鋼の強靭化

Toward Improved Ductility and Toughness

Kyoto International Conference Hall
October 25, 26, 1971.

日本鉄鋼協会
THE IRON AND STEEL INSTITUTE OF JAPAN
日本金属学会
THE JAPAN INSTITUTE OF METALS

目 次 / CONTENTS

Consideration of the Significance of Ductility and Toughness in Terms of Atomic Processes of Deformation and Fracture

H. Suzuki

University of Tokyo

Department of Physics

Ductility and toughness are not well-defined quantitative concepts but are the synthesis of various kinds of properties. These properties depend on some basic processes, such as relaxation of local stress concentrations, dissipation and absorption of mechanical energy, strain hardening and crack propagation. This paper is intended to review our understanding of these processes from an atomistic point of view. Especially the origin of the brittleness of body-centered cubic metals is discussed and some basic principles to avoid the brittle fracture of these materials are considered.

延性と靱性の原子論的基礎づけ

鈴 木 秀 次

東京大学理学部

延性と靱性は明快に定義できる定量的な概念ではなく，変形や破壊に関する諸性質を総合した概念である．これらの性質はより基本的な過程，例えば局所的応力集中の緩和，機械的エネルギーの消散及び吸収，加工硬化，亀裂の成長などに依存している．この論文においては，これらの過程について原子論的立場からどのように理解しているかを述べることにする．とくに体心立方金属が脆性を示す原因を論じ，またこの材料の脆性破壊をさけるときに必要な基本的な条件について考察する．

1. まえがき

金属及び合金が工業材料として特別に重要な地位を占めるのは主としてその延性と靱性による．しかしながら，これらの性質は物質に固有な明快に定義できる概念ではない．これらの性質はその物質の原子の配列状態——その材料の微細組織に依存するというだけではなく，これらの性質そのものが，材料の変形や破壊に関する諸性質を総合したものだからである．したがってこれらの概念を明らかにするには，結局，これらの性質に関係する諸過程を明確にする以外にないであろう．

この論文においては破壊がどのような過程でおき，それを阻止する原子的諸過程がどのように起こるかについての現在の我々の知識を概説する．そして鉄合金の延性と靱性が他種材料の中でどのような位置を占めるものであるかを明らかにし，これらを改善するための基本的な条件を整理することを試みたい．しかしそれらの議論に入る前に延性と靱性についての一般的な考察を次節に述べることにする．

2. 一般的考察

延性や靱性は簡単にいえば破壊がいかに起き難いかを示す性質であるということができるが，それだけではなく，変形に対する抵抗力の高いことが靱性の場合はとくに重要である．延性においてすら，水飴のように変形することは意味しないで，変形後の材料はある程度以上の降伏点をもつと暗黙のうちに期待している．

延性をあらわすのに最も便利な量は引張試験における伸びであるとされている．靱性を知るうえに一番手取り早いのはシャルピー試験である．しかしながら，これらの試験によって与えられる量は延性や靱性のある目安を与えるだけに過ぎない．引張試験における伸びの大きな材料は一般にロールで圧延するときに亀裂を生じ難いといえるが，これら二つの性質は正確に対応するものではない．シャルピー試験の結果はその試験の条件の下における靱性の一面を与えるのに過ぎないことも同様である．

シャルピー試験をもっと一般化すれば，応力—歪曲線の積分値ということができよう．衝撃的な力に体する材料の耐力は塑性変形によっても弾性変形によっても向上する．もしその材料の小体積が一様な応力，変形状態にあるならば，その対積に伝えられた運動エネルギーのうち，応力—歪曲線を実際の歪量まで積分した値だけ吸収および消散してしまう．弾性変形の場合にはそのエネルギーは材料の他の領域に伝えられ，破壊につながる可能性がある．しかし，ゴムを考えれば判るように，弾性定数の非常に小さな材料においては，硬い運動物体が衝突しても，接触した瞬間に大きな運動エネルギーを伝えることができるのではない．運動エネルギーは衝突物体のなす仕事として伝えられるが，それを伝え終るまでに物体とゴムは接触面積を著しく増大しており，局部的な衝撃力を空間的にも時間的にも拡げて弱めているのである．

ゴムはほとんど弾性的に変形するが，変形速度に依存する運動エネルギーの消散を伴うので，衝撃力を弱める上に有効な材料である．しかし，運動エネルギーの消散を伴わないとしても，弾性定数が小さいというだけでも衝撃力に対する安全性を増し得るのである．そのような例はプラスチックであって，ガラスに比べてはるかに衝撃力で破壊し難いのはおもに弾性定数が小さいことからきている．

Table 1 に幾つかの代表的な物質の弾性定数をあげておく．

Table 1. Elastic constants of some typical materials.

Material	Young's modulus (10^{11}dyne cm^{-2})	Shear modulus (10^{11}dyne cm^{-2})
Rubber	$\sim 10^{-4}$	
Polyethylene	0·076	0·026
Pyrex glass	6·2	2·5
Copper	12·6	4·6
Iron	21·4	8·14
Diamond	115	46

塑性変形は弾性変形に比べて，衝撃力に対する安全性を増す上に非常に有効である．塑性変形を起こす仕事として費やされた運動エネルギーは機械的エネルギーとして再び取出し得ない形で材料中で消散されてしまうのである．もちろん，エネルギーがすべて熱エネルギーにすぐに変換するわけでなく，一部分は格子欠陥のエネルギーとして材料内に蓄積される．しかし格子欠陥のエネルギーは高温で焼なますとき，格子欠陥の消失とともに熱エネルギーに変換してしまうのである．

靱性は，しかしながら，たんに応力—歪曲線の積分値だけであらわされるものではない．僅かな塑性変形はあっても，変形量はできるだけ小さいことが望ましい．すなわち，応力—歪曲線の形にも依存するのである．さらに Lüders 帯などの変形の不均一さ，材料の不均一さなどを考慮すると，多種類の応力—歪曲線を用いなければならないことになる．

塑性変形が起こるか破壊するかは亀裂の発生と成長を押えて塑性変形がどれだけ進行し得るかということにかかっている．したがって，次の2節で微小亀裂の発生と亀裂の成長条件を検討する．

3. 微小亀裂の形成

微小亀裂は局部的な応力集中によって形成されるか，または表面エネルギーの高い境界面に形成され得る．また表面の傷は内部に形成される微小亀裂と同様の性質をもち，応力の増大とともに成長伝播することがある．一般にもろい材料では表面の傷が破壊の核として重要であり，強化ガラスの例で知られるように，表面に圧縮応力が働くようにしておくことによって強度を著しく向上させることができる．これに対し，転位の移動の起き得るような金属合金などでは局部的な応力集中によって微小亀裂が形成される．このことを最も明瞭に示すのは次に述べる鉄のひげ結晶の塑性[1]である．

大きな鉄の単結晶の応力－歪曲線を液体窒素温度以下で測定することは困難である．すなわち，温度が低くなると急に降伏強さは上昇し，ある温度以下で脆性破壊を起こしてしまう．もちろん，結晶の純度を上げ，とくに格子間不純物を減らすと低温の延性を増加する．これまでの測定[2]では，鉄単結晶は 118°K においても滑らかな応力－歪曲線を示すが，78°K では鋭い降伏点を示したあと双晶変形による鋸歯状の応力－歪曲線となる．しかし，直径 0·1mm 程度のひげ結晶は 4·2°K においても容易に変形し，Fig. 1のように滑らかな応力－歪曲線を示す．降伏点の温度変化は Fig. 2のようになり，低温になるほど急激に上昇している．

ひげ結晶の場合転位源となり得る転位の数が少ないが，鉄のような b.c.c. 結晶中では容易に交差すべりを起こし得るので，転位の増殖が容易であり，かなり広い範囲にわたって一つの転位源から増殖された転位のみですべりが進行する．このため異なった Burgers ベクトルをもつ転位群が切り合ったり，反応するようなことはほとんどなく，応力集中を生じ難いのである．したがって微小亀裂を生ずることもできず，脆性破壊を起こさないのであるということができる．

析出物のない材料では結晶粒の小さいほど，脆性破壊を起こし難いことが知られている．ふつう程度の純鉄でも結晶粒の小さなものは 4·2°K の引張試験で非常に大きなくびれを生じて延性破壊を起こす[3,4]．多結晶材料では一つの結晶粒内で増殖された転位群は結晶境界を通過し得ないために堆積し，各転位の応力場が重ね合わされるために局部的に大きな応力を生ずる．

結晶粒の小さいほど，同一の外力のもとで堆積し得る転位の数は少ないから，応力集中も小さいのである．もちろん，多くの場合，結晶粒の微細化は微小亀裂の発生よりは亀裂の伝播を妨げる[5]ために靱性を増すのであるが，微小亀裂を発生するのに必要な外力も増大するのである．

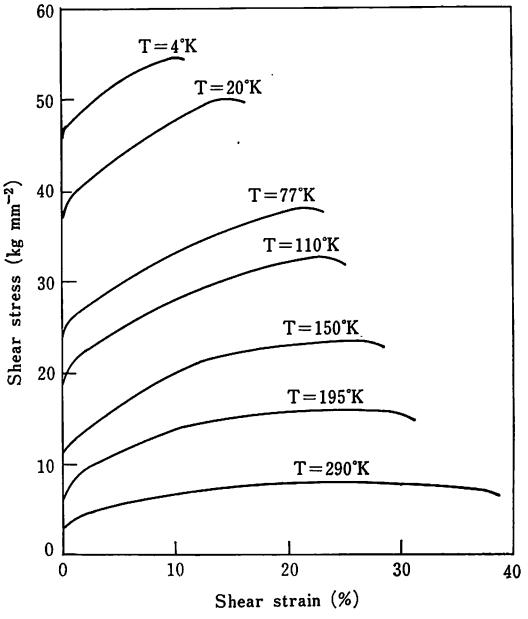

Fig. 1. Shear stress-shear strain relations of iron whiskers with radii between 60 and 120μ at the strain rate $\dot{\varepsilon}=5\times10^{-5}$ sec^{-1} (after R. Conte et al[1]).

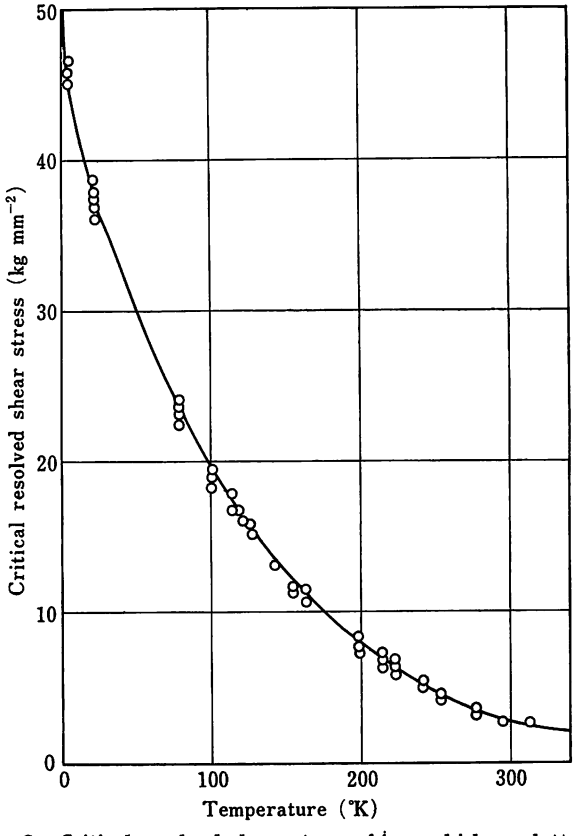

Fig. 2. Critical resolved shear stress of iron whiskers plotted against testing temperatures (after R. Conte et al[1]).

微小亀裂を発生する条件は，局部的な応力が理想的な結晶または結晶境界，相境界などに亀裂を作る応力に達することである．理想結晶に亀裂を作る応力は次のようにして求められる．

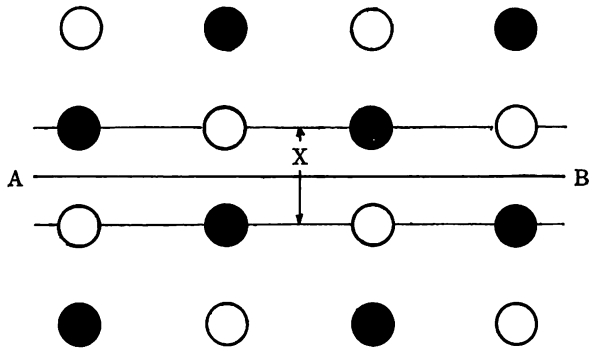

Fig. 3. Cleavage plane in a body-centered crystal.

いま Fig. 3 に示した結晶の AB 面で裂けるとしよう．裂ける過程で，AB 面のすぐ上とすぐ下の原子面の間隔 x が面内の場所によって変わらないと仮定する．裂けるときのエネルギーの増加を $U(x)$ とすると，$U(x)$ は次の性質をもっている．

$$\lim_{x\to\infty} U(x) = 2\gamma \qquad (1)$$

$$U(x_0) = 0 \qquad (2)$$

ここに γ は結晶の表面エネルギー，x_0 は外力のないときの原子面間隔である．また Hooke の法則はこのような局部的な変形に対しても近似的には成立つから，E を Young 率とすると

$$\left(\frac{dU(x)}{dx}\right)_{x=x_0} \simeq \frac{x-x_0}{x_0} E \qquad (3)$$

が成立つ．亀裂を作るのに必要な応力は $dU(x)/dx$ の最大値である．

ところで $U(x)$ は x の滑らかな関数であるから，(1), (2) の関係を満足する関数として次のようなものが考えられる．

$$U_1(x) = 2\gamma\left[1-\exp\{\lambda(x-x_0)^2\}\right] \qquad (4)$$

$$U_2(x) = \frac{\gamma}{2}\left[1-\cos\{2A(x-x_0)/\gamma\}\right]$$

ただし $$0 \le \frac{2A(x-x_0)}{\gamma} \le \pi$$

$$U_2(x) = 0 \quad \text{ただし} \quad \frac{2A(x-x_0)}{\gamma} > \pi \qquad (5)$$

(4), (5) 式の λ, A は定数で (3) 式からきめられ

$$\lambda = E/2\gamma x_0$$

$$A = (E\gamma/2x_0)^{1/2}$$

である．亀裂を作る応力は

$$F_{max} = \alpha\sqrt{E\gamma/x_0} \qquad (6)$$

と書かれ，(4) 式の場合には $\alpha = \left[\exp\left(-\frac{1}{2}\right)\right] \simeq 0.607$，(5) 式の場合には $\alpha = 1/\sqrt{2} \simeq 0.707$ となる．

Table 2 に代表的な物質の F_{max} の値を示す．極属材料では極めて高い値をもつが，イオン結晶ではかなり低い．これはイオン結晶ではイオン間の結合力の性質から弾性定数に比較して表面エネルギーの値が低くなるためである．金属の場合でも γ_B の表面エネルギーをもつ結晶境界，相境界で亀裂の作られるときには，(6) 式の γ の代りに $\gamma - \gamma_B/2$ を用いなければならないので，Table 2 の値より幾分小さくなり得る．

Table 2. Fracture stress of perfect crystals.

Crystal	Structure	Cleavage plane	E (kg mm^{-2})	γ (erg cm^{-2})	x_0 (10^{-8}cm)	$0.7\sqrt{E\gamma/x_0}$ (kg mm^{-2})
Ag	f.c.c.	(110)	8220	1140	1·44	1780
Au	f.c.c.	(110)	7940	1400	1·44	1940
Cu	f.c.c.	(110)	12600	1650	1·28	2820
Ni	f.c.c.	(110)	19700	1954	1·24	3900
Na	b.c.c.	(100)	912	94 ~110	2·14	140 ~151
Fe	b.c.c.	(100)	21400	1500	1·43	3320
W	b.c.c.	(100)	40500	2680 5510	1·58	5800 8330
KCl	rock salt	(100)	4800	56 ~163	3·14	206 ~350
NaCl	rock salt	(100)	4370	77 ~153	2·82	239 ~341
LiF	rock salt	(100)	7350	169 700	2·01	548 1120
MgO	rock salt	(100)	24500	1362	2·10	2880

どの結晶でも，一様に変形するさいには Table 2 の F_{max} に相当する応力は実現し得ない．異なったすべり系の交差点，結晶境界などに堆積した転位群の応力集中によってはじめて実現し得るのである．b.c.c. 金属の場合には変形双晶の交差が起こると応力集中はより大きくなり得るので，そのような場所が亀裂の発生点となることがある[6]．また金属間化合物が析出しているときには，周囲の変形で応力集中を受けて最初に金属間化合物が破壊し，それが亀裂の核となることが多い[7]．

4. 亀裂の伝播

微小亀裂は局部的な応力集中などによって形成されるが，破壊を起こすには外力の下で亀裂が成長しなければならない．もろい物質では，亀裂の成長によって外力のなす仕事が亀裂の表面エネルギーの増大を補い得るならば成長できる．そのときの破壊応力は Griffith[8] によって

$$\sigma = \beta\sqrt{E\gamma/c} \qquad (7)$$

と与えられている．ここに β は 1 の程度の定数，E は Young 率，γ は表面エネルギー，c は亀裂の長さの半分である．

もし亀裂を生ずる以外完全に弾性的に変形するならば，この応力はまた長さ $2c$ の亀裂の応力集中の最大値が F_{max} に達するような応力と等しくなるはずである．しかし，もし亀裂先端で塑性変形が起こって応力集中を緩和するならば，(7) 式の破壊応力は異なった表現を必要とする．もともと結晶中にあった転位が動き増殖するだけであるならば (7) 式の 2γ にそのような塑性変形によって消散されるエネルギーを加え合わせれば，劈開破壊として取扱うことができる[9]．しかしながら，亀裂先端の応力集中が F_{max} に達する前に転位対を形成してすべりが起こるときには，劈開は起こらず，すべりによる破壊になってしまう．

Friedel[10] は亀裂の先端で転位ループを作ることができないと結論したが，その議論は根本的に誤まっており，彼の計算を正しく解釈すると必らず転位を形成することになる．彼の計算では応力集中を大きく仮定し過ぎてい

るので，この結論もまた必ずしも正しくはない．ここでは簡単に亀裂を成長させるのに必要な応力 F_{max} と転位対を形成するのに必要な応力 σ_0 を比較してみる．完全転位対を作るのに必要な応力は $\mu/2\pi$ の程度であり，転位対間の距離が d だけ離れたときに必要な応力は刃状転位では $\frac{\mu b}{2\pi(1-\nu)d}$ である．亀裂先端の応力集中は大体 $1/\sqrt{d}$ に比例して減少するから，最も大きな応力集中の所で σ_0 を越えていれば，それが拡がっていく条件は満足される．

Table 3. Comparison between stresses required for the fracture of crystals and for the creation of dislocations in these crystals.

Crystal	F_{max} (kg mm^{-2})	$\frac{\mu b}{2\pi h}$ (kg mm^{-2})
Copper	2800	900
Iron	3300	1600
NaCl	250～360	590

Table 3に幾つかの結晶について F_{max} と σ_0 の値をあげておく．F_{max} は引張応力であり，σ_0 はせん断応力であり，亀裂先端附近の他の応力成分を求めていないので，両者の比較は簡単でないが，亀裂先端のすべり系の最大分解せん断応力は $F_{max}/2$ の程度とおいてもよいであろう．そうすれば表から判ることは，金属では f. c. c. であっても b. c. c. であっても脆性破壊を起こし得ないことになってしまう．これは実験結果と矛盾する．そこで著者[9]は次のような提案をした．

亀裂の先端では大きな応力のためにたんに弾性的に歪んでいるよりは，亀裂に垂直な方向に伸びた領域を作ることによって歪エネルギーを低下させることができる．そのような領域は周囲の結晶と双晶の関係をもち，Fig. 4の原子配列をもつとよい．この双晶の領域は亀裂先端の応力場と双晶境界エネルギーによってきまる形状をもが，b. c. c. 金属のように高い双晶境界エネルギーの場合つには図のように小さな領域に止まる．そして亀裂の側では引張応力が緩和しているので双晶境界エネルギーを減らすためにもとの結晶にもどるが，そのさいに裂目を前進させるのである．亀裂を作るエネルギーの一部は消失する双晶転位のエネルギーによって与えられ，それだけ応力集中を低下させることができる．また楔状の双晶領域先端の応力集中は双晶転位を作るだけでよいので，すべりを起こす転位を形成することはない．

上述の双晶領域は {100} 面に関して対称的に形成されるので，b. c. c. 金属の劈開面は {100} 面に平行になるのである．

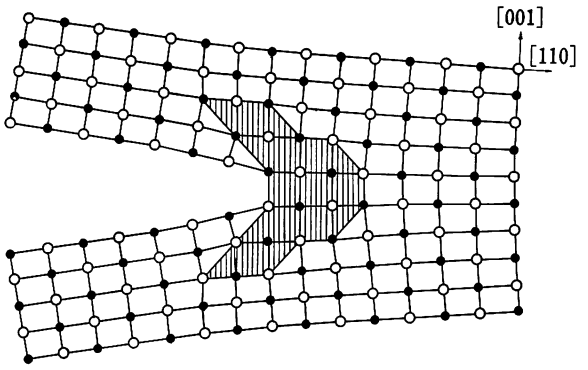

Fig. 4. A possible arrangment of atoms at the tip of a propagating crack in a body-centered cubic crystal.

同様の双晶領域は f. c. c. 金属の場合にも考えることが可能である．双晶領域は {110} 面に関して対称になるよう形成されると，この方向に $\sqrt{2}$ 倍に伸びる．しかし，f. c. c. 金属の双晶境界エネルギーは非常に低いので，双晶が楔型に作られ難い．Fig. 5 でまず応力集中で半転位対 A，B が作られたとしよう．A は亀裂の応力場によって亀裂の方に引きつけられるが，B は斥力を受ける．外力も B を亀裂から引離そうとするから，積層欠陥エネルギーと釣合う位置まで離れるであろう．第2の半転位対 C，D が作られても C は亀裂に引きつけられるが D は斥力を受ける．したがって亀裂先端の転位の形状は図 c) のようになる．亀裂先端の応力集中がさらに次の半転位を作り得るとしても d) のように積層欠陥を重ねる，すなわち，双晶薄片が形成され半転位が亀裂から離れるだけである．この双晶がある厚さになれば亀裂先端の形状は双晶変位によってきめられて，応力集中が急減し亀裂は成長できなくなる．このようにして f. c. c. 金属は劈開破壊を起こし得ないのである．

f. c. c. 金属と b. c. c. 金属の相異は積層欠陥エネルギーの相異に帰着されるが，もう少し定量的な議論を与えておこう．不完全転位に働く力は弾性応力を通しては $\tau b'$ であり，積層欠陥を通しては γ_s である．τ は不完全転位対を作るのに必要な力に比例し，$\tau \simeq \frac{\mu b'}{2\pi h}\sqrt{\frac{b}{r}}$ で近似してよい．ここに b は完全転位のバーガース・ベクトル，h はすべり面に平行な原子面間隔であり，r は亀裂先端からの距離である．不完全転位対間の距離は積層欠陥による張力，不完全転位対間の引力，亀裂附近の弾性応力が釣合ってきまる．まず不完全転位対の間隔が十分大きいとして引力を無視すると

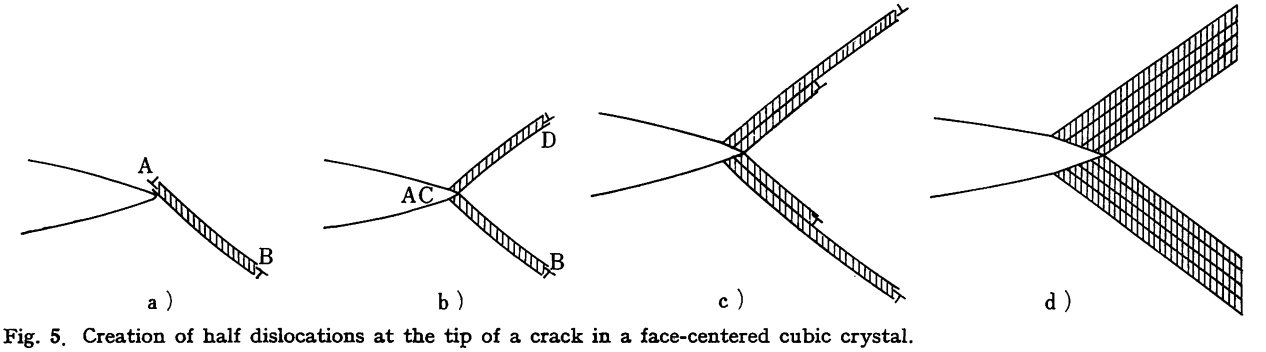

Fig. 5. Creation of half dislocations at the tip of a crack in a face-centered cubic crystal.

$$r=\frac{\mu^2 b'^4 b}{4\pi^2 h^2 \gamma_s^2}$$

b. c. c. 金属の場合，$h=\frac{a}{\sqrt{6}}$, $b'=\frac{a}{2\sqrt{3}}$, $\gamma_s=\frac{3}{4\sqrt{2}}\times\frac{\mu b}{\pi^2}$[12], $b=\frac{\sqrt{3}}{2}a$ であるから

$$r\simeq 0{\cdot}5\,b$$

この距離では転位対間の引力を無視できないが，引力であるから転位対が1原子距離も離れることのできないことに変わりない．双晶境界エネルギーは積層欠陥エネルギーの約 1/3 であるから，Fig. 4 の構造はかなりの拡がりをもち得るのである．

f. c. c. 金属では，$h=\frac{a}{\sqrt{3}}$, $b'=\frac{a}{\sqrt{6}}$, $b=\frac{a}{\sqrt{2}}$ であり，Cu で $\mu b\simeq 10^4$ dyne cm^{-1}, $\gamma_s\simeq 80$ erg cm^{-2} とおくと $r\simeq 20b$ である．この距離に対して転位対間の引力は亀裂先端の弾性応力に比べて無視できる．さらに次の面に積層欠陥を作れば，Fig. 5d) のように亀裂の成長をとめる双晶に発達する．f. c. c. 金属で最も積層欠陥エネルギーの高い Al の場合には $\mu b\simeq 7\times 10^3$ dyne cm^{-1}, $\gamma_s\simeq 200$erg cm^{-2} とおいて $r\simeq 6b$ である．b. c. c. 金属に比べれば非常に大きいが，転位対間の引力を補正すれば半分程度に減少するので，Fig. 5d) の形に双晶を成長させ得るか否か疑問である．Fig. 4 の形の亀裂先端の構造が作られると考えるのも困難であるが，その可能性を完全に否定することはできない．

しかし，他の f. c. c. 金属では r がもっと大きくなるのであって，f. c. c. 金属で劈開破壊が起こるとすれば Al に可能性があるだけで，他の金属では可能性はない．

5. 亀裂の伝播と塑性変形

b. c. c. 金属は積層欠陥エネルギーが高いという事情のために脆性破壊を起こし得るのであるが，もし結晶中に多数の転位が存在し，その移動によって亀裂先端の応力集中を緩和できるならば，脆性破壊は阻止される．転位密度が高ければ，転位の運動が比較的短距離起こるだけで応力緩和を起こすことができる．

ところで b. c. c. 金属のように交差すべりを容易に起こす場合にはらせん転位の対消滅が起き易く，転位密度を増すことは困難である．転位密度を高くする上に，転位の摩擦力は有効であるが，これは同時に亀裂近傍で転位の移動する領域を制限してしまう．しかし摩擦力の大きな転位密度の高い結晶中ではすべり転位も抵抗を受け，転位群の堆積やそれによる応力集中は起き難くなる可能性がある．

転位の運動に対する摩擦力のうち，Peierls 力，溶質原子によるものは，それだけでは亀裂の発生伝播に対する抵抗力とはなり得ない．

しかし，G-P 帯のような微細な coherent な析出物は亀裂の発生伝播に対しても抵抗力となり得るのである．この場合変動する内部応力場が亀裂先端の応力を変動させるので，逆向きの内部応力のある場所ではそれを打ち消すだけ応力集中を増さなければならない．小さな亀裂ほど析出物による内部応力によって大きな抵抗を受ける．内部応力の波長程度の亀裂の場合には，亀裂全体を含むような領域に働く外力が内部応力の振巾の程度にならなければならない．この程度の応力の下では転位は内部応力場を通ってほとんど自由に動けるようになると考えられる．すなわち，塑性変形も起きている．また異なったバーガース・ベクトルをもつ転位群が出合っても堆積する転位数は限られ，大きな応力集中を生じ難い．故に微細な coherent な析出物が硬化の主因となっているときには，一般に靱性をほとんど失わずに降伏強さを増大させ得る．

b. c. c. 金属の場合にはらせん転位だけが高い Peierls 力をもっている[13]．刃状転位は低い摩擦力を受けて堆積することができるので，局部的な応力集中を起こして亀裂を発生させることができる．とくに単結晶の場合には反応によって {100} 面に亀裂を発生するような2種類の転位群が出合って破壊を起こすほか，異なったバーガース・ベクトルをもつ転位群が切り合って双晶を発生し，双晶同志がぶつかったり，双晶境界に転位が堆積して破壊を起こす[6]．多結晶体では結晶境界に転位が堆積して亀裂を発生するのである．これらいずれの場合にも堆積するのはほとんど刃状転位とみなせるようなものである．

最初転位密度が低かったり，転位が C や N で釘付けされているときには，変形の初期には転位源の数は少ない．しかし，同一すべり上にならんだ刃状転位群が，他の同様な転位群に出会う頻度は結晶がある程度以上大きければ，かなり大きいことは容易に想像される．そのような場合に，もし変形応力がある程度以上大きければ，結晶の塑性変形がほとんど起こらないうちに亀裂が発生成長し，脆性破壊を起こす．

f. c. c. 結晶中のらせん転位は拡張していて，2本の半転位のバーガース・ベクトルが互いに平行でないために，全体としてらせん転位であっても交差すべりを起こし難い．したがって転位の運動に対する摩擦力が小さくとも，高い転位密度にすることができる．このように加工硬化した材料は伸びを減少することはあっても f. c. c. 構造であるから脆性を示すことはない．このほか f. c. c. 材料は Cu-Be 合金のように析出によって降伏強さを増し得るが劈開性の破壊は起こし得ない．ただ結晶境界への偏析が粒界を弱めたり，粒内の析出物がもろいために，粒界または粒内の析出物を結ぶ亀裂によって脆性破壊を起こす可能性がある．しかし，一般的にいって f. c. c. 合金は最も脆性破壊を起こし難い材料であるといえる．これに対して b. c. c. 金属は結晶それ自身が本質的に劈開を起こし得るのであるから，亀裂の発生と伝播を阻止するために種々の対策が講じられなければならないのである．

6. むすび

延性と靱性を亀裂の発生，伝播の原子的過程に結びつけて論じたが，極めて単純な場合に限られた．b. c. c. 金属がなぜ劈開性の破壊を起こし得るかということは，亀裂先端の原子配列がすべりを起こさずに原子面を剝がし得る特別の形をもっているからである．f. c. c. 金属で同様の原子配列が実現し得ないのは積層欠陥エネルギー，または双晶境界エネルギーが低いために，亀裂先端の双晶関係にある小領域が拡がってしまい，亀裂を伝播させるという機能を失ってしまうからである．もちろん，この他 b. c. c. 金属中の転位はパイエルス力などのために大きな摩擦力をもつが，f. c. c. 金属中では摩擦力が小さく，外力に対する塑性変形の応答速度が b. c. c. 金属では f. c. c. 金属よりも著しく遅いことも破壊の起き易さ

の相異の原因になっている．しかしこの相異は延性の相異であってb.c.c. 金属でだけ脆性破壊が起こることの原因ではない．

実用材料においては延性破壊であっても，伸びが実用上必要な大きさをもたなければ意味はない．延性を定量的に議論できるようになるには今後の研究にまたなければならない．

文　献

1) R. Conte, P. Groh, et B. Escaig : Phys. Stat. Sol., **28** (1968). p. 475
2) D.F. Stein and J.R. Low, Jr. : Acta Met., **14** (1966), p. 1183
3) Z.S. Basinski and A. Sleeswyk : Acta Met., **5** (1957), p. 176; 763; 764
4) R.L. Smith and J.L. Rutherford : Acta Met., **5** (1957), p. 761
5) A.H. Cottrell : Trans. AIME, **212** (1958), p. 192
6) R. Honda : J. Phys. Soc. Japan, **16** (1961), p. 1309
7) C.J. McMahon, Jr. and M. Cohen : Proceedings of the First International Conference on Fracture, Japanese Society for Strength and Fracture of Materials, Sendai (1966), Vol. 2, p. 779
8) A.A. Griffith : Phil. Trans. Roy. Soc., **A 221** (1920), p. 163
9) E. Orowan : Fatigue and Fracture of Metals, John Wiley & Sons, New York, (1952), p. 139
10) J. Friedel : Fracture, edited by B.L. Averbach et al, M.I.T. Press, Cambridge, Massachusetts (1959), p. 498
11) H. Suzuki : Proceedings of the First International Conference on Fracture, Japanese Society for Strength and Fracture of Materials, Sendai (1966), Vol. 2, p. 613
12) 鈴木秀次：転位論入門，アグネ (1967) 198頁.
13) H. Suzuki : Dislocation Dynamics, edited by A.R. Rosenfield et al, McGraw-Hill, New York, (1968), p. 679

The Effect of Composition and Microstructure on Ductility and Toughness

F.B. Pickering

British Steel Corporation Special Steels Division

ABSTRACT

Quantitative data are presented relating the microstructure and composition of a variety of structures in ferrous metals to ductility and toughness. The effects of second-phase particles and of nonmetallic inclusions are also quantitatively described.

1. INTRODUCTION

The properties of low-carbon ferrite-pearlite steels [1-3], low-carbon bainitic steels[4], and austenitic stainless steels[5] have been correlated quantitatively with the microstructural parameters and composition, and these types of steels form the basis of many structural materials. However, modern materials require to be formed and manipulated in a variety of ways, and apart from toughness, as for example measured by a notched-impact or fracture-toughness test, adequate performance during cold fabrication by bending, spinning, stretch forming, deep drawing, extrusion, wire drawing, etc, is required. It is often held that suitability for such processing, which demands high ductility, can only be assessed by type, or simulated type, testing. Such tests are difficult to perform and are frequently too time consuming for use with experimental alloys. There has therefore been a tendency in recent years to attempt to correlate performance under specific forming operations with the behavior of the steel in a simple test such as a uniaxial tensile test. Such an approach has obvious advantages, the test being widely accepted and rapidly carried out, so that it can readily be used to evaluate a wide range of steels or heat treatments in a development program.

It has also been found that there are relationships between certain parameters obtained from a tensile test and performance in an actual forming operation. For example, the uniform true strain prior to necking in a tensile test (ε^*) has been correlated with the ability of a material to be bent[6], and Butler[7] has also shown the value of ε^* in stretch forming, stretching and bulging operations. Other workers[8] have related ε^* to press formability. Bendability has also been related to the true strain at fracture[7,9], (ε_T), and Kegg[10] has suggested that this parameter can be related to the maximum reduction attainable during spinning. It has also been shown[7] that the ease of stretch forming and deep drawing depends on the rate of work hardening, and this parameter has been incorporated in a published formability index[11]. Cold-extrusion pressures also seem to be related to the K and n values of the conventional equation for the stress-strain curve[12], and much practical experience indicated that drawability increases with increasing total ductility or ε_T values.

Consequently there is an accumulation of evidence to suggest that the formability of materials is related to criteria or parameters derived from a tensile test. Therefore a knowledge of the metallurgical factors influencing these parameters is desirable, and quantitative relationships between microstructure, composition and true stress-true strain characteristics would be of value in the development of steels for cold forming operations.

In the work which will be described, it was found that the true stress-true strain curve was not described with sufficient accuracy by the relationship:-

$$\sigma = K\varepsilon^n \qquad (1)$$

This situation was not improved by using the Bridgeman correction, but it was possible to fit a relationship of the form:-

$$\sigma = a + b\ln\varepsilon + c(\varepsilon) \qquad (2)$$

Using this relationship, the work-hardening rate is given by:-

$$\frac{d\sigma}{d\varepsilon} = \frac{b}{\varepsilon} + c \qquad (3)$$

This conforms with the observation that $d\sigma/d\varepsilon$ decreases to a constant as ε increases, but it was found more convenient and accurate to determine $d\sigma/d\varepsilon$ as a function of strain by a numerical manipulation of the true stress-true strain data, using a digital computer. As $d\sigma/d\varepsilon$ varies with ε, the values of $d\sigma/d\varepsilon$ were evaluated at arbitrarily selected strains of $\varepsilon=0{\cdot}2$ and $0{\cdot}8$. The uniform true strain, ε^*, is the strain at maximum load before plastic instability and necking set in. It can be shown that the value of ε^* is that strain at which the flow stress and work-hardening rate are numerically equal, Fig. 1. Thus the factors

controlling ε^* could be resolved into those controlling the flow stress and those resulting from changes in $d\sigma/d\varepsilon$. Factors raising the flow stress relative to the work-hardening rate will give low ε^* values, whilst high work-hardening rates can give very high uniform ductilities. The method of evaluating the total ductility, ε_T, and the fracture stress, σ_{fr}, was simply to use the respective true strain and true stress at fracture.

It is the purpose of this paper to describe some of the relationships which have been observed in studies of the true stress-true strain characteristics of both ferrite-pearlite and austenitic structures, and to consider some of the microstructural and compositional parameters which influence the impact toughness of ferrite-pearlite steels containing up to eutectoid carbon content.

The method used to correlate structure and properties in both the ductility and toughness studies was a multiple linear regression technique, and the linear function of grain size employed was $d^{-1/2}$.

2. THE DUCTILITY OF FERRITE-PEARLITE STRUCTURES

2.1 The regression analysis

The regression analyses in steels containing up to ~0·25% C led to the following equations to describe some of the more important ductility parameters:–

(i) ***Flow stress*** at $\varepsilon=0{\cdot}2$ (σ_f) (kg/mm²)

$$\sigma_f=[16+0{\cdot}27\ (\%\text{pearlite})+2{\cdot}9\ (\%\text{Mn})+9{\cdot}0\ (\%\text{Si})+60\,(\%\text{P})+11\,(\%\text{Sn})+244\,(\%\text{N}_f)+0{\cdot}97\ d^{-1/2}]\times 1{\cdot}57 \quad (90\%\ \text{explained}) \qquad (4)$$

where N_f=free nitrogen not combined as a stable nitride

(ii) ***Work-hardening rate*** at $\varepsilon=0{\cdot}2$ (kg/mm²)

$$d\sigma/d\varepsilon=[25+0{\cdot}09\ (\%\text{ pearlite})+7{\cdot}2\ (\%\text{Si})+30(\%\text{P})+9{\cdot}9\ (\%\text{Sn})+89\ (\%\text{N}_f)+1{\cdot}0d^{-1/2}]\times 1{\cdot}57(55\%\ \text{explained}) \qquad (5)$$

(iii) ***Maximum uniform strain*** (ε^*)

$$\varepsilon=0{\cdot}27-0{\cdot}016(\%\text{pearlite})-0{\cdot}015(\%\ \text{Mn})-0{\cdot}040\ (\%\ \text{Si})-0{\cdot}043\ (\%\text{Sn})-1{\cdot}1(\%\text{N}_f)\ (60\%\ \text{explained}) \qquad (6)$$

(iv) ***Total strain at fracture*** (ε_T)

$$\varepsilon_T=1{\cdot}3-0{\cdot}020(\%\text{pearlite})+0{\cdot}30(\%\text{Mn})+0{\cdot}20(\%\text{Si})-3{\cdot}4(\%\text{S})-4{\cdot}4(\%\text{P})+0{\cdot}29(\%\text{Sn})+0{\cdot}015d^{-1/2}\ (65\%\text{explained}) \qquad (7)$$

(v) ***Fracture stress*** (σ_{fr}) (kg/mm²)

$$\sigma_{fr}=[32-0{\cdot}22(\%\ \text{pearlite})+16(\%\text{Mn})+18(\%\text{Si})-170(\%\text{S})-47(\%\text{P})+16(\%\text{Cr})+430(\%\text{N}_f)+2{\cdot}9\,d^{-1/2}]\times 1{\cdot}57(73\%\ \text{explained}) \qquad (8)$$

An assessment was made, using replicate property determinations, to show the errors associated with these equations. From this work it was quite clear that a large proportion of the residual error in the regression work arose from lack of reproducibility in the testing technique or in the behavior of the material.

2.2 The effect of microstructure

The two main microstructural variables were the amount of pearlite and the ferrite grain size. Although pearlite, over a limited range of low carbon contents, does not affect the yield strength[1–3], increasing pearlite does increase the flow stress. This is mainly due to the increased pearlite content

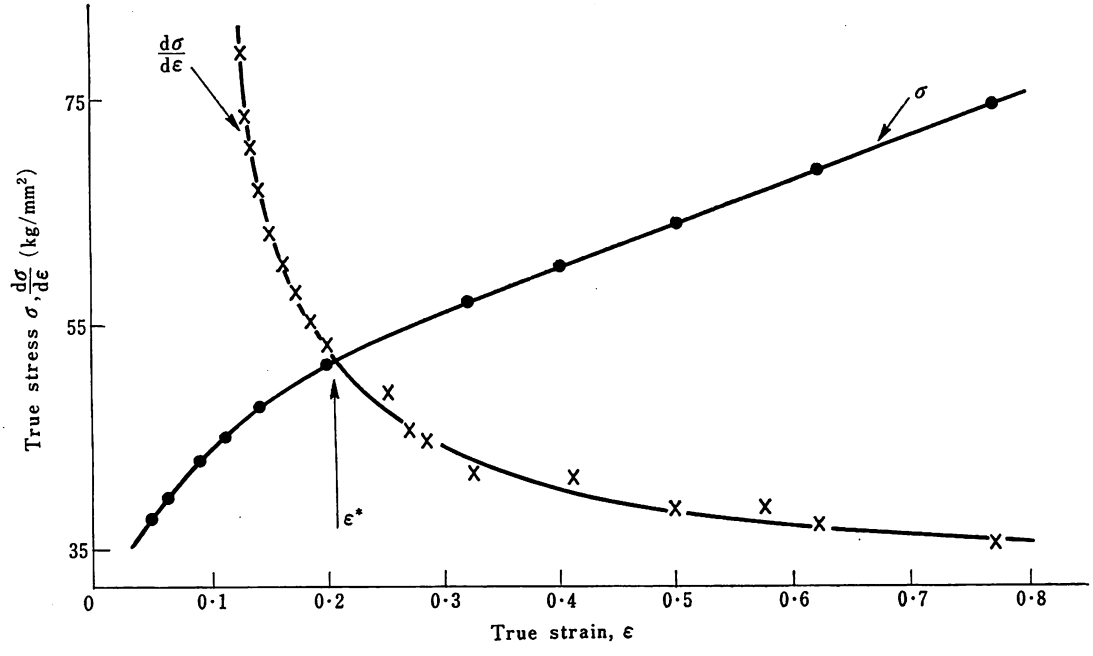

Fig. 1. Definition of maximum uniform strain (ε^*)

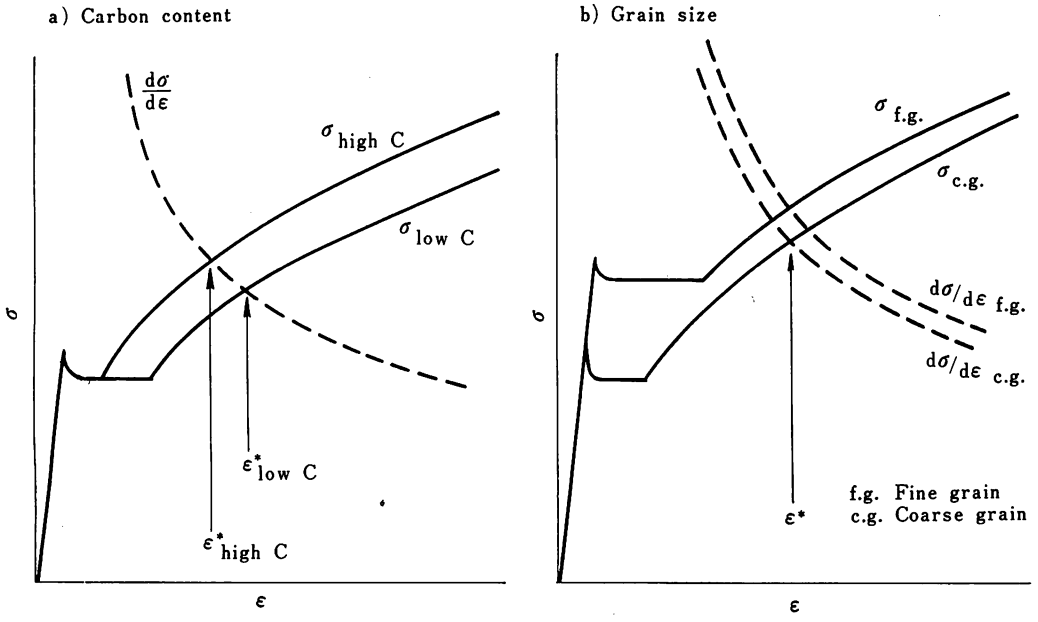

Fig. 2. Schematic effects of microstructure on ε^*.

decreasing the yield extension. Any effect on the yield extension will be important in controlling the flow stress at low strains because of the high work-hardening rate at such strains. In fact pearlite can be seen from equation 5 to have a relatively small, but positive effect on the work-hardening rate. Pearlite has perhaps the most important effect of the variables on the uniform extension, and it is significant that this detrimental effect cannot be offset by refining the ferrite grain size, which itself has no effect on ε^*. The reason why pearlite decreases ε^* is because of its much larger effect on the flow stress, by virtue of it shortening the yield extension, than on the work-hardening rate, Fig. 2 a). The lack of effect of ferrite grain size on ε^* is due to a refinement of the grain size producing a similar increase in both flow stress and work-hardening rate–equations 4 and 5 – Fig. 2 b). Because pearlite increases the flow stress, there is a pronounced effect for pearlite to decrease the total ductility at fracture, and this also results in a decrease in the fracture stress.

Experiments have also been carried out to assess the effect of spheroidizing the pearlite in steels containing up to the eutectoid carbon content. Spheroidizing resulted in a marked decrease in flow stress, but has no effect on the work-hardening rate. These effects became more pronounced as the carbon content increased, probably due to the fact that at high carbon or pearlite contents, the pearlite itself contributes to the yield stress and spheroidizing decreases the yield stress and the subsequent flow stress. The result was to cause spheroidization to produce a marked increase in the uniform elongation ε^*, Fig. 3, which became more pronounced with increasing carbon content, as might be expected. The total ductility at fracture, ε_T,

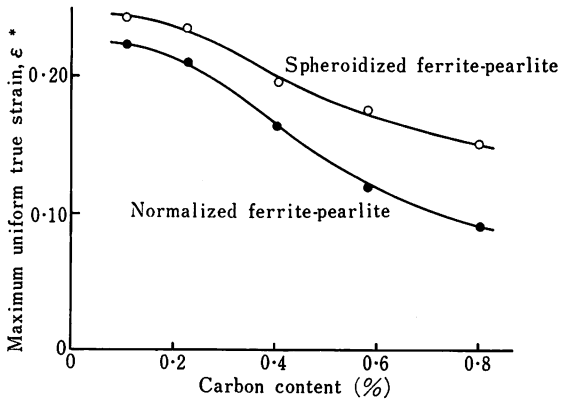

Fig. 3. Effect of carbon content and spheroidization on ε^*.

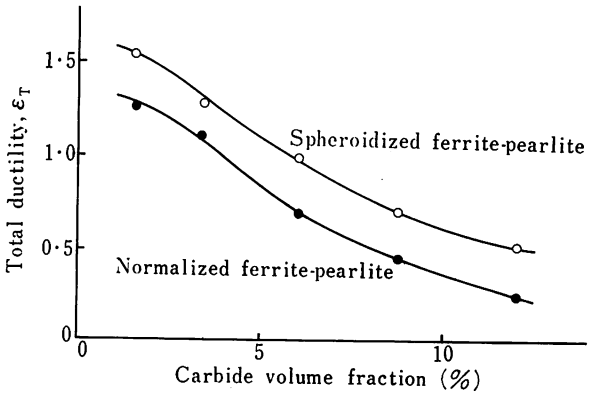

Fig. 4. Effect of carbon content and spheroidization on ε_T.

was also increased by the spheroidization treatment, Fig. 4. It can be seen that whilst ε_T decreased with increasing volume fraction of carbide, the effect of spheroidization was largely independent of carbon content. The fracture stress was virtually unaffected by spheroidizing, and therefore the greater total ductility at fracture imparted by the spheroidizing treatment was the result of the lower flow stress, which necessitated larger strains to achieve the virtually constant fracture stress at any given carbon level.

An investigation of the effect of the interlamellar spacing of the pearlite was confined to a eutectoid steel. This showed that as the interlamellar spacing became finer, so the flow stress and the work-hardening rate increased. These effects were self-cancelling, and no effect of interlamellar spacing was observed on the uniform strain ε^*. Despite the higher flow stress with a finer interlamellar spacing, a higher value of ε_T was observed. The reason for this is believed to be due to fine carbide lamellae being able to deform[13], whilst coarse carbide lamellae crack and initiate cavitation. Thus a greater total ductility is observed with a fine interlamellar spacing, due to the delayed cavitation as ductile fracture is approached.

As shown in equations 4 and 5, refining the grain size increases both the flow stress and the work-hardening rate, and due to the shorter slip distance requires more dislocations to operate at a given strain, thus producing a higher dislocation density[14]. These effects are self-cancelling so that a refinement of the ferrite grain size has no effect on the maximum uniform strain, ε^*. On the other hand, refining the ferrite grain size does cause an increase in the total strain at fracture, ε_T, equation 7. This is because the effect of grain size on the fracture stress is relatively greater than its effect on the flow stress, equations 4 and 8.

2.3 The effect of composition

The effects of solutes on the flow stress are shown in equation 4, and generally increase with increasing strain due to the fact that the substitutional elements, in particular, have a significant effect in increasing the work-hardening rate, equation 5. This effect is different from that observed for the interstitially dissolved nitrogen, which whilst having an appreciable effect on the work-hardening rate at low strains, has negligible effect at strains much in excess of $\varepsilon=0{\cdot}2$. This indicated that the nitrogen may not be entirely in interstitial solution. The observed effects of the substitutional solutes on the flow stress, besides being a partial result of their effects on work-hardening rates, may also be interpreted in terms of their effects on the friction stress. The relative effects of such solutes on the flow stress are directly proportional to their effects on the friction stress, and the work-hardening rate itself may well be related to the friction stress. For example, increasing solute content retards dislocation movement, increases the number of dislocations for a given strain and thus increases the number of dislocation interactions and thereby the work-hardening rate.

As can be seen from equation 6, free nitrogen either as precipitates or interstitially dissolved, markedly decreases the uniform strain, ε^*, and the substitutional solutes have a similar but much less marked effect. These effects can readily be related to the effects already described with respect to the flow stress and work-hardening rate; any element which increases the flow stress relative to the work-hardening rate decreasing the value of ε^*.

The equations described previously indicate that manganese, silicon and chromium all increase the fracture stress and the total strain at fracture, whilst phosphorus has the opposite effect. An element which increases the fracture stress relative to the flow stress, as is the case for manganese, silicon and chromium, will automatically increase the total strain at fracture, ε_T, and the converse is also the case for phosphorus. These results are therefore mutually compatible. Free nitrogen increases the fracture stress, but has no effect on the total strain at fracture, presumably because the increase in flow and fracture stresses due to nitrogen are virtually self-cancelling. It can also be seen from equation 7 that sulfur has a very detrimental effect on the total ductility, ε_T, and this will be discussed later.

2.4 The effects of second-phase particles

The effect of second-phase particles is most clearly observed in the reduction in total strain at fracture which they produce. The effect of sulfur in equation 7 is a reflection of the effect of manganese sulfides reducing ε_T, and this is not unnaturally associated with cavitation brought about by stress concentrations around the sulfide particles. Whilst equation 7 indicates a linear decrease in total ductility with increasing sulfur (or MnS) content, this is only over a relatively narrow range of sulfur contents. Much work[15,16] has shown that the total ductility, or strain at fracture, decreases non-linearly with increasing volume fraction of the second-phase particles, and Fig. 5 shows that to a first approximation the adverse effects of oxides, carbides and sulfides on total ductility are rather similar. As will be shown later, and in fact as indicated previously in Fig. 4, the actual shape and distribution of the second-phase particles have a major effect. The apparently identical effects of the different types of second phase are due to the fact that the sulfide and oxides occurred together with a considerable amount of carbide, which tended to mask the differences produced by the different types of particle.

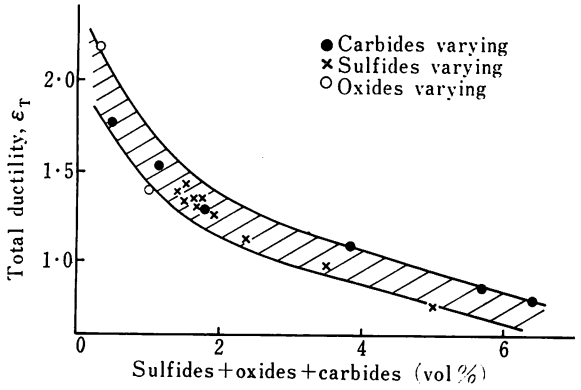

Fig. 5. Effect of second-phase particles on ε_T.

2.4.1 General theoretical considerations

The general mechanism of ductile failure is agreed to be one of void nucleation, void growth and finally void coalescence. Voids may nucleate either by cracking of a second-phase particle[17] or by decohesion of the metal-particle interface[16]. Growth of the voids follows and is enhanced by strain concentrations caused by the presence of the cracks or voids, which have been described by various equations. These all involve the strain concentration being proportional to the frontal radius of curvature of the crack or particle, and make varying assumptions regarding the radius to be ascribed in the different cases of particle cracking and interface decohesion. It can be shown, following the work of Gurland[16], that if all the second-phase particles behave identically, the total volume fraction of voids, f, can be given by:–

$$f = f_0 \left[(1 + k/r^2)\, e^{2(\varepsilon - \varepsilon_0)} - k/r^2 \right]^{1/2} \qquad (9)$$

for particle decohesion, and:–

$$f = f_0 \frac{3\, k^{1/2}}{2\, r} \left[e^{2(\varepsilon - \varepsilon_0)} - 1 \right]^{1/2} \qquad (10)$$

for particle cracking, where:–

f_0=initial volume fraction of particles

ε=true strain

ε_0=constant of integration and arises from the strain required to nucleate voids.

k=strain concentration factor

r=length : width ratio of the particles

Various criteria have then been employed to describe the onset of rapid growth of the ductile crack, which involves the inter-particle (or inter-void) spacing and the linking or coalescence of the voids. If the ratio of the void width to the near-neighbor inter-void spacing is the criteria for the onset of propagation of a ductile crack, then the relationship between the total strain at fracture, ε_T, and the amount and morphology of the second-phase particles, is given by:–

$$\frac{2}{3}\left(\frac{a}{S}\right)^2 = f_0 \left[1 + kr^2 \cdot e^{2(\varepsilon_T - \varepsilon_0)} - k/r^2 \right]^{1/2} \qquad (11)$$

for decohesion and:–

$$\left(\frac{a}{S}\right)^2 = f_0 \cdot \frac{3\, k^{1/2}}{2\, r} \cdot \left[e^{2(\varepsilon_T - \varepsilon)} - 1 \right]^{1/2} \qquad (12)$$

for particle cracking, where

a=half the width of the void

S=critical near-neighbor void spacing

It can be seen from these relationships that, as was shown in Fig. 5, the value of ε_T decreases exponentially as the volume fraction of particles increases. Also the equations show the well-known effect that increasing the length-width ratio of the second-phase particles gives a higher tensile ductility when the long axis of the inclusions is parallel to the tensile axis, compared with plate-like inclusions tested parallel to their minor axis.

2.4.2 The effect of sulfide particle shape

Experiments were carried out to illustrate the effect of sulfide particle shape on the ductility, and steels were prepared with either elongated or plate shaped sulfides, with major and minor axis respectively parallel to the tensile axis. It was observed that, as expected, an increase in the initial volume fraction of sulfides caused an increase in the void volume for any given tensile strain. The rate of increase in void volume with increasing tensile strain was in good agreement with the predictions made from the theoretical calculations. Also, a decrease in the length-width ratio of the sulfides, with respect to the tensile axis, increased the rate of growth of the voids with increasing strain, as again would be expected from the theoretical calculations. The experimental work showed that some void coalescence occurred at much smaller strains than would theoretically be required for the onset of a rapidly growing ductile crack, as shown in Photo. 1 a) in which the coalescence of voids in the region of a local concentration of inclusions has occurred. This emphasizes that the theory assumes a uniform particle spacing, which is not usually observed in practice, and as the criterion for failure is a critical ratio of inclusion width to inclusion spacing, the importance of local segregations of inclusions on the ductility at failure is clearly apparent. The importance of this factor with regard, for example, to lamellar tearing in welding is obvious. The critical void fraction for the onset of rapid ductile failure was calculated, for the steels examined, to give an average ratio of inclusion width: void diameter of 0·21. Actual measured ratios were in the range 0·3–0·6, and the slight disagreement between theory and observation is probably due to the heterogeneity of the sulfide distribution. The dependence of the void size on the inclusion size is clearly shown in Photo. 1 b); large inclusions are associated with large voids, as expected.

A comparison of longitudinal and transverse ductilities as a function of volume fraction of sulfides is shown in Fig. 6, and again the effect of

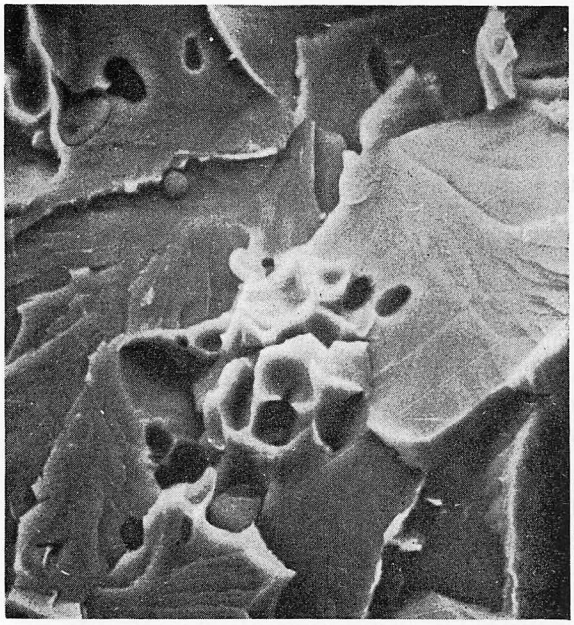

× 580

a) Premature void coalescence in region of local concentration of inclusions.

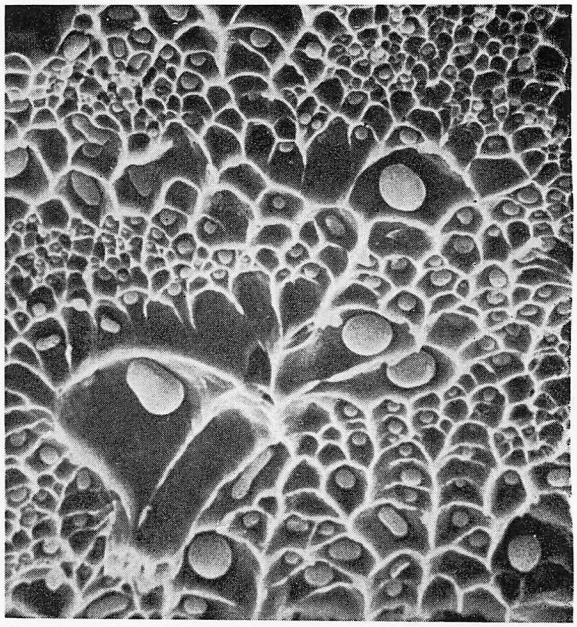

× 1350

b) Dependence of void size on inclusion size.

Photo. 1. Scanning electron micrographs of ductile fractures.

particle shape is clearly apparent, and is similar in magnitude to that predicted by equation 11 for particle decohesion. The effect of volume fraction of the sulfides could not be compared directly with the theoretical values due to the complicating effects of pearlitic cementite in the structures.

2.4.3 The effect of carbides

Although in very general terms sulfides, oxides and carbides behave similarly with respect to the total ductility ε_T, there is obviously an effect of particle morphology as already described. In addition there is a basic difference between sulfides and carbides in that carbides, unlike sulfides, do not crack or decohese at low strains. Consequently, with carbides in the structure, the steel can undergo significant deformation prior to void nucleation. In general, the carbides are observed to crack, and in a quenched-and-tempered steel which produces a uniform dispersion of fully spheroidized carbides, it was found that, using equation 12 for

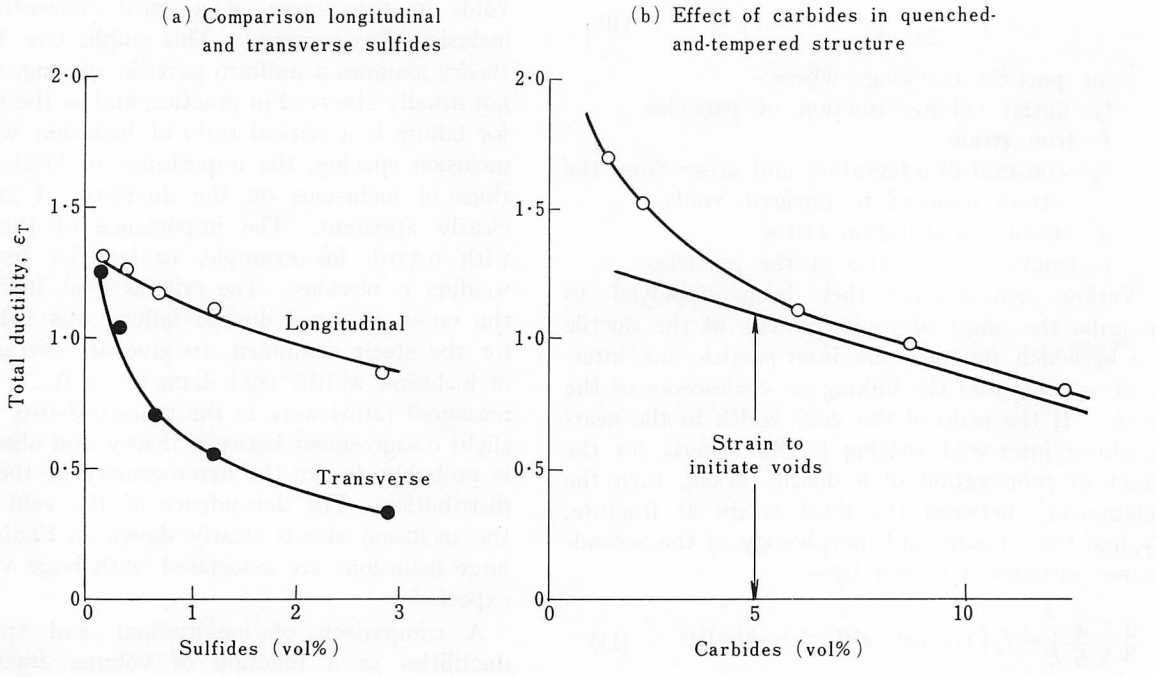

Fig. 6. Effect of shape and distribution of second phase on ε_T.

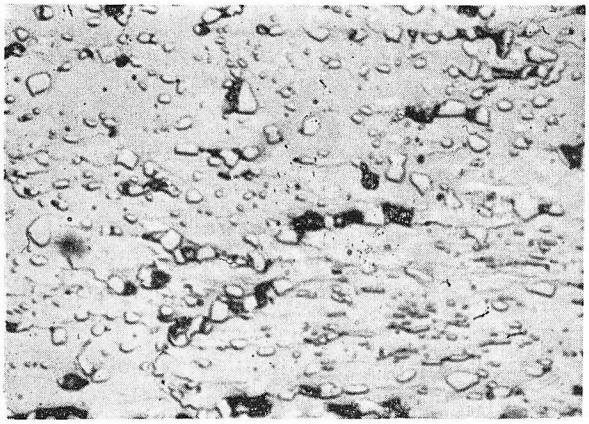

× 1100

a) Fracture of spheroidized carbides. Optical micrograph.

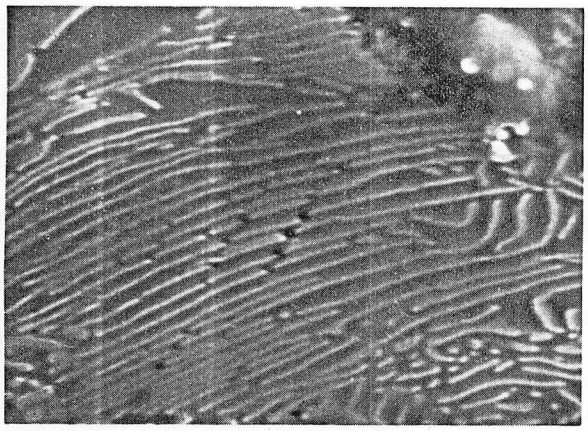

× 5250

b) Fracture across lamellae of pearlite. Scanning electron micrograph.

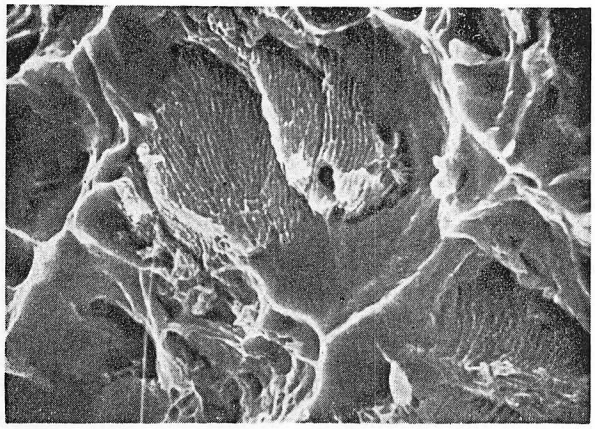

× 2200

c) Fracture of ferrite-pearlite structure. Scanning electron micrograph.

Photo. 2. Fracture of carbides.

particle cracking, the strain required to cause fracture after voids had been initiated was only a small proportion of the total strain, Fig. 6 b). In actual practice this strain to cause fracture after void nucleation may be greater than shown in Fig. 6 b), because the calculation assumes that all the carbides crack, and metallographic evidence indicated that this is not the case, Photo. 2 a). It can also be seen in Fig. 6 b) that the strain for the initiation of voids decreases with increasing volume fraction of spheroidal carbide, which would be expected because the cracking of cementite is stress dependent[18,19]. It would appear from the true stress-true strain work, that an appreciable proportion of the effect of carbides on ε_T is associated with the reduction of the strain required to attain the stress to crack carbides as the carbon content increases, i.e. the increased levels of flow stress. In the same manner as spheroidal carbides, pearlitic carbide may remain uncracked to considerable strain values, and this cracking is also stress dependent. However, due to the higher flow stress values of pearlite compared with spheroidite, the strain required for pearlitic carbide cracking is lower than that for cracking spheroidal carbides. Because of its lamellar structure, when a carbide lamella cracks strain is transmitted to adjacent lamellae, giving rows of cracks, Photo. 2 b), which coalesce[20] and give rise to sharp cracks across the pearlite. These cause a high degree of strain concentration and extend rapidly, which together with the lower strain (higher flow stress) for cracking, leads to pearlitic steels having significantly lower total ductilities than spheroidized steels, see Fig. 4. The voids in the pearlite nucleate normal ductile cusps, and fractures show the pearlitic structure in the base of the ductile dimples[20], Photo. 2 c). Pearlitic lamellae cracking is difficult to treat quantitatively, because the cracking is both stress and orientation sensitive, and because only a selected proportion of the pearlitic colonies crack at any given strain. In addition, the nature of the initial structure prior to spheroidization has an effect, as it controls the uniformity of dispersion of the carbide spheroids. Consequently, spheroidite resulting from the tempering of martensite has a higher total ductility than spheroidized ferrite-pearlite structures for a given carbon content, see Fig. 7.

2.4.4 The effect of oxides

Oxides were observed to behave qualitatively in a similar manner to sulfides, see Fig. 4; increasing the volume fraction gives a marked decrease in total ductility. Oxides however, probably act by means of a different mechanism, in that whilst sulfides decohese immediately at very low strain values, oxides readily crack, Photo. 3. Ductility is therefore probably best described by the particle cracking criterion, equation 12. However, it must be borne in mind that decohesion of the oxide-matrix interface also can occur, and the relative influence of these two mechanisms of void nucleation may well be dependent upon the type of oxide present in the steel. As will be discussed later, there is a marked interaction between carbides and oxides on the ductility of steels.

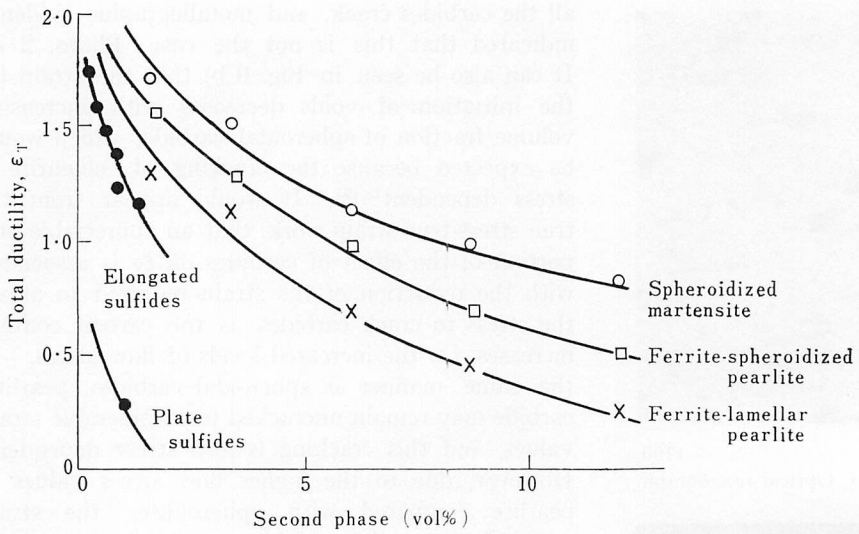

Fig. 7.
Summary of effect of morphology of second-phase particles on ε_T.

2.4.5 The effect of fine precipitates

Many high-strength low-alloy steels are designed so as to take advantage of the dispersion strengthening of a ferrite-pearlite structure by the precipitation of fine niobium or vanadium carbonitrides. In addition, niobium and vanadium produce a marked grain refinement of the ferrite after normalizing. Such grain refinement would be expected to give improvements in the total ductility, ε_T. Strengthening by the relatively small volume fraction of Nb(CN) in niobium-treated steels has been shown to increase the flow stress values, but not to have any material effect on the work-hardening rate. Consequently niobium dispersion strengthening is detrimental to the maximum uniform extension, ε^*, Fig. 8. It seems therefore that the effect of niobium in its grain-refining capacity would tend to be beneficial from the point of view of total ductility at fracture, ε_T, but niobium dispersion strengthening would adversely affect the uniform ductility, ε^*.

Some of the effects of second-phase particles and their morphology are summarized in Fig. 7. It can be seen that spheroidite resulting from tempered martensite gives better ductility for a given volume fraction of carbide than does a spheroidized ferrite-pearlite structure, because of the uniform dispersion of carbides compared with large local carbide contents occurring in patches. In turn, the spheroidized structures give better ductilities than ferrite-pearlite structures in which the pearlite is lamellar. Spheroidized carbides also lead to better ductilities for a given volume fraction of particles than do sulfides and oxides, and the reason for this has been suggested to be due to the delayed cracking of carbides compared with sulfides or oxides, which decohese or crack almost immediately strain is applied. In the case of sulfides, these are probably decohesed even prior to straining[21,22]. Plate shaped sulfides cause lower ductility than those elongated parallel to the tensile axis, and this has been shown to be due to the effect of the morphology on the rate of void growth. Finally, it is believed that much of the variation in ductility of ferrite-carbide aggregates can be attributed to variations in the flow stress at a given strain, or more correctly to the variations in strain necessary to raise the flow stress to a level capable of cracking the carbide particles.

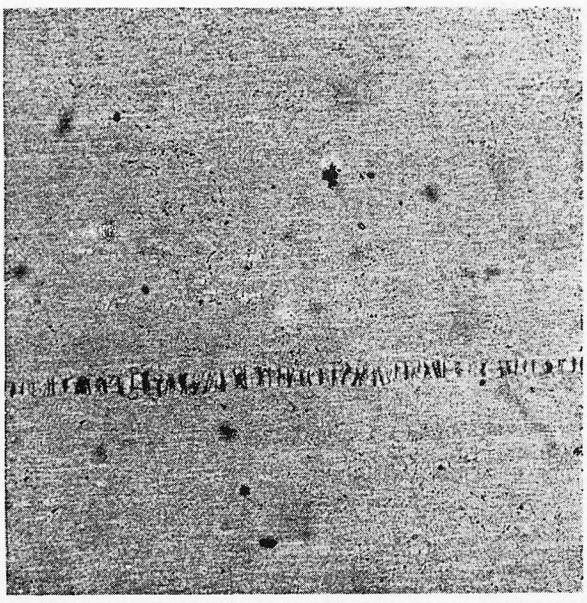

× 100

Photo. 3. Fracture of oxide stringer. Transverse cracks in brittle silicate stringer during straining. X-ray microradiograph, cobalt radiation.

2.5 Some practical considerations

2.5.1 The cold extrusion of steel

Kashar[12] has given an empirical relationship for the effective true strain (ε) in terms of the extrusion ratio, R, :-

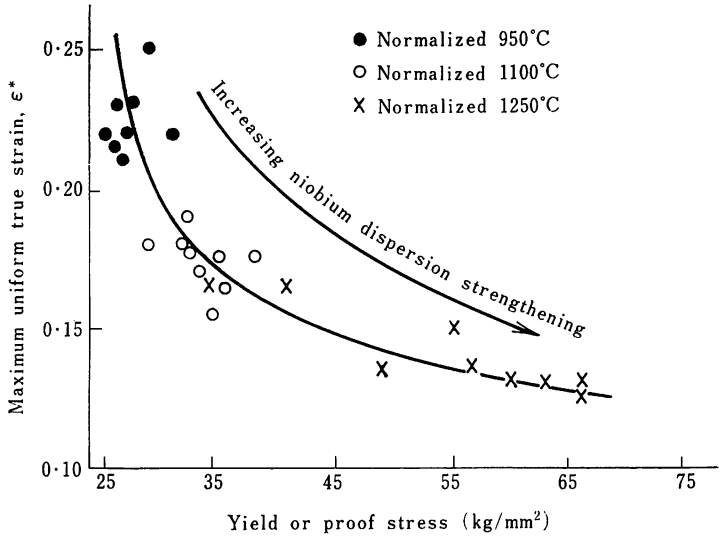

Fig. 8.
Effect of niobium dispersion strengthening on ε*.

$$\varepsilon = a + b \ln R. \qquad (13)$$

and showed that extrusion pressure was directly related to the area under the stress-strain curve.

Using equation 1 to describe the stress-strain curve, it is possible to obtain the extrusion pressure in terms of the extrusion ratio, yield stress, σ_y, the work-hardening coefficient, k, and exponent, n. From this it can readily be shown that increasing the yield stress will increase the extrusion pressure, as will increasing the work-hardening coefficient. Also, an increase in the extrusion ratio will increase the dependence of the extrusion pressure on the work-hardening coefficient, see Fig. 9. The effect of increasing the work-hardening exponent is more complex; at low strains an increase in the exponent decreases the work-hardening rate and thus the area under the curve and the extrusion pressure, Fig. 9. At higher strains the flow stress associated with a higher work-hardening exponent results in a greater area under the stress-strain curve, and at some critical strain, ε', the area under the stress-strain curves of low and high work-hardening exponent will be constant, providing the work-hardening coefficient does not alter. Thus at extrusion ratios less than strains equivalent to ε', a high value of work-hardening exponent will be beneficial, and only at the higher strains $>\varepsilon'$ will a low work-hardening exponent give any advantage. ε' will always be greater than unity.

Thus the factors required for low extrusion pressures are:–

(i) A low yield stress
(ii) A low work-hardening coefficient
(iii) A high work-hardening exponent if the extrusion ratio is moderately low; a low work-hardening exponent only being required at the highest extrusion ratios.

Using previously described data[23] and the equa-

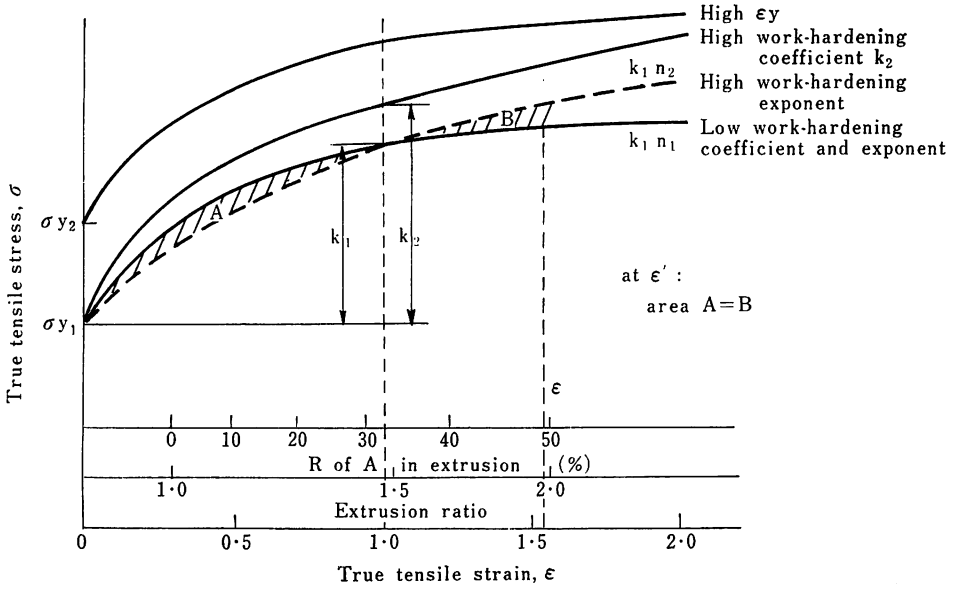

Fig. 9. Schematic relationships between true stress-true strain curve and extrusion.

tions given earlier in this paper, it is possible to identify the microstructural and compositional parameters which will give low yield stress values and work-hardening rates. In general it can be concluded that for the lowest extrusion pressures, a low pearlite (carbon) content, Fig. 10 a), a coarse ferrite grain size, Fig. 10 b), a slow cooling rate through the ferrite range to overage any precipitated iron carbides, and low solute contents are desirable. Consequently it is possible to begin to arrange the processing and analytical variables to achieve this, e.g. a controlled high finishing temperature with a slow cooling rate in a low-carbon steel would be beneficial.

However, the extrusion pressure itself is not the only criterion, and the steel must be able to give the appropriate properties after extrusion or after subsequent heat treatment. If it is desirable therefore to produce a high-strength, but readily extrudable steel, it is possible to decide which strengthening mechanism will be capable of producing the lowest increase in extrusion pressure. A vector diagram, showing the increase in extrusion pressure (at $\varepsilon=1\cdot5$) with increasing yield strength due to various strengthening mechanisms in low-carbon steels, is shown in Fig. 11, from which it can be seen that grain refinement and dispersion hardening are much more preferable strengthening agencies than carbon and manganese content. A mechanism which will lower the extrusion pressure whilst not affecting the yield strength of low carbon ferrite-pearlite steels is to spheroidize the pearlite. The vectors shown in Fig. 11 will change in magnitude with varying extrusion ratio, but not in their

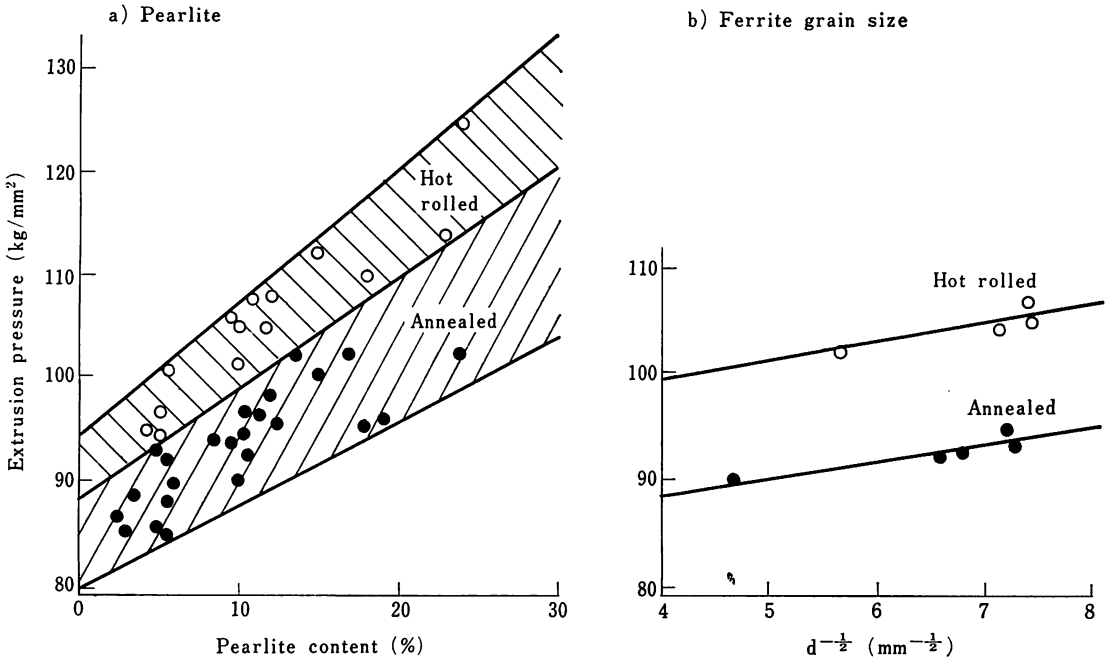

Fig. 10. Effect of microstructure on extrusion pressure at extrusion ratio of 1·5 in 0·1%C–0·5%Mn steel.

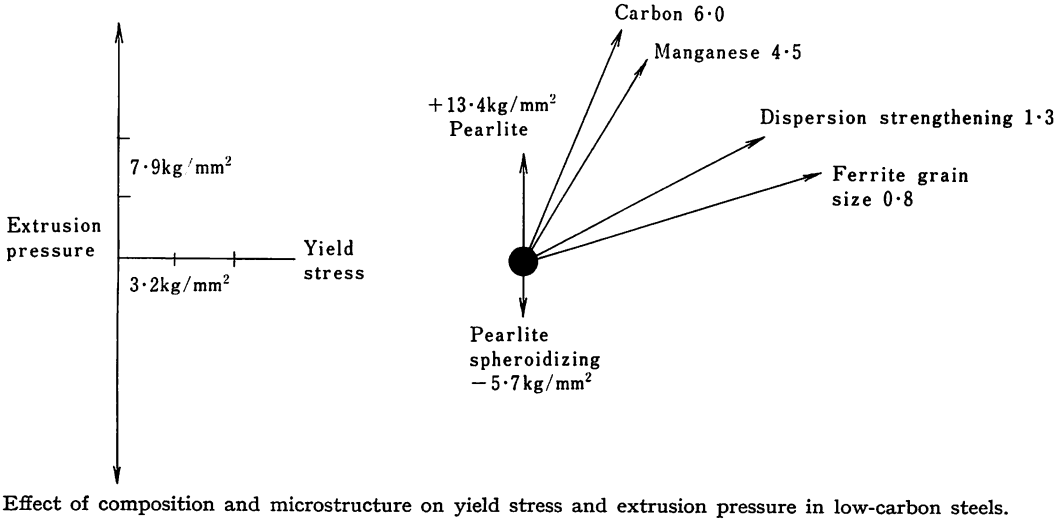

Fig. 11. Effect of composition and microstructure on yield stress and extrusion pressure in low-carbon steels.

relative order of effect. If the extrusion has to be quenched and tempered, hardenability may dictate the degree to which extrudability is to be sacrificed. However, it should be possible to optimize the composition which would give maximum extrudability for a given hardenability.

2.5.2 The use of low carbon contents

The advantages of low carbon contents both from the point of view of extrudability, high uniform ductility and high total ductility have already been illustrated. There are many other advantages of using low carbon contents, for example no great loss of yield stress, good impact toughness and weldability, etc. Reducing the carbon content to a very low level to achieve good formability however, has disadvantages because in air-melted steels the volume fraction of oxides tends to increase. Consequently there will be an optimum carbon content for maximum ductility, and lower carbon contents will give rise to lower ductilities due to the increase in oxide content. In a previous publication[23], it was shown that it is possible to calculate this optimum carbon content using an empirical hyperbolic relationship between ε_T and the volume fractions of oxides, carbides and sulfides, and the carbon-oxygen equilibrium[24]. This optimum carbon content is given by:–

$$\%\, C_{opt} = (p_{co}/5k_T)^{1/2} \qquad (14)$$

where $k_T = p_{co}/[C]\,[O]$

and $$\log_{10}(p_{co}/[C]\,[O]) = \frac{1056}{T} + 2{\cdot}131 \qquad (15)$$

P_{co} is the partial pressure of carbon monoxide, and [C] and [O] are the dissolved carbon and oxygen concentrations respectively, with T the absolute temperature. For a steelmaking temperature of 1600°C and air melting, C_{opt} is 0·02% with $\varepsilon_T = \sim 1{\cdot}6$. A reduction of carbon down to ~0·02% will therefore produce a benefit in formability, and as the steelmaking temperature can only be varied within small limits and $1/k_T$ does not vary greatly with temperature, varying the steelmaking temperature is unlikely to have a great effect either on C_{opt} or ε_T.

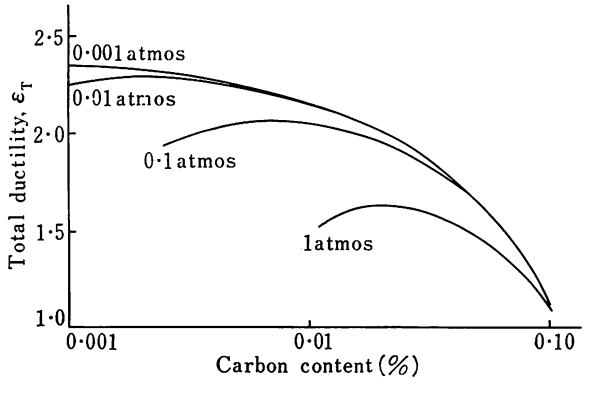

Fig. 12. Effect of reduced pressure and carbon content on total ductility.

On the other hand, lowering P_{co} by vacuum degassing has a marked effect, not only in increasing the maximum value of ε_T but also in decreasing C_{opt} to a level lower than the practicably attainable limits. Also, and most important, the value of ε_T for any given carbon content increases, as shown in Fig. 12, and this is quite marked even for a modest vacuum. Thus the use of low-carbon vacuum-degassed steel will undoubtedly give much improved formability.

2.5.3 Inclusion shape control

An important commercial development with respect to the effect of inclusion shape on the formability of steel has been the use of zirconium or rare-earth additions[25,26]. Normal manganese sulfides, particularly in hot-rolled strip, form greatly elongated stringers. Such stringers have a very deleterious effect on formability, particularly with respect to bends made parallel to the rolling direction. Tight bends lead to severe longitudinal cracking along the tensile edge of the bend, i.e. the transverse ductility is low. The addition of zirconium, cerium or calcium under controlled conditions can markedly alter the morphology of the sulfides, and also of the oxides. The sulfides particularly are prevented from forming elongated stringers, and occur as rounded globules, consequent upon the formation of higher melting point sulfides, which have much reduced plasticity at rolling temperatures. These globular sulfides, due to their low stress-concentration factors in the transverse direction, cause much less rapid void growth and consequently do not so markedly impair the transverse ductility, which is very much improved compared with a steel containing elongated sulfide stringers. Calcium, also, can effectively modify the plasticity of oxide inclusions with beneficial effects. It has been shown[26] that complete modification of the sulfide shape occurs at a cerium/sulphur ratio of about 1·5. In zirconium-treated steels, due to the nitride-forming capacity of zirconium, a minimum zirconium content of (6%N + %S) is required. In fact, due to its nitride-forming ability, zirconium is not suitable for use with a steel which owes its strength to nitride precipitation, i.e. a vanadium dispersion strengthened material, for which cerium is best suitable. Zirconium, however, can be used with a niobium steel.

These inclusion modifying additions can also greatly improve the transverse notched-impact properties, particularly with respect to the shelf energy, as will be described later.

3. THE TOUGHNESS OF FERRITE-PEARLITE STRUCTURES

The factors that control the impact toughness of

low carbon steels containing ferrite-pearlite microstructures have been the subject of intensive study over the past decade[1,2,3,27]. This has enabled a fairly comprehensive understanding to be reached of the effects of ferrite grain size, pearlite content, solid-solution hardening and dispersion strengthening on the impact properties, and from this work it has been possible to specify the strengthening mechanisms which have least deleterious effects on toughness.

3.1 The effects of strengthening mechanisms on impact resistance

Regression equations have been derived which can be used to predict both the yield stress and impact-transition temperature with reasonable certainty:-

$$\text{Yield stress (kg/mm}^2) = [3{\cdot}5 + 2{\cdot}1(\%\text{Mn}) + 5{\cdot}4(\%\text{Si}) + 23(\sqrt{\%\text{N}_f}) + 1{\cdot}13\text{d}^{-1/2}] \times 1{\cdot}57 \quad (16)$$

$$\text{Impact-transition temperature (°C)} = -19 + 44(\%\text{Si}) + 700(\sqrt{\%\text{N}_f}) - 11{\cdot}5\,\text{d}^{-1/2} + 2{\cdot}2(\%\text{ pearlite}) \quad (17)$$

This type of equation can then be used to correct properties to a constant level of composition and microstructure, from which the individual effects of the various strengthening mechanisms on the impact toughness can be assessed. These relationships can be expressed as the change in impact transition temperature per 1 kg/mm² increase in yield stress, and the resultant vectors for various microstructural and compositional strengthening mechanisms are shown in Fig. 13. It can be seen, that ferrite grain refinement is the most beneficial strengthening mechanism as it also improves the impact toughness, and this well-known effect has been widely applied. Aluminum and manganese are also beneficial in this respect, aluminum particularly so as it removes the detrimental element nitrogen as aluminum nitride. Solid-solution strengthening is detrimental as it causes an increase in impact-transition temperature, phosphorus and tin being very detrimental in this respect. Nitrogen either in interstitial solution or as iron nitride precipitates is also detrimental. Increasing the pearlite content is particularly harmful as in low-carbon steels it does not affect the yield strength but markedly raises the impact-transition temperature. Carbon reflects the detrimental effect of pearlite but also has a beneficial effect in that it depresses the transformation temperature and so refines the ferrite grain size; consequently it is not so detrimental as pearlite itself. Dispersion strengthening by copper, vanadium or niobium carbonitrides is only mildly detrimental, and by no means so bad as many solid-solution strengthening effects. The effect of dislocation strengthening, on very limited evidence, appears to be similar in overall effect to dispersion strengthening, possibly slightly worse with respect to the toughness. The results shown by the vectors in Fig. 13 clearly indicate why a low-carbon high-manganese, aluminum grain refined steel is a common choice for a high-strength low-alloy steel, and also why dispersion strengthening by Nb (CN) or V_4C_3 is frequently employed in notch-tough steels.

3.2 The strength and impact toughness of high-carbon steels

The effects described in the previous section were confined to low carbon contents less than 0·25%. As the carbon content is increased, and the pearlite content increases up to 100%, pearlite itself begins to play an ever increasing role in controlling the yield strength and toughness. An analysis of the effects on the yield strength in high-carbon steels has been carried out using the basic equation:-

$$\sigma_y = f_\alpha^n \sigma_\alpha + (1 - f_\alpha^n)\sigma_p \quad (18)$$

where:- f_α is the volume fraction of pearlite

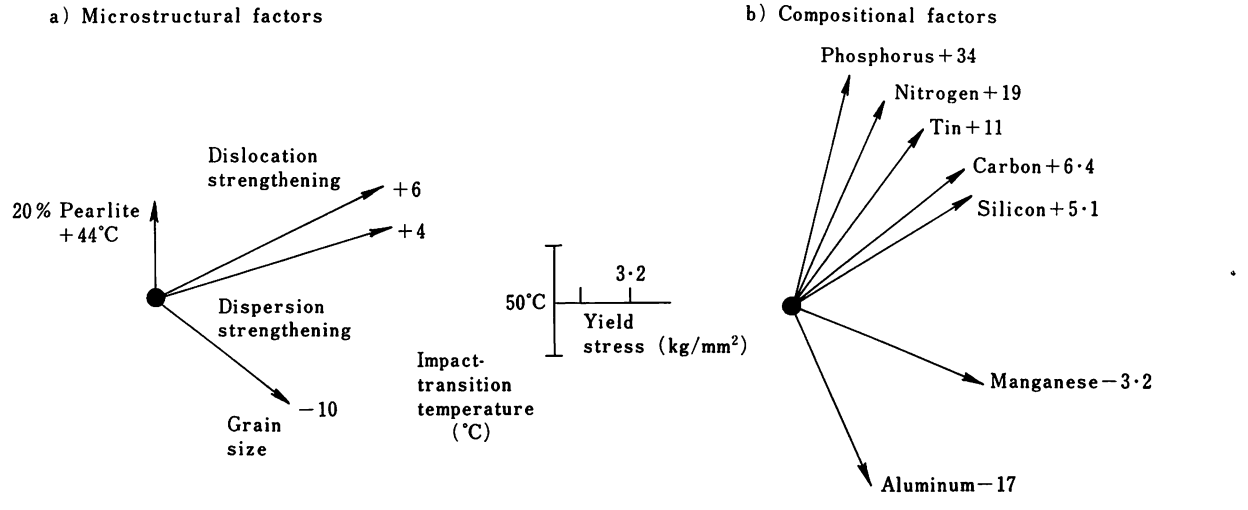

Fig. 13. Factors affecting yield strength and impact-transition temperature.

and σ_α, σ_p and σ_y are the yield strengths of ferrite, pearlite and the ferrite-pearlite aggregate respectively.

The index 'n' was used to allow the yield strength to vary non-linearly with pearlite content, and a value of n=1/3 gave the least residual error. It was found that the value of σ_α obeyed the Hall-Petch equation:-

$$\sigma_\alpha = \sigma_0 + k_1(\%\mathrm{Mn}) + k_2(\%\mathrm{Si}) + k_3(\%N_f) + k_y d^{-1/2} \quad (19)$$

where σ_0=friction stress

A similar equation was used for the value of σ_p, but involving the interlamellar spacing S_0. The pearlite colony size, p, and the cementite plate thickness, t, were found not to have significant effects on the yield stress, but did affect the 3·4 kgm/cm² impact temperature, which was used in place of the 50% brittle-transition temperature. Functions of $S_0^{-1/2}$, $p^{-1/2}$ and t were used in the equations describing the impact properties, and in this case the lowest residual error was when n=1.

The equation describing the yield strength was:-

$$\sigma_y(\mathrm{kg/mm^2}) = \{f_\alpha^{1/3}[2\cdot3+3\cdot8(\%\mathrm{Mn})+1\cdot13d^{-1/2}] + (1-f_\alpha^{1/3})[11\cdot6+0\cdot25S_0^{-1/2}] + 4\cdot1(\%\mathrm{Si})+27\cdot6(\%N_f)\}\times1\cdot57 \quad (20)$$

The equation illustrates the well-known dependence of the yield strength on the ferrite grain size, which gives a smaller contribution to the strength as the pearlite content increases. The pearlite contributes more to the strength as the composition approaches the eutectoid, and as is well known is very dependent on the interlamellar spacing. Considering the more complex analysis required, the various regression coefficients are remarkably similar to those obtained in the more limited analysis for low-carbon steels. Using this equation allows the effect of pearlite on the yield strength to be illustrated in terms of the various factors, but excluding interlamellar spacing, which was assumed constant, Fig. 14.

The 3·4 kgm/cm² impact-temperature was described by the equation:-

$$\mathrm{I.}\,(°\mathrm{C}) = f_\alpha - [46-11\cdot5d^{-1/2}] + (1-f_\alpha)[-335+5\cdot6S_0^{-1/2}-13\cdot3p^{-1/2}+3\cdot48\times10^6t] + 48\cdot7(\%\mathrm{Si})+762(\sqrt{N_f}) \quad (21)$$

Again the general similarity in the regression coefficients with those obtained over a restricted and low carbon content can be observed, and it is clear that grain refinement, low silicon and low free-nitrogen contents should be used for the optimum impact properties. Just as a refined ferrite grain size has a beneficial effect on the impact properties, so does a small pearlite colony size, and metallographic evidence has clearly shown that a pearlite colony boundary acts to impede the propagation of a cleavage crack. The morphological aspects of the

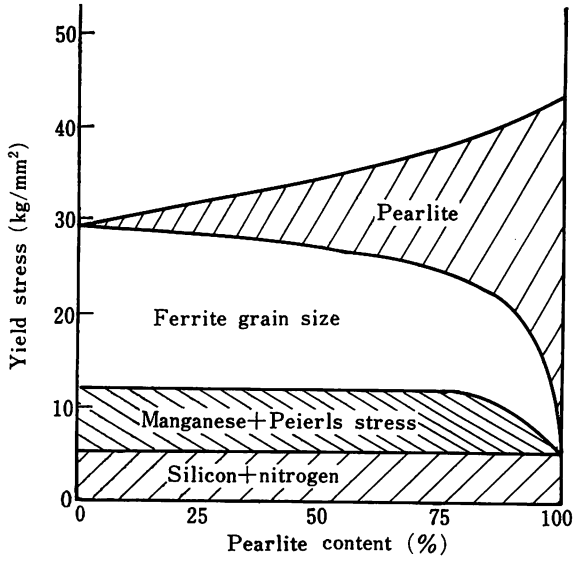

Fig. 14. Effect of pearlite on yield strength (0·9%Mn–0·3 %Si–0·007%N).

pearlite structure on the impact properties are complex in that a refinement of the interlamellar spacing is detrimental, but the usually simultaneously observed decrease in the carbide plate thickness, Fig. 15, is beneficial. In general, therefore,

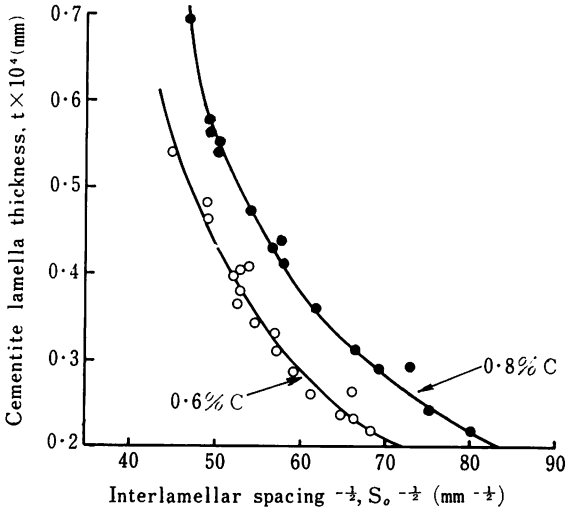

Fig. 15. Relation between interlamellar spacing and cementite lamella thickness.

there is a balance between a decrease in interlamellar spacing adversely affecting impact toughness, possibly through its effect in increasing the strength, and a simultaneous decrease in carbide plate thickness which improves the impact properties. Often they offset one another so that there is no net effect, but either effect can predominate causing an improvement or deterioration in impact toughness, and the effects are further complicated by any accompanying changes in pearlite colony size. As the two factors S_0 and t behave in opposite ways, there will obviously be an optimum interlamellar spacing

for the best impact toughness, Fig. 16. It is also clear that the dilution of the pearlite will be important, as increasing the carbon content of the pearlite will impair the impact properties because it will result either in an increased carbide plate thickness for a given interlamellar spacing, or a finer interlamellar spacing for a given carbide plate thickness. The pearlite dilution factor is defined as:-

$$D = 0{\cdot}8f_p/\%C \qquad (22)$$

i.e. D=1·0 for eutectoid pearlite and >1·0 for fully pearlitic hypoeutectoid steels.

It can be shown that the optimum interlamellar spacing for best impact toughness is related to the dilution factor by:-

$$S_{opt} = 6{\cdot}7 \times 10^{-6}(D - 0{\cdot}12)^{2/3} \qquad (23)$$

Thus, as shown in Fig. 17, the optimum interlamellar spacing increases as D increases, and the impact toughness gets progressively better, i.e. the 3.4 kgm/cm² temperature decreases. This of course is for a fully pearlitic structure, and it is clear that increasing the pearlite content for a given carbon content can be beneficial to toughness. However, the precise effect will depend on the balance brought about by decreasing the ferrite content by this

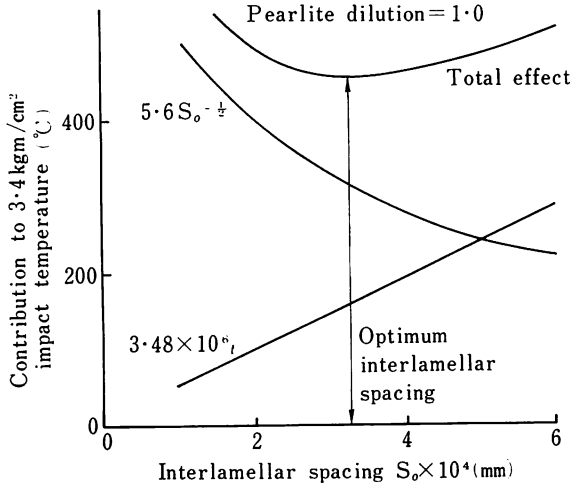

Fig. 16. Effect of pearlite interlamellar spacing on 3·4kgm/cm² impact temperature.

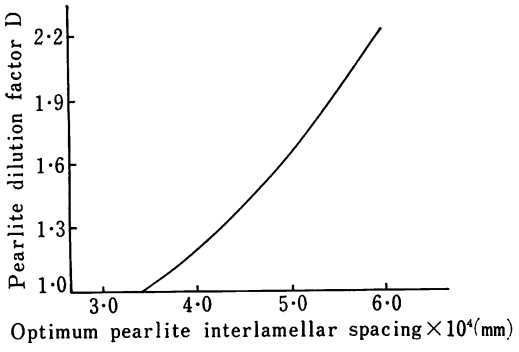

Fig. 17. Effect of pearlite dilution factor on optimum interlamellar spacing for impact toughness.

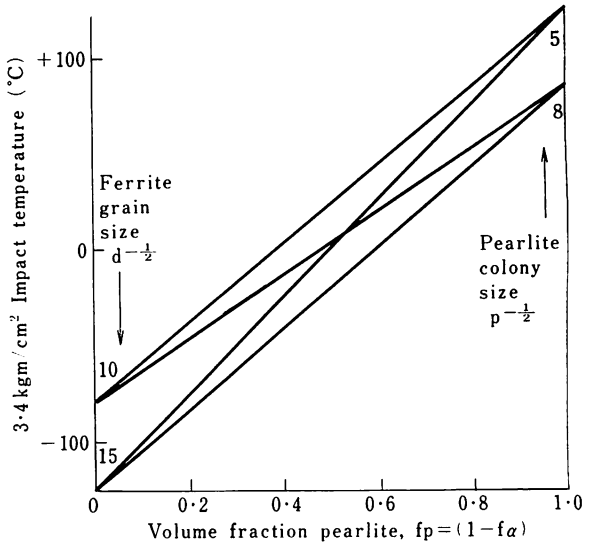

Fig. 18. Effect of ferrite grain size and pearlite colony size on impact toughness.

method, and especially if the impact toughness of the ferrite is very good (i.e. a very fine grain size) then increasing pearlite dilution could be detrimental to the impact resistance. Some general interrelationships of ferrite and pearlite morphology are illustrated in Fig. 18, and it can be seen that pearlite morphology is the more important in the higher carbon steels. In this context it is also necessary to bear in mind the effect of transformation temperature, brought about by alloy content, cooling rate or austenite grain size, on the morphologies of both the ferrite and the pearlite. In general it can be concluded that decreasing the transformation temperature will tend to be detrimental to impact toughness, although some depression of transformation temperature is essential to give fine ferrite grain sizes and fine pearlite colony sizes. An optimum combination of strength and toughness will be achieved by a minimum carbon content to comply with the strength requirements, grain refinement of the steel to give a fine ferrite grain size and pearlite colony size, and a minimum solid-solution hardening by nitrogen, silicon etc.

3.3 The effect of large carbide particles

McMahon[28] showed that large carbide particles can crack under applied stresses and cause the propagation of a cleavage crack through the ferrite of a low-carbon steel. Such an effect would adversely affect the impact toughness and lead to an increase in the impact-transition temperature[29]. The presence of coarse carbide filaments can occur in low-carbon steels, particularly at low manganese contents, by a degeneration of the pearlite, and in ferrite-pearlite steels large carbides can also be formed by a subcritical stress-relieving treatment. Such stress relieving has been observed to impair the impact properties[30], and so an investigation has

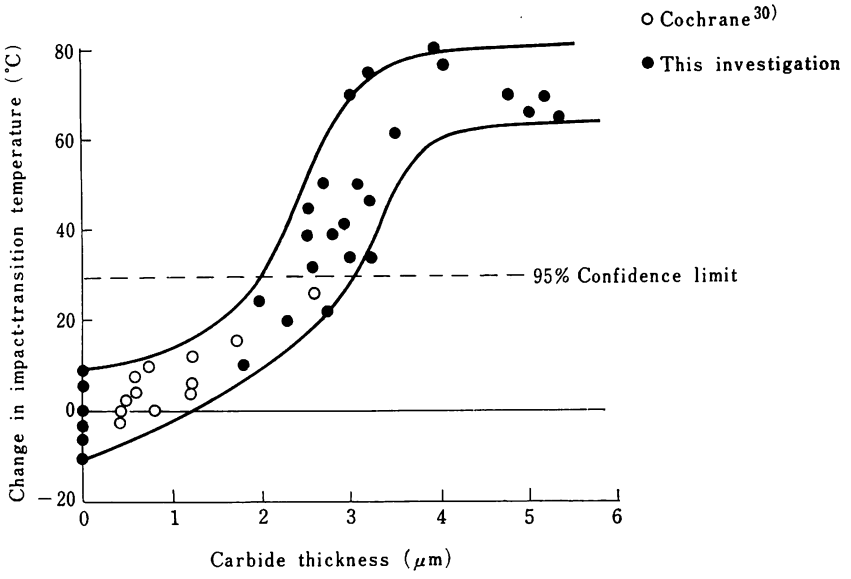

Fig. 19. Effect of carbide size on change in impact-transition temperature.

been made of the effect of coarse carbide particles on the impact properties of low-carbon low-manganese steels. In these steels, the size of the filamental or larger carbides decreased with increasing carbon and manganese content, and increased with slower cooling rates. The impact-transition temperatures were then calculated on the basis of equation 17, which accounts for compositional factors and the effects of pearlite and ferrite grain size. The differences between the observed and calculated transition temperatures are shown as a function of the carbide size (filament thickness) in Fig. 19. It can be seen that the impact-transition temperature was significantly higher than the calculated value when the carbide size exceeds $\sim 2\,\mu$m, and increased with increasing carbide size until it had been raised by as much as 80°C when the size of the carbides was 3–4 μm.

It was observed that cleavage in the ferrite was associated with cracking of the larger carbides, and the high strain rates and low temperatures used in impact testing obviously raise the macroscopic yield stress to a level capable of cracking the carbides. Thinner carbides may deform, thereby avoiding forming cracks, but it is also observed that these carbides can crack but that the cracks are subcritical in size and therefore do not propagate under the stress conditions in the impact test. The fact that the carbide cracking is definitely the cause of cleavage fracture is shown by the absence of mechanical twins. This clearly indicates that the cracked carbides can initiate propagating cleavage cracks at stresses lower than that necessary for mechanical twinning.

3.4 The effect of nonmetallic inclusions

It is a well-known phenomenon that the impact toughness of steels is adversely affected by a large inclusion content, and in particular there is general agreement that increasing inclusion contents decrease the ductile impact shelf energy value. However, the effect of inclusions on the impact-transition temperature is by no means so clearly defined, some evidence indicating little or no effect [31,32)], and other work indicating a clearly defined effect[33)]. In view of the ability of cracked carbides to raise the impact-transition temperature, it might be expected that brittle types of inclusions could behave in a similar manner.

In order to investigate the effect of inclusions on the impact toughness in more detail, controlled experiments were carried out on low-carbon manganese steels of varying sulfur contents; sulfides being a relatively readily controlled type of inclusion. The properties were examined in the longitudinal and transverse directions, using 19 mm-thick plate material. The effects of other compositional and microstructural variables were eliminated by use of the regression equation 17 to calculate the impact-transition temperature, and to compare this with observed effects. There was a clearly defined effect for increasing sulfur content, i.e. sulfide volume fraction, to lower the ductile-impact shelf energy, Fig. 20, and the shelf energy was much

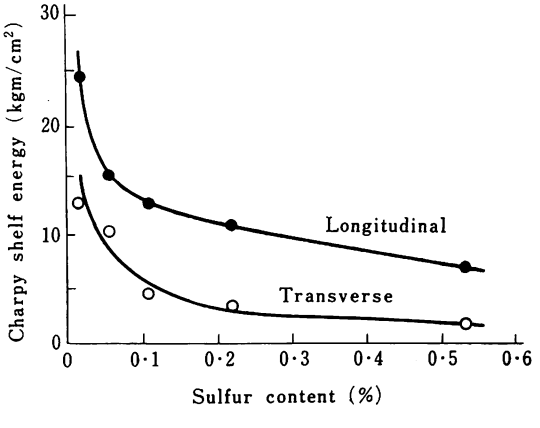

Fig. 20. Effect of sulfur content on Charpy shelf energy.

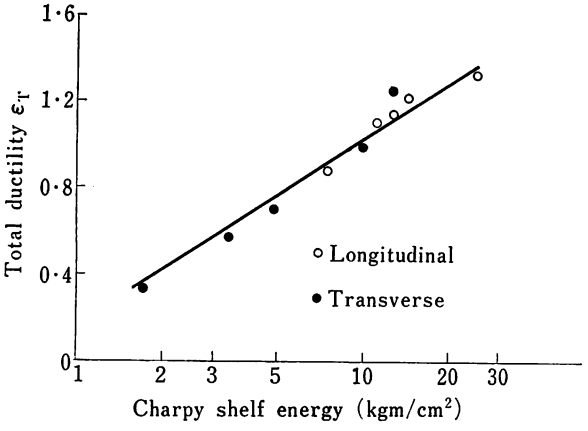

Fig. 21. Relation between total ductility and Charpy shelf energy.

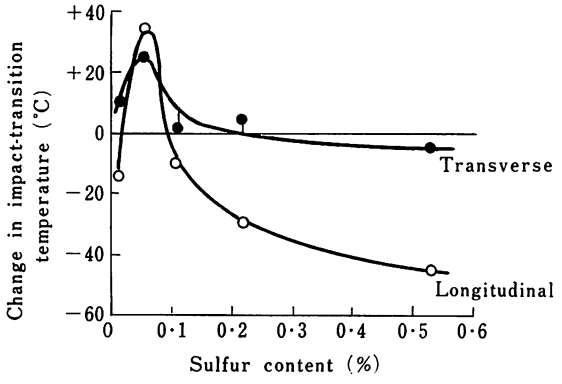

Fig. 22. Effect of sulfur content on impact-transition temperature.

lower in the transverse direction than in the longitudinal direction. This was in accord with general experience, and the qualitative similarity between the effect of sulfides on total ductility at fracture, ε_T. and impact shelf energy was most marked. In fact, there was a unique relationship between the impact shelf energy and the total strain at fracture, ε_T, measured in a tensile test, Fig. 21. A linear relation was observed between the value ε_T and the logarithm of the shelf energy value. With regard to the impact-transition temperature, the effect of sulfide volume fraction was similar in both the longitudinal and transverse tests, Fig. 22. Increasing the sulfur content up to ~0·05% increased the impact-transition temperature, due it is believed to the sulfide inclusions acting as sites for crack nucleation. A further increase in the sulfur content produced a progressive decrease in the impact-transition temperature and in the high-sulfur steels the transition temperature was in fact lower than that of the low-sulfur steel. Whilst increasing sulfur, i.e. sulfide inclusion, content would increase the number of sites for crack nucleation, it would also greatly increase the number of obstacles to crack propagation, the overall effect being to produce a decrease in impact-transition temperature. Particularly in the longitudinal tests, the elongated sulfide inclusions are most effective obstacles to crack propagation, the cleavage cracks having to propagate across many inclusion fibers. Hence the impact-transition temperature was lower in the longitudinal than in the transverse tests. Similar effects have been observed in the fracture of mild steel laminates[34], in which "crack arrester" and "crack divider" laminates correspond well with the longitudinal and transverse tests.

A practical application of current knowledge of the effect of inclusions on impact properties has been the use of inclusion shape control by zirconium or rare-earth additions to improve the transverse impact shelf energy in steels[26,35]. This work shows that by altering the shape of the sulfide inclusions from elongated stringers to a globular morphology, the transverse impact shelf energy is virtually doubled[26], and the longitudinal shelf energy is largely unaffected. The overall effect is that the ratio, longitudinal shelf energy: transverse shelf energy, approaches more nearly unity than for material to which no inclusion shape control has been applied, and this ratio decreases with increasing additions of either zirconium or rare earths[35]. Recently published evidence[35] indicates that rare-earth additions may give ratios of longitudinal: transverse shelf energies nearer to unity than is the case for zirconium additions. It has also been suggested that the optimum zirconium addition is that required to combine with both the nitrogen and the sulfur, but that above this optimum zirconium content the excess zirconium forms ZrC and $Zr_4C_2S_2$ phases, which lower the impact shelf energy. Recent evidence[36], whilst confirming the beneficial effects of zirconium on impact shelf energy, has indicated that in both as-rolled and heat-treated carbon-manganese steel, in both longitudinal and transverse tests, the addition of 0·15% Zr markedly raises the impact-transition temperature by ~50°C. It is possible that this effect is due to ZrN particles which were present, acting as crack initiators, but it could also be that zirconium eliminates the elongated stringers of sulfide and so prevents their crack arresting or crack dividing effects, previously referred to. These possible deleterious effects of zirconium should be borne in mind, particularly if large zirconium additions are used.

4. SOME ASPECTS OF THE DUCTILITY OF AUSTENITIC STEELS

In view of the fact that austenitic stainless steels have polygonal grain structures analogous to ferrite-pearlite steels, with delta ferrite corresponding to the pearlite, it was believed that quantitative relationships might be obtained between structure, composition and properties. This proved possible for the proof stress, tensile strength and tensile

ductility[5], but because of the complex effects introduced by variations in the stacking-fault energy, twinning frequency, strain-induced martensite and elemental partitioning between the austenite and delta ferrite, it has not yet been possible to analyse the results of room-temperature true stress-true strain tests with sufficient precision to formulate realistic regression equations.

The ductility is controlled by the interactions between the flow stress, work-hardening rate and fracture stress. The flow stress is affected by the tendency to form martensite during straining, and this automatically effects the work-hardening rate, causing discontinuities to appear in the ε vs $d\sigma/d\varepsilon$ curve. However, it is possible to obtain fairly accurate equations to describe the proof stress and tensile strength values, when the analysis is confined to stable steels which do not form strain induced martensite. It is useful therefore to consider some of the factors affecting the strength of austenite before proceeding to discuss ductility.

4.1 Factors affecting the strength of austenite

The equations which have been obtained to describe the strength of stable austenitic steels with M_d temperatures well below 0°C were:-

0·2% proof stress (kg/mm²)

$$=[44+23\%C)+35(\%N)+1\cdot3(\%Si)+0\cdot24(\%Cr)+0\cdot94(\%Mo)+1\cdot2(\%V)+0\cdot29(\%W)+2\cdot6(\%Nb)+1\cdot7(\%Ti)+0\cdot82(\%Al)+0\cdot16(\%\delta)+0\cdot46\,d^{-1/2}]\times1\cdot57 \quad (24)$$

where % δ=delta ferrite content
and d=mean grain diameter

Tensile strength (kg/mm²)

$$=[29+35(\%C)+55(\%N)+2\cdot4(\%Si)+1\cdot2(\%Mo)+5\cdot0(\%Nb)+3\cdot0(\%Ti)+1\cdot2(\%Al)+0\cdot11(\%Ni)+0\cdot14(\%\delta)+0\cdot82\,t^{-1/2}]\times1\cdot57 \quad (25)$$

where t is the twin spacing

With regard to the proof stress, the grain size has the well-known strengthening effect, but delta ferrite also has a marked strengthening effect over and above that which it causes by refining the austenite grain size. A recent analysis of this effect of delta ferrite indicates that it is due to strain concentration in the softer austenite phase, which therefore work hardens to a strain greater than the nominal 0·2%, and consequently gives a higher flow stress. Solid-solution strengthening is similar to that reported previously[37], and has been shown to be greatest for interstitial solutes, not so pronounced for ferrite-forming substitutional solutes and negligible for austenite-forming substitutional solutes. A good correlation exists between the lattice distortion and solid-solution strengthening produced by a solute element[38]. An interesting feature was the absence of any effect of twinning on the proof stress, which is because the variations in stacking-fault energy, as reflected by twin spacing, do not cause sufficient change in work-hardening rate to affect the low-strain proof stress value. Also, in very stable austenitic steels, martensite does not form at strains of 0·2%, and so the proof stress is not affected. However, further work on less stable compositions showed that up to 35% martensite in the solution-treated condition did not have any effect on the 0·2% proof stress, and indeed up to 20% martensite may lower it. This latter effect is due to the formation of more martensite in such unstable steels as soon as any strain is applied, so that the transformation strain causes the strain to exceed 0·2% at low stress values, and thus an abnormally low proof stress value is observed. This may be augmented by internal stresses associated with the prior martensite. With martensite contents greater than ~35%, the martensite itself becomes the main load-bearing phase, and consequently the proof stress value increases with increasing martensite content.

The tensile strength was dependent on the twin spacing rather than the grain size, equation 25. It is believed that the twin spacing reflects the stacking-fault energy rather than a major strengthening from twin boundaries themselves, a low stacking-fault energy (associated with a small twin spacing) resulting in a high work-hardening rate and a high tensile strength. However, whilst stacking-fault energy, as defined by twin spacing, has a major effect on tensile strength, in a high stacking-fault energy alloy in which there are no twins, the tensile strength will then increase as the grain size becomes finer. Again delta ferrite is a strengthening agent, but in this case in view of the dominant effect of work hardening, it is believed that partitioning of carbon and nitrogen to the austenite, thereby increasing the work-hardening rate, plays the major role. About 80% of the strengthening due to delta ferrite on the tensile strength can be accounted for in this way. The effects of solutes on tensile strength are complex, depending on their effects on solution strengthening, stacking-fault energy and work-hardening rate, and on the tendency to form strain-induced martensite prior to the limit of uniform extension. Solutes do however seem to have similar general effects on tensile strength to their solution-strengthening effects determined on the proof stress. The effect of martensite on tensile strength is also complex, and has been established on steels containing martensite prior to testing. Such steels, depending on their stability, may or may not form further strain-induced martensite. The tensile strength of such steels is found to increase linearly with the amount of prior martensite, Fig. 23, but the intercept of 19 kg/mm² at 0% prior martensite in these relatively unstable steels, is believed to represent strengthening by the martensite formed during straining up to the maximum uniform strain. The tensile strength in

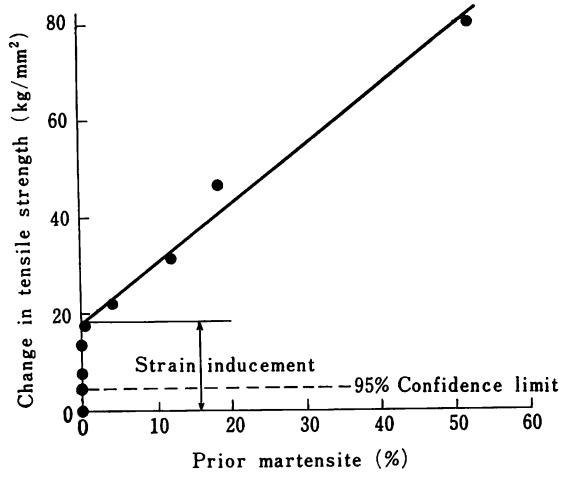

Fig. 23. Effect of prior martensite on tensile strength.

the presence of martensite can be described by:-

$$\text{Tensile strength (kg/mm}^2) = [T_e + 12 + 0{\cdot}82(\%\text{ prior martensite})] \times 1{\cdot}57 \quad (26)$$

where T_e is the tensile strength calculated from equation 25.

It can be seen that the factors controlling tensile strength are more complex than those controlling the proof stress, and this is shown by the less reliable nature of equation 25, which only explains 78% of the variation in tensile strength, compared with the 91% of the variation in proof stress explained by equation 24.

4.2 The work hardening of austenitic steels

In material which undergoes no phase change during straining, the work-hardening rate continually decreases with increasing strain, i.e. in a stable austenitic steel with M_d well below room temperature. In a steel in which strain-induced martensite is formed immediately strain is applied, the transformation strain augments the applied strain so that low apparent work-hardening rates are observed, which are lower than if no martensite had been formed. With the progressive formation of martensite however, the alloy is strengthened and the flow stress increases. This more than counterbalances the transformation-induced strain and so the work-hardening rate increases to reach a maximum value before finally decreasing at higher strains as the formation of strain-induced martensite ceases. These effects are shown in Fig. 24, and in these circumstances the effect of an alloying element on the work-hardening rate is not unique, but depends on the stability and M_d temperature of the base into which it is introduced. For this reason, it has not yet been possible to obtain simple or adequate predictive equations. The effects of the major alloying elements, nickel and chromium, on the work-hardening rate are shown in Fig. 25. The factor (Ni+2/3 Cr) was used on the basis that the amount of strain-induced martensite would be related to the M_d temperature, which in turn is

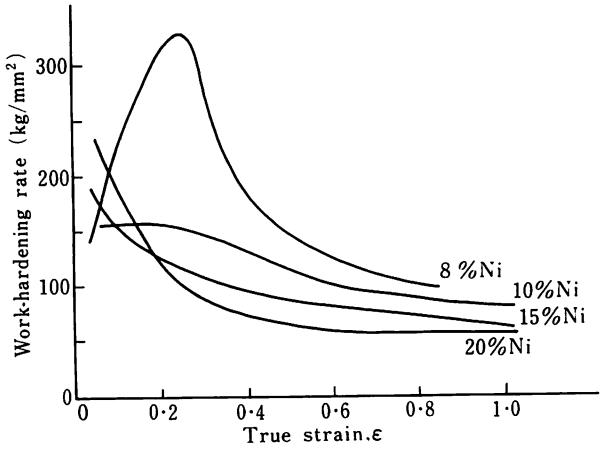

Fig. 24. Effect of nickel content on work-hardening rate of 18% Cr steels.

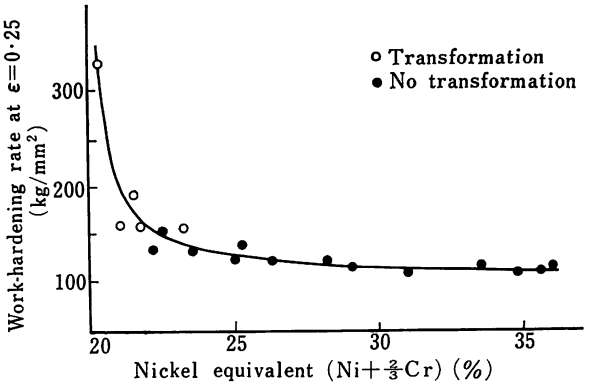

Fig. 25. Effect of nickel equivalent on work-hardening rate at $\varepsilon = 0{\cdot}25$.

related to M_s. Eichelman and Hull[39] showed that chromium was about two thirds as effective as nickel in depressing M_s, and hence Fig. 25 attempts to show work-hardening rate as a function of nickel equivalent. It can be seen that the work-hardening rate, at a strain where the effect of strain-induced martensite is very marked, decreases rapidly with increasing stability of the austenite. This effect could either be due to the maximum work-hardening rate decreasing with austenite stability, or more strain being required to induce martensite as the M_d decreases. Recent work[40], and evidence from experiments on unstable steels, suggest the former cause to be predominant.

The effect of stacking-fault energy on the work-hardening rate is important, elements which lower the stacking-fault energy causing an increase in the work-hardening rate. This effect may however be very marginal indeed in a high stacking-fault energy base composition, i.e. there is no unique effect. Thus, elements which increase the stacking-fault energy, i.e. nickel and copper[41] tend to decrease the work-hardening rate, as shown in Fig. 26. To a small extent aluminum and titanium also decrease the work-hardening rate, but no effect was observed

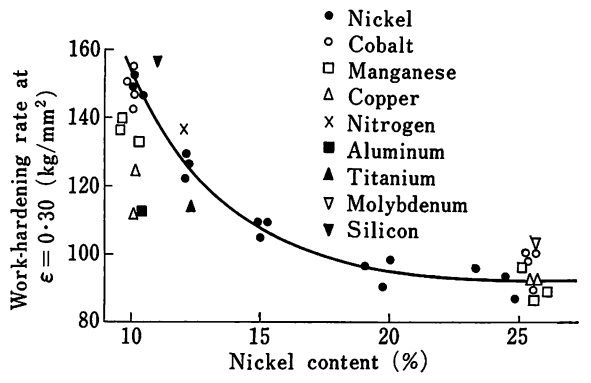

Fig. 26. Effect of various elements on work-hardening rate.

for niobium. Part of this effect may be due to the removal of nitrogen by aluminum and titanium. On the other hand, carbon and nitrogen lower the stacking-fault energy[41,42], and increase the work-hardening rate. Nitrogen has its main effect at small strains, but is almost ineffective at higher strains, whilst carbon on the other hand is effective at all strain values, albeit more so at the lower strains. The substitutional solutes silicon, tungsten and molybdenum all tended to increase the work-hardening rate, and the observed effects are in accord with the decreased stacking-fault energy reported to be produced by silicon[41] and molybdenum[43]. Vanadium has not been observed to materially affect the work-hardening rate. As has already been stated, the effects of any given element will vary depending on the base composition into which it is introduced, and this is clearly shown in Fig. 27 for silicon in a high stacking-fault energy base (16% Cr–25% Ni). Up to 2% Si there is no effect on work-hardening rate, but at 4% Si there is a marked increase in work-hardening rate as the silicon begins effectively to decrease the stacking-fault energy.

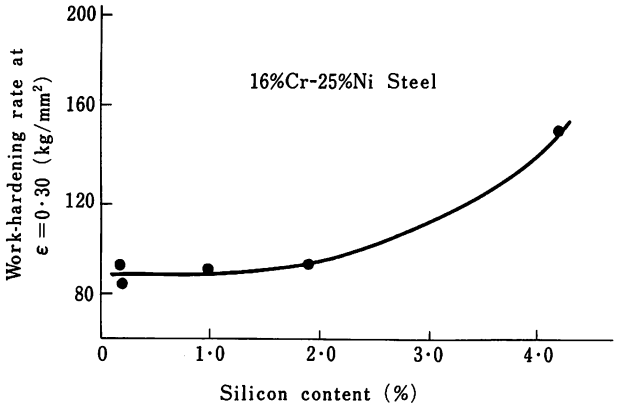

Fig. 27. Effect of silicon content on work-hardening rate.

It should be pointed out that this was not due to silicon forming delta ferrite in this high-nickel base, although delta ferrite does increase the work-hardening rate at low strains but tends to decrease it at higher strains. This is because delta ferrite is a high-strength low work-hardening phase, in contrast to austenite. Thus at low strains, strain is concentrated in the austenite which work hardens rapidly, until at higher strains the deformation becomes concentrated in the ferrite which only work hardens slowly.

The effect of martensite on work hardening is not simple, and whilst it would seem that martensite increases the work-hardening rate by a strain concentration effect, this is complicated by the fact that the presence of martensite prior to testing invariably leads to less strain-induced martensite.

Finally, it should be clearly appreciated that, in view of there being no unique effect of an alloying element which can be used to correct for variations in composition, care should be taken in interpreting results, particularly when an alloying element can depress M_d, combine with carbon or nitrogen, and introduce delta ferrite into the structure.

4.3 The ductility of austenitic steels

At present it has not been possible to analyse the results of an extensive series of experiments in order to produce a regression equation describing the maximum uniform strain, ε^*, and the total strain at fracture, ε_T. However, the reduction of area measured in the conventional tensile test has been described[5]:–

$$\text{R of A (\%)} = 77 + 0{\cdot}81(\%\text{Si}) + 0{\cdot}94(\%\text{Mo}) + 1{\cdot}3(\%\text{Cu}) + 1{\cdot}6(\%\text{Al}) - 0{\cdot}20(\%\text{Ni}) - 6{\cdot}6(\%\text{Nb}) + 0{\cdot}99\,t^{-1/2} - 1{\cdot}0\,d^{-1/2} \qquad (27)$$

This equation has limited predictive capabilities, only 63% of the observed variation being explained. Considerable uncertainty attaches to the coefficients, because even in relatively stable steels some strain-induced martensite may readily be formed at the high strains associated with fracture.

Microstructural and compositional parameters again have complex effects involving interactions between flow stress, work-hardening rate and fracture stress. Increasing the work-hardening rate relative to the flow stress will tend to increase the maximum uniform strain prior to plastic instability, ε^*. However, both these parameters depend on composition in terms of solid-solution hardening, stacking-fault energy and the formation of strain-induced martensite, and as has already been shown the strain-induced martensite can in turn have complex effects on the work-hardening rate. The total ductility, ε_T, occurs when the flow and fracture stresses are equal, i.e. at fracture. Thus increasing the flow stress relative to the fracture stress will decrease the value of ε_T, and the flow stress will depend on stacking-fault energy and strain-induced martensite. Non-linear effects of compositional and microstructural parameters are

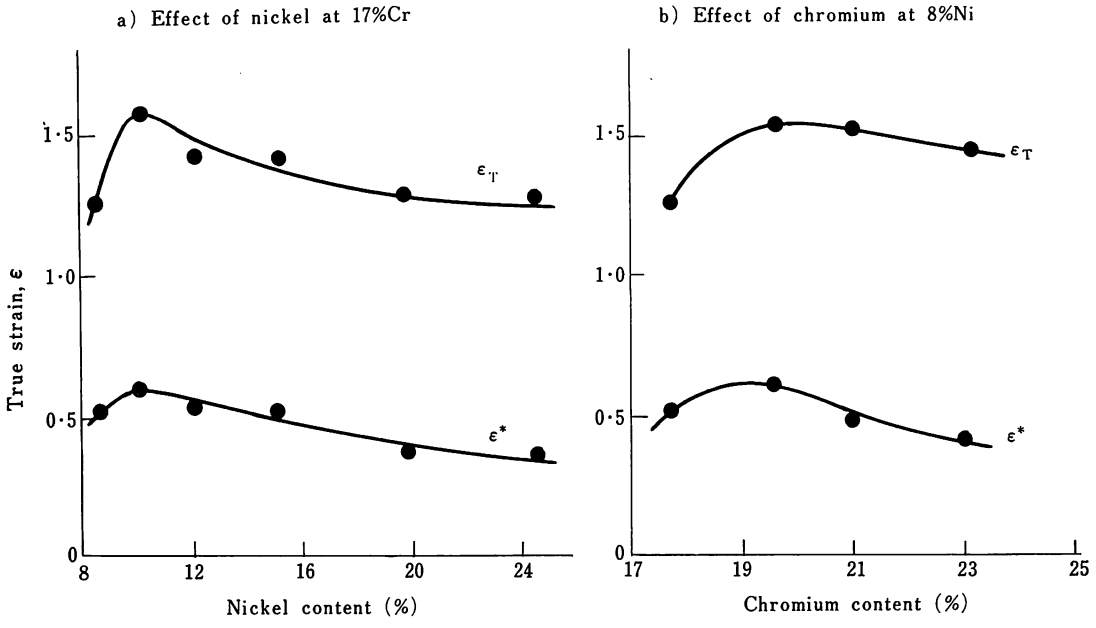

Fig. 28. Effect of nickel and chromium contents on ductility.

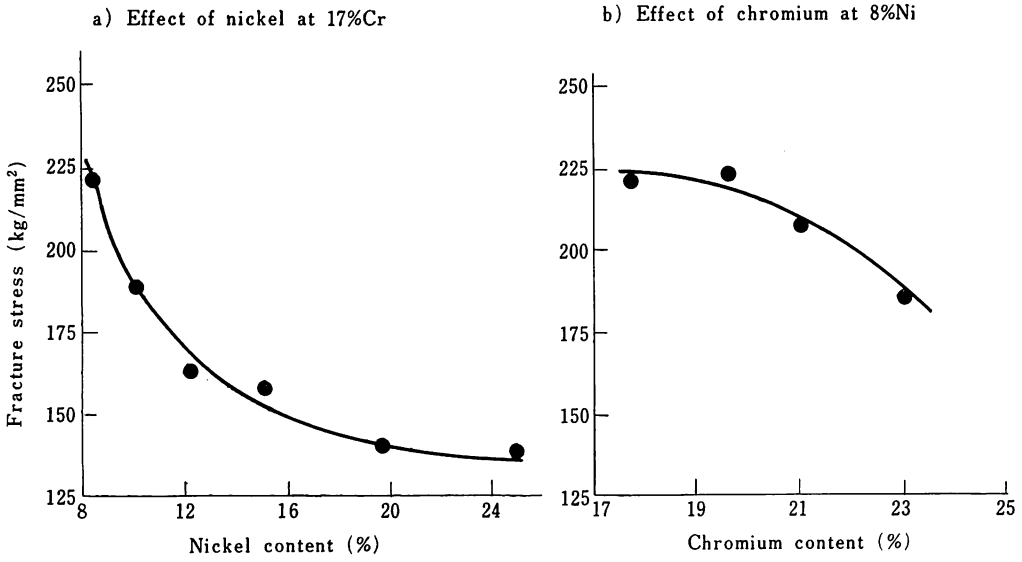

Fig. 29. Effect of nickel and chromium contents on fracture stress.

therefore observed on the various measures of ductility. A typical effect is shown for the major elements nickel and chromium, both of which give maxima in both ε^* and ε_T at specific alloy contents, Fig. 28. The maximum value of ε^* is due to the occurrence of strain-induced martensite at low nickel contents, which gives high work-hardening rates at strains approximating to ε^*, and thus increases the value of ε^*. With increasing nickel, less martensite is formed during straining, the work-hardening rate decreases, and whilst the flow stress is also decreased by the lower stacking-fault energy, the latter does not offset the former effect. Hence ε^* decreases with increasing nickel content. With regard to ε_T, this is dependent on the work-hardening rate, which controls the flow stress, and the fracture stress; the latter decreases both with increasing nickel or chromium, Fig. 29. At low nickel contents for example, much strain-induced martensite gives a high work-hardening rate and flow stress; thus ε_T is small. As the nickel content increases the flow stress decreases and ε_T increases, but with still higher nickel contents the decrease in the fracture stress predominates and so ε_T then decreases. Equation 27 describes this latter effect in the more stable higher nickel austenites, in terms of the reduction of area in a tensile test.

The general concept of the equivalence of flow and fracture stress in controlling ductile fracture may however be invalid, and rather the role of second-phase particles, i.e. inclusions, in controlling void nucleation and growth may be more important, as will be discussed later. Consequently it is possible that transformation-induced plasticity con-

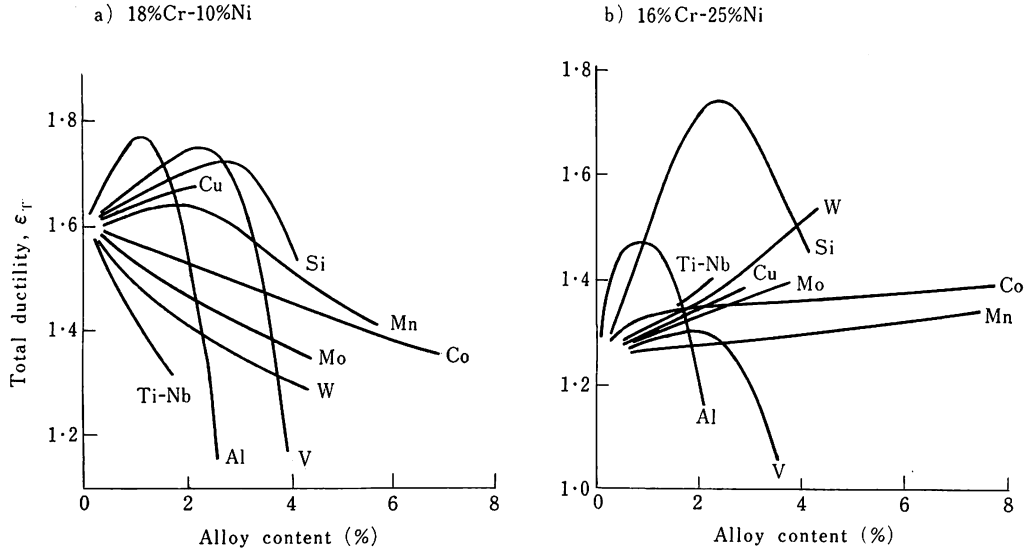

Fig. 30. Effect of alloying elements on total ductility.

tributes most vitally to the total ductility by not contributing directly to void growth. If this is the case, the maximum value of ε_T might be expected at a nickel (or chromium) content at which there was maximum transformation, i.e. transformation-induced plasticity. This in fact appears to be the case. Other elements also produce maximum ductilities at certain compositions, as shown in Fig. 30, and others such as cobalt seem to decrease ε_T in the less stable steels due to the suppression of strain-induced martensite, c.f. higher nickel contents. It can again be seen that there is no unique effect of an alloying element, which depends very much upon the base composition into which it is introduced.

In addition to the effects described previously, the alloying addition may introduce or suppress delta ferrite formation. The evidence so far available indicates that delta ferrite has only a a minor effect on ε_T or reduction of area. Approximately 10% delta ferrite seems to decrease the reduction of area by ~1%, or the value of ε_T by ~0·04 in an overall ε_T of about 1·6. The presence of martensite prior to straining decreases the maximum uniform strain ε^*, by increasing the flow stress relative to the work-hardening rate. The evidence so far available also suggests that prior martensite decreases ε_T, by decreasing the amount of subsequent strain-induced martensite formed during the test, and also due to its inherent brittleness. This is reflected in the reduction of area value, 10% martensite in the structure reducing the reduction of area by ~8%. On the other hand, as has already been shown, strain induced martensite formed during testing is very beneficial to ductility, the transformation strain augmenting the ductility but at the same time not apparently contributing to void growth during ductile failure. This effect has been exploited in the development of high-strength, ductile, stainless steels[44,45].

4.4 The effect of second-phase particles on ductility

The failure of an austenitic steel during any forming operation will almost invariably be due to ductile fracture, involving void nucleation and growth. The role of nonmetallic inclusions and other second-phase particles in this process is of the utmost importance, and investigations have been made into their effects. The effect of nonmetallic inclusions was investigated by controlling the sulfide content, using sulfur additions to a stable 16% Cr–25% Ni steel. The effect of the total volume fraction of both sulfides and oxides on the total ductility, ε_T, is shown in Fig. 31. The maximum uniform strain ε^*, was also decreased, but to a much less marked extent than ε_T. The relation between inclusion volume fraction and ε_T was qualitatively very similar to that observed in ferrite-pearlite steels, but the austenitic steels gave much lower ductilities than did ferritic steels. There are two possible reasons for this, the first being the angular shape of the oxides in the austenitic steels, which

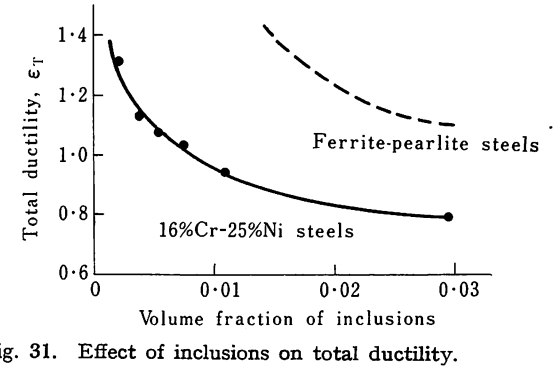

Fig. 31. Effect of inclusions on total ductility.

would give increased strain concentration and more rapid void growth. The second effect may have been due to segregation of the sulfides, causing local high volume fractions of particles so that void coalescence occurred at smaller strains than would be the case for randomly distributed particles.

Other forms of second-phase particles which occur even in solution-treated steels of the AISI 321 and 347 types, are the carbonitrides Ti(CN) or Nb(CN). The effect of volume fraction of Ti(CN) or Nb(CN) on ε_T is shown in Fig. 32, but excludes the effect of sulfides and oxides. Again the relationship was parallel to that observed for inclusions in ferrite-pearlite structure, but displaced to lower values of ε_T. This difference may also be associated with the similar effect discussed for the sulfides, but could also be due to some extent to the fact that the sulfides and oxides were not taken into account in assessing the volume fraction of second-phase particles. However it is clearly apparent that inclusions and Ti(CN) or Nb(CN) have equally as detrimental effects on the total ductility in austenitic steels as inclusions have in ferrite-pearlite steels.

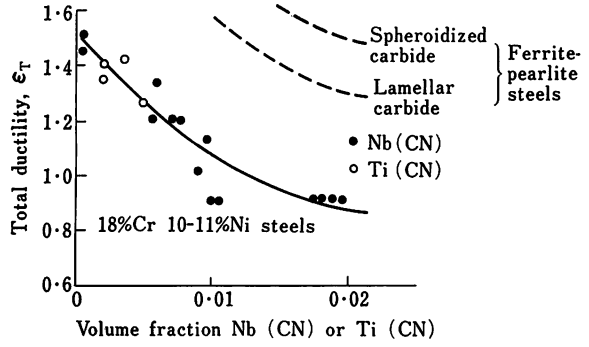

Fig. 32. Effect of Nb(CN) and Ti(CN) on total ductility.

5. CONCLUSIONS

A description has been given of some of the factors which control the ductility and toughness of ferrite-pearlite steels of the high-strength low-alloy type. Quantitative effects of both microstructural and compositional variations on the work-hardening, ductility and impact-toughness values have been described, and it has been shown that it should be possible to design steels for optimum formability using the criteria which have been established. In the past, advantage has been taken of such relationships to design high strength into structural steels, and at the same time preserve optimum impact toughness, and the present work has opened up the possibility also of designing for maximum strength and cold formability. However, even the most formable steel composition and structure can be rendered useless by excessive amounts of nonmetallic inclusions, and a considerable effort has been devoted to an attempt to quantify the effects not only of inclusions but also of carbide particles. It is clear that many advantages would accrue from a conjoint reduction in both carbon and inclusion content, and a suggestion for how this could be done has been made. The control of inclusion shape has also given rise to considerable improvements in both formability and toughness.

In the case of austenitic steels, the effects of microstructure and composition on ductility have been shown to be very complex. Consequently there is no unique effect of any given alloying element, rather its effect depending upon the base composition into which it is introduced. It is not possible therefore, at the present time, to derive reliable and realistic equations that could be used to predict flow stress, work-hardening rate and ductility for austenitic steels. Nevertheless a discussion of the possible interactions has been given and results which may help to a fuller understanding of the ductility of these steels have been presented. Again the major importance of inclusions on the ductility of austenitic steels has been emphasized and extended to include the deleterious effects of Ti(CN) and Nb(CN) particles. Using the information presented, it should be possible to appreciate better the metallurgical factors which may limit the formability of austenitic stainless steels, and to design alloys with improved ductility. However, much more systematic work is required before a complete and quantitative understanding of the structure-property relationships is achieved.

ACKNOWLEDGEMENTS

The author wished to thank Dr. K.J.Irvine, Head of Research, Special Steels Division, British Steel Corporation, for permission to publish this paper, and Dr. T. Gladman for many helpful discussions during the progress of the work described.

REFERENCES

1) T. Gladman and F.B. Pickering: I.S.I. Spec. Rep. No. 81, (1963), p. 10
2) K.J. Irvine and F.B. Pickering: J.I.S.I., **201** (1963), p. 944
3) K.J. Irvine et al.: J.I.S.I., **205** (1967), p. 161
4) F.B. Pickering: Transformation and Hardenability in Steel Symposium, Ann Arbor, Mich., (1967), p. 109
5) K.J. Irvine et al: J.I.S.I., **207** (1969), p. 1017
6) D.L. Paulson et al: Reg Conf. of AIMME, Spokane, Washington, (1955)
7) R.D. Butler: Sheet Metals Industries, (Sept. 1964), p. 705
8) H.L. Black and L.W. L'Herbier: Met. Prog., (June 1965), p. 62
9) J. Datske and C.T. Yang: J. of Eng. for Industry, (Nov. 1960), p. 309
10) R.L. Kegg: J. of Eng. for Industry, (May 1961), p. 119
11) C.F. Morris, Jr.: Space/Aeronautics, **37** (1961), no. 6, p. 87
12) L.J. Kashar: Trans. A.I.M.E., 239 (1967), p. 1461
13) F.B. Pickering: Iron & Steel, (March-April 1965)

14) D.J. Dingley and D. McLean: Acta Met., **15** (1965), p. 885
15) B.J. Edelson and W.H. Baldwin: Trans. ASM, **55** (1961), p. 230
16) J. Gurland and J. Plateau: Trans. ASM, **56** (1963), p. 442
17) C.T. Liu and J. Gurland: Trans. ASM, **61** (1968), p. 156
18) J.T. Barnby: Acta Met., **15** (1965), p. 903
19) E. Smith: Int. J. Fract. Mech., **4** (1968), p. 131
20) K.W. Burns and F.B. Pickering: J.I.S.I., **185** (1964), p. 889
21) D. Brooksbanks and K.W. Andrews: J.I.S.I., **206** (1968), p. 595
22) D. Brooksbanks and K.W. Andrews: J.I.S.I. **208** (1970), p. 582
23) T. Gladman, B. Holmes and F.B. Pickering: J.I.S.I., 208 (1970), p. 173
24) R.G. Ward: Physical Chemistry of Iron and Steelmaking. Arnold, (1962), p. 88
25) E.J. Licky et al : Journal of Metals, (July 1965), p. 767
26) M. Korchynsky and J. Stuart. London-Scandanavian Symposium on High Strength Low Alloy Steels, Nuremberg, (May 1970)
27) J.H. Bucher et al: Fracture, Academic Press, (1969), Chap. 5, p. 247
28) C.J. McMahon and M. Cohen: Acta Met., **13** (1963), p. 991
29) N.P. Allen et al: J.I.S.I., **174** (1953), p. 108
30) R.C. Cochrane: I.S.I./B.S.C. Conference on The Effect of Second Phase Particles on the Mechanical Properties of Steel, (March 1971)
31) W. Dahl et al: Stahl u. Eisen, **86** (1966), p. 796
32) L. Roesch et al: Mem Sci, Rev. Met., **63** (1966), p. 927
33) H.J. Kouwenhoven: Private Communication
34) J.D. Embury et al: Trans. A.I.M.E., **239** (1967), p. 114
35) J.H. Little and W.L. M. Henderson: I.S.I./B.S.C. Conference on The Effect of Second Phase Particles on the Mechanical Properties of Steel, (March 1971)
36) A. Nicholson: Private Communication
37) K.J. Irvine, D.T. Llewellyn and F.B. Pickering: J. I.S.I. **199** (1961), p. 153
38) B. Holmes and D.J. Dyson: J.I.S.I., **208** (1970), p. 469
39) G.H. Eichelman and F.C. Hull: Trans. ASM, **45** (1953), p. 77
40) D.C. Ludwigson and J.A. Berger: J.I.S.I., **207** (1969), p. 63–69
41) J. Nutting and D. Dulieu: I.S.I. Spec. Rep. No. **86**, (1964), p. 140
42) P.R. Swann: Corrosion, **19** (1963), p. 102
43) S. Barnartt, R. Stickler and D. Von Rooyal: Corrosion Science, **3** (1963), p. 9
44) V.F. Zackay et al: Trans. ASM., **60** (1967), p. 252
45) E.R. Parker and V.F. Zackay: Sci. Amer., **219** (1968), no. 5, p. 36

DISCUSSION-See pp. 341-342

Criteria of Ductility and Toughness for Fracture-Safe Design

E.A. Lange

U. S. Naval Research Laboratory

Metallurgy Division

ABSTRACT

Fracture-safe design procedures are the key to more effective utilization of high-strength structural metals. Significant advancements have been made in design models which provide interrelationships between the metallurgical, mechanical, and structural aspects. Recent developments in the theory of linear-elastic fracture mechanics (LEFM) have provided test methods and a basic analysis for the case of fractures occurring under elastic stress conditions for brittle materials. Other test methods and analytical procedures have been developed which can be applied to materials which have higher levels of fracture resistance and require stresses above the yield strength to propagate fractures.

Starting in 1961, a test method and an analytical procedure have been under development that could be applied to the full range, elastic and plastic, of structural steels. The test method for measuring fracture toughness is called the "Dynamic Tear" (DT) test, and the model used for analysis is called a "Ratio Analysis Diagram." All of the practical aspects of LEFM are incorporated in the DT-RAD system and current research is aimed at improving the quantitativeness of the plastic or plane stress fractures. Recent studies concerning the fracture extension resistance or "R-curves" for steels provide for separate characterization of metallurgical and mechanical parameters. This separation is a further significant advancement toward the ultimate goal of a generalized model for fracture-safe design. In particular, it permits computer analysis of the trade-offs in material, design, fabrication and inspection factors.

1. INTRODUCTION

An important requirement for effective utilization of high-strength structural metals is an effective program to provide fracture safety. Most conventional procedures for fracture safety involve rules and criteria that aim to preclude the initiation of cracks, and unfortunately, these approaches lead to designs with low nominal stress levels. A more realistic philosophy is to recognize that all large welded structures have built-in fabrication flaws and that fracture safety is a result of maintaining a positive relationship between the fracture toughness of the material and the driving force that the structure imposes upon the flaws. Fracture-safe design is then an optimization procedure involving material, design, fabrication and surveillance factors.

The first model for fracture-safe design was proposed in 1963 by Pellini. This model was specifically developed for the conventional pressure-vessel and structural steels, and it is called the Fracture Analysis Diagram, (FAD)[1]. Since this initial model was proposed, significant advancements have been made in fracture technology, and continued research has led to the development of more quantitative interrelationships between the multitude of metallurgical, mechanical and structural factors that influence the initiation and propagation of fracture[2-6].

One big step forward was the theoretical development of linear-elastic fracture mechanics (LEFM) and the publication of an ASTM tentative standard method, E399-70T, for determinining the plane strain (K_{IC}) fracture toughness of a material[7]. Since LEFM is based upon the theory of elasticity, its usefulness is limited, unfortunately, to fractures which can occur at elastic stress levels. Therefore, additional test methods and design models of broader scope are required to provide criteria for fracture-safe analyses when fracture occurs in the mixed mode or the fully plastic regimes.

The development of a test method for characterizing fracture resistance over the full range, elastic and plastic, was started in 1961 at the Naval Research Laboratory. This test method was called the

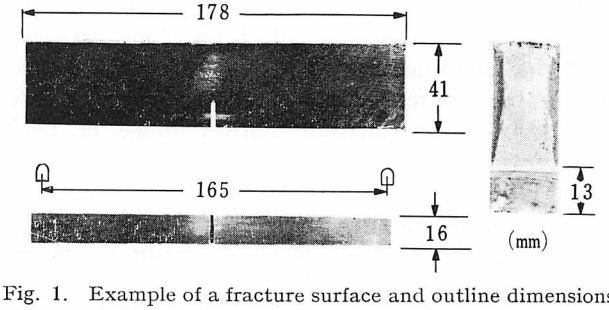

Fig. 1. Example of a fracture surface and outline dimensions of the 16mm DT specimen.

Dynamic Tear (DT) test, and it was designed to include all of the features of a LEFM test plus the features of significance to fully plastic fracture. The DT test has passed its initial development period, and standardization of a DT test method utilizing a specimen 16 mm in thickness (Fig. 1) is currently under development in ASTM Committee E-24.[8-10] The pertinent features of this specimen are use of saw-cut surfaces, a machined, deep notch with a sharp tip, and a net width approximately equal to twice the thickness.

The DT test provides for the measurement of resistance to fracture under a specific constraint condition. This feature permits DT test results to be correlated with test results from LEFM tests, and these correlations form the base of a model for fracture control analyses, which is called the Ratio Analysis Diagram (RAD). The RAD serves many practical needs in its current stage of development, and continuing research is providing a more quantitative analysis for the post-yield (plane stress or plastic) fracture region. The ultimate goal, of course, is a comprehensive model for fracture-safe design which will ultimately permit the development of a computerized fracture control plan involving the optimization of all pertinent factors related to the material, design, fabrication and inspection aspects.

This paper concerns primarily the characterization of steels which includes criteria of ductility and toughness for all types of products. Brief reviews of current models that are used in fracture-safe analyses are included to illustrate how couplings are developed between material properties and the mechanical requirements of various structures. It is shown how to select effective criteria for fracture resistance and thereby preclude catastrophic fracture from occurring within the framework of fabrication and operational controls that prevail for specific structures.

2. CHARACTERIZATION OF MATERIALS

Characterization of the performance of steels with respect to fracture resistance requires consideration of yield strength, temperature, strain rate and stress state. Yield strength is important because it is a measure of the driving force (elastic strain energy) for unstable, self-propagating, brittle fractures. Temperature and strain rate are important parameters because they affect the yield strength and the microfracture mode, which cause a transition in fracture resistance from a high level to a very low level in a relatively narrow range of temperature. Stress state is important because structures normally contain complex details that tend to produce a triaxial stress system which suppresses ductility. Mechanical constraint is, therefore, an important factor to be considered in the characterization of the fracture resistance of materials.

Because fracture resistance is a variable in any specific material, there is no one criterion that can serve as a singularity for this mechanical property. It is imperative, therefore, that engineers concerned about fracture safety consider the effects of design features and operational conditions on the fracture resistance characteristics of the various materials under the conditions encountered in service. Selection of adequate criteria of ductility and toughness is therefore a complex analysis, and several generalized characterization procedures have been developed to make fracture safety a practical element in day to day engineering design procedures.

2.1 Dynamic plane strain limits

The first step in a fracture-safe analysis is to determine whether there is a potential for a plane strain type of fracture. Plane strain fracture may be defined as unstable fracture that occurs at nominal elastic stresses with the maximum effective constraint in the thickness direction. The elastic strain energy that is released when a plane strain fracture initiates is sufficient to keep the fracture propagating without additional energy input from the loading system. That is why plane strain fractures are generally catastrophic. A definition of the constraint or thickness required to provide the level of constraint necessary for plane strain fracture has been proposed in accordance with LEFM theory as follows[2]:

$$B \geqq C\,(K_{IC}/\sigma_{ys})^2$$

where B is thickness, K_{IC} is the critical plane strain stress-intensity factor, σ_{ys} is yield strength, and C is a constant equal to 2·5. It has been found experimentally for steels that when fracture occurs under these conditions the fracture is indeed frangible, and the criterion based upon a thickness requirement can be considered the lower bound limit for plane strain conditions.

The above definition of plane strain limit conditions in terms of fracture resistance and constraint can be a useful relationship for an experimental determination of a dynamic fracture toughness ratio where the individual factors, K_{ID} and σ_{ys} are difficult to determine separately. For example, by simple mathematics the plane strain limits corresponding to the constraint capacity of 16 mm, 25 mm, and 62·5 mm thick sections are K_{ID}/σ_{ys} ratios equal to 2·5, 3·2 and $5\sqrt{\text{mm}}$, respectively. These limit conditions for plane strain fracture provide a coupling between the performance of a material in a dynamic impact test to fracture mechanics parameters and critical flaw size-stress relationships. The "dynamic" plane strain limit is particularly important for characterizing the fracture toughness of most steels because of their sensitivity to strain rate. Even though loading may

be static, a local, brittle pop-in crack can trigger a catastrophic fracture. The dynamic properties are thus the critical properties for fracture-safe design.

The complex interaction between the striker and the specimen under impact loading involves dynamic bending waves as shown from a mechanical analysis of the DT test[11]. The first conclusion drawn from this basic analysis is that the striking force cannot be used directly in an equation for static bending loads to calculate the nominal stress at the notch tip. The appearance of the force-time curve can be used, however, to indicate whether the fracture was truly frangible or whether the initial pop-in crack was arrested. If an initially unstable crack is arrested, the fracture is not completely frangible, and additional energy from the loading system is required to propagate the fracture through the net section. Using this simple criterion for defining fracture under frangible dynamic plane strain conditions, the limit conditions for dynamic plane strain fracture can be determined from a comparison of the appearance of force-time curves.

The procedure for establishing the dynamic plane strain limit using an instrumented DT test is illustrated by the two force-time traces shown in Fig. 2. The upper force-time trace illustrates the appearance of the trace for a truly dynamic plane strain fracture, i.e., only one impulse is obtained indicating that the elastic strain energy was sufficient to cause a completely unstable fracture. The lower trace illustrates the case where a small amount of additional energy was needed to supplement the elastic strain energy, and the limited amount of ductility associated with the purely dynamic plane strain condition has been exceeded.

The plane strain fracture condition in the DWT-NDT test has been analyzed in terms of LEFM parameters, and it has been shown that at the NDT temperature the fracture resistance level can be expressed as $K_{ID}/\sigma_{yd}=2\cdot5\sqrt{mm}$.[3] This level of resistance to dynamic plane strain fracture corresponds to the constraint capacity of a 16 mm-thick section. The NDT temperature is then the highest temperature at which a single impulse is observed in the force-time trace for a 16 mm DT specimen, upper trace in Fig. 2. When a 16 mm DT specimen is tested 6°C above the NDT temperature, a multiple trace, lower in Fig. 2, is obtained indicating that the dynamic plane strain limit and the NDT temperature have been exceeded. This method for establishing the NDT temperature is particularly useful when the appearance of the DT energy-temperature curve is difficult to interpret, and the DWT-NDT test method does not apply; for example, the DWT-NDT test is not recommended for quenched-and-tempered steels.

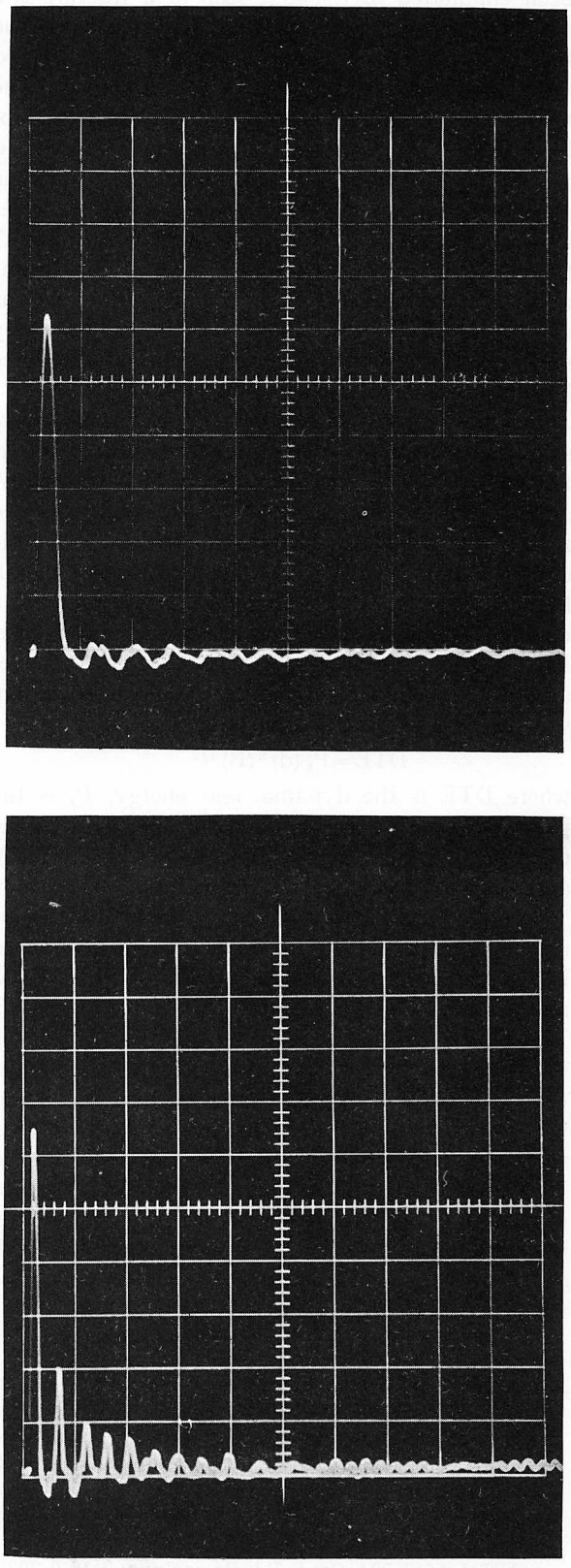

Fig. 2. Illustrating the use of the force-time trace from an instrumented DT test machine to determine the limit conditions for dynamic plane strain fracture. Upper single impulse trace is indicative of a plane strain type fracture; lower, multiple impulse trace is indicative of a nonplane strain type fracture.

2.2 Effect of size on nonplane strain fracture

After the potential for plane strain fracture has

been eliminated in the first step of a fracture-safe analysis, the next consideration is to determine the level of fracture resistance that can be developed under nonfrangible, nonplane strain fracture. The introduction of new, higher strength materials of limited fracture resistance has increased the need for improved analysis for size effects on nonplane strain fracture. These nonplane strain fractures have been termed "plane stress" or "plastic" fractures. An analysis for size effects is important also for comparing DT energy values from various specimens, and for this reason the effects of geometry on the plastic fracture resistance of steels have been investigated.

Included in the size effect investigations were samples of three steels as currently produced to the following ASTM specifications: A537 Grades A and B, and A517 Grade F.* The results obtained from these steels are shown to illustrate that the effects of size can be separated from the metallurgical aspects for the nonplane strain case in a manner similar to that for the plane strain case. For ductile type fractures that occur at stresses above the nominal yield strength, a relationship was developed for DT energy as follows:

$$DTE = P_r (d)^2 (B)^{1/2}$$

where DTE is the dynamic tear energy, P_r is the plastic instability resistance factor (PIRF), d is the distance the fracture propagates (the net width), and B is the section thickness.

An excellent agreement for the PIRF value calculated from DT specimens of various geometries in the three steels is demonstrated by the narrow scatterbands for the test results shown in Fig. 3. The DT specimens ranged from 6 to 76 mm in thickness with crack runs from one to three times the thickness. It can be seen that the PIRF value was consistent for all sections greater than 9 mm in thickness, but increased scatter was obtained for the PIRF values calculated from the equation when the section thickness was less than 9 mm. This scatter indicates that the simplified expression for DTE

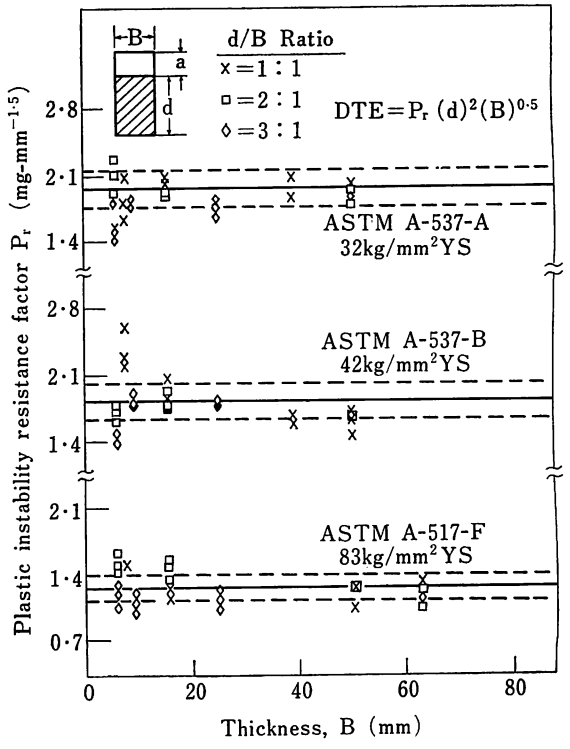

Fig. 3. Calculated plastic instability resistance factor (P_r) for DT specimens of various geometries in three steels, A537-A, A537-B, and A517-F. The dashed lines indicate ± 10% deviation from the average P_r value for each steel.

in the above equation may require modification for steels in thin sections (less than 9 mm).

The general equation for DT energy indicates that for plastic fracture the crack-run distance is a more important geometric feature than the thickness. This is in direct contrast to the effects of geometry on plane strain fracture. According to LEFM theory, an instability condition is reached when the stress-intensity at the crack tip reaches a critical value, and the distance that the crack propagates after initiation is not involved, but total instability is implied. Thus, the effects of size on plastic fracture resistance should not be considered to be a simple extension of the same LEFM parameters that relate to the elastic instability case. Another implication from the DTE equation for plastic fracture resistance is that the conventional technique for scaling structural models for experimental stress analysis does not apply directly to the scaling of models for fracture resistance. The conventional geometric analysis would indicate an exponent of unity for the "B" term rather than the 1/2 which is observed experimentally. These observations and other details concerning the significance of fracture extension resistance which includes the analysis of "R curves" are presented in Refs. (12 and 17).

2.3 Temperature and constraint

From earliest times the "temperature transition" feature of steels has been of concern, and notched-

* ASTM A537-70 ladle analysis: 0·24% C max, 0·70-1·35% Mn for 38·1 mm and under, 1·00-1·60% Mn for over 38·1 to 63·5mm, 0·035% P max, 0·040% S max. 0·15-0·50% Si. Grade A tensile properties: 49·2-63·3 kg/mm² tensile strength, 35·2 kg/mm² min yield point, 22·0% min elongation in 50·8 mm. Condition: normalized. Grade B tensile properties: 56·2-70·3 kg/mm² tensile strength, 42·2kg/mm² min yield point, 22·0% min elongation in 50·8mm. Condition: quenched and tempered.
ASTM A517-70A Grade F ladle analysis: 0·10-0·20% C, 0·60-1·00% Mn, 0·035% P max, 0·040% S max, 0·15-0·35% Si, 0·40-0·65% Cr, 0·40-0·60% Mo, 0·70-1·00% Ni, 0·002-0·006% B, 0·03-0·08% V, 0·15-0·50% Cu. Tensile properties: 80·9-94·9 kg/mm² tensile strength, 70·3 kg/mm² min 0·2% yield strength, 16% min elongation in 50·8 mm. Condition: quenched and tempered.

bar tests have been devised to characterize the drastic change in fracture resistance that occurs in a narrow, critical range of temperature. The notched-bar test using specimens of 10 mm in cross section as developed by Charpy in 1905 has remained the dominant test method for this important characteristic of steels for over 60 years. With the advent of welding and the development of steels with higher yield strengths, the limitations of Charpy-type specimens to adequately characterize the fracture properties of the higher strength steels and the limitations of Charpy energy values to serve as effective criteria for toughness became more evident. Unfortunately, the evidence was a more frequent occurrence of catastrophic failures in structures of significant economic importance.

The limitation of the Charpy test to provide a sufficient description of the fracture characteristics of steels for fracture-safe design primarily stems from the low level of constraint conditions in the specimens. In the Charpy V (C_V) notch specimen the notch is both shallow and dull. Also, the 10 mm thickness does not adequately model the constraint conditions that frequently triggers catastrophic, brittle fractures. Brittle fracture in the transition temperature region has been the subject of many investigations, and one recent study of a pressure vessel steel has included specimens with thickness ranging from 16 mm to over 300 mm[13]. This study was undertaken to establish a limit transition-temperature range (LTTR) and to develop a relationship between the LTTR and that for subthickness specimens. For practical day-to-day use, a subthickness specimen of practical size is needed that can effectively serve to characterize the fracture resistance of steels in thick sections. To illustrate the capability of the 16 mm DT test to provide an accurate characterization of the fracture properties

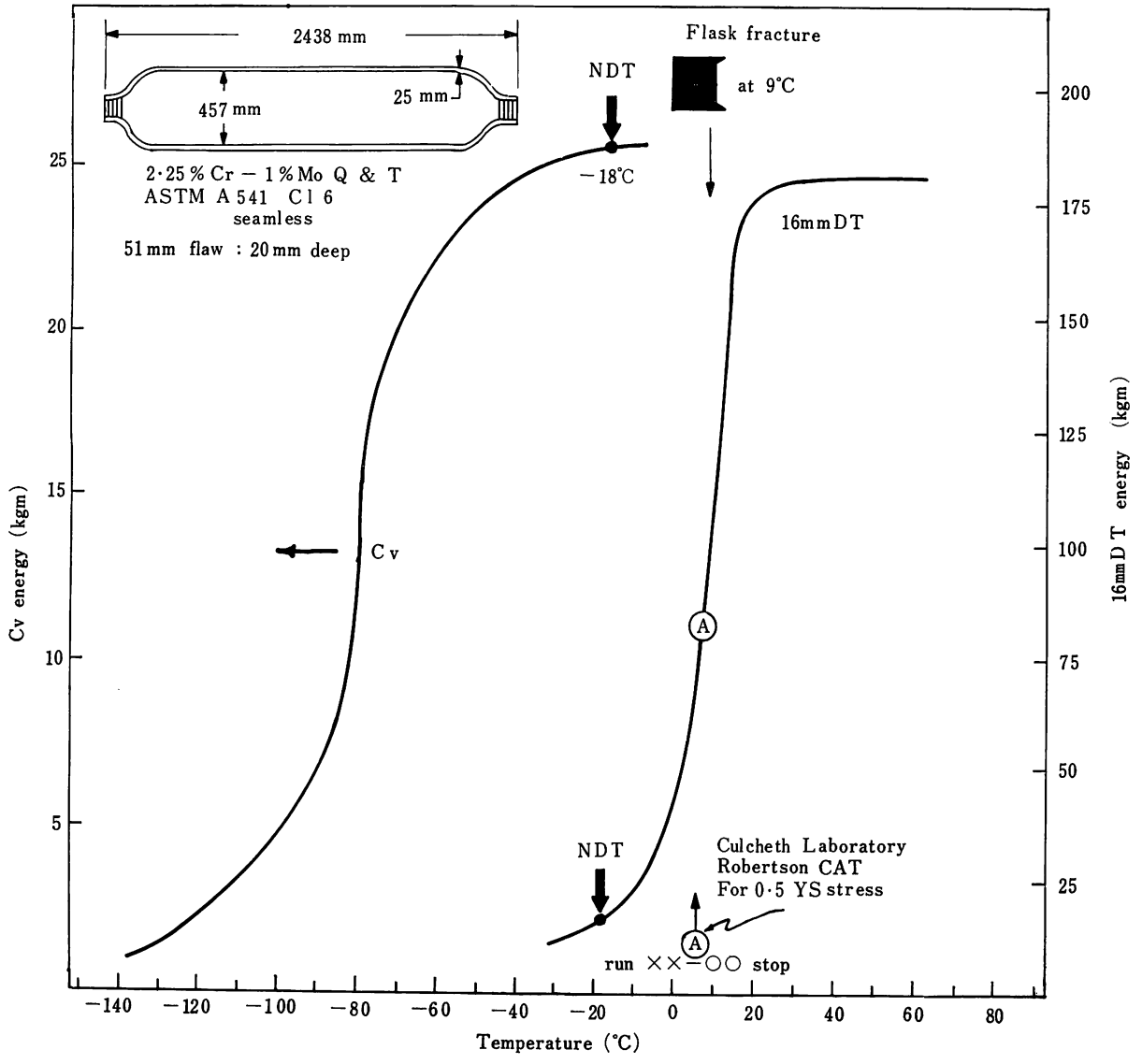

Fig. 4. Comparison of fracture resistance criteria from C_V, DT, NDT, and Robertson tests to the performance of a 2·25% Cr-1%Mo steel in a pneumatic burst test.

of various steels, several characterization studies including the LTTR experiments are described in the following sections.

In certain steels the temperature-transition region is very narrow, and the effect of constraint on fracture toughness can be very sensitive. For example, a 2·25 % Cr-1%Mo quenched-tempered steel was used to fabricate some seamless, pneumatic pressure vessels, and when the behavior of the vessels during burst tests was found to be erratic, an investigation of the fracture characteristics of the steel was conducted[13]. It was found that the transition in C_V energy with temperature was transposed entirely to a temperature region lower than that which corresponded to the temperature transition of the steel in the pressure vessel. Mixed-mode fractures occurred in the vessels at temperatures where a fully plastic, upper shelf level of performance was indicated by C_V test results.

In Fig. 4, the DWT-NDT tests and the crack arrest temperature (CAT) from the Robertson Crack Arrest test on this steel are compared. The displacement of the C_V energy-temperature relation to a nonrelevantly low-temperature range can be seen from a comparison of the results of the DT, NDT, and CAT tests. The start, or toe, of the transition-temperature range of DT energy for the steel in the pressure vessel is accurately indexed by the NDT temperature. The index for CAT conditions in the Robertson test occurs at approximately 12°C above the NDT temperature for this steel where the fracture resistance is substantially above the plane strain limit. The intent of this illustration is to emphasize the importance of the constraint aspects in the design of a fracture test specimen, and it illustrates why it is frequently difficult to establish an effective C_V energy criterion for a material. Because of this frequent temperature displacement of the C_V energy transition, a C_V energy criterion can only be certified if more definitive information is available concerning the fracture resistance characteristics of a specific steel.

The effect of constraint has been extensively investigated on the temperature transition of extremely thick sections of ASTM A533 Grade B* steel[14]. This steel is extensively used for nuclear pressure vessels because of its economical composition, good weldability, and high level of bainitic hardenability. When A533 steel is quenched in sections thicker than 100 mm, the material near the surface (approximately 16 mm) is transformed to lower temperature transformation products. However, most all of the section is metallurgically uniform resulting in a consistent level of yield strength and fracture resistance. The results from studies concerning the mechanical characteristics of this steel have been extensively reported, and only the results of Dynamic Tear tests using specimens ranging in thickness from 16 to 305 mm are shown to illustrate that the shift in the temperature transition with increasing constraint is limited.

The transition in DT energy with temperature for various specimens in A533 steel is shown in Fig. 5 where the data have been normalized at a constant upper shelf level to assist in the analysis of the constraint effect. Note that the DT energy values obtained from 16 and 25 mm specimens fall in a relatively narrow scatterband. As constraint is increased, the midpoint in the DT energy-temperature relationship is shifted by 22°C and then to 39°C for the 76 and 305 mm specimens, respectively. The lower plane strain region is extended also to higher temperatures with increased constraint, but as ductility overcomes the plane strain stress state, fracture resistance for all sections, regardless of size, increases very rapidly. The fracture resistance for this steel increased to very high levels under fully plastic fracture conditions. The results of other tests with extremely thick sections of A533 steel indicate that the effect of constraint on the midpoint of the temperature transition for steels saturates at 39°C for sections greater than 76 mm[14]. Therefore there appears to be a limit transition temperature range for steels in thick sections, and this maximum shift of 39°C appears to be the limit value for the shift in the midtransition temperature due to mechanical constraint.

2.4 Metallurgical gradients

The relationship between hardenability and alloy content is a well established principle of metallurgical design. When the hardenability does not correspond to the slower cooling rates of thick sections, a consistent microstructure and uniform mechanical properties are not developed from surface-to-center locations. For economical reasons, some current commercial quenched-and-tempered steels do not have sufficient hardenability to provide a consistent microstructure from surface-to-center in the thicker plate sections allowed in ASTM specifications. Although these products may have a significant gradient in mechanical properties from surface-to-center, the tensile strength properties are generally affected to a lesser degree than the fracture toughness characteristics. Characterization of materials with a gradient in properties from surface-to-center primarily concerns the temperature-transition aspects although the upper shelf may also be affected.

* ASTM A533-70 Grade B ladle analysis: 0·25 C max, 1·15-1·50% Mn, 0·035% P max, 0·040%S max, 0·15-0·30% Si, 0·45-0·60% Mo, 0·40-0·70% Ni. Class 1 tensile properties: 56·2-70·3 kg/mm² tensile strength, 35·2 kg/mm² min 0·2% yield strength, 18·0% min elongation in 50·8mm. Condition: quenched and tempered.

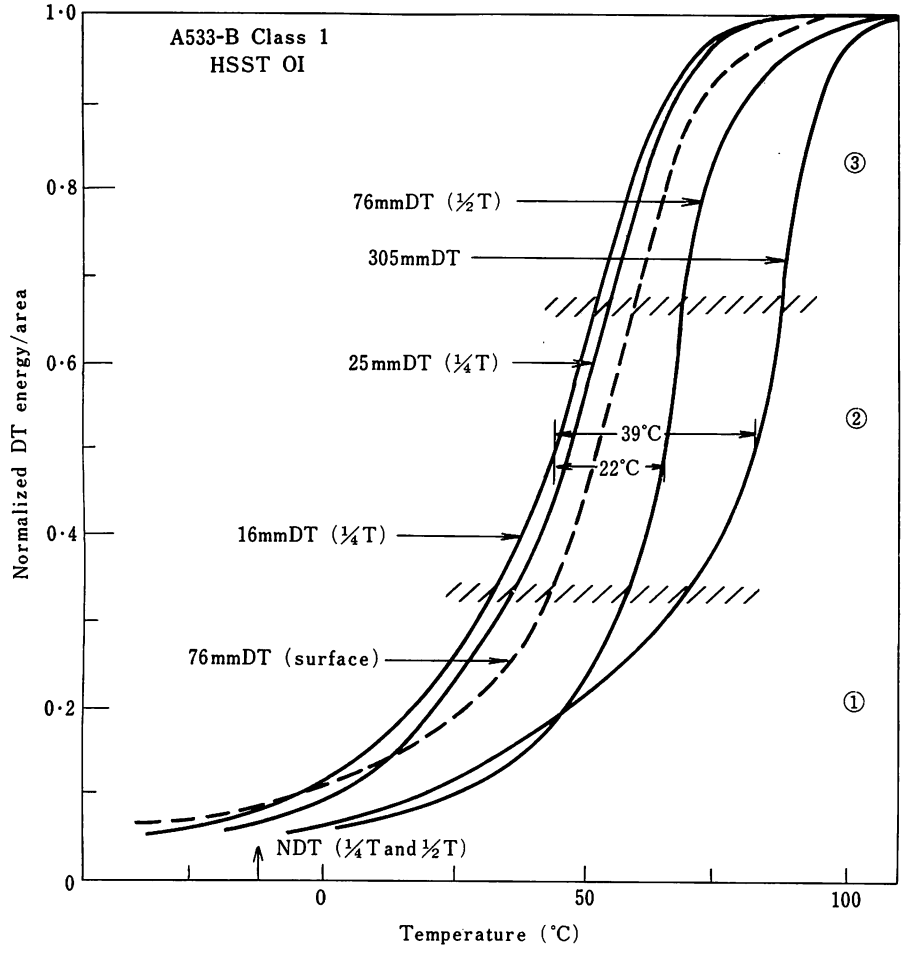

Fig. 5.
Illustrating the shift in the temperature transition of A533-B Class 1 steel with increasing section thickness. The energy-temperature transition curves for DT specimens from 16 mm to 305 mm in thickness are normalized to a constant upper shelf energy value. Note that both, toe and midtransition regions are shifted to a higher temperature with increasing constraint (thickness).

It is difficult to compare graphically the temperature-transition features of samples taken from surface-and-center locations using linear coordinates because of the sigmoidal shape of the DT energy-temperature relationship. Comparison of these relationships can be simplified by using a semi-log graph of DT energy in the temperature-transition region which tends to provide linear relationships. This is illustrated by the semi-log graph shown in Fig. 6 for DT energy values obtained from the surface-and-center regions of a 64 mm-thick plate in the A517-F steel.

The first observation from the position of the two curves in Fig. 6 for the 16 mm DT specimens is that there is a substantial gradient in fracture toughness from surface-to-center in the temperature-transition region. However, at temperatures corresponding to the upper shelf values, the DT energy values for the two locations are essentially the same. The NDT temperature of surface material was −84°C, and the NDT temperature for center material was −34°C. The limit of dynamic plane strain fracture for the full section was −62°C indicating that the integrated, full-thickness dynamic plane strain limit was affected more by the characteristics of the surface material than by the characteristics of the center material. Comparing the fracture resistance

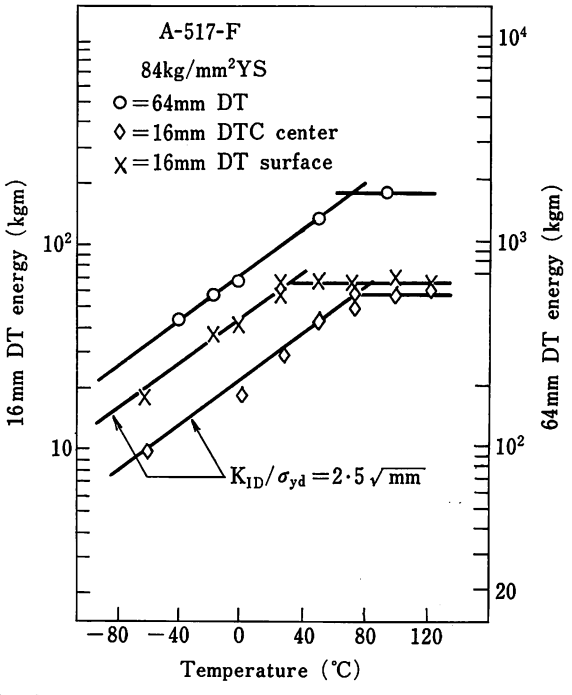

Fig. 6. Semi-log graph of DT energy as a function of temperature for subthickness and full-thickness DT specimens of A517-F steel in a 64 mm-thick plate. The plane strain limits for the 16 mm DT specimen for surface-and-center locations are noted at a K_{ID}/σ_{yd} level of $2\cdot5\sqrt{mm}$.

of surface material to that for the full section, the temperature shift in the plane strain fracture limit of 22°C due to the increased constraint capacity of a 64 mm-thick section over that for a 16 mm-thick section is considered nominal since it has been observed for other steels[14].

The lines on the semi-log plot in Fig. 6 through the DT energy data for the surface-and-center locations and the full-thickness points are parallel. This is not a consistent observation when DT energy-temperature relations are analyzed for other steels, and this observation should not be considered to be the general case. It can be also be noted that the temperature transition region for the A517-F steel in this plate extended over a long temperature range, 140°C. This indicates that in some steels fracture resistance does not build up rapidly in the low regions of the transition temperature range immediately above the plane strain limits. Additionally, there is a temperature region where flaws in the central portions of the plate can extend in a brittle fashion while ductility is maintained in the surface regions. Although ductile surface regions can provide significant fracture protection from surface flaws, this condition contributed to an unexpected, fast fracture in a pressure vessel that was undergoing a fatigue test[15].

The above example illustrates how the DT test can be used to characterize the fracture toughness of materials with a surface-to-center metallurgical gradient. It should be recognized that metallurgical gradients tend to complicate a fracture-safe analysis especially when the material operates in the transition temperature region. Therefore, the application of materials with metallurgical gradients to high-performance structures should be given a critical review and avoided if possible.

2.5 Statistical aspects

One very important factor that must be considered by design engineers is the variation in mechanical properties from lot to lot of material produced to a given specification. It is generally recognized that variations in mechanical properties exist, and for this reason, tensile properties are usually set at a minimum level. This same philosophy can be used for fracture-safe design when selecting criteria for fracture resistance, but in some cases the variation in quality of the economical materials is so great that it is practical to specify selection of material on a plate-to-plate basis. The system for selection of material that is optimum for any particular case is, of course, dependent upon specific circumstances.

The variations in fracture resistance that can be expected in normal production of steel products are illustrated in Fig. 7. The frequency distribution curves shown in Fig. 7 are for NDT temperatures that were obtained from plate products in various commercial steels, and a significant displacement of the frequency distribution curves for the NDT temperatures can be seen for various alloys and heat treatments. For some applications, the optimum approach for selecting materials would be to choose

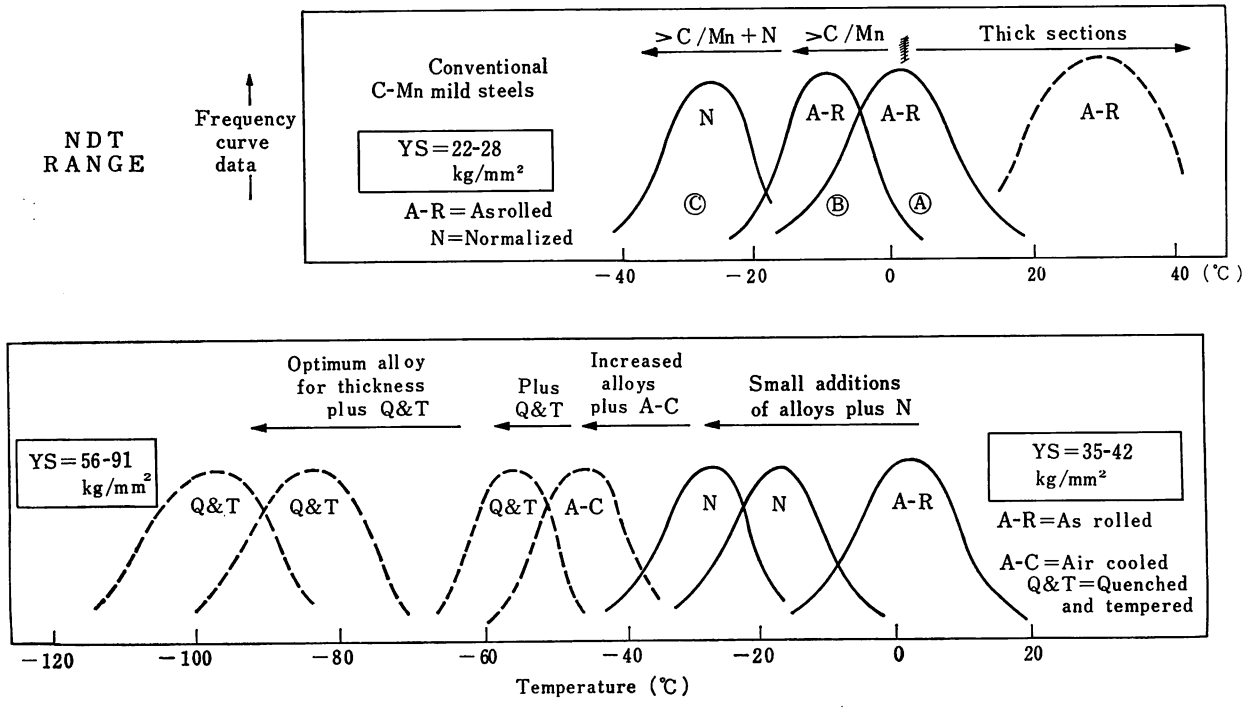

Fig. 7. Illustrating the statistical aspects of criteria for ductility and toughness. Frequency distribution curves for the NDT temperature for various steels indicate that the quality of specific steels varies over a wide range.

a steel whose entire NDT temperature distribution curve fell below the minimum service temperature. For other applications, the economical answer would be to select certain plates whose NDT temperatures were certified to be below the minimum service temperatures. The problem of assigning a specific NDT index, or any other fracture toughness criterion, to a specific type of steel is readily apparent from the width of the distribution curves for NDT temperatures in Fig. 7. Since catastrophic fracture starts from the interaction between a flaw and stresses on a localized scale, a minimum requirement should be that all critical regions should be fabricated from material of a known, minimum quality level. Hopefully, the general quality level of the more economical, high-strength steels will improve and become more consistent as fracture toughness criteria become more generally used in design procedures. Meanwhile, the statistical aspects with respect to quality level is an important consideration for fracture-safe design.

3. MODELS FOR STRUCTURAL ANALYSES

3.1 Linear-elastic fracture mechanics

When the fracture resistance of a material is sufficiently low to permit fracture to occur under plane strain conditions, the relationships between stress, flaw size, and critical stress-intensity factors can be calculated from LEFM theory. The analytical power of LEFM can be made more readily available for design considerations in graphical form as shown in Fig. 8 where a graphical representation of the following equation is shown:

$$K_{IC} = 1{\cdot}1\,\sigma\sqrt{\pi a}/\sqrt{Q}$$

The critical plane strain stress-intensity factor is K_{IC}, σ is stress, a is flaw size and Q is a geometry factor. The graph shown is for the case of a flaw with a length-to-depth ratio of three to one, and similar charts can be drawn for other stress and flaw conditions[7]. The relationships will change with various loading systems, but a surface flaw under tensile loading can be considered as a "worst" case condition.

The critical flaw sizes shown in Fig. 8 illustrate several important generalities concerning plane strain fracture. For example, it is readily apparent that extremely small flaws are critical in material at yield level stresses with fracture toughness levels less than a K_{IC}/σ_{ys} ratio of $2{\cdot}5\sqrt{mm}$. Such flaws would be difficult to detect by conventional inspection methods in large structures. In fact, critical flaw sizes indicated for elastic stress levels over the full range of LEFM analysis indicate that fracture-safe design predicated upon maintaining flaws below a certain critical size requires a rigorous inspection program including either periodic proof testing or a highly reliable system for flaw detection. It is therefore apparent that fracture-safe design based exclusively upon a LEFM model is practical only for those cases where the use of high-stfength, brittle material is required to provide an ultrahigh strength-to-weight ratio. The majority of structures and pressure vessels can be constructed with materials of higher fracture resistance, which precludes the potential for a strain type of fracture.

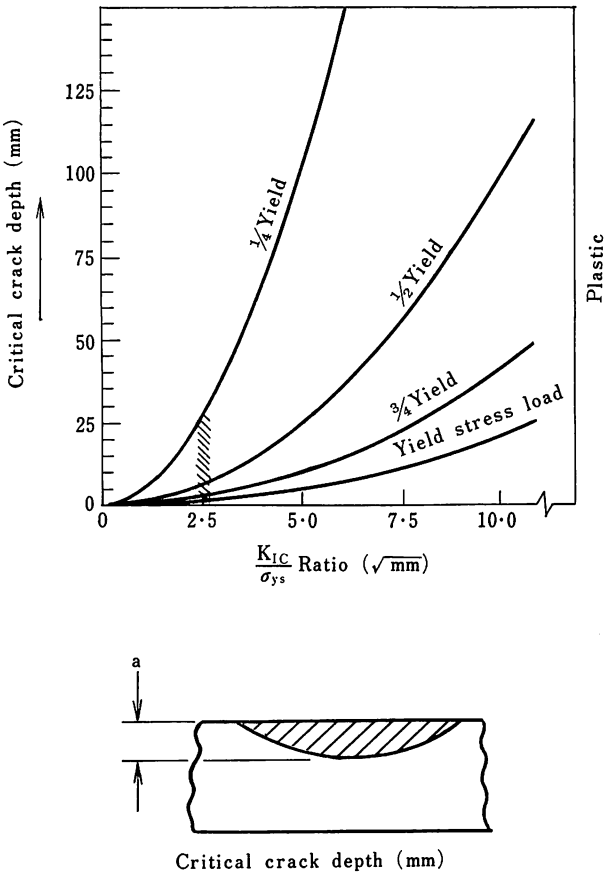

Fig. 8. Relationship of flaw size and stress requirements for the initiation of plane strain fracture as a function of K_{IC}/σ_{ys} ratios. The relationships shown are for a surface crack with a length to depth ratio of 3:1 under tensile loading.

3.2 Fracture analysis diagram

The FAD was the first model developed for translating criteria of fracture resistance into structural parameters. The FAD shown in Fig. 9 is for the general case involving sections 6 to 50 mm in thickness. The effects of added constraint for heavier sections can be factored in by an appropriate shift in the CAT curve[2]. Conditions for initiation and propagation are illustrated on the FAD, and the effects of the very rapid increase in fracture resistance in the temperature-transition region is readily apparent.

Valid use of the FAD for structural analysis of a

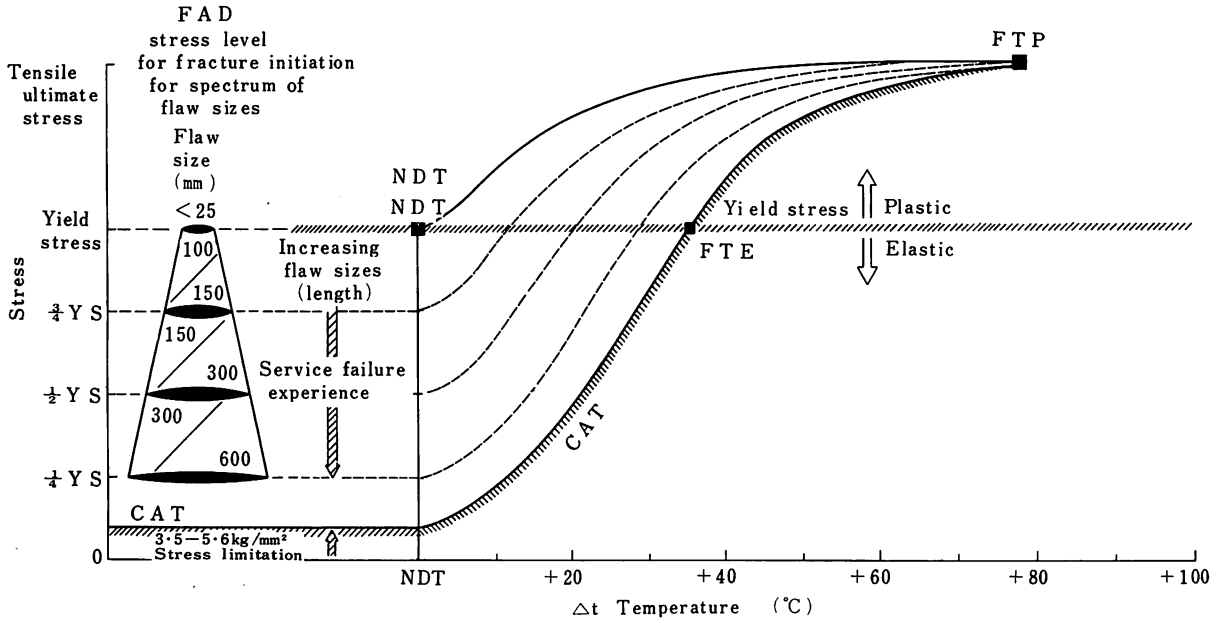

Fig. 9. Generalized Fracture Analysis Diagram (FAD) for steels.

specific steel requires the fracture resistance at the upper shelf level to be at an adequately high level with respect to yield strength, and the transition temperature range to be within that indicated on the temperature scale (67°C). These qualifications become critical for products which are given quench-and-temper heat treatments, especially when hardenability is insufficient for the sections involved. Illustrations of valid uses of the FAD for fracture-safe design of steel structures are extensive, and the reader is referred to the references for detail description of various applications[1-4].

3.3 Ratio analysis diagram

The model with wide range capability for translating fracture toughness criteria into structural parameters is the Ratio Analysis Diagram (RAD). The criteria of fracture toughness on the RAD are in terms of either DT energy or K_{IC} values, and these criteria apply to the upper shelf level regions above the temperature transition range. The general RAD for steels is shown in Fig. 10 with zones outlining the characteristics of specific classes of materials.

The slope of the ratio lines on the RAD illustrates the general requirement for an increase in fracture resistance as yield strength is increased in order to maintain a fixed level of structural performance. The upper bound of LEFM theory and the K_{IC}/σ_{ys} line analysis for providing the critical structural parameters are dependent upon the constraint capacity of the materials being considered. It is apparent from the zones outlined on the RAD that the most widely used commercial steels should never have a fracture problem at temperatures above the transition-temperature range. Operation within the temperature-transition range can lead to problems, and the FAD is the appropriate diagram for a fracture-safe analysis with these materials. However, as yield strength approaches the 70 to 105 kg/mm² range, criteria for fracture resistance become more critical at all temperatures, and a more precise analysis of fracture toughness in the temperature-transition region is required because the high margin of fracture resistance normally expected in steels at the critical temperature indexes may not be available.

From this brief discussion, it is apparent that the RAD contains a great amount of information concerning the performance of the whole system of steel alloys. In addition, for the high-strength steels the RAD provides a model that can readily be used for trade-off analyses involving yield strength, metal quality, design refinement, and flaw size control considerations. Detailed discussion of these analyses is provided in Refs. 4 and 16.

3.4 Plastic instability resistance diagram

A more recently developed model for translating criteria of plastic fracture resistance into structural parameters uses the R-curve approach[12]. For engineering purposes, the R-curve analysis classifies performance into one of a series of levels in a manner similar to that conventionally used for safety factors, i.e., whole number indices. This is considered adequate for most fracture control plans since the critical parameters pertaining to the material, structural and environmental aspects cannot be precisely defined or controlled in service. Therefore, an extremely precise criterion for plastic fracture resistance is not warranted, and final decisions must be on the conservative side.

The model for an R-curve analysis is shown in Fig. 11 where six levels of structural performance are indicated. The first three separations pertain

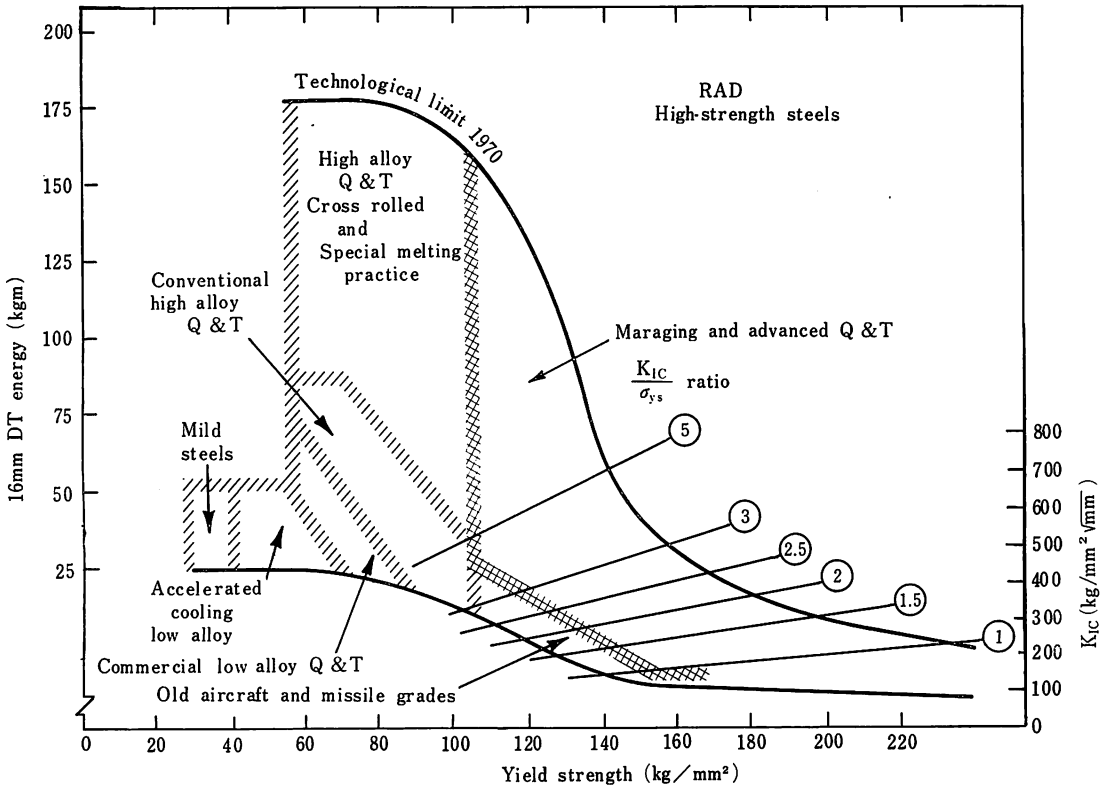

Fig. 10. Metallurgical zoning of Ratio Analysis Diagram (RAD) for steels indicating the mechanical characteristics of various generic types of steels.

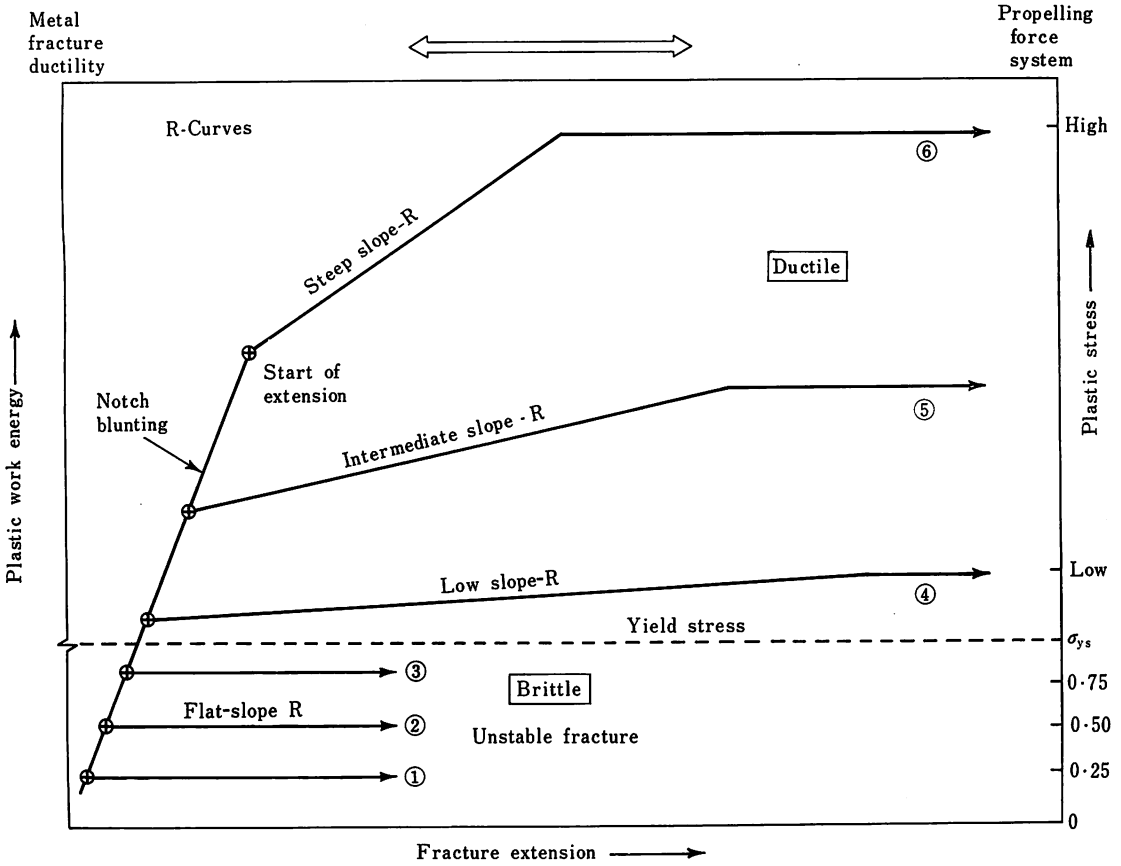

Fig. 11. Generalized R-curve analysis diagram showing a six-level fracture toughness classification system. The diagram illustrates that fracture ductility of the metal must increase with the propelling force of the structure to achieve fracture safety.

to fracture occurring under plane strain conditions, which are shown as horizontal lines. The horizontal lines indicate that resistance to crack propagation under plane strain conditions does not increase as the crack extends. In contrast, when fracture resistance is high and fracture occurs after net section yielding, resistance increases as the crack front extends.

A three-level classification in the two types of fracture behavior is indicated on the diagram. The appropriate level of fracture resistance depends upon design refinement and service conditions. For example, a structure with highly refined details and planned inspection periods may be fabricated in materials having a low R-curve slope. Structures with poorly designed details and regions which are essentially noninspectable require the use of materials with higher R-curve slopes to provide fracture safety. Any structure whose failure would be extremely catastrophic should be designed with materials of high R-curve slope. Further development of the R-curve model is currently planned to include structural parameters such as compliance, critical strains and critical loads. Detailed discussion concerning the current development of the R-curve model is provided in Refs. 12 and 17.

4. SUMMARY AND CONCLUSIONS

The development, standardization and the use of practical tests for assessing fracture toughness are the key to more effective utilization of high-strength steels. The Dynamic Tear test has been shown to incorporate the mechanical features necessary for accurately measuring fracture resistance over the broad range of performance encountered in commercial materials. Recently a coupling between DT energy and linear-elastic fracture mechanics parameters has been developed which will encourage more extensive use of the analytical capabilities of LEFM, although it is applicable only to brittle materials. More importantly, the DT test permits quantitative criteria to be established for the regime of mixed-mode fracture and for the regime of fully plastic fracture. Until a practical, quantitative analysis for calculating stress and strain conditions at structural details is developed, fracture-safe design in general engineering practice will rely heavily upon the fracture resistance of the material to compensate for the uncertainty of stresses and strains at complex details.

Plans for controlling fracture safety require procedures for selecting materials with an adequate level of fracture resistance. The Ratio Analysis Diagram (RAD) provides a graphical relationship between pertinent material and structural parameters. For many designs, the service temperatures are critical and the Fracture Analysis Diagram (FAD) is the relevant model. The more recently developed R-curve model provides an analysis for incorporating such structural features as compliance and redundancy. This latter model is not completely evolved at the present time, but many of its current features can be useful in decisions concerning trade-offs in material and design parameters. A good incentive to include fracture safety in design procedures should be the economic benefits from more effective utilization of the new, high-strength materials.

ACKNOWLEDGMENTS

The author expresses his appreciation for the technical guidance and encouragement of Mr. W.S. Pellini and the financial support of the Office of Naval Research, the Naval Ship Systems Command, Code 03422, and the Naval Facilities Engineering Command, Code 0321C. The extensive use of the work of his colleagues and the help of expert technicians for performing the experimental aspects of the work are also gratefully acknowledged.

REFERENCES

1) W.S. Pellini and P.P Puzak: NRL Report **5920**, (March 15, 1963)
2) W.S. Pellini: NRL Report **6713**, (April 3, 1968), WRC Bulletin **130**, (May 1968)
3) F.J. Loss and W.S. Pellini: NRL Report **6913**, (April 14, 1969)
4) W.S. Pellini: NRL Report **6957**, (Sept. 23, 1969)
5) A.S. Tatelman and A.J. McEvily, Jr.: *Fracture of Structural Materials*, (1967), Wiley
6) Vol. IV of *Engineering Fracture Design*, (1969), Academic Press
7) W.F. Brown and J.E. Srawley: ASTM Special Technical Publication **410**, (1966)
8) E.A. Lange, P.P. Puzak and L.A. Cooley: NRL Report **7159**, (Aug. 27, 1970)
9) E.A. Lange and F.J. Loss: NRL Report **6975**, (Nov. 17, 1969)
10) L.A. Cooley and E.A. Lange: NRL Report **6993**, (Jan. 16, 1970)
11) G.E. Nash: NRL Report **6864**, (Jan. 30, 1969)
12) W.S. Pellini and R.W. Judy, Jr.: NRL Report **7187**, (Oct. 19, 1970)
13) W.S. Pellini and P.P. Puzak: NRL Report **6030**, (Nov. 5, 1963)
14) F.J. Loss: NRL Report **7056**, (May 14, 1970), HSSTP TR-7
15) E.A. Lange, A.G. Pickett and R.D. Wylie: WRC Bulletin **98**, (Aug. 1964)
16) E.A. Lange: NRL Report **7046**, (May 4, 1970)
17) W.S. Pellini: NRL Report **7251**, (March 26, 1971)

DISCUSSION: See p. 342

Toughness and Effective Grain Size in Heat-Treated Low-Alloy High-Strength Steels

S. Matsuda T. Inoue H. Mimura Y. Okamura

Nippon Steel Corporation

Fundamental Research Laboratories

One of the most important factors controlling the toughness of steels is the ferrite grain size. This is true for ferritic steels, in which the cleavage facet is controlled by the ferrite grain size obviously revealed by metallographic methods. In heat-treated steels with a structure such as tempered martensite and bainite, however, the ferrite grain size can not be well defined because of the difficulty in characterizing adequately the crystallographic features due to the complicated microstructure. The aim of this paper is to show that toughness of heat-treated steels is closely related to the "effective grain size" which is defined as a region in which cleavage cracks go through in a nearly straight fashion.

From observations on the fracture surfaces of tempered martensite, it has been found that the fracture unit is much larger than the ferrite lath size, that the brittle fracture mode of low-carbon tempered martensite is cleavage and that the cleavage plane is equivalent to that of the ferritic steel. Photo. 1 shows a large fracture facet of low-carbon tempered martensite with etch pits showing that the fracture facet is cracked along the $(001)\alpha$ plane.

In tempered lower bainite, from observations on surfaces fractured just above the impact transition temperature ($_{v}Trs$), it is confirmed that microcrack is mainly formed by cleavage. It is to be noted that intercrystalline fracture along bainitic ferrite lath boundaries is frequently observed on the brittle fracture surface in addition to the transcrystalline cleavage.

In tempered upper bainite, the observations on the fracture surfaces are similar to those on tempered martensite.

Since the fracture mode of heat-treated steels is similar to that of the ferritic steel whose cleavage fracture unit is related to the ferrite grain size, it is expected that the natural choice of microstructural unit relevant to fracture may be a region bounded by high-angle grain boundaries in which cleavage cracks go through in a nearly straight fashion. If such a region in heat-treated steels is defined by a concept of "effective grain size", it must correspond to the microstructure having specific crystallographic orientation such as a ferrite grain.

Photo. 7 shows a nickel-plated fracture surface of low-carbon tempered martensite, etched with a new etching technique utilizing a modified Kalling reagent. A striped pattern with dark and bright contrasts is observed within each bundle (the group of parallel martensite laths is designated as a "bundle"). This striped pattern has been confirmed to reveal the crystallographic orientation difference. Namely, the dark and bright area corresponds to a set of two particular crystallographic orientations derived from 24 variants of the Kurdjumov-Sachs relationship. The packet of martensite laths formed by transformation following the same variant of the K-S relationship is hereafter designated as a "co-variant packet". It is noticed in Photo. 7 that the fracture path tends to alter direction at the co-variant packet boundaries. This implies that the effective ferrite grain relevant to fracture exactly corresponds to the co-variant packet, which is well defined when suitably etched. Photo. 8 shows the effect of the prior austenite grain size on the fracture characteristics of low-carbon tempered martensite. As the austenite grain size decreases, the size of the co-variant packet decreases and in all cases the cleavage fracture facets (effective grain size) are exactly related to the co-variant packets.

In tempered lower bainite the co-variant packet is always smaller than that of tempered martensite with the same austenite grain size. This offers a good explanation of the difference in size of cleavage facets between tempered martensite and tempered lower bainite having the same austenite grain size. Fig. 8 shows the effect of the bainite transformation temperature on the effective ferrite grain size. It is clearly seen that the effective ferrite grain size decreases as the transformation temperature is lowered.

Fig. 7 shows the effect of the effective ferrite grain size on the impact-transition temperature ($_{v}Trs$) of tempered martensite and tempered lower bainite. A linear relationship is obtained between $_{v}Trs$ and $\langle d\rangle^{-1/2}$ ($\langle d\rangle$ is the mean effective ferrite grain size). Thus, it can be said that the toughness in the heat-treated steels we studied correlates well with the "effective grain size." The results are summarized as

follows:

1) The concept of the effective grain size is very useful as a criterion for the toughness of heat-treated steels.

2) The brittle fracture mode of low-carbon tempered martensite and upper bainite is the (100)α cleavage.

3) The brittle fracture mode of tempered lower bainite exhibits two types of fracture: (100)α cleavage and intercrystalline fracture along the boundary between bainitic ferrite laths. But microcracks are mainly formed by cleavage.

低合金調質高張力鋼の靱性と有効結晶粒径

松田昭一　井上　泰
三村　宏　岡村義弘
新日本製鉄株式会社　基礎研究所

1. 緒　　言

脆性破壊の基本的な様式が劈開である場合には，結晶粒が靱性を支配する重要な因子になる．それは劈開クラックの伝播に対して粒界が大きな抵抗になるためである．フェライト鋼においては {100}α 面で劈開することがすでに明らかにされており，フェライト結晶粒が細かくなるにしたがって靱性は向上する．一方，調質鋼の基本組織である焼もどしマルテンサイト，焼もどしベイナイトの破壊様式については，Turkalo[1] が中炭素鋼の焼もどしマルテンサイト，焼もどし下部ベイナイトの脆性破面は各々の微視組織に対応して細かく，上部ベイナイトでは旧オーステナイト粒径に対応することを見出した以外，ほとんど明らかにされていない．それにもかかわらず，フェライト鋼の類推から調質鋼の優れた靱性はその緻密な組織によるといった曖昧な解釈がなされている．

オーステナイト変態生成物，特にマルテンサイト，ベイナイトの破壊様式についても最近かなり精力的に研究が行なわれているが，まだ統一的な結論が出されていない．例えば，Irani[2] は 13% Cr-0·23% C オースフォーム鋼の脆性破面単位は直線的で大きく，マルテンサイト板の大きさとは相関がないことを見出している．Beachem と Pelloux[3]，Srawley[4] も同様な結果を観察し，この型の破壊様式を擬劈開と称している．また，Lindborg と Averbach[5] は 0·3%C マルテンサイト鋼の脆性破面について結晶学的特徴を調べ，マルテンサイト板を単位にした数多くの小破面は単純な結晶方位をもっていないと結論している．

このような現状を省みると，オーステナイト変態生成物あるいはその焼もどし組織の脆性破壊を新しい視野から解明していくことが必要ではないかと思われる．本論文では，調質鋼の脆性破壊の様式がフェライト鋼のそれと基本的には同じであることを示し，そのことおよびフェライト鋼の劈開破面単位がフェライト粒に対応することより類推して調質鋼においても劈開破面単位を仮想的にフェライト粒と考え，それを“有効結晶粒”と定義する．そして，このように定義された有効結晶粒という概念が調質鋼の靱性評価の基準としてきわめて有効であることおよび有効結晶粒がある特殊な結晶方位からなる微視組織に対応することを示す．

Table 1. Chemical composition and heat treatment.

Steel	Chemical composition (wt%)						Heat treatment
	C	Mn	Si	Mo	Ni	Cr	
1	0·12	0·5	0·2	0·4	2·4	1·0	1300°C×30min WQ+600°C×1hr
							1000°C×30min WQ+600°C×1hr
							835°C×10min WQ(4times)+600°C×1hr
							1300°C×30min 420°CQ+600°C×1hr
							1000°C×30min 420°CQ+600°C×1hr
							835°C×10min WQ+835°C×10min 380°CQ+600°C×1hr
2	0·12	0·5	0·2	0·4	3·5	—	1300°C×30min WQ
							1300°C×30min WQ+600°C×1hr
							1300°C×30min 250°CQ
							1300°C×30min 250°CQ+600°C×1hr
							1300°C×30min 300°CQ
							1300°C×30min 300°CQ+600°C×1hr
							1300°C×30min 350°CQ
							1300°C×30min 350°CQ+600°C×1hr
							1300°C×30min 380°CQ
							1300°C×30min 380°CQ+600°C×1hr
							1300°C×30min 410°CQ
							1300°C×30min 410°CQ+600°C×1hr
							1300°C×30min 440°CQ
							1300°C×30min 440°CQ+600°C×1hr
							1300°C×30min 470°CQ
							1300°C×30min 470°CQ+600°C×1hr

2. 実験方法

電解鉄を素材にして真空溶解により 20kg の鋼塊を溶製した．鋼塊はアルゴン雰囲気中で 1250°C×40min 加熱後，仕上温度 950°C で 13mm に圧延した．圧延材より 12mm×12mm×55mm の角材を切出し，標準 2mm V ノッチシャルピー試験用の試料とした．

試料の化学組成と熱処理を Table 1 に示す．鋼 2 の合金元素の組合せは上部ベイナイト組織によく混入する高炭素島状マルテンサイトの量を少なくするのに効果的である．熱処理は鋼 1 については種々のオーステナイト粒度をもった焼もどしマルテンサイト，焼もどし下部ベイナイトを作ることを目的とし，鋼 2 については生成温度の異なるベイナイトおよび焼もどしベイナイトを得ることを目的として行なった．焼もどし条件は各組織とも最適靱性が得られる 600°C×1h に統一した．

3. 実験結果と考察

3.1 焼もどしマルテンサイトの微視組織と衝撃特性

Photo. 1 に示した透過型電子顕微鏡による観察結果から明らかなように，焼もどしマルテンサイトは高密度の転位を含んだラス状のフェライト粒と微細な炭化物の集合体から構成されている．Mf で指定した大きなフェライト粒（左肩に示した光学顕微鏡写真では白色に見える部分）は，マルテンサイト変態時に Ms 点直下で最初に変態したマルテンサイトが焼もどしを受けたものである．

Fig. 1 は焼もどしマルテンサイトの衝撃遷移温度におよぼすオーステナイト粒度の影響を示したものである．この研究では靱性評価の基準として 50% 破面遷移温度 ($_{v}$Trs) を採用した．Fig. 1 より明らかなようにオーステナイト粒径が小さくなるにしたがって $_{v}$Trs は下がる．

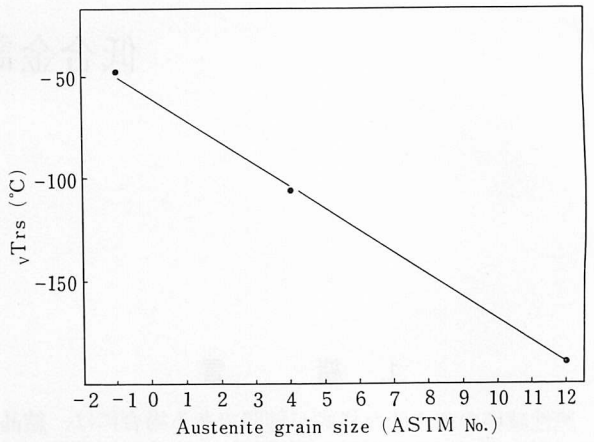

Fig. 1. Effect of prior austenite grain size on the impact-transition temperature $_{v}$Trs. Tempered martensite, steel 1.

フェライト鋼については Cottrell[6], Petch[7] によって提唱された理論式に基づいて数多くの実験が行なわれ，$_{v}$Trs と $d^{-1/2}$ または $\ln d^{-1/2}$ (d はフェライト粒径) との間に一次関係が成立つことが明らかにされている．一方，Fig. 1 の結果より焼もどしマルテンサイトにおける実効的な組織がラス状のフェライト粒と炭化物との集合体であるにもかかわらず，オーステナイト粒度と $_{v}$Trs との間にほぼ一次関係が成立っている．この明らかに間接的な関係を理解するためには，脆性破壊の観点からオーステナイト粒度が焼もどしマルテンサイトの微視組織におよぼす本質的な効果を明らかにすることが重要である．そのためには，まず焼もどしマルテンサイトの脆性破壊の様式をフェライト鋼のそれと対照して類似性を検討してみるのが最も効果的であろう．

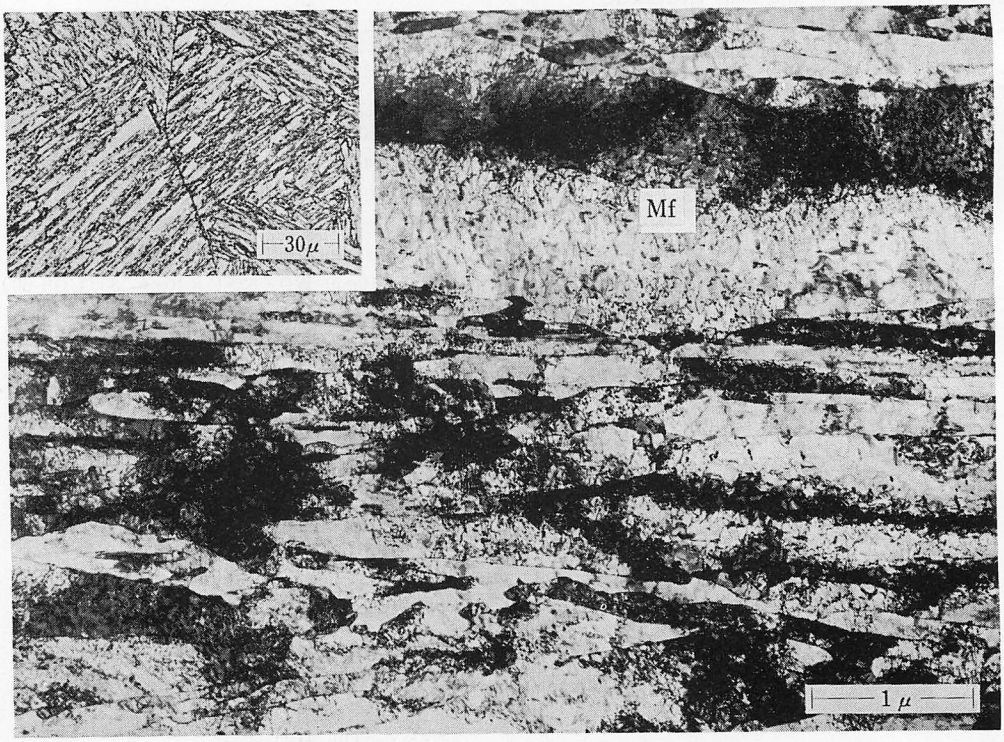

Photo. 1 Transmission electron micrograph of low-carbon tempered martensite in steel 1. An optical micrograph is shown in the upper left corner. Mf: first-formed martensite lath. 1300°C×30 min WQ+600°C×1hr.

3.2 焼もどしマルテンサイトの脆性破面の特徴

焼もどしマルテンサイトとフェライト鋼の脆性破壊の類似性を検討するためには，脆性破壊の発生から伝播への動的過程を究明することが厳密には必要である．しかし，現状ではこれを行なう効果的な手段がなく，破断した脆性破面の様式を解析することによって因果関係を推定し類似性を議論するのが唯一の方法である．

Photo. 2 はオーステナイト粒径が大きい焼もどしマルテンサイトの脆性破面である．破面は大きく全体として平らであるがその上にいくつかの微視的特徴が観察される．矢印は数多くの埋没クラック (submerged crack) が合体する時に接合部が塑性的にひきちぎられることによって生じたテアリッジ (tear ridge) を示しており，リバーパターン (river pattern) となってほぼクラックの伝播方向に走っている．テアリッジによって囲まれた領域には非常に繊細なリバーパターンが観察され，その方向はテアリッジを境にして変わっている．後者のリバーパターンはフェライト鋼の劈開面に観察されるそれと同じ機構に基づいて作られたものであろう．破面を軽く腐食して微視組織とテアリッジとの対応関係を調べてみると，Photo. 3 に示したようにテアリッジの位置はラス状のフェライト粒界に対応していることがわかる．また，ある場合には Photo. 2 とは異なり一点から発生したリバーパターンが扇状に拡がって平らな破面全体を覆うこともある．このような破面には微視組織に対応したテアリッジがあまり観察されないのが特徴である．これらの破壊様式の特徴より明らかなように，一つの平らな脆性破面は擬劈開ないしは劈開によって形成されていることがわかる．

Photo. 2. Fracture surface of tempered martensite in steel 1. Arrows show tear ridges. 1300°C×30 min WQ+600°C×1 hr.

Photo. 4は擬劈開した平らな破面に Table 2 に示した試薬を用いて直接エッチピットを現出し，破面の結晶方位を調べたものである．この腐食液は {110}α 面を選択的に腐食するのが特徴で，Photo. 4 において {110}α 面より構成されたエッチピットの型を解析するとすべて (001)α 面に沿って劈開していることがわかる．擬劈開であるにもかかわらず破面の結晶方位がほぼ一定であることは，隣接するラス状のフェライト粒がほぼ連続して同じ方位をもった結晶であることを示している．

焼もどしマルテンサイトの脆性破面にもタング (tongue) が観察される．このタングはフェライト鋼の劈開面によく観察されるもので，マトリックスと変形双晶との界面で劈開することによって形成されるといわれてい

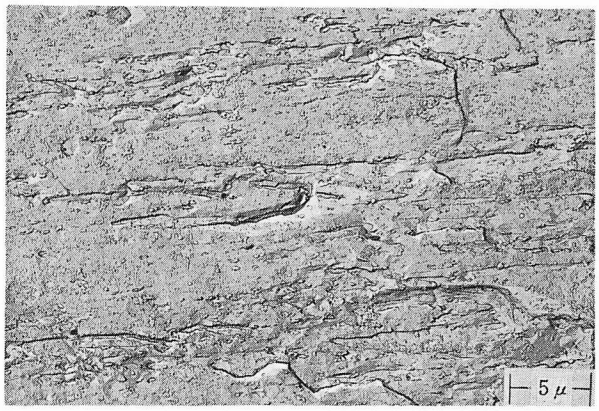

Photo. 3. Fracture surface of tempered martensite in steel 1, etched with saturated picral. 1300°C×30 min WQ+600°C×1hr.

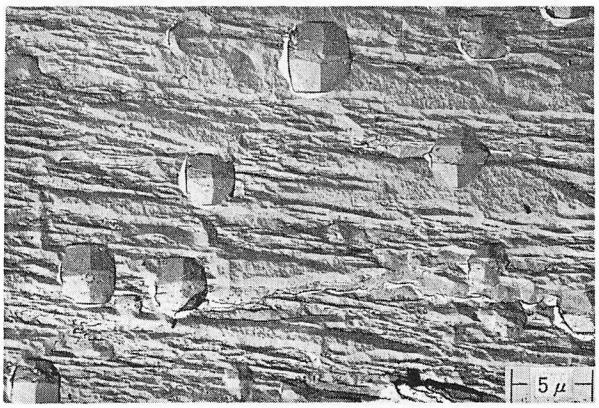

Photo. 4. An example of etch pits showing (001)α formed on a large brittle fracture facet of tempered martensite in steel 1. 1300°C×30 min WQ+600°C×1hr.

Table 2. Etchants and etching time.

Etchant A		Etchant B		Etchant C	
Reagent	Time	Reagent	Time	Reagent	Time
HCl 1cc + H_2O_2 20cc + H_2O 20cc	<5sec	Saturated aqueous solution of $FeCl_3 \cdot 6H_2O$ 20cc + HCl 10cc + H_2O 100cc	<50sec	HCOOH 25cc + H_2O_2 25cc + C_2H_5OH 25cc + H_2O 25cc	<5sec

Etchants A, B and C are used successively.

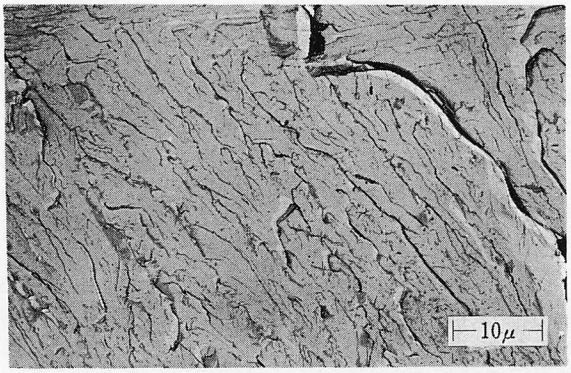

a) 1300°C×30 min WQ+600°C×1 hr.

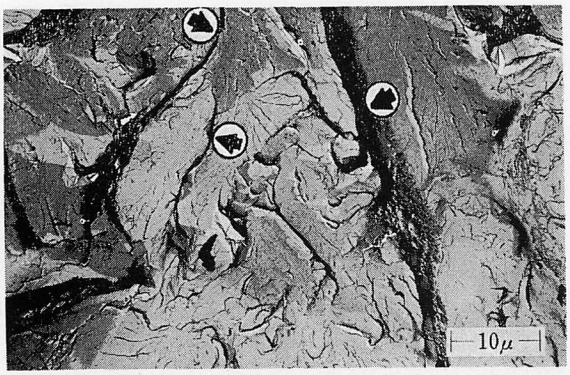

b) 1000°C×30 min WQ+600°C×1 hr.

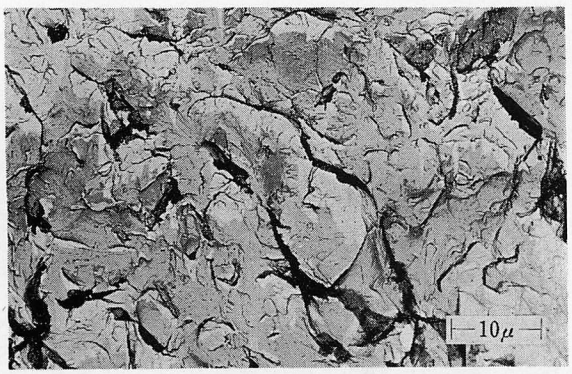

c) 835°C×10 min WQ (4 times)+600°C×1 hr.

Photo. 5. Fracture surfaces of low-carbon tempered martensite with various austenite grain sizes in steel 1. Arrows show tear lines.

る[8]．フェライト鋼の劈開破面の基本的な特徴は{100}α面で劈開すること，破面にリバーパターン，タングが観察されることなどであり，一方，焼もどしマルテンサイトの劈開破面にもこれらの特徴がすべて網羅されている．このことは焼もどしマルテンサイトの脆性破壊の機構がフェライト鋼のそれと基本的に類似していることを意味している．

Photo. 5a),b),c)は焼もどしマルテンサイトの脆性破面がオーステナイト粒度によってどのように変化するかを示したものである．オーステナイト粒径が大きい場合には(Photo. 5a))先にも述べたように擬劈開ではあるが全体として平らな大きい破面である．ところが，オーステナイト粒径が小さくなるにしたがって平らな破面単位（今後，劈開破面単位と呼ぶ）が小さくなり，隣接する劈開破面の境界には矢印で示したようにテアライン (tear line) が観察される(Photo. 5b), c))．また，テアラインをはさんだ2つの劈開破面には大きな色調の差がある．これはクラックの進行方向がテアラインの位置を境にして大きく変わっていることを意味している（テアラインとテアリッジの形成機構は同じである．本論文では1つの劈開破面上で観察される塑性的なちぎれをテアリッジと定義し，2つの劈開破面の境界で観察される塑性的なちぎれをテアラインと定義する)．フェライト鋼の脆性破壊の類推から，テアラインによって囲まれた劈開破面単位が焼もどしマルテンサイトの靱性を支配する要因になると解釈すれば，焼もどしマルテンサイトの靱性がオーステナイト粒度とともに変化する現象を定性的には理解することができる．これに関する詳しい議論は次節で展開する．

3.3 有効フェライト粒について[9-11]

衝撃破面遷移温度は粒界または粒内の炭化物から発生したミクロクラックが生長の過程で一度粒界によって停止され，新たにグリッフィスの条件が満たされた時に粒界を突破して伝播を開始し，最終的な脆性破壊に至らし

▼Fig. 2. Histogram obtained by lineal analysis of spacing d between two neighboring tear lines. The fraction of spacing is defined by $f_j \times d_j / \sum_i f_i \times d_i$, where d_i is the spacing and f_i, the frequency of spacing $d_i \pm 1 \cdot 25\,\mu$.
a) 1300°C×30 min WQ+600°C×1 hr.
b) 1000°C×30 min WQ+600°C×1 hr.
c) 835°C×10 min WQ (4 times)+600°C×1 hr.

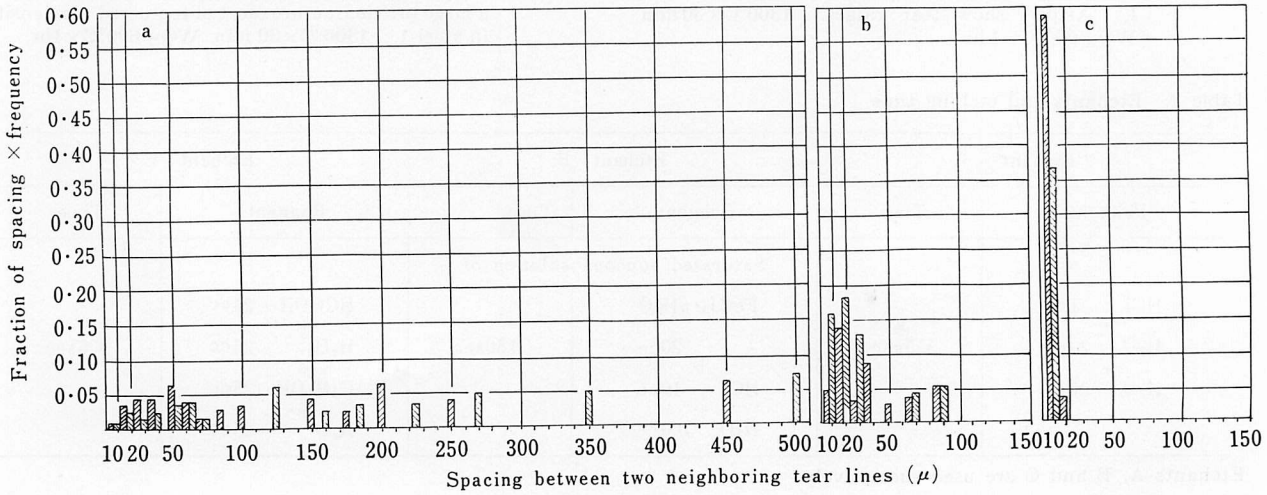

める温度であると解釈するのが最も自然であろう．このように解釈すると，ミクロクラックを停止し得る粒界すなわち最終的な脆性破壊を支配する粒界とは如何なる性質のものであるかが問題になる．ところで，フェライト鋼においては，劈開破面単位の大きさは光学顕微鏡においてはっきりと定義できるフェライト粒径にほぼ一致している．このことは脆性破壊に対して最も適切な微視組織の単位として大傾角粒界によって囲まれた領域を選ぶのが最も自然であることを示している．一方，焼もどしマルテンサイトにおいては微視組織が非常に複雑でその結晶学的特徴が十分に理解されていないため，フェライト粒をうまく定義することができない．しかし，フェライト鋼の劈開破面単位がフェライト粒に対することおよび両組織の破壊様式に類似性があることより類推して，焼もどしマルテンサイトにおいても劈開破面単位を仮想的にフェライト粒と考え，それを“有効フェライト粒”と定義する．

Fig. 3 はオーステナイト粒度の異なった焼もどしマルテンサイトの脆性破面より有効フェライト粒径をテアラインの間隔から求め，テアラインの間隔を横軸にその頻度を縦軸にして描いたヒストグラムである．各々のヒストグラムより有効フェライト粒径の平均値 $\langle d \rangle$ を求め，${}_{v}\mathrm{Trs}$ を $\langle d \rangle^{-1/2}$ に対してプロットすると Fig. 3 に示したようにきれいな一次関係が得られる．したがって，劈開破面単位の大きさという意味で定義した有効フェライト粒径が，焼もどしマルテンサイトの靱性を支配する要因になっていると考えてよさそうである．

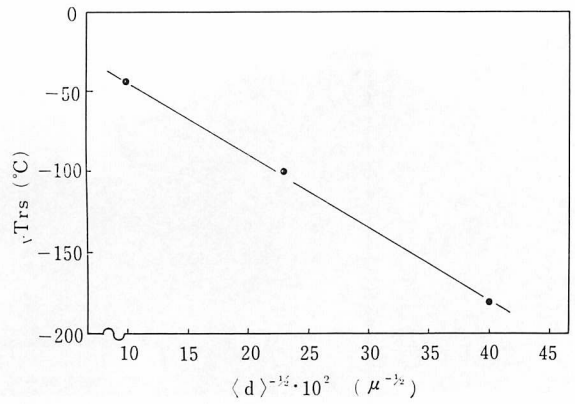

Fig. 3. Dependence of impact-transition temperature ${}_{v}\mathrm{Trs}$ on mean effective ferrite grain size $\langle d \rangle$. Tempered martensite, steel 1.

有効フェライト粒径はラス状フェライトの巾よりははるかに大きくオーステナイト粒径よりは小さい．一方，定義より有効フェライト粒は大傾角粒界によって囲まれた領域に対応しなければならない．そこで有効フェライト粒が焼もどしマルテンサイトの微視組織のうちどのようなものに対応するかということが問題になる．

3.4 テアラインと焼もどしマルテンサイトの微視組織との対応

Photo. 6 は焼もどしマルテンサイトの脆性破面を軽く腐食して破面と組織とを対応させたものである．テアラインの近傍は苛酷な塑性変形を受け組織がはっきりしない．しかし，比較的よく組織が現出されているところで対応関係を調べてみると次のことがわかる．テアライン

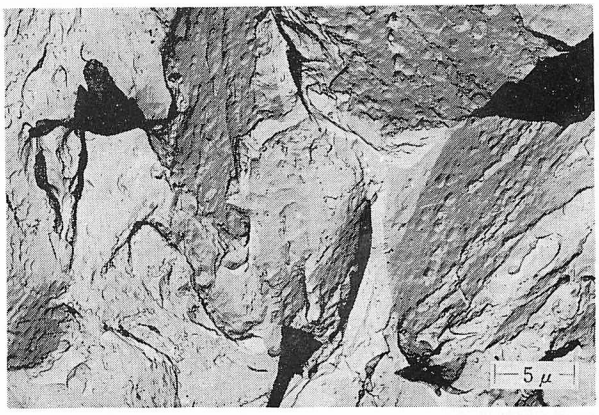

Photo. 6. An example of the fracture surface of tempered martensite in steel 1, etched with 2% nital+saturated picral. 1000°C×30 min WQ+600°C×1 hr.

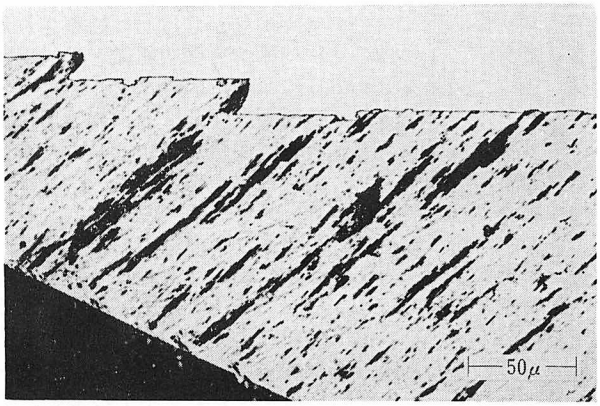

a) Type 1.

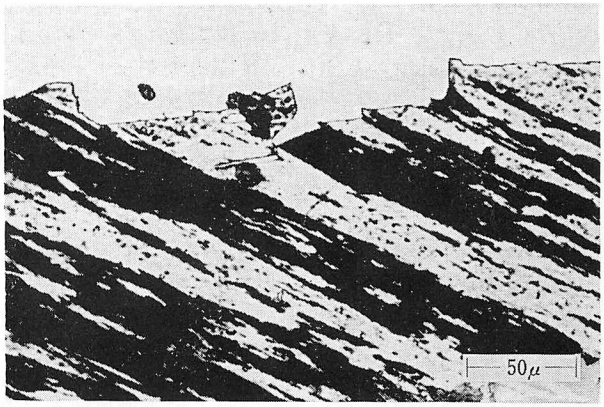

b) Type 2.

Photo. 7. Section of nickel-plated fracture surface of tempered martensite in steel 1, etched with modified Kalling reagent. Note change in direction of fracture at co-variant packet boundaries. 1300°C ×30 min WQ+600°C×1 hr.

によって囲まれた一つの劈開破面上の組織は平行に並んだラス状マルテンサイトの束（今後，平行に並んだマルテンサイトの束を“バンドル”(bundle) と称することにする．また，焼もどしによってマルテンサイトの結晶学的特徴は変わらないことを確かめている．したがって，結晶学的な観点から議論をする場合，焼もどしマルテンサイトをマルテンサイトと略しても何ら誤解を招かない）で構成されており，テアラインを境にしてマルテンサイ

Table 3. Modified Kalling reagent and etching time.

Reagent	Time
HCl 100cc + $CaCl_2$ 5g + CH_3CH 100cc	30sec

トのラス粒界の方向が変わっている．このことはバンドル粒界でテアラインが生じることを示しており，一方この粒界が大傾角粒界であることはマルテンサイト変態の結晶学的理論によって容易に証明できる．一般に旧オーステナイト粒界にもテアラインは生じるが，ある場合には粒界をはさんだ2つの破面が平らなこともある．

注目すべきことは一つのバンドルの中で微視組織との対応関係が明確でないテアラインがしばしば観察されることである．この種のテアラインと微視組織との対応関係を調べた結果をPhoto. 7に示す．Photo. 7a), b)はニッケルメッキをした破面の横断面をTable 3に示した修正カーリング液によって腐食して組織を現出したものである．通常の飽和ピクリン酸では1つのバンドルはほぼ一様に腐食されるが，修正カーリング液を使用するとバンドルの中に白黒の色調が観察される．この白黒の色調を持った帯状模様は方位の違った結晶を表わしている（この証明は次の節で行なう）．すなわち，白色部に対応する結晶は24通りの KURDJUMOV-SACHS のバリアント[12] (variant)のうちある特殊な関係にある2通りのバリアントのどちらか一方で変態したマルテンサイトの束を，黒色部は他方のバリアントで変態したマルテンサイトの束を表わしている．今後，同じK-Sバリアントで変態したマルテンサイトの束を“コバリアントパケット” (co-variant packet) と称し，略してパケットと呼ぶことにする．バンドルの中のパケットの分布をその特徴によって分類すると，

1) 1つのバンドルがほぼ同じ巾を持った2種類のパケットによって分割されている場合（Photo. 7a)，タイプ1) と

2) 一つのバンドルがほぼ一つのパケットから構成されている場合（Photo. 7b)，タイプ2）

とに大別される．特にパケットに注目して微視組織と破面とを対応させると，タイプ1ではクラックの方向はパケットの粒界で変わりそこにはテアラインが観察される．頻度は少ないがパケット粒界をはさんで両側の破面が平行なこともあるが，この場合にも概ね粒界にテアラインが観察される．タイプ2の破面は全体として直線的であり，所々にテアリッジが観察される．テアリッジの生じている位置には必ず結晶方位の異なった微細なパケットが観察される．

このことは，1つの劈開破面上に観察されるテアリッジ（Photo. 2, 3参照）は，ほぼ連続的につながった同じ結晶方位のパケットと量的には少ないけれどもそれらの間をうめている方位の異なったパケットとの境界で生じたものであることを示している．以上の実験事実より，バンドルの中で観察されるテアラインはパケットの粒界に対応すること，したがって，焼もどしマルテンサイトの脆性破面に生じるテアラインはほとんどすべて大傾角粒界に対応することが明らかになった．

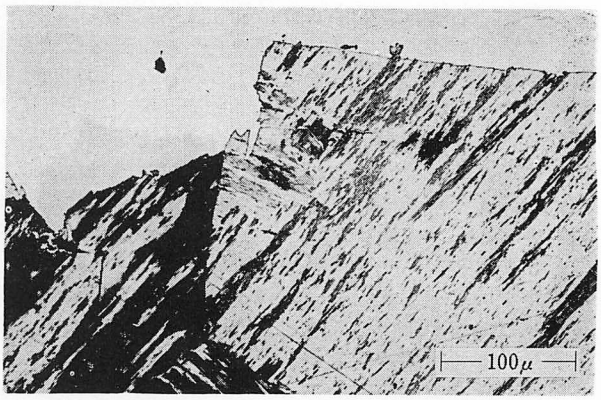

a) 1300°C×30 min WQ+600°C×1 hr.

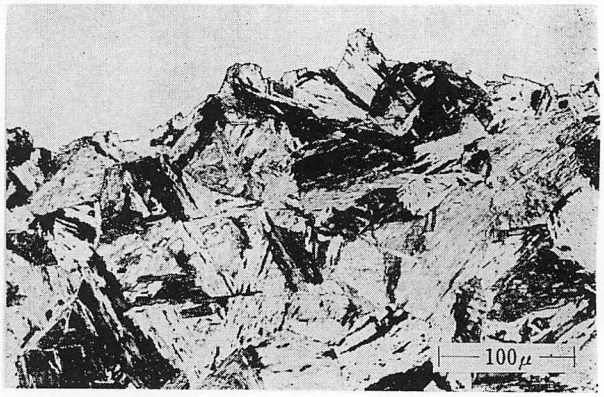

b) 1300°C×30 min WQ+600°C×1 hr.

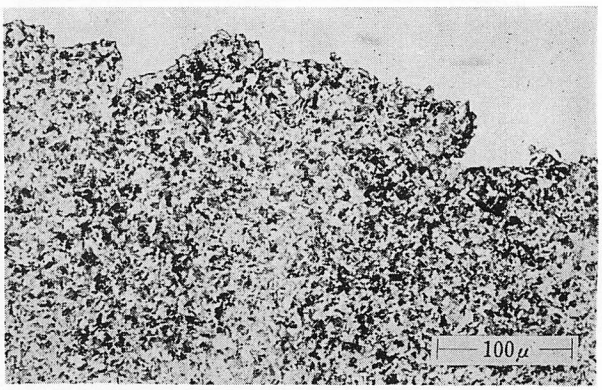

c) 835°C×10 min WQ (4 times)+600°C×1 hr.

Photo. 8. Relationship between the size of cleavage fracture facet and microstructure of tempered martensite with various austenite grain sizes in steel 1.

以上，主としてオーステナイト粒径が大きい場合の実験結果に基づいて議論したが，オーステナイト粒径が小さくなってもまったく同じである．Photo. 8a), b), c)はオーステナイト粒度の異なった焼もどしマルテンサイトの脆性破面を比較したものである．オーステナイト粒径が小さくなるにつれてバンドルおよびパケットの大きさが小さくなり，いずれの場合にも有効フェライト粒径はパケットの大きさとよく対応する．

3.5 低炭素マルテンサイトの結晶学的特徴

まず，前節で述べた修正カーリング液による腐食によって現出された色調の差が結晶方位の違いに対応することを示そう．Photo. 9a)は修正カーリング液による腐食

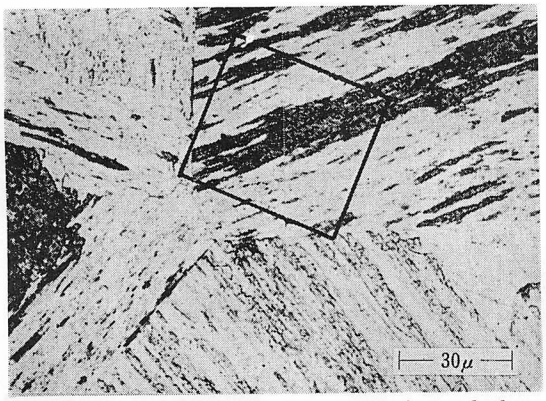

a) Microstructure of tempered martensite, etched with modified Kalling reagent.

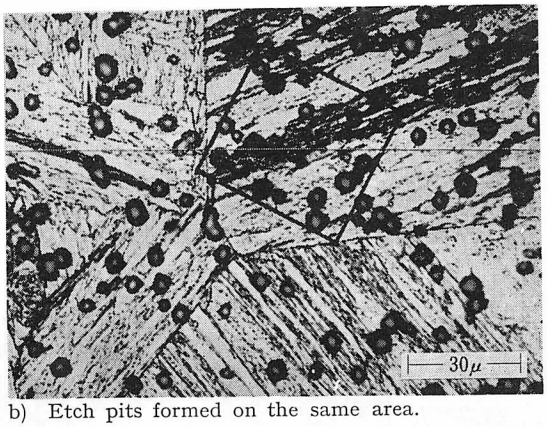

b) Etch pits formed on the same area.

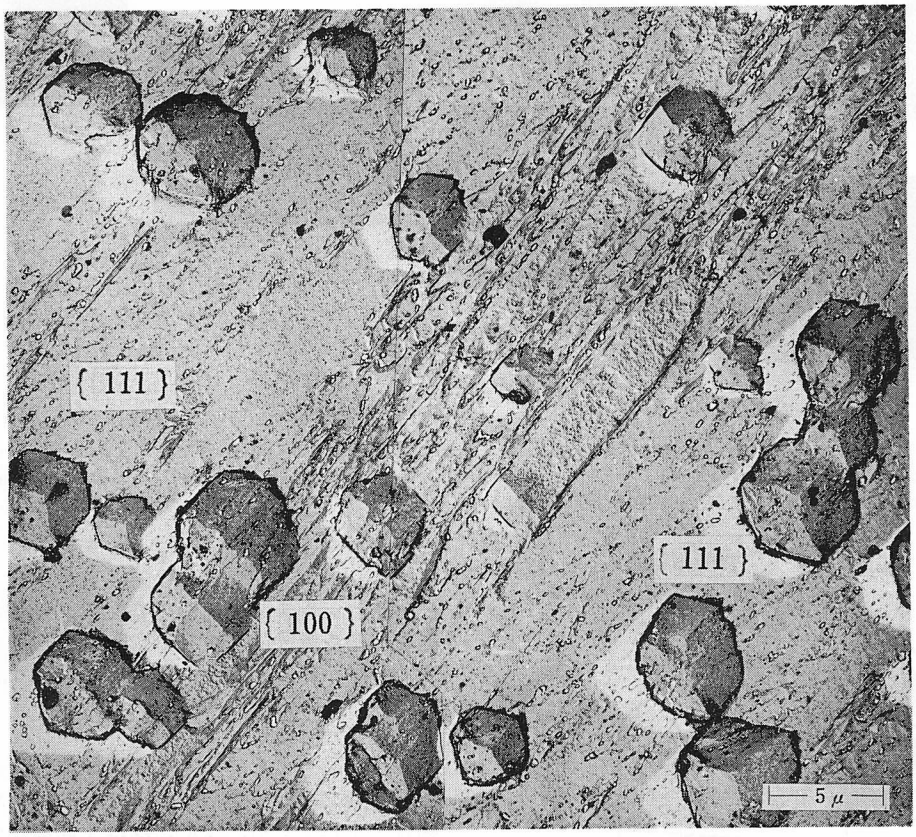

c) Framed area in b enlarged.

Photo. 9. Analysis of crystallographic orientation of white and dark etched areas in low-carbon tempered martensite.

像であり，b) はその上に Table 2 の試薬による腐食を重畳してエッチピットを現出しa) と同一視野を観察したものである．また，c)はエッチピット解析を容易にするため電子顕微鏡によって観察した結果を示したものである．

a) の枠内での白黒の色調に対応する c) の上でのエッチピットを解析することによって，色調の差が結晶方位の差を表わしていることがわかる．すなわち，白色および黒色は各々 {111}α, {100}α 面を表わしている．

1つのバンドルの中でのマルテンサイトの結晶学的特徴を透過型電子顕微鏡で調べた結果，

(1) 1つのバンドルの中のマルテンサイトは2組の K-S バリアントのみで変態し，

(2) 2組のバリアントはマルテンサイトラス1枚ごとに変わるのではなく 2〜3 枚から数 10 枚を単位として変わることなどが明らかになった．しかし薄膜で観察できる1視野はせいぜい 10μ×10μ であり，大きなパケット全体としての結晶学的特徴を正確に把握するためには連続的に写真をとり各々の視野での回折像を解析してみなければならない．Photo. 10a),b),11a),b) はその1例を示したものである．Photo. 11a) は平行に並んだマルテンサイトを 100〜150μ の範囲にわたって連続的に観察したものであり，b) はその制限視野回折像である．回折斑点は視野の全域にわたって (100)α と (111)α とで構成されているが，いずれの視野においても (100)α が優勢である．この結果は2組の K-S バリアントのどちらか一方が支配的であるが (この例では (100)α に相当するバリアント)，必ず他方のバリアント (この例では (111)α に相当) で変態したマルテンサイトが混入していることを示している．それに対して Photo. 10 a), b) では，10μ 程度の視野ごとに (100)α と (111)α が交互に現われる．しかし，この

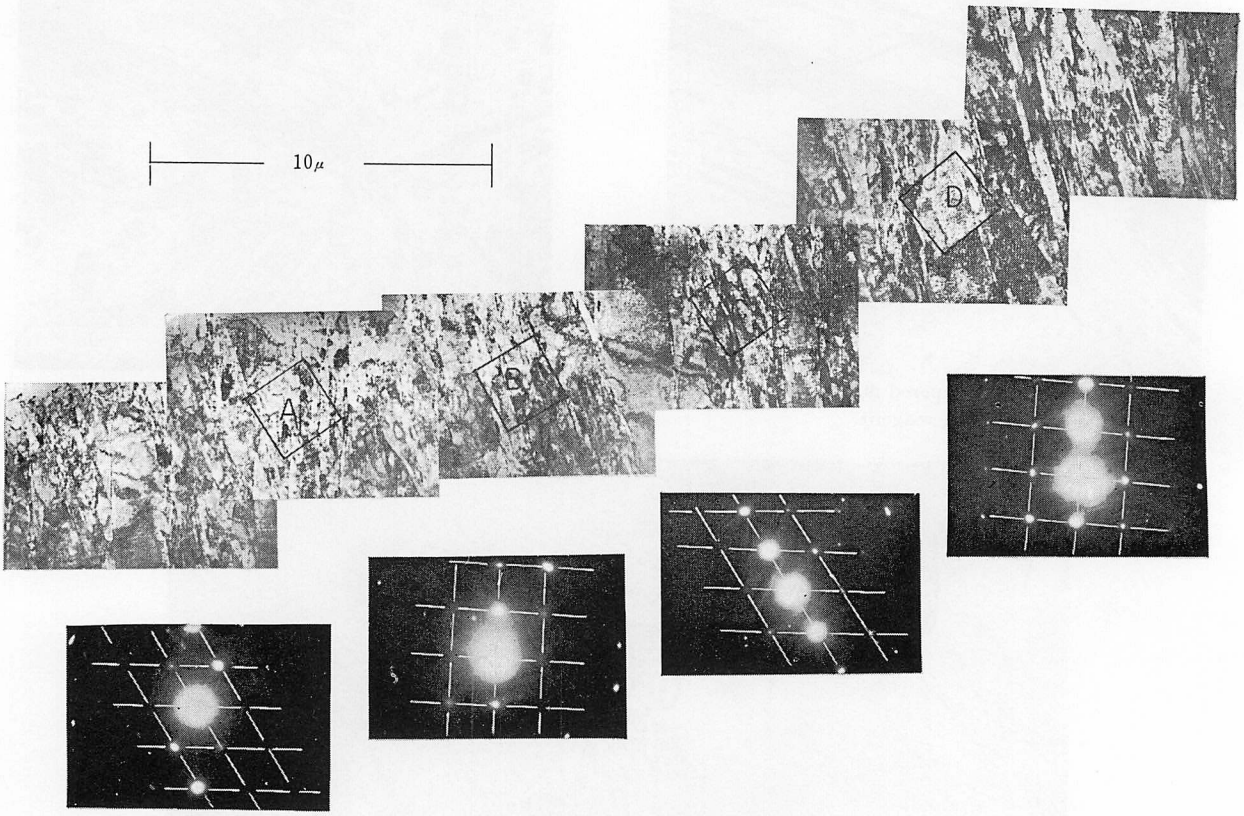

Photo. 10. Thin-foil electron micrograph and selected area electron diffraction pattern of successive martensite laths in steel 1. (Type 1 of Photo. 7) Areas showing strong (100)α pattern and (111)α pattern are observed alternatively. 1300°C×30 min WQ+600°C×1 hr.

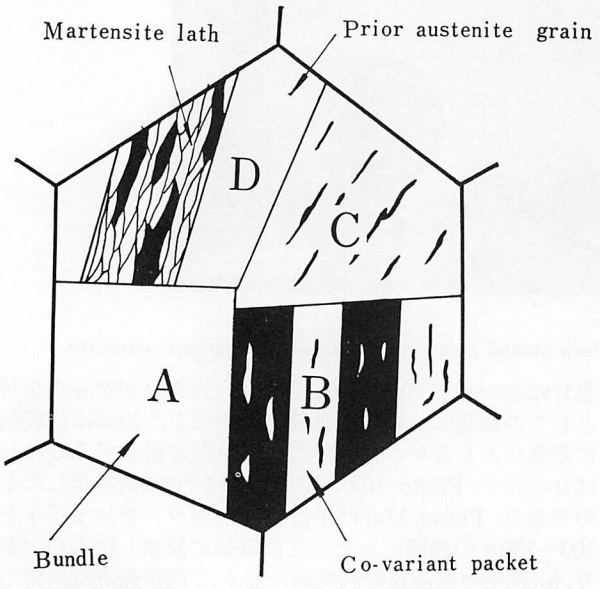

Fig. 4. Schematic drawing of four bundles of low-carbon martensite within a prior austenite grain. Section A represents a bundle, sections B and C show co-variant packets within a bundle and section D illustrates the substructure within a co-variant packet.

場合にも (100)α が優勢な視野には (111)α が，(111)α が優勢な視野には (100)α が反射の強度は非常に弱いけれども認められる．

透過型電子顕微鏡によるマルテンサイトの結晶学的特徴の解析と，光学顕微鏡によるそれとはよく対応する．Fig. 4 はマルテンサイトの結晶学的特徴を総合的に解析した結果を模式的に示したものである．この図には1個のオーステナイト粒内に4個のバンドルが示されており，A は平行に並んだラス状のマルテンサイトからなるバンドルを表わしている．

B は結晶方位の異なった2種類のパケットが交互に並んだ場合を，C はそのうちどちらか一方が非常に優勢な場合を示している．また，D は1個のパケットの中での結晶学的特徴を表わしたもので，隣接するマルテンサイトは基本的には同じ方位を持ち非常に小傾角な粒界によって分割されている．しかし，量的には少ないけれども方位の異なった極微細なパケットが必ず存在し，マトリックスに相当するパケットとは大傾角粒界によって分割されている．前節ではパケットを同一結晶方位を持ったマルテンサイトの束と定義したが，より厳密さを持たせるためにはほぼ同一結晶方位のマルテンサイトの束と再定義することが必要である．

旧オーステナイト粒界も一般には大傾角粒界である．しかしながら，粒界を境にして両側のオーステナイト粒内にのびたマルテンサイトのラス粒界の方向が平行に近い場合がしばしば観察される．

Photo. 12 a), b), c), d) はそのような領域の電子顕微鏡による観察結果の1例である．a) はオーステナイト粒界を中心にして撮影した明視野像であり，b), c) は制限視野 A，B の回折像である．b), c) の晶帯軸は〈111〉α で

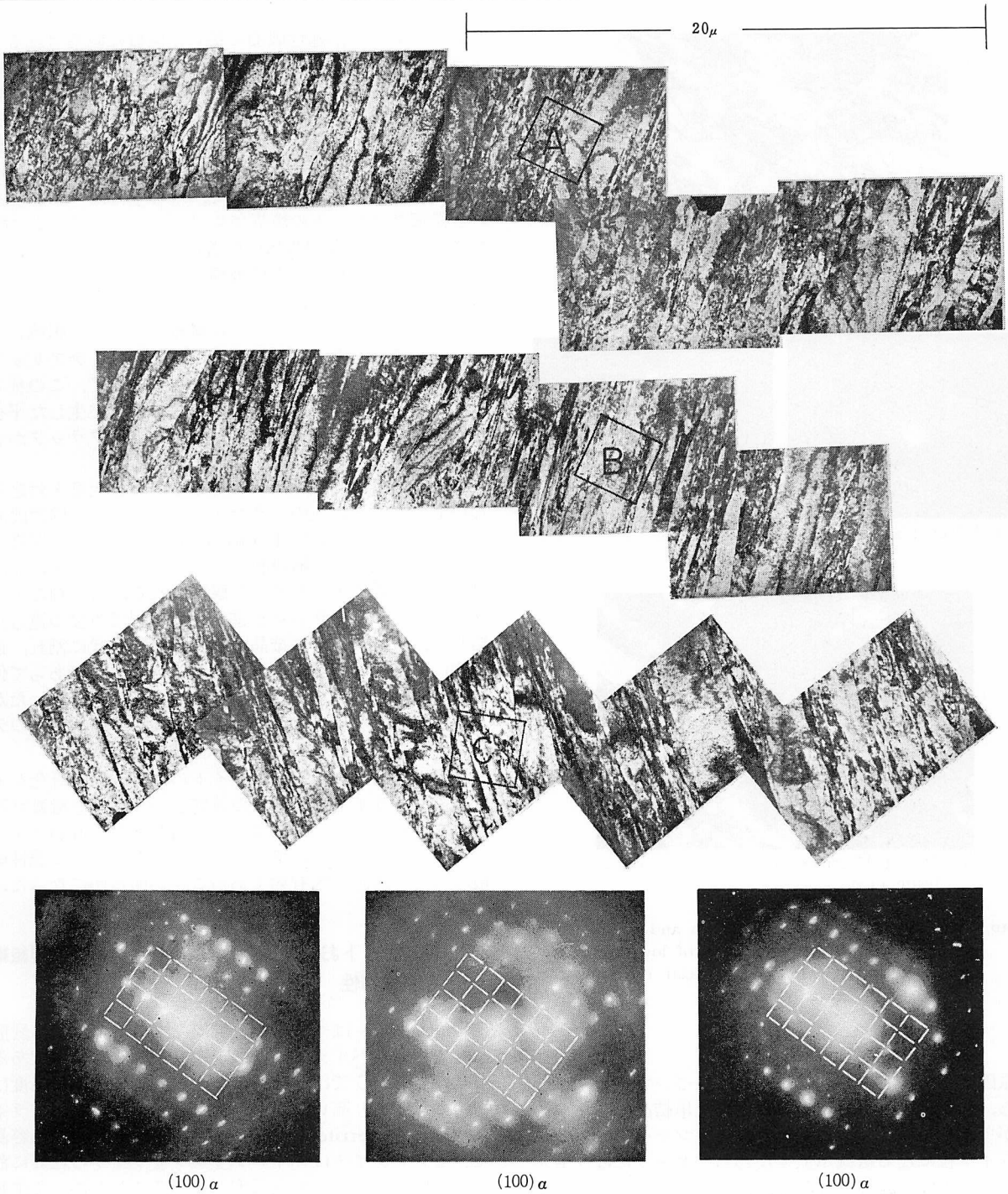

Photo. 11. Thin-foil electron micrograph and selected area electron diffraction pattern of successive martensite laths in steel 1. (Type 2 of Photo. 7) Pattern of (100)α is very strong in every area. 1300°C×30 min WQ+600°C×1 hr.

あり，回折像を重ね合せてみると〈111〉α 軸まわりの回転は非常にわずかである．

また，d) は c) の (110)α 斑点による暗視野像であるがほぼ全視野が反射している．このことはオーステナイト粒界がマルテンサイト変態によって大傾角粒界の性質を失なうこともあり得ることを示している．オーステナイト粒界についてのこのような結晶学的特徴は，腐食した脆性破面である場合にはオーステナイト粒界に沿ってテアラインが観察されない理由を説明するための強力な裏付けとなる．

以上述べたマルテンサイトの結晶学的特徴より明らかなように，微視組織の中で大傾角になり得る粒界はパケット粒界，バンドル粒界および旧オーステナイト粒界の大部分であり，これらの粒界は脆性破壊の観点からはフェライト鋼の粒界と同じものであるとみなすことができる．

また，ここで得られた結晶学的特徴は Marder[13,14]，Chilton[15] により Fe-C マルテンサイト，Fe-Ni マッシブマルテンサイトについて得られた結果と基本的には一致している．

3.6 有効フェライト粒とミクロクラックとの関係

フェライト鋼と焼もどしマルテンサイト鋼の破壊様式の違いは，前者が劈開であるのに対して後者が擬劈開であることである．焼もどしマルテンサイトが擬劈開にな

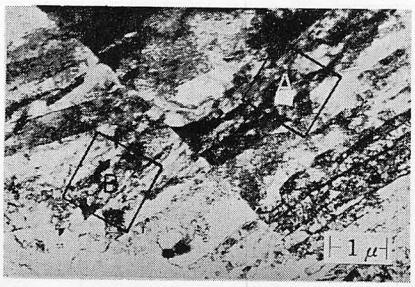

a) Bright-field image.

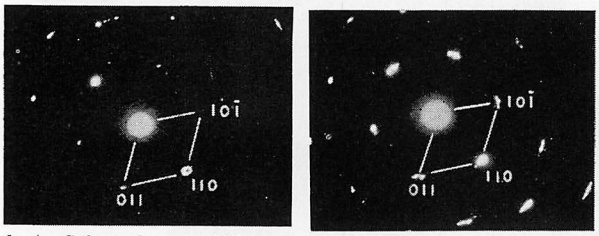

b,c) Selected area diffraction pattern.

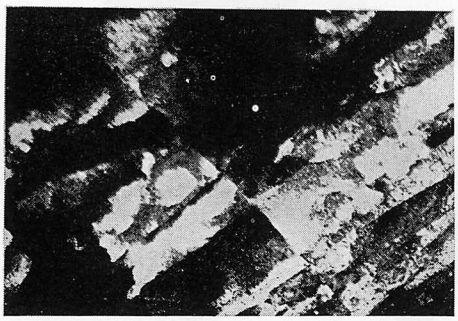

d) Dark-field image using the $(110)_\alpha$ diffracted beam in c.

Photo. 12. Thin-foil electron micrograph and selected area electron diffraction pattern of low-carbon tempered martensite, with special reference to a austenite grain boundary.

る原因はパケットの結晶学的特徴に基づいている．すなわち，フェライト鋼の1個の粒は完全な単結晶とみなすことができるのに対し，焼もどしマルテンサイトの有効フェライト粒になる組織単位すなわちパケットにはマトリックスと大傾角粒界で分割された極微細なパケットが存在する．もし，この微細なパケットによって1つの劈開破面単位の上に形成されるテアリッジが，単に有効表面エネルギーという意味で効いているばかりでなく破面遷移温度を支配する要因になっているとすると，劈開破面単位の大きさで有効フェライト粒を定義するわけにはいかない．このことを確かめる1つの有力な手段として延性領域での脆性ミクロクラックを観察する方法がある．これは，3節で述べた衝撃破面遷移温度に対する物理的な解釈より明らかなように，有効フェライト粒径はミクロクラックの大きさと対応しなければならないからである．

Photo. 13は遷移温度直上の延性域で破断した破面の1例である．肉眼では100% 延性破断したように観察されるが，所々に劈開ミクロクラックが観察される(領域 A, B)．ミクロクラックの大きさは大体 10～100μ 程度で，それらの周辺部が延性破面に接した位置に観察されるテアラインの特徴は，100% 脆性破壊した破面に観察されるテアラインの特徴と非常によく似ている．この観察結果は，延性破壊から脆性破壊への遷移はこのようなミクロクラックがグリッフィスの条件を満たして伝播を開始する時に生じることを意味している．注目すべきことは，ミクロクラックの破面は平らで，その上にはマトリックスと微細なパケットの境界で生じたテアリッジが必ず観察される（領域 A の矢印の位置）．このことより，テアリッジを生じる粒界は脆性破壊に対して無視することができると考えられる．

ある場合には，テアリッジは複雑に屈折して組織と対応しないこともある（Photo. 13，領域 B）．テアリッジ近傍でのリバーパターンの方向から判断して，この種のテアリッジは1つのパケットの数ケ所から発生した平行ではあるがわずかに高さの異なったミクロクラックが合体するときにできた偶然的なものである．

テアリッジと同様にテアラインの中にも組織と対応しないものがある．そのようなテアラインを含む劈開破面の1例とその概略図を Photo. 14 a), b) に示す．写真の下半分の劈開破面は階段状を呈しており，その階段部に対応する位置にテアラインが観察される．この種のテアラインはメインクラックが進行する過程で方位の違った結晶に出合った時その結晶の劈開面が階段状に割れ，最終的にそれらの間がつながる時にできたものであって何ら有効に働いていないと解釈することができる．したがって，Fig. 2のヒストグラムを求める際にはこの種のテアラインは勿論無視してある．

以上，焼もどしマルテンサイトの脆性破壊の研究を主としてフェライトの破壊との対応ということを指導原理として進めてきた．そして，その背景となる有効フェライト粒という概念が，焼もどしマルテンサイトの脆性破壊に対してきわめて有効であることが明らかになった．

3.7 ベイナイトおよび焼もどしベイナイトの微視組織と衝撃特性

Photo. 15 a) はベイナイト生成温度域で恒温的に変態させて作ったベイナイトの微視組織を示したものである(鋼2)．470°C では（鉛浴の温度で実効的な生成温度は指定の温度より高い），生長するベイニチックフェライト (bainitic ferrite) の先端での炭素拡散が比較的容易で，セメンタイトはベイニチックフェライトの粒界に沿って析出している．生成温度が下がるにしたがって生長端での炭素拡散が困難になり，セメンタイトはフェライト粒界ばかりでなく粒内にも析出する．Ms 点近傍 (350° C) ではますますその傾向が強くなり，粒界および粒内に均一に析出する．Ms 点以下ではベイナイトとマルテンサイトとの混合組織になり，生成温度が 250°C 以下では両組織の区別がむずかしくなる．Photo. 15 b) は a) の焼もどし組織である．生成温度をとわず，焼もどしによるベイナイトの形態変化はほとんど観察されない．

Fig. 5は変態ままのベイナイトおよび焼もどしベイナイトの破面遷移温度と硬さにおよぼす生成温度の影響を示したものである(鋼2)．変態ままのベイナイトでは生成温度が下がるにしたがって硬さは上昇するにもかかわらず $_{v}$Trs は下がり (410°C まで)，その温度から Ms 点直上の温度 (350°C) までは $_{v}$Trs はほとんど変化しない．

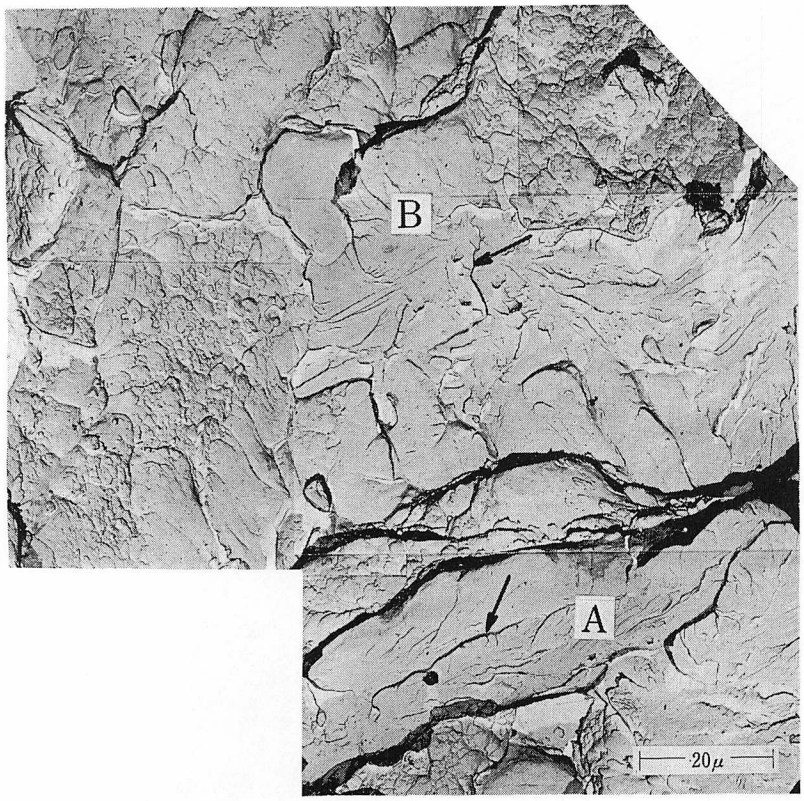

Photo. 13. An example of cleavage microcracks observed in the ductile temperature range just above the transition temperature of tempered martensite in steel 1. Arrows show tear ridges.
Testing temperature −40°C
($_v$Trs = −45°C)
Absorbed energy 27·7 kgm.
1300°C × 30 min
WQ + 600°C × 1 hr.

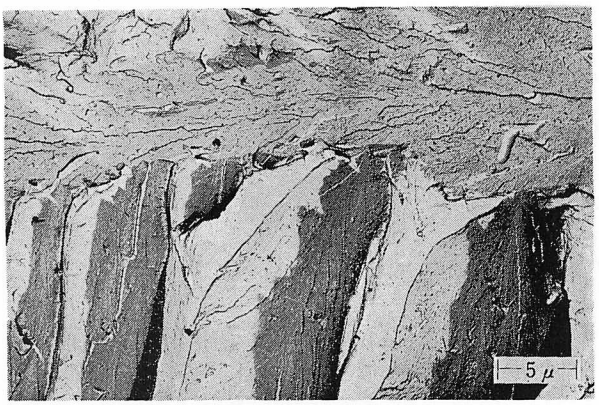

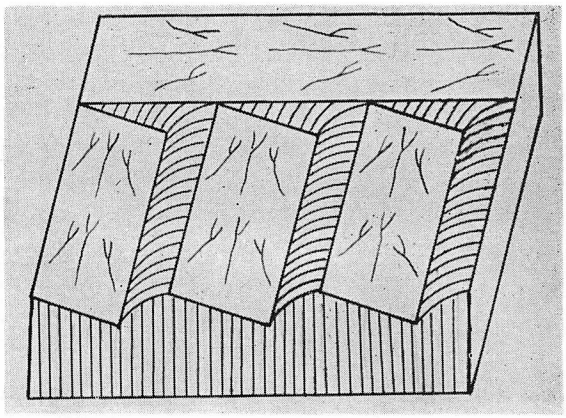

Photo. 14. An example of ineffective tear line.

生成温度が Ms 点以下になると硬さの上昇にともなって $_v$Trs も上昇する．焼もどしによる硬さの低下はマルテンサイトが最も著しく，つぎに下部ベイナイトであり，上部ベイナイトではほとんど硬さの低下がない（上部ベイナイト，下部ベイナイトという言葉は生成温度に基づいて使用する．したがって，結晶学的または反応速度論的な観点からの解析を加えて使い分けしたものではない）．焼もどしベイナイトの $_v$Trs におよぼす生成温度の影響は変態ままの場合の傾向とよく似ている．

注目すべきことは焼もどし下部ベイナイトと焼もどしマルテンサイトの硬さの差がほとんどないにもかかわらず，前者の $_v$Trs が後者に比較して 100°C も低いことである．Fig. 6 は鋼 1 について焼もどし下部ベイナイトと焼もどしマルテンサイトの破面遷移温度におよぼすオーステナイト粒度の影響を比較したものである．Fig. 6 より明らかなように，焼もどし下部ベイナイトにおいては $_v$Trs のオーステナイト粒度依存性が非常に小さくしたがって，オーステナイト粒径が大きくなるほど両組織の $_v$Trs の差は大きくなる．

低炭素ベイナイト鋼の強度と靱性との関係についてはすでに Irvine[16] によって詳しく調べられており (Ni-Cr-Mo 鋼)，Fig. 5 の変態ままの関係も Irvine の結果と定性的にはよく一致している．Irvine はベイナイトの強度と靱性との関係を実効表面エネルギーに基づいて評価し，上部ベイナイトから下部ベイナイトへの微視組織の変化にともなう靱性の向上は，ラスサイズ (lath size) の減少とセメンタイトの微細分散によるクラックの伝播抵抗の増加に基づくものであると考えた．しかしながら，Fig. 6, 7 の関係を実効表面エネルギーという概念によって統一的に説明することはむずかしい．そこで，組織と靱性との関係を首尾一貫した 1 つの概念で説明できるかどうかを究明するためにまず，ベイナイトの脆性破壊に対して有効フェライト粒という概念の適応性を検討してみよう．

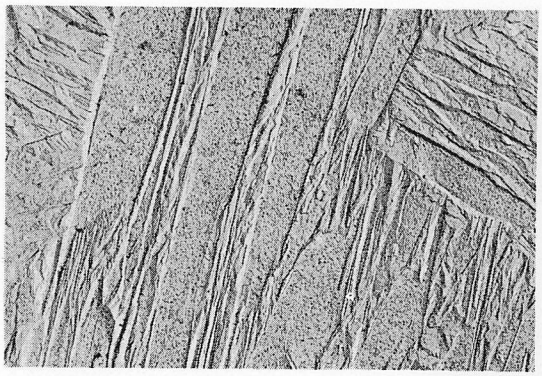

a) 1300°C×30 min WQ

e) 1300°C×30 min 380°C Q

b) 1300°C×30 min 250°C Q

f) 1300°C×30 min 410°C Q

c) 1300°C×30 min 300°C Q

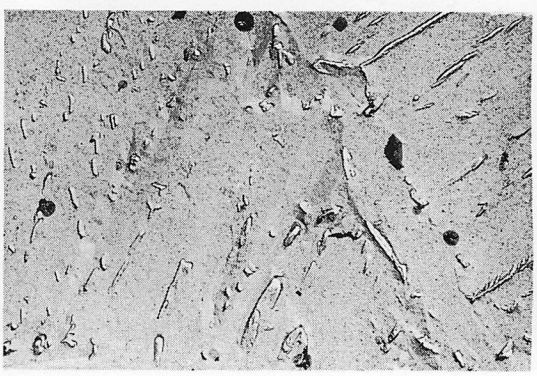

g) 1300°C×30 min 440°C Q

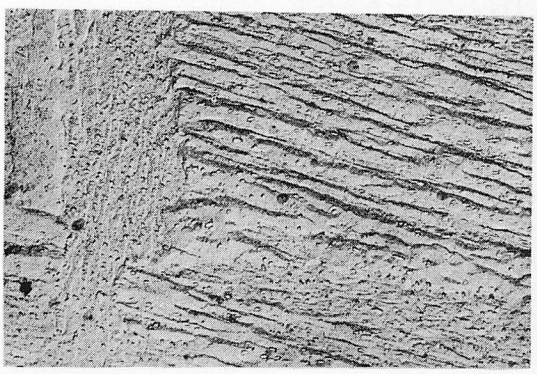

d) 1300°C×30 min 350°C Q

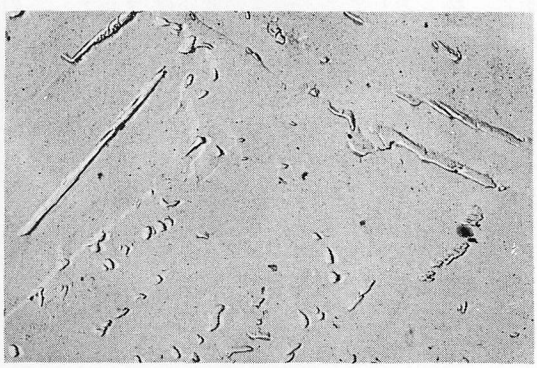

h) 1300°C×30 min 470°C Q

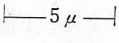

Photo. 15. (a) Microstructures of isothermally transformed bainite in steel 2.

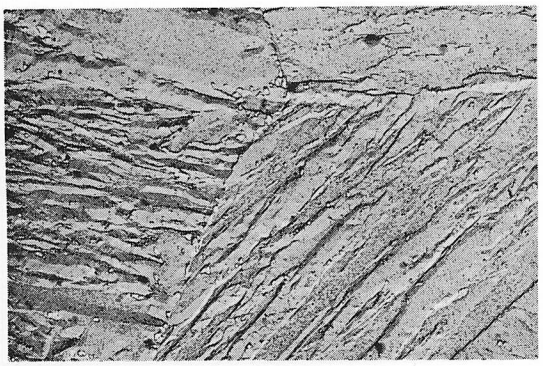

a) 1300°C×30 min W Q+600°C×1hr

e) 1300°C×30 min 380°C Q+600°C×1hr

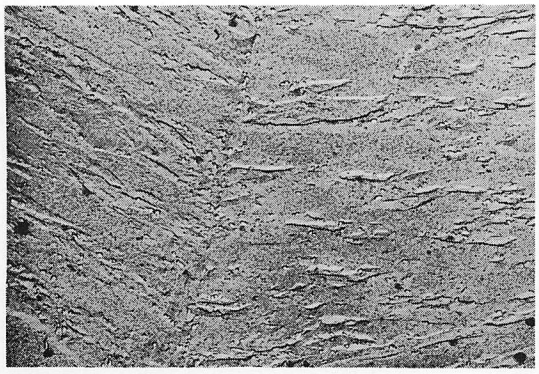

b) 1300°C×30 min W Q+600°C×1hr

f) 1300°C×30 min 410°C Q+600°C×1hr

c) 1300°C×30 min 300°C Q+600°C×1hr

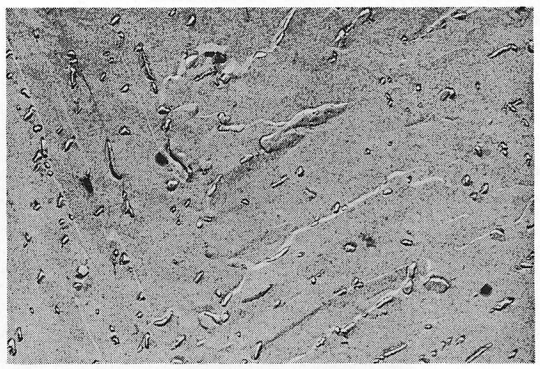

g) 1300°C×30 min 440°C Q+600°C×1hr

d) 1300°C×30 min 350°C Q+600°×1hr

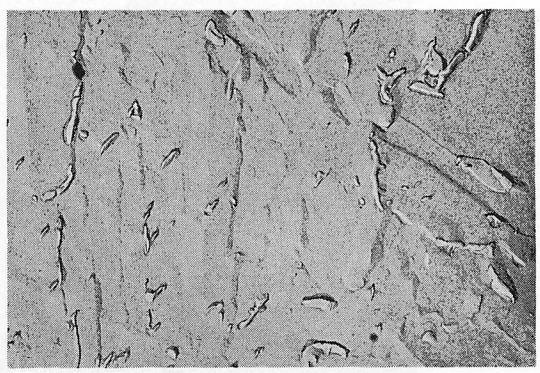

h) 1300°C×30 min 470°C Q+600°C×1hr

5 μ

Photo. 15. (b) Microstructures of isothermally transformed and tempered bainite in steel 2

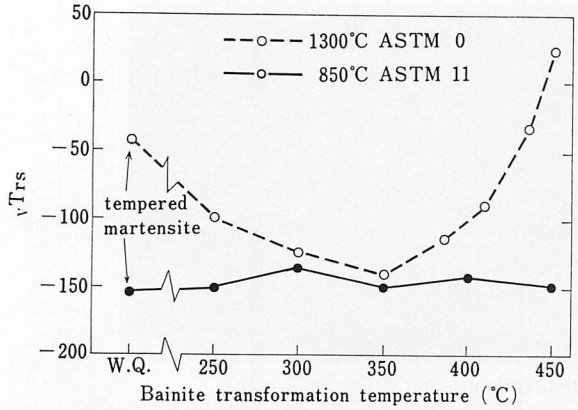

Fig. 5. Effect of bainite transformation temperature on the impact-transition temperature $_{v}$Trs. Tempered bainite, steel 2.

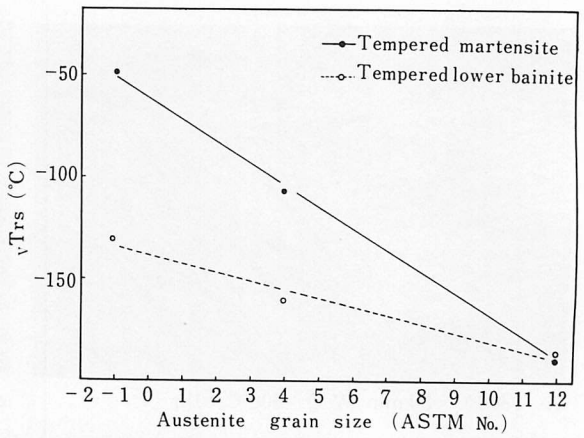

Fig. 6. Effect of prior austenite grain size on the impact-transition temperature $_{v}$Trs. Tempered martensite and tempered lower bainite, steel 1.

a) Tempered lower bainite 1300°C×30 min 420°C Q +600°C×1hr.

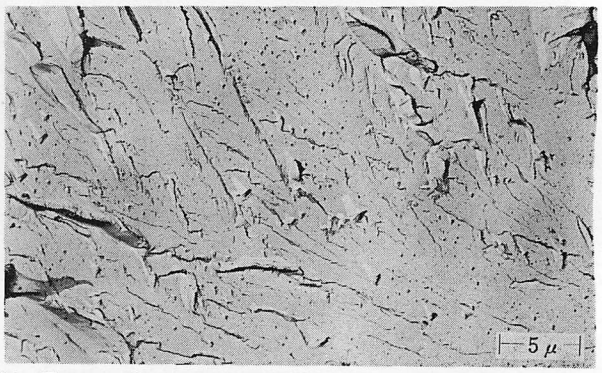

b) Tempered martensite 1300°C×30 min WQ 600 °C×1hr.

Photo. 16. Fracture surfaces of tempered lower bainite and tempered martensite in steel 1.

Photo. 17. Fracture surface of tempered lower bainite in steel 1. Enlarged micrograph is shown in the upper right corner. Note intercrystalline fracture along bainitic ferrite lath boundary is observed. 1300°C ×30 min 420°C Q+ 600°C×1hr.

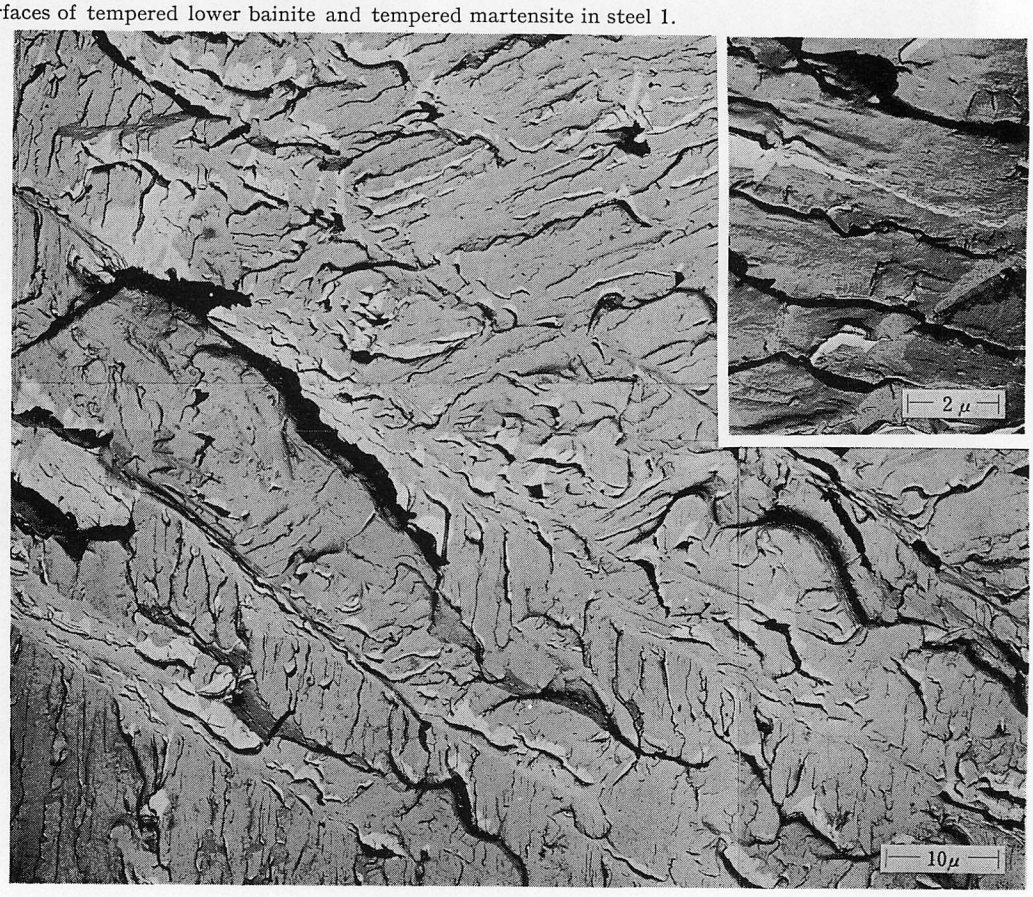

3.8 焼もどしベイナイトの脆性破面の特徴

議論を明解にするために主として焼もどしベイナイトについて説明する．Photo. 16 a) はオーステナイト粒径が大きい焼もどし下部ベイナイトの脆性破面でありその破面の特徴を印象づけるために，b) に同じオーステナイト粒度の焼もどしマルテンサイトの脆性破面を対照させて示す（鋼1）．

Photo. 16a), b) を比較することによって明らかなように，焼もどし下部ベイナイトの脆性破面にはテアラインが数多く観察され，平らな破面単位(劈開破面単位)が焼もどしマルテンサイトに比べてずっと小さいのが特徴である．1つの劈開破面上での微視的特徴は焼もどしマルテンサイトのそれとまったく同じであり，破面全体の感じはオーステナイト粒径が小さい焼もどしマルテンサイトのそれに非常によく似ている．この観察結果より，もし有効フェライト粒の概念が成り立つと仮定すれば，(次節で展開される議論の筋道により，有効フェライト粒の概念が成立つことが証明される)，同じオーステナイト粒度に対して焼もどし下部ベイナイトの方が靱性が優れている理由が理解されよう．しかしながら，この仮定の妥当性を評価するにあたって1つの問題を提起しなければならない．その問題は焼もどし下部ベイナイトの脆性破面には劈開割れ以外にベイニチックフェライトのラス粒界に沿った粒界割れが観察されることである．Photo. 17 はその1例であるが，この写真の破壊様式が粒界割れであることは次のような理由によって証明される．この写真では左上から右下方向にテアラインが走りそれによって脆性破面が分割されている．

さらにテアラインによって囲まれた破面は，ほぼ平行で等間隔に並んだテアリッジによって再分割されている．ところで，テアリッジで囲まれた小破面群の拡大写真を観察すると(Photo. 17の右肩)，小破面群の各々にはリバーパターンがまったく観察されず，しばしばマトリックスの炭化物が剝離して生じたと思われる凹凸の痕跡が観察される．また，このような特徴をもった破面の結晶方

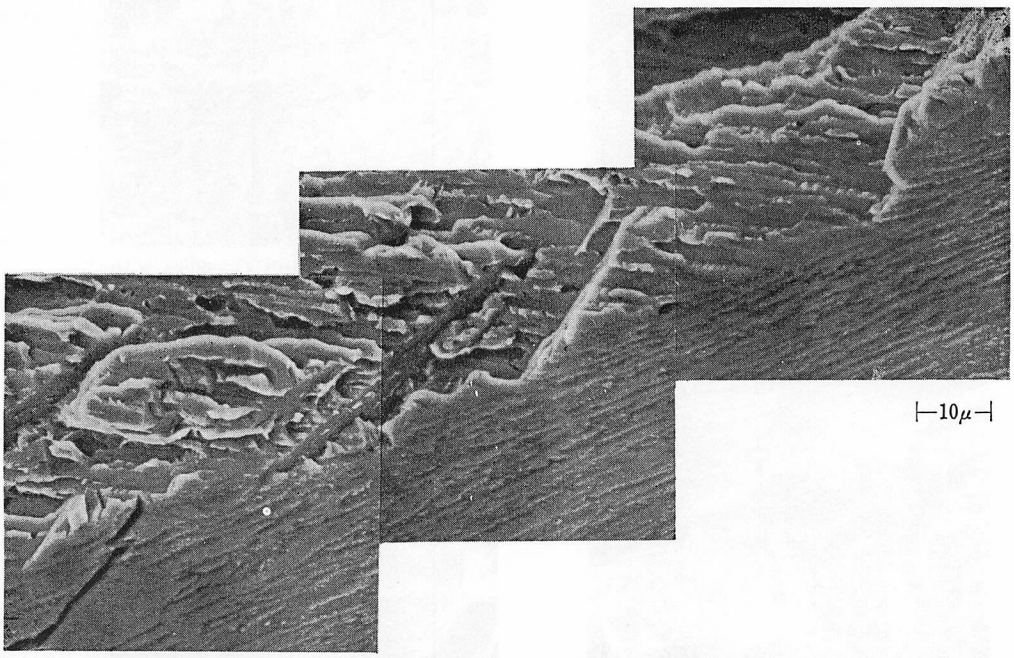

Photo. 18. Scanning electron micrograph of fracture surface and section of fracture surface of tempered lower bainite in steel 1. 1300°C×30 min 420°C Q+600°C×1hr.

Photo. 19. Fracture surface of tempered upper bainite in steel 2. 1300°C×30 min 470°C Q+600°C×1hr.

Photo. 20. An example of etch pits showing (001)α formed on a large brittle fracture facet of tempered upper bainite in steel 2. 1300°C×30 min 470°C Q+600°C×1hr.

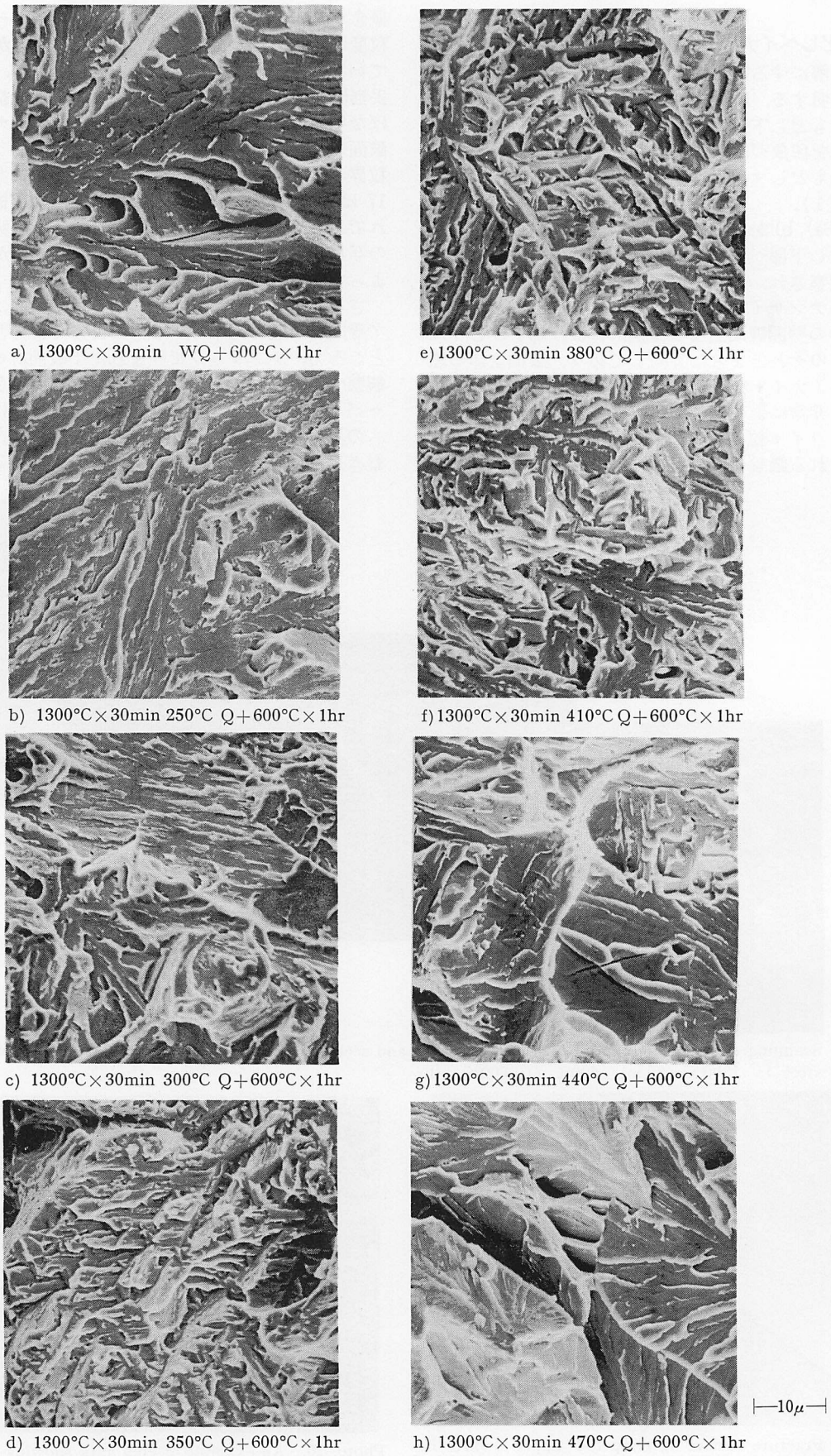

Photo. 21. Characteristics of fracture surfaces of tempered bainite in steel 2, with special reference to bainite transformation temperature.

位を調べると，{110}α または {110}α と {111}α の中間の方位の面が圧倒的に多い．さらに，走査型電子顕微鏡により破面と破面に垂直な断面を研磨腐食して同時に観察すると，Photo. 17 に類似した破面の垂直断面上でのクラックの方向はベイニチックフェライトのラス粒界に必ず沿っている．Photo. 18 はその 1 例を示したものである．一方，BCC 金属の劈開面は特殊な元素を除いて {100}α 面であること，低炭素マルテンサイト，低炭素ベイナイトの晶癖面は {110}α であることなどが証明されている．また，劈開割れの場合には破面にリバーパターンが観察されるのが普通である．

以上，破面観察による結果と bcc 金属の劈開破壊が具備すべき基本的な特徴とを対照させることにより，Photo. 17 に示したような特徴を持った破面の破壊様式はベイニチックフェライトのラス粒界に沿った粒界割れであると結論することができる．この節では焼もどし下部ベイナイトの脆性破壊の様式は擬劈開ないしは劈開以外に粒界割れを含むという現象の究明と，そのことが有効フェライト粒という概念の妥当性を評価する場合の基本的な問題点になるという指摘にとどめておく．

Photo. 19 は生成温度の最も高い焼もどし上部ベイナイトの脆性破面である（鋼 2）．平らな破面単位（劈開破面単位の大きさは同じオーステナイト粒度の焼もどし下部ベイナイトのそれに比べてはるかに大きく，むしろ焼もどしマルテンサイトのそれに近い．破面に観察される微視的特徴はフェライトのそれときわめてよく似ており，焼もどしマルテンサイト，焼もどし下部ベイナイトに比べて擬劈開の割合が減少する．Photo. 20 は焼もどし上部ベイナイトの脆性破面にエッチピットを現出し破面の結晶方位を調べたもので，(001)α 面で劈開することを示している（鋼 2）．これらの観察結果より，焼もどし上部ベイナイトの脆性破壊の様式はフェライト鋼とほぼ同じであり，したがって，焼もどしマルテンサイトの脆性破

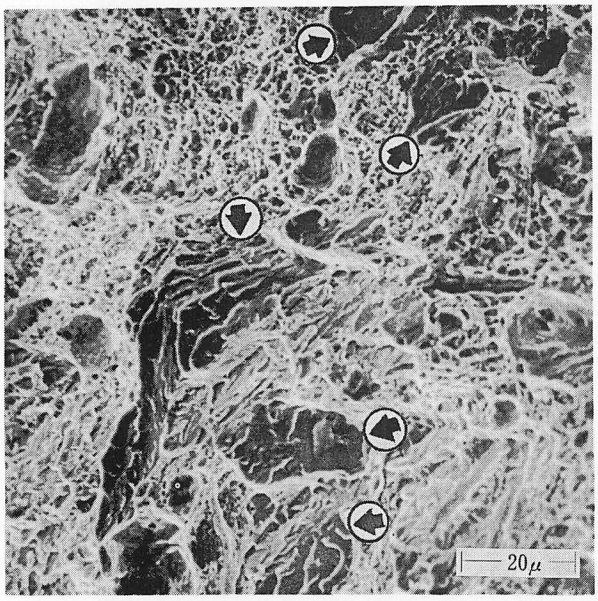

Photo. 22. An example of cleavage microcracks observed in the ductile temperature region of tempered lower bainite in steel 1. Arrows show cleavage microcracks. Scanning electron micrograph.
Testing temperature −95°C
Absorbed energy 24·4 kgm
1300°C×30 min 420°C Q+600°C×1hr

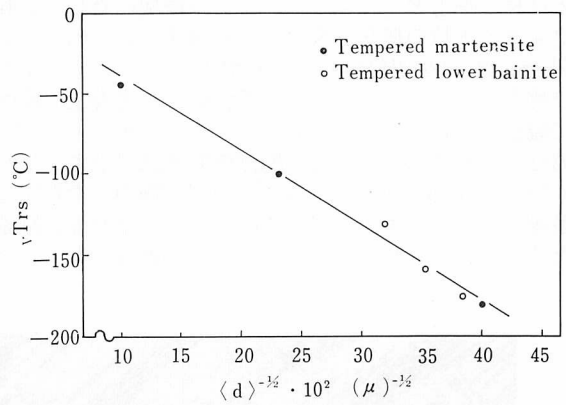

Fig. 7. Dependence of the impact-transition temperature $_v$Trs on mean effective ferrite grain size ⟨d⟩. Tempered martensite and tempered lower bainite, steel 1.

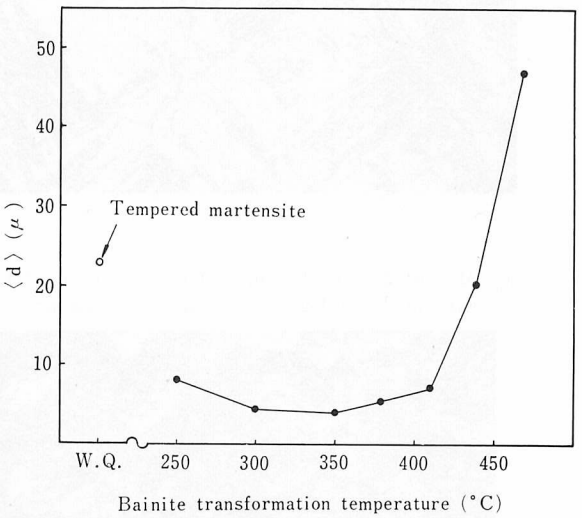

Fig. 8. Relationship between bainite transformation temperature and mean effective ferrite grain size ⟨d⟩, steel 2.

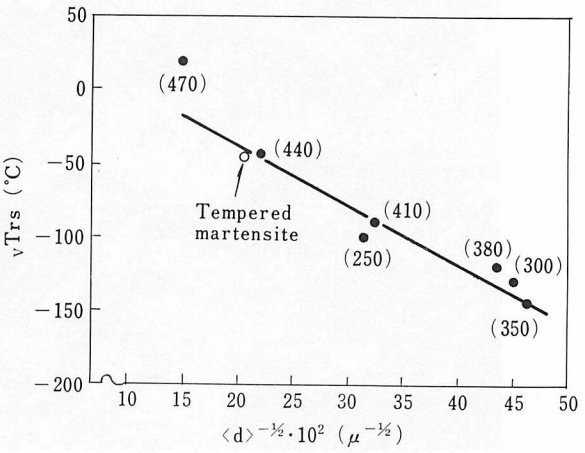

Fig. 9. Dependence of impact-transition temperature $_v$Trs on mean effective ferrite grain size ⟨d⟩. Figures in parentheses represent bainite transformation temperature. Tempered bainite, steel 2.

壊と同様に焼もどし上部ベイナイトの破壊に対しても有効フェライト粒の概念が成立つと結論することができる．

Photo. 21 は生成温度の異なる焼もどしベイナイトおよび焼もどしマルテンサイトの脆性破面を走査電子顕微鏡で観察した結果を示したものである．ベイナイトの生成温度が下がるにしたがって劈開破面単位は小さくなり，最も均一な下部ベイナイトが得られる 350°C で破面は一番細かくなる．生成温度が Ms 点以下になり混合組織になるとマルテンサイトの増加とともに破面も大きくなる．

3.9 焼もどし下部ベイナイトの有効フェライト粒について

前節で問題提起をしたように，焼もどし下部ベイナイトの脆性破壊の様式にはベイニチックフェライトのラス粒界に沿った粒界割れが混入している．もし，靱性評価の基準として採用した破面遷移温度に粒界割れが本質的な影響をおよぼすならば，フェライト鋼の破壊との対応という形で議論を展開することはできない．したがって，組織の如何をとわず首尾一貫した概念で脆性破壊をとら

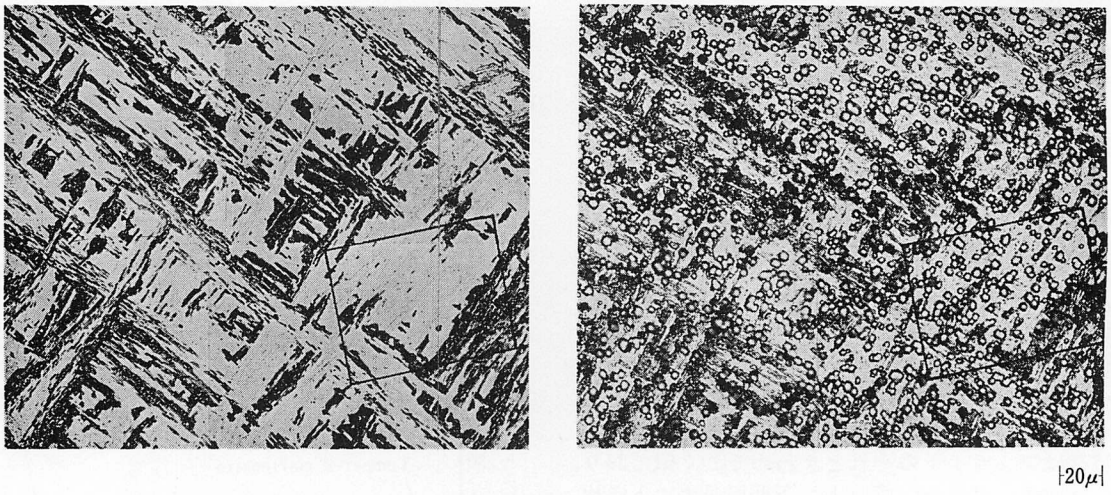

20μ

a) Microstructure of tempered lower bainite, etched with modified Kalling reagent. lower bainite.

b) Etch pits formed on the same area.

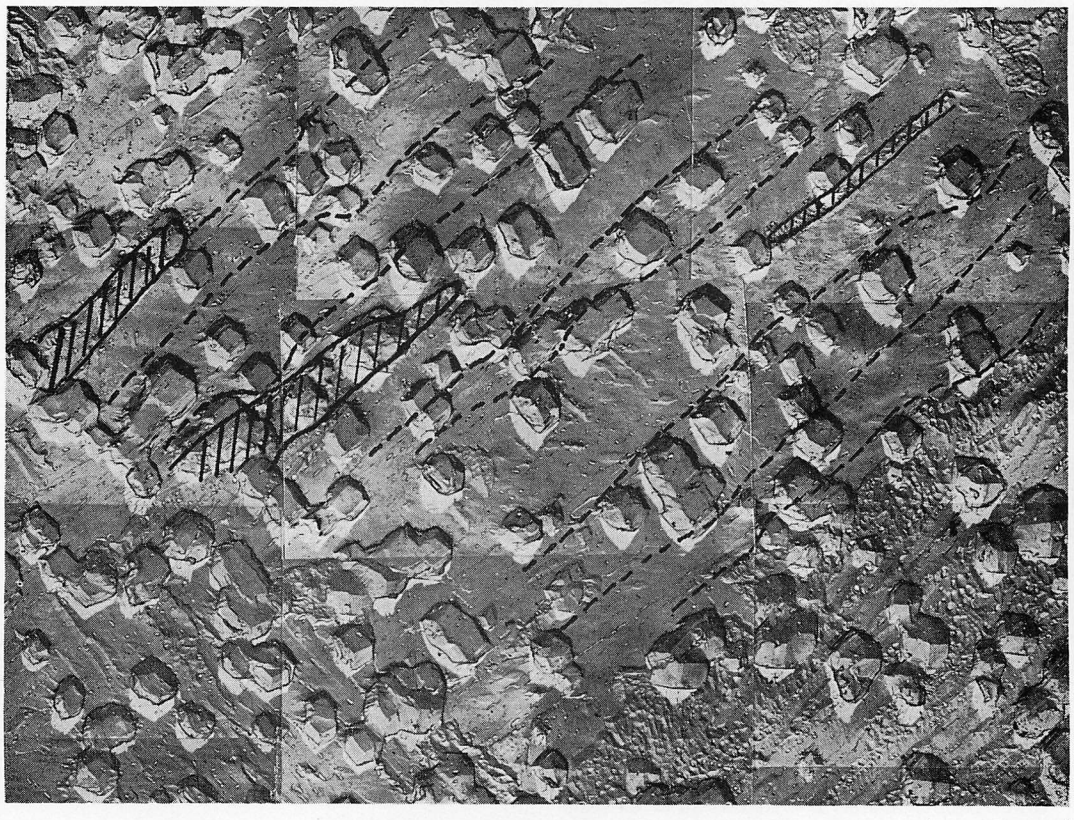

20μ

c) Framed area in b enlarged.

Photo. 23. Analysis of crystallographic orientation of white and dark etched areas in low-carbon tempered lower bainite.

えることを求めるならば，有効フェライト粒の概念に修正を加える必要があるかもしれない．ところで，3節で述べた破面遷移温度の解釈に基づいて考えると，延性域で観察される脆性ミクロクラックと完全に脆性破壊をした破面との間には因果関係が存在するはずである．

Photo. 22は破面遷移温度より上の温度で肉眼では100%延性破断したように見える焼もどし下部ベイナイトの破面を走査型電子顕微鏡で観察した1例である．大部分の領域は典型的なディンプルパターン(dimple pattern)を示しているが，所々矢印で示した位置に脆性ミクロクラックが観察される．脆性ミクロクラックの微視的特徴を注意して観察すると，ほとんどが劈開ミクロクラックで粒界割れは観察されない．また，完全に脆性破壊した試料について2次クラックを観察すると，2次クラックの先端付近に点在するミクロクラックは概ね劈開している．

したがって，これらのミクロクラックが最終的な脆性破壊に至らしめる芽となると解釈すれば，粒界割れは少なくとも破面遷移温度を支配する要因にはなっていないと考えることができ，幸いにも劈開破面単位で定義した有効フェライト粒の概念に修正を加える必要はないことがわかる．

Fig. 7 は鋼1について種々のオーステナイト粒度をもった焼もどしマルテンサイト，焼もどし下部ベイナイトの脆性破面より平均有効フェライト粒径 $\langle d \rangle$ を求め，$\langle d \rangle^{-1/2}$ に対して ${}_{v}\mathrm{Trs}$ をプロットしたものである．また，Fig. 8は鋼2の生成温度が異なる焼もどしベイナイトおよび焼もどしマルテンサイトについて $\langle d \rangle$ を求め，それとベイナイト生成温度との関係を示したものであり，Fig. 9は $\langle d \rangle^{-1/2}$ と ${}_{v}\mathrm{Trs}$ の関係をプロットしたものである．Fig. 7, 9 より明らかなように，各々の点は1次関係を示す1本の直線で表わし得ることがわかる．

これらの関係より明らかなように，有効フェライト粒径が一定であれば組織に関係なく破面遷移温度は一義的に定まることを意味している．いいかえれば，冶金学的な因子例えば，オーステナイト粒度，組織の差（マルテンサイトとかベイナイトとかいう意味での差）等は有効フェライト粒径を変えることによって調質鋼の靱性を支配する．

3.10 低炭素ベイナイトの結晶学的特徴

ベイナイトの生成温度とともに有効フェライト粒径が変わる要因を明らかにするためには，ベイナイトの結晶学的特徴を十分に理解することが重要である（焼もどしによってベイナイトの結晶学的特徴は変わらない．したがって，結晶学的特徴を議論する場合，焼もどしベイナイトをベイナイトと略しても何ら誤解を招かない）．

Photo. 23 a) は修正カーリング液による焼もどし下部ベイナイトの腐食像である．マルテンサイトに比べてバンドルが複雑に交錯しており，1つのバンドルの中での白黒の色調を持った帯状模様の巾（ベイナイトのコバリアントパケットの巾）がきわめて狭い．このパケットの巾はオーステナイト粒度が変わってもあまり変化しない．これらの結晶学的特徴は，同じオーステナイト粒度の焼もどし下部ベイナイトと焼もどしマルテンサイトとの靱性を比較すると前者の方が優れていることおよび焼もどし下部ベイナイトの靱性はオーステナイト粒度依存性が小さいことなどの現象とよく対応する．色調の差が方位差に対応すると仮定すると枠内の薄い灰色部は1つの結晶を表わしていることになり，したがって，下部ベイナイトにおいてもかなり大きなパケットが存在することになる．Photo. 23 b) は修正カーリング液による腐食の上にTable 2 の試薬による腐食を重畳してエッチピットを現出し a) と同一視野を観察したものである．また，Photo. 23 c) はエッチピットの解析を容易にするために電子顕微鏡によって観察した結果を示したものである．a) の枠内で薄い灰色部に対応する c) 上でのエッチピットを解析すると，結晶方位の異なった2種類のパケットが5μ程度の巾で交互に配列し，それらは大傾角粒界によって分割されていることがわかる（点線を境にして結晶方位は変わっている）。灰色部に隣接する黒と灰色からなる細かい帯状模様のうち灰色部に対応するパケットも同一結晶方位ではなく，2種類の結晶方位を持っている．

以上の観察結果から明らかなように，劈開破面単位に対応するパケットの大きさがマルテンサイトに比べて小さいこと以外に，1つのバンドルの中に少なくとも3種類の結晶方位の異なったパケットが存在するのが下部ベイナイトの特徴である．

上部ベイナイトではパケットの外形が塊状になりその大きさは下部ベイナイトに比べてはるかに大きく，むしろマルテンサイトのそれに近い．1つのパケットの中に観察される方位の異なった極微細なパケットの頻度はマルテンサイトに比べてずっと減少し，このことが擬劈開の割合を少なくする要因になっていると考えられる．

4. 結　　論

(1) 低炭素焼もどしマルテンサイト，低炭素焼もどしベイナイトの脆性破壊をフェライト鋼のそれと対応させて取扱うことができ，その背景となる有効結晶粒という概念の適用がきわめて有効である．

(2) 低炭素焼もどしマルテンサイト，低炭素焼もどし上部ベイナイトの脆性破壊の様式は擬劈開ないしは劈開である．

(3) 低炭素焼もどし下部ベイナイトの脆性破壊の様式には擬劈開ないしは劈開以外にベイニチックフェライトのラス粒果に沿った粒界割れがある．しかし，脆性破壊の発生には劈開破壊が優先する．

(4) 擬劈開ないし劈開面はいずれの組織においても $\{100\}\alpha$ 面である．

終りに当り，本研究に終止関心をよせられた基礎研究所所長大竹正博士，八幡製造所特殊鋼技術部長青木宏一博士および本稿執筆にあたり色々と御指導をいただいた基礎研究所第一基礎研究室室長長島普一博士，京都大学工学部高村仁一教授に深く感謝いたします．

文　　献

1) A.M. Turkalo: Trans. Met. Soc. AIME, **218** (1960), p.24
2) J.J. Irani: In "Physical Properties of Martensite and Bainite", ISI Special Report, **93** (1965), p. 193
3) C.D. Beachem and R.M.N. Pelloux: In "Symposium on Fracture Toughness Testing and Its Applications", STP **381**, (1965), 210, ASTM, Philadelphia
4) J. Srawley: ibid
5) U.H. Lindborg and B.L. Averbach: Acta Met., **14** (1966), p. 1583

6) A.H. Cottrell: Trans. Met. Soc. AIME, **212** (1958), p.192
7) N.J. Petch: Phil. Mag., **3** (1958), p. 1089
8) C. Crussard et al.: Trans. ASM, **51** (1959), p. 581
9) S. Matsuda, T. Inoue and M. Ogasawara: Trans. JIM, **9** (1968), p. 343
10) T. Inoue, S. Matsuda and K. Aoki: Trans. JIM, **11** (1970), p. 36
11) S. Matsuda, T. Inoue and Y. Okamura: Trans. JIM, **11** (1970), p. 371
12) G. Kurdjumov and G. Sachs, Z. Phys., **64** (1930), p. 325
13) A.R. Marder and G. Krauss: Trans. ASM, **60** (1967), p. 651
14) A.R. Marder and G. Krauss: Trans. ASM, **62** (1969), p. 957
15) J.M. Chilton and G.R. Speich: JISI, **208** (1970), p.184
16) K.J. Irvine and F.B. Pickering: JISI, **201** (1963), p. 518

討論 p. 343 参照

Temper Embrittlement of Low-Carbon Alloy Steels

C. Ouchi J. Tanaka T. Osuka*

Nippon Kokan Kaisha Technical Research Center

*Now at Fukuyama Works

Most of the past investigations on temper embrittlement of quenched-and-tempered steels have dealt with medium-carbon high-hardenability alloy steels containing both nickel and chromium. The present work was undertaken with 0·15% C–1·20% Mn steels heat treated to a tempered lower bainitic structure. The factors investigated included the effect of impurity elements, the effect of quenched structure and prior austenitic grain size, saturation and reversibility of embrittlement, mode of brittle fracture and effect of alloying elements such as nickel, chromium and molybdenum as well as auger electron-spectroscopic study.

1. Experimental procedure

The steels investigated were prepared from 50 kg induction-melted heats with the compositions given in Table 1. The ingots were heated to 1300°C and then rolled from 90 mm by 130 mm section to 60 mm thickness by 110 mm width. The 60 mm-thick slabs were reheated to 1250°C, except where otherwise stated, and rolled to 12 mm-thick plates followed by water quenching from 900°C directly after rolling (Fig. 1). Quenched plates were tempered at 630°C for one hour except where otherwise stated, and subsequently water cooled.

The reasons for utilizing this direct-quenching technique for the temper-brittleness study were the following: (1) to eliminate the segregation of alloying elements and impurities in the austenite; (2) to control the austenitic grain size by heating above 1250°C and selecting the rolling temperature; and (3) to get a homogeneous quenched microstructure with intentionally varied austenitic grain size since it is very difficult to obtain a homogeneous quenched microstructure in fine-grained 0·15% C–1·20% Mn steels with conventional quenching techniques.

Specimens were embrittled by isothermal reheating at 500°C for up to 500 hr or by extremely slow cooling (20°C/hr) from 600°C. V-notch Charpy impact tests were carried out for each heat-treated condition and evaluated on the basis of the 50% fibrous transition temperature ($_{v}$Trs) criterion. Microfractographs with a single-stage replica were taken to study the fracture mode as well as optical photomicrographs on a plane perpendicular to the fracture surface.

Mechanical properties are summarized in Table 2 to 4. The tensile-strength level was held between 60 and 75 kg/mm.^{2} The presence of impurity elements and variation in quenched structure, austenitic grain size and embrittling treatment had no significant effect on the strength level.

2. Results

The results obtained are summarized below:

(1) Embrittlement occured only when specific impurities were present in the steels (Fig. 2). Phosphorus had the largest effect with antimony, tin and arsenic following in that order (Fig. 3, Table 5).

(2) The degree of embrittlement was affected by the as-quenched structure. Lower bainite was much more sensitive to embrittlement than a mixed structure of lower bainite and ferrite (Fig. 4, Photo. 1).

(3) An effect of prior austenitic grain size on the transition temperature ($_{v}$Trs) was observed after the embrittling treatment but was scarcely noticeable in the unembrittled condition (Fig. 5).

(4) Saturation of embrittlement is observed after 50 hr holding at 500°C for manganese-phosphorus steels, while saturation of embrittlement is markedly retarded in manganese-molybdenum-phosphorus steels (Fig. 6, 7)

(5) Molybdenum decreased the susceptibility to embrittlement. An optimum effect was found with 0·2% Mo and no additional benefit was observed with a higher molybdenum addition (Fig. 6 and 8).

(6) A much greater degree of embrittlement was found in a manganese-chromium-phosphorus steel than in the manganese-phosphorus steels (Fig. 2). Large platelets of chromium carbide along the grain boundaries were observed in electron micrographs (Photo. 8).

(7) Severe embrittlement was observed in a manganese-nickel-phosphorus steel at an early stage of isothermal holding at 500°C. This embrittling tendency continued monotonically up to 500 hr without any saturation (Fig. 7).

(8) Heating specimens above 600°C led to a recovery of toughness. This reversibility was also observed

in respect to brittle-fracture mode, i.e., the change from intergranular to cleavage (Fig. 9, Photo. 3).
(9) From electron-microscopic studies of manganese-phosphorus steels, it was quite clear that no change in shape, size or distribution of carbides resulted from embrittling treatments (Photo. 6 and 7).
(10) Based on examination of the fracture surfaces in embrittled materials, it was fairly evident that the fracture had taken place along prior austenitic grain boundaries as well as in the carbide-ferrite interface rather than through the carbides themselves. In addition, decohesion of grain-boundary carbides was found on the intergranular fracture surface but no cracked carbide particles were detected. These observations suggest that the existence of grain-boundary carbides made the material more sensitive to temper embrittlement by splitting the interface between the ferrite matrix and the carbides (Photo. 4 and 5).
(11) In the early stages of embrittlement, increases in the transition temperature were accompanied by increased proportions of grain-boundary fracture; this relation, however, was no longer valid in the fully embrittled stage (Fig. 8, Photo. 2).

3. Discussion

The evidence of the present work leads to the conclusion that the mechanism of temper-embrittlement phenomenon can be treated essentially as the problem of equilibrium segregation of impurity elements to the prior austenitic grain boundaries as was originally proposed by McLean and Northcott and subsequently elaborated upon by McLean. Since the segregated boundaries with phosphorus, antimony, tin and arsenic have weaker cohesive forces than sound boundaries, intergranular fracture can easily take place.

Impurities segregate to the surface, i.e., high-angle grain boundary, external surface, interphase boundary or low-angle boundary by the Gibbs adsorption theorem for dilute solutions:

$$\Gamma \sim -\frac{c}{RT}\left(\frac{\delta\gamma}{\delta c}\right)_T \qquad (1)$$

where Γ is the surface concentration in excess of the bulk solute concentration C, $(\delta\gamma/\delta c)_T$ is the variation of surface free energy with concentration at T and R is the gas constant. This equation means that any impurity lowering γ tends to segregate to the surface if equilibrium is achieved. This tendency increases as T decreases and increases with $\delta\gamma/\delta c$. The driving force for equilibrium segregation is a reduction of free energy due to the diffusion of impurity atoms to a surface where misfit is more easily accomodated by the process. For a given boundary segregation, it is possible to show by a statistical thermodynamics argument that segregation is related to temperature by an expression of the form:

$$\mathrm{Cb} = \frac{\mathrm{ACe}^{\mathrm{Q/RT}}}{1 + \mathrm{ACe}^{\mathrm{Q/RT}}} \qquad (2)$$

where Cb is the grain-boundary concentration, C is the bulk concentration, T is the temperature in degrees absolute, A is a constant and Q is the excess lattice energy due to the presence of the impurity atoms. A is generally assumed to be unity. Q is estimated by Hondros as 16 000 cal g-atom^{-1} for the lattice strain energy of phosphorus in bcc iron.

The calculated grain-boundary concentration using 16 000 cal g-atom^{-1} for Q in the temperature range from 400 to 700°C is given by the solid lines in Fig. 11. As indicated by this figure, both steels containing less than 0·005% P heated at 500°C and more than 0·02% P heated at 600°C show fairly high equilibrium concentration at the grain boundaries. This is not consistent with the degree of embrittlement in these steels but the impurity segregation at sub-boundaries also has to be considered. Calculations carried out taking this factor into account are shown by the dotted lines in Fig. 11.

This kind of behavior for impurities was confirmed by an Auger spectroscopic study directly on the polished surface of the manganese-phosphorus steel. It was found that the phosphorus concentration at the very surface was extremely enriched when the specimen was held at 500°C while this enrichment disappeared after the specimen had been heated to 600 and 650°C for 0·5 hr. Furthermore, the phosphorus peak was again visible when the specimen was held at 500°C for 0·5 hr after heating at 650°C for 0·5 hr. This result confirmed the segregation of phosphorus to the surface at temperatures around 500°C (Fig. 10).

The effects of alloying elements can be categorized into three groups as follows: (1) effect on diffusivity of impurities: (2) effect on the shape of grain-boundary carbides; and (3) effect on the difference in toughness between the grain boundaries and the ferrite matrix.

Manganese and molybdenum apparently have markedly different effects on the diffusivity of phosphorus as shown in Table 6. Manganese accelerates the diffusion of phosphorus while molybdenum greatly retards it. These data clearly explain the difference between manganese-phosphorus and manganese-molybdenum-phosphorus steels. Chromium retards the diffusion of phosphorus to some extent but it seems that the shape of the grain-boundary carbides is more important in this case. It is believed that the large platelets of chromium carbide in the grain boundaries facilitate intergranular fracture more than small spherical carbides even at lower grain-boundary concentration of impurities. Although the effect of nickel on the diffusivity of impurities is unknown, its effect on the difference in toughness between grain boundaries and ferrite

matrix offers an explanation for the marked embrittlement of nickel-containing steels during the early stages of isothermal heating at 500°C. It seems reasonable to suppose that nickel improves the toughness of the ferrite matrix but has no effect on the cohesive strength of the grain boundaries. As a result, intergranular fracture can easily take place.

低炭素合金鋼の焼戻し脆性

田中淳一　大内千秋　大須賀立美*

日本鋼管株式会社　技術研究所

*現福山製鉄所

1. 緒　　言

焼入れ焼戻し型の低炭素高張力鋼はその高い強度と優れた切欠靱性および溶接性により，圧力容器，橋梁，その他の鋼構造物に広く採用されている．この種の高張力鋼は溶接施工後，溶接部の残留応力除去のため．しばしばSR処理 (stress relieving treatment) をうける．調質型高張功鋼は通常600°Cから650°Cの温度で焼戻しされているため，SR処理はこれよりやや低い温度に加熱後，徐冷を行なう．従って溶接部に加えて母材鋼板も焼戻し脆性域で徐冷されることになり，脆化を生じることがある．

焼戻し脆性は衝撃試験での延性一脆性遷移温度の上昇として認められるが，同時に脆性破壊の様式がへき開から粒界破壊に変化する．徐冷処理による脆化は500°C脆性と呼ばれ，現象の可逆性を有しており，低温焼戻し域で生じる500°F脆性（焼戻しマルテンサイト脆性）と区別される．

焼戻し脆性については，過去数10年間にわたって冶金学上の興味あるテーマとして数多くの研究がなされてきた．この間，Hollomon[1]，Woodfine[2]，Low[3]，McMahon[4]などによって優れたレビューがなされてきた．また焼戻し脆性の脆化機構については Balajiva[5] らの高純度鋼での研究以来，鋼中の不純物元素の粒界偏析に起因すこるとが明らかになりつつある．しかしながらこの方面の研究はNi-Cr鋼を対象にしたものが圧倒的に多く，単純な低炭素Mn鋼についての系統的な研究は数少ない．

本研究では低合金高張力鋼の基本成分系であるMn鋼を対象に，偏析傾向を有する不純物元素として知られているP, As, Sn, Sbの焼戻し脆性への影響を検討する．焼戻し脆性は焼入れ組織，オーステナイト粒度，合金元素など種々の冶金的因子の影響を強く受けるため，これらの諸点についても検討し，これらの諸結果と脆性破面や組織の電子顕微鏡結果をもとに，焼戻し脆性の統一な脆化機構について考察する．

2. 実験方法

2.1 供試鋼の化学成分

供試鋼は全て50kg高周波炉で溶製したが，その化学成分をTable 1に示す．いずれも純鉄（電解鉄）ベースで溶製しているため．添加した元素以外の不純物元素の含有量はきわめて少ない．P, Sn, As, Sbの分析はJISの化学分析法により行なった．

鋼番AはMn鋼での不純物元素の影響を調べるためP含有量を変えた系と，As, Sn, Sbを各々単独添加した系からなる．As, Sn, Sbは各々原子重量パーセントで0·030%を目標にしたが，Sbが目標より少なくなった．鋼番BおよびCではMn-P鋼の焼戻し脆性におよぼす焼入れ組織とオーステナイト粒度の影響を検討した．一方鋼番DではP含有Mn鋼の焼戻し脆性に及ぼす合金元素 (Mo, Cr, Ni) の影響を調べたが，Mo添加鋼は10kg鋼塊に注ぎ分け，Mo添加量の影響を調べた．また鋼番Eでは焼戻し脆性の可逆性を調べた．

2.2 供試鋼の作製方法

全ての鋼塊とも1300°C加熱後，130mm厚さから60mm厚さまで粗圧延した．60mm厚さの鋼片は1300°Cまたは1250°Cに再加熱後，12mm厚さまで熱間圧延し，圧延仕上り後900°Cから直接水冷した．

オーステナイト粒度は，Fig. 1a）に示すように，焼入れ前の圧延温度をコントロールすることによ〜変えたが，充分再結晶したオーステナイト粒を得るために圧延仕上り温度は900°C以上にした．一方焼入れ組織の調整は，Fig. 1b）に示すように圧延仕上り後，(1) 1分後に直接水冷，(2) 900°Cの加熱炉に1時間保持した後水冷，の2通りの方法で行なった．前者の方法では均一な低温ベイナイト組織，後者ではオーステナイト粒界に沿って2〜3μの厚さのフェライトの析出した組織のものを得た．なお焼入れ組織の影響を調べた鋼種以外は熱間圧延後直ちに焼入れる方式で調質し，組織的には均一なベイナイトである．熱間圧延一直接焼入れ方式を採用した理由は，(1) オーステナイト域での合金元素や不純物元素の偏析を除去する[6]．(2) 最高加熱温度を1250°C以上にして，オーステナイト粒度や焼入れ組織を調整する，などによる．

2.3 実験方法

焼入れした鋼板は一部の試料を除いて，630°Cで1時間加熱後水冷した．Mo添加鋼（鋼番D 1〜4）は650°Cで1時間の焼戻しである．一方脆化処理は (1) 600°Cで1時間加熱後20°C/hrで徐冷，(2) 500°Cで最長500時間までの等温加熱処理，の2通りの方法で行なった．

機械試験は常温での引張試験と2mmVノッチシャルピー衝撃試験を行なった．引張試験片形状は平行部9mm直径，長さ32mmのものである．

シャルピー衝撃試験で100%脆性破面を示した試料について，破面にニッケルメッキを施し，粒界破壊率（脆性破面中に占めるオーステナイト粒界に沿って破壊している割合）を測定した．測定は100個以上の粒についての平均値を算出した．また電子顕微鏡によるmicrostructureの観察や脆性破面のフラクトグラフィーを一

Table 1. Chemical analyses of steels investigated (wt %).

Steel		C	Si	Mn	P	S	Sn	As	Sb	Mo	Cr	Ni	Al
A	1	0·16	0·16	1·23	0·001	0·009	0·001	<0·001	<0·001	<0·01	<0·01	<0·01	0·043
	2	0·16	0·17	1·24	0·003	0·007	0·002	<0·001	<0·001	<0·01	<0·01	<0·01	0·059
	3	0·16	0·18	1·22	0·015	0·008	0·001	<0·001	<0·001	<0·01	<0·01	<0·01	0·050
	4	0·13	0·24	1·24	0·032	0·006	0·002	<0·001	<0·001	<0·01	<0·01	<0·01	0·040
	5	0·16	0·19	1·24	0·003	0·006	0·001	0·040	<0·001	<0·01	<0·01	<0·01	0·049
	6	0·15	0·20	1·21	0·002	0·008	0·062	<0·001	<0·001	<0·01	<0·01	<0·01	0·042
	7	0·14	0·24	1·29	0·002	0·006	0·001	<0·001	0·046	<0·01	<0·01	<0·01	0·052
B	1	0·17	0·52	1·39	0·003	0·007	0·007	0·001	0·001	<0·01	<0·01	<0·01	0·038
	2	0·15	0·43	1·31	0·029	0·007	0·007	0·001	0·001	<0·01	<0·01	<0·01	0·031
C	1	0·15	0·33	1·23	0·022	0·012	0·007	0·019	0·007	<0·01	<0·01	<0·01	0·044
D	1	0·16	0·21	1·28	0·024	0·008	0·006	<0·001	<0·001	<0·01	<0·01	<0·01	0·047
	2	0·15	0·16	1·21	0·024	0·007	0·006	<0·001	<0·001	0·08	<0·01	<0·01	0·036
	3	0·16	0·17	1·21	0·024	0·008	0·006	<0·001	<0·001	0·28	<0·01	<0·01	0·041
	4	0·16	0·16	1·25	0·024	0·004	0·006	<0·001	<0·001	0·47	<0·01	<0·01	0·049
	5	0·14	0·18	0·48	0·018	0·011	0·001	<0·001	<0·001	<0·01	1·60	<0·01	0·026
	6	0·10	0·16	2·06	0·030	0·009	0·002	<0·001	<0·001	<0·01	<0·01	2·09	0·041
E	1	0·17	0·25	1·30	0·034	0·004	0·002	<0·001	<0·001	<0·01	<0·01	<0·01	0·040

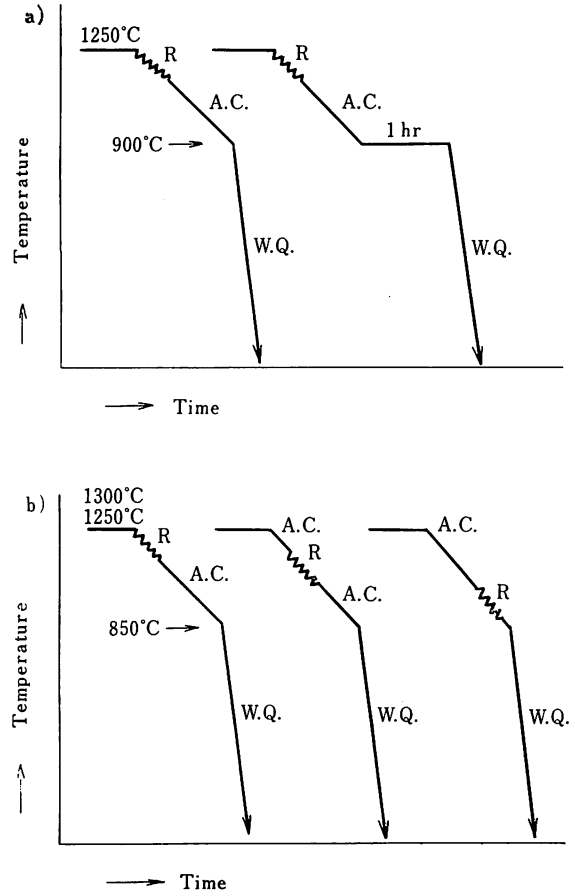

Fig. 1. Method of direct quenching after rolling.
a) Based on controlling quenched microstructure.
b) Based on controlling austenitic grain size.

段レプリカ電顕観察法で行なった.

更に不純物元素の偏析に関して粒界と同様の効果を持つ自由表面のオージェ電子分析を行ない，焼戻し脆性の可逆性との関連について検討した.

Table 2～4 に主な供試鋼の焼戻しままおよび脆化処理後の引張，衝撃特性を示す. 引張強度は 60～75 kg/mm² の範囲にあり，不純物元素や焼入れ組織あるいはオーステナイト粒度の相違による強度の較差は数 kg/mm² 以下である. また焼戻し後の徐冷処理や 500°C での等温長時間加熱などの脆化処理による強度の低下は 4kg/mm² 前後であり，比較的軽微である.

一方靱性については各鋼種とも焼戻しままの破面遷移温度は −70°C 前後である. また脆化処理後の靱性についてはシェルフエネルギーには著しい変化が認められず，大きく変化しているのは破面遷移温度である. 従って脆化度は焼戻しままと各脆化処理後の破面遷移温度の差をとって判定することにする.

3. 結　　果

3.1 不純物元素の影響

Balajiva[5] らは Ni-Cr 鋼での焼戻し脆性を生じる不純物元素は P, As, Sn, Sb であり，それらの不純物元素を含まない高純度鋼では脆化が生じないことを報告している. 一方 Low ら[7] は焼戻し脆性におよぼす不純物元素の作用は Ni や Cr などの主要元素の影響をうけることを示した.

本研究の第1の目的はこれらの不純物元素が低炭素 Mn 鋼の焼戻し脆性感受性にどのような作用をおよぼすかを検討することである. 衝撃試験での破面遷移温度と P 含有量の関係を Fig. 2 に示す. 焼入れ焼戻しままの靱性に対しては P 含有量はほとんど影響しない. しかし脆

Table 2. Mechanical properties of A steels.

Steel	Impurity	Austenitic grain size (μ)	Treatment	Tensile test				Impact test	
				Yield strength (kg/mm²)	Tensile strength (kg/mm²)	Elongation (%)	Reduction of area (%)	Eshelf (kgm)	$_{v}Tr_{s}$ (°C)
A-1	0·001% P	115	Q.T. [1]	54·8	63·7	29·1	78	24·0	−74
			Embrittled	53·0	61·1	30·0	76	20·9	−30
A-2	0·003% P	123	Q.T. [1]	56·8	65·3	29·1	78	21·2	−88
			Embrittled	53·2	61·6	26·9	75	20·0	−38
A-3	0·015% P	120	Q.T. [1]	58·8	66·6	29·3	76	21·0	−78
			Embrittled	56·4	61·4	26·5	74	20·3	32
A-4	0·032% P	130	Q.T. [1]	55·1	63·8	28·9	78	28·3	−82
			Embrittled	54·4	61·5	29·5	75	20·3	112
A-5	0·040% As	120	Q.T. [1]	54·8	63·7	29·1	78	24·0	−74
			Embrittled	53·0	61·1	30·0	76	20·9	−30
A-6	0·062% Sn	116	Q.T. [1]	55·0	63·9	28·9	78	29·8	−93
			Embrittled	54·4	61·9	30·0	76	23·3	−17
A-7	0·046% Sb	119	Q.T. [1]	56·9	64·7	23·4	76	23·6	−91
			Embrittled	54·2	62·4	28·0	75	20·0	−10

1) Embrittled : 500°C×500 hr

Table 3. Mechanical properties of B and C steels.

Steel	Micro-structure	Austenitic grain size (μ)	Treatment	Tensile test				Impact test	
				Yield strength (kg/mm²)	Tensile strength (kg/mm²)	Elongation (%)	Reduction of area (%)	Eshelf (kgm)	$_{v}Tr_{s}$ (°C)
B-1	Bainite	43	Q.T.[1] [3]	64·3	74·8	26·6	70	16·6	−68
			Embrittled	62·1	72·6	27·1	70	14·0	−47
	Ferrite +Bainite	40	Q.T.[1] [3]	58·9	72·2	27·3	69	14·8	−51
			Embrittled	57·2	71·0	26·8	69	13·6	−51
B-2	Bainite	47	Q.T.[1] [3]	67·3	76·5	24·5	68	10·4	−30
			Embrittled	65·0	74·1	23·9	67	12·1	90
	Ferrite +Bainite	44	Q.T.[1] [3]	62·9	74·6	26·4	68	15·2	−36
			Embrittled	60·8	73·0	26·0	67	13·2	12
C-1	Bainite	121	Q.T.[2] [4]	59·1	69·0	29·1	73	22·0	−80
			Embrittled	57·1	67·5	28·3	72	19·8	18
	Bainite	102	Q.T.[2] [4]	59·8	69·6	28·5	74	20·0	−82
			Embrittled	57·7	68·2	29·2	72	16·2	16
	Bainite	68	Q.T.[2] [4]	56·2	67·4	27·9	74	21·6	−80
			Embrittled	55·9	66·8	28·3	72	20·0	6
	Bainite	43	Q.T.[2] [4]	56·6	69·7	28·6	75	19·8	−83
			Embrittled	56·9	68·9	28·5	72	17·0	−11
	Bainite	37	Q.T.[2] [4]	63·8	71·6	28·3	74	19·0	−90
			Embrittled	55·8	66·3	30·6	73	18·6	−22

1) Q.T.: 600°C×1 hr Temper
2) Q.T.: 630°C×1 hr Temper
3) Embrittled : 500°C×30 hr
4) Embrittled : slow cooling (20°C/hr)

化処理後の靱性は強いP含有量依存性を示し，脆化度はP含有量に比例して大きくなる．オーステナイト粒度の影響については後述する．

一方脆化におよぼすAs, Sn, Sbの影響はTable 5に示す．1重量パーセント当りの遷移温度の上昇はPが最も大きく，ついでSb, Sn, Asの順である．Fig. 3にMn鋼での各不純物元素1重量パーセント当りの脆化度をBalajiva[5]らのNi-Cr鋼の結果と比較して示す．脆化度が最も大きい不純物元素はMn鋼ではPであり，Ni-Cr鋼ではSbである．後述するようにこれらの不純物元素は結晶粒界のmisfitを埋める形で偏析すると考えると原子パーセントで比較するのが合理的と思われるが，この場合にはTable 5に示すようにMn鋼でもSbが最も脆化度が大きい．しかし各不純物元素の脆化度を検討する場合，これらの不純物元素が各脆化処理により，平衡偏析濃度に達しているかどうか，あるいは同一偏析濃度でも偏析元素により脆化度が異なるかどうかを明らかにする実験データが必要である．後述するようにP以外の不純物元素についてはこれらの基礎データが不充分であり，各不純物元素の脆化度の相違の検討は今後の課題である．

Table 4. Mechanical properties of D steels.

Steel	Alloying element (%)	Treatment	Tensile test				Impact test	
			Yield strength (kg/mm²)	Tensile strength (kg/mm²)	Elongation (%)	Reduction of area (%)	Eshelf (kgm)	vTrs (℃)
D-1	Mo <0·01	Q.T. 1)	52·8	62·6	31·0	77	20·0	−72
		Embrittled					18·6	28
D-2	Mo 0·08	Q.T. 1)	59·3	65·0	29·4	76	20·0	−73
		Embrittled	56·5	65·4	28·4	73	17·2	−18
D-3	Mo 0·28	Q.T. 1)	65·8	73·3	26·4	74	19·5	−94
		Embrittled	64·4	72·2	25·6	71	18·1	−32
D-4	Mo 0·47	Q.T. 1)	69·2	76·8	25·6	73	19·0	−76
		Embrittled	68·2	76·6	22·8	68	17·6	−14
D-5	Cr 1·60	Q.T. 1)	64·7	70·8	24·9	77	22·8	−58
		Embrittled	62·6	67·5	24·7	76	19·5	106
D-6	Ni 2·09	Q.T. 1)	58·1	65·2	32·6	77	27·2	−72
		Embrittled	56·3	63·4	32·2	77	≧20·0	182

1) Embrittled : 500°C×500 hr

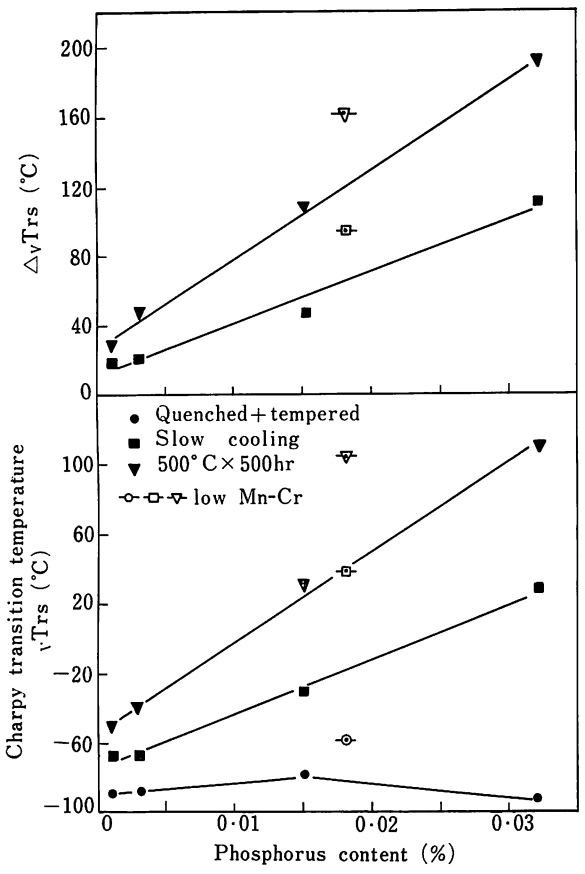

Fig. 2. Effect of phosphorus content on the embrittlement of low-carbon manganese steels (steels A1～4, and D5)

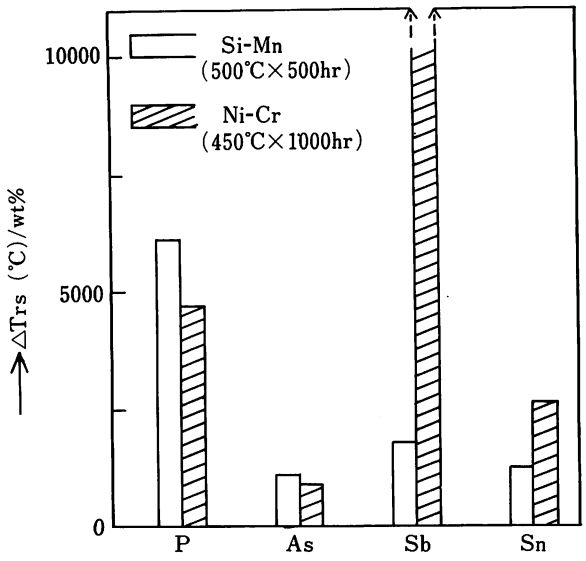

Fig. 3. Relative embrittling intensity of impurity elements in low-carbon manganese steels and nickel-chromium steels.

Table 5. Relative intensity of embrittlement by impurity elements in low-carbon manganese steel.

Steel	Impurity	Content		ΔTrs (°C)	ΔTrs/ wt %	ΔTrs/ at %
		wt %	at %			
A 4	P	0·032	0·058	197	6·160	3·410
A 5	As	0·040	0·030	44	1·100	1·470
A 6	Sn	0·062	0·029	76	1·230	2·610
A 7	Sb	0·046	0·021	82	1·780	3·830

3.2 焼入れ組織の影響

焼戻し脆性におよぼす組織の影響については，一般に低温変態生成物ほど感受性が高いことが知られている[7]．低炭素低合金高張力鋼の場合には不完全焼入れになると，焼入れ時にフェライトが析出した組織になる場合が多く，ここではこのようなフェライトの混在したベイナイト組織と均一な低温ベイナイト組織の焼戻し脆性感受性を比較検討した．

前節に記した方法で調質した時の焼入れ組織を Photo. 1 に示す．脆化処理は 500°C で 30 時間の等温加熱で行なった．結果を Fig. 4 に示す．この鋼種の場合，焼戻しままの靱性に対しては両方の組織の間に大きな差はない．一方脆化処理後の靱性は焼入れ組織の影響をうけ，特に P 含有量が高い場合には均一な低温ベイナイトの方

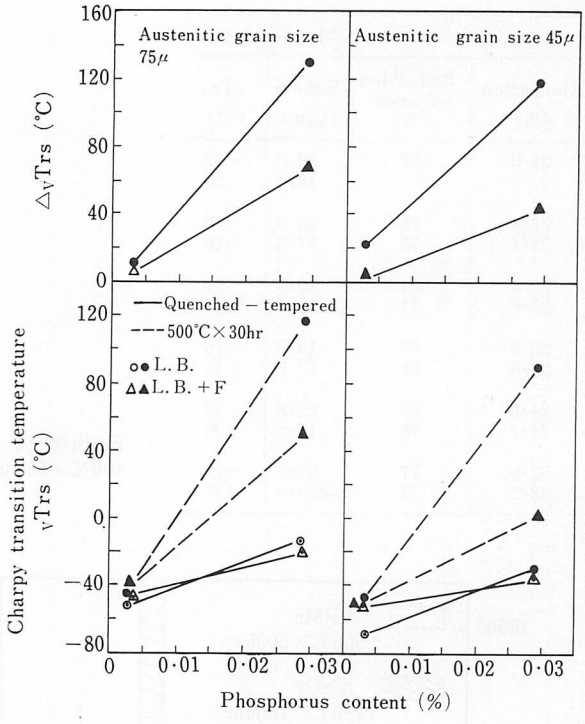

Fig. 4. Effect of phosphorus content and as-quenched microstructure on embrittlement in low-carbon manganese steels (steel B-1, B-2).

が脆化度が大きい．この傾向はオーステナイト粒径が変化しても同様であるが，P含有量が0·002% 程度になると組織によらず脆化度は非常に少ない．このような焼入れ組織の相違による脆化度の変化は，焼戻し脆性が不純物元素の粒界偏析に起因することを示していると考えられる．すなわち前オーステナイト粒界に沿ってフェライト相が析出している場合には，同じオーステナイト粒界でも粒界表面積が増加することになり，単位粒界面積当りの不純物元素の偏析濃度が低くなるため脆化度が少なくなると考えられる．

3.3 オーステナイト粒度の影響

Capus[9] は Ni-Cr 鋼での焼戻し脆性におよぼすオーステナイト粒度の影響を検討し，焼戻しままでは遷移温度の粒度依存性が小さい一方，脆化処理後には強い依存性を示すことを報告している．ここでは0·022% のPを含むMn鋼の焼戻し脆性におよぼすオーステナイト粒度の影響を調べた．前記の方法でオーステナイト粒度を調整した結果，40μ から 120μ の範囲の粒径が得られた．脆化処理は徐冷処理と 500°C での500時間の等温加熱処理で行なった．結果を Fig. 5 に示す，焼戻しままの遷移温度の粒度依存性は少なく，これはこの鋼種の特徴的な現象である[10]．一方脆化処理後には，遷移温度の粒度依存性は大きくなり，特に粗粒側での靱性の低下が大きい．後述するように 500°C で500時間の脆化処理は，Mn-P鋼ではこの温度での平衡偏析状態に達していると考えられる．すなわち粒度のいかんによらず，粒界のP濃度は同一のはずである．

従って粒界破壊の場合，粒界の結合強度が同じでも粗粒になるとクラックの発生と伝播が容易になることを示

a) No hold at 900°C before quenching.

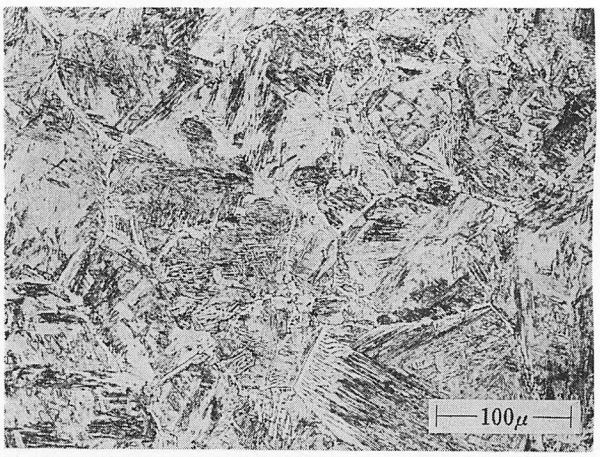

b) Held 60 min. at 900°C before quenching.

Photo. 1. Microstructures of steel B direct quenched from 900°C after rolling.

している．

3.4 合金元素の作用

焼戻し脆性が鋼中の不純物元素に起因することは今までに得られた結果から明らかであるが，同時にこの現象は合金元素の影響を強くうけるため，不純物元素と合金元素の相互作用について冶金的に検討することは重要である．経験的に Mn, Cr, Ni が脆化を促進させるのに対して，Mo は軽減することが知られている[4,7,11]．

ここではPを含むMn鋼の焼戻し脆性におよぼすMo, Cr, Ni の機能について検討する．Fig. 6 は Mn-P 鋼の500°C での等温加熱脆性におよぼす Mo の影響を示す．焼戻しままの遷移温度は Mo 含有量によってあまり変化していない．一方 500°C で等温加熱処理した時，Mo-free の Mn 鋼は 50 時間まで急激に脆化し，その後は遷移温度の上昇が飽和する傾向を示している，また Mo 添加鋼は Mn 鋼に比較して脆化度は小さくなるが，加熱時間に伴って遷移温度は直線的に上昇している．Mo 添加量の影響は脆化の軽減には0·2% で十分であり．それ以上添加しても大きな変化は認められない．

Fig. 7 は Mn-P 鋼（鋼番 E 1）と Mn-Ni-P 鋼（鋼番 D）の等温加熱脆化曲線を示す．Mn-P 鋼は Fig. 6 の結果と同様に脆化は 500°C で 50 時間の加熱で飽和する傾向を示し，これはオーステナイト粒度はよらない．これに対してほぼ同量のPを含む Mn-Ni 鋼は極めて強い脆

化を示しているが，特に 500°C に短時間加熱した時の脆化が大きい．

Cr の効果は Mn-P 鋼の結果を示す Fig. 2 中に示す．

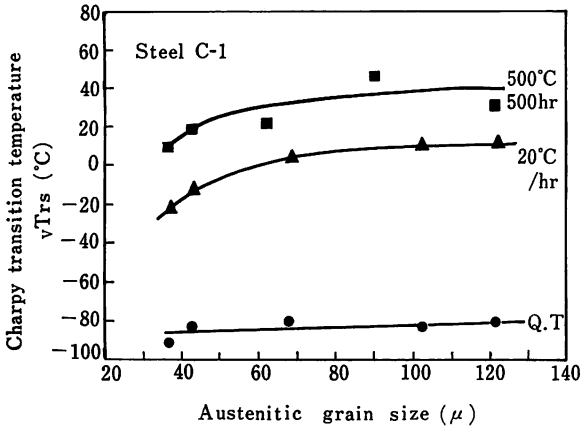

Fig. 5. Influence of austenitic grain size on the transition temperature of a manganese steel.

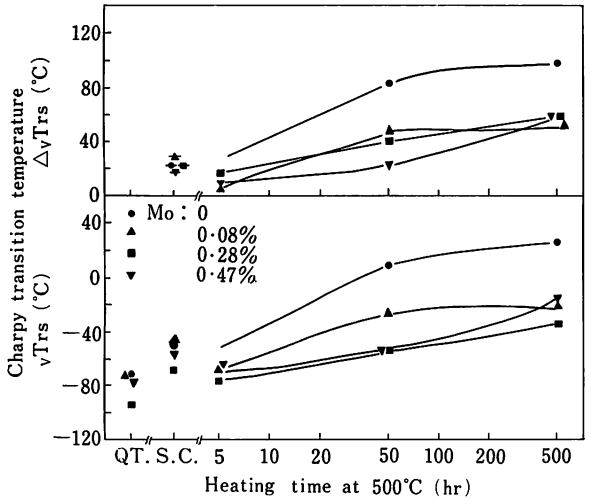

Fig. 6. The effect of molybdenum on the shift of transition temperature in manganese steel (steel D-1～D-4).

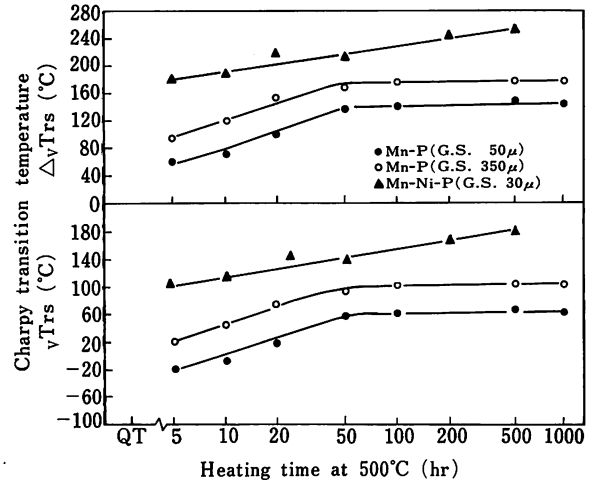

Fig. 7. The effect of manganese and nickel on the shift of transition temperature in manganese steel (steel D-6 and E-1).

同じ P 含有量の Mn 鋼に比較して Cr 鋼はより大きな徐冷脆化や等温加熱脆性を示している，これらの合金元素の脆化におよぼす作用については次節で考察する．

3.5 破壊の様式と現象の可逆性について

Photo. 2 は P 含有量の異なる Mn 鋼の脆性破面をニッケルメッキして観察したものである．高 P 含有鋼の破面は破壊が前オーステナイト粒界に沿っており，またピクリン酸飽和水溶液により粒界が優先的にエッチングされている．また P 以外の As, Sn, Sb などの不純物元素を含む鋼種の脆化材は，この腐蝕液では粒界のエッチングは認められなかったが，破壊は粒界に沿って伝播していた．

Fig. 8 には粒界破壊率と遷移温度の関係を示す．焼戻しのままではどの鋼種とも 100% へき開破壊であった．オーステナイト粒度の粗大化に伴う脆化度の上昇は粒界破壊率の増大に対応している．また Mo 添加鋼は Mn 鋼に比較して，同一脆化処理では粒界破壊率が減少しており，Mo 添加により不純物元素の粒界偏析率が減少することを示している．しかし 500°C での等温加熱時間が長くなるにつれて粒界破壊率は増大し，遷移温度の上昇と対応している．

焼戻し脆性の可逆性の検討は Mn-P 鋼（鋼番 E1）で行なった．500°C で 200 時間の脆化処理後 (Fig. 7 参照)，580°C から 640°C の温度域で各 1 時間再加熱し，水冷した．再加熱温度に伴う遷移温度と粒界破壊率の変化を Fig. 9 に示す．再加熱温度が 600°C 以上になると靱性は急激に回復し，640°C では焼戻しままと同じ遷移温度になっている．また Photo. 3 に示すように，再加熱温度の上昇に伴い，粒界破壊から粒内破壊に変化しており，また粒界のエッチング効果が消失している．すなわち不純物元素の粒界偏析は 500°C 前後で生じる一方，600°C 以上では粒界から粒内に再固溶していくことを示している．

4. 考　　察

4.1 フラクトグラフィーと組織の電子顕微鏡観察

Photo. 4, 5 に一段レプリカ法による脆性破面の電子顕微鏡観察結果を示す．Photo. 4 a), b) は焼戻しままの脆性破面であり，へき開破面上には高倍率でも炭化物のはくり的な様相は見られない．これに対して，脆化処理後の破面である Photo. 5 b), c) は粒界破壊を示しており，高倍率では粒界セメンタイトのはくり的な様相が認められる．また同じ脆化処理材でも粒内破壊をした所は，Photo. 4 d) に見られるように，へき開上にセメンタイトのはくり現象が認められる．

一方 Photo. 6 は Mn-P 鋼の焼戻しままおよび脆化処理後の一段レプリカ法による微細組織の電子顕微鏡観察結果を示す．Mn 鋼の焼戻し後のセメンタイトは 0·1～0·2 μ 直径の球状であり，焼戻し後の徐冷処理や 500°C で 500 時間の加熱処理によっても著しい炭化物の形状変化は認められない．またこのようなセメンタイトは粒界やベイナイト lath 上に優先析出しているために，粒内では planar な分布を示している．また Photo. 7 は Mn 鋼の薄膜電子顕微鏡観察結果であるが，ベイナイト lath の幅は 0·8μ から 1·0μ であり，やはり lath 上にセメンタイトの析出が生じている．これらの組織観察で見られるセメンタイトの大きさは粒界破壊の破面上に認めら

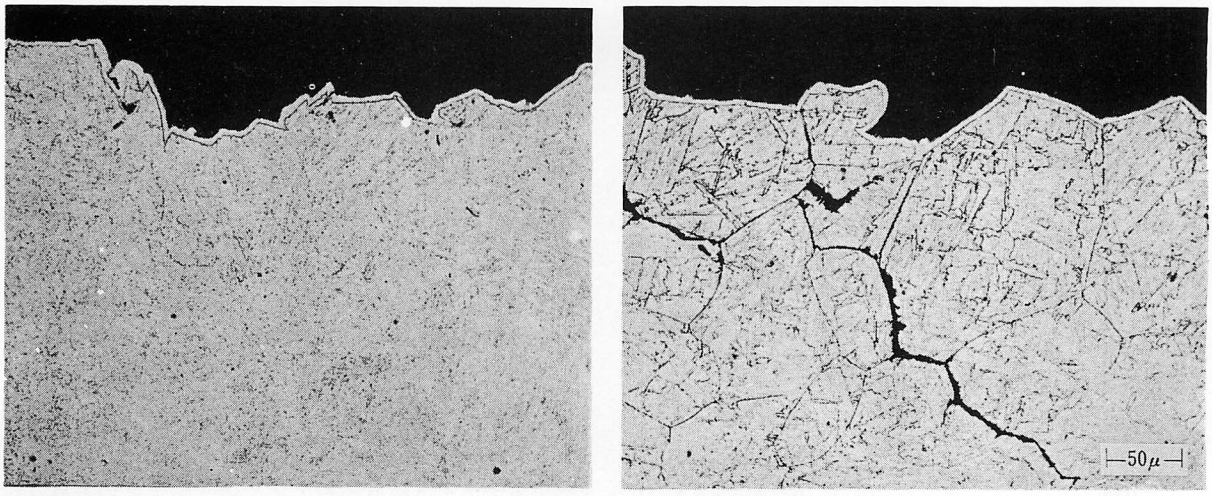

a) 0·001% P　　b) 0·032% P

Photo. 2. Brittle fracture appearance of impact specimens heated at 500°C for 500 hr. Etched with saturated aqueous picric acid containing 0·2% detergent.

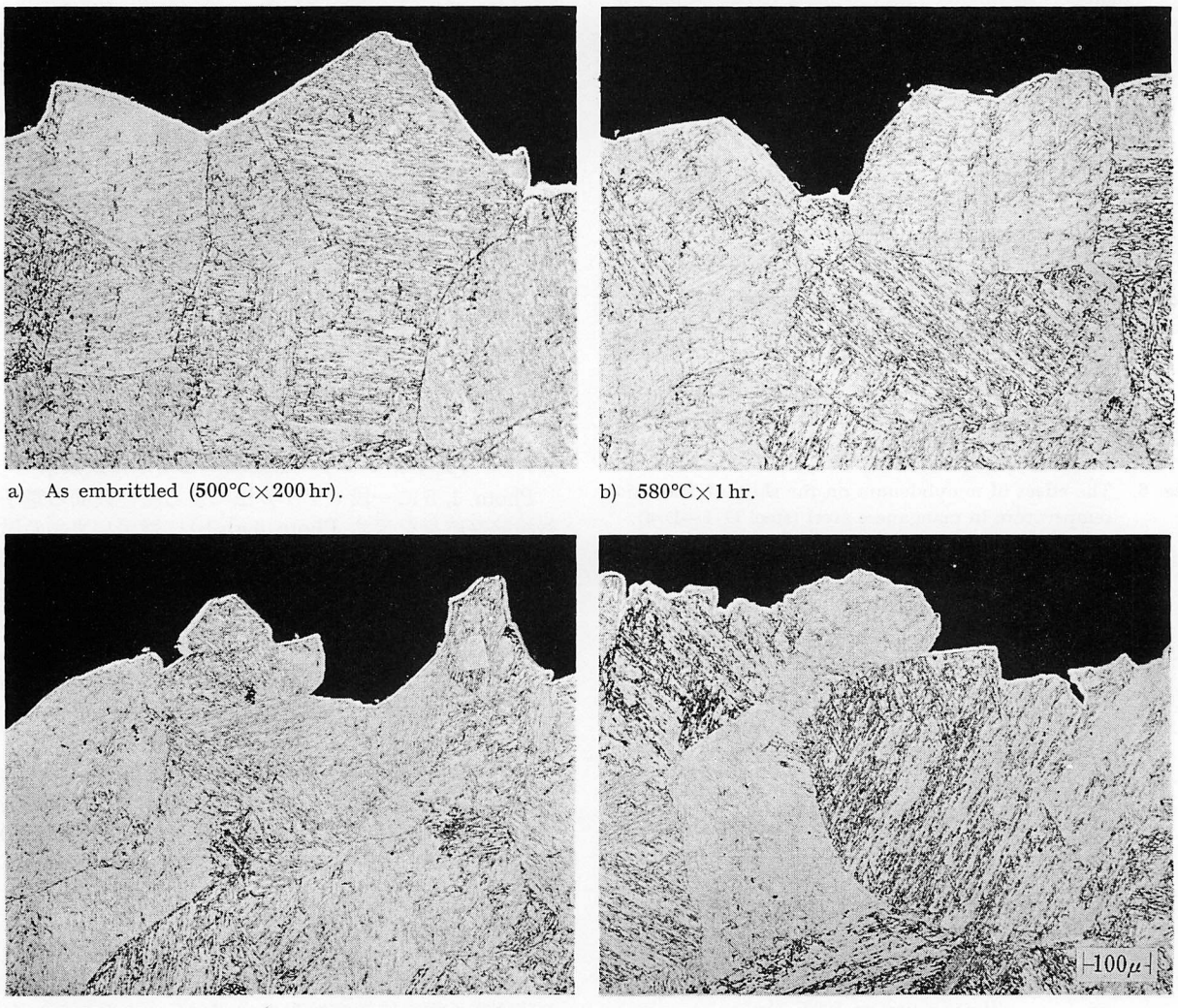

a) As embrittled (500°C×200 hr).　　b) 580°C×1 hr.

c) 610°C×1 hr.　　d) 640°C×1 hr.

Photo. 3. Change in fracture mode of de-embrittled steel E-1. Double etched by nital and picral.

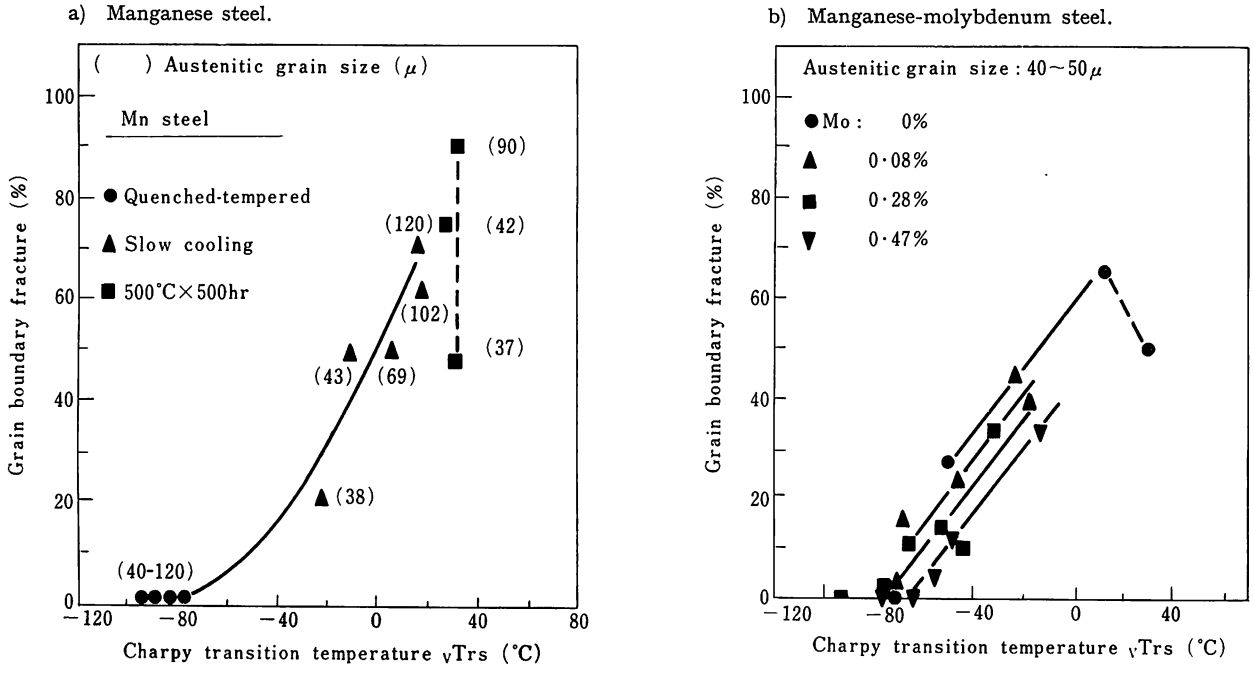

Fig. 8. The relation between transition temperature and grain-boundary fracture.

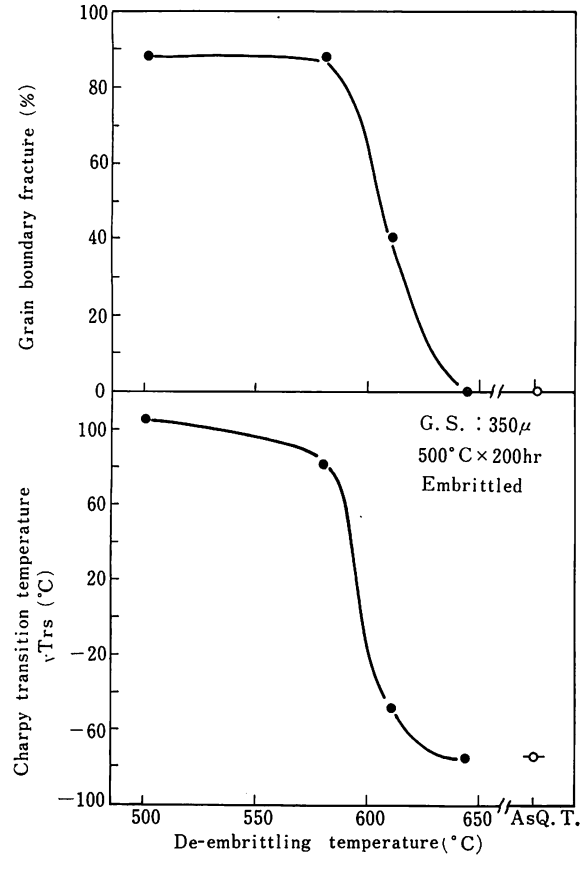

Fig. 9. Reversion of temper embrittlement by heating above the embrittling range (steel E-1).

れるセメンタイトのそれとほぼ同じである.

以上の破面と組織の電子顕微鏡観察結果で重要なことは，焼戻し脆性による粒界破壊の出現には粒界炭化物の存在が脆化を促進させていることである．すなわち鋼中の不純物元素は粒界に偏析すると同時に，粒界炭化物の回りに吸着し，その界面でのはくりを促進することが考えられる．Martin[12] らはオーステナイト化時に不純物元素がオーステナイト粒界に偏析し，その結果焼戻し時に粒界セメンタイトが plate 状に成長すること促進し，このような plate 状の析出物が脆化の原因とした．Mn 鋼の場合にはこのような形状の粒界セメンタイトは認められなかった．しかし Cr 鋼では Photo. 8 に示すように，粒界に扁平に伸びた Cr 炭化物が認められた．すなわち脆化度は不純物元素の粒界偏析濃度に対応する一方，偏析濃度が同じでも鋼種が異なり粒界炭化物の形状が変化すると，粒界破壊の難易性が違ってくる可能性がある．

またこのような粒界炭化物の回りへの不純物元素の吸着は subboundary 上に析出する炭化物にも同様に生じていることが考えられ，Photo. 4 d) に示すようなへき開破面上の炭化物の decohesion が生じると思われる．

4. 2 焼戻し脆性の脆化機構

焼戻し脆性におよぼす諸因子の検討結果から，この現象が鋼中の下純物元素の粒界偏析に起因することが明確になったと考えられるが，残された考察すべき点は，偏析の起因とその形態および脆化におよぼす合金元素の作用の機構についてである．

金属中の固溶原子の粒界偏析現象として従来報告されているものには，平衡偏析と非平衡偏析現象がある．後者は幾何学的な結晶粒界の厚さに比べてかなり厚い領域に偏析が生じるものであり[13,14]，粒界近傍の微小硬度測定で偏析の測定が可能である[15]．これに対して平衡偏析現象は粒界のきわめて薄い原子層に偏析するものであり，焼戻し脆性がこの現象に属することは最近に至り，オージェ電子分析[16~18] により直接明らかにされた．

平衡偏析現象は次式の Gibbs の吸着式で示されるものである．

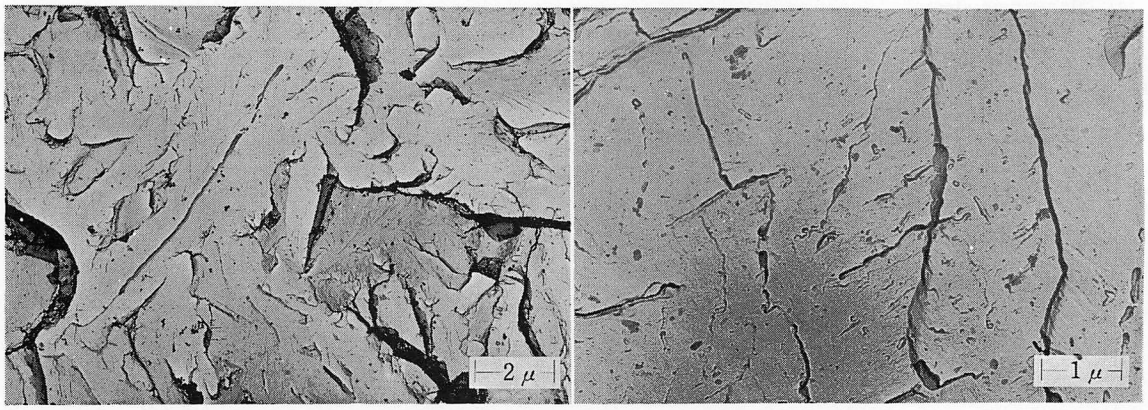

a) b) Cleavage fracture in quenched-and-tempered condition.

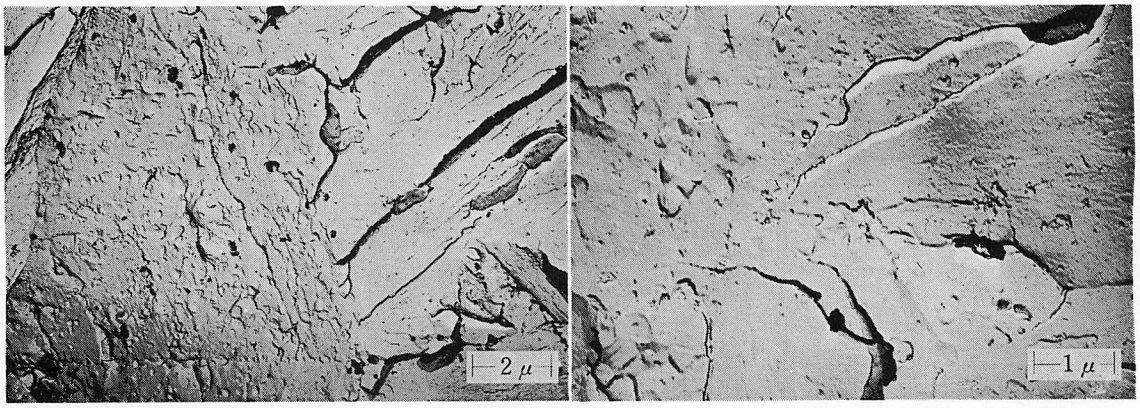

c) d) Cleavage and intergranular fracture in embrittled condition.

Photo. 4. Electron fractographs of the steel A-3.

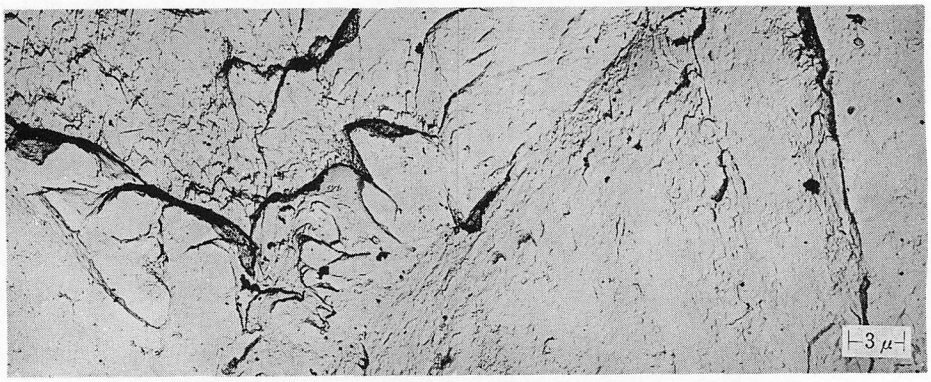

a) Intergranular fracture with dimpled rupture.

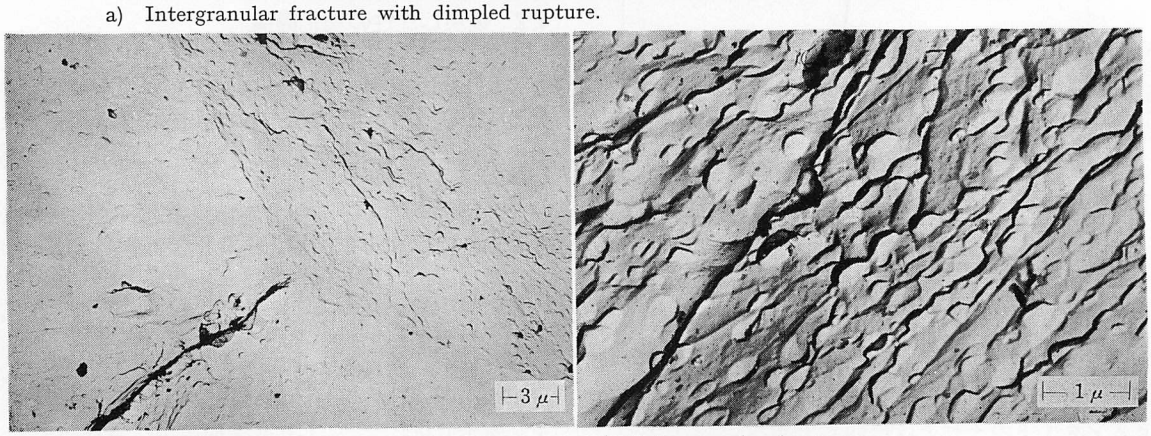

b) Intergranular fracture.

c) Intergranular fracture.

Photo. 5. Electron fractographs of the steel A-3 embrittled by heating 500 hr at 500°C.

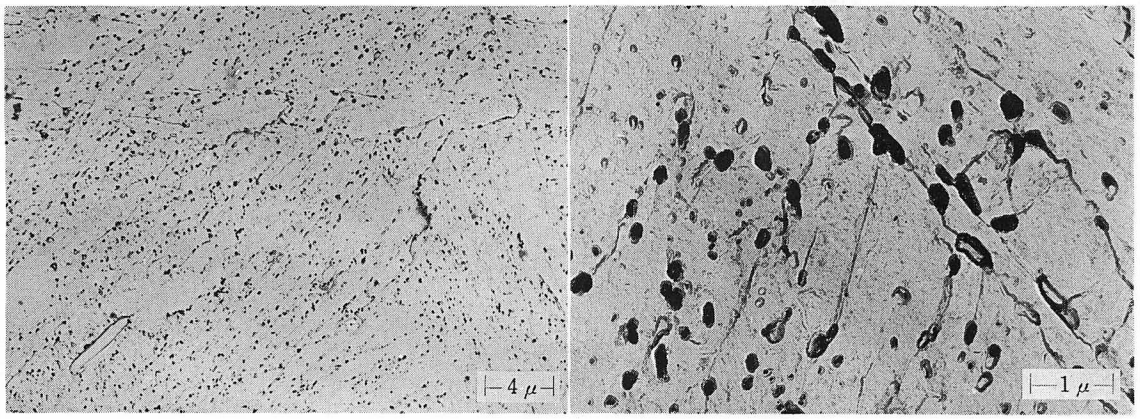

a) Quenched and tempered.

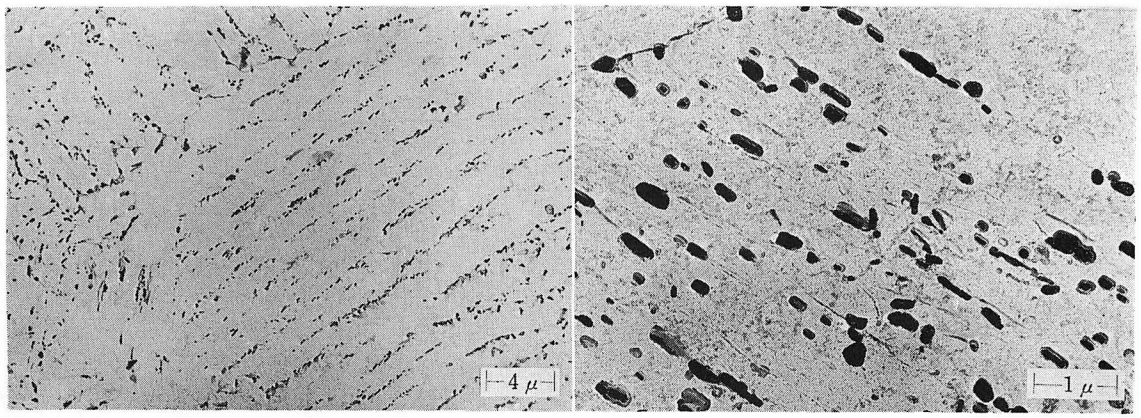

b) Embrittled by heating 500 hr at 500°C.

Photo. 6. Carbon extraction replica of the manganese steel (A-3).

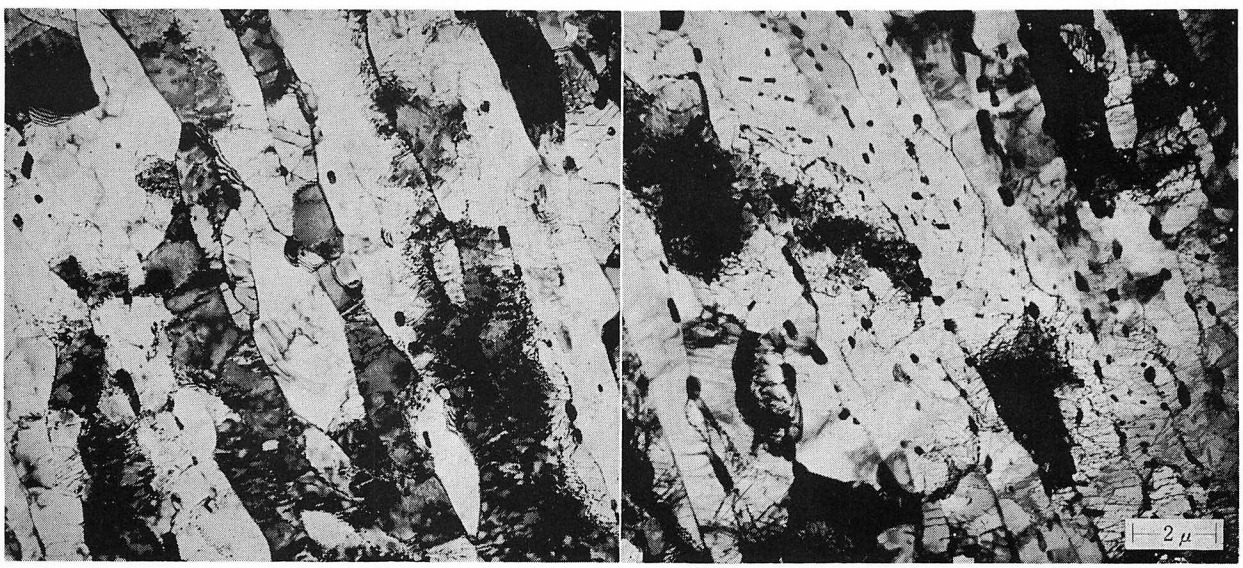

a) Quenched and tempered. b) Embrittled by heating 500 hr at 500°C.

Photo. 7. Transmission electron micrographs of manganese steel (A-3).

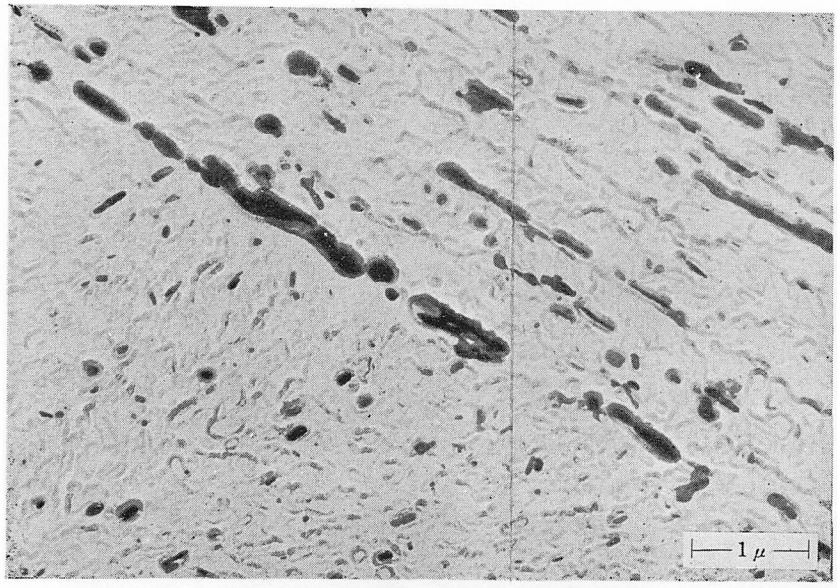

Photo. 8. Carbon extraction replica of chromium steel (D-5).

$$\Gamma \sim \frac{\partial}{\partial T} ln\left(\frac{\partial \gamma}{\partial C}\right)_T \qquad (1)$$

Γ ：単位面積当りの吸着量
C ：bulk の固溶原子の濃度
γ ：表面あるいは界面エネルギー
T ：絶対温度

すなわち吸着により表面ないしは界面エネルギーを低減する固溶原子は偏析する傾向をもち，偏析濃度は低温程大きい．焼戻し脆性が (1) 式で示される現象とすると，不純物元素は粒界のみならず鋼の自由表面にも偏析するはずであり[18]．また自由表面でも可逆性を有した偏析傾向を示すことが考えられる．

筆者と小野らは[19] Mn-P 鋼（鋼番 B-2）の自由表面での偏析現象とその可逆性の検討をオージェ電子分析で行なった．詳細は別途報告予定であるが，0·1mm の薄板に仕上げた試料を超高真空下（10^{-8}～10^{-9} torr）で直接通電で加熱しオージェ電子分析を行なった．結果を Fig. 10 に示す．500°C で 90 分保持後にはPのピーク（120 eV の位置）[20] がはっきり顕出されている．またその後 600°C および 650°C に各 30 分保持すると，Pのピークの高さには減少，消滅していく傾向が認められ，3.5 項に記した脆化の可逆性のきわめてよい対応を示している．また 650°C で 30 分保持後，500°C に 30 分保持すると，再びPのピークが出現しており，500°C 前後でPが偏析することが確認された．

粒界偏析の場合，温度 T での平衡偏析濃度 C_{gb} は次式で与えられる[21]．

$$C_{gb} = \frac{ACe^{Q/RT}}{1 + ACe^{Q/RT}} \qquad (2)$$

ここでQは固溶原子の存在による格子の過剰エネルギーである．また定数Aは振動エントロピーと関係した値であるが，通常 A=1 と仮定される．

Hondros[22] は粒界エネルギーの直接測定から，b. c. c 鉄中のPのQの値として 16 000 cal/mol を求めている．この値をもとに計算した 400°C から 700°C の温度での粒界でのPの平衡偏析濃度を Fig. 11 に実線で示す．500°C ではP含有量が 0·03 原子 % 以上では C_{gb}～1·0（これは粒界厚さを 3 原子層と仮定すると 30 原子 % に対応する[21]．）になることがわかる．しかし 500°C に加熱された 0·005% Pを含む鋼や 600°C 以上に加熱された 0·020 % 以上のPを含む鋼の平衡濃度は実際の脆化度から判定して高すぎる値である．後者は温度の上昇に伴うフェライト中のPの固溶濃度の変化などが原因していると考えられるが[23]，前者の点は前項に記したように不純物元素の subboundary への偏析量を補正して計算する必要

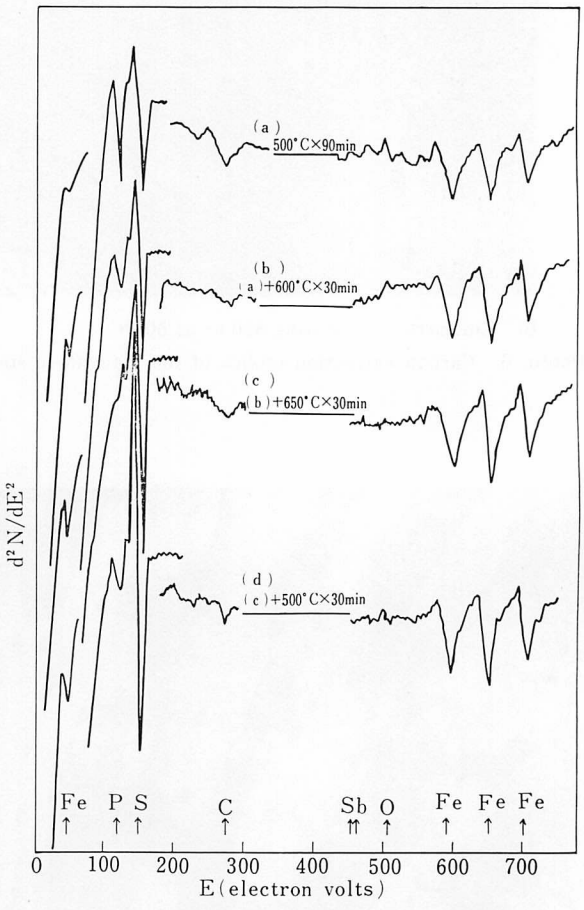

Fig. 10. Auger spectrum of the manganese steel with 0·029 % P after heating at temperatures from 500°C to 650°C.

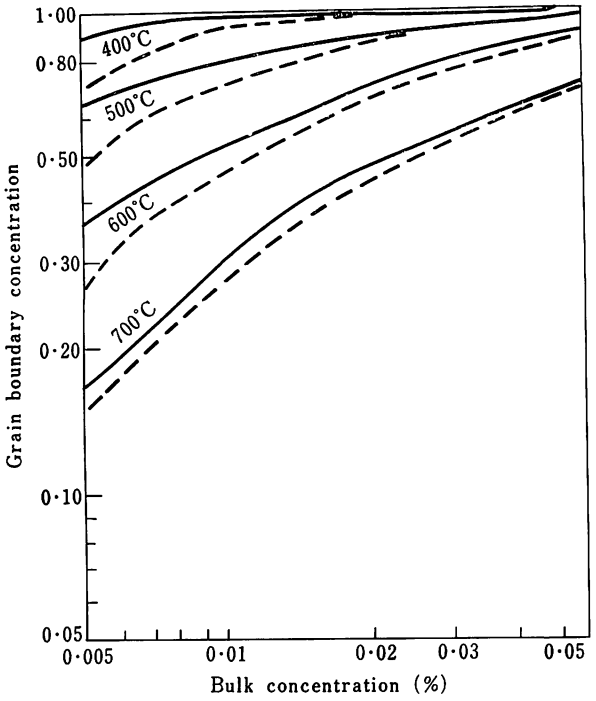

Fig. 11. Relation between grain-boundary concentration and bulk concentration as a function of temperature. Calculated with Q=16 000 cal/mole.

があることを示すものと思われる．脚注* に示すような仮定で計算した結果を Fig. 11 の点線で示す．このような補正で低濃度側での平衡濃度が減少することがわかる．

* subboundaryの厚さを1原子層とした時，単位体積当りのsubboundary の偏析 site の数，すなわち固溶限は粒界エネルギー γ_{gb} と subboundary エネルギー γ_{sb} の比に比例すると仮定すると，$2/da^2$ $(\gamma_{sb}/\gamma_{gb})$ になる．(d: cell の直径で Photo. 7 より約 1μ, a: 原子直径で 2·54Å)，すなわち subboundary の固溶限まで固溶原子が偏析する時に必要な bulk 濃度は $2a/d(\gamma_{sb}/\gamma_{gb})$ である．(γ_{gb}～700ergs/cm, γ_{sb}～50ergs/cm²)[24]．

更に subboundary の偏析に対しても平衡偏析を考慮して，Q=16000 cal/mol の値を用いて (2) 式により C_{gb} を計算し，この値を $2a/d(\gamma_{sb}/\gamma_{gb})$ に乗じて，bulk 濃度から差引いて計算した結果が Fig. 11 の点線で示されるものである．実際には subboundary の Q は 16 000 cal/mol よりも小さいことも考えられるので，この計算値は下限値を与える．

一方合金元素の作用については，脆化が不純物元素の粒界偏析に起因することを前提とした時，次の三点によって脆化と関連していることが考えられる．すなわち (1) 不純物元素の拡散速度への影響，(2) 粒界炭化物の形状の影響，(3) 粒界とフェライト地の相対的な靱性の変化である．

(1) の点に関しては焼戻し脆性が kinetics の問題として取り扱える点を重視する必要がある．すなわち Mn-P 鋼は 500°C で等温加熱処理した時，遷移温度の上昇が約 50 時間で飽和する一方，Mo 添加の Mn-P 鋼は単純な Mn-P 鋼よりも少ない脆化度ではあるが，500 時間まで単調に遷移温度の上昇を示す．逆に Ni 添加の Mn-P 鋼は最も大きな脆化度を示すと同時に，加熱時間に伴って単調な脆化度の上昇を示した．また Gould[25] は Mo-Ni-Cr 鋼では 850°F の加熱温度で約 10 000 時間後に脆化が飽和することを報告している．

McLean[21]は粒界での平衡偏析に達するまでの時間を取り扱い，次式を導びいた．すなわち温度 T での t 時間後の粒界の濃度 C_{gbt} は

$$\frac{C_{gbt}-C_{gbo}}{C_{gb\infty}-C_{gbo}}=1-e^{4Dt/\alpha^2\delta^2}erfc\left\{\frac{2\sqrt{Dt}}{\alpha\delta}\right\} \quad (3)$$

$C_{gbo}, C_{gb\infty}$ ：各々 $t=0$, $t=\infty$ 後の粒界濃度

α ： $\dfrac{C_{gb\infty}}{C_0}$

δ ：粒界の厚さ

C_0 ：偏析原子の bulk 濃度

(3) 式より温度 T での究極的な平衡濃度の 50% および 90% に達する時間 $t_{1/2}$, $t_{9/10}$ は各々次式で与えられる．

$$t_{1/2}\fallingdotseq\frac{9\alpha^2\delta^2}{64D} \quad (4)$$

$$t_{9/10}\fallingdotseq\frac{25\alpha^2\delta^2}{4D} \quad (5)$$

Gruzin[26] の求めた Fe, Fe-Mn, Fe-Mo, Fe-Cr 合金中での P の拡散係数より計算した $t_{1/2}$, $t_{9/10}$ の値を Table 6 に示す．(P 含有量が 0·04 原子パーセントの時 500°C での平衡偏析濃度は Fig. 11 よりほぼ 1 であり，$C_{gb\infty}\fallingdotseq$ 0·30%，また粒界の厚さを 3 原子層と仮定) このような計算結果から Mn が P の拡散を著しく促進する一方，Mo は拡散を遅らせることがわかり，また各鋼種の遷移温度の飽和する時間は 500°C での平衡偏析濃度に達す

Table 6. Time for equilibrium segregation.

Steel	Diffusion coefficient of phosphorus	D at 500°C (cm/sec²)	$t_{1/2}$ sec (hr)	$t_{9/10}$ sec (hr)
Fe	$1\cdot58\ \exp\left(-\frac{52300}{RT}\right)$	$2\cdot45\times10^{-15}$	$2\cdot6\times10^{5}$ (72·5)	$1\cdot2\times10^{7}$ (3220)
Fe+1·9% Mn	$1\cdot27\times10^{-4}\ \exp\left(-\frac{31400}{RT}\right)$	$1\cdot65\times10^{-13}$	$3\cdot9\times10^{3}$ (1·1)	$1\cdot7\times10^{5}$ (48)
Fe+1·3% Cr	$71\ \exp\left(-\frac{61700}{RT}\right)$	$1\cdot07\times10^{-15}$	$6\cdot0\times10^{5}$ (166)	$2\cdot6\times10^{7}$ (7400)
Fe+0·47% Mo	$7\cdot6\ \exp\left(-\frac{56000}{RT}\right)$	$2\cdot47\times10^{-16}$	$2\cdot6\times10^{6}$ (720)	$1\cdot2\times10^{8}$ (32000)

Remarks P content : 0·022 wt% (0·04 at %).
$\alpha=C_{gb}\infty/Co\fallingdotseq0\cdot30/0\cdot0004\fallingdotseq750$.
$\delta\fallingdotseq9\times10^{-8}$ cm

るに要する時間とほぼ対応することがわかる．すなわち等温脆化処理を行なった時，脆化度は不純物元素の粒界偏析濃度に比例して上昇し，粒界での偏析濃度がその温度での平衡値に近づくとそれ以上の脆化を生じないことを示している．

Cr の作用は Gruzin の求めた拡散係数では実際の脆化現象と対応しないが，前項に記したように少ない偏析濃度でも粒界炭化物が plate 状に析出すると粒界破壊がより容易に生じることが考えられる．

また Ni の作用に関しては不純物元素の拡散係数への影響は未知であり，ここではっきりしないが，等温加熱処理した時，短時間で急激に脆化する一方，500 時間まで単調に脆化していくことから，上記の (1) の他に (3) の因子が作用していることが推測される．すなわち Ni はフェライト地の靱性を向上させる一方，粒界の結合強度には大きな影響をおよぼさないとすると，不純物元素がわずかに粒界偏析した場合，より容易に粒界破壊が生じることが考えられる．

5. 結　　論

低合金高張力鋼の焼戻し脆性（500°C 脆性）におよぼす冶金学的諸因子の影響について検討した結果，以下の諸点が明らかになった．

(1) 焼戻し脆性は本質的に鋼中の P, As, Sn. Sb などの偏析傾向を有する不純物元素に起因する．

(2) Mn 鋼での不純物元素の脆化作用は P が最も大きく，Sb, Sn, As の順に小さくなる．

(3) 焼戻し脆性は焼入れ組織に敏感であり，低温変態生成物ほど脆化度は大きくなる．

(4) Mn 鋼の焼戻しままの遷移温度の粒度依存性は小さいが，脆化処理後には粒度依存性を示すようになる．またこの場合の遷移温度は粒界破壊率の変化と対応する．

(5) 焼戻し脆性におよぼす合金元素の作用は，(イ) 不純物元素の拡散速度への影響，(ロ) 粒界炭化物の形状の影響，(ハ) フェライト地と粒界の相対的な靱性の変化，の三点により説明できる．

(6) 焼戻し脆性は kinetics の問題として取り扱えるが，500°C で等温加熱処理した時，Mn-P 鋼は 50 時間加熱まで遷移温度は急激に上昇し，その後は飽和する傾向を示す．これに対して，Mo 添加鋼はより少ない脆化度であるが，500 時間まで単調に遷移温度の上昇を示す．

(7) このような現象はオーステナイト粒界での平衡偏析現象と P の拡散速度におよぼす Mn や Mo などの合金元素の作用により説明できる．

(8) 不純物元素の偏析は前オーステナイト粒界の他に，粒内のマルテンサイトやベイナイトの packet 粒界や lath 上にも生じる．これらの粒界上の炭化物の回りに不純物元素が吸着し，炭化物のはくりが生じやすくなり粒界破壊が促進される．

(9) 不純物元素の偏析現象は P 含有 Mn 鋼の表面のオージェ電子分析により直接明らかにされ，同時に脆化現象の可逆性はオージェ電子分析による偏析の可逆性の測定結果と極めて良い対応を示した．

謝　　辞

本研究を進歩させるに当って，堀川一男博士（日本鋼管技術研究所副所長），故久保田広行氏，天明玄之輔氏（同所次長）の御理解ある協力を戴いた．また本報告書をまとめるのに際しては，市之瀬弘之博士（同所課長）と小指軍夫氏（同所係長）から御討論，御教示をうけた．

更にオージェ電子分析を実施するに際しては，中山勝矢博士と小野雅敏氏（工業技術院電機総合研究所）の御協力を戴いた．

以上の方々に謝意を表します．

文　　献

1) J.H. Hollomon: Trans. ASM, **36** (1946), p. 473～540
2) B.C. Woodfine: J. Iron and Steel Inst., **173** (1953), p. 229～240
3) J.R. Low: Fracture of Engineering Materials (1964), p. 127～142 ASTM STP 407
4) C.J. McMahon: Temper Embrittlement in Steel (1968), p. 127～167 ASTM STP 407
5) K. Balajiva 他： J. Iron and Steel Inst., **193** (1959), p. 141～147
6) J.M. Capus: 4) に同じ，p. 3～19
7) J.R. Low 他: Trans. AIME., **245** (1969), p. 2481～2494
8) J.D. Murray 他： Low Alloy Steels (1968), p. 37～53 (Iron and Steel Inst.)
9) J.M. Capus: J. Iron and Steel, **200** (1962), p.922～927
10) H. Kubota 他： International Conference on the Science and Technology of Iron and Steel, Proceedings; to be published
11) A.Preece 他 : J. Iron and Steel Inst., **173** (1953), p. 387
12) M.A. Martin 他 : Metal Treat. Drop Forg., (1962),p.301～310
13) K.T. Aust 他： Acta Met., **16** (1968), p. 291～302
14) B. Chalmers 他 : Met. Trans., **1** (1970), p. 1095～1104
15) J.H. Westbrook 他： Acta Met., **11** (1963),p.1151～1163
16) P.W. Palmberg 他： Trans. AIME., **245** (1969), p. 1664～1666
17) D.F. Stein 他： Trans. ASM, **62** (1969), p. 776～783
18) H.B. Bishop 他： Acta Met., **18** (1970), p.813～817
19) 小野他： 投稿予定
20) D. Stein 他： J. Metals, **23** (1971), p. 39～44
21) D. McLean: Grain Boundaries in Metals, (1957), p. 116～149 (Oxford Univ. Press)
22) E.D. Hondros: Proc. Roy. Soc., **286A** (1965), p.479～498
23) C.J. McMahon Jr. 他： Trans. ASM., **60** (1967), p.699～706
24) J.B. Byrne: Recovery, Recrystallization and Grain Growth, (1965), p. 110～165 (Macmillan Co.)
25) G.C. Gould : 4) に同じ，p. 59～73
26) P.L. Gruzin 他： Fiz. Metal Metalloved., **17** (1964), p. 384～389

The Effect of Transformation Structures on the Toughness of Quenched-and-Tempered Low-Carbon Low-Alloy Steels

T. Kunitake F. Terasaki Y. Ohmori H. Ohtani

Sumitomo Metal Industries, Ltd

Central Research Laboratories

The effect of microstructural factors on the toughness of weldable low-carbon low-alloy high-strength steels was investigated. The toughness of various microstructures produced by continuous-cooling transformation was interpreted in terms of the fracture unit path and microstructural mode. Experimental data suggesting the role of carbide and dislocation density are presented and discussed.

The impact properties of three low-carbon low-alloy steels were determined in relation to both the cooling rate on continuous cooling after austenitization and the austenitic grain size. The steels investigated were a 0·15%C–1·3%Mn–0·2%Ni–0·13%Mo-0·03%V steel with a tensile-strength level of 60 kg/mm^2 (steel N) and two 80 kg/mm^2 tensile-strength steels with a chemical composition of 0·13%C–0·85%Mn–0·3%Cu–1·0% Ni–0·5% Cr–0·5% Mo–0·03%V-(B) (steel 7 without boron and steel 8 with). They were austenitized at temperatures up to 1200°C and then continuously cooled at rates from 1 to 4×10^{-4} sec (expressed as the cooling time from 800°C to 500°C). Tensile tests were made at room temperature and Charpy V impact tests were conducted at various lower temperatures.

The results showed the existence of an optimum cooling rate to produce the lowest impact transition temperature. For instance, the copper-nickel-chromium-molybdenum-vanadium steel exhibited a minimum transition temperature of –120°C after austenitizing at 900°C and continuous cooling at a rate corresponding to four seconds between 800°C and 500°C. Faster and slower cooling rates raised the transition temperature (Fig. 2). The optimum cooling rate varied with the hardenability of the steel and became slower as the hardenability of the steel increased. Raising the austenitizing temperature shifted the optimum rate to longer cooling times (Fig. 4).

Continuous-cooling transformation diagrams were determined for each steel with various austenitizing conditions. The optimum cooling rate was slower than the upper critical cooling rate (for the beginning of bainite formation) but faster than that corresponding to the formation of bainitic ferrite (Fig. 6 and 7).

Electron-microscopic observation revealed that the structure with superior impact properties was a duplex martensite-bainite structure with 10 to 20% bainite having a characteristic morphology. The carbide morphology in this bainite was similar to that in the lower bainite of a higher carbon steel, but trace analysis revealed that it had the same lath-like morphology with a $\langle 111\rangle\alpha\{110\}\alpha$, habit as that in upper bainite or lath martensite. This type of bainite in a low-carbon low-alloy steel has been designated as bainite III type[20] (Fig. 5).

The aspects of the brittle fracture surfaces were typical of quasi-cleavage surfaces with fine patterns like river-marks. The crystallographic orientation of the cleavage planes was determined by means of a facet pit technique using a goniomicroscope. The facet pit composed mainly of $\{110\}\alpha$ was produced on a section parallel to the direction of the crack propagation and nearly orthogonal to the fracture surface. From determination with the goniomicroscope of the orientation of the cleavage plane corresponding to the facet pit, it was concluded that the cleavage plane was $\{100\}\alpha$.

The unit crack path was determined by direct observation of the fracture surface with a scanning electron microscope. The cleavage fracture initiated inside the fracture unit near the boundary and it propagated radially to the boundary of the adjacent fracture unit where it was arrested. Each unit contained a fracture origin. The unit fracture path is defined as the mean diameter of the fracture facet in which the orientation differences of the ferrite laths in respect to a {100} plane are small.

In the ductile-brittle transition range, a ductile network enclosing the brittle fracture unit was observed but the fracture unit itself was found to be the same at all test temperatures.

There was a good correlation between the unit crack path and the transition temperature with the finer crack paths corresponding to lower transition temperatures. The duplex martensite-bainite (type III) structure with the best toughness had the finest fracture unit of all the continuous-cooling transformation

structures. In the linear plot of the transition temperature against the log (unit fracture path)$^{-1/2}$, two separate lines were obtained for the transformation structures produced on continuous cooling (Fig. 9). One of these covered both the martensite and the martensite-bainite (type III) structures, and the other represented the structures produced by slower cooling rates (bainitic ferrite (high-temperature bainite) and ferrite+bainite).

On studying the fracture path with a scanning electron microscope, it was observed that the fracture path changed direction at the interface of the martensitic matrix with the bainite (type III) lath. Accordingly, the orientation was different on both sides of the bainite (type III) lath. It was also noticed that, in the early stage of its formation, the bainite lath formed as if it had divided the austenite grain into several parts.

These observations suggested that the role of bainite (type III) in the duplex structure was the partitioning of the austenite grain prior to the martensitic transformation so the unit fracture path was reduced.

Tempering did not alter the general trend of the relation between toughness and cooling rate on continuous cooling although the absolute values of the transition temperature were different. After tempering at 650°C, a good linear relation was observed between the transition temperature and the logarithm of the (fracture unit)$^{-1/2}$ as was the case in the as-quenched steels (Fig. 11). The absolute value of the transition temperature shifted to a temperature about 40°C lower as compared with the as-quenched martensite and martensite-bainite structures.

Before recrystallization of the ferritic matrix on tempering, the lath orientation was essentially the same as in continuously cooled specimens so there should be no change in the unit fracture path. The results of the tempering experiments suggest the magnitude of the contributions of carbides (size, amount and distribution) and dislocation density to the toughness. With a fixed unit crack path, uniform distribution of fine carbides and decreased dislocation density yield superior toughness.

調質高張力鋼の靱性におよぼす変態組織の影響

邦武立郎　寺崎富久長
大森靖也　大谷泰夫
住友金属工業株式会社　中央技術研究所

1. 緒　　言

鋼の靱性を顕微鏡組織との関連において理解しようとする試みは，従来数多く行なわれている．一般的には，オーステナイト結晶粒や変態組織を微細化することにより低温靱性が向上することが知られている[1~15]．鋼の種々の顕微鏡組織の中で焼もどしマルテンサイトは良好な強度と靱性を有するので，焼入れ焼もどしを行なう調質型高張力鋼が多く使用されてきている[16]．

しかしながら調質高張力鋼の靱性を支配する因子について，定量的にすべて明らかになっていない．例えばオーステナイト粒度依存性も鋼種により異なっている[5]．これは低炭素低合金鋼においては，完全焼入れ組織（100% マルテンサイト）を得ることが容易ではなく[17]，変態組織が靱性におよぼす影響が複雑に介入してくることが一原因であろう．

本実験では，数種の低炭素低合金高張力鋼の連続冷却により得られた各種変態組織について，低温衝撃性質を詳細に検討した．

その結果，上位臨界冷却速度近傍の冷却速度で得られるマルテンサイトとベイナイトの混合組織が最もすぐれた衝撃性質を有することを見出した．そこでこのすぐれた衝撃性質を有する混合組織中のベイナイトの形態および存在状態を明らかにするとともに，シャルピー衝撃試験片の破面について，走査電顕を用いて，破面とその断面方向から観察を行ない，破面構成の様相と顕微鏡組織を直接対応させて観察することによって靱性に寄与する因子をできるだけ定量的に抽出しようと試みた．

2. 実験方法

2.1 供試鋼

供試鋼の化学成分を Table 1 に示す．鋼 N は，Mn-Ni-Mo-V 系の 60 キロ級高張力鋼である．鋼 7 および 8 は，Cu-Ni-Cr-Mo-V 系の 80 キロ級高張力鋼であり，鋼 8 には，B が添加されている．圧延条件を一定にして，熱間圧延により 7 mm 厚に圧延して後，以下の実験に供した．

2.2 熱処理および機械的性質

オーステナイト結晶粒度を変えるために，加熱温度を 900～1200°C とした．連続冷却時の冷却速度を種々変えることにより（800～500°C における冷却速度範囲は，冷却時間で表わせば 1～4×10⁴sec である*），マルテンサイト，ベイナイト，フェライト＋パーライトなどの各種変態組織を得た．これらの変態組織の連続冷却のまま，および 650°C×1hr の焼もどしを行なったものについて，機械的性質を測定した．

すなわち平行部の形状が 4t×6×30mm の試験片を用いて，インストロン試験機により引張試験を行なった．衝撃試験には 5×10×55 mm（2 mmV ノッチ）のサブサイズシャルピー試験片を用いた．

2.3 顕微鏡組織観察

2% ナイヌルによって腐食を行ない，光学顕微鏡により組織観察を行なった．微細組織の観察には，リン酸-クロム酸電解液を用いて薄膜を作成し，HU-200（加速電圧 200 KV）により直接観察を行なった．マルテンサイトおよびベイナイトについては，トレース解析により晶癖面と成長方向を求めた．

2.4 C.C.T. 曲線

種々の冷却途度で冷却した場合の組線変化を調べるために，連続冷却変態を測定した．Leitz 社製の熱膨張計（試料形状：3·8φ×50 mm）および Formastor 熱膨張計（試料形状：3φ×10 mm）を用い，変態時の長さ変化を測定した．

オーステナイト化温度に加熱保持後，種々の冷却速度で冷却し，長さ変化／温度の関係を記録した．熱膨張曲線の解析，組織観察，硬度測定などの結果を総合して C. C. T. 曲線を作成した．

2.5 破面の観察

シャルピー衝撃試験片の破面について，走査電顕を用いることによって破面構成の様相と顕微鏡組織を直接対応させた観察を試みた．破面の損傷防止と，破面と断面の交線を明確にするために，破面にあらかじめニッケルメッキを施し，断面方向を研磨した**．その後 2% ナイ

* 800～500°C における平均冷却速度は，200°C/sec～0·0075 °C/sec.

** 破面に垂直で，その破面との交線は，破壊の進行方向に平行なような断面である。

Table 1. Chemical composition of steels (%).

Steel	C	Si	Mn	P	S	Cu	Ni	Cr	Mo	V	B	Ti	sol. Al
N	0·15	0·34	1·25	0·027	0·017	0·03	0·19	0·02	0·13	0·03	—	—	0·032
7	0·12	0·30	0·83	0·004	0·005	0·30	1·11	0·53	0·49	0·03	—	—	0·038
8	0·14	0·25	0·89	0·004	0·005	0·27	1·04	0·54	0·50	0·03	0·004	0·03	0·044

タルで腐食を行ない組織を見出させたり，次の液を基本として[18]，ファセットピットを現出させた．ファセットピット液は，次の3種の試薬を順次用いて主として{110}面を現出させた．

A液：塩酸2cc＋過酸化水素水10cc＋水200cc.
B液：塩酸2cc＋塩化第二鉄の飽和水溶液20cc＋水200cc.
C液：蟻酸100cc＋過酸化水素水100cc＋エチルアルコール100cc.

それからニッケルメッキを剝離した後，走査型電子顕微鏡（JSM-2型）により，破面，破面と45°傾斜，90°傾斜（断面方向）の各々に垂直なる方向より観察し．破面と組織を直接対応させて観察した．脆性破面については．劈開破面の結晶方位は，研摩断面におけるファセットピットと破面の方位を傾角顕微鏡によって測定して決定した．

3. 実験結果

3.1 連続冷却時の冷却速度と機械的性質の関係

まず連続冷却のままについて述べる．鋼Nについて，冷却速度と機械的性質の関係をFig. 1に示す．加熱温度が950°C, 1000°Cの場合には，実験範囲の冷却速度では冷却速度が大きいほど50%脆性破面遷移温度（$_{v}$Trs）は良好である．しかし950°Cよりも1000°Cの方が曲線はやゝ徐冷側へ移行している．加熱温度が1200°Cになると，$_{v}$Trsは冷却速度と共に単調には変化せず$_{v}$Trsが最も良好となるoptimum pointがある．引張強さ（T. S.）の変化からも明らかなように，加熱温度によって焼入性が異なり，1200°C加熱では，950°C, 1000°Cに比較して焼入性が大きいことがわかる．

すなわち同一冷却速度でもオーステナイト化温度が異なれば得られる組織が異なることを示している．

鋼7の場合についてFig. 2に示す．鋼Nと異なる点は$_{v}$Trsのoptimum pointが加熱温度が低くてもみとめられることである．

鋼8の場合についてFig. 3に示す．冷却速度に対するoptimum pointは一層明確である．Fig. 4は，$_{v}$Trsに関しての最適冷却速度（Coで表わす）のオーステナイト化温度による変化を，3供試鋼について示したものである．これらの実験結果は，$_{v}$Trsに関するoptimum pointの位置は焼入性—冷却速度に対する組織変化—に大きく左右されることを示す．

次に，650°C×1hrの焼もどしを行なった場合についてもFig. 1～Fig. 3に示してある．焼もどし材では強度レベルは低下するが，$_{v}$Trsは冷却速度が大きい領域で著しく向上する．焼もどしによる$_{v}$Trsの変化については，後にふれるが，$_{v}$Trsの冷却速度による変化の傾向は連続冷却のままと同様であり，衝撃性質は連続冷却時の組織によって先ず大きく支配されることを示している．

3.2 顕微鏡組織観察

実験範囲の冷却速度で，冷却速度の低下につれて，マルテンサイト，マルテンサイト＋ベイナイト，高温で生成されたベイニティックフェライトから成るベイナイトと変化する．実験の冷却速度範囲の中で，冷却速度が最も小さい領域において鋼Nではフェライト＋パーライト，鋼7ではフェライト＋ベイナイトが生成する．しかし鋼8のフェライト生成の臨界冷却速度は更に小さい．Photo. 1に鋼Nについて代表的な冷却速度における光学顕微鏡写真を示す．$_{v}$Trsが良好となる組織は，マルテンサイト＋ベイナイトの混合組織であることが注目される．

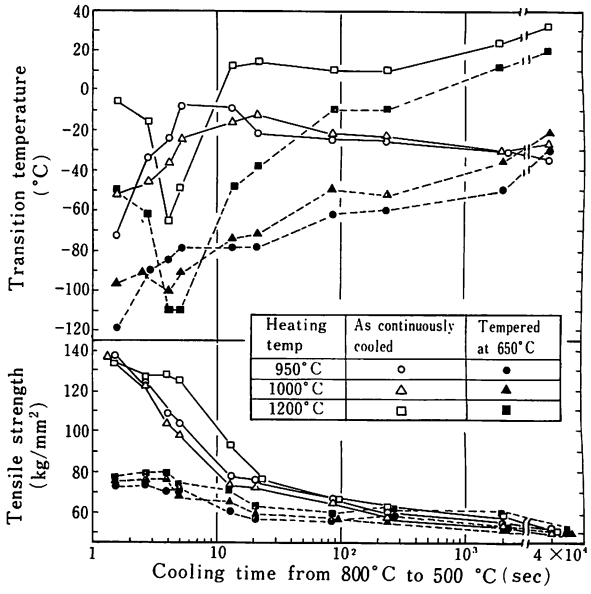

Fig. 1. Effects of cooling rate and heating temperature on the mechanical properties of manganese-nickel-molybdenum-vanadium steel (steel N).

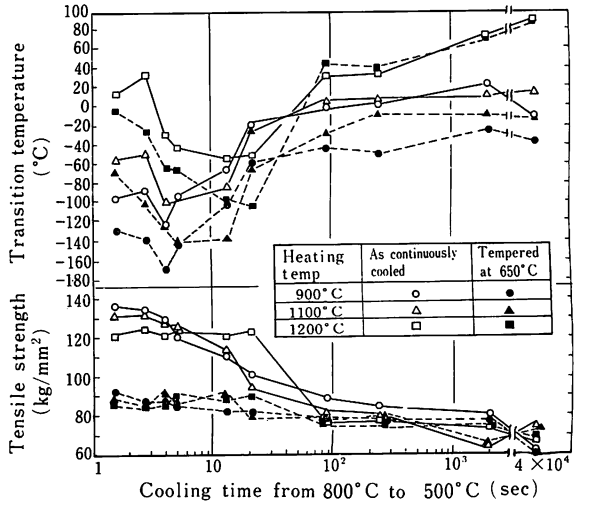

Fig. 2. Effects of cooling rate and heating temperature on the mechanical properties of copper-nickel-chromium-molybdenum-vanadium steel (steel 7).

この場合のベイナイトは，光学顕微鏡的にはマルテンサイトと区別し難い．しかし組織を詳細に観察すれば，マルテンサイトの場合は元のオーステナイト粒内において，lathの方向が揃っている単位が大きいが，混合組織ではオーステナイト粒内が更に細かく分割されている．冷却速度がさらに小さくなって，高温で生成されたベイナイトになれば衝撃性質が急激に劣化する．

稲垣ら[19]は溶接熱サイクル再現装置を用いて，急速加熱，冷却時のシャルピー衝撃性質を検討し，フェライト生成の臨界冷却速度において靱性が最も良くなることを示した．この実験においては，急速加熱のために加熱温度が同一でも冷却速度が小さくなれば，オーステナイ

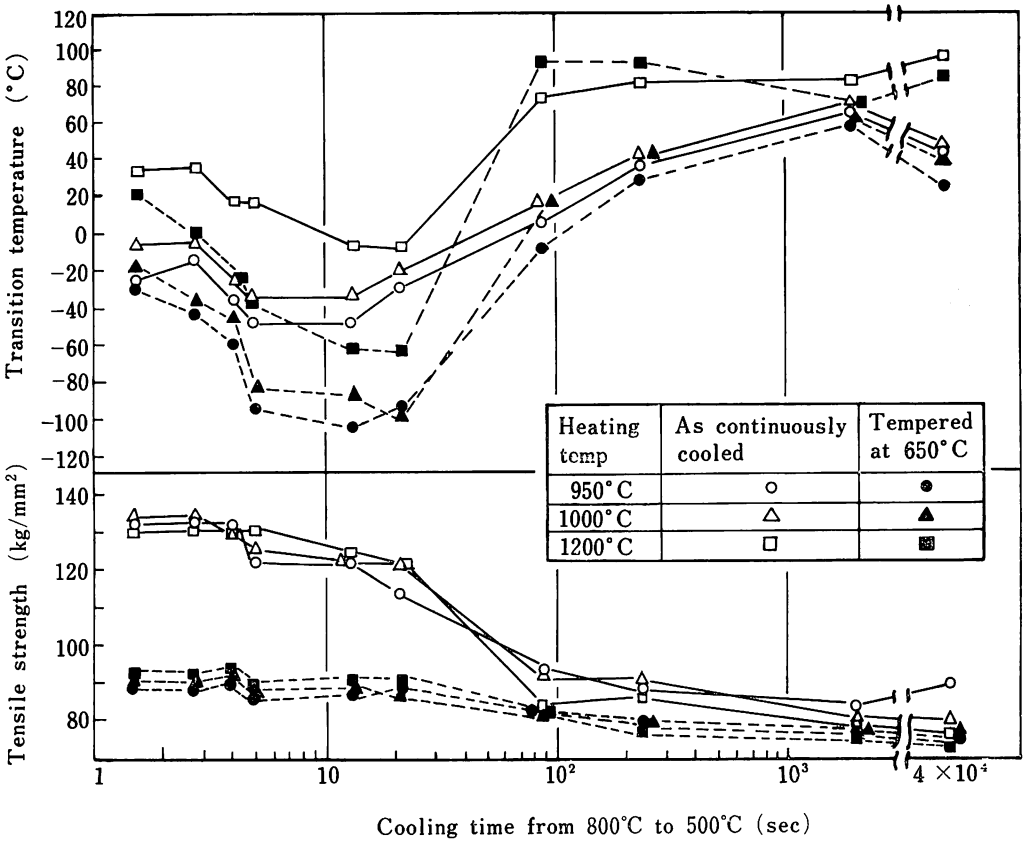

▲Fig. 3. Effects of cooling rate and heating temperature on the mechanical properties of copper-nickel-chromium-molybdenum-vanadium-boron steel (steel 8).

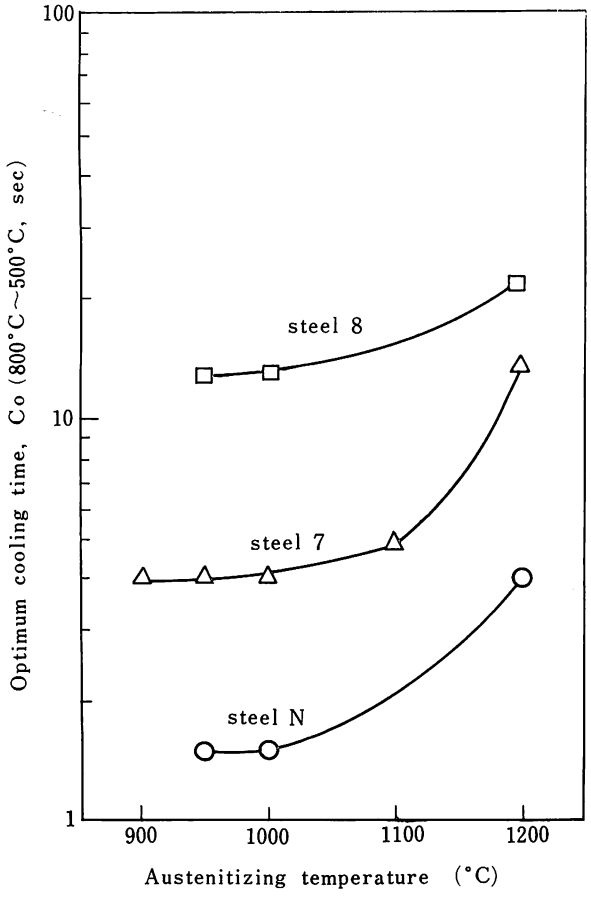

◀Fig. 4. Effect of austenitizing temperature on the optimum cooling rate for the lowest impact transition temperature (Co) where Co is expressed as the cooling time in seconds from 800°C to 500°C.

ト結晶粒の成長が起こることや，通常の加熱条件に比較して冷却時のフェライトの生成は促進されると考えられ，混合組織の構成（マルテンサイト，フェライト，中間段階組織）は本実験とは異なるが，完全マルテンサイト組織が必ずしも最良の靱性を示さない点においては本実験結果と一致する．

次に電顕による観察結果をのべる．Photo. 2 は低炭素鋼の lath マルテンサイトである．Photo. 3 は $_{\gamma}$Trs が optimum point となる混合組織中にみられるベイナイトであり，a) は明視野像，b) はセメンタイトの回折点を用いた暗視野像である．セメンタイトの形態は高炭素鋼の下部ベイナイトに極めて類似している．この場合の組織構成はマルテンサイトの割合はベイナイトよりもはるかに多いようである．

Photo. 4 は lath 内部にセメンタイトの析出を伴わないベイニティックフェライトから成るベイナイトを示す．トレース解析を行なった結果，マルテンサイト，ベイナイトいずれもフェライトに関する限り〈111〉α の成長方向と {110}α の晶癖面を有することが明らかになった[20]．したがっていずれのベイナイトもフェライトに関する限り上部ベイナイトの範疇に属する[21]．低炭素低合金鋼のベイナイトについて，炭化物の形態から B-I 型

a) ×500

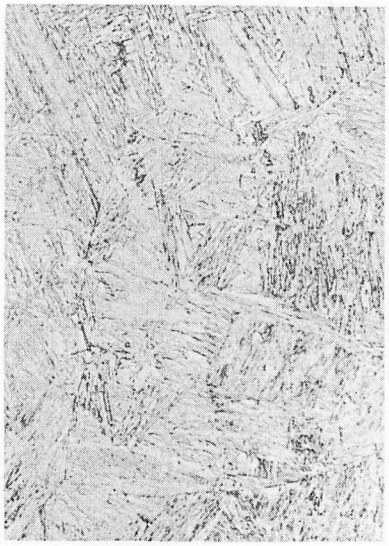

b) ×500

c) ×500

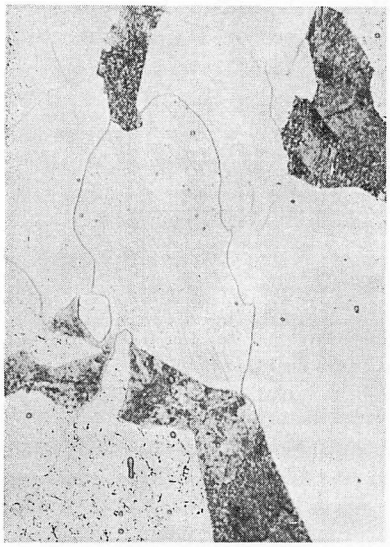

◀d) ×500

Photo. 1. Optical microstructures of manganese-nickel-molybdenum-vanadium steel (steel N).

	Cooling rate from 1200°C (°C/sec)	Tensile strength (kg/mm²)	$_{V}Trs$ (°C)
a)	200	132·9	− 6
b)	75	129·9	−66
c)	14	76·5	16
d)	0·0075	50·7	32

▼Photo. 2. Martensite formed in manganese-nickel-molybdenum-vanadium steel (steel N) cooled from 1200°C at 200°C/sec.

×20 000

×20 000

a) Bright field image.

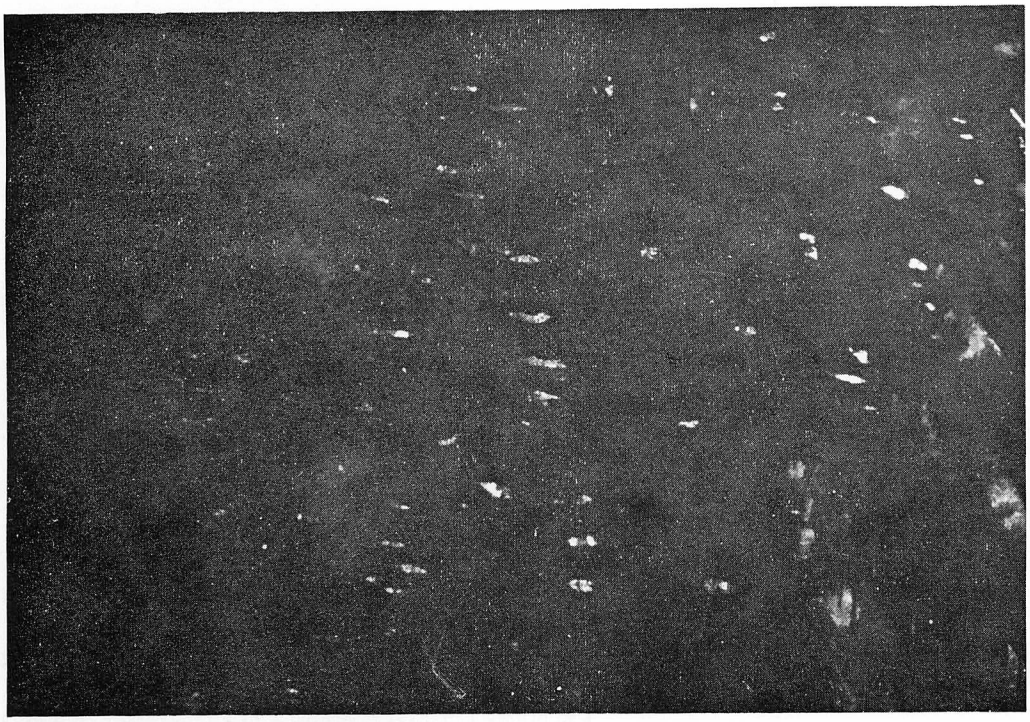

×20 000

b) Dark field image using a cementite reflection.

Photo. 3. Bainite formed in manganese-nickel-molybdenum-vanadium steel (steel N) during continuous cooling from 1200°C at 75°C/sec.

(ベイニティックフェライトより成る), B-II型 (フェライト lath 界面に沿ってセメンタイトが析出する), B-III 型 (lath の内部にもセメンタイトを析出し, その様相は下部ベイナイトに類似している), に分類した[20]. Fig. 5 は, この3種類のベイナイトを schematic に示したものである. Photo. 3 は B-III 型, Photo. 4 は B-I 型のベイナイトである.

3. 3 C.C.T. 曲線

鋼 N, 7, 8 の C. C. T. 曲線を作製した. 代表として鋼7についての C. C. T. 曲線を Fig. 6 に示す.

$_{V}$Trs が optimum point となる冷却速度 (Co) は, 鋼 N, 7, 8 の順に冷却速度の小さい方へ移動するが (Fig. 4 参照) C. C. T. 曲線と比較すれば, Fig. 7 に示すように上部臨界冷却時間 (C_B) よりも大きく, ベイニティック

Photo. 4. Bainitic ferrite formed in manganese-nickel-molybdenum-vanadium steel (steel N) cooled from 1200°C at 14°C/sec.

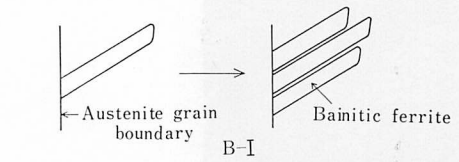

a) Between 600°C and 500°C.

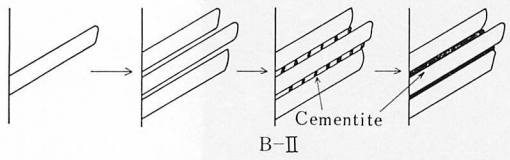

b) Between 500°C and 450°C.

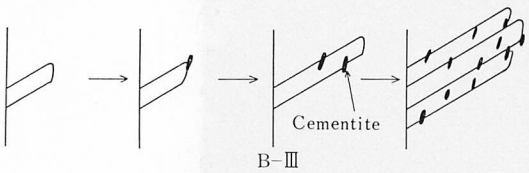

c) Between 450°C and Ms.

Fig. 5. Schematic representation of bainite formation

フェライト生成[20]，の臨界冷却時間(C_{BF})よりも小さい*．なおこの C_{BF} は，ほぼ HV 300 程度を与える冷却速度に対応している．

冷却速度 Co の近傍で生成されたベイナイトは主として Photo. 3 で示した B-III 型のベイナイトである．しかし冷却速度が小さくなって，ベイニティックフェライトが生成すると衝撃性質は劣化する．$_{\gamma}$Trs が良好な混合組織を得るためにはマルテンサイトと混在するベイナイトは連続冷却では必然的に B-III 型ベイナイトになっている．(Fig. 6 参照)

3. 4 オーステナイト粒度と衝撃性質

衝撃性質を良好にするには，オーステナイト結晶粒($d\gamma$)を微細にすることが有効なことはよく知られている[1-8]．Fig. 8 に鋼 7 について $\log. d\gamma^{-1/2}$ と $_{\gamma}$Trs の関係を示した．図中では冷却速度をパラメータとして示しているが，オーステナイト粒度が変わると同一冷却速度でも組織が同一でない難点がある．

しかしここで明らかなことは，オーステナイト粒度とよい相関関係にある場合には，冷却速度が大で主としてマルテンサイト，高温で生成されたベイナイト，あるいはフェライト＋パーライト組織の場合であり，しかもいずれも ASTM 粒度番号 1 当り約 15°C $_{\gamma}$Trs が変化し，従来の報告とよく一致する[4]．焼もどしマルテンサイトを対象として破面と組織の関係についての，関接的なしかし詳細な最近の実験から，破壊の単位として，有効結晶粒が提唱された[22]．またオーステナイト粒とフェライト粒の間には相関があり，フェライト＋パーライト組織の破面の観察から破面構成の単位はいくつかのフェライトを単位としていることが明らかとなった[23]．炭素鋼のパーライトにおいては，破壊の最小単位はパーライトコロニーとなっている[24,25]．これらの実験結果を考慮すれば，破壊の単位がオーステナイト粒度とよい相関を有するために，オーステナイト粒度とも実験的に比較的よい相関を示すものと推定される．

次に $_{\gamma}$Trs のオーステナイト粒度依存性が小さいのは，$_{\gamma}$Trs が optimum point を示す近傍の冷却速度で得られるマルテンサイト＋ベイナイト混合組織である．鋼 N では焼入性が小さいので，加熱温度が異なると同一冷却速度でも組織変化が大きいために，オーステナイト粒が大きくなれば衝撃性質が良好となる場合もある．鋼 7 では

* ここでは，C_B, C_O, C_{BF} は，いずれも 800～500°C の冷却時間で示した。したがって冷却速度が大であることは，これらの値が小さいことに対応する。

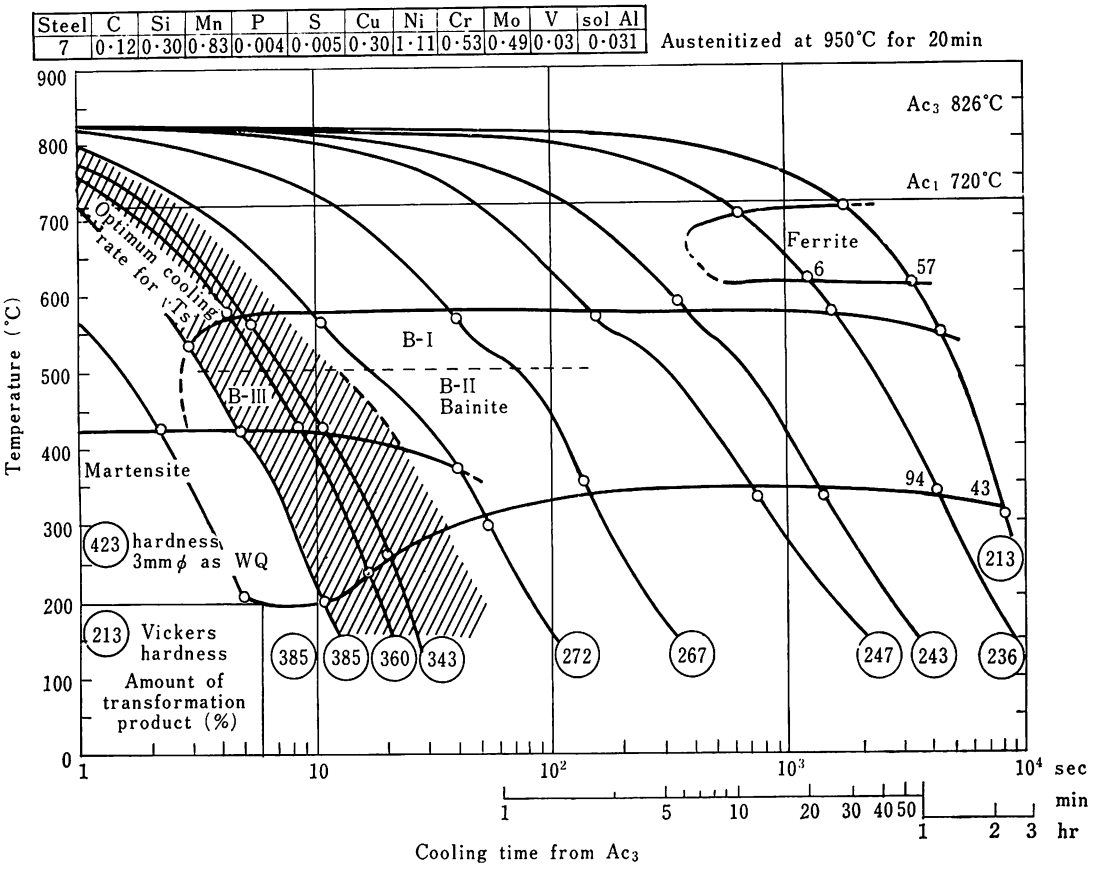

Fig. 6. Continuous-cooling transformation diagram for the copper-nickel-chromium-molybdenum-vanadium steel (steel 7). $_{V}$Trs is the 50% shear transition temperature.

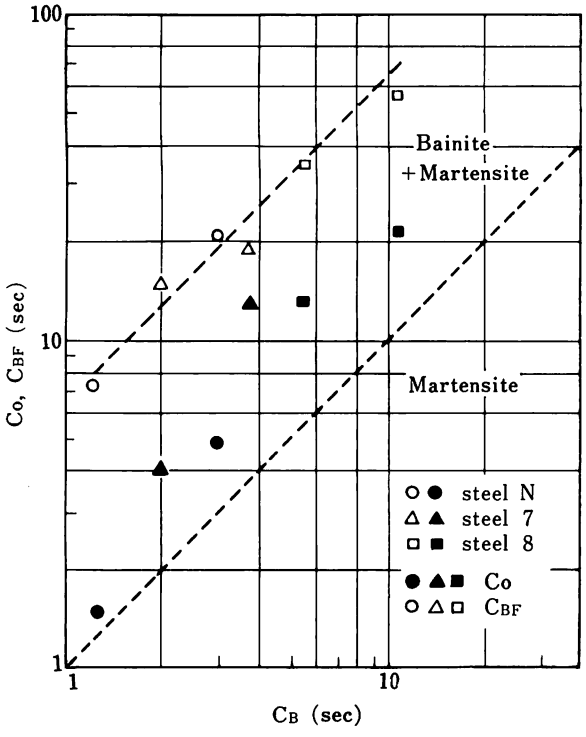

Fig. 7. Relation of optimum cooling rate for impact transition temperature (Co) and critical cooling rate for the beginning of bainitic ferrite formation (C_{BF}) to the critical cooling rate for the beginning of bainite formation (C_B) where all cooling rates are expressed as the cooling time in seconds from 800°C to 500°C.

加熱温度による冷却時の組織変化は鋼Nより小さく，$_{V}$Trsのオーステナイト粒度依存性はマルテンサイトの場合よりも小さい．これらのことは焼入れ焼もどしにおいては，焼入温度を高くすればオーステナイト粒は粗大化するが，それにもかかわらず衝撃性質は向上する場合（冷却速度）があることを示唆している．

3.5 走査電顕による破面の観察

Photo. 5～7は，鋼Nの1200°C加熱後連続冷却したもののシャルピー破面のうち，脆性破面について，a) 破面，b) 破面を45°傾斜，c) 破面を90°傾斜（断面方向）から観察し，破面と組織を直接対応させた写真を示す．これらは，おのおのPhoto. 2～4に対応している．いずれも微細な凹凸のある擬劈開破面と称されるものであり，river patternに類似した模様がみられ，破面の構成は不連続的である．

Photo. 5はマルテンサイトについて示したものである．同一破面単位内では，ファセットピットの形状は同一の方向を示しており，この領域内ではほぼ同一方位を有するlathから成り立っていることを示している．Photo 6はマルテンサイト＋B-III型ベイナイトの混合組織，Photo. 7は高温で生成されたB-I型ベイナイトの場合である．破面単位はPhoto. 6が最も小さく，Photo. 7が最も大きい．

劈開面の方位については，マルテンサイトでは(100)α以外の面も報告されているが[26]，傾角顕微鏡を用いて，ファセットピットおよびそれに対応した破面の方位を測定した結果，純鉄単結晶で示されたのと同様に[27]，微小な角度内で{100}から成り立っている．さらに破面の構

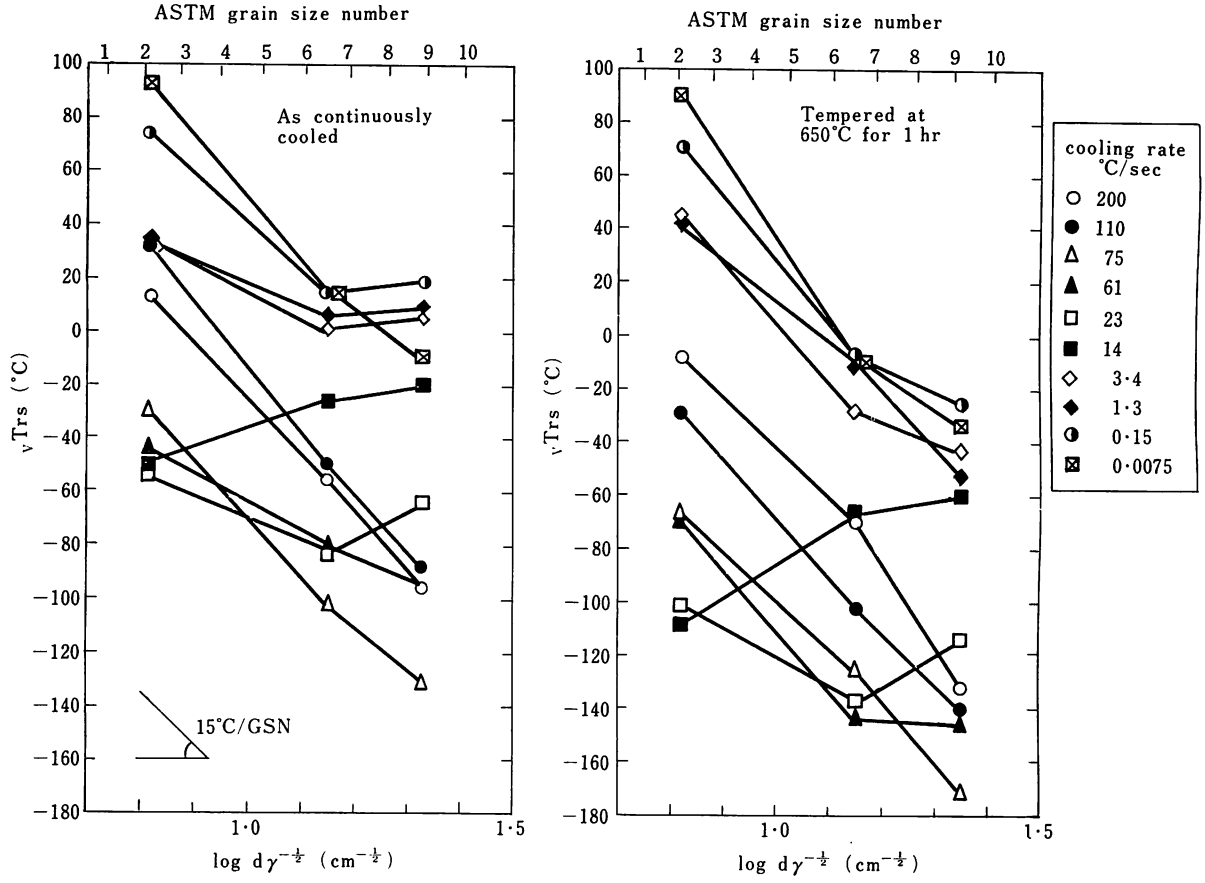

Fig. 8. Relation between austenitic grain size and 50% shear transition temperature for copper-nickel-chromium-molybdenum-vanadium steel (steel 7).

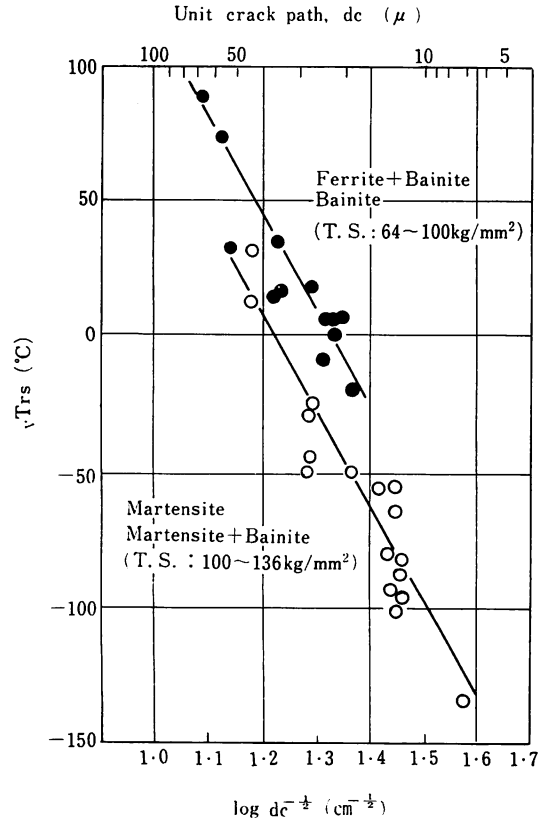

Fig. 9. Relation between unit crack path and 50% shear transition temperature for continuously cooled copper-nickel-chromium-molybdenum-vanadium steel (steel 7).

成を詳細に検討した結果，破面の単位として，「{100}を微小な角度内で共有する領域の大きさ」と定義した[23]．すなわち，この領域内では破面単位の境界近傍より破壊が発生し，放射線状に伝播して次の破面単位の境界で停止している．

この破面単位を構成する境界については別途詳細に検討を加えた[23]．この定義にしたがって，脆性破面より破壊単位の大きさ (dc) を測定し $_{v}$Trs との関係を検討した．

鋼7の連続冷却のままについて，$_{v}$Trs と log. $dc^{-1/2}$ の関係は，Fig. 9 に示すようにオーステナイト粒度で整理した場合に比較して良好な相関関係を有している．かつ強度的には 100 kg/mm² を境にして2つのグループに分かれる．これは従来，焼入性の比較として 50% マルテンサイトを目安としており[28]，本鋼種では 50% マルテンサイトの強度がほぼ 100 kg/mm² 程度であることと合せて考えると興味深い結果である*．引張強さが 100 kg/mm² 以下の場合は，フェライト＋ベイナイト，高温で生成したベイナイト (B-I 型) 組織であり，その破面は Photo. 8 で示すように river pattern が明瞭であり，破面単位は比較的塊状である．一方引張強さが 100 kg/

* これはまた，ベイニティックフエライトがあらわれるか否かの境界近辺にもほぼ相当する．

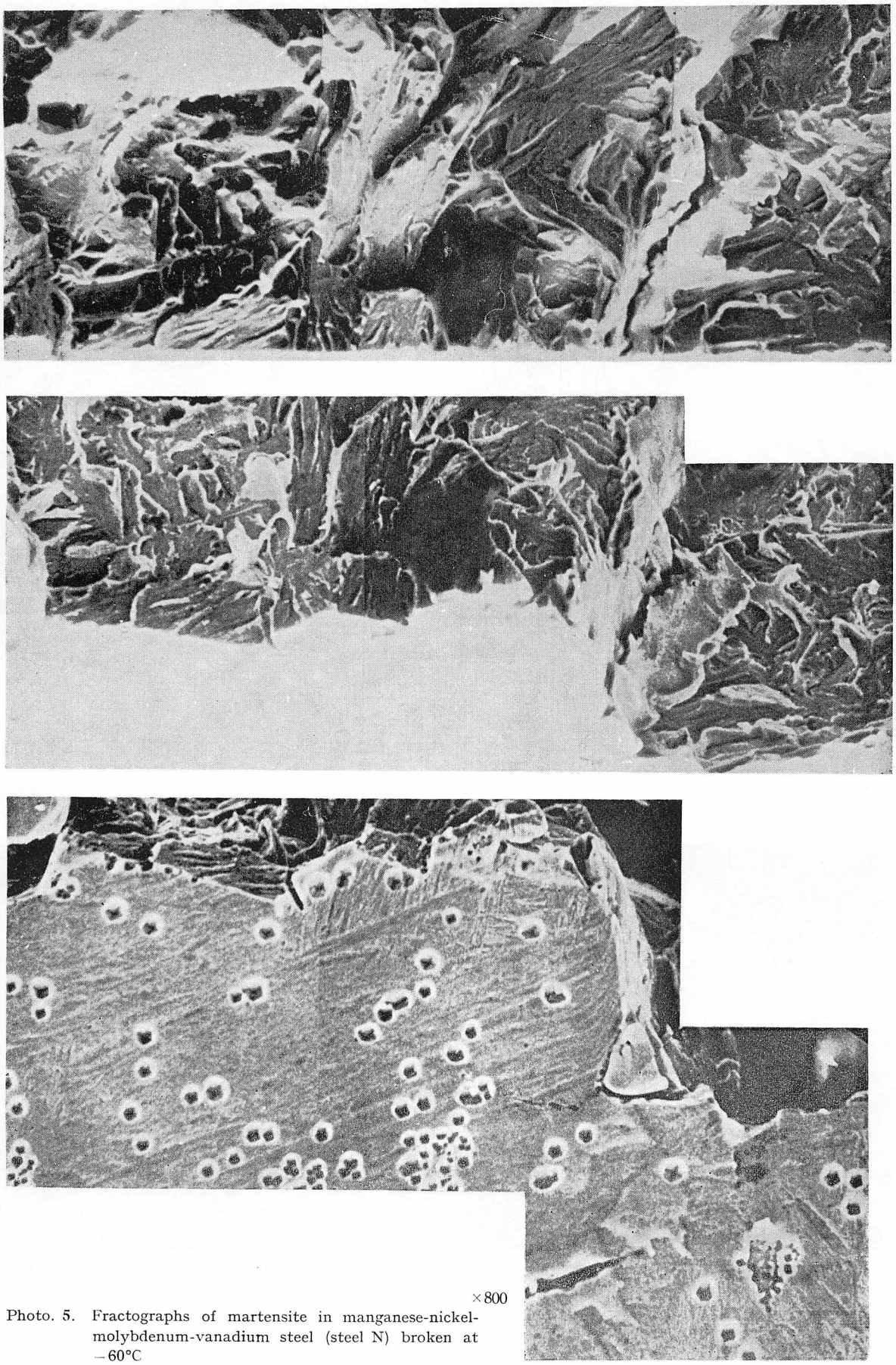

×800

Photo. 5. Fractographs of martensite in manganese-nickel-molybdenum-vanadium steel (steel N) broken at −60°C

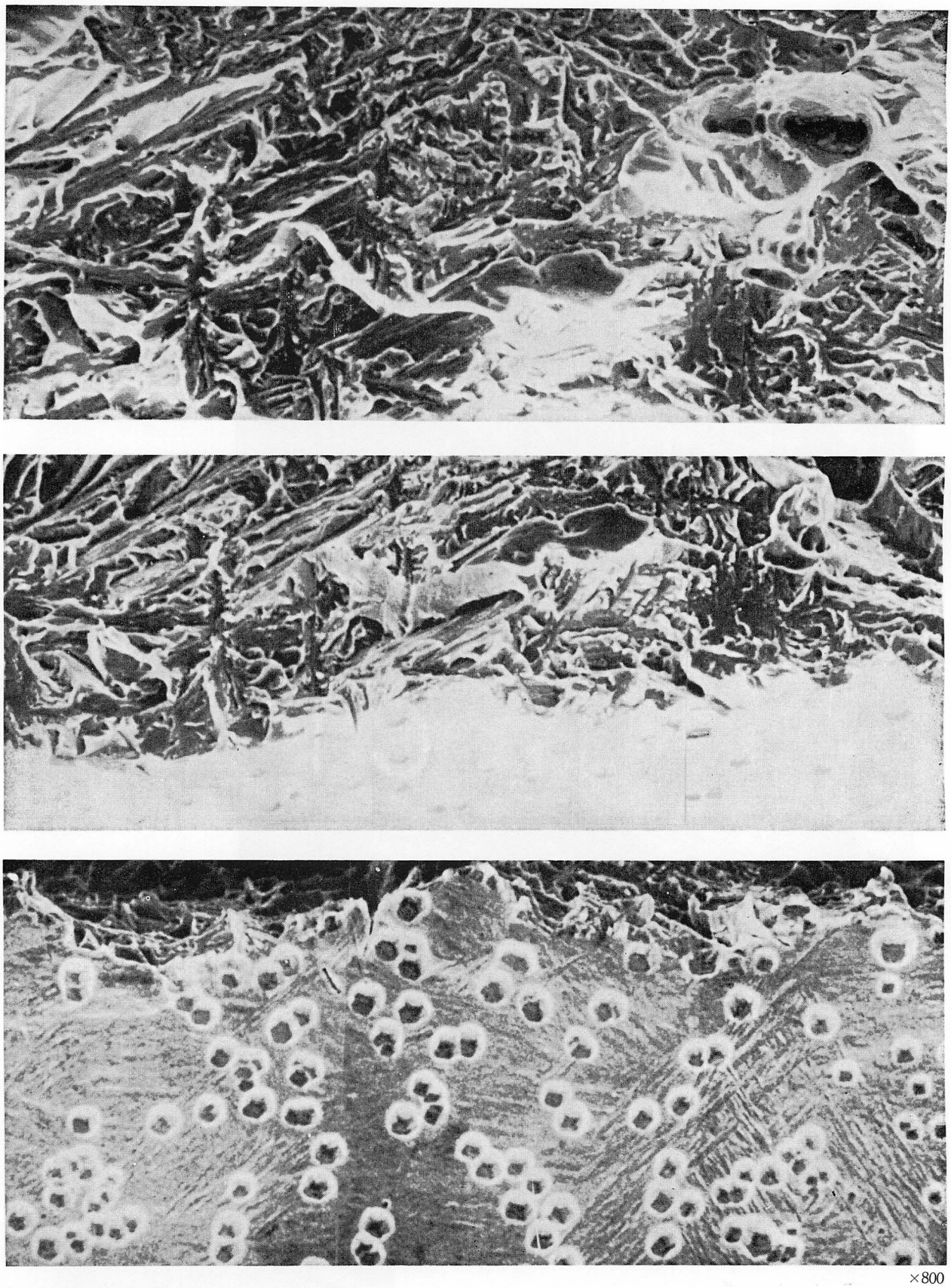

×800

Photo. 6. Fractographs of duplex martensite-bainite structures in manganese-nickel-molybdenum-vanadium steel (steel N) broken at −100°C.

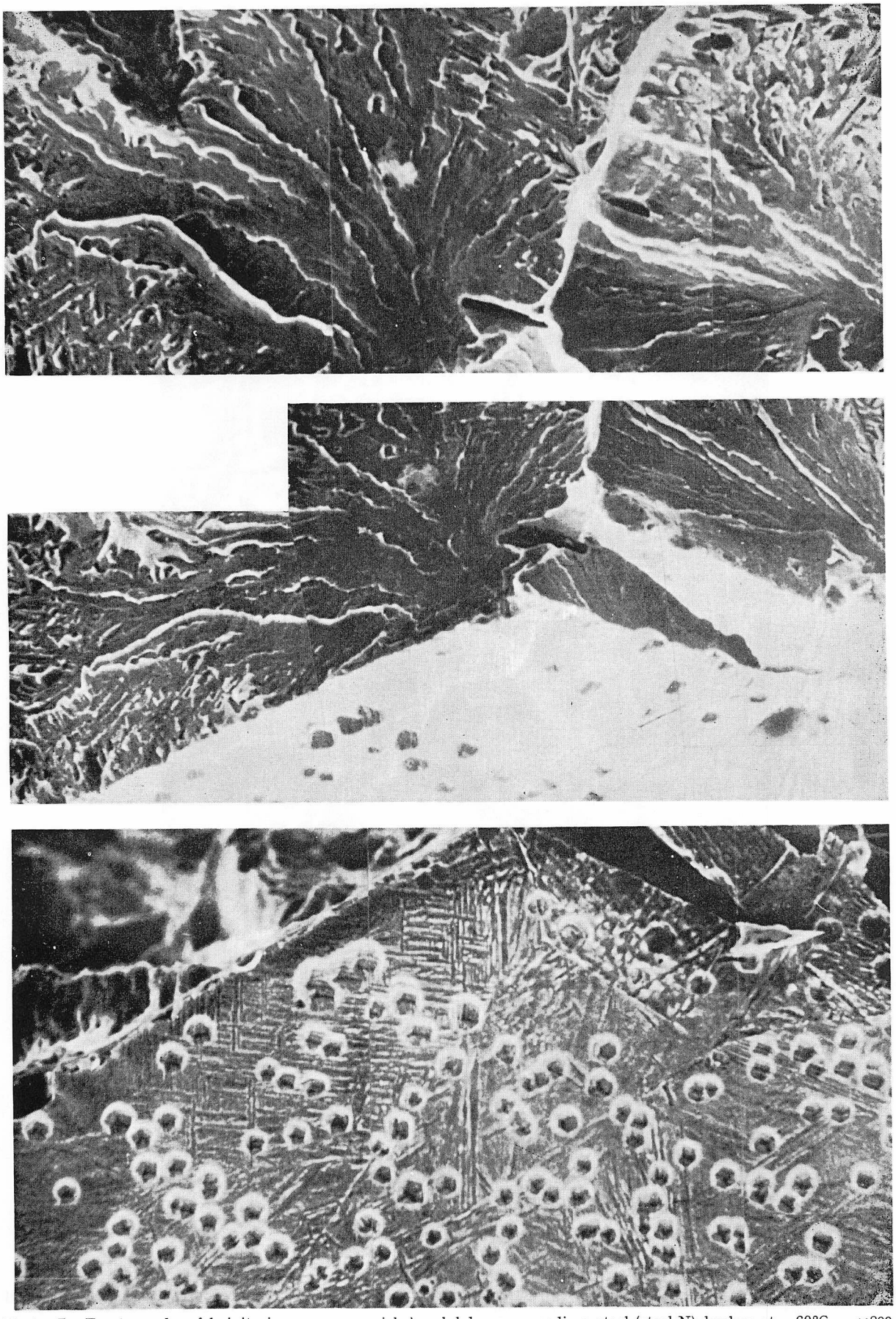

Photo. 7. Fractographs of bainite in manganese-nickel-molybdenum-vanadium steel (steel N) broken at −60°C. ×800

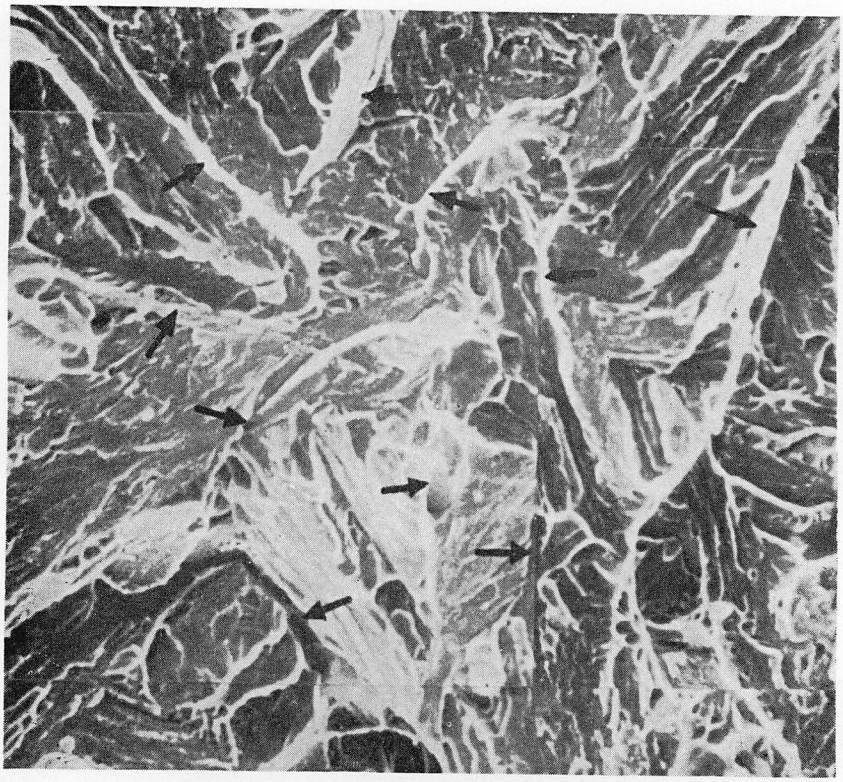

×600

Duplex martensite-bainite structure broken at −100°C.

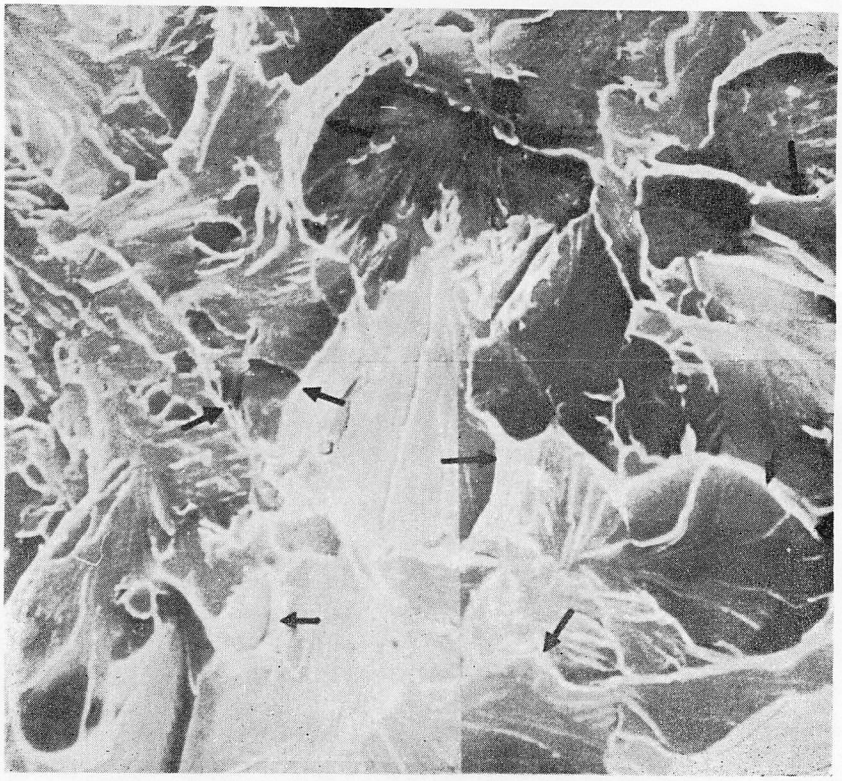

×600

Ferrite-bainite structure broken at −20°C.

Photo. 8. Unit crack path of typical microstructures formed in copper-nickel-chromium-molybdenum-vanadium steel (steel 7) during continuous cooling from 1200°C.

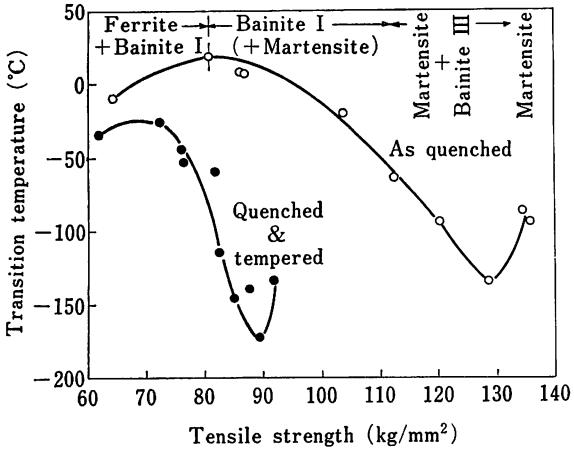

Fig. 10. Relation between tensile strength and transition temperature of copper-nickel-chromium-molybdenum-vanadium steel (steel 7).

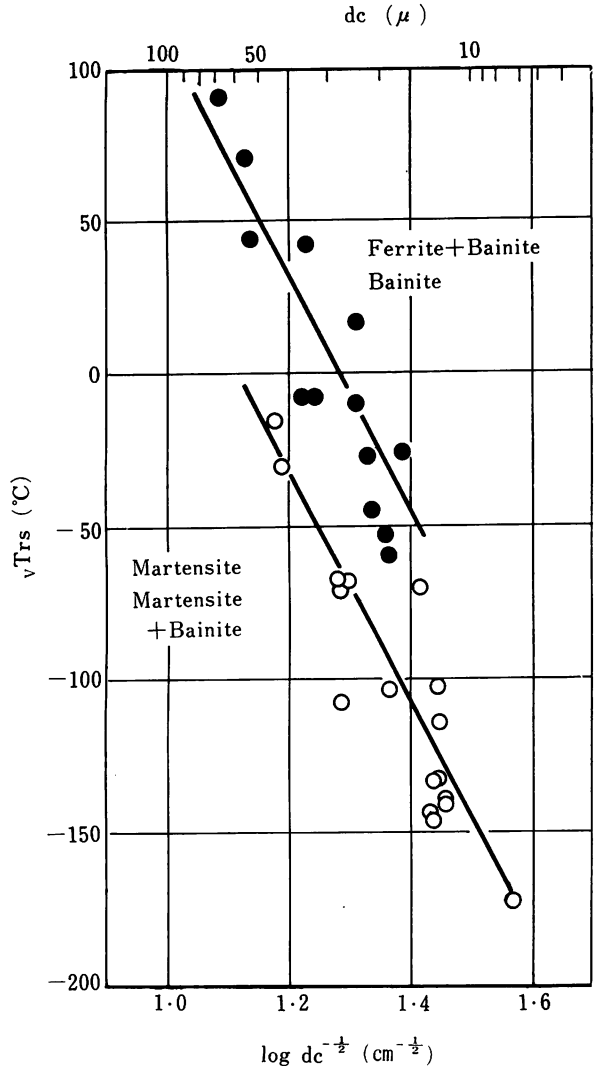

Fig. 11. Relation between unit crack path and 50% shear transition temperature, for copper-nickel-chromium-molybdenum-vanadium steel (steel 7), continuously cooled and tempered.

mm² 以上の場合は，マルテンサイト，マルテンサイト+B-III 型ベイナイト混合組織であり，river pattern は直線的でなく，かつ細長い単位も観察され微細組織が破壊の伝播に対して何らかの抵抗を有するものと推定される．破面単位の温度変化は小さいが，破断温度が高くなるとマクロ的には脆性破面を示していても，脆性破面をとりかこんで，微細な延性領域が網目状に存在するようになる．さらに温度が高くなれば破面単位の大きさの延性領域が現われる[29]．Fig. 10 は，冷却のままと焼もどし後の両者について，$_{v}$Trs の引張強さによる変化を示したものである．同一強度において，$_{v}$Trs を比較するとき，焼もどし後は冷却のままよりも低い $_{v}$Trs を示す．しかし，Fig. 2 にも示されているように，$_{v}$Trs の強度による変化の傾向には，冷却のままと焼もどし後で差異がない．焼もどし後についても，連続冷却のままと同様に $_{v}$Trs と $\log. dc^{-1/2}$ の関係をプロットすると，Fig. 11 に示すように直線関係が得られる．

4. 考　　察

連続冷却のままにおける $_{v}$Trs の冷却速度による変化は，650°C で焼もどしを行なっても連続冷却のままと，その傾向は変わらない．したがって上部臨界冷却度度近傍で生成された B-III 型ベイナイトを含むマルテンサイトの混合組織において．衝撃性質が最も良好なる現象は本質的には連続冷却時の組織で支配されており，冷却速度の低下にともなった冷却時それ自体における焼もどしの効果によるものではない．

本供試鋼のように低炭素低合金鋼では連続冷却により，マルテンサイトとベイナイトを単独に得ることが困難なために，おのおのの変態組織単独の靱性の評価が困難である．しかし，マルテンサイトとベイナイトを比較すると，炭化物の形態は両者において異なるが[20]，破面観察から炭化物にもとづくと考えられる差異は認め難い．また，マルテンサイトとベイナイトの晶癖面，成長方向はいずれも $\{110\}\alpha$, $\langle 111\rangle\alpha$ であり，lath が破壊に対して有効に作用するならば，ベイナイトはマルテンサイトよりも lath の厚さが小さくなることはないので[20]，この点においては特に差異はない*．

転位密度の差異は $_{v}$Trs の絶対値そのものには影響をおよぼすと考えられるが，焼もどし前後では冷却速度による靱性の変化の仕方は変わらないことが注目される．

従来，ベイナイトが強度靱性を有することは報告されている[13,30,31]．異なる組織の靱性は等しい強度レベルにおいて比較されるべきであるが，しかし同一強度レベルにするためには，一般にマルテンサイトは靱性に対して好ましくない低温で焼もどしを行なわねばならず，本質的な比較を行ない難い難点がある．本実験においては $_{v}$Trs を最も良くする最適冷却速度近傍では強度差が少なく，かつ，焼もどしを行なった場合には，強度差はほとんどなくなるので等しい硬度レベルでの靱性の比較が可能となる．

Photo. 9 は，ナイタル腐食により現出した混合組織と破面の対応を試みたものである．腐食の感受性が異なり，濃く腐食された領域で破面は境界になっている．

この組織は明らかに地のマルテンサイトより先に変態しており，ベイナイトか auto-temper されたマルテンサイトか明確ではないが，炭化物の析出の様相からは B-III 型ベイナイトと判断される．lath の一端で破面の

* ベイナイトの lath の巾は，変態温度の低下と共に小さくなり，Ms 点直上では，マルテンサイトの lath の巾と同程度になる[20]．

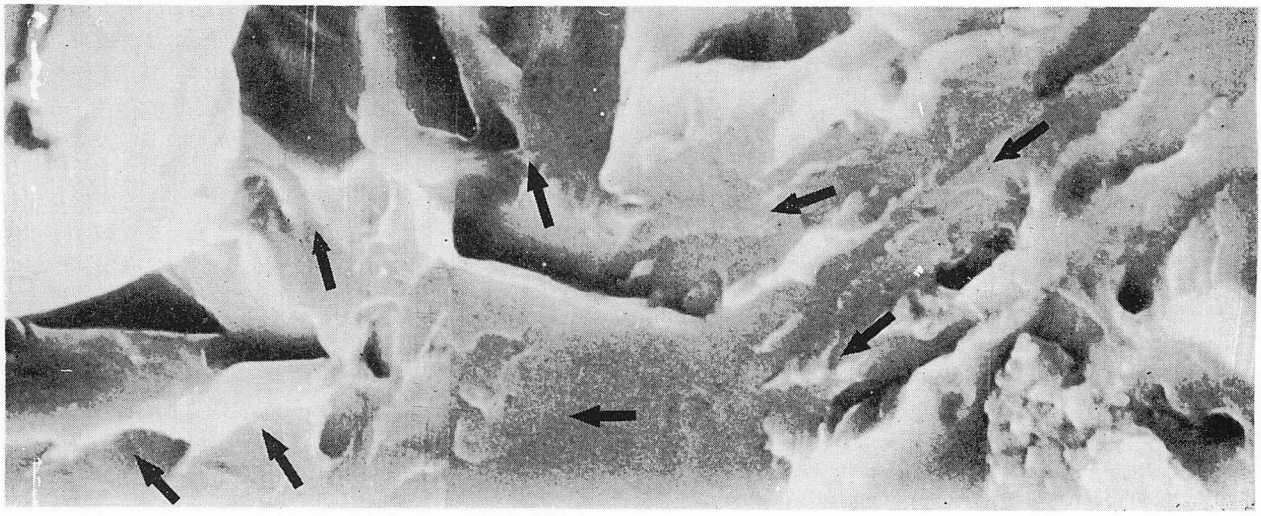

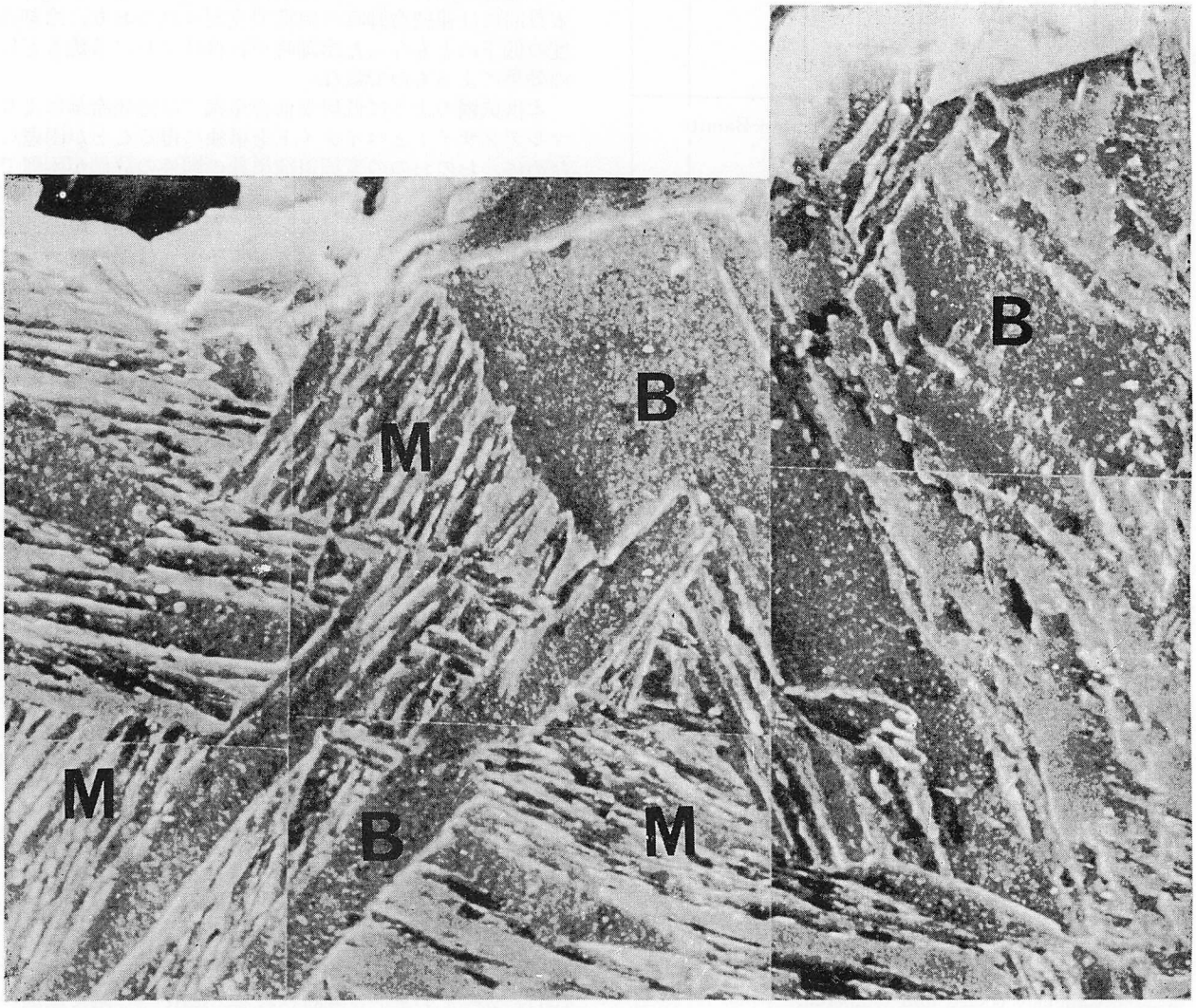

×10 000

Photo. 9. Correspondence of duplex martensite-bainite structure to fracture surface.

方向が変わっているが，lath 内で破壊の抵抗となっている証拠はなくベイナイトの lath そのものが脆性破壊に対して，特に有効とは思われない．最近 3%Ni-Cr-Mo 鋼において，マルテンサイトの方がベイナイトよりも靱性が大であるが，混合組織において，より靱性に富む現象が報告された[32]．この場合のベイナイトは下部ベイナイトであり，上部ベイナイトと芯異なるけれども，異なる組織の境界が重要であることを示唆してゐる．

破面の観察からは，破壊の単位 dc と $_{v}$Trs の間には，実験的に良い相関があることを示したが，劈開面が特定の面であることから鋼の靱性向上に対して一次的には，γ/α 変態時において結晶学的に {100} 面を全くランダムに分布させることができれば，有効であることが予測される．したがって極論すれば，鉄単結晶を用いた実験において示された如く[27]，破壊の進行に対して {100} 面の方位差が大きい組織を調整することができれば，その方向の靱性は著しく向上するであろう．

この点において混合組織が靱性に富むのは，ベイナイトの存在形態に起因すると考えられる．換言すれば，変態生成位置を増加させる点に関してオーステナイト結晶粒を微細化（オーステナイト粒の細分化）することと同様な効果をベイナイトが有するのであろう．Photo. 10は，B-III 型ベイナイトの生成の初期段階の顕微鏡組織を示したものであるが，ベイナイトの生成がもとのオーステナイト粒を分割する働きを有するとみなして不自然でないようにみえる．連続冷却によりこのような混合組織を得ようとするとき，ベイナイトは下部ベイナイトに類似した B-III 型ベイナイトである．オーステナイトの分割の効果は，どの組織によっても良いことになるが．破壊の単位 dc が同一でも衝撃性質が微細組織により異なることから (Fig. 9)，高温で生成するベイニティックフェライトによるときは，あまり有効であるとは考え難い．

×500

Photo. 10. Early stage of bainite III formation in austenite.

何故なら，ベイナイトの lath そのものや．{100}，面を共有する単位が大きいこと，未変態オーステナイトは C が濃縮され高 C 変態生成物が形成されることを挙げることができよう．また，マルテンサイトによる分割も有効と考えられるが，低炭素低合金鋼ではマルテンサイトの生成割合をコントロールすることは容易でない．

Fig. 11 に示されるように，鋼 7 は焼もどし後においても，冷却のままと同様に $_{v}$Trs と log. $dc^{-1/2}$ の間に良好な直線関係が存在している．これは焼もどし時，フェライトに再結晶が起こらない限りマトリックスの方位に変化がないことから予想されることである．しかしながら，焼もどし後の $_{v}$Trs の絶対値は，冷却のままのものより低温側へ移動している．すなわち，マルテンサイトおよびマルテンサイト＋ベイナイト (B-III) では，約 40°C 低温側へ動いている．ベイニテイックフェライトやフェライト＋ベイナイトでは，この移動量は，はるかに小さくなる．この移動は，焼もどしによる炭化物の析出状態，存在状態，大きさや転位密度の変化に寄せられるものであろり．しかし，その各々の因子の寄与を定量的に評価することは，本実験では可能でない．

以上，高張力鋼の低温衝撃性質に関する実験結果について，種々考察を試みたが，強度，マトリックスの靱性，微細な変態組織や析出物の影響などを合わせ考慮して，個々の効果と共に総合的に検討することは，今後に残された重要な課題である．

5. 総　　括

数種の高張力鋼について，オーステナイト粒度と冷却速度を変えて得られた各種変態組織について，その低温衝撃性質を比較した．シャルピー衝撃試験片の破面と顕微鏡組織を直接対応づけて観察を行ない，靱性に寄与する因子を抽出しようと試みた．得られた結果は，次の通りである．

1) 連続冷却のままの組織の破面遷移温度 ($_{v}$Trs) は冷却速度に対して単調には変化せず，ある冷却速度で $_{v}$Trs が最も良好となる．
2) この最適冷却速度は，焼入性の大きい鋼ほど冷却速度の小さい方に存在し，加熱温度の上昇と共に冷却速度の小さい方へ移行する．
3) 最適冷却速度は，ベイナイト生成の臨界冷却速度と関係を有し，C. C. T. 曲線との比較および電顕観察より，この場合，得られた組織はマルテンサイトとベイナイトの混合組織であることが明らかとなった．
4) この混合組織中のベイナイトの炭化物の形態は下部ベイナイトに類似しているが，フェライトに関する限り，lath マルテンサイトと同じ $\{110\}\alpha\langle 111\rangle\alpha$ の晶癖面と成長の方向を有する上部ベイナイトである．低炭素低合金鋼のベイナイトを 3 種類に分類しこのベイナイトを B-III 型と名付けた．
5) フェライト＋パーライト，マルテンサイト，主としてベイニティックフェライトより成る組織は，それぞれオーステナイト粒度とよい相関関係を有するが，マルテンサイト＋ベイナイトの混合組織においては，粒度依存性が小さく，ある冷却速度ではオーステナイト粒は粗大化するが，それにもかかわらず変態組織の点から，かえって $_{v}$Trs は良好となる場合がある．
6) 走査電顕により，破面と組織を直接対応づけて観

察を行なった．断面組織上のファセットピットおよび破面の方位を傾角顕微鏡により測定した結果，いずれの破面もその劈開面は {100}α であった．

7) 破面観察からは，マルテンサイト＋B-III 型ベイナイトの混合組織において，破壊の単位が最も小さくなり，ベイニティックフェライトが生成すると，破壊の単位が極めて大となる．

8) 破壊の単位として「{100}α を微少な角度内で共有する大きさ」と定義し，この領域が破壊の発生一伝播一停止の単位になっており，この単位 dc と $_{v}$Trs との間には実験的に良好な相関関係があることを示した．

9) マルテンサイト，マルテンサイト＋ベイナイト (B-III) とベイニティックフェライト，フェライト＋ベイナイト組織では，破面の様相は若干異なり，各々2つのグループに分かれて，$_{v}$Trs と $\log. dc^{-1/2}$ の直線関係を示す．すなわち，この2つのグループ間には dc が等しくても $_{v}$Trs の差を生ずる．これに対して破面単位の中の破面の様相が若干異なる．

10) マルテンサイト＋ベイナイト (B-III) 混合組織において，衝撃性質が良好となるのは，マルテンサイト変態に先行したベイナイト (B-III) がオーステナイト粒を，さらに細分する効果によるものと推定される．

11) 焼もどしを行なっても，$_{v}$Trs の連続冷却時の冷却度に対する変化の傾向は連続冷却のまゝと変わらない．しかし $_{v}$Trs の絶対値は良くなる．この変化は，炭化物の析出状態，存在形態，転位密度の変化に寄せられるものであろう．

おわりに，本研究の発表を許可された，中央技術研究所長，住友元夫博士に深甚なる感謝の意を表します．

文　献

1) R.A. Grange: Trans. ASM, **59** (1966), p. 26
2) 金沢，鈴木，今野：鉄と鋼，**56** (1970), No. 4, S. 306
3) D. Hadwick and K.R. Pirt: J. Iron Steel Inst., **196** (1960), p. 301
4) B. Cina and P. Jubb: ibid, **195** (1959), p. 329.
5) 久保田，大須賀，田中，大内：日本金属学会講演概要 (S. 45. 3), p. 156
6) W.S. Owen, D.H. Whitmore, M. Cohen and B.L. Averbach: Weld. J., **36** (1957) p. 503S
7) J.M. Hodge, R.D. Manning and H.M. Reichhold: Trans. Met. Soc. AIME, **185** (1949), p. 233
8) J.H. Gross and R.D. Stout: Weld. J., **35** (1956), p. 72S
9) N.J. Petch: Phil. Mag. **3** (1958), p. 1128
10) G. Burns and C. Judge: J. Iron Steel Inst., **182** (1956), p. 292
11) W. Barr and A.J.K. Honeyman; ibid, **157** (1947), p. 243
12) G. Birkbeck: ibid, **206** (1968), p. 909
13) E.S. Davenport: Trans. Met. Soc. AIME, **209** (1957), p. 677
14) J.C. Danko and R.D. Stout: Trans. ASM, **49** (1957), p. 189
15) E.H. Kottcamp, Jr. and R.D. Stout: Weld. J., **38** (1959), p. 435S
16) 邦武：鉄と鋼，**54** (1968), No. 6, p. 710
17) 邦武，大谷：住友金属，**19** (1967), No. 3, p. 311
18) T. Taoka, F. Furubayashi, and S. Takeuchi; Jap. J. Appl. Phys., **4** (1965), p. 120
19) 稲垣，三谷：金属材料研究所研究報告，**7** (1964), p. 408
20) 大森，大谷，邦武：鉄と鋼，**56** (1970), S457; **57** (1971), No. 10, p. 1690
21) Y. Ohmori and R.W.K. Honeycombe: Proc. Int. Conf. Sci. Tech. Iron and Steel, Tokyo (1970)
22) S. Matsuda, T. Inoue and M. Ogasawara: Trans. JIM, **9** (1968), p. 343. **11** (1970), p. 36
23) 寺崎，大谷：鉄と鋼，**56** (1970), No. 4, S. 211 (鉄と鋼投稿中)
24) A.M. Turkalo: Trans. AIME, **218** (1960), p. 24
25) 寺崎，大谷：鉄と鋼，56 (1970), No. 11, S. 550
26) U.H. Lindborg and B.L. Averbach: Acta. Met., **14**(1966), p. 1583
27) F. Terasaki: Acta Met., **15** (1967), p. 1057
28) J.M. Hodge and M.A. Orehoski: Trans. AIME, **167** (1946), p. 627
29) 寺崎，大谷：鉄と鋼，**57** (1971), No. 4, S. 239
30) 鈴木他：三菱重工技報，**4** (1967), No. 3, p. 271
31) 中島，荒木：鉄と鋼，**54** (1968), No. 4, S. 209, S. 522, **56** (1970), No. 4, S. 157
32) D.P. Edwards: J. Iron Steel Inst., **207** (1969), p. 1494

討論　pp. 346-347 参照

Low-Carbon Bainitic Steel with High Strength and Toughness

T. Terazawa H. Higashiyama S. Sekino

Nippon Steel Corporation

Technical Research Institute

As the manganese content of 0·04%C–0·7%Si–0·05%Nb steels was increased, the as-rolled strength increased abruptly at 2% Mn. This fact corresponded to a change in microstructure from polygonal ferrite-pearlite to bainite. In the ferrite-pearlite region, the addition of niobium did not alter the strength but in the bainite region there was a pronounced effect as a result of mutual interaction of niobium and manganese. The toughness of the niobium-free steels decreased sharply with increasing manganese over 1·3%.

The bainitic microstructure has two characteristics: the prior austenite grains from which it is formed are markedly elongated and unrecrystallized; and martensite islands are scattered through the ferrite matrix of the bainite. The transformation process after hot rolling is considered to take place as follows: First, at 650°C or below, acicular ferrite appears along the elongated prior austenite grain boundaries. Austenite-forming elements, such as carbon and manganese, are rejected into the untransformed regions where secondary transformation occurs with formation of martensite islands. Electron microscopic observation revealed no precipitate in the ferrite matrix or in the martensite islands. Dislocation density was high in the martensite islands, which also displayed transformation-twins, a typical microstructural feature of high-carbon martensite.

Chemical analyses of extracted carbides showed that manganese increased the solubility of Nb(CN). The higher soluble niobium content resulting from higher manganese may be the main reason why a bainitic microstructure is produced in this steel. Manganese may be replaced by elements such as nickel and/or copper as well as boron without deterioration and even with improvement of the mechanical properties of the parent metal and the weld. In the case of boron, simultaneous titanium additions are required to protect the boron against nitrogen during slab heating.

Carbon, unlike manganese, does not contribute much to the formation of bainite. It has a strong effect on mechanical properties only in the as-rolled condition. The influence of carbon and other alloying elements on mechanical properties is summarized in Table 1.

Hot-strip-mill-rolled low-carbon bainitic steel with a tensile-strength level over 80 kg/mm^2 was developed as a commercial product. When as-rolled specimens were tempered, the tensile strength decreased steadily with increasing tempering parameter while the yield strength first increased and then decreased. In the as-rolled state, yielding began at very low stresses. The fact that the yield strength increased in the initial stage of tempering seems to be due to elimination of the microstresses in the ferrite matrix that resulted from transformation to martensite in the as-rolled state. During further tempering, carbides first precipitated in the ferrite matrix and then the martensite islands decomposed to precipitate carbides. Actually, the hot-strip-mill-rolled low-carbon bainitic steel is annealed as a tight coil in the usual box furnace. Even with such a simple treatment, uniform mechanical properties can be obtained over the entire coil because of the comparatively gentle slope of the tempering curve.

When the bainitic steel was reheated between $Ac_1 \sim Ac_3$, the tensile strength increased but when it was reheated over Ac_3, the tensile strength decreased. In these cases, the strength changes could be explained by the percentage of martensite. When the steel was reheated between $Ac_1 \sim Ac_3$, the impact-transition curve remained the same as in as-rolled specimens but reheating over Ac_3 shifted the transition curve to higher temperatures. Hence, the low transition temperature of this steel seems to be inherent in the presence of ferrite formed from elongated austenite grains and is retained until the steel is reaustenitized.

The bainitic steel we have developed has a strongly laminated macrostructure so the fracture surface of impact specimens showed extraordinary striations. These striations were not evident when the specimen was fractured in the fully brittle temperature range or when the specimens had been reheated above the Ac_3 temperature. Therefore, it is believed that the striations may correspond to the prior austenite grain boundaries. Presence of such striations corresponded to a shift in transition temperature to lower temperatures and to a lowering of shelf energy. The features of the laminated structure could be observed more closely in bend tests where the prior austenite grain boundaries split and acted as barriers to crack propa-

gation. Cracks in the bend test produced almost a transgranular shear fracture. The very good bend characteristics of this steel do not stem from high elongation values but perhaps from the laminated structure.

Our bainitic steel has a unique preferred orientation with a highly dense (111) plane parallel to the surface. Because of this texture, there is very little difference in tensile strength between the longitudinal and transverse directions. When the strength level is considered, this steel also has good deep drawability.

As with other niobium steels, controlled rolling is essential for good impact properties. About 50% reduction in the low-temperature range is required with the optimum temperature for final rolling 800～1000°C. Too high a reduction in this temperature range, however, shifts the transition temperature to unnecessarily low temperatures and lowers the absorbed energy excessively.

When this bainitic steel was reheated in the austenitic temperature range, as in the heat-affected zone of a weld, the good toughness was lost. The HAZ toughness was much improved by partial replacement of manganese with nickel and/or copper as well as by lowering of the nitrogen content. An extremely low carbon content embrittled the heat-affected zone. A favorable HAZ microstructure consists of fine martensite lamellae distributed in parallel in the ferrite matrix while an unfavorable structure has martensite islands, especially larger ones, scattered in the ferrite matrix. Regression analyses showed that the favorable alloying elements for a tough heat-affected zone were carbon, manganese, titanium and nickel and the unfavorable ones, nitrogen and aluminum. The manganese content and especially the carbon content, however, must be restricted to minimize crack sensitivity of the HAZ. Thus, the carbon content of this steel is controlled between 0·04～0·10%.

強靱低炭素ベーナイト鋼

寺沢　健　東山博吉　関野昌蔵

新日本製鉄株式会社　八幡製鉄所　技術研究所

1. 緒　　言

Nbが鋼の合金元素として商用鋼に使われだしたのは比較的最近のことであり，合金元素としては新らしい．Nbの鋼中における挙動のうちよく利用されているのは，他の炭窒化物形成元素と同様に，フェライト(α)へのNb (CN) の析出による強化である．つぎに利用されNbのみに見られる大きな特徴は，オーステナイト(γ)への微細なNb (CN) の析出によって熱間圧延中のγ粒の再結晶を抑制することである．このため含Nb鋼は比較的高温で仕上圧延してもγ粒が伸長したままの未再結晶状態で$\gamma\rightarrow\alpha$変態を起し，それによりα粒が微細化し，従来の圧延ままの鋼と比較して強度のわりには靱性が良い．もしNbを含まない鋼でこのようなことを期待しようとすれば，さらに100°以上は仕上温度を下げなければならず，たとえそのような温度で変態がはじまらなかったとしても圧延機の能力や製品形状の上で多くの問題を生じて実現はむずかしい．

これらNbを利用した従来の鋼は組織的にみればフェライト－パーライト鋼であるが，BISRAではこのNbの効果とパーライトを減少させることの効果を組合せていわゆる“Pearlite Reduced Steel”を開発した[1]．これは通常の構造用鋼のC含有量よりもC量を一段と低くし，好ましくは0·04%以下とすることによってパーライトを含まないフェライトだけの組織としたものである．これによって靱性を大巾に向上させ，かつ溶接性を改善している．Nbの析出硬化と細粒化でパーライトをなくしたときの強度低下を補償しているのであるが，強度レベルはせいぜい45～60 kg/mm² 程度である．

最近の真空脱ガス法の普及によりこのような低C鋼が工業的に生産可能となったため，我々も“Pearlite Reduced Steel”の範ちゅうに属する成分系の検討を行なった．その結果低C，少なくともCを0·08%以下にしたとき，圧延ままで大巾に高張力化するには，Nbのような炭窒化物形成元素の添加のみ，あるいはフェライト－(パーライト)組織を変えない範囲の固溶硬化元素の添加では不可能であることがわかった．そして低C，含Nb鋼でMnを多量に添加することにより，組織をフェライト－(パーライト)からベーナイト状とすることで，強度，靱性が著しく向上することを見出した．我々とほぼ同じくしてスウェーデンのFagersta社も又極低C-Mn-Nb鋼の開発に成功した[2]．しかしMnが高いことは真空脱ガス法の利用をもってしても溶製が困難となるうえ，冷間割れ性，熱影響部および溶着鋼の靱性などの溶接性に問題が生ずる．そこでMnの一部をNi, Cuで置換し，さらにTi, Bの複合添加でMn量を減ずることでこれらの問題を解決した．また極低C化は圧延ままでの特性，あるいは溶接冷間割れ性には良いが，溶接熱影響部の脆化が大きい．すなわちCは溶接冷間割れ性を害さない程度まで添加されるべきである．

圧延ままでの特性の劣化は，圧延後焼戻しを行なうことによって防ぐのが良い．かくして我々は非調質高張力鋼として最適である低C-Mn-Ni-Cu-Nb鋼で，熱間ストリップ圧延薄板BHT 80，高張力形鋼BHT 75その他を開発した．以下この鋼の組織，機械的性質を論ずる．

2. 合金元素量と組織，機械的性質

Fig. 1は0·04% C-0·7% Si-0·05% Nb系でMnを増していったときの圧延ままにおける降伏強度($\sigma_{0.2}$)，引張り強さ(σ_B)，破面遷移温度($_v$Trs)，−40°Cにおける衝撃吸収エネルギー($_vE_{-40}$)の変化を示す．Mnが約2%のところから強度が急に上昇しているが，ここから組

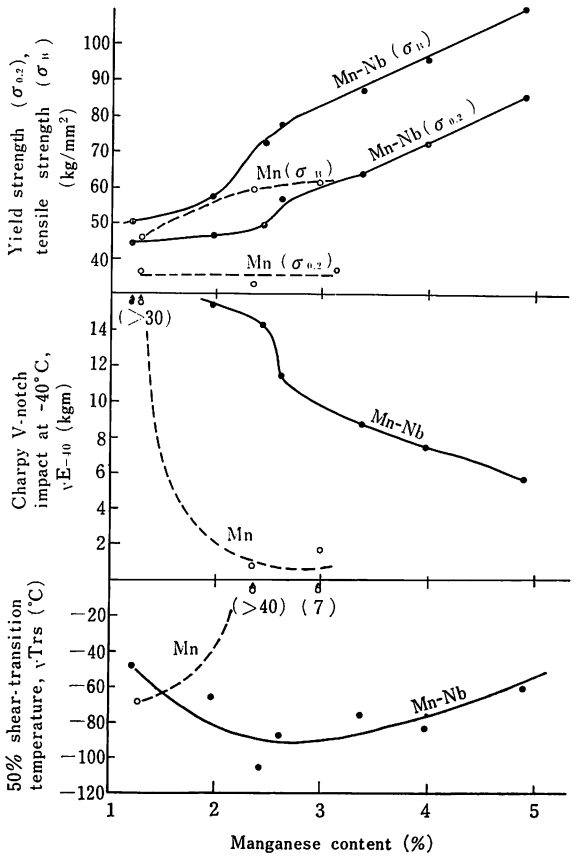

Fig. 1. Relation of tensile strength, yield strength, absorbed energy in V-notch Charpy impact test at −40°C and 50% shear-fracture transition temperature to manganese content in as-rolled 0·04%C-0·7Si%-Mn steels with and without 0·05% Nb. Thickness, 16 mm; finishing temperature, 880°C.

織がポリゴナルフェライトにわずかにパーライトを含む組織からベーナイト状組織に遷移する．Mn が 2·5% 以上で完全にベーナイト状組織になる．図中には Nb を含まない同一成分の鋼の性質の変化を比較のため示すがフェライト—パーライト組織の段階ではあまり差がないが，Nb を含むものがベーナイト状の組織に変わるとこから，Nb を含む鋼と含まない鋼の間で強度に大きな差が生じる．すなわち Mn と Nb の相互作用が顕著に現われる．靱性についても Nb を含まない場合は Mn が 1·3% 以上から著しく劣化することがわかる．

Photo. 1 にはこのときの光顕組織を示すが Nb を含まなければベーナイト状の組織が得られない．含 Nb，高 Mn 鋼で得られる圧延まま組織の特徴は変態前の γ 粒が未再結晶で著しく伸長していることである．そしてフェライト地の中にこまかいマルテンサイトが島状に分散している．

Photo. 2 は圧延後の冷却中に焼入れて圧延ままで得られる組織の生成過程を観察したものである．フェライトは約 650°C 以下で生成し始め，ポリゴナルフェライトとは異なるいわゆるアシキュラーフェライトであることがわかる．そして変態し始めでは核生成が起こるのは γ 粒界である．島状のマテテンサイトはフェライトの成長に伴ってはきだされた C やその他のオーステナイト形成元素が濃縮し Ms 点が下がった部分と考えられる．Photo. 3 に圧延まま材のレプリカによる電顕組織および薄膜透過電顕組織を示す．レプリカ組織でマルテンサイトは腐食されない島状の凸起として観察される．フェライト地，島状マルテンサイト中いずれも析出物は認められない．マルテンサイト中の転位密度は高く，高炭素マルテンサイトの特徴である変態双晶が認められる．

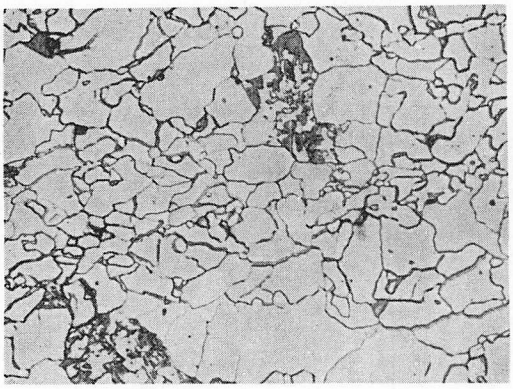

1·21% Mn-0·05% Nb

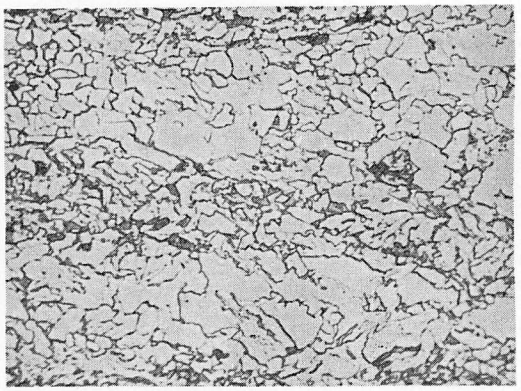

2·36% Mn-0·05% Nb

2·60% Mn-0·05% Nb

2·96% Mn-Nb free

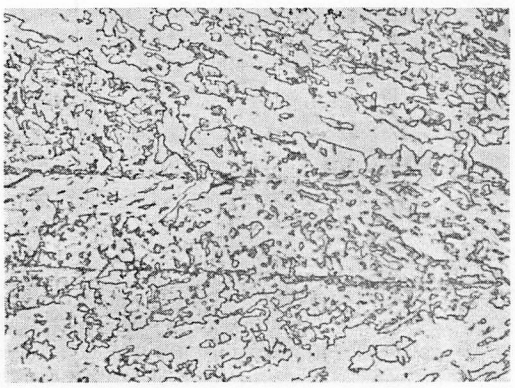

3·36% Mn-0·05% Nb ×500

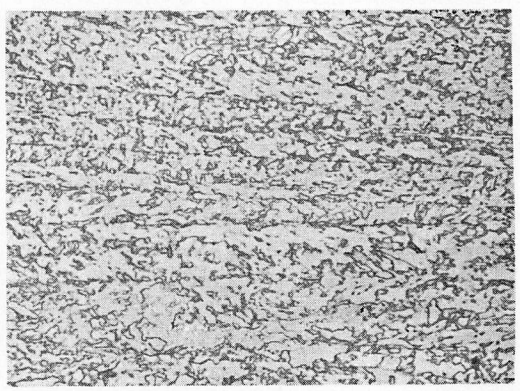

3·96% Mn-0·05% Nb ×500

Photo. 1. Change of optical micrographs of as-rolled 0·04% C-0·7% Si steels with manganese and niobium content.

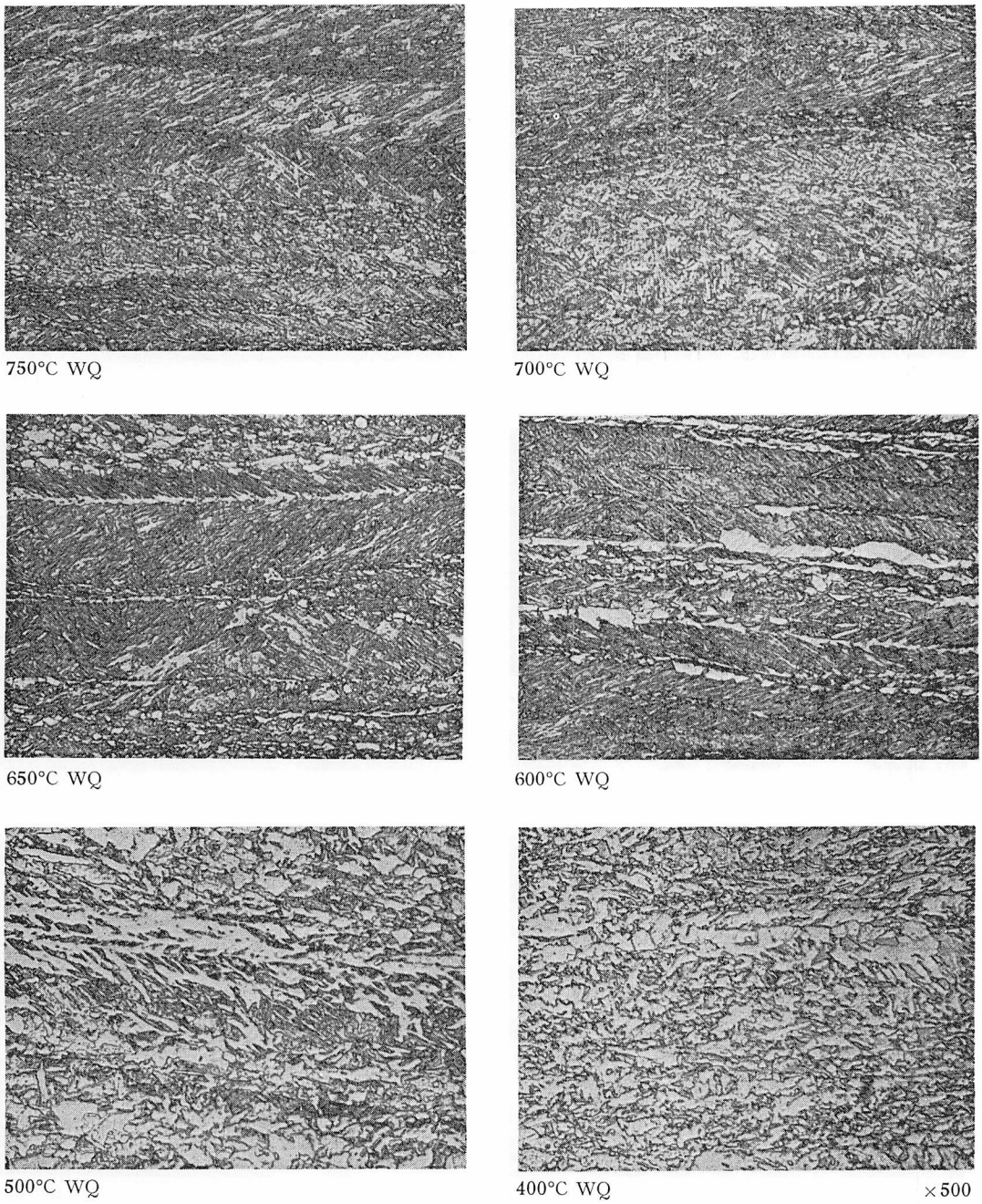

Photo. 2. Transformation process after hot rolling of 0·06% C-0·76% Si-2·46%Mn-0·05% Nb-0·001% B-0·02% Ti steel. Thickness, 12 mm; finishing temperature, 800°C. Nital etch.

Fig. 2 には Mn 量の違いによる圧延ままにおける塩酸可溶の sol Nb の変化を示す．Mn 量が増すにしたがって sol Nb 量が増すのは，単純に変態点の低下で説明できるが，1280°C 加熱と 1150°C 加熱における sol Nb 量の差が高 Mn 側で縮まるのは，Mn 量が高いときには Nb (CN) の溶解度が増すということにしないと説明できない．結局含 Nb 高 Mn 鋼がベーナイト状組織になり易い理由は，1つには高 Mn であることで変態点が下がること，1つには固溶 Nb のアシキュラーフェライト生成傾向にあるといえる．

Mn の上述のような効果は，γ粒界に偏析しフェライトの核発生を抑制する B の微量添加で置換可能である．B 添加でベイナイト状組織を得るに必要な Mn 量は約 0·5% 減少できる．B を添加する場合には，圧延前の加熱時に B を N から保護するために Ti の同時添加が必要である．B の焼入性に対する効果は B 量にはほとんど関係せず，効果があるかないかのいずれかである．

Mn はまた同じオーステナイト形成元素である Ni および Cu で置換可能である．その効果は Ni, Cu とも Mn の約 1/3 である．

C は少々の増量では Mn を置換できるほどのベーナイト状組織生成能を示さない．しかしベーナイト状組織になる Mn 量を有する鋼では大きな影響をもつ．Fig. 3 に C 量の機械的性質に及ぼす影響を示すが，圧延ままでとくに引張強さの上昇とそれに伴う伸びの低下，および靱性の劣化が C が増すにつれ大きくなる．

この C の影響は，焼戻しを行なうことにより軽減できる．焼戻し後は，強度および靱性ともほとんど C 量に関

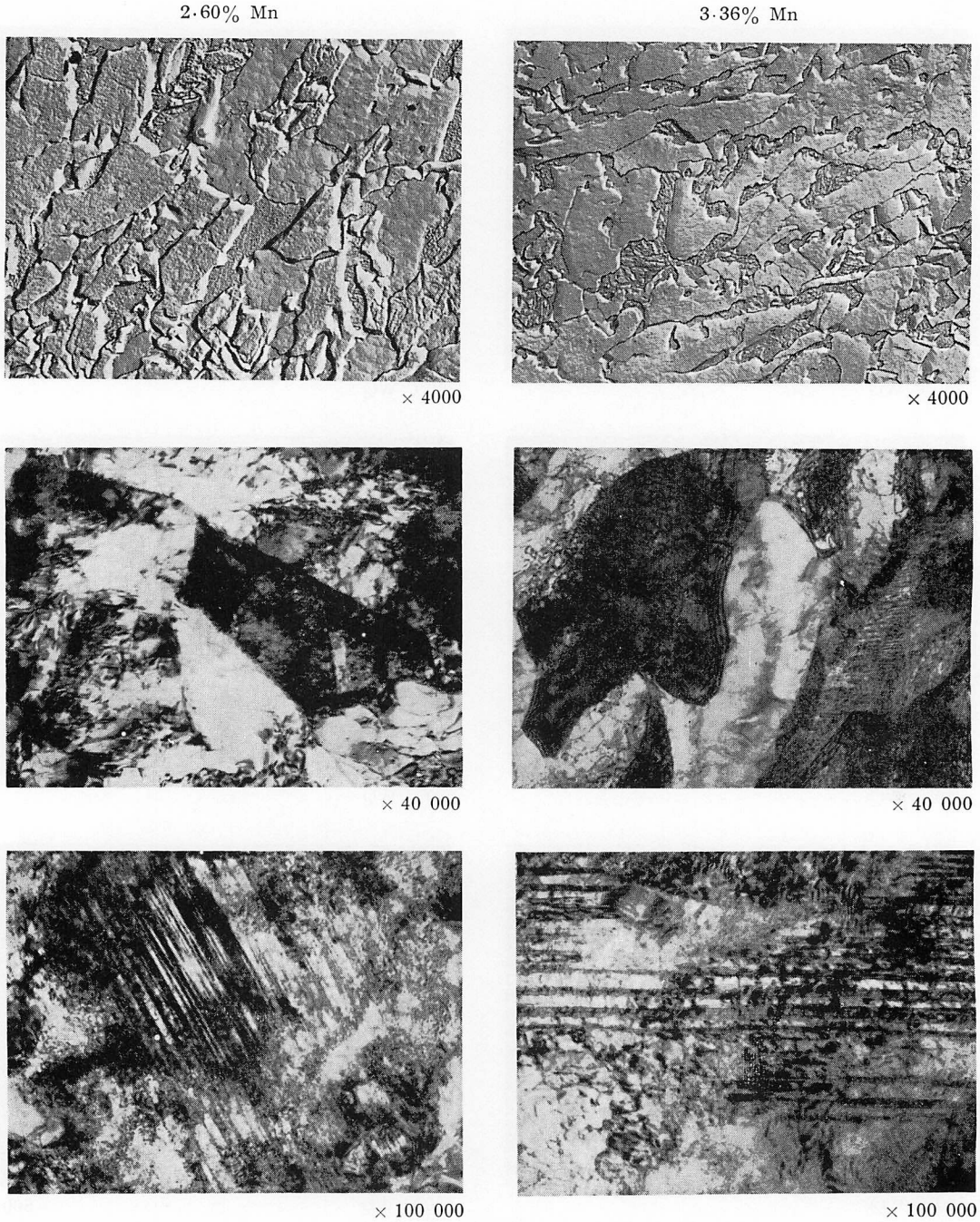

Photo. 3. Change of electron micrographs of as-rolled 0·04% C-0·7% Si-Mn-0.05% Nb steels with manganese content. Nital etch.

係しなくなる．ただし伸びは焼戻しで良くはなるが，Cの高いものほど低い．

これら合金元素の影響をまとめるとTable 1に示す回帰分析結果のごとくになる．この表で分析したものは全てBおよびTiが添加されている．

3. 機械的性質の特徴

ここでは代表的な成分についての機械的性質を述べる．前述の回帰分析結果に基づいて熱間ストリップ圧延で製造する80kg/mm²級高張力鋼板を開発したが，Table 2がその代表的成分例である．Table 3に圧延ままと焼戻し後の機械的性質を示す．Fig. 4にはこの鋼の焼戻し過程での強度変化を示す．引張強さは焼戻しによりゆるやかに低下するが，降伏点は一度増大して後次第に焼戻しパラメーターとともに減少する．圧延ままと焼戻し後の応力—ひずみ曲線をFig. 5に示すが，圧延ままでは低い応力で降伏が起こり明瞭な比例限，弾性限を示さない．焼戻しにより比例部分が長くなり降伏現象が明瞭となり，それにともなって降伏強度も上昇する．この焼戻しにより降伏強度の上昇する理由は次のように考えられる．この鋼の変態過程で島状マルテンサイトはCなどの濃縮によりMs点が下がっているため，周囲のフェライトが相当高い強度をもつようになる低い温度で変態し，そのマルテンサイト変態に伴う体積の膨張はミクロ的な残留応力として圧延ままでは残ることになる．その残留応力により圧延ままでは，低い応力で降伏が生じるのである．

Table 1. Result of regression analyses of the mechanical properties of 0·02～0·05%C-0·7%Si-1·5～2·2%Mn-0～1·6%Ni-0～1·0%Cu-0·02%Ti-0·001%B bainitic steels. (N=16; thickness, 16 mm).

Treatment	Mechanical properties	Coefficients					Multiple correlation coefficient
		C	Mn	Ni	Cu	Constant	
Heating temperature: 1150°C Finishing temperature: 850°C As rolled	YS(kg/mm²)	69·4*	11·7**	4·13**	4·45**	27·7	0·86
	TS(kg/mm²)	244·3**	25·4**	5·8**	4·3**	21·3	0·96
	El (%)	−151·9**	−5·06**	−1·8**	−1·6*	41·2	0·94
	$_{v}$Trs(°C)	665·0*	40·4*	23·8**	−3·1*	−212·0	0·74
	$_{v}E_{-40}$(kgm)	−94·2**	−4·68**	−1·3*	−0·9*	22·5	0·97
Heating temperature: 1150°C Finishing temperature: 850°C Tempering temperature: 625°C	YS(kg/mm²)	—	16·8**	4·7**	1·2*	31·6	0·88
	TS(kg/mm²)	—	15·2**	4·7**	—	44·0	0·86
	El (%)	30·7*	−3·3**	−1.7**	−0·6*	34·2	0·75
	$_{v}$Trs(°C)	−1369·0**	49·9**	12·9*	21·9*	−138·0	0·78
	$_{v}E_{-40}$(kgm)	—	−5·7**	−1·9**	—	21·0	0·86

* 50% probable
** 90% probable

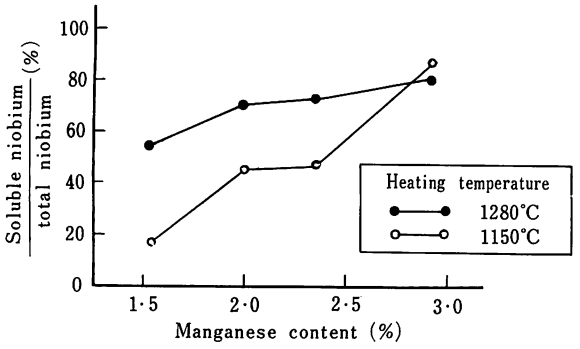

Fig. 2. Effect of manganese content on hydrochloric-acid-soluble niobium in as-rolled 0·04%C-0·7%Si-0·05% Nb steels. Thickness, 16 mm; finishing temperature, 880°C.

Table 2. Typical chemical analysis of hot-strip-mill-rolled bainitic steel (%).

C	Si	Mn	Cu	Ni	Ti	Nb	B	Al
0·05	0·38	2·16	0·81	0·82	0·02	0·05	0·001	0·05

Table 3. Mechanical properties of hot-strip-mill-rolled bainitic steel sheet. (Thickness, 4·5 mm).

	Direction	Yield strength (kg/mm²)	Tensile strength (kg/mm²)	Elongation (%)	Impact properties*	
					$_{v}$Eo (kgm)	$_{v}$Trs (°C)
As rolled	L	71	89	19	5·0	<−120
	T	64	87	18	3·5	<−120
600°C ×30min Tempered	L	75	79	21	5·5	<−120
	T	75	79	20	3·7	< −90

* 4·5 mm thick sub-size V-Charpy.

フェライトが軟化しこの残留応力で降伏するに至る温度で焼戻せば残留応力が除去されるため，除去された応力分だけ降伏強度は上昇する．

このようにこの鋼の焼戻しの初期過程は残留応力除去現象と考えられる．焼戻し過程の組織変化を光顕，電顕

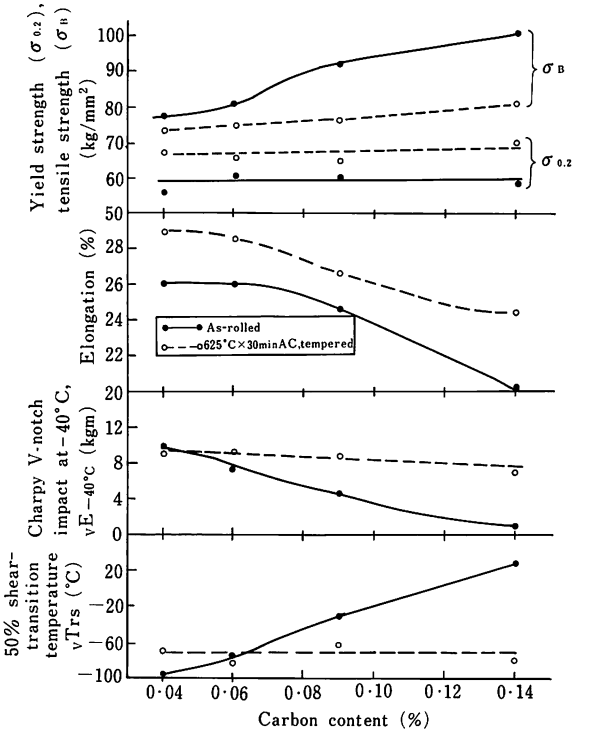

Fig. 3. Relation of mechanical properties to carbon content in 0·7%Si-2·1%Mn-0·05% Nb-0·02% Ti-0·001% B steels. Thickness, 16 mm; finishing temperature, 850°C.

で見たのが Photo. 4 である．島状マルテンサイトは焼戻しの初期にはなかなか分解しないが，フェライト地には微細な炭化物の析出が認められる．最後には，島状マルテンサイトも炭化物を析出して分解する．

この鋼は降伏強度を上昇させるため，圧延後タイトコイルのまま，通常の冷延焼鈍用ボックス炉で焼鈍している．焼戻し曲線が Fig. 4 に示すような，通常の調質鋼に比し非常にゆるやかであるので，コイル内の機械的性質の変動の少ないコイルが，このような簡単な処理で得られる．

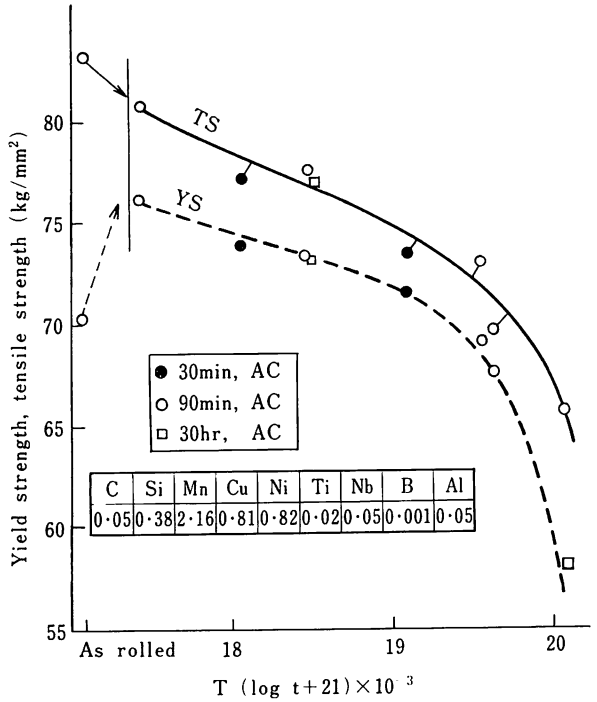

Fig. 4. Change of yield strength and tensile strength with tempering parameter.

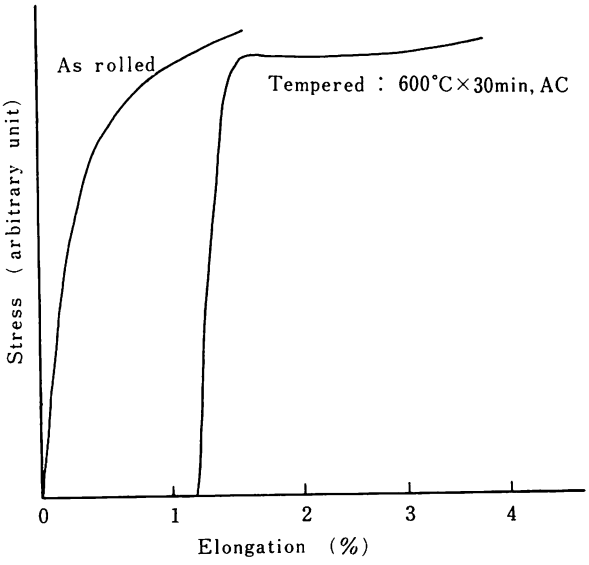

Fig. 5. Stress-strain curves of as-rolled and tempered specimens.

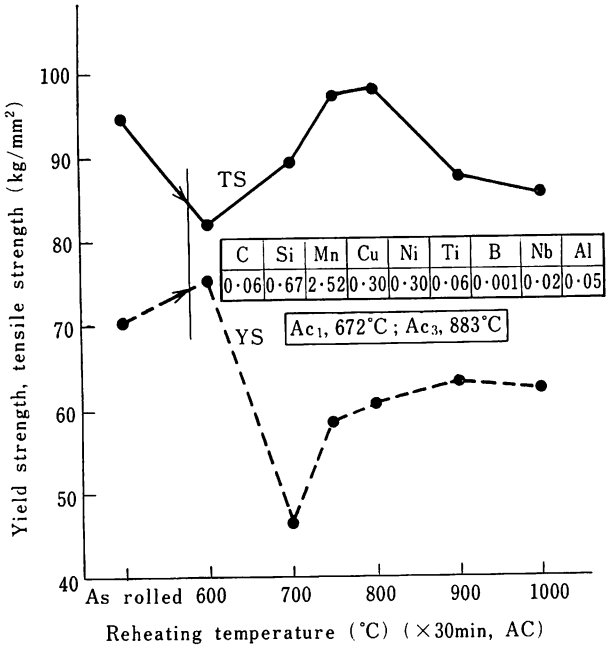

Fig. 6. Change of yield strength and tensile strength with reheating temperature. 4·5 mm-thick hot-strip-mill-rolled sheet.

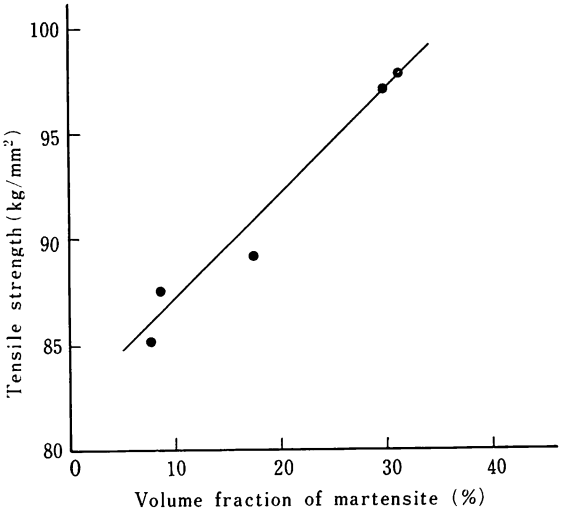

Fig. 7. Relation between tensile strength and volume fraction of martensite in reheated specimens.

変態点を越す再加熱での強度変化を Fig. 6 に示す．$\alpha+\gamma$ 域での再加熱で引張強さは増大し，降伏強度は低下する．γ 域に至ると再び引張強さは低下する．この間の組織変化を Photo. 5 に示すように，この引張強さの変化は島状マルテンサイトの量と相関がある．マルテンサイト量と引張強さの関係は Fig. 7 に示すとおりである．$\alpha+\gamma$ 域の再加熱でマルテンサイトの量が増加するのは，圧延ままで島状マルテンサイトの部分は，再加熱で始めにオーステナイト化し，それが他のフェライト部分に温度の増加とともに広がっていき，その後の冷却でオーステナイト化した部分は，オーステナイト形成元素の濃度は薄められるにせよ，その後の冷却で大部分は再びマルテンサイトに変態するからである．この再加熱における衝撃遷移曲線の変化を Fig. 8 に示す．靱性に対してはマルテンサイト量の影響はほとんどなく，完全 γ 域に再加熱されるまでは，遷移曲線は圧延ままの特徴を保持している．すなわち靱性を支配しているのは $\alpha+\gamma$ 域への再加熱で変化しないフェライト部分であるといえる．

この鋼は非常に強い層状組織をもっていることから，その衝撃試験における破面はきわめて特異な様相を示し，Photo. 6 に示すように破面にラミネーションが現われる．このラミネーションの破面での位置はほぼ一定しており，衝撃試験片のノッチ底における 3 軸応力の分布により決まるもののようである．完全脆性域ではこのラミネーシ

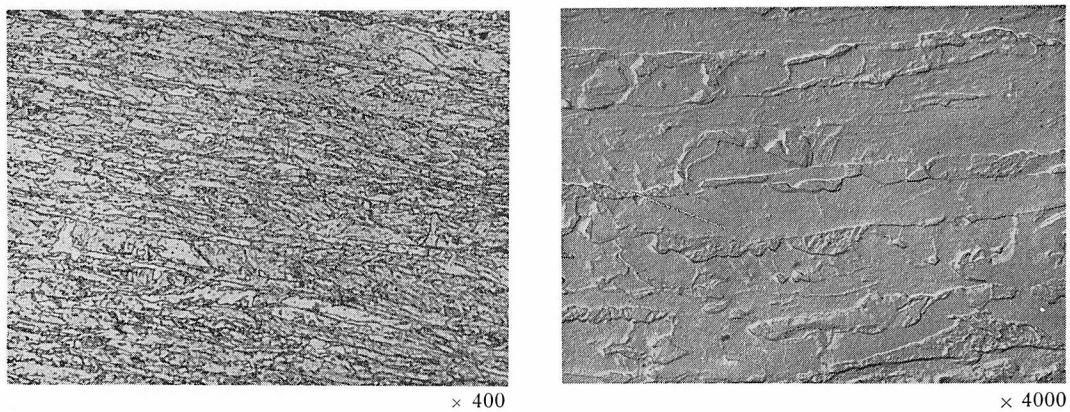

× 400　　× 4000

a)　As rolled

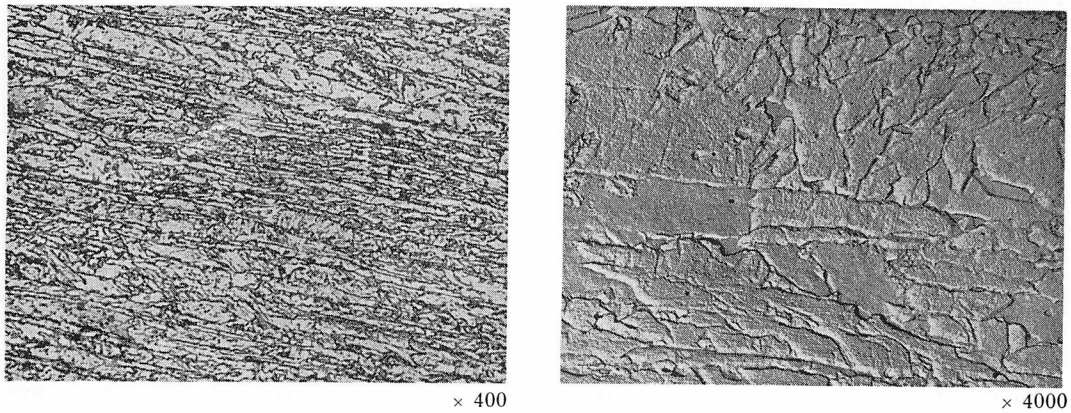

× 400　　× 4000

b)　500°C×10 min, AC

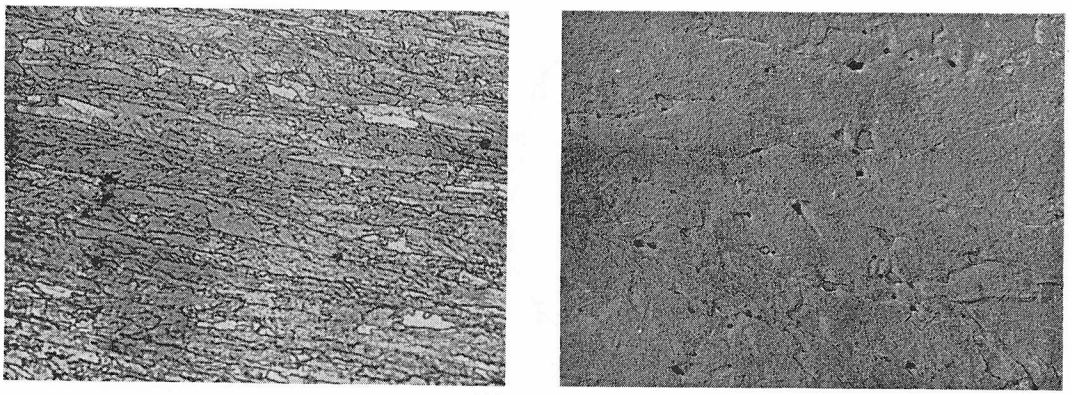

× 400　　× 4000

c)　600°C×30 hr, AC

Photo. 4.　Change of optical and electron micrographs of as-rolled low-carbon bainitic steel with tempering. Nital etch.

ョンはでない．又 Fig. 8 に示したγ域へ再加熱の場合もラミネーションはでず，ラミネーションの出現は組織が層状であることと対応している．このラミネーションは旧オーステナイト粒界で分離したものと考えられる．このラミネーションの出現がこの鋼の靱性を特徴づけている．すなわち層ごとに衝撃クラックが分割され，層は周囲の拘束を受けなくなるので3軸応力度が減少しなかなか脆性破壊しなくなり，その結果遷移温度が非常に低下する．しかし3軸応力度が減少するので変形させる応力は少なくてすむため吸収エネルギーは通常の鋼に比して低くなる．この間の事情は Fig. 8 にも示されている．

この層状組織の効果は曲げ試験を行なうとさらにはっきりと認められる．Photo. 7 は曲げ試験におけるクラックの断面であるが，層でクラックが伝播するのが阻止されており，旧オーステナイト粒界での分離がここでも生じている．曲げでのクラックは大部分の場合層を横ぎる剪断破壊であるが，ときには Photo. 8 のように旧オーステナイト粒界での破断も観察される．

この鋼の圧延まま材の強度と伸びの関係を多くのストリップ圧延の高張力鋼の中にプロットしたのが Fig. 9 であるが，この鋼が強度のわりに伸びが良いということにはならない．しかし曲げ性は他の高張力鋼に比べて非常に良好である．曲げ性と層状組織とはなんらかの関係があると考えられるが，はっきりしたことはいえない．

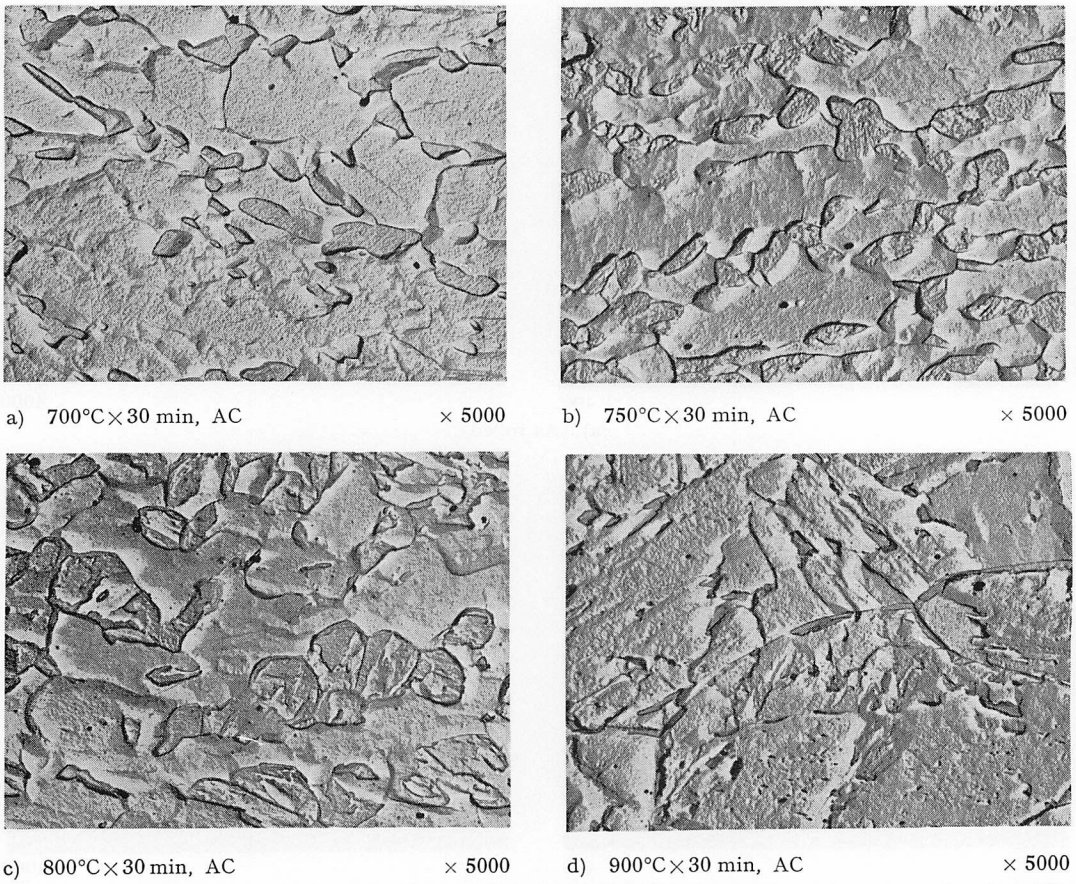

a) 700°C×30 min, AC × 5000　　b) 750°C×30 min, AC × 5000

c) 800°C×30 min, AC × 5000　　d) 900°C×30 min, AC × 5000

Photo. 5. Change of electron micrographs of hot-strip-mill-rolled low-carbon bainitic steel with reheating. Nital etch.

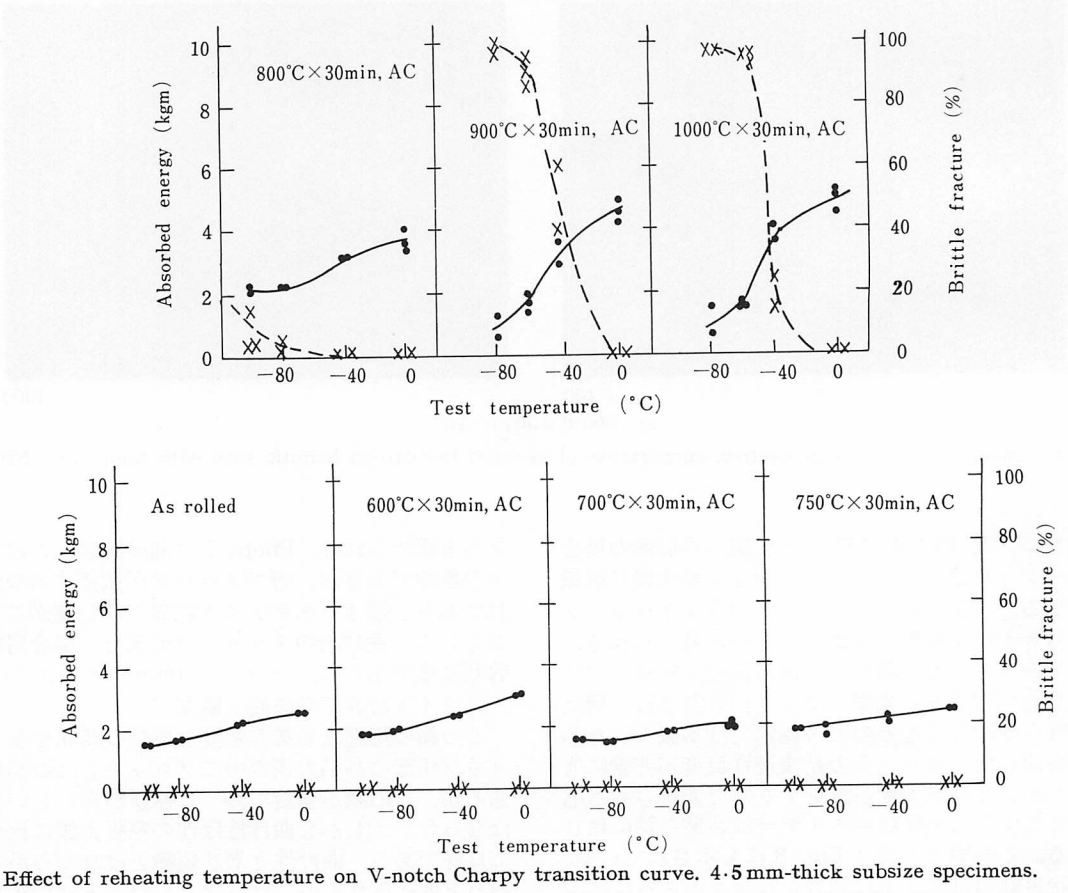

Fig. 8. Effect of reheating temperature on V-notch Charpy transition curve. 4·5 mm-thick subsize specimens.

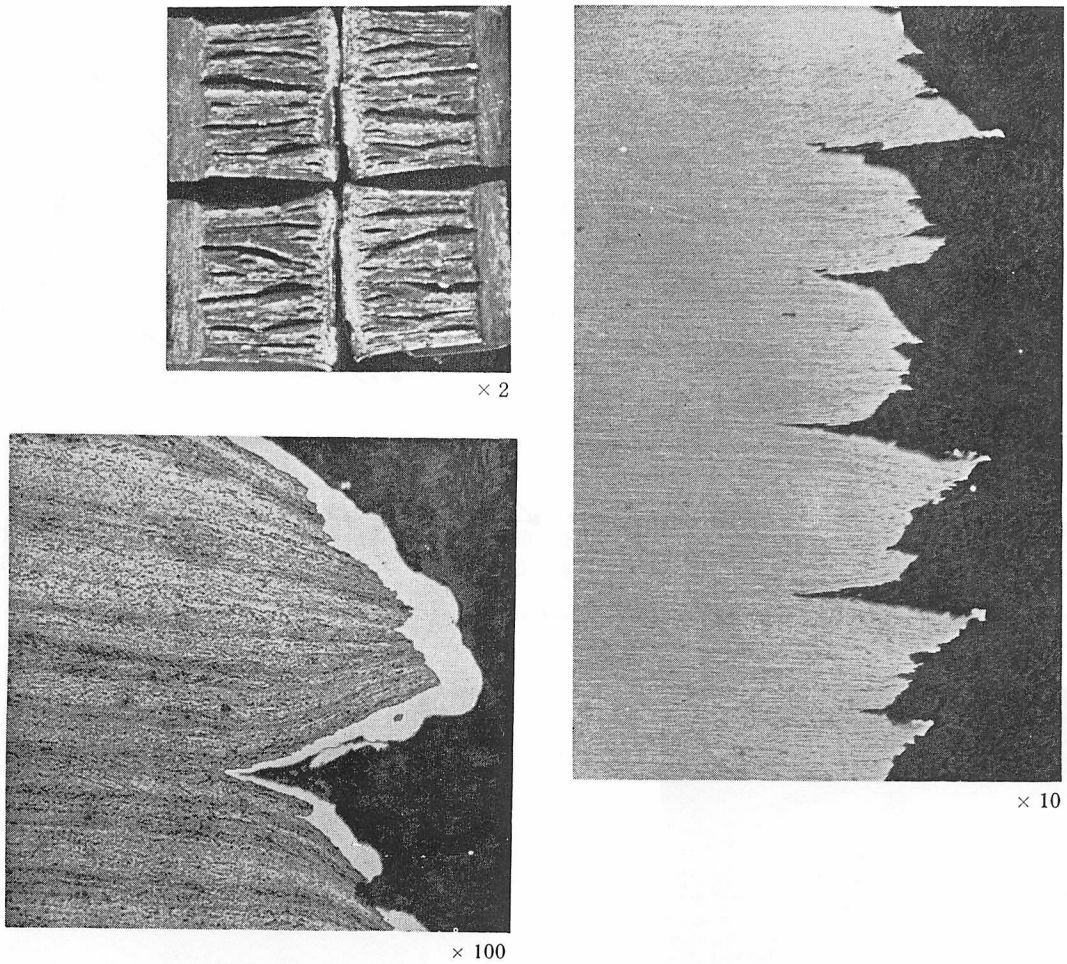

Photo. 6. Fractured surface of V-notch Charpy test piece and optical micrographs of its profile. Nital etch for micrographs.

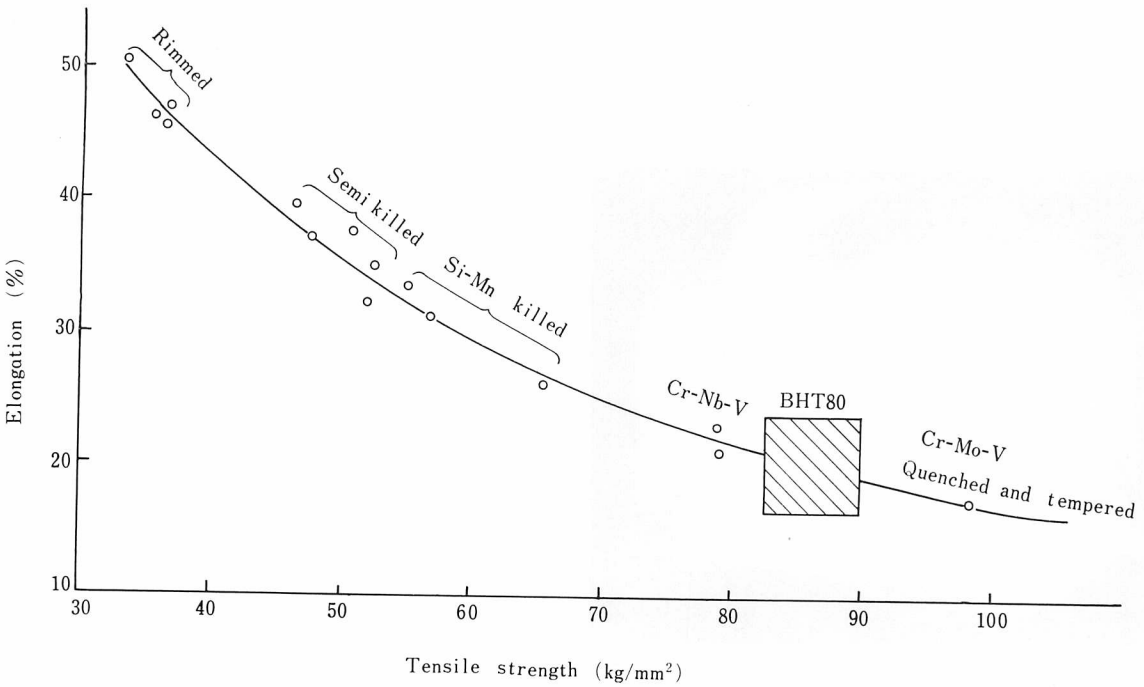

Fig. 9. Relation between tensile strength and elongation in 4·5 mm-thick sheet rolled on a hot-strip mill. Test piece, JIS No. 5; gage length, 50 mm.

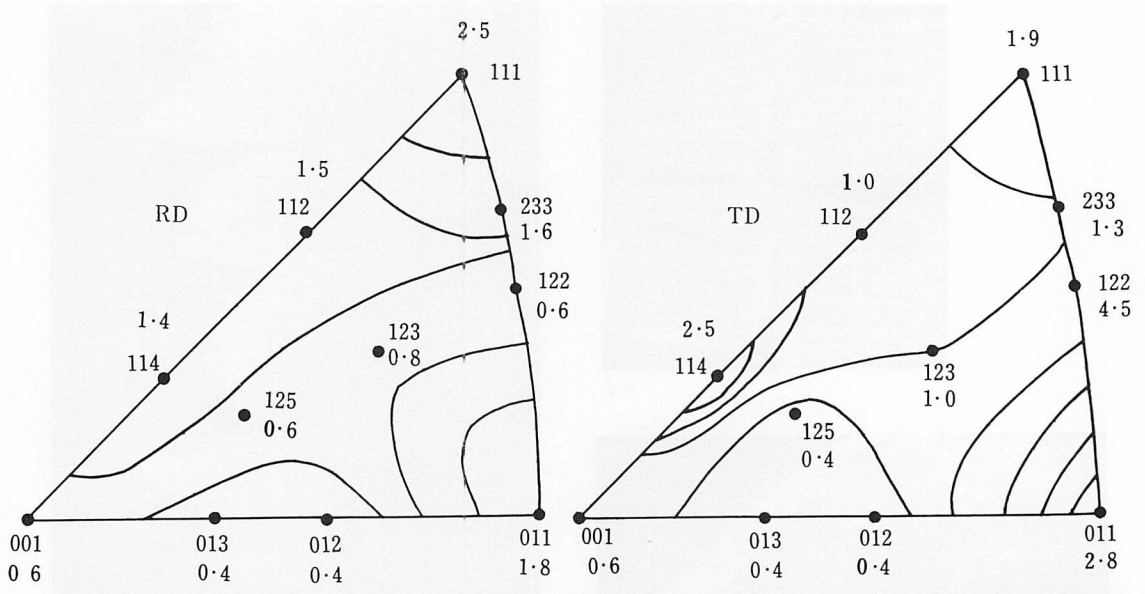

Fig. 10. Inverse pole figures of 4·5 mm-thick as-rolled sheet of low-carbon bainitic BHT-80. Chemical analysis is shown in Table 2.

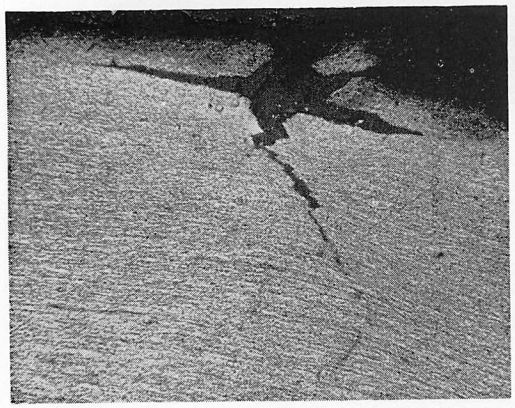

Photo. 7. Cross section of bend-test specimen of hot-strip-mill-rolled low-carbon bainitic steel. Nital etch.

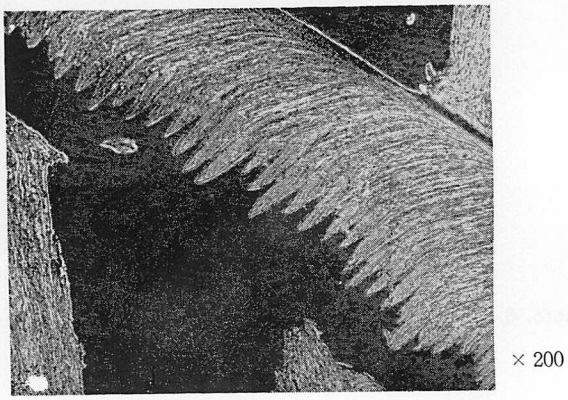

Photo. 8. Cross section of bend-test specimen of hot-strip-mill-rolled low-carbon bainitic steel. Nital etch.

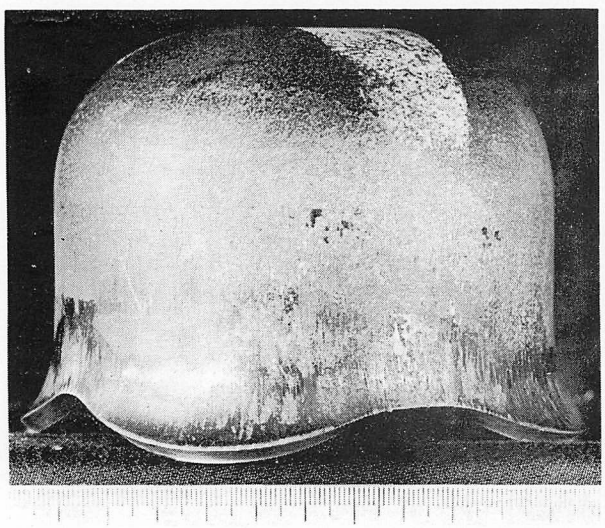

Photo. 9. Deep-drawn specimen of hot-strip-mill-rolled low-carbon bainitic steel. Thickness, 4·5 mm.

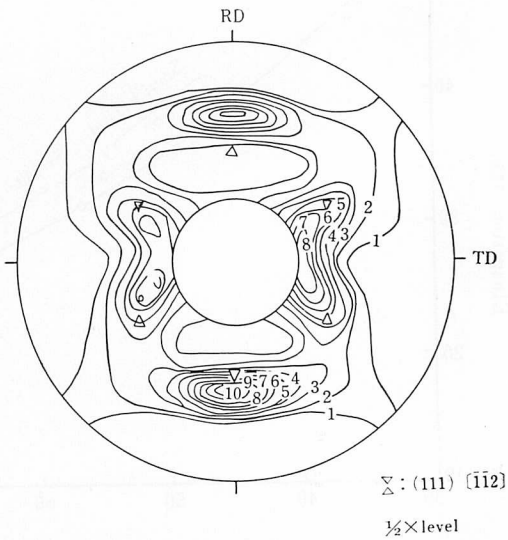

Fig. 11. (200) pole figure of the center of 4·5mm-thick as-rolled sheet of BHT-80. Chemical analysis is shown in Table 2.

先きに Table 3 に示したように，この鋼は圧延方向およびその直角方向での強度差がほとんどないかむしろ直角方向が強度が低い．通常のフェライトーパーライト鋼の熱延薄板では方向による強度差は非常に大であり，直角方向が強度が高いのが普通である．この鋼での異方性は Fig. 10 に示すような優先方位をもっていることで定性的ではあるが説明できる．すなわち辷り面上に高い剪断応力を受けるステレオ三角形上の下側の方位が直角方向で優先しており，それに反し圧延方向では剪断応力の低い上側の方位が優先しているからである．

Fig. 11 にはこの鋼の (200) 極点図を示す．顕著な集合組織を有しており，主方位は (111) [$\bar{1}\bar{1}2$] あるいはこれが少し傾いたものである．この集合組織は熱間圧延中の未再結晶オーステナイトの集合組織が，母相と格子関係のある変態によりフェライトに受け継がれたため生ずると考えれらる．オーステナイトの圧延集合組織の主方位が (110)[$\bar{1}\bar{1}2$] とすると，格子関係を Kurjumov-Sachs あるいは Nishiyama の関係にとるとき得られる集合組織に適合する[3]．この Fig. 11 の集合組織は板厚方向，および焼戻しでは変化しない．

このような集合組織をもっているので，この薄板の深絞り性は，同程度の高張力薄板と比べて非常に良い．Photo. 9 には実際ブランク径 200 mm のものを 100 mm 径にプレスした結果を示すが破壊を起さず絞り込んでいる．

4. 圧延条件と機械的性質

この鋼は，他の含 Nb 鋼と同様に，機械的性質，とくに靱性を高めるために低温圧延が必須である．Fig. 12 は圧延仕上温度を一定にして，パススケジュールを変えたときの強度，靱性の変化を示したものである．これらからわかるように，単に仕上パスのみを低温にすれば靱性が向上するわけではなく，圧下率で 50% 程度を低温圧下すべきことがわかる．低温域での圧下をあまり大きくとると，層状組織が非常に強くなり，前述の理由で遷移温度は不必要なほどきわめて低温側へ移行するものの，靱性域での吸収エネルギーの低下が大きく好ましくない．したがって圧下を行なうに適した温度域がある．これは厚板圧延とストリップ圧延とでは違うものの 800～1000°C の間にある．

Fig. 12 に示された試料の光顕組織と γ 粒を Photo. 10 に示す．パススケジュール E では，最終 2 パス目までは高温で圧下を受けているため，圧延されたオーステナイト粒は完全に再結晶している．靱性の最も良いパススケジュール B ではγ粒は未再結晶で伸長しており，地の組織もややこまかい．しかしオーステナイト粒度はさして変化なく，オーステナイト粒の細粒化よりも伸長度の方が靱性に効くことがわかる．

スラブ加熱条件と機械的性質の関係を Fig. 13 に示す．加熱温度が 1100°C 以下になると，強度の低下が目立つ

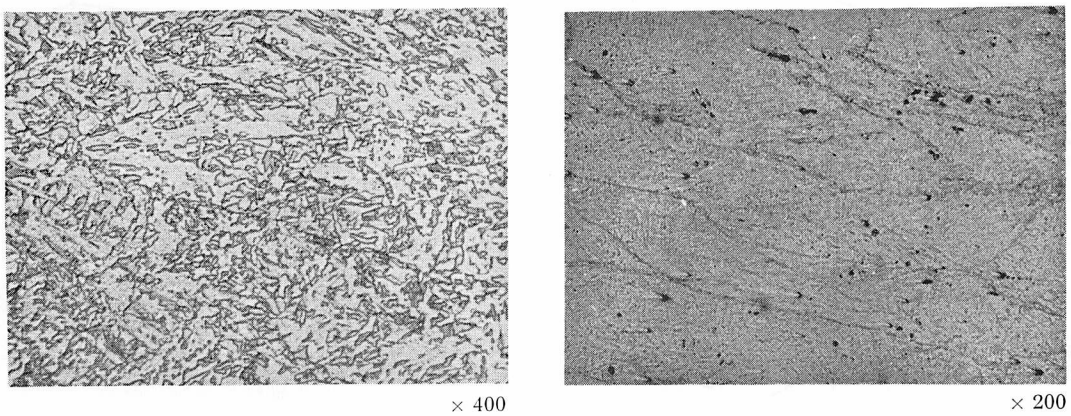

× 400　　× 200

Pass schedule B

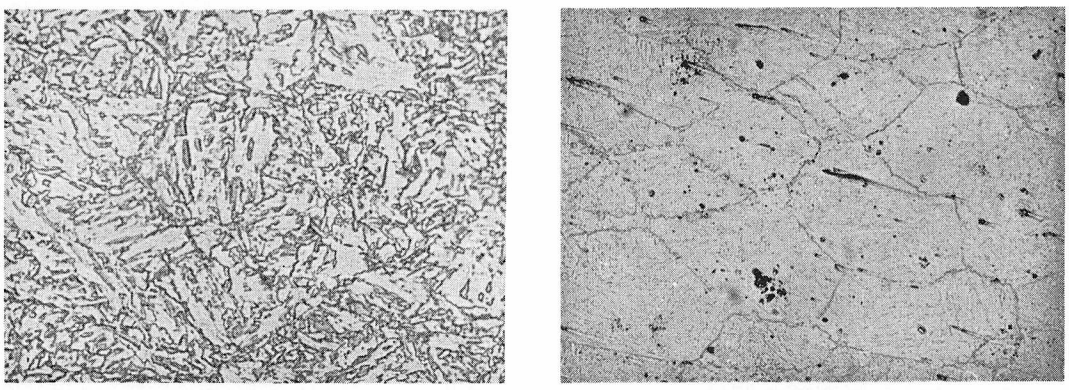

× 400　　× 200

Pass schedule E

Photo. 10. Change of optical micrograph with rolling conditions. ×400 micrographs, Nital etch; ×200, special etchant consisting of aqueous solution of 5% picric acid, 5% sodium laurylbenzenesulfonate and 30% alcohol to reveal grain boundaries.

Slab reheating temperature: 1250°C
Slab thickness: 50mm
Plate thickness: 15mm
●——● As rolled
○– –○ 600°C×30min, AC, tempered

Thickness (mm)	Rolling temperature (°C)				
33·5	>1100	>1100	>1100	>1100	>1100
28·5	990	1020	1050	1100	>1100
24·0	960	990	1020	1080	>1100
19·0	930	930	990	1050	>1100
15·0	900	900	900	900	900

C	Si	Mn	P	S	Al	Nb	Cu	Ni
0·07	0·76	2·26	0·009	0·013	0·03	0·04	0·40	0·26

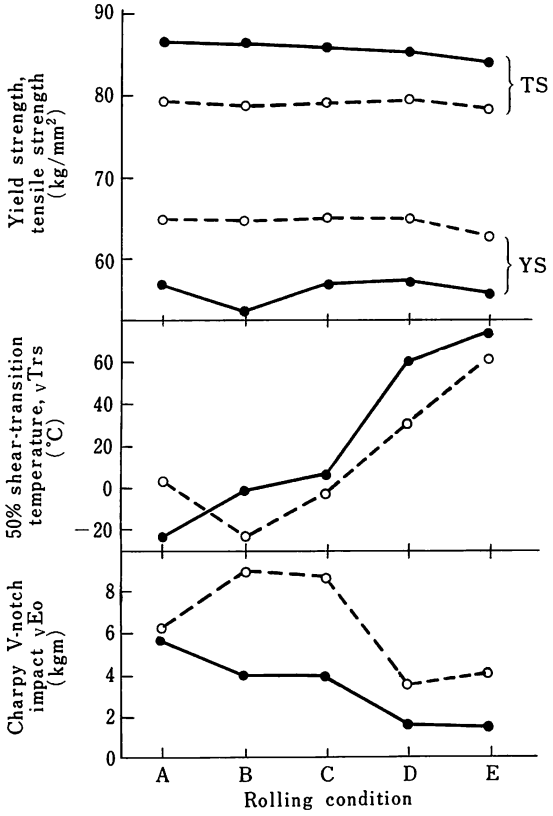

Fig. 12. Relation between rolling conditions and mechanical properties.

Slab reheating time: 2hr
Finishing temperature: 850°C
Temperature was controlled at 50mm thick.
Plate thickness: 16mm
Cooling condition: AC
●——● As rolled
○– –○ 625°C×30min tempered

C	Si	Mn	P	S	Nb	B	Al	Ti
0·06	0·76	2·46	0·016	0·010	0·05	0·001	0·03	0·02

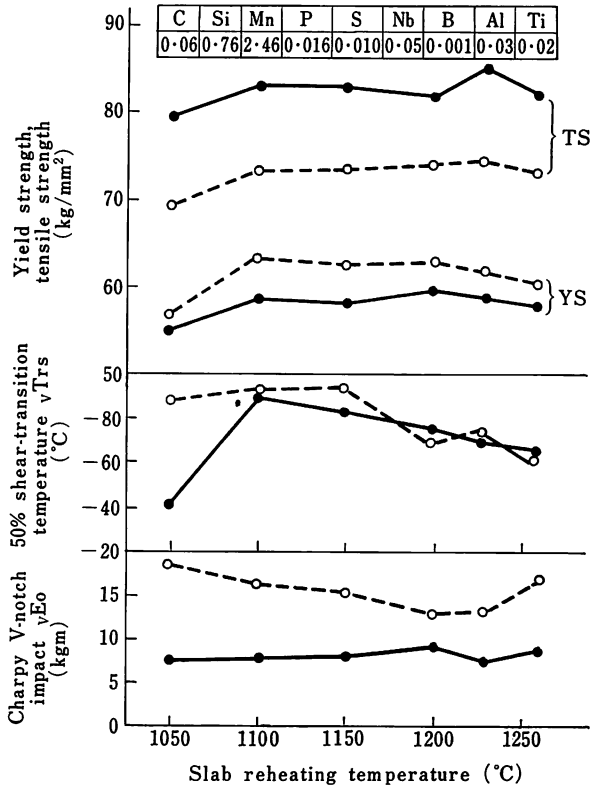

Fig. 13. Change of mechanical properties with the slab reheating temperature.

ようになり，加熱温度が 1200°C 以上と高くなると徐々にではあるが強度は上昇し靱性が低下する．このことから，スラブ加熱温度は 1150°C 附近が最良といえよう．

次に仕上温度の影響については，Fig. 14 に示すように，850°C 以下にすれば靱性は著しくよくなる．降伏強度は圧延ままではあまり変らないが，焼戻すと低温仕上すればするほど増加する．

5. 溶接熱影響部の靱性

この鋼は圧延組織で良好な靱性を得ているものであるため，圧延組織が失なわれるγ域へ再加熱されると，良好な靱性の特徴も失なわれる．溶接熱影響部のように，融点直下にまで加熱されるとオーステナイト粒の粗大化も加わり脆化を来たす．Table 4 に種々な成分と溶接熱サイクル後の靱性を示す．これからわかるように熱サイクル後の靱性は Ni, Cu の添加で著しく改善される．N は熱サイクル後の靱性に非常に有害である．極低 C 化も熱サイクル後の靱性を劣化させる傾向である．Mn のみの熱影響部の靱性に及ぼす影響を Fig. 15 に示す．Mn が 3% 程度のところに最良点がある．Mn 変化の場合と極低 C 材の熱サイクルの組織を Photo. 11 に示すが，靱性の良い組織は下部ベーナイト状で，マルテンサイトがラメラーとなっていてフェライトが細かく分割されているものであり，靱性が悪いものはマルテンサイトが島状でフェライトが粗大となっているものかあるいは地全体にマルテンサイトがでているものである．N は組織変化を通じない悪影響がある．Ni および Cu は Mn と同じく組織変化を通じて好影響を示す．

熱サイクル後の靱性について回帰分析を行なった結果を Table 5 に示す．靱性を向上させる元素は C, Mn, Ti, Ni, Cu で有害なものは Al と N である．

Mn のみの増量は実際の溶接において溶着鋼の靱性を劣化させるので Mn の増量は制限を受ける．Ni, Cu は溶着鋼の靱性を劣化させないので有利である．C は 0·10% を越すと急激に最高かたさを増し，溶接冷間割れを起すし，熱影響部も脆化させるので C は 0·04～0·10% に制限される．

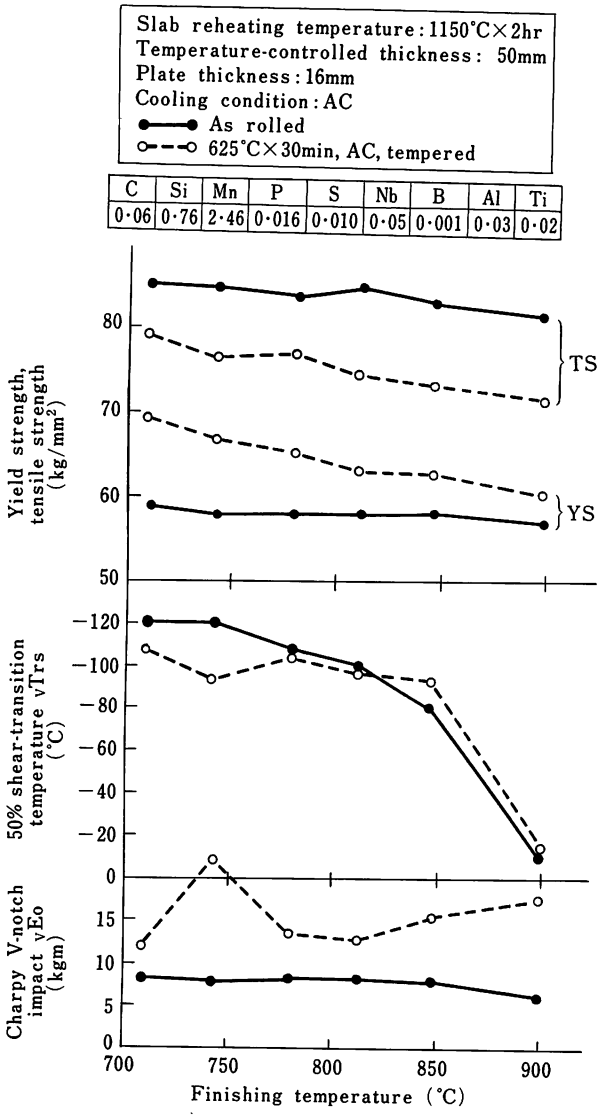

Fig. 14. Change of mechanical properties with the finishing temperature.

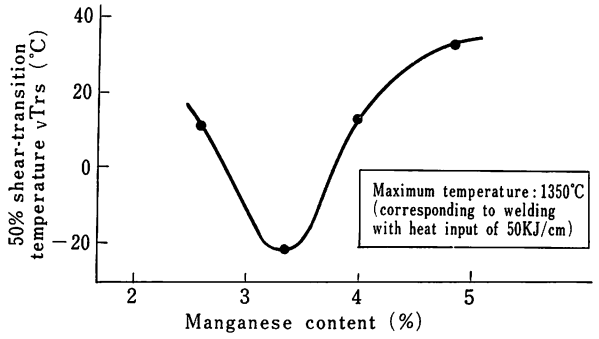

Fig. 15. Effect of manganese content in 0·04%C-0·7%Si-0·05%Nb-0·002%N steels on the transition temperature after a thermal-cycle-simulation test.

6. 結　　論

(1) 低 C-Mn-Nb 鋼は，Mn 量が 2·5% 以上で圧延までベーナイト状組織になり，きわめて優れた強度，靱性のバランスが得られる．Mn は Ni, Cu ならびに B で置換できる．Nb は Mn との相互作用により，固溶 Nb の形でベーナイト状組織になり易くするとともに，圧延中のオーステナイト粒の再結晶を阻止する作用により靱性を向上さす．C は圧延ままで強度を増すが延性，靱性の劣化が大きい．

(2) この鋼で得られるベーナイト状組織は，フェライトと細かく分散した島状のマルテンサイトとの混合組織である．

(3) この鋼を焼戻しあるいは焼鈍することにより，降伏強度を上昇させることができる．これは島状マルテンサイトの変態の際に生じたミクロ的な残留応力が除去されるためである．焼戻しあるいは焼鈍により，C の圧延ままにおける悪影響を軽減でき，延性および靱性を向上させることができる．

(4) この鋼の靱性は，衝撃破面におけるラミネーションの発生で特徴づけられ，靱性域での吸収エネルギーは高くないが，非常に低い衝撃遷移温度が得られる．

(5) 靱性は圧延条件により大きく支配され，低温で圧下量を大きくすると良い靱性が得られる．これは旧オーステナイト粒が未再結晶で延伸していることと対応する．

(6) オーステナイト粒が非常に延伸するストリップ圧延材は顕著な集合組織を有している．これは強加工を受けたオーステナイトに生じた集合組織が，格子関係のある変態により，フェライトの方位分布に伝わったものと考えられる．

Table 4. Impact properties after thermal-cycle-simulation test with 50 MJ/cm heat input.

	Chemical composition (%)												Impact properties		Remarks
	C	Si	Mn	P	S	Ni	Cu	Nb	Al	Ti	B	N	vEo (kgm)	vTrs (°C)	
1	0·04	0·76	3·36	0·008	0·010	—	—	0·05	0·02	—	—	0·0024	10·0	−2	C-Mn-Nb
2	0·03	0·33	2·97	0·014	0·010	—	—	0·08	0·04	—	—	0·0188	0·6	142	C-Mn-Nb
3	0·01	0·35	2·64	0·007	0·011	—	—	0·05	0·02	—	—	0·0083	1·0	68	C-Mn-Nb
4	0·05	0·69	2·62	0·020	0·007	0·50	0·54	0·05	0·04	—	—	0·0050	19·4	−16	ditto +(Ni, Cu)
5	0·03	0·30	2·42	0·009	0·005	—	—	0·04	0·04	0·02	0·001	0·0078	4·0	26	C-Mn-Nb +(Ti, B)
6	0·04	0·41	2·25	0·009	0·017	0·54	0·56	0·05	0·05	0·02	0·002	0·0089	12·0	−12	ditto +(Ni, Cu)
7	0·05	0·43	2·26	0·017	0·010	0·99	0·97	0·06	0·08	0·02	0·002	0·0059	8·5	−13	ditto +(Ni, Cu)

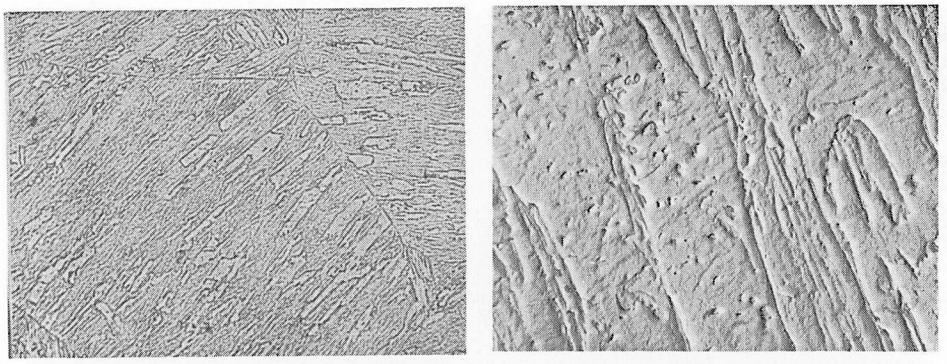

0·04%C-4·88%Mn

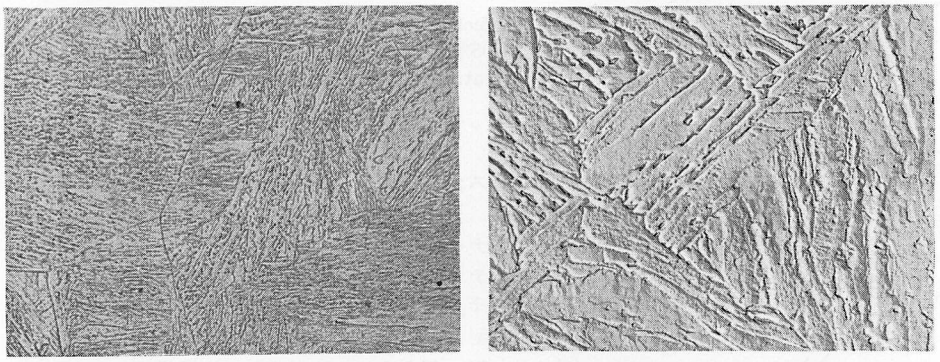

0·04%C-3·96%Mn

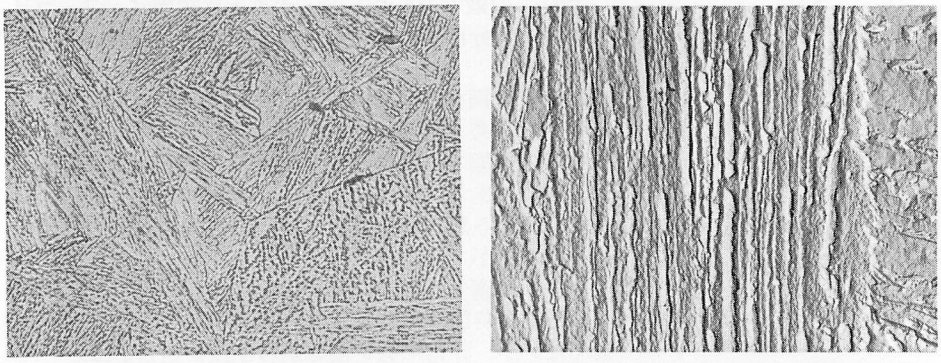

0·04%C-3·36%Mn

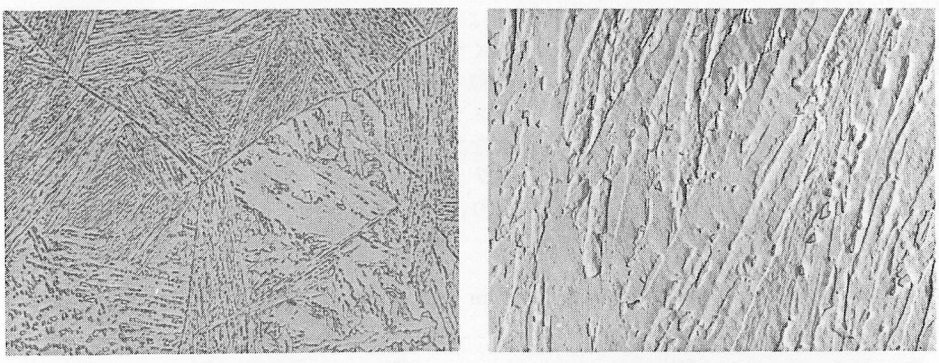

0·04%C-2·60%Mn

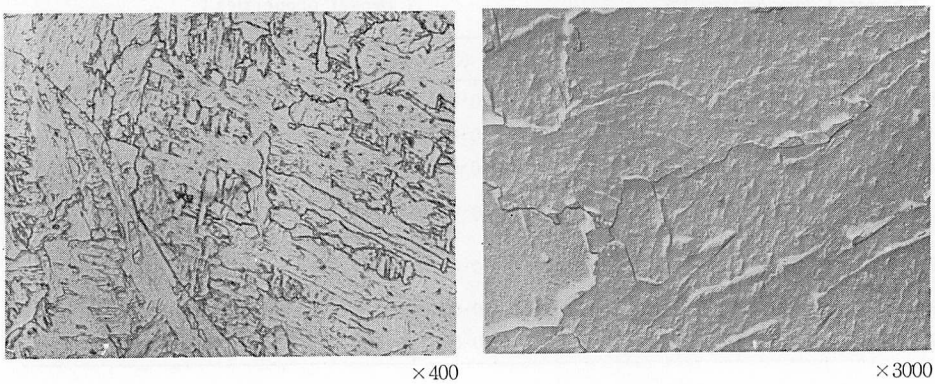

×400　　×3000

0·01%C-2·64%Mn

Photo. 11. Change of optical and electron micrographs of low-carbon bainitic steels after thermal-cycle-simulation test.

Table 5. Result of regression analyses of the impact properties after thermal-cycle-simulation test with 50 KJ/cm heat input.
(0·02～0·05%C-1·64～2·32%Mn-0·01～0·11%Al-0～0·11%Ti-0～1·55%Ni-0～0·54%
Cu-0·0076～0·024%N-0·7%Si-0·05%Nb steels. Number of data points, 24).

Impact properties	Regression coefficients								Multiple correlation coefficient
	C	Mn	Al	Ti	N	Ni	Cu	Constant	
$_{v}$Trs (℃)	−68·1	−17·8*	269·5**	−183·7**	1557·0**	−15·8**	−1·4	55·6	0·85
$_{v}$Eo (kgm)	47·8*	−0·4	−16·1	−8·8*	−80·8*	1·0	1·4	4·1	0·76

* 50% probable, ** 90% probable.

(7) 溶接熱影響部の靱性には，Ni, Cu の添加が有効であり，ある程度の C が必要である．N は熱影響部の靱性に非常に有害である．

謝　辞

本研究については Dr. Goda, Dr. Nagashima, Dr. Mimura その他多くの当社研究陣の指導，実用化にあたっては当社技術部の協力，ならびに実験については Mr. Toyofuku の尽力に負うところが大きい．ここに感謝の意を表する．

文　献

1) British patent, No. 1058146
2) Swedish patent, No. 8093/68
3) E.B. Kula, S.L. Lopata; Trans. AIME **215**, (1959), p. 980

討論　pp. 347-353 参照

Manganese-Molybdenum-Niobium Acicular Ferrite Steels with High Strength and Toughness

Y.E. Smith A.P. Coldren R.L. Cryderman

Climax Molybdenum Company of Michigan (Inc.)

an AMAX subsidiary, Research Laboratory

ABSTRACT

Hot-rolled, low-carbon manganese-molybdenum-niobium steels have been developed that have excellent combinations of high strength and toughness. The steels may be processed into spray-cooled and coiled strip or air-cooled and aged plate. Yield strengths of 48 to 70 kg/mm² may be obtained in either strip or plate. The steels have good impact resistance in both forms. Shelf energies of over 17 kgm/cm² and 50% shear transition temperatures as low as –60°C are attainable, as determined by the Charpy V-notch test.

The excellent properties are obtained by means of the transformation of the austenite to a very fine-grained acicular ferrite that is further strengthened by the precipitation of niobium carbonitride. The very high dislocation density and fine grain size of the acicular ferrite provide a large increment of "transformation strengthening." The presence of 0·2% to 0·4% Mo in the composition suppresses the formation of the conventional ferrite-pearlite structure so that acicular ferrite may be formed at the rates of cooling encountered in commercial processing. The manganese and niobium present also contribute to the control of transformation kinetics. A favorable aspect of the microstructure is that there is virtually no trace of the prior austenite grain-boundary structure; therefore a potential path of crack propagation has been eliminated. The low carbon, fine-grained microstructure also provides excellent formability and weldability.

A 0·05%C-1·6%Mn-0·25Mo-0·05%Nb steel is being produced as the first commercial application of the manganese-molybdenum-niobium acicular ferrite concept. This steel is being made for a 130 km section of 107cm diameter by 9·4mm-thick wall, spiral-weld gas pipeline that is being built across the central provinces of Canada. The pipe is being made to a 45·7 kg/mm² minimum yield strength specification and the 50% shear transition temperature of specimens taken transverse to the pipe axis is about −40°C.

Other applications that are envisioned include light-weight structural members for motor vehicles and structural plate for construction machinery, railroad cars, and shipbuilding.

1. INTRODUCTION

In recent years, trends toward more demanding designs and greater cost consciousness in the application of steel have resulted in a constant search for higher strength steels with adequate ductility and toughness. A large portion of this effort has been concentrated in the area of hot-rolled steels.* The large tonnage of these steels that is used creates an opportunity for considerable savings both in the weight and cost of finished products if the cost per unit of strength can be reduced.

Historically, carbon (as iron carbide) has been the primary strengthener of hot-rolled steel. Unfortunately, the low-cost strengthening that is available from this form of carbon must be used sparingly in a steel that must be welded in fabrication. The allowable carbon level of 0·25% or less has been found to be an extremely severe restriction with regard to obtaining high strength at low cost in a hot-rolled steel. Extensive efforts have been put forth to overcome this particular difficulty. Most of this work has been directed toward using a combination of refined grain size and precipitation hardening to strengthen the conventional ferrite-pearlite microstructure. Much of the progress to date has been limited to relatively light gages, 13mm thickness and under. Due attention has not been given to the fact that the ferrite-pearlite microstructure is not best suited either to extreme grain refinement or to precipitation strengthening. The practical limit of grain size refinement of the ferrite-pearlite structure in commercial products has been found to be about ASTM Grain Size 11 to 12. Furthermore, because of the excessive sensitivity of the precipitation to variation of the time-temperature aging parameter, there is considerable difficulty in obtaining precipitation strengthening homogeneously throughout a ferrite-pearlite structure on a commercial scale.

The manganese-molybdenum-niobium acicular ferrite steel described in this paper is designed on the

* Hot-rolled steels are defined here as steels that are either marketed or fabricated into products either in the as-hot-rolled or in the hot-rolled and stress-relieved (aged) condition.

basis of a new concept in hot-rolled steels.* The powerful effect of molybdenum in delaying the transformation of austenite to the high-temperature transformation products, polygonal ferrite and pearlite, is well known. In the manganese-molybdenum-niobium steel that is being discussed here, each of the four primary alloying elements, carbon, manganese, molybdenum, and niobium, contributes to controlling the transformation kinetics. Nevertheless, within the realm of the molybdenum-modified carbon-manganese-niobium steel compositions described below, the elements molybdenum and manganese provide the primary control over the extent to which the resulting microstructure will be composed of acicular ferrite.

The acicular ferrite matrix provides the potential for improving both the grain refinement and the precipitation-hardening components of the strengthening mechanism relative to those obtainable in ferrite-pearlite steels. Acicular ferrite is inherently fine-grained because of its relatively low transformation temperature and, in addition, it contains a substructure of high dislocation density. Because the matrix is transformed to ferrite at a lower temperature than is the case in the ferrite-pearlite steel, the precipitation of the strengthening phase is less rapid. This precipitation is much easier to control and therefore facilitates the development of homogeneous properties throughout a large plate or coil. The large strengthening component available from grain refinement and the generation of a highly dislocated substructure, i.e., "transformation strengthening", combined with the large additional component available from precipitation strengthening, makes it possible for the acicular ferrite steel to attain high yield strengths at unusually low carbon levels. This facilitates the attainment of excellent impact resistance, weldability, and formability.

2. EXPERIMENTAL METHODS

2.1 Materials

The steels used in the laboratory study were induction-melted as 25 to 34kg heats. Most of the heats were melted in an argon atmosphere, although a few were vacuum-melted and partially carbon-deoxidized prior to adding the argon atmosphere. All heats were deoxidized with aluminum, with less aluminum being used in the vacuum-melted heats. The steel was poured either into 9 or 14cm diameter seamless-steel tube molds, resting on copper chill blocks. Each copper chill had a 25 mm-diameter by 25mm-deep cavity that allowed a button for chemical analysis to be cast integrally with each ingot. The smaller molds were used for a split-heat technique whereby a series of three or four compositions were obtained from the same heat with the variation of a single compositional variable. All of the steels specifically referred to in the paper are listed in Table 1 with their chemical compositions. Those steels made by the split-heat technique have a two-letter designation, with the second letter indicating the order of pouring.

2.2 Forging and rolling

The cropped ingots were heated at 1205–1230°C and press-forged either to 38 or 44mm-thick slabs for subsequent rolling to 12·7mm-thick plate, or 19mm-thick slabs for rolling to 6·4mm-thick plate. Plates of 12·7mm thickness were rolled according to a wide variety of rolling schedules. The 12·7 mm-thick plates that were not rolled to special schedules were processed according to either one of the following schedules, after reheating for 50 minutes at 1260°C:

Schedule	Slab thickness (mm)	Reduction in thickness (%)			
		1230°C	1150°C	1095°C	870°C
A	38	25	—	45	48
B	44	20	29	44	34

Special schedules will be described later in the report. For all plates, an exposed-bead, Inconel-sheathed Chromel-Alumel thermocouple was inserted in a drilled hole in the slab prior to the first rolling pass. The temperature of each plate was continuously recorded during hot-rolling and subsequent cooling.

Plates of 6·4mm thickness were prepared by simulating the production of coiled strip. The same reheat temperature and temperature measurement technique were used as for the thicker plates. The 19mm-thick slabs were rolled to 33 and 50% reductions at 1150 and 870°C, respectively. After a delay of about five seconds, the rolled plates were spray-cooled to preselected spray-stop temperatures (near the respective simulated coiling temperatures). Following spray-cooling, some of the plates were air-cooled and some were placed in a recirculating air furnace at appropriate simulated-coiling temperatures to be program-cooled at 28°C/hr to simulate coil cooling.

2.3 Mechanical testing

Specimen blanks for tensile and impact specimens were cut from the as-rolled plates either in the longitudinal or transverse direction (or both). For aged properties, the blanks were aged one hour at

* Acicular ferrite is defined as a highly substructured, non-equiaxed ferrite that forms on continuous cooling by a mixed diffusion and shear mode of transformation that begins at a temperature slightly higher than the upper bainite temperature transformation range. It is distinguished from bainite for two reasons: (1) the limited amount of carbon available results in there being only a small amount of carbide present, and (2) the term bainite has been applied to such a wide variety of structures that it is somewhat indefinite.

Table 1. Chemical composition of laboratory steels (%).[a]

Steel	C	Mn	Mo	Nb	Si	Al	N	P	S	Other
AA	0·05	1·86	—	0·09	0·06	0·02	0·004	0·016	0·008	
AB	0·05	1·86	0·11	0·09	0·06	0·02	0·005	0·016	0·008	
AC	0·05	1·86	0·18	0·09	0·06	0·02	0·005	0·016	0·008	
BA	0·055	1·90	0·15	0·09	0·07	0·02	0·005	0·014	0·01	
BB	0·055	1·90	0·26	0·09	0·07	0·02	0·005	0·014	0·01	
BC	0·055	1·90	0·38	0·09	0·07	0·02	0·005	0·014	0·01	
BD	0·055	1·90	0·54	0·09	0·07	0·02	0·005	0·014	0·01	
CB	0·05	1·81	0·25	0·08	0·05	0·02	0·004	0·017	0·009	
CC	0·11	1·81	0·25	0·08	0·05	0·02	0·004	0·017	0·009	
CD	0·14	1·81	0·25	0·08	0·05	0·02	0·004	0·017	0·009	
DA	0·05	1·86	0·26	0·05	0·05	0·04	0·004	0·019	0·011	
DB	0·05	1·86	0·26	0·06	0·05	0·04	0·004	0·019	0·011	
DC	0·05	1·86	0·26	0·07	0·05	0·04	0·004	0·019	0·011	
DD	0·05	1·86	0·26	0·11	0·05	0·04	0·004	0·019	0·011	
E	0·04	1·80	0·25	0·09	0·06	0·02	0·003	0·011	0·007	
FB	0·05	1·89	0·20	0·05	0·20	0·03	0·004	0·011	0·004	
GA	0·045	1·87	0·24	0·07	0·05	0·03	0·005	0·015	0·005	
GB	0·045	1·87	0·24	0·07	0·05	0·03	0·005	0·015	0·016	
GC	0·045	1·87	0·24	0·07	0·05	0·03	0·005	0·015	0·033	
H	0·06	1·85	0·23	0·07	0·07	0·04	0·006	0·013	0·008	
J	0·05	1·80	0·25	0·07	0·07	0·04	0·008	0·013	0·010	0·10 Zr
K	0·05	1·86	0·26	0·07	0·05	0·03	0·002	0·021	0·009	
LA	0·045	1·91	0·25	0·05	0·22	0·06	0·008	0·012	0·016	0·015 Ti
MC	0·04	2·02	0·30	0·07	0·10	0·03	0·011	0·014	0·011	
N	0·055	1·91	0·35	0·075	0·05	0·03	0·005	0·015	0·020	
P	0·06	1·93	0·36	0·05	0·05	0·03	0·006	0·016	0·020	
Q	0·055	1·88	0·25	0·08	0·05	0·03	0·004	0·016	0·021	
R	0·06	1·94	0·26	0·05	0·05	0·03	0·005	0·016	0·019	
S	0·06	1·94	0·26	0·08	0·05	0·03	0·005	0·015	0·019	
T	0·055	1·87	0·26	0·05	0·05	0·03	0·005	0·016	0·020	
U	0·035	1·60	0·22	0·06	0·30	0·04	0·004	0·014	0·009	
V	0·035	1·59	0·21	0·09	0·27	0·04	0·004	0·011	0·008	
WA	0·05	1·87	0·23	0·045	0·05	0·02	0·004	0·011	0·007	
XA	0·02	1·86	0·24	0·09	0·05	0·02	0·004	0·010	0·008	
YA	0·05	1·43	0·27	0·10	0·07	0·03	0·004	0·018	0·017	
YB	0·05	1·43	0·27	0·10	0·07	0·03	0·004	0·018	0·017	0·02 Ce

[a] Within-heat variations in composition are underlined.

595 or 620°C. Tensile specimens from 12·7mm-thick plates had gage sections of 6·4mm diameter by 25 mm long. Those from 6·4mm-thick plates were flat specimens with gage sections 5·1 mm thick by 9·5 mm wide by 51 mm long. Tensile tests were conducted at room temperature in accordance with ASTM A-370 at strain rates of 18 and 120%/hr in the elastic and plastic ranges, respectively. Testing at these rates yields conservative strength data, since A–370 allows a strain rate of up to 375%/hr in the elastic range. Charpy impact tests were also conducted according to ASTM A–370, using either full size specimens from 12·7mm-thick plates or half-size specimens from 6·4mm-thick plates.

2.4 Metallography

Specimens were prepared for optical metallography by mounting specimens of the longitudinal cross sections of plates in Bakelite, polishing with diamond polishing wheels, finish-polishing electrolytically with 12·5 v/o concentrated H_2SO_4 in methanol, and etching with nital. Structures were also studied by electron microscopy, using carbon extraction replicas and transmission foil specimens. The extraction replicas were prepared from the Bakelite-mounted specimens by electropolishing in the methanol-sulfuric acid electrolyte, etching with a 1 to 1 mixture of 4% picral and 1% nital, depositing a carbon film, and stripping the replica from the

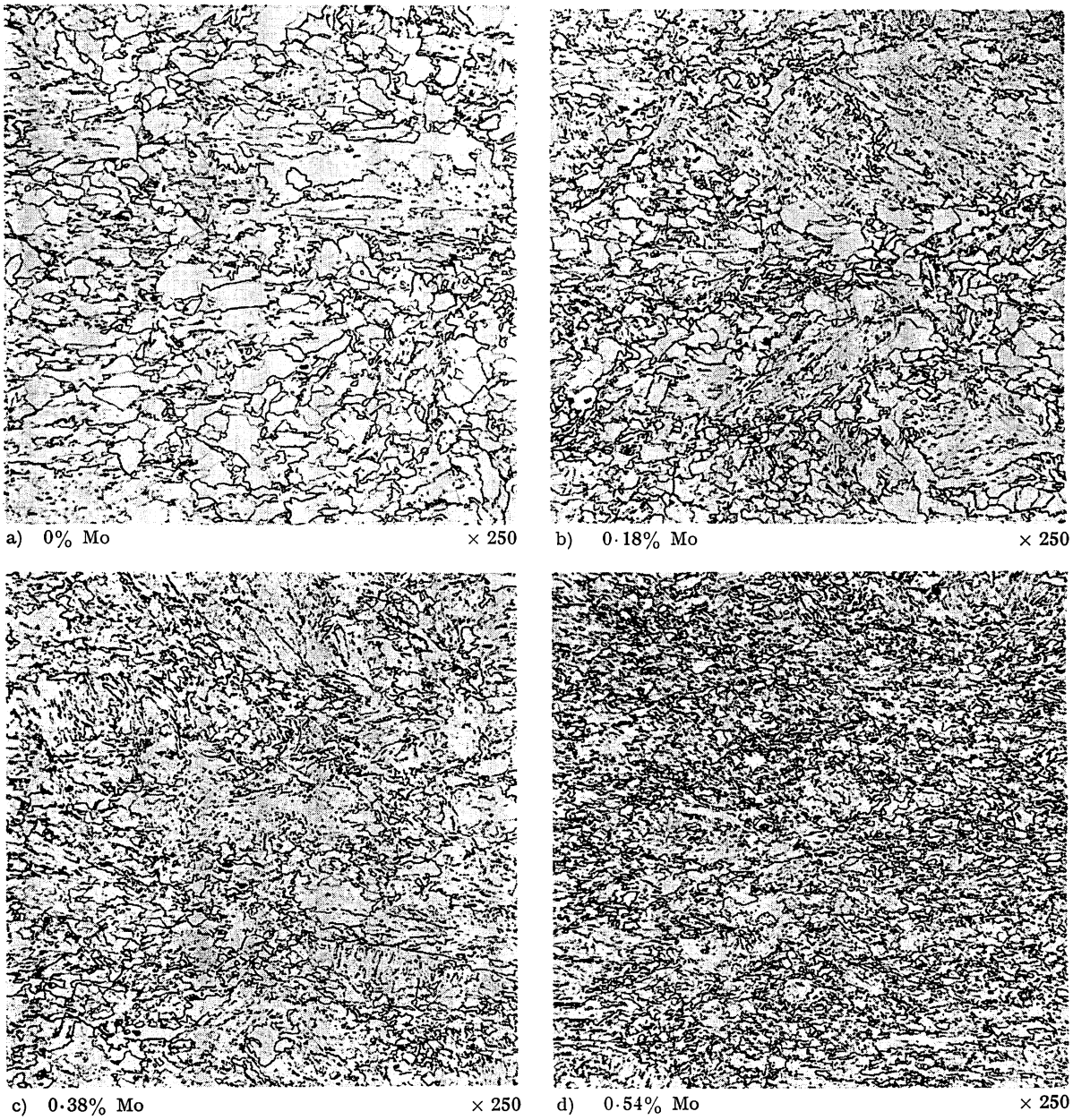

a) 0% Mo × 250 b) 0·18% Mo × 250

c) 0·38% Mo × 250 d) 0·54% Mo × 250

Photo. 1. Low-magnification optical micrographs showing effect of molybdenum on the microstructure of 12·7 mm-thick rolled-and-aged plates of 0·05/0·06%C–1·86/1·90%Mn–0·09%Nb steels.

specimen by immersion in a solution of 2·5% bromine in ethanol at —20°C. Transmission foil specimens were prepared by chemically milling 0·63mm-thick wafers to a thickness of 0·13mm, and then electrolytically thinning in a chromic-acetic acid electrolyte.

3. LABORATORY RESULTS AND DISCUSSION

3.1 Influence of composition

The composition of the manganese-molybdenum-niobium acicular ferrite steel that was initially selected for study was chosen with a particular set of objectives in mind. It was desired to develop a 56 kg/mm²-minimum yield strength steel, to be produced as 12·7mm-thick air-cooled plate, with good toughness, weldability and formability. The carbon content was nominally set at 0·05%. This low carbon level not only assured good weldability, but it facilitated the dissolution of approximately 0·1% Nb at the common slab reheat temperature of 1260°C. This unusually large niobium addition (relative to the more common 0·03% used in the higher strength grades of hot-rolled steels) provided a considerable capability for subsequent precipitation strengthening. To the above combination of carbon and niobium, 1·9% Mn and various molybdenum additions were added to provide sufficient control of the transformation kinetics so that acicular ferrite would be obtained in 12·7mm-thick air-cooled plate.

3.1.1 Molybdenum

The stepwise addition of up to 0·54% Mo to a

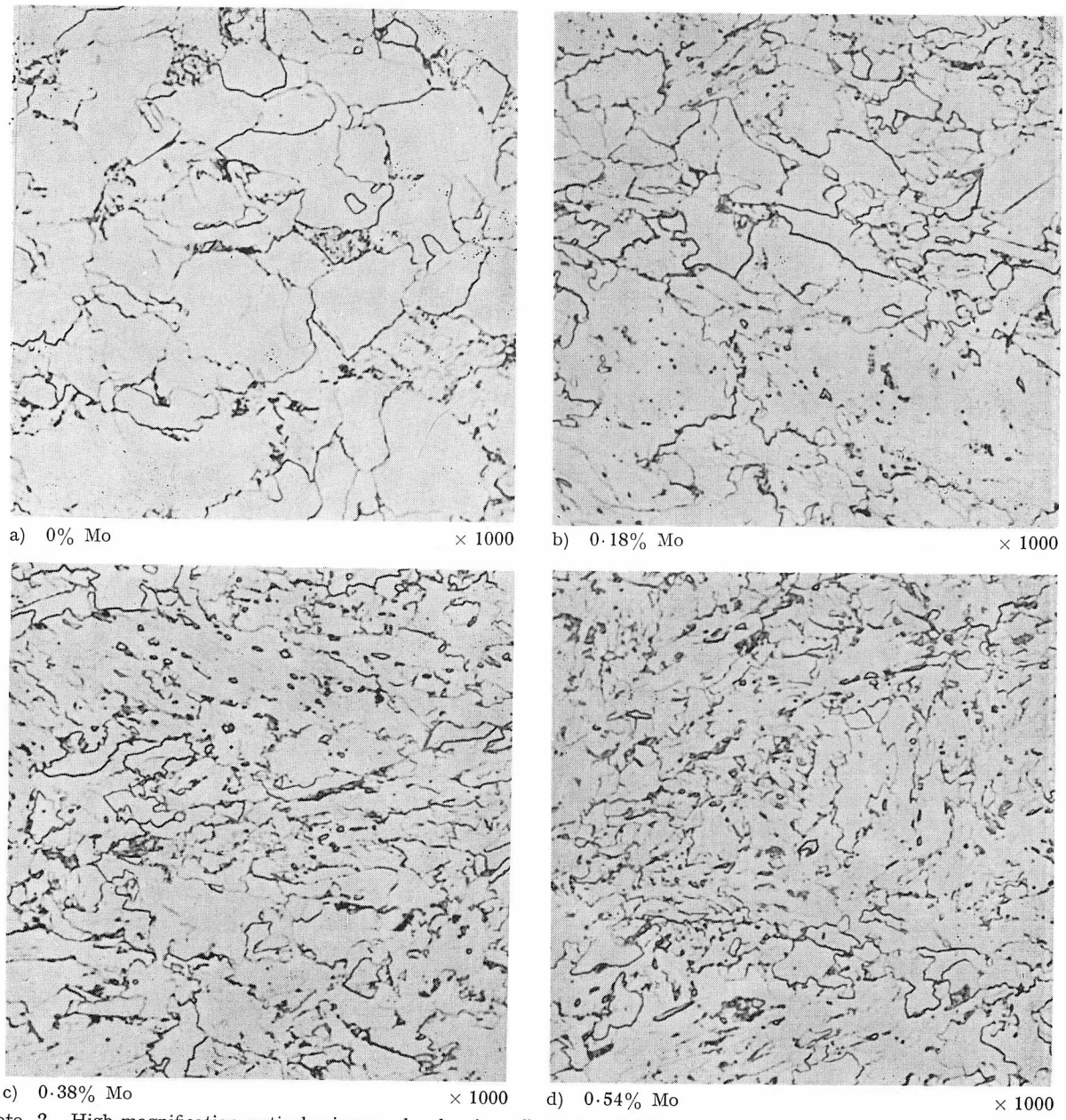

a) 0% Mo × 1000 b) 0·18% Mo × 1000

c) 0·38% Mo × 1000 d) 0·54% Mo × 1000

Photo. 2. High-magnification optical micrographs showing effect of molybdenum on the microstructure of 12·7 mm-thick rolled-and-aged plates of 0·05/0·06%C–1·86/1·90%Mn–0·09%Nb steels.

base composition of 0·05% C-1·9% Mn-0·09% Nb produced large increases in the acicularity of the structure of 12·7mm-thick air-cooled plates. At the highest level of molybdenum the structure was completely acicular. The effect of this microstructural change on the strength in both the as-rolled and aged conditions is presented in Fig. 1, which includes data from steels AA, AB, AC, BA, BB, BC and BD. The major point to be observed from this graph is that the addition of 0·25% Mo to a steel that has a 49 kg/mm² yield strength in the as-rolled condition makes it possible to increase the yield strength to 62 kg/mm² by a simple sub-critical-temperature aging treatment. Evidence for microstructural change brought about by the molybdenum addition is presented in Photo. 1, 2 and 3. The low-magnification photomicrographs of Photo. 1 emphasize the fineness of the acicular ferrite subgrains, which are in the grain size range of ASTM 13 to 14. The structures can be seen in more detail in Photo. 2. It may be observed in Photo. 2 that even when the microstructure is completely acicular, there is no indication of the locations of the prior austenite grain boundaries. The high dislocation density of the acicular ferrite substructure can be seen in the transmission photomicrographs of Photo.3.

The 0·09% Nb content of the steels of Fig. 1 has provided a maximum precipitation strengthening component of about 14 kg/mm², as a result of the aging treatment. It becomes obvious by comparing the data of Fig. 1 with the photomicrographs, however, that the degree to which this strengthening increment was realized was directly related to the fraction of the microstructure that was acicular.

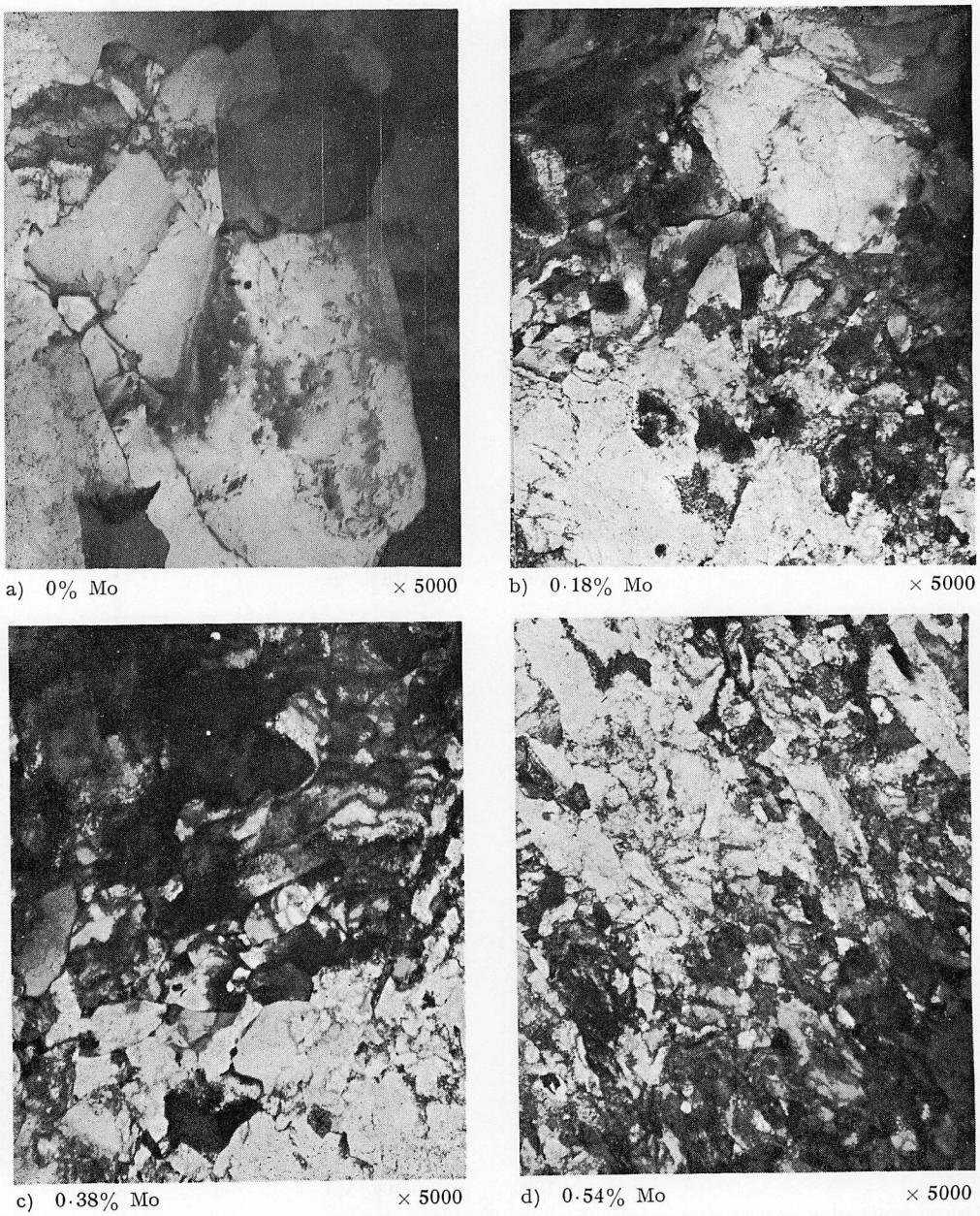

a) 0% Mo × 5000 b) 0·18% Mo × 5000

c) 0·38% Mo × 5000 d) 0·54% Mo × 5000

Photo. 3. Transmission electron micrographs showing effect of molybdenum on the microstructure of 12·7 mm-thick rolled-and-aged plates of 0·05/0·06%C–1·86/1·90%Mn–0·09%Nb steels.

This results primarily from the fact that acicular ferrite is transformed from austenite at a lower temperature than is polygonal ferrite. The very rapid rate of the precipitation of Nb(C,N) in the coarse polygonal ferrite during the course of the $\gamma \rightarrow \alpha$ transformation at the temperature range involved produces an overaged condition in as-rolled steel. In contrast, acicular ferrite ages only slightly as it is continuously cooled from hot rolling, because it forms at lower temperatures where the rate of Nb(C, N) precipitation is much slower. The result of these effects may be briefly reviewed in Fig. 1. Both the yield and tensile strength of the as-rolled steel decreased slightly because of the initial molybdenum addition. At this molybdenum level, the increased substructure strengthening of the small additional amount of acicular ferrite formed did not make up for the loss of some overaged, but nevertheless partially strengthened, polygonal ferrite. Further additions of molybdenum provided enough substructure strengthening to overcome this loss. Obviously, the effect of molybdenum upon the as-rolled properties is of minor importance. It is the marked beneficial influence of the molybdenum on the aged properties as described above, which has provided a steel of considerable practical significance.

It should be noted that the yield strength to tensile strength ratio increased during aging from about 0·70 to about 0·85. The ductility values, the elongation and the reduction of area were insensitive to aging, as well as to the strengthening effects produced by the molybdenum additions. Elongations ranged from 24 to 29% and reduction

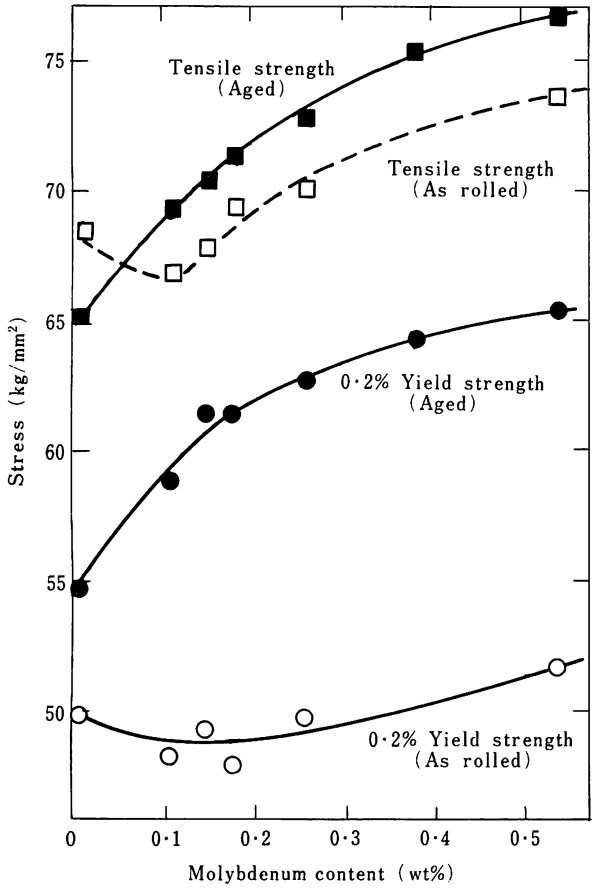

Fig. 1. Influence of molybdenum on the longitudinal tensile properties of 12·7 mm-thick plates of 0·05% C–1·9% Mn-0·09% Nb steel in the as-rolled and rolled-and-aged conditions.

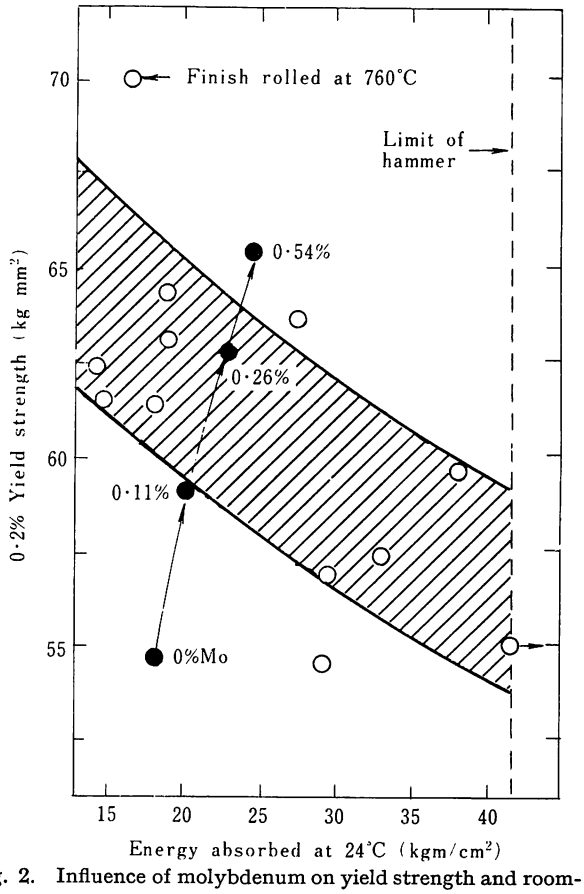

Fig. 2. Influence of molybdenum on yield strength and room-temperature impact energy of 12·7 mm rolled-and-aged plates of manganese-molybdenum-niobium steel, finish rolled at 870°C. (Open points show effects of varying other compositional and processing variables.)

of area values ranged from 71 to 78%.

The effects of the molybdenum content on the impact resistance of 12·7mm-thick aged plates, as determined by the Charpy V-notch test, are presented in Fig. 2 and 3. The shelf energies of these low-carbon steels tended to be quite high, as may be seen in Fig. 2. The solid points in this graph represent the series of steels whose tensile properties were presented in Fig. 1. It should be noted that despite the fact that the yield and tensile strengths were increased with higher molybdenum, the room-temperature impact energy (approximately equal to the shelf energy) also increased. The open circles in Fig. 2 represent steels with other compositional and processing differences at the 0·25% Mo level. In one steel at the 55 kg/mm²-strength level, specimens tested at room temperature stopped the hammer at the 41·4 kgm/cm² level. In general, these other 0·25% Mo steels tended to fall in a band that exhibits a trade-off of strength for toughness, as would normally be expected. It should be noted, however, that at the lower toughness end of this band where the yield strength rises to about 63 kg/mm², the room-temperature impact energy remained quite high—in the vicinity of 17 kgm/cm².

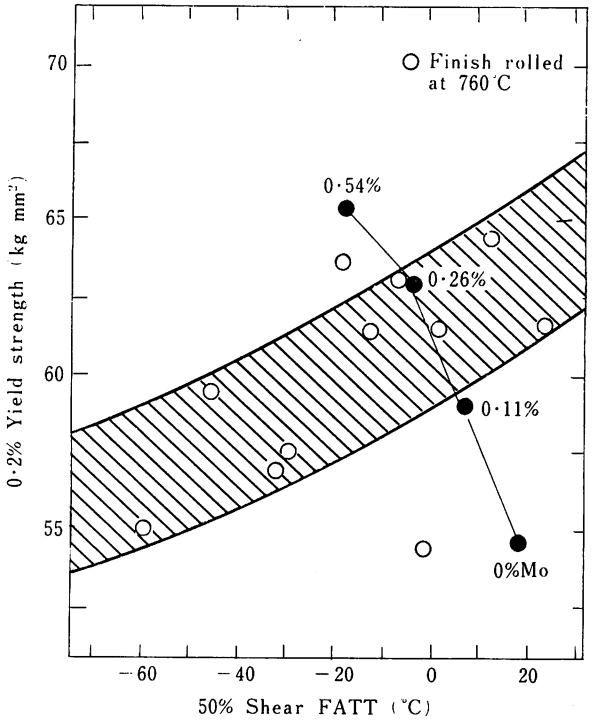

Fig. 3. Influence of molybdenum on yield strength and FATT of 12·7 mm-thick rolled-and-aged plates of manganese-molybdenum-niobium steel finish rolled at 870°C. (Open points show effects of varying other compositional and processing variables.)

The same fracture energy was exhibited by the steel that was finish-rolled at 760°C to provide a 69·6 kg/mm² yield strength.

The influence of molybdenum content on the impact resistance of 12·7mm-thick aged plates is even more striking when presented in terms of the 50% shear FATT,* as in Fig. 3. In combination with the large strength increase noted above, the 50% shear temperature of the 0·05%C-1·9%Mn-0·09%Nb base composition was shifted from 16°C to about −18°C by the addition of 0·54%Mo. The points representing the strength and toughness of other compositions containing 0·25% Mo are distributed mainly within a scatter band that tends to trade strength for toughness, as in Fig. 2. The data indicate that a yield strength of 56 kg/mm² can be attained with a 50% shear temperature below −18°C.

3.1.2 Carbon

As noted earlier, the historical role of iron carbide as the primary strengthener of hot-rolled steel is not valid in the case of the manganese-molybdenum-niobium steel. About 0·01 to 0·02%C is required in this acicular ferrite steel to facilitate precipitation strengthening, and any carbon in excess of that is present as an undesirable impurity as far as good mechanical properties are concerned. The laboratory-prepared steels were nominally 0·05 %C in consideration of the assumed limitations of commercial melting practice.

It was previously shown in a publication based on work at the Climax Laboratory, by Biss and Cryderman[1], that the continuous-cooling transformation of low-carbon low-alloy steels to bainitic structures results in the formation of a high-carbon microconstituent. This microconstituent may contain up to 1%C and, as a result, appears in the final microstructure as a mixture of martensite and retained austenite. In steels with as low as 0·1%C, the presence of this microconstituent exerted a deleterious influence on impact resistance. Although aging significantly reduces the martensite content of the microconstituent, harmful concentrations of cementite particles are left in its place. It has been the general observation thus far that as carbon is increased above 0·05% in the manganese-molybdenum-niobium acicular ferrite steel, the impact resistance tends to decrease. More than about 0·08% C is considered to be impractical, but this depends on the particular application. The strong influence of carbon is shown by the Charpy impact transition data on steels CB, CC, and CD in Fig. 4. It is believed that as the carbon level is increased, the above described martensite-austenite constituent and small accumulations of cementite contribute to the observed degradation of impact resistance.

* FATT is the fracture-appearance transition temperature.

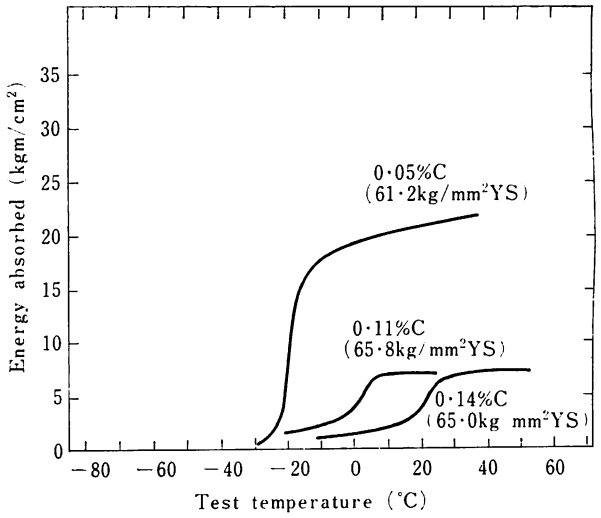

Fig. 4. Impact resistance in transverse direction of 12·7 mm-thick aged plates of 1·8%Mn-0·25%Mo-0·08% Nb steels at three levels of carbon content.

It was stated earlier that the carbon content has some influence on the hardenability of the acicular ferrite steel; i.e., it contributes to inhibiting transformation to polygonal ferrite in the high temperature range. When the carbon level is lowered to improve impact resistance, some increase in alloy (manganese or molybdenum) must be provided to maintain the acicular ferrite hardenability. This adjustment is a relatively small one.

3.1.3 Niobium

The primary effect of niobium in these manganese-molybdenum-niobium acicular ferrite steels is to combine with carbon (and some nitrogen) to form the Nb(C,N) precipitation-strengthening phase. The influence of the precipitation of Nb(C,N) on the yield strength of 12·7mm-thick air-cooled and aged plates of steels DA, DB, DC, and DD, within the range of 0·05 to 0·11% Nb, is presented in Fig. 5. Yield strength increased at the rate of 1·8 kg/mm² for each additional 0·01% Nb added, up to 0·09%. This strength increase was similar in both as-rolled and aged plates. The reason for the leveling off of the niobium strengthening effect was not established, but it is believed that the particular hot-rolling schedule that was used caused a coarse precipitation of Nb(C,N) in the austenite that consumed all of the niobium in excess of a certain level, so it was unavailable for the subsequent aging treatment. Observations to be described in a later section tend to support the latter suggestion. It is not known what this critical level of niobium is, but it would be expected to vary with the hot-rolling schedule.

The kinetic features of the Nb(C,N) precipitation in 0·05%C-1·9%Mn-0·25%Mo acicular ferrite steels (E and FB) are shown in Fig. 6. The low-and high-niobium steels have similar one-hour aging curves, with the only difference being the level

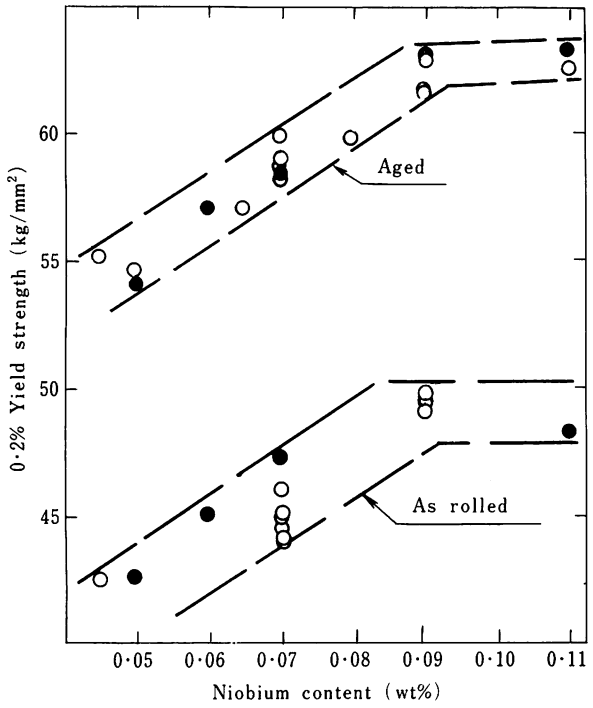

Fig. 5. Effect of niobium on yield strength of 12·7 mm-thick as-rolled and rolled-and-aged plates of 0·04/0·06%C–1·8/2·0%Mn–0·25%Mo steels, finish rolled at 870°C. (Solid points are for steels DA, DB, DC and DD of the same heat.)

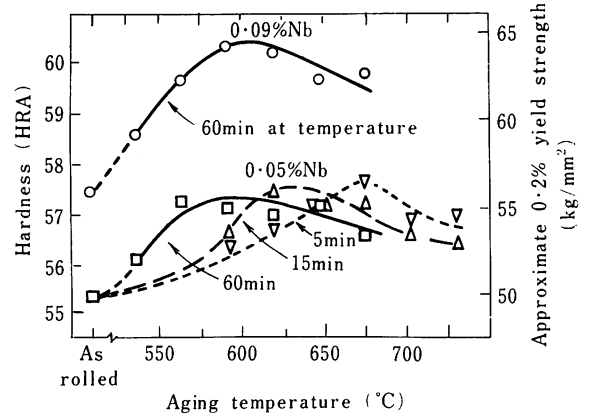

Fig. 6. Effect of aging treatment on hardness of 12·7 mm-thick plates of a 0·05%C–1·9%Mn–0·2%Mo–0·05% Nb steel and a 0·04%C–1·8%Mn–0·25%Mo–0·09% Nb steel.

of strength. The short-time isochronal curves for the low-niobium steel peak at successively higher temperatures. It was established by impact testing specimens aged at short times that toughness was not sacrificed by using the high-temperature short-time aging treatments, although there was a small sacrifice in yield strength. It is believed that optimizing the aging times and temperatures would eliminate the observed strength losses. These results served to demonstrate that short-time "in-line" production aging treatments are feasible.

In the course of examining the microstructures of the low- and high-niobium steels containing 0·25 % Mo, it was observed that the low-niobium steels had a higher percentage of fine-grained polygonal ferrite than the high-niobium steels. (It should be recalled from the earlier discussion that, for the processing parameters involved, 0·25% Mo did not convert the structure completely to acicular ferrite.) On the basis of this evidence, it was concluded that the niobium in solution in the austenite makes a significant contribution toward controlling the nucleation and growth of polygonal ferrite. This effect of niobium has also been observed by others[2].

3.1.4 Manganese

The manganese in this class of steels makes a major contribution toward inhibiting transformation to polygonal ferrite. It works in combination with the molybdenum in this regard. As manganese is reduced, the critical cooling rate for polygonal ferrite formation is increased. For 12·7mm-thick air-cooled plates, containing 0·05%C, 0·25% Mo, and 0·09% Nb, an excessive amount of polygonal ferrite appears at less than about 1·8 to 1·85% Mn. As the amount of polygonal ferrite becomes excessive, some of it appears as coarse-grained polygonal ferrite. The coarse polygonal ferrite grains are extremely harmful to impact resistance. Either low manganese or low molybdenum can lead to this result.

3.1.5 Silicon

Silicon was varied over the range of 0·05 to 0·3%. More than about 0·17% tended to reduce the impact resistance of aged plates for a given strength level. Sufficient data were not available to establish a quantitative increment for this effect. It was also found that the higher silicon levels resulted in the formation of a greater amount of polygonal ferrite at a given cooling rate. Although this tendency may easily be overcome by an adjustment of the manganese or molybdenum levels, silicon serves no useful purpose in the steel beyond its normal deoxidation function, and can just as well be kept low by the use of aluminum for deoxidation.

3.1.6 Sulfur

The influence of sulfur content was investigated over the range of 0·005 to 0·033%. Since sulfur appears in hot-rolled steel as sulfide stringers. it was expected that the primary effect of sulfur would be to exert its normal influence in degrading the impact resistance in the transverse direction. The data presented in Fig. 7 on steels GA, GB, and GC strongly support this hypothesis and emphasize the necessity of restricting the sulfur level. It is obvious from these results that the excellent impact resistance of the inherently tough acicular ferrite can be easily lost by a deleterious inclusion configuration. If the sulfur level cannot be kept low, it should be possible to maintain a relatively high level of toughness in the transverse direction

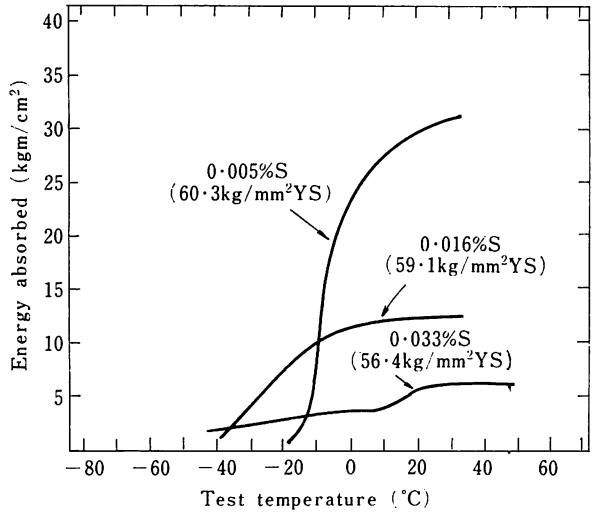

Fig. 7. Impact resistance in transverse direction of 12·7 mm-thick aged plates of 0·05%C–1·86%Mn–0·24% Mo–0·07%Nb steel at three levels of sulfur content.

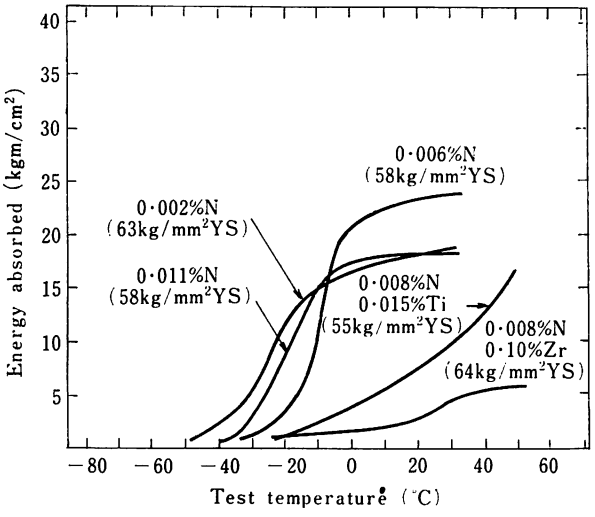

Fig. 8. Impact resistance in transverse direction of 12·7 mm-thick aged plates of 0·04/0·06%C–1·8/2·0% Mn –0·25/0·30% Mo–0·05/0·07% Nb steels at various nitrogen levels, with and without nitride formers.

by inclusion shape control, using rare earth additions. This has been done successfully in a hot-rolled vanadium-containing steel, as described by Luyckx, Bell, McLean, and Korchynsky[3].

3.1.7 Nitrogen

Nitrogen is present in the manganese-molybdenum-niobium acicular ferrite steel as an undesirable impurity. Of course, some nitrogen is present in the precipitation strengthening Nb(C,N) phase. The total elimination of nitrogen from the steel might change the precipitation characteristics in an undesirable manner, although this seems doubtful. Since such low nitrogen levels are out of the question for the normal commercial melting process, the nitrogen present should be treated as an undesirable impurity to be maintained at the lowest level possible. When the nitrogen content significantly exceeds 0·008%, some detrimental effects on strength-toughness balance should be expected to result. It is believed that high nitrogen causes excessive precipitation of Nb(C,N) in the austenite. This excessive loss of niobium from solution reduces the acicular ferrite hardenability, and the resulting microstructure may contain coarse polygonal ferrite. Even if the hardenability is not marginal, the yield strength of the aged steel will be reduced because of coarse Nb(C,N) precipitation in the austenite, which lowers the potential for subsequent precipitation strengthening after transformation. Attempts were made to mitigate the harmful effects of excess nitrogen impurity by an addition either of titanium or of zirconium. The effects of high nitrogen content, with and without such additions are shown by the Charpy data of Fig. 8 on steels H, J, K, LA, and MC. It may be concluded from these data that while nitrogen at the 0·01% level is mildly undesirable, the addition of either titanium or zirconium to tie up excess nitrogen is not a satisfactory solution because of notable losses in acicular ferrite hardenability.

3.2 Influence of processing variables

3.2.1 Austenite condition

At this stage of the study of ferrous metallurgy, it is widely recognized that the condition of the austenite prior to transformation is important with respect to the microstructure and mechanical properties of the final product. In the manufacture of hot-rolled steels with optimum strength-toughness properties, this consideration is most important. Outstanding combinations of strength and toughness are obtainable in manganese-molybdenum-niobium acicular ferrite steel by taking the maximum advantage of the benefits to be gained by proper prior austenite conditioning. After the presentation of the experimental observations, the detailed aspects of the phenomena involved will be discussed to the extent that they are presently understood. However, some introductory remarks are necessary at this point for the benefit of the reader who is completely unfamiliar with this alloy system.

The relatively large amount of niobium present in the manganese-molybdenum-niobium steel has a complex influence on austenite conditioning. It has been previously shown that the austenite of low-alloy steel is severely inhibited in its rate of recrystallization during hot working by the presence of 0·03 % Nb[4]. This effect is presumably due to the presence of a fine Nb(C,N) precipitate that pins grain boundaries. Such an effect must also be present in the higher niobium steel of present interest. Because of this effect, the amount of austenite grain refinement that is obtained upon hot working from a normal 1260°C preheat is somewhat limited. In addition, the restricted capability for recrystallization should make it possible to produce

a highly substructured austenite prior to transformation if sufficient mechanical deformation is carried out in the proper temperature range. The austenite conditioning process is further complicated by the fact that a coarse precipitate of Nb(C,N) may also be developed in the austenite. Further evidence of this will be presented below. Such coarse precipitation reduces the potential for the fine Nb(C,N) precipitation in the austenite and also in the subsequent acicular ferrite transformation product. All of the above described interrelated phenomena may be encountered under conditions that can occur in the normal commercial hot-rolling process; therefore, an understanding of the manner in which these physical metallurgical processes influence the final product is of importance to the mill metallurgist, as well as to the researcher.

In the laboratory study of the effect of processing variables on microstructure and mechanical properties, the variations that were made in processing parameters produced variations in the condition of the austenite. It will be shown below that these variations had major effects on strength and toughness.

3.2.2 Finish-rolling temperature

Steels P and N containing 0·06%C-1·9%Mn-0·35 %Mo plus 0·05 and 0·08% Nb, respectively, were preheated at 1260°C and rolled to 12·7mm-thick air-cooled plate at a series of finishing temperatures, by adjusting the rolling schedule as shown below. (Only the high-niobium steel was subjected to all six rolling schedules.) The yield strength and FATT

Finishing temperature (°C)	Rolling temperatures (°C) (20% Reduction)				
1000	1230	1175	1120	1065	1000
925	1230	1175	1120	1010	925
870	1230	1120	1040	955	870
815	1230	1120	980	900	815
760	1230	1120	925	845	760
705	1230	1120	870	790	705

of each of the respective aged plates are presented in Fig. 9. These results illustrate the general trend that has been observed in the acicular ferrite steel with respect to the effect of finish-rolling temperature. Lower finishing temperatures tend to produce better combinations of strength and toughness. There was no significant effect of finishing temperature upon the optical microstructure.

3.2.3 Intermediate-temperature deformation

Two sets of 12·7mm-thick plates were processed to investigate the effects of variations in the central range of the hot-rolling schedule, when low temperature finishing practice is used. In the first test, steels Q and R, containing 0·25% Mo with 0·08 and 0·05% Nb, respectively, were used to study the effect of varying the amount of hot reduction at

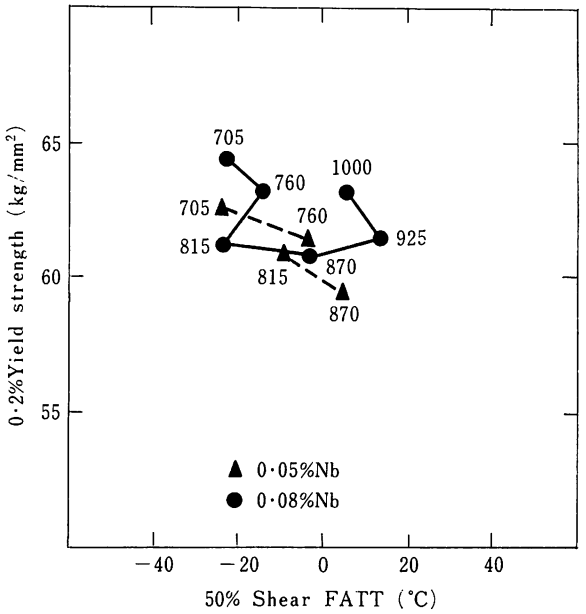

Fig. 9. Effects of finish-rolling temperature on strength and impact resistance of 12·7 mm-thick aged plates of 0·06%C–1·9%Mn–0·35%Mo steels at two levels of niobium content.

925°C. To make this change while maintaining the total rolling reduction constant, it was also necessary to vary the high temperature part of the rolling schedules. The schedules that were used are as follows:

% Reduction at temperature				
1230℃	1120℃	925℃	845℃	760℃
28	28	—	20	20
19	20	20	20	20
—	13	40	20	20

The yield strength and 50% FATT values of the aged plates of both the high- and low-niobium steels are shown in Fig. 10. The best results were obtained with the 20% reduction at 925°C. The very high level of yield strength, 68 kg/mm², was obtained in the high-niobium steel with no reduction in the range 1120–845°C. There were no significant differences observed in the optical microstructures as a result of the rolling schedule variations. Electron micrographs of carbon extraction replicas of the as-rolled plates of the high-niobium steel that were subjected to no reduction and 40% reduction, respectively, at 925°C, are presented in Photo. 4. The coarse Nb(C,N) precipitates in these electron micrographs could have precipitated only in the austenite. It is clear from a comparison of these two micrographs that the heavy 40% reduction at 925°C has resulted in a greater precipitation of the Nb(C,N). The very limited precipitation of the carbonitride in the plate that was not subjected to deformation at 925°C [Photo. 4 a)] allowed a much greater potential for precipitation strengthening, as demonstrated by its high yield-strength

level (Fig. 10). Such a high strengthening potential could not be developed in the low-niobium steel.

The second test of the effect of varying the rolling schedule in the intermediate-temperature range was conducted by altering the intermediate-pass temperature of plates of steel N containing 0·35% Mo and 0·08% Nb, in accordance with the rolling schedules shown below. The strength-toughness plot for the aged plates is presented in Fig. 11. For plates finished at 760°C the more favorable intermediate-pass temperature was 980°C.

Intermediate pass temperature (°C)	% Reduction at temperature						
	1230°C	1120°C	1040°C	980°C	925°C	815°C	760°C
925	19	20	—	—	20	20	20
980	19	20	—	20	—	20	20
1040	19	20	20	—	—	20	20

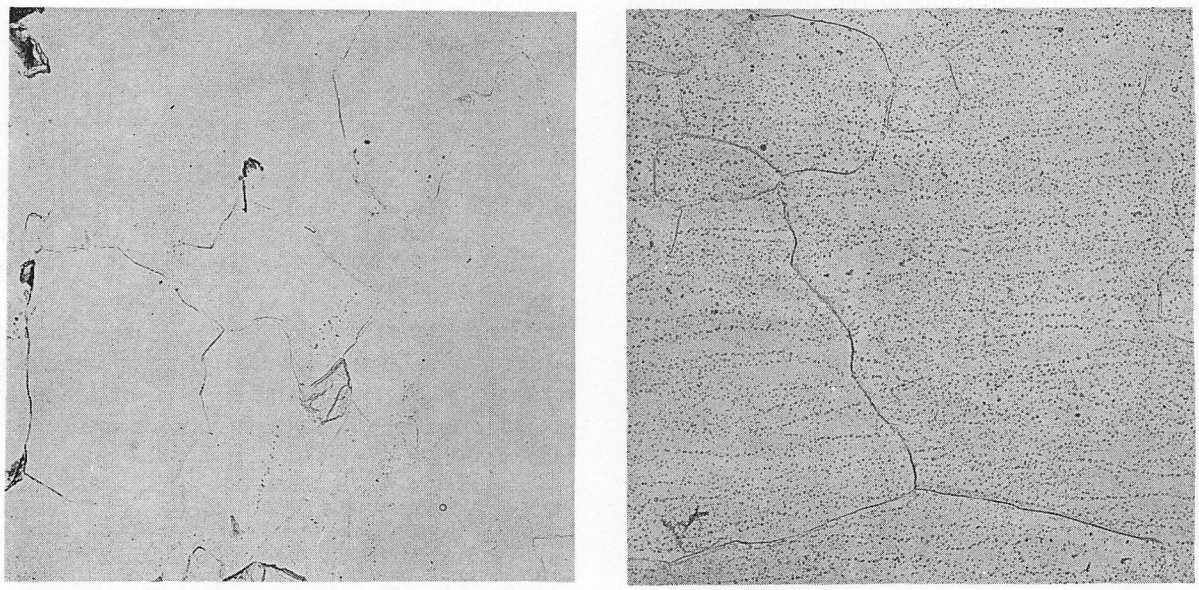

a) No reduction at 925°C × 10 000 b) 40% reduction at 925°C × 10 000

Photo. 4. Carbon extraction replicas from 12·7 mm-thick aged plates of a 0·06%C–1·9%Mn–0·25%Mo–0·08%Nb steel showing effect of difference in hot-rolling reduction at 925°C.

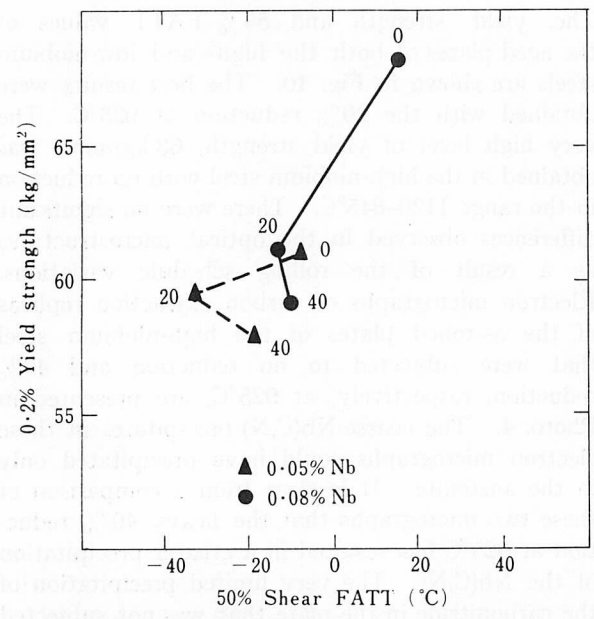

Fig. 10. Effects of percent reduction at 925°C on strength and impact resistance of 12·7 mm-thick aged plates of 0·06%C–1·9%Mn–0·25%Mo steel at two levels of niobium content, finish rolled at 760°C.

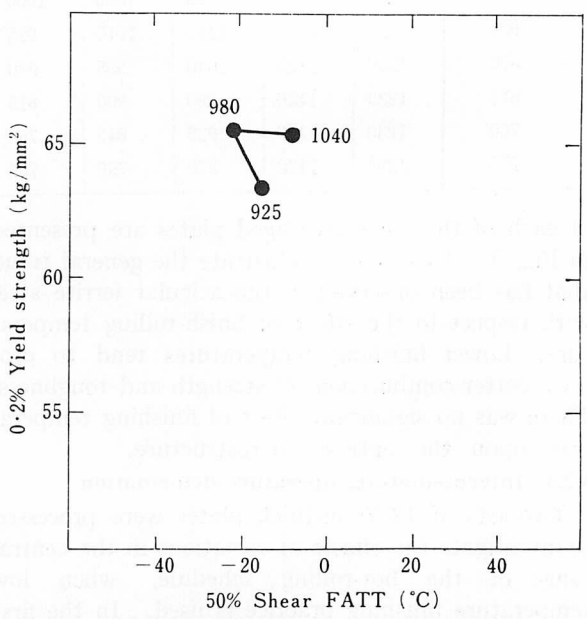

Fig. 11. Effects of intermediate-pass temperature on strength and impact resistance of 12·7 mm-thick aged plates of 0·06% C–1·9% Mn–0·35% Mo–0·08% Nb steel, finish rolled at 760°C.

3.2.4 Austenitizing temperature

Austenitizing temperature can be expected to have important effects on mechanical properties through its influence on the initial austenite grain size and the amount of niobium initially in solution. Test pieces of steels T and S, containing 0·25% Mo with 0·05 and 0·08% Nb, respectively, were subjected to austenitizing treatments of 1260, 1205, 1175, 1150 and 1120°C. The pieces were rolled to 25% reduction at each of the temperatures 1120, 1040, 955 and 870°C, with the exception of the one austenitized at 1120°C, which underwent the first rolling pass at 1095°C.

The effects of the variation in austenitizing temperature on the strength and impact resistance of this steel at both levels of niobium are shown in Fig. 12. The properties of the low-niobium steel were not sensitive to variation of the austenitizing temperature until it dropped below 1150°C. After austenitizing at 1120°C, the yield strength was noticeably decreased, apparently because of the incomplete dissolution of the niobium at this temperature. The properties of the high-niobium steel were much more subject to change by variation of the austenitizing temperature. The impact resistance was increased significantly without a noteworthy loss of strength by reducing the austenitizing temperature to 1175°C. A further reduction in austenitizing temperature resulted in a sharply reduced yield-strength level. The properties produced by austenitizing at 1120°C were similar to those of the low-niobium steel after the same treatment.

The optical microstructures of the high-niobium plates that were austenitized at 1260, 1175 and 1150°C are shown in Photo. 5 a), 5 b), and 5 c), respectively. An increased amount of somewhat coarser polygonal ferrite is present in material austenitized at 1150°C. Electron micrographs of extraction replicas taken from the high-niobium steel plates austenitized at 1175 and 1120°C are shown in Photo. 6. The plate austenitized at 1175°C contains a coarse Nb(C,N) precipitate that must have precipitated in the austenite. The steel subjected to the lower austenitizing temperature contains large, rod-shaped Nb(C,N) particles that apparently formed by agglomeration during austenitizing at 1120°C.

3.2.5 Simulated strip processing

Steels containing 0·04% C, 1·6% Mn, 0·2% Mo, and either 0·06 or 0·09% Nb (steels U and V, respectively) were processed to 6·4mm-thick simulated-coiled product to investigate the feasibility of producing acicular ferrite steel on a hot strip mill. The test pieces were rolled to the standard two-pass rolling schedule described earlier for simulated-coiled plates, finished at 870°C, and spray-cooled at about 22°C/sec to the simulated-coiling temperature. The plates were simulated-coiled at 680, 635, 605, 580 and 550°C after spray-cooling. It should be noted that the manganese-molybdenum-niobium steel must be coiled at about 675°C or below because this is approximately the maximum temperature of formation of acicular ferrite. Coiling at a significantly higher temperature will result in the formation of coarse polygonal ferrite. Plates were also air cooled after spray-cooling to 480°C to provide an extremely low-end point in the variation of the time-temperature aging parameter. Both strength and impact resistance are shown as functions of simulated-coiling temperature in Fig. 13. A yield

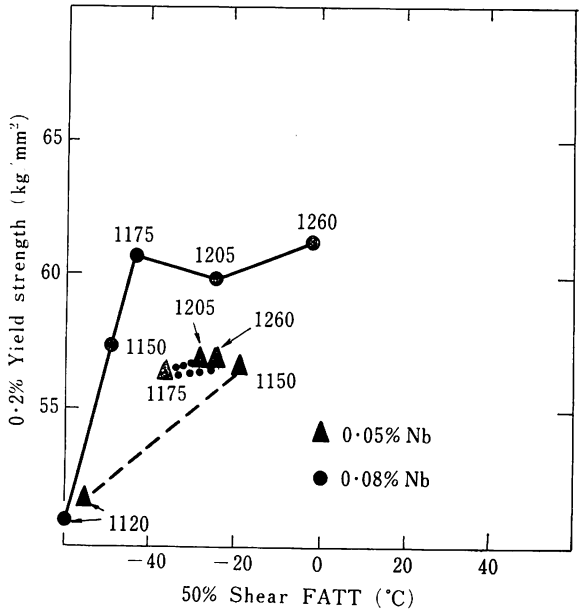

Fig. 12. Effects of austenitizing (slab reheat) temperature on strength and impact resistance of 12·7 mm-thick aged plates of 0·06%C–1·9%Mn–0·25%Mo steel at two levels of niobium content, finish rolled at 870°C.

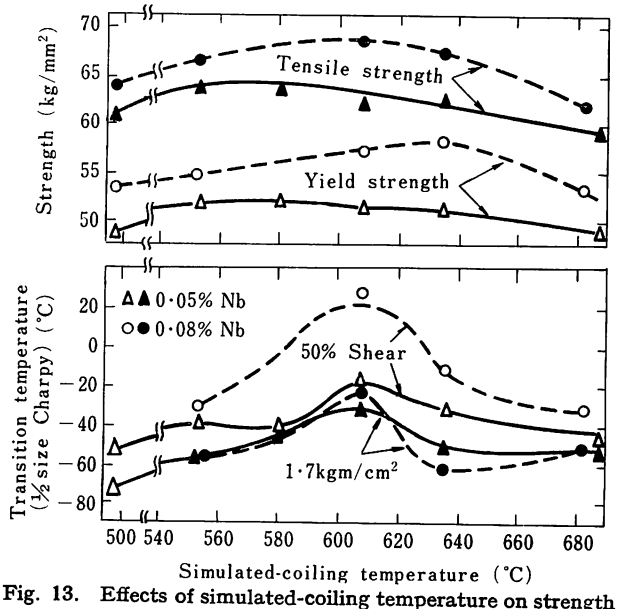

Fig. 13. Effects of simulated-coiling temperature on strength and impact resistance of 6·4 mm-thick plates of 0·04%C–1·6%Mn–0·2%Mo steel at two levels of niobium content.

a) 1260°C × 500

b) 1175°C × 500

c) 1150°C × 500

Photo. 5. Optical micrographs of 12·7 mm-thick aged plates of a 0·06%C–1·9%Mn–0·25%Mo–0·08%Nb steel showing effect of variation in austenitizing temperature.

strength of 56 kg/mm² was produced in the high-niobium steel, while over 49 kg/mm² was attained in the low-niobium steel. An extremely important attribute of the yield-strength data is the very low sensitivity of the yield strength to variations in coiling temperature. It should be noted that while the high-niobium material that was spray-cooled, followed by air cooling, had a yield strength of 53·5 kg/mm², the maximum strength observed was 58

▼Photo. 6. Carbon extraction replicas from 12·7 mm-thick aged plates of a 0·06%C–1·9%Mn–0·25%Mo–0·08%Nb steel showing effect of variation in austenitizing temperature.

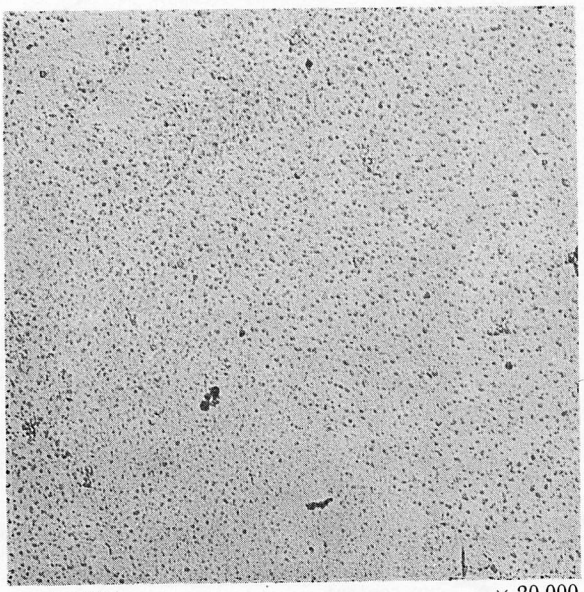

a) 1175°C × 20 000

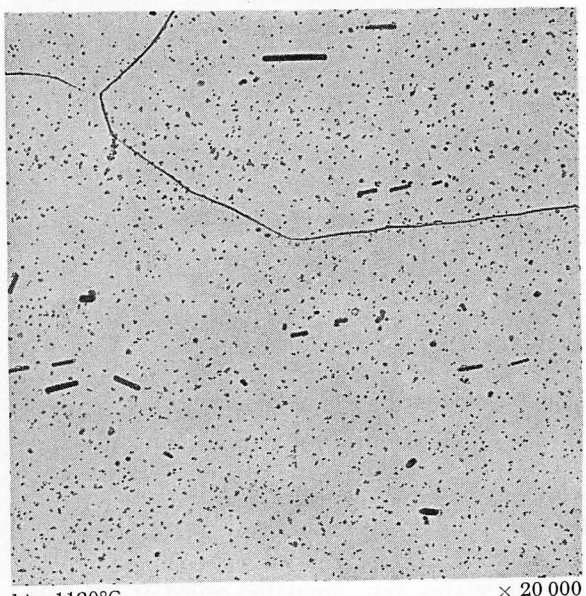

b) 1120°C × 20 000

Table 2. Processing parameters and mechanical properties of selected laboratory plates prepared by simulated coiling.

Steel	Cooling rate (℃/sec)	Coiling temperature (℃)	Yield strength (kg/mm²)	Tensile strength (kg/mm²)	Reduction of area (%)	Elongation (%)	50% Shear FATT (℃)	Microstructure
V	4	680	53·3	61·9	73	22	−32	9 (a)
V	23	550	54·6	66·4	71	19	−32	9 (d)
YA	11	680	54·0	60·3	72	22	−68	—
YA	7	645	62·3	88·3	69	21	−68	—
YB	8	680	54·8	61·3	71	20	−62	9 (b)
YB	8	645	63·2	69·5	68	18	−68	9 (c)

kg/mm². It may be recalled that the simulated-coiling process involved furnace cooling at 28°C/hr from the coiling temperature. Therefore, some test plates spent several hours above 480°C, while one plate was cooled rapidly to 480°C and then air cooled. This very large difference in the time-temperature aging parameter resulted in a strength difference of less than 5 kg/mm². Since the time-temperature aging parameter of a coiled mill product is subject to wide variation due to the gradient of cooling rates in the coil, this attribute is a most valuable one.

The impact resistance values of the simulated-coiled products were subject to somewhat more variation, as shown in the lower half of Fig. 13. The intermediate range of coiling temperature around 605°C is undesirable for the high-niobium steel because of the high FATT obtained in this range. About 650°C appears to be the desirable coiling temperature.

As indicated earlier, the 6·4mm-thick simulated coiled test plates were hot-rolled from 19mm-thick slabs. It was considered likely that a greater degree of hot reduction would produce steels more representative of what could be obtained in a mill product. Forged slabs, 38 mm in thickness, from steels YA and YB, both containing 1·4% Mn, 0·27% Mo, and 0·10% Nb, were austenitized at 1260°C and rolled to a five-pass schedule to more closely simulate a commercial hot strip mill. This schedule was as follows: 20%/1205°C, 25%/1120°C, 33%/1040°C, 33%/955°C, and 38%/870°C. These plates were spray-cooled at the somewhat slower rate of 8°C/sec and simulated coiled in the same manner as before at temperatures of 680° and 645°C. The mechanical properties of the two heats are summari-

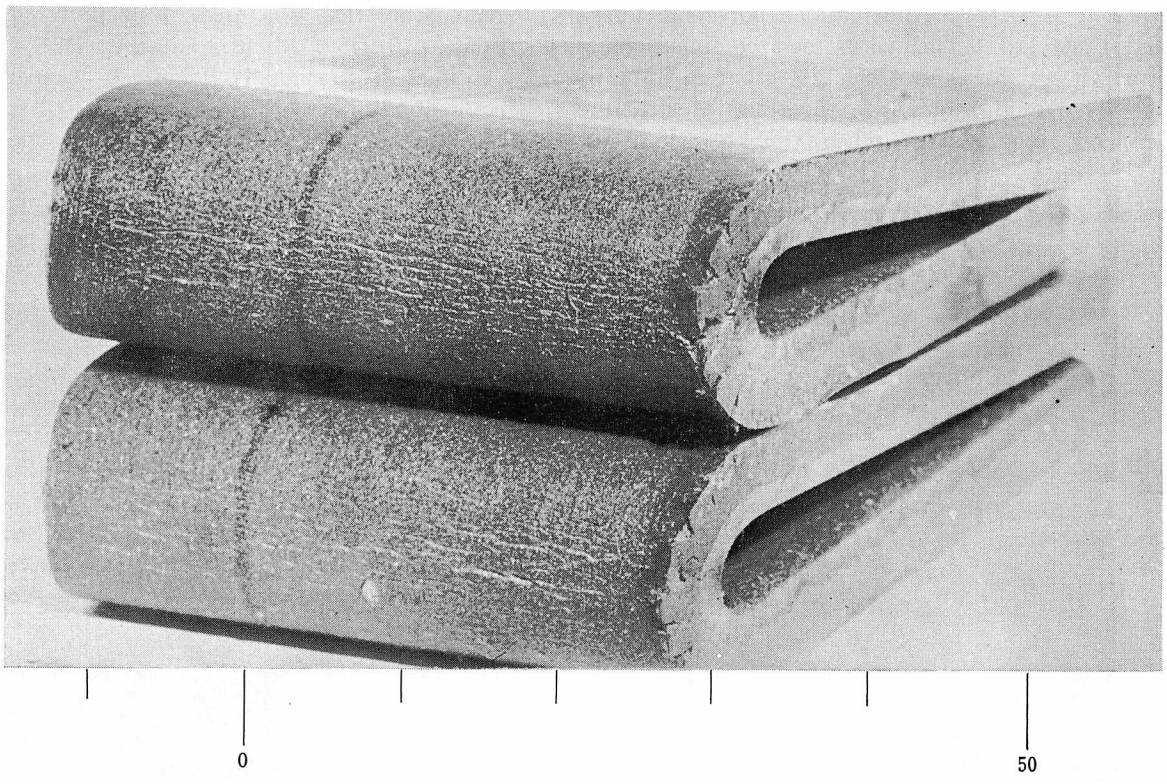

Photo. 7. Transverse guided-bend specimens of 6·4 mm-thick plates of manganese-molybdenum-niobium steel.

zed in Table 2, along with those of two simulated-coiled plates processed according to the normal two-pass rolling schedule. The strength-toughness balance was significantly better in the plates rolled to a five pass schedule.

3.2.6 Transverse bend tests

The 6·4mm-thick simulated-coiled plates of manganese-molybdenum-niobium steel were evaluated for formability by three-point bend tests on specimens with sheared edges. Two specimens of the 56 kg/mm² yield-strength material were bent 180° around a 3·2mm mandrel. The bent specimens are shown in Photo. 7, along with a scale divided in millimeters. It should be noted that the cracks that were initiated on the shear lip did not propagate and cause failure.

3.3 Optimization of microstructure

The effects of composition and hot-rolling parameters on the mechanical properties of the laboratory-prepared steels have been reviewed above. The question of (optical) microstructure was mentioned only briefly in the presentation of compositional effects by noting that as the microstructure became more and more acicular, while at the same time the amount of polygonal ferrite was reduced, the strength-toughness balance of the steel was improved. A major problem was encountered in attempting to rationalize all of the microstructures observed with their respective measured mechanical properties. It was found that a few of the observed structures contained large fractional amounts of what appeared to be fine-grained polygonal ferrite, and these steels had very good combinations of strength and toughnes. Such a situation appeared as only a mild anomaly in the trend of structure-property relationships when this transformation product was present as perhaps 25% of the total volume of the specimen material. On the other hand, when it appeared as the majority of the microstructure, as in some of the examples that will be shown below, it served as a test of the initial analysis of the influence of microstructure on properties, particularly with respect to toughness. A careful review of the microstructure and mechanical-property data, combined with data from transformation studies and the observations of other investigators, has made it possible to suggest a potential explanation for the observed phenomena.

3.3.1 Examples of a unique microstructure

The first structures that were observed to be in conflict with the general trend of increased strength and toughness with increased acicularity, were those represented by the two points to the far right end of the band in Fig. 2. The same two steels are represented by the two points to the far left end of the band of Fig. 3. Steel WA, the tougher of the two, contained 0·05% C and 0·045% Nb, while steel XA contained 0·02% C and 0·09% Nb. The microstructures of these two steels, which were processed according to the same schedule as the other steels represented in Fig. 2 and 3, are shown in Photo. 8. The structure of both steels appears to be predominantly fine-grained polygonal ferrite with scattered regions of acicular ferrite. Such structures were obtained in the course of this work whenever the composition involved was just short of providing sufficient hardenability to produce an acicular structure for the processing schedule and cooling rate that was used. Apparently, both the 0·05% C-0·045% Nb steel and the 0·02% C-0·09% Nb steel had virtually identical acicular ferrite hardenability.

The outstanding characteristic of this fine-grained

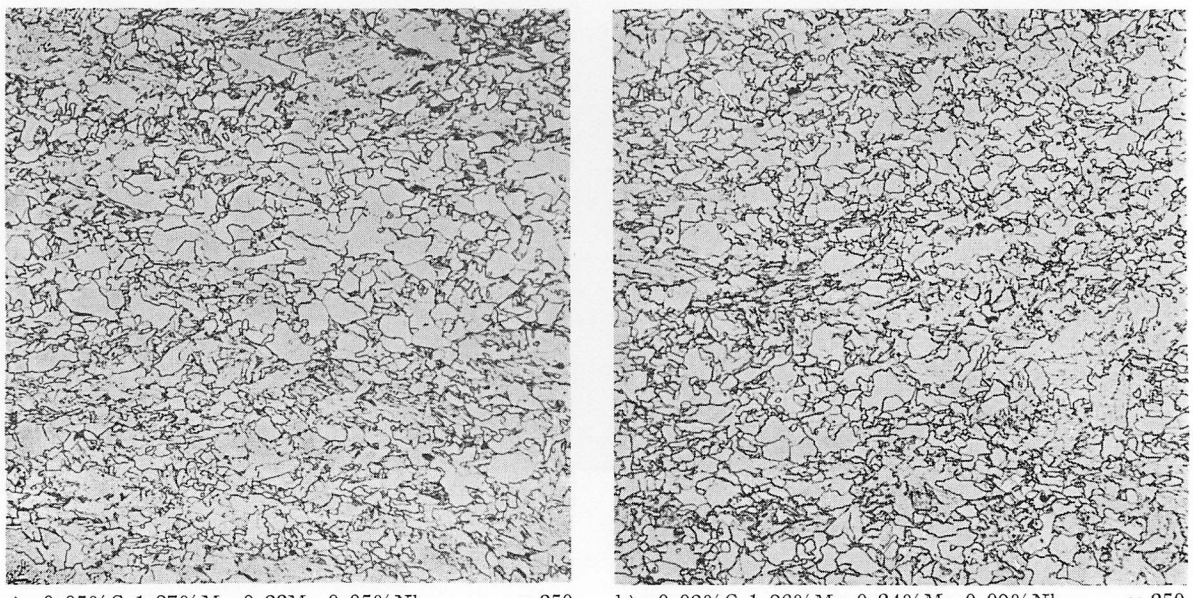

a) 0·05%C-1·87%Mn-0·23Mo-0·05%Nb × 250 b) 0·02%C-1·86%Mn-0·24%Mo-0·09%Nb × 250

Photo. 8. Fine-grained ferrite microstructures of 12·7 mm-thick plates.

structure is that it had high toughness in all instances where it was observed. The unusually good toughness of this structure, relative to that of the somewhat coarser polygonal ferrite observed as a fractional microconstituent in many of the steels tested, suggested that this "fine-grained ferrite," as it will be referred to henceforth in this paper, is a somewhat unique transformation product with properties significantly different from the orthodox polygonal ferrite transformation product. Evidence will be presented below to support this suggestion.

Another noteworthy example of the fine-grained ferrite structure is the simulated-coiled material shown in Photo. 9 c). The series of structures of Photo. 9 suggests an important criterion for the formation of the fine-grained ferrite structure. It must be formed within a relatively narrow temperature region just above the region of acicular ferrite formation. As the temperature of formation is increased just slightly, the product becomes correspondingly coarser and the transformation product loses its capability to be increased in strength by aging because the Nb(C,N) tends to precipitate as large (overaged) particles as the coarser polygonal ferrite is transformed. The mechanical properties of the steels whose structures are shown in Photo. 9 are summarized in Table 2. Both of the steels of Photo. 9 that were coiled at 680°C had relatively low yield strengths of 53·5 and 55 kg/mm²: Photo. 9 a) and b), respectively. The slightly higher yield strength and lower impact-transition temperature of the two accompanied the finer grain size [Photo. 9 b)]. The best combination of strength

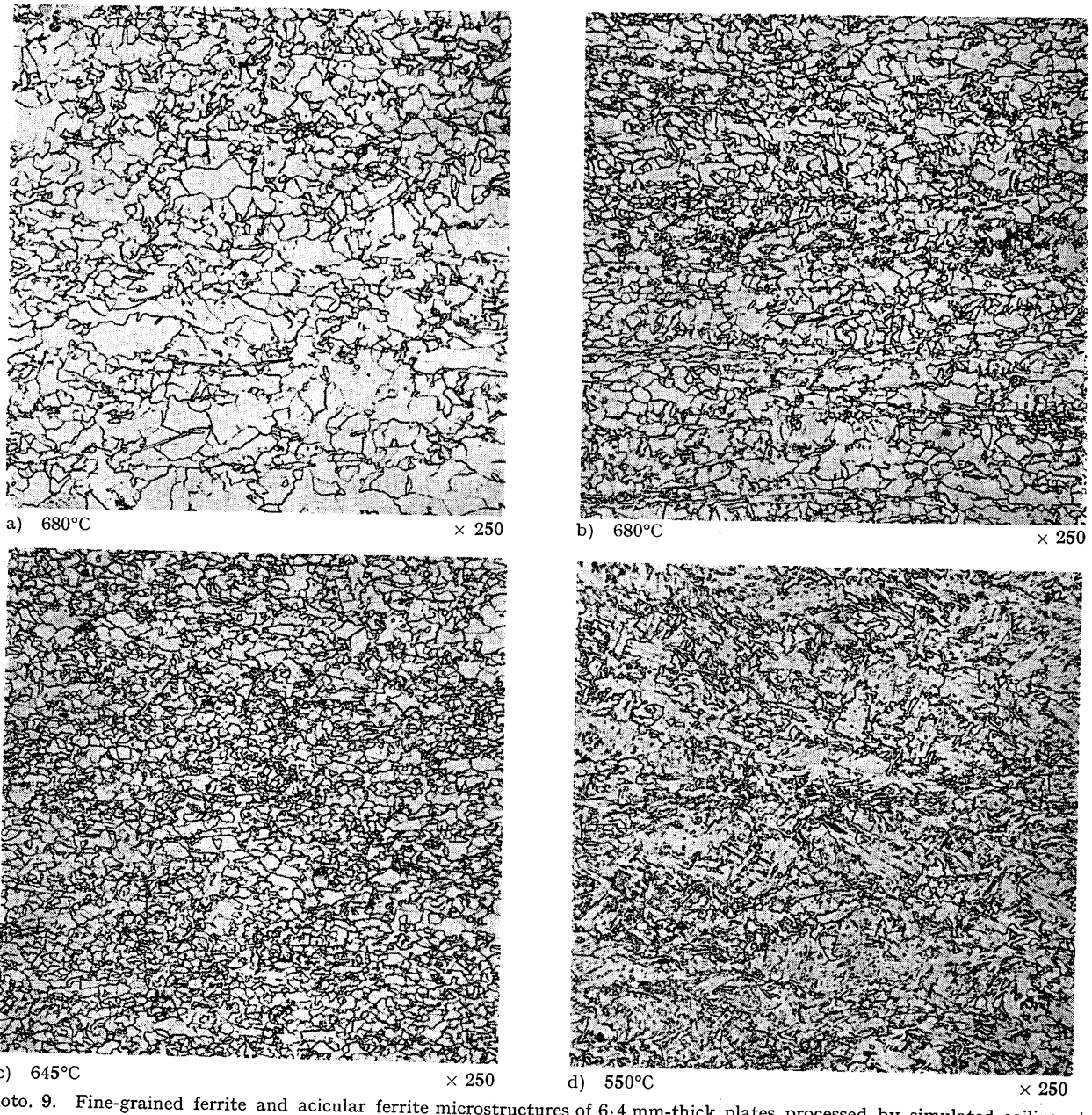

a) 680°C × 250
b) 680°C × 250
c) 645°C × 250
d) 550°C × 250

Photo. 9. Fine-grained ferrite and acicular ferrite microstructures of 6·4 mm-thick plates processed by simulated coiling at various temperatures.

and impact resistance was obtained with the fine-grained ferrite structure of Photo. 9 c). The acicular structure of Photo. 9 d) was lower in strength because very little aging took place at the relatively low simulated coiling temperature of 550°C.

3.3.2 Unique aspects of fine-grained ferrite

It was observed early in the development of the manganese-molybdenum-niobium steel that if the microstructure was composed of large amounts of coarse polygonal ferrite, the impact resistance would be poor. There was a larger difference than could be explained by the difference in grain size. Furthermore, it was known from the work of Gray and Yeo that the precipitation of coarse Nb(C,N) particles (>50 Å) takes place at the α/γ interface as polygonal ferrite is formed[5]. These particles are much too large to have a major strengthening effect. Therefore, polygonal ferrite in a niobium-containing steel normally contains overaged Nb (C,N) that forms as the polygonal ferrite is transformed from the austenite. The high strength level of the microstructure of Photo. 9 c) indicated that significant strengthening due to aging was taking place after transformation. It was tentatively concluded that the transformation reaction that formed the fine-grained ferrite structure was different in some way from the transformation that formed the somewhat coarser polygonal ferrite, since the Nb(C,N) was not involved in the transformation in the usual way.

Support for this tentative conclusion was presented by Repas[6]. He studied the precipitation of Nb(C,N) in 0·03% C-0·05% Nb steels containing varying amounts of manganese and nickel. The compositions used included a maximum of 2·6% Mn at 1% Ni and a maximum of 3·3% Ni at 1·2% Mn. The amounts of these two alloying elements were varied as a means of controlling the Ar_3 temperature of 12·7mm-thick hot-rolled and air-cooled plates (finish-rolled at 980°C). It was found that the Ar_3 temperature was decreased approximately linearly with increased manganese plus nickel content up to about 2%. The mode of precipitation of the Nb (C,N) in these steels was dependent upon the Ar_3 temperature. A 0·5% Mn-1·0% Ni steel had an Ar_3 temperature of 775°C and a ferrite-pearlite microstructure. The Nb(C,N) particles were in the normal size range (greater than 50 Å) and were distributed in their normal "row" configuration. A 1·2% Mn-1·7% Ni steel had an Ar_3 temperature of 660°C and the optical microstructure was again ferrite-pearlite, although the ferrite had a slightly "blocky" appearance. There was very little Nb (C,N) precipitation in this hot-rolled material. The few precipitates that could be found were less than 50 Å in diameter and were not aligned in rows, indicating that the precipitation had taken place in the ferrite after passage of the α/γ interface. Steels containing greater amounts of manganese plus nickel than the 1·2% Mn-1·7% Ni steel, and with correspondingly lower Ar_3 temperatures, had no Nb(C,N) precipitation in the hot-rolled condition. These higher alloyed steels also had more "blocky" ferrite structures than those containing less manganese plus nickel. In summary, as the Ar_3 temperature was decreased by increasing the alloy content, the ferrite boundaries acquired more and more planar segments. At the approximate Ar_3 temperature where the change in the character of the polygonal ferrite boundaries took place, Nb (C,N) ceased to precipitate during the $\gamma \rightarrow \alpha$ transformation. Repas concluded that the transformation must be proceeding by a somewhat different mechanism in this lower temperature range.

3.3.3 Dilatometer data

Repas showed that a low-temperature form of polygonal ferrite could be developed by increasing manganese and nickel to depress the Ar_3 temperature. In addition to the 1·3 to 2% Mn that is present in the subject manganese-molybdenum-niobium steel of this study, the influence of thermomechanical treatment is also of significance in controlling the temperature of transformation. This fact was clearly demonstrated by the results of deformation dilatometer studies that were conducted on a 0·05% C-1·9% Mn-0·2% Mo-0·09% Nb steel. The unique aspect of this dilatometer is that a specimen may be subjected to deformation in the austenite temperature range prior to controlled cooling transformation which is monitored dilametrically. This instrument has been previously described in detail in the literature[7]. Small cylindrical specimens of the above steels were austenitized at 1260°C, deformed to 25% reduction at 925° by axisymmetric compression to refine the grain size, and then continuously cooled at various rates. The continuous-cooling transformation diagram that was so determined is shown as dashed lines in Fig. 14. A second set of specimens were run in the same manner, except that they were subjected to a second 25% reduction at 840°C and immediately cooled according to the same set of cooling cycles without allowing time for recrystallization. The resulting continuous cooling transformation diagram, which is shown by the dotted lines in Fig. 14, is quite different from the first. Not only is the high-temperature ferrite nose moved to the left, as would be expected, but the temperature of initial $\gamma \rightarrow \alpha$ transformation has been lowered. This is in contrast to the results of similar experiments that have been run previously with slightly different steels[8]. Over a limited range of cooling rates, the initiation of transformation for the high-temperature ferrite microconstituent is at about 680°C. This is the same Ar_3 temperature at which Repas observed

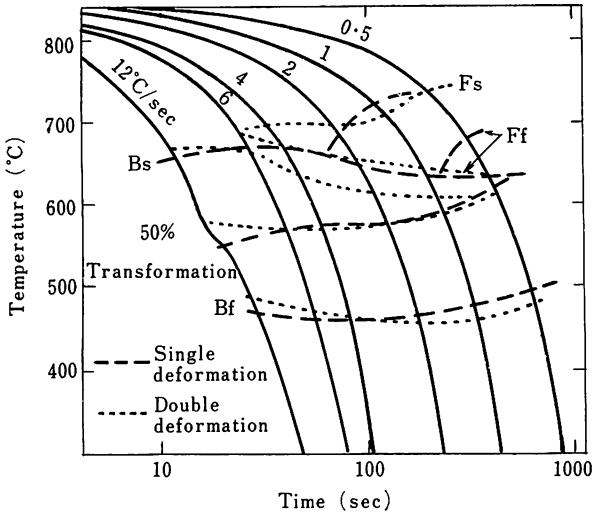

Fig. 14. Continuous-cooling transformation diagrams of a 0·05%C–1·9%Mn–0·2%Mo–0·09%Nb steel in two conditions: deformed and recrystallized (dashed lines); and deformed, recrystallized and deformed again without recrystallization (dotted lines).

polygonal ferrite formation without significant Nb (C,N) precipitation during $\gamma \rightarrow \alpha$ transformation. There is no indication, however, that this is a critical temperature that would be identical for a wide range of steel compositions. Nevertheless, it does appear that in the steels of present interest, there is a limited region of temperature just above the region of initial acicular-ferrite formation, in which a fine-grained ferrite forms that has Nb (C,N) precipitation characteristics that are for practical purposes identical to those of acicular ferrite; i.e., the niobium present does not precipitate during the transformation, but remains in solution to be brought out later on subsequent aging.

3.3.4 Conclusions about microstructure

It is well established that the microstructure of a steel is most important in determining the mechanical properties. The primary concern of the foregoing discussion of microstructure has been to attain the maximum toughness at a satisfactory level of strength. It was observed early in the paper that good toughness was developed along with high strength, using an acicular structure at the 0·05% C level. It was also found, however, that the fine-grained ferrite microstructure, that is believed to form in a narrow region of temperature just above the acicular ferrite range, had the best strength-toughness properties that were developed. To produce a virtually 100% fine-grained ferrite microstructure consistently, particularly on a commercial scale, may not be feasible. The major point that should be appreciated, based on the foregoing discussion, is that a mixed structure, such as might most easily be attained in this manganese-molybdenum-niobium steel, is not an undesirable feature. A transformation diagram of the proper configuration, such as that represented by the dotted lines in Fig. 14, can result in the formation of a consistent volume fraction of fine-grained ferrite mixed with acicular ferrite over a significant range of cooling rates. Since these two microconstituents have similar aging characteristics with respect to Nb(C,N), no problem is presented by the mixed structure.

4. TRANSLATION TO COMMERCIAL PRACTICE

The many differences that exist between laboratory scale and commercial scale melting and mechanical processing practice provide numerous difficulties in predicting the potential properties of a commercial product based on laboratory data. It was the awareness of this problem that led the authors to design processing methods to be used in the laboratory study that would be as similar as was economically possible to the existing production capabilities of the steel industry. This approach was demonstrated to have considerable merit because the first attempt at commercialization of the manganese-molybdenum-niobium acicular ferrite steel was an unqualified success. The properties of the first commercial material were better than those of the corresponding laboratory-scale material, as will be shown below in the section on Commercial Product. It is the purpose of the present section to review the important differences between laboratory and commercial practices for the various prospective products and to estimate what sets of mechanical properties might be developed under various commercial-processing practices.

4.1 Melting practice

4.1.1 General

The 25 and 34kg laboratory heats were melted in argon for the singular purpose of controlling the nitrogen content, which tends to be high (up to 0·012%) when small heats are induction melted in air. It was observed earlier that nitrogen levels in the vicinity of 0·01% tend to reduce toughness. This problem was initially believed to be more serious than was ultimately observed. In general, it is not of significance to the common production melting processes, because nitrogen does not normally run over 0·01%.

The major aspect of the composition of the manganese-molybdenum-niobium steel that is of importance to the steelmaker is the combination of low carbon (0·05%) and high manganese (up to 2%). This necessitates blowing the melt down to a somewhat lower level of carbon and then adding a slightly more costly grade of manganese than would normally be used to avoid adding back excess carbon.

4.1.2 Nonmetallic inclusions

The outstanding attribute of the manganese-molybdenum-niobium steel is the excellent toughness at high strength, both in terms of shelf energy

and fracture appearance transition temperature. Although the inherent toughness of the steel itself is high, this toughness can be reduced to a low level by the entrainment in the material of excessive amounts of inclusions, particularly those present as stringers. The laboratory steels were made with normal amounts of phosphorus and with sulfur levels slightly below common commercial practice on the basis that steels designed for toughness would involve careful control of sulfur content. Total rolling reduction, however, was not as high as would be expected in the production process. In general, it is believed that some differences would be expected in the effects of sulfide stringers on translation to mill practice.

A most important point to be made regarding the effect of inclusions is that an inherently tough microstructure makes inclusion control of prime importance. It is not reasonable to allow inherently tough material to be produced as a mediocre product simply by paying insufficient attention to the available methods for controlling the detrimental effects of inclusions. The geometry of sulfide inclusions may be controlled by rare-earth additions. It was noted above that a zirconium addition cannot be used in the manganese-molybdenum-niobium steel because it tends to reduce the acicular ferrite hardenability, and results in a higher fracture appearance transition temperature.

4.2 The hot-rolling process

The laboratory hot-rolling process for 12·7mm-thick plates suffered the primary limitation of an initial slab thickness of 44 mm. This dimension was limited by the maximum roll separation. Ingots had to be press-forged to this thickness for rolling. Therefore, the maximum total reduction by rolling was about 70%. As noted in the section on laboratory procedures, most of the work on simulated-coiled strip was conducted at the same total reduction, although some simulated-coiled material was prepared with over 80% total reduction in five passes instead of the usual two passes, and the improvement in properties was quite significant. Normally the amount of hot reduction under production conditions would be somewhat greater than this.

The hot-rolling process for a niobium-containing steel may be considered to consist of two primary stages. The first is the grain-refinement stage which takes place in the high-temperature range, perhaps above 1040°C, depending on composition and the amount of reduction, where deformation results in rapid recrystallization of the austenite. The second is the range below the temperature at which Nb(C,N) starts to precipitate and inhibit recrystallization, i.e., the thermomechanical-treatment range. To attain good toughness, there must be enough reduction in the upper range to obtain refinement of the very coarse grain size that forms at the normal 1260°C reheat temperature. In addition, there must be sufficient reduction in the lower temperature range to generate a high dislocation density in the austenite prior to transformation. The general improvement in the strength-toughness balance that was observed with low finishing temperatures is indicative of the beneficial effects of reduction in the low-temperature range.

It was observed earlier in the discussion concerning austenite conditioning that the precipitation characteristics of Nb(C,N) in the austenite during hot-rolling could have wide ranging effects in affecting the properties of the final product. Some of these effects were demonstrated by the variations in properties of the plates prepared in the laboratory. The properties of the commercial product can also be expected to be highly dependent upon the amount of reduction that the steel undergoes in the intermediate temperature range of about 870 to 1040°C. Heavy reductions in this range will produce coarse Nb(C,N) precipitation in the austenite, as in Photo. 4 b), and also lower the potential for subsequent strengthening by aging. The data of Fig. 10 and 11 are directly applicable to the production process, with the degree of the effect dependent upon the amount of deformation, the time for recovery between roll passes and the amounts of niobium, carbon and nitrogen in solution. The development of maximum strength in this type of steel would require cooling through the range of 1095 to 870°C without reduction and then finish rolling in the range 870 to 705°C.

The laboratory-prepared steels exhibited improved toughness when reduced austenitizing (slab reheat) temperatures were used. There is some question as to whether this would be beneficial in commercial practice (disregarding the question of feasibility in a given mill). The effect observed may be related to the limited amount of hot-reduction that could be imparted to the laboratory test plates in the high-temperature range where grain refinement could take place. The austenitic grain size of the slab reheated at 1175°C would be somewhat finer than those reheated at higher temperatures, and would not require as much reduction for grain refinement.

The laboratory hot-rolling process for simulating coiled-strip production is obviously somewhat idealized, relative to the normal production process. The difference in roll-pass schedule was noted above. One of the problems encountered with the test pieces was the spray-cooling step after hot-rolling. It was not possible, with the nozzles used, to get the desired cooling rate of 11–14°C/sec that was known to be feasible on many existing mills. Water spraying from both sides produced a cooling rate of about 19–25°C/sec and spraying from one side yielded about 7–8°C/sec. Actually any cooling rate (including air cooling) is acceptable, depending

upon the composition. Manganese must be increased from the nominal 1·5% for strip production if the cooling rate is less than 8°C/sec. The cooling rate is, therefore, of less importance than the maximum allowable coiling temperature.* The temperature of the coil should not be allowed to significantly exceed about 675°C. Otherwise, coarse polygonal ferrite will be formed and poor toughness will result.

The laboratory simulated-coiled material exhibited an unfavorably high impact transition temperature at the intermediate coiling temperature of 605°C as shown in Fig. 13. No explanation was found for this low toughness. It will be shown in the following section that low toughness is not observed in commercial product that is coiled at this temperature.

* This discussion is in terms of actual temperature. For comparison with the indicated coiling temperature on a commercial strip mill, a correction must be made for the difference in temperature between the surface temperature and that at center thickness. An additional correction must be made for the approximate 40°C rise of temperature in the coil due to recalescence, if a major part of the phase transformation occurs after the steel enters the coil.

5. COMMERCIAL PRODUCT

The first commercial application of the manganese-molybdenum-niobium acicular ferrite steel was for a 130km section of 107cm diameter by 9·4mm-wall spiral-weld gas pipeline in the central provinces of Canada. The specification called for minimum yield and tensile strengths of 45·7 and 54·1 kg/mm², respectively, with a minimum of 35% shear fracture at −4°C transverse to the pipe axis, as determined by the Battelle Drop-Weight Tear Test. A 0·05%C-1·55%Mn-0·25%Mo-0·06%Nb nominal composition was recommended to the Interprovincial Steel and Pipe Corporation, Ltd. of Regina, Saskatchewan. Based on the laboratory results described earlier for simulated-coiled test plates, it was expected that this composition would provide a yield strength level of 50·5 to 54 kg/mm² with adequate toughness. The first trial heats yielded

Table 3. Composition of commercial manganese-molybdenum-niobium acicular ferrite steel (IPSCO heat No. 17099) for X-65 line pipe (%).

C	Mn	Mo	Nb	Si	N	P	S	Ni	Cr	Cu
0·07	1·63	0·25	0·05	0·04	0·006	0·011	0·017	0·09	0·02	0·21

Table 4. Mechanical properties of manganese-molybdenum-niobium acicular ferrite steel for X-65 line pipe (IPSCO coil No. 86305).

Location and orientation	Yield strength (0·5% total strain) (kg/mm²)	Tensile strength (kg/mm²)	Battelle drop-weight tear test (50% shear)
Lead-end[a]			
Rolling direction	51·4	66·8	−40℃
Perpendicular to pipe axis	52·9	67·2	
Parallel to pipe axis	56·0	68·2	
Center			
Rolling direction	53·0	69·9	−34℃
Perpendicular to pipe axis	54·6	69·3	
Parallel to pipe axis	58·1	71·6	
Tail-end[a]			
Rolling direction	52·8	67·2	−37℃
Perpendicular to pipe axis	53·5	68·0	
Parallel to pipe axis	57·3	68·7	

[a] Lead-end and tail-end designations refer to uncoiling. The lead-end corresponds to the bottom-end of the ingot.

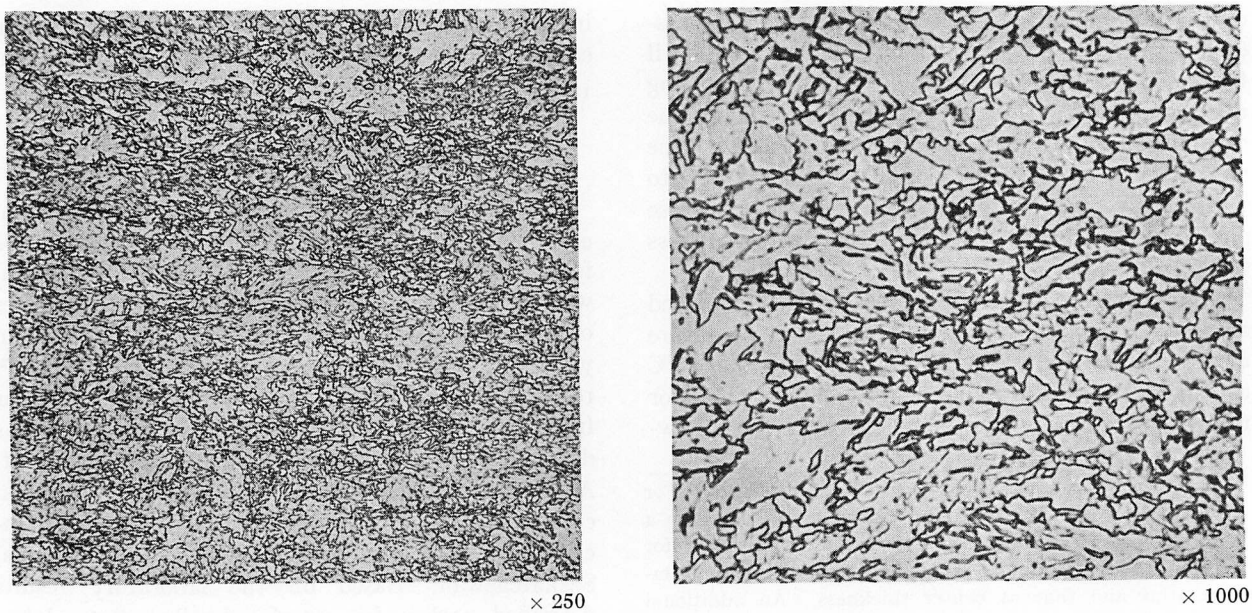

× 250 × 1000

Photo. 10. Representative microstructure of manganese-molybdenum-niobium X–65 linepipe steel.

× 10 000

Photo. 11. Carbon extraction replica from manganese-molybdenum-niobium X-65 line-pipe steel showing dense precipitation of coarse Nb(C,N) particles.

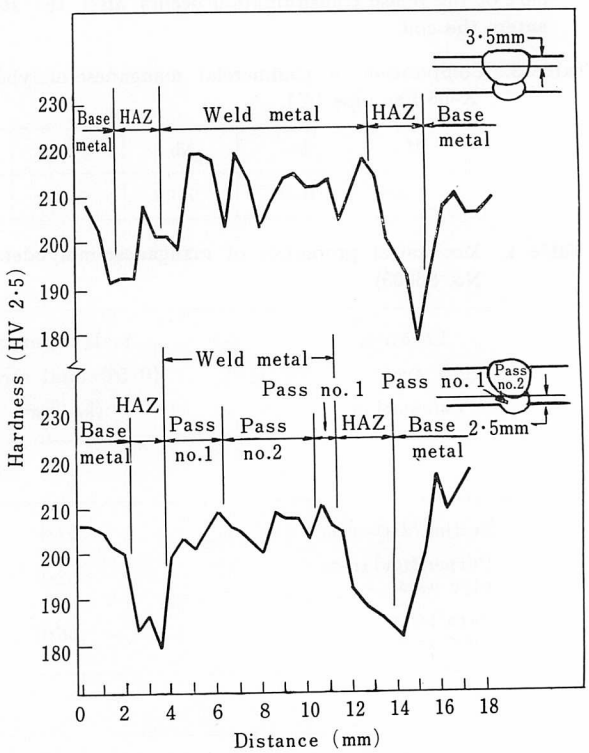

Fig. 15. Hardness profiles of submerged-arc spiral weld in manganese-molybdenum-niobium X–65 steel pipe.

highly satisfactory results, and production of the approximately 40 000 tons required for the 130km section of line was begun immediately.

The steel is melted in 35-ton electric furnaces by a semi-killed practice. It is poured into 74 by 178-cm bottle-top ingots, weighing about 18 tons. The ingots are soaked at 1315°C and rough-rolled to about 32mm-thick by 150cm wide. In the course of the rough-rolling process, the ends are cropped to yield a single, long slab that proceeds to a four-high mill with hot upcoilers. It has been observed that this molybdenum-containing steel has relatively non-adherent scale with good surface quality after rough-rolling. Finish-rolling is accomplished in five passes over the temperature range of about 1010 to 815°C. The strip then passes under a laminar-flow water-cooling bank, with spray-cooling on the underside. The strip is coiled so that the maximum temperature in the coil, due to recalescence, is about 605 to 620°C.

The chemical analysis of one of the first heats to be produced is presented in Table 3. The microstructure is shown in Photo. 10. The structure is a fine acicular ferrite. An electron micrograph of a carbon extraction replica taken from this material is presented in Photo. 11. This picture shows a

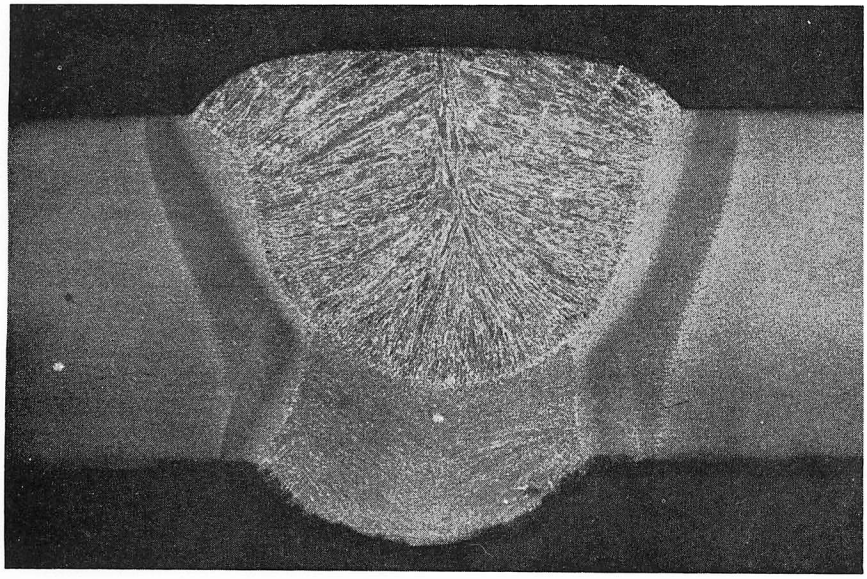

× 5

Photo. 12. Transverse section of submerged-arc spiral weld in manganese-molybdenum-niobium X-65 steel pipe.

dense array of relatively coarse Nb(C,N) particles that have apparently precipitated in the austenite. This is consistent with the laboratory observations that heavy hot-rolling reductions in the range between 870 and 1040°C produce Nb(C,N) precipitation in the austenite. Despite the loss of some niobium in this manner, the yield strength of the commercial product averages about 52·5 kg/mm² in the longitudinal direction. The mechanical properties of one coil from Heat 17099 are listed in Table 4. Since the coiled product is used to make spiral-weld pipe, the transverse direction of the pipe is about 27° from the longitudinal direction of the coiled strip. The linepipe specification requires testing specimens that are representative of the transverse direction of the pipe because that is the direction of maximum stress. It is clear from the data of Table 4 that the manganese-molybdenum-niobium acicular ferrite coiled product is extremely homogeneous in strength and toughness throughout the length of the coil. Longitudinal Charpy V-Notch specimens of 2/3 size were prepared from material at the center section of the coil and tested in accordance with ASTM A-370. The shelf energy was 15 kgm/cm² and the 50% shear FATT was −60°C.

The 9·4mm-thick strip is welded into pipe by a two-pass submerged-arc practice that uses a maximum heat input rate of about 14 kJ/cm, although the material is not known to be limited to this heat input. The first pass is on the inside diameter and the second, and larger pass, is on the outside diameter. The steel has been found to perform highly satisfactorily in the welding process. The low carbon content is believed to be an important asset, with regard to this favorable performance. A transverse section of a typical weld is shown in Photo. 12, with the outside diameter of the pipe at the top of the photograph. Two hardness traverses were made across this section with a Vickers hardness machine at a 2·5 kg load. The exact location of the traverses and the hardness values are presented in Fig. 15. These results show that there is some softening in the heat-affected zone, but no hardened regions.

6. SUMMARY

A family of low-carbon manganese-molybdenum-niobium acicular ferrite steels has been developed that takes advantage of a new concept in hot-rolled steels. This concept involves (1) the use of very low carbon contents for superior toughness, formability, and weldability, (2) lowering of the austenite-decomposition temperature by alloying with manganese, molybdenum, and niobium, and (3) controlling the final strength by regulating the amount of Nb(C,N) precipitation. It was found that good combinations of strength and toughness could be obtained by normal processing schedules. However, it was also observed that considerable variations in the strength-toughness relationships could be developed by adjustments in the hot-rolling schedule. The complex interrelationships that exist between the precipitation of Nb(C,N) in the austenite, austenite recrystallization kinetics, and subsequent transformation kinetics are believed to offer further opportunities for the development of even better combinations of strength and toughness than have been observed in the work reported herein.

The conclusion drawn from the results obtained in this study is that high levels of both strength and toughness can be obtained in a hot-rolled product if due attention is given to optimizing the balance between composition and processing variables. Molybdenum is required in the composition because of its strong effect in suppressing the formation of the conventional ferrite-pearlite microstructure.

REFERENCES

1) V. Biss and R.L. Cryderman: Met. Trans., **2** (1971), p. 2267
2) F. de Kazinsky, A. Axnas and P. Pachleitner: Jernkontorets Annaler, **147** (1963) no. 408
3) L. Luyckx, J.R. Bell, A. McLean and M. Korchynsky: Met. Trans., **1** (1970), p. 3341
4) G.A. Wilbur, J.R. Bell, J.H. Bucher and W.J. Childs: Trans. AIME, **242** (1968), p. 2305
5) J.M. Gray and R.B.G. Yeo: Trans. ASM, **61** (1968), p. 255
6) P.E. Repas: Transformation and Microstructural Aspects of Hot-Rolled Very-Low-Carbon Mn-Ni-Cb Steels, Presented at Spring Meeting of The Metallurgical Society of AIME, Las Vegas, Nevada, (May 1790)
7) Y.E. Smith and C.A. Siebert: Applications of Modern Metallographic Techniques, ASTM STP **480** (1970), p. 131
8) Y.E. Smith and C.A. Siebert: Met. Trans., **2** (1971), p. 1711

DISCUSSION-See pp. 347-353

Low-Temperature Brittleness of Iron and Steels

K. Kitajima

Kyushu University

A review is made of the recent research on fundamental mechanisms in the brittle fracture of iron and steels. The process of brittle fracture may consist of a number of stages ranging from microscopic to macroscopic dimensions, i.e., the stages of atomic dimensions, of the order of a grain size and the region of crystalline aggregates.

In the stage of atomic dimensions, the ductility of a crystal lattice is attributed to the balance between nucleation of cleavage cracks and dislocation loops under the given state of stress and is characterized quantitatively by the magnitude of the ratio σ_{th}/τ_{th} relative to the ratio σ_{max}/τ_{max}, where σ_{th} and τ_{th} are the critical normal and shear stresses of the crystal lattice, and σ_{max} and τ_{max} are the maximum normal and shear stresses operating in the cleavage and slip planes, respectively. The lattice ductility of iron is then discussed with relation to deformation of the bcc lattice and the nature of covalent-type bonding associated with unpaired d electrons in bcc transition metals.

As far as the role of plastic deformation in the mechanism of brittle fracture is concerned, the high lattice resistance of screw dislocations characteristic of bcc metals is responsible for the high yield stress at low temperatures or high strain rates, and the low lattice resistance of edge dislocations for the piling-up and coalescence of edge dislocations at the yield stress. On the other hand, the easy cross slip of screw dislocations can relieve local stress concentrations.

Experimental evidence on the initiation and propagation of cleavage cracks in single crystals of iron is critically reviewed from the above viewpoint. In particular, the growth of plastic deformation associated with the propagation of cleavage cracks at high velocities is attributed to the nucleation of dislocations at the tip of the crack. The activation energy of the nucleation of dislocations obtained experimentally is compared with that predicted theoretically, $k_s \sigma_{th}(\tau_{th}/\sigma_{th} - \tau_{max}/\sigma_{max})$. This gives an estimate $\sigma_{th}/\tau_{th} \simeq 0{\cdot}8\,\sigma_{max}/\tau_{max}$ at the tip of the crack, where σ_{max}/τ_{max} has the approximate value of five.

The effects of solid-solution alloying elements on the ductility of iron are discussed from the standpoint of lattice ductility and plastic deformation.

A review is presented for the phenomenological theories treating the initiation and propagation of cleavage cracks in an area of about one grain size. Next the differences in fracture characteristics of steels are explained on the basis of the role of the size and form of the precipitated particles.

Finally, some critical comments are made on the mechanisms relating microscopic and macroscopic processes, in particular, fracture stress, propagation of macro-cracks and the problem of size effects.

鉄鋼材料の低温脆性

北島一徳

九州大学　応用力学研究所

1. はじめに

鉄鋼材料は一般に高い降伏強度，抗張力とともに充分な伸びを持ちこれら大なる靱性のために各種の機械および構造物用材料として重要な位置を占めている．しかしながら半面低温あるいは衝撃荷重に際して特徴的な脆性破壊を示し，材料の使用上安全性の上から重要な問題とされてきた．

さて鉄鋼の低温脆性はその機構の上から大別して二つに分けられる．一つは劈開型破壊であり他の一つは粒界型破壊である．後者については純鉄の粒界破壊および低Ni-Cr合金鋼の焼戻し脆性等に見られるように一般に微量の不純物元素の役割が大きくその基本的な機構については近年新たな進展が見られているが，これについてはLowのReview[1]に詳しいので本文では省略したい．つぎに前者については，問題は基本的には体心立方鉄が劈開破壊を起こし易いという事実に帰着する訳であり，種々の合金元素，析出物形態および結晶粒度の役割もその立場から説明されねばならない．しかしながら現状では鉄が何故に劈開破壊を示すのかという基本的な問いにいまだ満足な解答は与えられていない。

その間の事情を見るためにまず多少の歴史的な記述をも含めて研究の現状を概観してみたい．

破壊の研究は理論的に推定される理想的な破壊強度が実際の破壊強度を大きく上廻る事実の指摘およびGriffith[2]の先在クラックの説等の古典的な研究にさかのぼるが，その後の研究はいくつかの流れに分かれて発展して来ている．まずその一つは破壊の巨視的な挙動を力学的に追求する立場である．そこでは鉄鋼の脆性自体の問題には触れず，むしろ破壊の特性をできるだけ数少ないパラメーターに帰着させようとする現象論的な立場である．すなわちLudwik，Davidenkovら[3]によって破壊応力，流動応力の概念が導入され，とくに物体の形状に依存する切欠効果およびそれによる遷移温度の変化等に合理的な説明が与えられた．この考えはさらに破面の伝播に伴う塑性仕事量[4]を問題にすることによって破壊力学の分野[5]が開拓されつつある．

つぎに破壊の機構を原子論的立場より解明しようとする研究は，結晶転位論の発展に伴ってZener[6]，Mott[7]らにより開始された．すなわち塑性変形の不均質性に伴う局所的応力集中によって原子的サイズのクラックを発生させる可能性が指摘され，一つのすべり面上に集積させられた転位のモデルが提案された．この考えはさらにStroh[8]，Cottrell[9]，Petchら[10,11]により発展させられ，結晶粒程度の領域における劈開クラックの発生について説明が与えられた．すなわち破壊応力や遷移温度の切欠効果，結晶粒度依存性等に説明が与えられ，金属組織学的研究に一つの有力な指針を与えている．しかしながらそれらのモデルの実証的裏付けはいまだ充分ではなく，むしろその後塑性変形についての詳細な研究が進み，とくに鉄のすべり帯特性，双晶と破壊との関連が明らかにされるとともに，モデルの適用にはなお種々の問題が残されていることが明らかにされて来た[12,13]．さらにまたこれらの理論は鉄が何故脆性を示すのかという問には答えることが出来ない．すなわち本質的には現象論的な域を出でていない．

鉄が低温で劈開破壊を起こし易い理由の一つは低温で降伏応力および流動応力が著しく上昇することである．この問題については近年体心立方格子金属の結晶構造自体の特性によってラセン転位の格子摩擦が大きいとする立場がHirsch[14]およびSuzuki[15]らにより提案され，これによって塑性変形の基本的な機構の解明に有力な緒が与えられるに至った．この方面の研究はさらに固溶元素の影響[16]等に関して現在発展の途上にある．

第二には，結晶格子自体の脆性特性である．たとえば前述転位モデルでは，転位の集積点において応力集中の結果局所応力が理想的破壊強度に到達して劈開クラックが発生すると仮定されている．しかしこれは自明の理ではない．すなわち理想的破壊応力程度の高い応力場では，劈開クラックの発生に先立って結晶格子のすべり変形が起こる可能性があり，脆性は両者のかねあいにより決められると考えられる．このことははじめStroh[17]によっても指摘されたところである．いま，劈開面およびすべり面に働く応力成分の最大値をσ_{max}，τ_{max}とするとき劈開破壊の発生条件は，$\sigma_{th}/\tau_{th}<\sigma_{max}/\tau_{max}$となる．こゝに$\sigma_{th}$，$\tau_{th}$は完全結晶の劈開およびすべり変形の臨界応力である．また右辺は応力状態に依存して物質によらない値であり，左辺は結晶格子自体の特性値である．従ってパラメーター(σ_{th}/τ_{th})は結晶格子の脆性を特性付ける常数にほかならない．この立場はKitajima[18]およびCottrell[19]らにより追求され，それぞれいくつかの方向に発展させられている．まずその一つは，与えられた結晶について原子間力よりσ_{th}，τ_{th}を決定することである．金属についての計算は現状ではきわめて困難であるが，本文ではBCC遷移金属の格子の脆性について出来るだけの手掛りを探究してみたい．いま一つはこの考えの帰結を実験事実につき追求することであろう．本文においてはこれに関して，純鉄単結晶における劈開クラックの伝播について行なわれた研究を紹介したい．なお，置換型固溶合金の脆性はこの立場から興味深い問題と考えられるので本文でも稍々詳しく論じたい．

本文においては以上の諸点につき研究の現状について紹介するとともに，破壊の全体の過程について微視より巨視的挙動を結ぶ機構につき問題点を指摘したい．

2. 鉄の脆性の基本的な性質

2.1 結晶格子の脆性

鉄の脆性に立入る前に格子の脆性一般について考察を加えておきたい．まず結晶の劈開破壊応力 σ_{th} の評価については Orowan[4] によれば原子間距離と引張応力との関係を $\sigma=\sigma_{th}\sin 2\pi u/\lambda$ によって近似すると

$$\sigma_{th}=\sqrt{\frac{E\gamma}{a}},$$

ただし a は格子常数，γ は表面エネルギーで，$2\gamma=\int\sigma du=\lambda\sigma_{th}/\pi$,
鉄の場合 $E=2\times10^{12}$ dyne/cm^2, $\gamma=1200$erg/cm^2, $a=2{\cdot}85$Å とするとき σ_{th} は 4800kg/mm^2 となる．転位を含まない whisker は完全結晶に近い特性を持つと考えられるが Brenner[20] によれば $(\sigma)_{max}\simeq1200$kg/mm^2 が得られている．なお高張力鋼では 300kg/mm^2 に達するものがある．Hull[21] は，W について低温で放電加工により微小なクラックを与え，ついで引張を加えて，劈開が伝播する応力より Griffith の関係を用いて γ を求めている．これは実験的に σ_{th} を追求する方法として興味がある．

つぎに結晶の剪断変形応力 τ_{th} については FCC 金属についての Mackenzie, Seeger らの考察[22] が知られている．いま容易すべりの方向 $(1\bar{1}0)$ [112] への剪断変形について考えると，隣接原子面間の相対的剪断変位が $a/6$ [112] の点では格子は近似的に体心立方格子位置を取り，また $a/2$[112] では双晶位置を取る．これらのことを考慮に入れて τ_{th} は比較的に小さい値 G/30 を持つと推定された．これは結晶がとり得る形態のうち面心立方および体心立方格子の位置は比較的に密な集合状態であり，一般にエネルギーの極小位置に相当すると考えられるからである．

同様の考察は体心立方格子の変形についてもなし得る．この場合変形の経路としては $(1\bar{1}0)$ および $(11\bar{2})$ すべ

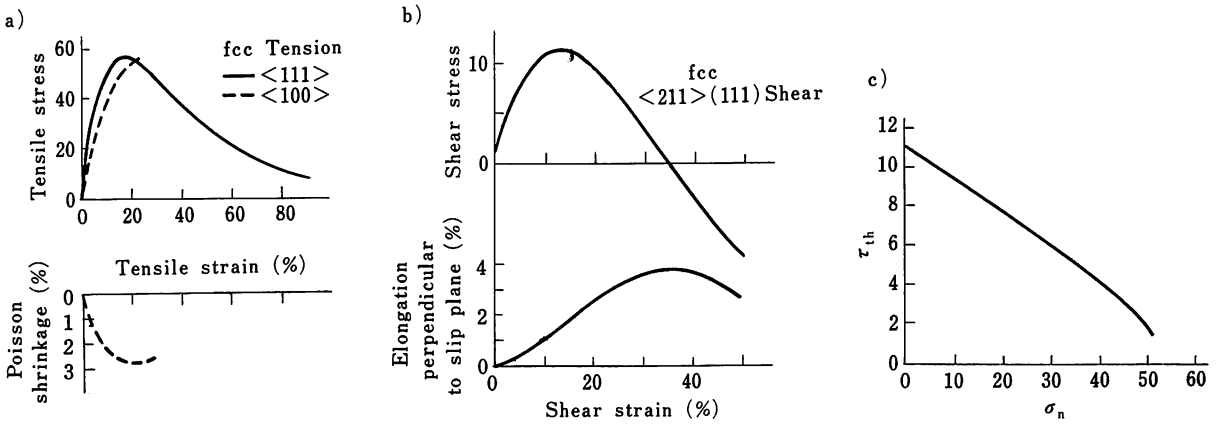

Fig. 1. Stress-strain characteristics of Lennard-Jones crystal with interatomic potential $\phi=-\frac{a}{r^6}+\frac{b}{r^{12}}$.

a) Tensile deformation, after Tyson[25]. b) Shear deformation, Tyson[25]. c) Effect of normal stress σ_n operating in slip plane on τ_{th}, Kelly et al.[25].

Table 1. Calculated values of σ_{th} and τ_{th}, after Kelly et al[25]. a_0, γ, E' and G' were determined by extraplating experimental values to 0°K. σ_{th} and τ_{th} for metals were calculated using the assumptions $\sigma_{th}=\left(\frac{E'\gamma}{a_0}\right)^{1/2}$, $\frac{\tau_{th}}{G'}=0.04$ (fcc), or 0·11 (bcc).

	Lattice constant a_0(Å)	E' $\left(10^{11}\frac{\text{dyne}}{\text{cm}^2}\right)$	Surface energy γ(erg·cm^{-2}) Measured	Surface energy γ(erg·cm^{-2}) Extrapolated	σ_{th} $\left(10^{11}\frac{\text{dyne}}{\text{cm}^2}\right)$	$\frac{\sigma_{th}}{E'}$	G' $\left(10^{11}\frac{\text{dyne}}{\text{cm}^2}\right)$	$\frac{\tau_{th}}{G'}$	τ_{th} $\left(10^{11}\frac{\text{dyne}}{\text{cm}^2}\right)$	$\frac{\sigma_{th}}{\tau_{th}}$
Cu	1·80	7·5	1730at 1000℃	3630	3·87	0·51	3·43	0·04	0·137	28·2
Ag	2·03	4·9	1130at 925℃	2930	2·66	0·54	2·20	0·04	0·088	30·2
Au	2·04	4·63	1350at 1000℃	3250	2·73	0·59	2·02	0·04	0·081	33·8
Ni	1·76	15·00	1725at 1455℃	4300	6·05	0·41	6·85	0·04	0·274	22·1
W	3·16	40·48	6300at 77℃	6415	9·08	0·22	16·35	0·11	1·80	5·04
			2900at 2000℃	7650						
α-Fe	2·85	14·33	1940at 1450℃ (δ-iron)	4520	4·79	0·34	6·48	0·11	0·71	6·75
Diamond	1·54	120·9			14·0	0·116	50·5	0·24	12·1	1·16
NaCl	2·75	5·75	118at 25℃	140	0·38	0·067	2·48	0·164	0·406	0·94

り面上の剪断変形に対応して2種類の経路が考えられる．

すなわち $(1\bar{1}0)$ については[23]，

$a/2\,[111]=a/8\,[110]+a/4\,[112]+a/8\,[110]$,

$(11\bar{2})$ については，

$a/2\,[111]=a/6[111]+a/3[111]$.

前者については，$a/6\,[110]$ の位置が近似的面心立方位置であり，後者については $a/6\,[111]$ の位置は双晶位置に相当する．従ってこれらの位置ではポテンシャルは極小値を取ることが予想される．

さて，具体的な物質について，原子間力を考慮に入れてなされた σ_{th} および τ_{th} の計算例はきわめて少ない．中心力場の場合 Lennard-Jones 型の結晶について Born[24]，Kitajima[18]，Tyson[25] らの計算がある．Fig. 1に Tyson による計算結果を示す．つぎにイオン結晶については Born-Meyer 型の原子間力を仮定して，Zwicky[26]，Tyson[25] らによって計算がなされている．

また Born[24] はこの問題を一般的に結晶の安定の問題として定式化している．すなわち種々の格子歪のもとにおける結晶の自由エネルギーを求め，付加的な微小変形に対する安定の条件より σ_{th} および τ_{th} の値が求められる．これによれば σ_{th} や τ_{th} の値は一般には外部応力の条件や変形の拘束条件に依存する．例えば Tyson の計算によれば，すべり面に垂直な圧縮応力 σ_n が増加すれば τ_{th} の値は増加する．Fig. 1c)．

また原子間力が中心でない場合の例として，ダイヤモンドに関する Tyson[25] の計算がある．

さて前述のように結晶格子の脆性は σ_{th}/τ_{th} により特性付けられるが，Table 1に，Kelly[25] らによりまとめられた種々の物質についての値を示す．この表によればFCC 金属では σ_{th}/τ_{th} は30程度の値を持ち，1程度の値を持つイオン結晶や共有結合型結晶に比較して延性的であること，および BCC 金属は両者の中間に位し，$\sigma_{th}/\tau_{th}\simeq 5\sim 6$ であることが示されている．

2.2 BCC 遷移金属の脆性

つぎに BCC 遷移金属の格子の脆性についていま少しく立入って考察を進めてみよう．

遷移金属の電子論的な計算については，エネルギーバンド構造等につき，現在かなりの知識が得られるに至っている[27]．しかしながらこれを基にしてさらに凝集エネルギーの計算に進むには多電子間の相互作用の取扱いに関して基本的な困難が残されており，現在の計算精度では結晶形の相違についてもいまだ定量的に説明するまでに至っていない．従って結晶格子の有限変形に関連する σ_{th} や τ_{th} の計算については，むしろ今後の新しい課題であると云えよう．

しかしながら問題の粗い取扱いについていくつかの途がないではない．たとえば Table 1に示すような結晶形に依存する脆性の相違を説明する目的には，近似的な原子間力を用いてある程度の推定が可能かもしれない．

Johnson[28] は BCC 結晶につき原子間力として中心力を仮定し，また第二近接原子までの相互作用を考慮に入れることによって種々の格子欠陥についての計算を行っているが，この方法をこの問題に適用することも興味がある。Chang[29] は Johnson の近似を用いてクラック先端付近の結合力の分布を FCC および BCC 鉄について比較し，後者では結合が断たれ易いことを示した．なお原子間力として中心力を仮定する方法の適用限界については下に示す非中心力の役割とも関連して多くの疑問が残される．

さて同じく BCC 金属についても，I 族のアルカリ金属は脆性を示さず V 族の V, Nb, Ta は VI 族の Cr, Mo, W および VIII 族の Fe に比較して脆性は少ないことが知られている．これらの相違は基本的には，遷移金属の d 殻不対電子による共有結合性の結合力に依存していることが考えられる．すなわち一価金属のアルカリ金属は純粋な金属結合であり，それらが BCC 結晶構造を取る理由は主として BCC 結晶が FCC結晶に比較して疎な構造を持ち，従って自由エネルギーに占めるエントロピー項の寄与が大きいためであるとされている．これに対比して遷移金属では d 電子の軌道函数が BCC 格子において共有結合を作り易い方向性を持っており凝集エネルギーへのそれらの寄与が大きいためであると考えられる[30]．このような共有結合的性格を持つ結合力は剪断変形への抵抗すなわち τ_{th} への寄与が大きいことは容易に推察される．なお自由電子的な結合力の τ_{th} への寄与は剪断変形に伴う体積変化が小さいことからも小さいであろうことが推察される。しかしながら σ_{th} については両者を含む凝集エネルギー全体が問題になるであろう．

さて共有結合に関与するものが d 殻の不対電子であるとするならばその数の増加とともに脆性が増すことになる．たとえば V, VI, VIII 族の V d^3s^2, Cr d^5s^1, Fe d^6s^2 について不対電子の数は 3, 5, 4 であるから V 族に比較して VI 族の脆性は大きく，VIII 族の Fe では逆に減少しはじめることが予想されよう．もっとも結晶中の d 電子の挙動は孤立原子のそれとは大きく異なる．結晶を組むことによって d 電子はバンド構造を示し，巡回電子的な性質を帯びる．さらに結合力については s バンドと d バンドとの相互作用その他多電子間の多くの相互作用が考慮されねばならずそれらの定量的な計算は今後の問題である．しかしながら一般に d 電子の局在的な性格[31]と共有結合的な性格も依然として大きいと推定されており，前述の推定も定性的な意味では肯定し得るものと考えられる．

なお凝集エネルギーの問題については，半経験論的な Engel-Brewer の理論[32] が知られている．この理論によれば孤立原子は結晶を組むことにより，電子状態に遷移が起こるとし，一方結合エネルギーの実測値より s および p 電子（両者は同等と仮定する．）および d 電子の1個当りの結合エネルギー，およびまた d 電子の s, p 状態への遷移に伴うエネルギーの変化を推定し，系の全エネルギーを最小にする条件より電子遷移の条件を定めている．このようにして期待される電子状態としてたとえば V; $d^{3.5}\,sp^{0.5}$, Cr ; $d^{4.5}\,sp^{0.5}$, Fe ; $d^{6.5}\,sp^{0.5}$ 等を得ている．つぎに結晶形を決めるのは s および p 電子の総数であり，d 電子の寄与は少ない（この点については電子論よりの推論とは一致しない．）としており，このようにして結晶形および凝集エネルギーに説明を与えている．この理論には多くの推察的要素が含まれているにもかかわらず，定量的評価を行なっている点に興味があり，また金属および合金の結晶構造の予知にある程度の成功を収めている．Leslie[33] はこの理論に基づいて鉄固溶合金の脆性に一つの説明を提出している．その内容の詳細およびこれに対する批判については後に述べる．

2.3 鉄の塑性変形特性と脆性

BCC 金属の脆性における塑性変形の役割については i)

低温における降伏応力の上昇 ii) 塑性変形の非均質性による応力集中 iii) 塑性変形に伴う応力集中の緩和の三つの要素が問題になる.

BCC 金属の降伏応力および流動応力が低温あるいは衝撃荷重に際して著しく上昇することは, FCC 金属に比較しての顕著な特徴であり, これによって応力のレベルが上昇し, クラックの発生および伝播を容易にする. 降伏応力の機構については, はじめ炭素による転位の固着が考えられたが, 近年になってこれを BCC 格子に固有の性質であるとする有力な説明が与えられるに至った. その詳細については本シンポジウム・鈴木秀次教授の講演[34] に譲るが BCC 金属では, その結晶構造に依存する転位の特性としてラセン転位の格子摩擦がきわめて大きいことが示された. その考え方は現在二つに分かれている. まずその一つは, ラセン転位は, いくつかの {112} および {110} 面において積層欠陥を伴って拡張し, 数個の部分転位に分解している. この場合転位が移動し得るためには, 積層欠陥は一つのすべり面上に一度収縮しなければならない. このことから転位の大きな移動抵抗が説明される[14]. いま一つは, ラセン転位の芯部分の原子の位置に着目すると, 結晶内の転位の位置によって芯のまわりの原子が互いに押し合い, エネルギーの高い状態を取る場合と, 無理のないエネルギーの低い状態を取る場合とが1原子間隔ごとに交互に存在しており, 従ってパイエルス応力が大きいとする考えである[15].

前者は現象論的ではあるが, 臨界剪断応力がすべり面に働く剪断応力の方向に依存する実験事実を説明することができ, また交叉すべりの説明等に利点を持っている. しかしながら積層欠陥の巾についての理論的な裏付けを欠いている. これに比較して後者ではその理論的根拠は明らかであるが, 実験値に比較して過大な計算値を与え, また前述の実験事実に対する説明が未完である. 両者の利点をより完結した理論に統合することは今後の課題であろう. いずれにせよ低温での降伏応力の上昇は基本的にはこれらの理論によって一応解決されたものと考えられる. なお注意すべきは, いずれの理論によっても, 刃状転位のパイエルス応力はラセン転位に比較してきわめて小さいと推定される点である. これも実験事実によって裏付けされる[13]. また BCC 金属の流動応力の歪速度依存性が BCC 金属に比較してもきわめて大きい理由も上述の理論により説明される.

つぎに塑性変形に伴う応力の集中および緩和の機構については, いづれも塑性変形の高次の特性でありいまだ充分な解明はなされていない. まず BCC 金属では, すべり系も多く, 等方的であり, またラセン転位はその構造から交叉すべり起こし易い特性を持っているので, すべりの非均質性による応力集中の発生には有利ではない. 実験事実によればすべり帯は巾を持ち均質的な微細すべりにより構成されており, また高温では交叉すべりによって特徴的な波状のすべりを示す. 交叉すべりの起こり易さは {110} すべりと {112} すべりの格子摩擦の差によると考えられ, これについては, 前述 Hirsch による説明[14] もあるが, 確定的ではない. 一般に低温では {110} すべりが優先して, 波状すべりは減少する.

一方 Cottrell[9] により示されたように二つの (110) すべり系の刃状転位は合体して

$$\frac{a}{2}[\bar{1}\bar{1}1]+\frac{a}{2}[111]\rightarrow a\,[001]$$

の反応により不動転位 $a[001]$ を形成し, これによって刃状転位の集積を起こす可能性がある. また刃状転位のパイエルス応力はラセン転位のそれに比較して小さいので, ラセン転位の格子摩擦に等しい応力下でも集積により局所的な応力集中を起こし得る.

なお双晶はすべりに比較して非均質性が大きいから応力集中には有利な機構であり, 後述のように純鉄におけるクラックの発生に大きな役割を持つ.

2.4 固溶合金元素の脆性に及ぼす影響

固溶元素の塑性および脆性に及ぼす影響については純金属についての研究の進展に伴って最近注目されて来ている.

まず塑性変形に及ぼす影響については, BCC 金属の著しい特徴として, 溶質原子が, 置換型[35,16] または侵入型[36] のいづれの場合についても一般には常温以上では固溶体硬化を, 低温では固溶体軟化を示す.

この機構については基本的には前述ラセン転位の大きなパイエルス応力の特性に関連して説明されるべきものである. Sato[37] および飯井[38] は溶質原子のまわりの応力場によってその近傍に kink 対が形成され易くなるものとして, 詳細な計算に基づき説明を与えている. またラセン転位のパイエルス応力は, 鈴木の理論によれば, 原子の整合的な並びに起因するものであるから, この配列を乱す要素は転位芯のパイエルスポテンシャルをむしろ低くする場合もあり得る (固溶軟化). なお障害物の寸法が大きくなるにつれて, 軟化より熱活性化型硬化さらに非熱活性化型硬化に移行することが, 実験事実により示されている[39].

一方同様に固溶体軟化を示す元素についても, 脆性を増加させる場合と脆性を減少させる場合がある[33]. Table 2. 一般にオーステナイト領域を減少させる合金元素 (Si, Al, Cr, Mo 等[33]) は脆性を増加させ, オーステナイト領域を拡げる合金元素 (Ni[40] Mn, Pt, Ir, Rh, Ru)[41] は, 脆性を減少させることが知られているが, Cr, Mn については, それらの影響は小さい[33]. (Table 2). この機構についても現在二通りの考え方がある. その一つは固溶元素が交叉すべりへの影響を通じて脆性に寄与するとする考えである。たとえば 3% Si-Fe 合金については, 純鉄に比較してすべり帯の模様はより直線的であり, 約

Table 2. Charpy impact characteristics for solid-solution alloys of iron, after Leslie et al[33].

Alloy content (%)	Grain size (ASTM No.)	Transition temperature (℃)	Maximum absorbed energy	
			(ftlb)	(kgm)
Fe	4 − 5	−34	75	10·3
Fe	0 − 2	−29	65	9·0
1·5Ni	5 − 6	−54	80	11·0
3Ni	7 − 9	−95	90	12·4
1·5Si	6 − 7	− 4	80	11·0
3Si	4 − 7	100	55	7·6
1·5Mn	6 − 8	−20	80	11·0
3Mn	7 − 9	− 7	80	11·0
1·5Cr	4 − 5	−18	75	10·3
3Cr	4 − 7	−23	75	10·3
6Cr	6 − 7	−23	85	11·7

240°C の遷移温度の上昇を示す[40]．一方 3% Ni については，50°K まで波状すべりを示し（純鉄ではすべり帯の波型より直線型への遷移が 120°K で起きる．）遷移温度は 70°C 低下する[40]．前節で述べたように，ラセン転位での交叉すべりを容易にする機構についてはまだ充分な説明は与えられていないが，交叉すべりによって一般に応力集中は緩和されるので，交叉すべりの容易さは脆性を減少させる有力な要素であろう．しかしながら VI 族元素 W，Mo 等は Fe に比較して交叉すべりを起こし易いにもかかわらず，より交叉すべりを起こし難い V 族元素 Ta，Nb，V に比較して脆性が大きい事実を指摘しておかねばならない．なお鉄固溶合金については流動応力の特性と脆性の間にあまり相関はないとされている．Fig. 2．

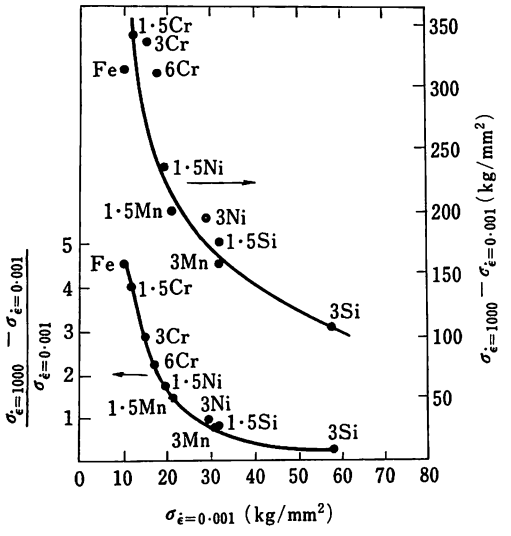

Fig. 2. Strain rate dependency of yield stress in solid solution alloys of iron, after Leslie et al[33].

いま一つの考えは，固溶元素によって結晶格子自体の脆性が変化させられるとする考えである．一般にオーステナイト域を拡げる作用は，BCC 格子と，FCC 格子のエネルギー差を少なくする作用である．前述のように BCC 格子の (110) 剪断変形に際して $a/6$ [110] の原子変位によって FCC 格子に近い位置を取ることが示されるが，実際の変形もこれに近い経路を通って変形すると考えられるので，FCC 格子とのエネルギー差の小さい程 τ_{th} は小さく，従って格子の延性は増加することが考えられる．たとえば実測によれば 9% Ni の固溶による α-γ 変態点の温度変化は約 300°C であり，これに伴う α と γ 相の自由エネルギー差の変化量は単位胞当りほぼ 0·04eV と推定される．一方鉄格子の臨界剪断応力下の弾性エネルギーは，$1/2\times\tau_{th}\times\gamma_c\times a^3\simeq 0\cdot15$eV，ただし γ_c は臨界剪断歪$\simeq\frac{\sqrt{6}}{8}$，$\tau_{th}\simeq G/10$，$G=8\times10^{11}$ dyne/cm²，$a=2\cdot86$Å，であるから τ_{th} の上述の意味の変化は大きさの程度において期待し得る．なお後述のクラックの伝播の際に説明されるように，脆性を支配する過程の活性化エネルギーは $k_s\,\sigma_{th}(\tau_{th}/\sigma_{th}-\tau_{max}/\sigma_{max})$ の形に表わされる[18]ため，BCC 遷移金属のように $\tau_{th}/\sigma_{th}\simeq\tau_{max}/\sigma_{max}$ の場合には τ_{th}/σ_{th} の小量の変化によっても脆性特性に大きな変化を及ぼすことが考えられる．

なお Leslie[33] は延性の増加は結晶格子の凝集エネルギーの増加によるものとし，これに寄与する要素として，結合にあずかる電子数および原子径を指摘し，Engel-Brewer 理論に基づいて鉄中の固溶元素の役割を説明している．それによれば Ni, Pt, Pd は凝集エネルギーを増加させ，Mn, Cr は影響は少なく，Si はエネルギーを減少させるとして前述の実験事実が説明されるとしている．これは興味ある考えであるが前に論じたように格子の脆性は，σ_{th}/τ_{th} に依存することを考慮すれば凝集エネルギーの増加をただちに脆性に結び付けることは出来ない．

さて前述の考察によれば，固溶による τ_{th} の変化，とくに，凝集エネルギー中の共有結合型成分の変化が重要である．問題の詳細は，電子論的研究の発展に待たねばならないが，定性的には，Ni;d^8s^2, Pd;d^{10}, Pt;d^8s^2 の固溶の効果は不対 d 電子の数を減少させて共有結合型の成分を減少させるためと考えられる．Si の影響についてはなお未詳であるが，s 電子はむしろ共有結合型成分に寄与するものと考えられる．いづれにせよ固溶元素の影響については格子の脆性すなわち σ_{th}/τ_{th} への影響は重要な要素であると考えられる．

3. 鉄鋼の脆性破壊の諸過程

本章においては鉄鋼の脆性破壊の諸過程について概観するとともに関連する実験事実，および現象論を含む種々の理論について述べる．脆性破壊の過程は微視的領域より巨視的領域にわたりいくつかの過程より成り立っているが，それらは i) 原子的領域，ii) 結晶粒内，iii) 結晶粒界を含む数個の結晶粒の領域，および iv) 巨視的な領域における諸過程に大別することが出来る。破壊の特徴として，これらの諸過程はそれぞれほぼ同等の重荷で全体の破壊の特性に寄与しているためそれぞれの過程における機構の特徴を明らかにするとともに，それらの間の相互の関連を明らかにすることがとくに必要である．

3.1 結晶粒程度の領域におけるクラックの発生と伝播

原子的領域において劈開クラックが発生し得るためには，巨視的な応力のほかに局所的な応力の集中が必要である．初期の理論においては，障害物によってせきとめられたすべり帯の先端に転位が集積する転位モデルが，Mott[7] および Stroh[8] により提出された。いま応力 τ のもとですべり帯上に集積する刃状転位の数を n とすれば転位の集積点では $\sigma_{max}\simeq\tau_{max}=n\tau$ の応力を生ずる．σ_{max} が σ_{th} に到達すればミクロクラックを生じ得る．ここに n は

$$L=\frac{Gbn}{\pi(1-\nu)\tau},\quad n\tau=\alpha'\sigma_{th} \tag{1}$$

によって与えられる．ここに b はバーカスベクトル，ν ポアソン比，$\alpha'\simeq1$，L は結晶粒径 d の 1/2 程度の値である．しかしながらこのモデルでは破壊の法則は臨界剪断応力の条件で支配されることになり，脆性破壊に特徴的な切欠敏感性すなわち三軸応力依存性を説明することができない．Cottrell[9]，Petch[10] および北島[11] らはさらに，クラックの結晶粒内の伝播に際して破面に塑性変形が発生することを考慮すれば，破壊の条件は (1) ではなくクラックの粒内における伝播の条件により決められることを指摘し，

$$\sigma_f=K\left(\frac{p}{\gamma}\right)^{1/2}\left(\frac{\sigma_{max}}{\tau_{max}}\right)^{1/2}\left(\frac{b}{d}\right)^{1/2} \tag{2}$$

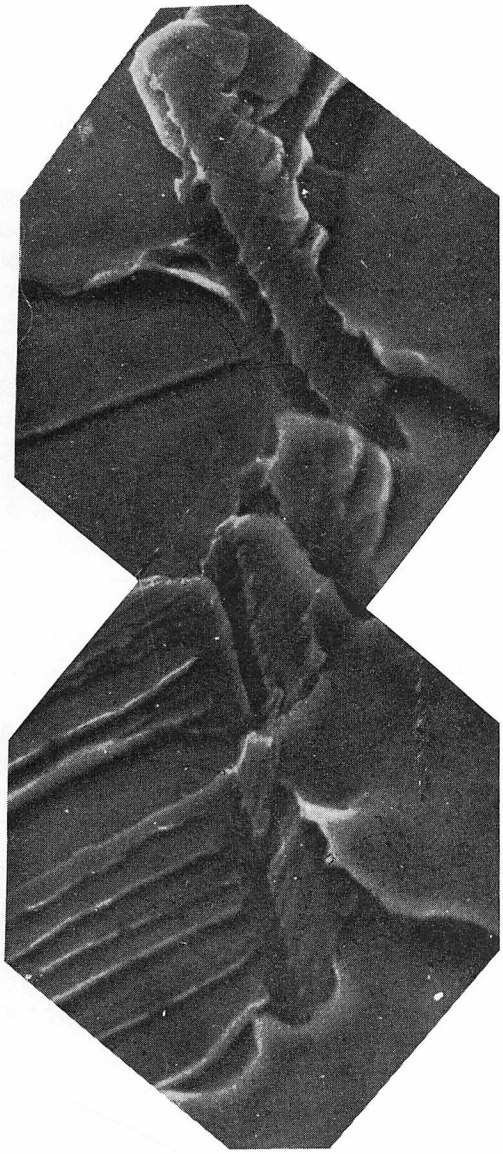

a) ×2000

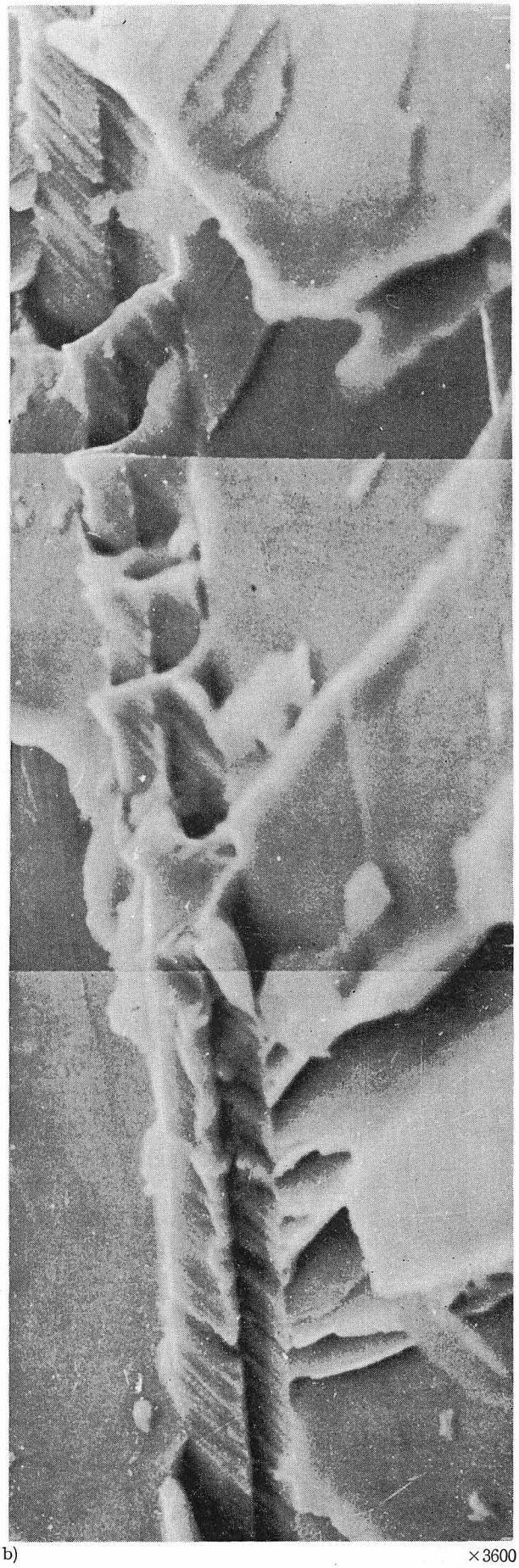

b) ×3600

Photo. 1. Scanning electron micrographs of crack origins accompanying a twin in a single crystal of pure iron.
a) Viewed along a direction not parallel to the plane of the twin.
b) Viewed along the direction parallel to the plane of the twin. The striations inside the twin show a shear-type fracture. A straight groove is formed along the center of the twin. A series of cleavage facets start from the ends of shear fracture facets along the twin boundary. A series of segments of twin as observed in a) is proved to be placed in a single twin as shown in b). The twin is cut by cleavage planes with various heights, after Kitajima[45].

を提出した．ここに p は塑性仕事量であり 10γ 程度の値を仮定すれば三軸応力依存性の実験事実を説明し得る．なおここで降伏の応力条件は実験事実によればPetchの式

$$\tau_y = \tau_i + kd^{-1/2} \qquad (3)$$

の形で与えられる．式 (2) を (3) に結びつけて遷移温度を求めることができる．これらの式を用いて破壊の種々の特性すなわち破壊応力および遷移温度の結晶粒度依存性，歪速度依存性等を説明することができており，いまなお現象論としての価値は失われていないが，各項の物理的意味についてはその後の研究によってかなりの改変が必要になってきた．

まず鉄のすべり帯の構造は前述のように巾を持ち (1) 式はそのまま妥当ではない．すなわち (1) 式の応力集中に対応するものとしてはすべり帯による巨視的応力集中とその内部における刃状転位の集積によるそれとの二段階の機構を考えねばならない．また (3) 式中の τ_i は主としてラセン転位の格子摩擦をあらわしているが，前述のようにすべり帯内部の刃状転位の集積に対しては応力 τ_y が働くと考えてよい．

なお寺崎[43]は一つのすべり面上にない多数の刃状転位による応力集中を考察してクラックの発生を論じている．

一方実験事実によれば純鉄単結晶についてすべりのみによるクラックの発生は見出されていない．むしろ劈開クラックは双晶に伴って発生しており，二個の双晶の交叉による例[44]および一個の双晶より多数のクラックが発生する例 Photo. 1[11,13,45]が報告されている．これらの例についてもクラックの発生の微視的機構は単純な上述のモデルでは説明し得ないことが示されている．また (3) 式の k については，はじめ炭素による転位の固着-Cottrell 効果- に結びつけて説明されたが，その後の実験によれば完全に固着された場合 k は温度に依存しないことが示された[46]．

3.2 劈開クラックの伝播

劈開クラックの伝播に伴う塑性変形の発生は前述のように破壊の条件に重要な役割を持つがその機構については二通りの考え方がある．その一つは Friedel[47]および Tetelman[48]によるもので，破面の近傍に先在する転位が破面に伴う応力場によって移動させられ，転位を多重形成する．Tetelman によればこの機構による塑性変形仕事 p はつぎのように表わされる．

$$p = \gamma[(\sqrt{5}/1{\cdot}7)\,\rho_0^{3/2} b^3 (8{\cdot}8\times10^2)(Vc/V)^2 T^{5/2}], \qquad (4)$$

ここに ρ_0 は初期の活動し得る Frank-Read 源の密度，Vc はクラックの臨界伝播速度である．Fig. 3, Photo. 2. 式 (4) に示されるようにこの機構では先在転位の密度が脆性に大きな影響を持つ．Gilman[49]はとくに転位の二重交叉すべりによる多重形成機構を重視し，それが結晶の脆性を支配する要素であるとしている．

いま一つの機構は，破面の先端において転位ループが核発生する機構である．すなわち破面の先端付近では σ_{max}/τ_{max} は5程度の値を持つが BCC 結晶格子では前述のように，σ_{th}/τ_{th} も5程度の値を持つため，破面の先端では劈開のみならず格子の変形により転位ループをも核発生し得る．これらが応力場により拡大すれば塑性変形を生じ得る．核発生の実験事実ははじめGilman[50]により指摘されたが，北島はさらに塑性仕事量 p を評価した[18]．

$$\log\frac{p}{K\tau_{max}b} \simeq 3\log\frac{\tau_{max}}{\tau_p} + \left(\frac{3kT}{A}+1\right)\log\frac{2Vc}{V} - k_s\sigma_{th}(\beta-\alpha)/kT \qquad (4)$$

ここに $\beta=\tau_{th}/\sigma_{th}$, $\alpha=\tau_{max}/\sigma_{max}$, K, A, k_s は常数，右辺第1，第2項は転位の移動抵抗，第3項は転位の核発生に寄与をあらわす．この機構によれば塑性仕事量は先在転位の数にはよらず格子自体の特性によって定められる．

両者の機構を比較すれば，まず前者すなわち既存転位の移動による機構の場合には，(4) 式によればクラックの進行速度 V が限界速度すなわち Reyleigh 波の速度 Vc の 1/100 程度より遅い場合にのみ問題になる．また交叉すべりによる転位の増殖機構を考慮に入れてもこの結論は大きくは変らない[48]．従ってこの理論によれば一度高速度 $V>Vc/10$ で伝播を開始したクラックは高温でも停止させることが出来ない．これに比較して，後者すなわち転位ループの核発生の場合にはクラックの速度が大きくても高温では p は大きくなり得る．鉄単結晶の実験結果によればクラック速度が数百米/秒の場合に高温 100～300°C で破面付近に形成される転位は核発生によるものであることが示された[45,51]．

すなわち厚さ 1·4mm，巾 40mm の純鉄単結晶の一端に切欠を付し液体窒素温度に冷却し，他端を約 350°C に加熱して引張試験を行なった．低温側に発生したクラックは約 300°C の付近で停止させられる．つぎに破面付近に発生した転位分布を etch pit 法により測定した結果を Photo. 3, Fig. 4 に示す．Fig. 4 に見られるように 100～200°C の領域では転位密度は初期転位密度の 100～1000 倍程度大きな値を持ち，またこのような高い転位密度の変形層は先在転位の平均間隔程度の薄い層内に局限されている．一方クラックの伝播速度はこの領域で

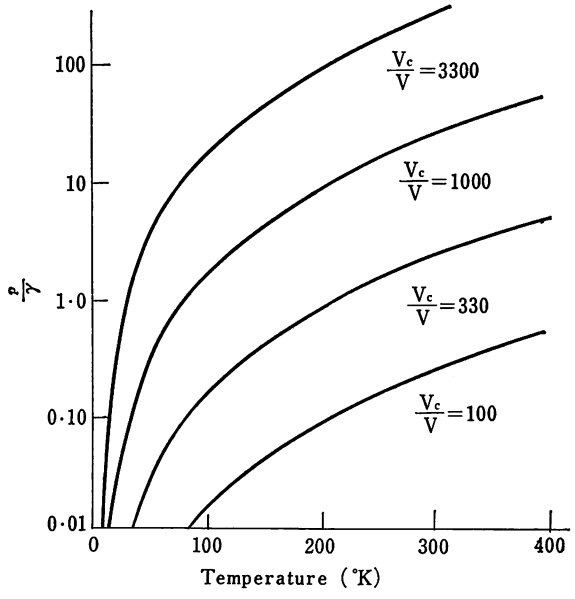

Fig. 3. Plastic work associated with the propagation of cleavage crack, calculated by Tetelman[48] using equation (4). Plastic work is caused by movement and multiplication of pre-existing dislocations near the tip of the crack.

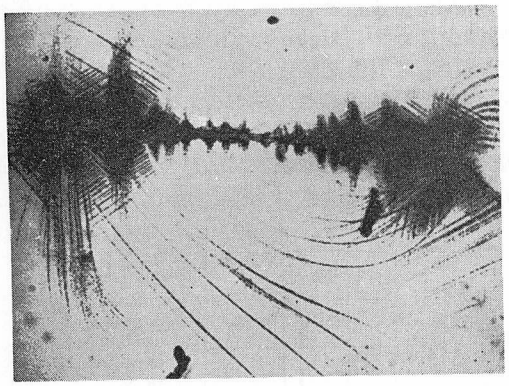

Photo. 2. Distribution of dislocations around a crack in an Fe-3%Si single crystal cathodically charged with hydrogen. Tetelman[48].

ほゞ 300m/sec$>Vc/10$ 程度の値を持つ．Fig. 5. これらの事実からクラックの先端に発生する塑性変形は転位の核発生によることが推論される．式 (4) より核発生の活性化エネルギーは $k_s\sigma_{th}(\tau_{th}/\sigma_{th}-\tau_{max}/\sigma_{max})$ と表わされるが Fig. 4 よりこの量はほゞ 0·20 eV の値を持つことが解る．従って推定値[18] $k_s\sigma_{th}\simeq 1\cdot 14$ eV を用いて $(\tau_{th}/\sigma_{th})=1\cdot 2(\tau_{max}/\sigma_{max})$ の評価が得られる．なお水素吸収により発生した 3% Si-Fe の破面についてもクラック速度の大なる部分では上述と同様のものと推定される塑

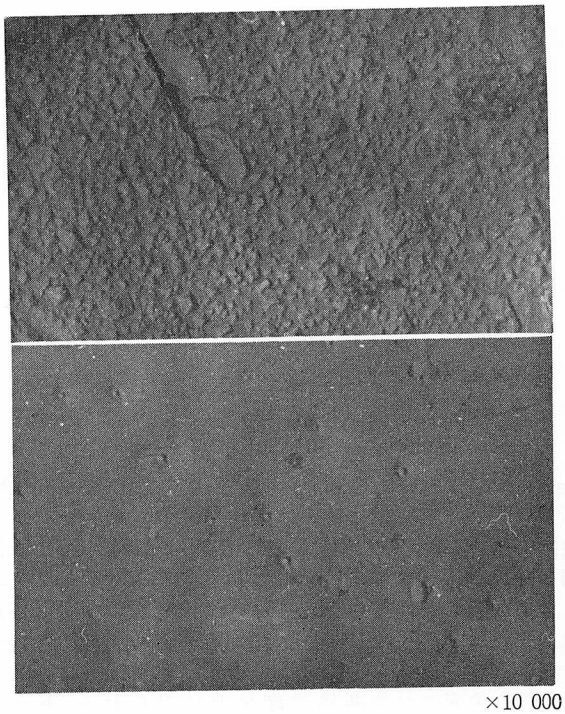

×10 000

Photo. 3. Etch-pit patterns of a surface cleaved at a temperature of about 100°C. Kitajima[45].
a) Surface as cleaved.
b) Surface after removing a 3μm layer.

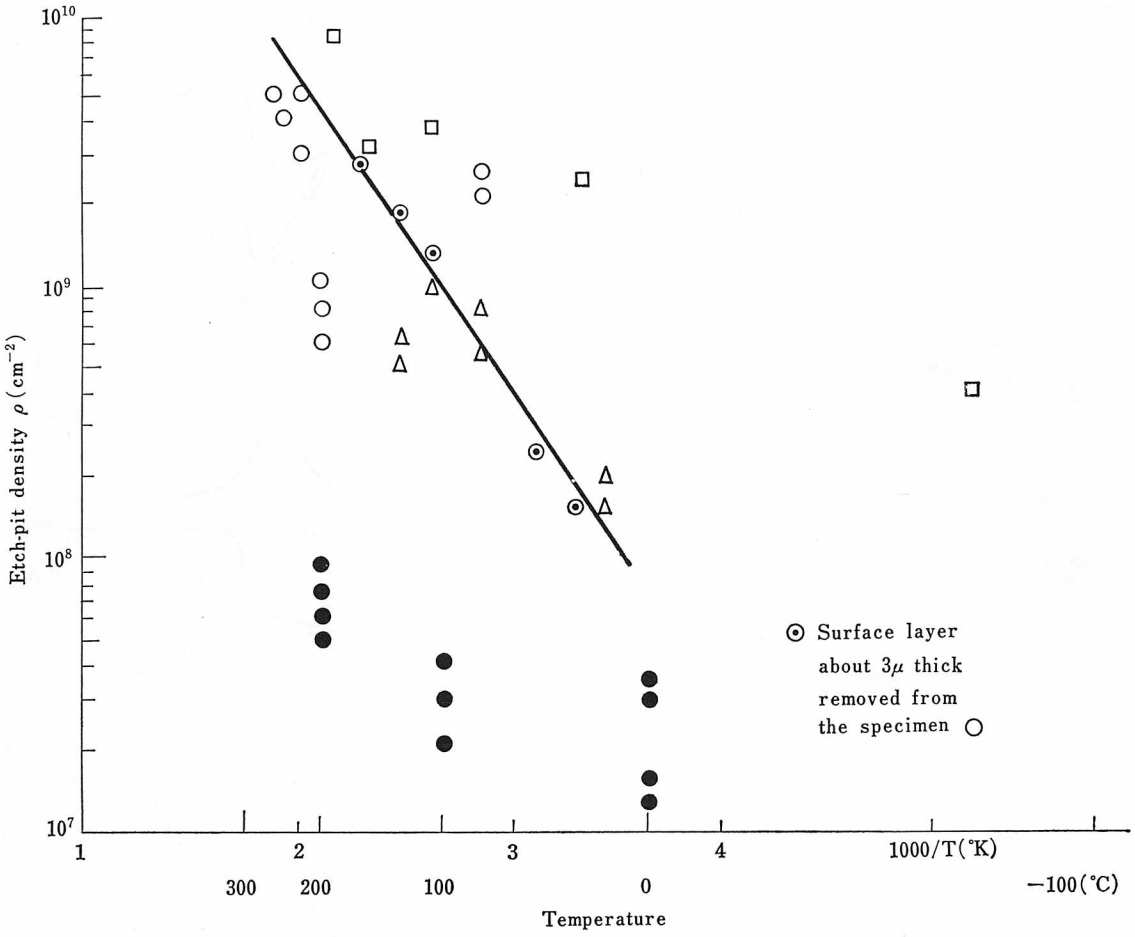

Fig. 4. Etch pit densities observed on the cleavage surface of iron single crystals, after Kitajima[45,51]

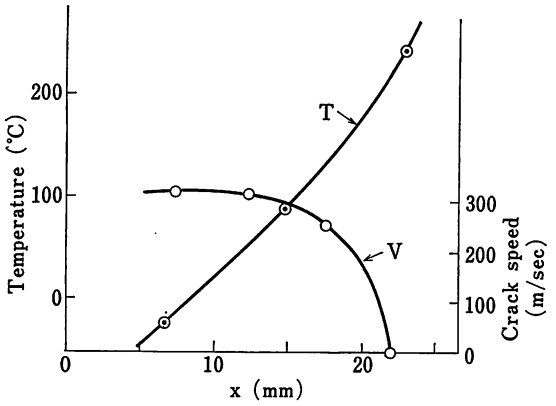

Fig. 5. Crack speed in single crystal of iron. Kitajima.[51]

性変形が見られる．Photo. 2. なお低温 <0°C では微細な双晶を含めて多数の双晶が核発生によって生じており，それらの塑性仕事量への寄与は大きいことが示される．なおまた高温では破面には流れ模様を欠き，きわめて滑らかな一見延性破面に似た様相を示すが，これは多結晶鋼の破面につき遷移温度付近に見られる ductile cleavage[52] および液体窒素温度で破断させた 9% Ni 鋼に見られる延性状の破面[53] に関連するものと言えよう．

3.3 析出物を含む鉄の脆性

炭素鋼では炭化析出物の大きさおよび形状の脆性に及ぼす影響がきわめて大きい[54]．微量の炭素 (0·02～0·04 %) を含む場合でも炉冷試料では粒界に炭化物が，また粒内には粗大な板状炭化物が析出しており，クラックは多くの場合それらより発生する[55,56]．Fig. 6, 7. これに比較して Mn を含む場合には炭化物は粒状になり脆性への影響は少ない[55]．Hahn ら[57] は炭素鋼につき種々の温度で行なった引張試験と試料内に停止したミクロクラックの分布とを対応させて調べており，それによればミクロクラックの密度は遷移領域に集中している．Fig. 8.

一般に純鉄や水中急冷鋼，Mn を多く含む鋼では遷移温度は低く遷移領域は狭い -純鉄型-．これに比較して

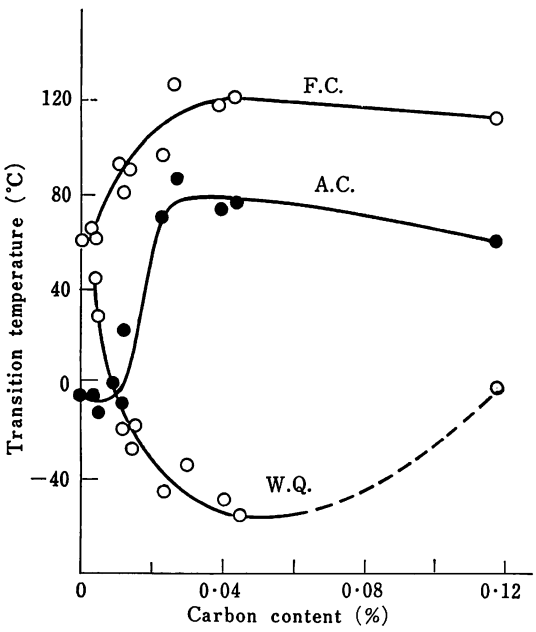

Fig. 6. Transition temperature of iron-carbon alloys measured with Charpy impact. W.Q. , water-quenched specimens, A.C. ; air-cooled specimens, F.C. ; furnace-cooled specimens. Intergranular fractures can be observed with carbon contents under 0·005%. Allen[55].

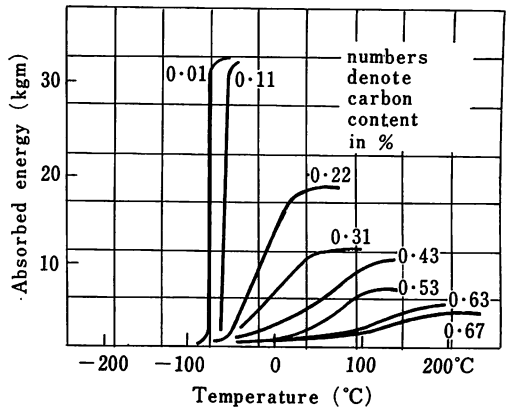

Fig. 7. Effect of temperature and carbon content of iron-carbon alloys on energy absorbed in Charpy test, after Rinebolt[54].

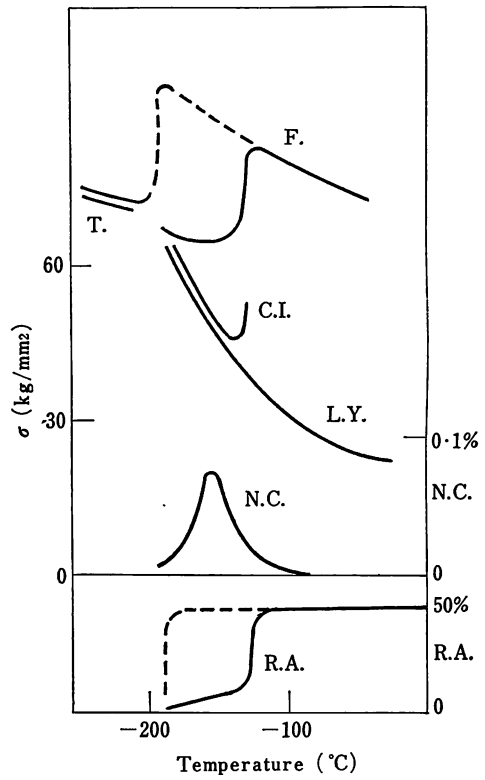

Fig. 8. Simple tensile test of low-carbon steel, Hahn et al[57]. Steel E: 0·22% C, 0·36% Mn, furnace cooled from 1250°C with a grain size of 0.106 mm. F. = fracture stress; T. = twinning stress; C.I. = crack-initation stress; L.Y. = lower yield stress; N.C. = ratio of number of cracks stopped within the grain to number of grains ; R.A.=reduction of area. The dotted line indicates the estimated characteristics of pure iron based on experimental data obtained on Steel M with 0·16% C and 1·30% Mn.

炉中冷却炭素鋼では遷移温度は高く遷移領域は広く，また切欠敏感性すなわち三軸応力依存性はより大きい—析出物型— Fig. 7. 両者における機構の相違は前述の実験事実をも考慮に入れてつぎのように説明することが出来る．すなわち析出物型ではミクロクラックはすべり帯が析出物によりせき止められたところに発生するが，この場合ミクロクラックは析出物のまわりの応力集中，割れまたは析出物境界の剝離等によって純鉄型に比較してかなり低い応力で発生する．また純鉄型の場合とは異なり変形がかなり進んだ後にも加工硬化により流動応力が上昇すればミクロクラックを発生し得る．またクラックの発生応力が低いためクラックは大きく生長し得ないで通常粒内または粒界によって停止させられる．

Fig. 9に長さLのすべり帯の端に転位の集積によって発生したクラック，式 (1)，が種々の応力状態 (σ_{max}/τ_{max}) のもとで伝播する過程を示す．たゞし $p=p_0(Vc/V)$ としている．図中 ξ_{oc} を通る太線はクラックが無限遠方まで伝播し得る条件，式 (2)，を示し，これより小または大なる応力の下ではクラックは停止または再加速される．Fig. 9よりまず純鉄型ではクラックの発生応力は高いためにクラックは高速度で伝播し，粒界を貫通し得るものと考えられる．この場合に破壊の条件は粒内での伝播条件，式 (2)，により記述される．これに比較して析出物型ではクラックの発生応力は低いために，粒内で停止させられるか，または粒界を貫通し得ず粒界で停止させられる．この場合さらに変形が進み加工硬化により応力が増大すれば，停止クラックの先端の隣接粒子内に新たなクラックを発生し，クラックの伝播が開始される．この条件は定性的に粒界での Orowan の条件によって表わされる．

$$\sigma_f=\sqrt{\frac{Ep_b}{d}} \qquad (6)$$

こゝに p_b は粒界での塑性仕事量であり実験によれば 10^5erg/cm^2 程度の値を持つ[58)59)]．なお p_b の物理的内容については粒界での塑性変形の外にも粒界析出炭化物などクラックの発生を支配する要素にも関連している．

(2) および (6) 式を比較すれば前述の二つの型すなわち純鉄型と析出物型の破壊特性の相違を説明することができる．Fig. 10.

なおミクロクラックを発生し得る析出物の限界大いさはその形にもよるがほぼ 1μ 程度と推定されている．また高密度の析出物はクラック伝播への障害ともなり得る．

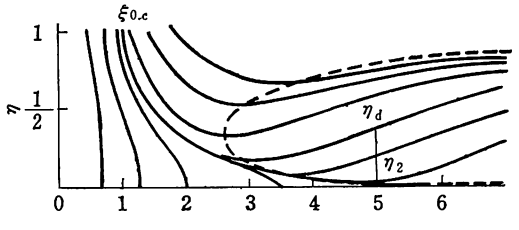

Fig. 9. Propagation of crack grown at tip of piled-up dislocations. Kitajima[18].

$\eta=\left(\frac{V}{V_c}\right)^2$, $\xi=\omega\left(3+\frac{c}{c_n}\right)$, $c_n=\frac{L}{2}\left(\frac{\tau_{max}}{\sigma_{max}}\right)$,

$\omega=\frac{\gamma}{2p_0}\left(\frac{L}{b}\right)\times\left(\frac{\tau_{max}}{\sigma_{max}}\right)\left(\frac{\sigma_{max}}{\sigma_G}\right)^2$, $\sigma_G{}^2=\frac{2E\gamma}{\pi(1-\nu^2)b}$, c=length of crack.

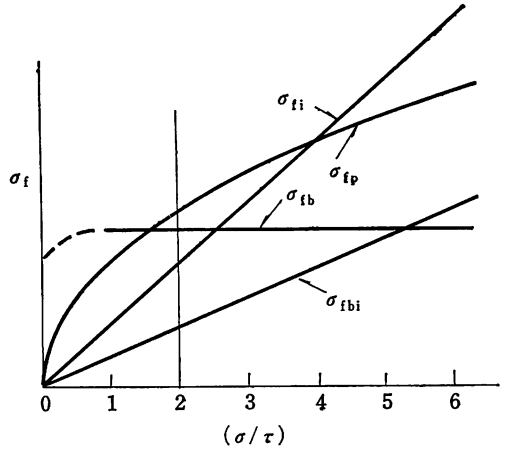

Fig. 10. Dependency of fracture stress σ_f on the triaxial ratio (σ/τ). σ_{fi}, σ_{fp}, σ_{fb} are fracture stresses calculated by equations (1), (2) and (6) respectively. σ/τ corresponds to 1 for the state of stress in torsion, 2 for simple tension and 6 for sharp notched specimens.

つぎに (2), (5) 式に示されるように結晶粒径 d の小さい程脆性破壊は起こり難いが，Mn, Ni は変態温度を低下させることにより，また AlN, NbC, VC 等の微細析出物 ($<0\cdot1\mu$) は変態および再結晶に際して結晶粒子の生長を阻害することにより d を小にする効果が著しい．

3.4 加工硬化および延性破壊

鉄鋼材料の流動応力の温度に依存する部分は前述のように主として，ラセン転位の格子摩擦によるものであるが，さらに転位間の弾性的相互作用に依存する加工硬化の成分を考慮しなければならない．これは転位密度の，従ってまた歪の平方根に比例するが[60)]より詳細には歪量および温度に依存する加工軟化（直線状転位組織よりもつれた転位の Cell 組織への遷移に伴う加工硬化率の減少．温度の高い程小さい歪で起きる．）を考慮に入れなければならない．鋼の引張試験の結果によれば加工硬化指数 n ($\sigma=A\varepsilon^n$)，従ってまた一様伸び ε_c ($n=\varepsilon_c$) は温度の低下とともにはじめゆるやかに増大しその後急激に減少する[61)]．

しかしながら断面収縮率および真破断応力は，これらとは別に延性破壊の条件によって決定される．延性破壊の発生は主として，粒界または粒内の介在物からその境界面での剝離によって起きることが報告されており[62)]大きな介在物からはより発生し易い．また発生の核となる介在物の大いさの限界は 1μ 程度と報告されているが[63)]，一般には応力に依存するであろう．歪の大きい領域では加工硬化率は前述のように小さくなるので完全塑性体の解析[64)]から推定されるようにすべりの場は局所的な領域に集中する傾向を持つ．このようにして一度発生した空洞はその端より局所すべりを誘発し，また空洞は幾何学的に引伸ばされて拡大し，さらに空洞同志の相互干渉によりその生長は加速される．すなわち不安定現象を伴って急激な破断につらなる．すべりの条件は最大剪断応力により支配されるが空洞の発生および生長の過程は静水圧的応力の成分の影響が大きく，圧縮応力の場合には延性を増し，張力の場合には延性を低下させる．

3.5 脆性破壊の巨視的取扱いにおける問題点

破壊の巨視的取扱いについては流動応力および破壊応力の概念に基づく連続体力学の近似による方法 -主として破壊の発生条件の解析に用いられる -といわゆる線型破壊力学の方法 -主として破壊の伝播の解析に用いられる- が知られている．これらは数学解析を援用して，観測される巨視的破壊特性より出来るだけ基本的な破壊の常数の導くことを目的としているが，一方前節までに述べた諸論はこれらの常数を微視的な立場より与えるものにほかならない．本節では両者を結ぶ際になお残されている二三の問題点について述べる．

3.5.1 脆性破壊の発生条件

脆性破壊の発生条件を純鉄型と析出物型に分けて考えるのは有用であろう．まず純鉄型では遷移領域は狭く破壊の発生条件は比較的に単純であると考えられる．これに比較して析出物型では遷移領域は広く，前述のように塑性変形および加工硬化の後に劈開クラックを発生し得るので，切欠試験片では応力や歪の解析がとくに困難になる．従来行なわれた塑性力学的解析との比較[65,66]によれば破壊の発生条件は最大垂直応力一定の条件に近いことが報告されているが，これは析出物型の場合の条件(6)に対応している．COD の測定もこの型の遷移領域における破壊条件を規定する方法として有効であると考えられる[67]．なお実際の破壊では，丸棒引張試験の場合には試験片の中心部に，また切欠試験片では切欠底付近(thumb nail) に延性破壊が最初に発生し，その先端から脆性破壊が発生している．これらの場合には延性破壊の発生に伴う応力集中および破断の際の衝撃が脆性破壊の発生に影響を持つことが考えられる．

3.5.2 脆性破壊の伝播条件

脆性破壊の伝播条件は実際の構造物等において重要であり，その特性の試験法も開発されている．そこでは塑性仕事量 p が重要な役割を持つ[68]．Fig. 11 に二重引張試験により求められた Kc 値の温度依存性を示す[69]．Kc は p と $Ep=Kc^2$ により結ばれる．Fig. 11 より p の活性化エネルギーを算出すると軟鋼 S25C より高張力鋼 HT80 に亘り，0·4eV～0·2eV 程度となる．もっともこれらの

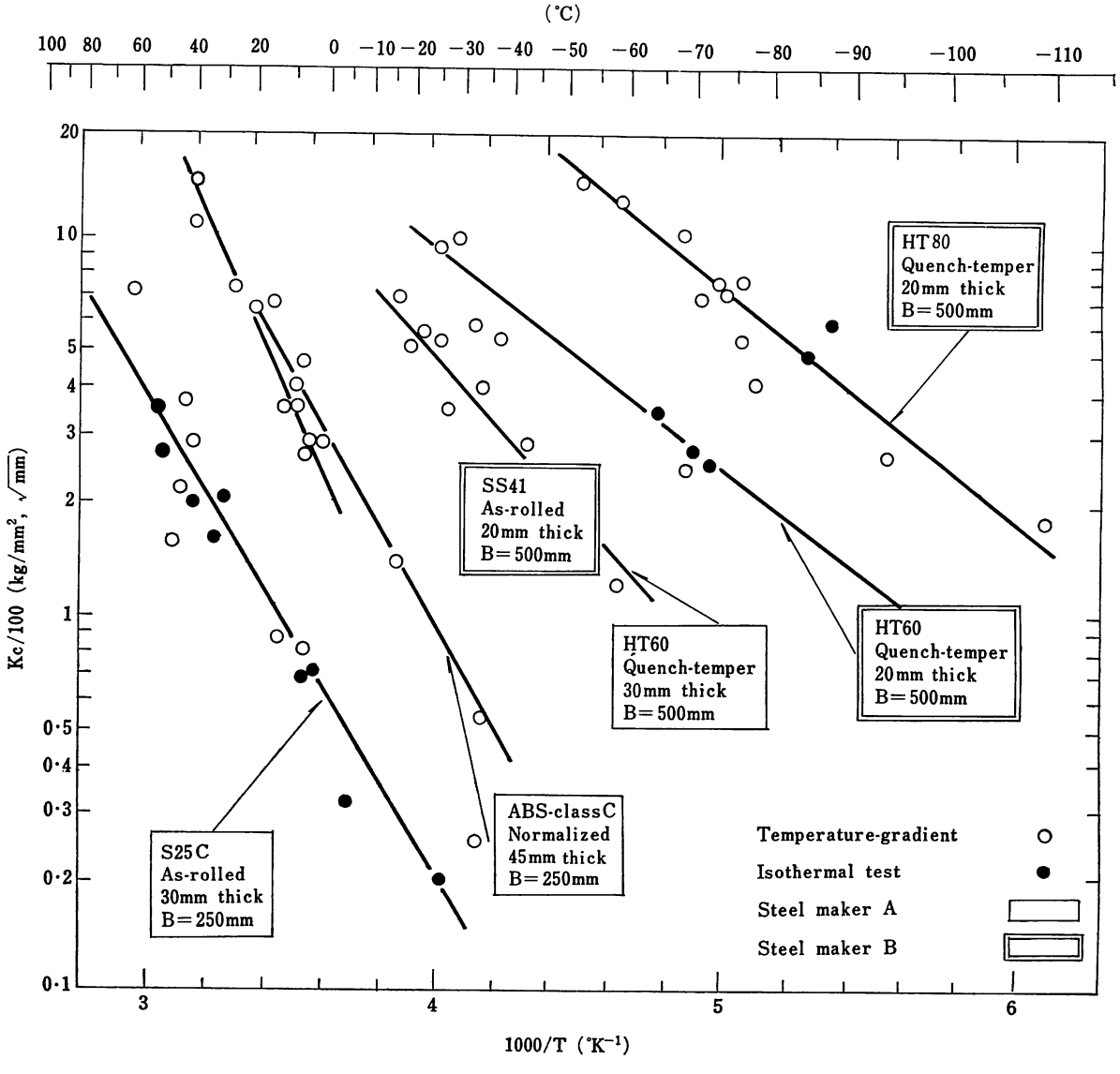

Fig. 11. Temperature dependency of K_c value of various steels obtained by double tension test. Koshiga.[69]

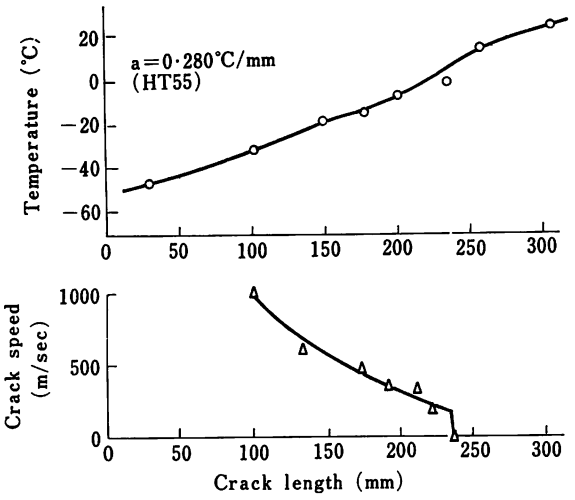

Fig. 12. Propagation velocity of crack measured on the steel plate with temperature gradient. Ikeda[70].

値はクラックの停止点における値であるから主として低速変形の活性化エネルギーに対応するものとして説明することが出来る．さて，脆性クラックの伝播を論ずるためには有限な速度を持つクラックについての動的な塑性仕事量の解析が重要と考えられる Fig. 12[70]．しかしながらその物理的内容については未知の要素がきわめて多い．いまクラックが 1000m/sec の速度で伝播する際に，変形層の厚さを 0·3mm，歪量を 3% として歪速度は 10^5/sec 程度となるが，このような高歪速度では通常の塑性変形とは様相が異なり，結晶粒内および結晶粒界では転位の核発生が行なわれていると考えられる．また鉄の衝撃変形の際に 10^5/sec を越える歪速度では主として双晶による変形が起きているという報告がある[71]．なお Hall[72] は進行破面の塑性仕事量を塑性波の伝播の立場より説明している．すなわち塑性変形領域の厚さ δ は

$$\delta = \frac{Cp}{C-Cp}\,\frac{C-V}{V}\,l$$

によって与えられている．ここに $C=\sqrt{E/\rho}$, $Cp=\sqrt{\frac{d\sigma}{d\varepsilon}/\rho}$ 塑性波速度，V クラック進行速度，l 破面に先行する塑性領域の巾である．

3.5.3 寸法効果と降伏現象

多結晶鋼の降伏は一般に Lüders 帯の発生とその伝播の過程より成るが，Lüders 帯の巾の大きさや，勾配を持つ応力場におけるその発生特性等については未知の部分が多い．一方丸棒の引張試験においても降伏応力に寸法効果の存在が知られており，切欠試験片においても切欠底の径や板厚が Lüders 帯の巾と同程度の場合にはこれらの寸法は切欠付近の応力の三軸状態に大きな影響を及ぼす[73,74]．また脆性破面の伝播についても shear lip の大いさは降伏条件を通じて Lüders 帯の巾に密接な関連を持っている．これらの諸要素は脆性破壊の寸法効果に説明を与えるものと考えられる．

文　献

1) Low, J.R., Jr.: Trans. AIME, **245** (1969), p. 2481
2) Griffith, A.A.: Phil, Trans. Roy. Soc., **A221** (1920), p. 163
3) Ludwik, Z.: Metallkde **15** (1924), p. 207. Davidenkov, N. N.: Dinamicheskaya Ispytania Metallov (1936), Moscow
4) Orowan, E.: Rep. Prog. Phys., **12** (1949), p. 185
5) Irwin, G.R.: Structural Mechanics, (Pergamon 1960, New York)
6) Zener, C.: Fracturing of Metals, (ASM 1948, Cleveland) 3
7) Mott, N.F.: Proc. Roy. Soc., **A220.** (1953), p. 1
8) Stroh, A.N.: Proc. Roy. Soc., **A223** (1954), p, 404
9) Cottrell, A.H.: Trans. AIME, **212** (1958), p. 192
10) Petch, N.J.: Phil. Mag., **3** (1958), p. 1089
11) Kitajima, K.: Rep. Res. Inst. Appl. Mech., Kyushu Univ., **5** (1957), p. 87
12) Low, J.R. Jr.: Progr. Mater. Sci., **12** (1963), p. 1
13) Kitajima, K.: Proc. 1st Intl. Conf. Fracture (JSSFM 1966, Sendai), p. 659
14) Hirsch, P.B., : Dislocation Dynamics (McGraw-Hill 1968, New York), p. 57, Phil. Mag., **8** (1963), p. 1895
15) Suzuki, H.: Dislocation Dynamics (McGraw-Hill 1968, New York), p. 679
16) Haasen, P.: Trans. JIM suppl., **9** (1968), XL
17) Stroh, A.N.: Advanc. Phys., **6** (1957), p. 418
18) Kitajima, K.: Proc. 1st Intl. Conf. Fracture (JSSFM 1966, Sendai), p. 647, 北島一徳，九州大学応用力学研究所所報 No. 19, (1962) p. 1
19) Cottrell, A.H., Kelly, A.: Endeavour, **25** (1966), p. 27
20) Brenner, S.S.: J. Appl. Phys., **27** (1956), p. 62
21) Hull, D.: Proc. 1st Intl. Conf. Fracture (JSSFM 1966 Sendai), p. 629, Phil. Mag., **161** (1969), p. 951
22) Mackenzie, J.K.: Thesis Bristol (1949), Seeger, A.: Handb. der Phys., **VII-2** (1958), p. 7
23) Cohen, J.B. et al.: Acta. Met., **10** (1962), p.894, Crussard, C.: Compt. Rend., **252** (1961), p. 273
24) Born, M.: Proc. Camb. Phil. Soc., **36** (1940), p. 160, p. 454
25) Kelly, A., Tyson, W.R., Cottrell, A.H.: Phil. Mag., **15** (1967), p. 567. Tyson, W.R.: Phil. Mag., **14** (1966), p. 925
26) Zwicky. F.: Z. Phys., **24** (1923), p. 131
27) Wakoh, S., Yamashita, J.: J. Phys. Soc. Japan, **21** (1966), p. 1712. Mott, N.F.: Adv. Phys., **13** (1964), p. 325
28) Johnson, R.A.: Phys. Rev., **134A** (1964), p. 1329
29) Chang, R.: Fracture (Chapman & Hall 1969, London), p. 306
30) 市川勲，水島三一郎：金属学会会報，**8** (1969), p. 384
31) Friedel, J. et al.: J. Phys. Chem. Solids, **25** (1964), p. 781
32) Hume-Rothery, W.: Progr, Material Sci., **13** No. 5 (Pergamon 1967, New York), p. 229
33) Leslie, W.C.: Trans. ASM, **62** (1969), p. 690
34) 鈴木秀次：本シンポジウム講演
35) Takeuchi, S. Yoshida, H., Taoka, T.: Trans. JIM **9** (1968), p. 715
36) Nakada, Y., Keh, S.: Acta Met., **16** (1968), p. 903
37) Sato, A.: Ph. D. Dissertation, Northwestern Univ. (1971), Proc. 2nd Intl. Conf. Strength Metal Alloys, Calif. (1970)
38) 飯井政博：金属学会，鉄鋼照射シンポジウム，昭 46, 6 月
39) 北島一徳：鉄鋼協会，鉄格子欠陥シンポジウム，昭 46, 10 月
40) Jolly, W.: Trans. AIME, **242** (1968), p. 306
41) Floreen, S., Hayden, H.W.: Trans. AIME, **239** (1967)
42) 北島一徳：破壊，結晶の強度 (朝倉書店，昭和 43) p. 231.
43) Terasaki, F.: Acta. Met., **15** (1967), p. 1057
44) Hull, D.: Acta. Met., **8** (1960), p. 11 Honda, R.: Proc. 1st Intl. Conf. Fracture (JSSFM 1966, Sendai) p. 615
45) Kitajima, K., Futagami K.: Electron Microfractography, ASTM STP No 453, (1969), p. 33.

第14回 材料強度と破壊国内シンポジウム, 昭44, p. 126
46) 鈴木秀次：鉄と鋼, **53**, **12** (1967), p. 1442
47) Friedel, J.: Fracture, Swampscott (MIT 1959, New York), p. 498
48) Tetelman, A.F.: Fracture of Solids, (Intersc. Publ. 1963, New York), p. 461
49) Gilman, J.J.: Proc. 1st Intl. Conf. Fracture, (JSSFM 1966, Sendai) p. 733
50) Gilman, J.J.: Trans. AIME, **209** (1957), p. 449
51) Kitajima, K.: Intl. Conf. Mech. Behav. Mater., Kyoto (1971)
52) Crussard, C., Borione, R., Plateau, J., Morillon, Y., Maratray, F.: J. Iron Steel Inst., **183** (1956), p. 146
53) 山本俊二, 高橋正道：鋼材の脆性破壊研究報告集, 学振 129 委, 昭 41, p. 209
54) Reinbolt, J. A., Harris, W. J., Jr., Trans. ASM, **44** (1952) p. 225
55) Allen, N.P.: J. Iron Steel Inst., **174** (1953), p. 108.
56) McMahon, C.J., Cohen, M.: Proc. 1st Intl. Conf. Fracture, (JSSFM 1966, Sendai) p. 779
57) Hahn, G.T., Averbach, B.L., Owen, W.S., Cohen, M.: Fracture, Swampscott, (MIT 1959, New York), p. 91
58) Averbach, B.L. : Proc. 1st Intl. Conf. Fracture, (JSSFM 1966, Sendai) p. 747
59) Yokobori, T.: Tech. Rep. Tohoku Univ., Vol. **28** (1964), p. 167.
60) Ashby, M.F.: Phil. Mag., **21** (1970), p. 399
61) 越賀房夫：鋼材の脆性破壊研究報告集, 学振 129 委, 昭 41, p. 383
62) Low, J.R.: The Fracture of Metals, Prog. Mater. Sci., **12** No. 1 (1963), p. 1
63) Roesch, L., Henry, G.: Electron Microfractography, ASTM STP No. 453, (1969), p. 3
64) Green, A.P., Hundy, B.B.: J. Mech. Phys. Solids, **4** (1956), p. 128
65) Hendrikson, J.A. et al.: Trans. ASM, **50** (1958), p. 656
66) Knoff, J.F.: Fracture, Brighton, (Chapman & Hall 1969, London), p. 205
67) Kanazawa, T., Machida, S., Momota, S., Hagiwara, Y.: Fracture, Brighton, (Chapman & Hall 1969, London), p. 1
68) 金沢武：金属材料の強度と破壊 (丸善, 昭 39), p. 197
69) 越賀房夫, 今沢理, 竹花荘治：造船協会論文集第 114 号, (1963)
70) 池田一夫：鋼材の脆性破壊研究報告集, 学振 129 委, 昭 41, p. 254
71) Rhode, R.W.: Acta Met., **17** (1969), p. 352
72) Hall, E.O.: Mech. Phys. Solids, **1** (1953), p. 227
73) Rosenfield, A.R., Pai, P.K., Hahn, G.T.: Proc. 1st Intl. Conf. Fracture, (JSSFM 1966, Sendai), p. 223
74) 栖原二郎, 栖原寿郎, 北島一徳, 辻勇：第二次鉄鋼研究委報告, 昭 38

討論 pp. 353–358 参照

Thermomechanical Treatment of Steels

M. J. May D. J. Latham

The Corporate Laboratories of
the British Steel Corporation

ABSTRACT

Several forms of thermomechanical treatment that have been applied to high- and low-alloy steels are described and the potential benefits of such treatments in terms of microstructural changes highlighted. The property levels that can be achieved by such treatments as ausforming (LTMT), controlled rolling (HTMT), isoforming and warm working in relation to those obtained by conventional heat treatment have been given for typical high- and low-alloy steels.

The metallurgical factors influencing toughness and ductility, as conventionally measured, are considered and the importance of mechanical test factors emphasized in relation to assessing the significance of property improvements arising from thermomechanical treatments.

The final part of the paper highlights the areas for potential application of thermomechanical treatments and emphasizes the need for information to facilitate design of suitable forming equipment for exploiting the potential of thermomechanical treatments over a range of temperatures as a means of producing various product forms with enhanced property combinations.

1. INTRODUCTION

In the last decade considerable research effort has been devoted to identifying the potential of controlled processing during the mechanical working of steels as a means of improving the combination of properties attainable in both high-alloy and low-alloy steels. Laterly the main objective has been to improve toughness and ductility at a given strength level over that obtainable by more conventional heat treatment.

Over the years, the term thermomechanical treatment has come into use to describe the controlled processing of materials to combine mechanical working with improvements in the mechanical properties of the final product. In general, these concern mechanically working a steel whilst, either in a stable or metastable austenitic condition prior to transformation, during transformation, or, as transformed from austenite, in order to promote microstructural modifications and refinement and/or interactions between dislocations and fine precipitates. Historically, ausforming was the first technique to which this generic title could be specifically applied. This involves large deformation of metastable austenite and hence can only be applied to steels having appropriate transformation characteristics. More recently, several alternative processes fitting controlled deformation schedules to the transformation characteristics of particular steels have been developed. The advantages of such treatments in terms of property combinations are reviewed in this paper and the microstructural factors responsible, highlighted.

The initial objective in thermomechanical treatment was as a means of producing ultra-high strength levels in finished products. However, it was soon appreciated that through use of thermomechanical treatments it was possible to increase both ductility and toughness of a wide range of finished and semi-finished products. More recently, attention has been focussed on utilizing controlled thermomechanical treatments as a means of improving ductility and toughness by, either refinement of the austenitic grain size, or, the production of a subgrain structure in the ferrite and more effective use of alloying elements for precipitation strengthening. In general, problems in the fabrication and use of steels arise from insufficient ductility or toughness. Consequently, it is not surprising, with the trend towards the application of higher strength steels, that thermomechanical treatments are now being exploited with this objective in view. Examples are given of typical property responses of steels to thermomechanical treatments and some of the results of recent studies at the British Steel Corporation Corporate Laboratories (formerly Bisra) highlighted.

It is important, however, to identify what is understood by improvement in ductility and toughness and the relevance of this in relation to a subsequent working operation or performance in service for a specific application. In the majority of studies involving thermomechanical treatments, improvements in ductility relate to increase in the total elongation or reduction of area at fracture of a uniaxial tensile specimen and improvements in toughness to a decrease in the impact transition temperature. These criteria are useful for laboratory investigations. However, one must not lose sight of the fact that the mechanical constraints of such tests are arbitrary and may suggest improvements

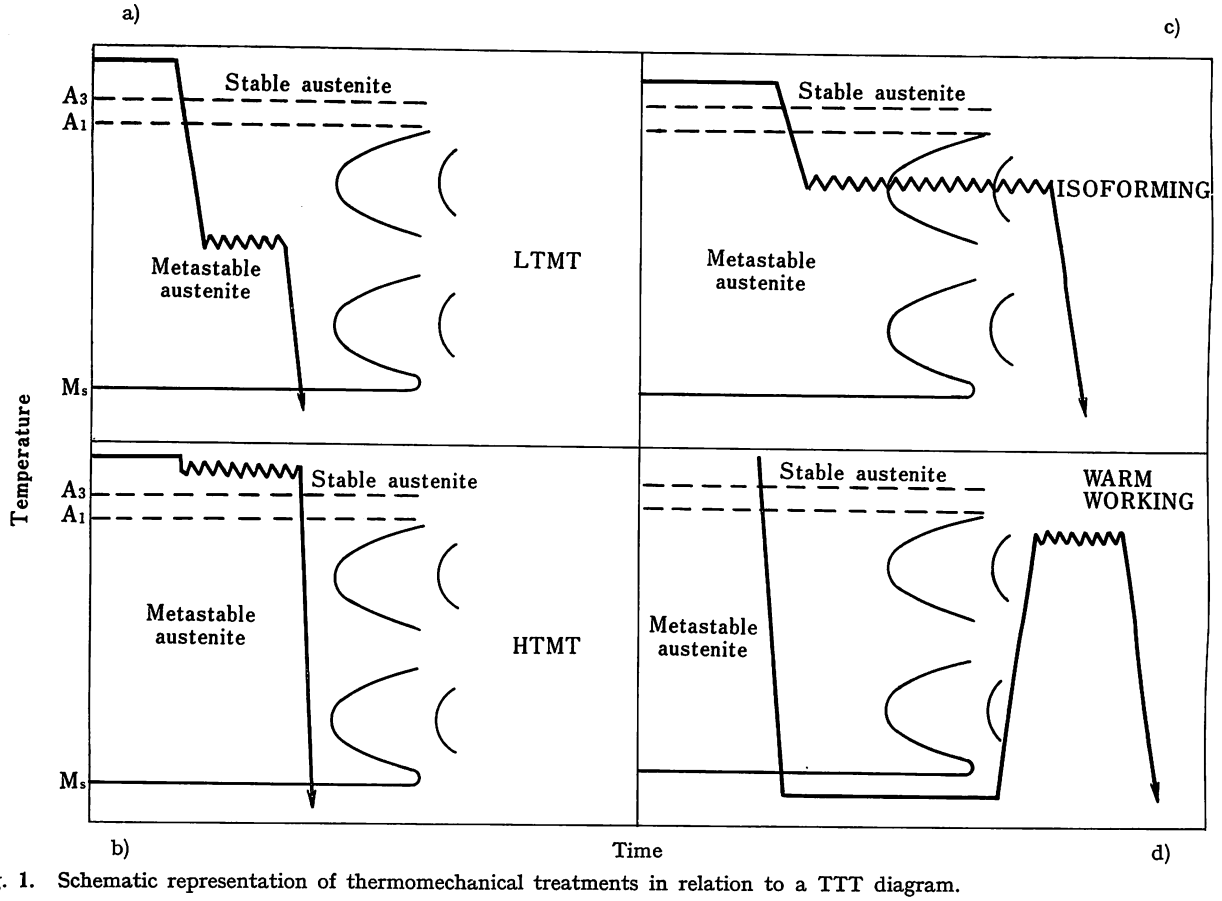

Fig. 1. Schematic representation of thermomechanical treatments in relation to a TTT diagram.

in notch ductility that are not realizable in practice, due to the different mechanical constraints imposed by a subsequent working operation or service application. These aspects are discussed and in the final part of the paper the likely realizable commercial potential for thermomechanical treatment identified.

2. INFLUENCE OF STEEL COMPOSITION AND PROCESS VARIABLES

With high- and medium-alloy steels several forms of thermomechanical treatment (TMT) have been adopted involving deformation of stable or metastable austenite prior to or during transformation. The type of treatment feasible is dependent on the transformation characteristics of the steel and can be carried out isothermally or over a range of temperatures. Several treatments involving deformation after transformation have also been studied and these are also considered. Fig.1 a)-d) shows schematically in relation to a TTT diagram the principle thermomechanical treatments investigated.

2.1 Deformation before transformation

2.1.1 Low-temperature thermomechanical treatment

This was one of the first treatments studied and consists of quenching a steel to a temperature in the metastable austenite bay and deforming a considerable amount prior to quenching to ensure a martensitic structure followed by tempering. Such a treatment has been termed ausforming and for this a steel must have a TTT diagram with a deep metastable austenite region. Consequently, most steels suitable for ausforming contain chromium and molybdenum, which lead to the formation of stable fine carbides at the deformation temperature (400 to 550°C) as does vanadium.

Control of the process variables such as austenitizing treatment, deformation temperature, and total percentage deformation and deformation schedule all influence the properties obtained for a given steel[1-3]. The tensile properties usually, but not always, improve as the deformation temperature is reduced, provided transformation does not occur during ausforming and optimum strengthening often requires deformations in excess of 60% reduction of area. For practical considerations it is necessary to avoid very low working temperatures in order to reduce the forming load.

By LTMT, it is possible to obtain improved strength without deterioration in ductility or impact properties or alternatively, for a given strength level, ausformed steels can be significantly tougher than conventionally treated steels. These improvements result from the deformation of the austenite leading

to precipitation and interaction of fine alloy carbides with dislocations which are retained during transformation to martensite. The resultant martensite contains not only a high dislocation density through transformations alone, but also that part inherited from low-temperature working[4]. On subsequent tempering, additional precipitation of carbides occurs in a fine spheroidal form and this results in improved impact properties, due to the absence of coarse lath-shaped carbides.

2.1.2 High-temperature thermomechanical treatment

This treatment differs from LTMT in that stable austenite is deformed at higher temperatures, as schematically represented in Fig. 1b), and involves deforming steels at temperatures just above Ac_3, followed by direct quenching and tempering. The maximum strengthening effect of HTMT depends on the ability to impart large deformations followed by quenching to prevent recrystallization[5]. The optimum schedule for HTMT is very much dependent on the steel composition and steels that recrystallize slowly such as some silicon-containing steels show marked improvements in properties after this type of treatment[6]. On the other hand, certain alloys recrystallize rapidly during deformation and the benefit of austenitic grain refinement is not so great[7], the incubation time and rate of recrystallization depending on the temperature of deformation.

Alternative treatments covered by Russian workers have also included deforming the steel in the temperature range between Ac_3 and Ar_3 or Ac_1; however, in the latter case the accelerated transformation of austenite to ferrite-carbide structures must be avoided or controlled[8]. HTMT can also be incorporated into a hot rolling schedule where the steel undergoes deformation on a falling temperature scale between 1000°C and 800°C. During such a controlled rolling sequence full or partial recrystallization occurs between rolling passes dependent on the temperature, degree of deformation and steel composition. The properties are influenced by the temperature, and amount of deformation of the final passes. The potential for increase in strength by HTMT is considerably less than by LTMT; nevertheless, the improvement in ductility and toughness can be considerable. In addition, as HTMT involves deformation at higher temperatures it is comparatively easy to apply on existing plant. Hence in recent years it has been adopted more readily as a commercial practice. The reasons for the improvement in properties by HTMT are not completely understood. Considerable refinement of the austenitic grain size can occur resulting in a fine martensitic structure on quenching. Carbide precipitation can take place during deformation at the lower temperature and high-alloy steels containing chromium, molybdenum, vanadium and niobium are particularly responsive to treatment, leading to increase in strength. However, with a reduced alloy content ($\sim 2\,^1/_2$wt% alloy addition) some steels although leading to elongated structures do not show marked strength improvements.

2.2 Deformation during transformation

Deformation during transformation to ferrite-pearlite has been applied to certain low-alloy steels, in order to modify the morphology and distribution of the cementite and prevent formation of lamellar pearlite which is known to be detrimental to toughness. The deformation schedule used is shown schematically in Fig. 1c) and has been termed isoforming[9]. The steel is quenched to an intermediate temperature in the region of the pearlite nose, deformed during complete transformation and air cooled. The characteristic feature of the microstructure is the formation of a very fine subgrain size together with small spheroidal carbides [9–10]. The deformation temperature must be high enough for polygonization to occur, normally between 600°C and 700°C, and deformations in excess of 60% are necessary to achieve a satisfactory microstructure. Small improvements in strength may be obtained by isoforming depending on the final subgrain size, but the main advantage is the considerable increase in toughness with greatly reduced impact transition temperatures.

Deformation of steel during isothermal transformation to bainite leads to a marked increase in strength but with a detrimental effect on the ductility and toughness[11].

2.3 Deformation following transformation

The properties of certain steels can also be improved by deformation following transformation, such treatments involve dynamic strain aging and warm deformation of martensitic and ferrite-pearlite steels.

In the former case, a steel may be deformed up to 2% between 150°C and 300°C at which temperatures aging occurs during straining. It has been reported, however, that by such treatments the fracture toughness is decreased[12]. By warm deformation of martensitic steels tensile strengths of 300 kg/mm² coupled with 30% reduction of area can be achieved, but in general such treatments mainly result in increased strength without an appropriate increase in ductility or toughness[13,14].

Working annealed ferrite-pearlite steels in the temperature range 250 to 300°C can lead to higher yield and tensile strengths compared with cold working followed by aging. However, deformation

Table 1. Mechanical properties for 5% Cr steel.

Details of TMT			Mechanical test data				
Austenitizing treatment	Deformation conditions	Tempering treatment	HV 30	Tensile strength (kg/mm^2)	Elongation (%)	Reduction of area (%)	Cv at 20°C (kgm)
1050°C × 1 hr	Conventionally rolled OQ (21 mm dia)	200°C × 1 hr	590	200	13	45	2·6
	Roll to FT 740°C, OQ (21 mm dia) (HTMT)	200°C × 1 hr	604	210	10	31	1·5
	Q to 480°C + WW 55% AC (LTMT)	200°C × 1 hr	738	247	9	19	0·8

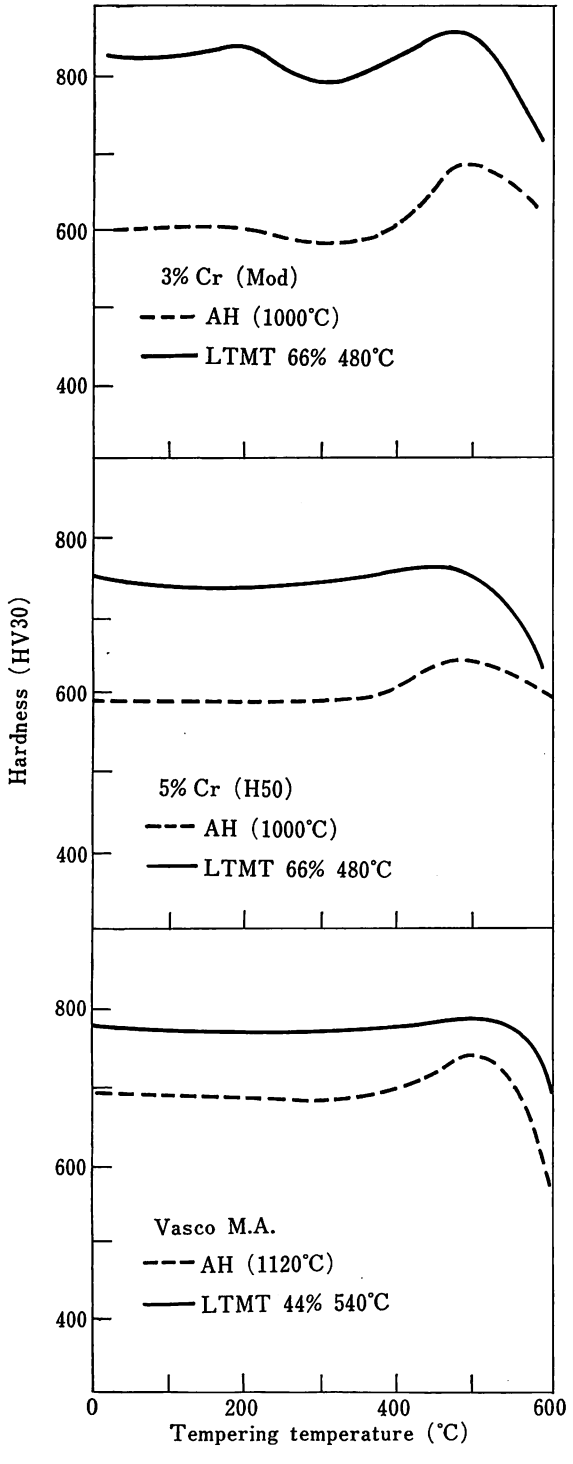

Fig. 2. Tempering response of ausformed (LTMT) tool steels.

in this temperature range also results in a decrease in impact resistance and ductility[15,16]. Useful property combinations can nevertheless be developed by working at higher temperatures and in the case of a spheroidized steel at 600°C can give a structure similar to that obtained by isoforming with similar properties[14].

Warm working of fully transformed steels at higher temperatures but below the onset of recystallization (below Ac_1) (Fig.1d)) can give improvements in strength depending on the degree of reduction. For annealed steels, capable of undergoing cold working, warm deformation offers no advantage in increasing the strength. However, strength improvements can be considerable with acicular ferrite structures containing secondary hardening additions[17].

The main advantage of warm working transformed steels is the markedly superior toughness compared with that after cold working or conventional heat treatment for equivalent strength levels. This is to a large extent controlled by the onset of recovery in the ferrite and the formation of subgrain structures[18]. This aspect is considered in more detail later in the paper.

3. TYPICAL PROPERTY RESPONSE OF STEELS TO THERMOMECHANICAL TREATMENTS

3.1 Tool steels

As has already been mentioned, the initial objective of ausforming (LTMT) was to increase the strength and hardness of alloy steel compositions within the range 0·3–0·6% C with 3–13% Cr and additions of molybdenum, vanadium and tungsten as used for punch and die tools. By LTMT it was possible to replace high-speed steels as punches (750–800 HV) and dies (650–700 HV)[17]. The typical tempering response of satisfactory ausformed tool steels is shown in Fig. 2 for a modified 3%Cr steel, 5%Cr and Vasco M.A. indicating little or no evidence of secondary hardening and enhanced resistance to overtempering.

The 5%Cr hot-work die steels have been studied in detail. The increase in strength after HTMT was

Table 2. Mechanical properties for En. 30B steel.

Details of TMT			Mechanical test data				
Austenitizing treatment	Deformation conditions	Tempering treatment	Lower yield strength or 0·2% proof stress (kg/mm²)	Tensile strength (kg/mm²)	Elongation (%)	Reduction of area (%)	Cv at 20℃ (kgm)
1200℃×1/2 hr	RH 1 hr 830℃, OQ (21 mm dia)	200℃×1 hr	139·2	173·6	14	54	2·5
		400℃×1 hr	132·3	174·0	—	—	1·6
	Roll to FT 850℃, OQ (21 mm dia) (HTMT)	200℃×1 hr	138·6	178·1	17	57	—
		400℃×1 hr	127·9	146·1	14	52	—
980℃×1 hr	Q to 500℃+WW 70% reduction AC (16 mm dia) (LTMT)	200℃×1 hr	146·1	226·0	12	37	2·1
		400℃×1 hr	163·0	176·9	10	38	2·8

Table 3. Mechanical properties for carbon-manganese-niobium and carbon-manganese-vanadium-silicon steels.

Details of TMT				Mechanical test data				
Steel	Austenitizing treatment	Deformation conditions	Tempering treatment	Lower yield strength or 0·1% proof stress (kg/mm²)	Tensile strength (kg/mm²)	Elongation (%)	Reduction of area (%)	Cv at 0 ℃ (kgm)
0·07% C 1·46% Mn 0·09% Nb	1250℃×1 hr	Rolled to FT 950℃, WQ (21mm dia) (HTMT)	600℃×1 hr	50·7	79·7	27	73	20·0
				68·7	76·5	30	76	11·1
		Rolled to FT 750℃, WQ (21 mm dia) (HTMT)	600℃×1 hr	52·6	80·6	28	74	24·9
				62·8	69·8	31	76	23·5
		Rolled to FT 1000℃, AC (21 mm dia) RH 950℃ WQ	600℃×1 hr	33·7	46·6	39	74	28·8
				39·4	46·9	49	82	28·5
0·10% C 1·52% Mn 0·72% Si 0·16% V	1250℃×1 hr	Rolled to FT 950℃, WQ (21 mm dia) (HTMT)	675℃×1 hr	76·5	116·4	19	41	2·8
				60·5	69·3	30	79	25·7
		Rolled to FT 750℃, WQ (21 mm dia)	675℃×1 hr	63·9	109·0	18	58	9·8
				57·2	65·2	38	80	27·9

not as pronounced as by LTMT but the ductility was improved as shown in Table 1 [19]. LTMT can lead also to large improvements in the fatigue endurance limit[20]. Further improvements in strength of ausformed H11 steel have been obtained by strain aging. Up to 2% strain at temperatures up to 320°C led to increases in the yield strength of from 30–67 kg/mm² [21].

Only a limited amount of work has been concerned with the application of LTMT to high-speed steels. Tamura et al[22] found that ausforming flat specimens of T1 steel up to 50% deformation at 500°C did not increase the strength but considerably improved the ductility. Additions of cobalt supressed this effect. A more marked response was obtained with a 6% W–4% Mo–4%Cr–2% V steel and there was no secondary hardening peak.

3.2 Engineering steels

The mechanical properties of thermomechanically treated engineering steels depend on the transformation characteristics and the processing conditions. In general low-alloy steels up to En. 24 (0·40%C–0·60% Mn–0·25% Si–1·20%Cr–1·5%Ni–0·30%Mo) do not have a sufficiently wide metastable bay for LTMT; however, steels of this type and also those with increased alloy content can show improved properties by HTMT. Table 2 shows mechanical property data for En. 30B (0·32%C–0·49%Mn–0·20 %Si–1·22%Cr–4·1%Ni–0·25%Mo) steel conventionally treated and after both LTMT and HTMT. The combination of properties resulting from HTMT is not significantly different from those obtained by conventional treatment.

The low-alloy steels that are not amenable to LTMT can be worked at higher temperatures to advantage, and more recent studies at the British Steel Corporation Corporate Laboratories have concentrated on investigating the potential of more simplified thermomechanical treatments on these steels. Such treatments known as controlled rolling, in which a steel undergoes deformation on a falling temperature scale between 1000°C and 800°C followed by controlled cooling, have formed the

basis for the development and manufacture of high-strength structural steel strip and plate. The controlled rolling of low carbon-manganese steels to low finish rolling temperatures improved the mechanical properties through ferrite grain refinement. This effect is considerably enhanced if strong carbide forming elements such as niobium and vanadium are added to the base composition and if the steel is quenched directly after controlled rolling (akin to HTMT) and subsequently tempered to promote precipitation hardening. Typical properties are shown in Table 3.

More recently, Dulieu et al[23] have subjected a range of 16 low-alloy steel grades to a controlled rolling schedule using up to 12 passes on a three-high merchant bar mill. Deformation occurred mainly in the range 950–750°C and after the final rolling pass bars were directly quenched in either water or oil. The results of several rolling trials on an En. 16 (0·40%C–0·23%Si-1·42%Mn–0·20%Mo) steel to establish the effect of billet soaking temperature and finish rolling temperature on properties after quenching and tempering are shown in Fig. 3. The strength after tempering at 550°C was relatively insensitive to start and finish rolling temperature; however, the fracture energy at 20°C showed a gradual improvement. Both strength and toughness were considerably improved over that obtained by conventional treatment. The properties of the material directly quenched and tempered at 200°C were comparable with those obtained in more highly alloyed nickel steels.

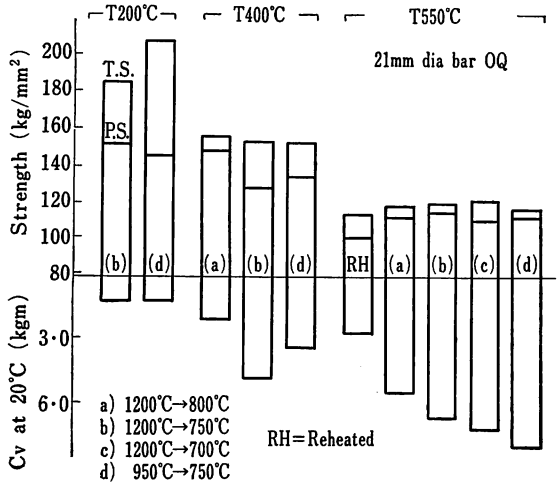

Fig. 3. The effect of roll-finishing temperature on the properties of En. 16 directly quenched and tempered.

From the mechanical property data it was concluded that the effect of direct quenching after controlled rolling (HTMT) as compared with conventional treatments, generally produced an increase in the yield strength of tempered martensitic steels. The magnitude was greatest in simple carbon and low-alloy steels and the relative strength increment decreased with increasing alloy content. This was primarily a reflection of appreciable differences in microstructure between the conventional and directly quenched conditions for the low hardenability steels. In many cases HTMT also resulted in increased impact resistance. Considerable latitude could be exercised in the rolling schedule, the basic requirement was for a minimum of 40% reduction at around 800°C but not necessarily achieved in a single rolling pass. The impact properties were, however, raised by increasing the deformation at the lower temperatures.

In ferrite-pearlite steels a considerable increase in toughness has been shown to be possible by thermomechanical treatment during transformation. The improvement in properties by isoforming is due to the formation of a very fine subgrain size through recovery of the ferrite, together with the formation of a finely dispersed spheroidal carbide precipitate. Alternative means of producing similar refined structures have been investigated using an En. 18 (0·48% C-0·25% Si-0·85% Mn-0·98%Cr)

Table 4. Treatments and mechanical properties for a 0·48 % C–0·98% Cr En. 18 steel.

Details of TMT			Mechanical test data					
Austenitizing treatment	Deformation conditions	Tempering treatment	HV 30	Lower yield strength or 0·1% proof stress (kg/mm²)	Tensile strength (kg/mm²)	Elongation (%)	Reduction of area (%)	Cv at 20°C (kgm)
950°C × 1 hr	Isoformed, 70% reduction at 600°C	—	312	86·0	104·3	25	63	22·1
		700°C × 1 hr	264	66·8	80·0	25	68	15·3
	Isoformed, 70% reduction at 550°C	—	343	111·7	124·0	17	53	3·0
1200°C × 1 hr	Hot rolled and WQ	600°C × 1 hr	—	101·4	113·1	17	50	3·3
		700°C × 1 hr	—	66·1	81·9	25	65	10·9
	Hot rolled and AC	—	333	62·4	109·6	15	32	0·7
950°C × 1 hr	Deformed, 70% reduction at 450°C, AC (LTMT)	—	394	115·6	132·6	11	24	1·1

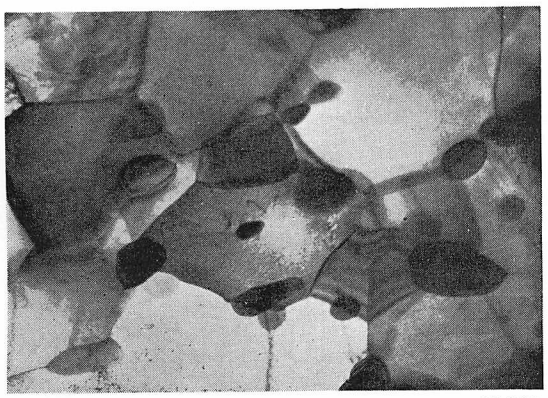

×25 000

Photo. 1. Thin-foil micrograph of 1% Cr steel isoformed at 600°C.

×25 000

Photo. 2. Thin-foil micrograph of 1% Cr steel isoformed at 550°C.

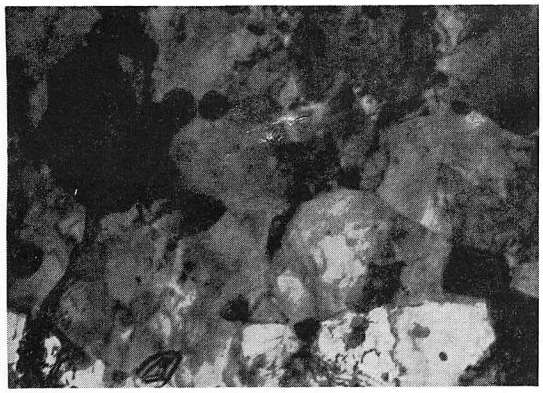

×40 000

Photo. 3. Thin-foil micrograph of martensitic carbon-manganese steel deformed at 600°C.

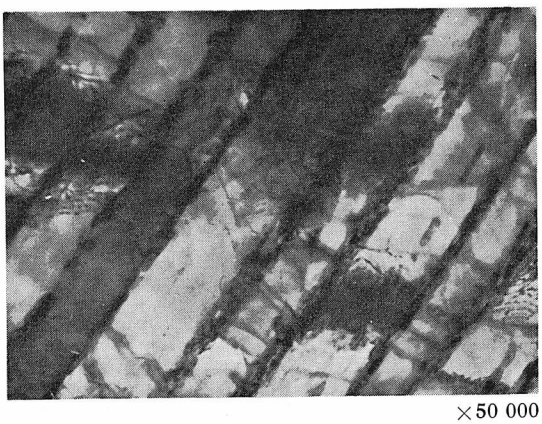

×50 000

Photo. 4. Thin-foil micrograph of pearlitic 1% Cr steel deformed at 600°C.

steel[24]. The mechanical properties after isoforming at 600°C are given in Table 4. Structural examination by electron microscopy revealed a fully recovered structure with dislocations re-arranged into subgrain boundaries and carbide particles often situated at triple points as shown in Photo. 1. Inferior toughness properties were obtained after isoforming at 550°C due to the presence of a non-recovered cellular structure involving dense tangles of dislocations in the cell walls as shown in Photo. 2. By isoforming it was possible to obtain a yield strength of 86 kg/mm² and an impact energy of 22·1 kgm with subgrain size of less than 0·5 μm. Such a structure was found to be resistant to recrystallization after tempering at 700°C.

A subgrain structure was also produced in localized areas by tempering martensite at 700°C for one hour; the subgrains were coarser and the properties inferior to those developed by isoforming at 600°C, as can be seen from Table 4. The properties obtained by hot rolling and LTMT are also included for comparison. Several lath carbides remained in the martensite unit boundaries which could account for the lower impact properties. Further tempering caused additional coarsening of the subgrains with a concomitant reduction in strength.

Deformation of a tempered martensite structure from a carbon-manganese steel by 70% at 600°C produced subgrains approximately of 0·4 μm diameter, associated with carbide particles of 500 Å as shown in Photo. 3. The yield strength obtained by this schedule was 80 kg/mm² with an impact toughness of 22·1 kgm being very similar to those obtained by isoforming this particular steel.

Deformation at 600°C (70% reduction of area) of a higher carbon 1%Cr steel previously isothermally transformed to pearlite at 650°C resulted in subdivision of the carbide lamellae into spheroidal particles 100–500 Å in diameter as shown in Photo. 4. The strength and impact properties were increased by warm working giving a yield stress of 76·5 kg/mm² and a Charpy impact value of 5·5 kgm. On tempering at 700°C, subgrains were formed having a diameter of 1 μm which led to a marked decrease in yield strength to 45·0 kg/mm² and increase in impact toughness. The strength increased with decreasing deformation temperature, but working below 500°C was not possible due to premature failure on drawing. Deformation at lower temperatures was, however, possible by utilizing extrusion as the mode of working. The strength and impact properties for the various treatments are presented in Table 5.

Table 5. Treatments and mechanical properties for a 0·38 %C–0·96% Cr En. 18 steel.

Details of TMT			Mechanical test data						
Austenitizing treatment	Deformation conditions	Tempering treatment	HV 30	Lower yield strength or 0·1% proof stress (kg/mm²)	Tensile strength (kg/mm²)	Elongation (%)	Reduction of area (%)	Cv at 20℃ (kgm)	5·5 kgm Tc (℃)
950℃ × 1 hr	Isoformed 70% reduction at 600℃	—	275	73·1	84·5	22	66	16·0	—
		700℃ × 1 hr	226	55·1	74·0	42	70	—	—
	Isothermally transformed (IT)	—	175	30·6	62·1	26	50	3·0	+ 75
	IT + WW 60% reduction at 600 ℃	—	273	76·5	87·6	14	51	5·5	+ 20
		700℃ × 1 hr	200	45·0	60·5	31	73	15·3	− 5
	IT + WW 70% reduction at 500 ℃	—	294	73·1	98·6	10	27	2·9	+ 50
		700℃ × 1 hr	190	46·6	59·2	29	67	12·7	− 10
	IT + WW 30% reduction at 450℃	—	280	67·4	87·6	9	18	0·5	>+100
		700℃ × 1 hr	189	45·0	61·1	27	57	3·5	+ 36
	Spheroidized Q + 700℃ × 16 hr	—	205	55·1	69·0	26	70	16·6	—
	Spheroidized, WW 70% reduction at 600℃	—	282	85·0	87·4	17	60	11·6	− 25
		700℃ × 1 hr	172	41·6	56·1	36	79	24·1	− 70

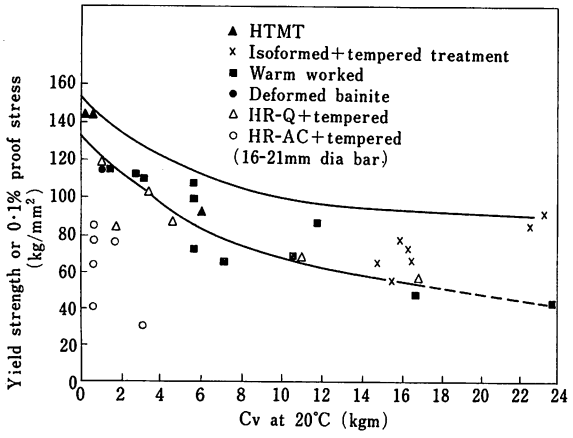

Fig. 4. Comparison of the mechanical properties that can be obtained in an En. 18 steel by conventional and thermomechanical treatments.

By spheroidizing the 1%Cr steel (via a treatment which consisted of prolonged tempering at 700°C after oil quenching from 950°C) 70% deformation at 600°C produced a yield strength of 85 kg/mm²; however, the impact energy was reduced due to only partial recovery of the structure. After tempering for one hour at 700°C the steel fully recrystallized. The properties for these conditions are also presented in Table 5.

From the results in Tables 4 and 5, of all the techniques used to obtain refined subgrain structures through recovery processes in the ferrite the best combination of strength and impact toughness is obtained by isoforming. This type of treatment is not amenable to certain mechanical working operations and in such cases warm deformation of a spheroidized structure or tempering of heavily deformed pearlite can produce a considerably refined subgrain structure with a corresponding improvement in properties.

Similar improvements in both strength and toughness have been obtained in other low-alloy steels by warm working a variety of initial microstructures in the range 500–650°C. The combination of properties was dependent on the precise working conditions. Working at the lower temperatures did not result in well defined subgrain structures and led to high strength-low toughness, whereas the higher working temperatures led to well developed subgrain structures giving lower strength levels with increased ductility and toughness[25].

The wide range of properties that can be developed in an En. 18 (1%Cr) steel by conventional and thermomechanical treatments is shown in Fig. 4. In addition to the treatments considered previously, the results of deformation during transformation to bainite and an HTMT treatment involving two finishing temperatures (985°C and 810°C) are included. The former treatment increased the strength without improving the toughness. A reduction in the finishing temperature prior to quenching gave a small increase in the strength and ductility of the tempered martensite but no improvement in the impact properties, even though the prior austenite grain size was refined from 35 μm to 18 μm.

From Fig. 4 it can be seen that an increase in

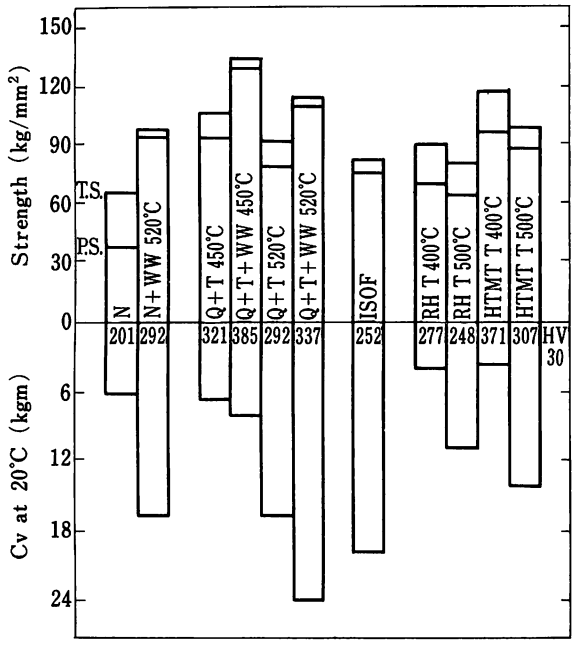

Fig. 5. Comparison of the mechanical properties that can be obtained in an En. 14A steel by conventional and thermomechanical treatments.

strength is accompanied by a decrease in impact energy, but for a given strength level the toughness levels obtained by thermomechanical treatments are greater than those that can be developed by conventional treatments.

The range of properties that can be developed in a much lower alloy content steel such as En. 14A (0·21%C–1·40%Mn–0·20%Si–0·14% Cr–0·16% Ni) steel is shown in Fig. 5. Warm working in the range 450–520°C is particularly effective in improving the combination of properties.

4. FACTORS INFLUENCING TOUGHNESS AND DUCTILITY

It has been shown for a variety of steels that both ductility (as measured by total elongation or percentage reduction in area at fracture of a uniaxial tensile specimen) and toughness (as measured by increase in impact energy at a given test temperature or decrease in transition temperature) can be improved by appropriate thermomechanical treatments. Such criteria are useful and will remain to be for laboratory investigations. However, the mechanical constraints of such tests are arbitrary and may suggest improvements in notch ductility that are not realizable in practice because of different mechanical constraints. It is therefore necessary to consider briefly the metallurgical and mechanical factors controlling both ductility and toughness. The former have been considered in detail at a recent conference[26] in the United Kingdom and are also dealt with by papers to this conference[27,28].

In ferritic steels the cleavage-fibrous impact transition temperature is markedly influenced by the ferrite grain or subgrain size. In general, the smaller the grain size the lower the temperature at which cleavage fracture occurs. The presence of large carbides in the form of pearlite colonies or large individual particles can crack and cause propagation of a cleavage crack under the applied stress, hence raising the impact transition temperature. The influence of nonmetallic inclusions is primarily with respect to the ductile shelf energy with little or no effect on the transition temperature per se. Increasing the volume fraction of nonmetallic inclusions markedly decreases the Charpy shelf energy. The type and morphology of the nonmetallic inclusions not only influence the Charpy shelf energy level but can lead to marked anisotropy between longitudinal and transverse properties, depending on the mode of deformation.

Thus, in order to increase the resistance to fibrous fracture and minimize anisotropy, it is necessary to control the shape and increase the spacing of inclusions which act as void nucleating sites. The same is true in relation to improved tensile ductility and relationships have been obtained relating Charpy shelf energy to tensile ductility.

In martensitic steels, there is no well defined cleavage-fibrous impact transition temperature. Raising the testing temperature leads to a gradual decrease in the proportion of quasi-cleavage fracture and an increase in ductile dimple fracture resulting in an improvement in the energy to fracture. The absolute level of impact toughness at a given temperature is very much dependent on the prior heat treatment of the steel. Previous work[29] has shown that the toughness of conventionally quenched-and-tempered martensitic steels is dependent on the distribution of precipitates at the martensite lath boundaries and the presence of coarse cementite precipitates. A marked increase in toughness was only obtained after tempering at higher temperatures with modification of carbide distribution and morphology. The improved toughness levels obtained by ausforming also resulted from an alteration in the precipitate distribution and size. However, vanadium-containing steels can show resistance to tempering following LTMT; fine dispersions of vanadium carbide can delay dislocation recovery and lead to inferior property combinations after tempering at high temperatures. As would be expected, the overall level of toughness is also influenced by the volume fraction and spacing of nonmetallic inclusions.

Thermomechanical treatments applied to alloy steels and, in particular LTMT, can lead to markedly directional structures. Although it would appear that prior austenitic grain size, shape and texture[23], and inclusion type and morphology have little effect on strength, both can greatly influence the level of ductility and toughness and lead to marked anisotropy. For crack propagation across the

direction of working, the fracture surface area is generally greater than that for the conventional case, and hence the toughness in that direction can be greatly enhanced. As might be expected, however, the toughness for crack propagation along the rolling direction is greatly reduced.

Nevertheless, the marked anisotropy can be used to advantage in certain applications provided any cracks arising in service have to propagate across the working direction, making use of the enhanced toughness.

Current methods of assessing resistance to fracture make use of fracture mechanics which takes into account the mechanical test factors influencing fracture, namely notch acuity, loading rate and state of stress. The notch acuity and loading rate have a pronounced effect on the fracture behavior and are fixed at arbitrary levels in conventional notched-bar testing. In addition the state of stress or constraint on plastic deformation imposed by the specimen is dependent on the specimen thickness in relation to the yield strength of the material. The local strain at failure at a given test temperature is dependent on the degree of relaxation of any triaxial stress system which is determined by the test conditions, specimen notch acuity and dimensions and rate of loading; under identical test conditions the degree of relaxation is decreased with increasing yield strength. Since this can have such a marked effect on the fracture behavior, one must consider any improvement in toughness in relation to yield strength and test factors. For fracture under essentially elastic conditions (at low strain levels) the crack tip conditions for failure can be conveniently characterized in terms of a critical crack tip stress intensity, K_{IC}, whereas failure after general yielding (at high strain levels) can be characterized in terms of the crack tip opening displacement, δ_c. These can be determined from analysis of load-displacement test data obtained using standardized testing procedures involving test specimens containing sharp cracks[30–33].

The influence of these factors on the measurement of toughness can be seen in Fig. 6 for a high strength martensitic steel and in Fig. 7 for a low strength ferritic steel. Fig. 6 shows the influence of tempering temperature on the impact toughness of a high-strength nickel-chromium-molybdenum-vanadium steel, together with test results from an identical specimen geometry in both impact and at a slow rate of loading, but containing an actual crack as opposed to the standard notch of a Charpy specimen. As can be seen the majority of the energy absorbed in fracturing the conventional Charpy V-notch specimen is associated with initiation of a crack from the relatively blunt machined notch. Equally important is that the shape of the fracture energy-tempering curve for the conventional specimen is completely different from that

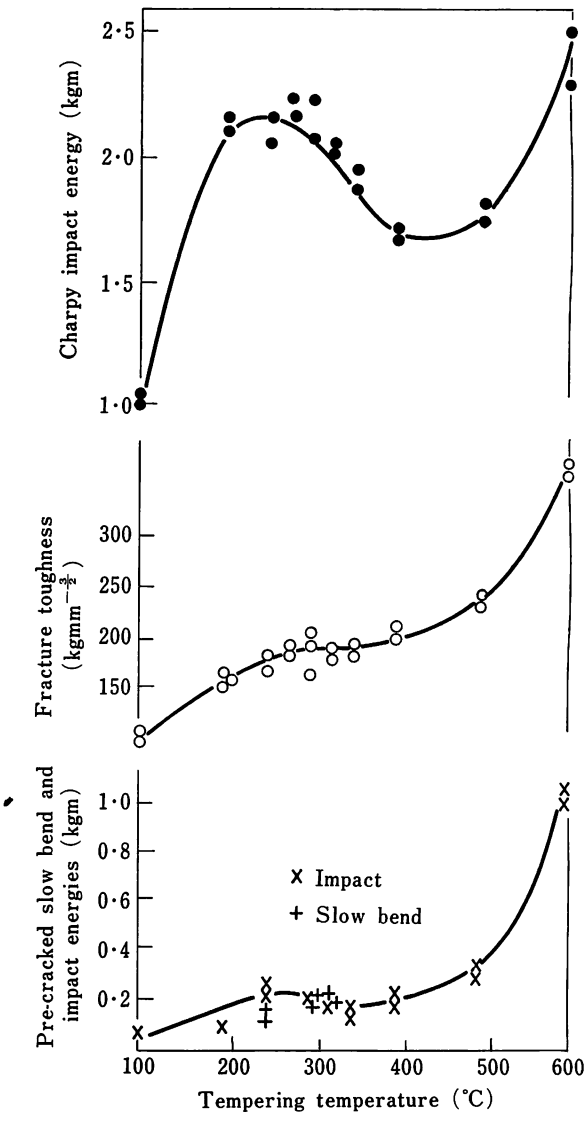

Fig. 6. The effect of tempering temperature on the fracture properties of a nickel-chromium-molybdenum-vanadium steel.

obtained using specimens containing sharp cracks.

The marked shift in transitional behavior in Fig. 7 for a structural steel relates solely to change in mechanical testing factors for a given metallurgical condition. This aspect further emphasizes the need to consider the relevance of shifts in transition temperature level in relation to the mechanical constraints likely to be experienced in a given design application.

Thus the real, rather than relative, significance of property combinations obtained by thermomechanical treatments can be only be evaluated by measuring the crack tip plasticity for failure under controlled conditions in relation to that required in a particular engineering application, to ensure satisfactory performance. This not only provides a means of realistically assessing the potential for improvement by thermomechanical treatment but facilitates economic comparisons with alternative

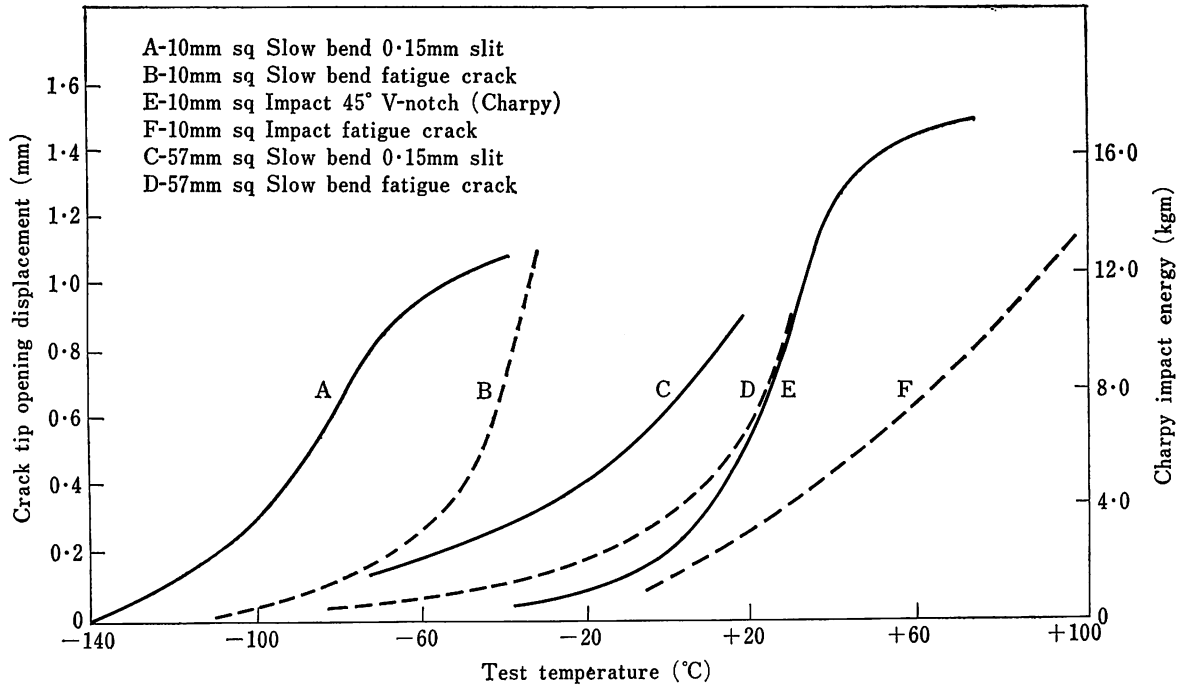

Fig. 7. Effect of specimen size, notch acuity and rate of loading on the transition characteristics of a structural steel.

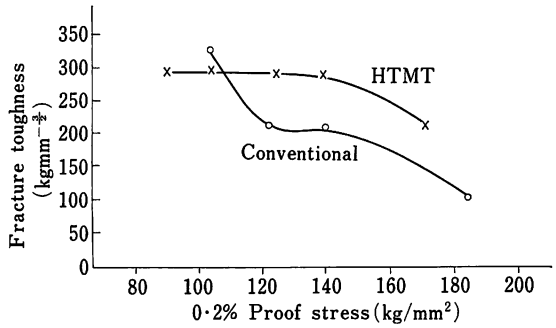

Fig. 8. The effect of HTMT on the longitudinal fracture toughness of a silicon-manganese spring steel.

approaches for obtaining similar property combinations

5. POTENTIAL APPLICATIONS OF THERMOMECHANICAL TREATMENTS

Although the basic mechanisms involved in the various thermomechanical treatments are not completely understood, the underlying factors responsible for the properties obtained and the different responses of steels to the various forms of TMT are largely known. From the majority of published data on the combinations of properties obtained for various treatments, it is not possible to assess the real significance of the reported improvements for reasons outlined earlier. In order to assess this it is necessary to consider both the strength and the fracture toughness, K_{IC}, or δ_c (the former is more relevant with higher strength steels) in that the crack tolerance is proportional to $(K_{IC}/\sigma_{ys})^2$, where K_{IC} is the plane strain fracture toughness and σ_{ys} is the yield or proof strength of the material. Thus for any increase in strength arising from a thermomechanical treatment, it is necessary to have an increase in fracture toughness such that the ratio $(K_{IC}/\sigma_{ys})^2$ is increased, if any real improvement is to be obtained. On this basis, thermomechanical treatments resulting in increased strength levels for an identical toughness level do not represent a real improvement in terms of overall fracture resistance. It is therefore considered by the authors that the main potential for thermomechanical treatments is as a means of increasing toughness at a given strength level in higher alloy steels by LTMT and HTMT. Also, alloying additions may be utilized more effectively through control of the microstructure and thereby upgrade the combination of properties possible in lower alloy steels to meet more stringent specifications by HTMT or warm working.

The application of HTMT to a 0·58%C-0·97%Mn-1·92%Si steel has been investigated with a view to improving the fatigue and fracture properties of leaf springs. By rolling to a finishing temperature of 830°C followed by direct quenching the fracture toughness was improved over that obtained by conventional treatment (hot rolled to 1050°C, A C, reheat 950°C × 1 hr, O Q) after tempering in the range 450–600°C. The strength and fracture properties are shown in Fig. 8 from which it can be seen that HTMT has resulted in a marked

increase in the longitudinal fracture toughness in the tempering temperature range 450–600°C. There was little effect of HTMT on the transverse fracture properties and the fracture surfaces showed marked anisotropy. However, for leaf spring application the mechanical anisotropy may be of value. Some measure of the advantage of HTMT over conventional practice, in terms of service application of leaf springs, can be obtained from consideration of the critical crack size likely to cause failure under a typical design situation, requiring a tensile strength of 140 kg/mm² and a yield strength of 120 kg/mm². The depth as of a surface flaw having a given aspect ratio (depth to length) with its major axis perpendicular to the direction of loading is for the HTMT material nearly double that for the conventionally treated material.

A further application considered has been the improvement in properties of sections by warm working at temperatures between 500 and 650°C. Significant increases in toughness have been obtained together with a small increase in strength. On warm working (3:1 extrusion ratio) of a heat-treated carbon-manganese-vanadium steel at 550°C, the strength was increased by 10·8 kg/mm² to 97·0kg/mm². The fracture energy per unit area for precracked specimens was trebled.

Most of the principle types of mechanical working operations can be used to deform steels under thermomechanical conditions. The main limitation with current equipment is the power required to achieve the large degrees of reduction necessary at the lower temperatures. Of the various types of thermomechanical treatment, HTMT is the most feasible since the forming loads are reduced at the higher temperatures and there is a greater flexibility in temperature control. Nevertheless, in hot rolling a need exists for information on the increase in rolling load with falling temperature, and a re-appraisal of roll pass design that might be appropriate under the exigencies of thermomechanical treatment. Developments in lubrication technology could partially offset the high rolling loads encountered. Designs of rolling mills suitable for the LTMT of flats and bars have been suggested.

Extrusion is particularly suited for the production of sections over a wide range of temperatures since large deformations can be achieved in a single operation and shapes can be formed to close tolerances, eliminating expensive machining operations. This latter aspect is of particular importance since machining of ultra-high strength material is a difficult operation. The use of the process for ausforming martensitic steels is being considered in the United Kingdom for specialized components. As discussed earlier, the process of extrusion also applies to the warm deformation of transformed steels and HTMT. Nevertheless, development of suitable tooling and lubrication practice is required for operation under unorthodox conditions imposed by TMT. Also, it cannot be expected that extrusion ratios typical of hot deformation will be attained at intermediate temperatures.

Forging in closed dies is at present limited by current design knowledge and die materials. The development of infrared heating techniques could substantially extend the working times allowing large forging reductions to be accommodated. Drawing is ideally suited for the processing of high strength wire by LTMT and in the production of bar by isoforming.

There is a need for process and plant development to facilitate forming under controlled conditions particularly when applied to shapes other than flats or bar. Although for many steels a variety of thermomechanical treatments can be shown to lead to improved combinations of properties, it is necessary that any improvements are considered in relation to property levels attainable by conventional means in other steel compositions.

6. SUMMARY

The potential of process control for the structural refinement of alloy steels to give enhanced strength-toughness combinations has been emphasized. Thermomechanical treatments can be selected to improve a specific mechanical property and this is particularly important in relation to improvement in fracture toughness at high strength levels. Also alloying additions may be utilized more effectively through control of the microstructure and thereby upgrade the combination of properties possible in lower alloy steels to meet more stringent specifications.

Sufficient is now known of the basic mechanisms responsible for improvements in properties as a result of various thermomechanical treatments. The main requirement now is for data to facilitate design of forming plant to cope specifically with the exigencies of the various forms of thermomechanical treatment.

Once this information is available it can be expected that certain aspects of thermomechanical treatment will come into greater commercial usage, as has been the case in recent years with the rapid acceptance of controlled rolling of structural steels.

REFERENCES

1) W.E. Duckworth and P.R. Taylor: High Strength Steels, ISI Special Report, **76** (1963), p. 61
2) W.E. Duckworth et al: J.I.S.I., **202** (1964), p. 135
3) F. Borik et al: Trans. ASM, **56** (1963), p. 327
4) W.E. Duckworth: Met. Rev., **128** (1968), p. 145
5) V.S. Ivanova and C.K. Gordienko: New Ways of Strengthening Metals, ISI **P 109** (1968)
6) S.J. Matas et al: AIME Proc. 5th Metal Working Conf., (1963), p. 143

7) R.A. Grange: Trans. ASM, **59** (1966), p. 26
8) M.V. Prindantsev and E.I. Ivantsova: Met. Sci. Heat Treatment, (Nov-Dec 1967), p. 900
9) J.J. Irani and D.J. Latham: Low Alloy Steels, ISI Special Report, **114** (1969), p. 55
10) J.J. Irani: Bisra Report MG/A/47/67
11) D. Kalish et al: J. Met., (1965), p. 157
12) V.F. Zackay et al: 1st Int. Conf. on Fracture of Materials, Sendai, (1965)
13) N.N. Breyer and N.H. Polakowski: Trans. ASM., **55** (1962), p. 667
14) D.J. Latham and D.K. Ganguli: Bisra Report MG/A/88/68
15) J.L. Peterson: Trans. ASM., **56** (1963), p. 304
16) J. Markula and S. Heiskanen: Jernkont. Ann., **150.5** (1966), p. 298
17) D.J. Latham and D.R. Stansfield: Paper presented at Ministry of Defence Conference on Thermomechanical Treatments of Metals, (April 1970), P1/UK/3A/70
18) D.J. Latham: J.I.S.I., **208** (1970), p. 50
19) P.R. Taylor and G. Hoyle: Bisra Report MG/E/172/65
20) V.F. Zackay and W.M. Justusson: High Strength Steels, ISI Special Report, **76** (1963), p. 14
21) V. Goel et al: J. Basic Eng., Trans. ASME, (1967), p. 871
22) I. Tamura et al: Trans. Japan Inst. Met., **7** (1966), p. 248
23) D. Dulieu, D.J. Latham, J.W. Bannister and S. Gibson: Bisra Report MG/73/70
24) R.L. Craik, M.J. May and D.J. Latham: Metals Eng. Quarterly, (Aug 1969), p. 12
25) D.J. Latham and D.R. Stansfield: to be published
26) The Effect of Second Phase Particles on the Mechanical Properties of Steels, ISI Special Report to be published (Nov 1971)
27) H. Suzuki: Consideration of the Significance of Ductility and Toughness in Terms of Atomic Processes of Deformation and Fracture. This volume, (1972), p. 1
28) F.B. Pickering: The Effect of Composition and Microstructure on Ductility and Toughness. This volume, (1972), p. 9
29) J.J. Irani et al: ASTM Special Technical Publication, **407** (1968), p. 168
30) Methods for Plane Strain Fracture Toughness (K_{IC}) Testing, British Standards Institution Draft for Development, (1971)
31) D. Elliott, E.F. Walker and M.J. May: Conference on Practical Applications of Fracture Mechanics to Pressure Vessel Technology, Institution of Mechanical Engineers, (May 1971). Bisra Report MG/S/7/71
32) F.M. Burdekin and M.G. Davies: ibid, (May 1971)
33) T. Ingham et al: ibid, (May 1971)

DISCUSSION See pp. 358~359

Microstructure and Mechanical Properties of Ausformed Steels

T. Araki* S. Watanabe** H. Miyaji**

*The University of Tokyo

**National Research Institute for Metals

The strengthening mechanism by ausforming has long been discussed in many respects and recently was seemingly well explained in terms of a characteristic subcell structure first proposed by the authors[1,2] for ausformed alloy steels. This cell structure also appears to account for the improved toughness that accompanies the enhanced strength of ausformed steels.

The two types of alloy steel shown in Table 1 were studied to determine the effect of ausforming on the relation between microstructure as observed by electron microscopy and their ductility, toughness and strength.

Table 1. Chemical composition of tested specimens (in weight %)*.

Steel	C	Cr	Ni	Mo	P	S	N	Remarks
5Cr-1	0·17	4·9	—	2·0	0·001	0·004	0·001	tensile tests
5Cr-2	0·19	5·0	—	1·9	0·001	0·004	0·001	Charpy tests
5Ni	0·17	—	5·3	2·0	0·001	0·003	0·001	tensile tests

* All steels include approximately : Mn=0·1%, Si=0·1%

All steels were melted in a vacuum induction furnace. Ausforming of steel billets homogenized at 1250°C was conducted by both rolling and forging of specimens first heated in a vacuum capsule to 1100°C and then air cooled to 600°C for ausforming. In most cases, the ausformed specimens were tempered at 200°C before mechanical testing.

The tensile specimens were machined to 3·5 mm dia ×25 mm gage length and tested at a rate of 0·5 mm/min in an Instron tester with a special extensometer. Standard V-notch Charpy specimens were tested in duplicate.

The following results were obtained:

(1) Transmission electron micrographs of the ausformed steels showed a characteristic subcell microstructure through or within the martensite laths. The average size of these cells in the 5% Cr-Mo steels decreased with increasing degrees of deformation. A similar trend was observed in the 5%Ni-Mo steel except the relation was not clear for low degrees of deformation. Photo. 2 illustrates the microstructure of the 5%Cr-Mo steel ausformed 75% and an electron diffraction pattern from the same micro-area. The ring formation of the diffraction pattern suggests an almost random orientation of each cell in covariant packets of martensite laths.

(2) Fig. 1 exhibits the effect of degree of deformation in ausforming on the tensile properties. The ultimate and yield strengths of the ausformed 5%Cr-Mo steel increased almost linearly with the degree of deformation and can be reasonably explained by refinement of the cell structure. In the case of the 5%Ni-Mo steel, lower degrees of deformation gave little or no increment in strength, as would be expected from the fact that cell formation and refinement were not clearly observed with low degrees of reduction.

(3) In respect to ductility, the uniform elongation remained constant with increasing amounts of strengthening in the ausformed 5% Cr-Mo steel whereas some drop in uniform elongation with increasing strength was seen in the ausformed 5%Ni-Mo steel. This observation is in agreement with the magnitude of the strain-hardening exponent n. The reduction-of-area and Charpy-impact values, which are thought to represent toughness, showed a distinct rise in the 5%Cr-Mo steel as the strength produced by ausforming increased.

(4) In both ausformed and non-ausformed steels, a marked increase in tensile strength was

consistently observed in the subzero temperature range below certain temperatures. The subzero ductility values of the ausformed steels were superior to those of the non-ausformed steels, which had impaired ductility at equivalent temperatures.

(5) The improved toughness and ductility of steels strengthened by ausforming are interpreted in terms of the nature of the specific cell boundaries in the microstructure. These boundaries are strengthened during deformation by a fine carbide precipitation in the metastable austenite, which is thought to be inherited by the martensite. The difference between the effects of nickel and chromium as an alloying element is explained by their distinctly different interaction in nucleating alloy carbides such as MoC in the cell structure (either cell boundaries or matrices) of the austenite being plastically deformed.

References (for the Abstract)

1) T. Araki, S. Watanabe, H. Miyaji: Trans. Jap. Inst. Metals, Proc. ICSMA, Supplem. to. **9** (1968), p. 111
2) S. Watanabe, T. Araki, H. Miyaji: Trans. Iron Steel Inst. Japan, Proc. ICSTIS, **11** (1971), p.1020

オースフォーム鋼の微細組織と機械的性質

荒木　透*　渡辺　敏**
宮地博文**

*東京大学工学部　**金属材料技術研究所

1. 緒　言

オースフォーム鋼の強度を支配する因子については，従来から多くの説[1,2,3]が提唱されてきた．しかし，これらの説は靱性に対する説明においてまだ十分でないように思われる．

筆者らは透過電子顕微鏡観察法により，加工オーステナイト中にも，またその変態によって生じたマルテンサイト中にも特有のセル構造が存在することを見出した[4]．この事実は，セル組織がまず準安定オーステナイトの加工中に発生し，変態に際してそのまゝマルテンサイト中に継承されることを示唆している．このような過程をへて形成されるセル組織は，オースフォーム鋼の機械的性質を決定する主要な因子であって，高い強度と適度の靱性を共有しうる原因は，個々のセルがかなり独立した結晶粒に類似した役割りを果しているためと考えられる．上述の効果は，セル境界が比較的大傾角のものであり，しかもその境界上，すなわちセル壁上に微細な合金炭化物が析出しているという特殊な構造に由来している．

本報告は，オースフォーム鋼の引張性質，衝撃特性あるいは焼もどしに伴うかたさの変化が，セル組織にもとづく強化機構の観点から合理的かつ統一的に説明し得ることを示し，あわせてセルの起源とその継承機構について考察を加えたものである．

2. 試料および実験方法

実験に用いた試料の化学組成を Table 1 に示す．

Table 1. Chemical composition of steels tested (wt. %).

Steel 鋼種	C	Cr	Ni	Mo	Mn	Si	P	S	N
5Cr 1	0·17	4·87	—	2·02	0·12	0·092	0·001	0·004	0·0012
5Cr 2	0·19	4·95	—	1·89	0·17	0·086	0·001	0·004	0·0014
5Ni	0·17	—	5·27	1·97	0·10	0·084	0·001	0·003	0·0012

原材料は電解鉄のほか，電解クロム，電解ニッケル，金属モリブデンなどを用い，高周波真空溶解炉によって 7 kg インゴットに鋳造した．これらのインゴットは 1100°C で鍛造，圧延後，1250°C×24 hr の拡散焼なましを行なって素材とした．オースフォーム試料は，あらかじめ所要の寸法に機械加工した素材を石英管中に真空封入し，1100°C×1 hr オーステナイト化処理をした後石英管を割って急冷し，600°C に 5 min 加熱してから加工を行なった．オースフォーム後，試料はすべて空冷された．5 Cr-1 と 5 Ni-1 は，種々の断面を有する丸棒素材から，最終的に 10 mmϕ にオースフォームされた．これらの試料はソルトバス中で 200°C×1 hr の焼もどしを行なった後引張試験片に機械加工された．試験片は 3·5 mmϕ の直径を有する丸棒試験片で，平行部の長さは 30 mm，標点距離 25 mm である．機械加工後，これらの試験片は水素ぜい性の発生を防止するため 200°C で 1 hr 真空焼もどしを行なってから直ちに試験に供した．

常温引張試験は 10 ton インストロン引張試験機によって行なった．ひずみ速度は 0·5 mm/min である．測定は一点について 2 本の値の平均をとったが，試料は大部分が中央で破断し，絞りも 50% を越えるかなり大きな値を示した．なお，伸びの検出にはインストロン社製伸び計を使用した．低温引張試験も行なったが，試験片の形状は常温引張試験のものと同じである．冷剤は 0～100°C まではアルコールと液体窒素を用いた．

シャルピー試験用の素材は，あらかじめ種々の断面を有する角棒を作製し，これを丸棒試験片と同様に石英管中に真空封入した．この場合は鍛造によって最終的に 11 mm×11 mm の断面に仕上げた．しかし，実際には予定の寸法にならず，いずれの試料も所定の加工度を与えることはできなかった．焼もどしの処理は引張試験片と全く同じである．なお試験片の形状は，JIS 4 号 V ノッチである．

電顕観察用の薄膜の作製に当り，as ausform 組織を電解する際は，電解中における試料の焼もどしを避けるために電解液として氷酢酸 135 ml＋水 7 ml＋クロム酸 25 g 溶液を用い，液温は 8～10°C，電流密度 300 mA/cm^2 で電解した．

3. 結　果

3.1 組　織

Photo. 1a) に 5 Cr 鋼の 40% オースフォーム組織を示す．この写真からも明らかなように，オースフォーム鋼の微細組織は直接焼入鋼の組織とは著しく異なり，マルテンサイトラス (lath) 内部に多数のセルが認められる．セル壁を構成する転位群は，低加工度の場合幅の広い帯状になっているが，加工度が増加するにつれて狭くなり，より明瞭に識別できるようになる．セルを観察するためには電子顕微鏡の倍率を低くする方がよく，写真はすべて直接倍率 5000 倍で撮影したものである．なお，Photo. 1b) はこの組織の制限視野回折像を示したものであるが，その範囲は写真中央部のほゞ全面回折となっている．各スポットは著しいアーキングを伴い，リングに近い形状を有していることが分る．これは，各セル間の方位差が冷間圧延などで生ずる通常のセルの場合と異なり，比較的大きな傾角を有することを示唆している．

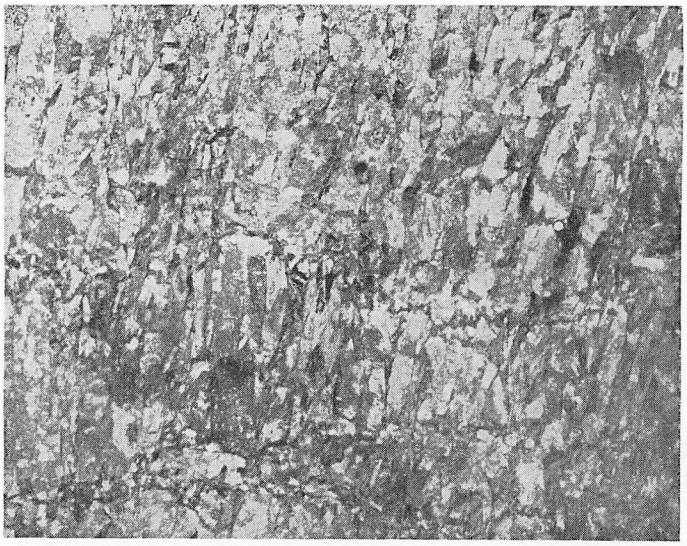

a) Transmission electron micrograph. ×10 000×2/3

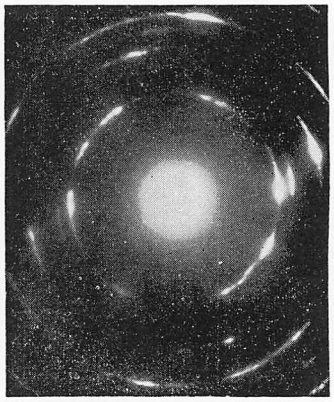

b) Diffraction pattern.

Photo. 1. Structure of 5%Cr–2%Mo–0·2%C steel (5Cr–1) after ausforming 40%.

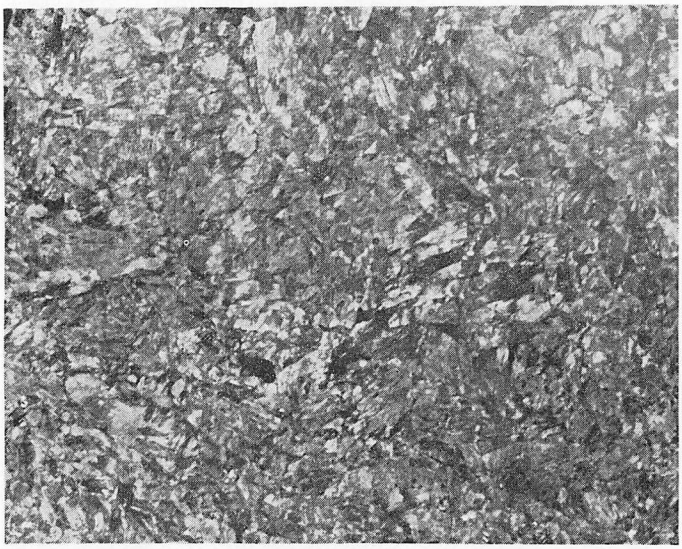

a) Transmission electron micrograph. ×10 000×2/3

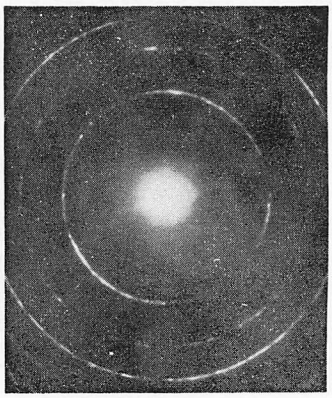

b) Diffraction pattern.

Photo. 2. Structure of 5%Cr–2%Mo–0·2% steel (5Cr–1) after ausforming 75%.

a) Transmission electron micrograph. ×10 000×2/3

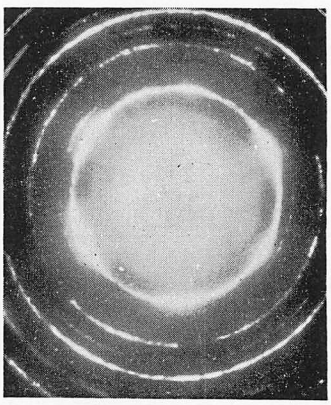

b) Diffraction pattern.

Photo. 3. Structure of 5%Cr–2%Mo–0·2%C steel (5Cr–1) after ausforming 75% and tempering at 200°C.

a) Transmission electron micrograph. ×10 000×2/3

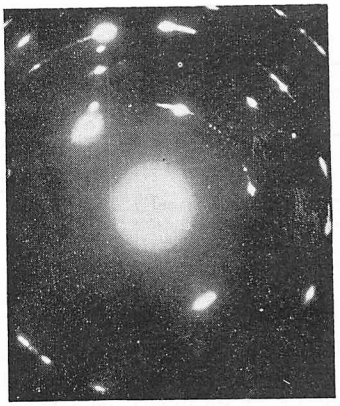

b) Diffraction pattern.

Photo. 4. Structure of 5%Cr–2%Mo–0·2%C steel (5Cr–1) after quenching and tempering at 200°C.

Photo. 2a) は，同じく 5Cr 鋼の 75% オースフォーム組織を示す．このような高加工度の場合は，組織中に通常のマルテンサイトラスの痕跡を認めることは困難である．Photo. 2b) は，この組織の回折像である．制限視野の範囲は，螢光板上のマークを目印しにして，Photo. 1b) と同じ大きさになるように配慮した．このように回折像がほとんど完全なリングに近づくことから，加工度の増加に応じてセル粒径の微細化と方位差の程度がさらに増大し，セル化が一段と進行したことを示すものと考えられる．

5 Ni 鋼の場合も，組織の基本的な特徴は 5 Cr 鋼と同じであり，高加工度のものではむしろ 5 Cr 鋼より明瞭な外観を呈していた．しかし，40% 以下の低加工度ではセル化が不明瞭で，転位密度の増加が主要な変化であるように見受けられた．

実際の試験は200°C焼もどし組織に対して行なわれているので，Photo. 3a) に 75% オースフォームした 5 Cr 鋼の焼もどし組織を示した．セル粒径などは Photo. 1a) と比較して全く変化していないことが分る．また Photo. 3b) に示す回折像には若干の回復現象が認められるが，依然として大きな方位差を有するセル組織が存在していることが分る．なお，Photo. 4a) には，比較のために直接焼入試料の焼もどし組織を示した．マルテンサイトラスの内部には，ε 炭化物と推定される微細な析出物が認められる．Photo. 4b) に示す回折像はわずかなアーキングを伴ったスポットであり，オースフォーム試料とは本質的に異なっている，

3.2 常温引張性質

Fig. 1 は 5 Cr 鋼と 5Ni 鋼の常温引張性質をオースフォームの加工度に対してプロットし，両鋼の性質の変化を比較したものである．いづれの加工度においても，5 Cr 鋼の強度は 5 Ni 鋼より優れている．両鋼の間に存在するもっとも特徴的な相違は，5 Cr 鋼の 0·2% 降伏強さ σ_y と引張強さ σ_B が加工度に比例してほゞ一様に増加しているのに対し，5 Ni 鋼では約 40% の加工度までそれらの増加に停滞がみられる点である．伸びの値は，5 Cr 鋼の場合，均一伸び δ_u も全伸び δ_t も加工度の全範

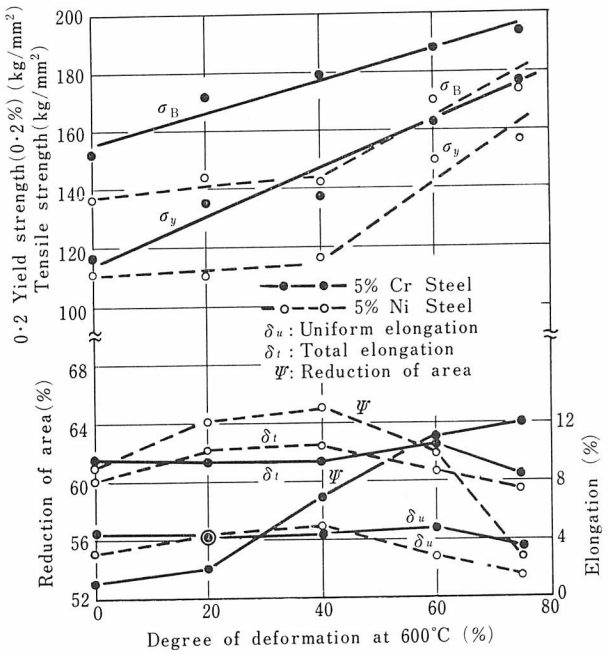

Fig. 1. Effect of degree of deformation during ausforming on the tensile properties of 5%Cr-2%Mo-0·2%C (5Cr-1) and 5%Ni-2%Mo-0·2%C steels tempered at 200°C×2hr after ausforming.

囲にわたって変化していない．5 Ni 鋼では，20% および 40% の範囲で伸びの値はむしろ増加しているが高加工度側では δ_u の低下がやゝ顕著になる．

両鋼の根本的な相違は，絞り ψ の変化に現われている．すなわち，5 Cr 鋼は加工度に比例して 52%から 64%までほぼ一様に増加する．これに対し，5Ni 鋼では伸びの変化と同様に 20%と 40%の間でいったん増加するが，60% 以上の加工度では急激な低下を示している．しかし，全体的に伸びの値は，強化の程度に比較すれば極めて良好なレベルを保持しているといえる．これは，主として本鋼が低炭素であるためと推定される．

Fig. 2 は，ひずみ硬化指数 n 値および δ_u/δ_t の値を加

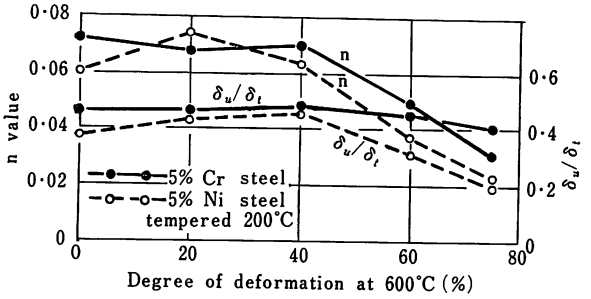

Fig. 2. Effect of degree of deformation during ausforming on the n value and the uniform/total elongation ratio of 5%Cr–2%Mo–0·2%C (5Cr–1) and 5%Ni–2%Mo–0·2%C steels.

工度に対してプロットしたものである．加工度0%の試料，すなわち直接焼入試料では，いわゆる“double n”挙動を示した．一方オースフォーム試料でも，低加工度の範囲では同様な現象がみられたが，5 Cr 鋼では60%以上の試料から，また5Ni 鋼では40%以上の試料から“single n”挙動に移行する明瞭な傾向がみられた．Morrison[5] によれば，“double n”挙動において塑性変形の後半の挙動を支配する n_c は結晶粒径に依存せずほゞ一定値を有するのに対し，前半の加工硬化挙動を支配する n_b は“single n”の場合の n_a と同様な粒度依存性を示している．この事実は，n_a と n_b が基本的に同格のパラメータとして取扱えることを示している．従って，“double n”挙動を示す場合は n_b を，また“single n”の場合には n_a をそのまゝ n 値として採用した．図から明らかなように，n 値は加工度と明瞭な相関を有し，5Cr 鋼では40%以上から，また5Ni 鋼では20%以上から顕著な低下を示している．一方，δ_u/δ_t の値は全伸び中に占める均一伸びの割合を表わすものであるが，その変化の傾向は伸びの変化と実質的に同じであった．しかし，全般的にみれば5 Cr 鋼の方が5 Ni 鋼より均一伸びの割合が大きいことを示している．この点は絞りの変化と逆の関係になっているが，絶対値としての伸びの変化を考えるならば，このような場合もありうることである．いづれにしても，強度と靱性の関係において両鋼の間に存在する差異は，後述するようなミクロ的要因に基づくものと考えられる．

3.3 低温引張試験

bcc 金属の降伏強さが試験温度に依存することはよく知られている．しかし，オースフォーム鋼の温度依存性については全く報告がないので，その靱性の本質を解明する一つの手掛りとして，75%オースフォーム試料と直接焼入試料の室温から液体窒素の温度までにおける引張試験を行ない，その挙動を比較した．Fig. 3 は 5 Cr 鋼について，また Fig. 4 は 5 Ni 鋼について行なった低温引張試験の結果を示す．常温引張試験の場合と比較すると，測定値にはかなりのバラツキがみられた．これはほとんどが1本の測定値によってプロットされていることと，試料の採取位置や種々の理由による前処理の相違に基づくものと推定される．しかし，全般的に言えることは，降伏強さの温度依存性が75%オースフォーム試料でも直接焼入試料とあまり差異がなく，平行的に変化しているということである．また伸びの値は，温度の低下によって強度が増大するにもかゝわらずやゝ増加した．しか

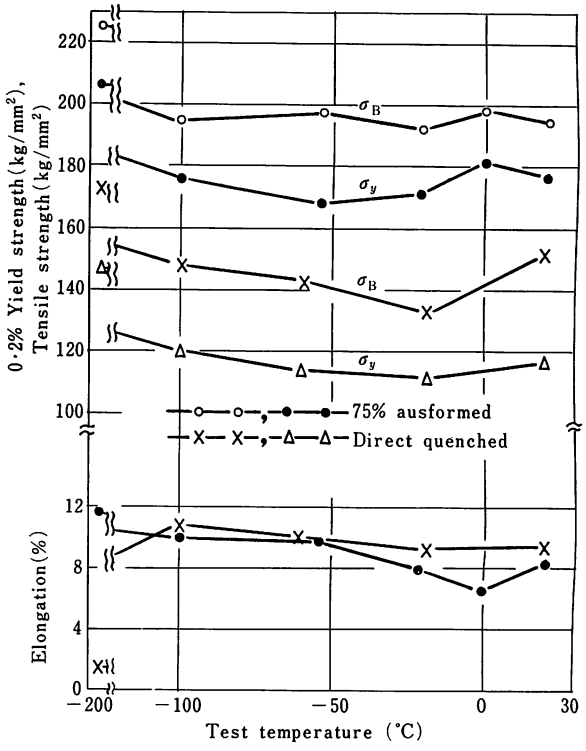

Fig. 3. Effect of test temperature on the tensile properties of 5%Cr–2%Mo–0·2%C steel (5Cr–1) ausformed 75% or direct quenched and tempered at 200°C×2hr.

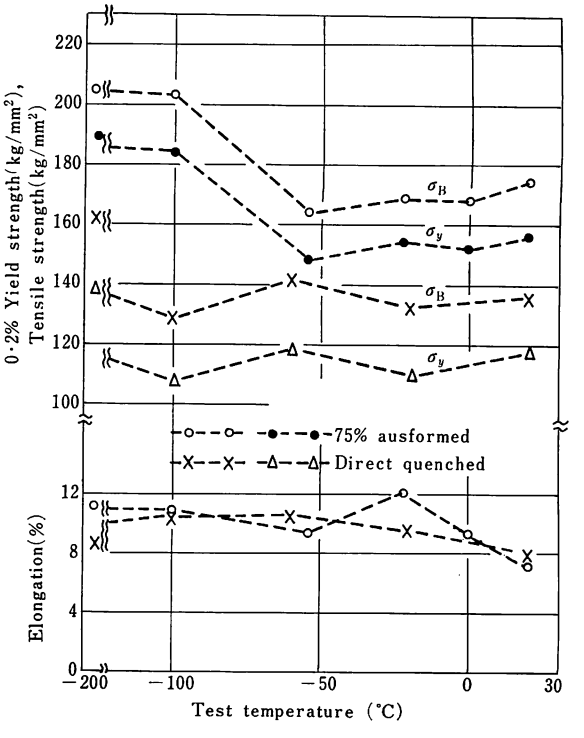

Fig. 4. Effect of test temperature on the tensile properties of 5%Ni–2%Mo–0·2%C steel ausformed 75% or direct quenched and tempered at 200°C×2 hr.

し，−196°C では 5 Cr 鋼はわずかに降伏したあとでぜい性的に破断したのに対し，5Ni 鋼では良好な伸びを示した．一方，オースフォーム試料では，いづれの鋼も良好な伸びを有することが注目される．全般的に低温における靱性は 5Ni 鋼の方が 5Cr 鋼より優れているといえる．

3.4 シャルピー衝撃試験

シャルピー試験は 5Cr 鋼についてのみ行なった．Fig. 5 にその結果を示す．

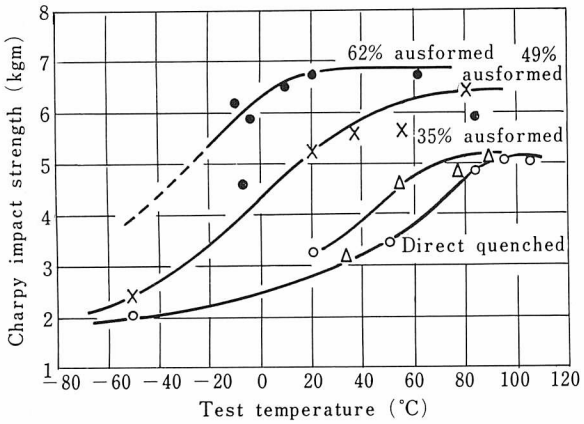

Fig. 5. Effect of test temperature and degree of ausforming at 600°C on the Charpy impact strength of 5%Cr–2%Mo–0·2%C steel (5Cr–2). All specimens tempered at 200°C×2 hr.

直接焼入鋼に比較してオースフォーム鋼は衝撃靱性が著しく向上し，遷移温度の低下は推定ではあるが 35% の加工度で約 20°C，49% の加工度で約 70°C，62% の加工度では実に 110°C に達している．しかも，単にエネルギー曲線が低温側に移行するばかりでなく，shelf energy の値も顕著に増大している．

一般的に言って，オースフォームした試料の破面は鈍い銀灰色のきめの細かい外観を呈し，直接焼入試料の延性破面とは異なった感じであった．また，肉眼でぜい性破面と延性破面を区別することはかなり困難であった．ただし，49% 加工度の試料のうち 21°C と −50°C で破壊したものは，延性破面中にへき開破面と推定される微小領域が不規則に散在していた．オースフォーム鋼では，破面の凹凸が激しいことも大きな特徴である．このような破面はクラックの伝播エネルギーを増加させ，遷移温度を低下させる一因になっているものと考えられる．低温で破壊した試料の破面には，ノッチルートの近傍から放射状に ridge が形成されているものもあった．一方，直接焼入試料の破面は通常の延性—ぜい性破面を有し，50% 破面遷移温度は +75°C 付近と推定された．

Photo. 5a) は +10°C で破断した 49% オースフォーム試料のノッチ直下の領域の走査電顕組織である．外観的に延性破面と思われたが，実際にも dimple pattern であることが分る．Photo. 5b) は側面に近い領域内のぜい性破面と考えられる部分を撮影したもので，dimple pattern と river pattern が混在した複雑な擬へき開破面を有している．facet の大きさは，直接焼入試料にくらべてかなり小さいように見受けられた．62% オースフォーム試料は，試験温度の範囲内ではぜい性破面と推定される領域は存在しなかった．

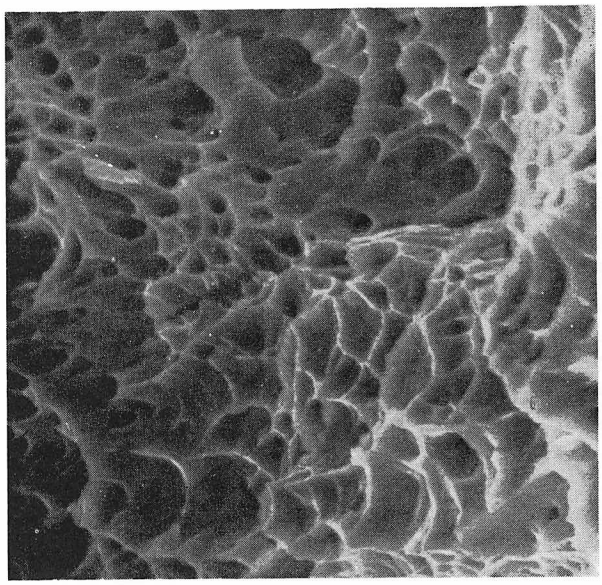

a) Dimple pattern observed in the vicinity of notch root.

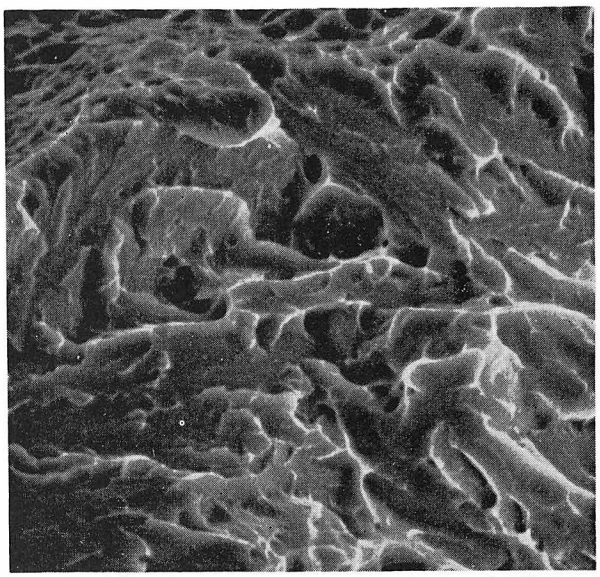

b) Complex quasi-cleavage pattern associated with some dimple parts observed near the shear-lip.

Photo. 5. Microfractographs of Charpy specimens of 5%Cr–2%Mo-steel (5Cr–1) after ausforming 49%.

4. 考　　察

筆者らは，オースフォーム鋼の機械的性質がマルテンサイト中に存在するセル組織によって影響されることを指適してきた[4]．この場合，各々のセルはあたかも独立した結晶粒に近い性質を有することが仮定されている．従って，もしこのような仮定が事実ならば，オースフォーム鋼の機械的性質は結晶粒微細化に伴う変化の延長上において記述されなければならない．しかし，結晶粒径と機械的性質との関係に関する研究は大部分がフェライト・パーライト鋼に関するものであり，焼もどしマルテンサイト組織に対してはほとんど報告がない．

邦武[6]は，高温で焼もどしを行なった低炭素低合金鋼の調質組織における強度が，炭化物粒子による分散強化，転位密度，固溶強化，フェライト結晶粒径および再結晶粒径などの総合効果として現われるものと仮定し，各項

の強度への寄与率を多重回帰分析によって求めた．その結果によると，降伏強さは主として炭化物の分散によって支配され，粒径の影響は小さい．これは，焼もどしマルテンサイトの亜粒構造による強化に対して否定的な結果を与えているようにも思われる．確かに，焼もどしマルテンサイト中では，転位の初期段階における移動の障壁として分散炭化物の方が亜粒界より強力であることは妥当であるように思われる．問題は粒界の構造に帰せられる．粒界強度は界面における方位差，偏析あるいは析出物の存在などによって決まるものであるが，オースフォームによって形成されるセル壁はある程度厚みを持った複雑な転位網中に微細な合金炭化物が析出しているような構造を持つと推定される．しかもセル間にはある程度の方位差が存在するので，焼もどしマルテンサイト中の多くの亜粒界よりはるかに強力な障壁であると考えられる．粒界強度は Petch の関係式における k_y 値によって代表されるので，以下に降伏強さ σ_y とセル粒径 ds との関係を求めてみた．

Table 2. Relation between deformation cell size (μ) in martensite and degree of deformation (%).

Deformation(%)		20	40	60	75
ds(μ)	5Cr	1	0·73	0·44	0·32
	5Ni	2	1	0·40	0·35

Table 2 は，5Cr 鋼および 5Ni 鋼の加工度と ds の関係を示したものである．高加工度の試料については，原則として倍率 10 000 倍の組織中で，一辺 50 mm の正方形中に存在するセルの数から ds を算出した．しかし障壁としてのセル壁の判定にはかなり任意性がある．加工度 20% のものは算定がさらに困難であり，測定値は定性的なものと考えるべきであろう．この場合，ds としてはマルテンサイトラスを横断しているセル壁間の距離を測定して求めた．5Ni 鋼の場合 40% の試料は 20% のものとやゝ類似した組織を有するが，一方 60% と 80% の試料も互いに類似していた．これらは Fig. 1 の結果にも反映されている．

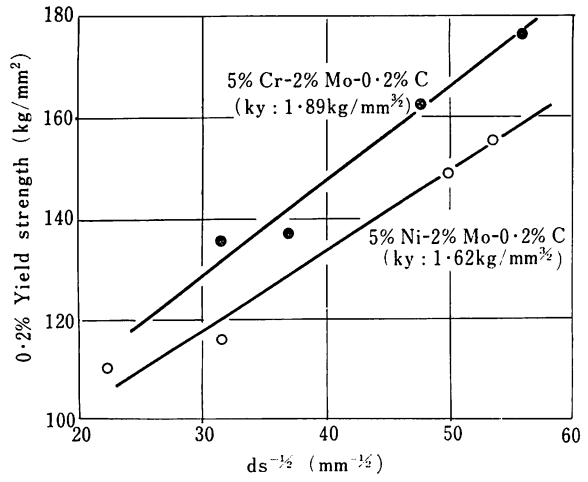

Fig. 6. Relation between yield strength and inverse square root of cell size of ausformed nickel-molybdenum and chromium-molybdenum steels.

Fig. 6 は σ_y と $ds^{-1/2}$ との関係をプロットしたものである．両鋼種ともほゞ直線関係を有するが，低加工度の試料ではこの関係からはずれる傾向がある．k_y 値は 5Cr 鋼では 1·89 kg/mm$^{3/2}$，5Ni 鋼では 1·62 kg/mm$^{3/2}$ である．一方 Grange[7] が低合金構造用鋼などのまえオーステナイト粒径に対して求めた k_y 値は 2·11 kg/mm$^{3/2}$ であって，5Cr 鋼の値に近い．これは 5Cr 鋼のセル壁が極めて強力なものであることを示している．一方 5Ni 鋼ではやゝ強度が低下しているものと考えなければならない．この原因は，セル壁上への炭化物の析出に関係するものと考えられる．すなわち，Ni のようにフェライト中の C の活量係数を高める元素を添加すると，炭化物の析出成長は主としてマトリクス中で起こりやすい．これに対して Cr の添加は，後述するようにセル壁上への析出を促進する効果が大きい．

上述の効果は，オーステナイトからマルテンサイトにセルが継承される問題にも関連がある．すなわち，オーステナイト中における C の活量係数を高め，粒内析出を促進するような元素の添加は，低加工度の範囲においてセルの継承を困難にするものと考えられる．Fig. 1 において，5Ni 鋼の低加工度試料で強度上昇に停滞がみられるのは，この現象に関係があるものと推定される．一方加工度が高くなってセル粒径が減少すれば，相対的にセル壁上への析出が促進されるので，急激な上昇が認められるようになる．Borchers ら[8] は 5%Cr-3%Ni 鋼をオースフォームすると，強化に 3 つの段階が現われることを見出した．すなわち約 25% までのやゝ明瞭な強度上昇とそれに引続く約 50% までの極めて緩慢な上昇，およびそれ以上の加工度における急激な上昇である．この傾向は上記の鋼ではそれほど明瞭でないが，これに 3 %の Co を添加すると著しくなる．彼らはこの現象を，第 1 段階では積層欠陥の発生，第 2 段階では拡張転位の動的回復による効果，第 3 段階では微細な炭化物の析出に基づく分散強化によって説明している．

しかし，筆者らの研究によれば，後述するように積層欠陥エネルギーの低い鋼でも，温度を上げて加工すれば転位は拡張せず，かえってセル化を起こす．彼らの結果は，本来強度が一様に上昇すべきはずであるのに，Co の添加によって低加工度の範囲内における強化が抑制されたと考える方が妥当であるように思われる．この場合，低加工度側での強度は直接焼入試料と同様な炭化物の分散強化によって支配されるのに対し，高加工度側では次第にセルによる強化が支配因子になると考えればよい．Turkalo と Low[9] は，高温で焼もどされたマルテンサイトの強度が Gensamer の関係からはずれ，その場合炭化物分散によって定まる平均自由行路の代りに結晶粒の大きさを用いれば，同一直線上にのることを見出した．この理由は，高温焼もどしを行なうと炭化物がほとんど結晶粒界に並ぶので，フェライトの平均自由行路を定めるものとして炭化物の代りに結晶粒界を用いた方が妥当だからであるとしている．

オースフォーム鋼でも，高加工度の場合には炭化物がセル壁上に偏存する傾向があるため，似たような効果が期待できる．しかし，Fig. 6 の結果から明らかなように，同じ ds の値に対して 5Cr 鋼と 5Ni 鋼の間にはかなりの相違がみられる．この事実は，オースフォーム鋼の強化がすべてセル粒径 ds のみによって整理できないことを示している．5Ni 鋼では炭化物の分散による相乗的な効果も無視できないものと思われる．このような事情は，

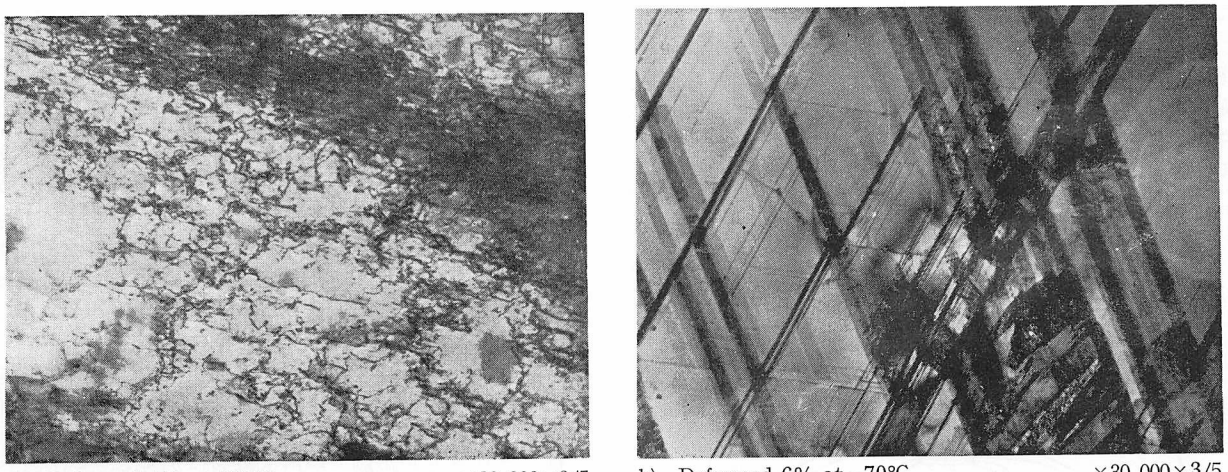

a) Deformed 4% at 500°C. ×30 000×3/5　　b) Deformed 6% at −70°C. ×30 000×3/5

Photo. 6. Transmission electron micrographs of 25%Mn–2%Mo–0·2%C steel.

絞りの変化にも現われている．すなわち，5Cr 鋼ではセル内部の摩擦応力が小さいと考えられるので，靱性の変化は単純な結晶粒微細化と同等にあつかうことができる．この場合，ds の減少とともにセル壁上での集積転位の数も減少する．従って強度が増加するにもかゝわらず塑性拘束が起こりにくく，絞りを生ずるためのボイド形成の応力も高くなる．

これに反し，5Ni 鋼ではセル内部の摩擦応力も強力に寄与しているため，絞りが低下する傾向にあるものと推定される．

低温引張試験の結果については，厳密な考察を行なうことは困難である．しかし，オースフォーム試料では，少なくとも −50°C の温度まで降伏点の温度依存性が直接焼入試料のものより小さいと言えるが極低温ではかなり増大する．伸びは全体的に 5Ni 鋼の方がやゝ優れており，両鋼ともオースフォームによる向上がみられ，特に極低温において向上が著しい．このような挙動は恐らく残留オーステナイトにも影響されているものと考えられる．

シャルピー衝撃値についてもオースフォームの効果は顕著であるが，このような挙動も ds の変化によって定性的に説明できる．特に shelf energy が加工度と共に増加することは，Fig. 1 の ψ の変化と対応するものであり，セル組織による強化機構の一つの証拠とみなすことができる．また一方，Fig. 2 に示すように ds の減少と n 値の減少が対応していることも，同様にセル組織による強化を間接的に裏付けている．

つぎに，マルテンサイト中に存在するセルの起源とその継承について考察する．Photo. 6a) は，25% Mn–2% Mo–0·2%C 鋼を 500°C で約 4% 加工したオーステナイト中に発生したセル化の中間段階を示すものである．加工度が増せばセル組織が明瞭になる．Photo. 6b) は同じく −70°C で約 6% 加工した場合の組織であるが，Photo. 6a) の組織と著しく異なり，多数の積層欠陥や ε 相が発生している．このように積層欠陥エネルギーの低い鋼を加工する場合は，加工温度が重要な意味をもつ．積層欠陥の高い鋼ではセル化に関する限り加工温度はあまり問題にならない．しかし，セル壁上に微細な炭化物が析出することが継承の条件であるならば，このような鋼でも温度をあげて加工しなければならないことの意味が明らかになる．いづれにしても，オースフォームによって準安定オーステナイト中に形成される炭化物を伴っ

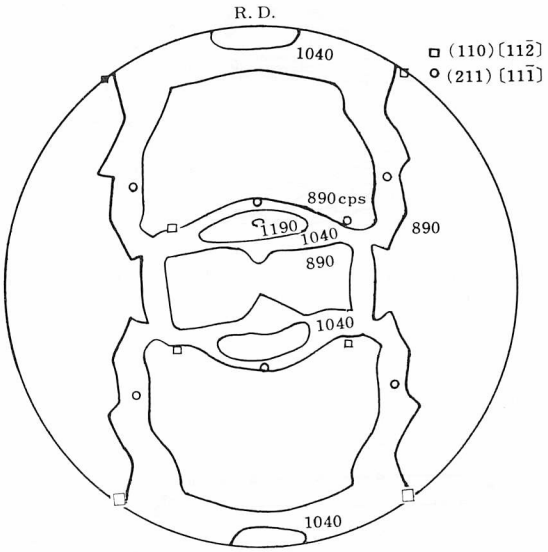

a) (200)γ pole, rolled 80% at 500°C.

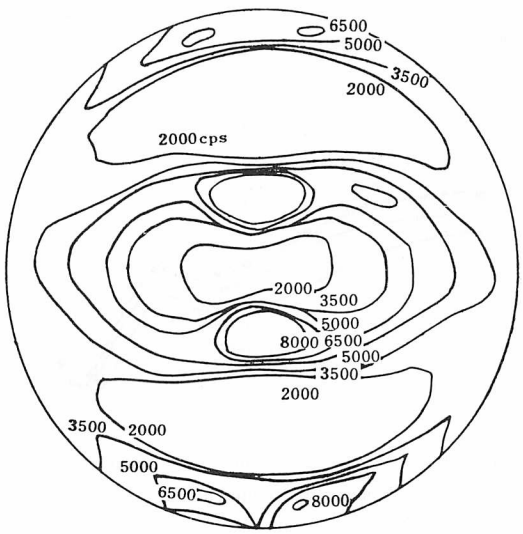

b) (110)α pole, after transformation.

Fig. 7. Rolling texture of a 30%Ni–0·3%C steel.

たセル組織が，強化の第1条件である．

このようにして形成されたセル組織は，マルテンサイトへ継承される際に格子変態を経由しなければならない．従って，そのまゝの形状で継承されるためには一定の条件が必要である．Fig. 7 は 30%Ni-0·3%C 鋼を 500°C で 80% 圧延した場合の加工オーステナイトおよびそれをサブゼロ冷却してマルテンサイトに変態させた場合の集合組織である．図のような集合組織をもつオーステナイト組織から，24通りの等価な格子関係に従ってマルテンサイト変態が起こるものとして計算極点図を画くと，Fig. 7b) に示すマルテンサイトの実測極点図とはあまりよく一致しない．しかし，上述の方位を有するオーステナイトが圧延を受ける際にもっともすべりが起こりやすいと考えられる面，すなわち作動すべり系に属する面だけが格子不変面として選択されると仮定すれば，計算極点図は実測のものとよく一致する．これを Fig. 8 に示した．たゞし変態は K–S 関係に従うものとした．

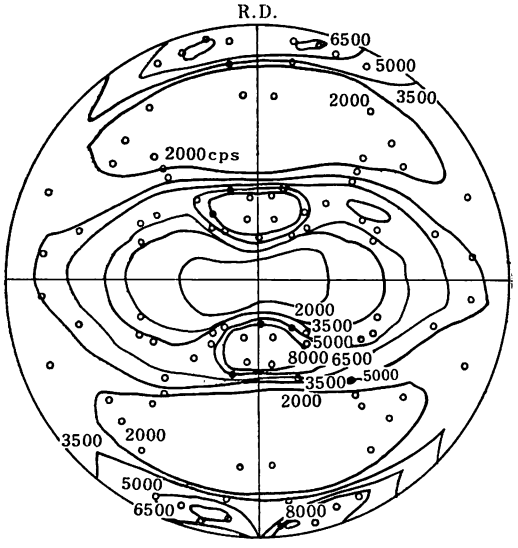

Fig. 8. Comparison of measured and calculated pole figures/(110)α pole.

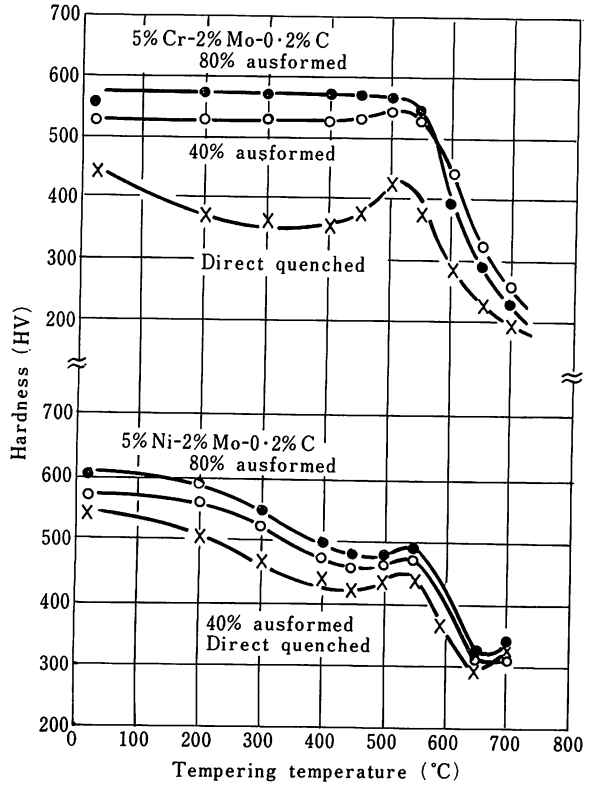

Fig. 9. Effect of degree of ausforming and tempering temperature on hardness of 5%Cr–2%Mo–0·2%C and 5%Ni–2%Mo–0·2%C steels.

このような結果は，作動すべり面，すなわちセル化を生ずるオーステナイトの {111} がそのまゝマルテンサイトの {110} に継承されることを示すものである．

継承されたセル組織と機械的性質との関係についてはすでに述べたが，以下に焼もどしに伴うかたさの変化とセル組織の関係について考察する．Fig. 9 は Table 1 に示す鋼とほとんど同じ組成を有する試料の焼もどしによるかたさの変化を，オースフォーム鋼と直接焼入鋼について比較したものである．5Cr 鋼では加工度の増加とともに二次硬化のピークが減少するが，5Ni 鋼では80%の加工度においても明瞭なピークが存在する．抽出レプリカによる炭化物の観察によれば，5Cr 鋼では主としてセル壁にそって粒状炭化物の成長がみられるのに対し，5Ni 鋼ではセル内部に整合炭化物が析出してこれが針状に成長する現象が認められた．このような結果はピークの挙動を合理的に説明しうるものである．また薄膜観察では 5Ni 鋼の方が容易に再結晶したが，5Cr 鋼ではセル組織が高温の焼もどしまで維持された．再結晶挙動におけるこのような相違は，粒界炭化物の影響によるものである．

5. 結　　論

1. オースフォームした鋼の微細組織中には特有のセル構造がみられ，この組織がオースフォーム鋼の機械的性質を決定する主要な因子である．5Cr 鋼では加工度とともにセル粒径の微細化が明確にみられるが，5Ni 鋼では低加工度側でこの傾向がやゝ不明瞭であった．
2. 5Cr 鋼の強度は加工度とともにほゞ直線的に増大するが，5Ni 鋼では低加工度の範囲で強度の上昇に停滞がみられる．
3. オースフォームによる延性の挙動は，5Cr 鋼の場合強度上昇にもかゝわらず一様伸びの低下がみられないのに対し，5Ni 鋼では高加工度において若干の低下がみられる．この差は n 値の挙動とも合致する．一方，延性破壊による靱性を代表する絞りとシャルピー，およびぜい性せん移温度は，5Cr 鋼の場合いづれも加工度の増大による強化とともに明らかに上昇を示した．このような現象もセル粒径の効果によって説明することができる．5Ni 鋼の絞りは，低加工度での上昇と高加工度での低下の傾向がわずかに見られた．
4. オースフォーム鋼は極低温において直接焼入鋼にみられるのと同等以上の強度上昇を示すが，反面延性と靱性において若干増加の傾向がみられる点が異なる．
5. セル組織の継承に関連し，5Cr 鋼と 5Ni 鋼の挙動には差違が認められる．この差は，セル壁上への炭化物の析出挙動に対する Cr および Ni の相互作用の差に基づくものと考えられる．

文　　献

1) J.C. Shyne, V.F. Zackay and D.J. Schmatz: Trans. Amer. Soc. Met., **52** (1960), p. 346
2) P.M. Kelly and J. Nutting: J. Iron Steel Inst., **197** (1961), p. 199
3) 田村，吉村，茨木，多賀谷：日本金属学会誌，27 (1963), p. 206
4) 渡辺，荒木，宮地：鉄と鋼，55 (1969)，p. 797. Trans. JIM, 9 (1968), p. 111
5) W.B. Morrison: Trans. ASM, **59** (1966) p .825
6) T. Kunitake: Trans. ISIJ, **7** (1967), p. 254
7) R.A. Grange: Trans. Amer. Soc. Met., **59** (1966), p. 26
8) H. Borchers and J. Möller: Arch. Eisenhüttenw, **9** (1970), p. 853
9) A.M. Turkalo and J.R. Low, Jr.: Trans. AIME, **212** (1958), p. 750

討論 pp. 358-359 参照

Ductility Enhanced by Martensitic Transformation in Metastable Austenitic Iron Alloys

I. Tamura T. Maki

Kyoto University

The characteristics of transformation-induced plasticity (TRIP) and the effect of strain rate on TRIP in several metastable austenitic iron alloys were studied. The chemical composition, Ms and Md temperatures of alloys are shown in Table 1. These alloys are transformed from austenite to martensite in entirely different manners. The martensite formed is α' martensite (lenticular partially twinned martensite) in the iron-nickel-carbon alloy, α' (dislocated lath martensite) and ε' martensite in the iron-chromium-nickel alloy, and ε' martensite in the iron-manganese-carbon alloy. Since these features are related to the stacking fault energy of austenite, ε' martensite is apt to be formed in an alloy with a low stacking fault energy of austenite. The tensile tests were carried out at various temperatures between +240°C and −196°C with several strain rates in the range of $5\cdot5\times10^{-4}$ and $1\cdot65\times10^{-1}$/sec ($5\cdot5\times10^{-4}$/sec was mainly used) Microstructural observations and the determination of martensite content by X-ray analysis were carried. out on specimens after tensile testing.

The results obtained are briefly summarized as follows:

(1) In all alloys, a high elongation is obtained by strain-induced martensitic transformation. The peak elongation value exists at some test temperature between Ms and Md. In tests at the temperature showing the maximum elongation, the strain-hardening exponent increases continuously with the strain. The effective condition for enhancement of the transformation-induced plasticity is that the martensite is constantly formed little by little during deformation up to fracture. When the martensite is plentifully formed in the early stages of deformation, or the total amount of martensite formed is too small, the elongation is not as large. The elongation does not simply depend on the total amount of martensite induced during deformation but also on the conditions of martensite formation.

The following two points can be considered as the main reasons why a high elongation is obtained when martensite is formed constantly during deformation. The first one is suppression of necking. When martensite is formed little by little during deformation, the strain-hardening exponent increases continuously with the strain and at last reaches a much larger value than that of austenite at the high strains near fracture. Consequently, the uniform elongation becomes larger when martensite is formed gradually during deformation. Secondly, the suppression of initiation and propagation of microcracks is considered. The stress concentrated locally during deformation is relaxed by the formation of martensite, and hence the initiation of microcracks is prevented. Furthermore, even if microcracks are initiated, the stress concentration at the tips of microcracks is also relaxed by the formation of martensite, and so the propagation of microcracks is suppressed. Thus, it can be considered that transformation-induced plasticity is caused both by the suppression of necking and by the suppression of initiation and propagation of microcracks.

The temperature gap between Ms and Md is very different among the three alloys. The gap is about 80°C in the iron-nickel-carbon alloy, about 200°C in the iron-chromium-nickel alloy and about 450°C in the iron-manganese-carbon alloy. The difference in the temperature gap between Ms and Md may be closely connected with the difference in type of martensite formed by deformation. In the iron-manganese-carbon and iron-chromium-nickel alloys with a low stacking-fault energy of austenite, ε' martensite is formed by deformation. The ε' martensite is easily induced by strain, so the Md temperature increases. The temperature range showing the high elongation is quite different among the three alloys in accordance with the difference of the temperature gap between Ms and Md. The elongation-temperature curve has a very sharp peak in the iron-nickel-carbon alloy, a fairly broad one in the iron-chromium-nickel alloy and a very broad one in the iron-manganese-carbon alloy, as shown in Fig. 14. The iron-chromium-nickel alloy shows a fairly high elongation even at temperatures below Ms, while in the case of the iron-nickel-carbon alloy the elongation decreases rapidly below Ms. This fact may result from differences in the amount of retained austenite prior to tensile testing and the differing conditions of martensite formation during deformation. Thermally transformed martensite of the iron-nickel-carbon alloy is formed with burst phenomenon. In

the iron-chromium-nickel alloy, martensite is formed without bursts and the increase in the amount of martensite produced on cooling is less than in the iron-nickel-carbon alloy. Furthermore, when martensite is formed from retained austenite during deformation below Ms, the martensite of the iron-nickel-carbon alloy is formed plentifully at an early stage of deformation, but in the case of the iron-chromium-nickel alloy martensite is formed gradually with strain. These are considered to be the reasons why fairly large transformation-induced plasticity occurs in the iron-chromium-nickel alloy even at temperatures below Ms. In the iron-manganese-carbon alloy, where the ε' martensite is formed gradually with strain even at low temperatures, a high value of elongation is obtained over a wide temperature range. Transformation-induced plasticity depends greatly on the transformation behavior of martensite.

The tensile strength increases with decreasing test temperatures below Md. The change in tensile strength with test temperature is in good agreement with the martensite content after fracture. In the iron-nickel-carbon and iron-chromium-nickel alloys, the 0·2% proof stress drops at a temperature near the Ms. This fact is caused by the stress-induced martensitic transformation at low stress levels before yielding of the austenite. This phenomenon is remarkable in the iron-nickel-carbon alloy because the martensite is formed in bursts. Below Ms, the proof stress increases rapidly in the iron-nickel-carbon alloy and slightly in the iron-chromium-nickel alloy because of the existence of thermally transformed martensite prior to the test.

(2) The effect of strain rate on the transformation-induced plasticity has some relation with the environment of the specimens during testing. The elongation decrease with increased strain rate is less when the tests are made in liquid than when they are made in gas. This relation is especially notable in the iron-nickel-carbon alloy having a small temperature gap between Ms and Md as shown in Fig. 14 and Fig. 15. This can be explained by the temperature rise of the specimen due to increased strain rate. In the iron-chromium-nickel and iron-nickel-carbon alloys, however, the elongation decreases with increased strain rate even in the liquid bath where hardly any temperature rise of the specimen during deformation is observed. In these cases, as illustrated in Photo. 3, the amount of strain-induced martensite is scarcely affected by strain rate. The effect of strain rate on metastable austenitic stainless steel has been simply explained by the temperature increase of the specimen during deformation. It seems, however, that the effect of strain rate is not so simple. It may be considered that fracture occurs more easily and sooner with increased strain rate.

In the iron-manganese-carbon alloy where the ε' martensite is induced by deformation, the strain-rate dependency of tensile properties is very low.

準安定オーステナイト鉄系合金のマルテンサイト変態誘起延性

田村今男　牧　正志

京都大学工学部

1. 緒　　言

準安定オーステナイトをMd点以下の温度で加工するとマルテンサイト変態がおこる，このような準安定オーステナイト鉄合金を種々な温度で引張試験をおこなうと，変形中にマルテンサイトが生成するような温度領域で伸びが著しく大きくなる[1~7]．この現象はマルテンサイト変態誘起塑性 (Transformation-Induced Plasticity) と呼ばれており，従来，主にFe-Cr-Ni系ステンレス鋼におけるこの現象について研究がなされている．

1967年，Zackay ら[8]によって開発された高い強度と良好な伸びを兼ねそなえもつTRIP鋼はこの現象を巧みに応用したものであり，超強靱鋼開発の新しい方向を示すものとして注目すべきものである．しかし，これらの基礎となるマルテンサイト変態誘起塑性現象に関する系統的な研究は未だ少なくその本質の解明が必要である．

本研究はマルテンサイト変態のおこる代表的な鉄系合金を用い，マルテンサイト変態誘起塑性現象の合金系による特徴および歪速度の影響を調べ，各合金系の相違点，類似点を明らかにし，より本質的な解明を目指そうとするものである．

2. 実 験 方 法

鉄系合金において生成するマルテンサイトは，bccまたはbct構造の α' マルテンサイトと，hcp構造の ε' マルテンサイトの2種類がある．これらはオーステナイトの積層欠陥エネルギーと密接な関係があり，積層欠陥エネルギーの低い合金ほど ε' マルテンサイトが生成しやすい傾向がある．本研究では，α' マルテンサイトが生成する合金としてFe-Ni-C，ε' マルテンサイトが生成する合金としてFe-Mn-C，α' と ε' の両者が生成する合金としてFe-Cr-Niを用いた。試料は高周波真空溶解により作製したもので，その化学組成，Ms点およびおおよそのMd点をTable 1に示す．これらを熱間鍛造により約10mm厚にしたものをFe-Ni-CおよびFe-Cr-Ni合金は1200°Cで，Fe-Mn-C合金は1000°Cで20時間真空中にて均一化処理を施した後，冷間圧延，真空焼鈍を繰返して0·5mm厚の板にした．これから圧延方向に平行に引張試片を作製した．試験片の形状はFig. 1に示すように厚さ0·5mm，平行部の長さ30mm，巾10mmの板状試験片である．オーステナイト化処理としてFe-Ni-CおよびFe-Cr-Ni合金は1150°C 3時間，Fe-Mn-C合金は1000°C 2時間，おのおの真空中にて加熱後，Fe-Ni-Cは炉冷，Fe-Cr-Ni，Fe-Mn-C合金は油焼入れを行なった．

Table 1. Chemical composition, Ms and Md temperatures of specimens.

	Composition (wt%)					Ms (°C)	Md (°C)
	Ni	Cr	Mn	C	Fe		
Fe-Ni-C	28·81	—	—	0·26	bal	− 60	≈+ 25
Fe-Cr-Ni	11·47	18·89	—	0·006	bal	− 70	≈+130
Fe-Mn-C	—	—	24·22	0·26	bal	−180	≈+260

以上の処理を施した後，試料表面の酸化膜，脱炭層を除去するため軽く電解研磨を行なった．なお各合金のMs点は，Table 1に示したようにすべて0°C以下であるため，処理後，室温では完全にオーステナイト一相である．引張試験はインストロン型島津オートグラフを用い，+240°C～−196°Cの種々な温度で行なった．引張速度は主に1mm/min（公称歪速度 $5·5\times10^{-4}$/sec）であり，さらに歪速度の影響を調べるためには1mm/min～300mm/minと変化させた．なお，所定の試験温度を得るために+240°C～0°Cでは油，水を用い，0°C以下は液体窒素を気化させて冷却する低温恒温槽を用いた．歪速度の影響を調べる際に，0°C～−80°Cの間で一部アルコールとドライアイスの組合せによる液体冷媒をも用いた．さらに引張試験後の試片を用い，光学顕微鏡により組織観察，X線回折によるマルテンサイトの定量をおこなった．

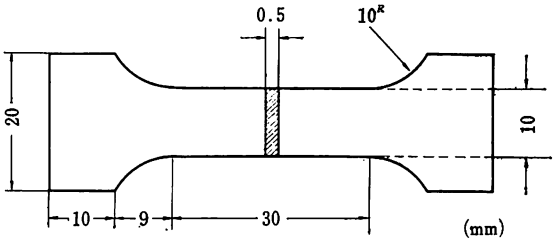

Fig. 1. Shape and dimensions of the tensile specimen.

3. 実 験 結 果

3.1 各種鉄系合金のマルテンサイト変態誘起塑性現象

各種鉄系合金における準安定オーステナイトを種々な温度で引張試験したときの結果を示す．この場合歪速度は $5·5\times10^{-4}$/secであり，試験雰囲気は0°C以上240°Cまでの高温側では油および水，0°C以下は液体窒素を気

化させることによって一定温度に保持する低温恒温槽を用いた.

3.1.1 Fe-Ni-C 合金

Fe-29%Ni-0·26%C 合金の種々な温度での代表的な応力—歪曲線を Fig. 2 に示す.

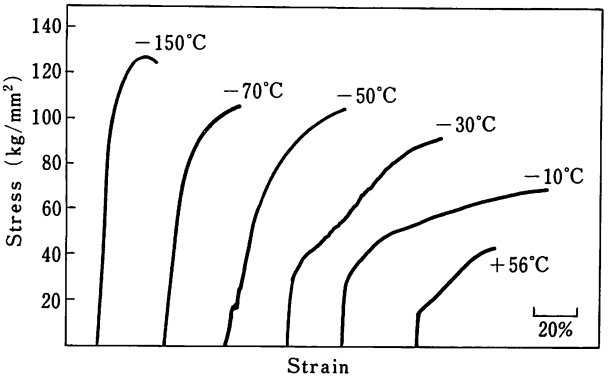

Fig. 2. Stress-strain curves of Fe-29% Ni-0·26%C alloy.

ここに示すように，変形中にマルテンサイトが生成する場合，応力—歪曲線にセレーションが観察された．+56°C は Md 点以上であるためオーステナイトのみの変形であるが，−10°C 試験では約 20%歪後から細かいセレーションが破断に至るまで連続的に生じている．なお後で示すが，−10°C 試験で伸びが最高，つまり顕著な変態誘起塑性が認められた．試験温度がさらに低くなり −30°C の場合には数 % 歪よりセレーションが生じ，その振巾も大きい．また，セレーションが生じると曲線の傾斜（加工硬化）が大きくなっている．本合金の Ms 点は −60°C であるが，試験温度が Ms 点直上および直下の −50°C や −70°C では，オーステナイトが降伏する以前に，つまり低応力でマルテンサイトが誘発されるため，応力—歪曲線の立上り部ですでに大きなセレーションが生じる．−70°C の場合は Ms 点以下であるので，試験前にある程度のマルテンサイトが存在しており，このセレーションは残留オーステナイトの応力誘起マルテンサイト変態によるものである．−150°C では試験前に多量のマルテンサイトが生成しており，ほとんどマルテンサイトの変形と考えられる．以上示したように，応力—歪曲線には試験温度が Ms 点近傍へと低くなるにつれてより少歪でセレーションが開始し，その振巾が大きくなる．このセレーションは変形中のマルテンサイト生成に帰因するのであるから，このことから Ms 点近傍になる程，より少歪でより多量にマルテンサイトが生成するのがわかる．

Fig. 3 に試験温度と 0·2% 耐力，引張強さ，および伸びの関係を示す．0·2% 耐力は温度が下がるにつれて上昇する．Ms 点近傍では，図中 2 本の曲線で示してあるが，これは Ms 点近傍ではオーステナイトが降伏する以前に低応力で多量のマルテンサイトが生成するようになるため，この変態によってひずみを発生するが，点線で示した曲線はそのひずみを無視した場合の曲線であり，著者らの以前の論文[5~7] ではこの曲線を示してある．しかし，応力によって誘発された変態によるひずみを考慮して 0·2%耐力をとると実線で示したように Ms 点近傍で低下する[9~11]．Ms 点以下に温度が下がるにつれて 0·2% 耐力が急激に上昇するが，これは試験開始前にすでに多量のマルテンサイトが生成しているからである．引張強さは Md 点より低温になると急に上昇している．これは後述するようにマルテンサイトの生成量と非常によい対応を示す．一方，伸びは試験温度が Md 点より低くなると急激に上昇し，−10°C 近傍で最高値を示し，その後低温になるにつれて急激に減少している．このように，伸びの peak は Md 点と Ms 点の間に存在しており，最高伸びは 90% をこす大きなもので，典型的なマルテンサイト変態誘起塑性を示している．

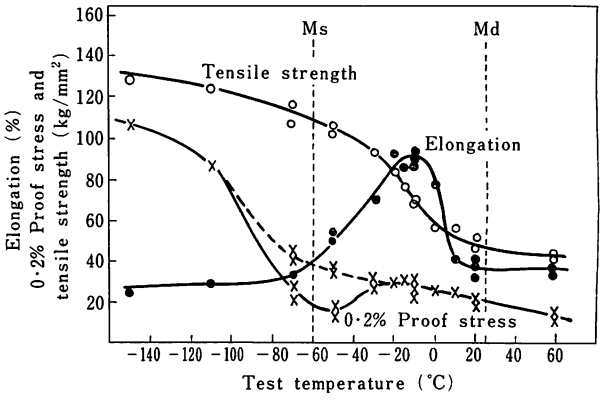

Fig. 3. Effect of test temperature on the tensile properties of Fe-29%Ni-0·26%C alloy.

応力—歪曲線にマルテンサイト生成によるセレーションがみられ，このようなセレーションがおこる場合，曲線の傾斜（加工硬化）が大きくなる傾向があった．そこで．加工硬化の挙動を調べるために，各試験温度で得られた真応力—真歪曲線から各歪の微少領域で $\sigma=K\varepsilon^n$ が成立するとして，各種領域間で 10% 歪ずつの平均の加工硬化指数を求めた結果を Fig. 4 に示す．Md 点以上の +58°C，Ms 点以下の −70°C ではほとんど一定であるが，最高伸びが得られた −10°C では歪量の増加とともに刻々加工硬化指数が上昇しているのが特徴である．一方，Ms 点近傍の −30°C の場合，少歪で急激な上昇を示している．このように，変形中にマルテンサイト変態がおこる場合には真応力—真歪曲線は $\sigma=K\varepsilon^n$ という一つの n 乗硬化式が成立せず，加工硬化指数 n は歪とともに大きく変化する．ただし，ここで得た加工硬化指数は本来の加工硬化ではなく，オーステナイト中に硬いマルテンサイトが生成したためにおこるみかけの加工硬化指数である．加工硬化の挙動を表わす別な尺度として，加工硬化率 $d\sigma/d\varepsilon$ の変化を調べた結果を Fig. 5 に示す.

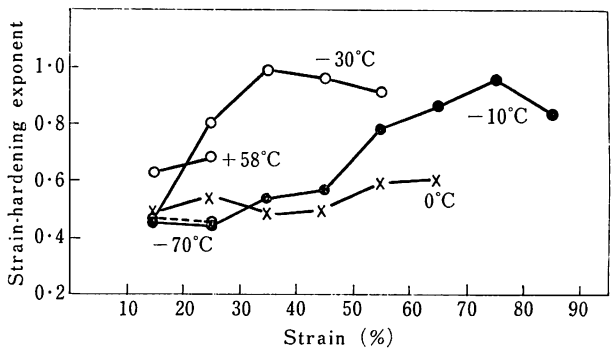

Fig. 4. Variations in the strain-hardening exponent with strain in Fe-29%Ni-0·26%C alloy.

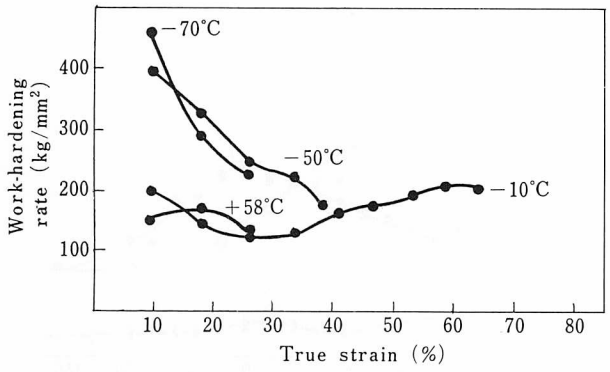

Fig. 5. Variations in the work-hardening rate with strain in Fe–29%Ni–0·26%C alloy.

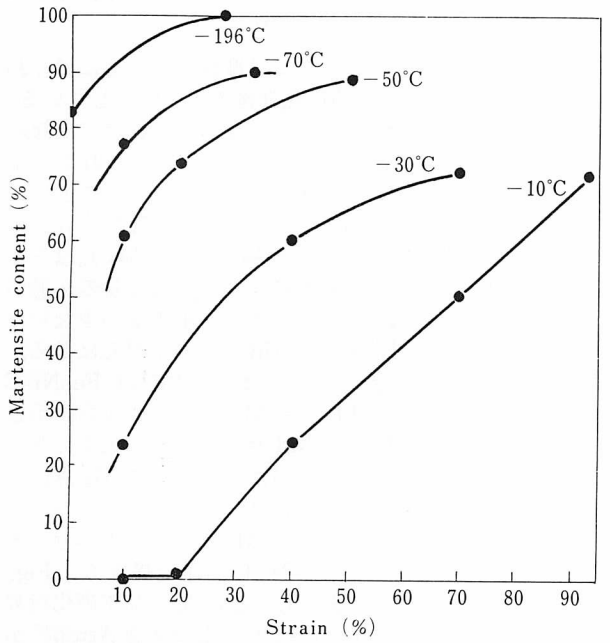

Fig. 6. Martensite content of Fe–29%Ni–0·26%C alloy as a function of strain at various test temperatures.

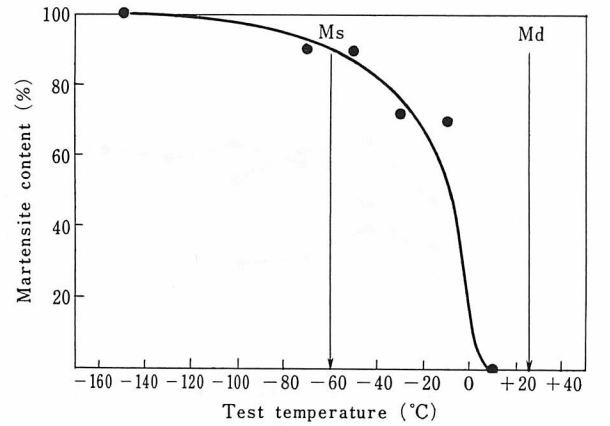

Fig. 7. Effect of test temperature on the martensite content of Fe–29%Ni–0·26%C alloy after tensile fracture.

全体に加工硬化率は歪増加とともに減少するが，伸びが最高となった −10°C の場合，歪量が 20～30% までは低下するが，その後再び上昇するという特異な挙動を示す．

以上示したような加工硬化挙動は，変形中のマルテンサイトの生成傾向と密接に関連するものである．

Fig. 6 は各温度で種々な加工度の歪を与え，そのときに生成するマルテンサイト量をX線により定量した結果である．−10°C 試験では最初 20% 歪位はオーステナイトのみの変形であり，その後歪増加とともにマルテンサイトがほぼ直線的に増加しているが，低温になるほど変形の初期に多量のマルテンサイトが生成する．Fig. 7 は各温度で試験したときの破断後の試片の平行部でのマルテンサイト量を示す．各温度で変形量，すなわち破断伸びが異なるが，破断後のマルテンサイト生成量は低温になるほど多くなっている．+10°C では試片破断部にマルテンサイトが生成していたが，平行部では非常に少な

a) Deformed 40% in tension at 0°C. ×1050

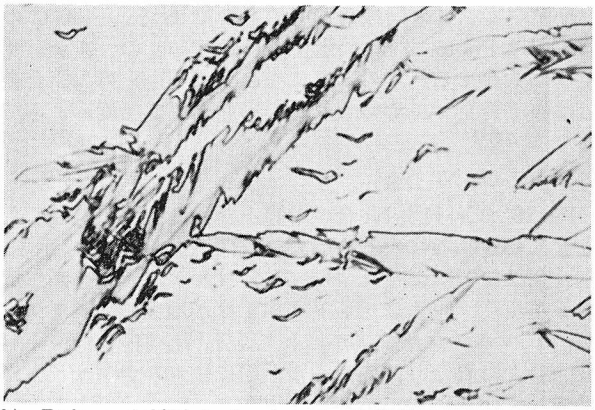

b) Deformed 20% in tension at −30°C. ×600

c) Deformed 5% in tension at −50°C. ×250

Photo. 1. Optical micrographs showing morphology of strain-induced martensite in Fe–29%Ni–0·26%C alloy (Ms = −60°C).

い．最高伸びが得られた −10°C では破断後約 70%，Ms 点直上の −50°C では約 90% のマルテンサイトが生成している．

このように，低温になるほど破断時のマルテンサイト量は多くなっているが，伸びは Ms 点直上では急激に低下している．このことは，伸びは変形中に生成されたマルテンサイト量のみに依存するものではなく，少しづつ破断に至るまで徐々にマルテンサイトを生成してゆくことが変態誘起塑性を大きくする要因であることを意味している．また，Fig. 3 に示した引張強さの変化は破断時のマルテンサイト量の変化とよく対応している．なお，Fe-Ni-C 合金では加工によって誘発されるマルテンサイトはいずれも α' マルテンサイトであるが，良好な伸びが得られた 0°C〜−20°C 近傍で生成するマルテンサイトは Photo. 1 a) に示すような特異な形態を呈するものが生成する．このようなマルテンサイトは透過電子顕微鏡観察によれば変態双晶のない dislocated martensite であり，結晶方位関係はほぼ K-S 関係を満たしていた．このマルテンサイトは歪とともに比較的徐々に生成するもので，変態誘起塑性にきわめて有効である．一方，Ms 点近傍の −50°C では Photo. 1 c) に示すように，加工によってレンズ状マルテンサイトが生成する．これらは mid-rib のある partially twinned martensite であり，単に冷却によって生成するマルテンサイトと同様な形態のものである．これらは比較的変形初期に burst 現象を伴って生成する．なお，Ms 点以下の温度での変形により残留オーステナイトから生成する加工誘発マルテンサイトもこれと同様な形態のものである．−30°C の加工では Photo. 1 b) に示す如く両 type のマルテンサイトが共存する．このように Fe-29%Ni-0·26%C 合金では加工誘発マルテンサイトの形態が生成温度によって異なる[6,12]．

3.1.2 Fe-Cr-Ni 合金

Fe-19%Cr-11%Ni 合金を種々な温度で引張試験したときに得られた代表的な応力—歪曲線を Fig. 8 に示す．本合金は加工により α' および ε' マルテンサイトが生成するが，ε' マルテンサイトは加工度が増すにつれて減少し，α' マルテンサイトが増してくる[13]．前述の Fe-Ni-C 合金とは異なり，応力—歪曲線にはマルテンサイトが生成しているにもかかわらずセレーションはほとんど認められなかった．しかし，Ms 点直上の −60°C などでは歪量増加に伴って加工硬化の度合が大きくなっている．

Fig. 9 に試験温度と 0·2% 耐力，引張強さ，および伸

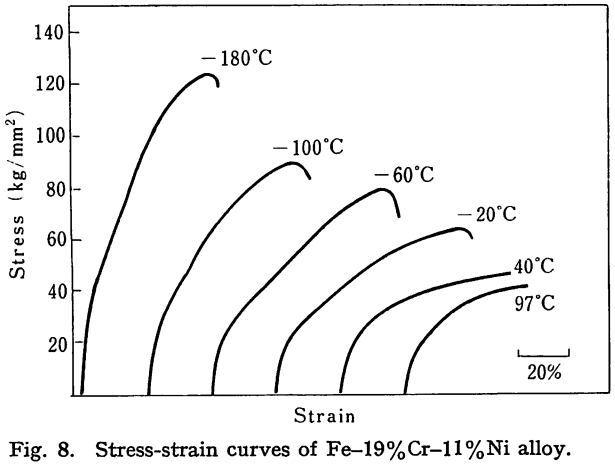

Fig. 8. Stress-strain curves of Fe-19%Cr-11%Ni alloy.

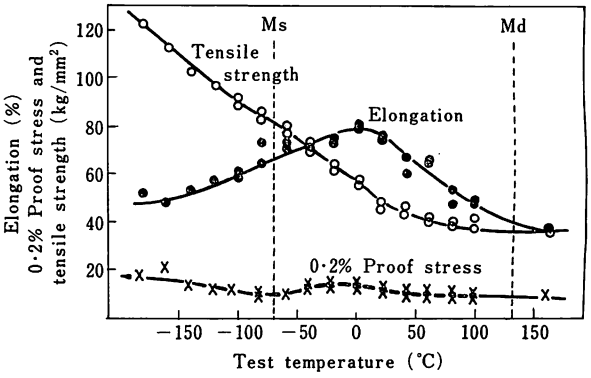

Fig. 9. Effect of test temperature on the tensile properties of Fe-19%Cr-11%Ni alloy.

びの関係を示す．0·2% 耐力は温度低下とともにごくわずかに上昇しているが，Ms 点近傍で少し低下している．これは Fe-Ni-C 同様，このような Ms 点近傍では低応力でマルテンサイトが誘発されるためと考えられる．また，Ms 点以下の温度でも 0·2% 耐力はわずかに上昇している程度で，Fe-Ni-C と比べてその上昇の度合が小さい．これは Fe-Cr-Ni 合金の場合には，Ms 点以下でも Fe-Ni-C のように burst による一度に多量の変態がおこらないので，試験前のマルテンサイト量が少ないためと考えられる．引張強さは Md 点より上昇しはじめ，低温になると上昇が急になる．また，伸びは Fe-Ni-C 合金の場合と同様に Md 点と Ms 点の間で最高を示している．ただし，Ms 点と Md 点の温度差が大きくなっており，伸びの良好な温度領域が広い．特に Ms 点以下でも大きな伸びを示しており，オーステナイトのみが変形する場合（Md 点以上）より Ms 点以下の方がむしろ伸びが大きいという点が Fe-Ni-C 合金と異なる．Fig. 10 に各試験温度での歪量変化にともなう加工硬化指数の変化を示す．最高伸びが得られ顕著な変態誘起塑性がおこる 0°C の場合，加工硬化指数は歪とともに刻々上昇している．一方，+80°C，−125°C ではほぼ一定，もしくはわずかに上昇している程度である．

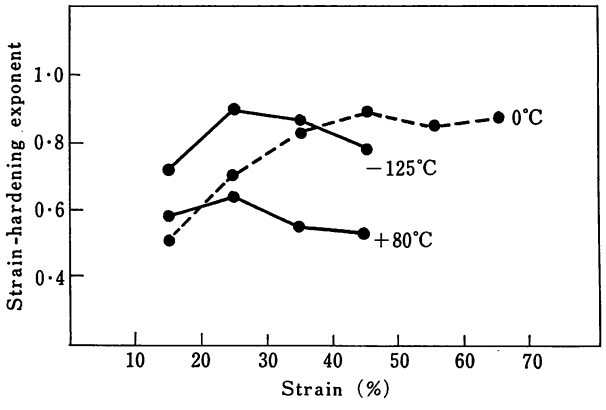

Fig. 10. Variations in the strain-hardening exponent with strain in Fe-19%Cr-11%Ni alloy.

3.1.3 Fe-Mn-C 合金

Fe-24%Mn-0·26%C 合金を種々な温度で引張試験したときに得られた応力—歪曲線を Fig. 11 に示す．本合金では ε' マルテンサイトが生成することを X 線により確認した．Ms 点は −180°C であるが，Md 点は破断後

の組織観察によれば +240°C 試験でもごくわずかのマルテンサイトが試片破断部に生成しており，約 260°C 前後と考えられる．それ故，すべての試験温度で変形中に ε' マルテンサイトが生成するが，応力—歪曲線には Fe-Ni-C 合金のようなセレーションは認められなかった．なお，+240°C 試験では比較的細かいセレーションが観察された．しかし，このセレーションは歪速度を増加すると認められなくなる．このようなことから，この 240°C でのみ現われたセレーションは侵入型固溶原子（炭素）による動的歪時効によるものと考えられる．

Fig. 12 に試験温度と 0·2% 耐力，引張強さおよび伸びの関係を示す．図に示したように，Fe-Mn-C 合金は Ms 点と Md 点の温度態が非常に大きいのが特徴である．0·2% 耐力，引張強さともに試験温度低下につれてほゞ直線的に上昇している．一方，伸びは全温度範囲で非常に良好であり，+150°C 近傍で伸びが最高となり，変態誘起塑性現象が認められる．Fig. 13 に代表的な温度での引張試験により得られた加工硬化指数と歪量の関係を示す．このように，本合金では Ms 点と Md 点の温度差が大きいため，あらゆる温度で加工硬化指数が歪とともに刻々上昇する傾向を示している．Photo. 2 に +80°C および −196°C 変形での マルテンサイト の生成状態を示す．+80°C では少歪ではオーステナイトのみの変形であるが，約 20% 歪でわずかに ε' マルテンサイトが生成しはじめる．一方，−196°C 変形の場合 5% 歪ですでに ε' マルテンサイトが生成し，その後歪増加とともに生成量が増加していく．

以上，代表的な 3 種の鉄系合金の結果を述べたが，すべての合金で，明瞭なマルテンサイト変態誘起塑性がおこることが明らかとなり，伸びの peak はいずれも Md 点と Ms 点の間に存在している．しかし，Fig. 14 に示すように Md 点と Ms 点の温度差が合金系により非常に異なり，オーステナイトの積層欠陥エネルギーが低いものほど，つまり Fe-Ni-C, Fe-Cr-Ni, Fe-Mn-C の順に広くなっている．その結果，伸びの良好な温度領域が非常に異なっている．

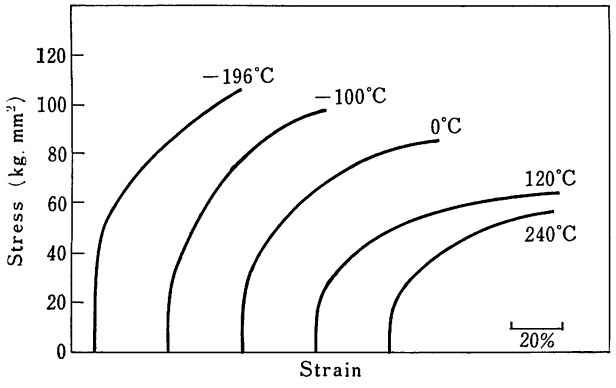

Fig. 11. Stress-strain curves of Fe–24%Mn–0·26%C alloy.

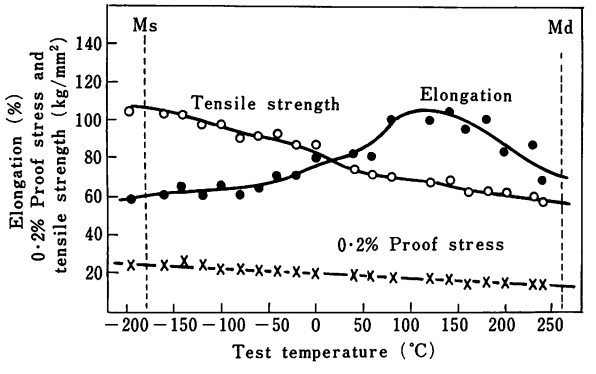

Fig. 12. Effect of test temperature on the tensile properties of Fe–24%Mn–0·26%C alloy.

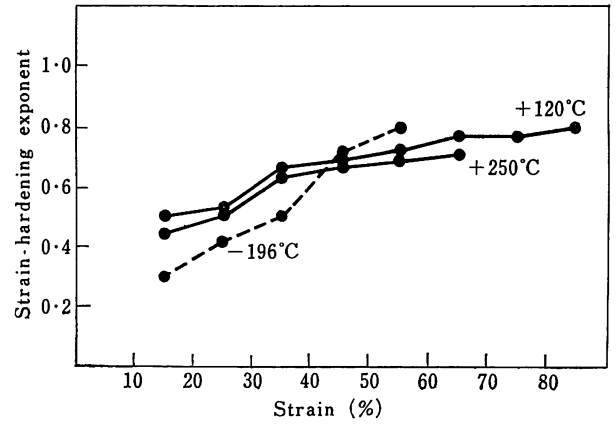

Fig. 13. Variations in the strain-hardening exponent with strain in Fe–24%Mn–0·26%C alloy.

3.2 マルテンサイト変態誘起塑性におよぼす歪速度の影響

いままで述べた実験結果は歪速度 $5{\cdot}5\times10^{-4}$/sec の場

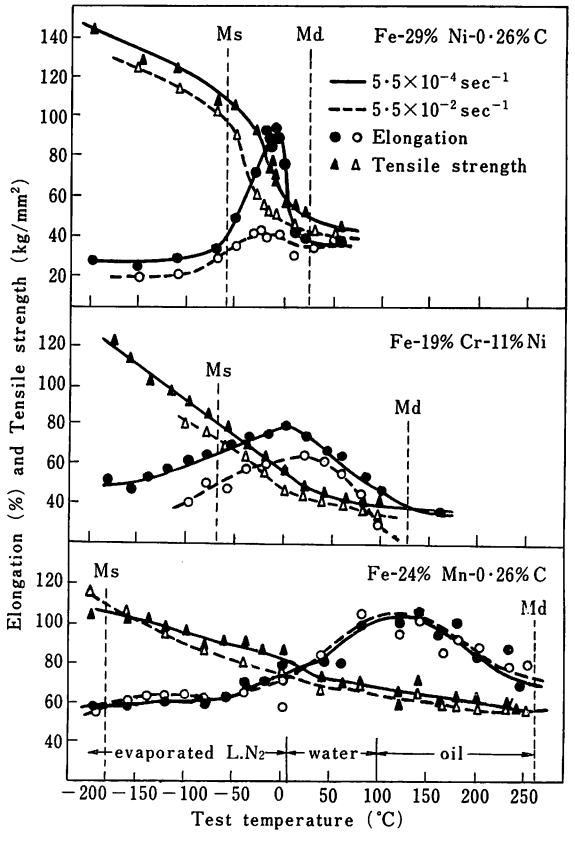

Fig. 14. Effect of strain rate on the tensile properties at various temperatures of Fe–29%Ni–0·26%C, Fe–19% Cr–11% Ni and Fe–24%Mn–0·26%C alloys.

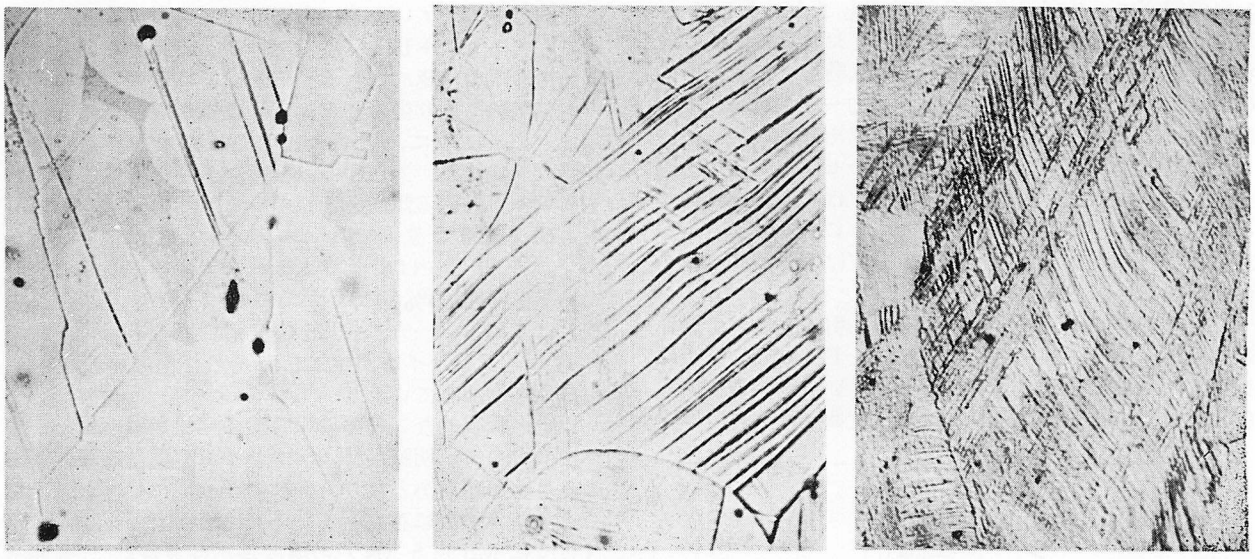

a) 20%　b) 40%　c) 60%　×1 000

Deformed at +80°C

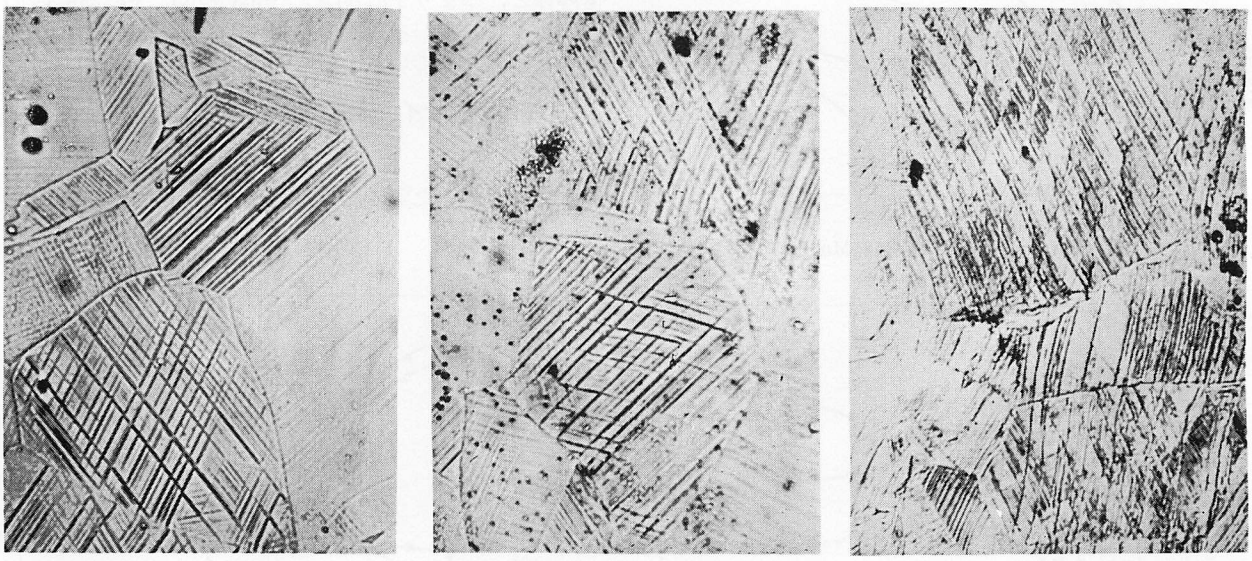

a) 5%　b) 20%　c) 58%　×1 000

Deformed at −196°C

Photo. 2. Variations in optical microstructure with strain of Fe–24%Mn–0·26%C alloy deformed in tension.

合について示した．次に各合金でのマルテンサイト変態誘起塑性現象に及ぼす歪速度の影響を調べるため，歪速度 $5\cdot5\times10^{-2}$/sec で各温度で引張試験した結果を，歪速度 $5\cdot5\times10^{-4}$/sec の場合の結果と併せて Fig. 14 に示す．これから明らかなように，歪速度が増加すると Fe–Ni–C 合金では伸びが急激に低下し，変態誘起塑性が非常に低下する．Fe–Cr–Ni 合金はわずかに低下するか，Fe–Mn–C 合金はほとんど変化がない．このようにオーステナイトの積層欠陥エネルギーが低くなるほど歪速度の影響は小さくなる傾向が認められた．

本実験では試験雰囲気が 0°C 以上は油，水の液体であるが，0°C 以下は液体窒素を気化させて得たものである．歪速度の影響を調べる場合，歪速度増大に伴う試験片の温度上昇が問題となる．この試験片の温度上昇は液体中試験では小さく，大気中（気体中）では大きい．Fe–Ni–C 合金の場合，最高伸びが得られた温度（−10°C）では気体雰囲気中の試験であるため，試験片の温度上昇による効果が大きく現われたものと考えられる．そこで，Fe–Ni–C 合金を歪速度 $5\cdot5\times10^{-4}$/sec で最高伸びが得られた −10°C で試験雰囲気を変化させて歪速度の影響を調べた結果を Fig. 15 に示す．図中，実線はアルコールとドライアイスによる液体雰囲気，破線は液体窒素を気化させる気体雰囲気での結果である．気体雰囲気では歪速度が増すと急激に伸びが低下してしまう．ところが，液体雰囲気試験ではその低下の度合は少ない．試験中の試験片の実際の温度上昇を測定した結果，歪速度 $5\cdot5\times10^{-4}$/sec の場合には気体中，液体中ともに試片の温度上昇はほとんどない．しかし，歪速度増加につれて，気体雰囲気中では試験片温度が急激に上昇し，歪速度 $5\cdot5\times10^{-2}$/sec では破断時に約 20°C の温度上昇があった．一方，液体雰囲気中では試験片の温度上昇は非常に小さく，歪速度 $1\cdot65\times10^{-1}$/sec の場合で高々 4°C の上昇である．このように歪速度の影響を調べる場合にその試験雰囲気の相違によりその結果は大きく異なる訳で，これらは実際の試験片の温度上昇効果によることは明らかである．しかし，試片の温度上昇が非常に少ない液体雰囲気中で

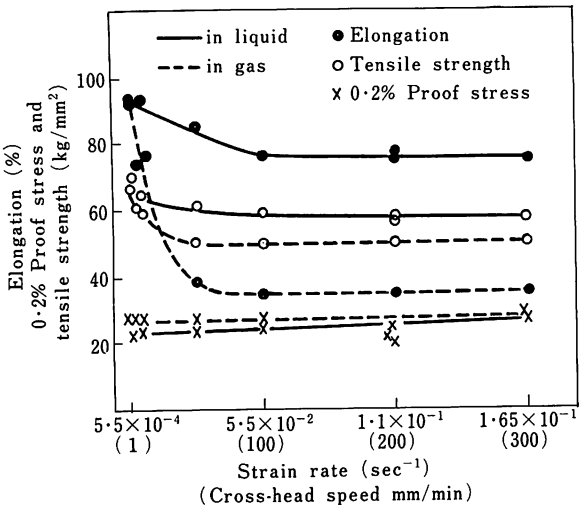

Fig. 15. Effect of strain rate on the tensile properties of Fe-29%Ni-0·26%C alloy tested in liquid (acetone with dry ice) and in gas (evaporated liquid nitrogen) at −10°C.

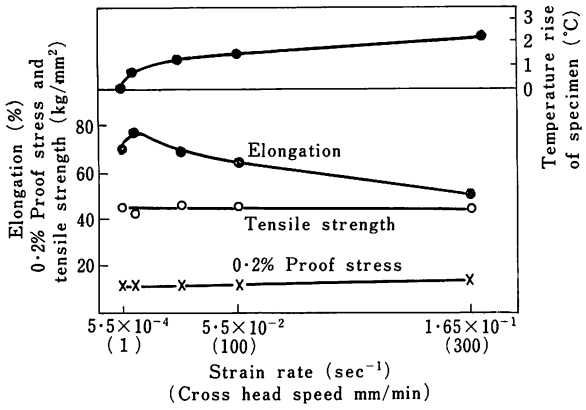

Fig. 16. Effect of strain rate on the tensile properties and the temperature rise of the specimen during deformation of Fe–19%Cr–11%Ni alloy tested in water bath at +40°C.

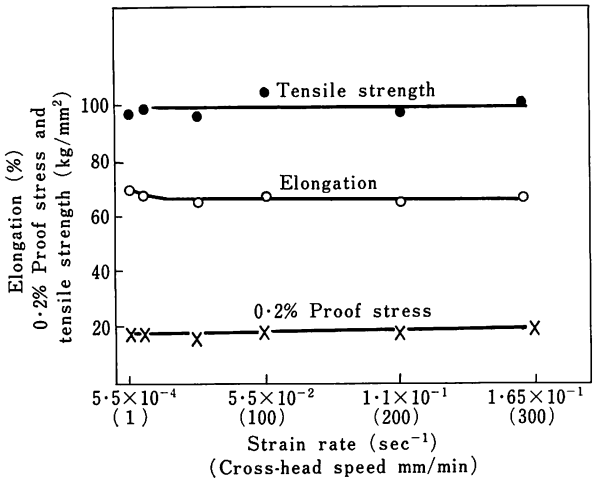

Fig. 17 Effect of strain rate on the tensile properties of Fe-24%Mn-0·26%C alloy tested in water bath at + 80°C.

の引張試験においても，Fig. 15 に示したように歪速度増加に伴って伸びが低下している．

Fig. 16 に Fe-Cr-Ni 合金を +40°C の水中で種々な歪速度で試験したときの結果を示す．歪速度上昇につれて 0·2% 耐力，引張強さはほとんど変化しないのに対し，伸びは低下している．図上部に試験中の試片の破断時の温度上昇（試片の温度は歪増加とともに上昇していき，破断時に最高となる）を示しているが，歪速度が上昇しても試験片の温度上昇は高々 2°C である．このように，試験片の実際の温度上昇がほとんどないにもかかわらず伸びが低下することは，歪速度の影響を試片の温度上昇のみでは単純に説明できず，歪速度増加そのものが伸びの減少になんらかの影響を及ぼすことを明瞭に示している．Fig. 17 は Fe-Mn-C 合金を +80°C の水中で種々な歪速度で試験したときの結果を示す．このように，Fe-Mn-C 合金の場合歪速度の影響はほとんどなく，すべての場合非常に良好な伸びを示している．これは Fe-Ni-C や Fe-Cr-Ni 合金と大きく異なることである．

4. 考　　察

4.1 変態誘起塑性

本研究で用いた 3 種の合金はそれぞれ生成するマルテンサイトが異なる．つまり，Fe-Ni-C 合金で α' マルテンサイトが，Fe-Cr-Ni 合金で α' と ε' の両マルテンサイトが，Fe-Mn-C 合金で ε' マルテンサイトが生成する．さらに α' マルテンサイトでも Fe-Ni-C 合金はレンズ状の partially twinned martensite であり，burst 現象を伴って変態するものであり，Fe-Cr-Ni 合金は lath martensite である．このように生成するマルテンサイトの種類や性質がそれぞれ異なる．これはオーステナイトの積層欠陥エネルギーの相違に帰因するものである[14]．

このように生成するマルテンサイトが相違するにもかかわらず，すべての合金で Ms 点と Md 点の間の温度で異常に大きな伸びが観察された．この大きな伸びは変形中にマルテンサイトが生成することによるのであるが，Fig. 7 に示したように，伸びは必ずしも変形中に生成した全マルテンサイト量のみに依存するのではなく，マルテンサイトの生成状態（生成する時期，形態，量など）が重要である．伸びが最高となった場合，3 種の合金で共通していることは，組織観察の結果，変形の初期（約 20% 歪位まで）はオーステナイトのみが変形しており，その後マルテンサイトが歪増加とともに刻々生成することであり，この場合，加工硬化指数は歪増加とともに連続的に上昇していた．

変形中にマルテンサイトが刻々生成する場合に伸びが増大する原因として，第 1 に necking の抑制が考えられる．一般に，加工硬化指数 (n 値) が大きいほど necking がおこりにくく，均一伸びが大きくなる．本研究のように変形中にマルテンサイトが刻々生成する場合には加工硬化指数が一定ではなく，歪とともに増大する．このように歪増加につれて加工硬化指数が連続的に上昇することは，局部的にくびれが生じてマルテンサイトが生成された領域では，その部分で実質的に加工硬化指数が大きいように働き，オーステナイトのみの変形（Md 点以上）の場合より非常に necking がおこりにくくなり，均一伸びが増大するものと考えられる．このような necking の抑制効果については，Fe-Cr-Ni ステンレス鋼の研究で，すでに Moskowitz ら[1]，深瀬ら[2] によっ

て指摘されている．第2の原因として，割れの発生，伝播の抑制が考えられる．変形がすすみ，局部的に応力集中をおこしたとしても，その部分でマルテンサイト変態がおこることにより応力集中が緩和されるため，割れの発生がおさえられる可能性がある．また，微少な割れが生じても，それが伝播する際，その先端にマルテンサイトが生成することによって応力を緩和し，伝播の抵抗となる[15]．

以上のような作用をするマルテンサイトは，変形がある程度進んだ段階で少しずつ，刻々と破断に至るまで生成する場合に伸びの増加に有効にきく訳で，Ms 点近傍のように変形初期に多量にマルテンサイトが生成すれば，その後の変形はほとんどマルテンサイトでおこり，そのため早期破断がおこり，また，Md 点直下のように生成するマルテンサイトが非常に少ない場合には，均一伸び増大に充分に作用し得ず，伸びが少なくなる．その結果として Md 点と Ms 点の間のある適当な温度で伸びが最高となる．

4.2 各種合金の相違点

3種の合金での大きな相違点は，Md 点と Ms 点の温度差が非常に異なることである．Fe-Ni-C 合金では約 80°C，Fe-Cr-Ni 合金で約 200°C，Fe-Mn-C 合金は約 450°C にも及んでいる．これはオーステナイトの積層欠陥エネルギーの低い合金では，加工によって ε' マルテンサイトが容易に生成するためと考えられる．この結果，伸びの良好な温度範囲が Fe-Ni-C では狭く，Fe-Mn-C では非常に広くなっている．Fe-Cr-Ni では両者の中間である．

また，Ms 点近傍およびそれ以下の温度での伸びが各合金で大いに異なる．これは生成するマルテンサイトの種類および変態機構の相違によるものと考えられる．つまり，Fe-29% Ni-0·26% C では冷却によって生成する α' マルテンサイトは mid-rib のあるレンズ状を呈し，自触媒作用による burst 現象を伴って一度にかなり多量のマルテンサイトを生成するのに対し，Fe-19% Cr-11% Ni では生成する α' マルテンサイトは Schiebung 変態による，いわゆる lath martensite である．また，Fe-24% Mn-0·26% C は ε' マルテンサイトを生成するが，これも burst 現象がおこらず，生成量は比較的少ない．さらに，Ms 点以下の試験で残留オーステナイトから加工によって生成するマルテンサイトも，Fe-Ni-C 合金の場合，変形初期に多量に生成してしまうので伸び増加にあまり寄与しないが，Fe-Cr-Ni のような lath martensite の場合には Ms 点以下でも変形初期に出つくしてしまうことがなく，変態誘起塑性に有効に働きうるものである．ε' マルテンサイトは低温での加工でも一度に出つくしてしまうことはなく，歪とともに刻々生成するために，Fe-Mn-C では低温でも充分に変態誘起塑性がおこり，伸びが大きくなるものである．このように，合金系のオーステナイトの積層欠陥エネルギーの相違に帰因するマルテンサイトの種類，変態様相の相違が，マルテンサイト変態誘起塑性の傾向に大きく影響を及ぼす．

4.3 歪速度の影響

変形中にマルテンサイトが生成する場合の歪速度の影響については，Fe-Cr-Ni 合金ですでに多くの研究がなされている[1,2,16~18]．Moskowitz ら[1]は歪速度が増すと

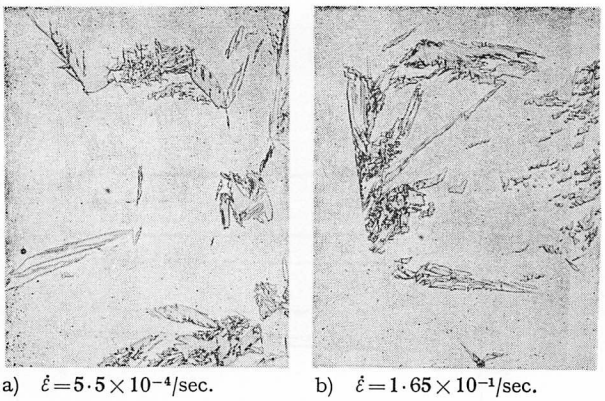

a) $\dot{\varepsilon}=5\cdot5\times10^{-4}$/sec.　b) $\dot{\varepsilon}=1\cdot65\times10^{-1}$/sec.　×350

Photo. 3. Optical micrographs of Fe-29%Ni-0·26%C alloy deformed 36% in tension at −10°C in liquid bath.

気体雰囲気中では伸びが著しく低下するが，液体雰囲気中試験では歪速度増大にもかゝわらず伸びはほとんど変化しない結果を得，結局，歪速度の影響は単に試験片の温度上昇のみで説明できるとしている．確かに歪速度増加により多かれ少なかれ試験片の温度上昇はおこり，特に変形中にマルテンサイト変態がおこるような場合にはその効果が大きく現われる訳で，重要な問題である．本研究においても，Fe-Ni-C 合金で Fig. 14, Fig. 15 に示したように，気体中での試験では試片温度上昇が大きく，その影響が非常に大きく現われた．しかし，Fig. 15, Fig. 16 に示したように，Fe-Ni-C および Fe-Cr-Ni 合金では試験片の温度上昇がほとんどないか，もしくは非常に少ない液体雰囲気試験でも歪増加によって伸びは低下している．このことは歪速度の影響を単に試片の温度上昇のみでは説明できないことを示している．試片の温度上昇がほとんど無視できる状態，つまり液体雰囲気試験で歪速度変化によってマルテンサイトの生成量が変化するかどうかを調べるため，種々な歪速度で同じ量の変形を施して組織観察をおこなった結果，歪速度が変化してもマルテンサイトの生成状態は歪速度に無関係で，主に歪量によってきまっていた．その1例を Photo. 3 に示す．これは Fe-Ni-C 合金を −10°C でドライアイスとアルコールによる雰囲気中で歪速度を変化させ，同じ歪量だけ変形した後の光学顕微鏡組織である．歪速度が変化してもマルテンサイト量はほとんど変化していない．このように歪速度が増大してもマルテンサイト生成状態はほとんど変化がないにもかかわらず伸びが減少することは，充分に変態誘起塑性がおこらないうちに，早期に破断がおこるものと考えられる．ε' マルテンサイトの生成する Fe-Mn-C 合金の場合は Fig. 17 に示したように歪速度の影響がほとんど認められなかった．

得られた結果から，Fe-Ni-C，Fe-Cr-Ni 合金のように α' マルテンサイトが生成する合金では，歪速度増加により伸びの低下がおこり，ε' マルテンサイトが生成する Fe-Mn-C 合金では歪速度の影響をうけない．これらは歪速度増大による早期破断の難易と生成するマルテンサイトの種類との関連として説明されるべきであるが，その詳細については今後の研究にまたなければならない．

5. 結　　論

Ms 点が室温以下にある3種の Fe-29% Ni-0·26% C, Fe-19% Cr-11% Ni および Fe-24% Mn-0·26% C 合金

を用い，種々な温度で引張試験をおこない，マルテンサイト変態誘起塑性に関する合金系の特徴および歪速度の影響について研究した結果，次のことが明らかとなった．

(1) オーステナイトの積層欠陥エネルギーの相違により生成するマルテンサイトの種類が異なり，Fe-Ni-C 合金では α' マルテンサイト，Fe-Cr-Ni 合金では α' および ε' マルテンサイト，Fe-Mn-C 合金では ε' マルテンサイトが生成する．

このように生成するマルテンサイトの種類の相違にもかかわらず，すべての合金で顕著なマルテンサイト変態誘起塑性現象がおこり，伸びは Ms 点と Md 点の間の温度で最高となる．伸びが良好となる場合には加工硬化指数が歪とともに刻々増加するのが特徴である．最高伸びの得られる条件は，最初ある程度の歪まではオーステナイトのみで変形し，その後マルテンサイトが歪とともに破断に至るまで刻々と生成されることである．たとえ加工誘発マルテンサイトが生成しても，変形初期に多量のマルテンサイトが生成するならば良好な伸びは得られない．このように伸びは必ずしも変形中に生成したマルテンサイト量のみに依存するのではなく，マルテンサイトの生成状態が重要である．

(2) 3種の合金で Ms 点と Md 点の温度差が非常に異なる．Fe-Ni-C 合金はせまく，Fe-Mn-C 合金は非常に広く，Fe-Cr-Ni はその中間である．この結果，伸びの良好な温度範囲が非常に異なり，Fe-Ni-C 合金では変態誘起塑性は非常にせまい温度域でしかおこらないのに比べ，Fe-Mn-C 合金は非常に広い温度範囲で伸びが良好である．このような合金間の特徴は，オーステナイトの積層欠陥エネルギーの相違によるマルテンサイトの種類，変態様相の相違に帰因する．

(3) マルテンサイトの変態誘起塑性に及ぼす歪速度の影響は，試験雰囲気によって大きく異なる．つまり気体雰囲気中では伸びが歪速度増大によって急激に低下するが，液体雰囲気中試験では伸びの低下は少ない．このことは歪速度増大による試験片の温度上昇から説明される．しかし，試片温度の上昇がほとんどない液体雰囲気中試験の場合でも，歪速度が増加すると Fe-Ni-C，Fe-Cr-Ni 合金では伸びが低下した．ただし，この場合マルテンサイトの生成状態は歪速度増大によってもほとんど変化がなかった．このことは，歪速度の影響は従来から言われているように単に試験片の温度上昇のみでは説明できず，歪速度が増大することによる早期破断がおこるものと考えられる．ε' マルテンサイトの生成する Fe-Mn-C 合金では歪速度の影響はみられない．

文　献

1) J.P. Bressanelli, A. Moskowitz: Trans. ASM, **59** (1966), p. 223
2) 深瀬，江波戸，大久保，村尾：日本金属学会誌，**32** (1968), p. 38
3) F. Abrassart, F. Lecroisey, A. Pineau: Mem. Sc. Rev. Met., **66** (1969), p. 805
4) G.P. Sanderson, D.T. Llewellyn: JISI, **207** (1969), p. 1129
5) 田村，牧，波戸，油井：日本金属学会誌，**33** (1969), p. 1383
6) I. Tamura, T. Maki, H. Hato: Trans. ISIJ, **10** (1970) p. 163
7) I. Tamura, T. Maki, H. Hato, Y. Tomota, M. Okada: Proc. of 2nd Int. Conf. on the Strength of Metals and Alloys. at Asilomar (1970), p. 901
8) V.F. Zackay, E.R. Parker, D. Fahr, R. Busch: Trans. Amer. Soc. Metals, **60** (1967), p. 252
9) 田村：塑性と加工，**12** (1971) p. 149
10) G.T. Bolling, R.H. Richman: Phil. Mag., **19** (1969), p. 247
11) G.T. Bolling, R.H. Richman: Acta Met., **18** (1970), p. 673
12) 田村，牧，波戸：日本金属学会誌，**33**, (1969), p. 1376
13) C.J. Guntner, R.P. Reed: Trans. ASM, **55** (1962), p. 399
14) J.F. Breedis: Trans. Met. Soc. AIME, **230** (1964) p. 1583
15) S.D. Antolovich: Trans. Met. Soc. AIME, **242** (1968), p. 2371
16) G.W. Form, W.M. Baldwin, Jr: Trans. ASM, **48** (1956), p. 474
17) D.V. Neff, T.E. Mitchell, A.R. Troiano: Trans. ASM **62** (1969), p. 858
18) 平野，須藤，柚鳥：日本金属学会誌，**33** (1969), p. 975

討論 pp. 358-359 参照

Ductility of Age-Hardenable Martensitic Iron Alloys

M. Tanaka J. Yamamoto

Tokyo Institute of Technology

The 18%Ni maraging steel is a well-known type of material combining high strength and good toughness. The hardening of this steel is mainly due to the precipitation of stable intermetallic compounds such as Ni_3Ti and Ni_3Mo. A pronounced age-hardening response has also been observed in iron-nickel-manganese, iron-nickel-cobalt and iron-manganese-cobalt martensitic alloys.

The major hardening factor is considered to be strain hardening due to formation of a coherent precipitate or zone during decomposition of the matrix. Therefore, high ductility of these age-hardenable alloys at high strength levels can hardly be expected unless improvements in the microstructure are produced.

The present study was concerned with the effects of precipitation of austenite and carbide on the mechanical properties of the age-hardenable iron-nickel-manganese ternary alloy and its modifications.

The results obtained in this study are summarized as follows:

(1) It was concluded that the existence of precipitates (such as stable intermetallic compounds, carbides) and austenite, which are only partially coherent or incoherent with the matrix, is very effective in improving the combination of high strength and good toughness in the age-hardenable martensitic iron-nickel-manganese alloys.

(2) A considerable loss in ductility accompanied by premature failures during test was observed when the strongly age-hardenable Fe-12%Ni-6%Mn alloy was treated to maximum hardness. The ductility of this alloy recovered in the overaged state containing about 10 vol % precipitated austenite. Some of these overaged alloys showed a high elongation value at -196°C due to transformation-induced plasticity.

(3) The Fe-4%Ni-2%Mn alloy was not age hardenable. With the addition of aluminum, chromium and molybdenum, however, it could be age hardened to high strengths. Moreover, the addition of 0·1% C to this modified alloy was very effective in increasing toughness at high strength levels.

(4) Depending on the microstructure of the aged Fe-12%Ni-6%Mn alloy, two modes of yielding (continuous and discontinuous) were observed in the load-elongation curves. This behavior could be explained by the difficulty in generating and propagating dislocations. It was estimated that the critical size of precipitated particles that impedes dislocations from cutting is about 400～500 Å.

時効硬化性マルテンサイト鉄合金の強靱性について

田中　実　山本　襄

東京工業大学　精密工学研究所

1. 緒　論

時効硬化性マルテンサイト鉄合金の一種として18% Ni マルエージ鋼が開発され，高強度と良好な靱性を有するものとして知られている[1~5]．この合金は炭素含有量がきわめて少なく，その金属組織学的な特徴は，立方晶マルテンサイトの過飽和固溶体から Ni_3Ti あるいは Ni_3Mo のような安定な金属間化合物の析出[6~9]によって時効硬化することである．

Fe-Ni および Fe-Mn 2元合金が類似の平衡状態図を有し，いずれもマルテンサイト組織を形成するので，著者らは18% Ni マルエージ鋼の Ni の一部を Mn によって置換することの可能性を検討するために，その基礎的研究として Fe-Ni-Mn 3元マルテンサイト合金について2，3の実験を試みた．18% Ni マルエージ鋼に対して不純物としての Mn は，靱性を著しく低下せしめること[1,10]，また Mn 量が2%までは強靱性を害することなく Ni と置換し得ること[11]などが報告されている．

著者らの Fe-Ni-Mn 3元マルテンサイト合金についての実験結果はきわめて興味深いものであり，Fe-Ni および Fe-Mn の2元合金のマルテンサイト組織は非時効硬化性であるにもかゝわらず，Fe-Ni-Mn 3元合金のそれには著しい時効硬化性が認められた[12,13]．これと同時に Fe-Ni-Co[14,15] および Fe-Mn-Co[16] 3元合金のマルテンサイト組織においても顕著な時効硬化性が認められた．そしてこれらの3元合金の時効硬化は，いずれも過飽和のマルテンサイト組織が $(\alpha+\gamma)$ の2相混合の平衡状態の組織になる過程においておこることで軌を一にしており，安定な金属間化合物を析出する18% Ni マルエージ鋼の硬化機構とは異なるものであることを明らかにした．

Fe-Ni-Co 合金と Fe-Mn-Co 合金は，両者とも，時効に際して (i) FeCo に Ni あるいは Mn が固溶した規則格子が形成されるための硬化が観察され，(ii) 溶質原子濃度の高い γ 相が析出し，この γ 相と共軛する溶質原子濃度の低い α 相の析出のためにマルテンサイト相内に格子ひずみを生じ，著しく硬化するものと認められた．これに対して Fe-Ni-Mn 3元マルテンサイト合金では，時効に際して基質内に bcc 相の2相分離がおこり，溶質原子濃度の高い bcc 相（NiMn と考えられる）の zone の形成に伴う整合ひずみに起因するひずみ硬化が時効硬化の主原因であると認められた[13,17]．また Fe-Ni-Mn 3元合金に炭素をはじめ2，3の元素を添加すれば，炭化物あるいは適当な金属間化合物の析出が期待される．したがって，このような Fe-Ni-Mn 合金は，時効硬化性マルテンサイト鉄合金の金属組織と強靱性とを関連せしめて調べるのに好適な試料の一つと考えられる．著者らが行なった一連の実験的研究の結果，時効硬化性マルテンサイト鉄合金は，「均質な金属組織の内部に微細な析出物（オーステナイト，炭化物あるいは金属間化合物）が非整合に均一に分散した状態が最も強靱であろう」と結論された．

本報告は，このような結論に達した Fe-Ni-Mn マルテンサイト合金の金属組織と強靱性についての実験的研究の概要を述べたものである．

2. Fe-Ni-Mn 3元合金の時効硬化と強靱性について

Fig. 1 は Fe-Ni-Mn 3元合金の時効硬化領域および硬化量（時効前と最高時効かたさとのかたさの差）を示したものである[12]．この合金の時効硬化はマルテンサイト組織領域にのみ認められ，硬化の著しい範囲は Ni 12%，Mn 6% の組成を中心として，Fe-24%Ni，Fe-12% Mn の組成点を結ぶ線を長軸方向とする細長い楕円状に拡がっている．

Fig. 2 は代表的な3種類の Fe-Ni-Mn 合金と Fe-

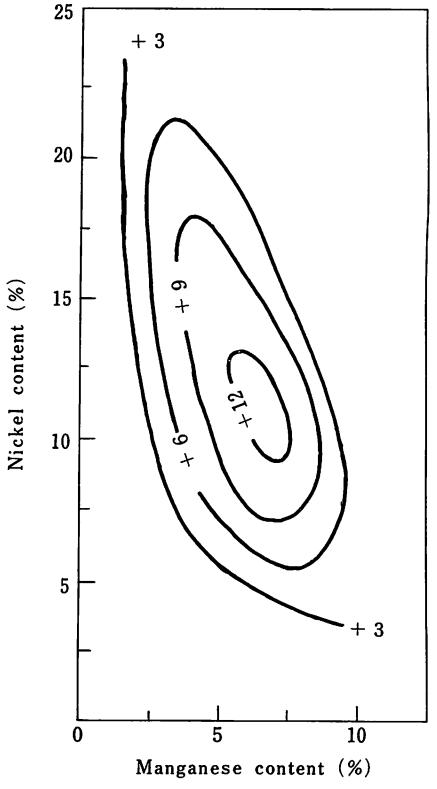

Fig. 1. Equihardness increment contour lines for age hardening of iron-nickel-manganese alloys. Hardness units are on the Rockwell A scale.

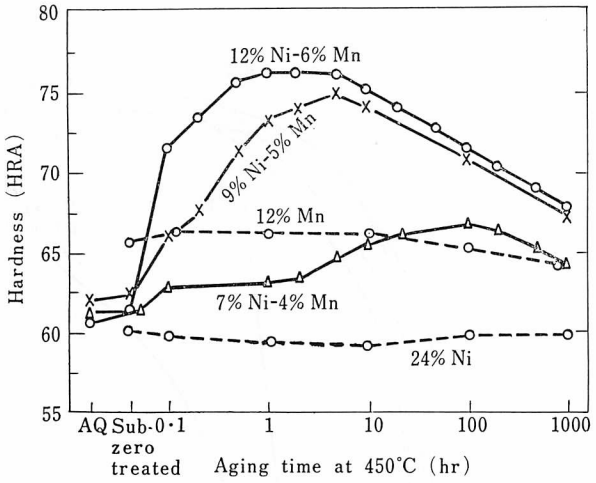

Fig. 2. Effect of aging time on the hardness of iron-nickel-manganese alloys water quenched from 900°C and subzero treated at −196°C.

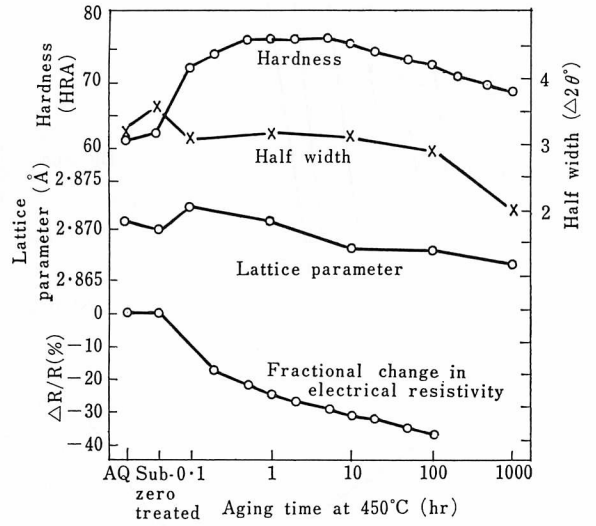

Fig. 3. Effect of aging time on some properties of the 12% Ni–6%Mn alloy water quenched from 900°C and subzero treated at −196°C.

24%Ni および Fe–12% Mn 2元合金の等温時効硬化曲線[13]で，2元合金では硬化が全くおこるのに対し，3元合金では著しい硬化がおこることを示した一例である．Fig. 3 は，Fe–12%Ni–6%Mn 合金を 900°C より水冷後 −196°C にサブゼロ処理して 450°C で等温時効した場合のかたさ，X 線回折線 (211)α' の半価幅，基質の格子定数および電気抵抗の測定結果[13]である．すなわち，硬化に伴って電気抵抗および格子定数は減少し，半価幅は焼入れ後一度減少するがその後多少増大する．

Photo. 1 は 12%Ni 6%Mn 合金の 900°C 焼入状態，450°C に 1hr 加熱して最高時効かたさにした状態および 500°C に 1000hr 加熱した過時効状態の透過電顕組織[13]である．Photo. 1 a) はマッシブなマルテンサイトで，多数の lath があり，各 lath の内部にはきわめて多くの転位が存在している．Photo. 1 c) は $(\alpha+\gamma)$ の2相混合組織で，γ 相の量は 30 vol% 程度である．Photo. 1 b) には全面にきわめて微細な粒子が存在しており，電子回折像から解析するとこの粒子は 10〜100Å 程度の大きさで板状の bcc 構造のもので，基質と整合関係を有しており，おそらく bcc NiMn 相であろうと推定される．そしてこの粒子の析出による整合ひずみが，Fe–Ni–Mn 合金の時効硬化の主原因と結論された．さらにこの結論は，この種の合金の復元現象についての実験結果[18]によっても確かめられている．

Fig. 4 は 12%Ni 6%Mn 合金についての常温における引張試験の結果[19]である．引張試験には直径 4 mm，平行部 20 mm，全長 70 mm の試片を用いた．この合金は時効硬化に伴って急激に脆化し，いわゆる早期破断をおこして，かたさに対応する引張強さは得られない．この状態では伸び，絞りはほとんどなく，きわめて脆い破断状況を呈する．時効温度が高くなり過時効状態になると，引張強さを測定することが可能となり，伸び・絞りの値は増加する．この引張試験は，大気中溶解の 5 kg 程度の鋼塊を直径 10 mm に鍛伸したものを素材とした結果であるので，さらに消耗電極型の電気炉によって 12% Ni 6%Mn 合金を約 40 kg 真空溶解・真空鋳造して素材とし，機械的諸性質の測定を行なった．この試料の主なる化学成分は，12·08%Ni，6·01%Mn，0·010%C であって，Si, P および S などの不純物はそれぞれ 0·01% 以下，0·005% 以下および 0·012% 以下である．この試料

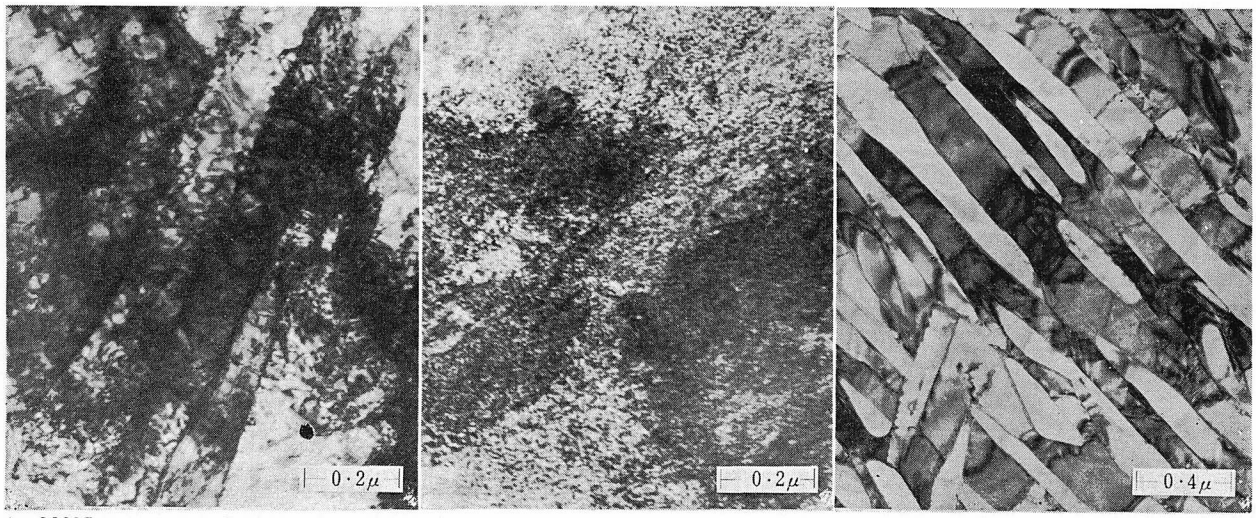

a) 900°C water quenched　b) 450°C×2hr　c) 500°C×1000hr

Photo. 1. Transmission electron micrographs of the Fe–12%Ni–6%Mn alloy.

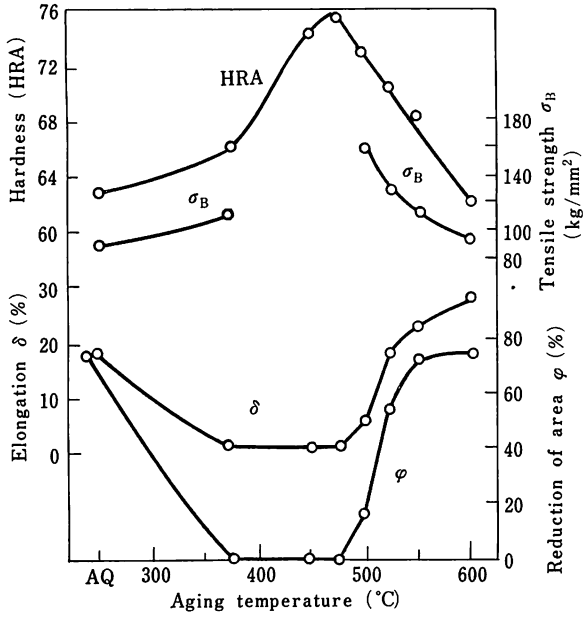

Fig. 4. Mechanical properties of the 12%Ni–6%Mn alloy aged for one hour at the indicated temperatures after water quenching from 900°C.

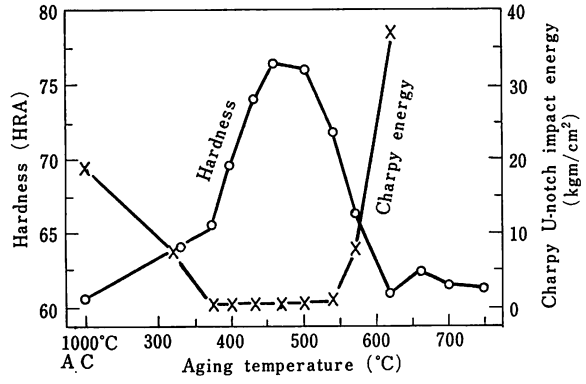

Fig. 5. Hardness and Charpy impact energy of the 12%Ni–6%Mn alloy aged for one hour at the indicated temperatures after air cooling from 1000°C.

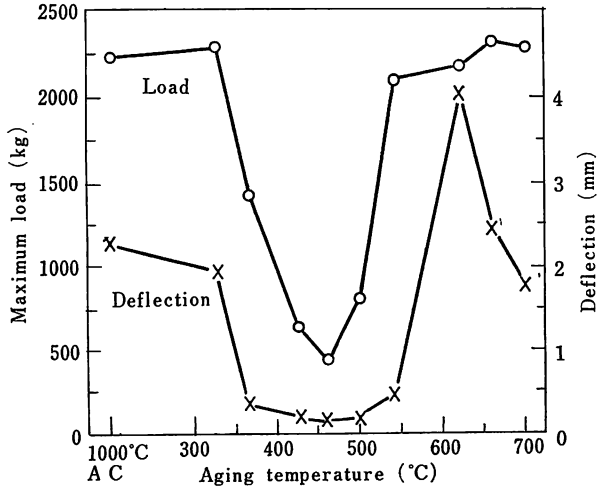

Fig. 6. Maximum load and deflection of the aged 12%Ni–6%Mn alloy in static bending tests using standard U-notch Charpy test pieces.

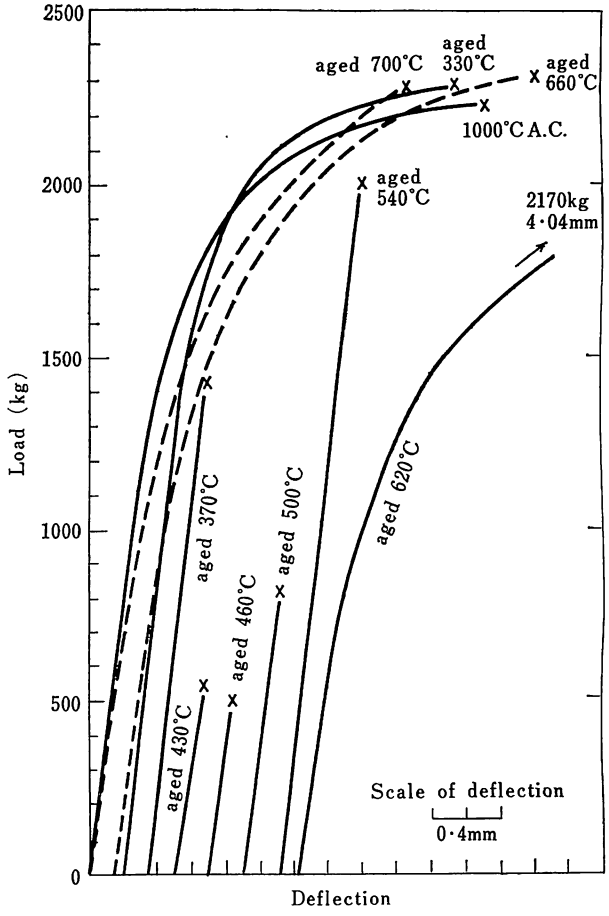

Fig. 7. Load-deflection curves for the aged 12%Ni–6%Mn alloy in static bending tests.

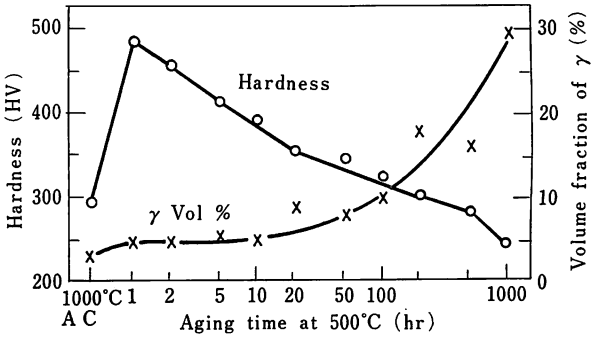

Fig. 8. Effect of aging time on the hardness and volume fraction of precipitated austenite in the aged 12%Ni–6%Mn alloy.

を用いて得られた実験結果は次のとおりである．

Fig. 5 は，1000°C 空冷後各温度に 1hr づつ等時時効したときのかたさとシャルピー試験(2 mmU 型切欠標準試片使用) の結果であり，Fig. 6 は静的曲げ試験によって破断せしめた際の最高荷重と最大撓み量である．静的曲げ試験は試片，試片の支点間距離および荷重を与える刃型などすべてシャルピー試験の場合と同様にして行なった．Fig. 7 は静的曲げ試験の際の荷重—撓み線図の一例である．1000°C 空冷のものでは比較的靱い破断過程を示し，シャルピー値も大きいが，370～540°C に時効した状態では曲げ荷重—撓み線図はほとんど直線的で塑性変形がおこらず脆い状態の破断となり，シャルピー試

験の結果もこれを示している．620°C で時効したものは完全に軟化しており，著しく靱い破断を呈する．時効温度が 660°C，700°C のものは，時効中に析出した γ 相が冷却中にマルテンサイトに変態するため，その破断挙動はほぼ 1000°C 空冷の試片と類似したものになる．620°C で時効したものと，660°C あるいは 700°C で時効したものとでは，かたさはほぼ同一であるのに金属組織を異にするため破断挙動が著しく相違する．このような Fe-Ni-Mn 合金の過時効状態における破断挙動の著しい変化は，γ 相の析出量と関連するものと推定される．

Fig. 8 は 1000°C から空冷した 12%Ni 6%Mn 合金を 500°C で等温時効したときのかたさと γ 相の析出量を測定した結果で，Photo. 2 はそのときの金属組織の変化を示したものである．かたさは 500°C×1hr の時効で HV

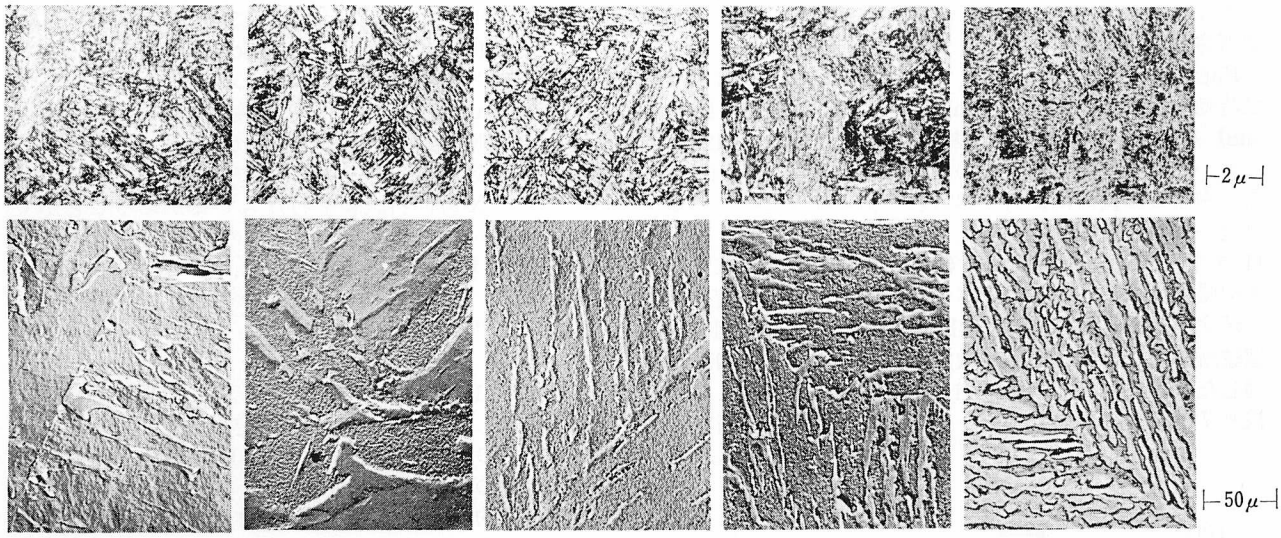

Photo. 2. Optical and electron replica micrographs of the Fe–12%Ni–6%Mn alloy isothermally aged at 500°C after air cooling from 1000°C.

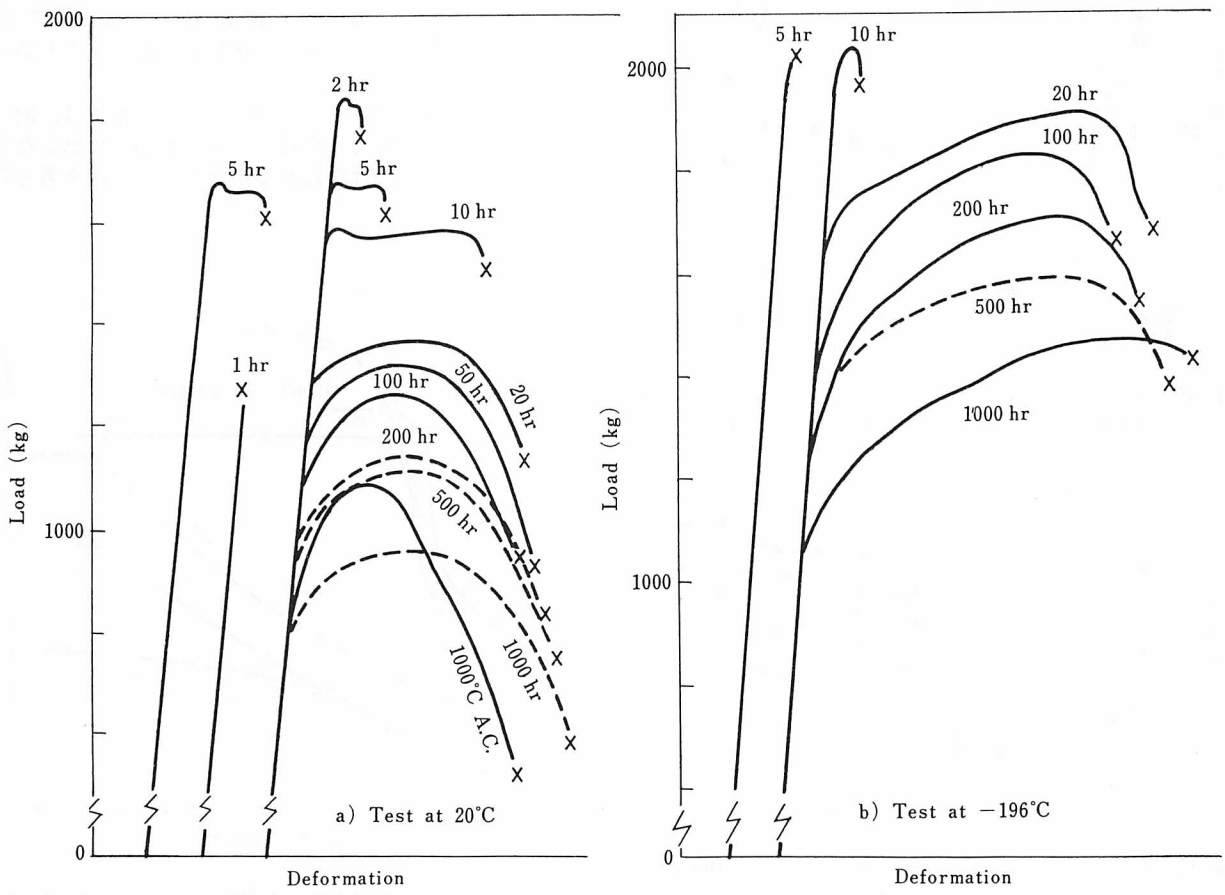

Fig. 9. Tensile load-deformation curves for the 12%Ni–6% Mn alloy isothermally aged at 500°C.

500程度に硬化し，その後時効時間の増加とともに軟化する．この軟化に伴ってγ量は次第に増加しており，500°C×1000hr の時効では約 30 vol% になる．このγ量は島津製作所製自記 X 線回折装置 (VD-1A) により Cr Kα線を用い，(111)γと (110)αの回折線の強度の比により求めた．Photo. 2 の光学顕微鏡写真ではγ相の存在は不明瞭であるが，レプリカ電顕写真ではγ相が細長く析出していることが認められ，500°C×1000hr 時効のものではα相とγ相とが層状に混合していることが観察される．

Fig. 9 は 1000°C 空冷のままおよびこれを 500°C で等温時効した試片（直径 4 mm，平行部 20 mm，全長 70 mm）をインストロン型試験機により 20°C と −196°C において引張試験したときの荷重—伸び線図の一例である．またこの試験によって得られた引張強さと絞りおよび均一伸びと全伸びを示したものが Fig. 10 および Fig. 11 である．すなわち，1000°C 空冷のままのものは常温で引張強さ 90 kg/mm², 伸び 19%，絞り 78% 程度の値を示すが，これを 500°C で 1hr 時効したものは常温で早期破断を呈しきわめて脆い状態となる．500°C で 2hr 時効したものは常温では引張強さ 153 kg/mm², 伸び 1·4%，絞り 7% 程度の値となるが，−196°C では早期破断を呈する．500°C で 5hr 以上の時効をした試片は常温と −196°C で引張試験が可能となり，20hr 以上時効をした試片では −196°C における伸びおよび絞りの値が急激に増加していることが認められる．また Fig. 9 の荷重—伸び線図で明らかのように，10hr 時効試片では常温の試験で上部降伏点が観察され，不連続降伏がおこるが，20hr 以上時効した試片では上部降伏点が不明瞭になり，50hr 以上時効した試片では完全な連続降伏を示すようになる．100hr 以上時効した試片には，−196°C の試験において荷重—伸び線図に serration が認められるようになり，伸びの急激な増加がおこる．

この serration は，γ相が引張変形によってマルテンサイトに変態するためであり，これは試片を −196°C に浸漬した前後，および −196°C で引張変形を与えた試片について X 線回折試験を行なって確かめることができた．したがってこの場合の伸びの増加は変態誘起塑性 (TRIP) 現象によるものである．

Fig. 12 は 12%Ni 6%Mn 合金を 500°C で等温時効したものの U 型切欠標準試片によるシャルピー試験の結果であって，500 hr および 1000 hr 時効したものでは遷移温度が −100°C 付近に認められ，−196°C における衝撃値も著しく大きいことが注目される．1000°C 空冷のままのものは，500 hr および 1000 hr 時効したものとほぼ同程度の遷移温度である．

以上の静的引張試験と静的および衝撃曲げ試験の結果を綜合すると，500°C×500 hr 時効状態のものは，常温で引張強さ 93～94 kg/mm², 0·2% 耐力 80 kg/mm², 全伸び 20%，均一伸び 11%，絞り 63～60%，−196°C で引張強さ 132～135 kg/mm², 0·2% 耐力 111～115 kg/mm², 全伸び 25%，均一伸び 17·5%，絞り 42～43% の成績を示し，常温でも低温でも比較的強靱であると認められる．

Fe-12% Ni-6%Mn 合金についての実験結果は，均一マルテンサイト組織内に時効によってγ相が析出したために強靱性の改善が行なわれることを示す一例と考えられる．

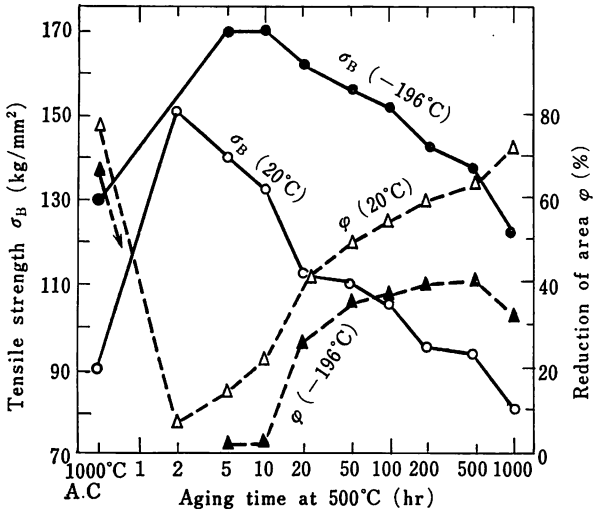

Fig. 10. Effect of aging time on the tensile strength and reduction of area of the 12%Ni–6%Mn alloy.

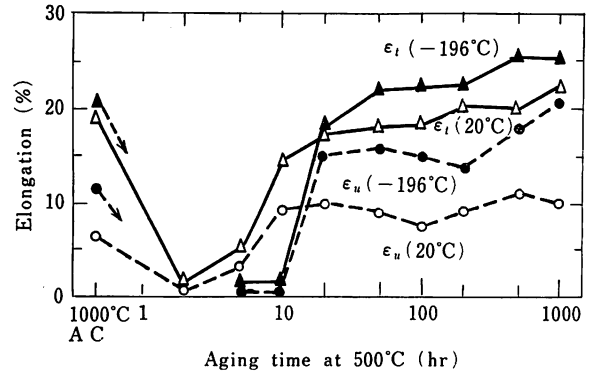

Fig. 11. Effect of aging time on the elongation of the 12% Ni–6%Mn alloy. ε_t denotes total elongation and ε_u uniform elongation.

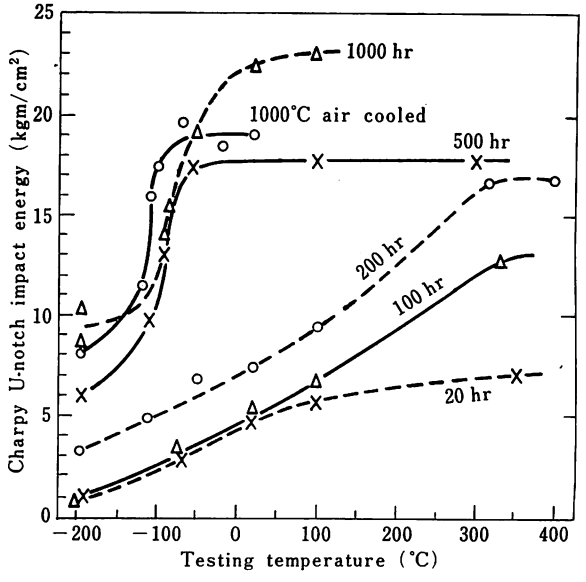

Fig. 12. Effect of aging time at 500°C on the impact properties of the 12%Ni–6%Mn alloy.

3. 2, 3の合金元素を含む Fe-Ni-Mn マルテンサイト合金の時効硬化と強靱性について

Fig. 1 で示したように Fe-Ni-Mn 合金の時効硬化性は12%Ni 6%Mn 合金が最大であって，これよりも Ni および Mn の含有量が増加しても減少しても低下する．

Fig. 13 は 12%Ni 6%Mn 合金 (900°C 水冷)，8%Ni 4%Mn 合金 (900°C 水冷)，および 8%Ni 4%Mn 合金に Mo, Cr, Co を添加した合金 (1050°C 水冷) を 370～600°C に 1hr づつ等時時効したときのかたさおよび引張試験を行なった結果[19]である．12%Ni 6%Mn 合金についての結果は Fig. 4 と重複している．すなわち，12% Ni 6%Mn 合金では時効かたさが高くなると早期破断を呈するが，8%Ni 4%Mn 合金では最高時効かたさが HRA 65 程度になり，この状態で引張強さ 110 kg/mm², 伸び 12%，絞り 50% 程度の比較的強靱な性質を示すようになる．8%Ni 4%Mn 合金に Mo, Cr, Co などを添加したものでは，時効硬化性は著しく増大し，12%Ni 6% Mn 合金のそれとほぼ同程度になる．そしてこのような硬化に伴って引張強さは増加し，伸び，絞りは急激に減少する．しかしこの場合は，12%Ni 6%Mn 合金に見られたような早期破断はおこらず，475°C で時効したものでは引張強さ 180 kg/mm², 伸び 10%，絞り 30% 程度の値が得られた．

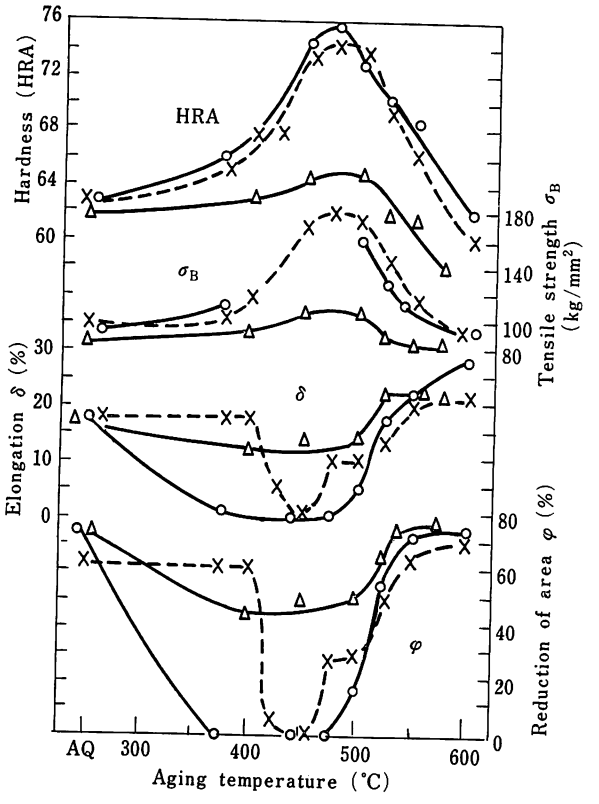

Fig. 13. Mechanical properties of three iron-nickel-manganese base maraging alloys.
- ○ Fe–12%Ni–6%Mn alloy (water quenched from 900°C)
- △ Fe–8%Ni–4%Mn alloy (water quenched from 900°C)
- × Fe–8%Ni–4%Mn–2%Mo–4%Co–4%Cr alloy (water quenched from 1050°C)

Fig. 14 は Fe–4%Ni–2%Mn 合金に Al, Cr, Mo を添加したものと，これにさらに 0·1% 程度の C を含有せしめたものとについての試験結果[19]である．Fe–4%Ni–2%Mn 合金では全く時効硬化性は認められぬが，これに Al を 1% 程度添加すると時効硬化するようになる．Al のほかに Cr, Mo が添加されているのは，靱性の改善が期待されたためである．これらの2種類の合金を比較すると，C を含有するものは硬化に伴って引張強さが増大するにもかゝわらず伸び，絞りの減少がほとんどないことが注目される．

以上の予備実験結果に基づき，12%Ni 6%Mn 合金の場合と同様に消耗電極型電気炉によって，2種類の供試鋼 A, B をそれぞれ約 40 kg づつ溶製し，直径 16 mm の鋼棒として機械的諸性質と金属組織との関連性を調べた．Table 1 は供試鋼 A および B の化学成分を示したものである．

Fig. 15 は鋼 A および B を 1000°C から空冷後 200～700°C にそれぞれ 1hr づつ等時時効したときのかたさ，基質の格子定数および電気抗抵の測定結果[20]である．鋼 A は 500°C の時効で，鋼 B は 550°C の時効で最高かたさに達し，硬化に伴って格子定数および電気抵抗は減少する．鋼 B は炭素を 0·09% 含有しているため，1000°C 空冷の状態で鋼 A よりも高いかさたを示す．しかし鋼 B の時効硬化量は鋼 A よりも少なく，鋼 B の最高かたさ

Table 1. Chemical composition of steels A and B (%).

Steel	C	Ni	Mn	Cr	Mo	Co	Al
A	0·02	6·72	4·02	3·75	1·94	3·84	—
B	0·09	4·12	2·20	1·13	1·36	—	0·94

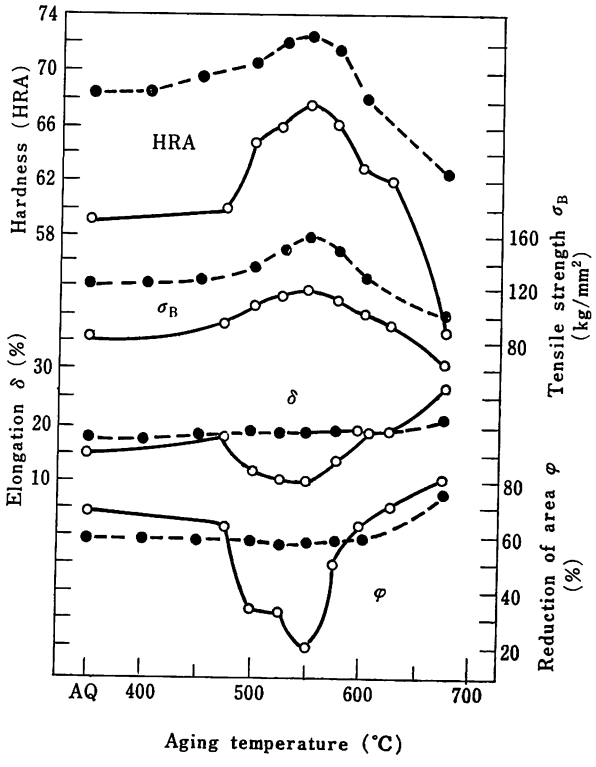

Fig. 14. Effect of carbon content on the mechanical properties of Fe–4%Ni–2%Mn–1%Al–1·5%Cr–1·5%Mo alloy.
● 0·1% C ○ under 0·03% C

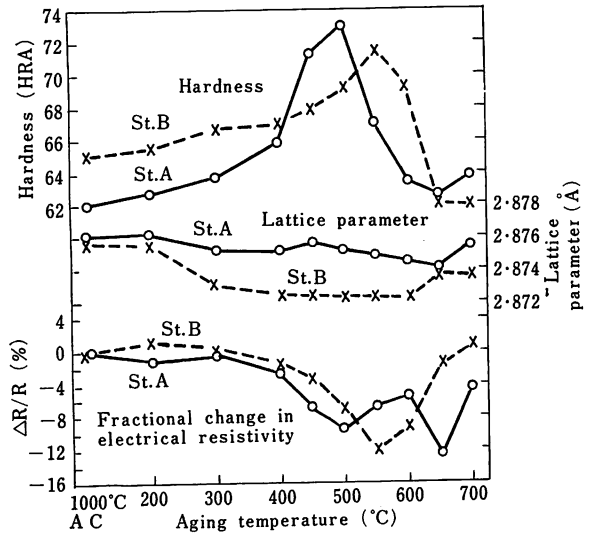

Fig. 15. Effect of aging temperature on some properties of steels A and B after air cooling from 1000°C.

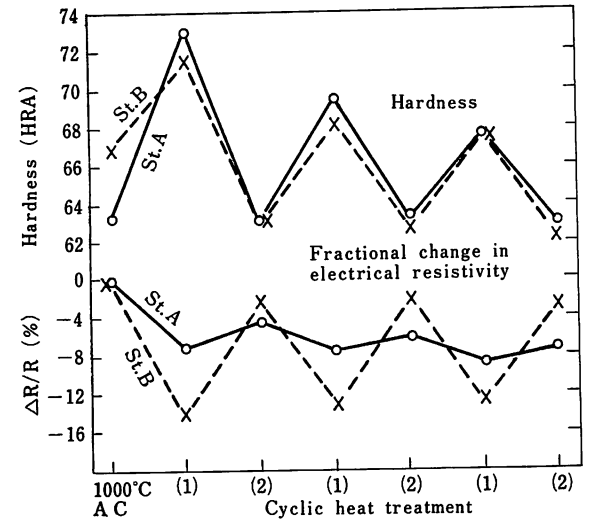

Fig. 16. Effect of cyclic heat treatment on the hardness and electrical resistivity of steels A and B. Heat treatment (1) denotes 475°C×1 hr for steel A and 550°C×1 hr for steel B. Heat treatment (2) denotes 600°C×0·5 hr for steel A and 650°C×0·5 hr for steel B.

は鋼Aよりも多少低くなっている．鋼Aは過時効状態でγ相が析出し易く，600°C×1hr 時効で約 10 vol%，650°C×1hr 時効で約 25 vol%，700°C×1hr 時効で約 6 vol% の γ 相が残留する．700°C 時効の場合は多量のγ相が析出するが，冷却中に再びマルテンサイトに変態し，残留γ相の量は少なくなる．

Fig. 16 は鋼AおよびBを 1000°C 空冷後，最高かたさに硬化する時効温度と，過時効状態になる温度に繰返し加熱した場合のかたさと電気抗抵の変化[20]を示したものである．鋼AもBもこの繰返し加熱で硬化と軟化がおこり，到達最高かたさは加熱の繰返しとともに次第に低くなる．この際の電気抵抗の変化は，鋼Aでは次第に減少するのに対し，鋼Bではかなり大きく，3回の繰返し加熱でほとんど同様の挙動を示している．これは鋼Aではγ相が次第に増加しているのに対し，鋼Bでは硬化に際して析出，過時効では析出物の基質への再固溶の現象が繰返されているためと推定される．

Photo. 3 および Photo. 4 は鋼AおよびBの透過電顕組織である[20]．鋼Aの 1000°C 空冷の状態は転位密度の高い lath の集合したマルテンサイト組織であり，475°C×1hr の時効状態になっても転位密度は多少減少するが，組織的に著しい変化は認められない．600°C×1/2hr の時効では過時効状態で，転位は大部分消失しており，γ相の存在が観察される．この状態のγ相の量は 4～9 vol% である．600°C×1/2hr 時効後 475°C に 1hr 再加熱したものでは，基質における転位は少なく，γ相を含んだ組織であり，γ相の量は再加熱によってほとんど変化はない．

Photo. 4 の鋼Bでは，1000°C 空冷の状態で針状の析出物が認められることが特徴的で，この析出物は電子回折の結果 Fe_3C にほぼ間違いないと推定された．この析出物は 550°C×1hr の時効で最高かたさになった状態においても存在している．650°C×1hr の加熱で過時効状態にしたものでは，基質中に細い針状析出物が直交するように存在しており，この析出物は Mo_2C であろうと推定している．しかし鋼Bのこれら2種類の析出物については目下検討中である．

鋼AとBの金属組織で最も大きな相違点は炭化物の存在である．両供試鋼の基質のマルテンサイトの硬化機構は，(i) 鋼Aでは Ni_3Mo が析出する以前にマルテンサイトが Fe-Ni-Mn 3元合金の場合と同様に2相分離し，その後 Ni_3Mo の析出がおこることによって硬化し，(ii) 鋼Bでは Fe_3C の分散強化と NiAl の析出によって硬化するものと考えられる．いずれにしても鋼AおよびBは，前節で述べた Fe-Ni-Mn 3元合金の硬化状況とはかなり異なっている．

Fig. 17 は鋼AおよびBを 1000°C 空冷後，それぞれ 475°C と 550°C で等温時効したときのかたさ，格子定数，電気抵抗の変化[20]を示したもので，鋼Bが鋼Aよりも格子定数，電気抵抗が著しく減少することは炭化物の析出の有無によるものと考えられる．

Table 2 は鋼AおよびBについて直径 4 mm，平行部 20 mm，全長 70 mm の試片を用いて引張試験を行なっ

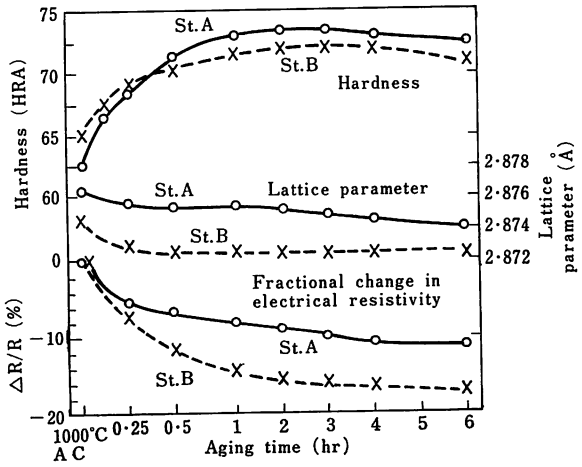

Fig. 17. Effect of aging time on some properties after isothermal aging at 475°C for steel A and at 550°C for steel B.

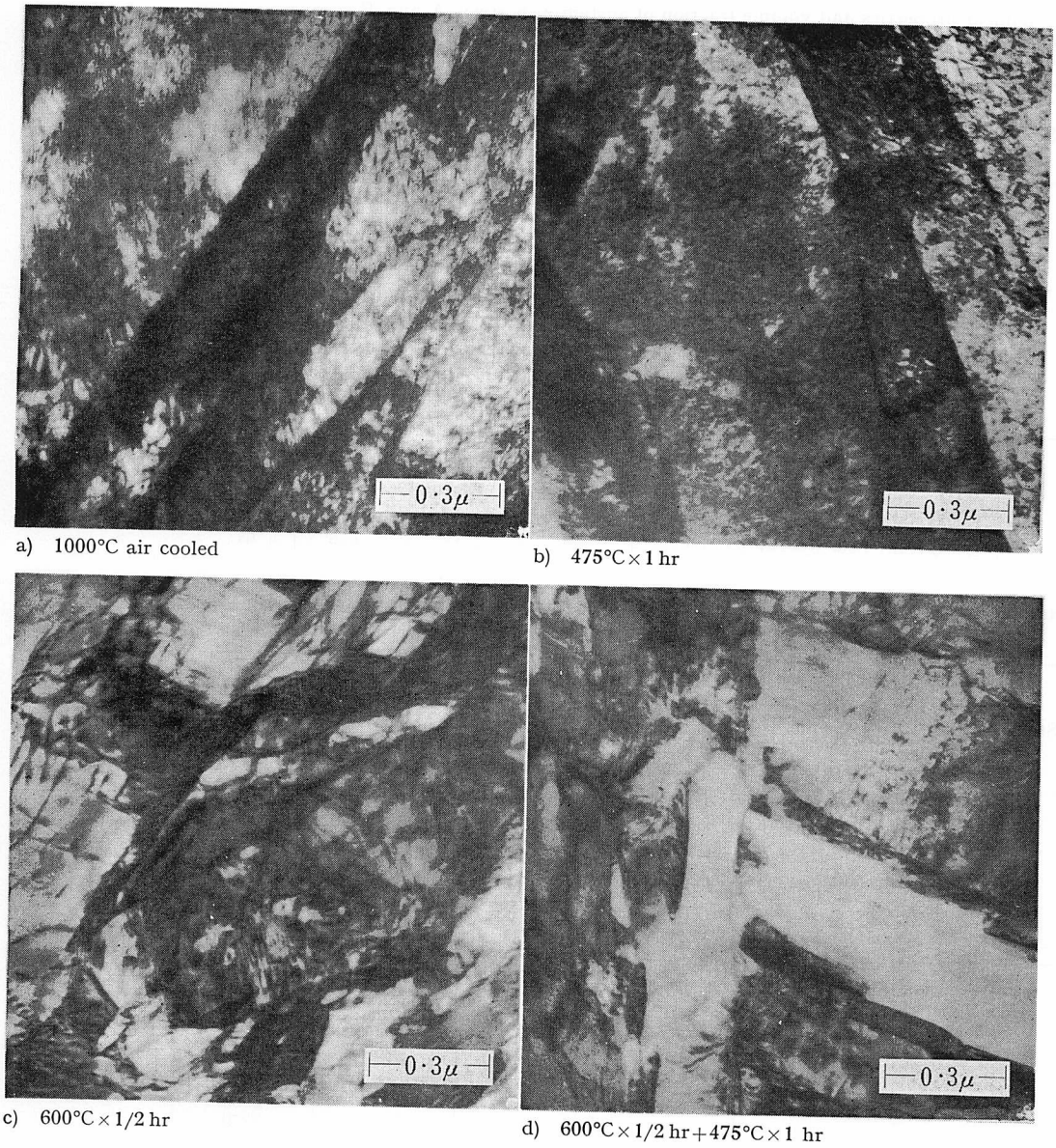

a) 1000°C air cooled　b) 475°C×1 hr

c) 600°C×1/2 hr　d) 600°C×1/2 hr+475°C×1 hr

Photo. 3. Transmission electron micrographs of steel A.

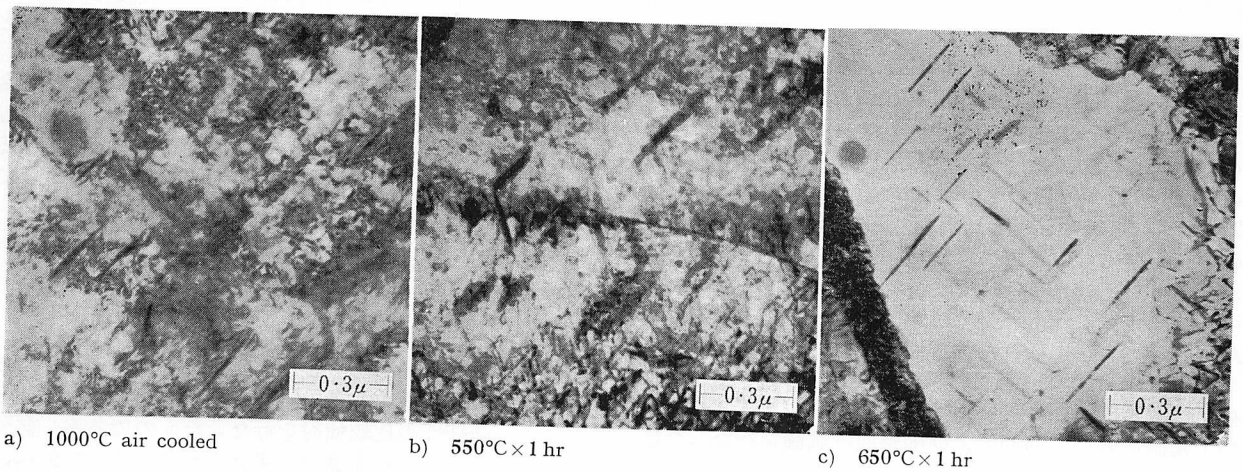

a) 1000°C air cooled　b) 550°C×1 hr　c) 650°C×1 hr

Photo. 4. Transmission electron micrographs of steel B.

Table 2. Mechanical properties and volume fraction of austenite in steels A and B.

Steel	Heat treatment	Hardness (HRA)	Tensile strength (kg/mm²)	Elongation (%)		Reduction of area (%)	Amount of austenite (vol%)
				Total	Uniform		
A	1000℃ air cooled	60	100	14	6·7	72	0
	475℃×1hr aged	67	—	—	—	—	0
	600℃×½hr aged	61	93	19	7·5	73	9
	600℃×½hr+475℃×3hr	70·5	143	8	4	47	9
	600℃×1hr aged	61	93	22	9·7	76	30
	600℃×1hr+475℃×2hr	65	112	15	6·0	60	29
	600℃×4hr aged	62	93	22	10	74	40
	600℃×4hr+475℃×2hr	61·5	93	18	11	74	48
B	1000℃ air cooled	63·5	121	14·2	5·1	64	5
	550℃×2hr aged	72	153	13·4	5·8	53·5	5
	650℃×1hr aged	61	104	17·8	5·9	64	5
	650℃×1hr+550℃×2hr	69	123	15·2	6·5	64	5

Table 3. Results of bending tests on steels A and B using standard V-notch Charpy test pieces.

Steel	Heat treatment	Static test			Impact test	
		Maximum load (kg)	Deflection (mm)	Absorbed energy (kgm)	Maximum load (kg)	Absorbed energy (kgm)
A	1000℃ air cooled	—	—	—	1100	13·0 (unbroken)
	475℃×3hr aged	1160 860	0·25 0·15	0·16 0·07	1100	0·4
	600℃×½hr+ 475℃×3hr aged	2720 2760	0·60 0·62	0·97 0·97	1500 1300	1·1 0·9
B	1000℃ air cooled	—	—	—	2300 2300	8·5 10·7
	550℃×2hr aged	2840 2400	0·69 0·51	1·14 0·60	2700 —	1·9 2·3
	650℃×1hr aged	—	—	—	2340 2960 2370	2·1 2·7 2·1

た結果[20]を示したもので，最右欄には試片に存在するγ相の量をX線により測定した結果が付記してある．鋼Aにおいては，1000°C 空冷後 475°C×1hr の時効で最高かたさになると，早期破断を呈し，伸び・絞りは測定不可能であり，600°C で過時効状態にすると次第にγ相の量は多くなり，引張強さはほとんど変化せぬが，均一伸びは次第に増加する．600°C×1/2hr の過時効処理後 473°C×3hr の再加熱を行なったものは，引張強さ 143 kg/mm², 伸び 8%, 絞り 47% の値を示して，かなり強靱性を有するものと認められた．鋼 B では，1000°C 空冷後 550°C×2hr の時効で最高かたさに達した状態で，引張強さ 153 kg/mm², 伸び13%, 絞り 53% を示し，鋼 A に比べてさらに優れた強靱性を有している．

Table 3 は，鋼 A および B を 1000°C より空冷後時効したものについて，V型切欠標準シャルピー試片を用いて常温において静的および衝撃曲げ試験を行なった結果である．静的曲げ試験は前節で述べたものと同様に行なった。これらの結果においても，鋼 A を 600°C で過時効処理後 475°C で再加熱して硬化せしめたもの，および鋼 B を 550°C で時効したものが，鋼 A および鋼 B においてそれぞれ高いかたさのレベルで比較的靱性を有し，鋼 A よりも鋼 B の方が強靱性に優れていることが認められる．

以上の試験結果より，Fe-Ni-Mn マルテンサイト合金では，Ni および Mn の含有量を減少せしめても，Al, Cr, Mo を添加することによって時効硬化性を維持することが可能であり，少量の C の添加は強靱性の改善にきわめて有効であることが明らかになった．

4. 考　　察

この研究は，Fe-Ni-Mn, Fe-Ni-Co および Fe-Mn-Co などの 3 元合金のマルテンサイト組織が著しい時効硬化性を示すことを金属組織的に探究した結果と関連せしめて，強靱性の比較検討を行なったものである．試験の結果は，従来から常識的に考えられていたように，「微細な析出物が基質と非整合に，均一に分散した状態」が強靱であり，このような金属組織の得られるような合

金の化学成分あるいは熱処理条件を選択することが必要であると結論された．

鋼の金属組織と強靱性を関連せしめるときには，A.H. Cottrell[21] が提案した式，

$$(\sigma_i d^{1/2} + k_y) k_y = \beta \mu \gamma$$

が一応の目安になるものと考えられる．ここに σ_i は摩擦応力，d は結晶粒の大きさ，k_y は Petch の実験式の固着応力の係数，μ は剛性率，γ は亀裂の表面エネルギー，β は定数である．一般に鋼の強化法は σ_i を大きくするものであり，上式の左辺は右辺より大きくなるので強化とともに脆くなる傾向がある．したがって周知のように，結晶粒径あるいはこれに相当する上式の d の値を小さくすることが，靱性を低下することなく強化する有力な方法になる．

本研究の結果は上式の σ_i の値を適当に調節することにより同一の強度水準ならば靱性を高めることが可能であり，また靱性が同一の水準であれば強度を高めることが可能であることを示したものと考えられる．そしてこのような考え方が，強靱性を問題とする場合に金属組織学的にも実用的にも重要であることを提案したい．

Fig. 18 および 19 は，本研究で得られた引張試験結果から引張強さと伸びおよび絞りの関係を示したもので，図中の斜線の領域は一般の高張力鋼，調質鋼について公表されている値[22]に相当する．すなわち，鋼 B は引張強さが 150 kg/mm² 程度の水準においてはほぼ従来の調質鋼と同等の性質を示しており，熱処理の簡便なことおよび熱処理による寸法変形の少ないことなどを考慮するとき精密機械部品あるいは機械構造部材として利用範囲の多い鋼種の一つであろうと認められる．

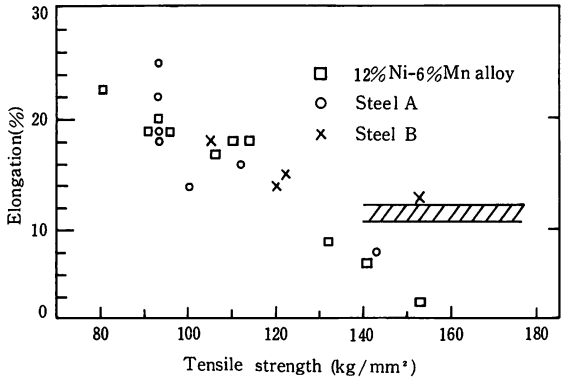

Fig. 18. Relation between tensile strength and total elongation of the 12%Ni-6%Mn alloy as well as steels A and B. The cross-hatched area corresponds to values for commercial high-strength steels.

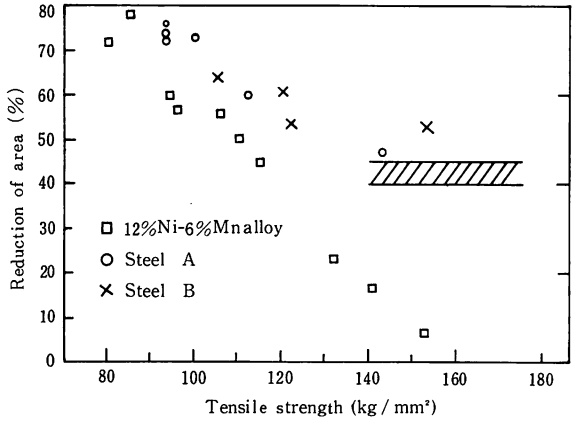

Fig. 19. Relation between tensile strength and reduction of area of the 12%Ni-6%Mn alloy as well as steels A and B. The cross-hatched area corresponds to values for commercial high-strength steels.

12%Ni-6%Mn 合金の靱性は，引張強さが 110 kg/mm² 以上の強度水準においては必ずしも良好でない．しかし本研究で使用した Fe-Ni-Mn 3元系を基とする時効硬化性合金では，γ 相の析出が比較的容易であり，この γ 相の TRIP 現象を利用して強靱性を改善する可能性が見出されたことは注目すべきであろう．また本研究においてこの合金の引張試験で観察された荷重—伸び線図の形状と金属組織との関係にはきわめて興味深いものが得られたと考えられる．すなわち，Fig. 9 における荷重—変形曲線において不連続降伏が 500°C×10 hr 時効試片では明瞭に認められ，500°C×20 hr 時効試片では不明瞭になり，500°C×50 hr 時効試片では消失して連続降伏をするようになる．このような挙動の変化は，過飽和マルテンサイト組織が分解する際に生成される zone の大きさおよび γ 相の析出量などと関連せしめて理解できる．

焼入状態における均一なマルテンサイト組織では，比較的転位密度は大きいが，基質は軟かく，局部的に転位の運動は容易な筈である．そして転位が動くと転位林に出会う機会が多く，多数のジョグが形成されるであろう．したがって，連続降伏がおこり加工硬化はかなり著しくおこるものと推定される．500°C×1 hr の時効で最高のかたさに達したものは，Photo. 1 の透過電顕による観察結果では 10～100 Å 程度の大きさの zone が形成されている．このような硬化状態では，変形は局部的におこり，可動転位は容易にこの zone を切断するので脆い状態を呈するものと考えられる．500°C で 2～10 hr 時効したものでは，析出した zone は次第に成長するが，なお基質と整合性を維持しており，析出 γ 相の量は 5% 程度で 500°C×1 hr 時効状態とほとんど同じである．したがって，こりは基質内で局部的に集中しておこることが予想され，顕著な不連続降伏現象を呈するのであろう．降伏伸びは時効時間の増加に伴って増大する．これは zone の成長によるものであろう．500°C×5 hr の時効試片では，5% 程度の全伸びが得られており，zone の大きさは転位によって切断されぬような臨界の大きさ以上になっているものと考えられる．

500°C×100 hr の時効試片では析出粒子の大きさは 1000 Å 程度と推定され，析出物の基質との整合関係は失なわれていることが観察されている．このような析出粒子の大きさは，450°C×100 hr の時効では 400～500 Å，450°C×1000 hr の時効では 500～1000 Å で，後者の場合の析出粒子は基質と非整合状態であることも観察されている．したがって，500°C×(50～500) hr の時効試片では，(i) 析出粒子はかなりの大きさに成長しているため転位によって切断されず，(ii) γ 相の量は時効時間とともに次第に増加しており，(iii) 基質は軟化すると同時に転位密度は減少しているため，変形をうけると転位の発生は容易で，クロススリップも容易におこり得る状態であり，連続降伏のおこることが可能になると推定される．500°C×20 hr の時効試片では，連続降伏のような挙動が認められるが，50～500 hr の時効試片よりも加工硬化量が少ない．これは (i) 転位の動き易い状態と，

(ii) 転位の発生し易い状態との両者が混在した金属組織になっているためと考えられる.

500°C×1000hr の時効試片では，γ 相は 30 vol% 程度存在しており，γ 相は析出物としてよりもむしろ ($\alpha+\gamma$) の2相混合組織における組織成分であり，ひずみの増加とともに転位は容易に発生し，転位密度が増大して，連続降伏をおこすものと考えられる.

以上は 12%Ni 6%Mn 合金の変形挙動を金属組織と対応せしめて考察したものであるが，このような析出硬化型鉄合金の強靱性は，析出粒子の分散強化[23] を主体として論ぜられる.

分散強化量 $\Delta\sigma_T$ は，周知のように，

$$\Delta\sigma_T = \frac{\alpha\mu b}{D} = \frac{\alpha\mu b f^{\frac{1}{2}}}{d}$$

で表示される．ここに μ は剛性率，b はバーガースベクトル，D は粒子間距離，f は粒子の存在量，d は粒子の直径，α は常数で大体1である.

12%Ni 6%Mn 合金においては d が 100Å 以下ではきわめて脆い状態を示し，1000Å 程度になれば十分な靱性が観察された．したがって転位が析出粒子を切断せぬための臨界直径は 400～500Å 程度と推定される.

供試鋼 A および B についても上記のような考察を行なうことができる．供試鋼Bは炭素を含有しているため炭化物が微細に分散しており，さらに金属間化合物が析出し得るものであって，このような析出硬化型鉄合金は今後一層研究すべきものと思われる.

5 結　　論

時効硬化性マルテンサイト鉄合金の強靱性について，Fe-Ni-Mn 3元合金およびこれに2，3の元素を添加して炭化物あるいは金属間化合物を析出せしめた合金を供試料として．金属組織と機械的性質との関連性を実験的に研究した結果を総括すると次のとおりである.

(1) 時効硬化性マルテンサイト鉄合金は，均質な金属組織の内部に微細な析出物（オーステナイト，炭化物あるいは金属間化合物）が非整合に均一に分散した状態が最も強靱である.

(2) Fe-12% Ni-6%Mn 3元マルテンサイト合金では，最高時効かたさの状態においてきわめて脆く，早期破壊がおこるか，過時効状態にしてオーステナイトの析出量が 10 vol% 程度になると，比較的高いかたさ水準でも靱性の顕著な改善が認められた．またこのようなオーステナイトの析出した状態では，−196°C で変態誘起塑性が観察された.

(3) Fe-4%Ni-2%Mn 合金では全く時効硬化性は認められぬが，Al, Cr, Mo を添加することにより著しい時効硬化性が付与されると同時に強靱となり，さらに 0·1 %程度の炭素の添加によって強靱性の優れたものになることが見出された.

(4) Fe-12%Ni-6%Mn 3元合金では時効過程において不連続降伏あるいは連続降伏をおこす現象が観察され，これらの変形挙動の変化は，マルテンサイト組織が2相分離して ($\alpha+\gamma$) の混合組織になる過程で，基質から析出する粒子の大きさおよびその整合性によって説明することができた．そして転位が析出粒子を切断せぬための粒子の臨界直径は 400～500Å 程度と推定された.

この研究の一部は東京工業大学金属工学科大学院院生小林経明，学部学生オクタビオ・マモン，早坂民雄の諸君の助力によって行なわれたことを記し，謝意を表する．またこの研究に種々協力・援助された東京工業大学精密工学研究所鈴木朝夫助教授，淀川正進博士に謝意を表する次第である.

文　　献

1) R.F. Decker et al.: ASM Trans. Quart., **55** (1962), p. 58
2) S. Floreen: ASM Trans. Quart., **57** (1964), p. 38
3) G.W. Tuffnell and R.L. Cairns: ASM Trans. Quart., **61** (1968), p. 798
4) W.A. Spitzig et al.: ASM Trans. Quart., **61** (1968), p. 635
5) K. Bungardt et al.: Arch. Eisenhüttenw., **39** (1968), p. 719
6) R.K. Pitler and G.S. Ansell: ASM Trans. Quart., **57** (1964), p. 220
7) G.P. Miller and W.I. Mitchell: JISI, **203** (1965), p. 899
8) J.M. Chilton and C.J. Barton: ASM Trans. Quart., **60** (1967), p. 528
9) I.L. Cheng and G. Thomas: ASM Trans. Quart., **61** (1968), p. 14
10) S. Floreen and G.R. Speich: ASM Trans. Quart., **57** (1964), p. 714
11) W.R. Patterson and L.S. Richardson: ASM Trans. Quart., **59** (1966), p. 71
12) 田中・鈴木・淀川：日本金属学会誌，**31** (1967), p. 1075
13) 田中・鈴木・淀川：鉄と鋼，**54** (1968), p. 776
14) 田中・鈴木・小村：日本金属学会誌，**31** (1967), p. 1016
15) 田中・鈴木：日本金属学会誌，**34** (1970), p. 711
16) 鈴木：日本金属学会誌，**31** (1967), p. 1081
17) 鈴木：日本金属学会誌，**32** (1968), p.1019
18) 淀川：日本金属学会誌，**34** (1970), p.407
19) 田中その他：鉄鋼技術国際会議 (1970) で発表
20) 田中・山本：日本金属学会講演会 (1970 年 10 月) で発表
21) A.H. Cottrell: Fracture, ed. by B.L. Averbach et al., (1959), p. 20 [John Wiley and Sons]
22) Metal Progress **96** (1969), No. 4, 153
23) E. Hornbogen: Die Verfestigung von Stahl, p. 1, Symposium sponsored by AMAX (1969)

討論 pp. 359-360 参照

The Effect of Primary Carbides on the Toughness of High-Speed Tool Steels

K. Kiyonaga

Hitachi Metals, Ltd. Metallurgical Research Laboratory, Yasugi Works

In order to investigate the effect of primary carbides on the toughness of molybdenum high-speed tool steel (SHK9), various mechanical tests such as static bend tests, impact tests, torsion tests, tensile tests and fatigue tests were conducted on specimens that were changed and controlled artificially in the degree of segregation, size and shape of primary carbides.

In the first experiment using two different-size ingots (208 and 268 mm square), the effect of forging ratio on the microstructure and bend toughness was studied. The results showed that the static bend strength increased appreciably at first but steadily approached saturation at higher forging ratios (Fig. 3). This change in bend toughness was slower in specimens cut from the larger ingot and also from the transverse direction of forged bars. These findings could not be explained by macroscopic carbide segregation, such as the width of carbide nets or streaks, but were related presumably to the microscopic states of the primary carbides, namely, the density, size and shape of primary carbides in the segregated parts (Fig. 4, Photo. 2 and 3).

In the second experiment, various mechanical properties were investigated in samples with different primary carbide structures produced by variation of the process condition of ingots from the same heat. The carbide states were measured by an image analyzing computer with the results shown in Table 4 and 5, Fig. 5 to 9 and Photo. 4 to 6. Table 6 is the general assessment of the carbide state in these samples based on the above data.

The austenitic grain size and amount of residual austenite of these samples after quenching from 1220°C are shown in Table 7. Although there is no clear difference in the amount of residual austenite, the austenitic grain size was larger in samples with coarser primary carbides.

The results of the static bend tests are shown in Fig. 11 and 12. When the toughness of the various samples is compared on the basis of the maximum absorbed energy at the same hardness level, the bend toughness is seen to have been superior in samples with smaller austenitic grain size and a good degree of carbide homogeneity.

Charpy impact tests were conducted at room temperature as well as at temperatures up to 600°C with the results shown in Fig. 13. There was a significant increase in Charpy impact values at test temperatures between 150 and 300°C. Above 550°C, the differences among samples became smaller. The effect of primary carbides was similar to that observed in static bend tests but the degree of carbide segregation seemed to have a greater effect on impact values than on the results of static bend tests.

Static torsion tests were carried out on the Shimazu RET-50 type torsion tester using the specimen shown in Fig. 14. The results are shown in Table 9. In this case, the effect of carbide segregation was more evident than with impact values.

Fatigue tests were conducted on the Ono type rotating-beam fatigue testing machine using the specimen shown in Fig. 15. The difference from one sample to another was small at high stress levels and large at low stress levels, as shown in Fig. 16, which indicates that the samples with good carbide homogeneity and few coarse carbides gave good results.

The shape of the tensile-test specimen was devised to minimize the notch effect as much as possible (Fig. 17). The results on hardened specimens are shown in Table 10 and those on annealed specimens in Table 11. The tensile toughness in these tests seemed to depend greatly on the degree of carbide segregation.

After the above mechanical tests, the fracture surfaces of the specimens were observed macro- and microscopically. The state of the fracture surfaces indicated no clear difference among samples. As a result of these observations, however, it became obvious that most of the fracture surface presented a quasi-cleavage type fracture characteristic (Photo. 12) with a ductile fracture present in local sites. For instance, fractures with a dimple structure were found in hardened tensile and impact specimens as shown in Photo. 13. As indicated in Photo. 15 and 16, instances were frequently observed where carbides were cracked on the fracture surfaces, and also where carbides were torn from the matrix at the interface of the

two phases as shown in Photo. 17. Evidently the course of crack propagation was quite complex and was affected by both carbides and grain boundaries.

The fracture surfaces were also observed in Hitachi HSM-2 type scanning microscope. Photo. 20 is the tensile fracture of an annealed specimen, which denotes complete dimple fracture. Torn and cracked carbides can be found on the fractures illustrated in this photograph. Traces were also found where carbides had been removed from the matrix. Although Photo. 21 presents the fatigue fracture surface, striations peculiar to fatigue fracture surfaces could not be observed. In this photograph, a coarse carbide projects out on the surface as shown by arrow a and this carbide seems to have been torn from the interface between the carbide and matrix. In this case, the circumference of the carbide lacks the irregularities of small carbides (Photo. 19 or 20). It seems to indicate that coarse carbides were torn easily from the matrix without much plastic deformation. Photo. 23 indicates the origin of a fatigue crack that presumably resulted from the tearing of a large carbide.

In order to estimate the ease of crack propagation, notch toughness was determined using specimens with the shape shown in Fig. 18. As indicated in Table 12 and Fig. 20, there was a good correlation between notch toughness and hardness.

Many factors other than primary carbides affect the toughness of high-speed tool steels. Predominant among these factors are the amount of dissolved carbide, the amount of precipitated carbide and its morphology, homogeneity of structure, austenitic grain size and chemical composition.

The author investigated the chemical analysis of quenched-and-tempered matrices and the transmission electron microscopic structure of the matrices. The results are shown in Table 13, Photo. 24 and 25. According to these results, sample Y, which had the worst degree of carbide segregation and showed inferior toughness in most of the mechanical tests, presented great differences in vanadium content between the carbide-segregated parts and normal parts. Matrix structures by transmission electron techniques were almost the same in all samples. As shown in Photo. 24 and 25, dislocations were piled up around residual carbides and there was a stress concentration at the circumferences of the carbides, which might induce cracks or tears in the carbides when further mechanical stress was imposed.

Table 15 summarizes the mechanical properties of the samples. A comparison of Table 15 with Table 6 demonstrates the effect of primary carbides on the toughness of high-speed tool steel. It is concluded that toughness depended on the resistance to cracking or tearing of large carbides in the segregated parts. Table 14 indicates the number of cracked or torn carbides in hardened tensile specimens. The larger the carbide and also the more complex the carbide shape, the higher was the probability of crack occurrence in the carbides. MC carbide seemed to crack or tear more easily in tensile deformation than M_6C carbide with similar shape and size. Confirmation of the previously known inhomogeneity of large carbides in high-speed tool steels is given by the electron probe microanalyzer results on large carbides shown in Photo. 27.

The conclusion reached from this investigation is that the toughness of high-speed tool steel is affected by the degree of carbide segregation and size. The degree of carbide segregation should not be measured simply by the width of the segregated parts but must be assessed by the carbide density (percent of carbide area) in the segregated parts. The carbide size should be measured by the amount of coarse primary carbides with dimensions over 5μ and an irregular shape caused by coagulation. These factors will have an unfavorable influence on the occurrence of cracks and their propagation through cracking or tearing of large carbides as a result of the imperfection of carbide crystals and the high dislocation density in the area between adjoining carbides.

The author considered the relation between toughness and carbide cracks, where the critical fracture stress was calculated from notch toughness values on the assumption that a microcrack resulted from a coarse carbide (Fig.23 and 24). As a result, it was concluded that a crack in an individual coarse carbide could not by itself be the origin of a cleavage fracture and that another mechanism was necessary such that the microcracks would connect with each other to grow large enough to cause a cleavage fracture. Various properties, however, had a good correlation with the value of [matrix area in carbide-segregated parts/maximum carbide length]$^{1/2}$. This parameter was introduced from the Griffith-Orowan criterion with some modifications.

高速度工具鋼の靱性におよぼす一次炭化物の影響

清永欣吾

日立金属株式会社　安来工場　冶金研究所

要　旨

Mo系高速度工具鋼（SKH 9）の靱性におよぼす一次炭化物の影響を検討ずるために，人為的に炭化物状態，すなわち，炭化物密集度（ミクロ的偏析度），炭化物粒度，形状の異なる試料を作製し，静的曲げ試験，衝撃試験，捩り試験，疲れ試験などを行ない，これらの性質に対し，炭化物のいかなる状態がいかに影響をおよぼすか研究した．

その結果，炭化物状態の上記性質に与える効果は試験法により若干異なるが，炭化物密集度の影響がもっとも強く，つぎに形状，粒度の順と考えられる．しかし，一般に炭化物密集度の大きいものは，炭化物の形状が悪く，また，5μ以上の融合した粗大炭化物が多い傾向にあり完全な要因分解は困難であった．破面は擬劈開状で局部的塑性変形があり，一部 dimple pattern も認められた．炭化物亀裂がマクロ的あるいはミクロ的破壊面の起点となっている例が多く観察された．これらの結果より，一次炭化物が靱性に影響をおよぼす機構を考察した．

1. 緒　言

高速度工具鋼の性能は単に化学成分や熱処理によって定まるものではなく，鋼材の製造法によって種々変化するものである．とくに高速度工具鋼あるいは冷間ダイス鋼のごときレデブライト鋼においては，熱処理によって変化しがたい一次炭化物の状態が品質に大きな影響を与えることが経験的に知られており，一次炭化物分布あるいは粒度などに関し，厳重な規格が実施され[1,2]，また，一次炭化物の状態改善のため，振動鋳造法[3]，接種法[3~5]，特殊溶解法[6]，紛末冶金法[7,8]など多くの製造法が研究され検討されている．

しかし，一次炭化物のいかなる状態が品質に対してどのような影響をおよぼすかについて，詳細な報告はほとんどみられない．本研究では，まず，一次炭化物の分布状態に対し，主要な効果を及ぼす鋳造比が高速度工具鋼SKH 9（AISI·M 2）の性質に与える影響を明らかにし，鋳造による一次炭化物のいかなる状態の変化が，性質に直接的な影響をもつかを検討した．

つぎに，上記の検討から得られた結論をもとに，鋼塊形状，熱間加工工程など所謂通常ランニング工程で容易にかえ得る製造条件を変動して，一次炭化物状態の異なる同一チャージ，ほぼ同一寸度の鋼材を製造し，各種性質を調査した．その結果から，高速度工具鋼の品質，とくに靱性に関する一次炭化物組織の評価法に対し，実際的な見解を与えるとともに，靱性に及ぼす一次炭化物の効果の機構について検討を加えた．

2. 鍛造比の影響

高速度工具鋼は鋳造状態でレデブライト共晶のネットワークを有する為，いちじるしく脆弱である．鍛造および圧延は単に製品の形状に仕上げるばかりでなく，熱間加工によって脆弱なレデブライト共晶を破壊し，一次炭化物を分散させ，靱性を向上させる事にその目的がある．

本研究では先づ2種類の鋼塊について炭化物分布および靱性におよぼす素延鍛造比の影響を検討した．

2.1 試料の調整

試料としては1 ton 高周波炉で溶製した SKH 9 (AISI·M 2) の 208 mm 角，および 268 mm 角鋼塊をそれぞれ鍛造比 4, 8, 12, 16, 24, 36 の丸棒に鍛造後焼なましたものを用いた．試料の化学成分を Table 1 に示す．

2.2 オーステナイト結晶粒度と熱処理硬さ

各鍛造丸棒より 12 mmϕ×10 mm の試験片を削出し，900°C×10 分予熱後，1220°C×2 分塩浴中に浸漬し，油焼入した．焼もどしは 560°C×1hr，4 回繰返した．

Fig. 1 に鍛造比と焼入時のオーステナイト結晶粒度 (Snyder-Graff 分割法）の関係を示す．鍛造比の増大にともない，結晶粒が微細化する傾向が認められる．焼入，焼もどし硬さは鍛造比によってほとんど変化せず，ほぼ一定であった．

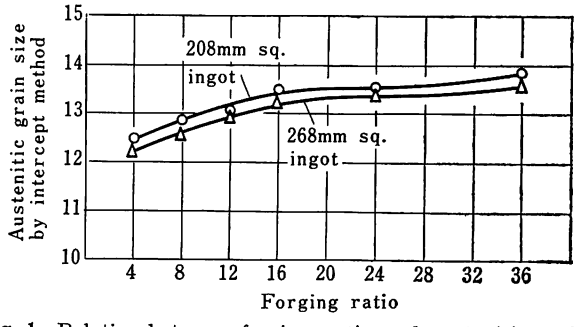

Fig. 1. Relation between forging ratio and austenitic grain size.

Table 1. Chemical composition of samples (%).

Kind of steel	C	Si	Mn	P	S	Cr	W	Mo	V	Cu
SKH9 (AISI·M2)	0·83	0·30	0·31	0·017	0·006	4·24	6·44	5·06	1·84	0·06

2.3 静的曲げ試験

各丸棒素材より 3×5×30 mm の試験片をそれぞれ 3, 5, 30 mm の辺が鍛造方向に平行になるような3方向（それぞれ N, R, P, Fig. 2）から削出し，予熱 900°C×5分，焼入 1220°C×40 秒油冷，焼もどし 560°C×1 hr 空冷 2 回の熱処理を施し静的曲げ試験を行なった．静的曲げ試験は 10 ton アムスラー型万能試験機を用い，支点間距離 20 mm の台座の上で 3 mm の辺に平行に V 字形の押金具により中央一点負荷して行なった．

Fig. 3 に鍛造比と P, N および R 方向より採取した試験片の静的曲げ強さの関係を示す．

各方向の試料とも鍛造比の増大にともない初めは静的曲げ強さを増大するが，やがて飽和に達する傾向があり，曲げ強さが飽和に達する鍛造比は鋼塊サイズの大きいほど大となっている．N と R 方向より採取した試料の曲げ強さはほとんど差がなく，ともに P 方向の試料の曲げ強さの約 60% の値で，この比は鍛造比によりあまり変わらない．

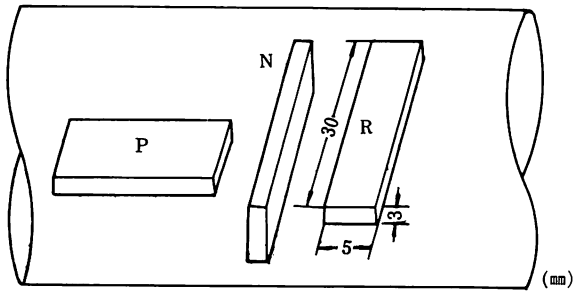

Fig. 2. Sampling position of bend-test specimens.

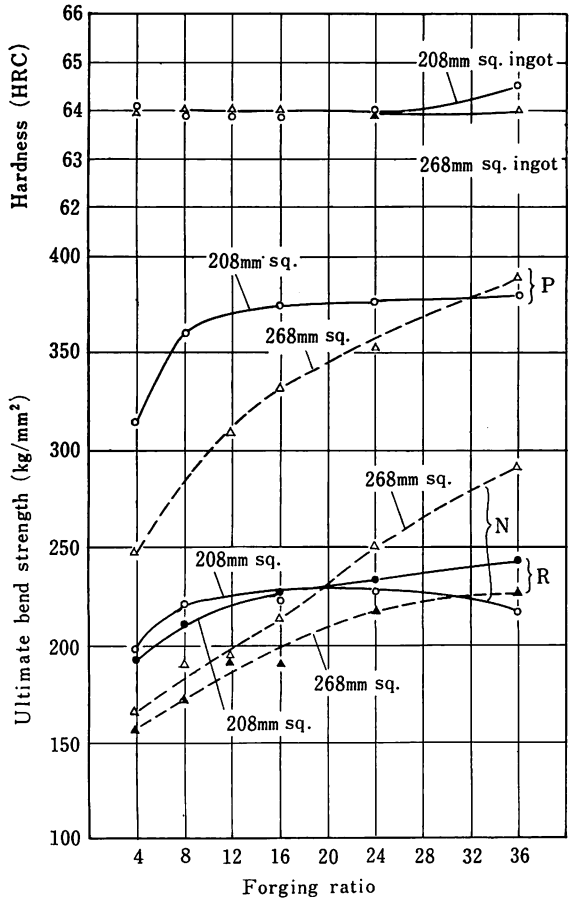

Fig. 3. Relation between forging ratio and static bend strength on the specimens sampled from P, N and R directions of bars.

2.4 ミクロ組織

各試料の焼なまし状態における二次炭化物については鋼塊サイズ，鍛造比によりほとんど変化が認められなかった．同様に焼入焼もどしを行なった各試料のマトリックス組織に関しても，さきに示したオーステナイト結晶粒度を除き，鋼塊サイズおよび鍛造比による本質的な差は認められなかった．

しかし，鋳造時のレデブライト共晶に由来する一次炭化物の分布形態は鍛造比の増大にともない，いずれも，net 状から hook 状をへて streak 状に変化した．Photo. 1 は 268 mm 角鋼塊の場合の鍛造比による一次炭化物分布状態の変化を示したものである．Net→hook→streak 状の変化の過程は鋼塊サイズの小さいほど加速させられた．また鍛造比が増大するにつれて一次炭化物の集団が分散して，細かく引き伸ばされてくるとともに，隣接した炭化物集団が融合してくる傾向が認められた．

次に，鍛造方向に平行な断面における炭化物集団の縞巾を 60 個測定し，その度数分布を求めた．Fig. 4 はその平均縞巾，最大縞巾（大きい方から 6 ケの縞巾の平均値）および平均縞間隔と鍛造比の関係を示したものである．平均縞巾は縞巾分布が鍛造比により不規則に変化するにもかゝわらず，ほとんど一定であり，また最大縞巾あるいは平均縞間隔は鍛造比の変化にともなって類似した変化を示し，鍛造比 8～12 で極小値が現われている．

以上は一次炭化物のマクロ的な分布状況を示すものであるが，静的曲げ試験を行なった試料を用いて鍛造方向に平行な方向の一次炭化物のミクロ的分布形態を調査した．Photo. 2 に示すように，いずれの鋼塊においても，鍛造比の増大にともない，共晶内の一次炭化物は次の変

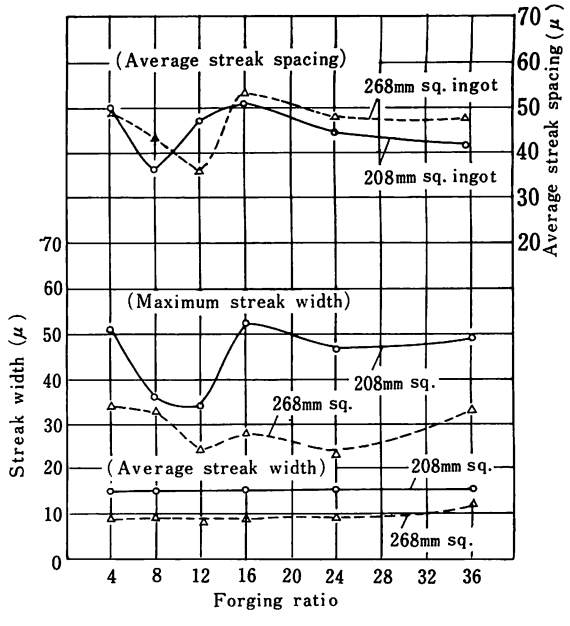

Fig. 4. Change of carbide streak widths and spacings due to forging ratio.

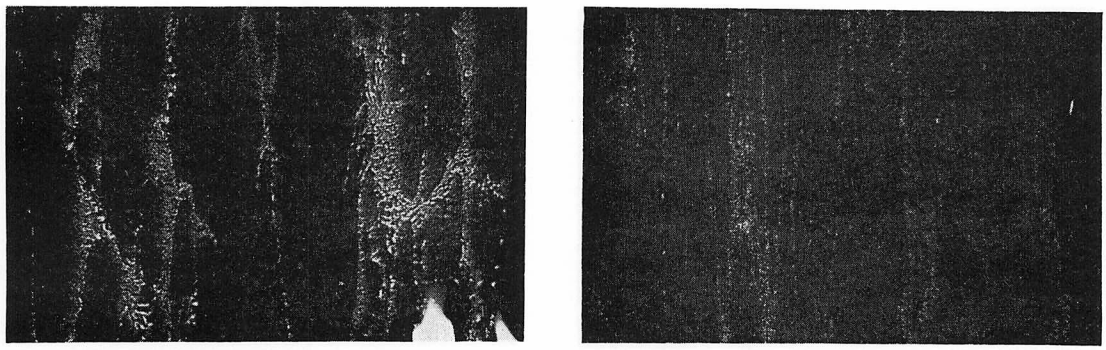

F. R. =4　　F. R. =16

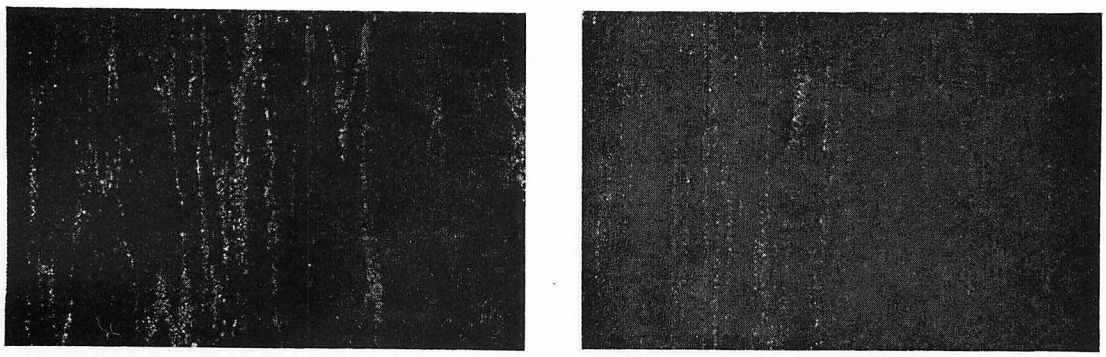

F. R. =8　　F. R. =24

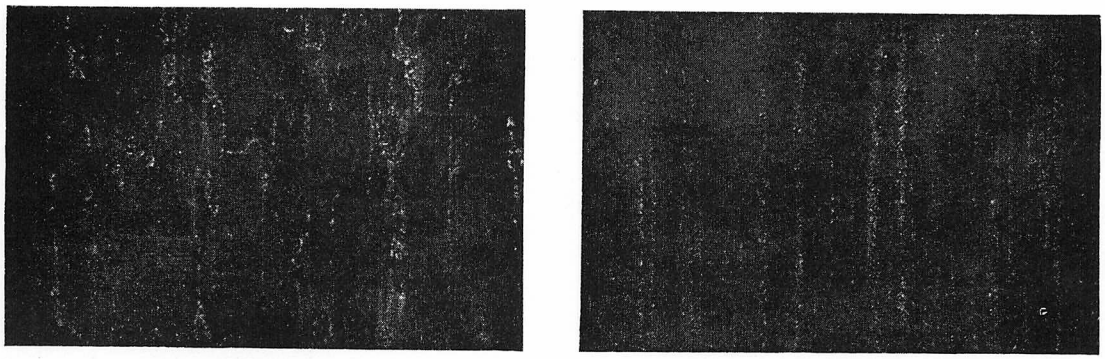

F. R. =12　　F. R. =36　　×100

Photo. 1. Change of carbide distribution in a 268 mm-square ingot due to forging ratio.

化を辿る．

(1) 形状；連結的な複雑な形状→分離的な簡単な形状

(2) 集合度；密→疎

上記のうち，集合度の変化についてはあまり明瞭でないが，形状の変化は明らかに鋼塊サイズの大きなものほど遅くなっている．

Photo. 3 は 268 mm 角鋼塊の鍛造方向に直角な断面における一次炭化物分布の変化を示すもので，この場合も平行方向の場合と同様に，一次炭化物の形状と集合度の変化が明瞭に認められるが，形状の変化は平行方向に比べ遅くなっている．このように直角方向の断面においても，炭化物が分散して集合度が粗になることは注目される．

2.5 一次炭化物分布と靱性の関係

高速度工具鋼の靱性が炭化物分布に大きく依存していることは疑いのないことであり，実際，高速度工具鋼の品質は炭化物分布によって評価され，炭化物分布に関する厳しい仕様が設けられている．しかしながら，一次炭化物のマクロ的分布は，既述のごとく，静的曲げ強さと一義的関係になく，鍛造比により複雑な挙動を示す．本研究によれば，むしろ炭化物のミクロ的な分布形態，すなわち，一次炭化物の形状，集合度，粒度などが靱性に直接の影響を与えているものと考えられる．

静的曲げ強さは，鍛造比の増大にしたがって，初めは急激に増大し，やがて飽和に近づく．すなわち，まず共晶内部の連続的な複雑な形状の一次炭化物が破砕され球状化する過程が，低い鍛造比に対する靱性の急激な上昇に対応し，次に球状炭化物が分散，均一化する過程が，靱性の漸増し，飽和に近づく過程と一致すると説明される．

この変化が鋼塊サイズの大きいほど遅いのは，鋳造時共晶組織が大きく発達し，炭化物粒度が大きいこと，鍛造効果が中心部まできゝにくいことなどによるものであろう．P と N, R 方向の靱性の違いは，鍛造比 8 以下では主として，炭化物の形状が鍛造方向に長いため，鍛造

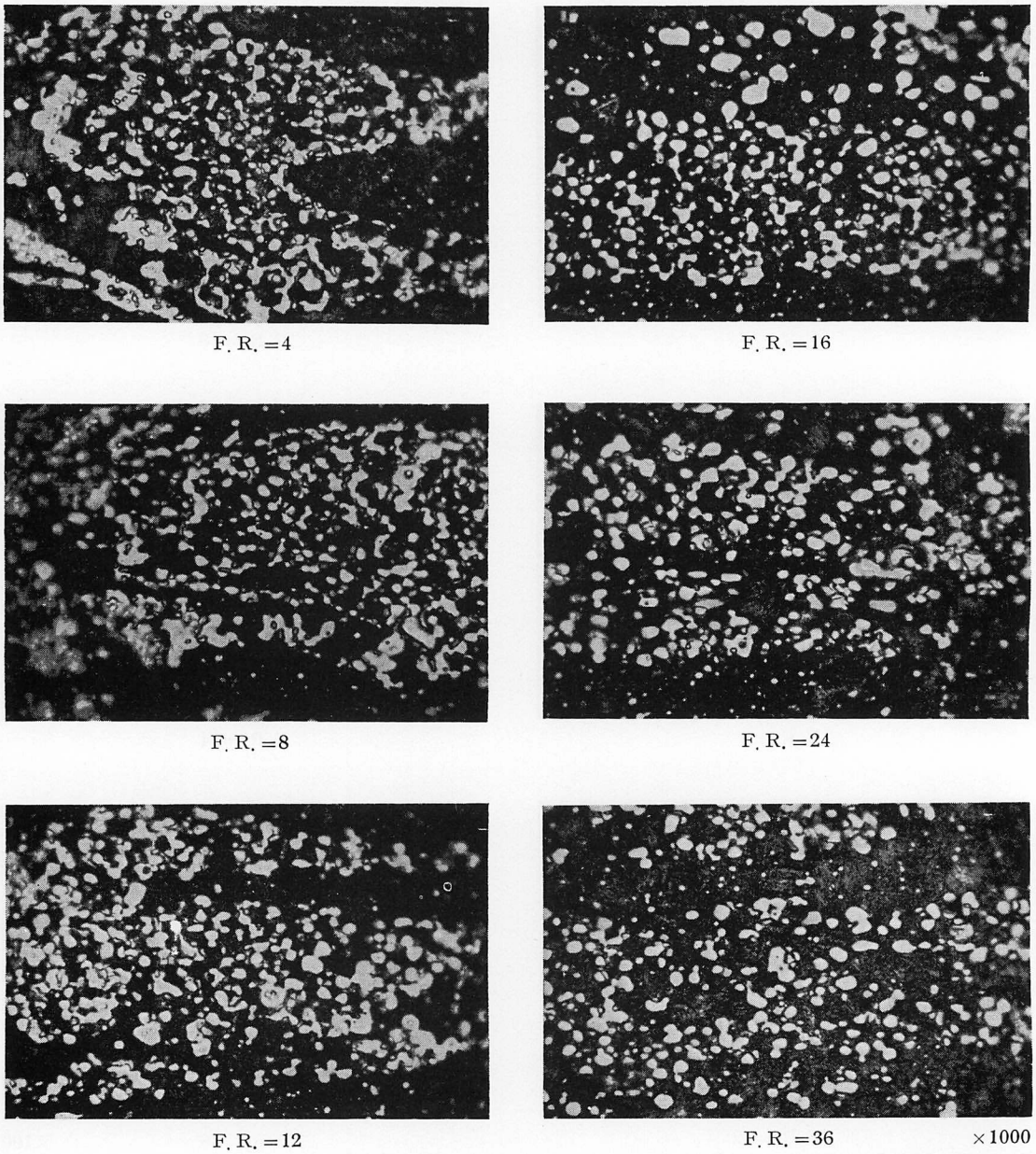

Photo. 2. Change of carbide distribution in the carbide-segregated portion in a longitudinal section of a 268 mm-square ingot.

比の大きい所では炭化物の縞状偏析に沿う方向のクラックの伝播が直角方向に比し極めて容易であることに基づくものと考えられるが，検討が必要である．

いずれにしろ，鍛造比の増大により一次炭化物の形状，粒度，集合度とも良い方向へ移行するため，実用的には高い鍛造比が望ましい．しかしながら鍛造比増大のため，大型鋼塊を用いれば，粒度は粗大になりやすい欠点を生ずる．それ故，靱性の高い高速度工具鋼を製造するに当り，一次炭化物の形状，粒度，集合度のうち，いずれが靱性に対し，より大きな影響を及ぼすか，炭化物はどのような機構で靱性に影響を与えるのか，これらの疑問点をさらに明瞭にする必要がある．

3. 一次炭化物の分布状態と諸性質の関係

前章で示したように，高速度工具鋼の靱性は一次炭化物の存在状態，とりわけその形状，粒度，集合度によって定まると考えられるが，このうち，どれが主要な要因であるかを確認するために，この3要素の各々を独立に変化させた試料を作製し，諸性質を比較した．

3.1 試料の作製

Table 2 に示す化学成分の SKH 9 (AISI·M 2) につき鋼塊形状，分塊および圧延加熱条件等を適当に組合せ，Table 3 に示すほゞ同寸度（約 30 mmφ）の6個の試料

Table 2. Chemical composition of samples (%).

C	Si	Mn	P	S	Cr	W	Mo	V	Cu
0·86	0·26	0·28	0·022	0·004	4·10	6·05	4·85	1·81	0·04

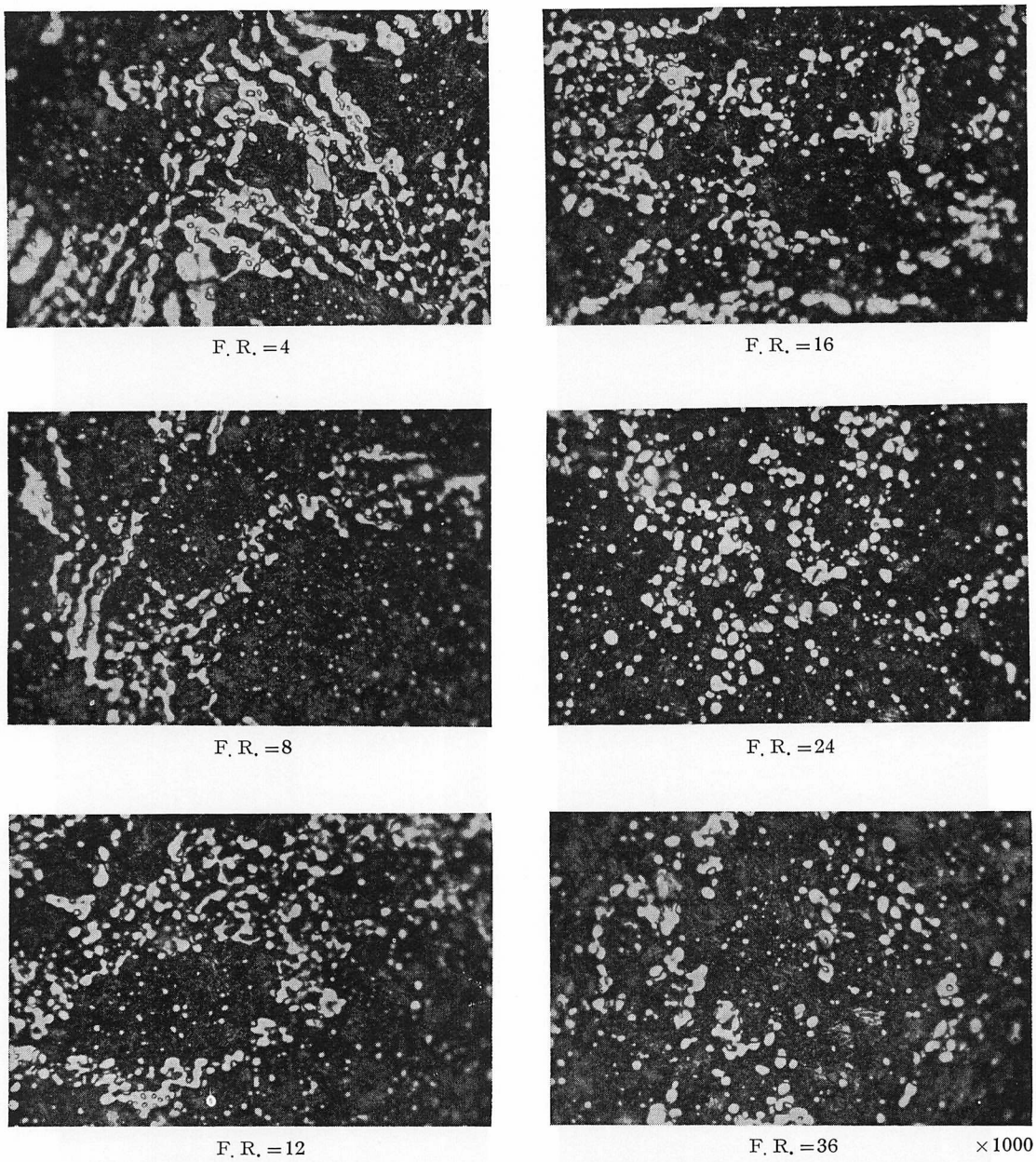

Photo. 3. Change of carbide distribution in the carbide-segregated portion in a transverse section of a 268 mm-square ingot.

Table 3. Target states of primary carbides in samples.

Mark	Size	Distribution density	Shape
H	large	low	good*
B	large	low	bad*
X	large	high	bad
C	small	low	good
F	small	low	bad
Y	small	high	bad

* good : spheroidal
bad : irregular

素材を製造した.

各試料素材は仕上圧延後, 820°C×5 hr 徐冷の焼なましを行ない, 各種試験片の切出しを行なった.

3.2 試料のミクロ組織

各試料の D/4 位置におけるミクロ組織を Photo. 4 ないし 6 に示す. Photo. 4 は低倍率で一次炭化物の分布状況を示し, Photo. 5 は高倍率で縞状偏析部の一次炭化物の状態, Photo. 6 は非偏析部の組織を示している. いずれも, 後述の機械的性質との関連をもたせるために, 1220°C 焼入, 560°C×1hr 2 回焼もどしした状態の組織である.

一次炭化物の形状および分布に関しては, 粒度の大きい H, B が比較的良好であり, 炭化物形状の悪い Y では, 融合した粗大な一次炭化物が見られる. 非偏析部の炭化物については, H, B, X と F, C, Y では明瞭な差が認められ, 前者では Photo. 6 のごとく 2～3 μ の比較的大きい一次炭化物が多く含まれている.

各試料の炭化物の状態をより定量的に表わすために,

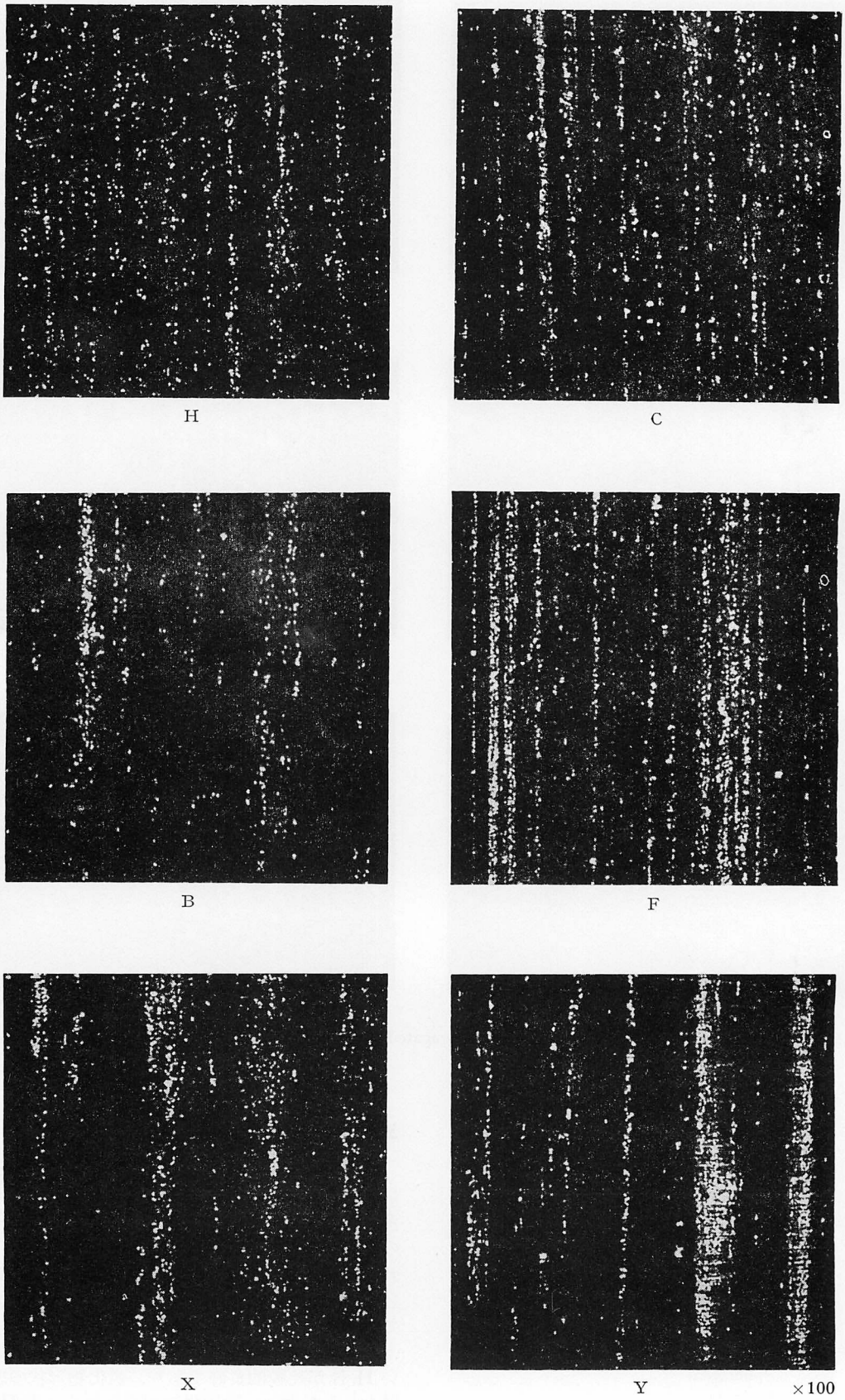

Photo. 4. Carbide distribution as hardened.

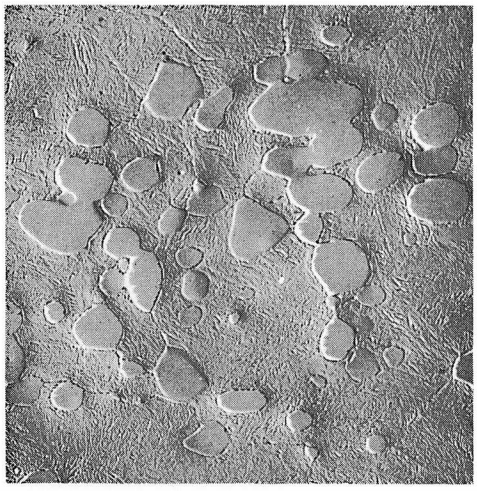

H

C

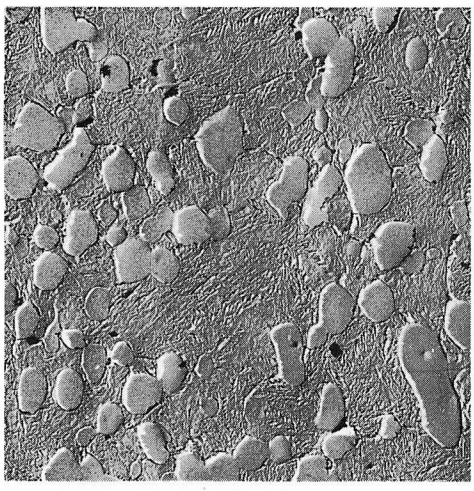

B

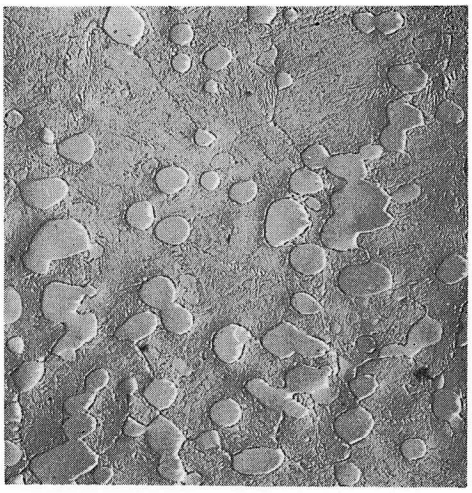

F

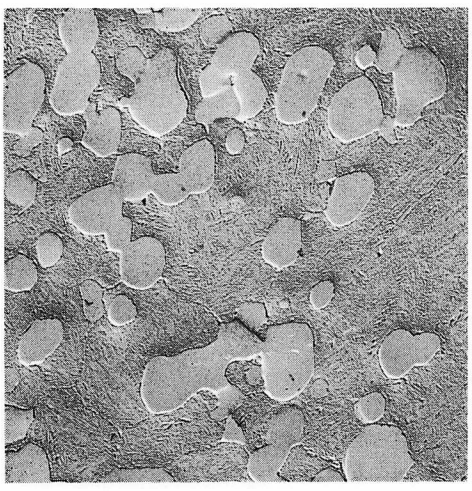

X

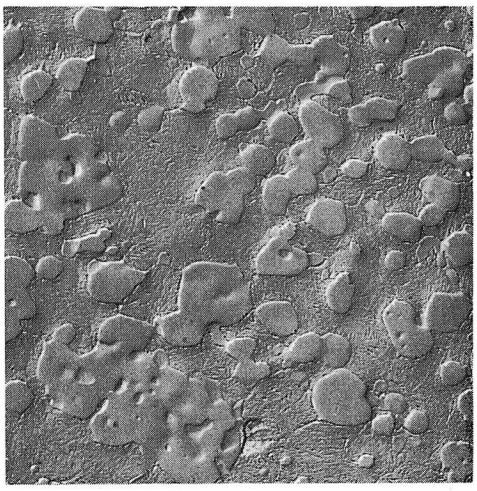

Y ×3000

photo. **5.** Carbide distribution in the streaks.

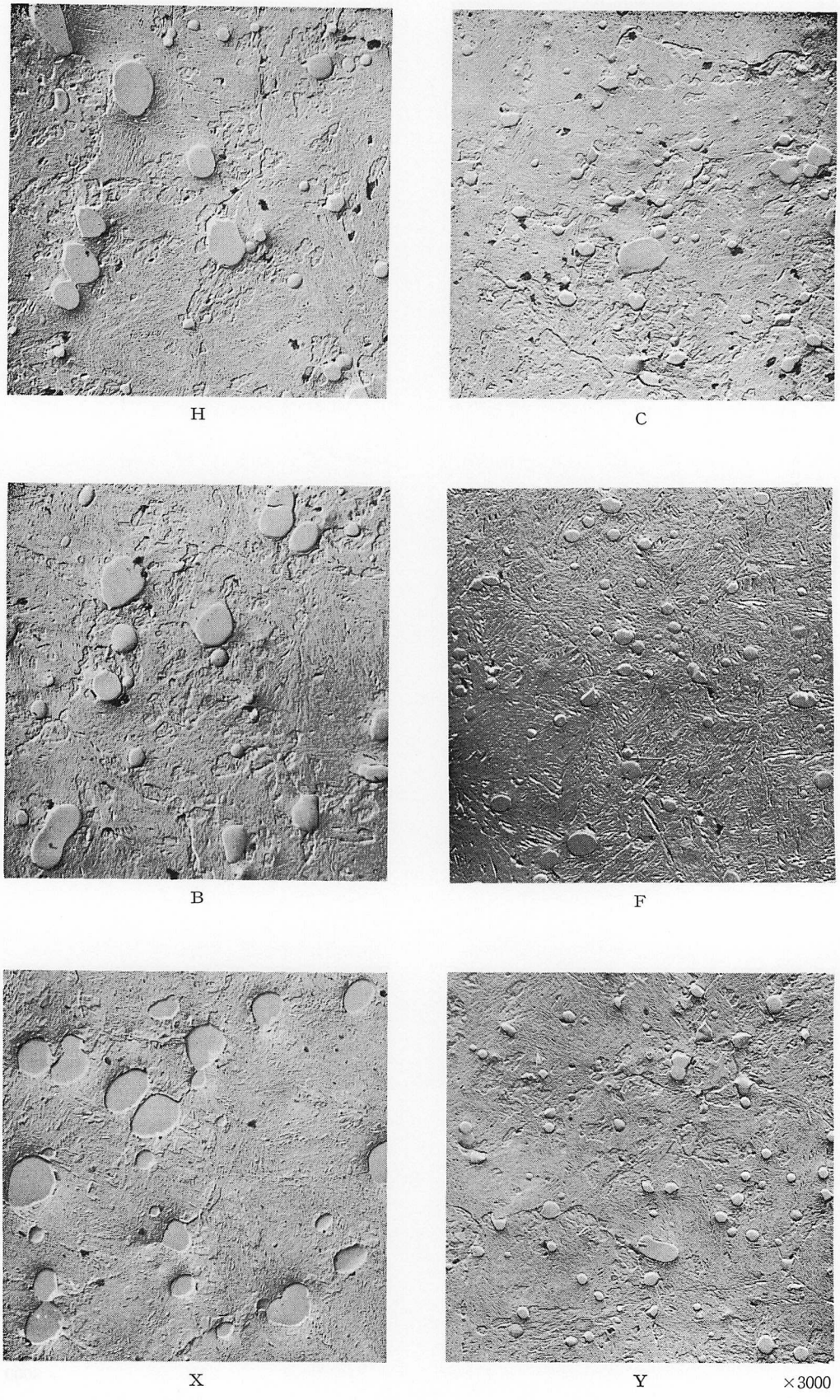

Photo. 6. Carbide distribution in the field of homogeneous structure.

Quantimet (Image analyzing computer) を用いて，炭化物サイズ分布，偏析度，面積率などを測定した[9,10]．

3.2.1 炭化物偏析

焼入焼もどし（1220°C 油冷，560°C×1 hr 2回）した試料の D/4 位置組織を，10% Nital で腐食し，炭化物を白く，マトリックスを黒く腐食させた状態で，倍率5600倍で Quantimet のブラウン管上に組織を投影し，250×60 mm（実寸約 45μ×11μ）の視野中の炭化物面積率を圧延方向と直角方向に 200 視野（実寸約 2 mm）にわたり連続測定した．

測定結果を Fig. 5 に示す．非偏析部の炭化物面積率は約 2～3%，偏析部は 20～30% で非偏析部の約 10 倍の炭化物が存在する．10% 以上の炭化物を有する偏析縞数は 2 mm 当り H は 11 個，B は 15 個と少なく，他は 22～23 個で大差ない．しかし，20% 以上の炭化物量を含む偏析の大きい縞は Y がもっとも多く，次に X であり，C, F は同程度に少ない．Fig. 6 は 200 個の測定値の頻度分布を対数確率紙にプロットしたもので，概ね対数正規分布をなすことがわかる．H, B の炭化物偏析が少なく，Y はとくに偏差が大きい．

3.2.2 炭化物の粒度分布

前項と同様，Quantimet を用い，綜合倍率 10 500 倍，ブラウン管スクリーン上視野 300×200 mm の炭化物数，粒度分布，面積率を 50 視野にわたり測定した．結果を Table 4 および Fig. 7 に示す．ただし，2·5μ 以上の粗大炭化物については，頻度が少ないため，1000 倍の顕微鏡下で 0·3 mm² にわたり直接計測した．結果を Fig. 8 に示す．

これらの結果によれば，F, C, Y は 1μ 以下の炭化物が多く，逆に B, H, X は 1·5μ ないし 5μ の炭化物が多い．さらに，7·5μ 以上の粗大炭化物は Y, F が多い．

残留炭化物量は平均約 10% 程度であるが，範囲はかなりバラツク，上限は共晶部分に当るが，共晶偏析部の炭化物については次項で別に検討した．

3.2.3 偏析部炭化物の粒度分布

Quantimet により綜合倍率 8000 倍，スクリーン上視野 160×65 mm（実視野 163μ²），10 視野中の炭化物面積率，粒度分布を炭化物偏析部のみを対象として測定した．測定視野としては，視野が完全に偏析部の中に入る

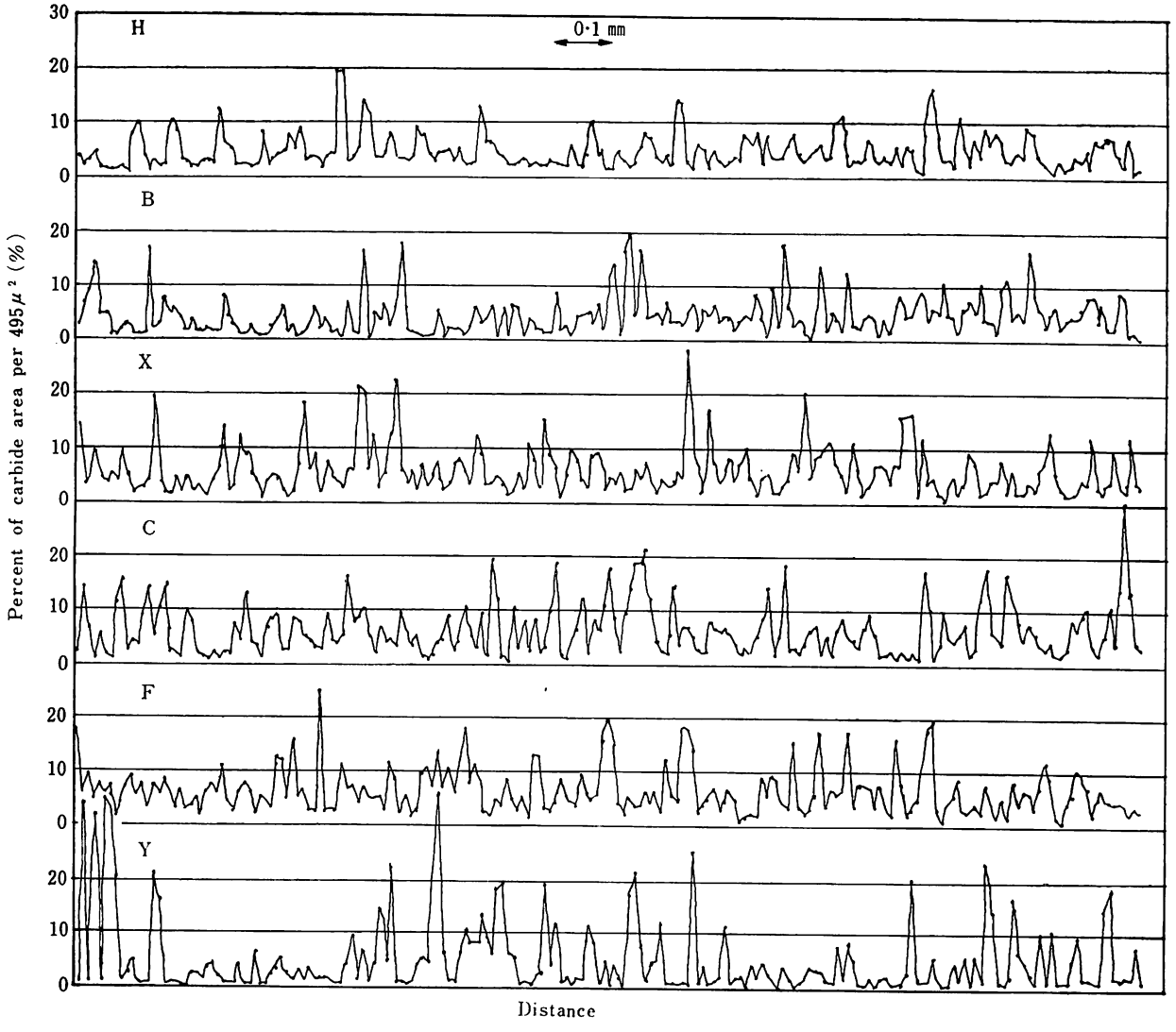

Fig. 5. Change of carbide area existing in the continuous fields.

Table 4. Amount and size of carbides in the hardened samples.

Sample	Average carbide area (%)	Number of carbide per 0·1mm²	Carbide size	
			Median size (μ)	Average area of carbides (μ^2)
H	11·5	8 200	1·02	1·4
B	13·1	10 000	1·00	1·3
X	9·1	5 980	0·90	1·5
C	10·3	15 800	0·70	0·65
F	10·8	19 500	0·40	0·56
Y	11·3	11 300	0·65	1·00

Table 5. Amount and size of carbides in the carbide segregated parts*.

Sample	Average carbide area (%)	Number of carbides per 0·1mm²	Carbide size	
			Median size (μ)	Average area of carbides (μ^2)
H	32·4	9 800	1·85	3·31
B	37·8	12 400	1·75	3·05
X	38·6	12 000	2·00	3·20
C	32·6	16 400	1·55	1·99
F	35·9	13 000	1·50	2·76
Y	36·9	15 200	1·45	2·40

* On carbides with length more than 0·5 μ.

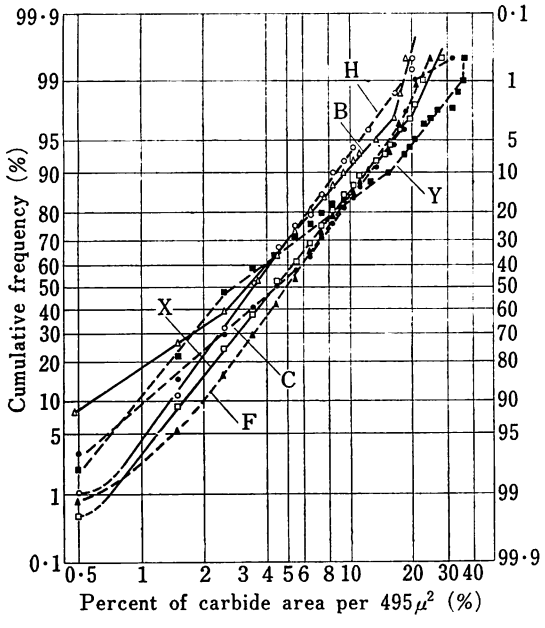

Fig. 6. Cumulative frequency of carbide area in each field with 495 μ^2.

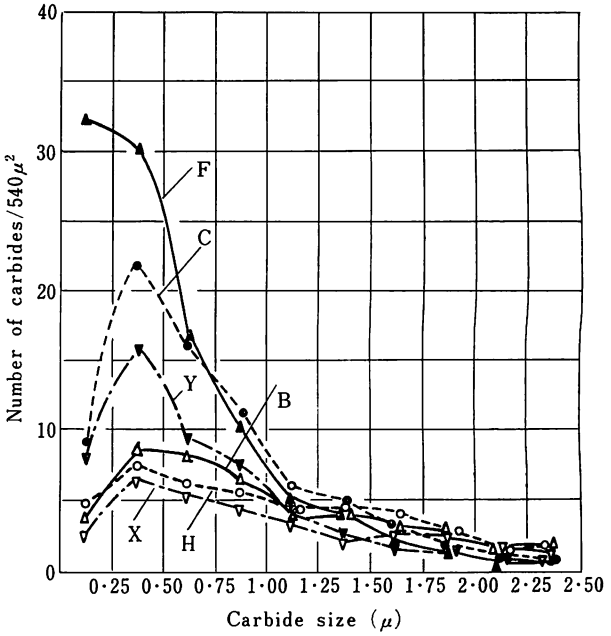

Fig. 7. Carbide size distribution of the carbides less than 2·50 μ.

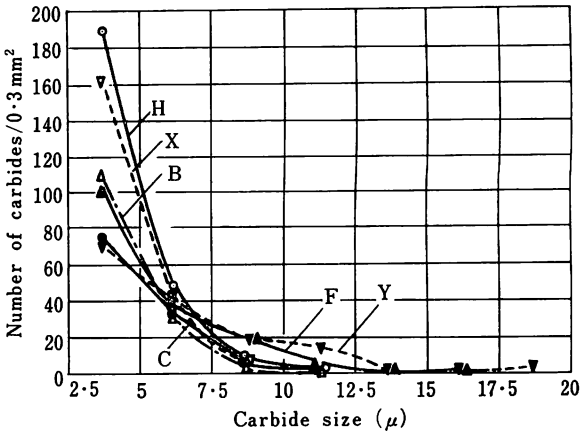

Fig. 8. Number of carbides over 2·5 μ in length and 1 μ in width, per 0·3 mm².

ような大きな偏析部で，しかも，計数が困難な複雑な形状の炭化物が少なく，また，視野一杯に拡がるような6μ 以上の炭化物が存在しない視野を選択した．
結果を Table 5 および Fig. 9 に示す．

試料 Y, F, C の炭化物が微細であり，H と C の偏析度が低いことが明瞭に示されている．また，試料 Y は4μ 以上の炭化物が急激に増加する傾向が認められ，Fig. 8 の結果とよく一致している．

3.2.4 炭化物の形状

炭化物の形状はそれが角ばっている場合，切欠効果によって靱性を害することが考えられる．その意味で球形であることが望ましい．既に示したように鍛造によって鋳造時に存在する羽毛状あるいはスケレトン状の共晶炭化物は次第に破壊され，同時に熱履歴も加わって球状化して行くが，かなり細丸に圧延されても異形の共晶炭化物が残存する場合がある．また，圧延時に融合粗大化し

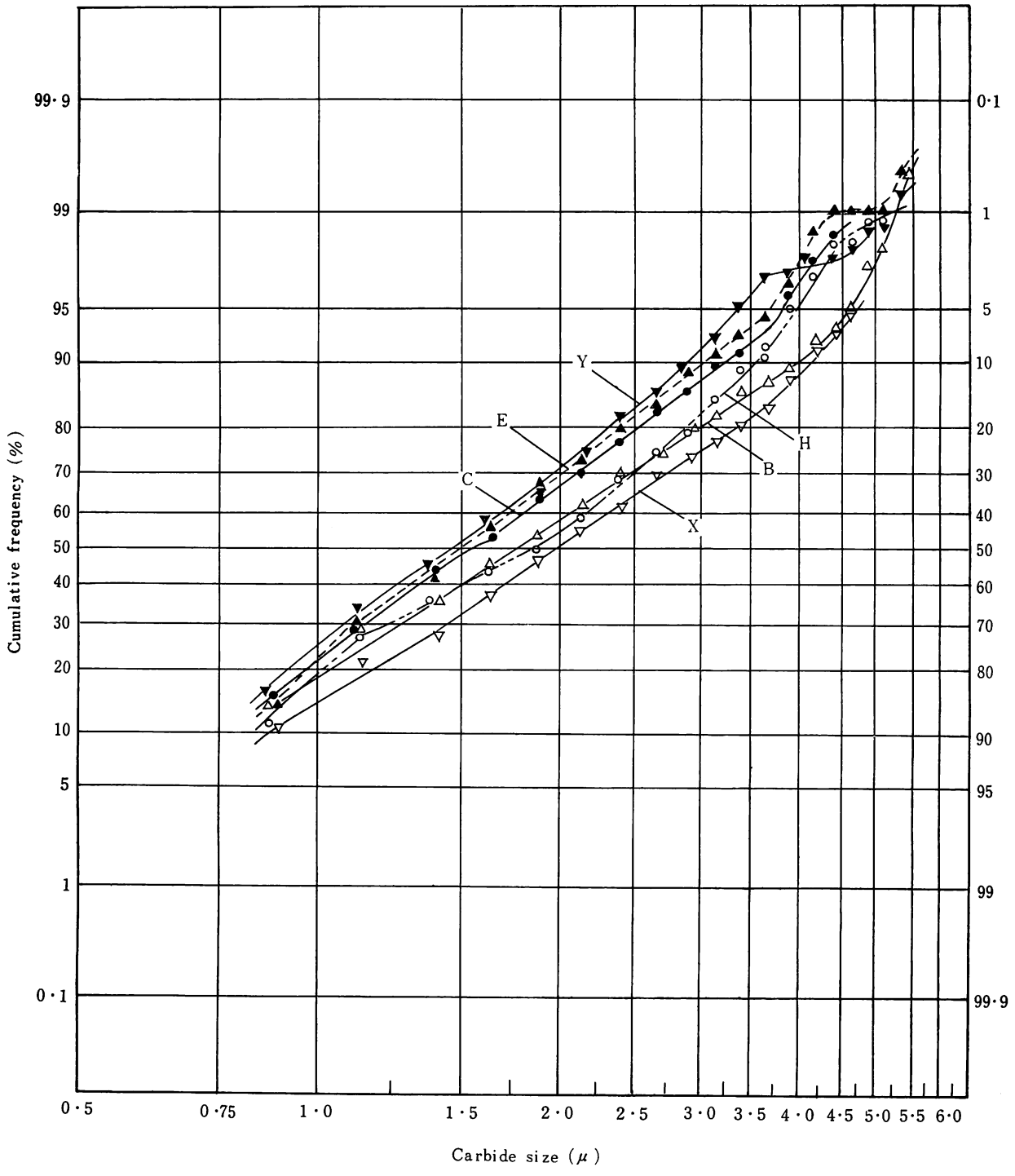

Fig. 9. Carbide size distribution at the carbide-segregated parts of carbides with length more than 0·5 μ.

た共晶炭化物は形状が大きく，5μ 以上の炭化物は概ねこの種の炭化物で形状も異形のものが多い．

試料Hの炭化物はもっとも球状に近く，Bがそれに次ぐ．Xには比較的異形のものが多い．試料 Y, F, C とも異形の粗大炭化物が存在し，その量はYがもっとも弱く，Fがそれにつぐ．

このような異形で粗大な共晶炭化物は，結晶学的に種々の欠陥を含んだものと考えられる．

3.2.5 各試料の炭化物状態のまとめ

以上炭化物組織の調査結果を要約して Table 6 に示す．

Table 6. General assessment of the carbide state in samples.

Sample	Degree of carbide segregation (1)	Carbide size in average field		Carbide in segregated part		Carbide shape
		Average size (2)	Number of carbides over 5μ (3)	Amount (4)	Size (5)	
H	good	large	medium	less	large	good
B	good	large	less	medium	large	fairly good
X	under medium	large	less	medium	large	medium
C	medium	fine	least	less	small	medium
F	medium	fine	more	medium	medium	under medium
Y	bad	fairly fine	most	medium	medium to large	bad

(1) Refer to Fig. 5 and 6.
(2) Refer to Fig. 7 and Table 4.
(3) Refer to Fig. 8.
(4) Refer to Table 5.
(5) Refer to Table 5 and Fig. 9.

3.3 熱処理性質

18φ×10 mm の試験片により焼入焼もどし硬さ，オーステナイト結晶粒度，残留オーステナイト量を比較した．

Fig. 10 は 850°C 予熱，1220°C の塩浴に 2 分浸漬後油冷，500～600 に各 1 時間，繰返し焼もどしした場合の硬さを示したものである．F, C, Y のごとく，炭化物微細な材料ほど最高二次硬さ，焼もどし抵抗は大きい．しかし焼入温度 1240°C 以上では試料間の差は減少する．

Table 7. Austenitic grain size and amount of residual austenite after quenching from 1220°C.

Sample	Austenitic grain size*	Amount of residual austenite (%)
H	12·6	19
B	13·2	20
X	11·0	21
C	17·7	22
F	14·8	20
Y	15·9	20

* Intercept method (Snyder-Graff)

1220°C で焼入した状態におけるオーステナイト結晶粒度および残留オーステナイト量を Table 7 に示す．オーステナイト結晶粒度は試料 C, Y, F が微細であり，一次炭化物粒度が平均的に大きい試料 H, B および X は粗大である．残留オーステナイト量は X 線回折法（Mo ターゲット，Zr フィルター）により，γ(220)，α(211)

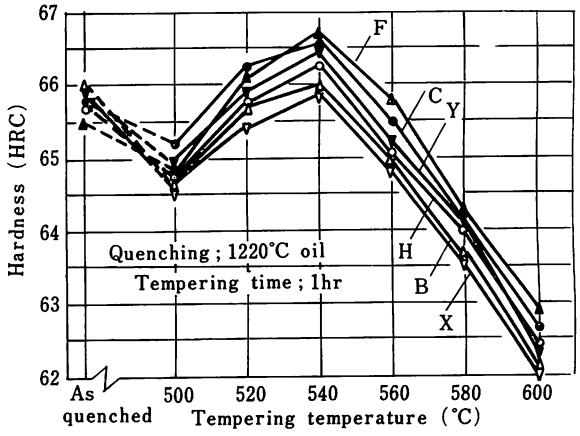

Fig. 10. Relation between tempering temperature and hardness.

Table 8. Heat treatment and testing machines for mechanical tests.

Kind of test	Heat treatment (°C)		Number of specimens	Testing machine	Notes
	Quenching	Tempering			
Static bend test	1200, 1220 1240×1min oil	540, 560, 580 ×(1+1)hr	5	10ton Amsler, universal	One point loading at center
Charpy impact test	1220×2min oil	560×(1+1)hr	5	15kgm Charpy testing machine	Notch : 10mmR Temperature: RT～600°C
Static torsion test	1220 oil	560×(1+1)hr	5	Shimazu torsion tester RET−50 type	Strain measurement by strain gage
Fatigue test	1220 oil	560×(1+1)hr	about 10	Ono-type rotating beam fatigue	
Tensile test	1220 oil	560×(1+1)hr	3	30ton Amsler, universal	Strain measurement by strain gage
Tensile test	as annealed		2	30ton Amsler, universal	Strain measurement by strain gage

回折線強度より求めたが，19～28% で試料間に有意差はないと考えられる．なお，560°C×(1+1)hr 焼もどした状態では γ 相の明瞭なピークは認められなかった．

3.4 機械的性質

既述のような炭化物状態の異なる試料を用いて，種々の機械的性質に及ぼす一次炭化物の影響を調査した．各試料に施した熱処理条件と試験機等を Table 8 に示す．

なお，試験片はいずれも圧延方向に平行な方向より採取した．採取位置は素材径が小さいため断面位置によらず無作為とした．

3.4.1 静的曲げ試験

5φ×70 mm の試験片を用い，支点間距離 50 mm，中央一点負荷による静的曲げ試験を行なった．

試験結果を Fig. 11 に示す．一般は焼入温度が低く，焼もどし温度の高いほど曲げ試験における破断までの吸収エネルギーは大きくなるが，硬さは低下する．一定の硬さに対し，最大吸収エネルギーを与える熱処理条件は，種々の熱処理条件において硬さに対する吸収エネルギーの関係をプロットすれば得られ，これにより材料間の靱性を比較することが可能である[11]．Fig. 12 はその意味で各試料の硬さに対する最大吸収エネルギーの関係を示したものである．

この結果より C, F, H が靱性にすぐれ，X, Y が劣ることがわかる．すなわち，炭化物集合度の密なものが靱性を劣化する傾向がある．そして，この差に対し，HRC

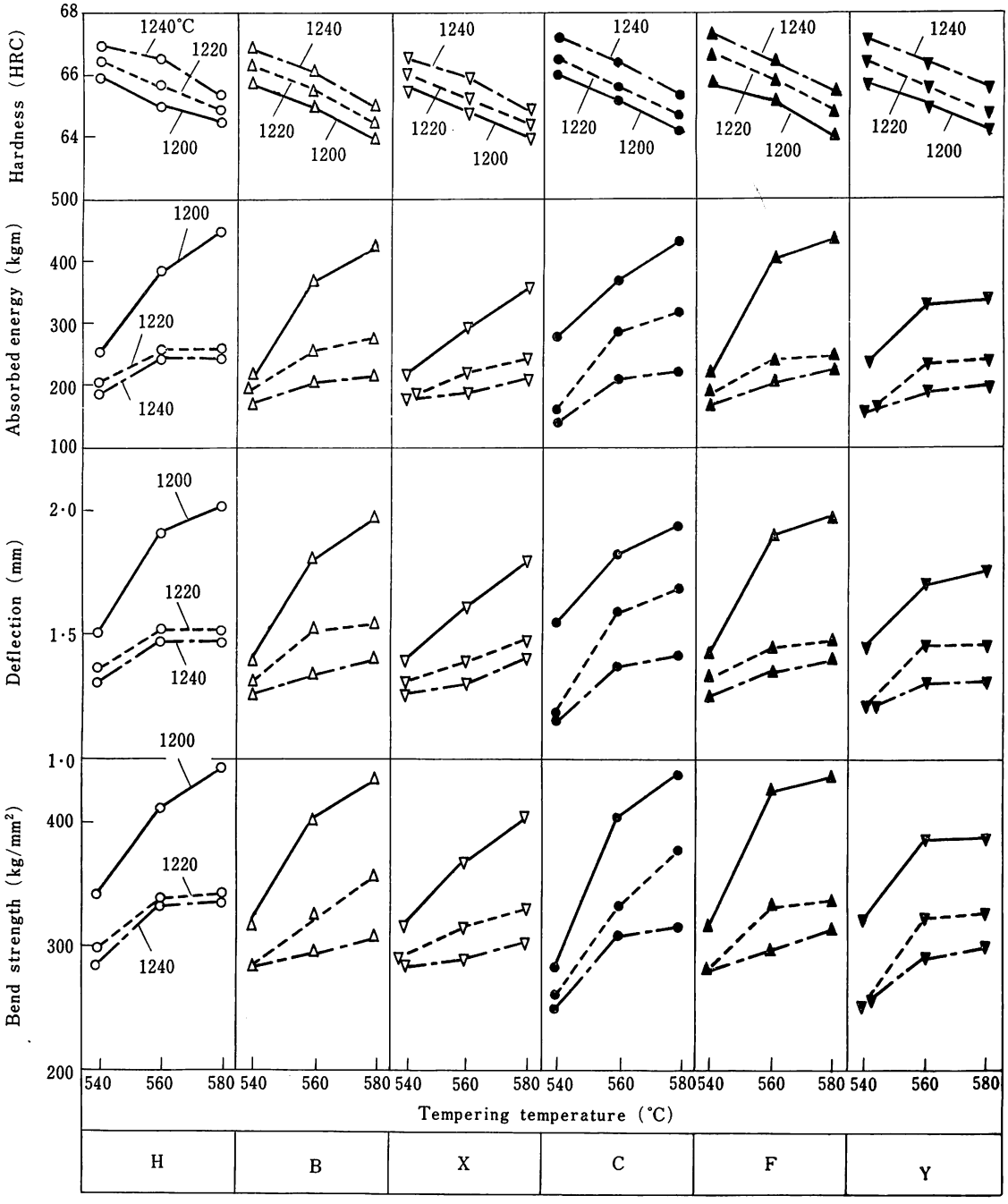

Fig. 11. Results of static bend tests. Specimen size: 5 mm dia ×70 mm, strain rate 0·36 mm/min in deflection. Heat treatment: 1200～1240°C×1 min oil; 540～580°C×(1+1)hr. Values represent average of five pieces.

64～65 の硬さ，換言すれば，1200°C 焼入，560～580°C 焼もどし条件における吸収エネルギーが支配的な影響を与えている．

3.4.2 シャルピー衝撃試験

高硬度材の衝撃値は極めて小さいため，切欠なし，あるいは 10～12·5 mm R の C ノッチの衝撃試験がよく行なわれている[12,13]．こゝでは，10 mm R ノッチを採用した．高速度工具鋼の高温衝撃値は殆んど公表されていないが，実際切削時には刃先の昇温はいちじるしい．高合金鋼では青熱脆性温度が上昇し，500～600°C 付近に現われる場合もあるので，実用的見地から室温～600°C での試験を行なった．室温を越える温度での保持時間は 10 分とした．結果を Fig. 13 に示す．試験温度 150°C～300°C 間で衝撃値は増大し，300°C 以上では，F および Y を除き変化が少ない．試験温度 550°C 以上では試料間の差は少なく，したがって，300～500°C 間で試料間の差は大きい．青熱脆性はほとんど現われていないが，500～600°C 間で Y を除き若干の低下が認められる．

試料 H, C, B が良い結果を示し，Y, X が劣る結果を示している．この結果は静的曲げ試験の場合と類似はしているが，Y の低下が大きい点，F が悪いグループに入る点で若干趣を異にしている．すなわち，静的曲げ試験が比較的オーステナイト粒度に依存する傾向が強く，それに炭化物集合度の影響が加味されているのに対し，衝撃試験では炭化物集合度の影響が遙かに大きく現われているように思われる．

こゝで注目されることは，室温シャルピー値が試料間で大差があることで，試料 C に対し，Y は 60% の値しかない．これは従来の試験結果よりみて，化学成分の変化（Co, V, C 量の変化による鋼種間の差）以上に炭化物状態が衝撃靱性に大きな影響を及ぼすものであることを示唆している．

3.4.3 静的捩り試験

島津製作所製 RET-50 形捩り試験機を用い，Fig. 14 に示す形状の試験片により，静的捩り試験を行なった．

本機は定速トルク負荷試験を行なうようになっているが，塑性変形域は負荷応力に対する歪の変化が激しいので手動により調整し，歪速度がほゞ一定となるようにした．すなわち

試験片外周部の負荷剪断応力約 150 kg/mm² まで
$0{\cdot}46\times10^{-3}$ (min^{-1})，150kg/mm² 以上は
$0{\cdot}70\times10^{-3}$ (min^{-1})

歪量の測定は，Fig. 15 に示す試験片の中央平行部にストレンゲージを軸方向と 45° の方向をなすようはりつけ測定した．なお試験片表面における剪断応力 τ_a は

$$\tau_a = 2M/\pi a^3 \cdots\cdots\cdots\cdots (1)$$

たゞし，a は円柱の半径，M は負荷ねじりモーメントで表わされる．

剪断応力 τ_a と試験片表面の剪断歪 ε_a の関係ならびに破断応力および破断歪を Table 9 に示す．なお，永久変形量 0·005% 以下の領域で，τ_a—ε_a の関係を 11 試料の平均より求め，$\tau_a = E/(1+\nu)\times\varepsilon_a$ より縦弾性係数 E を求めた結果，τ_a が 73 kg/mm² 以下の比例域において，$E = 2{\cdot}26\times10^4$ kg/mm² を得た．たゞし，ポアソン比 $\nu = 0{\cdot}28$，この E の値は振動法により測定した値 $2{\cdot}2350\times10^4$ kg/mm² と良い一致を示している．

Table 9 の結果によれば，破断時の最大剪断応力は約 240 kg/mm² で大差なく，試料 Y のみ低い値（216 kg/mm²）を示す．破断時の伸びも Y のみ極めて低く（0·32%）他は約 1% 程度である．耐力に関しては，永久変形 0·2% 以下で試料間で有意差は認められない．

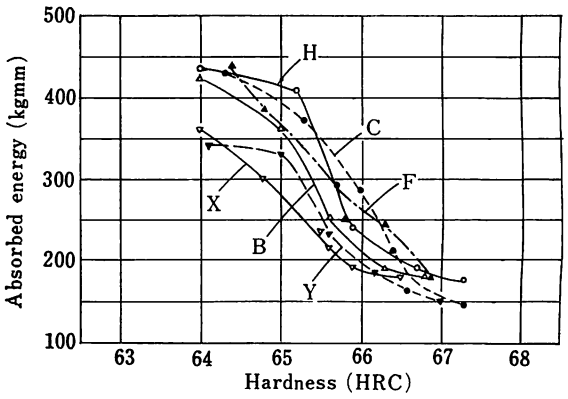

Fig. 12. Maximum absorbed energy of samples at each hardness level.

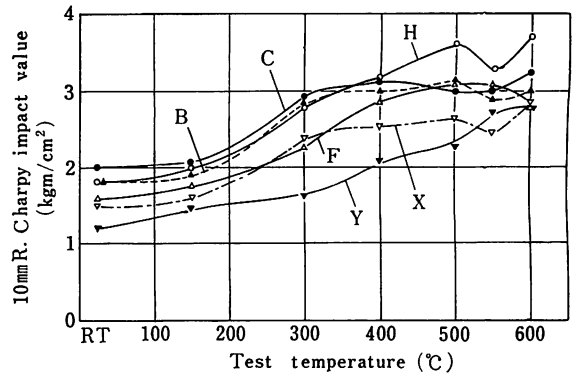

Fig. 13. Test temperature vs Charpy impact value. Values represent average of five pieces. Heat treatment: 1220°C×2 min oil ; 560°C×(1+1)hr. Hardness HRC 65～66.

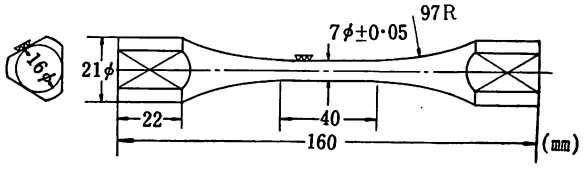

Fig. 14. Dimensions of torsion-test specimen.

3.4.4 回転曲げ疲労試験

Fig. 15 に示す試験片により小野式回転曲げ疲労試験を行なった．熱処理は 1220°C×2 分油冷，560°C×1 hr 2 回焼もどしである．試験結果を Fig. 16 に示す．

試料 C, H がすぐれ，B, Y, F が劣る結果を示している．試料間の差は短時間側で少なく，長時間側で開く傾向を示している．

3.4.5 引張試験

高速度工具鋼のような高硬度材は従来ほとんどデータが得られていなかった[14]．この理由は，引張試験を行なう際に，摑み部や R 部分で破断し満足すべき試験を行なうことができなかったためと考えられる．本報においては試験片の形状および引張速度の重要性を考慮し実験を行なった．

Table 9. Results of static torsion tests.

Sample	Shear stress corresponding to each plastic deformation (kg/mm²)									Rupture strength * (kg/mm²)	Strain * (%)
	Plastic deformation (%)										
	0·005	0·01	0·02	0·05	0·10	0·20	0·50	1·00	1·50		
H	134	143	153	171	187	205	227	242	—	242	1·290
B	125	135	147	167	182	200	223	236	239	237	1·101
X	126	134	146	165	182	199	219	233	—	237	1·288
C	133	141	152	170	186	204	228	240	—	239	0·975
F	127	134	148	169	186	205	229	242	249	235	0·927
Y	132	140	151	170	187	204	—	—	—	216	0·324

* Average of 5 pieces.

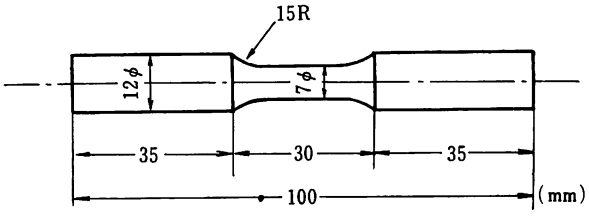

◀Fig. 15. Dimensions of fatigue-test specimen.

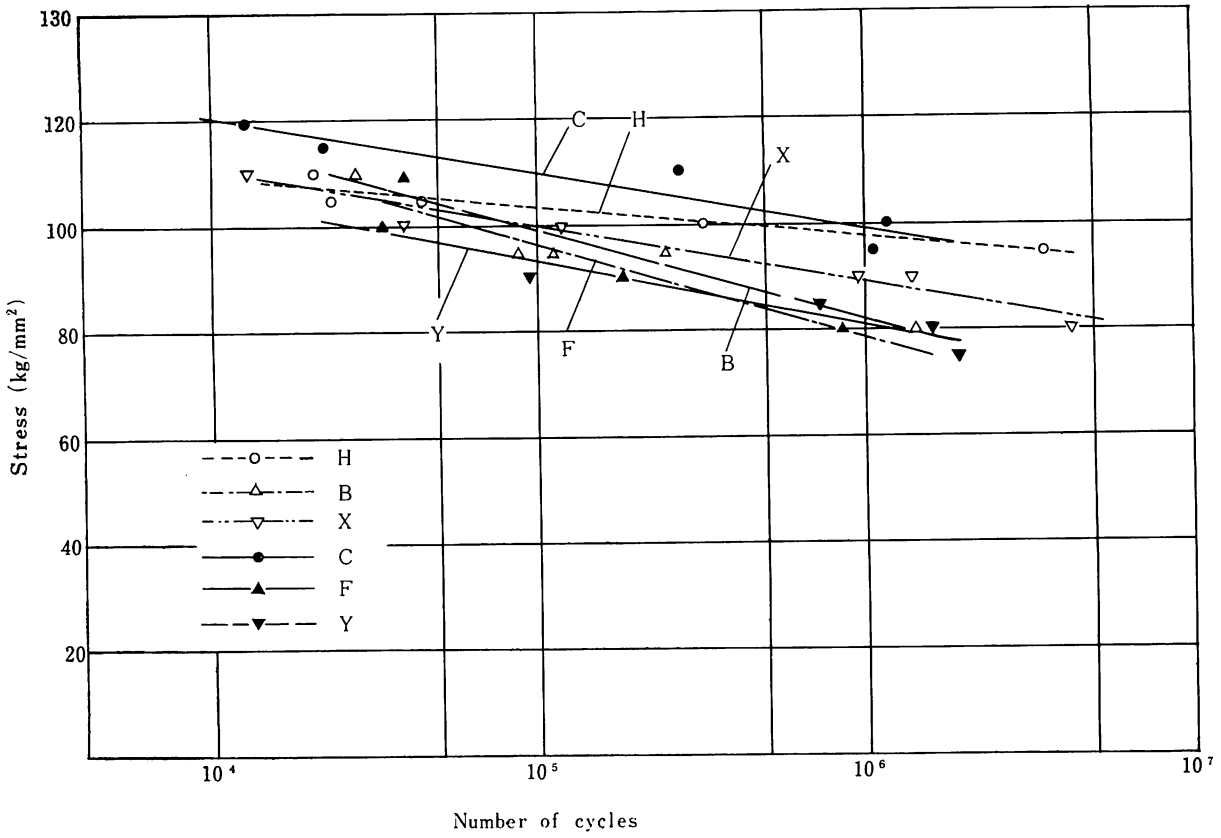

Fig. 16. Results of rotating-beam fatigue tests.

試験片の形状は Fig. 17 に示すように，極端に切欠効果を少なくするよう考慮した．この試験片の特徴は

(i) 平行部は 30 mm 存在し，約 4D に近い．
(ii) R 部の曲率半径を十分大きくとった．(200 mm)
(iii) 両端を除き，曲線と直線の接続は連続である．

次に，微少の歪まで測定するために，電気低抗歪ゲージを試験片の平行部に 2 枚貼りつけた．歪計は静歪計を使用した．引張試験機は 30 ton アムスラー型万能試験機を使用したが，一定の歪速度を得ることが難かしく，やゝ速く引張った試験片は平行部外で破断し，破断時の荷重も低く測定された．

そのため，平行部で破断させるために荷重伸び曲線が

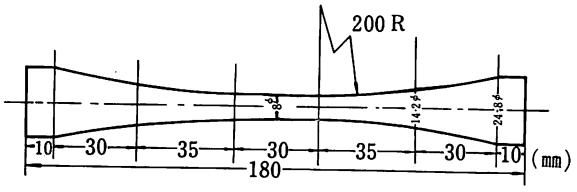

Fig. 17. Dimensions of tensile-test specimen.

比較的急な部分では 0·01～0·015%/min (200～300 kg/min.) の速度で引張り，焼なまし材のごとく歪が大きく現われるものは歪が大きくなるにつれて歪速度をやゝ増した．たゞし，負荷重速度はやゝ遅くなっている．

以上のような試験法により荷重—歪曲線を作成し，引張り強さ，各耐力，伸び絞り値を求めた．焼入焼もどし材（1220°C 油冷，560°C×1hr 2回焼もどし）および焼なまし材に関する試験結果を Table 10 および Table 11 に示す．なお，焼なまし材の場合は硬さを揃えるために，いずれも 950°C×30 分空冷後，750°C×3～5hr の低温焼なましを行ない，硬さを HRB 93～94 に揃えた．

Table 10 において，伸び≒絞りとしている．焼入焼もどし材のごとく，局部絞りがなく，微小の絞りの場合は，塑性変形の際，体積一定とすると，$A_0 L_0 = A_f L_f$，たゞし A_0, L_0 は最初の断面積および長さ，A_f, L_f は破断後の断面積および長さ，絞り ψ は

$$\psi = (A_0 - A_f)/A_0 = \{A_0 - A_0(L_0/L_f)\}/A_0$$
$$= 1 - L_0/L_f \fallingdotseq (L_f - L_0)/L_0 = \varepsilon \quad (\text{伸び})$$

のごとく，ほゞ ε に等しい．

Table 10 の結果によれば，試料 H は引張強さ，伸びともももっともすぐれ，Y および X が低い値を示している．耐力についても，Y がもっとも低く，X がそれにつゞく．

Table 11 の焼なまし材の場合は，H, C, F が引張強さ，伸び，絞りともすぐれている．耐力は試料間で大差はないが焼入焼もどし材の場合と同様，試料 X. Y がわずかに低い傾向がある．

3.5 破面の観察

3.5.1 破面のマクロ的観察

シャルピー衝撃試験片のマクロ的破面の状況は，衝撃値の絶対値の差があるにもかゝわらず，試料間で有意差を認め得なかった．

いずれも，切欠底部の中央にクラックの起点が存在し，直ちに四方へ放射状に拡がる fibrous-radial 破面があり[15]，引きつゞき光沢を有する滑かな曲率の cleavage 破面につながっている．この部分にはクラックの進行に沿う radial ridge が局部的に認められ，低温で試験されたものほど，この Ridge が多い．Cleavage 破面の部分は多くの曲面が重なった複雑な形をしており，低温試験材ほどその傾向が強い．

試験温度が上昇するにつれて，次第に cleavage 破面の面積は減少し，fibrous-radial 破面の割合が増大する．しかし，衝撃値の低い Y がとくに cleavage 破面が多いとか，radial ridge が少ないというような現象は認められなかった．fibrous な破面を部分的にせよ有することは，多数のミクロ的なクラック起点が存在し，クラック伝播の際に多少の塑性変形を伴うことを暗示している．また，cleavage 破面の複雑な形状は割れ伝播速度が局部的に異なり，独立して個々の破面が成長し，あるいは一時的に停留するというような複雑な割れ伝播を行なっているためと考えられる．代表的な破面の状況を Photo. 7 に示す．

Table 10. Results of tensile tests on hardened specimens*.

Sample	Tensile strength (kg/mm²)	Yield strength (kg/mm²)				Elongation ≒Reduction of area (%)	Hardness (HRC)
		0·002%	0·005%	0·01%	0·02%		
H	247·6	135·1	147·9	165·3	185·8	0·091	66·4
B	231·7	134·8	146·4	161·0	184·6	0·069	65·5
X	212·8	128·0	144·0	159·4	175·9	0·052	65·6
C	232·0	140·9	148·6	161·4	185·1	0·060	66·2
F	222·0	134·9	143·8	161·5	183·1	0·055	66·1
Y	191·8	126·7	137·0	154·4	175·7	0·029	65·9

* Average of 3 pieces

Table 11. Results of tensile tests on annealed specimens*.

Sample	Hardness (HRB)	Yield strength (kg/mm²)						Tensile strength (kg/mm²)	True fracture stress (kg/mm²)	Elongation (%) GL=25mm	Reduction of area (%)
		0·02%	0·05%	0·1%	0·2%	0·5%	1%				
H	93·3	22·3	24·5	27·5	31·8	40·7	49·9	76·8	113·0	25·3	40·6
B	93·8	22·4	24·6	27·2	31·4	39·9	48·8	73·9	100·7	21·0	34·3
X	93·2	22·1	24·2	26·7	31·0	39·1	47·7	72·2	99·5	20·7	32·6
C	93·5	22·0	24·0	27·0	31·4	40·4	50·4	75·7	112·9	24·0	39·7
F	93·1	22·1	24·5	27·3	31·8	40·9	50·3	75·8	110·6	25·1	40·0
Y	94·0	21·8	23·8	26·5	30·8	39·6	49·0	73·3	101·7	20·4	35·5

* Average of 2 pieces.

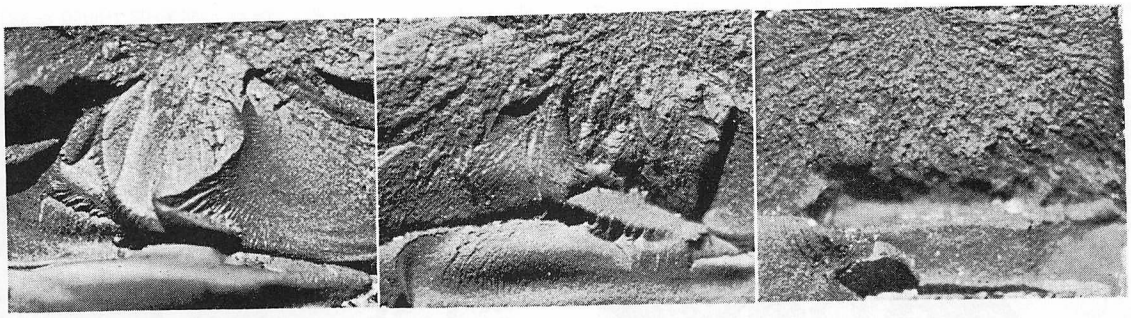

at room temperature　　at 300°C　　at 600°C

Photo. 7. Fracture surface of Charpy specimens (sample X).

捩り試験の場合の破断状況を Photo. 8 に示す．破片が多数できるのは，剪断破壊と引張破壊が組合わさって破壊したためで，つかみ側が約 45° の面を向いているのは引張りによる劈開破壊が主体であるためと考えられる[16]．

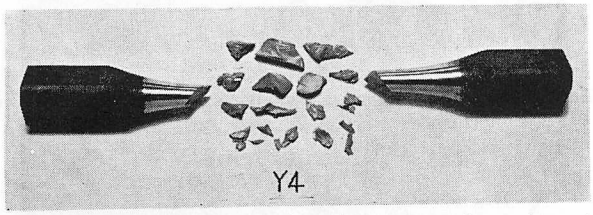

Photo. 8. Ruptured state of torsion-test specimens (sample Y).

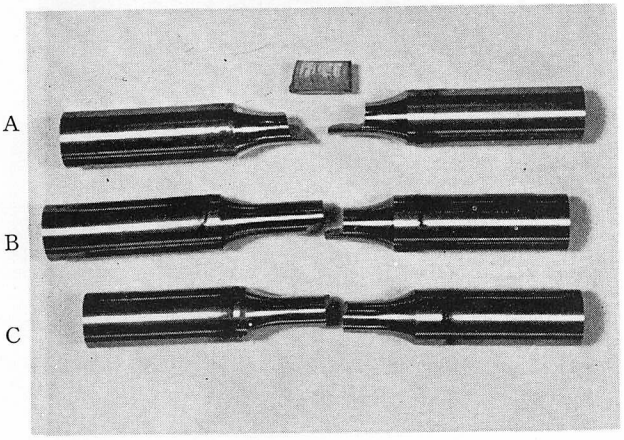

Photo 9. Ruptured state of fatigue-test specimens.

破面は多少の tear ridge を含む平滑な cleavage 破面を示す．

疲労試験片の破面は Photo. 9 のごとき形状を示し，まず軸に対し垂直にクラックが進行し，直径の約 2/3 進行してから恐らく破断時に軸に平行に進行方向をかえ，最後に軸に垂直に破断する．Photo. 9 の (A), (B) がその例で，応力の高い場合の破壊に多い．(C) は疲労限に近い場合に多い破壊様式で，この場合はほゞ軸に垂直な面で破壊が進行している．

疲労クラックの起点はすべて一個所より起こり，外周部にある．疲労破面は平滑で，疲労特有の Beachimarking

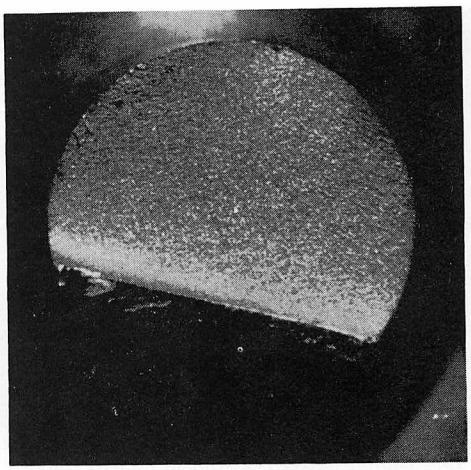

Photo. 10. Fracture surface of a fatigue-test specimen. (Sample B: 95 kg/mm², N=86 800.)

Photo. 11. Fracture surface of tensile-test specimen.

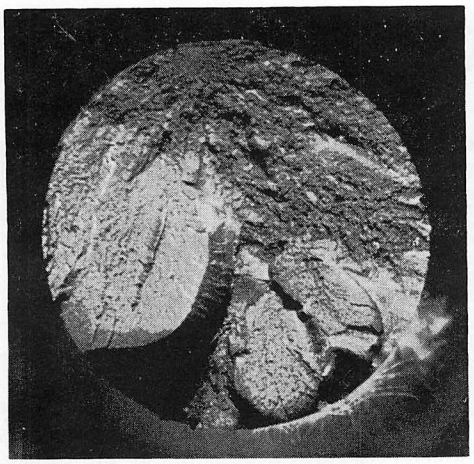

Hardened specimen (Sample Y)

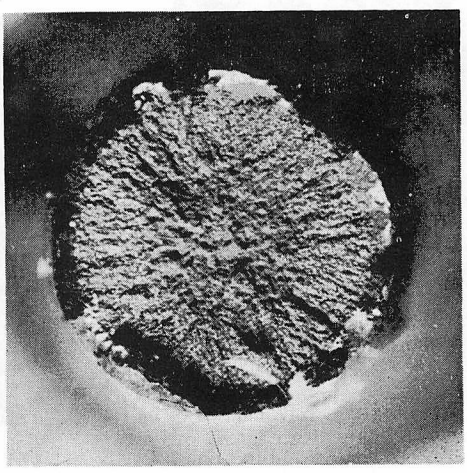

Annealed specimen (Sample H)

は認められない．Photo. 10 は疲労破面の一例で，このように起点部に欠陥らしいものが存在する場合がある．試料間で破面のマクロ的な差は認められない．

引張試験片の破面の例を Photo. 11 に示す．焼入焼もどし材では破壊の起点は外周部に近く，radial 破面に続いて，大部分の面積 (80～90%) を占める cleavage 破面に連なる．焼なまし材の場合は破壊の起点はほゞ中央にあり，fibrous-radial 破面が大部分で，円周部に若干 shear lip がみられる．なお，試料間で明瞭な破面の相違は認められない．

×3000×4/5

Photo. 12. Typical quasi-cleavage fracture. (Sample C, Charpy fracture at room temperature.)

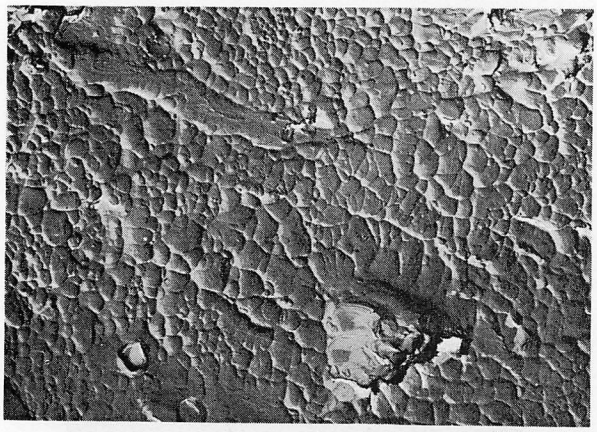

×3000×4/5

Photo. 13. Dimple pattern existing at Charpy fracture surface of sample H fractured at room temperature.

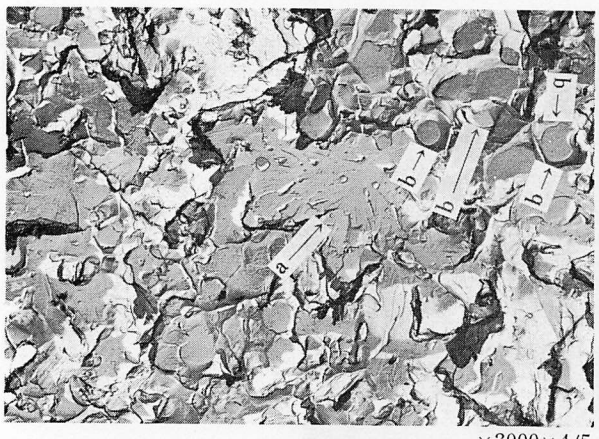

×3000×4/5

Photo. 14. Dimple-like fracture associated with larger carbides and local fracture origin. (Sample X, tensile fracture of a hardened specimen.)

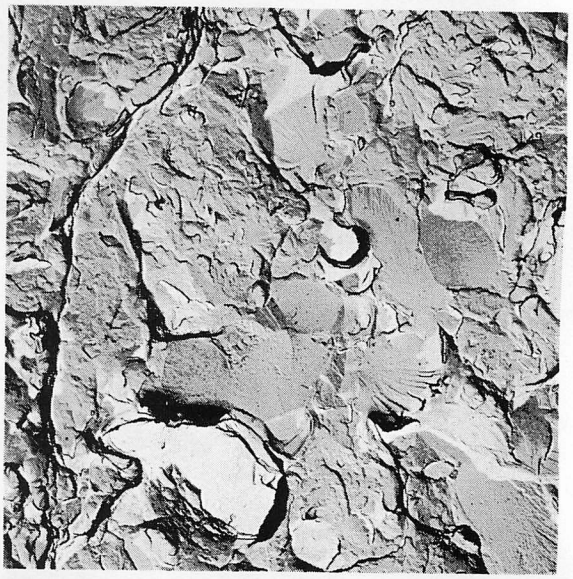

×8000

Photo. 15. An example of carbide-cleavage on the fracture surface.

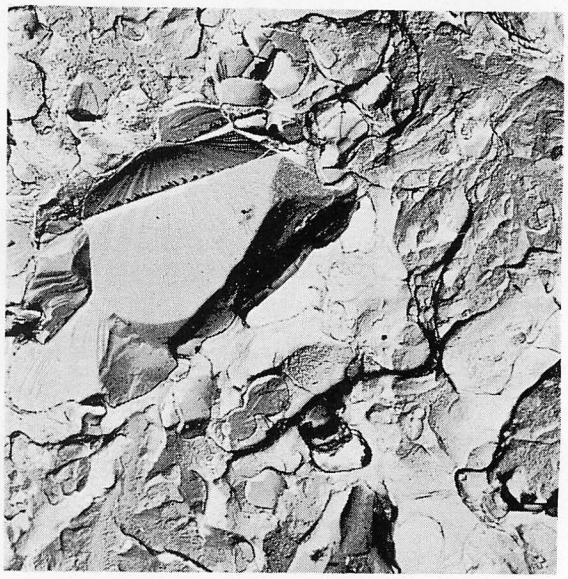

×8000

Photo. 16. Etched structure on the fracture surface.

×3000×4/5

Photo. 17. Carbides separated from matrix at the carbide-matrix interface. (Sample F, static bend fracture.)

3.5.2 破面のミクロ的観察

二段レプリカ法による破面の電子顕微鏡観察，および走査型電子顕微鏡による破面の直接観察を行なった．

a. Microfractography

破面を酢酸セルロースフィルムに転写し，これに Cr を斜めより真空蒸着，つぎに黒鉛を真空蒸着後，酢酸セルロースを酢酸メチルで溶かし，電子顕微鏡観察用試料とした．試料採取位置はクラック発生起点付近である．

破面は静的曲げ試験，疲労試験，捩り試験，シャルピー衝撃試験，引張試験とも，大部分粒内を通る擬劈開 (quasi-cleavage) 破面[17] のような様相で，いずれも非常によく類似している．代表的な破面を Photo. 12 に示す．

しかし，引張試験，シャルピー衝撃試験の破面には一部 dimple pattern が認められ，その他の試験片では認められなかった．この dimple pattern 部には 1μ 以上の大きな炭化物は存在せず，あっても 0·1～0·2μ の極めて微細な炭化物である (Photo. 13)．この部分は，マクロ破面の radial marking に相当する所であり，炭化物偏析部ではなく，縞状の中間の炭化物分布の少ない所に相当すると考えられる．

Photo. 14 の矢印 b で示す部分は一種の dimple でその起点にある炭化物は 1～2μ のやゝ大きなものである．炭化物の面が平滑であることから，この炭化物は劈開割れを起こしていると考えられる．

また，矢印 a の先端の炭化物割れが，その下に拡がる局部的脆性破面の起点になっている様子がわかる．

Photo. 15 に破面に存在する炭化物の劈開割れと思われる他の例を示す．これが真に炭化物であるか，あるいはマトリックスの一部の割れの状態かを確認するために，Nital で腐食し，破面の再観察をした．その場合の破面の状況を Photo. 16 に示す．これから，明らかに Photo. 15 に示す組織は炭化物の破面であることがわかる．しかし，このような炭化物の劈開破壊面は破面のすべてに現われているのでなく，試料 F, Y, X に多く，試料 H, B, C に少ない．また，引張試験片，シャルピー試験片よりも捩り，疲れ試験片の破面に観察され，とくに疲れ試験片ではほとんどの視野 (40×60μ^2) に 1 ケ以上の炭化物割れ面が観察された．

Photo. 17 の矢印 c で示すように，炭化物とマトリックスの界面で剝離しているものも多い．Photo. 18 は粒界に存在する炭化物の剝離部分が割れ起点となっている例を示す．多くの観察結果によれば，炭化物を起点とする局部的な割れが多数存在し，割れの径路も複雑である．また，結晶粒界は cleavage step を形成している場合が多い．このように，炭化物と結晶粒界が割れ伝播に対し大きな影響をもち，複雑な破面を形成しているものと考えられる．

b. 走査電顕による観察

日立走査電子顕微鏡 (HSM-2 形) を用いて，破壊の起点を中心に，破面の観察を行なった．

Photo. 19 に引張試験片の破面を示すが，丁度起点に相当する部分は，破断時に摩擦による引掻摩耗を起こしており，とくに欠陥部を見出すことはできなかった．しかし，ミクロフラクトグラフィで見たように，破面の起伏の中心に炭化物またはその抜け孔が観察された．Photo. 20 は焼なまし材の引張破面で完全な dimple 破面である．こゝでは明らかに破面に剝離した炭化物，および亀裂を起こした炭化物が認められ，また粗大炭化物の抜け跡らしいものも認められる．Photo. 21 は疲労破面の状況を示すが，疲労破面特有の striation はみることができず，シャルピー，捩りなどの破面と同様に起伏の多い破面を形成している．Microfractography で観察された quasi-cleavage 破面がこれに相当する．Photo. 21 の矢印 a で示すような粗大炭化物が破面に突出し，炭化物とマトリックスの界面で剝離したような様相を呈している例もある．破面に現われた粗大炭化物の周囲は，Photo. 19 あるいは Photo. 20 にみられたような，微細な

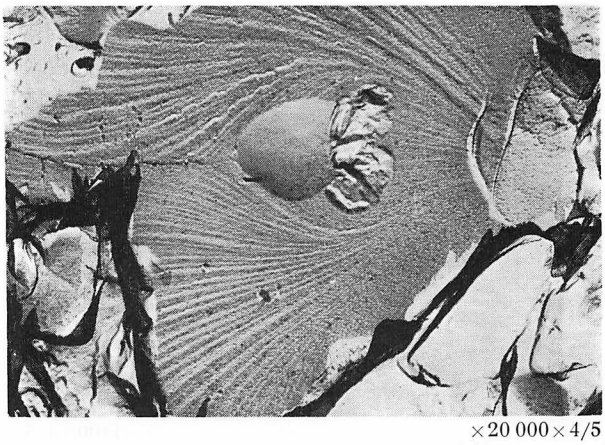

×20 000×4/5

Photo. 18. Microcrack originated at a carbide separated from the matrix.

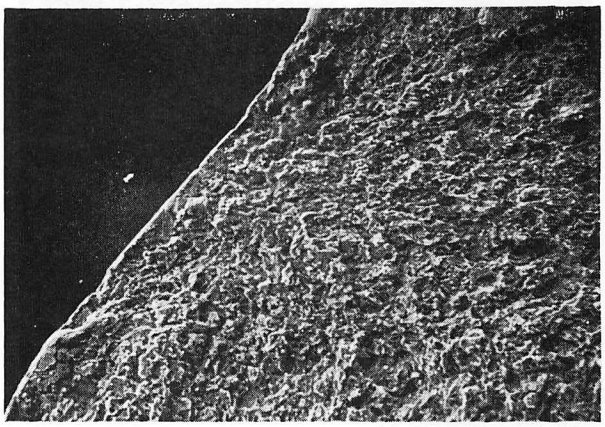

×370×4/5

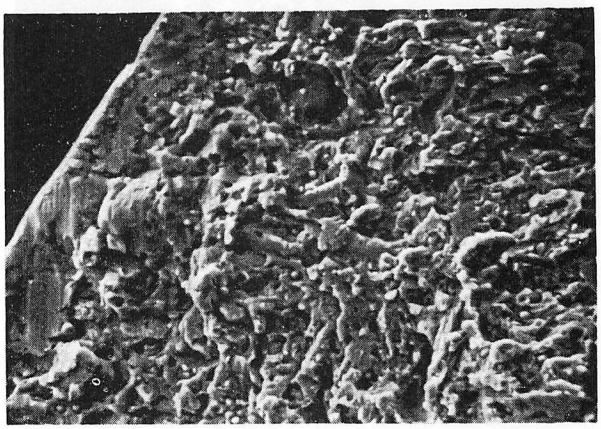

×1100×4/5

Photo. 19. Fracture surface of a tensile specimen. (Sample X at the origin of crack.)

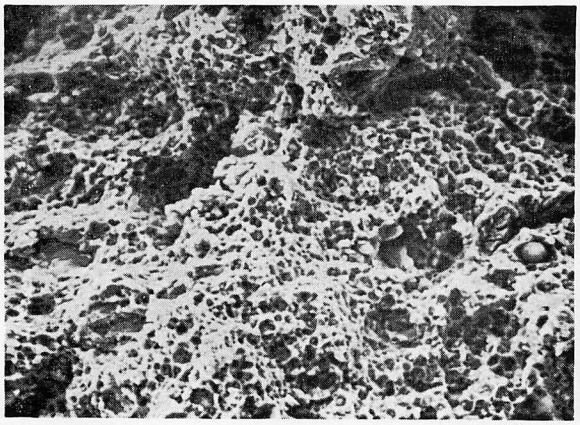

×1100×4/5

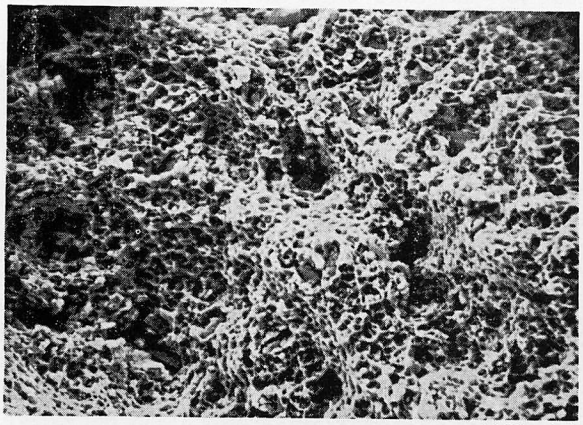

×1100×4/5

Photo. 20. Fracture surface of an annealed tensile specimen (sample Y).

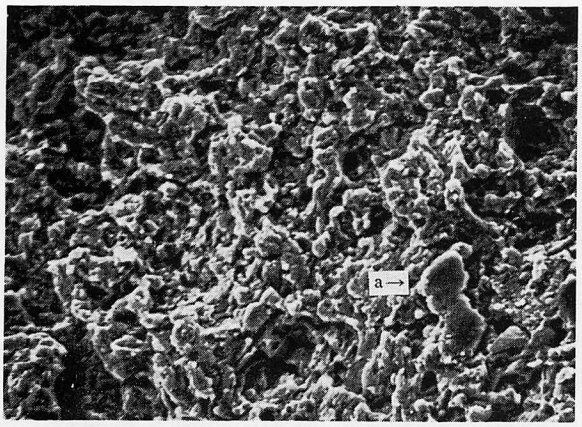

×1100×4/5

Photo. 21. Fracture surface of a fatigue specimen. (Sample Y: 90 kg/mm², N=95 000).

炭化物の周辺の局部的な盛り上りや凹みが少ないようである．これは，粗大炭化物とマトリックスの界面での剝離が塑性変形をほとんど伴わず劈開破壊的に進行したことを示すものであろう．Photo. 22 は疲労破面の起点で，明らかにある相の脱落が破壊起点となったことを示している．そのある相は，炭化物か結晶粒のいずれかであろうが，大きな形状より，結晶粒の粒界亀裂に起因する剝離と思われる．

Photo. 23 は試料 H の疲労破面の起点で a は恐らく炭化物の脱落によるものであろう．この横にみえる b は組織が粒界および粒内において崩壊しつゝある様相を呈し

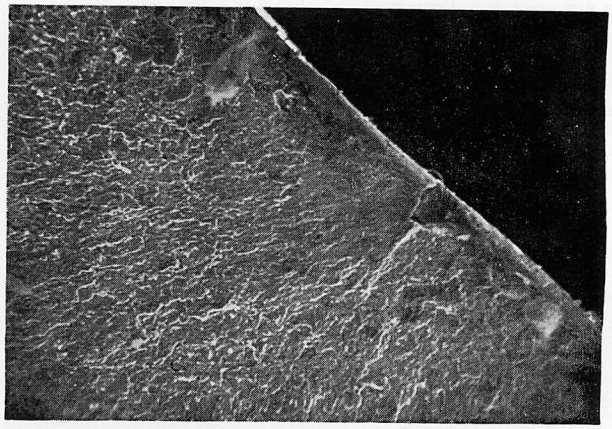

×370×4/5

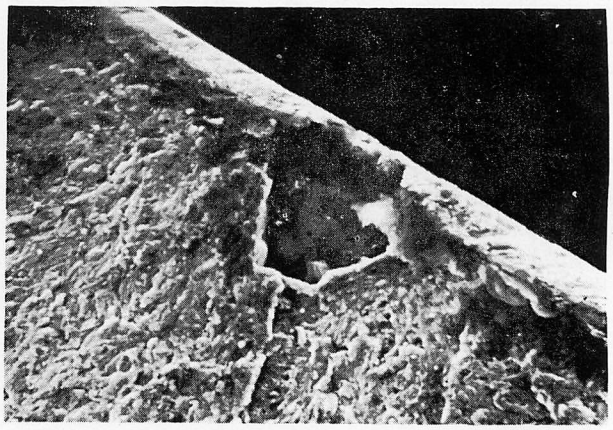

×1100×4/5

Photo. 22. Fracture surface of a fatigue specimen. (Sample Y: 100 kg/mm², at N=39 400, at the origin of crack.)

ているが．詳細は不明である．なお白く光っている c は起点の目印のためにつけた銀粉である．疲労破面の場合，起点近傍はミクロ的にも平滑な破面をしており，やゝ内部はミクロ的には他に比し平滑ではあるが，ミクロ的には他と同じ quasi-cleavage 破面となる．また，割れ起点部の最外層は，どの試験片でも塑性変形による組織の流れが認められる．

3.6 破壊靱性の測定

3.6.1 試験方法

Fig. 18 に試験片の形状を示す．焼なまし状態でこの形状に仕上げた後，日立実動荷重疲れ試験機 (HFT-10) でノッチ部に疲れクラックを入れた．つぎに予熱 900°C×5分，焼入 1220°C×1分35秒油冷，焼もどし 560°C×(1+1) h 空冷の熱処理を行ない，30 t アムスラー万能試験機で引張って破断荷重を求めた．疲れクラックを熱処理前に入れたのは，熱処理後では停留する疲れクラックを入れることができず，ノッチ部に疲れクラック発生後直ちに全破壊が生じたためである．Fig. 19 に破断後の試料の測定個所を示す．

Fig. 18 に示す試験片の破壊靱性値 K_{IC} は次式で求められる[18]．

$$K_{IC}^2=8\cdot43\left(\frac{P}{B}\right)^2\cdot\frac{1}{W}\cdot\left(\frac{a}{W}\right)\left[1-4\cdot22\left(\frac{a}{W}\right)+15\cdot4\left(\frac{a}{W}\right)^2\right] \quad \cdots\cdots (2)$$

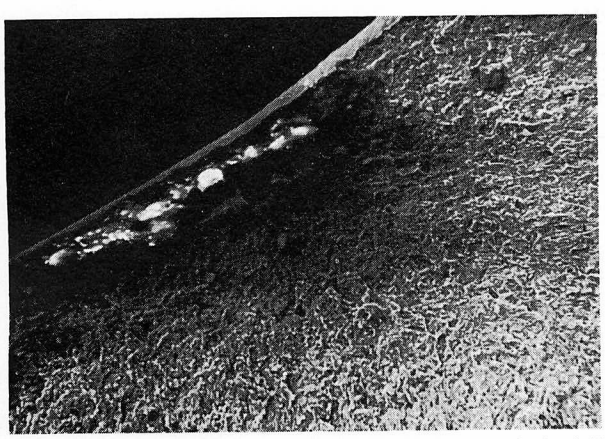

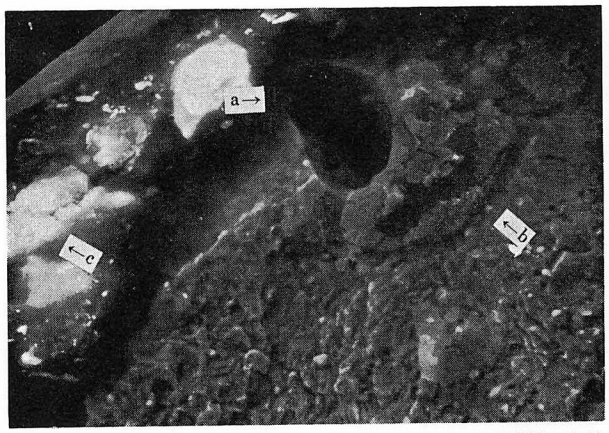

Photo. 23. Fracture surface of a fatigue specimen. (Sample H: 95 kg/mm², N=3 537 700, at the origin of crack

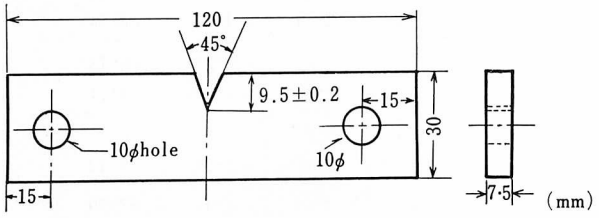

Fig. 18. Dimension of notch-toughness specimen.

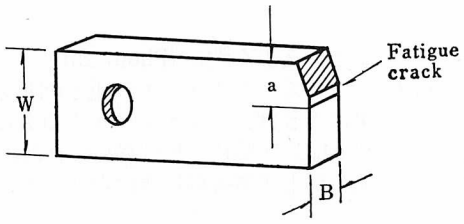

Fig. 19. Measuring position after fracture.

Table 12. Notch toughness of samples.

Sample	K_{IC} $\left(\frac{kg\sqrt{mm}}{mm^2}\right)$	Hardness (HRC)
H	62·9	63·8
B	61·7	63·6
X	59·8	64·2
F	48·3	64·9
Y	46·9	65·0

ただし，P：破断荷重 (kg)，B：厚さ (mm)，W；巾 (mm)，a：ノッチ深さ＋クラックの長さ (mm)．

3.6.2 試験結果

Table 12 に示すように，試料 H, B, X の破壊靱性値が高く，F および Y が低い．しかし，値は 45～63 kg/mm²$\sqrt{mm}$ であり，マルエージング鋼の約 300 kg/mm²$\sqrt{mm}$ (σ_B 200 kg/mm²)，熱間ダイス鋼の約 200 kg/mm²$\sqrt{mm}$ (AISI・H13, HRC 45) と比較すれば，遙かに小さい．Fig. 20 は K_{IC} と硬さの関係を示したもので，K_{IC} が硬さと強い相関を示していることがわかる．

3.7 その他の要因に対する検討

高速度工具鋼の靱性に関し，多くの研究が行なわれてきたが，主に化学成分および熱処理の影響を論じたものであった．化学成分の影響を除き，靱性におよぼす要因として，炭化物固溶量，析出炭化物量，オーステナイト結晶粒度，組織の均一性，残留炭化物の分布と形状が挙げられる．本論文は最後の項目について論じたものであるが，その他の項目についても各試料につき検討しておく必要がある．オーステナイト結晶粒度については 3.3 に示したので，こゝでは他の項目について調査した結果を述べる．

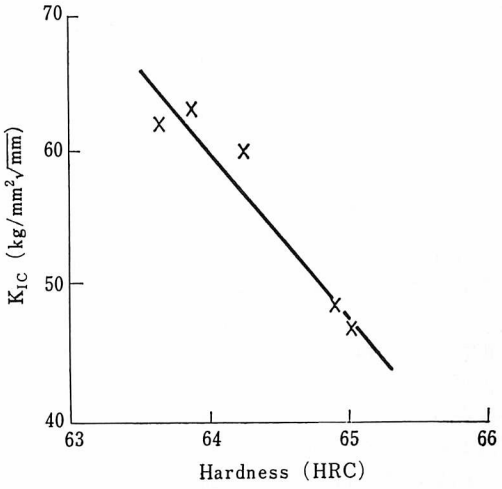

Fig. 20. Relation between hardness and K_{IC} values of the samples.

3.7.1 マトリックスの化学成分

EPMA (Electron Probe Microanalyzer) により，熱処理後の炭化物偏析部および正常部の化学成分を調査した．測定条件は次のとおり．

装置　Hitachi XMA-5
加速電圧　25 KV
試料電流　0·03μA
スポット径　0·7μ 以下

Table 13 に試料 H, X, C, Y に関し分析した結果を示す．表中の測定値は純金属に対する試料の元素の二次 X 線強度比から，コンピューターにより Philibert 法 (吸収効果補正) および Reed-Long 法 (螢光励起効果補正) に基く補正を行ない求めた結果である[19]．ただし，C 是は正確でないので参考値としてカウント数を示した．

Table 13. Chemical composition of matrix, determined by EPMA.

Sample	Field	Site*	Chemical composition (%)							
			C**	Si	Mn	Cr	W	Mo	V	Fe
H	1	a	897	0·23	0·18	5·20	2·63	3·41	1·40	86·95
		b	396	0·27	0·14	4·50	2·93	3·01	1·35	87·79
	2	a	976	0·26	0·19	5·15	2·40	3·18	1·41	87·41
		b	256	0·26	0·15	4·05	2·91	2·75	1·22	88·66
X	1	a	295	0·19	0·18	5·11	2·81	3·47	1·66	86·57
		b	291	0·25	0·15	4·22	2·84	2·66	1·28	88·59
	2	a	343	0·22	0·19	4·42	2·80	2·84	1·38	88·15
		b	281	0·24	0·17	4·49	2·59	2·65	1·25	88·61
C	1	a	711	0·19	0·20	5·34	3·00	3·81	1·97	85·48
		b	367	0·20	0·16	4·10	3·16	3·12	1·24	88·01
	2	a	393	0·22	0·21	4·84	2·96	3·09	1·35	87·33
		b	273	0·22	0·14	3·96	3·14	2·84	1·17	88·54
Y	1	a	317	0·23	0·17	5·09	2·92	3·23	2·23	86·13
		b	305	0·25	0·15	4·03	3·21	2·83	1·38	88·14
	2	a	279	0·20	0·20	5·10	2·66	3·29	1·96	86·57
		b	161	0·28	0·16	3·90	3·10	2·81	1·26	88·49
Average			409	0·23	0·17	4·59	2·88	3·06	1·47	87·59

* a=carbide segregated parts; b=normal parts adjacent to a.
** Number of counts per 20 sec-background counts.

測定視野は各試料ともそれぞれ1，2の2視野を選び，その視野中の縞状偏析部および縞状間の非偏析部で炭化物が存在しない5位置を選び分析した．Table 13 中の数字は5視野の平均値を示している．

この結果によれば，炭化物偏析部と非偏析部で元素の分配が異なり，炭化物偏析部に濃縮しやすい元素は Mn, Cr, Mo, V，非偏析部に濃縮しやすい元素は Si, W となっている．試料間の差は明瞭ではないが，偏析が著しく，かつ機械的性質のもっとも劣った試料 Y の V 量が偏析部でとくに多いのが注目される．また，平均炭化物サイズの大きい H, X と比較して，試料 C, Y の W, Mo, V のマトリックス中含有量が大きく，より多く固溶している傾向がみられる．

3.7.2 マトリックスの透過電子顕微鏡組織

炭化物偏析部と正常部で，マトリックスの微細組織が違うかどうか検討するため，薄膜による透過電子顕微鏡観察と，その電子回折を行なった．

試料は熱処理後 0·20～0·25 mm に平行研摩し，Bollmann 法により薄膜を作製した．電解液には燐酸—無水クロム酸を使用した．加速電圧は 100 KV である．

試料 C, F, X, Y 相互間でマトリックス組織に大きな差はなかった．代表的な組織を Photo. 24 に示す．マトリックスは多数のマルテンサイト双晶，結晶粒界，残留炭化物を含み，マルテンサイト中の転位密度が非常に高い．

炭化物偏析部分は薄膜試料作製の際，急速に腐食され，均一な薄膜作製が困難であったが，偏析部と正常のマトリックスの間にマルテンサイト晶の形状，転位密度に関し差は認められなかった．しかし，炭化物の周囲に局部的にいちじるしく転位が集積し，輪郭がぼけているものが数多く観察された．これは炭化物の周囲に歪が集中していることを示すものであり，破壊の起点となり易いことを示しているといえよう[20]．(Photo. 25)

試料 Y, C についてマトリックスの電子回折を行なったが，その結果によれば，マルテンサイト以外にオーステナイトおよび M_6C のスポットが認められた．たゞし，試料間および偏析部と正常部間に差はなかった．

3.8 炭化物の割れおよび剝離について

鋼の残留炭化物が靱性に対し大きな影響をもつことは周知のことであり，例えば高速度工具鋼の一次炭化物を除いたマトリックス鋼がすぐれた靱性をもつことは良く知られている[21]．C. T. Liu および J. Gurland[22] の研究によれば，球状化組織の高炭素鋼の引張破壊の場合，炭化物の亀裂または剝離によって micro voids が発生し，これらが連続して破壊に到ることを示し，破断強さは炭化物サイズの小なるほど大きいことを示している．

本研究で多くの機械試験の破面観察の結果，炭化物の割れおよび剝離が，ミクロクラックあるいはメインクラックの起点となっている例を見出したが，これをさらに検討するために，破断後の引張試験片について，炭化物と割れの関係を調査した．

焼なまし材では炭化物の割れまたは剝離はいちじるしく，2μ 以上の炭化物はほとんど亀裂を起こしていた．焼入焼もどしした試験片でも，破断部近傍では 5μ 以上の炭化物に多数の割れまたは剝離を生じていた．

Table 14 は破断面から 10 mm 離れた場所に存在する炭化物のうち，長さ 5μ 以上の粗大な炭化物について，サイズ毎に亀裂および剝離した炭化物数を計測した結果である．なお，観察倍率×1000，観察面積 1·03 mm^2 である．代表的な炭化物の割れおよび剝離状況を Photo. 26 に示す．

Table 14 に示すように，炭化物サイズが大きいほど

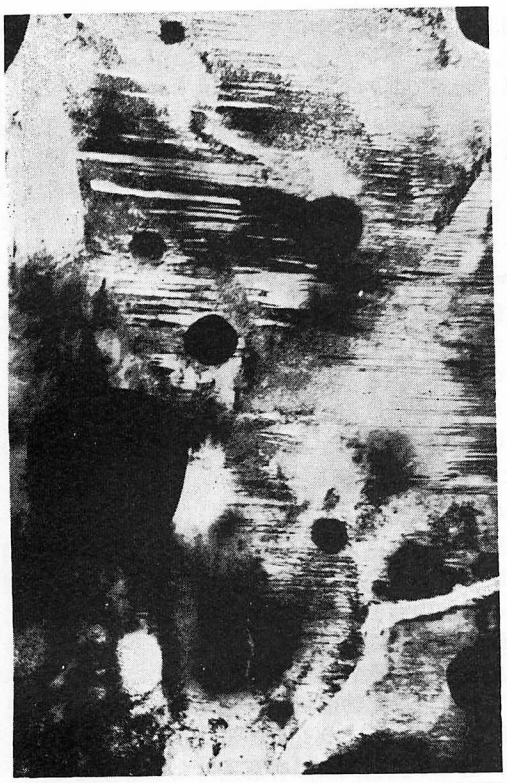

Sample C ×20 000

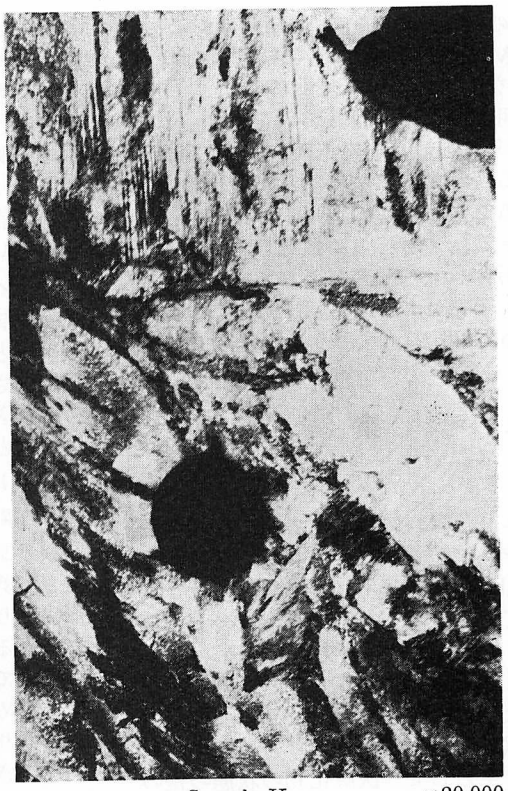

Sample H ×20 000

Photo. 24. Typical transmission electron micrographs.

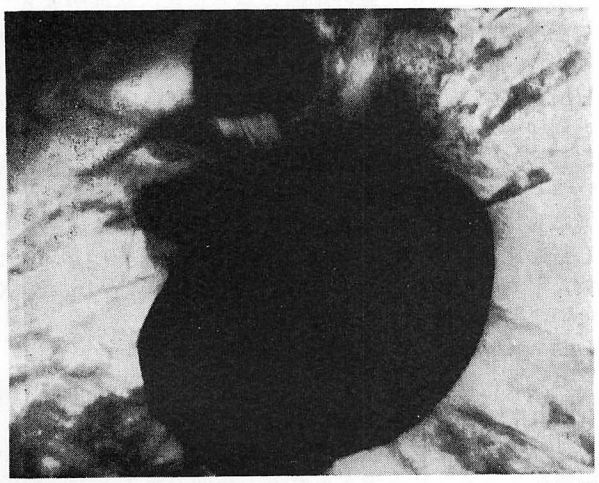

Sample X ×20 000

Photo. 25. Dislocation density around carbides.

割れあるいは剝離の発生率が高く，また，割れの方が剝離よりも発生率が高い．同一の炭化物長さ区分でも，試料により炭化物の割れ率が異なるのは，主として炭化物の形状に差があるためである．すなわち，試料 C は 5μ 以上の炭化物数は比較的多いが，球状に近いため割れ率は低い．試料 Y および X の炭化物割れ率が高いのは炭化物形状が悪いためである．観察結果から割れやすい炭化物を示すと次の通りである．

長さ 5μ 以上で，しかも

1) 長さ/巾の大きいもの
2) くびれたもの
3) ひとで状のもの

一次炭化物中の M_6C は上述のような異形の炭化物となりやすいが，MC 炭化物は M_6C と融合して複雑な形状になる場合をのぞき，一般に多少角ばった単純な形状のものが多い．各試料を村上試薬で腐食し，MC 炭化物の割れ率を測定したが，1～5μ のサイズのもので 20～

Table 14. Number of cracked or torn carbides with length over 5μ in hardened tensile specimens after rupturing in an area of 1·03 mm².

Sample	Elongation (%)	Number of cracked carbides (1)				Number of carbides torn from matrix				Percent of cracked to total carbides over 5μ (%) (2)			
		Carbide size (μ)			Total	Carbide size (μ)			Total	Carbide size (μ)			Total
		5-9	10-15	>15		5-9	10-15	>15		5-9	10-15	>15	
H	0·080	12/220(3)	4/16	—	16/236	5/220	2/16	—	7/236	7	38	—	10
B	0·041	14/228	4/30	1/3	19/261	6/228	2/30	1/3	9/261	9	20	67	11
X	0·048	47/204	8/11	—	55/215	5/204	0/11	—	5/215	26	64	—	26
C	0·060	14/265	7/25	1/3	22/293	3/265	1/25	—	4/293	7	32	33	9
F	0·038	28/202	3/16	3/6	34/224	4/202	5/16	0/6	9/224	16	50	50	19
Y	0·038	46/231	49/79	15/26	110/336	3/231	2/79	4/26	9/336	21	64	73	35

(1) Contains carbides with both cracks and tears in one grain.
(2) Number of cracked carbides/number of observed carbides.
(3) Contains torn carbides.

30%，5～10μ のもので約 40～50% の割れ率を示し，試料間に差はない．MC 型炭化物は同一サイズ形状の M_6C に比較し，割れを生じ易いようである．

高速度工具鋼中の粗大炭化物の組織が均質でないことは既に知られているが，Photo. 27 の EPMA による線分析結果からも知られる．粗大炭化物の割れが炭化物中の格子欠陥に影響されることは容易に想像できるが，割れた両片の組織に差がある．すなわち，独立した個々の炭化物が融合成長した場合，その融合部において亀裂を発生することが考えられるため，両片の EPMA による分析を行なったが，Photo. 28 に示すように，有意差を発見することはできなかった．

4. 考　察

4.1 結果の要約

炭化物状態を変化させた試料について各種の機械試験を行ない，試料間に特性差のあることが判明した．結果を綜括して示すと Table 15 の通りである．

このように，すべての性質にわたり，Hはすぐれた機械的性質を示し，Cがこれに次ぐ．一方，試料Yはきわめて機械的性質が悪く，Xも捩り試験をのぞき悪い．Fは試験項目により異なった成績を示す．これらの性質の差はすべて炭化物の状態のみで説明することは困難かも知れないが，ここでは主として一次炭化物の状態の差の面から考察を加えてみる．

4.2 機械的性質と炭化物の状態について

4.2.1 静的曲げ試験

静的曲げ試験は高硬度工具鋼の強度および靱性測定法として最も広く使用されている[23]．筆者らの研究によれば[11]，少なくとも HRC 65 以上の硬さでは SKH 9 の曲げ塑性変形量はほとんど0になり，曲げ強度と破断時のたわみはほゞ比例する．このような領域では強度が同時に靱性を表わす．またこの領域では劈開型の破壊形式をとり，劈開強さが靱性を定める要因と思われる．O. Mülders 等によれば，高速度工具鋼の曲げ強さは結晶粒直径の平方根の逆数に比例することを示し，また，組織の均一性の大なるほど増加することが知られているが[24]，本研究のように同一熱処理，化学成分の場合，曲げ靱性値は Table 7 の結晶粒度の関係のみでは説明できない．組織の均一性を Table 6 の炭化物偏析度で考えれば，これと結晶粒度の両方から説明できる．すなわち，Hが良いのは炭化物偏析度が良いため，C, F が良いのは結晶粒度細かく，偏析度が中位であるため，X が悪いのは結晶粒度，偏析が悪いため，Y が悪いのは偏析がいちじるしく悪いためであろう．炭化物粒度が大きいほど静的曲げ特性が低下するという実験結果もあるが[25]，Table 6 の結果では説明できない．以上より，静的曲げ靱性に対してはオーステナイト結晶粒度と一次炭化物偏析度の双方が影響し，その効果は，強いて言えば前者の方が大きいといえる．

4.2.2 シャルピー衝撃値

衝撃試験では劈開強さが剪断強さの3倍以上ないと脆性破壊となるといわれるように[26]，静的曲げ試験以上に劈開強さの影響は大となる．剪開強さは炭化物偏析によって顕著な影響を受けると考えられる．それ故，静的曲げ試験とほゞ同様な傾向をとるが，炭化物偏析，形状の悪い F は低い衝撃値を示している．

4.2.3 捩り試験

捩り試験では剪断応力と垂直応力は等しくなり，劈開強さが剪断強さより小さいときは脆性破壊となる．破壊形式よりみて，両者とも大差ないと思われるが，垂直応力による破壊がやゝ優先しているようであり，破面も脆性破面である．Y が低い捩り強さを示すのは劈開強さが低いためであり，炭化物偏析，形状などが悪いためと思う．捩り破壊の歪は，バラツキが多く，絶対値も低い．Y を除き，他の5試料間では有意差はないと考える．

4.2.4 引張試験

捩り試験より更に脆性破壊を起こし易い条件であり，破面は擬劈開面を呈した．引張強さの大きいものは伸びも大であったが，伸び率は0·1%以下で，捩りの場合の1/10 以下であった．試料間の順位は，概ね曲げ，衝撃と同様であったが，それらよりも，さらに炭化物偏析の影響が強いようである．破面に多数の炭化物の割れが観察されている．焼なまし材の場合は，試料 F がよくなり，逆に B は悪くなっている．焼なまし材の場合は，焼もどし材と比較して，さらに小粒の炭化物まで破砕され，それ故，平均炭化物粒度の小さい C, F は有利となり，B, X は逆に靱性を低下すると考えられる．

4.2.5 疲労試験

一次炭化物の極めて少ない高速度鋼のマトリックス鋼 (例えば VASCO-MA) はすぐれた疲労強さを示すが，これは一次炭化物が疲労強さに対し，何らかの形で悪い影響を与えるためと考えられる．今回のテストで，疲労破面の起点に粗大炭化物に起因するものが認められたが，5μ 以上の粗大炭化物の多い F, Y が悪い結果を与えた

Table 15. Summary of mechanical properties of samples.

Sample	Bend test	Charpy impact	Torsion test		Tensile test				Notch toughness	Fatigue test		General assessment
					Hardened		Annealed					
			Strength	Strain	Strength	Elongation	Strength	Elongation		Under 10^5 cycle	Over 10^6 cycle	
H	◎	○	◎	◎	◎	◎	◎	◎	◎	○	◎	Superior
B	○	○	○	○	○	○	△	△	◎	○	△	Good
X	△	△	○	◎	△～×	△	△～×	△	○	○	○	Fair
C	◎	◎	○	○	○	○	◎	○	—	◎	◎	Superior
F	◎	△	○	○	△	△	◎	◎	△	○	△	Good
Y	△	×	×	×	×	×	△	△	△	△	△	Bad

◎ Superior ○ Good △ Fair × Bad

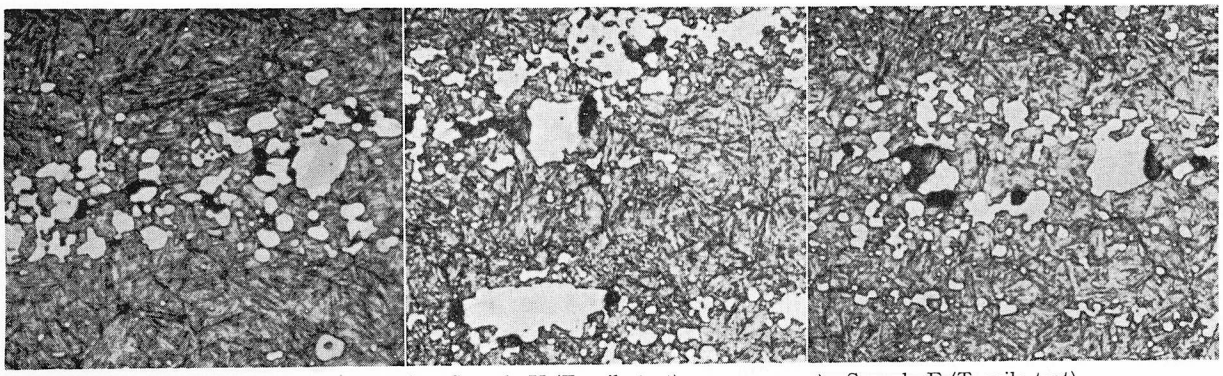

a) Sample X (Tensile test)　b) Sample Y (Tensile test)　c) Sample F (Tensile test)

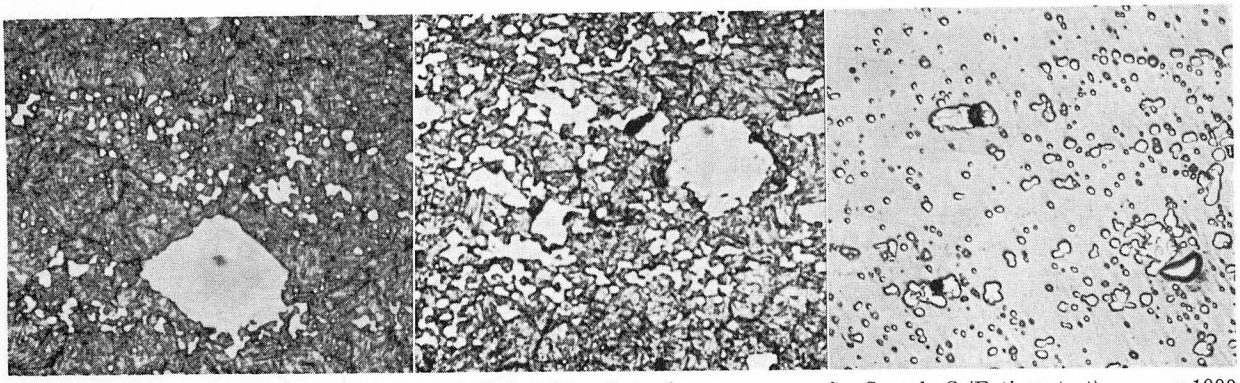

d) Sample C (Tensile test)　e) Sample Y(Tensile test)　f) Sample C (Fatigue test)　×1000

Photo. 26. Microcracks and voids in the vicinity of the fracture surface of hardened specimens.

ことに符合している．また，偏析部の炭化物量の少ない C, H が良い結果を与えたことから，偏析部炭化物密度が疲労破壊の起点または伝播に大きな影響をもつことが想像される．

4.2.6 破壊靭性

高速度工具鋼のような多量の炭化物を含み，かつ硬さの高い材料についての破壊靱性値はまだ公表されていない．それ故，一次炭化物がどのような影響を与えるかはよく分っていない，Fig. 20 の結果より，一次炭化物の偏析が極端に K_{IC} を低下させるとは考えられず，むしろ，マトリックスの影響が大きいと考えられる．破壊靱性試験では予め疲労クラックを入れているので，一次炭化物の割れによる初期クラックの発生効果が除かれるためと思われる．

上記のように，高速度鋼の機械的性質に対し，一次炭化物の状態が大きな影響を与えることがわかるが，その影響の仕方は画一的でない．しかし，高速度鋼の機械的性質は結晶粒度のほかに，炭化物偏析度と粗大炭化物量が大きな関係をもち，試験条件により，そのいずれかの効果が大になると考えられる．粗大炭化物は主としてマトリックスからの剝離，またはそれ自身がもつ格子欠陥あるいは応力集中源により，また炭化物偏析は割れの伝播しやすさにより，それぞれ影響をもつと考えられる．

4.3 靱性におよぼす一次炭化物の役割

炭化物状態と靱性に関しては，鋼の場合よりも粉末冶金法による超硬質合金についてよく研究されている．WC-Co 系焼結合金では，炭化物の平均自由距離が一定の場合，Co 量の多いほど曲げ破断強さが大きく，また一定 Co 量の脆性域において，平均自由距離の大きいほど曲げ破断強さが大であることが知られている[27]．これらの関係は Co 量の代りにマトリックス面積率を用いれば高速度工具鋼にも適用できるであろう．

脆性材料では，一般に Griffith-Orowan 理論が破壊強さとミクロ組織的パラメータの間の定量的関係を表わす．すなわち

$$\sigma=K\left[\frac{EP}{l_c}\right]^{1/2}$$

こゝに，σ：臨界破断応力，K：定数，E：弾性係数，p：破断仕事量，l_c：初期クラックの長さ．

Kreimer[28] は WC-Co 合金にこれを利用し，

$$\sigma^2=\mathrm{AEC}+\mathrm{K}$$

の実験式を得ている．ただし，A, K：定数，E；弾性係数，C：Co 量(wt %)．炭化物サイズは定数 K に影響をおよぼすとしている．ともかく，炭化物とマトリックスよりなる脆性材料においては，炭化物量（またはマトリックス量）とそのサイズが靱性を定める主要因子と考えられる．本鋼では靱性が偏析度と強い相関を有していたゝめ，上記の関係は炭化物偏析部で考える必要がある．

高応力下で発生する粗大炭化物の割れまたは剝離が破壊の起点となり，これが応力集中により拡大して完全破壊になると仮定する．この場合，粗大炭化物が微小クラックの起源となり，偏析部の炭化物量がクラック伝播抵抗に関係すると考えられる．それ故，Griffith-Orowan の式において，破断仕事量 p の代りに，Kreimer の考え方を導入して，偏析部のマトリックス面積率を代入，また l_c に最大炭化物長さを代入し，〔偏析部マトリックス面積率 / 最大炭化物長さ (μ)〕$^{1/2}$ に対する各種機械的

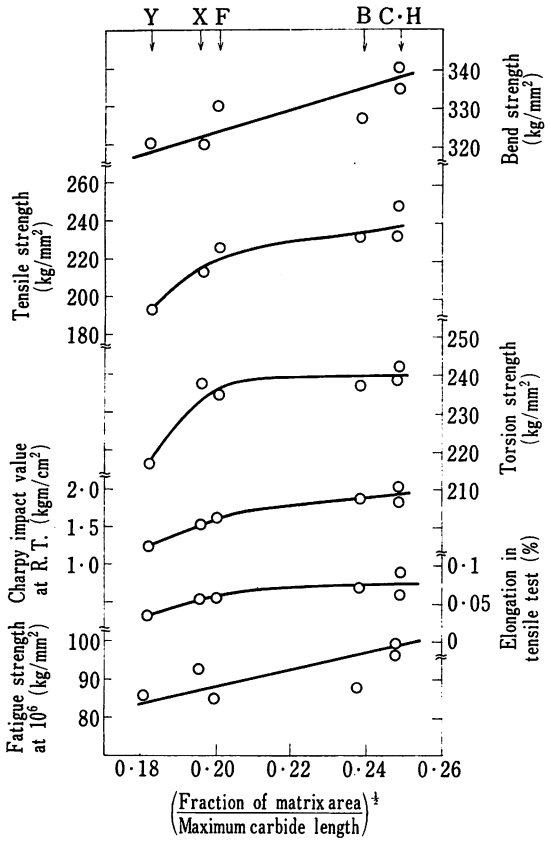

Fig. 21. Various properties vs (Fraction of matrix area in the segregated parts/maximum carbide length)$^{1/2}$.

性質をプロットしてみた．結果を Fig. 21 に示す．直線関係は得られていないが，比較的密接な関係が得られている．なお，単に偏析部の炭化物面積率，炭化物の平均自由距離，偏析部炭化物サイズでは良い相関は得られなかった．上記のごとく，機械的性質と一次炭化物の関係は上記のパラメータを用いてある程度定量的評価が可能である．しかし，鍛造比が小さく，炭化物形状がいちじるしく悪い場合は，別個の検討が必要と思われる．

しかしながら，粗大炭化物の割れまたは剝離が果して成長するクラックの起源となりうるであろうか．筆者は Table 12 に示すごとく試料の破壊靱性値を測定した．今，Fig. 22 に示すように，半月形のクラックが平板材の表面に存在する場合，応力σによりこのクラックが脆性破壊に進展する臨界応力σ_fは次式で求まる[18]．

$$\sigma_f=\frac{\pi}{2}K_{IC}\sqrt{\frac{1}{1{\cdot}2\pi a_0+0{\cdot}2\left(\frac{K_{IC}}{\sigma_{ys}}\right)^2}}$$

同様に円形クラックが鋼材内部に存在する場合 (Fig. 22-2)) の臨界応力σ_fは次式で求まる[18]．

$$\sigma_f=K_{IC}\sqrt{\frac{1}{\pi a_0+\frac{(1-0{\cdot}3^2)}{6}\left(\frac{K_{IC}}{\sigma_{ys}}\right)^2}}$$

K_{IC}=60, 50, および 40 kg/mm$^2\sqrt{\text{mm}}$ として，a_0 とσ_fの関係を求めると Fig. 23 および 24 のようになる．この結果より，クラックが表面に出た場合の方が若干臨界破壊応力は小さくなることがわかる．また，同一クラ

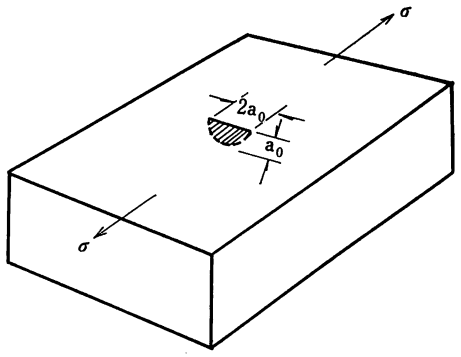

1) Semicircular crack on the surface of a plate

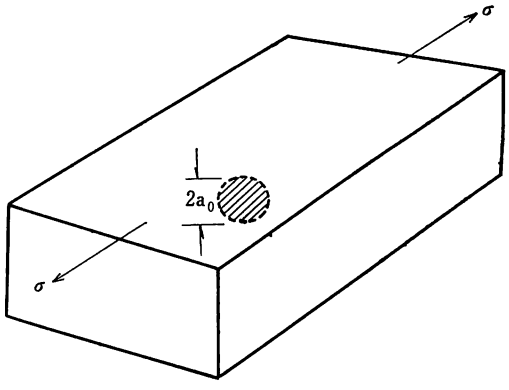

2) Circular crack inside a plate

Fig. 22. Existence condition of a crack.

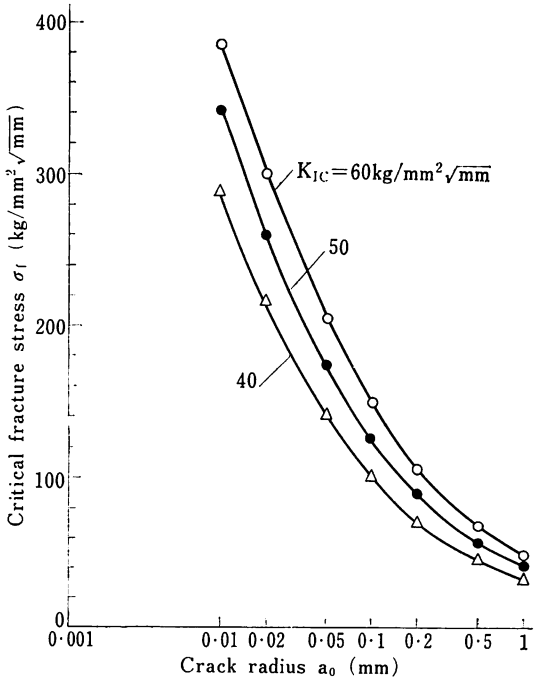

Fig. 23. Relation between critical fracture stress σ_f and crack radius a_0 where a crack is present on the outer surface of a plate (σ_{ys}=180 kg/mm^2)

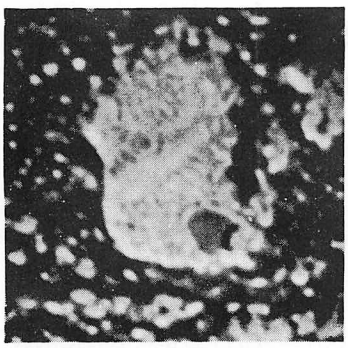

RE

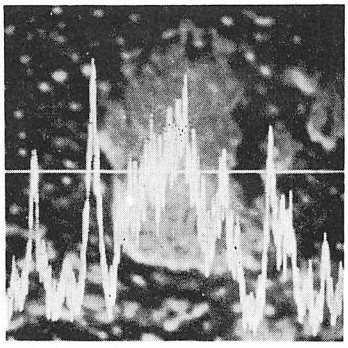

C

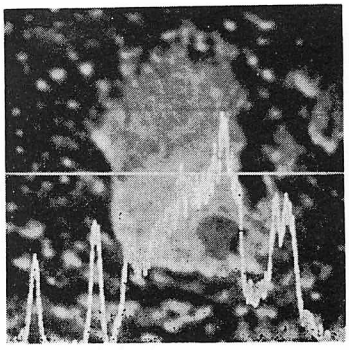

V

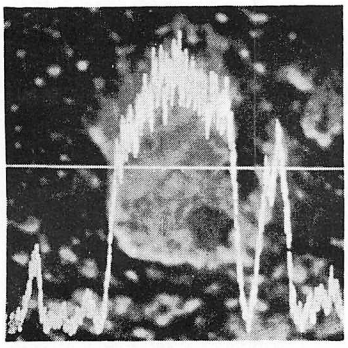

Mo

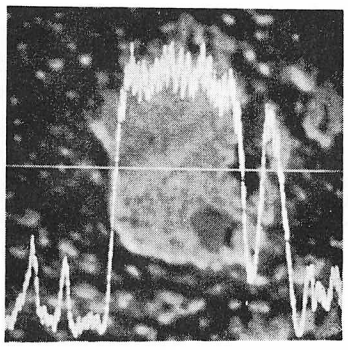

W

Photo. 27. Line analysis on a coarse primary carbide in sample Y.

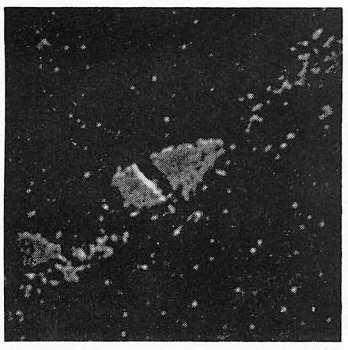

×650

(1) Microcrack of a large carbide

	C	Cr	Mo	W	V
a.	2·71	4·28	12·37	20·97	10·28
b.	2·84	4·31	12·32	21·80	11·01

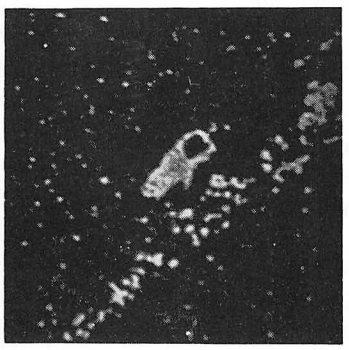

×650

(2) MC carbide, coalesced with a M_6C carbide

	C	Cr	Mo	W	V
a.	2·58	4·23	11·80	17·70	12·73

(3) Microcrack of a large carbide

	C	Cr	Mo	W	V
a.	2·75	5·18	12·90	19·35	9·40
b.	—	4·98	13·19	17·66	19·68

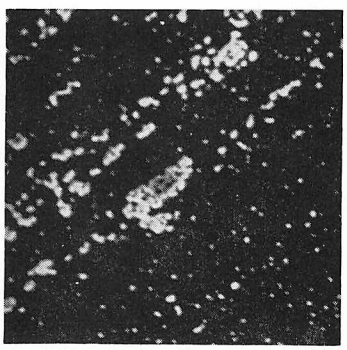

(4) M_6C carbide with minute MC carbides

	C	Cr	Mo	W	V
a.	—	4·98	13·19	16·52	12·52 ~17·91

Photo. 28. Secondary electron images and X-ray point analysis of large carbides, cracked or uncracked, in a hardened tensile specimen of sample Y.

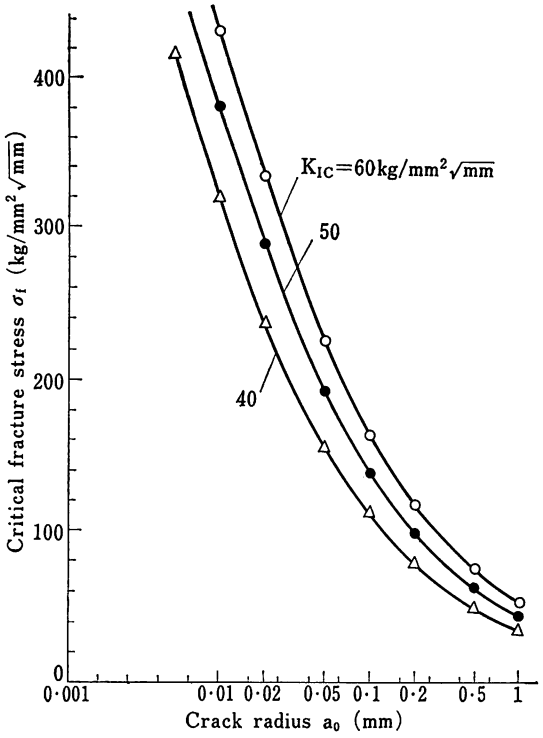

Fig. 24. Relation between critical fracture stress σ_f and crack radius a_0 where a crack is present inside a plate (σ_{ys}=180 kg/mm^2).

ック半径の場合，K_{IC} の値は臨界破断応力はかなり相違が認められる．試料の引張強さは約 230kg/mm^2 であり，真破断応力もほとんどこれに等しいので，σ_f=230kg/mm^2 における a_0 を求めると，約 0·02～0·05mm，つまり，クラック巾にして 40～100μ 程度である．この値は粗大炭化物の巾，10～20μ よりかなり大きい．それ故，独立した粗大炭化物の割れはそれ自身，伝播するクラックの直接起源とはなり得ない．高速度工具鋼の破壊のメカニズムを説明するには，他のメカニズムが必要である．例えば，偏析部の炭化物に発生した多数の割れや剝離が結合連結し，40～100μ のクラックに成長する可能性が考えられる．実際，破面には多くの独立したクラックが認められ，クラック伝播の方向もかなり複雑であった．炭化物偏析部のマトリックスは非偏析部と比較して固溶合金量多く（Table 13 参照）また近接する炭化物の周囲には転位の集積による内部歪の増大があるので，その部分の K_{IC} はかなり低いことが推定される．このようにして，粗大炭化物ならびに偏析の顕著な材料は，例えば試料 Y のごとく応力付加の早期に内部クラックが成長し，σ_f が低下すると考えられる．

本実験結果によれば，Table 15 に示したように試料の靱性は試験方法によって若干相違を示した．これは応力条件以外に歪速度によって偏析部における内部クラックの成長が変化するためでないかと考えられる．炭化物の割れおよび剝離は塑性変形により炭化物とマトリックスの界面に転位が集積し大きな応力集中を起こすためと推察され，炭化物とマトリックスの弾性係数の差，炭化物形状の複雑さがそれを助長すると考えられる．さらに，Photo. 27 に示したような粗大炭化物の不均質性もそれらを加速したと思われる．

5. 結　　言

Mo 高速度工具鋼 (SHK 9) の靱性，疲労性質などにおよぼす一次炭化物の影響を確認するため，鋼塊形状，鍛造比，加工条件を変えて種々の一次炭化物状態の試料を作製し，各種の機械的性質を検討した．得られた結果を要約すると次の通りである．

(1) 静的曲げ強さは，鍛造比の増大にしたがい，初めは急激に増大し，やがて飽和に近づく．この変化は，鋼塊サイズの大きい場合遅く，また，鍛造方向に垂直な方向より採取した試験片の方が平行に採取した試験片より遅い．

(2) 鍛造比の増大による静的曲げ強さの変化は，炭化物偏析の巾などマクロ的に観察される偏析度とは直接関係しない．鍛造比の増大による炭化物状態のミクロ的変化，すなわち，偏析部内の炭化物集合度，大きさ，形状の変化と関連するものと考えられる．

(3) ほゞ同一寸度の製品を製造方式をかえて種々の炭化物状態の試料を作製し各種の機械試験を行なった結果，静的曲げ靱性はオーステナイト結晶粒度，炭化物集合度で計測される炭化物偏析度に大きく依存し，シャルピー衝撃値はほゞ同様であるが，炭化物偏析度の影響が強くなる．

(4) 捩りおよび引張強さは静的曲げ，衝撃値よりさらに，炭化物偏析度の影響が強く現われ，結晶粒度の効果は減少する．引張の場合は粗大炭化物が悪影響をおよぼし，焼なまし材のごとく塑性変形量の大なる場合ほど炭化物粒度の影響が大きい．

(5) 疲れ強さに対しては，炭化物偏析度が小さく，粗大炭化物の少ない試料が良い結果を与えた．

(6) 破壊靱性値は約 45～65kg/mm$^2\sqrt{\text{mm}}$ を示し，硬さと良い相関を示した．

(7) 多くの破面を観察した結果，粗大炭化物の割れまたは剝離が破壊の起点となったり，あるいは多数のミクロクラックの局部的な破壊起点となっている例を見出した．炭化物の亀裂は 5μ 以上の大きさの炭化物に多く，しかも形状が複雑なものに多かった．MC 型炭化物は M_6C 型炭化物より，亀裂または剝離を起こしやすいと判断された．

(8) 各種性質は〔偏析部のマトリックス面積率 / 最大炭化物長さ〕$^{1/2}$ の値と良い相関を示し，この値の大きいほど各種機械的性質は改善された．

(9) 破壊靱性値と破面の考察結果を参照して，高速度工具鋼の破壊のメカニズムについて考察を加えた．

(10) 以上より，高速度工具鋼の靱性を良くするには，偏析部の炭化物をできるだけ分散させ，最大炭化物サイズを小さく，できるだけ 5μ 以下にすること，また一次炭化物の形状を球状化することが重要と思われる．

本研究を遂行するに当り，終始，御指導，御鞭撻をいたゞいた日立金属（株）安来工場，橋本冶金研究所長をはじめ，試料作製に積極的に協力された製造部門各位および実験を担当していたゞいた吾郷，渡辺，芥川，市川，秦，瀬崎研究所員に深く謝意を表する．最後に，本研究を鉄鋼の靱性向上に関する京都国際学会へ投稿することを許可され，かつ御激励をいたゞいた当社宮下常任顧問，溝口常務取締役安来工場長，浅田取締役に厚く御礼申し上げる．

文　献

1) GOST 5952–63
2) VDEh Stahl Eisen Prüfblatt 1615
3) E. Ineson and G. Hoyle: Met. Treatment, (July 1956)p. 257–262
4) K. Tesche and W. Beuthner: DEW Techn. Ber., **4** (1964), no. 2, p. 51～62
5) E. Bernart, V. Dlouhy: Hutnik, **18** (1968) no. 4, 165～167
6) H. Fielder, H.J. Eckstein: Neue Hütte, **13** (1968), no. 5, p. 268～278
7) P. Hellman: Stora Kopparberg, Jun. **16** (1970)
8) A.R. Johnson and J.C. Hamaker: Metals Engineering Quarterly, **9** (1964), no. 3, p. 6
9) C. Fisher and M. Cole: The Microscope, Second Quarter, **16** (1969), p. 81
10) A. Rose, H. Mathesius and H.P. Hougardy: Archiv Eisenhüttenwes., **40** (1969), p. 323
11) 新持，清永，奥野：鉄と鋼，**50** (1964)，p. 678
12) G. Steven: Metal Progress, **75** (1959), no. 5, p. 76
13) 沢：機械の研究，**18** (1966)，p. 77
14) 浦野，芥川：日立評論，**52** (1970)，no. 7，p. 654
15) J. Nunes, F.L. Carr and F.R. Larson: Techniques of Metals Research, **2** (1968), p. 388, 1968, Interscience Publishers
16) 森本：鉄と鋼，**57** (1971)，No. 1，p. 116
17) 志村：日本金属学会会報，**9** (1970)，no. 5，p. 289
18) J.E. Srawley and W.F. Brown, Jr: ASTM Special Technical Publication **381**, (1965), p. 190
19) X線マイクロアナライザーにおける定量分析法（日立製作所）
20) 新持，清永，沢田：水曜会誌，**16** (1968)，no. 7，p. 454
21) A.M. Bayer: Metal Progress, **97** (1970), no. 4, p. 86
22) C.T. Liu and J. Gurland: Trans. ASM, **61** (1968), p.156
23) S. Wilmes: Stahl und Eisen, **18** (1961), p. 676
24) O. Mülders and H.H. Weigand: Schweizer Archiv., **32** (1966), no. 3, p. 68
25) 辻，増田，碓永：鉄と鋼，**52** (1966)，p. 680
26) VASCO Metallurgical Bulletins No. 2
27) J. Gurland: Microstructural Aspects of the Strength and Hardness of Cemented Tungsten Carbides, (Dec. 1969) Brown Univ. Providence R. 1
28) G.S. Kreimer: Strength of Hard Alloys (1968), N.Y. Consultants Bureau

討論 pp. 360–361 参照

Effects of Composition on Ductility and Toughness of Ferritic Stainless Steels

M. Semchyshen A.P. Bond H.J. Dundas

Climax Molybdenum Company of Michigan (Inc.)

an AMAX subsidiary, Research Laboratory

ABSTRACT

Brittle-to-ductile transition temperatures were determined by impact tests for a series of ferritic stainless steels containing 14 to 28% Cr and 0 to 5% Mo. The effect on ductility of variation in carbon, nitrogen and titanium content was determined for steels containing 18% Cr and 2% Mo. In general, transition temperatures increased with increasing chromium content but were relatively insensitive to molybdenum content. Increases in carbon and/or nitrogen content caused a pronounced increase in the transition temperature. Stabilization of the steels with titanium alleviated the deleterious effects of high-temperature exposure on ductility, for example, as would be encountered as result of welding. Otherwise, the titanium-modified steels exhibited transition temperatures commensurate with their carbon and nitrogen contents. The effects of chromium, carbon and nitrogen variations on the tensile ductility of welded specimens were similar to those noted in the impact tests. On the other hand, increasing molybdenum contents appeared to improve the postweld ductility of the steels. The relationships of the carbon and the nitrogen content of the steels to mechanical properties are reflected in the corrosion behavior of the alloys; that is, the higher the carbon and/or the nitrogen, the greater is the susceptibility of the steels to intergranular corrosion. All of the steels studied exhibited excellent resistance to stress-corrosion cracking.

1. INTRODUCTION

Ferritic stainless steels have long been of interest to the designer and the metallurgist because of potentially lower costs compared with austenitic grades and because of their resistance to stress-corrosion cracking in the presence of chloride ions. The factors that have prevented the widespread utilization of conventionally-melted ferritic grades have been limited room-temperature toughness together with embrittlement and increased sensitivity to intergranular corrosion after welding or heating at high temperatures.

As long ago as 1951, Binder and Spendelow[1] and Hochmann[2] demonstrated that the toughness of straight chromium ferritic steels was sensitive to the combined carbon and nitrogen content. Binder and Spendelow showed, for example, that the limiting carbon plus nitrogen content consistent with good toughness in a nominally 18% Cr steel was about 0·05%. A comparable value for a 25% Cr steel was closer to 0·03%.

More recently, Wright[3] confirmed a maximun carbon plus nitrogen level of 0·03% for a steel containing 26% Cr, 1% Mo and 0·22% Ti to give acceptable toughness in 3mm-thick sheet. Somewhat higher tolerances for interstitial elements were reported for thinner sheet.

Binder and Spendelow[1] achieved low interstitial contents in vacuum-melted laboratory-scale heats by using extremely high-purity charge materials. Such a practice was, of course, not put into commercial production because its implementation would negate the economic advantages of the ferritic grades. Thus the concept of low-interstitial ferritic grades was not exploited until recent years when new steel-making techniques such as oxygen-argon melting, vacuum refining and electron-beam refining progressed to the point of economic feasibility.

Of particular interest is the electron-beam continuous-hearth refining process as described by Knoth[4]. This process has the advantage of exposing molten metal to a high vacuum for a relatively long time period. The process is currently being used commercially to produce a high-purity ferritic stainless steel containing nominally 26% Cr and 1% Mo[5,6].

The objective of the work reported here was to define the effects of composition on the toughness and ductility of ferritic steels containing from 14 to nominally 28% Cr. Laboratory heats were prepared to study the effects of chromium, carbon, nitrogen and molybdenum on the properties of ferritic steels. Stabilization with titanium or niobium was also studied.

2. MATERIALS AND PROCEDURES

The laboratory heats prepared for this study are described in Table 1. As indicated in this tabula-

Table 1. Composition of alloys studied.

Heat	Composition (%)								
	Cr	Mo	Ni	C	Si	Mn	N	Ti	Nb
High-purity alloys[v]									
V537A	13·68	0·08	—	0·003	—	—	0·004	—	—
V537B	13·60	1·88	—	0·002	—	—	0·004	—	—
V98	16·93	1·04	—	0·002	0·05	—	NA[a]	—	—
V99	16·98	2·99	—	0·003	0·06	—	0·005	—	—
V530A	17·35	0·01	—	0·002	—	—	0·003	—	—
V530B	17·61	2·02	—	0·004	—	—	0·004	—	—
V468	19·70	2·01	—	0·003	—	—	0·010	—	—
V472A	22·52	2·00	—	0·003	—	—	0·011	—	—
V233A	25·66	0·005	0·13	0·002	NA	—	NA	—	—
V233B	25·26	2·05	0·13	0·002	NA	—	0·017	—	—
V470	25·02	1·99	—	0·003	—	—	0·013	—	—
V234A	25·58	3·49	0·13	0·002	NA	—	NA	—	—
V233C	25·25	5·24	0·13	0·002	0·019	—	0·013	—	—
V471	26·15	0·99	—	0·003	—	—	0·016	—	—
V472B	27·86	2·00	—	0·007	—	—	0·021	—	—
High-purity alloys[p]									
P270A	16·76	—	—	0·002	—	—	0·010	—	—
P270B	16·74	—	—	0·002	—	—	0·022	—	—
P270C	16·87	—	—	0·003	—	—	0·032	—	—
P270D	16·71	—	—	0·004	—	—	0·057	—	—
P271A	16·81	—	—	0·012	—	—	0·009	—	—
P271B	16·76	—	—	0·018	—	—	0·009	—	—
P271C	16·69	—	—	0·027	—	—	0·009	—	—
P271D	16·81	—	—	0·061	—	—	0·007	—	—
P526	17·60	1·96	—	0·001	—	—	0·004	—	—
P527A	17·58	1·97	—	0·010	—	—	0·004	—	—
P527B	17·61	1·95	—	0·018	—	—	0·004	—	—
P528A	17·63	1·96	—	0·012	—	—	0·009	—	—
P528B	17·67	1·95	—	0·019	—	—	0·009	—	—
P529A	17·41	1·95	—	0·008	—	—	0·019	—	—
P529B	17·48	1·93	—	0·018	—	—	0·018	—	—
P531A	17·77	1·98	—	0·002	—	—	0·009	—	—
P531B	17·77	1·99	—	0·002	—	—	0·018	—	—
Commercial-purity alloys[c]									
4073A	18·45	1·97	0·11	0·034	0·13	—	0·045	0·47	—
4073B	NA	NA	NA	NA	NA	—	NA	0·81	—
4073C	NA	NA	NA	NA	NA	—	NA	1·27	—
4073D	NA	NA	NA	0·035	NA	—	0·023	1·86	—
4354A	17·61	0·035	0·09	0·028	0·22	0·55	0·032	—	—
4354B	NA	0·96	NA	NA	NA	NA	NA	—	—
4354C	NA	2·06	NA	NA	NA	NA	NA	—	—
4354D	NA	3·51	NA	NA	NA	NA	NA	—	—
4354E	17·31	4·67	NA	0·031	NA	NA	0·033	—	—
4355A	24·24	0·046	0·12	0·035	0·23	0·59	0·046	—	—
4355B	NA	0·97	NA	NA	NA	NA	NA	—	—
4355C	NA	2·37	NA	NA	NA	NA	NA	—	—
4355D	NA	3·52	NA	NA	NA	NA	NA	—	—
4355E	24·19	4·94	NA	0·033	NA	NA	0·043	—	—
4356A	17·75	2·07	0·06	0·036	0·22	0·41	0·031	—	0·02
4356B	NA	NA	NA	NA	NA	NA	NA	—	0·13
4356C	NA	NA	NA	NA	NA	NA	NA	—	0·32
4356D	NA	NA	NA	NA	NA	NA	NA	—	0·61
4356E	17·59	1·85	NA	0·030	NA	NA	0·033	—	0·93

v Vacuum-induction melted.
p Melted and cast in 350 mm absolute argon atmosphere.
a NA=not analyzed, but in the range of the series.
c Air-induction melted.

tion, heats were prepared either by vacuum melting, melting in a partial pressure of argon or air melting.

A majority of the materials available for this study were made by the split-heat technique. In this procedure, fractions of the melt were cast, each preceded by a desired change in melt composition. Heats prepared in this manner are indicated in Table 1 by the use of letters (A through E) appended to the heat numbers.

All ingots were cast to a size of 60-mm diameter. The ingots were conditioned and rolled to either 12 or 3 mm-thick plate. No effort was made to achieve optimum working schedules. Working schedules within each finished plate size were repeated as closely as possible in order to minimize variations from this source.

Standard (10 mm-square) Charpy V-notch specimens and quarter size (2·5 by 10 mm) specimens were machined from 12 and 3 mm plate, respectively. Specimens were tested at temperatures selected to define the brittle-to-ductile transition.

Tensile tests were performed on flat specimens either annealed or welded by a tungsten-inert-gas technique.

Selected corrosion data on experimental ferritic stainless steels were obtained.

3. UNSTABILIZED STEELS

The effect of varying carbon and nitrogen content was investigated in alloys of several differing base compositions. Fig. 1 shows the effect of carbon content on the impact energy absorbed by quarter-size specimens of rather pure 17% Cr alloys. There is a clear (but rather small) increase in impact-transition temperature as carbon content increases in specimens annealed at 815°C. Similar tests on 17% Cr alloys containing nitrogen did not reveal a significant nitrogen effect in the range from 0·01 to 0·057% (Fig. 2). The carbon effect is in agreement with the observations of Binder and Spendelow[1].

The same two series of alloys were tested in impact after heat treatment at 1150°C to simulate the conditions in the heat-affected zone after welding. The results (Fig. 3 and 4) show that this heat treatment greatly accentuates the deleterious

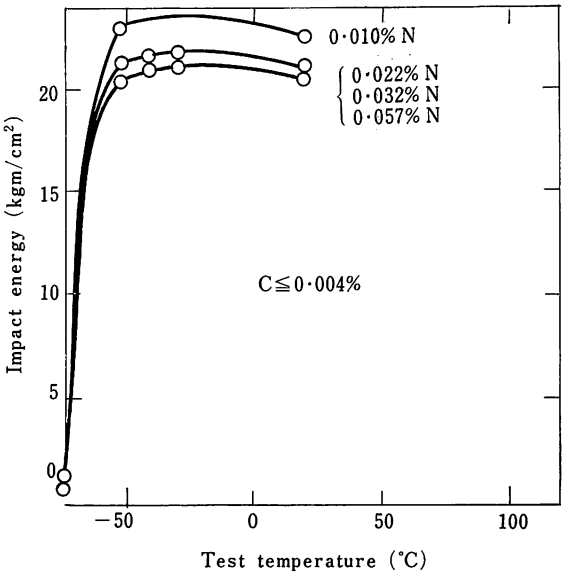

Fig. 2. Transition curves for quarter-size Charpy V-notch impact specimens of 17% Cr-0·010 to 0·057%N ferritic stainless steels (Heats P270A-D) heat treated at 815°C for 1 hr and water quenched. ASTM grain size range 6–7.

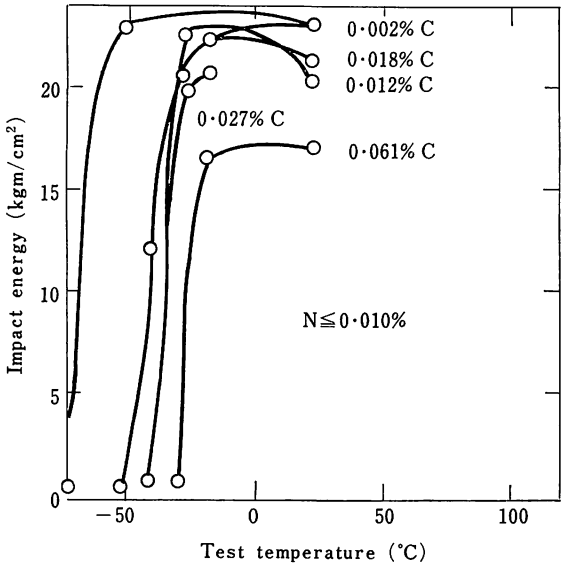

Fig. 1. Transition curves for quarter-size Charpy V-notch impact specimens of 17% Cr-0·002 to 0·061% C ferritic stainless steels (Heats P270A, P 271A-D) heat treated at 815°C for 1 hr and water quenched. ASTM grain size range 6–7.

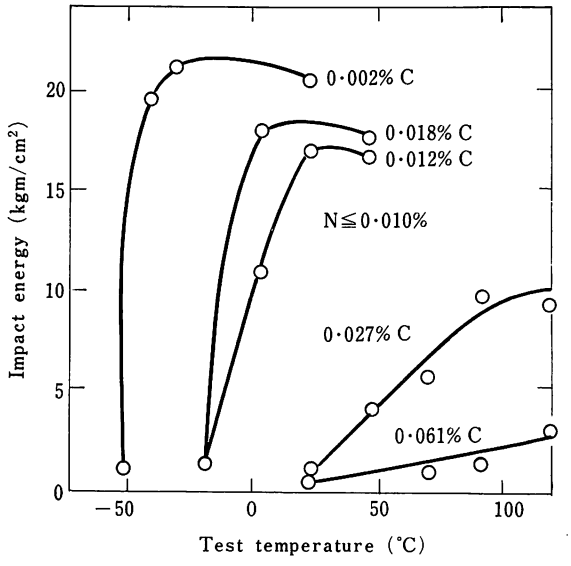

Fig. 3. Transition curves for quarter-size Charpy V-notch impact specimens of 17% Cr–0·002 to 0·061% C ferritic stainless steels (Heats P270A, P271A–D) heat treated at 815°C + 1150°C for 1 hr and water quenched. ASTM grain size range 1–5.

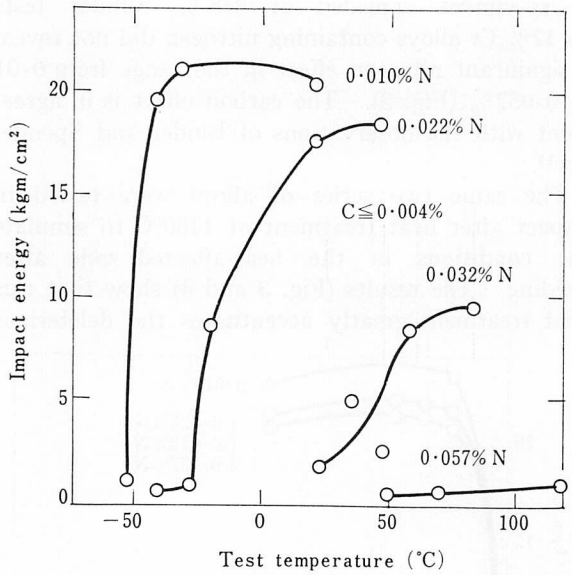

Fig. 4. Transition curves for quarter-size Charpy V-notch impact specimens of 17% Cr–0·010 to 0·057% N ferritic stainless steels (Heats P270A-D) heat treated at 815°C + 1150°C for 1 hr and water quenched. ASTM grain size range 1–2.

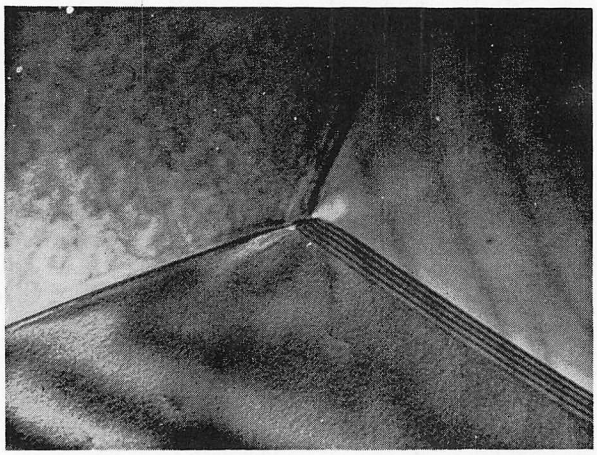

×25 000

Photo. 1. Transmission electron micrograph of ferritic steel containing 16·76% Cr, 0·002% C, 0·010% N.

×25 000

Photo. 2. Transmission electron micrograph of ferritic steel containing 16·74% Cr, 0·002% C, 0·022% N.

effects of carbon and nitrogen on impact resistance. These results are in agreement with the work of Hochmann[2] who showed, particularly in the case of nitrogen, that exposures in the neighborhood of 1200°C were necessary to delineate the effect of impurity elements.

The two alloys of highest carbon and nitrogen content contained a considerable amount of untempered martensite after the 1150°C treatment, and this must account in part for the very high transition temperatures of these alloys. However, the remainder of the alloys contained little or no martensite so that factors other than martensite formation contribute to the effect of carbon and nitrogen.

The alloys containing only chromium and 0·01% C or 0·02% N contained grain-boundary precipitates while the highest-purity alloy remained free of grain-boundary precipitates after quenching from temperatures above 925°C. The microstructure shown in Photo. 1 confirms the absence of precipitate in low-interstitial alloys and, in Photo. 2, the presence of precipitate in less-pure alloys. It is concluded that the precipitation of chromium carbonitrides, mainly at grain boundaries, is the principle cause of the observed increases in transition temperature of the alloys containing increasing amounts of carbon and/or nitrogen and quenched from 1150°C. Demo[7] analyzed precipitates extracted from sensitized 25% Cr steel. A combination of X-ray diffraction, transmission electron diffraction and chemical analysis led to the conclusion that the precipitates actually consisted of a mixture of $M_{23}C_6$ and β-Cr_2N.

The effects of carbon and nitrogen in a base alloy of 18% Cr and 2% Mo were studied in some detail using full-size Charpy bars in this case. The deleterious effect of carbon and nitrogen on impact properties is again clearly evident (Table 2). Nitrogen alone is less harmful than carbon. For example, at 0·004% N, an increase in carbon content from 0·002 to 0·01% resulted in a 60°C increase in transition temperature. On the other hand, at a constant carbon content of 0·002%, an increase in nitrogen content from 0·004 to 0·01% resulted in only a 10°C increase in transition temperature. As carbon content increases, the degrading effect of increased nitrogen content is more clearly evident.

The difference between the transition temperatures observed for the 17% Cr alloys and for the 18% Cr-2 Mo alloys is the result of two factors: First, the molybdenum-free specimens were quarter size, and this type of specimen inherently produces a lower transition temperature. Second, and most important, the stock from which the full-size, molybdenum-containing specimens were machined received considerable less hot-cold work during conversion from ingot to plate. As indicated in Fig. 5, the combined effect of specimen size and

Table 2. Charpy V-notch transition temperatures for full-size specimens of 18% Cr-2% Mo steels annealed one hr at 815°C.

Nominal nitrogen content (wt %)	Minimum temperature (°C) to absorb 20 kgm/cm²		
	Nominal carbon content (wt %)		
	0·002	0·01	0·02
0·004	−25	35	25
0·01	−15	95	95
0·02	25	80	130

Table 3. Charpy V-notch transition temperatures for full-size specimens of 18% Cr-2% Mo steels annealed one hour at 1150°C.

Nominal nitrogen content (wt %)	Minimum temperature (°C) to absorb 20 kgm/cm²		
	Nominal carbon content (wt %)		
	0·002	0·01	0·02
0·004	−25	60	125
0·01	−15	125	160
0·02	60	160	170

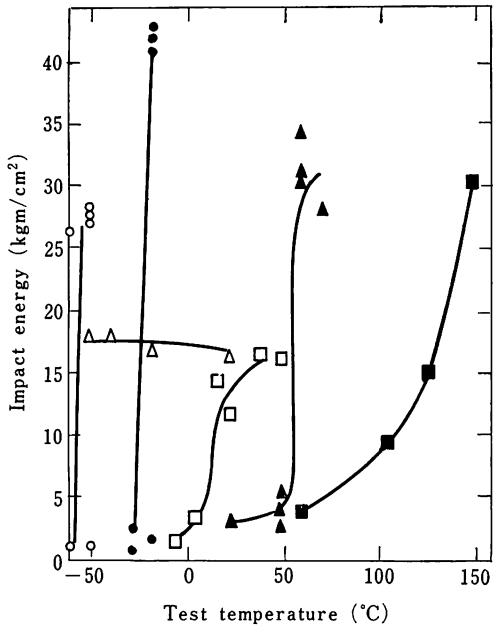

Fig. 5. Transition curves for quarter- and full-size Charpy V-notch impact specimens of three ferritic stainless steels.

Specimen			Composition (%)		
Quarter size	Full size	Heat	Cr	Mo	(C+N)
○	●	P526*	18	2	0·005
□	■	P529B*	18	2	0·036
△	▲	V470**	25	2	0·016

* Annealed 1 hr at 815°C and water quenched.
** Annealed 1 hr at 980°C and water quenched.

level of hot-cold work in the present program can result in differences in transition temperature from about 25°C to over 100°C.

Heat treatment at 1150°C generally raised the transition temperature of the 18% Cr-2% Mo alloys from the present study (Table 3). None of these steels contained martensite after quenching from 1150°C, so the effect on transition temperature must be attributed to grain growth and the distribution of carbonitride precipitates.

The effect of molybdenum content on impact properties at chromium contents of 17–18% and 25–26% was studied in some detail. Fig. 6 gives the results for 17% Cr alloys with low interstitial contents. As expected from the previous data, the low interstitial alloys suffered a rather small increase in transition temperature as a result of the 1150°C heat treatment (Fig. 7) as compared to the base anneal at 815°C. Increasing molybdenum content from 0 to 3% had no marked effect on transition temperatures; the effect of molybdenum was undoubtedly overshadowed by other variables.

Similar tests were carried out on 25% Cr alloys

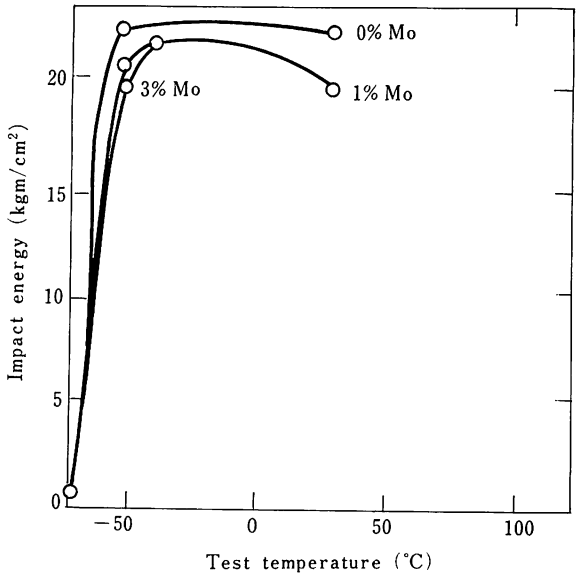

Fig. 6. Transition curves for quarter-size Charpy V-notch impact specimens of 17% Cr-0 to 3% Mo-(C+N)≤ 0·012% ferritic stainless steels (Heats P270A, V98–99) heat treated at 815°C for 1 hr and water quenched. ASTM grain size range 6–7.

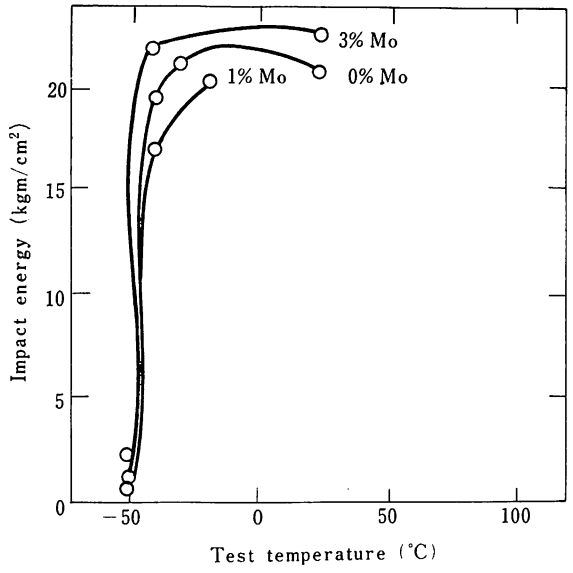

Fig. 7. Transition curves for quarter-size Charpy V-notch impact specimens of 17% Cr–0 to 3% Mo–(C+N)≤ 0·012% ferritic stainless steels (Heats P270A, V98–99) heat treated at 815°C + 1150°C for 1 hr and water quenched. ASTM grain size range 0–1.

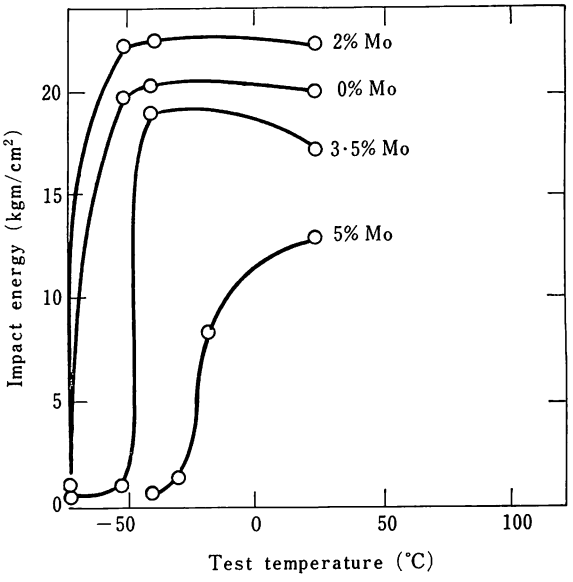

Fig. 8. Transition curves for quarter-size Charpy V-notch impact specimens of 25% Cr–0 to 5% Mo–(C+N)≤ 0·019% ferritic stainless steels (Heats V233A-C, V234A) heat treated at 980°C for 1 hr and water quenched. ASTM grain size range 1–3.

(Fig. 8). The base annealing treatment was at 980°C, a temperature that did not produce visible manifestations of chi or sigma phase in any of the alloys. The 2% Mo addition increased the upper shelf energy slightly, while the 3·5 and 5% additions tended to increase transition temperature and decrease the upper shelf energy. Quenching from 1150°C did not increase transition temperatures of any of the alloys (Fig. 9), but in fact decreased the transition temperature of the 5% Mo alloy. This suggests that the 980°C anneal did allow the presence of a slight amount of sigma or chi phase even though it was not readily evident in the microstructure. Phase diagram work by McMullin and coworkers[8] indicated, in fact, that a 25% Cr alloy containing 5% Mo is within the ferrite plus chi region at 900°C. Quenching from the higher temperature would avoid the formation of a second phase.

An indication of the impact-transition temperatures that can be obtained from commercial electron-beam-refined 26% Cr-1% Mo alloy is given in Fig. 10[5]. The range of values plotted here represents both longitudinal and transverse specimens machined from rolled bar of 63mm-square section. The scatter band is the result (in addition

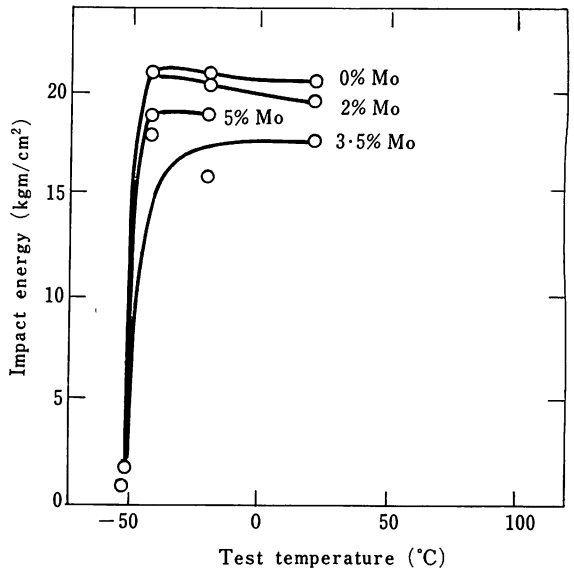

Fig. 9. Transition curves for quarter-size Charpy V-notch impact specimens of 25% Cr–0 to 5% Mo–(C+N)≤ 0·019% ferritic stainless steels (Heats V233A-C, V234A) heat treated at 980°C + 1150°C for 1 hr and water quenched. ASTM grain size range 0–1.

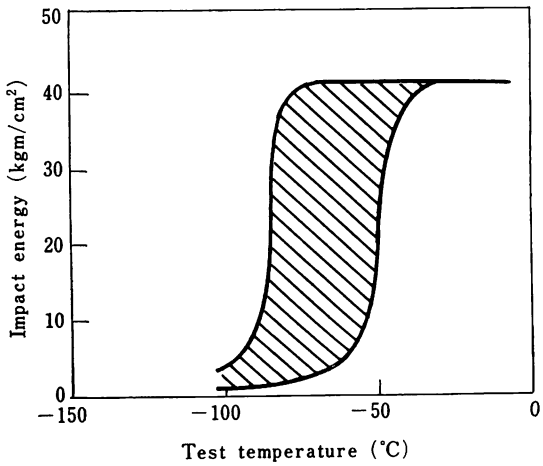

Fig. 10. Charpy V-notch impact-transition temperature range for commercially produced, electron-beam melted ferritic stainless steel containing 26% Cr and 1% Mo.

to specimen orientation) of variations in thermal treatment and cooling rate.

Impact-transition tests were carried out on a series of air-melted alloys representing combined carbon and nitrogen contents generally above 0·06 % total. The higher interstitial content caused a definite increase in transition temperature of all alloy types. The effect of molybdenum was similar to that observed in the low-interstitial alloys; in the 18% Cr series quenched from 815°C, molybdenum contents up to 2% had little effect on impact toughness (Fig. 11). In the 18% Cr-3·5% Mo steel, a small amount of chi phase was present, and a larger amount was observed in the 18% Cr-5% Mo steel. This may be the principal cause of the decrease in impact properties at these molybdenum contents. Quenching from 1150°C (Fig. 12) resulted in much higher transition temperatures for all of the alloys. The extreme effect on the molybdenum-free alloys was accounted for by the formation of untempered martensite.

The high-interstitial 25% Cr alloys annealed at 815°C had higher transition temperatures than the corresponding 18% Cr alloys (compare Fig. 13 and 11); the effect of molybdenum in the 18% and 25% Cr steel was almost identical. The molybdenum additions up to 2% had little effect on transition temperature. An intermetallic compound, probably

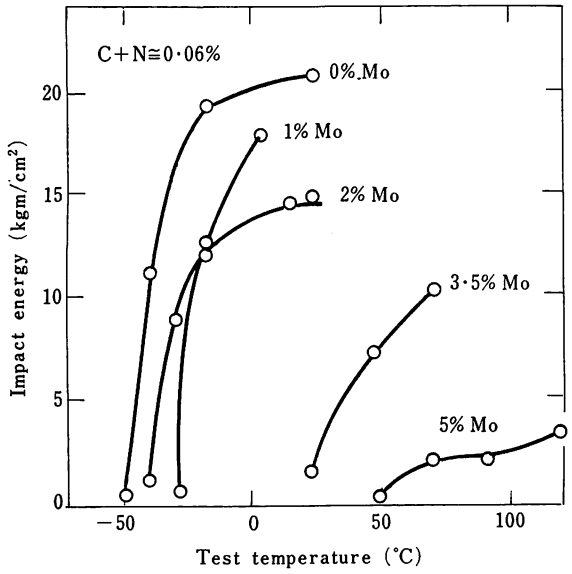

Fig. 11. Transition curves for quarter-size Charpy V-notch impact specimens of air-melted 18% Cr–0 to 5% Mo ferritic stainless steels (Heats 4354A-E) heat treated at 815°C for 1 hr and water quenched. ASTM grain size range 6–7.

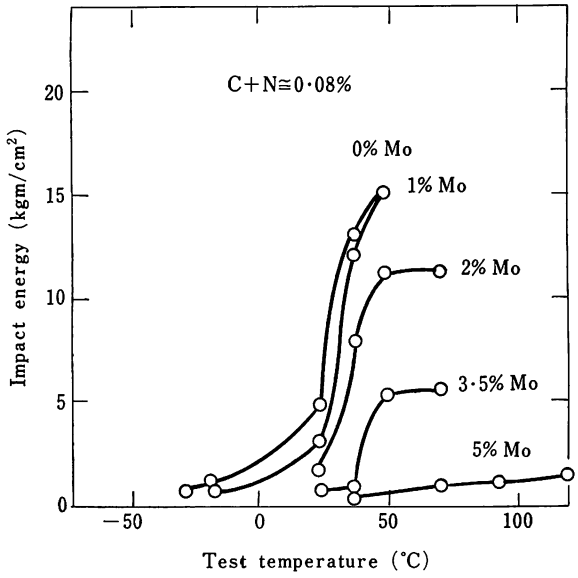

Fig. 13. Transition curves for quarter-size Charpy V-notch impact specimens of air-melted 25% Cr–0 to 5% Mo ferritic stainless steels (Heats 4355A-E) heat treated at 815°C for 1 hr and water quenched. ASTM grain size range 6–7.

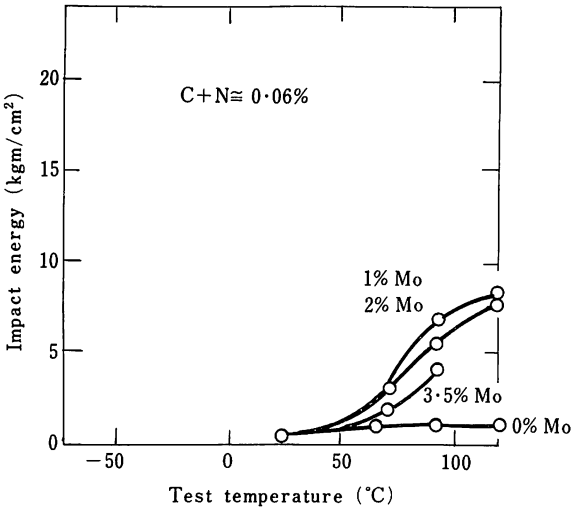

Fig. 12. Transition curves for quarter-size Charpy V-notch impact specimens of air-melted 18% Cr–0 to 3·5% Mo ferritic stainless steels (Heats 4354A-D) heat treated at 815°C + 1150°C for 1 hr and water quenched. ASTM grain size range 1–3.

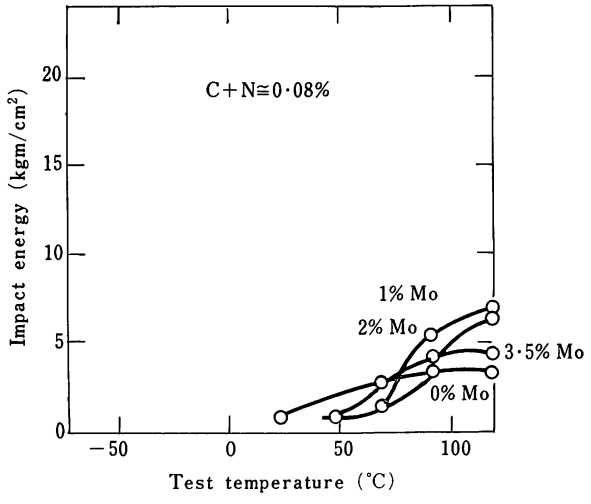

Fig. 14. Transition curves for quarter-size Charpy V-notch impact specimens of air-melted 25% Cr–0 to 3·5% Mo ferritic stainless steels (Heats 4355A-D) heat treated at 815°C + 1150°C for 1 hr and water quenched. ASTM grain size range 0–1.

chi, was present in the 3·5 and 5% Mo alloys and probably accounted for the very poor impact resistance of these alloys. The results obtained on quenching from 1150°C (Fig. 14) were nearly identical with those obtained on the 18% Cr alloys (Fig. 12). It is concluded that the toughness of high interstitial ferritic stainless steels quenched from 1150°C is mainly determined by the precipitation of carbonitrides.

Comparison of Fig. 11 and 13 suggests that an increase in chromium content from 18 to 25% results in a significant increase in transition temperature of air-melted (high-interstitial) alloys. These results are in agreement with those of Binder and Spendelow[1] which showed a marked increase in sensitivity to carbon plus nitrogen content above about 20% Cr.

The effects of chromium content on the transition temperatures of vacuum-melted (low-interstitial) alloys containing 2% Mo are shown in Fig. 15 and 16. The observed increases in transition temperature associated with increasing chromium are in contrast to the results of Binder and Spendelow[1] who showed a decrease in (Izod) transition temperature in *high-purity*, straight chromium steel as chromium increased from 12 to 25%. These conflicting results may be explained on the basis of grain size. The specimens used to describe the transition temperatures plotted in Fig. 15 and 16 were obtained from relatively lightly worked plates. The resulting microstructures were coarse-grained. In contrast, the steels used in Binder and Spendelow's study had somewhat finer grain sizes. It has been demonstrated[9] that the impact-transition temperature of ferritic stainless steels is quite sensitive to grain size. For example, a reduction in grain size from ASTM 2–3 to ASTM 5–6 resulted in a 60°C decrease in transition temperature. Thus the vacuum-melted steels represented in Fig. 15 and 16 represent an increasing sensitivity to interstitial content with increasing chromium content that would not be manifested in fine-grained high-purity steels.

Tensile tests were carried out on flat specimens machined from 3mm-thick plate representing selected compositions. Specimens were taken either from annealed plate or from blanks containing a tungsten-inert-gas weld oriented paralled to the tension axis.

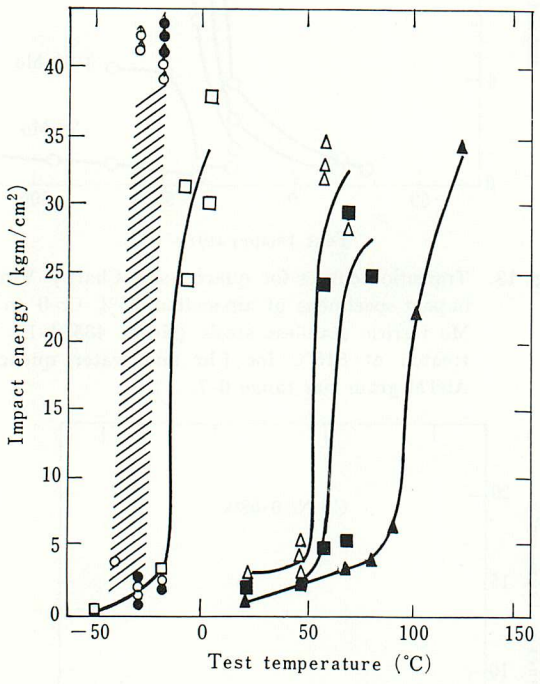

Fig. 15. Results of Charpy V-notch impact tests on full-size specimens of vacuum-induction melted ferritic stainless steels containing 2% Mo and 14 to 28% Cr. 14% Cr and 18% Cr steels annealed 1 hr at 815°C, and water quenched. 20 to 28% Cr steels annealed 1 hr at 980°C and water quenched. ASTM grain size No. 1.

○ 14% Cr–2% Mo (Heat V537B)
● 18% Cr–2% Mo (Heat V530B)
□ 20% Cr–2% Mo (Heat V468)
■ 22·5% Cr–2% Mo (Heat V472A)
△ 25% Cr–2% Mo (Heat V470)
▲ 28% Cr–2% Mo (Heat V472B)

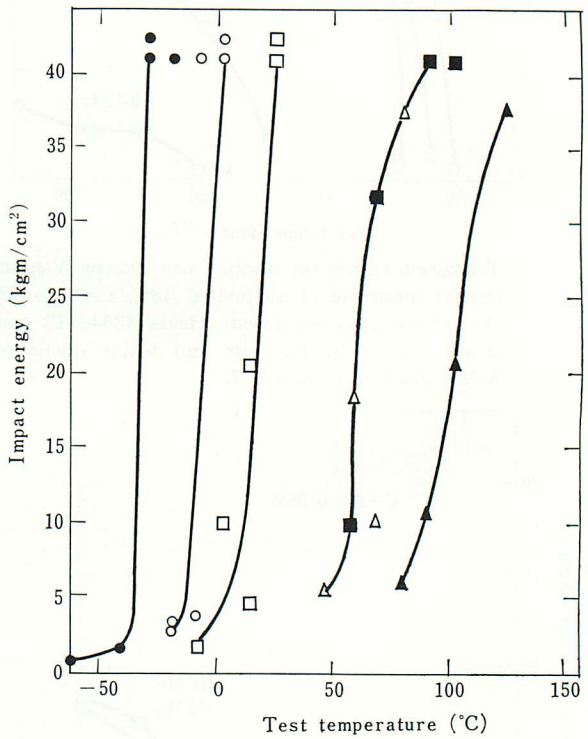

Fig. 16. Results of Charpy V-notch impact tests on full-size specimens of vacuum-induction melted ferritic stainless steels containing 2% Mo and 14 to 28% Cr. Specimens annealed at 980°C + 1150°C for 1 hr and water quenched. ASTM grain size No.00.

○ 14% Cr–2% Mo (Heat V537B)
● 18% Cr–2% Mo (Heat V530B)
□ 20% Cr–2% Mo (Heat V468)
■ 22·5% Cr–2% Mo (Heat V472A)
△ 25% Cr–2% Mo (Heat V470)
▲ 28% Cr–2% Mo (Heat V472B)

Table 4. Results of tensile tests on ferritic alloys.

Alloy	Nominal composition (wt %)				Condition	0·2% Yield strength (kg/mm²)	Tensile strength (kg/mm²)	Elongation in 50mm %
	C	N	Cr	Mo				
V233A	0·002	0·015	25	—	Annealed	29·4	41·5	35
					Welded	34·5	41·9	10
Comm*	0·005	0·015	26	1	Annealed	32·2	45·6	44
					Welded	37·5	50·3	26
V233B	0·002	0·015	25	2	Annealed	35·3	47·6	31
					Welded	39·4	41·8	21
V234A	0·002	0·015	25	3·5	Annealed	38·0	51·7	30
					Welded	44·4	54·6	22
V233C	0·002	0·015	25	5	Annealed	43·3	57·2	29
					Welded	49·6	62·3	18
P526	0·001	0·004	18	2	Annealed	24·7	42·4	32·5
					Welded	26·9	43·2	30·7
P531A	0·002	0·01	18	2	Annealed	28·3	44·3	35
					Welded	30·4	43·8	35·5
P531B	0·002	0·02	18	2	Annealed	29·0	45·4	33
					Welded	37·8	49·2	22
P527A	0·01	0·004	18	2	Annealed	23·9	41·6	25
					Welded	34·5	46·3	21·5
P527B	0·02	0·004	18	2	Annealed	24·5	42·9	31·5
					Welded	39·7	50·8	15·5
P529A	0·01	0·02	18	2	Annealed	28·7	46·0	30·5
					Welded	43·9	54·3	7·5
P529B	0·02	0·02	18	2	Annealed	29·2	46·5	27
					Welded	50·3	62·3	10
4356A	0·04	0·03	18	2	Annealed	31·4	49·9	36
					Welded	34·0	50·0	22

* Commercial alloy produced by electron-beam refining[5,26].

Test results are given in Table 4. Typical data representing 13-mm plate rolled from electron-beam-melted 26% Cr-1% Mo are included for comparison purposes.

Considering the steels containing nominally 25% Cr, increasing tensile strengths were associated with increasing molybdenum contents over the range from zero to 5%. Tensile ductility of annealed samples was unaffected over the same range in molybdenum content.

The low-interstitial 25% Cr alloy suffered a significant loss in ductility on welding. Molybdenum additions were helpful in retaining greater ductility in the as-welded condition. On the other hand, the higher purity 18% Cr-2% Mo alloys were least affected by welding, as evidenced by elongation values nearly as high after welding as prior to welding. Increased interstitial content was clearly detrimental to weld ductility of the 18% Cr-2% Mo alloys. The effect of carbon was more pronounced than that of nitrogen, since 0·01% C reduced elongation of the as-welded specimen while 0·01% N did not.

In view of the observed effects of interstitials (particularly carbon) on toughness and ductility and on sensitivity to welding, it was considered desirable to define some interstitial effects on corrosion properties of ferritic stainless steels.

Sensitivity to intergranular corrosion after welding or other high-temperature heat treatments has been a serious problem with ferritic steels. Control of carbon and nitrogen content to suitably low levels prevents intergranular corrosion[10–13], as is shown in Table 5. It will be noted that the tolerance for nitrogen, at least, increases with increasing chromium and molybdenum content. It has been reported that electron-beam-melted 26% Cr-1% Mo steels with very low interstitial contents are immune to intergranular corrosion even in the welded condition[3].

Wert[14] has shown that small molybdenum additions reduce the diffusion rate of nitrogen in iron-molybdenum-nitrogen alloys. This then may be one of the important contributions of molybdenum toward the intergranular-corrosion properties of ferritic stainless steels. Kawabe, Nakagawa and

Mukoyama[15] have shown the same mechanism to be important in austenitic stainless steels containing molybdenum.

The effects of both chromium and molybdenum in facilitating the attainment of passivity are clearly demonstrated by exposure to inorganic acids (Table 6). This result is in accord with anodic polarization measurements made at our laboratory[16–18].

It can be seen, however, in the case of alloys that are corroding in the active state, that corrosion rate decreases with increasing molybdenum content, but increases with increasing levels of chromium. In oxygen-saturated sulfuric acid, for example, the 25% Cr steel corroded at a rate over eight times that of the 25% Cr-2% Mo steel. Increasing the chromium content of the molybdenum-free steels from 18% to 25% resulted in over a four-fold increase in corrosion rate in the same medium.

Resistance to pitting corrosion is also markedly improved by lowering the carbon and nitrogen content to very low values[14,18]. The results in Table 7 illustrate the effect of interstitial levels and also show the very beneficial effects of increased chromium and molybdenum content on pitting resistance. The pitting resistance displayed by the low-interstitial high-alloy ferritic steels is greater than has been observed for any iron-base, austenitic alloy.

The ferritic stainless steels have demonstrated great superiority to austenitic stainless steels in resistance to stress-corrosion cracking[19,20]. It has been found, however, that the nickel, copper and cobalt content of ferritic steels must be kept at low levels to preserve resistance to stress corrosion cracking[10].

Table 5. Results of modified Strauss test[27] for susceptibility to intergranular corrosion of unstabilized ferritic stainless steels.

Alloy	Nominal composition (wt %)				As annealed[a]			As welded[b]
	Cr	Mo	C	N	815℃	1040℃	1150℃	
P270A	17	—	0·002	0·01	Pass[c]	Pass	Fail	—
P270B	17	—	0·002	0·02	Pass	Fail	Fail	—
P271A	17	—	0·01	0·009	Pass	Fail	Fail	—
P526	18	2	0·001	0·004	Pass	Pass	Pass	Pass
P531A	18	2	0·002	0·01	Pass	Pass	Pass	Fail
P527A	18	2	0·01	0·004	Pass	Pass	Fail	Fail
V468	20	2	0·003	0·01	Pass	Pass	—	Fail
V472A	22·5	2	0·003	0·011	Pass	Pass	—	Fail
V233B	25	2	0·002	0·017	Pass	Pass	—	Pass
V471	26	1	0·003	0·016	Pass	Pass	—	Fail[d]

a Samples were heat treated for 1 hr at indicated temperature and water quenched.
b The weld was made using the tungsten-inert-gas technique with no filler metal added.
c Evaluated by bending the specimen through 180° and examining the bend for cracks using a magnification of 20X.
d Commercial electron-beam-refined 26% Cr-1% Mo steel reportedly passes the modified Strauss test after welding.

Table 6. Results of 24 hr exposure tests in inorganic acids at 25°C.*

Alloy	Nominal composition (wt %)		Corrosion rate (mg/dm²/day)		
	Cr	Mo	1N H_2SO_4 O_2	0·1N HCl O_2	1N HCl N_2
V537A	14	0	1 550	1 160	135
V537B	14	2	1 080	501	208
V530A	18	0	4 330	1 080	832
V530B	18	2	1 420	0	267
V468	20	2	2 330	0	710
V472A	22·5	2	1 920	0	936
V233A	25	0	20 000	4 500	39 400
V233B	25	2	2 450	0	1 260
V234A	25	3·5	0	0	556
V233C	25	5	0	0	307
V471	26	1	3 760	0	2 560
V472B	28	2	2 250	0	1 590

* Specimens activated with magnesium at start of test.

Table 7. Results of tests in 10% $FeCl_3 \cdot 6H_2O$+0·1N HCl.

Alloy	Nominal composition (wt %)				Corrosion rate (mg/dm²/day)		
	Cr	Mo	C	N	25℃	50℃	70℃
4354 A	18	0	0·03	0·03	7200	—	—
4354 C	18	2	0·03	0·03	5300	—	—
4354 E	18	5	0·03	0·03	220	—	—
V530A	18	0	0·002	0·003	214	—	—
V530B	18	2	0·004	0·004	177	—	—
V468	20	2	0·003	0·01	14	—	—
V472A	22·5	2	0·003	0·011	0	—	—
4355 A	25	0	0·04	0·05	1200	—	—
4355 C	25	3·5	0·04	0·05	560	—	—
V233A	25	0	0·002	—	40	—	—
V233B	25	2	0·002	0·017	0	380	—
V234A	25	3·5	0·002	—	0	0	415
V233C	25	5	0·002	0·013	0	0	0
V471	26	1	0·003	0·016	0	—	—

4. STABILIZED STEELS

Several comprehensive studies have been made aimed at stabilizing ferritic stainless steels with additions of titanium or niobium[11,21,22]. Lula, Lena and Kiefer[11], for example, concluded that titanium and niobium additions were not effective in eliminating intergranular corrosion of ferritic steels in very highly corrosive environments such as boiling 65% HNO_3 and HF-HNO_3 mixtures, but the presence of these elements did raise the sensitizing temperature.

For the present program, air-melted heats of the 18% Cr-2% Mo steel were made with titanium additions up to 2% and niobium additions up to 1%. Specific compositions are shown in Table 1.

Titanium contents up to about ten times the combined carbon plus nitrogen content of the 18% Cr-2% Mo steel had no significant effect on impact-transition temperature (Fig. 17). Additions resulting in titanium residuals of 1·27 and 1·86% resulted in the precipitation of a second phase that markedly increased impact-transition temperature.

Titanium-stabilized steels containing 18% Cr and 2% Mo have been made commercially using an oxygen-argon melting technique. Minimum titanium contents in the range from 10 to 12 times the combined carbon plus nitrogen contents are speci-

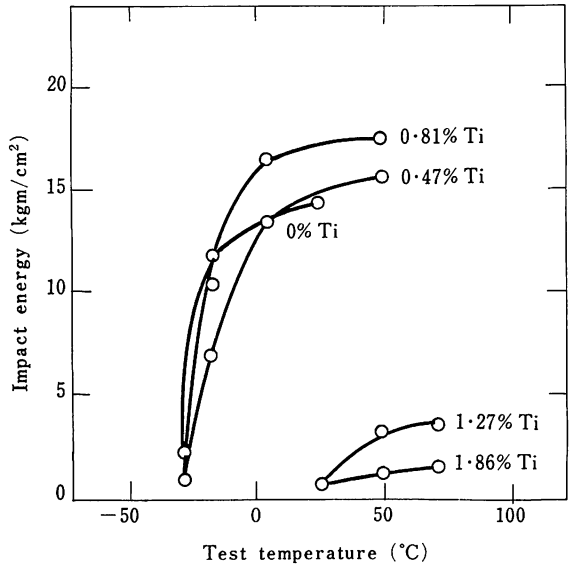

Fig. 17. Transition curves for quarter-size Charpy V-notch impact specimens of air-melted 18% Cr–2% Mo–0 to 1·86% Ti ferritic stainless steels (Heats 4354C, 4073A-D) heat treated at 815°C for 1 hr and water quenched. ASTM grain size range 6–7.

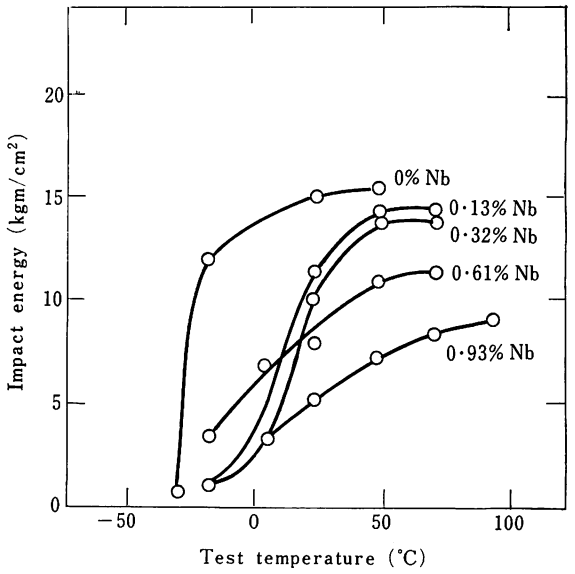

Fig. 18. Transition curves for quarter-size Charpy V-notch impact specimens of air-melted 18% Cr–2% Mo–0 to 0·93% Nb ferritic stainless steels (Heats 4354C, 4356B-E) heat treated at 815°C for 1 hr and water quenched. ASTM grain size range 6–7.

fied. It is reasonable to assume from the evidence presented in Fig. 17 that titanium contents in the range from 0·25 to 0·35% would have an insignificant effect on the transition temperature of annealed 18% Cr-2% Mo steel.

Niobium additions between 0·1 and 0·9% tended to increase the transition temperature of 18% Cr-2% Mo alloys in the annealed state (Fig. 18). No second phases were observed in any of the alloys, but niobium did retard recrystallization to the extent that the 0·93% Nb alloy was not fully recrystallized after one hour at 815°C. This may account for the lack of a well defined transition temperature for the 0·93% Nb steel.

Titanium and niobium were both effective in retarding the increase in transition temperature associated with heat treatment at 1150°C (Fig. 19 and 20). Titanium appears more effective than niobium in reducing degradation in toughness associated with high temperature exposures. A titanium content of 0·47%, for example, limited the increase in transition temperature (resulting from heating to 1150°C) to only about 30°C.

From the studies performed here, it is evident that titanium carbonitrides and, to a somewhat lesser extent, niobium carbonitrides are less harmful to the toughness of ferritic stainless steels than chromium carbonitrides. A difference in precipitate size and distribution has, in fact, been observed in ferritic stainless steels with and without titanium. In general, precipitates in titanium-containing steels are larger, less randomly distributed, and less soluble at high temperatues.

Tensile test results on annealed or tungsten-inert-gas welded plate samples of stabilized steels are given in Table 8. It is evident that the titanium-stabilized steel suffered less loss in room-temperature ductility after welding than the niobium-stabilized grade. The niobium-stabilized steel lost ductility to about the same extent as the unstabilized high-interstitial alloy reported in Table 4. Thus, in this test as well as in the impact tests, titanium was more effective than niobium in preventing degradation of mechanical properties of 18% Cr-2% Mo alloys as a result of welding or high-temperature heat treatment.

As indicated in Table 9, nominal titanium and niobium contents of 0·5 and 0·6%, respectively, were effective in preventing susceptibility to intergranular corrosion in the modified Strauss test.

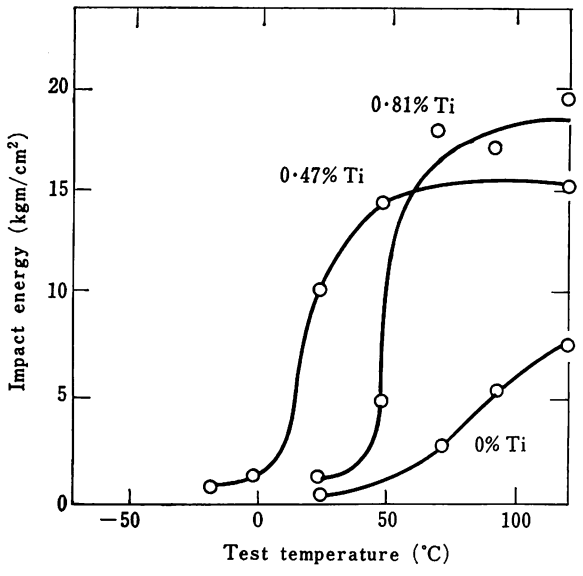

Fig. 19. Transition curves for quarter-size Charpy V-notch impact specimens of air-melted 18% Cr–2% Mo–0 to 0·81% Ti ferritic stainless steels (Heats 4354C, 4073A-B) heat treated at 815°C + 1150°C for 1 hr and water quenched. ASTM grain size range 1–3.

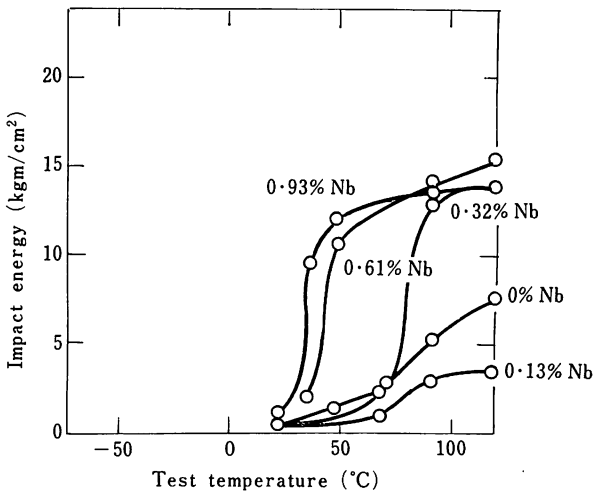

Fig. 20. Transition curves for quarter-size Charpy V-notch impact specimens of air-melted 18% Cr–2% Mo–0 to 0·93% Nb ferritic stainless steels (Heats 4354C, 4356B-E) heat treated at 815°C + 1150°C for 1 hr and water quenched. ASTM grain size range 1–4.

Table 8. Results of tensile tests on stabilized ferritic alloys.

Alloy	Nominal composition (wt %)						Condition	0·2% Yield strength (kg/mm²)	Tensile strength (kg/mm²)	Elongation in 50 mm (%)
	C	N	Ti	Nb	Cr	Mo				
4073A	0·03	0·04	0·5	—	18	2	Annealed	27·5	47·1	34
							Welded	30·7	48·4	30
4356D	0·03	0·03	—	0·6	18	2	Annealed	31·5	51·7	28
							Welded	30·5	51·0	21

Table 9. Results of modified Strauss test[26] for susceptibility to intergranular corrosion of 18% Cr-2% Mo ferritic stainless stabilized with titanium or niobium.

Alloy	Nominal composition (wt %)				As annealed[a]				
	Ti	Nb	C	N	815℃	930℃	1040℃	1150℃	Welded[b]
4354C	—	—	0·03	0·03	Pass[c]	Fail	—	—	—
4073A	0·5	—	0·03	0·04	Pass	Pass	Pass	Pass	Pass
4356C	—	0·3	0·03	0·03	—	Pass	Fail	Fail	—
4356D	—	0·6	0·03	0·03	—	—	Pass	Pass	Pass
4356E	—	0·9	0·03	0·03	—	—	Pass	—	Pass

[a] Samples were heat treated for 1hr at indicated temperature and water quenched.
[b] The weld was made using the tungsten-inert gas technique with no filler metal added.
[c] Evaluated by bending the specimen through 180° and examining the bend for cracks using a magnification of 20 ×.

5. APPLICATIONS

Existing and potential applications for high-purity ferritic stainless steels such as 18% Cr-2% Mo and 26% Cr-1% Mo are based on considerations of economics and property advantages compared with austenitic grades.

The thermal conductivity of these ferritic grades is approximately 20% higher than that of the most common austenitic steels. Some applications of the ferritic grades are based on the fact that they exhibit thermal expansion coefficients significantly lower than the austenitic stainless steels. The electrical resistivity of the 26% Cr-1% Mo alloy is almost 30% lower than that of SUS 27 stainless steel.

Typical room-temperature tensile properties of the two high-purity ferritic grades are compared below with SUS 27. Materials are in the annealed condition.

Type	0·2% Yield strength (kg/mm²)	Tensile Strength (kg/mm²)	Elongation (%)
18-2	28·1	47·8	33
26-1	37·3	50·6	33
SUS 27	24·6	56·3	60

The ferritic steels generally have lower work-hardening coefficients than the austenitic grades. Because of this property, the high-purity ferritic steels are particularly well suited to flow forming operations such as cold heading.

Many potential applications for the high-purity ferritic grades are based on superior corrosion properties in a wide variety of environments[4,5,10,22-25].

Areas where high-purity ferritic stainless steels have been considered include the following:

Chemical equipment
Refinery equipment
Fertilizer manufacturing equipment
Pulp and paper manufacturing equipment
Food and beverage processing equipment
Marine hardware
Desalination equipment
Waste treatment equipment
Heaters and dryers
Heat exchangers
Transport tanks
Fasteners

6. CONCLUSIONS

Data developed for this program confirm the sensitivity of impact resistance and weld ductility of ferritic stainless steels to carbon and nitrogen contents. The results are summarized for 17% Cr steels in Fig. 21. Although quantitative relationships have not resulted from the present work, the limiting values of carbon plus nitrogen contents consistent with good ductility and toughness are probably related to grain size.

In fully ferritic alloys, molybdenum had little effect on transition temperature, as illustrated in Fig. 22. Moderate molybdenum contents had a clearly beneficial effect on tensile ductility after welding.

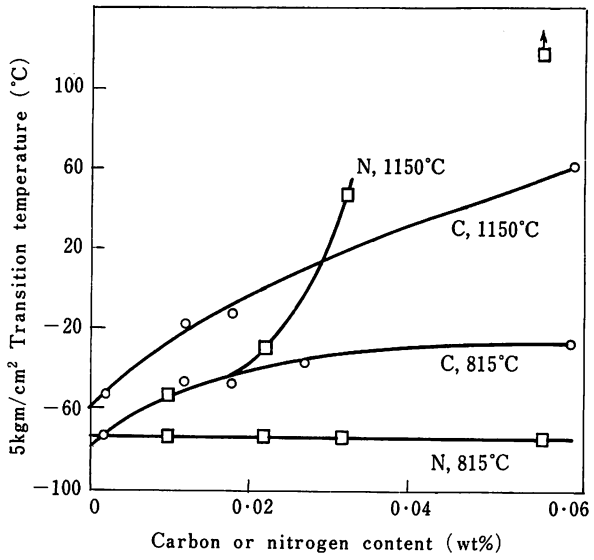

Fig. 21. Transition temperatures for quarter-size Charpy V-notch specimens of 17% Cr steels (Heats P270 A-D and P271A-D) water quenched from the indicated temperatures as a function of carbon or nitrogen content.

The combination of molybdenum contents of 3·5% or higher and an annealing temperature of 815° to 980°C sometimes resulted in the presence of intermetallic compounds, such as chi or possibly sigma. The presence of these phases had an adverse effect on toughness.

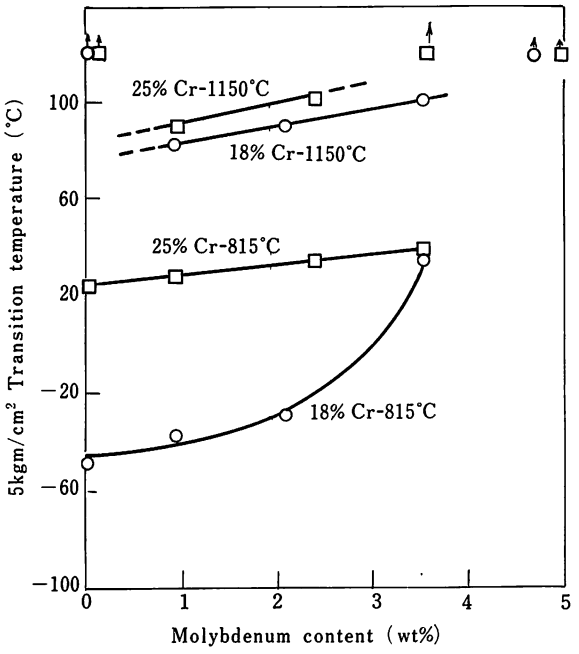

Fig. 22. Transition temperatures for quarter-size Charpy V-notch specimens of air-melted commercial-purity ferritic stainless steels (Heats 4354A-E and 4355 A-E) water quenched frem the indicated temperatures as a function of molybdenum content.

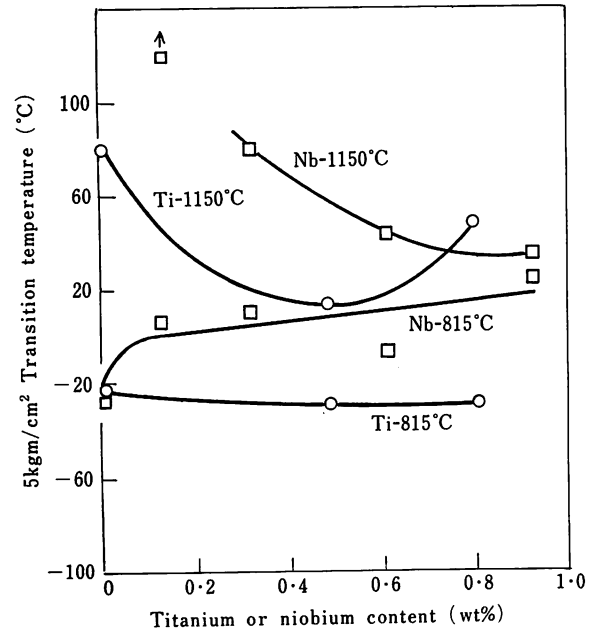

Fig. 23. Transition temperatures for quarter-size Charpy V-notch specimens of air-melted commercial-purity 18% Cr-2% Mo steels (Heats 4073A-D, 4354C and 4356B-E) water quenched from the indicated temperatures as a function of titanium or niobium content.

In alloys of higher interstitial content such that the formation of austenite was possible at 1150°C, both increased chromium and molybdenum contents helped minimize the degradation of impact resistance occasioned by high-temperature heat treatment, reflecting the suppression of austenite formation and the subsequent formation of untempered martensite on cooling.

Stabilizing additions of titanium or niobium were helpful in reducing the detrimental effects of high-temperature heat treatment on the impact resistance of air-melted (high-interstitial) alloys (Fig. 23). Titanium was also helpful in maintaining weld ductility of such alloys. However, niobium was somewhat harmful to the impact resistance of properly annealed alloys.

The 18% Cr–2% Mo steel is a versatile material that can be produced by high-vacuum techniques or by other methods with titanium stabilization. Adequate toughness and tensile ductility (either as annealed or welded) are manifested by both the low-interstitial and the titanium-stabilized grades of the 18% Cr-2% Mo steel. Both grades are resistant to intergranular corrosion in the annealed or welded conditions as evidenced by the results of the modified Strauss test.

REFERENCES

1) W.O. Binder and H.R. Spendelow, Jr.: Trans. ASM **43** (1951), p. 759
2) J. Hochmann: Rev. Met. **48** (1951) no. 10, p. 734
3) R.N. Wright: "Mechanical Behavior and Weldability of a High Chromium Ferritic Stainless Steel as a Function of Purity" Presented at the Annual Meeting of the National Association of Corrosion Engineers, Chicago, 1971
4) R.J. Knoth: "Electron Beam Continuous Hearth Refining and its Place in the Specialty Steel Industry" Presented at the Specialty Steel Seminar, Pittsburgh, 1969
5) Anon.: Preliminary Data Sheet EB26 Cr+1 Mo, Airco Vacuum Metals Div. of Air Reduction Co., Inc.
6) Anon.: Uniloy EB26–1, a High Purity Ferritic Stainless Steel, Universal-Cyclops Specialty Steel Division of Cyclops Corp., 1970
7) J.J. Demo: "Mechanism of High-Temperature Embrittlement and Loss of Corrosion Resistance in AISI Type 446 Stainless Steel" Presented at the Annual Meeting of the National Association of Corrosion Engineers, Philadelphia, 1970
8) J.G. McMullin, S.F. Reiter and D.G. Ebeling: Trans. ASM **46** (1954), p. 799
9) Personal communication, Edelstahlwerk Witten A.G.
10) A.P. Bond: Trans. AIME **245** (1969), p. 2127
11) R.A. Lula, A.J. Lena and G.C. Kiefer: Trans. ASM **46** (1954), p. 197
12) A.P. Bond and E.A. Lizlovs: J. Electrochem. Soc. **116** (1969), p. 1305
13) R.J. Knoth, G.E. Lasko and W.A. Matejka: Chem. Eng. **77** (1970), no. 11, p. 170
14) C. Wert: Trans. AIME **294** (1952), p. 602
15) Y. Kawabe, R. Nakagawa and T. Mukoyama: Trans.

Iron and Steel Inst. of Japan **8** (1968), p. 353
16) E.A Lizlovs and A.P. Bond: J. Electrochem. Soc. **116** (1969), p. 574
17) E.A. Lizlovs and A.P. Bond: J. Electrochem. Soc. **118** (1971), p. 22
18) A.P. Bond and E.A. Lizlovs: Werkstoffe u. Korrosion, **21** (1970), p. 336
19) A.P. Bond and H.J. Dundas: Corrosion **24** (1968), p. 334
20) F.K. Kies, I.A. Franson and B. Coad: Chem. Eng. **77** (1970), no. 6, p. 150
21) L. Balaban and M. Patriciu: Metalurgia (Bucharest) **21** (1969), no. 1, p. 30
22) E. Brauns, W. Schwenk and H.E. Buehler: Stahl u. Eisen **84** (1964), p. 790
23) R. Oppenheim: DEW-Tech. Ber. **7** (1967), p. 49
24) Anon.: Vaculoy 26-1 Stainless Steel, Jones & Laughlin Steel Corporation
25) C.D. Schwartz, I.A. Franson and R.J. Hodge: Chem. Eng. **77** (1970), no. 8, p. 166
26) R. J. Knoth: "Weldability of E-Brite 26-1, A Status Report," Airco Vacuum Metals, Feb. 3, 1971.
27) ASTM A262-70

Embrittlement of High-Strength Steels by Hydrogen Absorption

A. Tokuda K. Ohnishi

The Japan Steel Works, Ltd.

Research Center, Muroran Plant

The phenomenon of hydrogen embrittlement in high-strength steels has been investigated in detail for a long time. In spite of many hypotheses, however, its mechanism has not yet been completely solved because of inadequate data on the behavior of hydrogen in steel and on the role of hydrogen in embrittlement. Consequently, we are studying hydrogen occlusion, hydrogen diffusion and hydrogen embrittlement in hot-rolled high-strength steel plate and high-strength low-alloy steel forgings. Our investigations on the directionality of hydrogen occlusion, diffusion and embrittlement in hot-rolled steel plate and on the hydrogen-induced delayed failure of high-strength low-alloy steels are reported in this paper.

1. Directionality of hydrogen occlusion and diffusion in hot-rolled steel plate

Since hydrogen embrittlement of steel appears in the temperature range of -80 to +150°C, it is interesting to study the behavior of hydrogen diffusion and occlusion in steel within this temperature range.

The published data on the low-temperature diffusion rate of hydrogen in steel are very scattered; moreover, the data depart from the extrapolation of high-temperature data at about 150 to 300°C and fall sharply at lower temperatures (Fig. 1). The scatter of these data is caused not only by the measuring methods for diffusion rate but also by hydrogen trapping in defects such as cracks. microcavities, pores, precipitates and nonmetallic inclusions. These defects in hot-rolled steel plate may have a directional distribution resulting from hot rolling. Therefore, hydrogen absorption and diffusion in hot-rolled steel plate were investigated from this point of view.

Hydrogen diffusion and occlusion in steel plate were found to be directional. That is, the amount of hydrogen occlusion in specimens parallel to the hot-rolled surface was higher than that of specimens taken through the plate thickness (Fig. 2 and 3). The hydrogen diffusion rate was fastest in the direction of rolling, slower transverse to the rolling direction and slowest in the through-thickness direction (Fig. 5). This directionality of hydrogen diffusion, however, gradually diminished as the temperature increased.

Next the site of hydrogen evolution was determined by microscopic observation of the specimen surface. The indications were that hydrogen was actively evolved from the nonmetallic inclusion-matrix interface in the steel plates but that there was scarcely any evolution from the matrix (Photo. 3 and 4).

These results point to the possibility that hydrogen is trapped in the interface between the matrix and nonmetallic inclusions and that this trapping retards hydrogen diffusion into the plate.

2. Directionality of hydrogen embrittlement in steel plate

The influence of hydrogen concentration is especially remarkable among the various factors affecting hydrogen embrittlement of steel. As already shown, hot-rolled steel plate displays a directionality in hydrogen occlusion that may relate to embrittlement of steel plate by hydrogen occlusion. Tensile test pieces were taken from the hot-rolled plate in various directions. After immersion in a 0·5% HAc+2000 ppm H_2S solution, these specimens were analyzed for hydrogen and tested for hydrogen embrittlement and recovery.

The degree of embrittlement varied with the direction from which each test piece was taken from the steel plate. Specimens parallel to the rolling direction had greater hydrogen embrittlement than those from the thickness direction (Fig. 7).

Hydrogen embrittlement of steel appears during plastic deformation as a result of hydrogen dissolved in the steel. This is a reversible phenomenon since the ductility is recovered by effusion of hydrogen during aging. The rate of recovery is determined by the hydrogen diffusion rate, aging temperature and aging time.

The results of aging at 22°C are shown in Fig. 9. As can be seen, the recovery of ductility increased with aging time, and the recovery rate was highest in the specimen Y-Z taken from the thickness direction and lowest in specimen X-Y parallel to the rolling surface. Thus, we noticed a high degree of directionality in the recovery of ductility. The recovery rate increased with the aging temperature but at higher temperatures there was no directionality such as was seen near to room temperature (Fig. 10).

Fish eyes were observed in the fractured surface of the embrittled specimen. The fish eyes were formed as a function of hydrogen charging time and extended over the plane parallel to the rolled surface. The facet of the fish eye was quasi-cleavage, which is characteristic of hydrogen embrittlement, while the balance of the fracture was of a ductile dimple type (Photo. 6).

When the test pieces were aged after hydrogen charging, they showed a high degree of ductility recovery. Nevertheless, even after aging, the fish eyes on the fracture surface remained on the plane parallel to the rolled surface.

Hydrogen embrittlement of steel as a phenomenon occurs at low strain rates during plastic deformation and is limited to a temperature range of –80 to +150°C. The embrittlement is considered to be caused by the interactions of the multiplication and pile-up of dislocations at plastic deformation zones and of the concentration of atomic hydrogen on these dislocations. Generally, commercial steels have vacancies, dislocations, grain boundaries, inclusions, precipitates and other defects that are heterogeneous to the material as in the case of segregation of constituent elements or that are regarded as defective for hydrogen atoms. Hydrogen occlusion is concentrated and accumulated in these heterogeneous parts and defects. It is certain that hydrogen embrittlement originates in portions that are high in hydrogen concentration.

The heterogeneity of hydrogen concentration in rolled steel plate has already been discussed. Large quantities of hydrogen are occluded around nonmetallic inclusions and embrittlement begins at fish eyes within this region.

3. Delayed failure of chromium-molybdenum steels

The crack propagation in static fatigue of hydrogen-charged chromium-molybdenum steels was investigated using a Kelvin bridge attached to the test pieces. Crack propagation in hydrogen-induced delayed fracture of chromium-molybdenum steels has three stages: I, slow growth; II, intermediate growth; and III, rapid growth. The propagation rate in each stage varied with strength and structure of the material. Based on the results of these investigations, the fracture toughness was determined (Fig. 13 and Table 3). Hydrogen occlusion caused a pronounced decrease in the toughness of high-strength steel.

高張力鋼の水素吸収に伴う脆化について

徳田　昭　大西敬三

株式会社 日本製鋼所 室蘭製作所 研究所

ま え が き

水素は鋼材の製造過程から使用中に至るまで，さまざまな径路から侵入し，水素脆性をはじめ白点，銀点，ふくれ，水素侵食などの悪影響をおよぼすことは改めていうまでもない．これらの問題については，空真溶解，真空造塊，その他の脱ガス処理などによって，工業的にかなり回避できるようになったが，今なお根本的には解決されていない．とくに近年広く利用されつつある高張力鋼において，硫化物腐食割れ，応力腐食割れ，メッキ脆性，水素による遅れ破壊など，いずれも水素脆性と関連するものとして重視されているが，高張力鋼は少量の水素吸収によって著しい脆性を引きおこすことから，水素脆性の機構究明と根本的な対策が強く要求されている．

しかしながら水素脆性に関するこれまでの研究報告は，そのほとんどが水素脆性の現象追求にとどまり，深く解析されてはいない．それは水素の鋼材内への侵入，拡散径路や脆化に対する水素の役割などが明らかでないからである．

本報告では，鋼の水素吸収，拡散と水素脆性などに関連した試験結果を紹介し，御参考に供したい．

1. 水素吸収と拡散

鋼の水素脆性は，常温付近，低歪速度域においてみられる現象であるが，水素脆性に対し鋼材内部の水素吸蔵の不均一さと塑性変形過程における水素の拡散が重要視されている．

鉄鋼の低温における水素の拡散速度は，近年多くの研究者によって調べられているが[1~9]，Fig. 1にまとめて示すように，その多くは高温からの外挿よりはるかに遅く，しかもその値は大きくバラツいている．高温における水素の拡散に要する活性化エネルギーは約 2～3 kcal/mol であるのに対し，低温では約 6·5～10 kcal/mol と非常に高い．低温における水素拡散速度の異常な低下は，上記の事柄と関連し，欠陥部分へ水素が“trap”され，拡散し難いことによるものであろう．また測定値の異常なバラツキは，測定方法によることもあるが，鋼材内の欠陥の存在状態に大きく影響されるといえる．

したがって，熱間圧延鋼板においては，鋼材内の欠陥の存在状態に方向性を有し，水素吸収や拡散状態は鋼板の圧延方向と何らかの関連性があるものと考えられる．

Fig. 2 および 3 は鋼板の圧延方向を基準とし，4×20×60 mm の板状試験片をさまざまな方向から採取して，水素の吸収状態を調べた結果である．供試材は Table 1 に示すように溶接構造用鋼板 (SM-41) ならびに調質型高張力鋼板 (HT-80) である．水素添加は 0·5% CH_3COOH＋2000 ppm H_2S 水溶液中への浸漬によった．

腐食に伴う水素の吸収状態については，鋼板の圧延方向によって吸収速度や吸収量などが異なる．

Fig. 2 に HT-80 についての結果を示す．まず HT-80 の水素吸収量については，ロール面と平行な X-Y 面のものは Z 面のものより多く，さらに同じ X-Y 面でも鋼板内部より採取したものは表層部に比べ吸収量が多い．

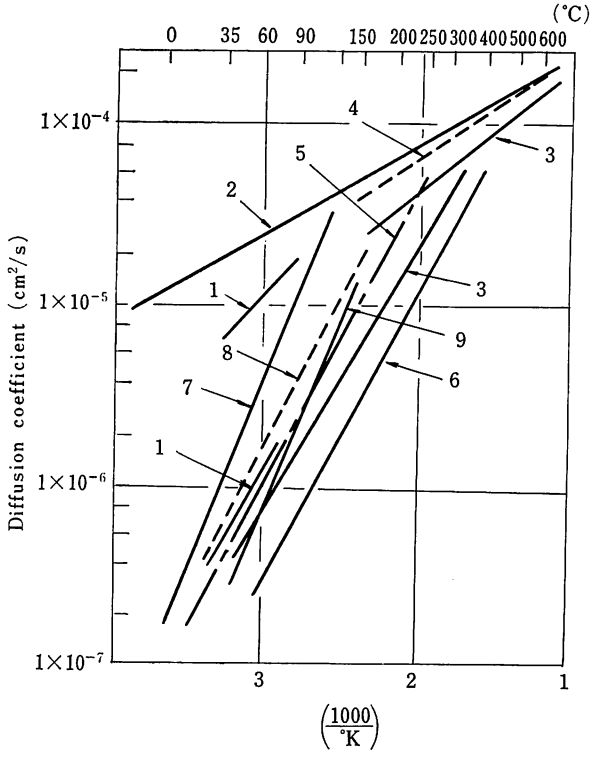

Fig. 1. Published data for the diffusion coefficient of hydrogen in iron and steels. (The numbers indicate the referenced publications.)

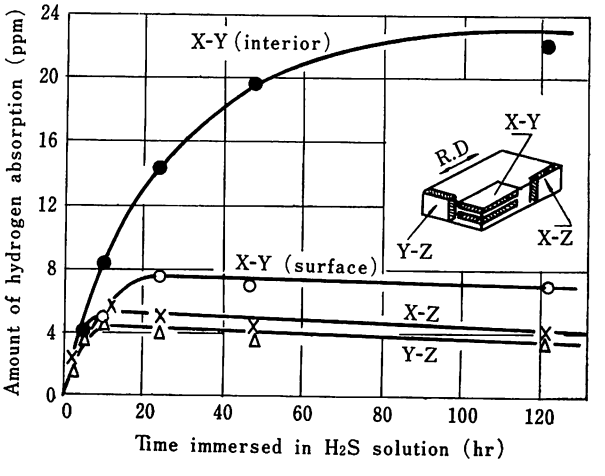

Fig. 2. Relation between immersion time and amount of hydrogen absorption as a function of direction relative to rolling for specimens of HT-80.

Table 1. Details of specimens used.

Grade	Chemical composition (%)									Yield point (kg/mm²)	Tensile strength (kg/mm²)	Elongation (%)	Heat treatment
	C	Si	Mn	P	S	Ni	Cr	Cu	Mo				
SM-41	0·11	0·23	0·73	0·021	0·012	0·14	0·09	0·20	0·07	34·8	49·6	49·6	As rolled
HT-80	0·12	0·24	0·73	0·018	0·016	1·14	0·45	0·22	0·35	79·9	83·1	35·1	Quenched and tempered

また水素吸収の飽和速度については，Z 面がもっとも早期に飽和に達し，ついで X-Y 表層部が飽和に達するが，X-Y 中心部では飽和速度は非常に遅い．このように水素吸収状態が鋼板の各面によって著しい相違を示すのは，ブリスターや水素割れの発生と密接な関係があり，ブリスターを多数形成する X-Y 面の試料は水素吸収量が多く，ブリスターを生じない Z 面の試料では吸収量が少ない．

一方 Fig. 3 に示した SM 材の場合は，HT-80 にみられたような各面の著しい差異はないが，水素吸収の傾向は大体類似している．この傾向は別の HT-80 と SM 材とについて試験した結果でも同じであった．SM 材において大きな差を生じないのはブリスターや水素割れの発生状態と試験片の厚さとによるものと考えられる．すなわち SM 材に発生するブリスターや水素割れは比較的微小であるため，試験片の厚さ 4 mm ではたとえ Z 面から採取したものでも，その中に多くの水素が吸蔵されると考えられる．

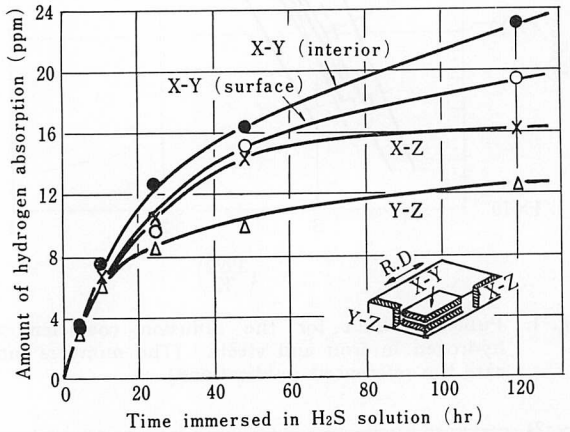

Fig. 3. Relation between immersion time and amount of hydrogen absorption as a function of direction relative to rolling for specimens of SM-41.

以上のように水素の吸収状態が鋼板の各面によって異なった傾向を示すのは，鋼板の圧延方向と水素侵入速度とが密接な関係を有するばかりでなく，水素吸収に伴うブリスターや水素割れの発生とも関係があることを物語っている．鋼板に生ずるブリスターや水素割れはロール面と平行な面に沿ってのみ生ずるが，このことは鋼材の熱間加工の方向，鋼中不純物の存在状態などと関係があると考えられる．この点について 0·1%C 鋼の鋼塊をさまざまな加工度に鍛造し，ブリスターや水素割れなどの発生状態を調査した．その結果，Photo. 1 に一例を示すように，鋳造ままの部分にはブリスターが発生せず，鍛造された部分にのみブリスターが発生しているのが判った．すなわち鋼材が熱間加工を受けるとブリスターを生じやすくなる．このことは加工に伴う組織の方向性，欠陥の分布状態などと関係があると考えられるが，加工による非金属介在物の変形とその分布がもっとも重大な影響を与えているものと考える．事実，試験片の内部を観察してみると，ブリスターや水素割れはいずれも非金属介在物から発達したものであることが判った．

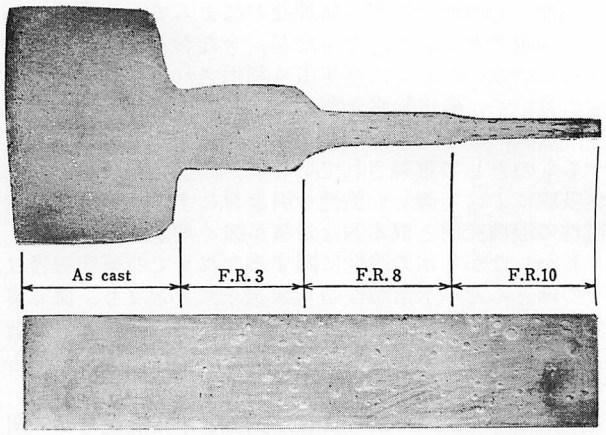

Photo. 1. Effect of hot working on hydrogen blistering. (F.R.: forging ratio).

Photo. 2 および 3 は水素割れが非金属介在物と結びついて大きく発達した例である．ただしこの場合の非金属介在物とは粘性変形しやすい介在物のことであり，酸化物系介在物のように変形しがたいものは割れとの関係が密でない．

以上に述べたようにブリスターや水素割れの発生は非金属介在物と密接な関係を有するが，これは介在物の部分に水素が集積しやすいことを示す．この場合，水素の集積の場所は介在物そのものではなく，介在物と鋼基地との界面となるであろう．すなわち介在物は鋼基地との界面において空隙を形成しているか，または不整合状態で存在しているので，その界面は拡散侵入した水素の“たまり”(trap) となるものと考えられる．したがって“たまり”は介在物の存在と密接な関係をもつことになる．実際に筆者らは介在物周辺（界面）に水素が集中しやすいことを確かめた．

Fig. 4 は板厚 1·0 mm の試験片の片側から水素を添加し，透過面にシーダ油を塗装して，裏面から透過，放出する水素を，水素気泡として観察したものである．

Photo. 3～4 に示すように，水素は透過面に存在する非金属介在物と基地との界面から活発に放出される．

圧延鋼板においては，水素吸収量および吸収速度に方向性があることを知ったが，水素拡散速度についても同様に方向が認められる．Fig. 5 は水素吸収試験片に水素を添加し，さまざまな温度に一定時間放置後の残留水素量から水素拡散速度を求めた結果である．水素拡散の計

specimen surface (X—Z)

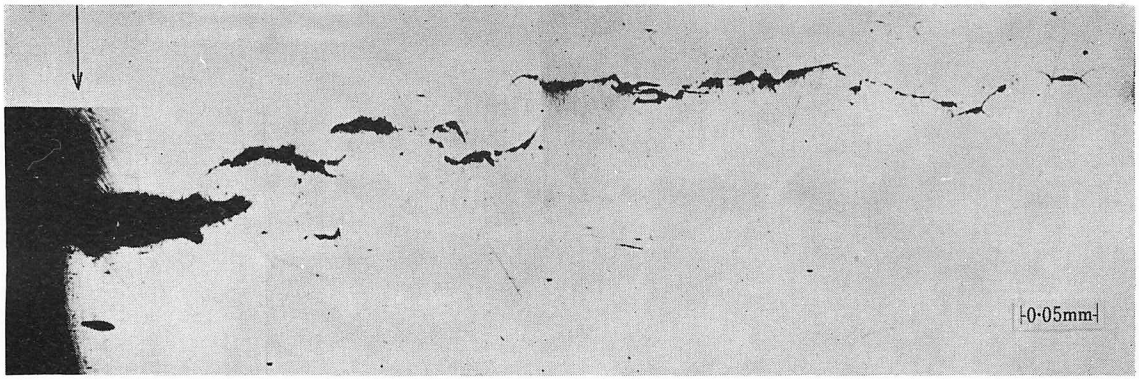

immersed 14 days

Photo. 2. Hydrogen crack connected with nonmetallic inclusions in SM-41 specimen; X-Z, observed surface Y-Z.

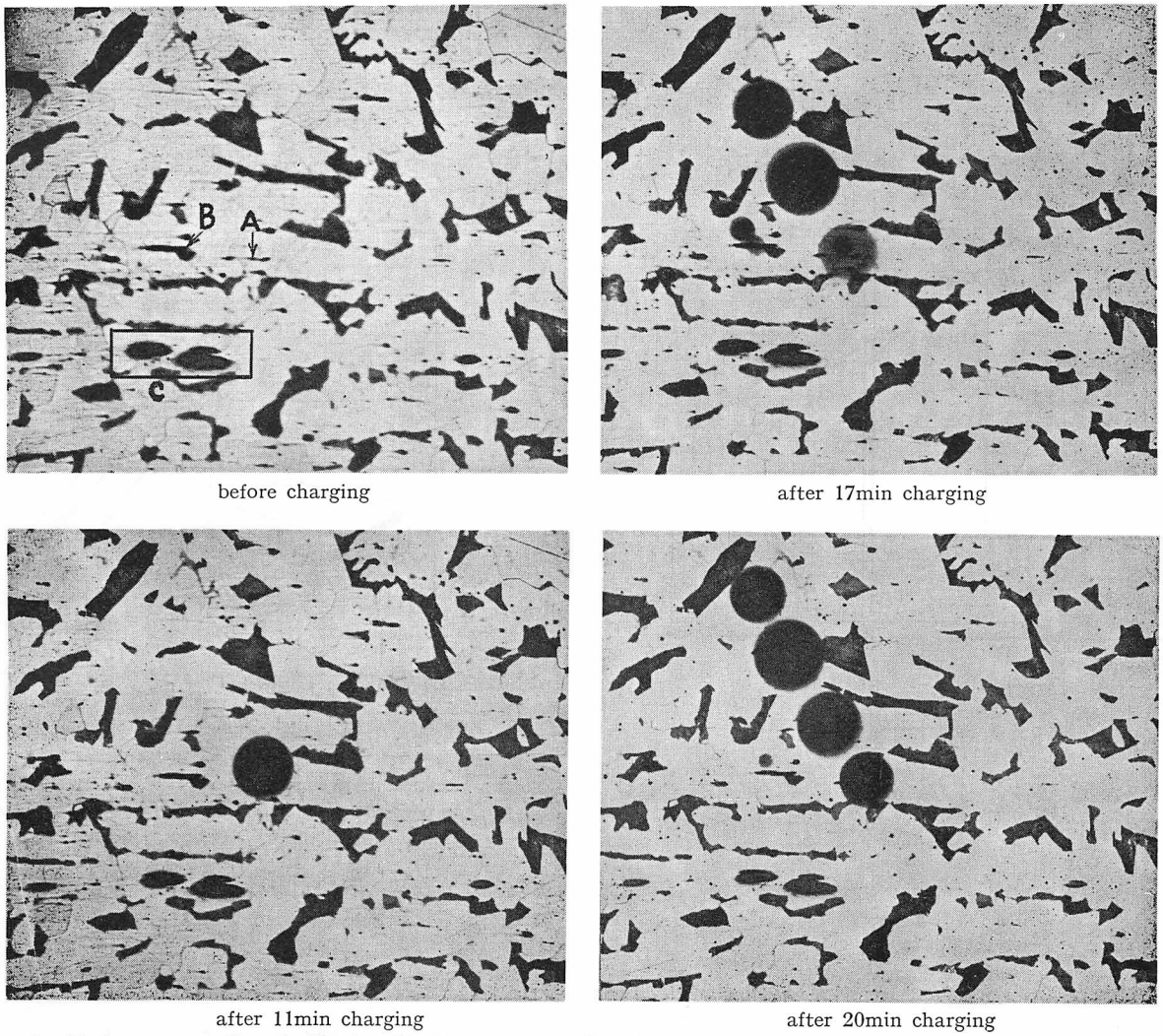

before charging　　after 17min charging

after 11min charging　　after 20min charging

Photo. 3. Hydrogen evolution on SM-41. Hydrogen bubbles issued from nonmetallic inclusions.

算は次式によった.

(初期条件) 試験片内部に添加した水素濃度は均一に分布し, $t=0$ で濃度は C_0 (一定) である.

(t 時間後の水素濃度) Fick の第2法則により次式で計算した.

$$C_t=C_0\frac{8}{\pi^2}\sum_{n=1}^{\infty}\frac{(-1)^{n-2}}{2n-1}\exp\left(\frac{-(2n-1)^2\pi^2D_t}{4L^2}\right) \quad (1)$$

ここに C_t: t 秒後の水素濃度, D: 拡散恒数 cm²/sec, L: 板厚の 1/2, cm である.

(2) 式により $C_t/C_0=0{\cdot}5$ となるまでの時間を各温度および各方向について測定し, 拡散恒数 D を求めた.

図から明らかなように, 低温において水素の拡散恒数にはかなり差異があり, X-Yはもっとも拡散速度が遅く, Y-Zはもっとも早い. このような水素拡散の方向性は高

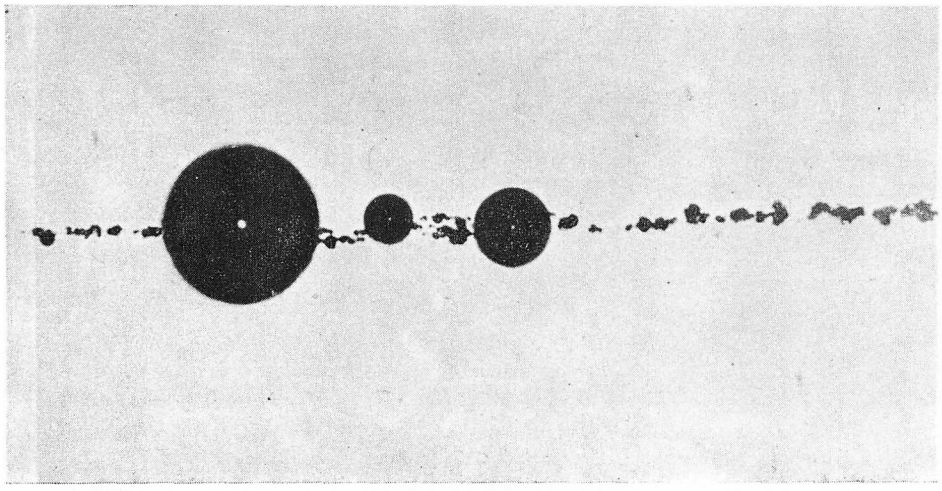

Photo. 4. Hydrogen evolution from Al_2O_3-inclusion in SM-41.

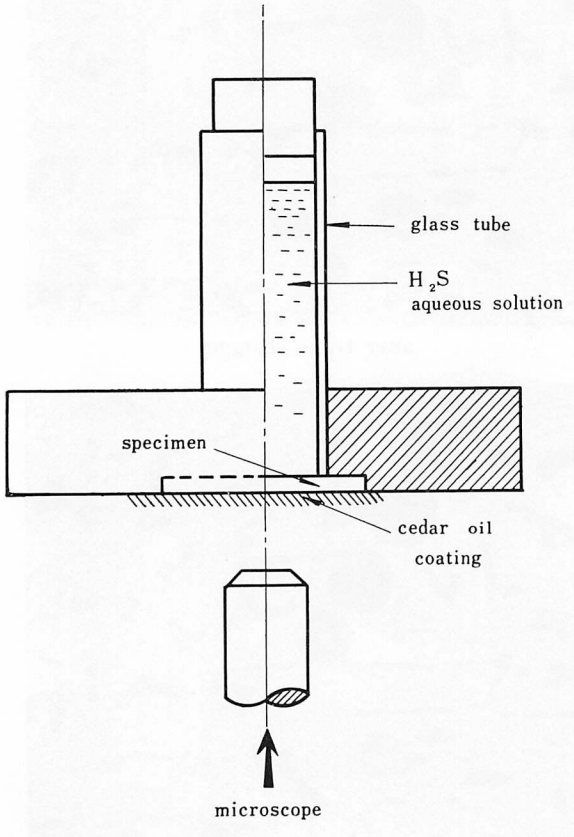

Fig. 4. Experimental apparatus for observation of hydrogen evolution.

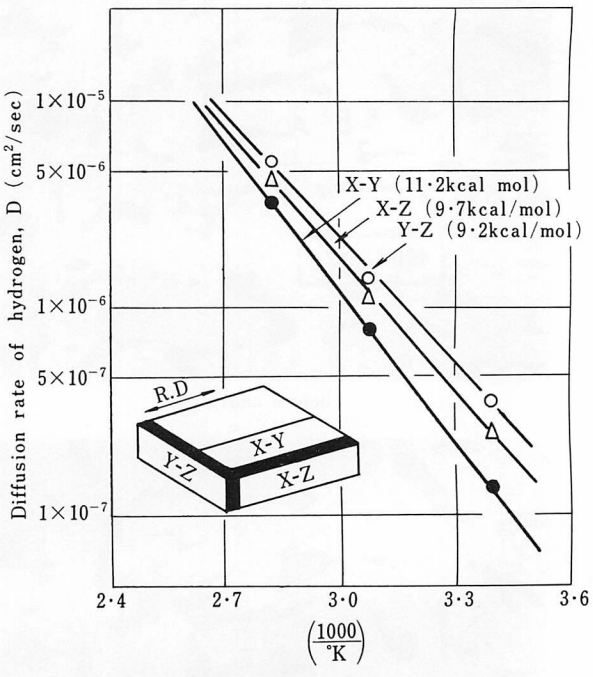

Fig. 5. Relation between diffusion rate of hydrogen and temperature as a function of direction relative to rolling of steel plate.

温になるにしたがってしだいに顕著でなくなる．

このような水素拡散速度の方向性は，上述の鋼板内の“trap”の存在分布状態に方向性があることと関連づけられる．

Evans[10] は鋼の水素拡散におよぼす非金属介在物の種類の影響について検討した．その結果によるといずれの介在物においても水素を捕捉し，みかけの拡散を遅くするが，介在物の種類には無関係であると述べている．結局，水素の拡散は介在物そのものに影響を受けるのではなく，介在物と基地との界面に欠陥が存在し，その形状や大きさに影響されることを意味している．

2. 圧延鋼板における水素脆化の方向性

鋼の水素脆性に影響をおよぼす因子は種々あるが，水素濃度の影響はとくに顕著である．前節で圧延鋼板には水素の吸蔵や拡散速度などに方向性があり，それらは熱間加工の方向（非金属介在物の分布）と密接な関係があることを知った．このように圧延鋼板において，水素吸蔵や拡散速度に方向性を有するなら，水素脆性にも方向性を有すると考えられる．そこで，圧延鋼板における水素脆化の方向性について検討を行なった．

試験に用いた材料は，Table 1 に示す HT-80 であるが，Fig. 6 に示す要領で板状の引張試験片を採取し，水

素吸収板および水素吸収後の時効材について脆化の割合を調査した．

水素による鋼材の脆化は，伸び，絞り，切欠引張強さおよび真破断応力の低下を測定することによって検知されるが，平板状引張試験片を使用したので，水素脆化度は伸びの減少率から求めた．

$$I(\%)=\frac{l-l'}{l}\times 100 \qquad (2)$$

ここで I：脆化度，l：水素添加前の伸び，l'：水素添加後の伸びである．

水素添加に伴う脆化の割合は，Fig. 7 に示すように，約 12 時間までは，いずれも水素添加時間とともに大きくなり試料の採取方向による差は明らかでないが，その後は脆化の割合は小さくなり，方向性が顕著にあらわれる．鋼板からの採取方向による水素脆化の差異は，X-Y (中心部) がもっとも脆化率が大きく，ついで X-Y (表層部) が大きかったが，X-Z や Y-Z では脆化率が小さく，約 10 時間以後は脆化度はほとんど変化しなかった．

このように鋼板からの採取方向によつて脆化量に差異を生ずるのは，Fig. 2 と関連し，水素吸収量の多い X-Y は脆化率が高く，吸収量の少ない板厚面のもの (X-Z, Y-Z) では脆化率が低いと言えよう．そこで Fig. 2 と Fig. 7 とより吸収水素量と脆化率との関係で整理したのが Fig. 8 である．図から明らかなように，いずれの試料も図中の直線近くにあり，水素吸収量約 6 ppm まではほぼ直線的に水素量の増加に伴って脆化率は高くなり，脆化率80%にまで達するが，それ以上では水素量の増加に伴う脆化率の上昇は小さくなる傾向を示した．したがって同じ水素濃度レベルで脆化率をみた場合，試料採取方向による脆化の方向性はないといえ，結局脆化の方向性とは，水素吸蔵量の方向性に依存していると考えられる．

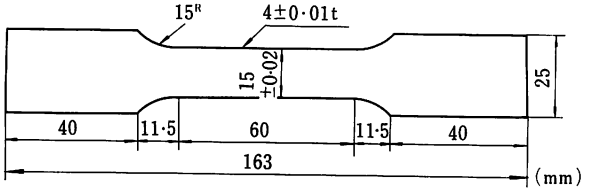

Fig. 6. Dimensions of test piece.

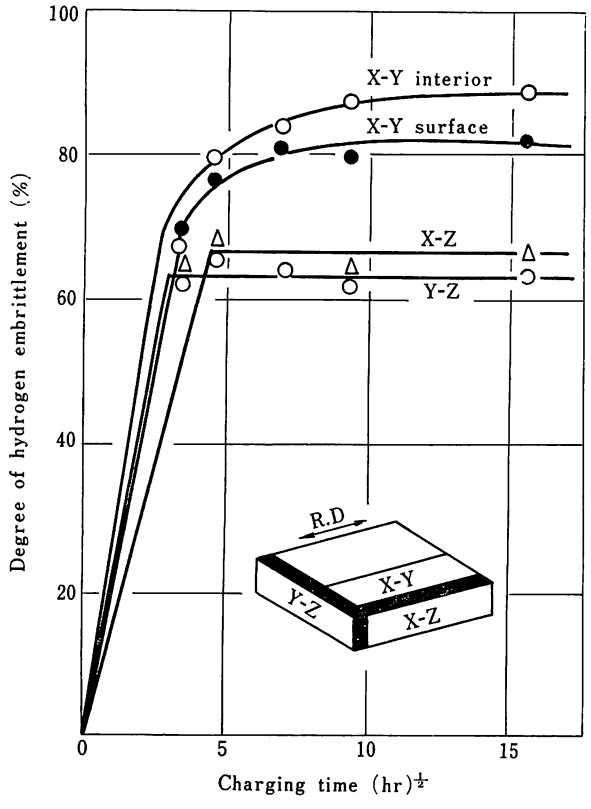

Fig. 7. Variation of hydrogen embrittlement with charging time as a function of direction relative to rolling.

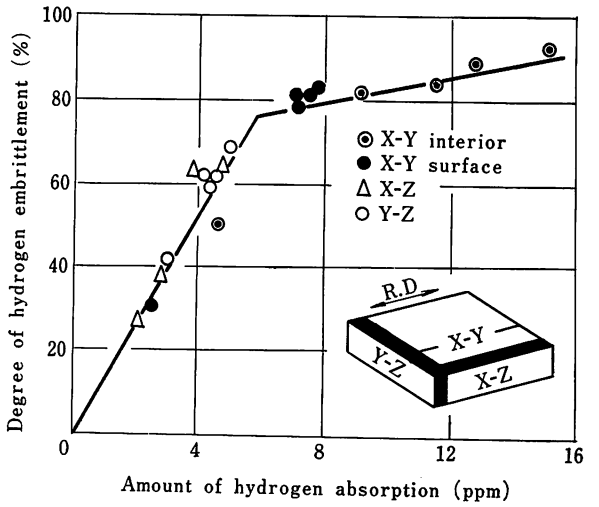

Fig. 8. Relation between amount of hydrogen absorption and hydrogen embrittlement.

鋼材の水素脆性は，鋼材内に固溶した水素により塑性変形過程であらわれるが，時効によって水素を拡散，放出させることにより延性が回復する可逆的現象である．

この場合，回復速度は鋼中の水素の拡散速度，時効温度，時効時間などによって決定される．圧延鋼板においては水素吸収と拡散速度に方向性を有するので，時効による延性の回復速度にも方向性があると考えられる．

そこで時効による延性の回復についての検討を行なった．水素添加時間は 12 時間であるが，これは Fig. 2 との関係から判るように，水素吸収量がいずれも約 4 ppm となるようにしたものである．水素添加後の時効温度は 22°, 52°, 82° および 150°C である．22°C の結果を Fig. 9 に示す．図から明らかなように時効時間とともに延性の回復は大きくなっているが，回復速度は Y-Z がもっとも早く，X-Y がもっとも遅い．このように延性の回復には顕著な方向性が認められた．たとえば時効 10 時間において，Y-Z は約 54% の回復率であるのに対し，X-Z は約 43%，X-Y は 32% の回復率である．時効温度が 52°C の場合は 22°C の場合より全体に回復速度は早くなり，20 時間程度の時効でいずれも 80% 以上の回復を示した．この場合もやはり，Y-Z の回復がもっとも早く，X-Y はもっとも遅い．さらに時効温度が 82°C, 150°C となるのにしたがって延性の回復は一層早くなる．この場合室温付近でみられたような回復速度の方向性はなくなり，いずれも 1 時間以内に 80% 以上の回復率を示した．

次に，これらの結果からそれぞれの試験片について，水素脆化した材料の 50% の回復率に達するまでの時効時間を各温度で求め，Fig. 10 を得た．これによると回復の早い Y-Z は他のものに比べて温度依存性は小さく，回復速度の遅い X-Y はもっとも温度依存性が大きいと

言える．この図から Arrhenius の関係による回復に要する活性化エネルギーを求めた結果，図中に示すように Y-Z は 7·4, X-Z は 8·2, X-Y は 10·3kcal/mol であった．

Photo. 5 は各方向の試験片の水素添加後の破面状況である．水素添加前の破面は十分な延性を示し，X-Y, X-Z および Y-Z はいずれも大きな断面収縮を呈しているが，水素添加 4 時間後のものでは，断面収縮がやや小さくなり，破面の至る所に微小な fish eye（銀白色）が認められた．水素添加 12 時間後では脆化はさらに進み，断面収縮の割合は非常に小さくなっている．この破面の中にみられる fish eye は水素添加 4 時間のものよりさらに大型となっている．さらに水素添加 48 時間のものでは断面収縮がほとんどなくなり，破面内に認められる fish eye も一段と大きくなっている．このころにあらわれる fish eye はもとの鋼板のロール面と平行な面 (X-Y 面) に沿って拡がっているのが特徴で，X-Y のものでは試験片平面と平行な拡がりを呈し，X-Z および Y-Z では試験片の厚さ方向に拡がった形を呈している．

fish eye 近傍の破面を電子顕微鏡によって観察したところ，Photo. 6 a) にみられるように，fish eye の部分は水素脆性の特徴をあらわす quasi-cleavage が観察された．しかし fish eye の全面がこのような脆性破面で

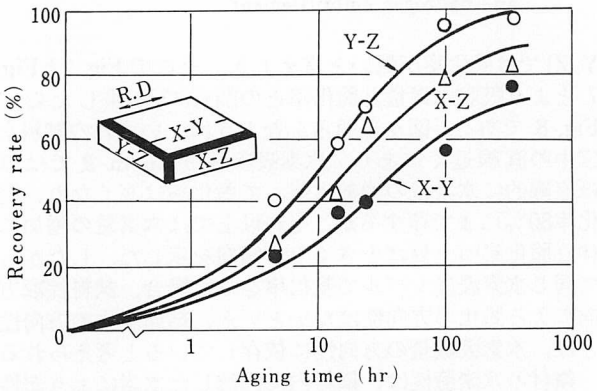

Fig. 9. Recovery of ductility by aging at 22°C.

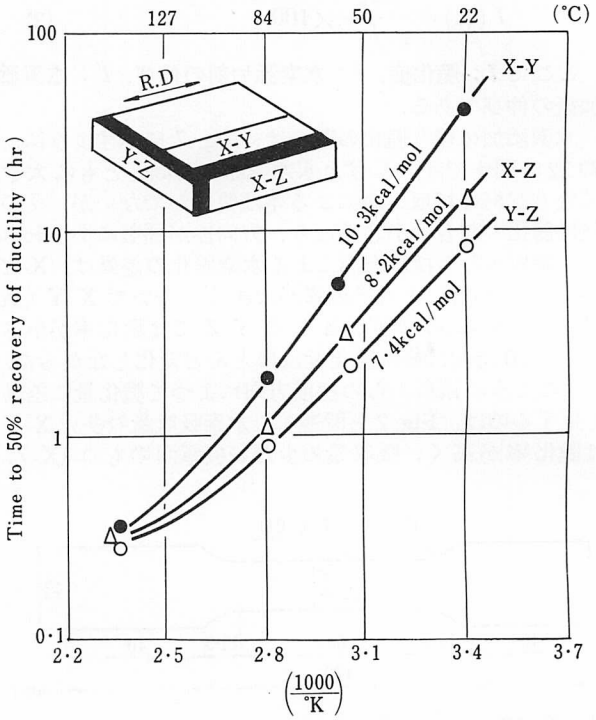

Fig. 10. Effect of aging temperature on recovey of ductility.

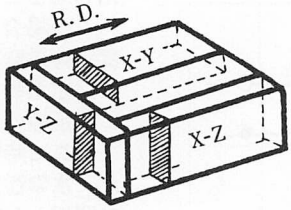

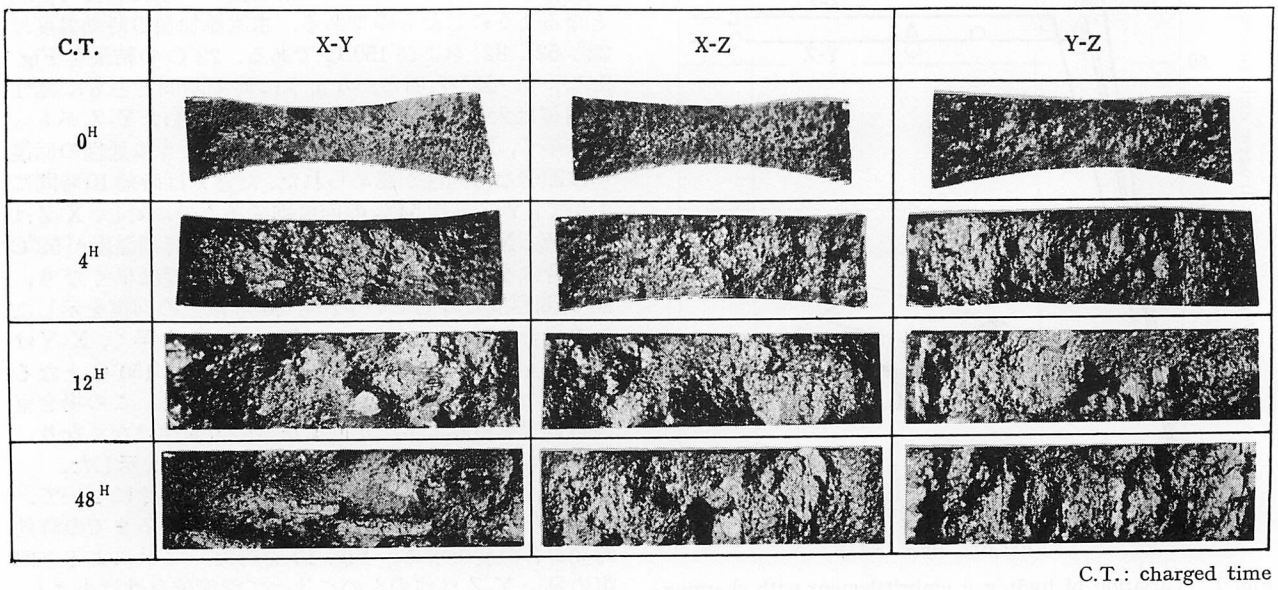

C.T.: charged time

Photo. 5. Fractured surface of hydrogen-charged specimen.

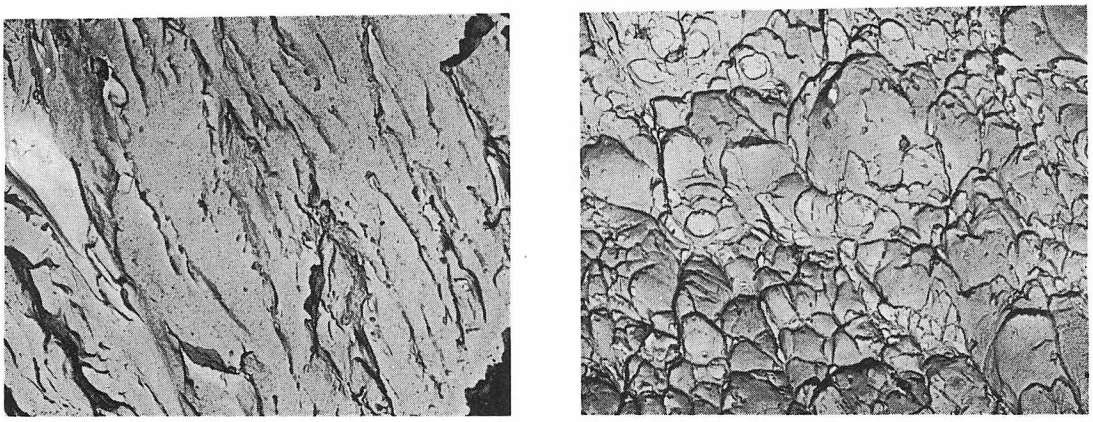

a) b) ×5000

Photo. 6. Hydrogen evolution from Al_2O_3-inclusion in SM-41.

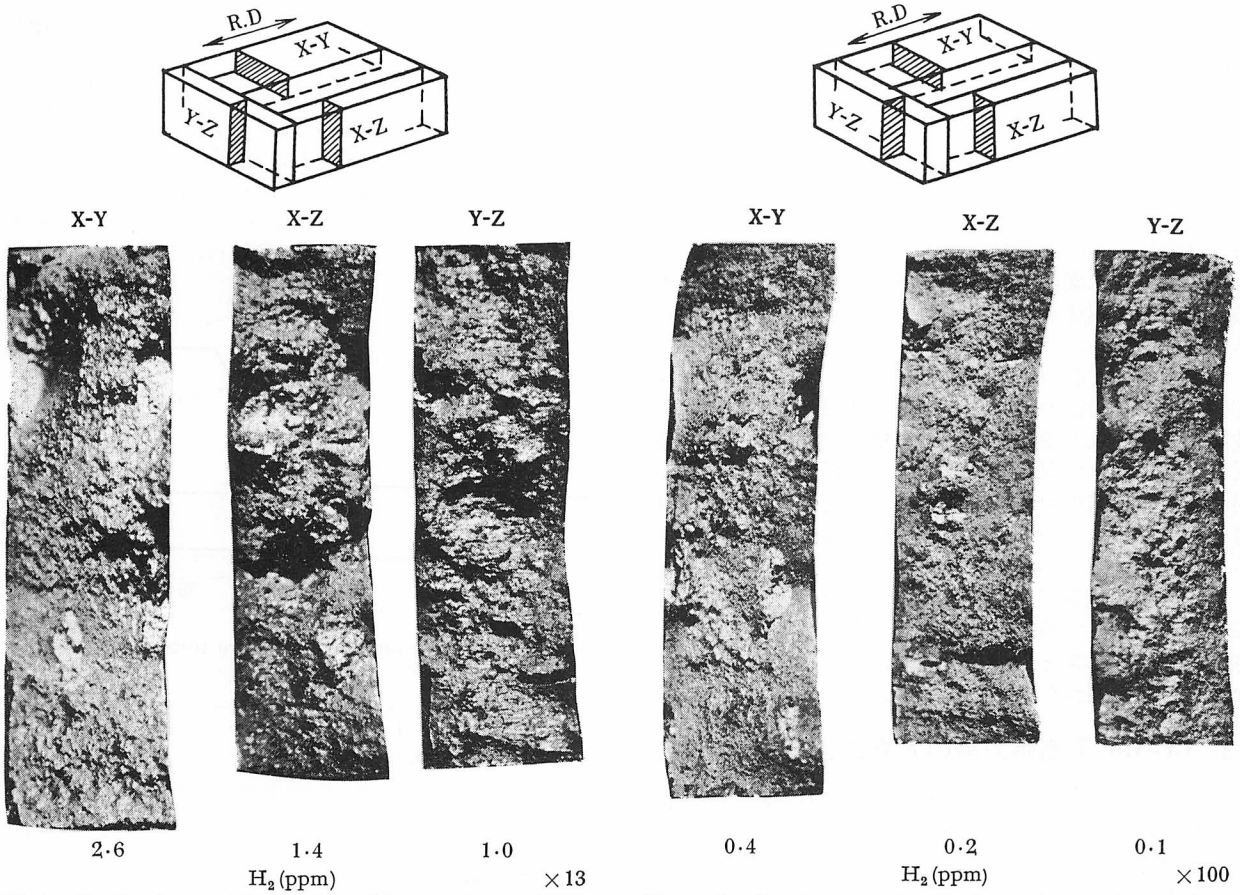

Photo. 7. Fracture surfaces of specimens after aging at 22°C.

Photo. 8. Fracture surfaces of specimen after aging at 22°C.

はなく，fish eye の内部においても Photo. 6 b) にみられるような靱性を示す dimple 模様が観察された．この dimple 模様は fish eye の外周辺や fish eye から隔った所にも認められた．

次に 12 時間水素添加後時効処理を行なった試験片の破面を観察した．12 時間添加した状態の破面はすでに，Photo. 1 に示した通りであるが，その後 22°C で 13 時間放置したものでは，延性の回復がかなり顕著にあらわれてくる．この場合，Photo. 7 に示すように Y-Z の回復がもっとも早く，fish eye は少なく，破断面積はもっとも小さい．これに対し X-Y は回復が遅く破面の所々にまだ fish eye が認められ破断面積も大きい．100 時間時効後では，fish eye の数および大きさはさらに少なくなっているが Photo. 8 にみられるように，X-Z の破面には依然として fish eye が明瞭に認められる．Y-Z や X-Z の破面には fish eye が僅かではあるが認められた．これらの fish eye は，いずれの試料においても前述のようにもとの鋼板のロール面と平行に形成していた．この観察結果から fish eye は水素添加に伴って，ロール面と平行に平面的な拡がりをもって形成するばかりでな

Table 2. Details of material tested

	Chemical composition (%)									Proof stress (kg/mm²)	Tensile strength (kg/mm²)	Elongation (%)	Reduction of area (%)
	C	Si	Mn	P	S	Ni	Cr	Mo	V				
A	0·38	0·29	0·76	0·015	0·011	0·16	2·90	0·18	—	29·0	61·7	24·9	37·4
B	0·81	0·40	1·03	0·025	0·020	1·02	1·01	0·38	—	53·9	90·3	1·4	3·0
C	0·23	0·21	0·43	0·016	0·016	4·00	1·53	0·48	0·13	103·6	113·2	18·4	53·5

く，水素添加後の時効に伴う fish eye の消失においても，ロール面と平行な面に沿って強く残存するのが特徴といえる．

鋼材の水素脆性は，現象的には，低歪速度下でかつ塑性変形過程中においてあらわれ，脆性を示す温度も −80°～+150°C の範囲に限られており，脆化には塑性変形部分における転位の増殖，堆積とこれら転位群への水素原子の濃化とが相互に作用するものと考えられている．

一般に工業用材料では化学成分の偏析など材質的に不均一な部分や水素原子にとって欠陥と見做し得る原子空孔，転位，粒界，介在物，析出物その他の欠陥が存在する．水素の吸蔵はこれらの不均質部分や欠陥に濃化集積するもので，水素脆化も水素濃度の高い部分から生ずることは明らかである．

圧延鋼板内における水素濃度の不均一さについては前項で述べたように，非金属介在物周辺に多量に吸蔵され，脆化は介在物を中心とした fish eye から始まっている．したがって，水素添加した鋼板が脆化する過程では水素濃度と密接な関係があり，次のような過程で脆化がおこると推察される．

(i) 水素吸蔵量が少なく脆化率も低い間では非金属介在物や炭化物周辺の転位群に水素が捕捉され，さらに塑性変形時に転位の増殖ならびに堆積が進み，そのとき捕捉されていた水素原子も転位とともに移動，集積するが，同時に周辺の基地中からも水素原子が侵入して水素脆性亀裂を生ずる．この場合，水素濃度が低いため，形成する水素脆性領域は小さい．

(ii) 水素吸蔵量が多く脆化率が高くなると，非金属介在物周辺に水素が過剰に蓄積されて水素割れを形成し，さらに多くの水素を吸蔵するので，水素脆化はこれらの介在物と水素割れを中心として拡大される．

3. Cr-Mo 系高張力鋼の水素による遅れ破壊

われわれは冷間圧延用ロールの置き割れをはじめ，極厚鋼板の超音波不良，高張力鋼溶接部の低温遅れ割れ，大型鍛鋼品の偏析割れなど，いずれも遅れ破壊に関連した現象として広く経験している．これらの現象の共通している点は，鋼材が大型鍛鋼品であり，破壊点近くには水素が存在し，かつ高い応力が残留しているが破壊はいずれも常温またはその付近の低温域において発生することである．

遅れ破壊については，従来 Sachs[11,12] や Troiano ら[13~18] によって研究されてきたが，これら研究データの多くは静的疲労曲線を求めることで終っていた．このような曲線を求めることは，鋼材の遅れ破壊に対する感受性の相対的な値を知る上に効果はあるが，実際の鋼材に対する破壊の危険性を具体的かつ定量的に求めることは全く難しい．

そこで，遅れ破壊試験中での，亀裂発生から伝播，破断に至るまで，亀裂の生長状況を調査し，亀裂の伝播に対する水素の役割，つまり水素による破壊靱性値の低下割合などについて検討した．

Table 2 に示す3鋼種を供試材とし，Fig. 11 の形状の試験片を製作し試験に供した．試験片への水素添加は陰極電解によった．

Fig. 12 に各供試材の疲労亀裂を伴った場合の静的疲労曲線を示す．図中の付与応力値は，切欠部の断面における最大曲げ応力（引張応力）を示したものである．いずれの材料も水素添加によって切欠引張強さは低下している．水素添加材の切欠引張強さ以下における，破壊時間の遅れは鋼種によって異なっている．まず A 鋼については，94 kg/mm² の切欠引張強さが，水素 9 ppm の添加によって 71 kg/mm² に低下し，付加応力の低下に伴う破壊時間の遅れが約 61 kg/mm² まで続き，60 kg/mm² で静的疲労限に達した．B 鋼は A 鋼より脆い材質であり，水素添加前の切欠引張強さは供試材中もっとも低く，74 kg/mm² である．この材料は水素 3 ppm の添

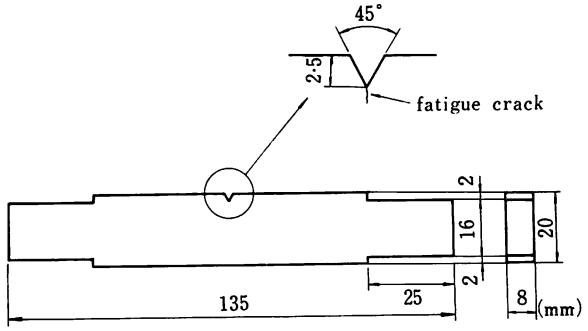

Fig. 11. Test piece for delayed failure tests.

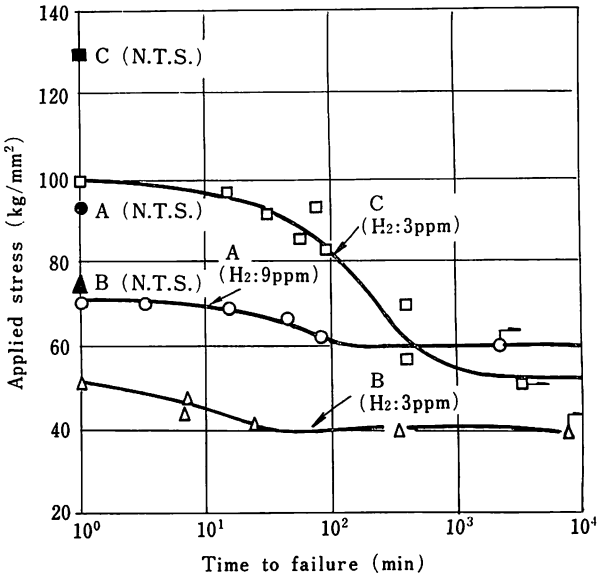

Fig. 12. Static fatigue curves for steels A, B and C.

加によって 51 kg/mm² に低下し，40 kg/mm² で静的疲労限に達する．静的疲労限に達するまでの時間は約 30 分であり，A 鋼に比べ低水素濃度であるにも拘らず破壊応力の低下は著しい．C 鋼は供試材中もっとも強度が高くしかもすぐれた靱性を有する材料であるが，水素吸収 (3 ppm) によって切欠引張強さは 129 kg/mm² から 99 kg/mm² にまで低下し，約 10^3min の遅れで静的疲労限 52 kg/mm² に達している．これらの曲線から，水素脆化に対する感受性を比較すると，もっとも強い脆化を示すのは B 鋼であり，次いで C 鋼であると言える．A 鋼は水素脆化の感受性が鈍く，水素脆化を検知するためには多量の水素を添加する必要があり，9 ppm の水素添加でも破壊応力の低下は僅かである．

遅れ破壊過程における水素脆性亀裂の発生から伝播，破壊に至るまでの各段階の模様を Kelvin Bridge によって電気的に測定した．測定結果を Fig. 13 に示す．Fig. 13 a) は A 鋼について測定した結果であるが，試験開始直後に電位の上昇がみられその後，時間の経過とともにきわめて僅かながら電位が上昇する傾向にあり，そして破断時に至って瞬時に電位が増加する．

B 鋼においては Fig. 13 b) にみられるように，試験開始とともに遂次電位の上昇がみられ，約 0·3 μV の増加後，やや停滞し，次に階段状に電位は上昇する．電位の上昇速度は，1·0～1·5 μV 付近から電位の上昇が早まり，瞬時破壊に移行している．B 鋼の場合は，A 鋼に比べ亀裂の進行状態が異なる．すなわち，A 鋼は応力付加直後に一定亀裂長さに達し，潜伏期間を経過した後，直ちに破壊に至るが，B 鋼の場合は応力付加後，亀裂生長は，段階的であり，図に矢印で示すように，金属音を発して亀裂を生じ，一定期間生長が停止した後，再び金属音を発して亀裂を生じ，限界亀裂長さに達して破断に至っている．

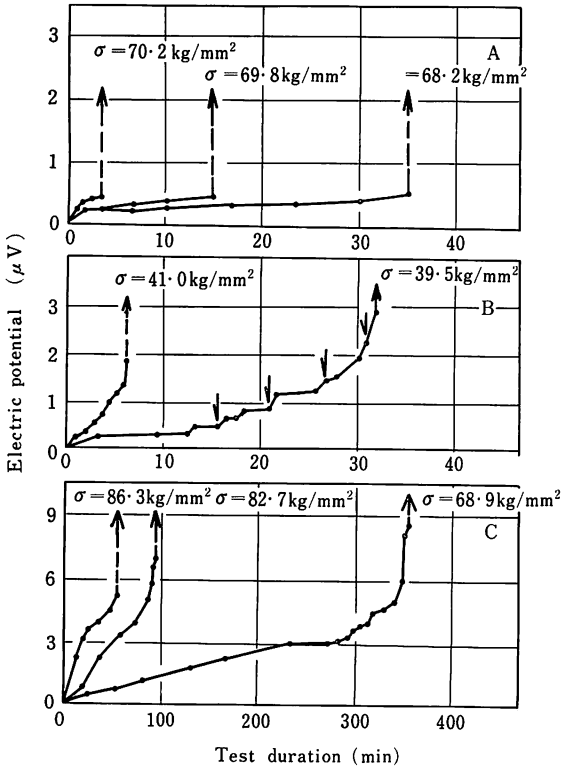

Fig. 13. Crack growth during static fatigue tests.

C 鋼については Fig. 13 c) のように，試験開始後，ほゞ一定の速度で亀裂が生長し，3～4 μV に達してやや停滞した後は，亀裂の生長は著しく速くなり，5～8 μV に達して破断に至っている．C 鋼においても付加応力の高い方が亀裂の生長速度は大きく，付加応力の低い場合ほど遅くなっている．付加応力の低い場合においては，亀裂の生長段階に明瞭な差異が認められる．また，最終破断に至るまでの電位の増加量は付加応力によって明らかに差異がみられ試験初期におけるやや遅い亀裂の生長段階に引続き，亀裂生長がやや速くなる段階があり，最終段階に入って著しい亀裂の生長段階がある．

以上の 3 鋼種について亀裂の発生から伝播破断に至るまでには，3 つの段階があり，第 I 段階は slow growth，第 II 段階は partially rapid growth，第 III 段階は rapid growth にそれぞれ分類される．A 鋼の場合は第 I 段階が非常に顕著であり，第 II 段階がほとんどなくて第 III 段階に移っている．B 鋼は第 II 段階が長く，第 I 段階は短い．C 鋼では第 I 段階，第 II 段階および第 III 段階の各段階が顕著に認められ，その生長速度は連続的である．

Fig. 13 は亀裂の生長状況を電位の変化で示したが，この図より，水素脆性亀裂の生長過程における破壊靱性値 K の変化について検討を加えた．各鋼材の破壊靱性値 K は，水素吸収によって著しく低下しているが 破断時間の長い場合すなわち，付加応力の低い場合ほど亀裂の初期伝播の際の K 値は低くなっている．亀裂の生長過程における K の変化については，亀裂生長初期段階においては K はもっとも低く，試験時間の経過とともに K はしだいに増加し一定時間経過後に K の上昇は顕著となり，やがて破断に至る傾向が認められる．

Table 3 に各試料の水素添加前後の破壊靱性値 K_{IC} を示した．いずれも水素吸収によって破壊靱性値は著しく低下しているのが判る．

Table 3. Fracture toughness of steels A, B and C.

	σ_s (kg/mm²)	H_2 (ppm)	K_{IC} (kg√mm/mm²)	
			H_2 uncharged	H_2 charged
A	29·0	9	216	149
B	53·9	3	130	89
C	103·6	3	280	132

以上の結果から，遅れ破壊過程における水素脆性亀裂の伝播は，亀裂先端部への水素の拡散集中速度と水素による材料の脆化率に依存しながら緩慢に進むが，一定亀裂長さ（限界亀裂長さ）に達すると不安定破壊に移って急速破断に至ると言える．不安定破壊時の亀裂の伝播は非常に早く，伝播には水素は直接関与しない．

む す び

鉄鋼の水素脆性に関係したデータを簡単に紹介した．現状では，転位一水素間の相互作用が水素脆性に重要な役割をもつことが認識され，この方面の研究が積み重ねられつつある．しかしながら，水素脆性の定量的な検討を行なうには，まだまだデータ不足であり，次の点が明らかにされなければならない．

(1) 塑性変形過程での水素の挙動の把握.

(2) void 内の水素圧の測定ならびに水素圧の脆化に関与する程度の確認（果して水素脆化に，void 内の水素圧が有効であるか否かについての検討）.

(3) 表面エネルギーは水素によってどの程度低下するのか，その低下量の把握.

(4) 水素脆性と結びつけられる欠陥の具体的表示.

しかしこれらの問題を把握することは非常に難しい．したがって，一方では巨視的破壊力学の立場から水素脆性を取扱うことも大切である．最近，水素雰囲気中での鋼材の破壊や高張力鋼の応力腐食割れなどの問題に破壊力学的検討がなされつつある．

文　献

1) R.C. Frank: Internal Stress and Fatigue in Metals, Elsevier Publishing Co., (1959), p. 411
2) C. Sykes, H.H. Burton and C.C. Gegg: J. Iron Steel Inst., **156** (1947), p. 155
3) T.M. Stross and F.C. Tompkins: J. Chem. Soc., (1956), p. 230
4) W. Eichenauer, H. Kunzig and A. Pebler: Z. Metallk., **49** (1958), p. 220
5) E.W. Johnson and M.L. Hill: Trans. Met. Soc. AIME, **218** (1960), p. 1104
6) P.L. Chang and W.D.G. Bennett: J. Iron Steel Inst., **170** (1952), p. 25
7) J.D. Hobson: J. Iron Steel Inst., **189** (1958), p. 315
8) F.R. Coe and J. Moreton: J. Iron Steel Inst., **204** (1966), p. 366
9) W. Heller and W. Janiche: Stahl. u. Eisen, **83** (1963), p. 145
10) G.M. Evans and E.C. Rollason: J. Iron and Steel Inst., **207** (1969), p. 1484
11) E. P. Klier, B.B. Muvdi and K. Sachs: Trans. AIME, **202** (1957), p. 106
12) K. Sachs and A. Morgan: J. Iron Steel Inst., **206** (1968), p. 357
13) P.P. Fromberg, W.J. Barnett and A.R. Troiano: Trans. ASM, **47** (1955), p. 892
14) W.J. Barnett and A.R. Troiano: J. Metals, April (1957), p. 486
15) H.H. Johnson, J.G. Morlet and A.R. Troiano: Trans. AIME, Aug. (1958), p. 528
16) E.A. Steigerwald, F.W. Schaller and A.R. Troiano: Trans. AIME **215** (1959), 1048; **218** (1960), p. 832
17) J.G. Morlet, H.H. Johnson and A.R. Troiano: J. Iron Steel Inst., **186** (1958), p. 37
18) A.R. Troiano: Trans. ASM, **52** (1960), p. 54

Delayed Fracture by Atmospheric Embrittlement and Microstructure

C. Asada S. Fukui

Daido Steel Company Ltd.

With the objective of studying the problem of delayed fracture in high-strength steel used under common atmospheric conditions, such as high-strength bolts for joining steel constructions, we investigated the mechanism of delayed fracture under wet atmospheric conditions as well as the influence of metallographic factors on the characteristics of delayed fracture.

Circumferentially grooved specimens were tested under sustained bending stress in pure water, solutions containing small amounts of hydrochloric acid up to 0·1 N, solutions with up to 3% NaCl and slightly acidified solutions saturated with H_2S.

A shear lip on the tensile side of the delayed-fracture surface was observed as shown in Photo. 1. This lip indicated that the delayed fracture first occurred below the surface of the test piece. The thickness of this shear lip depended on the notch radius of the test piece and it was recognized that this thickness was almost the same as the distance from the surface to the position of maximum triaxiality of stress (Fig. 4).

Hydrogen analyses of test pieces immersed in these various solutions confirmed that the steel absorbed hydrogen under such atmospheric conditions and that the delayed-fracture limit decreased as the amount of hydrogen absorbed during test increased. From these results it was conjectured that the role of hydrogen absorption was the most important factor in determining the delayed-fracture strength under the various atmospheric conditions covered by the present study.

As indicated in Fig. 6, tempering temperature had a complicated effect on the delayed-fracture limit of hardened steel in 0·1 N HCl solution. A common behavior to all steels was a low value of the delayed-fracture limit after tempering at 350°C. The maximum delayed-fracture limit was reached with higher tempering temperatures.

When steels were tempered at temperatures above that giving the maximum value of delayed-fracture limit, the delayed-fracture ratio (ratio of 30 hr strength in delayed fracture to static bending strength) showed an almost constant value. From this it is presumed that the lowering of delayed-fracture limit in this area is attributable to decreasing load-carrying capacity rather than to increased delayed-fracture susceptibility.

In investigating the initiation and propagation of delayed fracture cracks in steel it was found that the early cracks occurred in the prior austenitic grain boundaries but that their propagation depended upon tempering conditions. In those steels that showed a low value of delayed-fracture limit because of tempering at around 350°C, the cracks propagated along the prior austenitic grain boundary (Photo. 3 and 4). Electron-microscopic investigation of microstructure revealed carbides precipitated along the prior austenitic grain boundaries (Photo. 5 and 6).

The delayed-fracture limit of steel isothermally transformed to bainite was higher than that of quenched-and-tempered steel, especially at the high-hardness level (Fig. 8). When the bainitic steel was tempered at 550°C, an abnormally sharp decrease in delayed-fracture limit was observed so the delayed-fracture limit became the same as that of quenched-and-tempered material having the same hardness.

Platelike carbides connected in a row along the prior austenitic grain boundaries were observed in the isothermally transformed and tempered steels that had shown an abnormally high drop in delayed-fracture limit (Photo. 8). Such grain-boundary precipitates were not found in the steels that had not been tempered after isothermal transformation (Photo. 7). When the isothermally transformed steels were tempered at a sufficiently high temperature, the grain-boundary carbides were spheroidized (Photo. 9).

An investigation of the relation between internal strain as determined by X-ray diffraction techniques and the delayed-fracture ratio of quenched-and-tempered steel confirmed that there was a good correlation between these two values. Even here, however, abnormally low values of the delayed-fracture ratio were obtained in test pieces heat treated so as to precipitate carbides along the prior austenitic

grain boundaries.

The influence of reduction by cold drawing was examined for a steel having spheroidized carbides. The hardness increased monotonically with the degree of cold working but the delayed-fracture limit decreased. The fact that the delayed-fracture limit reached a maximum at about 15% reduction resulted from the increased load-carrying capacity due to work hardening rather than from a decreased susceptibility to delayed fracture (Fig. 10).

When cold-drawn steel was annealed, the hardness reached a maximum with an annealing temperature of 400°C. The delayed-fracture ratio increased gradually with annealing temperatures up to 300°C and then more rapidly with higher annealing temperatures. In other words, the relation between hardness and delayed-fracture ratio was not simple in this case (Fig. 11). Annealing temperature had exactly the opposite effect on internal strain so the relation between internal strain and delayed-fracture ratio remained valid. These facts are believed to suggest that internal strain is a major factor among the hardening mechanisms of steel especially influencing the delayed-fracture strength.

環境脆化による遅れ破壊と金属組織

浅田千秋　福井彰一

大同製鋼株式会社　中央研究所

概　　要

鋼構造物接合用の高力ボルトのようにごくありふれた環境中で使用される高力鋼の遅れ破壊の問題を対象として湿潤環境中での遅れ破壊の機構ならびに遅れ破壊特性におよぼす金属組織学的要因の影響について調べた．

純水 0·1 規定以下の微量の HCl を含む水溶液，3% 以下の NaCl を含む水溶液ならびに H_2S で飽和した微酸性水溶液中において，切欠付き円筒試験片について曲げ応力下で遅れ破壊実験を行なった．いずれの環境中で遅れ破壊した試験片でも，その破断面の引張応力側には破壊がまず内部から発生したことを示す Photo. 1 のようなせん断唇が認められた．このせん断唇の厚さは試験片の切欠半径によって異なり，表面から三軸応力性最大なる位置までの距離とほぼ一致することが認められた (Fig. 4)．これらの環境に浸漬した試験片の水素分析の結果，鋼は環境から水素を吸収することが確かめられ，さらにその遅れ破壊強度は水素吸収量の多い環境ほど低下することがわかった．これらの結果から，本研究で取扱った各種の環境中における遅れ破壊に対して，鋼中に吸収された水素の役割がきわめて重要なことが推察された．

焼入した鋼の 0·1 規定 HCl 水溶液中における遅れ破壊強度は Fig. 6 に示すように焼もどし温度によって複雑な変化を示すが，各鋼に共通した挙動として焼もどし温度 350°C 附近で低い遅れ破壊強度を示し，さらに焼もどし温度を高めると極大値を示す．この高温焼もどしによる遅れ破壊強度の極大値以上の温度で焼もどすことにより，鋼の遅れ破壊強度比（遅れ破壊における 30 時間強度と静曲げ強度との比）はほぼ一定値を示すことから，この領域における遅れ破壊強度の低下は鋼の遅れ破壊感受性の増大によるものではなく，載荷能力の低減によるものと考えられる．

鋼の遅れ破壊き裂の発生および伝播について調べた結果，初期的なき裂は前オーステナイト粒界に発生するが，その伝播径路は焼もどし条件によって異なり，350°C 附近の焼もどしによって遅れ破壊強度が低値を示すものではき裂の伝播径路も前オーステナイト粒界に沿っていた (Photo. 3, 4)．電子顕微鏡による金属組織観察の結果，このような試料では特長的に前オーステナイト粒界部に Photo. 5 および 6 に見られるような炭化物が連なって析出していることが認められた．

恒温変態処理してベイナイト組織とした鋼はとくに高硬度域での遅れ破壊強度が焼入焼もどし鋼にくらべて高いが (Fig. 8)，この場合にも 550°C で焼もどしたものはその他の温度で焼もどしたものにくらべて異常に遅れ破壊強度は低下し，同一かたさをもつ焼入焼もどし材と同等の遅れ破壊強度となる．恒温変態処理材の場合にも焼入焼もどし材の場合と同様に異常に遅れ破壊強度が低下したものでは前オーステナイト粒界部に板状の炭化物が連なって析出している (Photo. 8)．恒温変態処理ままのものにはこのような粒界析出物は認められず (Photo. 7)，また十分に焼もどし温度が高いものでは粒界部の炭化物も球状化していた (Photo. 9)．

焼入焼もどし鋼について X 線回折法により内部ひずみを測定し，遅れ破壊強度比との関係を調べた結果，遅れ破壊強度比は内部ひずみと良い相関を示すが，この場合にも前オーステナイト粒界に炭化物が析出するような処理を施したものでは遅れ破壊強度比が異常な低値を示すことがわかった (Fig. 9)．

十分に炭化物を粒状化した鋼について冷間引抜による減面率の影響を調べた．冷間加工によってかたさは単調に増加し，反対に遅れ破壊強度比は低下した．遅れ破壊強度は減面率 15% 附近に最大値を示したが，これは加工硬化による載荷能力の増大によるもので，遅れ破壊に対する感受性が減じたためではない (Fig. 10)．他方，強い冷間引抜を施した鋼の焼なましにおいて，かたさは焼なまし温度 400°C で最大を示すが，遅れ破壊強度比は焼なまし温度 300°C まではゆるやかに増加し，300°C をこえると急激に増加する．すなわち，この場合にはかたさと遅れ破壊強度比との関係は単純ではない．しかし焼なましによる内部ひずみの変化は度遅強れ破壊強度比の変化と反対の関係にあり，両者の変化はよく対応している．これらの事実は鋼の強度機構のうちで，とくに内部ひずみが遅れ破壊強度に対して大きな影響を与える因子であることを示すものと考えられる．

1. まえがき

鋼構造物の軽量化という要求のため各種の高力鋼が開発されたが，その使用に際して従来の低強度鋼では問題とならなかった遅れ破壊が生ずることがあることがわかり，高力鋼の適用に対して大きな隘路となっている．

従来，電気メッキなどによって水素を吸収した鋼が遅れ破壊することは水素脆化遅れ破壊としてよく知られているが，高強度に調質された鋼ではとくに水素を吸収するような処理が施されていないような場合でも遅れ破壊を生ずることが報告されており[1,2]，また高力鋼の遅れ破壊強度に対して大気中の湿気が大きな影響をもつことが知られている[3]．摩擦接合に用いられる高力ボルトは常に高い応力を受けているうえに，橋梁のように露天に設置された鋼構造物の接合部の間隙には雨水が侵入したり，大気中の水分が結露することにより湿潤な環境が形成されており，高力ボルトは遅れ破壊に対して極めて危険な状態にあるといえる．このようにごくありふれた環境中における高力鋼の遅れ破壊を対象として，破壊の機構を調べ，また遅れ破壊特性におよぼす金属組織学的要因の影響について検討した．

2. 遅れ破壊試験方法

湿潤な環境中における遅れ破壊を実験するために Fig. 1に示すような片持曲げ式の負荷機構による遅れ破壊試験機を用いた．また試験片の形状はボルトのねじ部の応力集中係数を参考とし，応力集中係数3·45の切欠をつけた Fig. 2 のごとき形状のものを用いた．

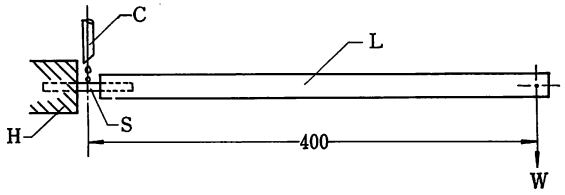

S : Specimen　　W : Loading weight
L : Loading lever　　C : Corrodant supplier
H : Specimen holder

Fig. 1. Testing apparatus for delayed-fracture experiments.

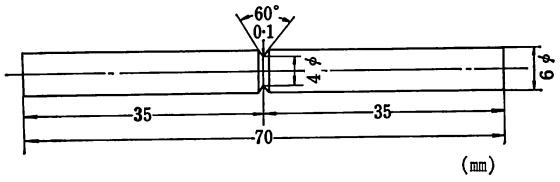

Fig. 2. Test piece shape for delayed-fracture tests.

遅れ破壊試験は試験片の切欠部に所定の曲げモーメントを加えたのち，試験水溶液を切欠部に滴下しつつ破断までの時間を測定することによって行なった．水溶液は試験片の切欠部が乾くことがないように毎分4～6滴の速さで滴下するように調節した．試験結果は負荷した曲げモーメントを切欠部の断面係数で除した商，すなわち表皮最大曲げ応力の値で整理した．

試験はおもに 0·1 規定 HCl 水溶液で行なったが，その他，大気，水，NaCl 水溶液，H_2S 飽和酢酸水溶液でも行なった．水はすべて純水装置によって精製した脱イオン水で，精製直後の酸度は pH 6·8 であった．NaCl および HCl 水溶液は日本薬局法試薬一級品を用いて調整した．HCl 水溶液の酸度は pH メータによって測定し，0·1 規定 HCl 水溶液はメチルオレンジを指示薬として滴定法により濃度を定めた．H_2S 飽和酢酸水溶液は 0·5 % 酢酸水溶液を貯えたびんに H_2S を通じて飽和せしめたもので，H_2S は硫化鉄に稀塩酸を加えて発生させたものである．

3. 遅れ破壊機構

Table 1 に示す鋼について各種の環境中における遅れ破壊試験を行なった．その結果を Fig. 3 に示す．静曲げ強度は遅れ破壊試験片と同形の試験片を用いて漸増荷重によって破断した時の強度である．静曲げ強度よりも低い応力を負荷した場合でも水溶液中では遅れ破壊を生じ，いずれの試験環境中においても負荷応力を低めると破断までの時間は長くなる．そしてある程度以下に負荷応力を下げると破断時間が急に増加するような限界応力値が存在することを示している．遅れ破壊寿命あるいは限界応力値は環境の種類によって異なる．陰極チャージによって予め水素を添加した鋼の遅れ破壊においては，本実

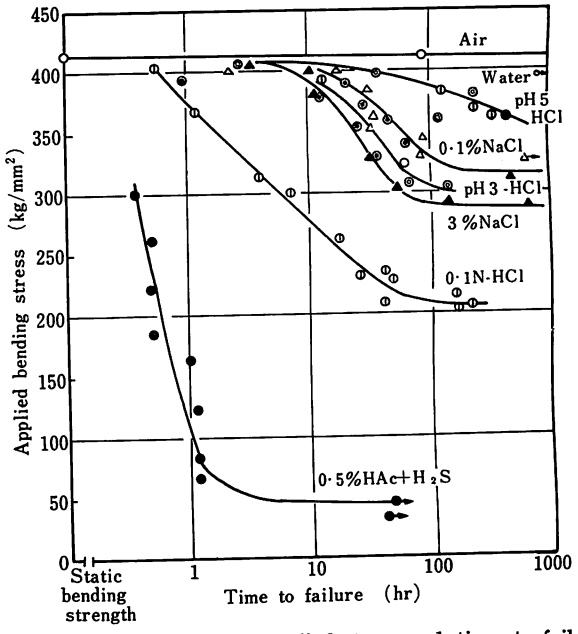

Fig. 3. Relation between applied stress and time to failure for steel B in various environments.

Table 1. Materials used in the delayed-fracture experiments.

Chemical composition (wt %).

	C	Si	Mn	P	S	Cu	Ni	Cr	Mo	Ti
Steel A	0·36	0·25	0·66	0·021	0·013	0·20	0·10	0·98	0·19	—
Steel B	0·21	0·75	1·34	0·013	0·009	0·16	0·14	1·67	—	0·13

Heat treatment and mechanical properties.

Steel	Heat treatment	0·2 % proof stress (kg/mm²)	Tensile strength (kg/mm²)	Elongation (%)	Reduction of area (%)
A	Austenitized at 850°C for 30 min, oil quench, tempered at 550°C for 1hr	115	124·5	9	57·5
B	Austenitized at 885°C for 30 min, oil quench, tempered at 300°C for 1hr	126	150	9·3	47·5

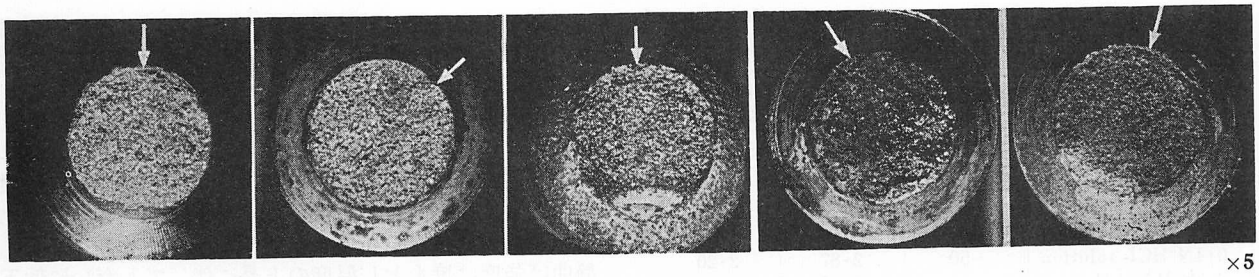

×5

Fractured after 89·5 hr in air	Fractured after 22·7 hr in water	Fractured after 49·8 hr in 0·1N HCl	Fractured after 33·9 hr in 0·1% NaCl	Fractured after 17·3 hr in 3% NaCl

Photo. 1. Fracture surfaces of specimens tested under sustained load in various environments showing a shear lip at the tensile side of the specimen (arrows).

験の場合と同様な限界応力値が存在するほか，高応力側でさらにもう一段破断寿命が急増する上限界応力が存在することが指摘されている[4]．本実験供試材の場合には上限界応力はほとんど静曲げ強度に一致しているが，他の鋼では明らかな上限界値を示すものもあり[7]，一般的にはこれらの水溶液中遅れ破壊の場合の応力一破断時間曲線の形状は水素脆化遅れ破壊の場合と同様であるといえる．ただ，水溶液中遅れ破壊の場合には破断時間の応力依存性が水素脆化遅れ破壊の場合よりも大きく，応力破断時間曲線の傾斜部がゆるやかになっている．

以上のように水溶液中に長時間保持されることにより破壊強度は明らかに低下するが，水溶液の作用としては腐食反応における陽極的な効果と陰極的な効果とが考えられる．腐食環境中における遅れ破壊の場合に陽極的あるいは陰極的効果のいずれが主導的な役割を持つかを見分ける方法として，しばしば分極下における遅れ破壊実験が行なわれるが，この方法では実際に破壊が進行するき裂先端部での局所的な腐食環境の変化のため，必ずしも実際の現象を捕えていないという指摘もある[5]．また，微視的には陽極部分と陰極部分とが入り混ってき裂が進行していくという観察結果もあり[6]，両作用の主導性を弁別することはなかなか困難である．

Photo. 1 は各種の環境中で遅れ破壊した試験片の破断面の例である．いずれの場合にも引張応力側の表層部にせん断唇状のせん断破壊部が認められる．このせん断唇は破壊が表面からではなく，内部から発生したことを示すものである．Photo. 2 は試験片が破断する前に遅れ破壊試験を中断し，試験片の軸を含む曲げ平面で切断したときに引張応力側の切欠底部に発見されたき裂である．

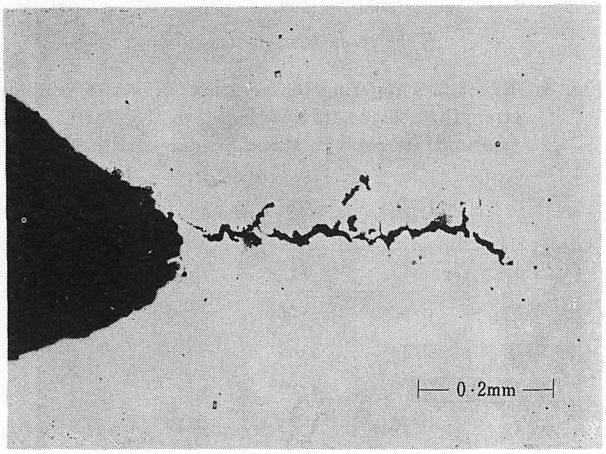

Photo. 2. Subsurface crack observed on the axial section of the specimen after sustained loading in 0·1N HCl solution.

これは遅れ破壊き裂の初期のもので，さらに成長して表面に通じるが，その際に表層附近でせん断破壊に転化するものと考えられる．その経過が破断面におけるせん断唇として認められるのである．

遅れ破壊した試験片の破断面に生ずるせん断唇の厚さは試験片の切欠半径によって異なることがわかった．Fig. 4 は切欠半径の異なる試験片を 0·1 規定 HCl 中で遅れ破壊した際のせん断唇の厚さの測定値をそれぞれの試験片の応力分布と比較して示したものである．せん断唇の厚さはほぼ表面から半径方向応力最大の位置までの距離と一致している．Johnson らによると水素脆化遅れ破壊の場合にき裂発生点は切欠によって生ずる 3 軸応力性最大の位置で，切欠底に塑性変形が生ずると 3 軸応力性最大の位置は半径方向応力が最大となる位置と一致するという[8,9]．本実験におけるせん断唇厚さとき裂発生点との対応は明らかではないが，Johnson らの所見との対応は興味深い．

以上の実験結果は本研究で取扱った各種の環境中における遅れ破壊がおもに腐食反応における陰極的挙動によ

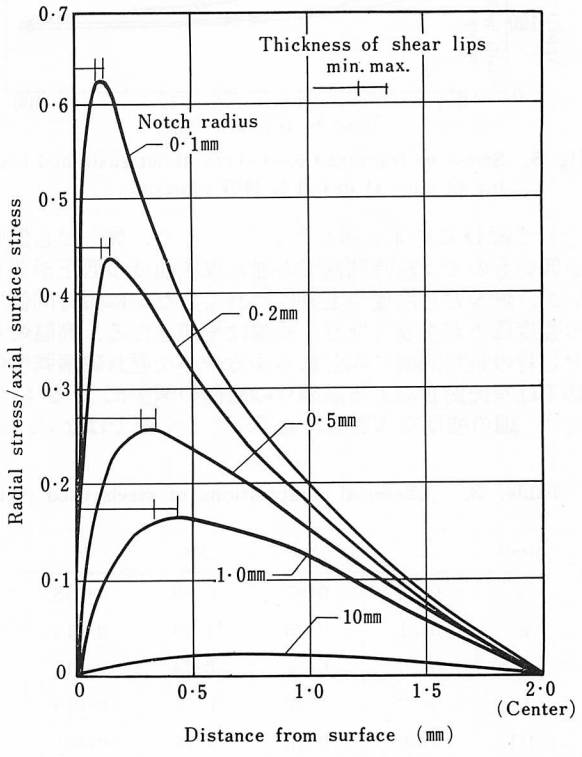

Fig. 4. Relation between distribution of radial stress and thickness of shear lip measured from notch surface.

Table 2. The results of hydrogen analyses of steels immersed in various environments.

Environment	Immersion time (hr)	Hydrogen content (ml/100g)	
		Steel D-1	Steel B
Air	—	0·24	0·22
pH5 HCl solution	50	0·28	0·18
3% NaCl solution	100	0·66	1·03
0·1N HCl solution	50	2·87	2·20
0·5% HAc+H_2S	50	7·06	9·36

って鋼中に吸収された水素に起因することを示唆する．Table 2 は直径 6mm，長さ 70mm の試験片を各種の水溶液に浸漬したのち，その水素含有量を調べた結果である．水素の抽出は 1000°C で行なったが，水溶液に浸漬することにより水素量が増加することが認められる．また Fig. 3 の遅れ破壊試験結果と対比すると水素増加量の多い環境ほど遅れ破壊強度が低下する傾向が認められる．

4. 金属組織の影響

Table 3 に示す化学成分の鋼を焼入れ後各種の温度で焼もどしした場合の 0·1 規定 HCl 中における遅れ破壊強度を調べた．Fig. 5 は負荷応力一破断時間曲線の一例

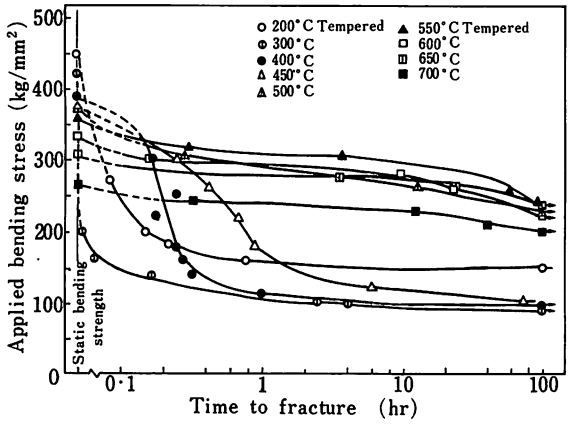

Fig. 5. Stress vs fracture-time curves under sustained loading of steel D in 0·1 N HCl solution.

として鋼 D の結果を示したものである．焼もどし温度が低いものでは短時間側での遅れ破壊強度の低下が著しいが，焼もどし温度の上昇につれてしだいに短時間側での強度低下が少なくなり，曲線は平坦となる．高温焼もどし材の長時間側にみられるゆるやかな遅れ破壊強度の低下は全面腐食による試験片の直径の減少によるもので[7]，鋼の強度の本来の遅れ破壊強度としてはこのような全面腐食の影響が少ない領域で比較するのが適当で，本研究では 30hr で破断するときの応力値をとり遅れ破壊限度と呼ぶこととする．

Fig. 6 は各鋼の焼もどしにともなう静曲げ強度，遅れ破壊限度および遅れ破壊限度比の変化を示す，ここに遅れ破壊限度比とは遅れ破壊限度の静曲げ強度に対する比の値で，遅れ破壊抵抗性を示す指標となるものである．静曲げ強度は焼もどし温度の上昇に伴ってしだいに低下するが，Cr, Mo, V 等を含む鋼では焼もどし軟化抵抗性に対応する静曲げ強度の低下の停滞が認められる．遅れ破壊限度は焼もどし温度によって複雑な変化を示すが，各鋼に共通した挙動として，まず 200～300°C 焼もどし

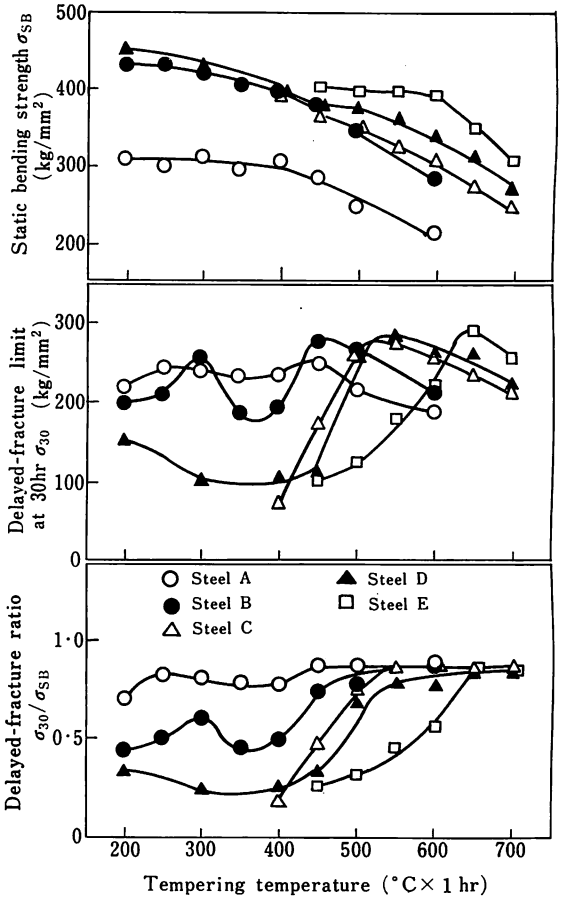

Fig. 6. Effect of tempering temperature on static bending strength, delayed-fracture limit in 0·1 N HCl solution and its ratio to static bending limit.

Table. 3. Chemical compositions of steels used (%).

Steel	C	Si	Mn	P	S	Cu	Ni	Cr	Mo	Others
A	0·20	0·27	0·68	0·018	0·019	0·13	0·05	1·00	—	—
B	0·21	0·75	1·34	0·013	0·009	0·16	0·14	1·67	—	Ti 0·13
C	0·39	0·27	0·74	0·015	0·017	0·15	0·06	1·01	—	—
D	0·37	0·27	0·73	0·019	0·014	0·14	0·10	1·01	0·19	—
D1	0·36	0·25	0·66	0·021	0·013	0·20	0·10	0·98	0·19	—
E	0·36	0·64	0·82	0·015	0·008	0·10	0·04	1·38	0·59	V 0·15

で極大値，350°C 附近での焼もどしにより極小値を示し，さらに焼もどし温度を高めるとしだいに遅れ破壊限度は上昇し，再び極大値を示したのち低下していく．焼もどし温度による遅れ破壊限度比の変化についてみると焼もどし温度の低い領域での変化は遅れ破壊強度の場合とまったく同様であるが，遅れ破壊限度が高温側の極大値を示す温度よりも高い焼もどし温度域では遅れ破壊限度比はほぼ一定値 0·85 を示している．すなわち，これらの温度で焼もどした鋼の遅れ破壊抵抗性はほぼ一定で，遅れ破壊限度が焼もどし温度の上昇に伴って低下するのは静曲げ強度の低下に示されるように鋼の載荷能力が減ずることによるものであることがわかる．

焼もどし温度の低い領域における遅れ破壊限度の変化に関しては Hughes ら[10] も同様な結果を報告している．Hughes らは焼入鋼の焼もどしにおいて 250°C 附近まで存在する ε 炭化物が水素と強い親和力をもつという

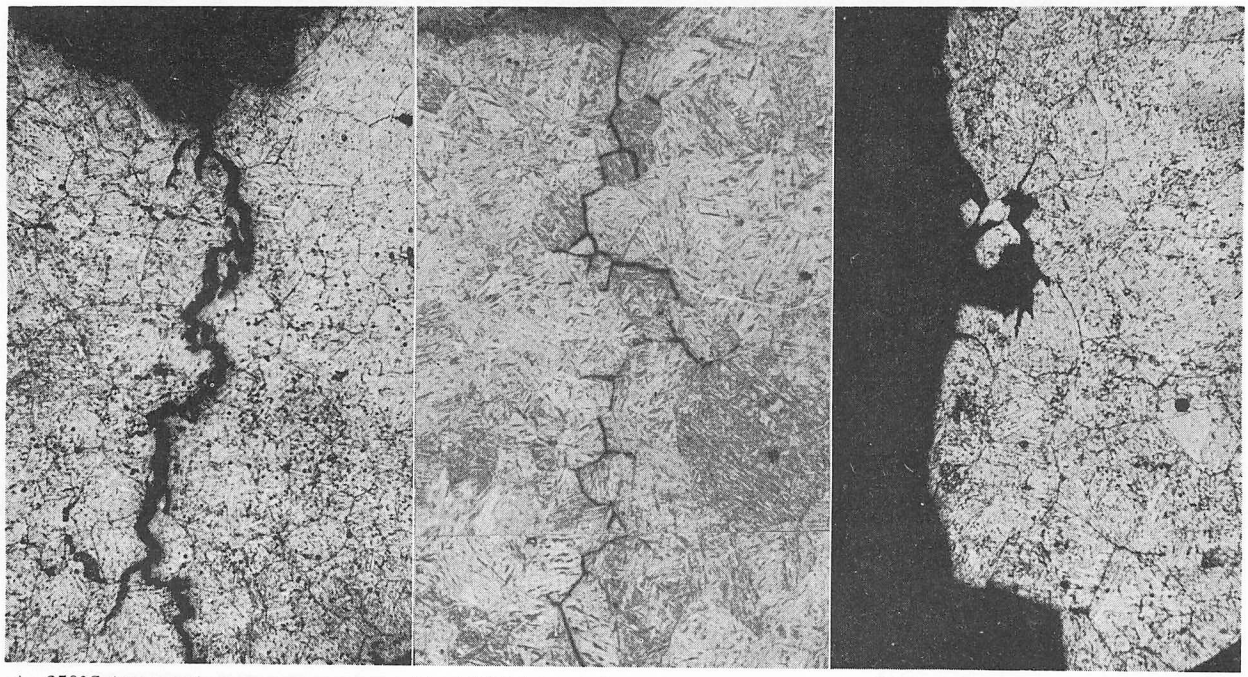

a) 250°C tempered　b) 400°C tempered　c) 500°C tempered　×100

Photo. 3. Crack propagation path on delayed fracture of steel B in 0·1 N HCl showing transcrystalline fracture (a and c) and intercrystalline fracture b). Etched by saturated picric-acid solution (a and c) or 1% nital b).

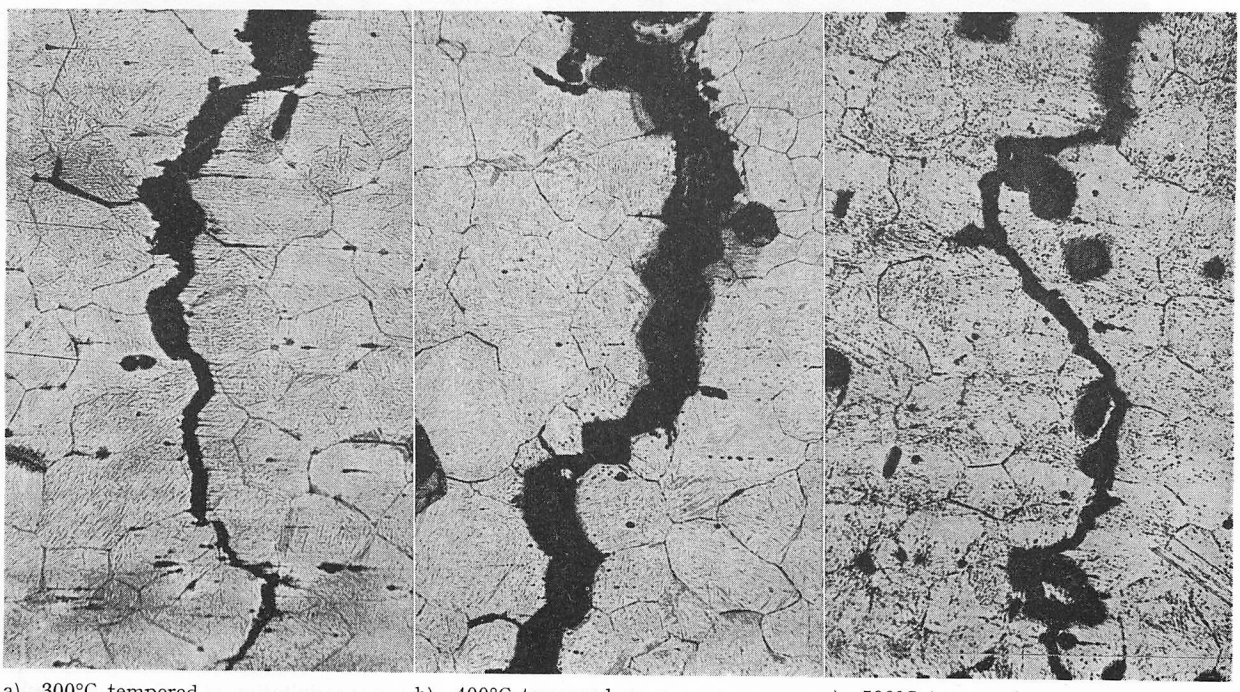

a) 300°C tempered　b) 400°C tempered　c) 500°C tempered　×100

Photo. 4. Crack propagation path on delayed fracture of steel D in 0·1 N HCl. Etched by saturated picric-acid solution.

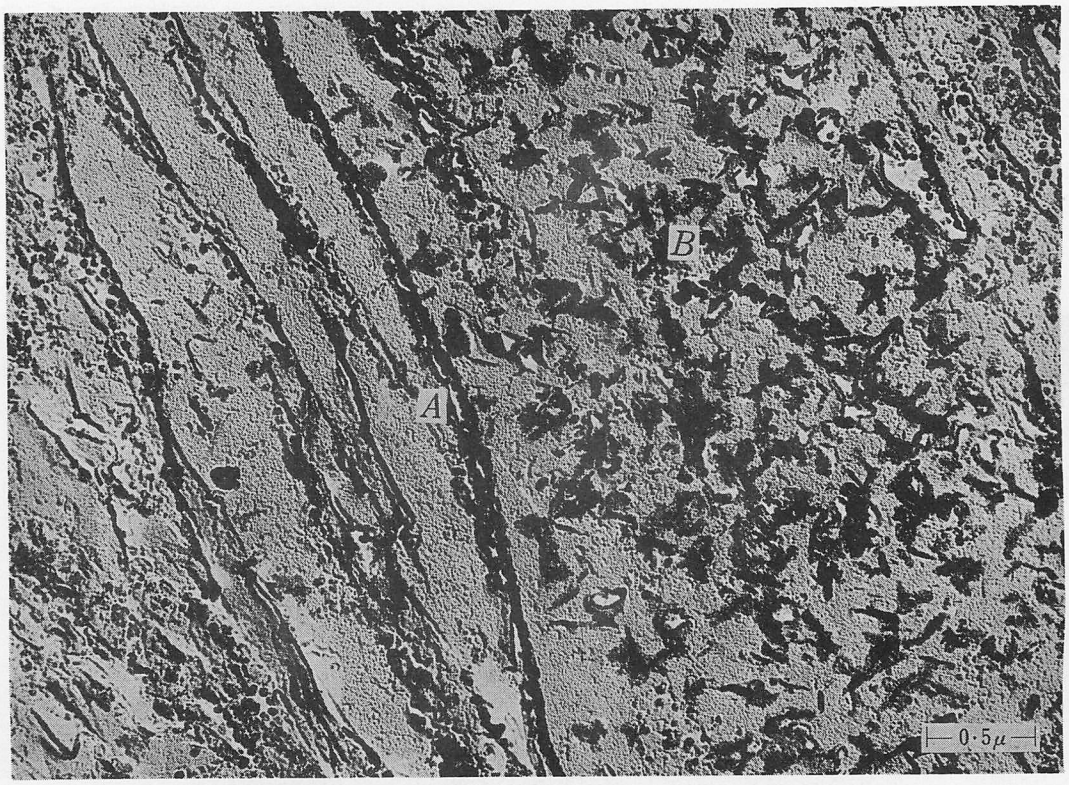

Photo. 5. Electron micrograph of extraction replica for steel B tempered at 400°C showing carbide precipitation at prior austenitic grain boundary (A) and flaky cementite (B).

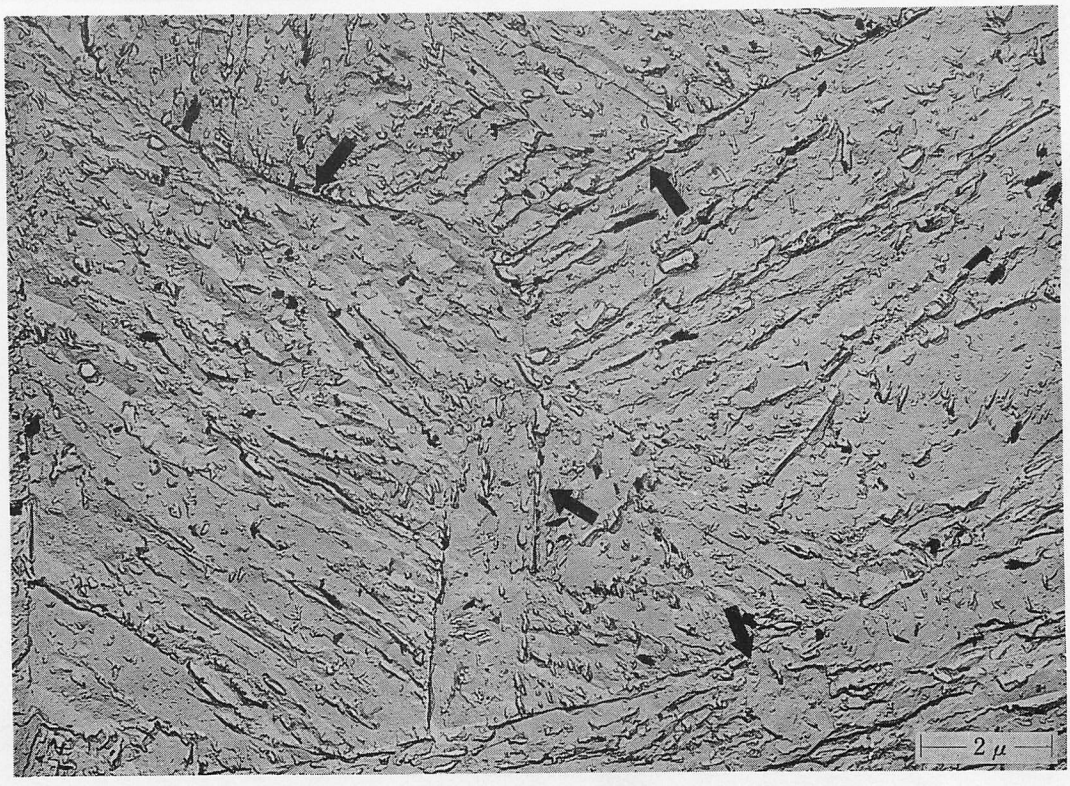

Photo. 6. Electron micrograph for steel D tempered at 450°C showing grain-boundary precipitation of carbides (arrows).

Berg の報告[12]を引用して，ε炭化物の水素捕捉効果により破壊発生部への水素の拡散を妨げるために遅れ破壊限度が増加すると説明している．

Siはε炭化物を安定化する元素であるといわれるが[11]，本実験においてもSi含有量の少ない鋼Aや鋼Cでは200～250°Cの焼もどしで遅れ破壊限度の極大値を示し，またSi含有量の多い鋼Bではそれよりやや高い300°C焼もどしで極大値を示しており，その点からはHughesらの説明は矛盾しない．他方，Davisら[13]は各種の鋼の焼もどし温度による食塩水中での遅れ破壊寿命の変化を調べて500°F脆性領域で遅れ破壊寿命が短縮することを認めた．彼らはこの領域における破壊が前オーステナイト粒界に沿って生ずることから，Klingerら[14]の500°F脆性に関する研究結果と対応して，前オーステナイト粒界に形成された板状セメンタイトによって遅れ破壊強度の低下が生ずると考えているようである．Lillysおよび Nehrenberg[15]は13% Cr 鋼の5%NaCl 水溶液噴霧中における遅れ破壊寿命について調べ，900°F 焼もどしで最も遅れ破壊感受性が大きくなることと前オーステナイト粒界に形成されたCr 炭化物とが対応することを示している．またこの鋼の場合セメンタイトが析出しはじめる500°F 附近で遅れ破壊感受性は最も小さくなるという．

Photo. 3 および Photo. 4 はそれぞれ鋼Bおよび鋼Dの遅れ破壊き裂伝播径路を示す．遅れ破壊限度が極小を示すような温度で焼もどした試験片では遅れ破壊き裂は前オーステナイト粒界に沿って伝播しており，この焼もどしによって前オーステナイト粒界部の遅れ破壊に対する抵抗性が低下していることがわかる．また Photo. 4 において主き裂から離れたオーステナイト粒界部に滲みが認められるが，これは主き裂とは独立して生成した遅れ破壊き裂の初期的なもので，これからみても前オーステナイト粒界部が遅れ破壊き裂の生成場所として重要な役割を演じていることがわかる．

Photo. 5 および Photo. 6 はそれぞれ鋼Bを400°Cで焼もどしたものおよび鋼Dを450°Cで焼もどした試料の電子顕微鏡的組織である．これらに認められるように前オーステナイト粒界部には炭化物が密に連なって析出している．焼もどし温度をさらに上昇すれば，これらの粒界部の炭化物は粒状に凝集していく．このような前オーステナイト粒界部の炭化物の析出状況は中間温度での焼もどしによる遅れ破壊強度の低下と関連をもつように思われる．

いわゆるオーステンパー処理は低温焼戻し脆性を示すような強度レベルの鋼の靱性を改善する方法として有効なことが知られている[16]．そこで鋼Eに相当するCr-Mo-V 鋼について各種の温度で恒温変態処理を行ない，ベイナイト組織とした試験片について遅れ破壊強度を測定した．

Fig. 7 は400°Cで恒温変態してベイナイト組織としたものおよびそれを焼もどしたものの0·1 規定 HCl 水溶液中における負荷応力—破断時間曲線である．焼もどし温度の上昇によって静曲げ強度はしだいに低下するが遅れ破壊限度は550°C焼もどしではむしろ低下し，600°C以上の焼もどしで回復している．このようにオーステンパー処理した鋼でもある範囲の温度で焼もどしを施すと遅れ破壊強度の低下をきたす．Fig. 8 には恒温変態処理およびその後の焼もどしによってかたさを調整したCr-Mo-V 鋼の静曲げ強度，遅れ破壊限度などとかたさとの

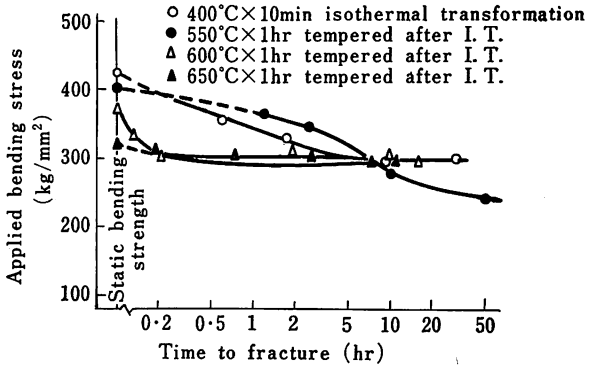

Fig. 7. Stress vs fracture-time curves under sustained load in 0·1 N HCl solution for chromium-molybdenum-vanadium steel isothermally transformed at 400°C and tempered after isothermal transformation.

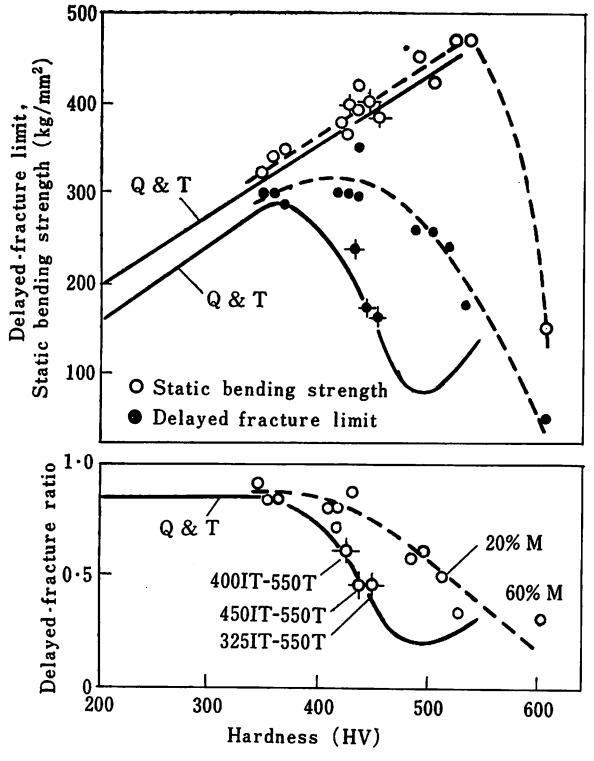

Fig. 8. Relation between hardness and delayed-fracture characteristics for isothermally transformed and tempered chromium-molybdenum-vanadium steel in comparison with quenched-and-tempered steel.

関係を通常の焼入焼もどし処理のものと比較して示した．恒温変態処理材は焼入焼もどし材にくらべてより高いかたさHV 400 程度まで遅れ破壊限度は上昇を示し，遅れ破壊限度比の低下も少ない．しかしかたさHV 400 をこえるとこれらはいずれも低下していく．ここで興味深いのは恒温変態処理後550°Cで焼もどしたものはその他の焼もどし温度で処理したものにくらべて異常に遅れ破壊限度が低く，同一かたさの焼入焼もどし材と同等の遅れ破壊限度を示すことである．

Photo. 7 は325°Cで恒温変態したCr-Mo-V 鋼の電子顕微鏡組織である．この状態では前オーステナイト粒界部にとくに炭化物が多く析出しているようなことはなく，粒内に微細な炭化物の析出が認められる．しかしこ

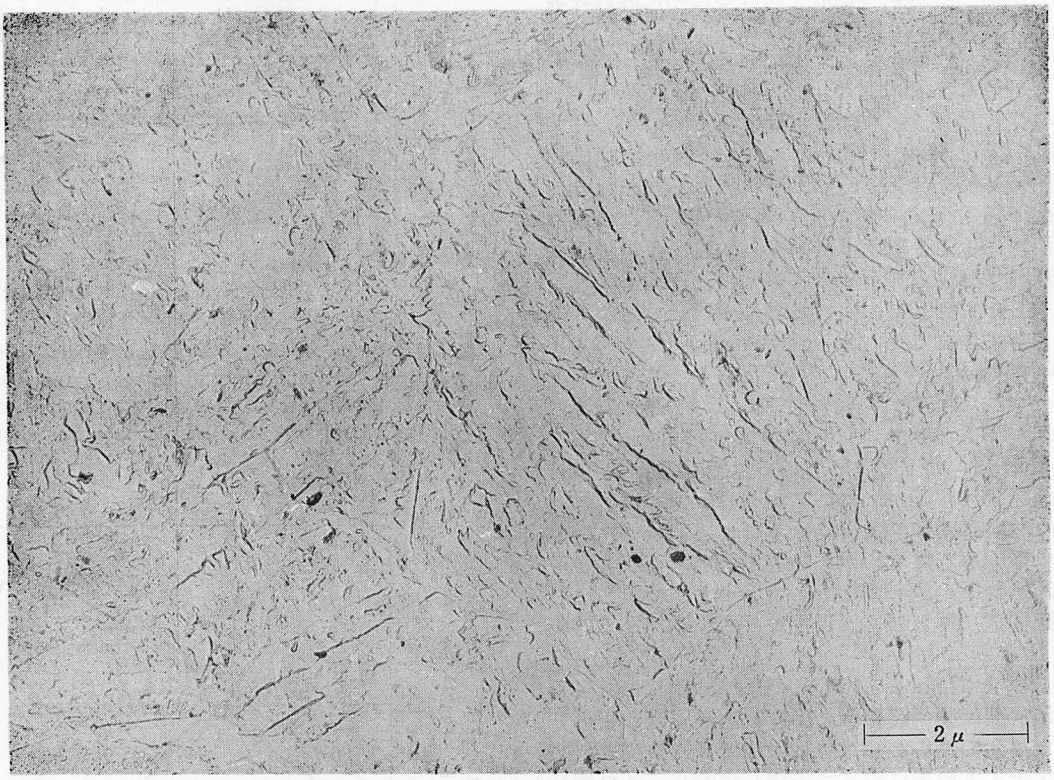

Photo. 7. Electron micrograph of chromium-molybdenum-vanadium steel isothermally transformed at 325°C.

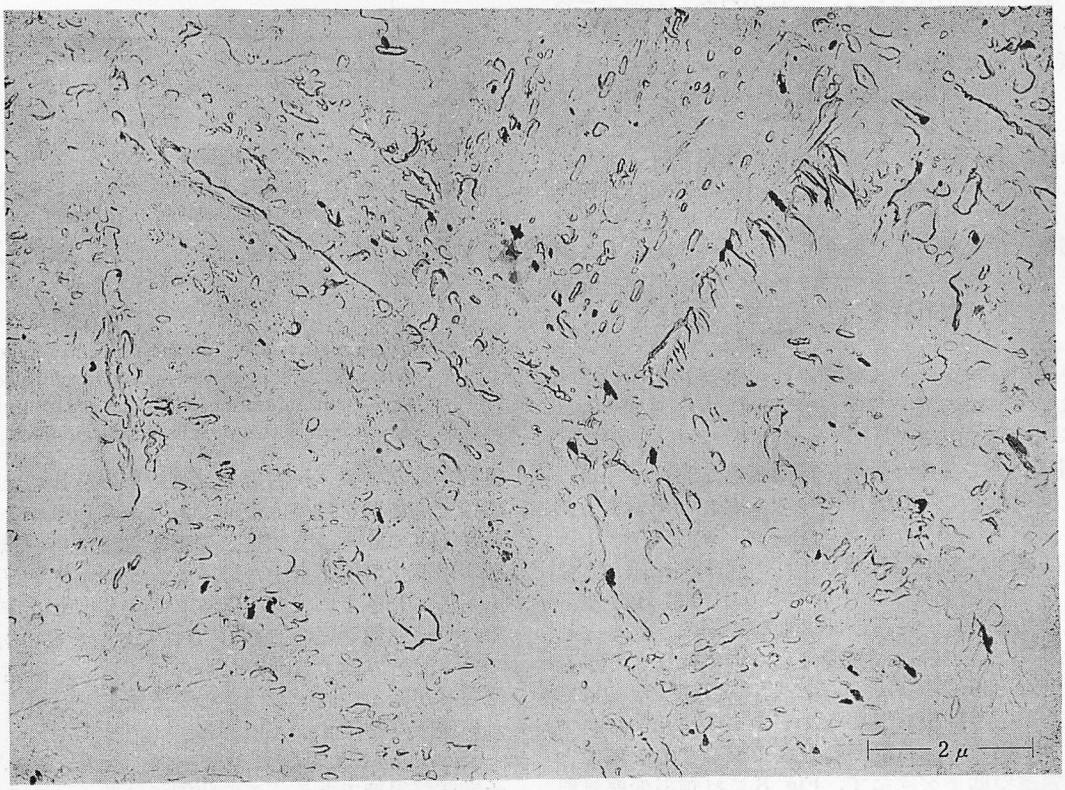

Photo. 8. Electron micrograph of chromium-molybdenum-vanadium steel tempered at 550°C after isothermal transformation at 325°C showing carbides compactly precipitated at prior austenitic grain boundary.

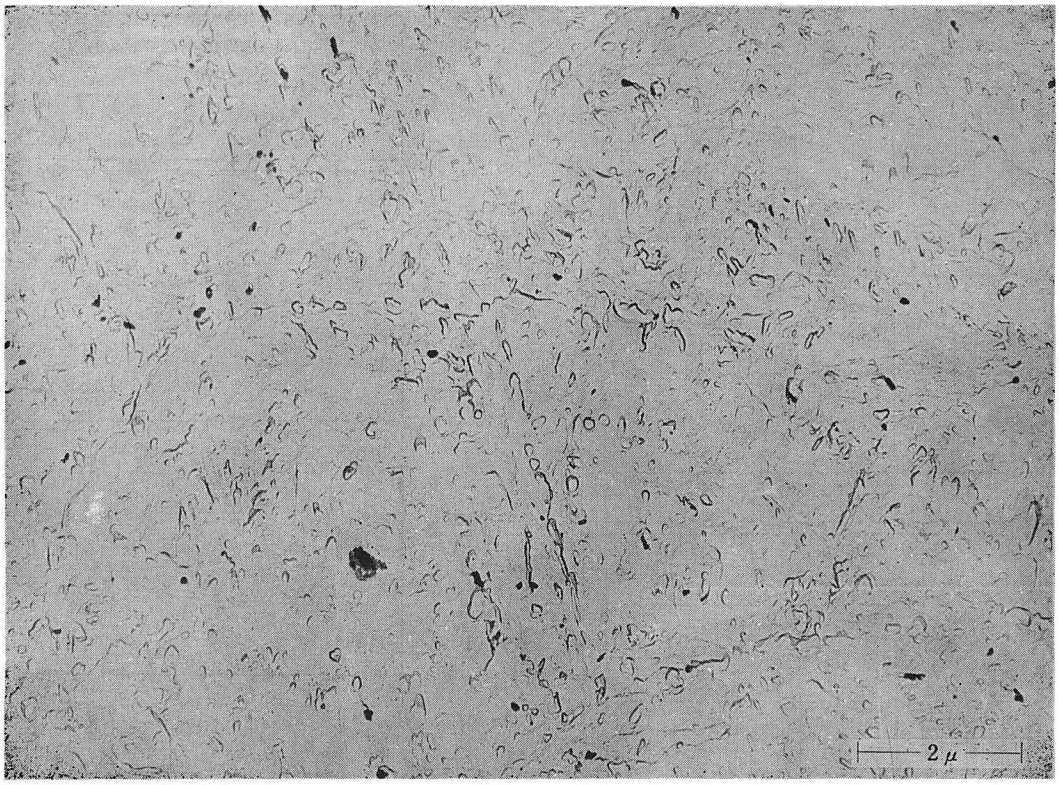

Photo. 9. Electron micrograph of chromium-molybdenum-vanadium steel tempered at 600°C after isothermal transformation at 325°C showing spheroidized carbides at prior austenitic grain boundary.

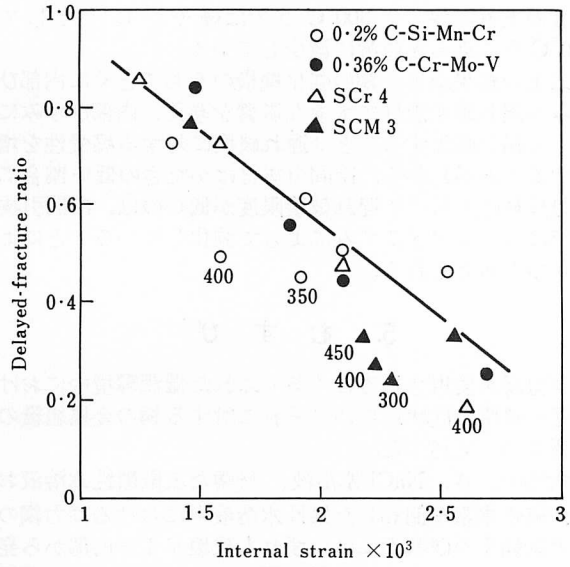

Fig. 9. Relation between internal strain and delayed-fracture ratio for several quenched-and-tempered steels.

Table 4. Chemical composition of steel used for tests on the influence of cold drawing on the delayed-fracture characteristics (%).

C	Si	Mn	P	S	Cu	Ni	Cr	Mo
0·38	0·31	0·71	0·013	0·021	0·18	0·08	0·95	0·18

れを 550°C で焼もどしたものでは Photo. 8 のごとく前オーステナイト粒界部に板状の炭化物が連なって析出している．さらに 600°C で焼もどしたものでは Photo. 9 のごとく前オーステナイト粒界部の炭化物は球状化していることがわかる．

これらのことから，HV 350 以上のかたさ領域において恒温変態処理材の遅れ破壊強度が焼入焼もどし材のそれにくらべて高いのは，前オーステナイト粒界部における炭化物の析出状態の差異によるものと考えられる．

前オーステナイト粒界部に不適当な炭化物が析出していない恒温変態処理材の場合でも HV 400 以上のかたさではかたさの上昇に伴って遅れ破壊強度が低下する．焼入焼もどし材の場合にも同様な傾向が認められる．いっぽうこれらの鋼のかたさは地鉄の固溶炭素，変態時に生成した内部ひずみ，分散炭化物粒などによって支えられる．遅れ破壊強度がかたさによって変化することはこのような鋼の強化機構と関連することを示唆するものと考えられる．

Fig. 9 は各種の鋼を焼入れ後焼もどしした際の内部ひずみと遅れ破壊限度比との関係を示すものである．ここに内部ひずみとしては Fe の (110) 面および (220) 面からの回折 X 線の幅広がりから Hall の式を用いて算定したものである．Fig. 9 にみられるように遅れ破壊限度比は前オーステナイト粒界に炭化物が析出して異常な低下を示した点を除けば内部ひずみ量と良い相関を示す．

鋼の内部ひずみと遅れ破壊限度との関係を確かめるために冷間引抜加工によって内部ひずみを与えた鋼の遅れ破壊特性を調べた．供試材は Table 4 に示す化学成分の鋼で，予め冷間引抜と A_1 変態点以下の温度での焼なましによって十分に炭化物を粒状化させたのち，所定の引抜減面率まで冷間引抜を施し，これより遅れ破壊試験片

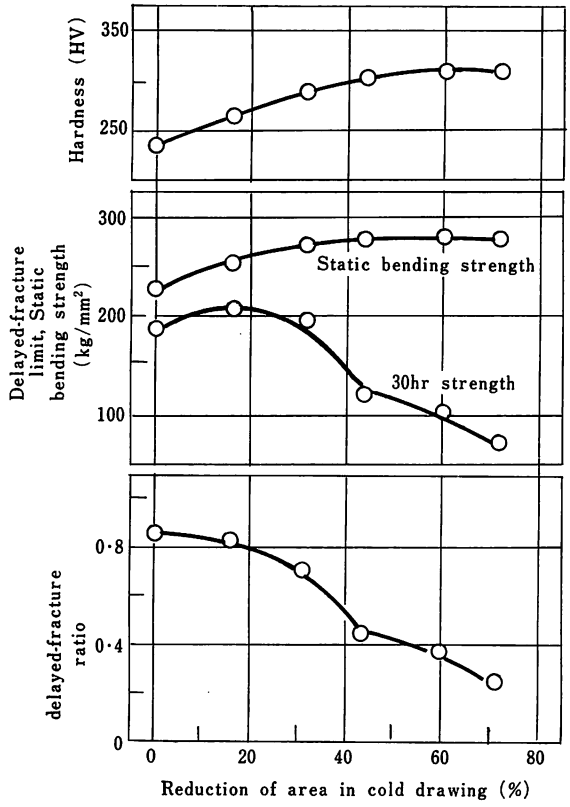

Fig. 10. Effect of reduction of area in cold drawing on hardness, static bending strength, 30 hr strength and strength ratio in delayed fracture under sustained load in 0·1N HCl solution.

を切出して 0·1 規定 HCl 水溶液中で遅れ破壊試験を行なった．試験片は切欠断面部で素材断面積の 60% 以上を削除しているので冷間引抜による巨視的残留応力の影響は除外されている．

Fig. 10 は冷間加工率による遅れ破壊限度，遅れ破壊限度比，静曲げ強度およびかたさの変化を示したものである．遅れ破壊限度は冷間加工率 15% 附近に最大を示すが，これは静曲げ強度の上昇によって示されるように鋼の載荷能力が増大したことによるもので，遅れ破壊に対する抵抗性を示す遅れ破壊限度比でみると冷間加工率の増加につれてしだいに遅れ破壊に対する抵抗性が減ずることがわかる．

Fig. 11 は引抜による冷間加工率 71·5% の試料について焼なまし温度による遅れ破壊限度比，かたさおよび内部ひずみ量の変化を示す．遅れ破壊限度比は焼なまし温度の上昇につれて 300°C まではゆるやかに，そして 400°C をこえると急激に増加していく．かたさは焼なまし温度 400°C までは上昇し，それ以上で漸減する．冷間加工したフェライトの焼なましに際して 200°C 程度までの低温加熱によって侵入型固溶原子による転位のピン止めが行なわれ，降伏点が上昇する．本供試材のように分散炭化物粒を含む鋼では完全に転位のピン止めが行なわれるには炭化物粒の再固溶を要するため 350～400°C の高温加熱ののちに降伏点の最大値に達するといわれる[17,18]．この場合には冷間加工率によってかたさを調整した場合と異なり，かたさと遅れ破壊限度比との間には単純な関

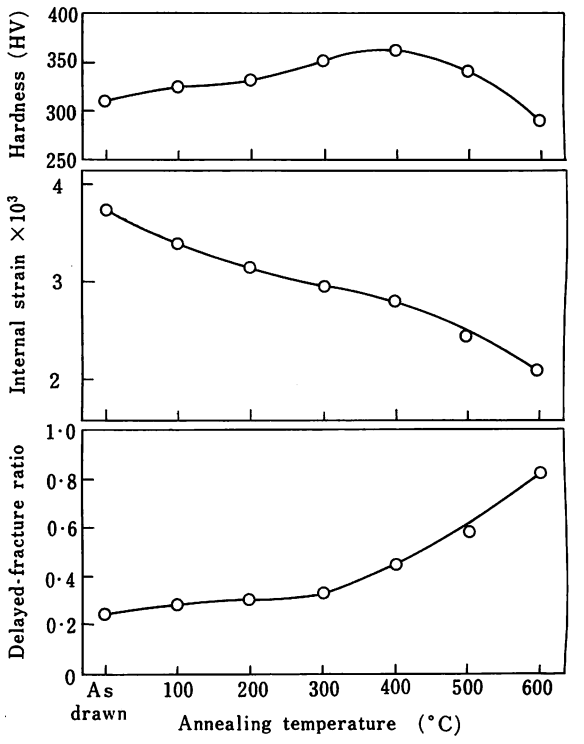

Fig. 11. Effect of annealing temperature on hardness, internal strain and delayed-fracture ratio of steel cold drawn to a 71·5% reduction of area.

係が成立たない．これに対して焼なましによる内部ひずみの変化はちょうど遅れ破壊限度比と反対に，焼なまし温度の上昇に伴って 300°C までは緩やかに，そして 300°C をこえると急激に減少していく．

以上の結果から，鋼の強化機構のうちでとくに内部ひずみが遅れ破壊限度に大きな影響を与え，内部ひずみによって鋼を強化することは遅れ破壊に対する感受性を増大することがわかる．冷間引抜材はかたさの低い割合に熱処理材にくらべて遅れ破壊限度が低いのは，冷間引抜材ではおもに内部ひずみによって強化していることによるものと考えられる．

5. むすび

高力鋼が使用されるごくありふれた湿潤環境中における遅れ破壊の性状ならびにそれに対する鋼の金属組織の影響について述べた．

大気中，水，NaCl 水溶液，稀薄な塩酸酸性水溶液および硫化水素を飽和した酸性水溶液中における高力鋼の切欠試験片の破断面にはいずれも破壊がまず内部から発生したことを示すせん断唇が認められた．このせん断唇の厚さは切欠半径によって異なり，表面から三軸応力性最大なる位置までの距離とほぼ一致した．またこれらの環境中で鋼は明らかに水素を吸収することが確かめられた．環境中での遅れ破壊強度は水素吸収量の多い環境ほど低下した．これらの結果から本研究で取扱った環境中での遅れ破壊に対して鋼中に吸収された水素の役割がきわめて大きいことがわかった．

焼入れした鋼の遅れ破壊強度は焼もどし温度の上昇につれて次第に上昇するが，前オーステナイト粒界部に炭化物が連なって析出した場合には異常に遅れ破壊強度が

低下する．恒温変態処理によって強化した鋼はかたさHV 350以上の高硬度域では焼入焼もどし材よりも遅れ破壊強度は高いが，この場合にも前オーステナイト粒界部に連なって炭化物が析出するような焼もどしを施した場合には焼入焼もどし材と同程度まで遅れ破壊強度が低下する．遅れ破壊き裂は前オーステナイト粒界に沿って発生し，結晶粒界に連なって炭化物が析出したものではき裂の伝播径路も前オーステナイト粒界に沿っている．これらの結果から熱処理によって強化した鋼の場合，前オーステナイト粒界の性状が遅れ破壊強度に大きな影響を及ぼすことが推察された．

上記のような前オーステナイト粒界部の炭化物による異常な遅れ破壊強度の低下を除けば，遅れ破壊強度はかたさと良い相関を示す．しかし冷間引抜のようにおもに内部ひずみによって強化した鋼の遅れ破壊強度は熱処理によって強化した鋼にくらべて同一かたさでも著しく低い．X線解析によって求めた内部ひずみ量によって整理すると，冷間加工材でも熱処理材でもその遅れ破壊強度比は内部ひずみ量によって一義的に決まる．このことから鋼の強化機構のうちとくにひずみ強化は遅れ破壊強度の低下を招くおもな要素であることがわかった．

文　献

1) A. Büttinghaus, H.G. Brandt, E. Keil und B. Richman: Stahl u. Eisen, **86** (1966), 2, p. 542
2) R.H. Raring and J.A. Rinebolt. Trans. Amer. Soc. Metals, **48** (1956), p. 198
3) G.L. Hanna, A.R. Troiano and E.A. Steigerwald: Trans. Amer. Soc. Metals, **57** (1964), p. 658
4) A.R. Troiano: Trans. Amer. Soc. Metals, **52** (1960), p. 54
5) H.P. Leckie: Preprint of the Conference on Fundamental Aspects of Stress Corrosion Cracking, (1967), Ohio State Univ
6) N.A. Tiner and C.L. Gilpin: Corrosion, **22** (1966) 10, p. 271
7) S. Fukui and C. Asada : Tetsu to Hagane 54 (1968), p. 1290
8) H.H. Johnson, J.M. Morlet and A.R. Troiano: Trans. Met. Soc,. AIME, **212** (1958), p. 528
9) W.J. Barnett and A.R. Troiano: Trans. Met. Soc. AIME, **209** (1957), p. 486
10) P.C. Hughes, I.R. Lamborn and B.B. Liebert: J. Iron Steel Inst., (1965), p. 154
11) C.J. Altstetter, M. Cohen and B.L. Averbach: Trans. Amer. Soc. Metals, **55** (1962), p. 287
12) T.G. Owe Berg: Amer. Ceram. Soc. Bull., **40** (1961), p. 78
13) R.A. Davis, G.A. Dreyer and W.C. Gallaugher: Corrosion, **20** (1964), p. 93
14) L.J. Klinger, W.J. Barnett, R.P. Frohmberg and A.R. Troiano: WADC TR 53205, (July 1953)
15) P. Lillys and A.E. Nehrenberg: Trans Amer. Soc. Metals, **48** (1956), p. 327
16) C.Asada, Y.Motomiya and A.Yamamoto : Denkiseikō **28** (1957), p. 351
17) E.T. Stephenson and M. Cohen: Trans. Amer. Soc. Metals, **54** (1961), p. 72
18) D.V. Wilson and B. Mintz: Trans. Amer. Soc. Metals, **54** (1961), p. 728

Delayed Failure of High-Strength Steels

S. Yamamoto* T. Fujita**

*Kobe Steel, Ltd. Chemical Machinery and Equipment Group

**Kobe Steel, Ltd. Central Research Laboratory

The delayed failure properties of conventional quenched-and-tempered steels and of maraging steel were investigated. Notched-tensile sustained-load tests with a stress-concentration factor Kt=10 were conducted in distilled water (Fig. 1, 2). The results are summarized as follows:

1. Initiation and growth of cracks

As far as our tests are concerned, the delayed failure crack initiated on the surface of the notch root of the specimen having a notch radius of 0·03 mm. Crack propagation was mostly along the former austenitic grain boundary in case of quenched-and-tempered steel and underaged 18% Ni maraging steel but through the former austenite grains of the latter when fully aged.

2. Temperature dependence

Increasing the test temperature from 25 to 80°C accelerated the delayed failure phenomenon about 30 times in terms of time to failure. The apparent activation energy was about 13 000cal/mole. This means that the chemical reaction between the material and the environment plays a major role in determining the rate of the process so the delayed failure of high-strength steels in water is a branch of the vast field of environmental embrittlement (Fig. 3, 4).

3. Mechanism

Delayed failure, sometimes called delayed fracture, stress-corrosion cracking or static fatigue, is one type of the broad phenomenon of embrittlement caused by environmental attack, which includes so-called season cracking, hydrogen attack, stress-corrosion cracking in stainless steels and so forth.

Nomenclature in this field is somewhat confused at the present time. The term "delayed failure" generally designates the time-dependent failure of high-strength steels under static tensile stress in a comparatively moderate environment. There are two types of delayed failure. In the one case, the fracture is definitely caused by excess hydrogen in the steel; examples would be flaking or failure of cadmium-plated components. In the other case, with which we are now involved, appreciable amounts of hydrogen are not always detected, at least on a macroscopic scale.

Delayed failure tests in a 0·3% NaCl solution under impressed current showed that an anodic dissolution or stress-corrosion mechanism was operative (Fig. 9). On the other hand, the positive result of the tritium (hydrogen isotope) absorption experiment in water might suggest a hydrogen embrittlement mechanism (Table 1). Hydrogen adsorption on the surface must also be considered. It seems that all three mechanisms are involved in the delayed failure of high-strength steel in water or under open-air service conditions.

4. Strength level

From the practical point of view, sensitivity to delayed failure has a close relation with the strength level of the material. All conventional low-alloy steels with yield strengths above 110 kg/mm² or equivalent ultimate tensile strengths above 120 kg/mm² became sensitive to delayed failure in water when tested with Kt=10 (Fig. 5).

This fact seems to confirm the concept about the unreliability of high-strength steels generally held in the past. It might be pointed out that the conventional authoritative steel specifications based on previous service experience and huge amounts of experimental data depending mainly on rather obscure measures of reliability such as elongation and reduction have been appropriate in respect to the correct selection of steels, whose reliability has now been clearly and quantitatively revealed by the delayed failure test. If chemical composition and heat treatment, especially tempering temperature, are in accordance with the steel specification, the ultimate tensile strength of constructional steel to be used as a tension member in open air is kept below 120 kg/mm².

Our test results correlate well with actual service tests on bolts. Material with a delayed failure strength in 10 000 hr higher than the ultimate tensile strength has also been found to be safe in actual loaded bolt tests.

5. Heat treatment

The tempering temperature of low-alloy steels and the aging temperature of 18% Ni maraging steel have some effect on delayed failure properties.

Improper heat treatment such as underaging of 18% Ni maraging steel at about 440°C caused an unanticipated drastic decrease in delayed failure endurance (Fig.7). Temper brittleness observed after tempering a low-alloy steel with 0·2% C at about 350°C could also be correlated with a lowering of the delayed failure endurance. A decrease in delayed failure endurance likewise occurred in steels tempered below 200°C although low-alloy steels with 0·2% C have about the same strength after tempering below 200°C as after tempering at 250°C and display good ductility even as quenched (Fig. 6).

The common cause for all these cases of decreased delayed failure endurance would seem to be incomplete precipitation of the intermetallic compound or carbide.

6. Environmental factors

Electrical contact of the steel with zinc or magnesium is detrimental because hydrogen penetration occurs. A vapor-phase inhibitor dissolved in water, which is believed to be adsorbed on the steel surface, has a remarkable effect in preventing failure.

It should be pointed out that the prevention of failure is not always identical to prevention of corrosion. Cathodic protection such as a zinc coating is detrimental from the standpoint of delayed failure while simple, electrochemically inert but nonporous coatings on the steel surface (painting, plastic coating or even dissolved vapor-phase inhibitor) are effective in preventing delayed failure.

高張力鋼の遅れ破壊

山本俊二* 藤田達**

株式会社 神戸製鋼所

機械事業部化工機本部* 中央研究所**

1. まえがき

強力鋼の遅れ破壊とは，シーズン・クラッキング，ステンレスの応力腐食割れ，酸洗脆化などを含む環境脆化現象の一分野である．対象とする環境は常温の空気中での使用および降雨を予想する水中の条件である．典型的な実用例は橋梁などに広く採用されている摩擦接手用高張力ボルト，PC 鋼棒などで，戸外で使用する引張強さ 120 kg/mm² 以上の材料が問題となる．

環境脆化では一般に環境がきびしいほど，合金量が少なくて強度の低いものでも起こりやすくなり，逆に環境がゆるやかであると強度の高いものでも起こりにくくなる．鋼では環境が水の場合，その影響による脆化が問題となる強度レベルが 120～150 kg/mm² 付近にあるということである．水素を電解で大量にチャージするさらにきびしい環境では，より強度の低い軟鋼でもブリスターを発生するなどの脆化が起こる．

水中での強力鋼の遅れ破壊は未だ水素脆化か，塩化物水溶液中でのステンレスの破壊のような応力腐食割れ (stress corrosion cracking) かは明らかでないが，上記の有害な環境の存在のほかに一般に外力の存在を必要とする．なお鋼塊の白点 (flaking) や，ブリスターのように大量の過飽和の水素がガス状で析出するような場合には，原則として外力・残留応力などがなくても割れが発生しうると考えられる．

強力鋼の遅れ破壊は外力の存在の下で起こるのであるが，その外力は静的負荷でも惹起されるものであり，破面は似ているが疲労破壊とは区別される．

次に脆性破壊と比較してみると，その典型である低温脆性破壊は低温における鋼の降伏点の上昇すなわち降温による転位の易動度の低下に原因がある．これに対し強力鋼の遅れ破壊では，なるほど高強度化のための転位の易動度の低下にともなう脆化は存在しておりこれは低温脆性と同様に考えてよいが，ほかに環境と材料表面の化学的な反応，たとえば材料の溶解，水素の吸着・侵入などの現象が大きな影響をもち，これらの表面現象が温度に対し正の依存性を持つことから，現象全体は常温付近では温度が高いほど起こりやすくなり単なる脆性破壊とは区別される．これらの点は工業界では事故原因調査および対策確立の際忘れてはならないことである．

2. 遅れ破壊試験法

遅れ破壊の試験法としては，電解により水素をチャージした後，あるいはしながら負荷する方法，酸水溶液中で負荷する方法などいろいろあるが，高張力ボルトなどを対象とする場合には，使用環境条件と試験環境条件を同じにしたほうが定量的にも実用化しうるデータがえられるので，今回は水中で負荷することにした．

試片形状も実際のボルトにネジのような応力集中部があることを考慮して，Fig. 1 のような応力集中係数 K_t が約 10 の切欠をもつ試片に引張静的負荷を与えることにした．試験の順序はまず短時間で引張試験を行ない，破断荷重を切欠底面積で除算し切欠強さ σ_N を求める．次に σ_N よりも低い応力を水中で負荷し遅れ破壊が起こるまでの破断時間を順に求めてゆき，Fig. 2 のごとき応力一破断時間曲線をえがき，遅れ破壊感受性を調査する．

本報告では約 100 時間までの試験で遅れ破壊感受性を判定しているが，実用化に際し必要ある場合には約 1 ケ年までの試験を行なう．日本鋼構造協会接合小委員会ボルト強度班で行なった JIS 規格 F13T ボルト (引張強さ 130 kg/mm² 以上) の使用可否判定についての協同研究[1]では，本試験法による結果と，同一材料同一熱処理の実物ボルト締付曝露試験の結果を比較したが，非常によい一致をしめし，本試験法で 1 ケ年で破断応力が引張強さ以下に下がる材料は曝露試験でもボルトの破断を起こしている．

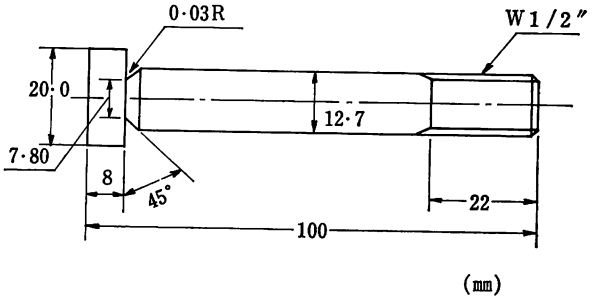

Fig. 1. Specimen for delayed failure test with stress-concentration factor Kt≃10.

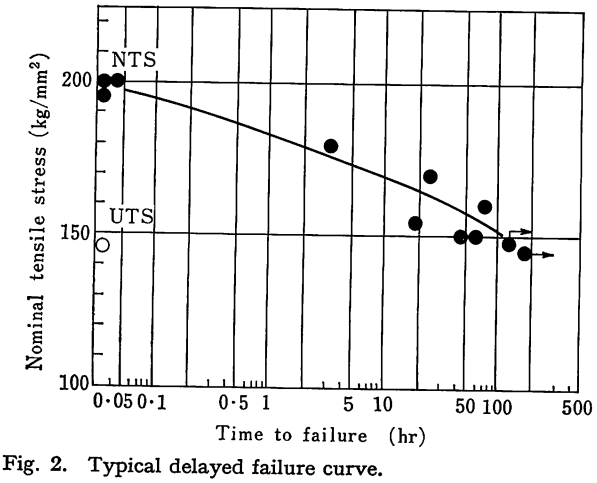

Fig. 2. Typical delayed failure curve.

負荷装置としてはクリープ試験機と同様な挺子式装置，歯車式引張試験機，荷重検定器と似たループ式装置などを用い，環境には蒸溜水を使用する．

3. 遅れ破壊現象の特性

引張強さ 120～200 kg/mm² 級の強力鋼の水中負荷での遅れ破壊試験により認められる特性は以下のようになる．

3.1 クラックの発生と成長

水中で，Fig. 1 の試片に負荷を与えておくとその切欠底部にクラックが発生し，それが徐々に内部に進行する．Fig. 1 のごとき切欠先端 R が 0·02～0·04 mm のように小さいものの場合我々が調べた範囲では，クラックは切欠底表面に発生したものと判断されたが，R が大きいものでは切欠底表面直下の内部で発生したと認められる報告もあり今後の検討を要する．水中での遅れ破壊については後述のように水素脆化割れか，応力腐食割れ機構か判然としないのが現状であるが，もし内部から割れが発生することが確められれば，少なくとも水素脆化機構は存在するといえると考えられる．

発生した遅れ破壊クラックが進行する経路は，焼入焼もどしした低合金鋼の場合，前オーステナイト粒界にそっている場合が多い．ただし必らずしも前オーステナイト粒界のみにそうとはかぎらず，光学顕微鏡上で wavy な様相を呈するものもあり，ときには分岐したり再び集合するものもみられる．水中遅れ破壊クラック進行部の破面を電顕のフラクトグラフィにより観察すると多く dimple 状であることが認められており，その解釈は今後の問題とされている．

一方マルエージ鋼でのクラックの進行経路は粒内であり，しかも光学顕微境で観察すると直線状である．結晶面との関連がうかがわれ，調査の要がある．

以上のべたクラックの発生と進行に要する時間がすなわち Fig. 2 の破断時間である．クラックが長くなり純断面積が減少し，最後に瞬時に破断を起こすものであるが，その時の破壊はまず通常の不安定破壊と考えてよいであろう．

3.2 温　度

水中での遅れ破壊は，常温付近では Fig. 3 でしめすように温度が高いほど起こりやすくなる．室温 (25°C) にくらべ 60°C では約 10 倍早く，80°C では約 30 倍加速されている．これは材料表面と環境である水との化学反応が律速段階となっていることを示すものと考えられ，単なる材料の高強度化に伴う脆化のみが原因ではない．

Fig. 4 はこのデータから見掛けの活性化エネルギーを求めたもので，12 000～14 000 cal/mole なる値が得られる．

この値は鋼中における水素の拡散エネルギーである 2 000 cal/mole[2]，あるいは水素と転位との結合エネルギーとみられる 6 400 cal/mole[2] とも差があり，今回のような水中での遅れ破壊現象では単なる水素の拡散が律速段階とはなっていないようである．上記の値がなにを示すかについては不明であるので，今後材料表面と水との相互作用について研究をすすめる要がある．

常温付近では高温ほど遅れ破壊が起こりやすいということは，実際に冬期より夏期に事故が多いという経験とも一致している．またこの種の破壊では，疲労限度のような応力の限界値が存在しないので数年のような長時間後に破断の起こる可能性があり注意を要する．逆に温度をあげて促進試験を実施すれば，長時間後の破壊の様相を予想できるという事情がある．

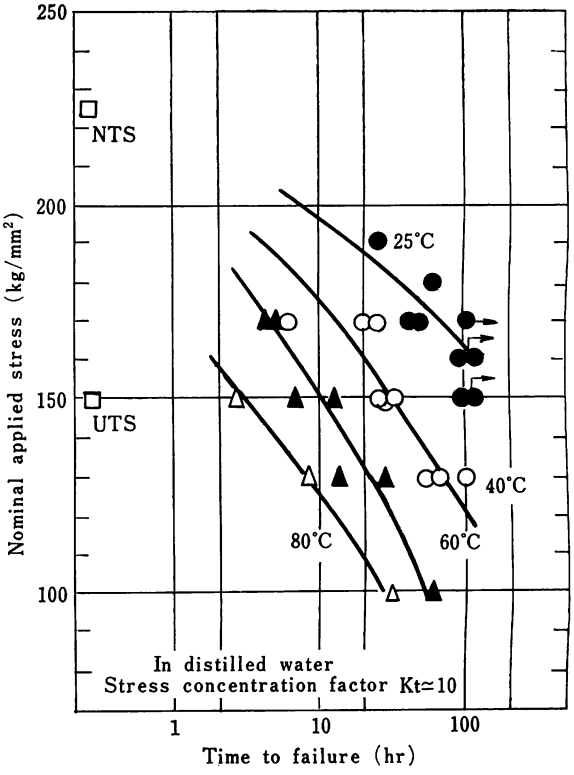

Fig. 3. Temperature dependence of delayed failure.

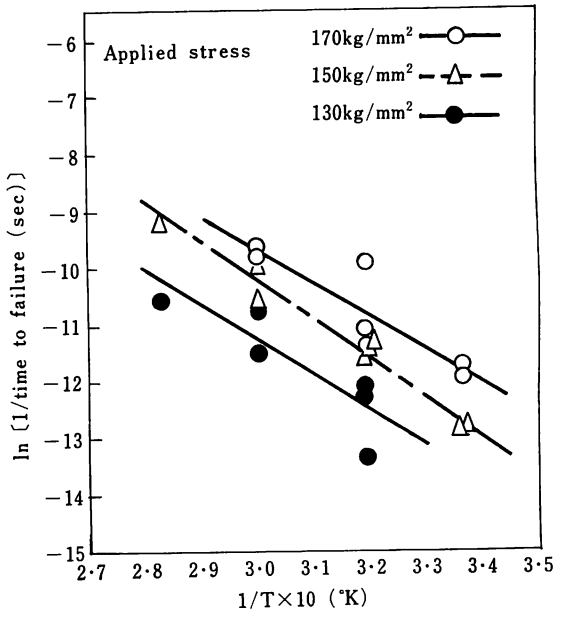

Fig. 4. Apparent activation energy (data from Fig. 3).

3.3 強度レベル

耐遅れ破壊性に大きな影響があり，実用上最も重要な因子は対象材料の強度レベルである．

Fig. 5 は横軸に多種の低合金鋼およびマルエージ鋼

の0·2% 耐力をとり，縦軸に 100 時間遅れ破壊強さをとったものである．1つの点はそれぞれ約 10 本の試片による Fig. 2 の曲線より求めており，低合金鋼 (Conventional steel) にかぎれば，すべての鋼種はほぼ1本のバンドで表現されている．すなわち耐力が約 110 kg/mm² までは，遅れ破壊はほとんど問題とならず，切欠強さ σ_N とほゞ同じ値を示すが，それ以上では遅れ破壊に感受性をもちはじめ，実用に際してはなんらかの考慮を払うべきものであることを示している．

従来高強度材料の安全性は材料の伸び，絞り，衝撃値のような延性値で判断していたが，これらは強度の上昇につれ低下一方の特性値であり，高強度鋼の使用限界の推定に困難があった．これに対し遅れ破壊性質の結果によれば，大気中あるいは戸外で，鋼材料を多少の切欠形状を許して安全に使用できる範囲は 0·2% 耐力で 110 kg/mm², 引張強さで 120 kg/mm² までであろうと明確に判断できる．歴史的に従来から低合金鋼は通常引張強さ 100 kg/mm² に焼きもどして使用されてきており，これは遅れ破壊現象を明確に把握してはいなかったが，経験的に材料の難点を避けてきたことによると思われ，約言すれば従来の鋼材料の規格は妥当であったといえる．

実用上は同じ引張強さでも，耐遅れ破壊性の良否に多少の差があるので，後述のように化学成分・焼もどし温度に考慮を払うが，その程度は Fig. 5 から 0·2% 耐力に換算してほぼ ±10 kg/mm² ぐらいである．

Fig. 5 にはマルエージ鋼のデータもかかげているが，

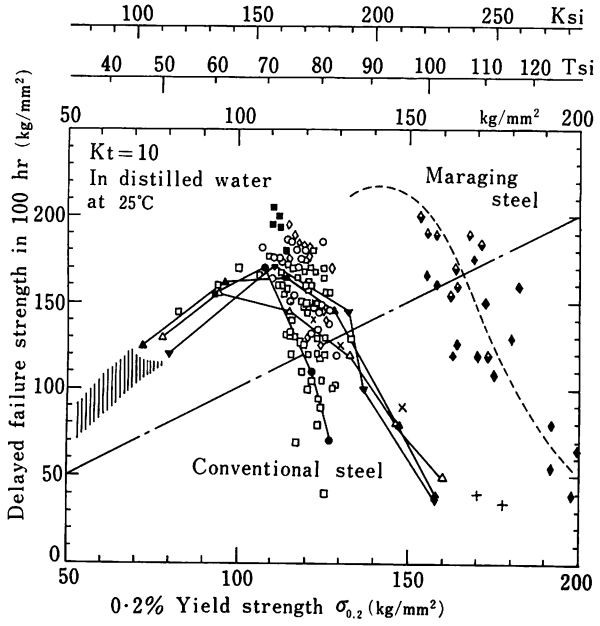

Fig. 5. Delayed failure strength vs 0·2% yield strength.

遅れ破壊が問題となるのは 0·2% 耐力で 140 kg/mm² 以上であると推定され，低合金鋼よりかなり優れている．鋼材における遅れ破壊研究の最終目標の1つは低合金鋼の critical 強度である 110 kg/mm², およびマルエージ鋼の約 140 kg/mm² が何によって決められているかということにあり，それが解明されれば改善の可能性についても推定が可能となるであろう．

3.4 熱処理

前述のように材料面からみて遅れ破壊に最も大きな関係のあるものはその強度であるが，熱処理にともなう材料の組織も遅れ破壊感受性に影響を与える．そのうちで重要なものの1つが炭化物，金属間化合物の析出状態に関連ありと思われるものである．

Fig. 6 は 0·20% C-Mn-Cr 鋼の通常の焼もどし性能曲線に 100 時間遅れ破壊強さを書き加えたものである．これによれば，焼入れのまゝの状態と 350°C 焼もどしの状態で遅れ破壊に敏感になっていることがわかる．後者は低温焼もどし脆性と遅れ破壊とが関連あることを示すが，前者は他の機械的性質とほとんどかかわりがない．

Fig. 7 は 300 ksi 級マルエージ鋼の時効温度と機械的性質および遅れ破壊強さとの関係を示したものである．過時効側では強度の低下にしたがい，伸び・絞りなどの延性値が回復し遅れ破壊も起こりにくくなっているが，時効が不充分である 440°C の時効で伸び・絞りなどが高いにもかかわらず異常に遅れ破壊に敏感となっている．光学顕微鏡による断面観察によれば過時効側では前述のようにクラックは粒内を直線的に進行しているが，不足時効側では粒界を進行し枝わかれして多くのクラックを生じている．

先の低合金鋼の焼入れのまゝとマルエージ鋼の不足時効の状態で共通にいえることは，何らかの析出の前段階であるということである．ほかに類似の現象としては，低合金鋼を焼入れ焼もどししたのち 20 時間までのうちに負荷すると遅れ破壊を起こしやすいが，100 時間以上常温に放置すると鈍感になるという例がある．この場合は焼もどし後のわずかな析出現象も関係あるということになる．

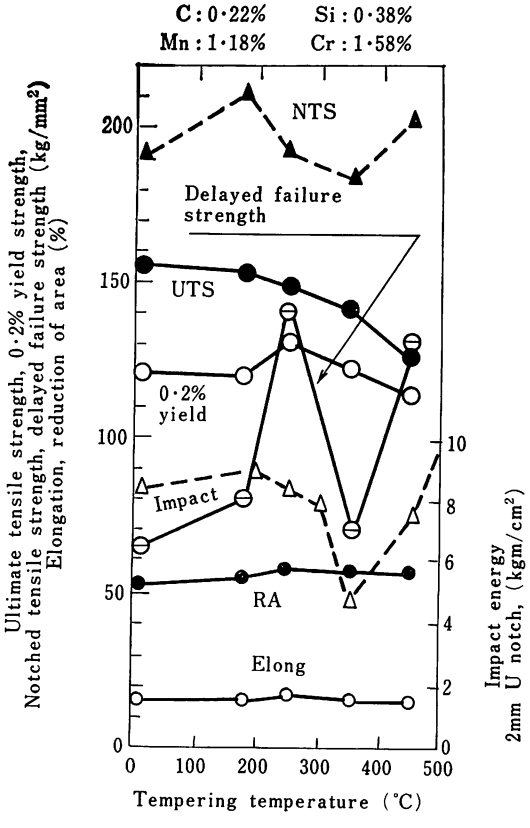

Fig. 6. Tempering temperature vs mechanical properties and delayed failure strength of 0·2%C manganese-chromium steel

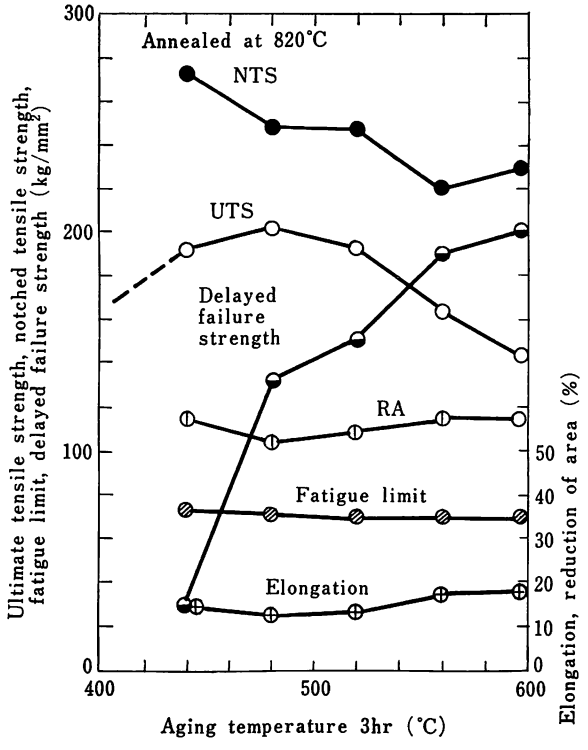

Fig. 7. Aging temperature vs mechanical properties and delayed failure strength of 18%Ni–300 ksi maraging steel.

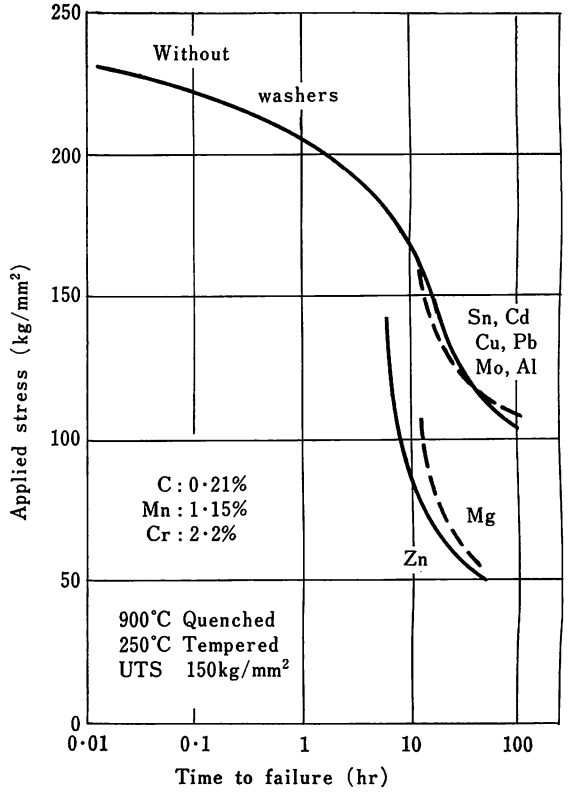

Fig. 8. Effect of contact with other metals on the delayed failure of 0·2% C manganese-chromium steel in distilled water at 25°C.

このように析出の状態は遅れ破壊と密接な関係のある場合がみられるので，今後の遅れ破壊の研究の一つの突破口ではないかと感じられる．

3.5 環境についての考察

Fig. 8 は純金属の約 1 mm 厚さのワッシャを試片にかませて水中で負荷した遅れ破壊試験の結果である．

Sn, Cd, Cu, Pb, Mo, Al のワッシャをかませた場合にはワッシャのない場合と差はないが，Zn, Mg のように鉄より卑なる金属で，しかも Al のように強固な酸化膜をつくらないもののワッシャは遅れ破壊を助長する．すなわち陰極防食作用があるために Zn メッキのように被覆材として効果のあるものは，有害であるといえる．これは多分水素が陰極である試片に一部侵入するためと推定される．メッキ材として用いられた場合でも完全に鋼表面を被覆することは不可能であるので，ポーラスな部分が電池作用を起こすため危険である．

Table 1 は純水 15 cc に水素の放射性同位元素を 1 キュリー加えた中へ，鋼試片をそのまゝおよび曲げ応力をあたえながら浸漬したのち取出し，カウンターにて β 線を測定したものである．結果によれば応力のありなしにかかわらず鋼中に水素が侵入したことは確かなようである．それが遅れ破壊にどのように影響するかはさらに検討する必要があるが，純水中における遅れ破壊現象においても水素の挙動は常に注意せねばならぬ．

先に Zn メッキのように防食法として効果のある対策が，必ずしも遅れ破壊防止法とならないことを示したが，水との接触を完全にふせぐプラスティックのコーティングや単なる塗料は一般に有効である．ほかに気化性防錆剤 (VPI) のように水中においても金属表面に吸着する

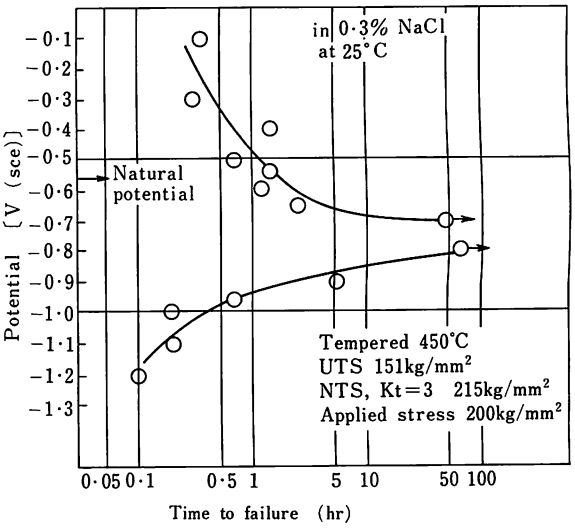

Fig. 9. Delayed failure test in 0·3% NaCl solution at 25°C under polarized conditions.

物質を水に加えることも効果がある．この場合は試片表面に VPI が吸着し鋼と水との化学反応が妨げられたため防食にも有効であると同時に遅れ破壊防止にも役立ったものと判断される．なお VPI はいずれは気化するものであるので実用には問題が残る．

Fig. 9 は応力集中係数 3 の引張強さ 151 kg/mm² の試片に 0·3% NaCl 水中で同一負荷をかけ，ポテンショスタットで試片と対極間に電流をながし，試片の電位を自然電位から陽分極あるいは陰分極させた状態で遅れ破壊

Table 1. Tritium penetration into steel surface.

Material	UTS (kg/mm²)	Applied* stress (kg/mm²)	Soaking** time (hr)	Counting rates by gas flow counter (Q gas)***	
				Condition	Counts/min****
AISI 4120	140 (250°C Tempered)	about 120	20	Rinsed	1050±15
				Rinsed and polished	190± 3
				Rinsed and polished again	125± 5
		0	20	Rinsed	259± 5

* Specimen, 0·17×4·0×11·75 mm; two point loading distance, 10·6 mm.
** In tritium water, 1 curie/15cc.
*** Q Gas=He+1% isobutane.
**** Background, 10 counts/min.

試験を行なったものである．結果によれば自然電位から陽分極させると破断時間がみじかくなる一方，陰分極させると長くなる．しかしさらに陰分極させると再び破断時間は短かくなる．

このような傾向は一般に次のように解釈されている．すなわち上側の曲線は陽極支配の破壊（アノード割れともいう）でありいわゆるクラック先端部の選択的溶解によりクラックが進行する応力腐食割れであり，下側の曲線は陰極支配の破壊（カソード割れともいう）でこの場合は水素脆化と考えられる．

Fig. 9 の場合，自然電位すなわち電流のながれていない状態ではアノード割れの範囲に属するゆえ，0·3% 食塩水中の遅れ破壊は応力腐食割れと判断される．

4. 考　　察

以上の如き結果から水中での遅れ破壊の原因として考慮せねばならぬ機構は次のようなものと思われる．

1) 水素脆化

放射性同位元素による試験から，水からの水素の侵入が存在するが，侵入した水素はいずれ水素ガスとして析出し，高強度鋼の場合はクラックの発生と成長をうながすことが考えられる．

また他の実験[3]で，3% 食塩の沸とう水中では試片内部よりクラックが発生するという結果がえられていることもあり水素脆化機構を看過できない．

2) 水素吸着

クラック付試験片の外界を水素ガスあるいはアルゴンガスなどにおきかえることにより水素の吸着の影響が明らかである[4]ので，特にクラックの成長について，この影響を考慮する必要がある．

3) 応力腐食割れ

0·3% 食塩水中分極遅れ破壊試験では本機構が進行していると判断されるので，水中においても同じ機構の存在が類推される．

1) 2) の機構は同時に成立しうるが，分極試験によれば水素脆化と応力腐食割れが両立しうるとは考えにくい．水中の条件はほぼ両者の中間に位置し，わずかの環境の変化がどちらかの機構が支配的になるのかもしれない．

いずれの場合にも材料の高強度化はこれらの過程を促進させることは間違いないものと考えられる．

文　　献

1) JSSC, 日本鋼構造協会誌 "特集　高力ボルトの遅れ破壊" Vol. 6, No. 52, 1970年4月
2) R. Gibala: Trans. AIME, **239** (1967), p. 1574
3) H.L. Logan and J.M. Wehrung: Corrosion, **22** (1966), p. 265
4) G.G. Hancock and H.H. Johnson: Trans. AIME, **236** (1966), p. 513

The Effect of Neutron Irradiation on the Toughness and Ductility of Steels

T. C. Reuther K. M. Zwilsky

U. S. Atomic Energy Commission
Division of Reactor Development and Technology

ABSTRACT

The fundamental impact of neutron irradiation on metals is the displacement of atoms from normal lattice sites, the consequent generation of extensive lattice defect structures and the production of impurity elements by transmutation reactions. The consequence of these irradiation produced changes is to alter the plastic flow and plastic instability behavior in highly specific ways depending upon the steel, its thermal, mechanical and irradiation history and the specific test conducted. In light of this fundamental perspective, current research and technology findings on the effect of neutron irradiation on engineering properties and behavior of steels for use in current and advanced reactor designs are reviewed.

In particular, irradiation effects on the ferritic steels for pressure-vessel application in light-water reactors and on the austenitic stainless steels for fuel cladding, structural and vessel applications in sodium-cooled fast-breeder reactors are examined. In general both types of a steel exhibit an increase in hardness and tensile yield strength and a decrease in tensile ductility and fracture toughness with neutron exposure. The ferritic steels also show an increase in ductile-to-brittle transition temperature and the stainless steels exhibit a loss of ductility at elevated temperatures in both tensile and creep testing. It is shown that the susceptibility of both categories of steel to neutron irradiation damage can be reduced by careful attention to chemistry and/or microstructure. Data, models and theories that examine the bases of these effects are cited. The extrapolation of irradiation test data to the prediction of material performance in other neutron flux and spectra environments are reviewed in terms of the *damage function* concept of the neutron energy dependence of observed property changes. The influence of irradiation embrittlement on deformation and failure mode are examined by example in the analysis of irradiated fuel pin performance.

1. INTRODUCTION

1.1 Introduction and scope

The physical sequence of events that determines the effects of neutron irradiation on the toughness and ductility of steels is complex. The phenomena include the many ways in which the crystal lattice and the microstructural defects and impurities of the steels respond to the spectrum of displacement and transmutation reactions imposed by neutron irradiation. The complexity of this radiation damage is compounded by the subsequent (or concurrent) response of the irradiated steel to testing or operational conditions of time, temperature, environment, load and strain. Treatment of the subject ranges from atomistic and crystal dynamics through microscopic, macroscopic and large structure observations. For each of these scales of observation, especially for the latter, treatment is further compounded by recognition that ductility (and toughness) like beauty is in the eye of the beholder, and thus subject to many varying definitions and interpretations.

Toughness and ductility represent manifestations of various integral measures of the details of plastic flow and microcracking, and the development and propagation of plastic or structure instability throughout the spectrum of continuum material behavior, micrometallurgy and dislocation dynamics. In terms of the design and operation of nuclear power reactors, the appropriate ductility definitions lie in the experience of the designer, the specific component, materials and environment, the acceptance criteria of the quality assurance specifications and the operating and safety criteria that must be observed as much as in the scientific understanding of the phenomena.

In view of this complexity of definition, we shall not attempt a comprehensive review of the scientific or engineering behavior, or property parameters to which either the materials scientist or the engineer might wish to refer; rather, we shall make an effort to illustrate the principle phenomena that are involved using selected current engineering data.

Phenomena and observations that indicate the direction of metallurgical and engineering developments which show promise of easing the burden or significantly reducing the adverse effects of neutron irradiation on the pressure-vessel steels for use in light-water reactors (LWR) and the austenitic stainless steels that are being used in the fuel clad, core structural and heat transport systems of the liquid-metal fast-breeder reactors (LMFBR) will be cited.

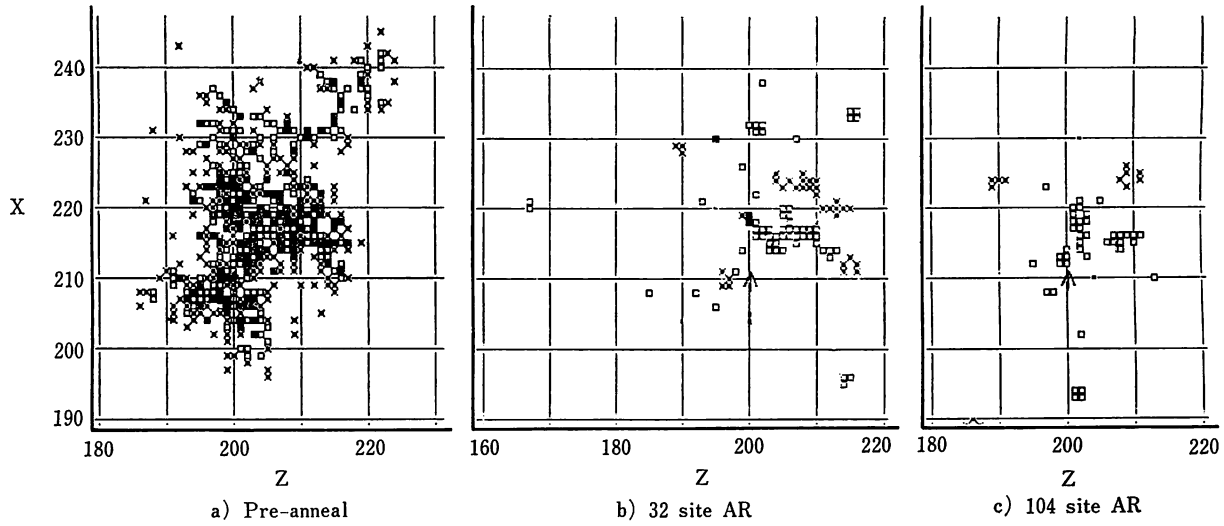

a) Pre-anneal b) 32 site AR c) 104 site AR

Fig. 1. Computer simulated displacement cascade. A projection onto one plane of a typical 20 keV displacement cascade. Squares and x's represent vacancies and interstitials, respectively. Take-off point of the primary knock-on atom is 200, 200, 200; the direction is shown by the arrow. Coordinates are in half-lattice units (1·8Å).[3]

a) The output of the cascade simulation; the input to the annealing simulation.

b) The result of a simulated 500°C short term ($\sim 10^{-4}$ sec real time) anneal when the annihilation region contains 32 sites.

c) Same as b) for a 104 site annihilation region.

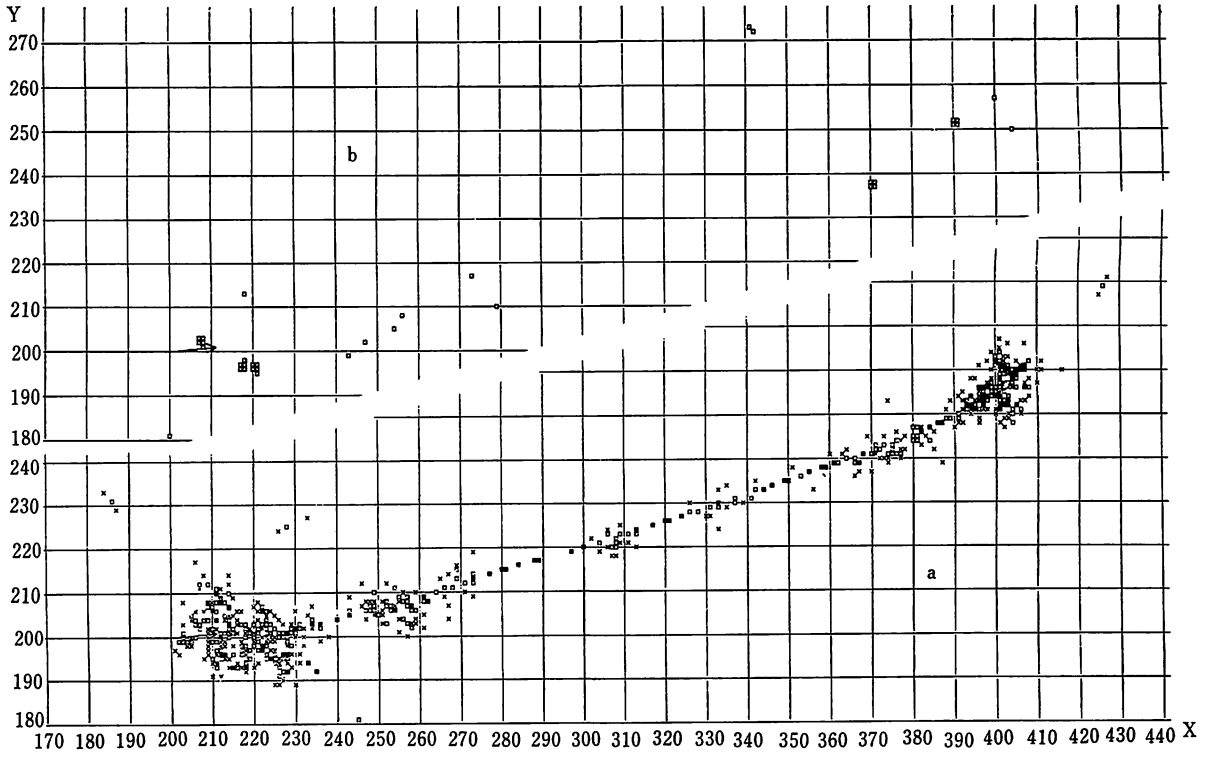

Fig. 2. See caption for Fig. 1. This is a non-typical, quasi-channeled cascade, in which a series of low-energy loss collisions confined between a particular pair of atomic planes permit a substantial increase in the dimensions of a cascade[3].

a) The input configuration.

b) The result of a simulated 500°C short term anneal with a 104 site annihilation region.

1.2 Elementary damage phenomena and general behavior

The irradiation of crystalline materials with neutrons having energies greater than several tens of electron volts produces damage to the crystal in the form of atoms displaced from their normal lattice sites. For neutron energies in the kilovolt range, the primary knock-on atom (PKA) in turn will have energies great enough to displace other atoms from their lattice sites in a collision cascade, thereby producing a distribution of interstitial-vacancy pairs and clusters of vacancy and interstitial atoms over a region of up to several thousand atomic volumes depending upon PKA energy[1]. The definition and observation of this primary damage state and the immediate interaction of it with the parent crystal are not subject to direct observation. However, the phenomena have been treated in considerable detail with computer crystal simulation techniques developed by Beeler[1].

These crystal simulation techniques have been extended and applied to the elevated-temperature annealing of alpha and gamma iron[2,3]. Examples of computer simulated collision cascades in gamma iron in the primary defect state before and after annealing at 500°C for 10^{-4} seconds are illustrated in Fig. 1 and 2. Two conclusions follow from these kinds of observations. Most of the displacement damage (about 80%) is removed by annealing in very short times; however, there is both a dynamic production of singular defects and a net production of interstitial and vacancy clusters. High temperatures favor larger vacancy clusters and yield three times as many vacancy as interstitial clusters[2]. With continued irradiation these grow, eventually forming visible dislocation loops and voids, Photo. 1. a), b). During irradiation the excess concentration of point defects also leads to accelerated precipitation reactions, Photo. 2. a), b) and to irradiation-enhanced creep[4]. Other reactions involve formation of defect-impurity complexes[1,5,6].

A second form of elementary irradiation damage is the production of impurity elements by transmutation reactions. The formation of helium in stainless steel by (η, α) reactions was identified in 1965 as the probable cause of elevated-temperature embrittlement of stainless steel[7], and the study of this phenomena continues to be of major importance in assessing the performance of stainless steel in irradiation environments[8].

The effect of the above kinds of irradiation-induced structural and chemical changes on the mechanical properties of steels is manifest in a variety of ways which depend upon the steel, the kind of test and test conditions, the irradiation environment including temperature, flux and spectrum and the post-irradiation history. In general, the tensile behavior of both the pressure-vessel steels[9,10] and the austenitic stainless steels[11] irradiated and tested at relatively low temperatures (<120°C for ferritic steels and $<0{\cdot}5T_m$ for the austenitics) exhibit a strong increase in yield strength with increasing fluence, a decrease in the work-hardening rate and a consequent early onset of plastic instability resulting in low uniform elongation. For example, the uniform elongation of several pressure-vessel steels tested at room temperature following irradiation at <120°C is reduced from the range of 10 to 20% to less than 2% at a fluence of about 1×10^{19} n/cm^2, E>1Mev. In contrast, the reduction in area measure of ductility was not changed significantly[9]. This irradiation hardening is the principle generalization that is common for the two kinds of steel. Higher irradiation and test temperatures result in complex behavior for both types of steel and these will be treated separately along with other properties of engineering significance. For ferritic steels, the most important phenomenon is the transition temperature behavior, while for the austenitics the elevated-temperature ductility loss is of major consequence.

Before examining the separate irradiation behavior of the two kinds of steel, some comments are in order regarding the literature on studies of irradiation effects. The open literature on the effects of irradiation on reactor structural materials tends to be concentrated in special conference and symposia publications. The major such compendia of recent years[12-16]* and the recent reviews on pressure-vessel steels for LWRs[17,18] and stainless steels for fast reactors[19] provide a comprehensive entry into the literature. More recent data may be found in laboratory publications as well as in the nuclear and general metallurgical and engineering literature. Much of the data that appear in the open literature represent parameter type of experimentation designed to isolate particular phenomena in order to investigate specific scientific or engineering questions. Consequently, irradiation temperatures of much of the literature data are different than current or projected reactor service temperatures, and post-irradiation testing may be at still other temperatures, either higher or lower. Parametric data always will be necessary to explain mechanistic behavior. However, to simplify interpretation and to assess the engineering significance of irradiation phenomena, the irradiation conditions including temperature, flux and spectra should approximate service conditions, and testing should be conducted at irradiation temperatures unless a specific data

* The August 1971 issue (Vol 17, No. 1) of Nuclear Engineering and Design is a special issue containing 15 papers, which include much of the data developed under the Heavy Section Steel Technology program of the U.S. Atomic Energy Commission.

requirement calls for other testing conditions (e.g., determination of ductile-brittle transition temperature behavior). This, of course, is easier said than done because of the limits of experimental irradiation facilities. Experimenters have developed extremely clever and well engineered vehicles to

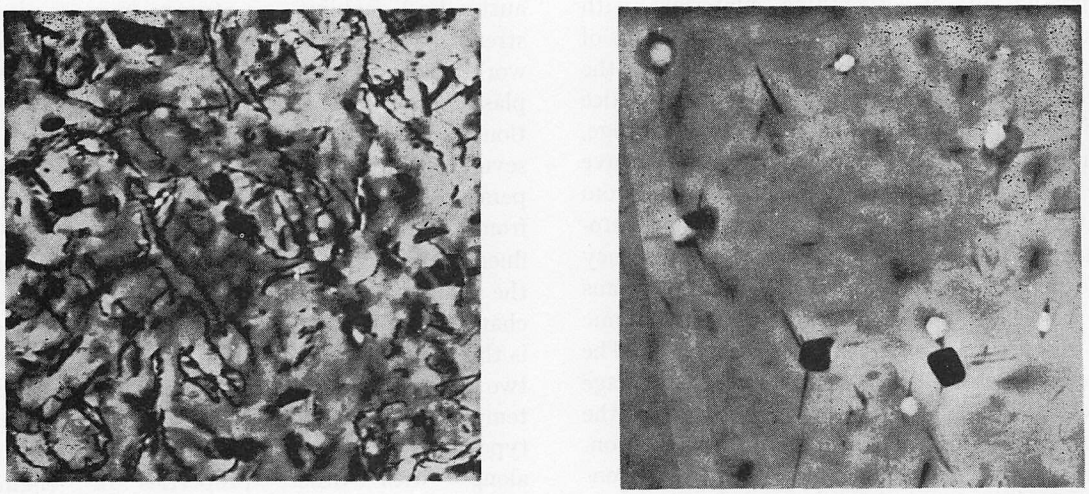

a) Dislocation structure. b) Voids. ×70 000

Photo. 1. Transmission electron micrographs of dislocations a) and voids b) in type 316 stainless steel irradiated at 590°C to $1{\cdot}9\times10^{22}$ n/cm² (>0·1 MeV)[66].

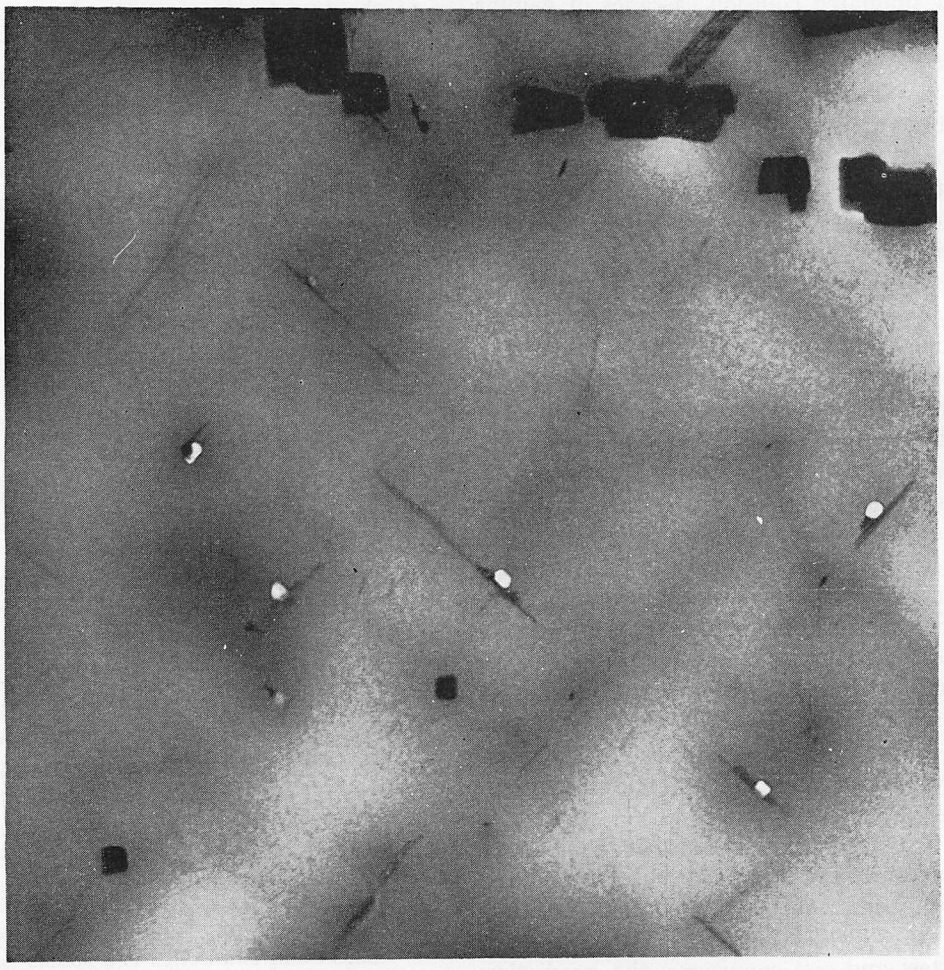

Photo. 2. Transmission electron micrographs of precipitates and voids in irradiated Type 316 stainless steel.
a) Voids are preferentially associated with rod-shaped intermetallic particles. Cuboidal precipitates are $M_{23}C_6$. Irradiated at 740°C to 3×10^{22}n/cm² (>0·1 MeV).

extend these limits[20]; however, varying conditions of irradiation experiments tend to be characteristic of the literature and the reader needs to be alert to it. In subsequent sections of the present review, where appropriate and where data are available, an effort has been made to select examples that meet the criteria of comparable irradiation, test and application temperatures.

2. EMBRITTLEMENT OF FERRITIC PRESSURE-VESSEL STEELS

2.1 General

In general, the effect of neutron irradiation on the carbon and low-alloy steels that are in use for nuclear pressure-vessel applications[17] is to increase the hardness, the initial flow stress (yield strength) and the tensile strength; to decrease the work-hardening coefficient, the tensile ductility (as measured by uniform elongation) and the fracture toughness; and to increase the ductile-brittle transition temperature. For nuclear pressure-vessel applications, toughness or resistance to fracture constitutes a property of major importance to safe operation. Consequently, toughness requirements are explicitly defined in the regulatory safety criteria and engineering codes[21,22].

The essential objective of the criteria currently in effect in the USA is to require that vessels be operated at pressure only at temperatures above the ductile-brittle transition temperature (DBTT) on the basis that gross plastic overload then is required for fracture. The DBTT in turn is defined by (or indexed to) the *nil-ductility transition* (NDT) temperature as measured by the drop-weight tear test[23]. In practice* the temperature transition behavior is established by the Charpy-V notch ductility energy, Cv, versus temperature curve, and this in turn is indexed to the NDT. For the Cv versus temperature behavior of the common nuclear vessel steels, the temperature corresponding to the 5·2 kgm/cm² Cv energy level has been widely accepted as the established index to NDT behavior for both unirradiated and irradiated steels; and current code criteria[22] use this as the reference index to establish the effect of irradiation on the transition

* Small specimen tests are required for extensive irradiation testing and for surveillance irradiation the Charpy-V specimen is generally used.

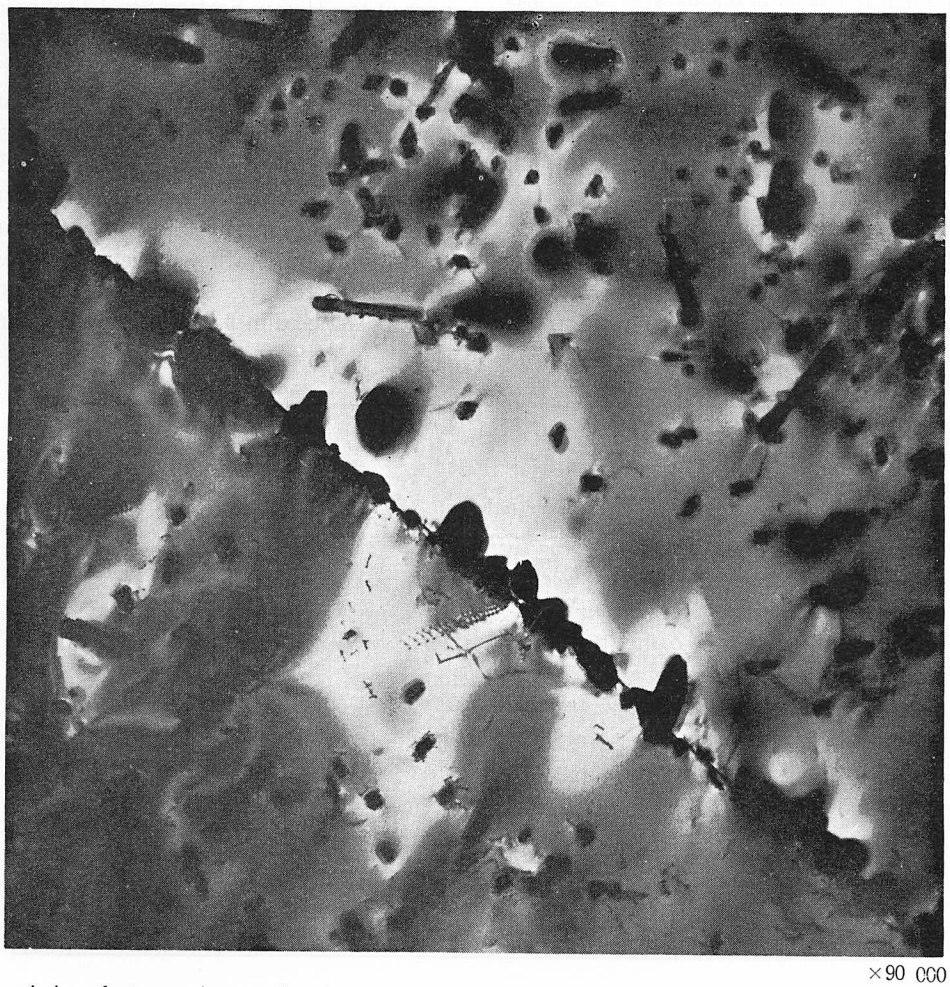

×90 000

Photo. 2. Transmission electron micrographs of precipitates and voids in irradiated Type 316 stainless steel.
b) Massive $M_{23}C_6$ carbide precipitation in Type 316 stainless steel. Denuded zone adjacent to nearly continuous boundary film. Irradiated at 840°C to 3×10^{22}n/cm² (>0·1 MeV).

temperature of A302B* and A533B steel**. We shall return to this point later, for accumulated NDT and Cv data suggest that the 5·2 kgm/cm² fix may be neither consistent nor necessarily conservative[24].

Alternate fracture analysis of reactor vessels may be made using plane strain fracture toughness, K_{IC}, and linear-elastic fracture mechanics (LEFM) flaw-size, stress calculations[25]; however, both measurement and analysis appear to be restricted to the frangible region near or below the NDT temperature for the tough steels now in use for reactor vessels[24].

2.2 Notch ductility behavior

The typical effect of irradiation on the Cv, temperature behavior of a pressure-vessel steel is illustrated schematically in Fig. 3. Three characteristic features of irradiation embrittlement are illustrated:

a) the shift of the Cv vs. temperature curve to higher temperature,
b) the reduction in the full shear fracture energy, and
c) the change in shape of the curve, in particular the rate of change in slope dCv/dT, in the initial part of the curve.

The first order and most general effect is the increase in the ductile-brittle transition temperature, which nearly always is accompanied by a reduction in the full shear fracture energy. Generalizations cannot be made regarding the slope change; irradiation may at times produce a more distinct transition behavior (dCv/dT changes sharply) while at other times a more sluggish rise of Cv with increasing temperature is observed. The latter point may be of considerable significance in defining an arbitrary energy level as the reference at which a change in transition temperature is measured.

Suggested fracture mechanisms of cleavage and ductile rupture also are indicated in Fig. 3. Correlation of fracture transition behavior for unirradiated and irradiated steels with fracture appearance has been made by many observers, e.g., Wechsler and Berggren[27], Wullaert[29], and Mager[25], using macroscopic descriptive terms such as *percent fibrous fracture*, *percent brittle fracture*, and *percent crystalline fracture*, respectively. More recently as part of the Heavy Section Steel Technology program, Hunter, *et al*, in cooperation with Hawthorne, *et al*, at NRL have made microfractographic observations of the fracture surface of unirradiated and irradiated Charpy-V specimens of A533B steel using scanning electron microscopy (SEM)[26,28]. Typical observations are shown in Photo. 3. For this particular steel, irradiation at 120°C produced a very sharp transition temperature behavior. Fracture of the irradiated steel at 105°C, 3·8 kgm/cm², contained 30% plastic dimpling distributed largely at the

* ASTM A302–70 Grade B ladle analysis: 0·20% C max for plates 25·4 mm and under in thickness; 0·23% C max for plates over 25·4 to 50·8 mm in thickness; 0·25% C max for plates over 50·8 mm in thickness, 1·15–1·50% Mn, 0·035% P max, 0·040% S max, 0·15–0·30% Si, 0·45–0·60% Mo. 56·2–70·3 kg/mm² tensile strength, 35·2 kg/mm² min yield point, 18% min elongation in 50·8 mm. Condition: see specification; generally normalized and tempered.

** ASTM A533–70 Grade B ladle analysis: 0·25% C max, 1·15–1·50% Mn, 0·035% P max, 0·040% S max, 0·15–0·30% Si, 0·45–0·60% Mo, 0·40–0·70% Ni. Tensile requirements depend on class. Condition: quenched and tempered.

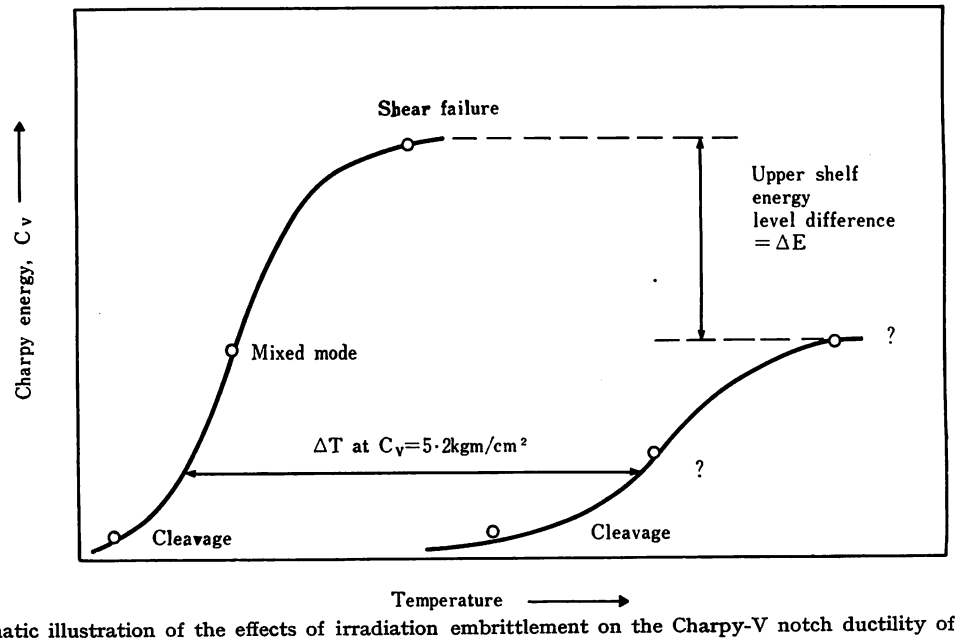

Fig. 3. Schematic illustration of the effects of irradiation embrittlement on the Charpy-V notch ductility of ferritic steel[26].

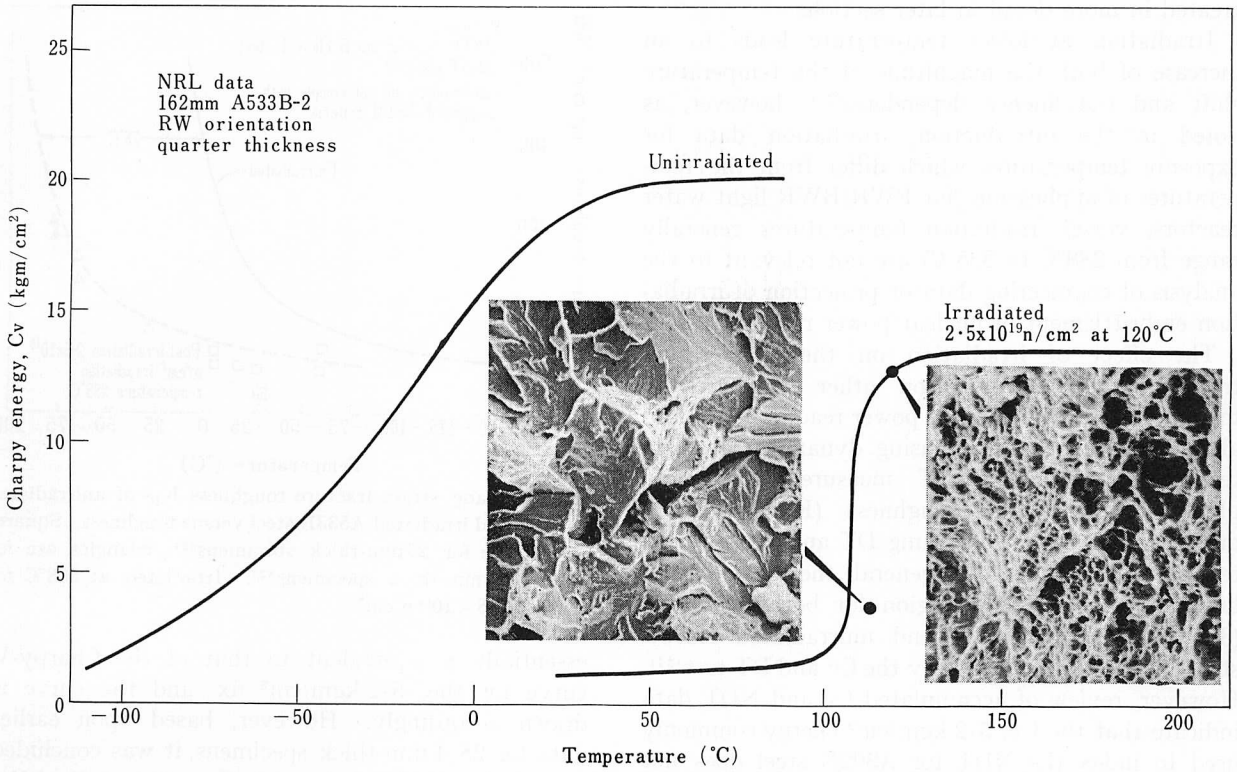

Photo. 3. Pre- and post-irradiation Charpy-V energy versus temperature curves for A533B steel and scanning electron fractographs of the irradiated steel[26].

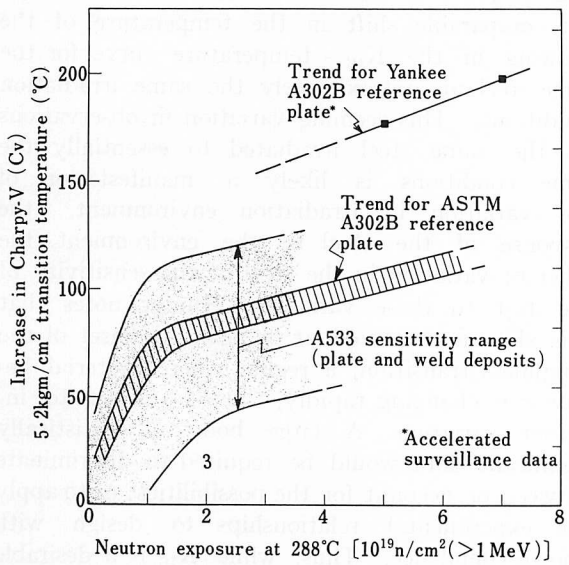

Fig. 4. Fluence dependence of Charpy-V 5·2 kgm/cm² transition temperature of A302B and A533B steels. Data are for the 152 mm-thick ASTM A302B reference plate, the 206 mm-thick Yankee reactor surveillance plate and numerous A533 steel plates and weld metals[30].

specimen edges with cleavage fracture dominating throughout most of the specimen. At 110°C, 13·2 kgm/cm² the fracture surface was 100% ductile rupture. This sharp transition temperature behavior is thus associated with the equally sharp change from a cleavage to a ductile rupture fracture mode.

2.3 Fluence dependence of transition behavior

The integral neutron exposure or fluence, φt, dependence of the Cv, 5·2 kgm/cm² transition temperature shift for plate and welds of several heats of A533B steel irradiated at 288°C is given in Fig. 4[30]. The trend band for a reference heat of A302B steel and surveillance data for a heat of A302B that is very sensitive to neutron-irradiation embrittlement also are included. Two points are noted: 1) the fluence dependence rises sharply starting at an exposure of about $0{\cdot}1\times10^{19}$n/cm² to about 2×10^{19}, beyond which damage accrues at a slower rate; 2) the variations in sensitivity to irradiation embrittlement of these steels from plate to plate and heat to heat within commercial specifications are seen to be as large as the primary effect being determined. Conservative design must be based upon the maximum sensitivity within the observed variance. Surveillance testing of actual construction materials is conducted as an integral part of normal reactor operation, and the results are used to establish the operating temperature/pressure envelope and lifetime based upon performance. However, the initial design must be based upon the projected minimum performance for the specified material. Metallurgical factors may contribute to the observed variance, but composition variation in residual elements appears to be the dominant cause of the large observed variation in the sensitivity of steels to irradiation embrittlement[31]. This point will be

treated in more detail in later sections.

Irradiation at lower temperature leads to an increase of both the magnitude of the temperature shift and the fluence dependence[32]; however, as noted in the introduction, irradiation data for exposure temperatures which differ from the temperatures of application (for PWR/BWR light water reactors, vessel irradiation temperatures generally range from 288°C to 335°C) are not relevant to the analysis of engineering data or projection of irradiation embrittlement of nuclear power reactor vessels.

The effect of irradiation on the temperature transition behavior and on other measures of toughness of A533B steel at power reactor conditions also have been examined using dynamic tear (DT) testing, drop-weight NDT measurements[24] and plane strain fracture toughness (K_{IC}) measurements[25]. Investigations using DT and drop-weight testing indicate that in general the temperature limits of the transition region for both irradiated (307°C, $3{\cdot}7\times10^{19}$n/cm^2) and unirradiated A533B steel may be characterized by the Cv and DT tests[24]. However, review of accumulated Cv and NDT data indicate that the Cv, 5·2 kgm/cm^2 energy commonly used to index the NDT for A302B steel does not yield consistently conservative results for A533B steel[24]. This effect appears to follow from variations in the shape of the Cv versus temperature curve. For A533B steel, Loss, Hawthorne and Serpan[24] recommend measurement of the DBTT shift at the 6·9 kgm/cm^2 energy level for specimens in the transverse orientation and 8·6 kgm/cm^2 for specimens in the longitudinal orientation.

Plane strain fracture toughness K_{IC} measurements have been made on A533B steel irradiated at 288°C as part of the Heavy Section Steel Technology (HSST) program[25,33,76], and as noted above, measurement of K_{IC} appears to be limited to the frangible region near or below the NDT temperature. The exhaustive investigation of Wessel on fracture mechanics specimens up to 305 mm thick[34] demonstrated that a sharp increase occurs in plane strain fracture toughness of unirradiated A533B steel as the region of the NDT temperature is approached. These K_{IC} data parallel the fracture energy curve measured for similar sized specimens by DT testing at NRL[35]. Both sets of data are compared by Loss, Hawthorne and Serpan[24]. For irradiated (288°C, $2{-}5\times10^{19}$n/cm^2, E>1 Mev) A533B steels, data have been obtained on 25·4 and 50·8 mm-thick fracture mechanics specimens[25,33,76]. The K_{IC} versus temperature curve, Fig. 5, for the irradiated steel is displaced to higher temperature from that of the unirradiated steel and a temperature dependence paralleling that reported by Wessel for the unirradiated steel is indicated. Based upon test data for the 50·8 mm K_{IC} specimens and Cv data for the same material[25], Mager[33] suggests that the temperature shift of K_{IC} due to irradiation

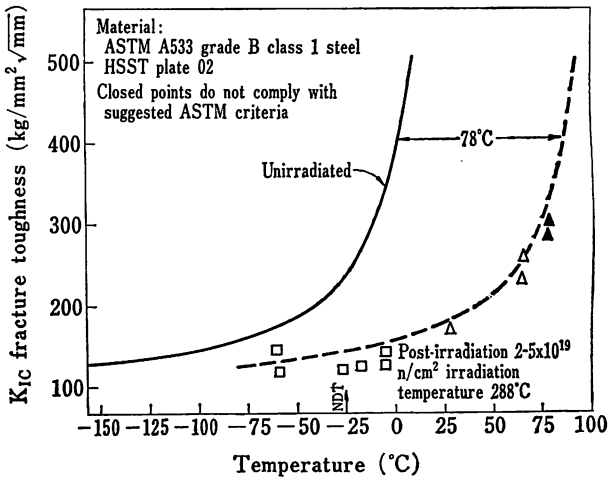

Fig. 5. Plane strain fracture toughness K_{IC} of unirradiated and irradiated A533B steel versus toughness. Squares are for 25 mm-thick specimens[25], triangles are for 50 mm-thick specimens[33]. Irradiated at 288°C for $2{-}5\times10^{19}$ n/cm^2.

essentially is equivalent to that of the Charpy-V curve for the 5·2 kgm/cm^2 fix and the curve is drawn accordingly. However, based upon earlier data for 25·4 mm-thick specimens, it was concluded that the irradiation induced temperature shift of K_{IC} was always less than the 5·2 kgm/cm^2 Cv shift[25]. Hunter and Williams[28] observed a somewhat larger but comparable shift in the temperature of the upswing in the K_{IC} - temperature curve for the same steel at approximately the same irradiation conditions. This seeming variation in observations on the same steel irradiated to essentially the same conditions is likely a manifestation of the variation in irradiation environment, the response of the steel to the environment, the inherent variation in the steel or the sensitivity of the test to these variables. Hunter notes that this shift is meaeured at or near the onset of the toughness transition, a region where material behavior is changing rapidly, thus is subject to inherent variation. A large body of statistically significant data would be required to discriminate between or account for the possibilities; or to apply the experimental relationships to design with known confidence. Thus, while K_{IC} is a desirable measure of toughness because of the implicit quantitative capability of LEFM, the current limited quantity of data and the restriction to the frangible region of toughness limit application of this technique at present when irradiation effects must be considered for tough pressure-vessel steels.

2.4 Upper shelf fracture toughness

The fracture of steels above the temperature transition does not necessarily assure high energy, high ductility rupture. Steels with high yield strength may fracture by low energy tearing above the temperature transition and neutron irradiation

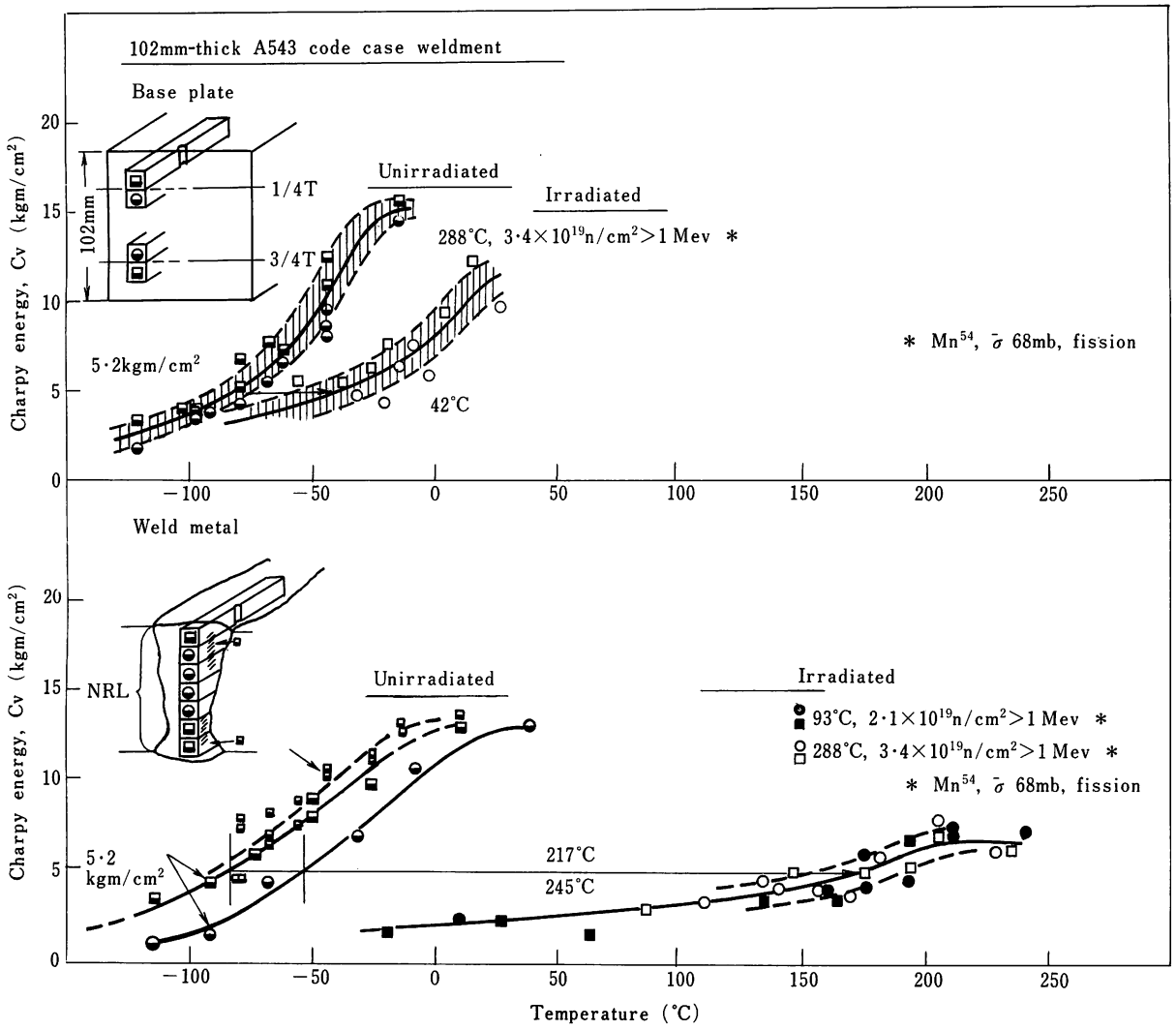

Fig. 6. Charpy-V fracture energy curves for unirradiated and irradiated plate and weld metal of A 543 steel[40].

can raise yield strength several fold and may reduce the full shear fracture energy in addition to producing a shift in the transition temperature. For steels subject to low-temperature or high-level irradiation, and for steels which are highly sensitive to irradiation damage, this reduction of shelf energy can be large. Fig. 6 illustrates this for high-copper A543* weld metal. Fractographic observations by scanning electron microscopy verify mixed mode or low energy tearing at the 214°C (~6·9 kgm/cm²) test condition[26].

Thus with the possibility of low energy fracture, consideration should be given to evaluation of fracture toughness or resistance to tearing above the transition temperature. For ultra-high strength steels, plane strain fracture toughness and analysis by LEFM may be used; however, for the relatively tough reactor vessel steels, valid K_{IC} measurements cannot be made at temperatures much above the NDT as has been discussed above.

Pellini and his colleagues at the U.S. Naval Research Laboratory have developed and advanced alternate approaches to fracture analysis for tough materials based upon drop weight NDT and the DT tests, the Ratio Analysis Diagram (RAD), the Fracture Analysis Diagram (FAD), and the Crack Arrest Temperature (CAT)*. The RAD in which the DT fracture energy (upper shelf) is plotted against yield strength is central to the approach and is the means of representing the material fracture data. The RAD is a convenient display of a large amount of information that permits ready comparison of the relative performance of different materials to one another and with respect to major categories or modes of fracture behavior. Entry to

* ASTM A543–70 Grades A and B ladle analysis: 0·23% C max, 0·40% Mn max, 0·035% P max (Grade A) and 0·020% P max (Grade B), 0·040% S max (Grade A) and 0·020% S max (Grade B), 0·20–0·35% Si, 2·60–3·25% Ni for plates to 102 mm in thickness; 3·00–4·00% Ni for heavier plates, 1·50–2·00% Cr, 0·45–0·60% Mo, 0·03% V max. Tensile requirements depend on class. Condition: quenched and tempered.

* These concepts have been treated in some detail elsewhere in this symposium by Lange[36], and are summarized by Pellini[37] and are applied to analysis of pressure-vessel wall toughness gradients by Loss, *et al.*[30]

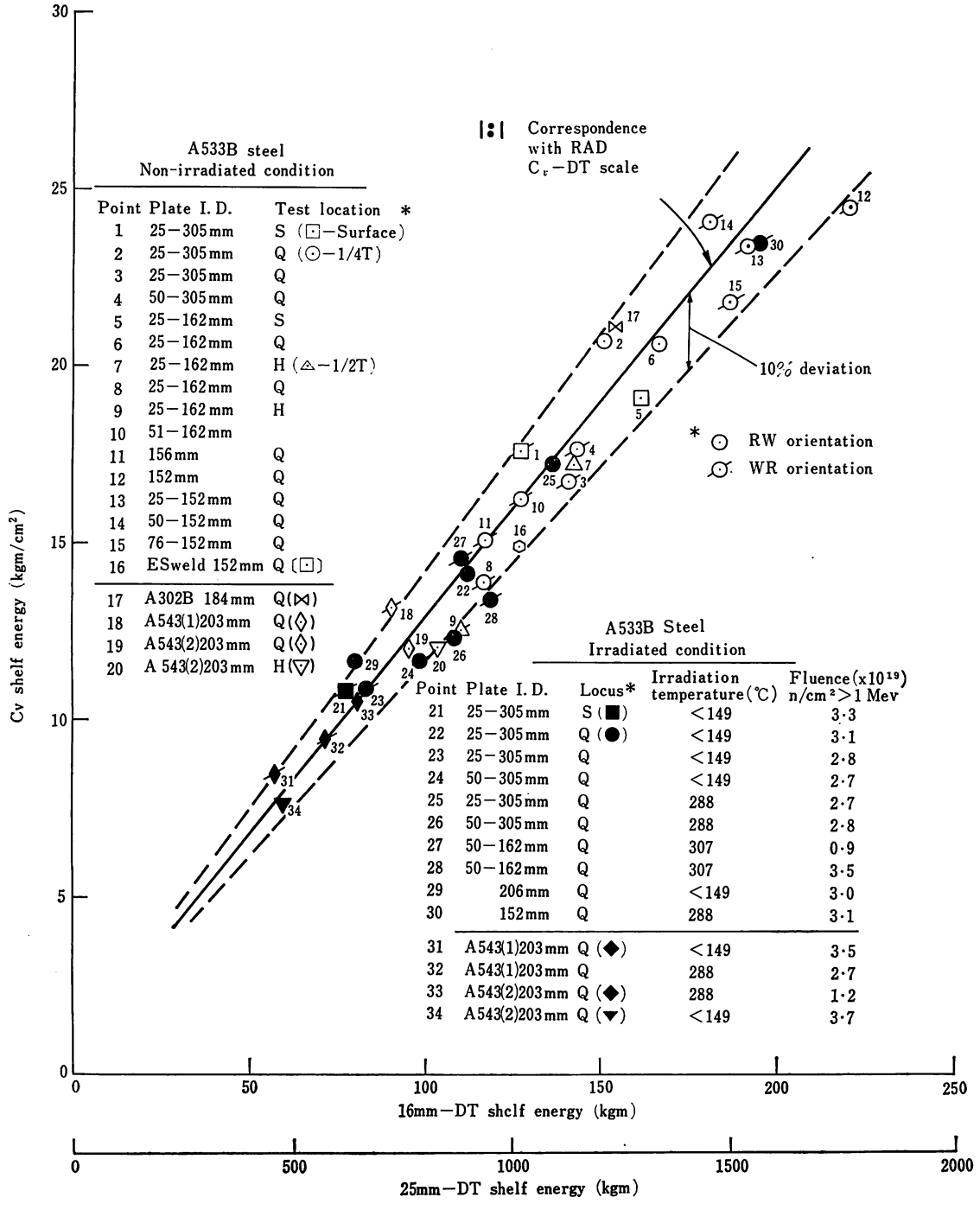

Fig. 7. Correlation of Charpy-V shelf energy with dynamic tear shelf energy for A533B steel in the irradiated and unirradiated condition and for material from various plates[24].

the diagram requires DT data or correlation to it by other measures of fracture toughness plus tensile yield data. In a reassessment of fracture safe operating criteria for reactor vessel steels, Loss, Hawthorne and Serpan[24] obtained a correlation of Cv shelf energy with DT shelf energy for numerous plates of A533B steel in both the unirradiated and irradiated condition and with various metallurgical histories, Fig. 7. This correlation establishes the validity of constructing a RAD for A533B steel based upon Cv upper shelf fracture data and the resultant diagram is given in Fig. 8[24].

The upper shelf K_{IC} correlation included on Fig. 8 has been obtained for high-strength steels and is assumed to apply to the A533B steel. The radial ratio lines of constant K_{IC}/σ_{ys} establish regions of fracture behavior on the diagram. Material falling below $K_{IC}/\sigma_{ys}=2{\cdot}5$ will be subject to fracture initiation by flaws of 5–10 mm and analysis could be made by LEFM. As one moves to higher ratios,

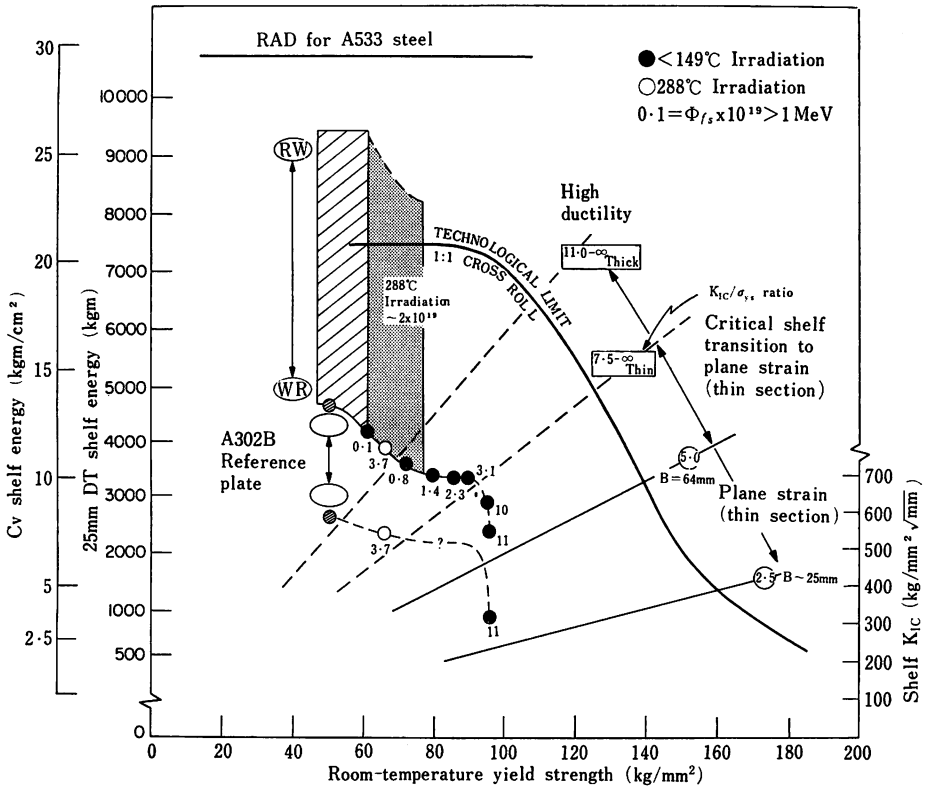

Fig. 8. Ratio Analysis Diagram (RAD) pre- and postirradiation Charpy-V shelf energy characteristics of an A302B reference plate and numerous A533 plates and weld metals[24].

materials exhibit rapidly increasing toughness in the presence of flaws. Above the "∞" lines for thin or thick material respectively, gross plastic deformation is required for fracture propagation in the presence of large flaws.

The Cv upper shelf fracture energy data of Hawthorne[38] for irradiated (228°C 2×10^{19}n/cm², E>1Mev) and unirradiated A533B steels of various heat treatments are shown by the shaded and cross hatched regions, respectively. Specimen fracture plane orientation relative to the rolling direction is indicated (RW indicates fracture normal to rolling direction, WR indicates planes parallel to rolling direction) and these are noted to bound the upper and lower fracture energy. Data points for the reference heat of A302B steel (see Fig. 4) also are plotted.

The data trend on the RAD for the A302B steel has several interesting features. Irradiation leads to an initial rapid decrease in full shear fracture energy and a concomitant increase in yield strength for neutron exposures over the range of 10^{18} to about 10^{19}n/cm². This is followed by a continued increase in yield strength at a constant level of Cv shelf energy to about 4×10^{19}n/cm² and yield strength approaching 98 kg/mm². An apparent strength transition then leads to a rapid drop in fracture toughness and plane strain fracture appears to be possible for even relatively thin sections.

All data for the A533B steel fall above the trend band for A302B steel and for the indicated exposure of 2×10^{19}n/cm² at 288°C, all data fall above the 7·5-∞ ratio line, thereby implying that gross plastic overload is required to propagate cracking for sections of less than 76 mm. For thick sections mechanical constraint could lead to plane strain fracture up to the estimated ratio line of $K_{IC}/\sigma_{ys}=$ 11-∞. It would thus appear that for the weak direction, irradiated A533B steel could fracture in a brittle mode (for Cv of 10·3 kgm/cm², σ_{ys}=67kg/mm²) in the presence of a large flaw[24].

The RAD diagram thus may be used to represent key aspects of the effect of irradiation on upper shelf Cv fracture behavior of A533B steel; however, the DT-Cv correlation should be established for each steel being considered and the K_{IC}/σ_{ys} ratio lines for heavy sections must be established.

In awareness of the kinds of results illustrated in the above sections, the Atomic Energy Commission recently has published for comment proposed amendments to the general design criteria for nuclear plants that would specify minimum fracture toughness requirements for the pressure boundary material of such power plants[39]. These requirements are based upon the theoretical methods of elastic fracture mechanics and include specification of drop-weight testing for unirradiated steel to establish NDT, and Charpy-V notch testing for

unirradiated and irradiated steel to establish the Cv curve including the upper shelf fracture energy level. Criteria included specify minimum adjusted Cv fracture energy at the lowest pressurization temperature, minimum Cv upper shelf fracture energy for irradiated and unirradiated steel and consideration and allowance of section size and specimen orientation.

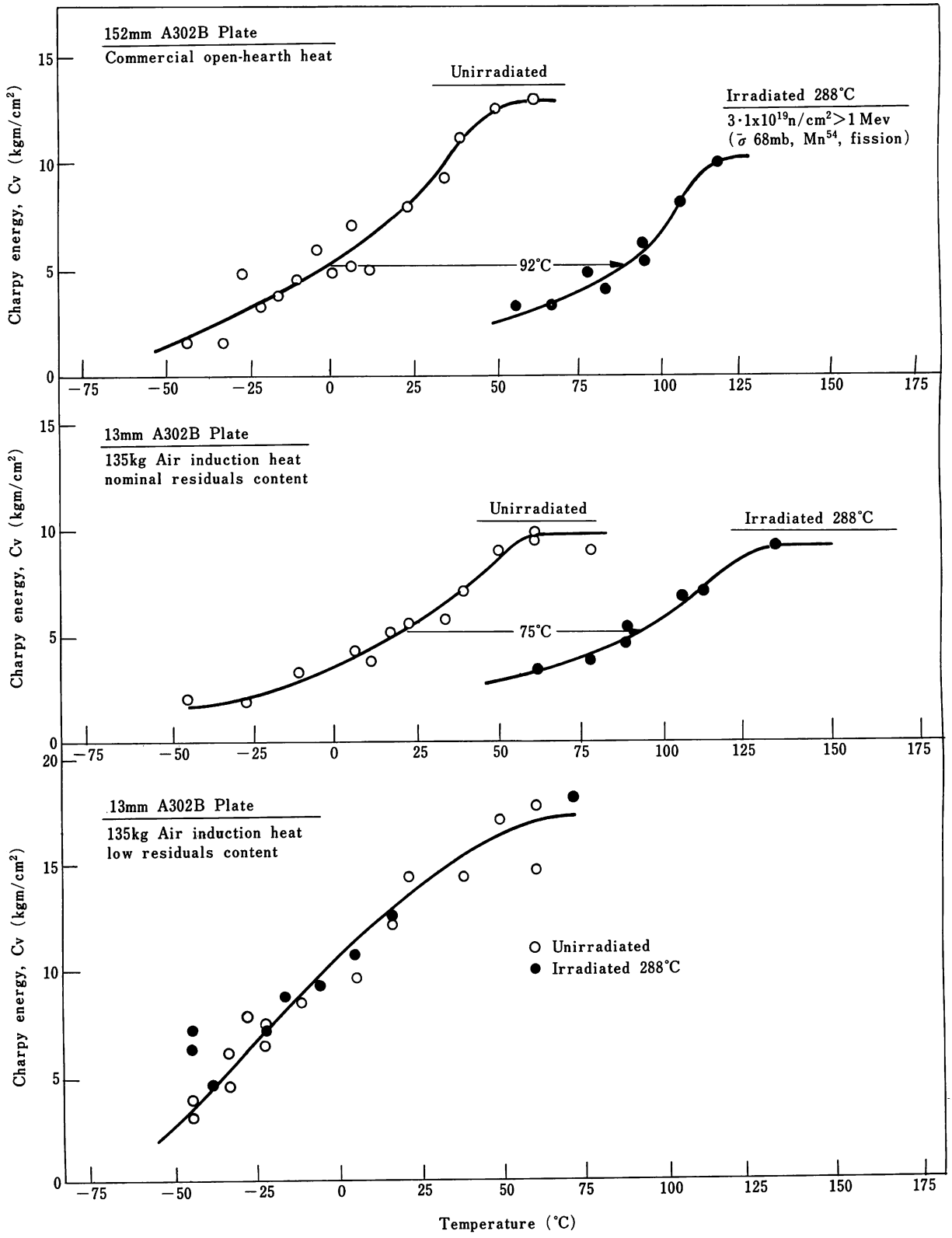

Fig. 9. Comparison of radiation-embrittlement sensitivities (as measured by changes in the Charpy-V notch 5·2 kgm/cm² transition temperature) of one large commercial heat and two "air-induction" heats of A302B steel with nominal and low-residual element contents following 288°C irradiation[31].

2.5 Metallurgical approach to reduced embrittlement

The magnitude of and the variance in the effect of neutron irradiation on the toughness and ductility of reactor pressure-vessel steels seemingly suggest that nature intends to be unkind to or to impose a rather severe burden on the engineer who must design or operate such vessels. In response to this challenge of nature, many investigations have been undertaken to examine the effect of metallurgical structure and alloy composition and the variable of the irradiation environment on hardening and embrittlement. For the steels of engineering significance to reactor vessels, minor effects have been identified with structure and chemistry (e.g., ref. 5, 10) but until recently results of engineering significance which reduced either the magnitude or the variance of irradiation embrittlement of the vessel steels effectively had not been isolated. A firm and technologically important exception to this observation is the recent work conducted at the U.S. Naval Research Laboratory and published in a series of papers and reports over the past three years[31, 40, 41]. Investigators at NRL working with steel producers and fabricators have established the identity of copper and phosphorus as the principle contributors to the embrittlement of both plate and weldments of reactor vessel steels after irradiation at 288°C.

In the course of investigating the effect of residual elements on the response of several pressure vessel steels and weldments to irradiation at 288°C, Potapovs and Hawthorne[31] found that in laboratory heats of A302B steel with "low residuals content" there was a total absence of irradiation embrittlement as measured by Cv testing, Fig. 9. Copper and phosphorus were indicated as significant contributors to the irradiation embrittlement sensitivity in A302B plate from the 135 kg laboratory heats and in A543 steel weld metal[31]. Some evidence suggested some influence or synergistic effect of other "residual" elements, but clear conclusions were not indicated.

In follow-on work the initial indication of the effect of copper and phosphorus on the irradiation response of weld metal was verified in the statistically comprehensive investigation of Hawthorne, Fortner and Grant[40] for 60 kg/mm² yield strength weld metals of quenched-and-tempered A543 and A542* steels with varying copper, phosphorus, nickel and manganese. Typical data for A542 weld metal with varying copper content are illustrated in Fig. 10 for 288°C irradiation. Both the Cv transition temoerature shift (△TT) and the drop in the upper shelf Cv fracture energy (△E) are affected by the composition variables. Data for these quantities were fitted empirically to analytical expressions by regression analysis yielding:

$$\triangle TT(°C)=[118+14800(\%P)+990(\%Cu)]0\cdot55 \quad (1)$$

$$\triangle E(kgm/cm^2)=[-2-100(\%Cu)]0\cdot17 \quad (2)$$

The results of the Cv transition temperature shift are summarized graphically in Fig. 11 for the 2·25% Cr-1%Mo weld metal deposits of varying copper, nickel and manganese. Nickel and manganese did not significantly influence the response of the weld metal to irradiation but did influence the transition temperature of the preirradiated welds which varied from −45°C to −1°C. Irradiation embrittlement virtually was absent from the low-copper welds –the Cv 5·2 kgm/cm² transition temperature shift was 11°C and the reduction in Cv upper shelf fracture energy was less than 1·7 kgm/cm². The low-copper welds also exhibited Rockwell C hardness changes of about one-half that of the high-copper series of

* ASTM A542–69a ladle analysis: 0·15% C max, 0·30–0·60% Mn, 0·035% P max, 0·035% S max, 0·15–0·30% Si, 2·00–2·50% Cr, 0·90–1·10% Mo. Tensile requirements depend on class. Condition: quenched and tempered.

Table 1. Chemical composition: specifications and NRL check analysis of special heat of A533B steel.

Determination	Chemical composition (wt%)												
	C	Mn	Si	Ni	Mo	Cu	P	S	As	Sb	Sn	Bi	Other
Melt purchase specifications													
Ladle	0·25 max	1·15/1·50	0·15/0·30	0·40/0·70	0·45/0·60	0·08 max	0·007 max	0·007 max	0·01* max	0·01* max	0·02* max	0·02* max	low as possible max
Check	—	1·10/1·55	0·13/0·32	0·37/0·73	0·41/0·64	0·10 max	0·010 max	†	0·01* max	0·01* max	0·02* max	0·02* max	—
Ingot 1 ††	0·17	1·22	0·19	0·58	0·50	0·03	0·008	0·008	<0·03	<0·01	<0·02	<0·005	0·02 V 0·015 Al (0·010–0·012 Al)
Ingot 2 ††† (copper modification)	0·17	1·21	0·20	0·56	0·50	0·13	0·008	0·007	<0·03	<0·01	<0·02	<0·005	0·02 V 0·015 Al (0·010–0·013 Al)

† % P+%S≦0·022 * % As+% Sb+% Sn+% Bi≦0·05

†† Average of Plates A and B.

††† Average of Plates C and D.

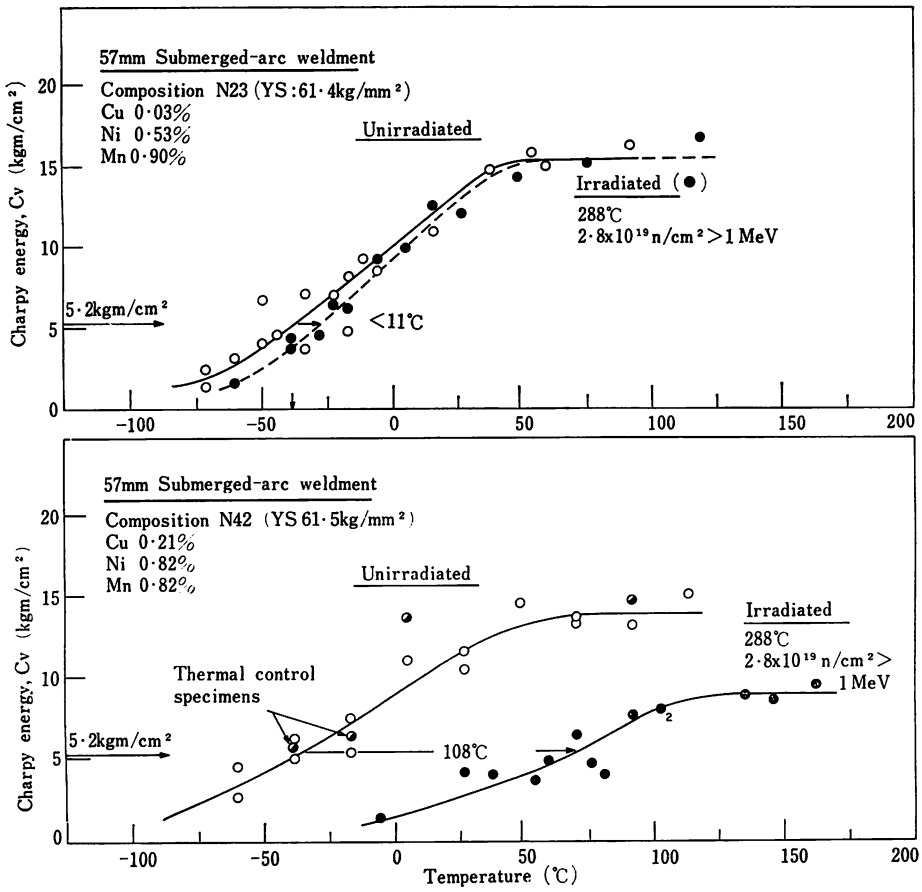

Fig. 10. Typical effect of low versus high copper content on the radiation - embrittlement resistance of 2·25% Cr-1% Mo-0·40% Si-0·10%C weld deposits. Low-copper composition exhibits very low, essentially nil, sensitivity to radiation-induced embrittlement at a temperature comparable to reactor vessel service[40].

Experimental weld performance comparison
(Irradiated 288℃, 2·8x10¹⁹ n/cm²>1 MeV)

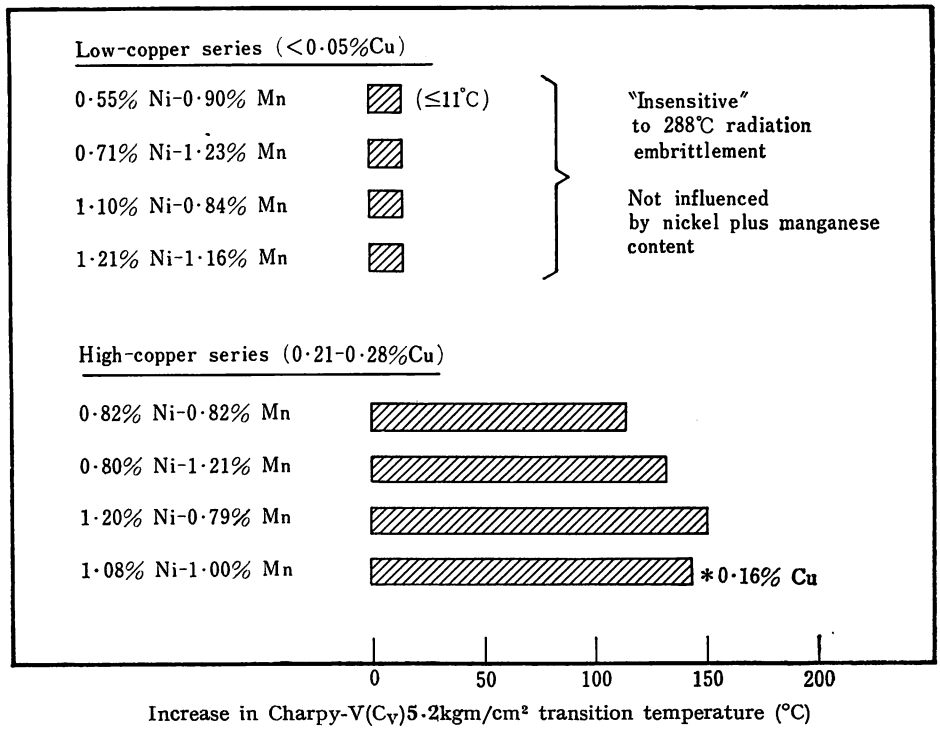

Fig. 11. Summary of observed radiation embrittlement resistance of high- and low-copper welds. Primary division of behavior along the line of low versus high copper content is quite evident[40].

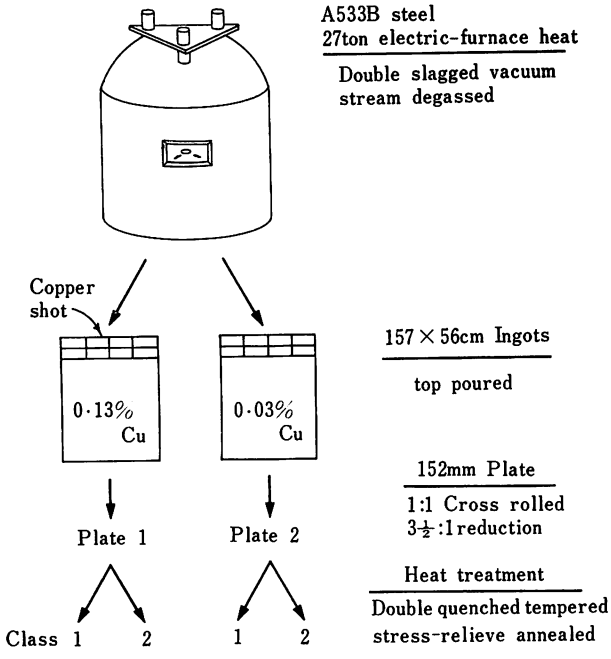

Fig. 12. Schematic plan of processing of special commercial heat of A533B steel for radiation-sensitivity studies[41].

welds. Hawthorne, Fortner, and Grant[40] thus demonstrated that submerged-arc weld compositions can be tailored to have a high resistance to radiation damage at elevated (288°C) irradiation temperatures.

The striking influence of copper and phosphorus on the irradiation performance of the plate from the laboratory heats of steel led the Atomic Energy Commission to sponsor a scale-up program to investigate the possibility of obtaining similar effects by appropriate specification and control of steel processing on a commercial basis. In this program, which was conducted by the NRL[41], a 27-ton heat of A533B steel was procured with specified composition and metallurgical control (with the goal of the lowest possible copper and phosphorus content) in accord with the chemistry specification of Table 1 and the processing schematically illustrated in Fig. 12. The processing schedules were selected to permit examination of composition and metallurgical structure variables. Preirradiation characterization included tensile, drop-weight NDT, and DT testing.

Charpy-V and DT specimens were irradiated at 288°C and at <149°C to fluences of 2·5 to 3×10^{19} n/cm². Typical Cv versus temperature data for the 288°C irradiation for the 0·03% Cu and 0·13% Cu plate are given in Fig. 13. The transition temperature shift and the shelf energy drop for the low-copper steel both are less than one-third that of the higher copper plate. Comparison of the Cv and DT test performance is illustrated in Fig. 14 for the 288°C, 3×10^{19} n/cm² and for the <149°C, $2\cdot5\times10^{19}$ n/cm² irradiation of the low-copper steel. The mid-energy shift of transition temperature for the DT and Cv tests is in agreement for both the 288°C and <149°C irradiations. DT test results indicate a post-irradiation NDT temperature of <25°C for the low-copper Class 2 plate after 288°C exposure to $3\cdot1\times10^{19}$ n/cm².

Consistent with the observations on the laboratory heats, both the high- and low-copper plates appear to be equally sensitive to embrittlement at the lower irradiation temperature. The shift in transition temperature for the <149°C irradiation is comparable to that of the ASTM A302B reference heat Fig. 4. The reduced sensitivity of the low-copper steel to embrittlement at the higher temperature also is reflected in tensile yield data. The tensile yield strength of the unirradiated plate represented in Fig. 14 was 46·5 kg/mm². Data for the irradiated plate are given in Fig. 14 and it is seen that the higher temperature irradiation increased the yield strength by only 6% while the lower temperature irradiation increased it by about 75%.

Data are not included in this review, but no discernable difference was observed for the influence of copper on the sensitivity to embrittlement for either the Class 1 or Class 2 strength condition.

The significance of the reduced sensitivity of the low-copper (primary melt analysis) heat of A533B steel to irradiation embrittlement is readily apparent when the data are examined in perspective with data representative of general commercial production. In Fig. 15 the present data for plate and weld metal are displayed along with the established trend band for Cv transition temperature

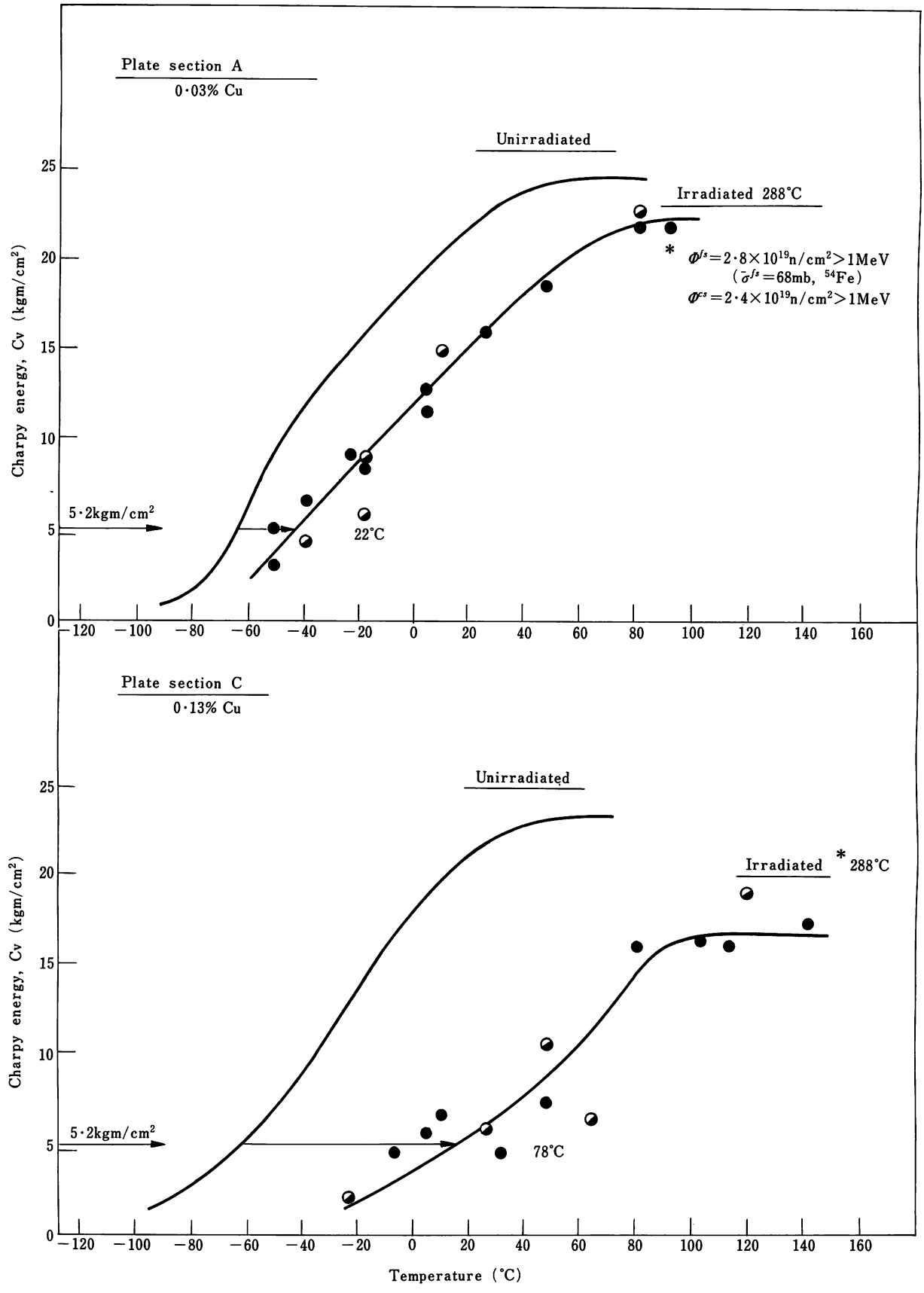

Fig. 13. Charpy-V assessments of the radiation-embrittlement resistance of plate sections of low- and high- copper A533B steel. Very low sensitivity to radiation embrittlement is indicated for the primary melt analysis represented by plate section A. The melt modification which increased copper content to 0·13% is seen to have a strong detrimental effect on radiation performance. Irradiated at 288°C to $2\cdot4\times10^{19}$n/cm² (>1 MeV)[41].

data for A533B steel and the ASTM reference heat of A302B. The sensitivity of both the plate and weld metal with a low copper content to irradiation-induced shift of the DBTT is about one-third that of the A302B reference plate and significantly less than the best A533B production steels. The scale-up investigation thus demonstrates that the specification and production of A533B steel that is highly resistant to neutron-irradiation embrittlement are within present industrial capability.

On the basis of these investigations a revised specification for reactor pressure-vessel steels has been proposed and is currently under review by the ASTM. The draft specification limits copper to 0·10% (max) and phosphorus to 0·012% (max)[42].

2.6 Fracture mechanisms and irradiation embrittlement of ferritic steels

The microscopic and macroscopic aspects of flow

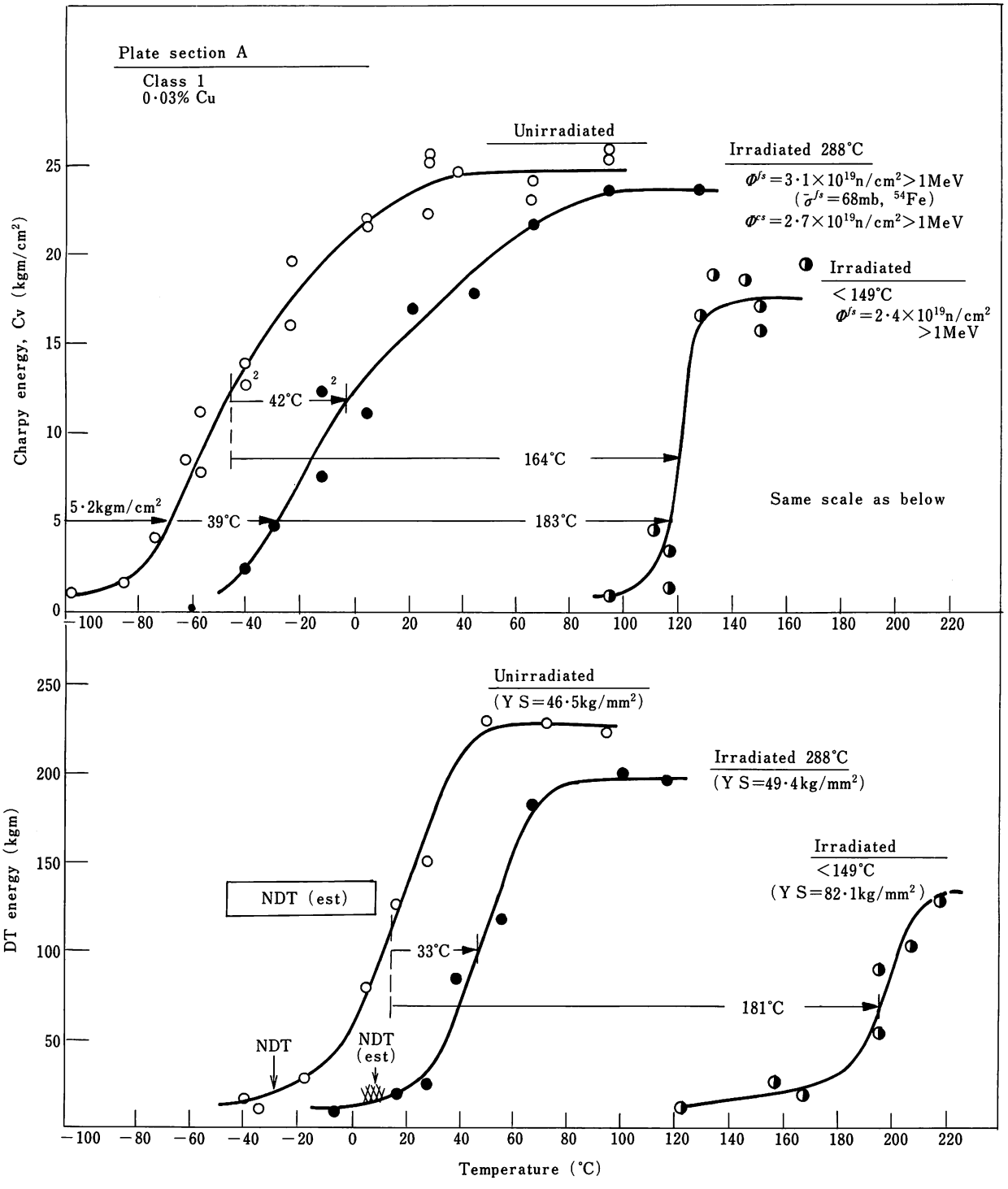

Fig. 14. Comparison of Charpy-V and dynamic-tear test performance of plate section A at the quarter thickness location[41].

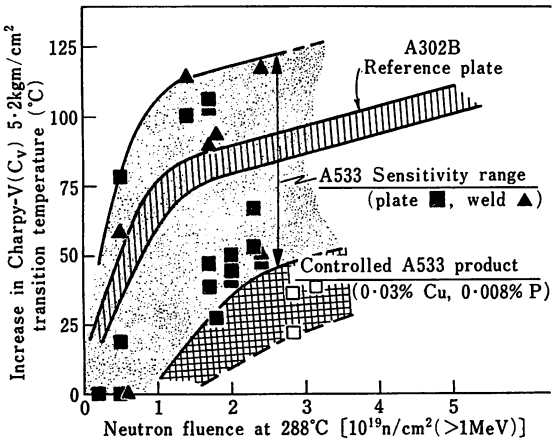

Fig. 15. Increase in Charpy-V notch 5·2 kgm/cm² transition temperature with neutron exposure at 288°C. The performance of plate sections representing the primary melt analysis of the special melt of low-copper A533B steel (open data points) is compared to the performance of the ASTM A302B reference plate and conventional A533 materials representative of current reactor vessel construction[41].

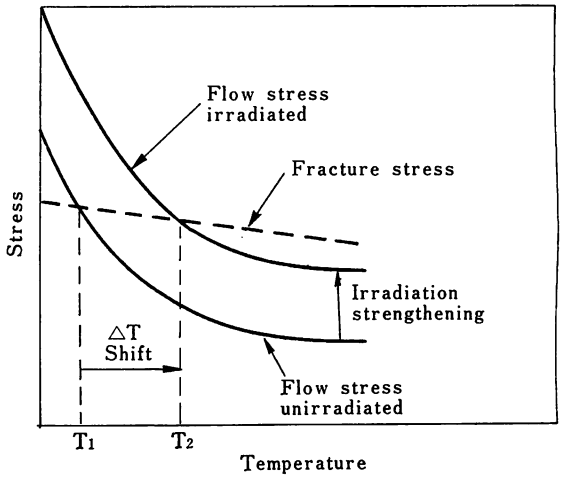

Fig. 16. Schematic diagram illustrating how irradiation strengthening can produce a shift in transition temperature[6,27].

and fracture which lead to the temperature transition from brittle cleavage to ductile rupture for ferritic steels have been treated in extensive detail by Tetelman and McEvily[43]. In essence, the transition occurs at that temperature at which the intrinsic (or cleavage) fracture stress σ_f equals the flow stress σ_y for given conditions of microstructure, grain size, strain rate and constraint. At lower temperatures $\sigma_f < \sigma_y$ and fracture occurs before macroscopic plastic flow. At higher temperatures $\sigma_f > \sigma_y$ and rupture occurs by ductile tearing. Variation in either σ_f or σ_y thus may cause a shift in the ductile-brittle transition temperature (DBTT).

For irradiated steels it follows that the usual irradiation induced increase in σ_y will produce an upward shift in the DBTT as illustrated schematically in Fig. 16. In contrast, the presence or absence of any effect of irradiation on σ_f is not at all obvious by deduction. The question must be examined experimentally.

Wechsler, *et al*[27] studied the relationship between the increase in the tensile yield stress and the DBTT measured by Charpy-V impact testing of A212B* steel irradiated at 60°C. Results of tension and impact testing were reported to be consistent based upon a critical cleavage stress deduced from tensile testing. No evidence was noted for an irradiation-induced change in the cleavage stress. It was concluded that irradiation embrittlement as manifest in a shift of DBTT is largely a consequence of irradiation hardening and not a change in the fracture processes *per se*.

Similar conclusions follow from more recent investigations that were undertaken to examine the origin of the influence of copper on the sensitivity of A533B steel to irradiation embrittlement[6,44,45]. In cooperative experimentation, Hellerich and Hunter[44] conducted scanning electron fractographic observations on specimens from the studies of the U.S. Naval Research Laboratory[31,40,41]. No distinction was observed between the fracture appearance of irradiated and unirradiated steels for either the ductile rupture or the cleavage mode of fracture. For either condition, 100% cleavage always occurred below NDT and 100% ductile rupture always was observed at full shelf-energy levels. Furthermore, for irradiated steels which exhibit a large reduction in full shear (upper shelf) fracture energy (e.g. welds of type A543 steel, Fig. 6), the fracture surface was reported to have a mixed mode or to be similar to a low-energy tear surface which is characteristic of high-strength steels. Of further significance, there was no evidence of a preferential fracture path along grain boundary or precipitate interfaces for either cleavage or high or low energy tearing for either the high- or low-copper steels[6,44]. Based upon these SCM fractography observations both (6) and (44) conclude that irradiation influences the conditions at which a given fracture mode may occur, but that for a given fracture mode, there is no essential difference between irradiated and unirradiated steels or between low- and high-copper steels.

Fracture surfaces also were examined by Auger electron spectroscopy. No segregation of copper or phosphorus was observed on the fracture surface of irradiated specimens[6,45]. Post-irradiation hardness-recovery measurements showed that the low-copper steel was hardened only slightly at the 288°C

* ASTM A212 has been superseded by ASTM A515 and A516. These specifications cover carbon-steel plate for pressure vessels. Condition: see specifications; generally normalized and tempered.

irradiation temperature relative to the increase for the high-copper steel but that the recovery behavior for the two steels is similar[6,45]. The similar recovery behavior lead Smidt[6] to suggest that the difference in irradiation hardening that is observed is likely one of the relative magnitude of the dynamic recovery during irradiation in the two different composition steels rather than a basic difference in mechanism.

As was noted earlier, tensile data included on the DT curves for the low-copper steel, Fig. 14, also indicate only a slight increase in the flow stress after 288°C irradiation in parallel to the small shift of the transition temperature. However, the lower temperature irradiation (<149°C) leads to a 75% increase in flow stress and a concomitant 183°C increase in the 5·2 kgm/cm^2 transition temperature[41]. Smidt[6] concludes that most of the evidence of scanning electron fractography, Auger spectroscopy, hardness recovery and some preliminary transmission electron microscopy points to a model in which vacancies interact with copper to form defect complexes, which are more numerous and more stable than those which exist in the absence of copper. These complexes retard the dynamic recovery process during irradiation and thereby increase irradiation hardening, which in turn leads to a greater shift in the transition temperature for the higher copper steels.

The transition temperature behavior of irradiated steels thus appears to be adequately explained by irradiation strengthening according to the classic concept of transition temperature as suggested schematically in Fig. 16 and not by changes in the cleavage fracture stress. By comparison, neither the mechanistic explanation nor the phenomenological description of upper shelf fracture energy has been adequately developed for irradiated steels. The RAD provides a useful representation of the data and shows promise as a predictive tool in conjunction with the other approaches to fracture analysis which are under development[24,30,37].

3. EMBRITTLEMENT OF STAINLESS STEEL

3.1 Effect of radiation on microstructure

Changes in the microstructure of stainless steel are a function of irradiation temperature, fluence and neutron energy spectrum. A range of mechanical properties is obtained as a function of these variables, and it is important that irradiation and test temperature coincide as closely as possible for a realistic assessment of properties at a given temperature. Brager, *et al.*[46] and Bloom[47] have recently discussed the microstructure of irradiated stainless steel as a function of temperature and fluence. Photo. 4 and 5 from the work of Bloom[47] illustrate the development of dislocation structure and void structure, respectively, as a function of fluence and irradiation temperature for annealed Type 304 stainless steel irradiated in a fast flux. Dislocation damage was not observed in specimens irradiated to 1×10^{18}n/cm^2 at 370°C (Photo. 4). After irradiation to $1{\cdot}4\times10^{20}$n/cm^2 at 370°C, interstitial dislocation loops with diameters to about 1000Å were observed. The concentration of these defects decreased with increasing irradiation temperature for this same fluence, and no damage was visible above 524°C. As the fluence was increased at temperatures below about 550°C, the concentration of faulted interstitial loops increased and their size increased with increasing temperature. At temperatures above 550°C, the Frank dislocation loops unfaulted and formed dislocation networks. Irradiation at high fluences and relatively low temperatures produced considerable image overlap in the electron microscope making it more difficult to develop accurate quantitative data. Values for the number density of faulted loops range from $<1\times10^{12}$ to 1×10^{16} cm^{-3}.[47]

The development of the void structure as a function of fluence and temperature is shown in Photo. 5. Voids are not observed below a certain fluence threshold and this threshold increases with increasing irradiation temperature. Void concentration increases with increasing neutron fluence and decreases with increasing irradiation temperature. The mean void diameter increases with increasing irradiation temperature but does not appear to change significantly with fast fluence. At low void concentrations a significant fraction of the voids is associated with either dislocations or precipitate particles. The upper temperature limit for void formation for the Type 304 stainless steel illustrated in Photo. 5 is about 650°C for fluences of about 5×10^{22}n/cm^2. At higher irradiation temperatures cavities are observed which are believed to be helium bubbles as described later. These usually are much smaller than voids formed at slightly lower temperatures and often are found in grain boundaries, whereas voids formed at lower temperature are not. The number density of voids illustrated in Photo. 5 varies from 10^{12} to 10^{16}cm^{-3} depending on temperature and fluence, leading to density decreases up to 4 volume percent.

The microstructural development of irradiated annealed Type 316 stainless steel is similar to that of Type 304, although some important differences have been identified[46]. The fluence threshold below which no voids are found is increased in Type 316 and the average void diameter is somewhat smaller. Although swelling behavior for other stainless steels can differ markedly from Types 304 and 316, structural features such as dislocations, coherent and incoherent precipitates, and grain boundaries exert a much larger effect on swelling

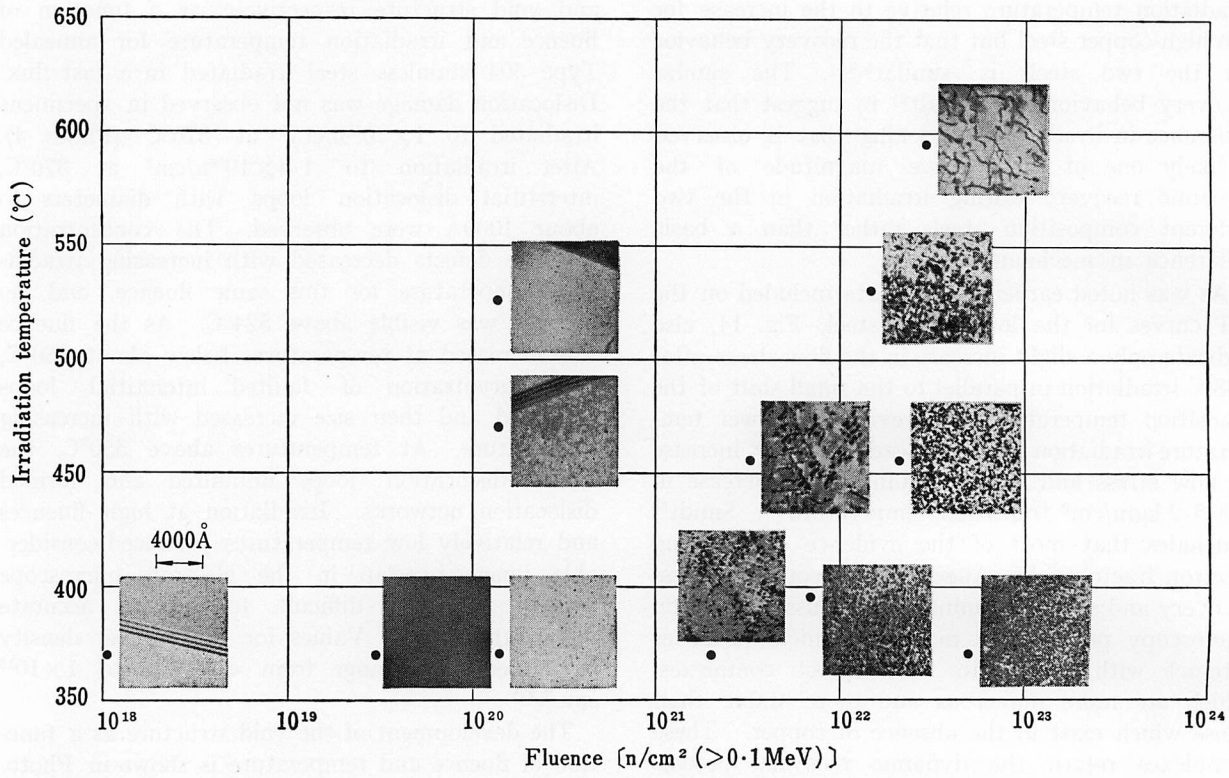

Photo. 4. Dislocation structures formed in annealed Type 304 stainless steel during fast neutron irradiation[47].

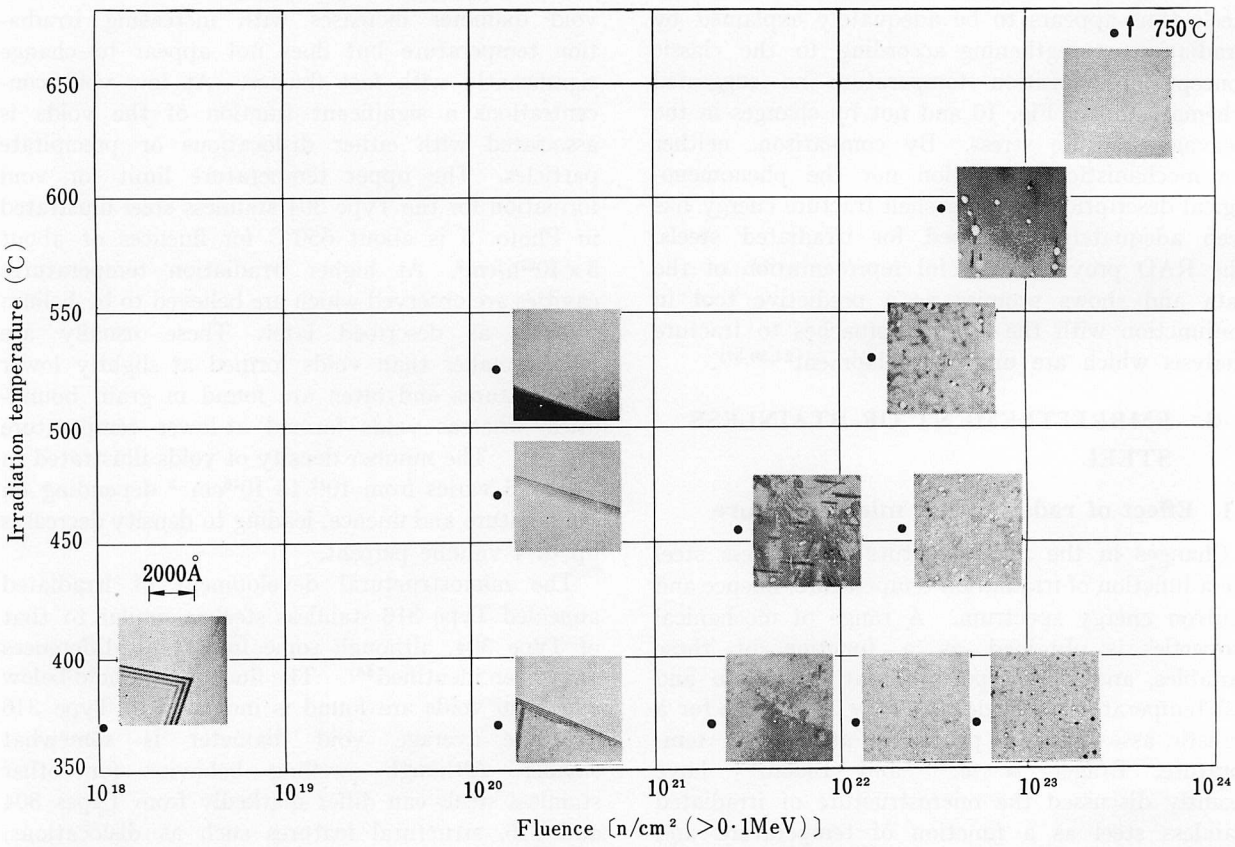

Photo. 5. Cavities formed in annealed Type 304 stainless steel as a result of fast neutron irradiation[47]

characteristics. Cold working of Type 316 stainless steel by 25 or 75% has been found to essentially eliminate swelling to fluences of 3×10^{22}n/cm^2.[48] Thus, changes in metallurgical structure can influence void nucleation and growth and a very large matrix of experimental conditions will have to be investigated before the phenomenon of swelling is completely understood. Theoretical treatments of loop and void nucleation, their interaction, annihilation and growth are available and may shorten the time for a complete understanding to be obtained[49,50].

The third microstructural feature arising from irradiation is the precipitation of fine carbides and/or intermetallic particles. Specimens of Type 304 stainless steel irradiated in the 370 to 425°C region at fluences above 1×10^{22}n/cm^2, often contained high concentrations of coherent $M_{23}C_6$ precipitates on the order of 50 to 3000Å in size[46]. Voids were not found on these coherent particles. In the 450–600°C temperature range larger particle and rod-like precipitates were observed; the latter believed to be the FeCr sigma phase. Most of the voids were found to be associated with a majority of the rod shaped precipitates and not with the carbide particles. An illustration of this is shown in Photo. 2 (a) for annealed Type 316 stainless steel irradiated at about 740°C to a fluence of 3×10^{22}n/cm^2.[51]

3.2 Effect of radiation on properties below 0·5 T_m

Stainless steel does not exhibit a ductile-to-brittle transition temperature similar to the ferritic steels described earlier. The effects of radiation are therefore more gradual as a function of fluence, and lead to a continuous spectrum of properties rather than either ductile or brittle behavior. From a fast-reactor point of view many of the core components operate below $0\cdot5T_m$ of stainless steel (approximately 560°C) and the effects of radiation may be design limiting.

The effects of irradiation on stainless steel in this temperature region in general lead to a large increase in yield strength together with a large decrease in uniform strain and decrease in the work-hardening coefficient. These characteristics are illustrated in Fig. 17 for a series of Type 304 true stress-true strain curves at 480°C[52]. The true fracture strain decreases with increasing fast fluence from approximately 28 to less than 1% over the fluence range investigated, while yield strength increases by a factor of 4 to 5. The true fracture stress by comparison changes little (except at the highest fluence). Saturation of tensile properties appears to occur after exposures of about 4×10^{22} n/cm^2 (E>0·1Mev) with residual uniaxial tensile elongation of approximately 2%[19].

Fig. 18 is a plot of true yield stress (PEL stands for Proportional Elastic Limit) as a function of fluence[52]. The initial increase in true yield stress up to perhaps 25 kg/mm^2 is probably due to hardening from point interstitial loops. At higher fluences, voids become increasingly important as the principle contributors to hardening. An empirical relationship between microstructure and flow properties of irradiated stainless steel has been developed for this set of tensile data. The increase in yield stress is related to the microstructure, which is represented empirically by a dimensionless structural parameter K which is a function of void volume V, and void spacing $\bar{l}$.[52] The plot of true yield stress vs. $K/\bar{l}$ is shown in Fig. 19. It represents one of the first attempts to correlate mechanical property data with void volume, size and distribution. It is too early to know whether the parameter has applicability beyond the relatively narrow set of data from which it was derived, but it is a step in the right direction in being able to relate and thus predict mechanical properties on the basis of microstructural features.

The effect of irradiation on stress-rupture properties of annealed Type 316 stainless steel is shown in Fig. 20[53]. Only the curve at 538°C will be discussed in this section; the other curves are discussed later. The rupture life at 538°C after a fluence of $1\cdot2\times10^{22}$ n/cm^2 is reduced about a factor

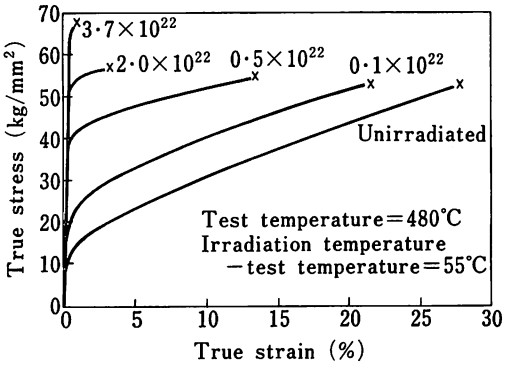

Fig. 17. True stress versus true strain for a series of annealed type 304 stainless steel tensile specimens as a function of fast fluence[52].

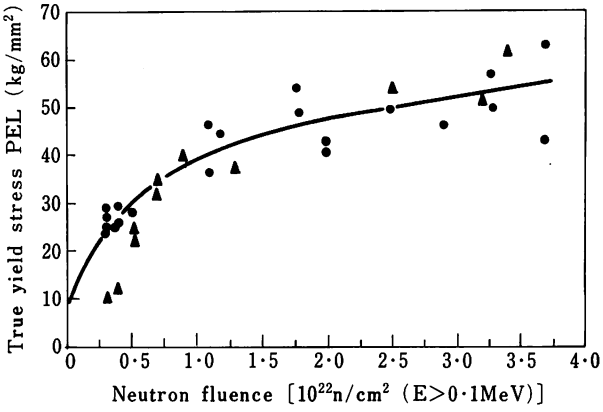

Fig. 18. True yield stress as a function of fast neutron fluence for irradiated specimens of annealed type 304 stainless steel.[52]

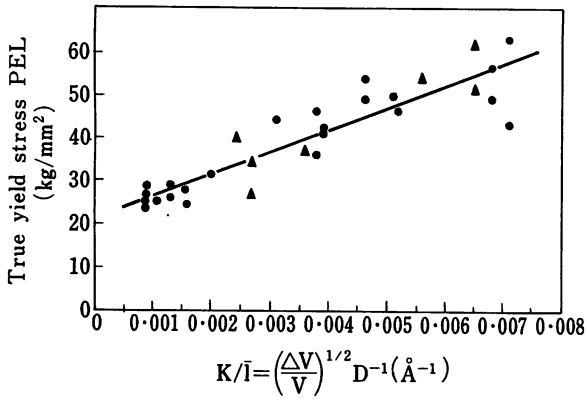

Fig. 19. True yield stress as a function of void structural parameter[52].

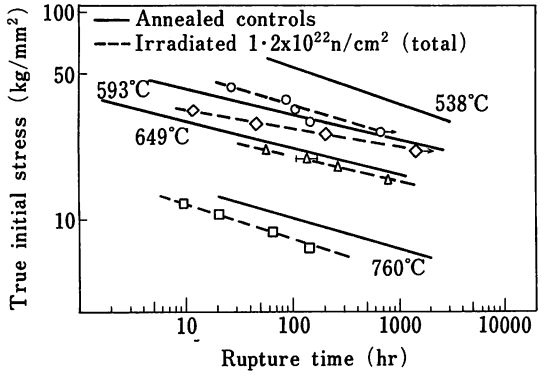

Fig. 20. Log stress-log rupture time curves for annealed Type 316 stainless steel irradiated in a fast flux[53].

of 20, while total elongation values are reduced from the range of 14–39% for the unirradiated to 4 to 18% for the irradiated specimens. The steady-state creep rate after irradiation was found to be increased by up to one order of magnitude. A clear mechanism for these observations has not yet been elucidated. One possible explanation for the increased creep rate is that it results because of the observed accelerated (irradiation-induced) coarse precipitation and consequent loss of solution strengthening in the irradiated materials. (Photo. 2b). Secondary creep rates also were found to increase in unirradiated specimens when these were aged above 600°C in order to precipitate carbides.

At the 538°C test temperature the substantial loss in rupture life for the irradiated specimens is believed to be primarily the result of higher creep rates with only a small contribution ascribed to loss of ductility. It is clear that explanation of the much larger loss in rupture life observed at 538°C compared to the higher test temperatures must be sought in microstructural changes that predominate in the lower temperature regime, rather than in helium embrittlement which predominates at higher temperatures as is described later.

3.3 Effect of radiation on properties above $0{\cdot}5T_m$

The principle effect of irradiation on elevated-temperature properties is a loss in ductility which usually is not associated with large changes in either yield or ultimate strength. This loss in ductility, moreover, cannot be eliminated by annealing at high temperatures. There now is general agreement that helium produced by transmutation reactions is responsible[7,54–58]. An excellent review and summation of current data on helium generation as a function of metal composition, impurities and neutron energy recently has been presented by McElroy and Farrar[8]. In thermal reactors it has been assumed that the major source of helium was the (η, α) reaction with boron for which the cross section is very large. At a thermal neutron fluence of about 10^{20}–10^{21}n/cm² the ^{10}B effectively would be consumed and helium production was expected to cease. Recent data, however, showed anomalously high helium production rates in both nickel and stainless steel[59,60]. The increased helium production in thermal neutron spectra is postulated to be due to secondary (η, α) reactions with ^{59}Ni or ^{58}Co which are formed from the precursor ^{58}Ni by (η, α) and $(\eta$, proton) reactions, respectively[60]. In a thermal neutron environment the helium production in stainless steel and nickel is thus proportional to the nickel content. The rate was related to the equivalent thermal neutron fluence (φt) by McElroy and Farrar[8] as

$$\text{He (atoms/gm nickel)} = 9{\cdot}8\times10^{-19}\ (\varphi t)^{1{\cdot}68}$$

This expression is applicable to fluences ranging between $\sim3\times10^{20}$ and $\sim1\times10^{23}$n/cm².

In fast neutron spectra, on the other hand, the production of helium is dominated by primary (η, α) and $(\eta$, proton) reactions with nickel, iron and chromium and the rate is given by McElroy and Farrar[8] as a function of fast fluence (E>3·68 Mev) as

$$\text{He (atoms/gm of material)} = K\varphi t$$

(where K is approximately 10^{-4}). Fast flux effects are often

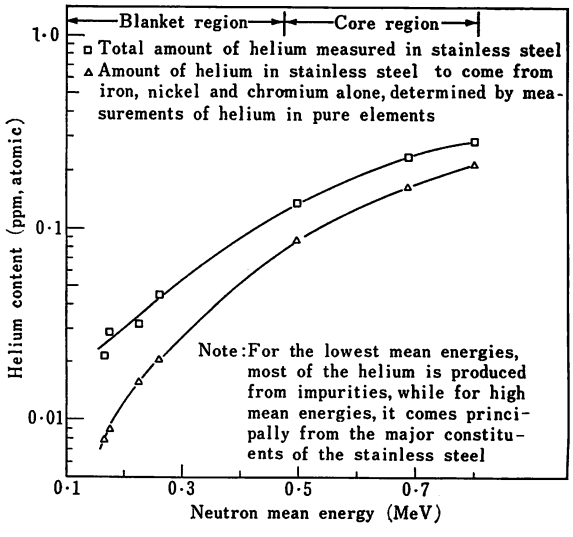

Fig. 21. Spectral effects of helium production for a constant total fluence (>10^{-10} MeV) of $1{\cdot}3\times10^{21}$n/cm².[8]

correlated with neutrons having energies above 0·1, 1·0, or 3·68 MeV. Fig. 21 illustrates how helium content varies as a function of neutron mean energy for an experiment containing iron, nickel, chromium and 304 stainless steel conducted in several core and blanket locations of the sodium-cooled fast reactor, EBR-II[8]. The total fluence is low, only $1{\cdot}3\times 10^{21}$n/cm,^{2} resulting in low helium values. It can be seen however, that helium content increases with neutron mean energy, and that iron, nickel and chromium alone do not account for the total helium as measured in stainless steel. For the lowest mean energies most of the helium is produced by impurities, while at the higher energies it comes primarily from iron, nickel and chromium.

Even though a great deal has been learned about helium production in the last two years, much additional data is needed, especially on energy-dependent (η, α) cross sections of elements in structural alloys and better definition of neutron spectra.

Helium, regardless of how it is produced, has a very low solubility in the matrix of stainless steel and will precipitate under stress to form bubbles at relatively low temperatures. Bubbles located at

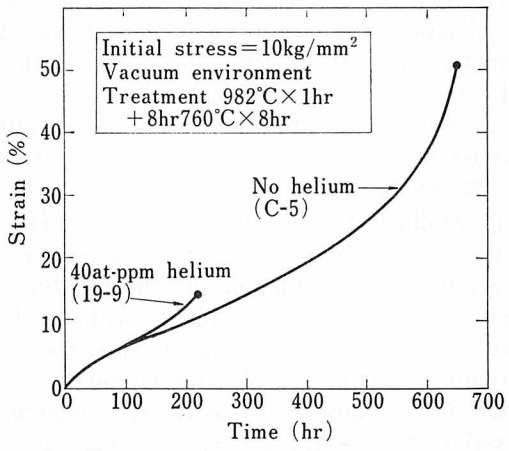

Fig. 22. Creep curve at 700°C for Type 316 stainless steel with and without helium injection[61].

grain boundaries are particularly important, for the boundary and bubbles appear to interact under stress leading to accelerated grain-boundary fracture behavior under conditions that normally tend to produce intergranular fracture (in the absence of irradiation). Irradiated alloys fracture intergranularly at strains where grain-boundary cracking

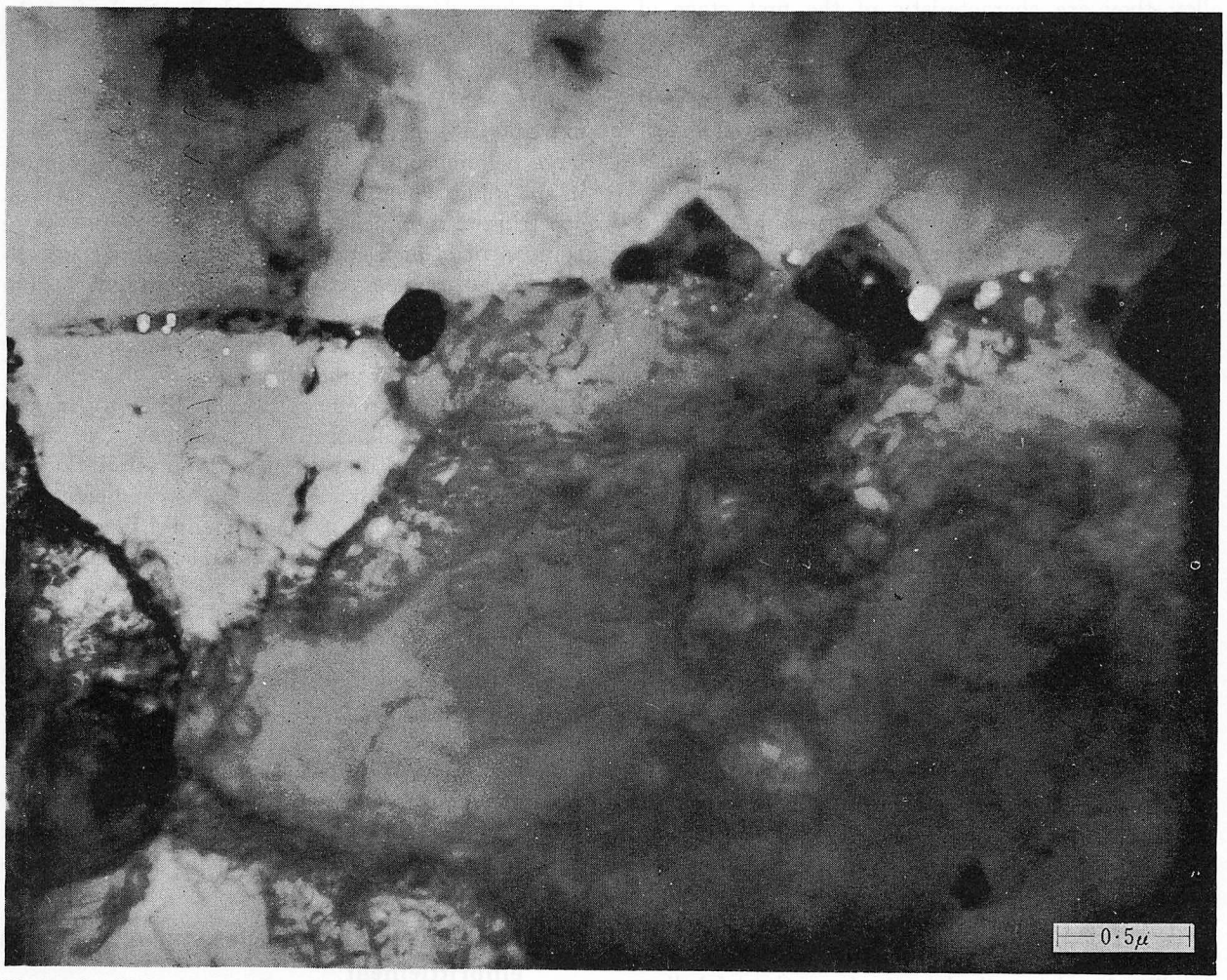

Photo. 6. Helium bubbles in Type 316 stainless steel after injection of $4{\cdot}0\times 10^{-5}$ atom fraction helium and testing at 700°C. Rupture life=316 hr, elongation=13%[62]

in unirradiated alloys is either absent or just beginning. Furthermore, fewer cracks are found in an irradiated alloy at fracture, indicative of the fact that cracks propagate much faster than in unirradiated alloys[57]. The influence of this embrittling behavior on mechanical properties is illustrated in Fig. 22, Photo. 6 and Fig. 23.

Fig. 22 illustrates the influence of 40 ppm He on the creep of Type 316 stainless[61,62]. The major effect of helium was a reduction in rupture time and strain at rupture. The sample without helium failed in a transgranular manner while the sample containing helium failed intergranularly. Interrupted tests followed by destructive examination showed that intergranular cracks begin as small voids on grain boundaries early in the second stage of creep and that the voids become more numerous and link to form cracks. Although the curves in Fig. 22 were generated on samples into which the helium was cyclotron injected rather than produced by neutron irradiation, the behavior is typical. Steady-state creep rates generally are not strongly affected by irradiation although increases have been observed on occasion[53,63]. It appears that when higher creep rates are observed in an irradiated alloy they are characteristic of the first stage of creep and that a normal second stage is not established due to premature fracture of the specimen[63]. The variations in creep rates observed are sensitive to temperature and stress as well as test specimen. Stress-rupture testing of tubular specimens, for instance, can lead to apparently higher values of secondary creep rate, since diametral measurements usually are made at the beginning and end of the test and an "average" creep rate is assigned. At high temperatures where primary creep may be large, this "average" deviates more and more from the secondary creep rate[53].

The existence of helium bubbles primarily on or near a grain boundary is shown in Photo. 6[62]. This particular sample with a helium content of 40 ppm was creep tested at 700°C and had a rupture life of 316hr. In many cases the bubbles are attached to carbide particles on the grain boundary.

Reduction in tensile properties due to helium embrittlement is shown in Fig. 23[64]. The uniform elongation for unirradiated 347 stainless steel drops off gradually as a function of temperature. By comparison, the uniform elongation of the irradiated specimens is considerably reduced at room temperature, drops off as the temperature is increased and rises again to a maximum at 525°C as the low-temperature radiation damage is annealed out. Between 525° and 575°C, in the region of change-over from low-temperature hardening to high-temperature embrittlement, the uniform elongation drops off very rapidly from 16 to 1·8%. This ductility loss is ascribed to the formation of helium bubbles at the grain boundaries leading to premature

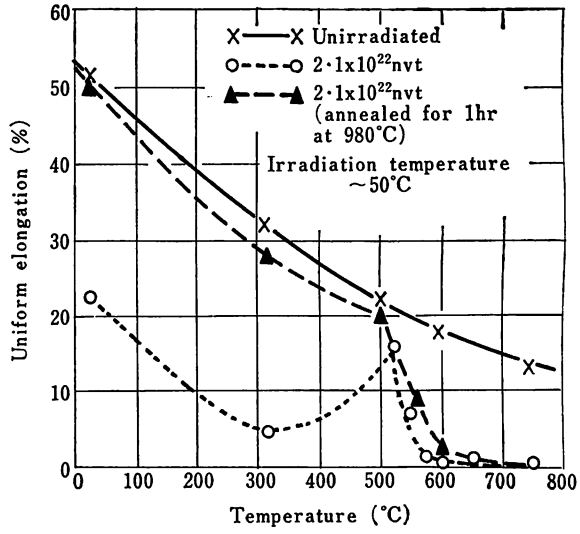

Fig. 23. Tensile ductility as a function of temperature for Type 347 stainless steel unirradiated and irradiated at 50°C.[64]

fracture. Annealing of the irradiated steel leads to recovery of ductility at temperatures of 500°C and below; however, at temperatures greater than 500°C no ductility recovery was observed indicating that the helium damage is not annealed out. In fact the helium bubbles were found to persist even after annealing at 1350°C[64].

The examples shown in Fig. 23 present an extreme case of embrittlement because of the very large helium content. Irradiations were performed in the ETR, which is a reactor with a large thermal spectrum but which contains an unusually large component of high energy neutrons. This combination of neutron energy spectra results in high helium contents due to secondary reactions as discussed previously. The measured helium content in the specimens was 917 ppm[65].

Reduction in creep-rupture life due to helium embrittlement is illustrated in Fig. 20[53]. At 538°C the reduction is due to carbide precipitation as discussed previously. At the higher temperatures, the reduction is due to helium embrittlement. In general, the curves for irradiated and unirradiated specimens are parallel, except for the 593°C test temperature where the rupture life of the irradiated specimens exhibits a somewhat higher stress dependence. Total elongation values at 593, 649 and 760°C were reduced to the 5–14% range, from values that were about 25% at 593°C, 35–66% at 649°C, and up to 72% at 760°. It can be expected that at neutron exposures greater than the $1{\cdot}2\times10^{22}$n/cm^2 shown in Fig. 20, the ductilities would be affected to an even greater degree reaching values as low as 1–2% total strain.

3.4 Metallurgical approach to reduced helium embrittlement

Considerable progress has been made in reducing

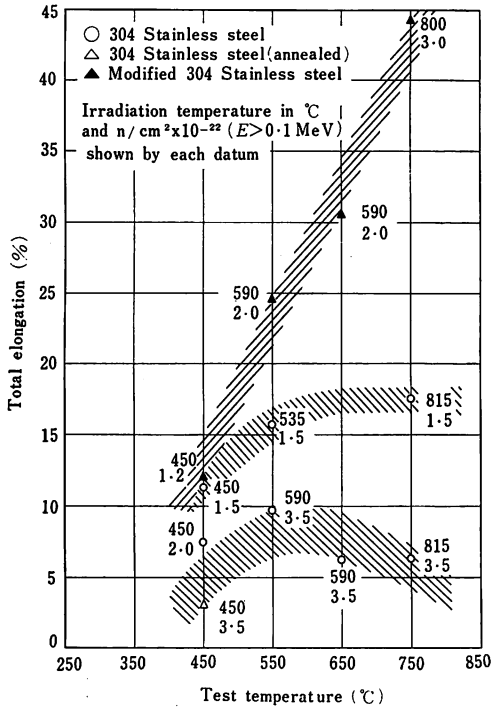

Fig. 24. Tensile ductility of standard and titanium-modified Type 304 stainless steel after irradiation in EBR-II[66].

the elevated-temperature embrittlement due to helium by alloying additions to stainless steel. Titanium, in particular, has been found to be very effective[57]. Fig. 24 from the work of Bloom and Weir[66] shows constant or decreasing tensile ductility as a function of test temperature for irradiated Type 304 stainless steel while showing sharply increasing ductility for irradiated Type 304 stainless steel modified with approximately 0·2% Ti. The cause for this is believed to be a change in the helium bubble distribution, leading in turn to a change in fracture behavior. In the standard alloy, nearly all grain boundaries contained helium bubbles whereas in the modified alloy bubbles occurred in clusters usually within the grain, and were found in grain boundaries only when the latter intersected such a cluster[57]. It was further observed that helium bubbles occurred near precipitates within the grains and it was postulated that since boron is segregated to such precipitates the amount of helium in the grain boundaries where boron normally resides was reduced. The irradiated modified alloy did not contain intercrystalline cracks and only voids lying parallel to the applied load were observed. Tests on the irradiated standard alloy, by comparison, showed extensive intercrystalline cracking. These effects are illustrated in Photo. 7. The top part in the figure shows the creep curve anb fracture surface for irradiated standard Type 304 stainless steel. The strain at fracture is only 0·5% and the fracture surface has the classical appearance of intergranular fracture. The bottom part of the figure shows the creep curve and fracture surface for a specimen of irradiated titanium-modified Type 304 stainless steel, tested under approximately equivalent conditions. The strain at fracture is 17% and the fracture has a typical ductile appearance. This implies a strong influence of titanium on fracture behavior, most likely due to a change in the location and distribution of helium bubbles.

The influence of titanium modifications on mechanical properties of other alloys is also under investigation. Included in these are Type 316 stainless steel and Incoloy 800.

4. IRRADIATION EFFECTS IN DESIGN

In applying irradiation effects data to the design of nuclear power reactors, caution must be exercised in translation from the experimental irradiation conditions (of temperature, flux and spectra) to the design conditions. Furthermore, the applicability of conventional post-irradiation mechanical property data must be considered in light of specific loading conditions and/or failure mode or criteria of particular components. Illustrations of examples of some approaches to these questions are given in this concluding section.

4.1 Damage function analysis

The consideration of temperature and fluence has been treated in the preceding sections, but the influence of neutron spectra requires further discussion. Displacement damage is dependent upon neutron energy[67,68] but the direct translation from theory based upon first principles to engineering property data does not exist. An empirical engineering approach has been applied to this problem through the development of *damage function* analysis[69-71]. In concept a *damage function*, G(E), is an energy-dependent cross section that describes the reaction rate to obtain a given property change as a function of neutron irradiation. Thus a property change, *Si*, in a given neutron spectra is given by

$$Si = \int_t \int_E G(E)\, \varphi(E, t)\, dE\, dt$$

where φ (E, t) is the flux at energy E and time t.

In application, a set of such integral equations for a given measured property change in various spectra is solved by an iterative computer code to obtain an empirical G(E) energy-dependent damage function. The determined G(E) then may be applied to another spectra to predict the property change.

This approach to the correlation and prediction of irradiation effects data has been applied to Charpy-V transition temperature shift data for A302B pressure-vessel steel[70] and to tensile properties of irradiated stainless steel[71]. A set of predicted yield strength versus fluence curves for Type 304

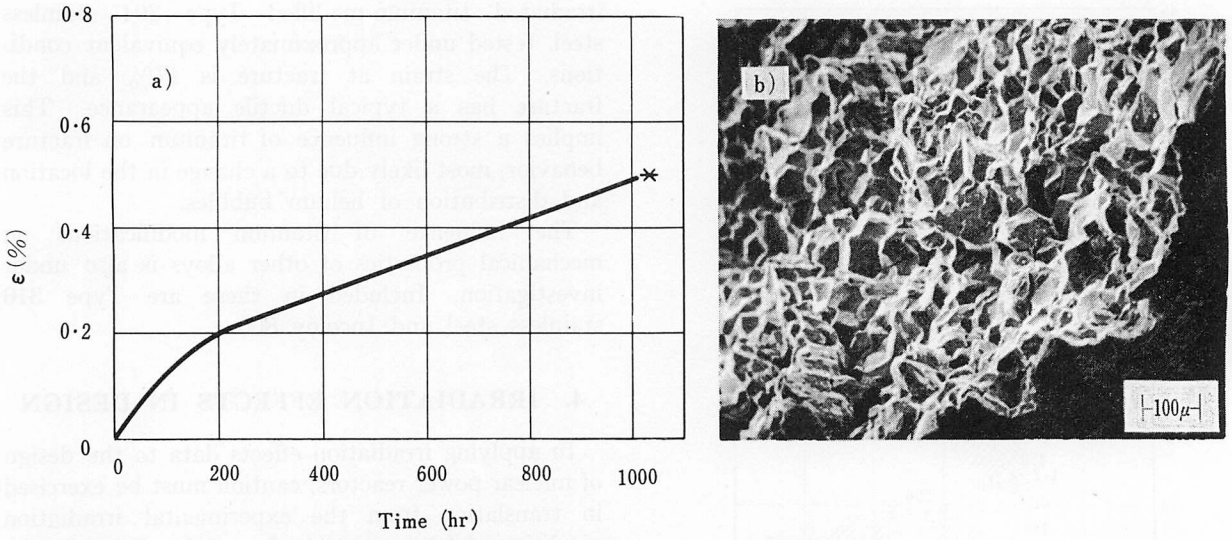

Standard alloy irradiated in EBR-II to $1{\cdot}5\times10^{22}$n/cm²(>0·1MeV) at 535°C, tested at 550°C and 24·6kg/mm².
a) Creep rupture curve. b) Scanning electron micrograph showing intergranular, brittle fracture.

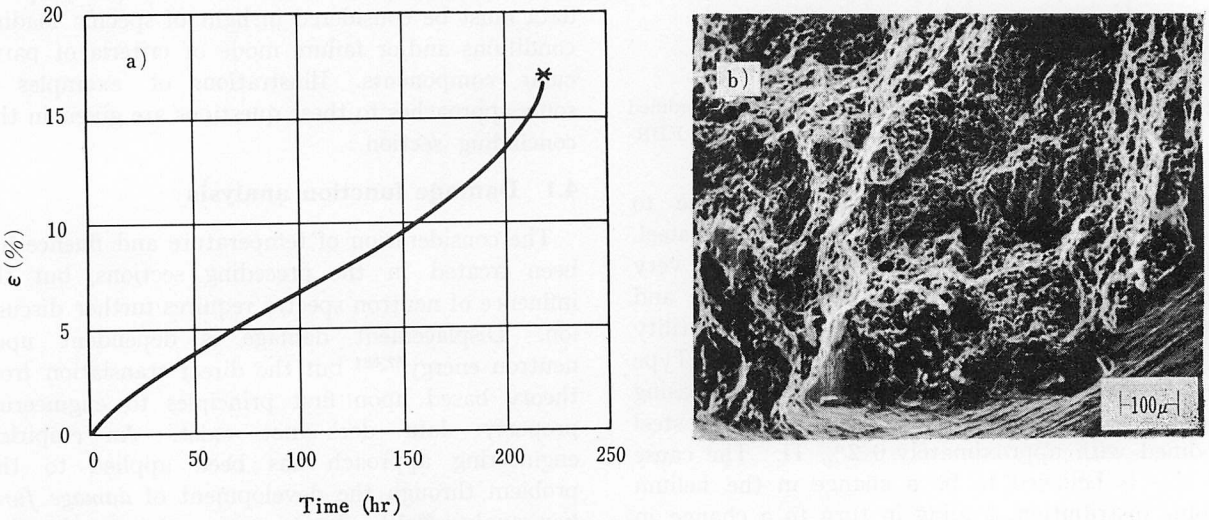

Titanium-modified alloy irradiated in EBR-II to $3{\cdot}0\times10^{22}$ n/cm² (>0·1MeV) at 590°C, tested at 600°C and 19·4kg/mm².
a) Creep-rupture curve. b) Scanning electron micrograph showing transgranular, ductile fracture.

Photo. 7. Creep curves and fractographs for irradiated standard Type 304 stainless steel and irradiated titanium-modified Type 304 stainless steel[66].

stainless steel in various locations in the Fast Test Reactor (FTR) is given in Fig. 25. Derived property change versus fluence curves such as these are being used to provide guidance in the analysis, correlation and application of irradiation effects data to reactor design.

4.2 Performance analysis and failure mode

Examples from the testing of irradiated stainless-steel tubing and the data analysis of fast-reactor fuel-pin performance serve to illustrate the need for detailed treatment of load and strain history in predicting the time and mode of failure.

Data for Type 316 stainless steel uniaxial creep-rupture specimens irradiated at 482°C to a fluence of $1{\cdot}2\times10^{22}$n/cm² and tested at 649°C result in total elongation values in the 10–20% range. By comparison, data for Type 316 stainless-steel tubing (5·3 mm diameter by 0·2 mm wall) irradiated under the same conditions and tested at 649°C in biaxial creep-rupture tests show changes in diameter values between 0·9 and 5·7%[53]. There is little doubt that pressurized biaxial testing is more representative of fuel-pin performance than is uniaxial testing; however, just how close it is in simulating performance accurately remains open to question. In one attempt to develop a test procedure more prototypical of fuel-pin performance, a ring ductility test was developed to measure the maximum circumferential ductility of small sections of tubing[72]. A cylindrical mandrel is inserted into a ring cut from irradiated tubing and deformed by compression, thereby imparting a circumferential strain to the ring. Diametral fracture strain is observed to be

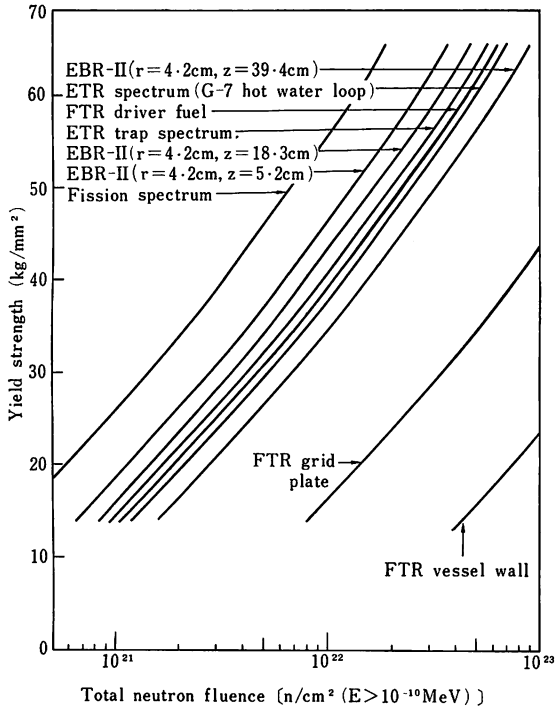

Fig. 25. Yield strength for Type 304 stainless steel versus total fluence for different spectra (test and irradiation temperature of ~450°C)[71].

much greater for the ring test than for pressure-type burst tests.

This behavior has been rationalized by Franklin[73]. As the mandrel presses against the ring, radial and tensile hoop stresses develop in the ring and, if a frictional force exists between the ring and mandrel, an additional compressive axial stress is generated. If a small portion of the ring becomes plastically unstable, local deformation occurs until the instability criterion is no longer satisfied, or until failure occurs. As the local instability propagates, the ring attempts to move relative to the mandrel. Since the friction force opposes this motion, some of the load is transferred from the deforming region to the mandrel and this process continues until the instability criterion is no longer met. Franklin concludes that under conditions where instability is precluded considerably more useful ductility may be available in irradiated materials than is indicated by elongation measurement. Reduction in area is suggested as a better measure of the ability of a material to deform locally, consistent with the observation that reduction in area values decrease much more slowly as a function of irradiation than elongation data[73]. Of course, if failure occurs by plastic instability the meaningful measure of ductility from a structural point of view is uniform elongation.

There are other factors as yet not completely understood that influence the deformation behavior of fuel cladding. Boltax, *et al*[74] have recently analyzed the measured diameter increase of a number of fuel pins in the USA fuel-irradiation program which exhibited pin diameter increases of up to 5·6% after a fluence on the cladding of about 8×10^{22}n/cm² (E>0·1Mev). Table 2 shows the results of an OLYMPUS-II computer code analysis for two of these fuel pins. This code was developed for the analysis and prediction of irradiation performance of fast-reactor mixed-oxide fuel pins. It can be seen that of the total calculated strain for pin F2V, 59·4% is ascribed to clad swelling, 34·7% to irradiation creep and only 5·9% to thermal strain. Pin F2G likewise shows large parts of the total strain related to clad swelling and irradiation creep. These two phenomena produce changes in diameter which do not strain the cladding in the same way as the thermal strain. Clad swelling arises from void formation in a fast flux and is accompanied by a decrease in density as already discussed. Geometrically, the non-conservative volumetric swelling causes the tube to expand outward. Irradiation creep occurs under the influence of a neutron flux at temperatures where thermal creep is low and decreases with increasing temperature[4,74]. Both of these irradiation effects provide relief mechanisms that permit accommodation of a greater amount of fuel swelling and/or fission gas pressure without thermally straining the cladding to the point of failure. Thus while the cladding may be able to withstand only 1–2% thermal strain before failure, several times that amount is available for deformation under the proper conditions of flux, temperature and load.

Another feature of cladding behavior that is important to fuel-pin performance is the cladding failure mode. The stress-rupture failure mode of stainless-steel tubing ranges from high-energy burst

Table 2. Summary of OLYMPUS-II analysis of two F2 fuel pins[74].

Pin no.	Clad composition	Measured total strain %ΔD/D	Calculated values %ΔD/D				Percent of total strain		
			Total strain	Clad swelling	Irradiation creep	Thermal strain	Clad swelling	Irradiation creep	Thermal strain
F2V	316	3·8	3·52	2·09	1·22	0·21	59·4	34·7	5·9
F2G	347	5·6	5·78	2·35	1·49	1·94*	40·6	25·8	33·6

* Includes start-of-life strain of 0·45 due to interaction of fuel and cladding at startup.

to pinhole leaking. Yaggee and Li[75] have analyzed a large body of biaxial creep to rupture data in terms of failure mode. They have reported that a rather sharp demarcation of stress (σ) and strain rate separates the burst and leak failure modes for stainless-steel tubing. A low (σ, $\dot{\varepsilon}$) failure occurs by leaking while at high (σ, $\dot{\varepsilon}$) a burst failure mode obtains. The latter is found to be in accord with plastic instability criteria and the former is observed to be due to grain-boundary sliding and cracking[75].

In light of these two observed failure mechanisms, if the logic expressed by Franklin obtains, mechanical instability will not develop in the cladding due to loading from fuel swelling; consequently, a leak type of failure mode would be expected due to grain-boundary sliding and cracking.

From a mechanical point of view, the benign pinhole or leak type failure mode is more desirable than high-energy burst. We note that the irradiation-induced embrittlement due to helium is manifest by grain-boundary cracking. Thus, while helium embrittlement reduces available thermal strain, the inherent enhanced grain-boundary cracking also would be expected to promote the more benign leaking failure mode in a fuel pin.

5. CONCLUSIONS

In this review we have illustrated the effects of neutron irradiation on the toughness and ductility of steels. The direct effects may be very severe and have large uncertainty, and may be limiting in terms of the design and operation of reactor components. Current and developing knowledge of irradiation damage provides a basis for the specification and control of the metallurgical structure and chemistry of steels that can ameliorate or reduce the magnitude of and the variance in neutron embrittlement. In the move toward improved ductility and toughness, increased understanding and appreciation of the details of the deformation and fracture behavior of irradiated steels and the continued development of the analytical tools to treat these phenomena will, in conjunction with an expanding body of physical data on irradiation effects, serve to reduce the uncertainty in design and lead toward more full utilization of actual material capability.

ACKNOWLEDGEMENTS

The authors wish to acknowledge that the material in this paper is based on the excellent and dedicated work of many people in several laboratories of the U.S. Atomic Energy Commission and its contractors as well as other organizations both in the United States and elsewhere.

We are especially grateful to the following for stimulating discussion during the preparation of this review: L.E. Steele and J.R. Hawthorne and their colleagues of the U.S. Naval Research Laboratory; J.J. Holmes, C.W. Hunter, and W.N. McElroy of Hanford Engineering Development Laboratory; C.Y. Li of Argonne National Laboratory; and E.E. Bloom of Oak Ridge National Laboratory.

The authors also wish to express their appreciation to the individuals who supplied the illustrations used in this paper.

Finally, we wish to express appreciation to the sponsors for the invitation to present this review and the support and encouragment of J.M. Simmons and our colleagues in the Fuels and Materials Branch in preparing it. Special thanks are due to Mrs. LaRue Weddle for manuscript typing.

REFERENCES

1) J.R. Beeler, Jr.: Radiation Damage in Reactor Materials, **2** (1969), p. 3–29
2) D.C. Doran: Radiation Effects, **2** (1970), p. 249–267
3) D.G. Doran and R.A. Burnett: Interatomic Potentials and Simulation of Lattice Defects, Plenum, New York, to be published
4) E.R. Gilbert and L.D. Blackburn: WHAN-FR-**30**, WADCO Corporation, (Oct. 1970). Also, Second International Conference on Strength of Metals and Alloys, Pacific Grove, Calif., (Aug. 30-Sept. 4, 1970)
5) E.A. Little and D.R. Harries: ASTM STP **457**, (1969), p. 215–241
6) F.A. Smidt and L.E. Steele: IAEA Working Group Meeting on Engineering Aspects of Irradiation Embrittlement of Reactor Pressure Vessels, Vienna, (May 1971)
7) R.S. Barns: Nature, **206** (1965), p. 1307
8) W.N. McElroy and H. Farrar: International Conference on Irradiation Produced Voids in Metals, Albany, New York, (June 1971)
9) E.P. Kleir, J.R. Hawthorne and L.E. Steele: NRL Report **6649**, (Dec. 1967), Also see Reference 18, Figure 54, p. 81
10) P.W. Flynn and T.A. Trozera: ASTM STP **457**, (1969), p. 180–214
11) J.J. Holmes, R.E. Robbins and A.J. Lovell: ASTM STP **457**, (1969), p. 371–389
12) Irradiation Effects in Structural Alloys for Thermal and Fast Reactors, ASTM STP **457**, (1969), Symposium: San Francisco, Calif. (June 1968)
13) The Effects of Radiation on Structural Metals, ASTM STP **426**, (1967), Symposium: Atlantic City, New Jersey, (June 26-July 1, 1966)
14) Radiation Damage in Reactor Materials, Proceedings of a Symposium (2 volumes) IAEA, Vienna, (1969)
15) Effects of Radiation on Structural Metals, ASTM STP **484**, (1971), Symposium: Niagara Falls, (June 29-July 1, 1970)
16) International Conference on Irradiation Produced Voids in Metals, Albany, New York, (June 1971)
17) R.H. Stern, Jr. and L.E. Steele: Nuclear Engineering and Design, **10** (1969), p. 259–307
18) L.E. Steele: Atomic Energy Review, **3** (1969), no. 2
19) T.T. Claudson, E.E. Sinclair, B.R.T. Frost, A. Boltax, H. Pearlman, C.N. Spalaris and J.R. Weir: Fourth Atoms for Peace Conference, Geneva, (Sept. 1971)
20) National Symposium on Developments in Irradiation Testing Technology, Sandusky, Ohio, (Sept. 1969), CONF–690910, U.S. Atomic Energy Commission (1969)
21) Federal Register, **36** (Feb. 1971), no. 35, p. 3259
22) ASME Boiler and Pressure Vessel Code, Nuclear Power Plant Components, Section III, NB–2300, (July 1971)
23) ASTM Standard E–208–66T, Part 31, (May 1969)
24) J.F. Loss, J.R. Hawthorne and C.Z. Serpan: Trans. ASME Journal of Basic Engineering, (1971), Preprint # 70-WA/Met-1
25) T.R. Mager and F.O. Thomas: HSST Technical

Report #5, WCAP-7328, Westinghouse Electric Corp., (Oct. 1969). Also, T.R. Mager: Radiation Damage in Reactor Materials, Proceedings of a Symposium (2 volumes), IAEA, Vienna, (1969)
26) W. Hunter, C.L. Hellerick and J.A. Williams: Heavy Section Steel Technology Program, Semiannual Progress Report, ORNL-**4512**, (Aug. 1969), p. 77-90
27) M.S. Wechsler, R.G. Berggren, N.E. Hinkle and W.J. Stelzman: Reference **12**, p. 242-260
28) C.W. Hunter and R. Williams: HSST Semiannual Progress Report, ORNL-**4653**, (Aug. 1970), p. 31-38
29) A.S. Tetelman and A.J. McEvily, Jr.: Fracture of Structural Materials, John Wiley and Sons, Inc., New York, (1967), p. 116
30) F.J. Loss, J.R. Hawthorne, C.Z. Serpan, Jr. and P.P. Puzak: NRL Report **7209**, (Sept. 1970). Also see reference 18, p. 68, Fig. 43
31) U. Potapovs and J.R. Hawthorne: Nuclear Applications, **6** (Jan. 1969), p. 27-46
32) L.E. Steele: Atomic Energy Review, **3** (1969), p. 50, Fig. 31
33) T.R. Mager: HSST Program Technical Report # 5, WCAP-**7561**, Westinghouse Electric Corp., (Aug. 1970)
34) E.T. Wessel: Symposium on Fracture Toughness Concepts for Weldable Structural Steels, UAEA, Culcheth-Risley, England, (April 1969)
35) F.J. Loss: NRL Report **7056**, (May 1970)
36) E.A. Lange: This Conference
37) W.S. Pellini: NRL Report **7251**, (March 1971)
38) J.R. Hawthorne: Nuclear Engineering and Design, **2** (1970), p. 427-446
39) Federal Register, **56** (July 1971), no. 129
40) J.R. Hawthorne, E. Fortner and S.P. Grant: Welding Journal Research Supplement, **35** (1970), p. 553-561
41) J.R. Hawthorne: NRL Report **7121**, (May 1970), ASTM STP **484**, (1971), To be published
42) A. Van Echo: Private Communication
43) A.S. Tetelman and A.J. McEvily, Jr.: Fracture of Structural Materials, John Wiley and Sons, Inc., New York, (1967), Section III
44) C.L. Hellerich and C.W. Hunter: BNWL-SA-**2298**, Battelle Northwest Lab., (Feb. 1969)
45) F.A. Smidt, Jr.: NRL Memo Report **2259**, QPR, (Feb. 1-April 30, 1971), p. 21-34
46) H.R. Brager, J.L. Straalsund, J.J. Holmes and J.F. Bates: WHAN-FR-**16**, WADCO Corp., (Dec. 1970)
47) E.E. Bloom: International Conference on Irradiation Produced Voids in Metals, Albany, New York, (June 1971)
48) J.J. Holmes and J.L. Straalsund: Trans. ANS, **13** (1970), p. 559
49) S.D. Harkness and C.Y. Li: International Conference on Irradiation Produced Voids in Metals, Albany, New York, (June 1971)
50) R. Bullough and R.C. Perrin: International Conference on Irradiation Produced Voids in Metals, Albany, New York, (June 1971)
51) H.R. Brager and J.L. Straalsund: The Microstructure of Fast Reactor Irradiated Type 316 Stainless Steel, presented at AIME-IMS Spring Meeting, (May 1971), to be published
52) A.L. Ward and J.J Holmes: HEDL-SA-**198**, WADCO Corp., (June 1971)
53) A.J. Lovell and R.W. Barker: ASTM STP **484**, (1971)
54) W.R. Martin and J.R. Weir: Nature, **202** (1964), p. 997.
55) D.R. Harries: J. Brit. Nucl. Energy Soc., **5** (1966). p. 74
56) W.R. Martin and J.R. Weir: ASTM STP **426**, (1967), p. 440
57) E.E. Bloom and J.R. Weir: ASTM STP **457**, (1969), p. 261
58) J. Moteff: National Symposium on Developments in Irradiation Testing Technology, Sandusky, Ohio, (Sept. 1969), p. 3
59) H.R. Brager and R.E. Robbins: Trans. AIME, **242** (1968), p. 2010
60) J. Weitman, N. Daverhog and S. Farvolden: Trans. ANS, **13** (1970), p. 557
61) D. Kramer: Atomics International Quarterly Technical Progress Report **12993**, (April 30, 1971), p. 49
62) K.R. Garr, D. Kramer and C.C. Rhodes: Atomics International Report **12932**, (April 15, 1970)
63) E.E. Bloom: Oak Ridge National Laboratory TM-**2130**, (March 1968)
64) M. Kangilaski, J.S. Perrin and R.A. Wullaert: ASTM STP **457**, (1969), p. 67
65) M. Kangilaski and A.A. Bauer: Trans. ANS, **14** (1971), p. 168
66) E.E. Bloom and J.R. Weir: Unpublished data, courtesy of Oak Ridge National Laboratory
67) D.G. Doran: HEDL-TME-**71-42**, WADCO Corp., (April 1971)
68) G.E. Russcher: BNWL-**1093**, Battelle Northwest Lab., (Sept. 1969)
69) W.N. McElroy, R.E. Dahl, Jr. and C.Z. Serpan, Jr.: Nucl. Appl. Technol., **7** (1969), p. 561
70) C.Z. Serpan, Jr. and W.N. McElroy: Radiation Damage in Reactor Materials, Proceedings of a Symposium (2 volumes), IAEA, Vienna, (1969), p. 33
71) W.N. McElroy, R.L. Simons and L.D. Blackburn: Trans. Am. Nucl. Soc., **13** (1970), p. 144
72) H. Busboom, W. Kimball, A. Withop and F. Comprelli: Trans. ANS, **2** (1968), p. 483
73) D.G. Franklin: The Ductility of Irradiated Type 304 Stainless Steel and Its Applications to Fuel-Element Design, to be published in Journal of Nuclear Materials
74) A. Boltax, A. Biancheria, B.L. Harbourne and T.P. Soffa: Mixed Oxide Fuel Pin Performance Analysis Using the OLYMPUS Computer Code, presented at ANS Conference on Fast Reactor Fuel Element Technology, (April 1971), to be published
75) F.L. Yaggee and C.Y. Li: ANL **1317**, Argonne National Laboratory, (Feb. 1971)
76) C.W. Hunter and J.A. Williams: Nuclear Engineering and Design, **17** (1971), p. 131

Ductility Improvements in Superalloys

R.G. Dunn D.L. Sponseller J.M. Dahl

Climax Molybdenum Company

ABSTRACT

Some recent developments concerning ductility improvements in superalloys are discussed. Particular emphasis is placed upon ductility or workability improvements that are achieved without sacrificing elevated-temperature strength properties. Because of the economic and technological impact that the aircraft gas turbine exerts on the superalloy industry, the ductility improvements are specifically directed toward aircraft engine applications. Two of the developments involve hafnium alloying and directional-solidification effects on cast-superalloy ductility properties. The two remaining developments relate to ductility and workability improvements in wrought superalloys and involve a discussion of thermomechanically processed and powder-metallurgy components.

1. INTRODUCTION

Compositions of some of the more important superalloys in current use are presented in Table 1. These alloys are utilized on the basis of their superior strength properties and their environmental resistance in the 600 to 1200°C temperature range. Most alloys contain chromium for high-temperature environmental resistance and one or more of the following elements for strengthening effects: molybdenum, tungsten, niobium, tantalum, titanium, aluminum and carbon. Precipitation of intermetallic compounds, dispersed carbides and solid-solution strengthening are utilized to promote enhanced elevated-temperature properties.

The history of superalloys dates back a scant four decades. They were originally developed for reciprocating engine turbosuperchargers. Today they have assumed an essential role in many of our advanced transportation and power technology systems. For example, superalloys are used in aircraft, marine, industrial, and vehicular gas turbines, space vehicles, steam-power generating equipment, and metalworking tools. An indication of the relative importance that superalloys hold in today's materials technology can be gained from the fact that the estimated annual worldwide sale of superalloy products is approaching $1 000 000 000.

The emergence of the gas turbine as the preeminent prime mover for flight propulsion has been the principal stimulus for advancements in superalloy technology. Aircraft gas turbines presently account for an estimated 60 to 70% of superalloy consumption.

For the future, the industrial, marine and vehicular turbine markets are expected to undergo a period of rapid growth and will account for an increasing share of future superalloy production. In spite of a diminished market participation, however, the aircraft gas-turbine industry is expected to maintain a leadership position in superalloy technology.

It is the objective of this paper to discuss four recent developments involving ductility improvements in superalloys. Two of the developments involve hafnium alloying and directional solidification effects on cast-superalloy ductility properties. The other two developments relate to ductility improvements in wrought superalloys obtained by thermomechanical processing and powder-metallurgy techniques. All of these developments originated with aircraft gas turbines and were stimulated by the design requirements for advanced commercial and military engines. In an effort to provide a better understanding of these ductility developments, they are discussed in terms of recent design trends and performance characteristics of specific aircraft engine components; namely, cast superalloy turbine airfoils and wrought superalloy discs. Although all the developments discussed originated with and at present principally relate to the aircraft gas turbine, it does not mean that they will be restricted to aircraft engine applications. In fact, several of the developments are being seriously considered for other superalloy markets.

2. ENGINE TRENDS AND COMPONENT REQUIREMENTS

2.1 Aircraft gas-turbine design trends

Doll[1] has reviewed salient aircraft gas-turbine design trends and related them to future superalloy needs. The design trend for both subsonic and supersonic aircraft has been away from turbojet and toward turbofan engines. Higher bypass ratios (ratio of fan air that bypasses the turbine to that which goes through the turbine) are being used in

Table 1. Nominal compositions of representative superalloys (%).

Alloy Designation	C	Cr	Ni	Co	Mo	W	Nb	Fe	Ti	Al	B	Zr	Other
						Cast alloys							
Alloy 713LC	0·05	12·0	Bal.	—	4·5	—	2·0	—	0·6	5·9	0·01	0·10	
B-1900	0·10	8·0	Bal.	10·0	6·0	—	—	—	1·0	6·0	0·015	0·08	4·3 Ta
GMR-235D	0·15	15·5	Bal.	—	5·0	—	—	4·5	2·5	3·5	0·05	—	
Haynes Stellite Alloy No. 21	0·25	27·0	3·0	Bal.	5·0	—	—	1·0	—	—	—	—	
IN-100	0·15	10·0	Bal.	15·0	3·0	—	—	—	4·7	5·5	0·015	0·06	1·0 V
IN-738	0·17	16·0	Bal.	8·5	1·8	2·6	0·9	—	3·4	3·4	0·01	0·10	1·8 Ta
MAR-M 200	0·15	9·0	Bal.	10·0	—	12·5	1·0	—	2·0	5·0	0·015	0·05	
MAR-M 246	0·15	9·0	Bal.	10·0	2·5	10·0	—	—	1·5	5·5	0·015	0·05	1·5 Ta
MAR-M 509	0·60	24·0	10·0	Bal.	—	7·0	—	—	0·2	—	—	0·5	3·5 Ta
M 22	0·13	5·7	Bal.	—	2·0	11·0	—	—	6·3	—	—	0·6	3·0 Ta
NX-188	0·04	—	Bal.	—	18·0	—	—	—	—	8·0	—	—	
TRW-NASA VI A	0·13	6·1	Bal.	7·5	2·0	5·5	0·5	—	1·0	5·4	0·02	0·13	9·0 Ta 0·3 Rh 0·43 Hf
WI-52	0·45	21·0	—	Bal.	—	11·0	2·0	2·0	—	—	--	—	
X-40	0·50	25·5	10·5	Bal.	—	7·5	—	2·0	—	—	0·01	—	
						Wrought alloys							
A-286	0·05	15·0	26·0	—	1·25	—	—	Bal.	2·2	0·2	0·003	—	0·3 V
Hastelloy X	0·10	22·0	Bal.	1·5	9·0	0·6	—	18·5	—	—	—	—	
Haynes Alloy 188	0·10	22·0	22·0	Bal.	—	14·0	—	1·5	—	—	—	—	0·08 La
Incoloy Alloy 901	0·05	13·5	42·7	—	6·2	—	—	Bal.	2·5	0·3	—	—	
Inconel Alloy 600	0·08	15·5	Bal.	—	—	—	—	8·0	—	—	—	—	
Inconel Alloy 625	0·05	21·5	Bal.	—	9·0	—	—	2·5	0·2	0·2	—	—	
Inconel Alloy 718	0·04	19·0	Bal.	—	3·1	—	5·1	18·5	0·9	0·5	—	—	
L-605	0·10	20·0	10·0	Bal.	—	15·0	—	—	—	—	—	—	
N-155	0·15	21·0	20·0	20·0	3·0	2·5	1·0	Bal.	—	—	—	—	0·15 N
Nimonic 80A	0·06	19·5	Bal.	1·1	—	—	—	—	2·5	1·3	—	—	
Nimonic 90	0·07	19·5	Bal.	18·0	—	—	—	—	2·4	1·4	—	—	
Nimonic 105	0·20	14·6	Bal.	20·0	5·0	—	—	2·0	1·2	4·7	—	—	
Nimonic 115	0·15	15·0	Bal.	15·0	3·5	—	—	—	4·0	5·0	—	—	
Rene 41	0·09	19·0	Bal.	11·0	10·0	—	—	—	3·1	1·5	0·01	—	
Rene 95	0·15	14·0	Bal.	8·0	3·5	3·5	3·5	—	2·5	3·5	0·01	0·05	
S-816	0·38	20·0	20·0	Bal.	4·0	4·0	4·0	4·0	—	—	—	—	
Udimet 500	0·08	19·0	Bal.	18·0	4·0	—	—	—	2·9	2·9	0·005	—	
Udimet 700	0·15	15·0	Bal.	18·5	5·2	—	—	—	3·5	4·3	0·030	—	
Waspaloy	0·08	19·5	Bal.	13·5	4·3	—	—	—	3·0	1·3	0·006	0·06	

advanced subsonic transport engines. Efforts to reduce specific fuel consumption and improve the thrust-to-weight ratio favor higher engine operating temperatures. A schematic comparison of gas and metal temperatures for a typical advanced supersonic engine is presented in Fig. 1. As a result of these design trends, the proportion of superalloys used in aircraft gas-turbine engines has been increasing and is expected to continue to do so (Fig. 2). Superalloys account for approximately 40% of the weight of a current subsonic commercial transport engine depicted in Photo. 1. Superalloys are used in the latter stages of the high-pressure compressor and in the combustor and turbine sections.

2.2 Turbine airfoil requirements

Because performance and efficiency of the engines are intimately related to gas temperatures, there has been a continuing trend to higher turbine-inlet temperatures (Fig. 3). Generally speaking, first-stage turbine airfoils (i.e., blades and vanes) have

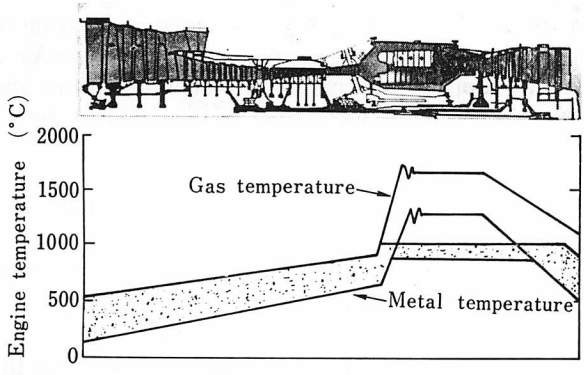

Fig. 1. Advanced supersonic engine operating temperatures.

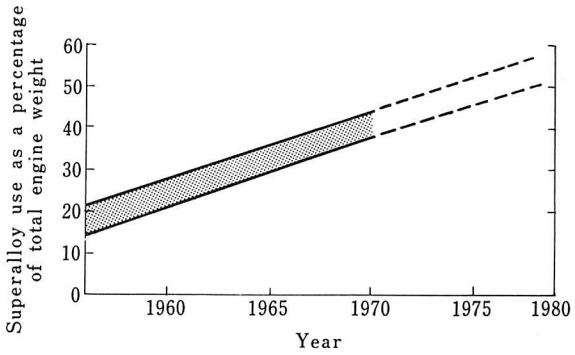

Fig. 2. Superalloy use in aircraft turbine engines.

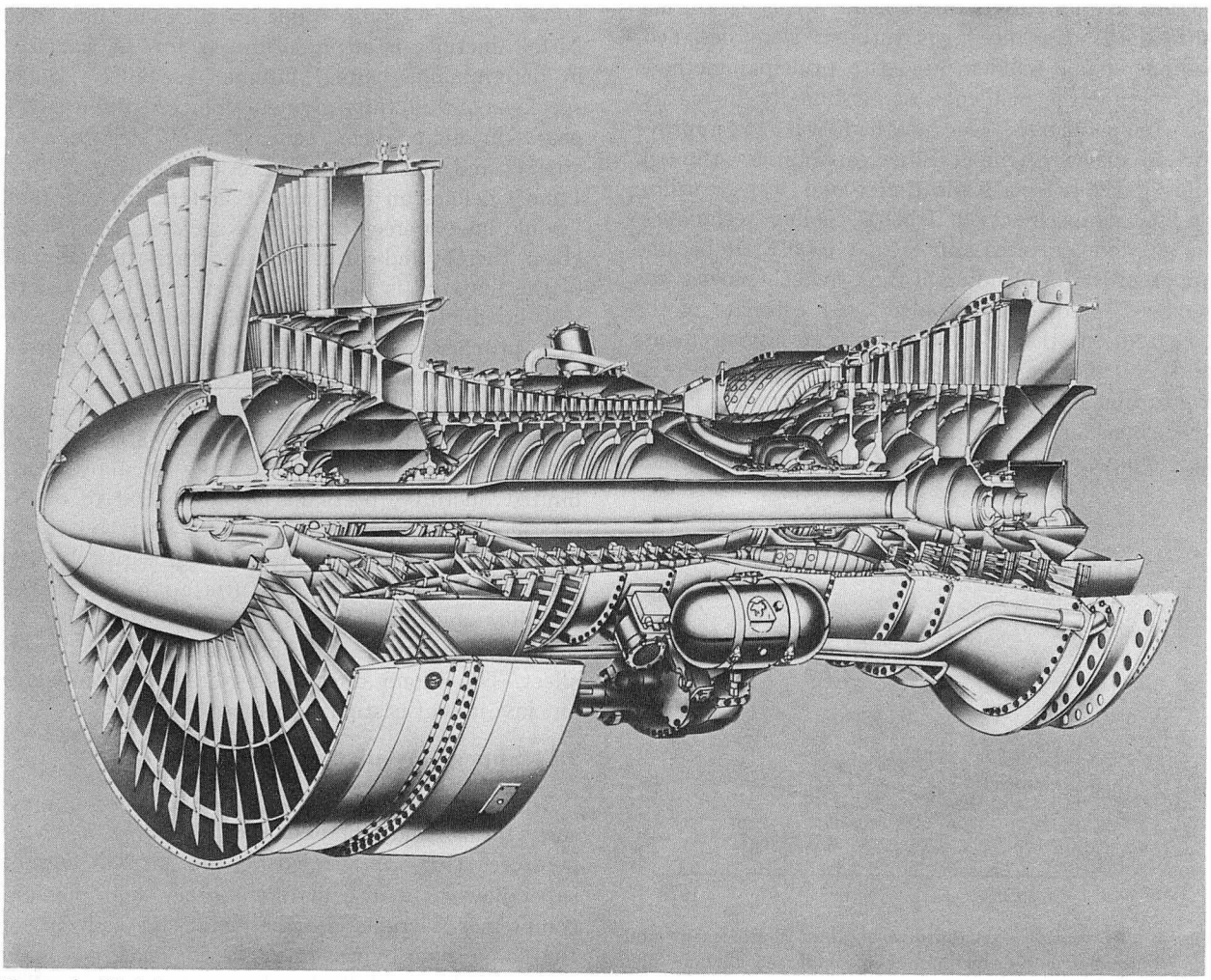

Photo. 1. High-bypass commercial aircraft gas-turbine engine.

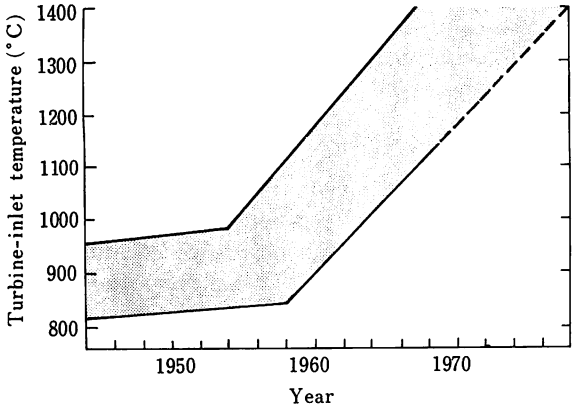

Fig. 3. Turbine-inlet temperature progression.

been the pacing items for engine advancements. Turbine airfoils receive the full potential of the hot gases from the combustor and have the task of converting thermal energy into mechanical work to drive the compressors. Successful turbine airfoil materials require a balanced interrelation of the following properties: strength, ductility, and oxidation, corrosion and erosion resistance.

In the early days of engine development when turbine-inlet temperatures were relatively low, engine manufacturers used solid wrought turbine airfoils. As advanced gas turbines were designed, various engine builders used two principal methods of meeting the challenge of continually increasing gas temperatures. One method was to improve airfoil elevated-temperature capabilities through alloy development, while the second was to utilize design advancements and blade cooling techniques. As gas temperatures approached 1000°C, it became apparent that a blending of the two technologies was required to solve the problem. An estimate of the contributions that alloy development advancements and each of three cooling techniques make to increasing turbine inlet temperatures[2] is presented in Fig. 4.

Turbine airfoil alloy advancements were realized through increased utilization of precipitation, carbide

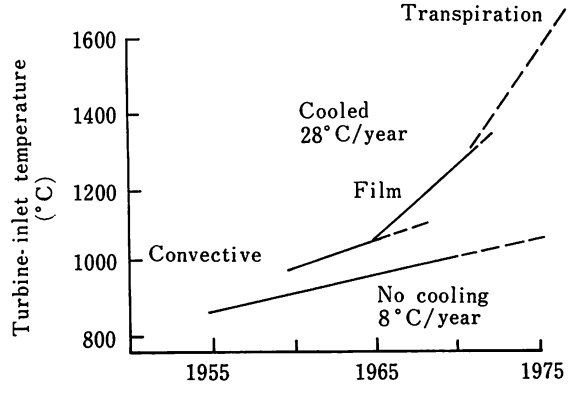

Fig. 4. Respective contributions of alloy development and blade-cooling techniques to increased turbine-inlet temperature capability.

forming, and solid-solution strengthening elements. In general, the alloying necessary to achieve improved elevated-temperature strength continuously lowered the melting temperature and raised the solvus temperature of the strengthening precipitate phase. Increases in strength obtained by compositional variation were achieved only with a loss in workability and ductility. Since it was recognized that high-temperature strength was generally incompatible with workability, it became apparent that further development of airfoil materials could only occur with the use of cast alloys. Moreover, many of the alloying elements used in advanced superalloy compositions are very reactive. As a result, emphasis was placed on vacuum-melting and investment-casting techniques in the development of new airfoil materials.

In developing advanced turbine-airfoil materials, there has been a continuing emphasis for more strength at higher temperatures. The service lives of many blades are limited by creep (or lengthening) under the combined effects of thermal and mechanical stresses. For stationary parts, the deflection or bow of an airfoil usually defines the life of a component. Creep property improvements in airfoil superalloy materials have been achieved, however, at a considerable sacrifice in ductility. Airfoil ductility is an important factor, particularly in determining thermal fatigue resistance. Doll[1] speaks about ductility giving a component "forgiveness" in that there can be a redistribution of stresses and plastic deformation rather than failure. Lund[3] defines an ideal airfoil material as one that "would have a creep curve showing good third stage creep, thereby indicating that the strength potential of the material is being consumed and that failure will be ductile and predictable, but would have little primary creep and a low minimum creep so as to extend the time to one percent creep."

As mentioned previously, the continued quest for airfoil materials with improved strength at temperature has produced a series of alloys with limited ductility, particularly in the 600 to 800°C intermediate-temperature range. Two relatively recent developments, however, appear to have reversed this trend to the utilization of limited ductility superalloys. One involves the use of hafnium to improve ductility through an alloying effect. The second, directional solidification, involves an investment-casting advancement.

2.3 Superalloy-disc requirements

The continuing trend to higher compressor pressure ratios and increased compressor-exit temperatures (Fig. 5) has led to the introduction of superalloys as a disc material in the high-pressure compressor section. Furthermore, the advent of the large high-bypass-ratio engine has not only increased the size but also the number of superalloy

turbine discs. In a typical high-bypass-ratio commercial transport gas turbine, superalloy discs can account for 10 to 15% of the engine weight.

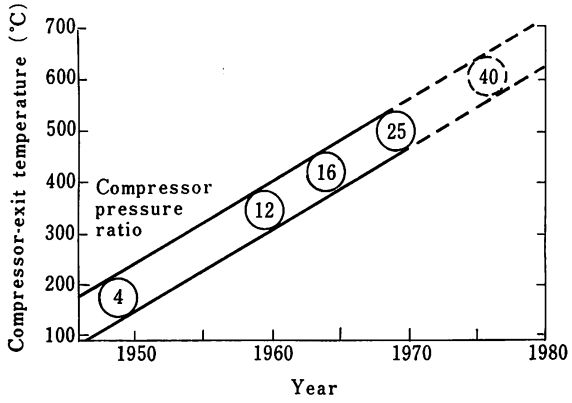

Fig. 5. Compressor-exit temperature progression.

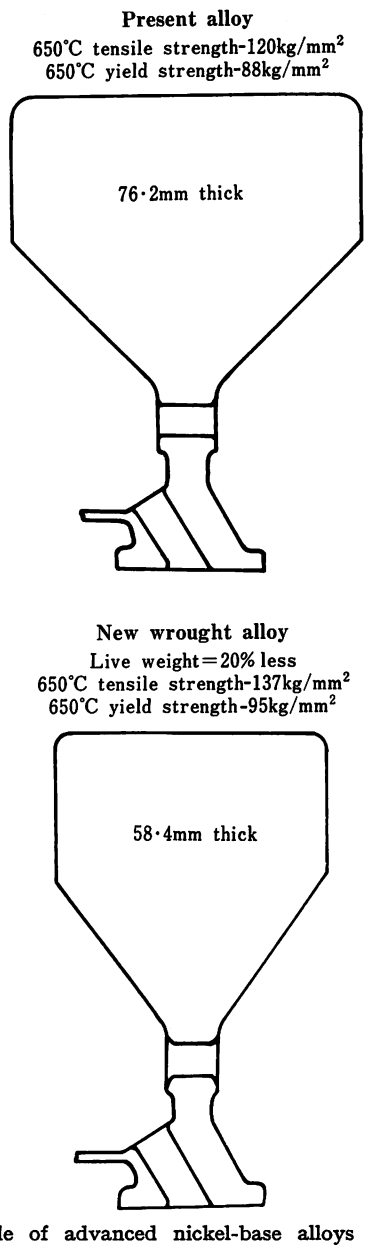

Fig. 6. Role of advanced nickel-base alloys in size and weight reduction of disc components.

Consequently, the superalloy disc is an important problem area in gas turbine technology.

Superalloy discs generally are creep- and low-cycle-fatigue-limited applications of materials which still must have sufficient yield strength and burst margins to be usable[4]. For advanced engines, a minimum service life objective of 50 000 hr has been proposed[1]. Consequently, future alloy and process development must concentrate on new superalloy discs with improved yield, ultimate, low-cycle-fatigue, and creep strengths. Bradley and Donachie[5] have indicated the substantial savings to be expected from the development and application of advanced superalloy discs (Fig. 6). In addition to engine weight savings, a reduction in physical size is very important, for there is virtually no room for the thicker discs required for future advanced engines if they are to be fabricated from present day materials. Because finish-machined superalloy discs can weigh as little as 10 to 20% of the weight of a rough forging, material and machining costs are also important. Thus, it is desirable to have sufficient material ductility whereby inherently high-strength superalloys can be fabricated into intricate shapes. Recent developments in thermomechanical processing and superalloy powder technology indicate that significant progress is being made toward achieving these objectives.

3. HAFNIUM IN SUPERALLOYS

Cochardt[6] was probably one of the first to report the use of hafnium as an alloying element in airfoil materials. He described the use of up to 1·5% Hf in a series of wrought nickel-chromium-iron and cobalt-nickel-chromium-base alloys that were notch ductile and had good rupture ductility in the 650 to 870°C temperature range. Data were presented whereby the presence of 0·5% Hf not only improved the rupture ductility but also increased the rupture life.

Cochardt believed that the beneficial effect of hafnium was due in part to the fact that hafnium compounds have an extremely high free energy of formation. He postulated that the presence of hafnium precluded the formation of grain-boundary films of deleterious compounds (i.e., oxides, sulfides, nitrides, etc.). It was proposed that the hafnium compounds formed were not harmful to the alloy since they tend to assume a generally spherical form and are found dispersed throughout the grains rather than being concentrated along grain boundaries. Cochardt, however, presented no data to support his hypothesis. Although the idea may have some merit, as is discussed in subsequent sections of this report, it is believed that this is not the principal reason whereby hafnium improves the ductility properties of superalloys.

At the time of the disclosure (i.e., 1961), little or no commercial advantage was taken of Cochardt's discovery. This could have been due in part to the fact that low rupture ductility was not a serious problem with the wrought airfoil superalloy in use at that time.

More recently Collins[7] studied the effect of hafnium along with 13 other alloying elements in the development of the investment-cast turbine airfoil alloy TRW-NASA VI A. Latin square and fractional-factorial statistical designs were used to formulate the alloy compositions. It was concluded that hafnium was one of a group of six elements "most influential in improving stress rupture life. In general, the elements and levels which increased the life also increased tensile strength, but they normally decreased ductility and workability."

About the same time, Lund, Hockin and Woulds[8] were studying the effects of refractory alloy elements on nickel-base investment-cast turbine airfoil materials. They found that hafnium had a beneficial effect on the strength and ductility properties of many cast superalloys including B-1900, Alloy 713LC, Alloy 713C, MAR-M 200, MAR-M 246, IN-100 and Udimet 700.

At present, hafnium-modified B-1900, hereafter referred to as B-1900-Hf (also known as MM-007), is probably the most important commercial application of hafnium in superalloys. For the future, however, hafnium-modified Alloy 713LC, hereafter referred to as Alloy 713LC-Hf (also known as MM-004), may prove to be the most important application. Consequently, the remainder of the subject discussion on the hafnium effect will be restricted to modifications of B-1900 and Alloy 713LC.

3.1 Hafnium effects on strength and ductility

The B-1900 alloy is an investment-cast nickel-base material that is commonly specified for first-stage turbine blades in commercial transport aircraft engines. One of the characteristics of this alloy is that it exhibits erratic creep ductility at intermediate temperatures (e.g., 760°C). This is particularly true for tests performed on specimens machined from actual turbine components. As shown in Table 2[9], the typical properties determined on cast-to-size specimens are generally better than those determined on specimens machined from blades. In contrast, the presence of 1·3% Hf in B-1900 (B-1900-Hf) markedly improves the mechanical properties of specimens machined from blades. As shown in Table 2, the B-1900-Hf alloy has better strength and ductility properties, both at room and elevated temperatures[10], than B-1900.

An analysis of a number of 760°C-66·1 kg/mm² creep tests performed on B-1900 revealed the prior-creep data had a skewed distribution[9] (Fig. 7). Further analysis of the creep data revealed the skewed distribution was a composite of two populations representing the specimens that had respectively failed in second- and third-stage creep. Moreover, the prevalence of second-stage creep failures was considerably greater in heats made from revert materials. A similar analysis of B-1900-Hf creep data revealed no second-stage creep failures

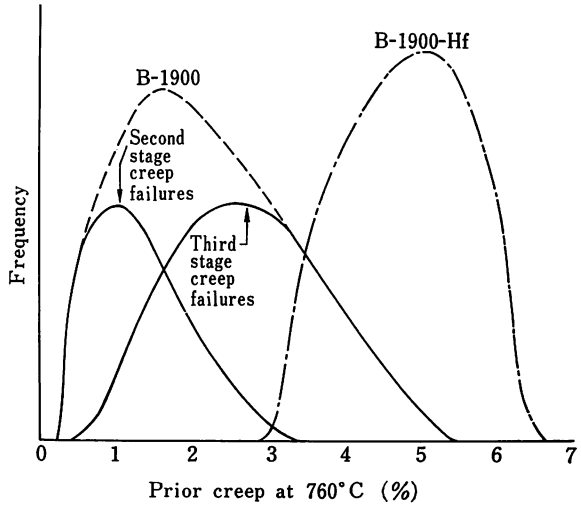

Fig. 7. Frequency analysis of B-1900 and B-1900-Hf creep-rupture failures.

Table 2. Typical mechanical properties for B-1900 and B-1900-Hf.

	B-1900		B-1900-Hf
	6·4 mm dia cast to size	4·5 mm dia from turbine blade	4·5 mm dia from turbine blade
Room temperature			
Ultimate tensile strength (kg/mm²)	94·9	80·9	89·2
0·2% yield strength (kg/mm²)	75·9	74·1	76·0
Elongation (%)	7·0	5·5	8·9
Creep rupture at 760 °C and 66·1kg/mm²			
Life (hr)	75·0	19·0	86·0
Prior creep (%)	2·5	1·6	4·8
Stress rupture at 980 °C and 20·4kg/mm²			
Life (hr)	35·0	30·0	43·0
Elongation (%)	7·0	5·0	7·0

and what appeared to be a somewhat more normal distribution of third-stage creep failures having a larger mean creep value than B-1900 with no significant difference between virgin and revert heats. The presence of hafnium, at least in short-term testing, has little or no effect on the primary- and secondary-creep rates of B-1900 (at 760°C), but merely extends the point of failure well into the third-stage creep range, thereby increasing the creep ductility and life.

Alloy 713LC is important because it is probably the most popular nickel-base alloy used for turbine airfoil castings. The cast integrally bladed turbine disc for small gas-turbine engines is a significant application for Alloy 713LC. The design of an integral wheel may be limited by any of the following modes of failure: burst, creep, low-cycle-fatigue, or thermal fatigue. Thus, for such an application, both room- and intermediate-temperature strength and ductility properties are important. Tensile and rupture properties determined on specimens machined from wheels[10] are presented for standard and hafnium-modified (1·3% Hf) Alloy 713LC (i.e., Alloy 713LC-Hf) in Table 3. As shown, the presence of hafnium markedly increases the room-temperature ultimate strength and elongation. It has a somewhat less pronounced effect on the 760°C rupture life and ductility.

3.2 Effect of hafnium on fracture toughness

Hockin[11] evaluated the effect of hafnium on the plane strain fracture toughness of several investment-cast nickel-base superalloys. Using standard ASTM procedures, it became apparent that specimens in excess of 25-mm thick should be used to determine the valid true fracture toughness. Such section thicknesses would not, however, be representative of air-cooled turbine components because of the effect that section size variations have on cooling rate, microstructure, and resultant mechanical properties. Consequently, a mathematical method based on thinner section data was used to determine true fracture toughness (i.e., K_{IC}). Such an evaluation indicated that respective K_{IC} values for B-1900 and B-1900-Hf are 117·3 kg/mm^2 $\sqrt{\text{mm}}$ and 139·6 kg/mm^2 $\sqrt{\text{mm}}$. Hockin concluded that the use of hafnium in cast nickel-base alloys can significantly improve the fracture toughness.

3.3 Effect of hafnium on physical metallurgy

Light micrographs and replica electron micrographs are presented for B-1900 in the as-cast plus heat-treated (1080°C×4 hr; 900°C×10 hr) condition in Photo. 2 and 3. The heat treatment is intended to simulate a coating cycle. The microstructure principally consists of a script type or elongated carbide network and γ' in a γ matrix. The results of metallographic examinations and X-ray analyses of bulk extractions revealed the script network principally consists of MC type carbides (a_0= 4·37Å)[12]. There was some evidence of blocky M_6C type carbides in heat-treated specimens but none in as-cast samples. From the appearance of the MC carbides, it would seem that the M_6C carbides formed from residual matrix carbon rather than a decomposition of the MC carbides. There was also some evidence of M_3B_2 type borides.

The microstructure of the B-1900-Hf alloy in the as-cast plus heat-treated condition is presented in Photo. 4 and 5. As shown, the presence of hafnium changes the morphology and distribution of the carbide network. Moreover, there are some differences in γ' morphologies. Hafnium appears to promote the formation of eutectic γ/γ'. The results of X-ray analyses of bulk extractions indicate that MC carbides having at least three different lattice parameters (a_0=4·38–4·60Å) are present[12]. There are indications of M_3B_2 borides, but no evidence of M_6C carbides either before or after heat treatment.

A comparison of micrographs from Alloy 713LC and Alloy 713LC-Hf indicates that hafnium similarly affects the morphology and distribution of carbides and γ' microconstituents (Photo. 6 to 9). Results of X-ray analyses[13] on bulk extractions indicate the presence of three MC carbides (a_0=4·45–4·54Å).

The microstructures of the B-1900 and B-1900-Hf samples were analyzed with a microprobe. The

Table 3. Mechanical properties of Alloy 713LC and Alloy 713LC-Hf (specimens machined from cast wheels).

	Alloy 713LC		Alloy 713LC-Hf	
	Rim	Hub	Rim	Hub
Room temperature				
Ultimate tensile strength (kg/mm^2)	77·3	70·4	93·8	91·8
0·2% yield strength (kg/mm^2)	71·2	67·8	70·2	69·8
Elongation (%)	6·3	3·9	14·8	12·5
Creep rupture at 760 °C and 59·8 kg/mm^2				
Life (hr)	35·7	23·6	58·2	63·4
Prior creep (%)	2·1	1·3	3·0	3·4
Creep rupture at 925 °C and 16·2 kg/mm^2				
Life (hr)	38·4	35·7	30·3	33·5
Prior creep (%)	6·8	9·1	12·0	11·2

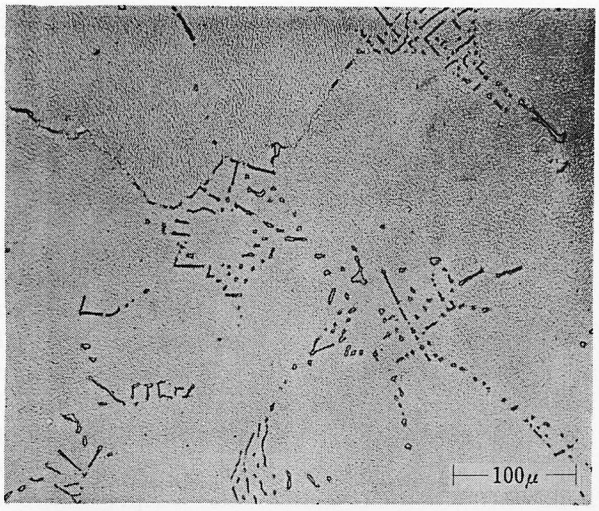

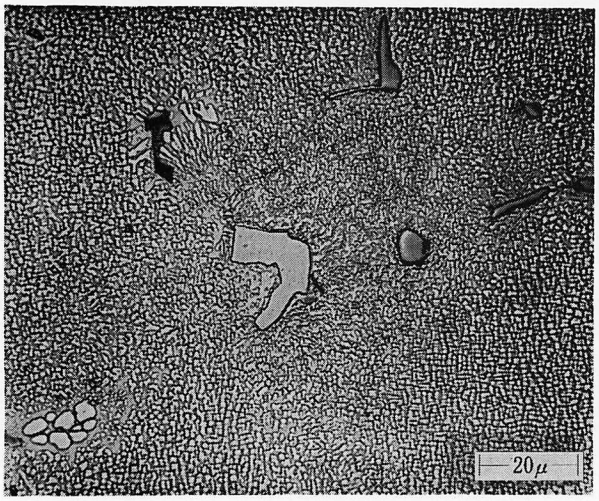

Photo. 2. Microstructure of B–1900.

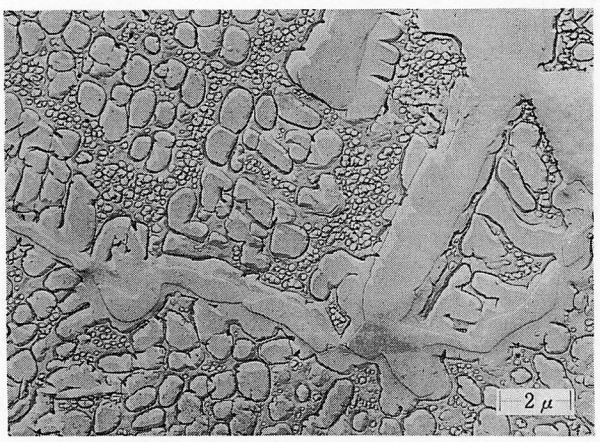

Photo. 3. Microstructure of B–1900.

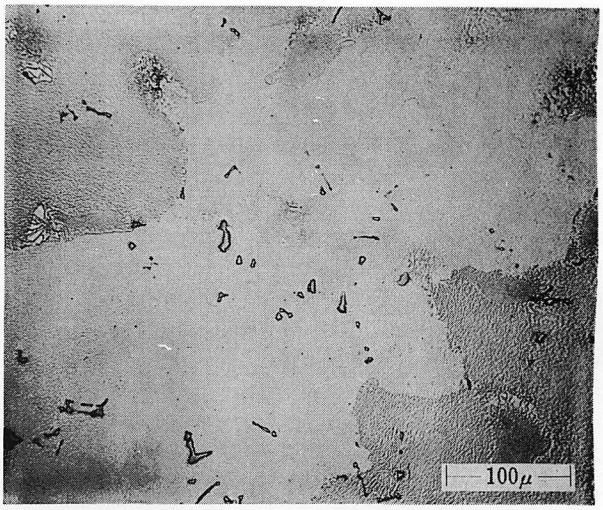

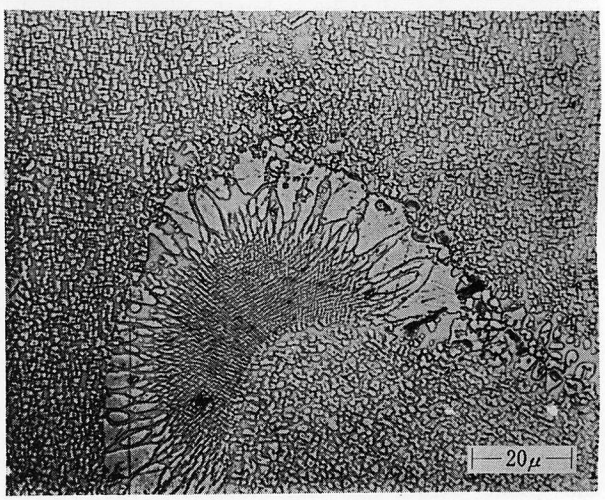

Photo. 4. Microstructure of B–1900–Hf.

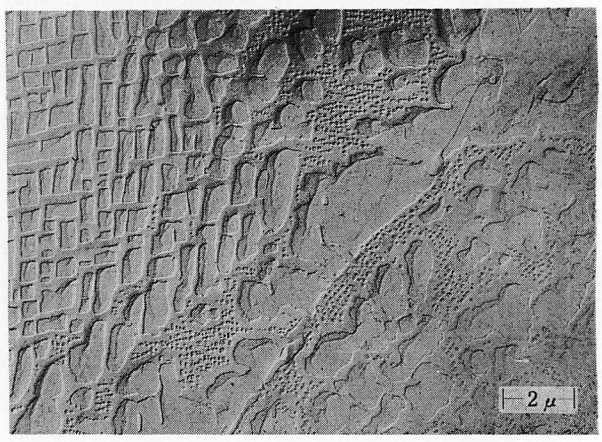

Photo. 5. Microstructure of B–1900-Hf.

analysis of two different carbides in B-1900 is presented in Photo. 10. The X-ray images indicate a high concentration of titanium and tantalum in the small circular carbide (MC) and a high molybdenum concentration in the semicircular carbide (M_6C). Chromium is absent from the MC and only slightly concentrated (i.e., above the matrix) in the M_6C. A line scan of the same microstructure is presented in Fig. 8.

Data on a typical carbide area in B-1900-Hf are presented in Photo. 11 and Fig. 9. The MC carbide has a high concentration of tantalum and hafnium, less titanium than the carbide in the hafnium-free alloy, very little molybdenum and almost no chromium. An examination of the line scan reveals a concentration envelope at the outer perimeter of the carbide. The outer perimeter has a higher hafnium and a lower molybdenum content. There

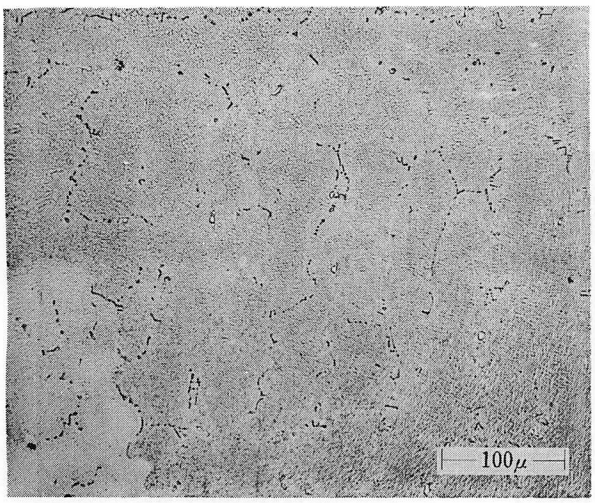

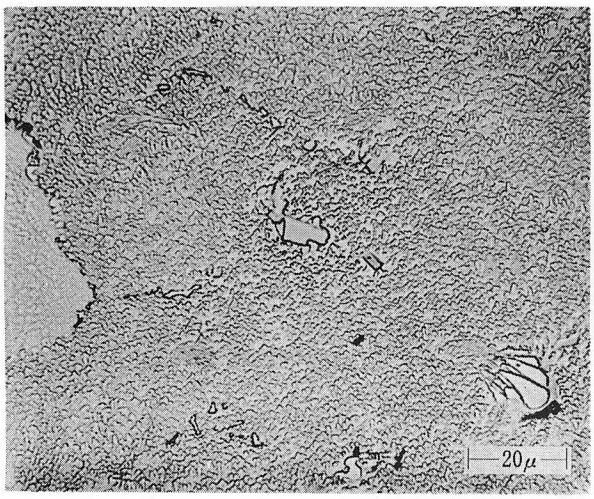

Photo. 6. Microstructure of Alloy 713LC.

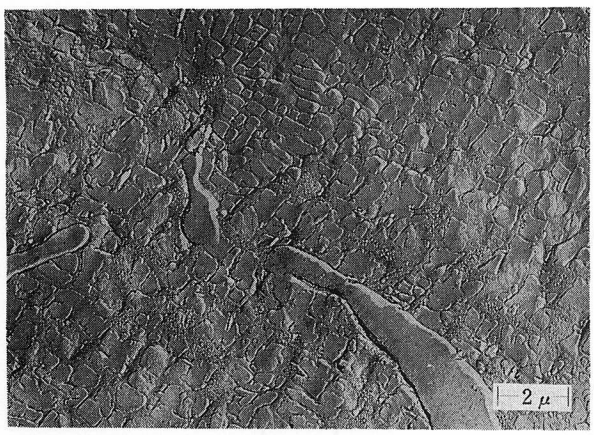

Photo. 7. Microstructure of Alloy 713LC.

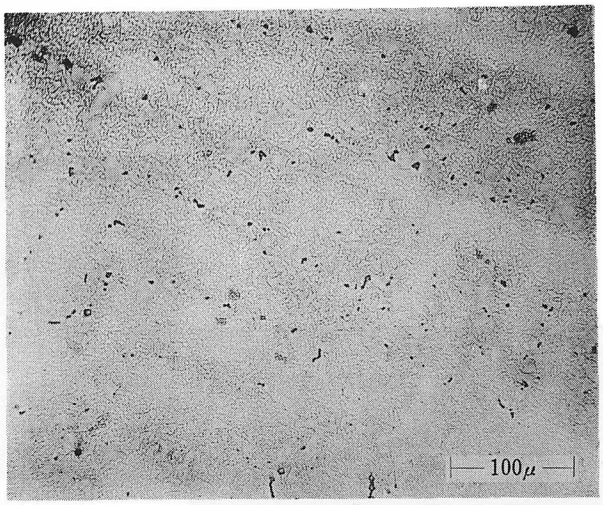

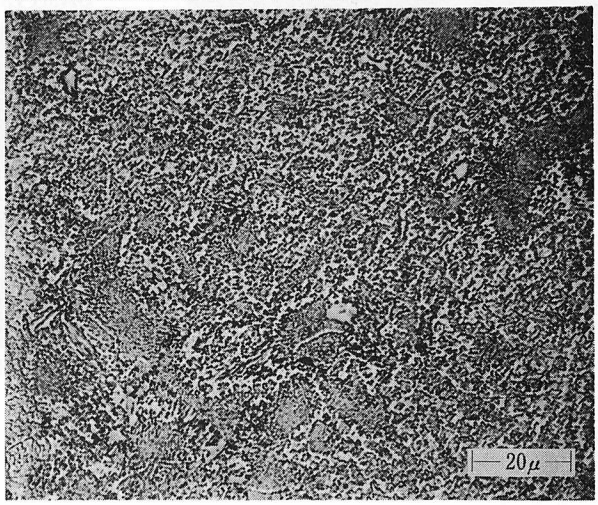

Photo. 8. Microstructure of Alloy 713LC-Hf.

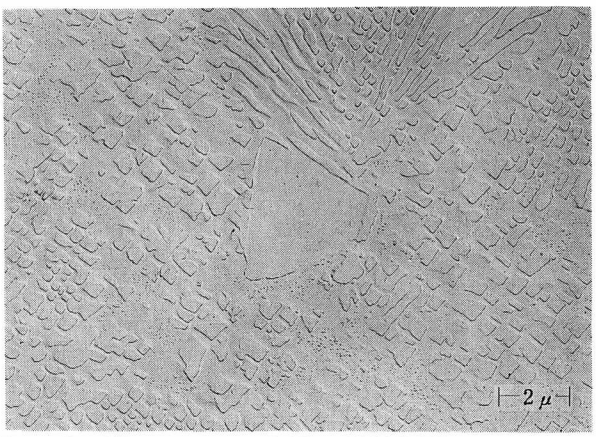

Photo. 9. Microstructure of Alloy 713LC-Hf.

was insufficient evidence to support the X-ray results that there are three or four distinctly different carbides present.

Results of microprobe analysis in a representative eutectic γ/γ' area in B-1900-Hf are presented in Photo. 12 and Fig. 10. As shown, the chromium and molybdenum are primarily partitioned to the γ phase, while the hafnium and tantalum are primarily partitioned to the γ' phase. There are some indications of molybdenum-rich particles along the eutectic cell.

The X-ray images and line scan data for a carbide area in Alloy 713LC are presented in Photo. 13 and Fig. 11. The smaller MC carbide has higher niobium and titanium contents and a significantly lower chromium content than the matrix. The larger carbide is primarily enriched in molybdenum and chromium. Similar X-ray images and line scan data for Alloy 713LC-Hf are presented in Photo. 14 and Fig. 12. As compared to the matrix, the MC

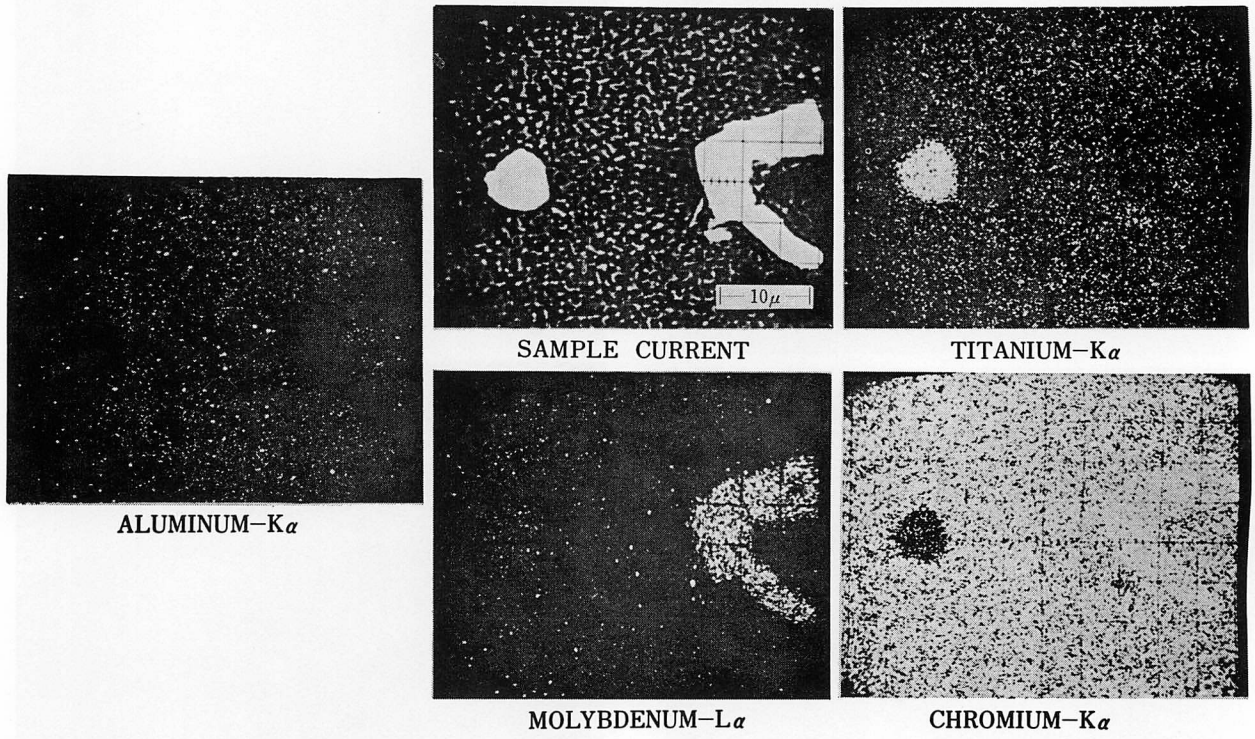

Photo. 10. Elemental X-ray images of carbides in B–1900.

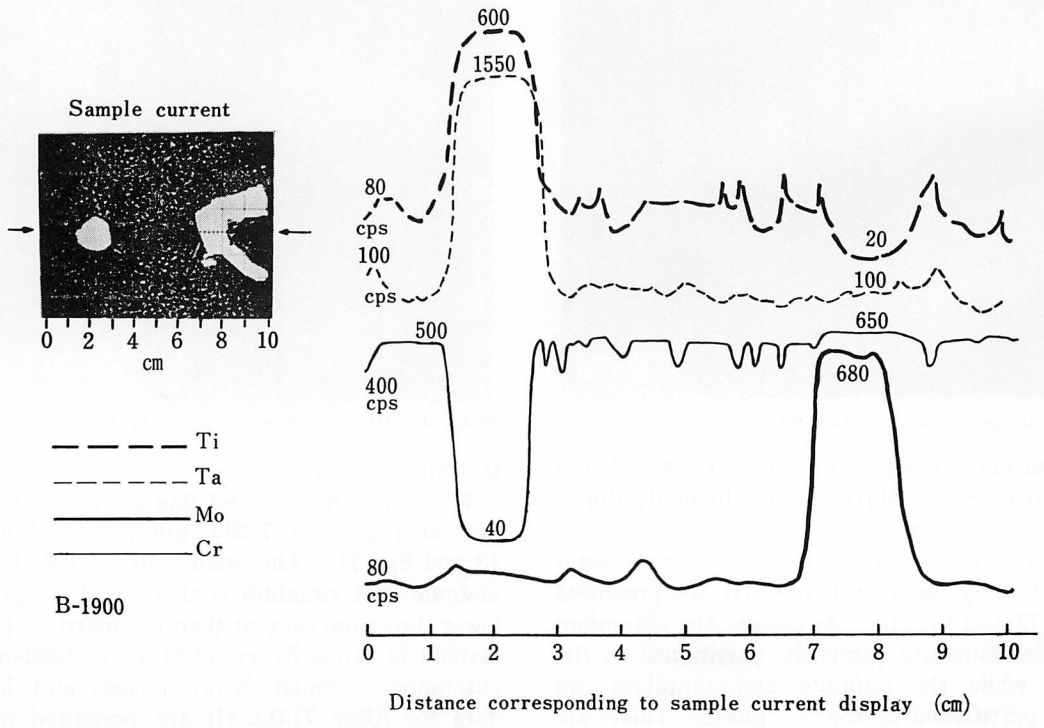

Fig. 8. Elemental line traces for four elements in B–1900.

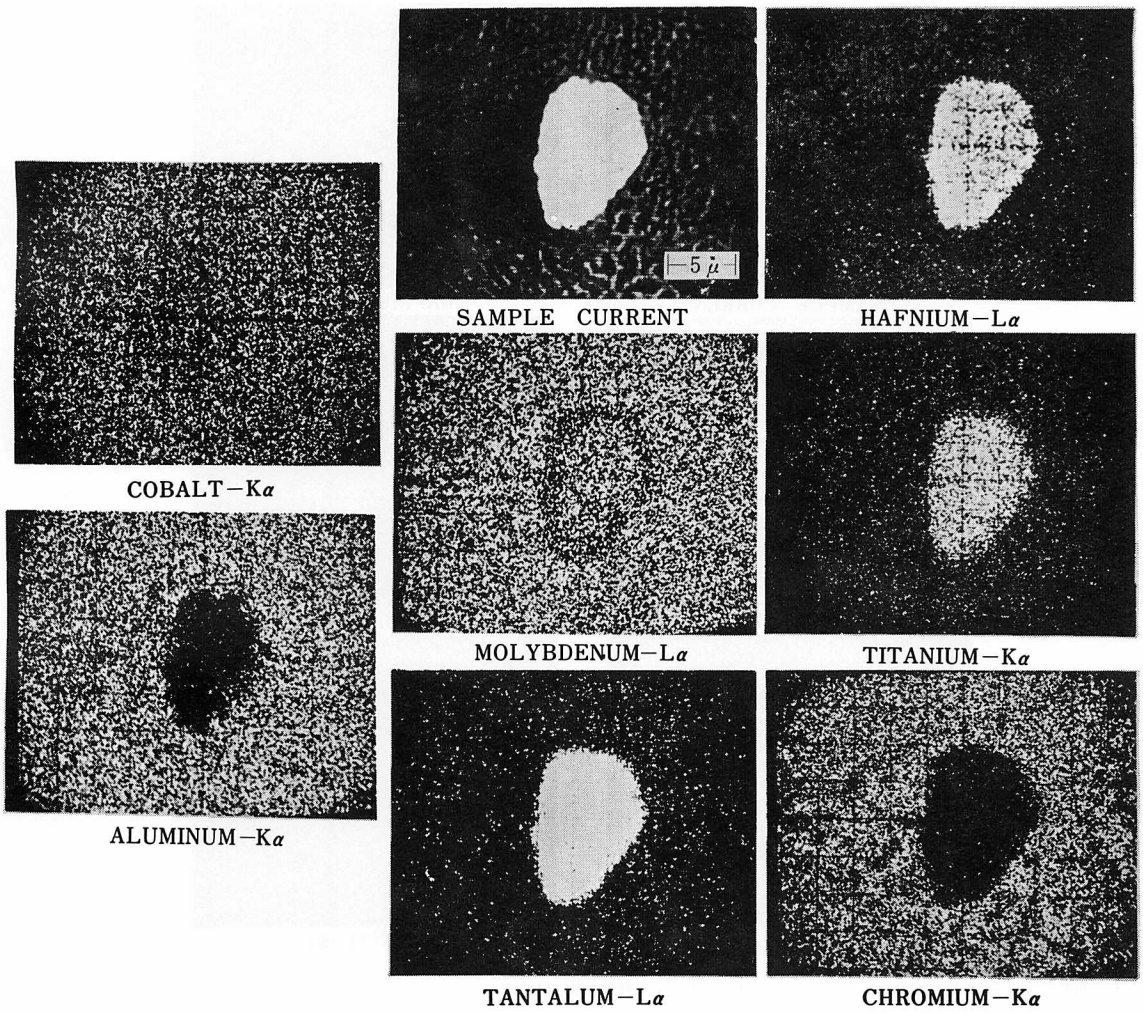

Photo. 11. Elemental X-ray images of a carbide in B–1900–Hf.

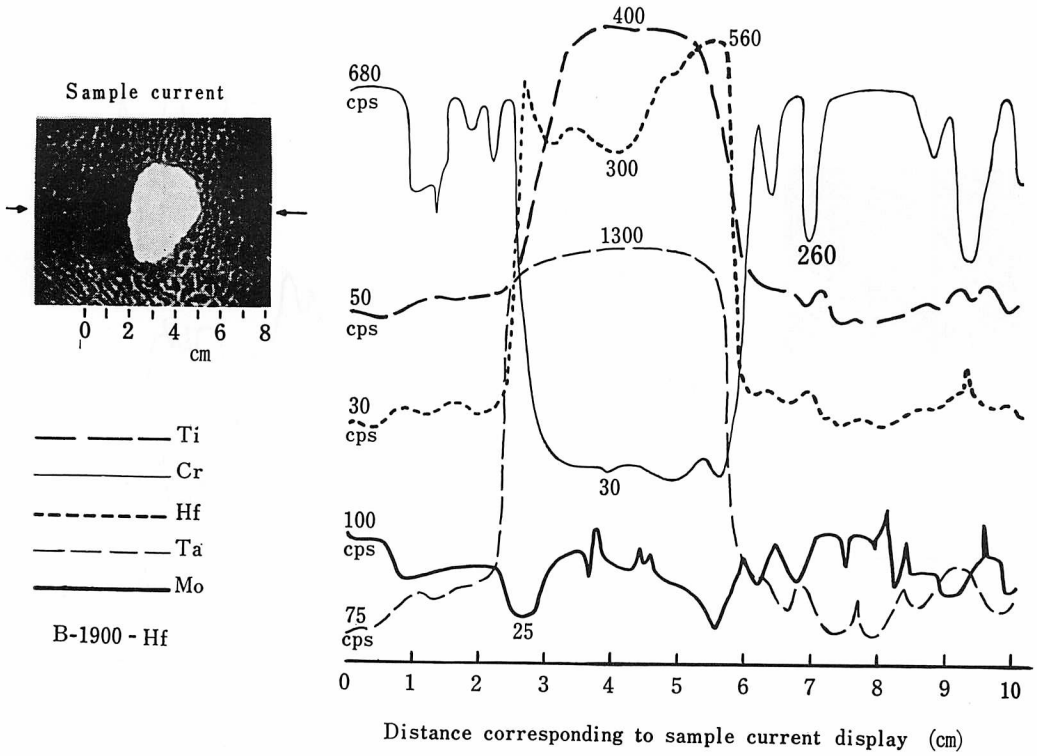

Fig. 9. Elemental line traces for five elements in B–1900–Hf.

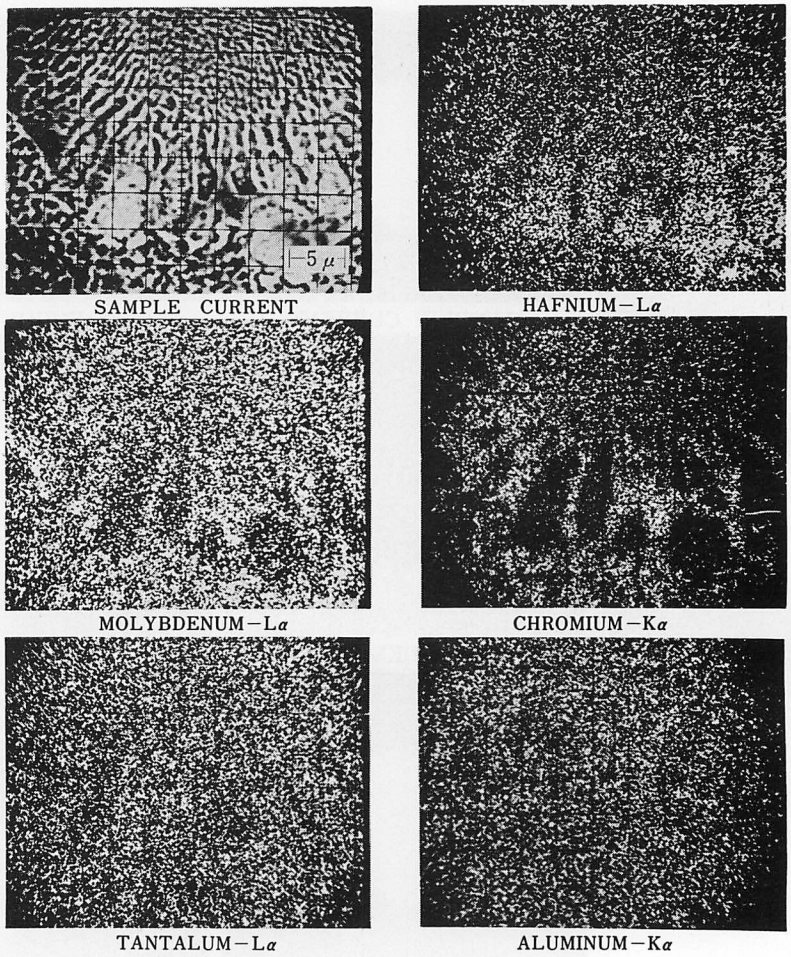

Photo. 12. Elemental X-Ray images of eutectic γ/γ' in B-1900-Hf.

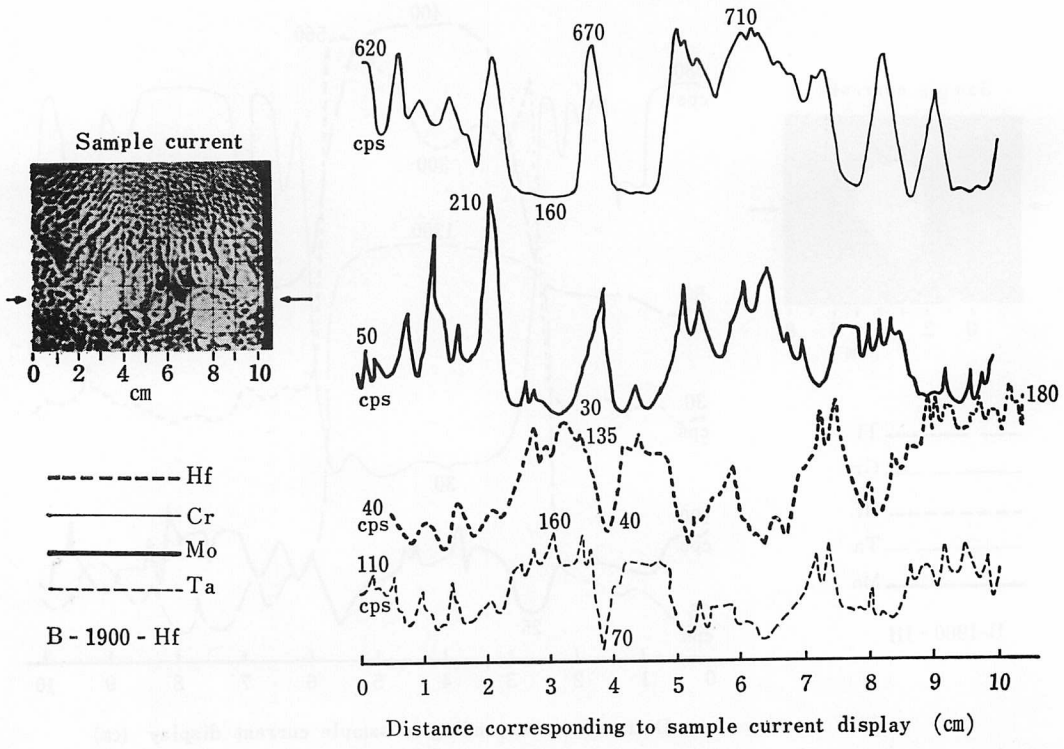

Fig. 10. Elemental line traces for four elements in B-1900-Hf.

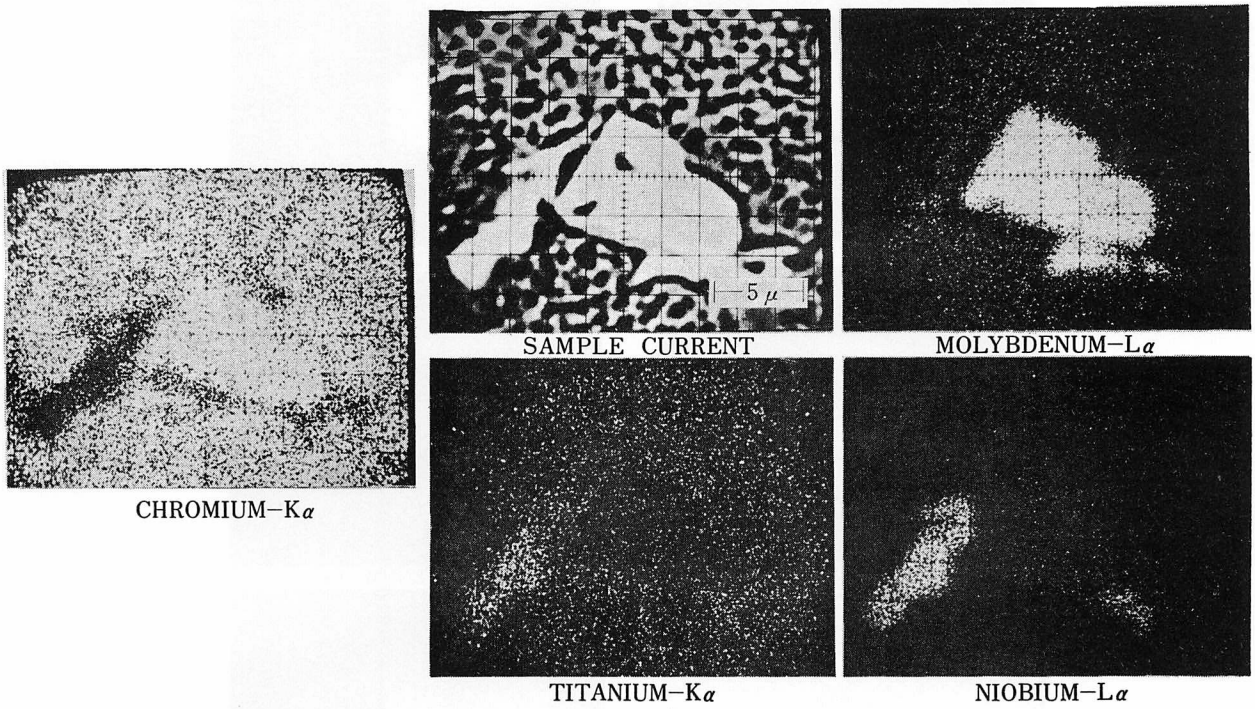

Photo. 13. Elemental X-ray images of carbides in Alloy 713LC.

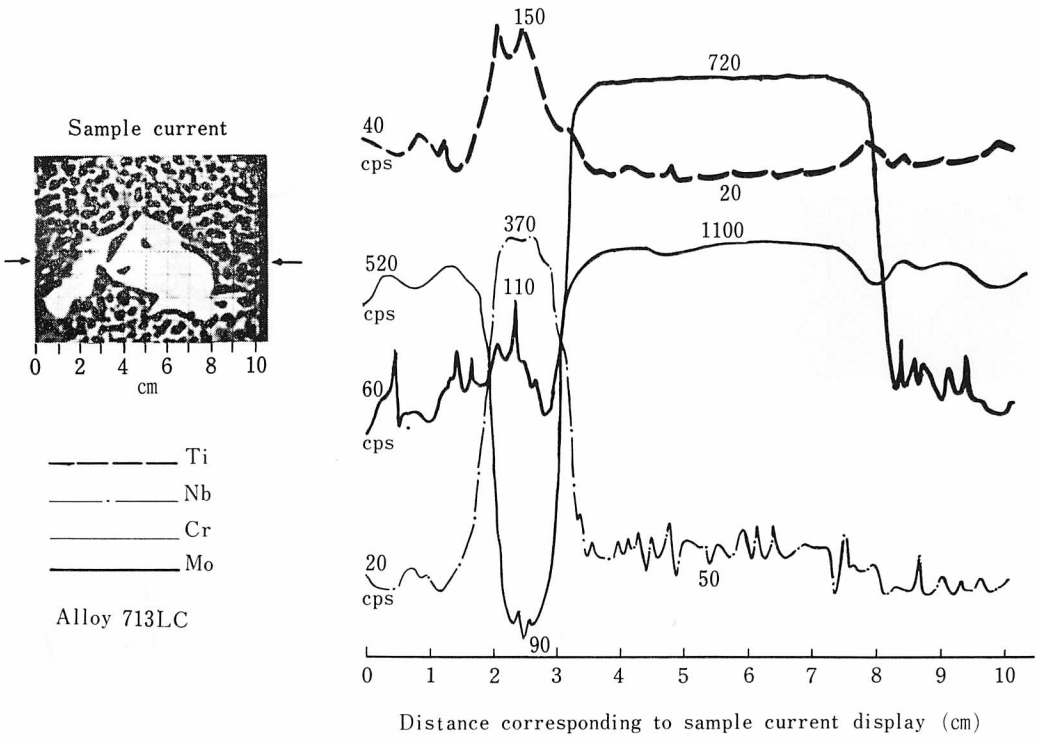

Fig. 11. Elemental line traces for four elements in Alloy 713LC.

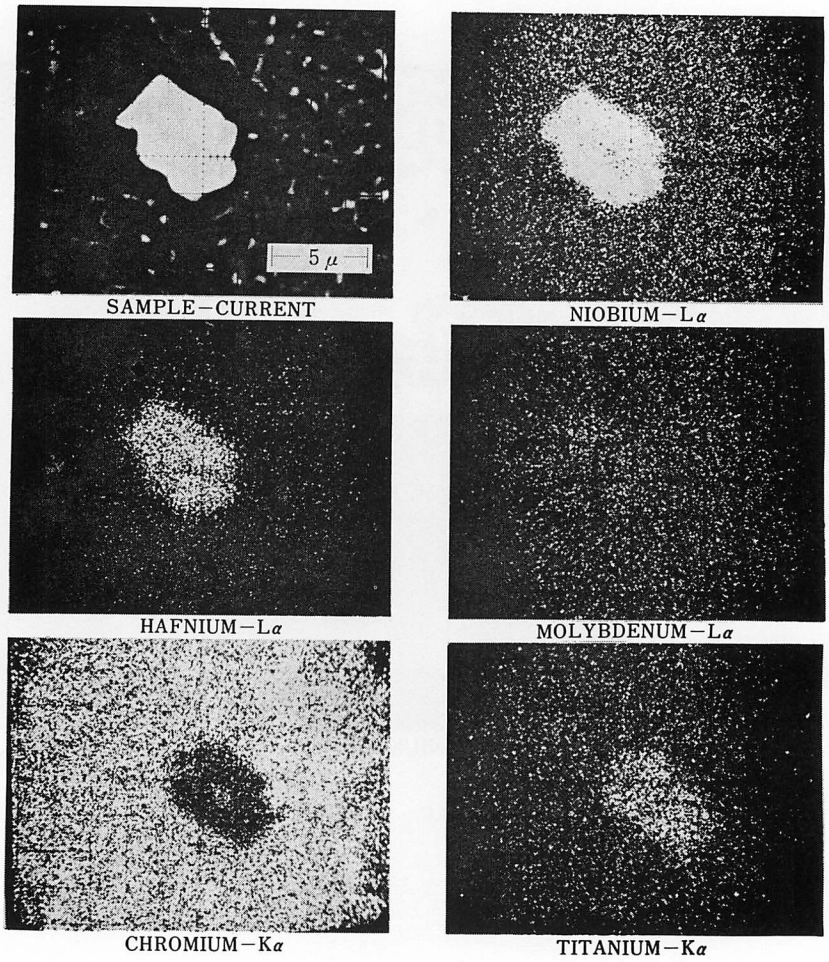

Photo. 14. Elemental X-ray images of a carbide in Alloy 713LC–Hf.

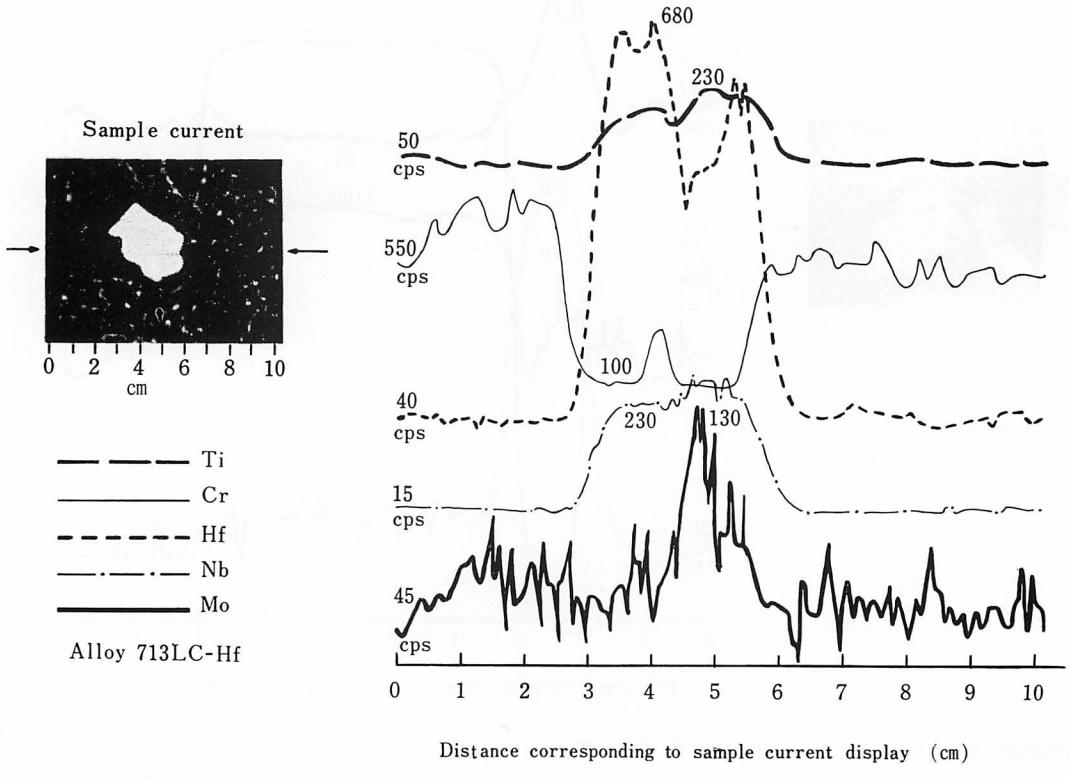

Fig. 12. Elemental line traces for five elements in Alloy 713LC–Hf.

type carbide is enriched in hafnium, niobium, titanium and molybdenum and depleted in chromium. Titanium in Alloy 713LC-Hf does not appear to behave the same way as it did in B-1900-Hf in that the presence of hafnium does not result in a significantly reduced titanium concentration in the MC carbide. In a manner similar to the B–1900–Hf, however, there was a distinct concentration envelope at the outer perimeter of the carbide in the Alloy 713LC–Hf.

The foregoing brief analysis of the microstructures does not define the mechanism by which hafnium improves the properties of cast nickel-base superalloys. It does, however, clearly show that hafnium markedly alters the morphology and composition of the various microconstituents. Because the creep-rupture properties of a superalloy are determined by the microstructure, it is reasoned that the beneficial effects of hafnium can principally be attributed to its microstructure altering effects rather than, as proposed by Cochardt, its scavenging action for tramp elements.

4. DIRECTIONAL SOLIDIFICATION

There have been many investigations concerning the role that grain boundaries play during elevated-temperature creep deformation and subsequent rupture. Particular emphasis has always been placed on the grain boundary because most undesirable events occur at this location during elevated temperature deformation. Such undesirable occurrences as grain-boundary sliding, excessive precipitation, adjacent denuded zones, and void formation are primarily concentrated at grain boundaries oriented normal to the principal stress axis. One proposed course of action to deal with this problem would be to reduce or possibly eliminate the transverse grain boundaries. By developing a columnar grain structure parallel to the principal stress axis, it is possible to eliminate the transverse grain boundaries. Such reasoning stimulated the development of the directional-solidification process.

The directional-solidification casting process produces a columnar grain structure in superalloy turbine-airfoil castings. Two conditions must be met to produce the desired structure: (1) heat flow must be unidirectional causing the solid-liquid interface at the growing grains to move in one direction, and (2) there must be no nucleation in the melt ahead of the advancing interface. It is possible to obtain a unidirectional structure and control grain orientation by establishing a strong thermal gradient in the solidifying melt. A schematic view of a laboratory mold to produce directionally-solidified turbine blades is presented in Fig. 13. The mold has a water-cooled copper-chill and is equipped with a two-zone winding molybdenum resistance-heater. The superalloy heat is melted and the blades cast in vacuum. A steep temperature gradient established by the water-cooled copper-chill is controlled by gradually reducing the power, first from the bottom winding, then from the top

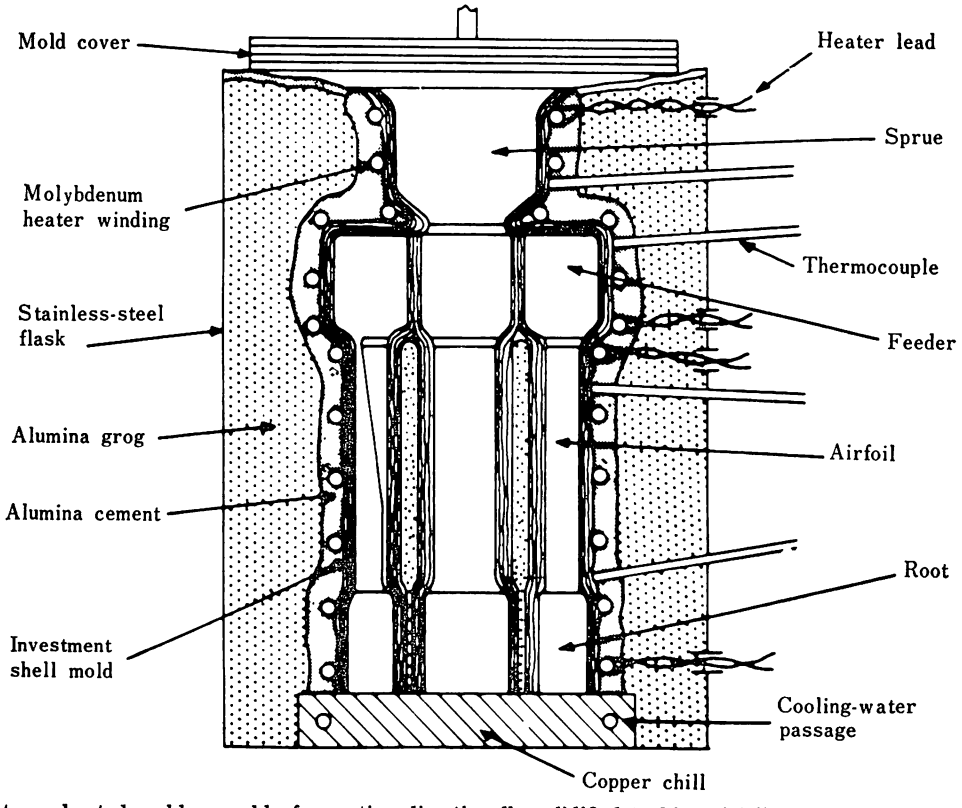

Fig. 13. Resistance-heated mold assembly for casting directionally solidified turbine airfoils.

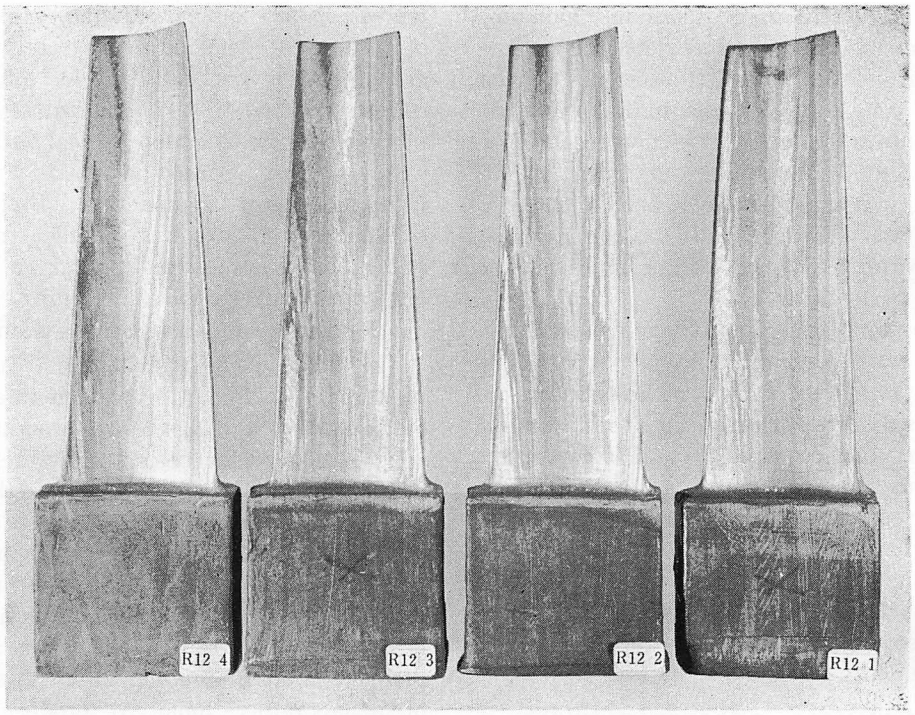

Photo. 15. Directionally-solidified turbine-blade castings in the macroetched condition showing the columnar grain structure.

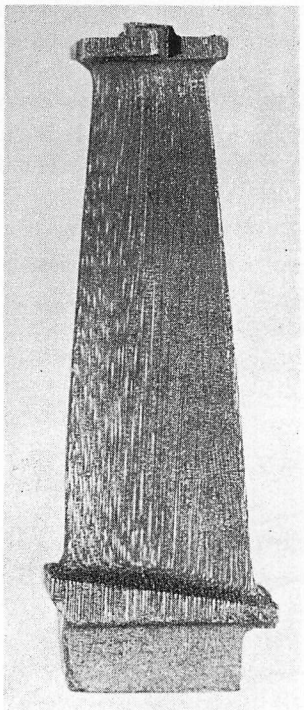

Photo. 16. Macroetched monocrystal turbine blade showing parallel dendritic structure and complete absence of grain boundaries.

as the columnar grains grow upward. Examples of directionally-solidified blades produced by the foregoing process are presented in Photo. 15. The blades have been macroetched to reveal the columnar grain structure. The development of the directional-solidification process and current production methods for turbine airfoils have been discussed in detail by Versnyder and Shank[14]. They also describe techniques whereby it is possible to cast monocrystal airfoils having a preferred (001) orientation (Photo. 16).

The 760°C and 980°C stress-rupture properties of four superalloys for both the conventionally-cast and the directionally-solidified conditions are presented in Table 4. With only one exception (i.e., MAR-M 246, 760°C, 63·3 kg/mm^2), directional solidification provides a marked improvement in both rupture life and elongation. It is with the latter property that directional solidification has a particularly dramatic effect. Rupture elongation data for a number of conventionally-cast and directionally-solidified superalloys[15] are presented in Fig. 14. As shown, the alloys fall into two distinct scatter bands. The lower band refers to the conventionally-cast material having elongation values ranging from less than 5% at 760°C to less than 10% at 1095°C. In contrast, the minimum elongation for directionally-solidified alloys is in excess of 5% at 760°C and more than 15% at 1095°C.

A marked reduction in turbine-airfoil edge cracking as a result of thermal fatigue can be realized with directionally-solidified components. This is probably the single most important attribute of the process. Thermal fatigue generally is an intergranular phenomenon. The absence of transverse grain boundaries at leading and trailing edges of airfoils eliminates the principal origin of failure. Furthermore, the lower modulus of elasticity associated with the anisotropic grain structure in directionally-solidified components also improves

Table. 4. Comparison of rupture properties as conventionally cast and as directionally solidified.

	Rupture test at 760 °C and 63·3 kg/mm²				Rupture test at 980 °C and 21·1 kg/mm²			
	Conventionally cast		Directionally solidified		Conventionally cast		Directionally solidified	
Alloy	Life (hr)	Elongation (%)	Life (hr)	Elongation (%)	Life (hr)	Elongation (%)	Life (hr)	Elongation (%)
MAR-M 200	20	1	790	13	35	4	68	24
IN-100	110	3	210	8	20	4	25	30
B-1900	150	3	220	13	35	7	50	18
MAR-M 246	700	5	143*	4	75	6	113	20
M 22	10	1	230	12	75	9	40	40

* Load was 70·3 kg/mm² rather than 63·3 kg/mm². This translates to a life of approximately 600 hr.

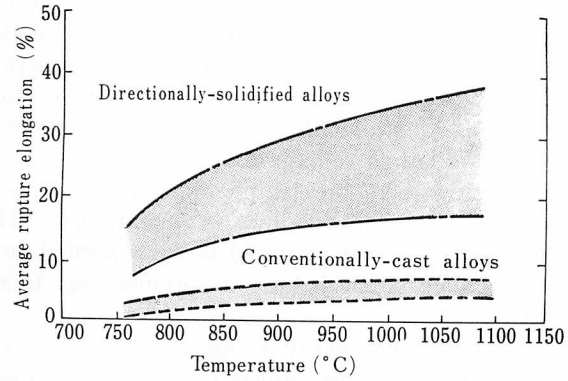

Fig. 14. Comparative rupture ductilities of conventionally cast and unidirectionally-solidified superalloys.

thermal fatigue resistance.

In discussing the potential of directional solidification, Versnyder and Shank mention that the development opens a new approach to alloy design; new alloys specifically tailored to the particular characteristics of the process can be expected. They cite NX-188 as being an example of such an alloy. The 18% Mo–8% Al nickel-base alloy has a higher melting point than almost all other superalloys, exceptional creep-rupture properties and structural stability[16]. The alloy can be readily cast into sound complex configurations through conventional or directional-solidification casting techniques.

The NX-188 alloy is unique from the fact that it utilizes the Ni_3Al (i.e., γ') phase as a structural material (Photo. 17). In contrast to other superalloys, the basic dendrite consists of γ' rather than γ; therefore, the γ' constitutes the continuous phase or matrix with γ as the irregular secondary phase. The small lathlike precipitate in the γ was identified as M_6C carbides by selected-area electron diffraction. The interdendritic areas contain a γ plus α-molybdenum eutectic. Maxwell reasons that the maximum solubility of molybdenum in the γ' phase is 4 to 6%. Reportedly, the principal function of the molybdenum is to serve as a solid-solution strengthener for the dispersed γ phase.

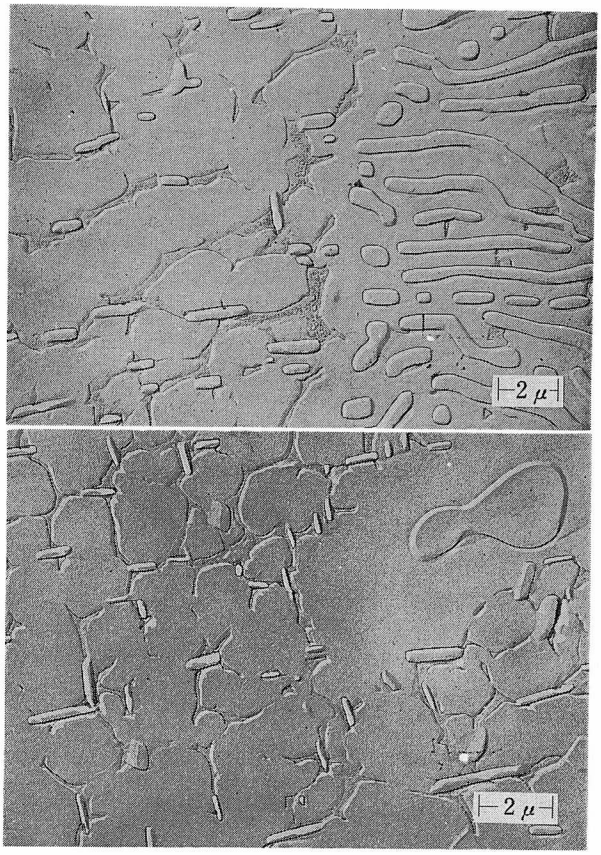

Photo. 17. Microstructure of NX-188.

Although it can be used in the conventionally-cast condition, NX-188 shows a remarkable response to directional solidification. Basically, the alloy is grain boundary limited and directional solidification eliminates a potential origin of failure. As shown in Fig. 15, directional solidification produces improvement in minimum creep rates, rupture life and elongation prior to fracture in 1205°C, 2·1 kg/mm² creep testing. Furthermore, the creep-rupture strength of directionally-solidified NX-188 is vastly superior to cast cobalt-base alloys (Fig. 16) and, as illustrated in Fig. 17, superior to cast nickel-base alloys at temperatures in excess of 1090°C. In fact, the alloy had usable strength properties at temperatures up to 1230°C. These strength proper-

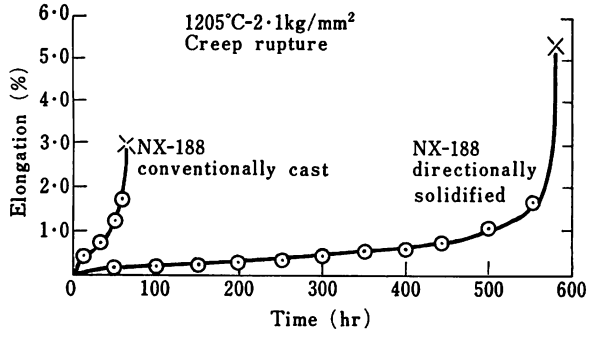

Fig. 15. Effect of casting technique on creep-rupture properties of NX–188[16].

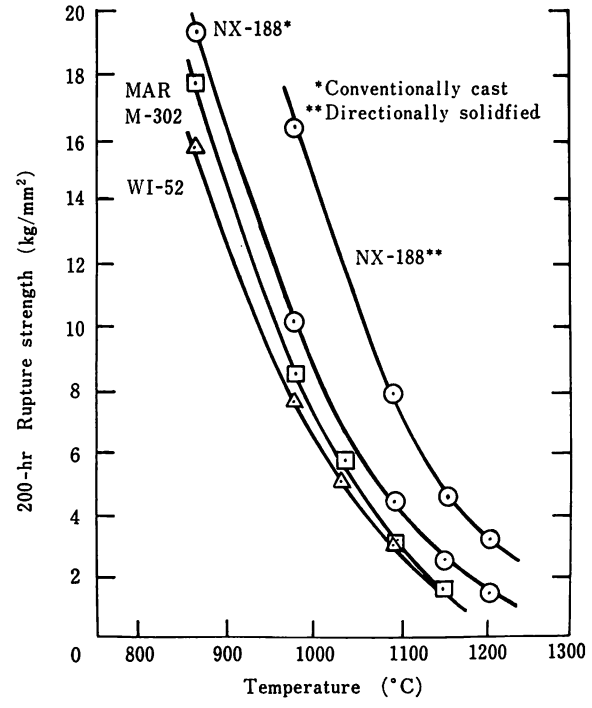

Fig. 16. Comparative rupture strengths of cobalt-base vane alloys and NX–188[16].

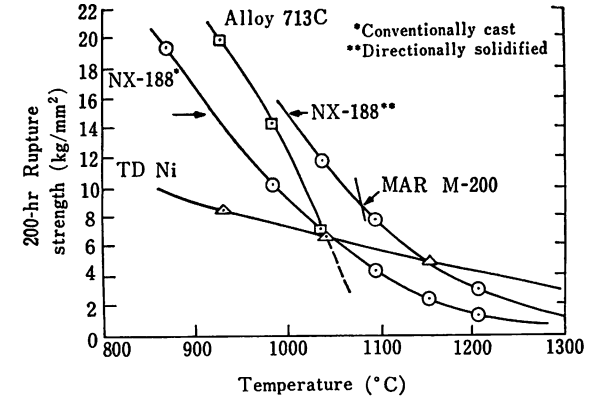

Fig. 17. Comparative rupture strengths of nickel-base vane alloys and NX–188[16].

ties combined with good thermal-fatigue resistance make NX–188 a particularly attractive alloy for turbine-vane applications in advanced design turbine engines.

5. THERMOMECHANICAL PROCESSING

Thermomechanical processing is frequently employed in the fabrication of wrought superalloy components. In general, controlled processing techniques are utilized to improve the mechanical properties of the resultant product. There has been a recent development reported by Moore and Athey[17], however, where thermomechanical processing is used to achieve a somewhat different effect. They have developed a technique (known by the trade name GatorizingTM) whereby unforgeable superalloys are processed in compression under controlled conditions of temperature and reduction to place them in a temporary condition of low strength and high ductility. They are subsequently forged to a desired configuration in heated dies at a temperature where the temporary condition of low strength and high ductility is maintained. The forged parts are then returned to their normal condition of high strength by conventional heat treatment.

As discussed previously, engine design criteria for wrought discs require superalloys with improved elevated-temperature strengths. While the high-temperature strength demands have been satisfied, generally they have been achieved at the expense of fabricability. As a result, advanced superalloys have limited fabricability or are even considered unworkable (i.e., cast alloys) by normal forging techniques. Gatorizing, however, is a thermomechanical process whereby it is possible to forge such alloys into intricate shapes.

A particular combination of temperature and compressive working, preferably extrusion, is required to place cast superalloys in a condition of low strength and high ductility. Billets are extruded at a temperature within about 250°C of the normal recrystallization temperature of the alloy. A reduction of at least 4 to 1 is the practical minimum necessary at the most preferred working temperature. Deformation reduces the normal recrystallization temperature, and recrystallization occurs spontaneously during extrusion. The "hot-cold-working" process should occur at a low enough temperature so that there is a substantial inhibition to grain growth. The resultant grain structure reportedly cannot be resolved by conventional light microscopy.

The IN–100 alloy is a high-strength superalloy that among other applications is used for cast turbine airfoils in advanced military aircraft engines. The alloy has inadequate high-temperature ductility to be considered forgeable and is used almost

exclusively in the cast condition. Moore and Athey[17] presented stress-rupture elongation data for extruded IN–100 bar stock to illustrate the properties that controlled thermomechanical processing can impart to a superalloy. As shown in Table 5, it is possible to achieve rupture elongations in excess of 1300%.

Table 5. Rupture elongation properties of extruded* IN-100 bar stock.

Test temperature (°C)	Elongation (%)
870	45
900	240
925	217
980	556
1040	1330
1095	1220
1150	230

* 16 to 1 reduction at 1150°C plus 16 to 1 reduction at 1095°C.

From all indications, the controlled extrusion process embodied in the Gatorizing development places the superalloy in a superplastic condition. Superplasticity is commonly referred to as the ability of an alloy to endure large essentially neck-free deformations at very low stresses[18]. The deformation generally occurs at or greater than half the absolute melting temperature and is highly strain-rate sensitive. A finely divided microstructure incorporating a stable second phase to inhibit grain growth is another condition. The deformation characteristics and microstructure of Gatorized alloys appear to conform to the conditions for superplastic behavior.

In the subsequent fabrication process, extruded superalloy bar stock is forged under controlled strain rates to obtain superplastic deformation. Induction-heated dies are used and the forging operation takes place in an inert atmosphere. The TZM molybdenum-base alloy and high-strength superalloys have been suggested as suitable die materials. To preclude grain growth, the forging operation must take place at a temperature below the recrystallization temperature. Upon completion of the fabrication operation, the normal grain structure and mechanical properties are restored with solution and aging heat treatments.

A comparison of conventional and superplastic forging characteristics of Astroloy (Udimet 700), a somewhat difficult-to-forge alloy, illustrates the advantages of thermomechanical processing. Conventional forging to a disc configuration at 1175°C requires an approximate stress of 31·6 kg/mm². Gatorized Astroloy can be processed to the same configuration at a temperature of 1040°C and a stress of 0·8 kg/mm² using low strain rates. Thus, conventional forging requires almost 40 times the stress along with a 140°C increase in temperature to achieve the same results as thermomechanical processing.

Moore and Athey conducted many forging tests on IN–100. In one such test, it was discovered that the die had developed a hairline crack. The crack was reproduced in a pancake forging in the form of a thin-walled fin. A further indication of the ductility of the material could be gained from the fact that the grain structure on the surface of a die could be reproduced on the exterior of a pancake forging. Furthermore, they forged IN–100 billets in a die designed to cause metal flow diametrically inward and then axially forward into a die cavity. This produced an article with a thin-wall annular flange.

The forging results have been so successful that it is now considered feasible to forge high-strength cast superalloys into turbine discs. Perhaps more significantly, it appears that these alloys can be forged into integrally bladed discs (Photo. 18). In addition, this new thermomechanical process offers great promise of forging simplification and cost saving.

6. POWDER METALLURGY

All of the major aircraft gas-turbine producers are actively pursuing development programs on powder-metallurgy superalloys for disc and shaft components. Some industry sources estimate that powder metallurgy could capture 40 to 50% of this market by 1980[19]. Chemical homogeneity is one of the principal advantages of using superalloys in powder form. Improved workability and reproducible mechanical properties can be realized because of the improved homogeneity. Large conventionally-processed superalloy discs can inherit chemical segregation from the cast billets which can lead to forging problems, localized phase instability, and

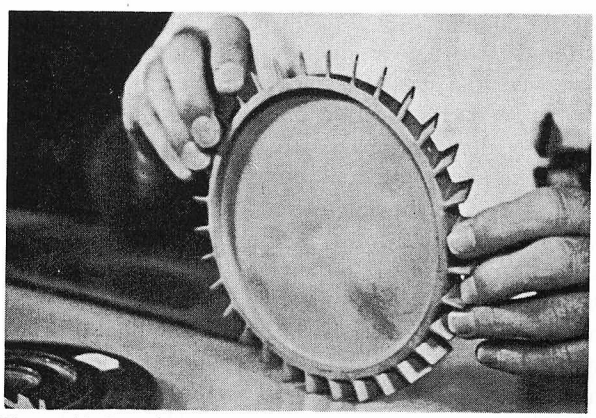

Photo. 18. Integrally bladed IN–100 Gatorized™ turbine disc.

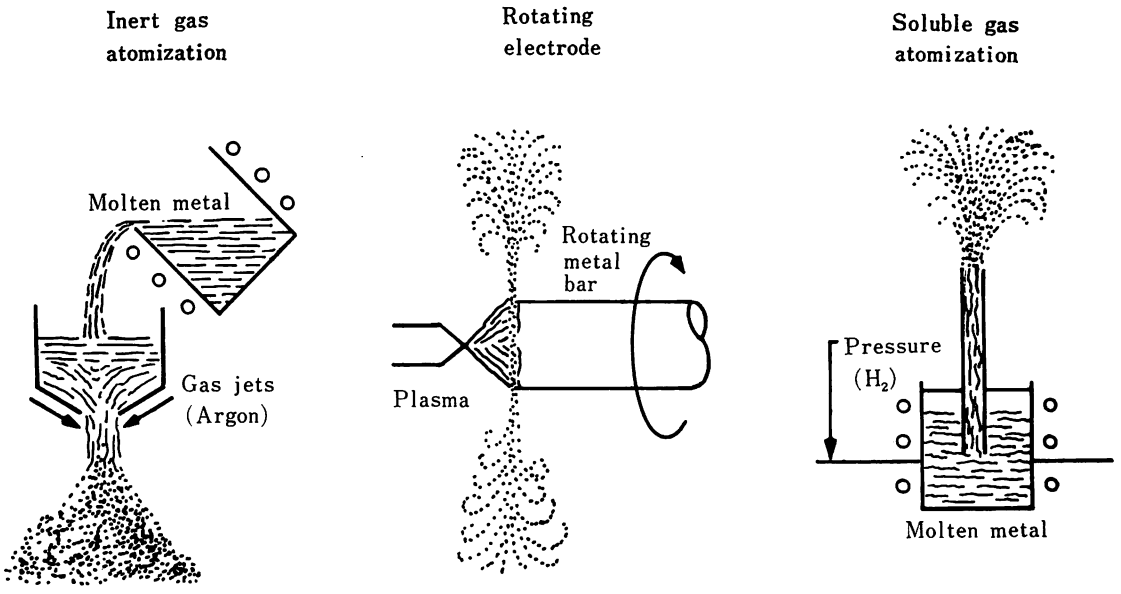

Fig. 18. Three major methods of producing superalloy powders.

erratic mechanical properties. Moreover, the use of pressed-and-sintered forging preforms can markedly improve material utilization and reduce scrap losses. In addition, cast compositions produced in powder form can be forged using superplastic forming techniques.

Bufferd and Gummeson[20] have reviewed the various methods of producing prealloyed superalloy powders and the procedures for manufacturing gas turbine components. The three methods for producing superalloy powders are (Fig. 18): inert gas atomization, rotating electrode, and soluble gas atomization. The principal consolidation techniques are (Fig. 19): hot-die pressing, hot isostatic pressing, and hot extrusion. Hot extrusion produces the best interparticle bonding and is used to consolidate approximately 90% of all prealloyed superalloy powders.

It is very important that the interstitial content of the atomized powder be low (<100 ppm O) to preclude insoluble compound formation. In densified material, the presence of such compounds (particularly in a continuous network) at prior powder boundaries will result in an extremely brittle material with poor high-temperature properties. Moreover, the use of high extrusion ratios (>6:1) insures good cross-section uniformity and eliminates prior powder (i.e., particle) boundaries.

In general, powder-metallurgy superalloy products have a fine grain microstructure. Even in solid bars consolidated from high-purity powders with relatively clean prior particle boundaries, inevitably there are some interstitial impurities that are insoluble in the matrix. These combined with undissolved grain-boundary carbides restrict grain growth beyond an ASTM 4 to 5 grain size during a solution anneal heat treatment. This can be a drawback, especially at high service temperatures, by limiting the elevated-temperature strength properties of superalloy powder metallurgy components. Reichman and Smythe[21], however, have developed a proprietary thermomechanical process whereby it is possible to grow large grains in superalloy powder-metallurgy products. In fact, they report that it was possible to obtain a single

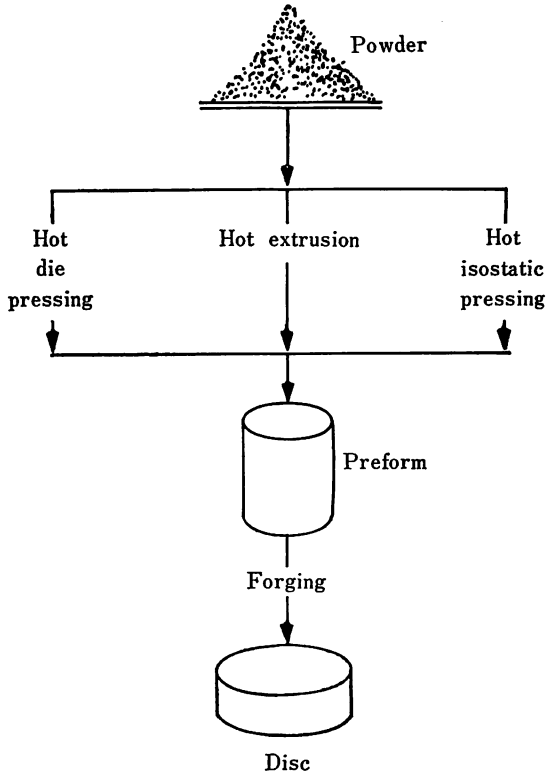

Fig. 19. Production cycles for producing a superalloy disc by powder-metallurgy means.

Table 6. Tensile properties of thermomechanically processed* powder-metallurgy Udimet 700.

	Room temperature	760 °C
Ultimate tensile strength (kg/mm²)	162	114
0·2% yield strength (kg/mm²)	113	106
Elongation (%)	28	33
Reduction of area (%)	30	35

* Extruded 10.6 to 1 at 1095°C plus TMP (proprietary deformation and annealing process).

Table 7. Tensile properties of powder-metallurgy IN-100.

Process treatment*	Room temperature				650 °C			
	Ultimate tensile strength (kg/mm²)	0·2% yield strength (kg/mm²)	Elongation (%)	Reduction of area (%)	Ultimate tensile strength (kg/mm²)	0·2% yield strength (kg/mm²)	Elongation (%)	Reduction of area (%)
A	218	208	12	8	181	170	10	16
B	179	125	27	25	144	127	15	12
C	120	91	10	15	115	88	8	10

* A Extruded 10·6 to 1 at 1095°C and rolled 3 to 1 at 1095°C.
B Extruded 10·6 to 1 at 1095°C and rolled 3 to 1 at 1095°C. Heat treatment: 1175°C×4 hr oil quench+650°C×24 hr air cool+760°C×8 hr air cool.
C Extruded 10·6 to 1 at 1095°C and superplastically deformed 100% in tension at 1095°C. Heat treatment: 1245°C×56 hr air cool.

crystal in a 6·4 mm-dia. tensile specimen. As shown in Table 6, the tensile-elongation properties of Udimet 700 are excellent.

Using powder-metallurgy techniques, it is also possible to produce wrought products from cast-superalloy compositions. Room temperature and 650°C tensile data[22] are presented for powder-metallurgy IN-100 in Table 7. As shown, it is possible to obtain remarkably high strength with good ductility properties in this alloy by powder-metallurgy techniques.

7. SUMMARY

There have been some recent developments in improving the ductility of both cast and wrought superalloys. Of particular importance is the fact that these improvements have been achieved without sacrificing elevated-temperature strength properties. Hafnium is particularly effective as an alloying element in improving the ductility of cast nickel-base turbine-airfoil materials. The presence of hafnium can eliminate erratic creep ductility at intermediate temperatures (e.g., 760°C) by extending the point of failure well into the third-stage creep range, thereby increasing the creep ductility and life. It also improves the plane strain fracture toughness of cast nickel-base alloys. It is believed that hafnium improves properties by altering the morphology, distribution and composition of the various microconstituents.

Directional solidification is a casting process that produces a columnar grain structure in superalloy turbine airfoil castings. The absence of transverse grain boundaries at leading and trailing edges of airfoils eliminates the principal origin of failure; consequently, ductility and thermal-fatigue properties are improved. The NX-188 alloy is specifically suited to the particular characteristics of the directional-solidification process. This advanced superalloy is unique in that it utilizes the γ' (Ni_3Al) phase rather than the γ phase as a structural material. The 18% Mo-8% Al nickel-base alloy has a high melting point, exceptional creep-rupture properties and structural stability.

There has been a recent thermomechanical processing development (known by the trade name GatorizingTM) whereby unforgeable superalloys are processed in compression under controlled conditions of temperature and strain to place them in a temporary condition of low strength and high ductility. From all indications the process places superalloys in a superplastic condition, and advanced materials having very limited fabricability can be forged into intricate shapes.

Powder-metallurgy techniques are being used to fabricate wrought superalloy components. Superalloy powder-metallurgy components have improved chemical homogeneity which can reduce or eliminate forging problems, localized phase instability, and erratic mechanical properties. Moreover, the use of densified forging preforms can increase material utilization and cast compositions can be forged using superplastic forming techniques. Remarkably high strength with good ductility at 650°C has been achieved in IN-100 alloy by powder-metallurgy techniques.

ACKNOWLEDGMENTS

Particular credit is due K. E. Kienholz for the microprobe analyses, L. W. Walker the light microscopy and V. Biss the electron microscopy.

The authors would like to acknowledge the helpful discussions of E.F. Bradley, W. P. Danesi, J. Hockin, C.H. Lund, J.N. Mushovic, S.H. Reichman and J. Walsh. We are also indebted to Martin Metals Division, Martin Marietta Corporation, for supplying metallographic samples and mechanical property data; to Pratt & Whitney Aircraft Division, United Aircraft Corporation for supplying many of the illustrations; and to Federal Mogul Corporation for supplying unpublished mechanical-property data.

REFERENCES

1) W.P. Doll: International Symposium on Structural Stability in Superalloys, Seven Springs, Pa., (Sept. 1968)
2) G.J. Wile: The Transportation Industry 1968–1978 Symposium, Ann Arbor, Mich., (Sept. 1968)
3) C.H. Lund: Ninth Annual British Investment Casters Technical Association Conference, London, England, (May 1968)
4) D.G. Phinney, E.F. Bradley, M.J. Donachie, Jr.: Metals Progress, **97** (1970), No. 3, p. 68–75
5) E.F. Bradley, M.J. Donachie, Jr.: New England Regional Conference, AIME, Schenectady, N.Y., (April 1970)
6) A.W. Cochardt (Westinghouse Corporation): U.S. Patent No. 3,005,705, (Oct. 24, 1961)
7) H.E. Collins: NASA CR–54507, (June 20, 1967)
8) C.H. Lund, J. Hockin, M.J. Woulds: German Offen. 1,921,359, (Nov. 13, 1969), Italian Patent 861,727, Belgian Patent 736,244
9) J. Hockin, W. Taylor: Second World Conference on Investment Castings, Düsseldorf, Germany, (June 1969)
10) Martin Metals Company
11) J. Hockin: "The Effect of Hafnium on Fracture Toughness of Nickel-Base Superalloys", to be published
12) W.P. Danesi: personal communication
13) Martin Metals Company: MM–004 data sheet
14) F.L. Versnyder, M.E. Shank: Materials Science and Engineering, **6** (1970), No. 4, p. 213
15) B.J. Piearcey, B.R. Terkelson: Trans. AIME, **239** (1967), p. 1143
16) D.H. Maxwell: Metals Engineering Quarterly, **10** (1970), No. 4, p. 42–54
17) J.P. Moore, R.L. Athey (United Aircraft Corporation): U.S. Patent 3,519,503, (July 7, 1970)
18) D.H. Avery, W.A. Backofen: Trans. ASM, **58** (1965), p. 551
19) "Powdered Steel a Tough Customer", Business Week, (Jan. 2, 1971), p. 37
20) A.S. Bufferd, P.U. Gummeson: Metal Progress, **99** (1971), No. 4, p. 68
21) S.H. Reichman, J.W. Smythe: International Powder Metallurgy Conference, New York, N.Y., (July 1970)
22) S.H. Reichman (Federal Mogul Corporation): personal communication

The Effect of Composition and Microstructure on Ductility and Toughness: F.B. Pickering

(pp. 9-31)

M. Nagumo (Nippon Steel Corporation, Fundamental Research Laboratories).

The work at British Steel Corporation presented by Dr. Pickering should be appreciated for the systematization of the effects of many metallurgical variables on ductility of steel. The true strain, ε_T, as determined by tensile test is a good measure of formability for some working processes. However, in order to assess the effects of metallurgical variables for different working processes, the critical condition at which ductile fracture takes place should be established. The nature of ductile fracture which Dr. Pickering presumed is likely to be based on the Gurland's model. The model, which is explained in the paper, is essentially a strain criterion of ductile fracture. I would like to point out that the strain criterion is insufficient.

Fig. 1 shows a result of compression test of 0·35%C steel, conducted by Mr. Yamaguchi of our laboratories. The fracture strain as defined by circumferential strain on the surface at the onset of cracking strongly depended on both the shape factor of cylindrical specimens, i.e. the initial diameter to height ratio, and the constraint of specimens by compression dies. The shape factor and constraint both change the stress state on the free surface of specimens. Therefore, it is evident that the critical condition of the onset of ductile fracture depends on both the stress and strain states.

From microscopic aspect, the fracture strain implies the ultimate strain that the material can sustain. However, the transmission electron micrograph of Fig. 2 shows that heavy deformation takes place in a very small region just below the fracture surface as ductile fracture proceeds. The picture was taken with a spheroidized 0·2% C steel bar fractured by tension. The fracture surface was electroplated with iron and subjected to thin foil preparation. The amount of localized deformation can be estimated from the dislocation cell structures, and it is much larger than "fracture strain" in usual definition. The latter is estimated by the dislocation density at some distance below the fracture surface. This observation means that the condition at the onset of ductile fracture was attained when the specimen still retained the ability of further straining.

My conclusion is that the effects of metallurgical variables should be analyzed with respect to both the stress and strain states for each working process.

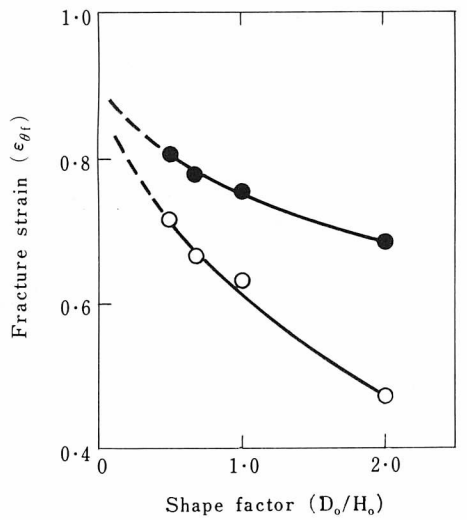

Fig. 1. Fracture strain at compression test of 0·35%C steel. Fracture strain is defined as the circumferential strain at fracture. The shape factor is the ratio of initial diameter to height of specimen. Solid circles are the data of compression test using a flat die without lubrication, and open circles are those using grooved dies.

Fig. 2. Transmission electron micrograph of the area just below the fracture surface. A spheroidized 0·2% C steel bar was fractured by tension. The fracture surface was electroplated with iron and subjected to thin foil preparation. The fracture surface is from the upper right to the lower left. Electroplated iron is right side of fracture surface.

Author's Response.

I would agree with Dr. Nagumo that the stress-strain state is critical with regard to the criteria governing the onset of ductile fracture, for example, hydrostatic compression leads to very high ductility. I would point out, however, that whilst agreeing that when ductile fracture occurs in practice, the metal is capable of further deformation, this is simply because the overall deformation at fracture is controlled by the growth and coalescence of voids around second-phase particles. If the second-phase particles are removed, very much larger overall deformations at fracture are obtained. Thus, the local deformation between voids, as assessed by dislocation densities, is very much greater than would be expected from the macroscopic necking strain. Nevertheless, it is this latter

strain that is technologically important, for example in processes such as bending. In other forming processes, such as stretch forming, the criteria are very different, and it is true that assessments made with the actual forming process involved are the only really satisfactory measure of service performance. In assessing the general metallurgical characteristics of a steel during forming, however, the use of these "type" tests would be very expensive and time consuming, and a fairly good appreciation can be achieved by the much more simple true stress-true strain uniaxial tensile test.

Criteria of Ductility and Toughness for Fracture-Safe Design: E. A. Lange

(pp. 33-44)

K. Ikeda (Kobe Steel Ltd.).

According to the results of Dynamic Tear test in Japan, the Dynamic Tear test has good correlation with the brittle-fracture arresting temperature as well as the NDT temperature in NRL drop weight test. Generally, the brittle-fracture initiation temperature has no good correlation with the brittle-fracture arresting temperature for the same crack length in a plate. Consequently, the D T test has no good correlation with the brittle-fracture initiation characteristics.

In your diagram, only the effect of notch length and plain strain condition in the base metal is mentioned.

When we have investigated the brittle-fracture casualties of welded structures such as pressure vessels and so on, it was observed frequently that the brittle fracture initiated in the welded joint. Therefore, the brittle-fracture initiation characteristics of HAZ or bond and weld metal are the most significant.

The brittle-fracture initiation characteristics of bond or weld metal are greatly influenced by the welding heat input and the welding procedures such as shielded arc, submerged arc, electroslag, electrogas welding and so on. In addition, at the cross joint or the T-joint, the brittle-fracture initiation temperature is severely influenced by the welding residual stress. As we observed already, the angular distortion and the misalignment also greatly affect the brittle-fracture initiation temperature. Of course, the effect of structural discontinuity on brittle-fracture initiation should be taken into account, too.

When you mention the application of D T test results for base metal to the safety design of welded structures by designers, why don't you take these above mentioned factors related to the welding into account? How do you apply your evaluation of steel quality to the brittle-fracture initiation in welded joint of welded structures which always include welded joints?

In Japan, we have already analyzed and clarified precisely the effect of these various factors on brittle-fracture initiation characteristic by using wide-plate test specimens including the deep notch test specimens, and the design of welded structures to prevent brittle fracture is in progress for various kinds of boundary conditions.

M. J. May (The British Steel Corporation, Corporate Laboratories).

I agree entirely with the emphasis given by Mr. Lange in his paper on the importance of taking into account constraint in the characterization of the fracture resistance of materials. In addition to thickness and notch acuity, however, equally important with ferritic steels is the very large effect of loading rate. This can be seen by reference to Fig. 1*, together with other mechanical test factors influencing fracture characterization.

The approach suggested by Mr. Lange in his paper is based on the premise of use of criteria to identify conditions for crack arrest or avoidance of crack propagation; no consideration, however, is given to criteria for crack initiation. In certain situations reliance on crack arrest or avoidance of propagation is essential but in many cases such an approach is impracticable or uneconomic in relation to material selection and the alternative approach of avoidance of crack initiation must be used. This approach for structural steels makes use of an extension of linear elastic fracture mechanics to general yielding by determining the local strain that can be developed at a sharp crack for crack initiation and failure in terms of the crack tip opening displacement.

By determining the crack initiation characteristics of the parent plate, weld metal, heat affected zone, etc., over a range of test temperatures it is possible to identify potential regions for crack initiation and to select the parent steel, welding consumables and processes to minimize the likelihood of crack initiation in a structure. The results from small-scale tests can then be validated by appropriate wide-plate tests into which, in addition, other mechanical and geometric factors can be introduced.

This approach has been developed in several laboratories in the UK and has the advantage that just as one can, with LEFM, relate the fracture resistance to the size of crack to cause failure under given loading conditions, proportional to $(K_{IC}/\sigma_{ys})^2$, so one can, under GYFM, relate the fracture resistance to σ_C/ε_y. Generalized equations relating COD to overall strain levels and crack length have been developed from experimental studies and making use of a theoretical analysis with the strip yield model. Although such equations are not fully developed more refined analyses are being developed through elastic-plastic analyses using finite element techniques. This approach has the advantage that relationships between crack size, and geometry and loading conditions can be developed directly rather than through correlations with other test methods.

It therefore depends on the design conditions which of the two approaches is the most appropriate, namely avoidance of initiation of fracture from weld regions or reliance on avoidance of crack propagation by the parent plate. The latter requirement can often be conservative on use of materials, although in certain structures it is an essential design requirement.

Author's Reponse.

The author is grateful for the comments on his paper by Dr. Ikeda. He agrees with Dr. Ikeda that the performance of a welded joint requires a test that models the design, residual stress pattern, temperature and strain rate that represent the worst case conditions to be encountered in the real structure. The wide-plate test can accomplish this objective but not the Dynamic Tear test. However, the more economical Dynamic Tear test can be used to characterize the fracture resistance properties of plates and weld metals. Using this information, materials and welding procedures can be selected with sufficient fracture resistance so that hidden flaws and residual stresses are not sufficient to cause brittle fractures to initiate. The expensive wide-plate test is then saved to develop information on the weldability characteristics of base materials and the effectiveness of joint design.

I would also agree with Dr. May that selection of a criterion depends on the design aspects, including welding.

* Fig. 1 of the discussion is the same as Fig. 7 on p. 167.

Toughness and Effective Grain Size in Heat-Treated Low-Alloy High Strength Steels:

S. Matsuda, T. Inoue, H. Mimura, Y. Okamura

(pp. 45-66)

T. Araki (University of Tokyo) and H. Nakajima (NRIM).

We have much appreciated the series of fine research work conducted by the authors since years. We would like to offer some comments and questions on the relation between the transition temperature and the size of fracture unit. Fig. 1 shows some transition temperature values of 0·34%C-1·8%Ni-1%Cr-0·3%Mo steel isothermally transformed at 350°C to bainite having a hardness of HRC 41·6 and also at 305°C to HRC 47·2.

When the bainite or martensite of this steel is tempered so as to get the same hardness of HRC 32, the series of tempered transformed structures show a linear relation between $_{v}$Trs and inverse square root of the fracture unit size, d, of the Charpy specimen.

Matsuda, Inoue and others exhibited in their paper two similar linear plots on two types of 0·12%C nickel steel as shown in Fig. 1, curve 1 and 2, though those plots do not have the same hardness. As mentioned by the authors the fracture unit size, or mean effective ferrite grain size, is thought to be a controlling factor of the toughness of those steels.

In the case of 0·34% C steel, one can see the gradient of the line is much steeper than that of those two low carbon nickel-steels. And there is a difference between steel 1 and 2 having the same carbon content.

As an opinion, it seems we cannot ignore some other factors than the fracture unit when the carbon content increases. Sizes and precipitation morphology of the carbides may affect results to some extent.

May we ask for the authors' comments on this point? And, the second question is:

How much, do you think, is a maximum difference between crystallographic orientations of laths in one co-variant packet which acts as a fracture unit?

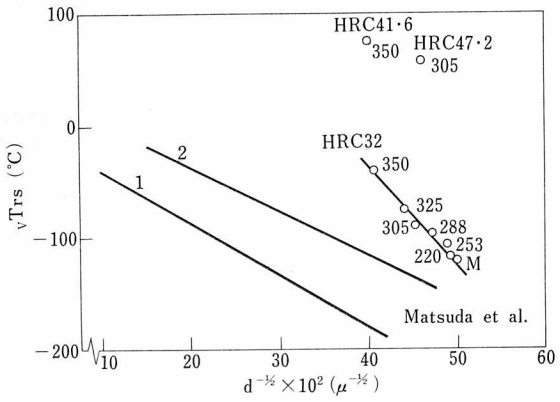

Fig. 1. Relation between transition temperatures and inverse square root of fracture unit size, d. Curves 1 and 2 correspond to Fig. 3 and 9 in the paper, respectively.

Authors' Response (T.Inoue).

On the first question we agree with the remark of Prof. Araki et al. The effective grain size uniquely determines the toughness of heat-treated steels with the same chemical composition. Of course the toughness changes with chemical composition, for example, $_{v}$Trs of a ferritic steel decreases as the nickel content increases even if the ferritic grain size is same.

Also sizes and amounts of carbides may affect the toughness, because they change the stress which can propagate microcracks as a Griffith crack.

On the second question we have not yet made accurate measurements of the differences between crystallographic orientations of laths. But they are expected to be smaller than 2∼3 degrees in view of following two results:

1) The intensity distribution of electron diffraction patterns did not change as specimens were tilted by a few degrees.

2) In Photo. 4, it can be seen that edges of etch pits are straight through the lath boundaries.

Temper Embrittlement of Low-Carbon Alloy Steels:

C. Ouchi, J. Tanaka, T. Osuka

(pp. 67-82)

H.G. Suzuki and M.Ono (Nippon Steel Corporation, Fundamental Research Laboratories).

Auger analysis examined by Ouchi et al. is very ingenuous and interesting to make clear the mechanism of temper brittleness of alloyed steels. We also think there is some correlation between the free surface and the grain boundary. However, it is necessary to correlate the segregation to grain boundaries with that to free surfaces.

The present purpose of this discussion is to present the direct evidence of segregation of tin to the prior grain boundaries by Auger electron spectroscopy.

Vacuum-melted 0·1%C-3%Mn-1%Sn alloys were prepared. After austenitizing for 2 hr at 1300°C, specimens were water quenched, then tempered for 1 hr at 675°C followed by water quenching. Embrittlement treatment was done for 5 hr at 550°C. By this treatment, brittle fracture occurred almost intergranularly. Auger electron spectroscopy was used to detect the segregating elements. A display type LEED apparatus with four spherical grids was used as an energy analyzer. The details of the apparatus used were described elsewhere[1]. Standard V-notch Charpy specimens were

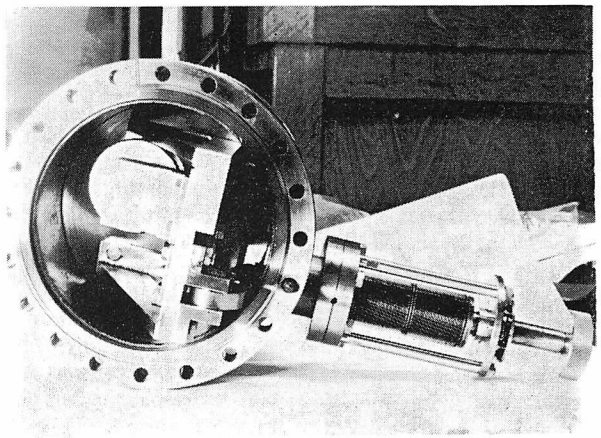

Photo. 1. Low-temperature cleavage manipulator for LEED apparatus.

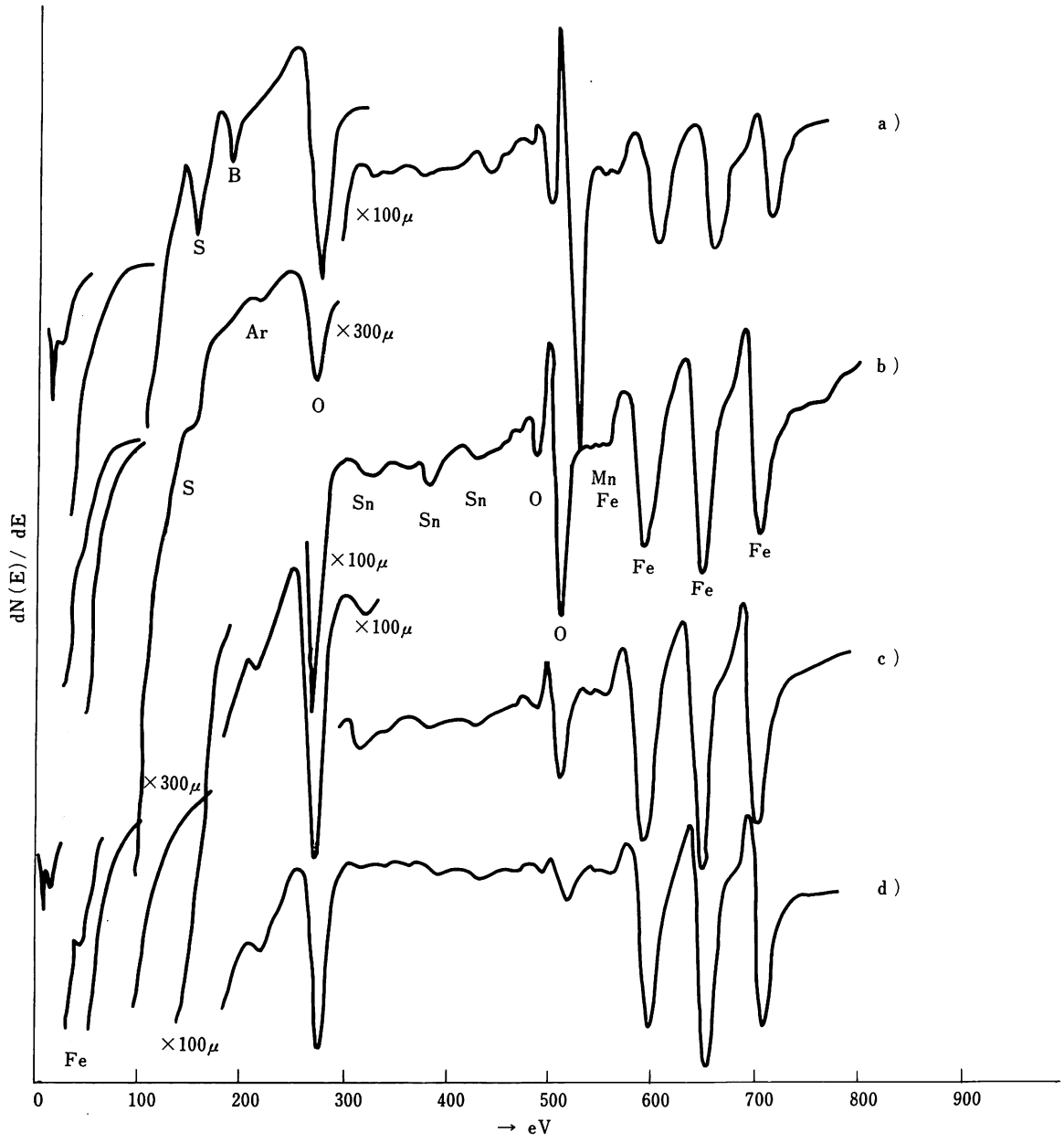

Fig. 1. Auger spectra from the fracture surface of 0·1%C-3%Mn-1%Sn steel (embrittled and broken in the air at −196°C) before and after sputtering of surface.
a) As fractured. b) After 20 atomic layers removed. c) After 40 atomic layers removed. d) After 60 atomic layers removed.

broken both in the air at liquid nitrogen temperature and in a high-vacuum chamber.

A specially designed low-temperature cleavage manipulator, which is shown in Photo. 1, was used in order to fracture a specimen in a high-vacuum chamber. The details will be described in another report[2]. After analyzing a given surface layer, the layer was removed by sputtering with Ar^+ ions and the next layer was analyzed.

Fig. 1a) shows the derivative of energy distribution function dN(E)/dE of electrons emitted from the intercrystalline surface of the specimen which was fractured in the air at liquid nitrogen temperature. The change of dN(E)/dE due to the sputtering by Ar^+ ion bombardment is also shown in Fig. 1b) -d). No peaks corresponding to tin appeared in the case of the as-fractured surface (Fig. 1a)). It is noted, however, that tin peaks were observable after about 20 atomic layers being removed by sputtering (Fig. 1b)), and decreased with further sputtering (Fig. 1c)-d)).

From these results, it is concluded that the qualitative analysis of tin segregated to the grain boundary can be successful even when the specimen is broken in the air, but the adsorption and surface oxidation prevent one from the accurate examination.

Fig. 2 shows dN(E)/dE of electrons emitted from the fresh intercrystalline surface of the specimen fractured in the vacuum chamber at the temperature of −160°C. All of specimens were fractured intergranularly, which was confirmed by scanning electron fractograph as shown in Photo. 2. The amount of segregated tin was obtained by the comparison of the tin peak height at the fracture surface with those obtained from the interior of the same specimen. This figure also shows absence of sulfur and oxygen peaks. The peak height ratio of tin to iron is shown in Fig. 3 as a function of distance from the fracture surface by sputtering off

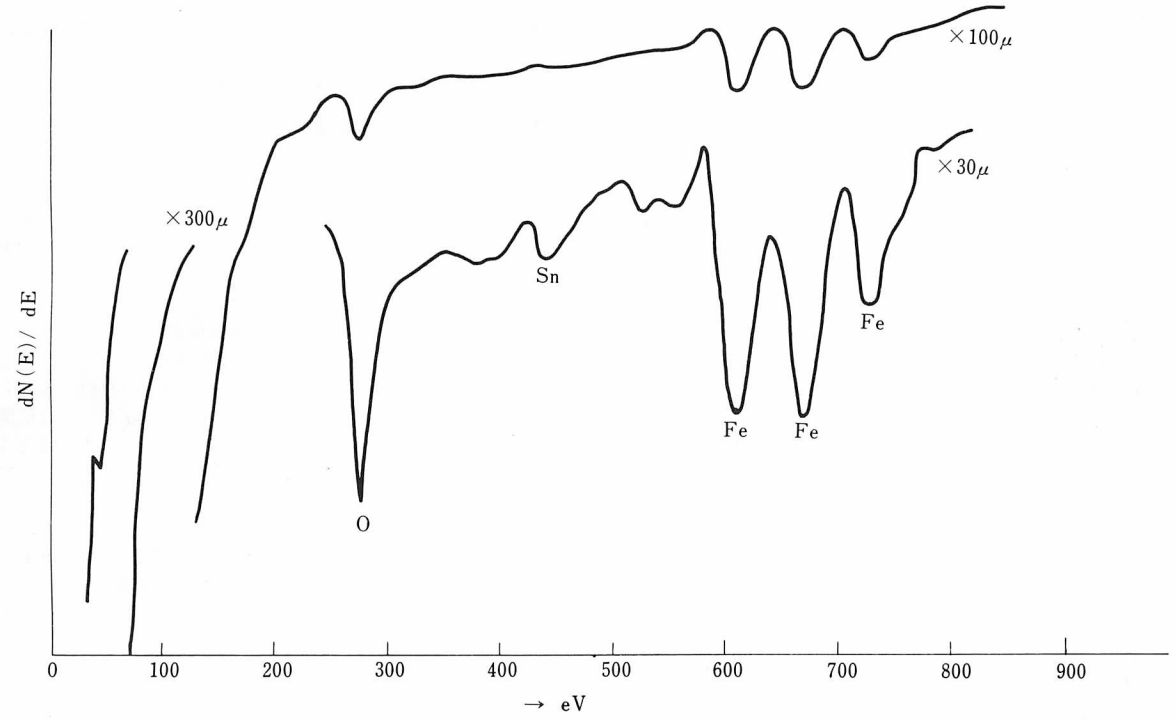

Fig. 2. Auger spectra from as-fractured surface of 0·1%C-3%Mn-1%Sn steel (embrittled and broken in the vacuum chamber at −160°C).

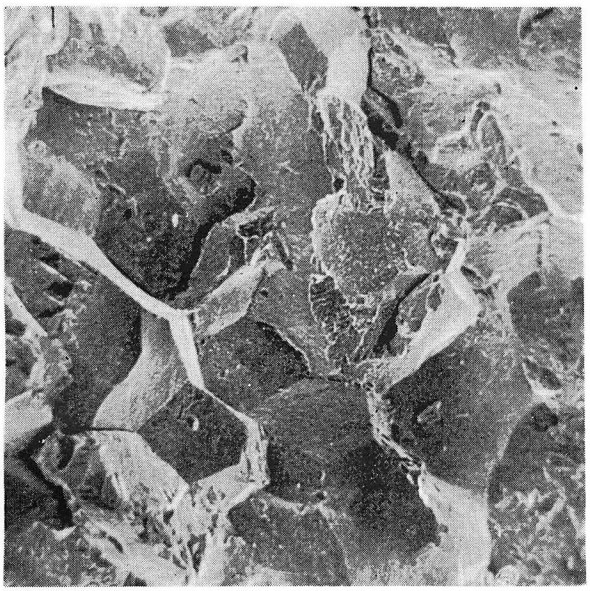

×100

Photo. 2. Scanning electron fractograph from Auger specimen, fractured at −160°C.

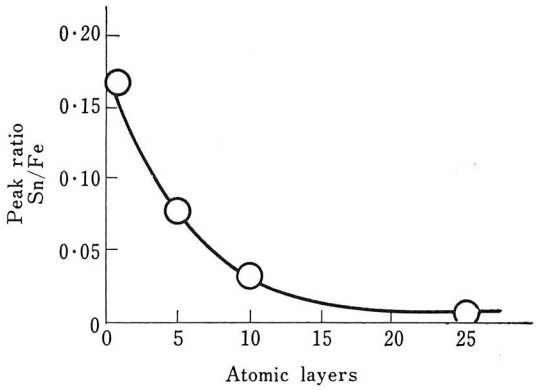

Fig. 3. Sn/Fe peak height ratio of the dN(E)/dE at various depths from the intergranular fracture surface of embrittled 0·1%C-3%Mn-1%Sn steel.

successive layers. If the peak height of the dN(E)/dE peak for each element is assumed to be proportional to the amount of the element present[3,4], it is concluded that tin is segregated to the grain boundaries at a concentration level about seven times that of the bulk in this experiment.

1) K. Nakayama, M. Ono and H. Shimizu: Presented at Int. Conf. on Solid Surface, 1971, Boston, U.S.A. To be published
2) To be published
3) D.F. Stein, A. Joshi and R.P. Laforce: Trans. ASM., **62** (1969), p. 776
4) R. Weber and A. Johnson: J. Appl. Phys., **40** (1969), p. 314

Authors' Response (J. Tanaka).

It is most interesting to detect the grain boundary itself with Auger analysis technique directly as Dr. Suzuki had demonstrated in his comment. However, it can be said that the role of the free surface as the segregation sites of impurities such as phosphorus, antimony, tin etc. is quite the same as the role of the grain boundaries. Therefore, there should be a clear qualitative relationship between the concentration of impurity atoms at the free surface and at the grain boundary. It seems that quantitative studies on the relationship between the free surface concentration and the grain boundary concentration is not meaningful at the present time, because of the accuracy of the Auger analysis technique. Qualitatively speaking, Auger analysis on the free surface can be still a good tool for grain boundary problems. For example, the result of Auger analysis on the free surface sometimes shows good correlation with mechanical properties of embrittled materials. Fig. 1 shows the

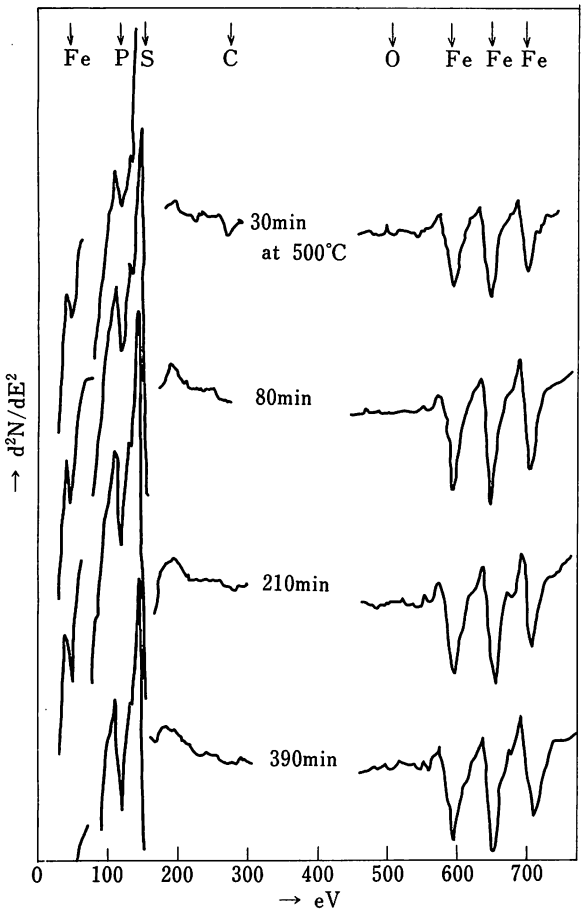

Fig. 1. Auger spectra from the free surface of 0·029%P-manganese steel, measured at 500°C.

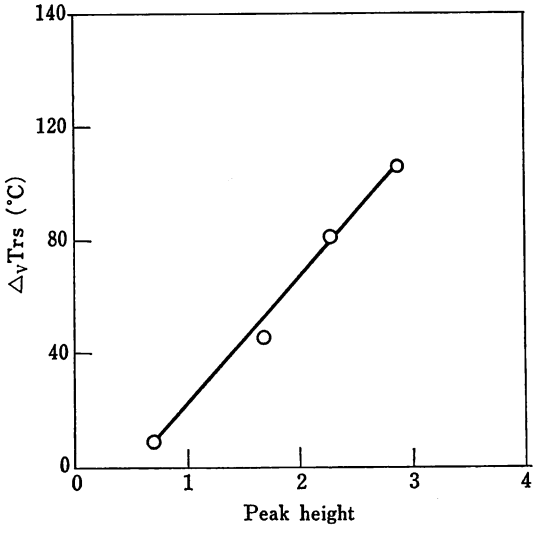

Fig. 2. Relationship between the variation of $_{V}$Trs (50% shear FATT) and peak height of the phosphorus spectrum.

variation of the phosphorus peak height of the Auger spectrum during isothermal holding at 500°C. This increase in the peak height corresponds very well to the increase of $_{V}$Trs (50% shear FATT) as demonstrated in Fig. 2. This means that the degree of embrittlement can be explained with the relative impurity concentration at the free surface.

調質高張力鋼の靱性におよぼす変態組織の影響

邦式立郎，寺崎富久長，大森靖也，大谷泰夫

榎並禎一（川崎製鉄技研）

(pp. 85-100)

邦武らは調質高張力鋼の靱性について研究し，焼入れ冷却速度を変えたとき，マルテンサイトに少量のベイナイトが混在するような冷却速度のところで最も低い遷移温度が得られることを示した．同様の結果は我々の研究室でも得られている．Fig. 1は板厚 7·5 mm の調質高張力鋼の板表面から板厚中心部までの各位置におけるエネルギー遷移温度を示す．焼入れ冷却速度は板厚表面部が最も早いが靱性の最も良好な位置は表面ではなくて少し板厚中心寄りである．この靱性の最も良好な位置は焼入れのままでマルテンサイトに少量のベイナイトが混在する位置に相当し，これより焼入れ冷却速度が早くても，遅くても遷移温度は高い．

このとき，走査型電顕による破面観察でもぜい性破壊の単位破面の大きさは，遷移温度の低い混合組織のほうが焼もどしマルテンサイト組織よりも小さいという傾向も確認されており，混合組織における良好な靱性の原因は主として組織の微細化によるという考えは妥当と考えます．

いっぽう我々は 5% Ni-0·5% Mo 鋼を用いて完全焼入れ-焼

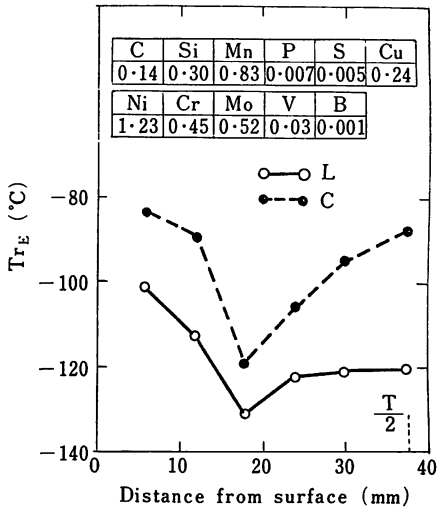

Fig. 1. Transition temperature of a 80kg/mm² high-strength steel in the longitudinal and through-thickness directions as a function of distance from the surface.

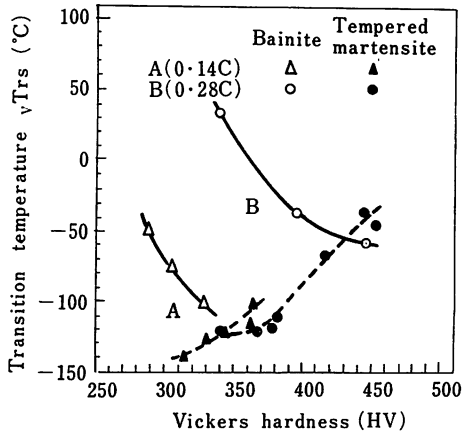

Fig. 2. Transition temperature of 5% Ni-0·5% Mo steel as a function of carbon content and structure.

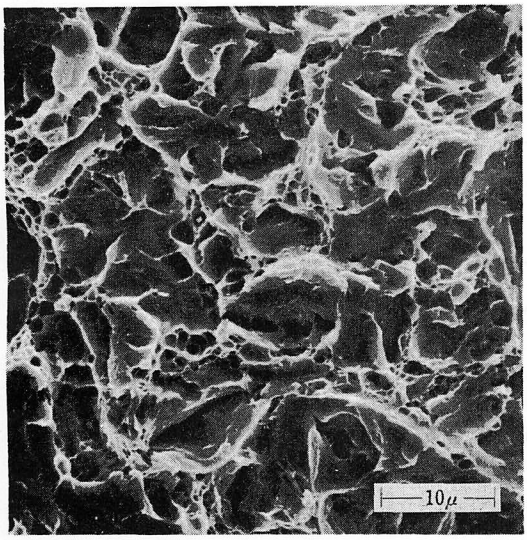

a) Tempered martensite.

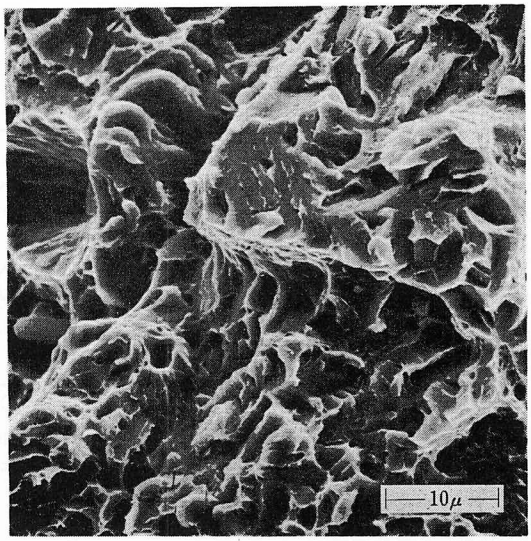

b) Bainite.

Photo. 1. Structure of fractured surface of 5% Ni-0·5% Mo steel.

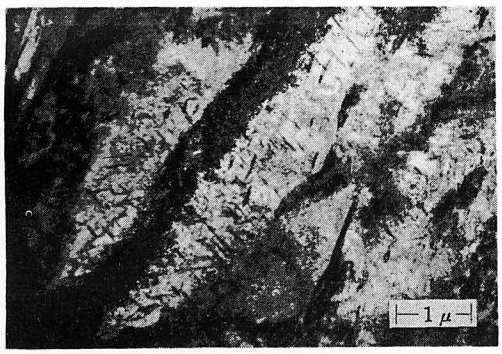

a) Tempered martensite.

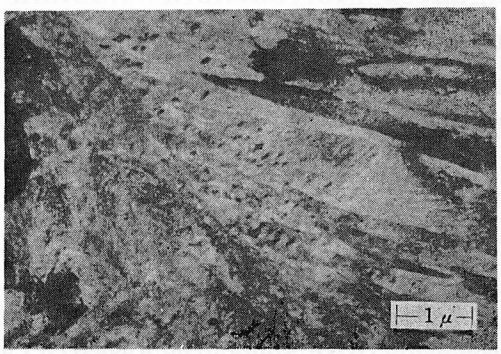

b) Bainite.

Photo. 2. Precipitates on fractured surface of 5% Ni-0·5% Mo steel.

もどし，恒温変態処理によりそれぞれ焼もどしマルテンサイト，ベイナイトの単一相からなる組織を得，これらの靱性を同じ硬さで比較した[1]．この結果を Fig. 2 に示す．B 鋼の高硬度側ではベイナイトの靱性が焼もどしマルテンサイトのそれより良好である．このときの破面観察では Photo. 1 に示すように単位破面の平均的大きさには差が認められず，Photo. 2 に示すように析出物の形態に差が認められた．このことから両者の靱性の差にたいしては析出物の形態の差が重要であると考えられる．以上のことから調質高張力鋼の靱性にたいしては破面の大きさと同時に析出物の形態も十分考慮する必要があると考えます．

参考文献

1) 腰塚，鎌田，船越： 鉄と鋼，57 (1971)，S 721，p. 379

著者回答

本研究の結果と合致する例として，板厚 75 mm の調質高張力鋼板の，板厚方向の各位置における遷移温度の測定結果を提示していただき，厚くお礼申し上げる．

さて，0·28%C-5% Ni-0·5% Mo 鋼の，低温変態ベイナイト（おそらく B III 型ベイナイトと考えられる）と，焼もどしマルテンサイトを等しい強度（HV≈450）において比較する時，前者のじん性が後者にくらべてややすぐれていることから，破壊の単位の大きさだけでなく，析出物（ここでは炭化物である）の形態も十分考慮する必要があろうと指摘されている．

著者らも，調質鋼のじん性が破壊の単位だけですべて決定されるとは考えていない．遷移温度の絶対値には，破壊の単位だけでなくて，他の因子も寄与するであろう（p. 99-100 の総括，11 参照）．これを例えば次のような表現によって表わすことができよう．

$$vTs = K + k \cdot \log(dc)^{-1/2}$$

K は，侵入型や置換型元素の固溶，炭化物の量や形態，転位密度などによって異なる値をとるであろう．従って破壊の単位が等しくても，他の影響因子が異なれば，遷移温度の絶対値は異なる筈である。著者らの種々の連続冷却変態組織についての実験において，Fig. 9 に示すように，遷移温度と破壊の単位の関係において，2 本のほぼ平行な直線が得られた。その一は，マルテンサイトや，マルテンサイトと B III 型ベイナイトの混合組織に対するものであり，他は主として B I 型ベイナイト〈高温における変態によって生じたベイナイト〉からなる組織に対するものであった．これは，この二つのグループの組織の間に，炭化物や，転位密度などの因子の大きさにおいて，やや顕著な相異があることを示唆するものであろう．

しかしながら，炭化物の量や存在形態など個々の因子が遷移温度に対しておよぼす影響は，いまだ定量的に明らかでなく，これを明らかにすることは今後の課題である．これを明らかにするには，破壊の単位を媒介として考察を進めることが必要であろう．そのような手がかりを与えるものとして，破壊の単位の測定は大切といえる．

Low-Carbon Bainitic Steel with High Strength and Toughness: T. Terazawa, H. Higashiyama, S. Sekino (pp. 101-117)

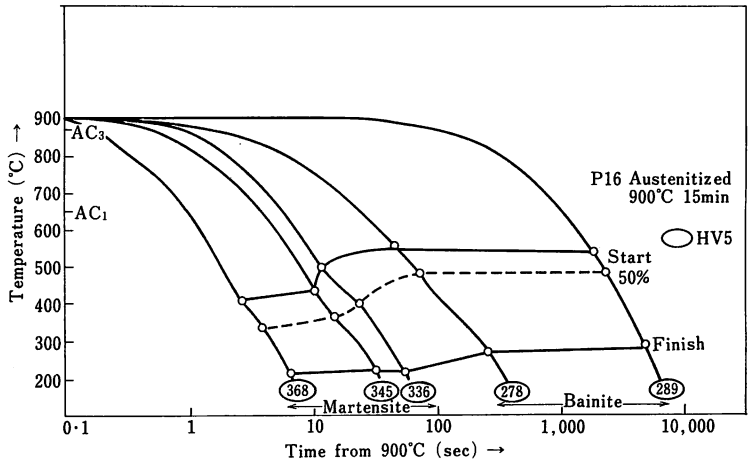

Fig. 1. CCT diagram for P16.

Manganese–Molybdenum–Niobium Acicular Ferrite Steels with High Strength and Toughness: Y. E. Smith, A. P. Coldren, R. L. Cryderman

(pp. 119-142)

A. Brownrigg (BHP Melbourne Research Laboratories).

I would like to make a few comments on the paper by Terazawa et al. on low-carbon bainitic steels, as similar work has been carried out at the B.H.P. Melbourne Research Laboratories in order to develop an as-rolled high-strength structural steel having similar properties to quenched-and-tempered steels. These steels, containing 0·03–0·06%C, 3·5–4%Mn and 0·5–0·8%Si have transformation curves which show an extensive flat topped bainite region (Fig 1). As described by Terazawa et al., the low-carbon bainite structure consists of small ferrite grains (as laths or blocks) with a high dislocation density and containing pools of martensite, occasionally twinned. As the transformation does not begin until below 550°C, it is unlikely that manganese or any other substitutional alloying element is rejected into the untransformed austenite, and the build up of carbon alone in these regions is probably responsible for their lower transformation temperature and different appearance. When the transformation temperature is depressed to lower temperatures, by increasing the cooling rate or the addition of more manganese, there is insufficient thermal energy for carbon diffusion and a low-carbon martensitic structure is obtained.

In contrast to the results of Terazawa et al. (in their Fig.1), niobium has been shown to have only a small effect on tensile properties of the low carbon bainitic steels. Fig. 2 shows the effect of finishing temperature on 28 mm plate for 3·5% Mn steels with and without niobium, which have a difference in ultimate tensile strength of only 2 kg/mm². The chemical compositions of these steels are given in Table 1.

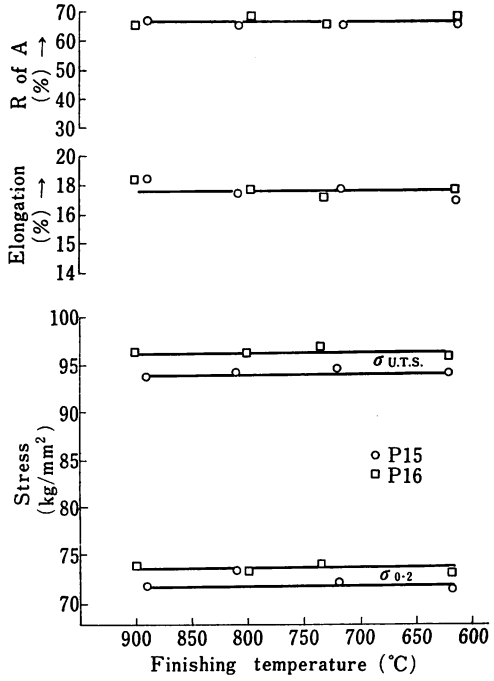

Fig. 2. Longitudinal tensile properties of 28 mm plate.

Table 1. Steel composition (wt%).

	C	Mn	Si	S	P	Cr	Ni	Nb
P15	0·055	3·54	0·66	0·022	0·010	0·17	0·13	<0·005
P16	0·058	3·53	0·69	0·025	0·011	0·17	0·13	0·042

In the niobium steel secondary hardening due to NbC precipitation occurs on tempering and a comparison of the hardening effect after different heat treatments shows that most of the niobium is in solution in the as-rolled condition (Fig. 3). Therefore, these results confirm that when the Bs temperature is lower than 600°C, strengthening by NbC precipitation is absent or only very slight[1]. The niobium in solution has no effect on the transformation behavior, and the CCT curve of the niobium-free steel is similar to that shown in Fig. 1. We are unable to confirm the existence of a manganese-niobium interaction, and consider the main

role of niobium is in retarding austenite recrystallization so that niobium steels can be rolled to higher finishing temperatures than niobium-free steels. Also as-rolled niobium steels can be slightly stronger because of the greater amount of reduction given to the unrecrystallized austenite. This strengthening effect is a type of ausforming process, where the strength of the steel is improved by the dislocations introduced into the unrecrystallized austenite on deforming at low finishing temperatures.

It is unusual that the authors' Fig. 1 shows no effect on manganese on yield strength in the niobium-free steels. We have confirmed other workers[2,3] results that the tensile properties of low carbon alloys are sensitive to the manganese

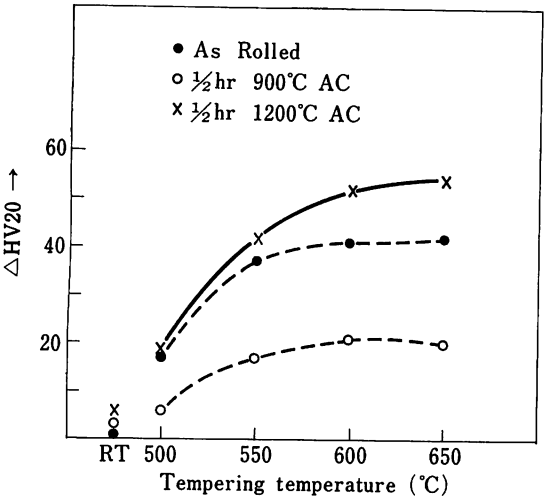

Fig. 3. Difference in hardness between P15 and P16 as a function of tempering temperature.

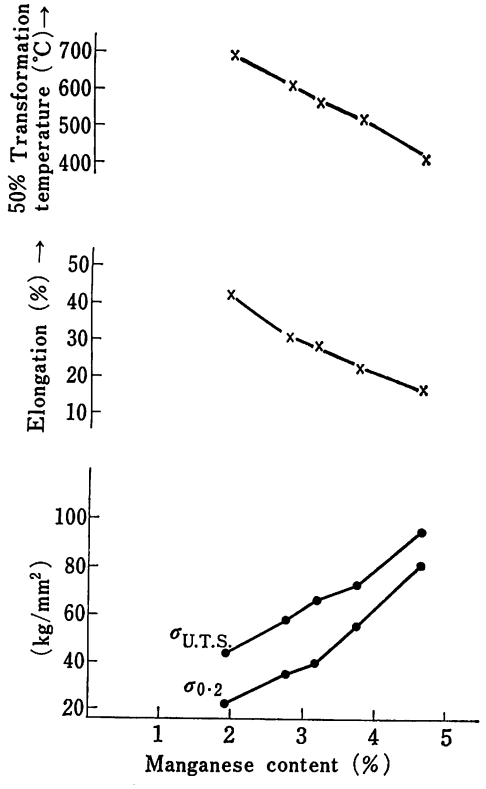

Fig. 4. Properties of 0·04%C-0·3%Si alloys, normalized 1/2 hr at 950°C.

content, and Fig. 4 shows the effect of manganese on the tensile properties of alloys containing 0·04%C and 0·3%Si, normalized from 950°C. In these specimens only the 2% Mn alloy transformed to equiaxed ferrite, while the others had low-carbon bainite structures. The increase in strength is due to two factors: solid solution hardening by manganese and the increased dislocation density of the bainite ferrite as the transformation temperature is lowered. As the former contribution is low (4·5–9kg/mm² per 1% Mn estimated from work on carbon free iron-manganese alloys[4,5]) the main effect of manganese is to provide substructure strengthening by suppressing the equiaxed ferrite reaction, and this can be achieved at 2·5% Mn (with 0·04%C). However at manganese contents up to 3% the properties are still somewhat sensitive to cooling rate and equiaxed ferrite can be produced if the cooling rate is slow enough. Addition of other substitutional alloying elements, such as silicon or molybdenum, to the 3·5% Mn base can provide further solid solution strengthening and also substructure strengthening by lowering the Bs temperature. An important feature of the tensile results of Fig. 4 is the PS/UTS ratio which increases from 0·5 at 2% Mn to 0·85 at 4·6% Mn. These ratios are lower than those for specimens water quenched to give low-carbon martensite, where a value of 0·9 is commonly observed.

From initial work it would appear that there is considerable scope for the development of a series of low-carbon steels containing manganese as a major alloying element in order to achieve strengths greater than those attainable by ferrite-pearlite structures at reasonable cost.

1) A.P. Coldren, R.L. Cryderman and M. Semchyshen: Steel Strengthening Mechanisms. Symposium sponsored by AMAX, p. 17
2) G.M. Chubinidze and F.N. Tavadze: Metal Science and Heat Treatment, (1967), p. 643
3) A. Mercier and R. Lêvêque: Rev. Met., **67** (1970), p.413.
4) Y.I. Matrasov and V.I. Krasnykh: Metal Science and Heat Treatment, (1969), p. 237
5) W.P. Rees, B.E. Hopkins and H.R. Tipler: JISI, **169**, (1951), p. 157

I. Kozasu (Nippon Kokan K. K. Technical Research Center).

Mr. Terazawa and his coauthors discussed beneficial effects of alloying copper and nickel to their low-carbon bainitic steel. On the other hand, Dr. Smith and his coworkers stressed the importance of molybdenum as an alloying element in their acicular ferrite steels. Since all of these steels seem to be essentially identical in microstructure, it may be of some interest to compare the effects of copper, nickel, chromium and molybdenum on the mechanical properties of low-carbon high-manganese niobium steels. Table 1 is a part of the results obtained at the writer's laboratory by multiple regression analysis on laboratory-melted steels with similar basic compositions as the above. The steels were air melted in a 50 kg induction furnace. The final rolling was carried out on 60 mm thick blocks to give a finished thickness of 12 mm with controlled rolling of 50% of the total rolling reduction below 900°C. Mechanical testing was done in the as-rolled state and also after heating to 650°C for 30 min. It is apparent from the results that, in respect to tensile strength, manganese and molybdenum had the same strengthening effect and that the effect of copper and nickel was a third to half that of manganese or molybdenum compared at the same alloying content. The effect of these alloying elements on 50% FATT was not conclusive although a slight rise in transition temperature was noted for molybdenum.

Table 1. The effect of alloying elements on mechanical properties of 0·06%C–2·0%Mn–0·05%Nb steels (nominal composition) calculated by multiple regression analysis (N=36).

Change of property	State	Mn	Cu	Ni	Cr	Mo
(Range (wt %)		1·8-2·3	0-1·0	0-1·0	0-1·0	0-0·5
ΔTS	As rolled	19·8**	8·2**	10·3**	16·6**	26·4**
(kg/mm²/1%)	650°C×30min	26·0**	8·0**	9·7**	10·2**	20·0**
Δ50% FATT (°C/1%) of full size Cv	As rolled	ns	ns	-17·0+	-9·3+	12·1+
	650°C×30min	ns	ns	ns	ns	38·5*

Significance limit ** 99% * 95% + 90% ns <90%

J.L. Mihelich (Climax Molybdenum Company).

The paper by Mr. Terazawa and his coauthors as well as the one by Dr. Smith and his associates focus on a new metallurgical concept: low-carbon bainitic/acicular ferritic steels, which possess high strength and favorable toughness in the as-rolled condition. Although each takes a somewhat different alloying route — low-carbon high-manganese plus molybdenum or nickel-copper-chromium — similar acicular structures, more typical of lower than upper bainite, have been achieved. I believe that Mr. Kozasu's quantitative results on the effect of molybdenum, nickel, copper and chromium (presented as a discussion) demonstrate the relative metallurgical importance of these elements in the acicular ferritic structure.

As pointed out by the authors and subsequently reinforced by the discussion to this series of papers, the low-carbon bainitic steels by virtue of their excellent combination of strength, toughness and weldability are considered especially attractive for natural-gas transmission pipe lines being installed in semi-arctic or arctic regions. In addition to the over 65 km of manganese-molybdenum-niobium acicular ferrite X-65 spiral-welded linepipe discussed in the paper by Dr. Smith and his associates, IPSCO, in Western Canada, has delivered approximately 6 km of X–70 pipe applying this basic composition. Similarly, X-75 and X-80 pipe appear to be feasible with this approach.

M.R. Krishnadev (Université Laval Faculté des sciences).

First let me congratulate Dr. Smith and his associates on carrying out an excellent piece of work. I would like to call the author's attention to the following facts:

(1) The authors state in their paper that silicon serves no useful purpose in the steel beyond its normal deoxidation function. Tither and Kewell, however, have observed that the addition of 0·7%Si improves the impact properties of carbon-manganese-niobium steels[1].

(2) Recently it has been observed[2] that an improvement in strength may be realized in nickel-copper-niobium steels by warm working. Is it possible and practical to enhance the strength of these carbon-manganese-molybdenum-niobium steels by warm working?

1) G. Tither and J. Kewell: JISI, **208**, (1970), p. 686
2) E. Snape: Met. Trans., **1**, (1970), p.1375

M.J. May (The British Steel Corporation, Corporate Laboratories).

I would agree with the authors, Y.E. Smith, A.P. Coldren and R.L. Cryderman, that acicular ferrite structures have the greatest potential for providing combinations of strength and toughness, making use of a low-carbon acicular transformation product coupled with a fine grain size and high dislocation density that can be subsequently hardened on tempering by the precipitation of a fine dispersion of alloy carbides.

It is to this objective, as many of you are aware, that work in recent years at the BSC Corporate Laboratories (formerly Bisra) has been directed, through controlled rolling followed by direct quenching. Tither and Kewell[1-3] have studied the influence of alloying additions to a 0·07–0·10% C–1·5% Mn base on the mechanical properties of steels directly quenched after controlled rolling to finishing temperatures of 950°C and 750°C with those obtained by reheating to 950°C and quenching. Alloying additions covered were niobium, vanadium, silicon, aluminum and copper in various combinations and at various levels. Depending on the hardenability, the structures ranged from acicular ferrite, Widmanstätten ferrite and upper bainite to martensite.

The addition of niobium (or vanadium) resulted in a slight reduction in hardenability in the reheated quenched state as the NbC and V(CN) were not completely redissolved on reheating for one hour at 950°C. This prevented, on reheating, austenitic grain growth giving grain-size control but gave rise to a greatly reduced precipitation-strengthening response on subsequent tempering. A typical structure is shown in Photo 1. On the other hand, directly quenching from the rolling mill at a finishing temperature of 950°C gave an acicular ferrite structure with niobium in solution,

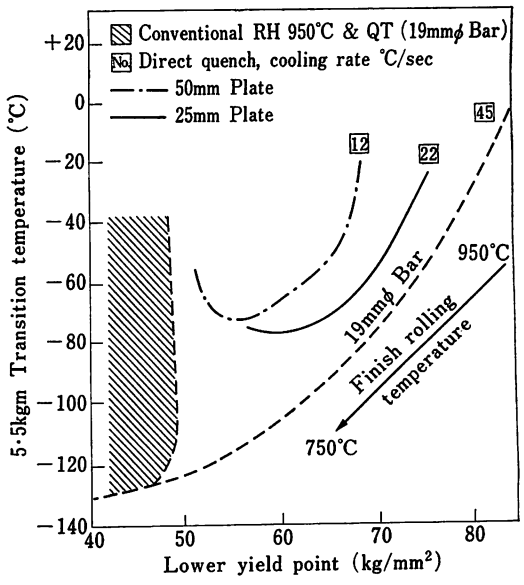

Fig. 1. Summary of the quenched-and-tempered mechanical properties obtained in low-carbon low-alloy steels.

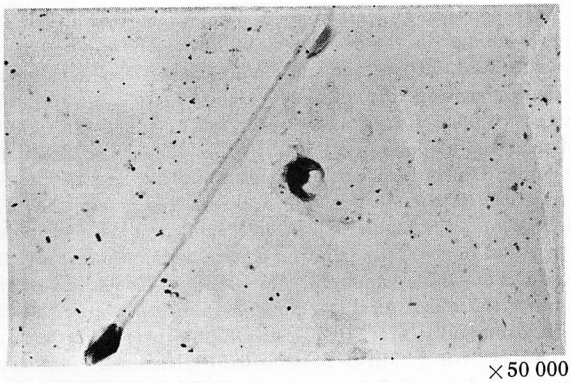

×50 000

Photo. 1. Precipitate of Nb(CN) on prior austenite grain boundaries.

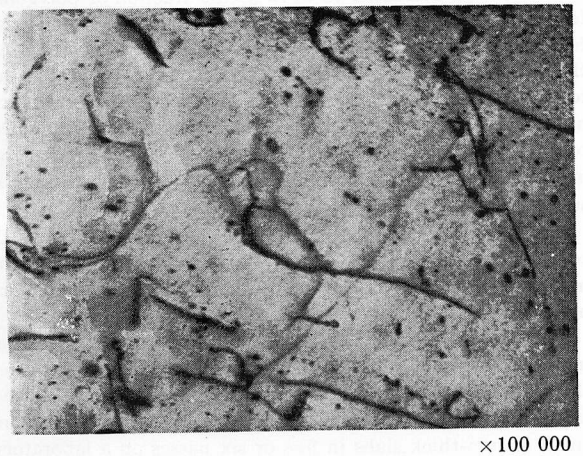

×100 000

Photo. 2. Precipitate of Nb(CN) on dislocations.

which on subsequent tempering showed a very fine dispersion of Nb(CN) (50–100Å particle size) leading to effective pinning of dislocations as shown in Photo. 2. Such precipitation would normally have a marked effect on the ductile-brittle transition temperature; however, the refinement in grain size obtained by controlled rolling and direct quenching tended to counteract this effect.

For maximum effective use of alloying additions for strengthening, it is necessary to minimize precipitation in the austenite or during transformation and to ensure this it is necessary to cool sufficiently fast after final rolling. The combination of properties that can be obtained is summarized in Fig. 1, and shows that very attractive combinations of properties can be realized in relatively thick sections.

The acicular ferrite route, whether it be achieved by controlled processing or modification of transformation characteristics by alloying additions such as molybdenum, nickel, copper and boron, has a further advantage in that "as quenched" the steel is of low strength with very good toughness and therefore readily formable, which is not true with the conventional reheat quenched-and-tempered steels.

In conclusion it would appear to us that acicular ferrite structures provide the means of obtaining optimum combination of strength and ductility and for several current specifications for pipelines it will be necessary to utilize controlled processing (finishing temperature and cooling rate) together with controlled alloy additions to obtain the high levels of strength and toughness required. Alloying additions certainly provide flexibility in the cooling requirements after rolling but because of economics and welding requirements (low carbon equivalent) it is preferable to utilize water, i.e. fast cooling, rather than alloying additions as far as possible.

1) J.J. Irani and G. Tither: ISI Special Report, **104** (1967), p. 135
2) G. Tither and J. Kewell: JISI, **208**, (1970), p. 686
3) G. Tither, J. Kewell and M.G. Frost: Paper presented at conference on Effect of Second Phase Particles on Mechanical Properties, Scarborough (1971)

Authors' Response (T. Terazawa).

As for the strengthening effects of copper, nickel, chromium and molybdenum on the low-carbon high-manganese niobium steels, our data coincide with Mr. Kozasu's work for the most part. It must be pointed out that the strengthening effects of these elements can be expected only on the steels with high manganese content, more than 1·8% or so. For example, as shown in Table 1,

Table 1. The effects of chromium additions on the mechanical properties of 0·05%C–1·0%Mn–0·05%Nb steels.

Steel	Chemical composition (%)								State	Yield point (kg/mm²)	Tensile strength (kg/mm²)	Impact properties	
	C	Si	Mn	P	S	Nb	Al	Cr				vTrs (°C)	vEo (kgm)
A	0·05	0·68	1·02	0·005	0·008	0·05	0·02	1·38	As rolled	40·8	51·0	—26	35·8
									625°C Tempered	41·6	50·7	—28	32·1
B	0·05	0·68	1·03	0·005	0·008	0·05	0·02	1·96	As rolled	40·9	51·3	— 5	26·4
									625°C Tempered	40·9	50·9	—28	25·8

16mm thick plate, vacuum melted in 100 kg furnace, finished at 850°C after controlled rolling.

Table 2. The effects of molybdenum additions on the mechanical properties of 0·05%-2·3%Mn–0·05%Nb steels.

Steel	Chemical composition (%)								State	Yield point (kg/mm²)	Tensile strength (kg/mm²)	Impact properties	
	C	Si	Mn	P	S	Nb	Al	Mo				vTrs (°C)	vEo (kgm)
C	0·05	0·76	2·32	0·005	0·010	0·05	0·02	0·25	As rolled	57·2	81·0	−30	11·7
									625°C Tempered	65·6	78·4	−14	11·2
D	0·05	0·75	2·33	0·006	0·010	0·05	0·03	0·47	As rolled	53·5	84·9	+ 9	4·3
									625°C Tempered	69·8	84·5	+26	5·8

16mm thick plate, vacuum melted in 100 kg furnace, finished at 850°C after controlled rolling.

the strengthening effect of chromium is scarcely observed in the low manganese range, in spite of a large chromium addition. As for the effects of molybdenum on the toughness of these steels, our data (shown in Table 2) suggest that the addition of molybdenum may be more detrimental than Mr. Kozasu's results.

Authors' Response (Y.E. Smith, A.P. Coldren, R.L.Cryderman).

It is difficult to comment on the findings of Mr. Kozasu without more detailed information on the particular compositions, processing, actual levels of strength and toughness, and microstructures. In general, his conclusion regarding the influence of molybdenum on strength is in agreement with our results and his observed influence of molybdenum on toughness (transition temperature) is in disagreement with our results. One serious problem with the type of comparison that is being made by Mr. Kozasu is that it assumes that each of the alloying elements studied influences transformation characteristics in the same way but in differing degrees. The effects of the various alloying elements on transformation characteristics are, however, not the same. Most important to the control of both strength and toughness is the effect of delaying transformation that occurs above 700°C. Molybdenum is much more effective than the other elements in delaying this transformation.

An example of the effectiveness of molybdenum, in comparison with nickel, copper and chromium, in controlling transformation is the IPSCO experience. Prior to the introduction of the manganese-molybdenum-niobium steel at IPSCO, a combination of nickel, chromium and copper was being used along with manganese, vanadium and niobium for the manufacture of X-65 skelp. Three major changes in the properties of the product resulted from the shift to the manganese-molybdenum-niobium steel: (1) the minimum yield strength was increased to qualify the product as an X-70 steel; (2) the toughness was increased in terms of both Charpy V-notch shelf energy and fracture-appearance transition temperature; and (3) both strength and toughness properties were distributed within a narrower range than for the previous product, i.e., the production process was easier to control. This last point is illustrated by Table 1 presenting the results of a statistical analysis performed by the Quality Control Department of TransCanada PipeLines, Ltd. on data from 457 sections of pipe representing 457 heats. The average tensile and impact properties are presented in Table 1, along with the corresponding standard deviations. This is a representative sampling from about 65 km of 107cm-diameter pipe. For any given property, 95% of the product will fall within a range of (mean±2 (standard deviation)); therefore it is obvious by the small numbers in the standard deviation column that this product was very homogeneous.

In response to Dr. Krishnadev, Tither and Kewell reported improvements in the toughness of both carbon-manganese-niobium and carbon-manganese-vanadium steels as a result of increasing the silicon from 0·4 to 0·7%. The steels contained 0·08–0·10%C and were finish rolled at 950°C, quenched at a cooling rate of 9°C/sec or higher and tempered at either 600 or 675°C. Although they did not define the mechanism of the effect of silicon on the toughness, they did observe that the higher silicon level increased the fraction of ferrite (as opposed to bainite) in the microstructure of the carbon-manganese-vanadium steels. Our recent investigations of the effect of silicon included silicon levels of 0·05, 0·17, 0·30 and 0·42%. These silicon additions were made to a 0·05%C–1·9% Mn–0·24%Mo–0·07%Nb steel that was finish rolled to 12·7 mm plate at 870°C and air cooled at about 2°C/sec. The microstructure of the 0·05%Si steel was acicular ferrite with less than 10% polygonal ferrite. As the silicon increased to 0·42%, the fraction of polygonal ferrite increased to over 60% and somewhat larger polygonal ferrite grains were present. It has generally been observed that as coarse polygonal ferrite appears in these steels, the toughness is reduced. Presumably, the loss of hardenability brought about by the higher silicon level could be regained by the addition of roughly 0·05%Mo or 0·1%Mn but the more practical approach would be simply to leave the silicon out.

We have studied the data published by Snape with considerable interest and have considered investigating the influence of warm working on the manganese-molybdenum-niobium steels although no work has yet been done.

The oral question as to whether the manganese-molybdenum-niobium steel can be produced as plates thicker than 13 mm may be answered by the recently obtained laboratory data of Table 2. These plates were rolled from small 85 mm-thick slabs in five or six passes on a laboratory mill, finished at 815°C and air cooled. The toughness of these plates is relatively good but it is believed that commercial rolling of plates to the same thickness would produce even lower transition temperatures at the same strength levels because of the higher reduction ratios that result from greater slab thicknesses. However, slightly increased hardenability (alloy content) may be required in the commercial plate to compensate for the slower cooling rates of large plates.

We would like to thank Dr. May for his contribution. We certainly agree with his conclusions as to the advantages of an acicular ferrite structure. The economics of water quenching vs alloying depend to a large degree on the product in question and the individual mill. Certainly, from a commercial standpoint, we feel the flexibility and reliability conferred by alloys have a beneficial influence on overall economy.

Table 1. Statistical analysis of 457 pipe sections of 107 cm diameter 9·4 mm-thick X-65.*

Property	Mean	Standard deviation
Yield strength (kg/mm^2)	52·9	1·8
Ultimate tensile strength (kg/mm^2)	65·1	2·45
Yield/tensile ratio	0·81	0·02
Elongation (%)	33	2·0
Charpy energy at −4°C (kgm/cm^2)**	20	3·0
Charpy FATT (50%) (°C)**	−43	8
BDWTT (50% shear transition) (°C)	−44	11

* Information from the Quality Control Department of TransCanada PipeLines, Ltd.
** 2/3 size specimens.

Table 2. Mechanical properties in the longitudinal direction of 19 and 25mm-thick plates of 0·06%C–2·0%Mn-Mo-Nb steels.

Steel	Thickness (mm)	Condition	0·2% Yield strength (kg/mm²)	Charpy V-notch test	
				energy at −18°C (kgm/cm²)	50% shear FATT (°C)
0·35% Mo - 0·05% Nb	19	As rolled	47·8	20·7	−43
		Aged 620°C× 1 hr	59·9	29·5	−48
0·29% Mo - 0·09% Nb	19	As rolled	46·0	26·8	−57
		Aged 620°C× 1 hr	56·2	30·7	−57
	25	As rolled	45·2	19·0	−43
		Aged 620°C× 1 hr	56·2	27·1	−34

Low-Temperature Brittleness of Iron and Steels:

K. Kitajima (pp. 143-156)

S.Nagashima (Nippon Steel Corporation, Fundamental Research Laboratories).

It is well known that the 9%Ni steel is the only ferritic steel that has an excellent toughness at low temperatures and can be used safely even at temperatures as low as −196°C. However, because of the deficient nickel supply, the high nickel content makes the steel very expensive. Consequently, development of a more economical steel with the same low-temperature characteristics as the 9% Ni steel has been desired.

In the present comment, the author would like to describe briefly the development of a new steel for low-temperature use, based on the results of investigations clarifying the factors that control the low-temperature toughness of the 9%Ni steel[1-4].

1. 9%Ni steel

In general, the 9%Ni steel is used in the quenched-and-tempered as well as in the normalized-and-tempered condition. Fig. 1 shows the relation between the Charpy impact value at −196°C and the tempering temperature of 9%Ni steel. Data at room temperature and also −145°C were added to this figure. It is clear that the steel shows excellent impact values higher than 10 kgm/cm² when it is tempered at appropriate temperatures, such as those ranging between 500 and 600°C. But, the impact values are extremely low with tempering temperatures lower than 500°C and also at temperatures higher than 600°C.

The reason why the steel tempered at temperatures lower than 500°C shows inferior impact energy is explained well by normal temper embrittlement. This conclusion follows from a study on the influence of cooling rate after tempering on the impact energy of steels as well as microfractographic examinations.

The embrittlement of steels tempered at temperatures higher than 600°C is explained as being caused by the instability of austenite islands formed during tempering.

The low-temperature toughness of austenite islands

The role of the austenite islands formed by tempering 9% Ni steel has been considered to be as follows[1]:

a) The austenite islands act as sinks for impurity atoms during the scavenging process through tempering.

b) These austenite islands act as shock absorbers since fcc alloys have an excellent toughness even at low temperatures. Nevertheless, it is questionable from Fig. 2 and 3 that the austenite islands act as shock absorbers in the Charpy impact tests. These figures show mechanical properties and the volume fraction of residual austenite as a function of tempering temperature. It is evident at room temperature

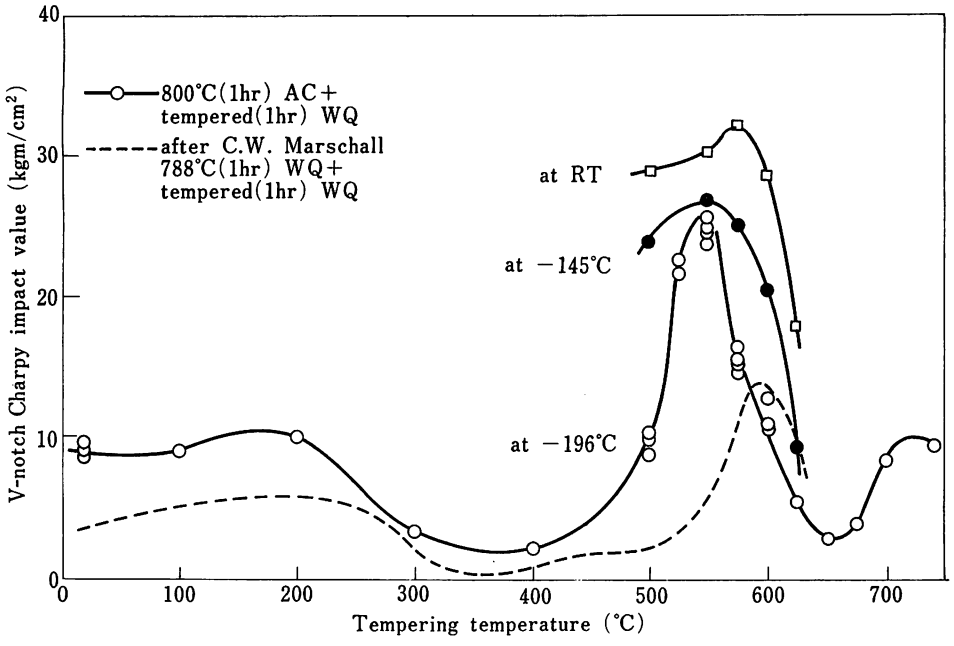

Fig. 1. Effect of tempering temperature on the Charpy impact value of 9% Ni steel.

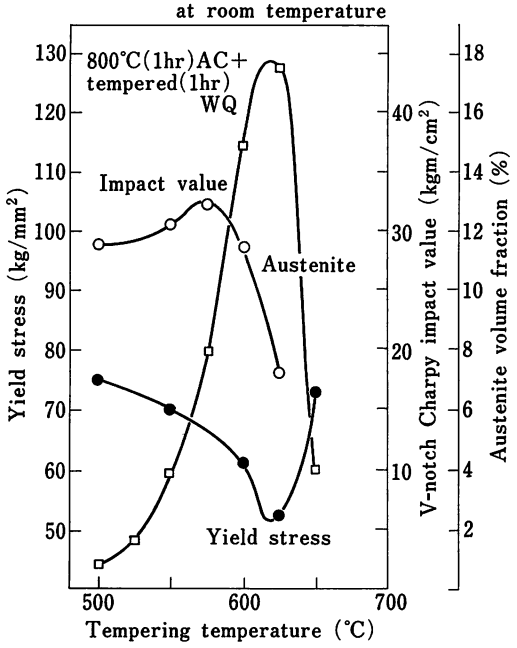

Fig. 2. Effect of tempering temperature on the mechanical properties and volume fraction of austenite in 9% Ni steel, at room temperature.

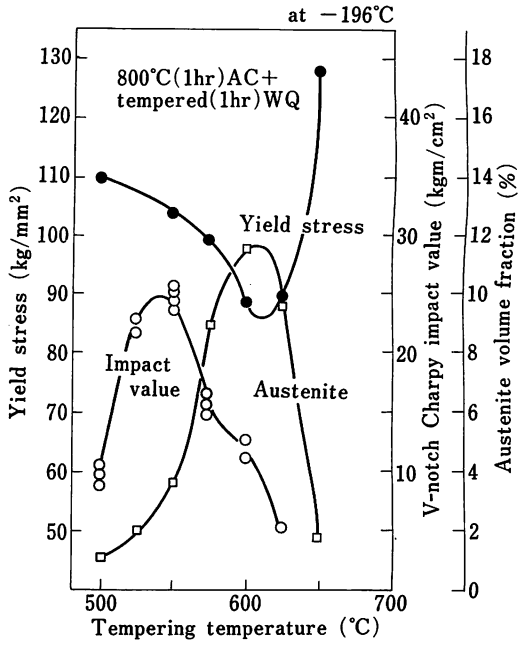

Fig. 3. Effect of tempering temperature on the mechanical properties and volume fraction of austenite in 9% Ni steel at −196°C.

as well as at −196°C that the tempering temperatures showing the peak of impact energy are different from those of the maximum volume fraction of austenite[3]. This shows clearly that the austenite islands are not always effective in producing good toughness.

The austenite islands were extracted electrolytically from steels tempered at various temperatures and then the chemical composition was determined with the results listed in Table 1[2,5]. The main chemical composition of the steel itself is also shown. It is surprising that alloying elements such as nickel, manganese and copper are enriched in the austenite phase to such a degree during tempering. The carbon content, however, is questionable because the cementite phase was mixed with the extracted residues.

Charpy impact tests were performed on an austenitic steel having a composition similar to that of the austenite islands formed by tempering at 600°C for one hour. Photo. 1 shows the section of the notch root of the Charpy specimen; the dark etched region is martensite transformed by impact deformation at −196°C[3]. From this photograph it is obvious that the austenite islands formed in 9%Ni steel during tempering are not always stable during impact deformation.

The factors controlling the low-temperature toughness of 9%Ni steels

When the steel is air cooled from 800°C, it has a mixed microstructure of martensite and bainite. A tempered specimen of this steel has a fairly fine microstructure, as

Table 1. Chemical compositions of electrolytically extracted residues (%) from heat-treated 9%Ni steel.

Heat treatment (tempering)	Residue (%)	Volume of cementite in residue (%)	C	Fe	Ni	Mn	Cu
400°C× 1 hr	0·85	—	7·48	57·7	7·73	1·96	2·56
× 8 hr	0·98	—	6·54	59·1	7·55	2·29	2·95
500°C× 1 hr	1·63	50	5·7	62·8	12·20	3·92	5·22
550°C× 1 hr	3·10	19	2·75	62·6	16·90	3·46	3·46
× 8 hr	5·28	8	1·79	64·5	19·28	3·08	2·57
600°C× 1 hr	2·21	16	4·1	61·5	15·70	3·13	2·94
× 8 hr	1·54	5	5·0	50·2	18·20	1·86	3·71
650°C× 1 hr	0·60	—	10·5	30·9	15·10	2·38	3·79
× 8 hr	0·51	—	12·1	27·9	13·23	2·49	4·68

Chemical composition of 9% Ni steel (wt%)

C	Si	Ni	Mn
0·09	0·26	9·60	0·72

shown in Photo. 2, with excellent impact energy at low temperatures[3].

On the other hand, when slowly cooled from 800°C at a rate such as 120°C/hr, this steel has a microstructure composed of ferrite and cementite. The microstructure after tempering shows a rather coarser ferrite grain as indicated in Photo. 3[6]. Such slowly cooled specimens give poor low-temperature toughness regardless of the tempering treatment. These experiments show that in order to obtain excellent low-temperature toughness, it is not sufficient to have a ferritic matrix containing 9%Ni but a uniform microstructure composed of fine ferrite and uniformly dispersed fine carbides as shown in Photo. 2 is necessary. The following conclusion is deduced from the relation between Charpy

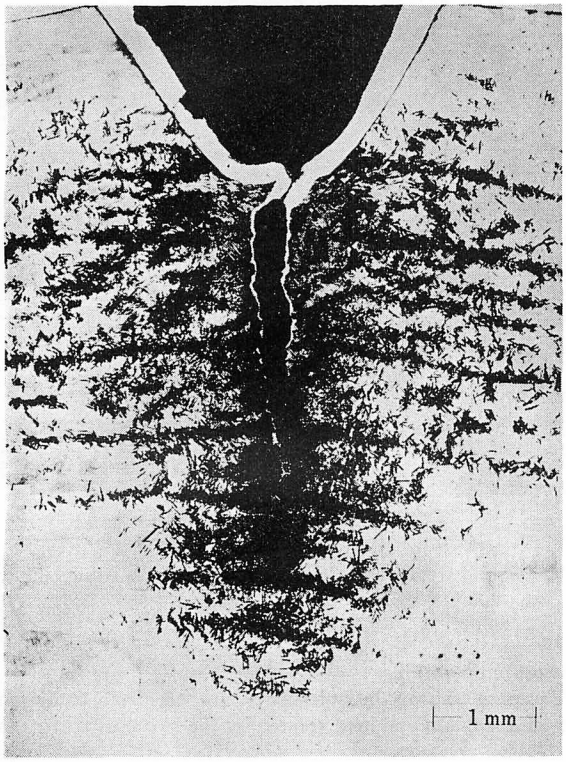

Photo. 1. Martensite phase (dark etched zone) formed by impact deformation at -196°C. The chemical composition of steel was 0·4%C–3·0%Mn-20%Ni.

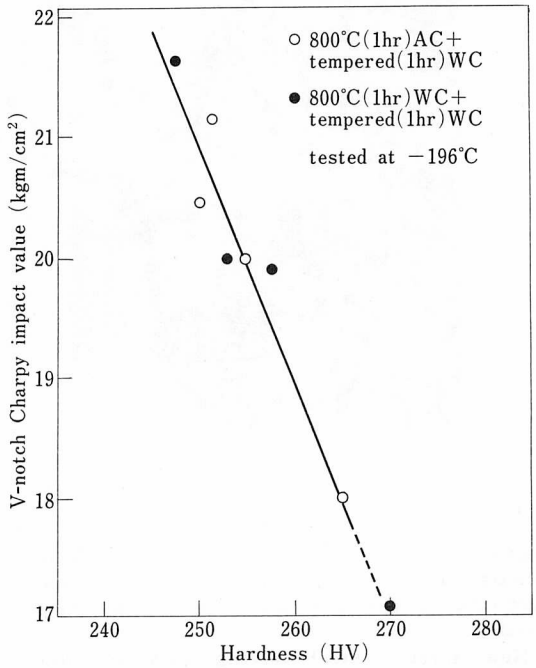

Fig. 4. Relation between Charpy impact value and the hardness in heat-treated 9%Ni steel.

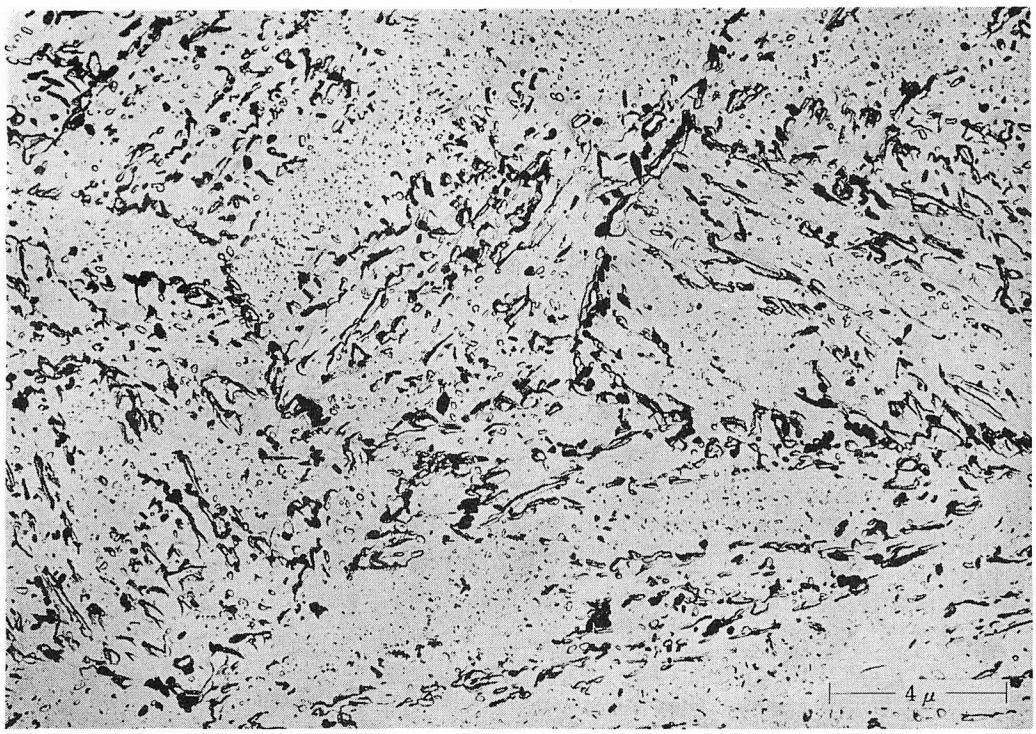

Photo. 2. Electron micrograph of 9%Ni steel air cooled from 800°C and tempered. The chemical composition of the steel was 0·1%C–0·8%Mn-9%Ni. The heat treatment was 800°C×1hr AC+550°C×1hr WQ.

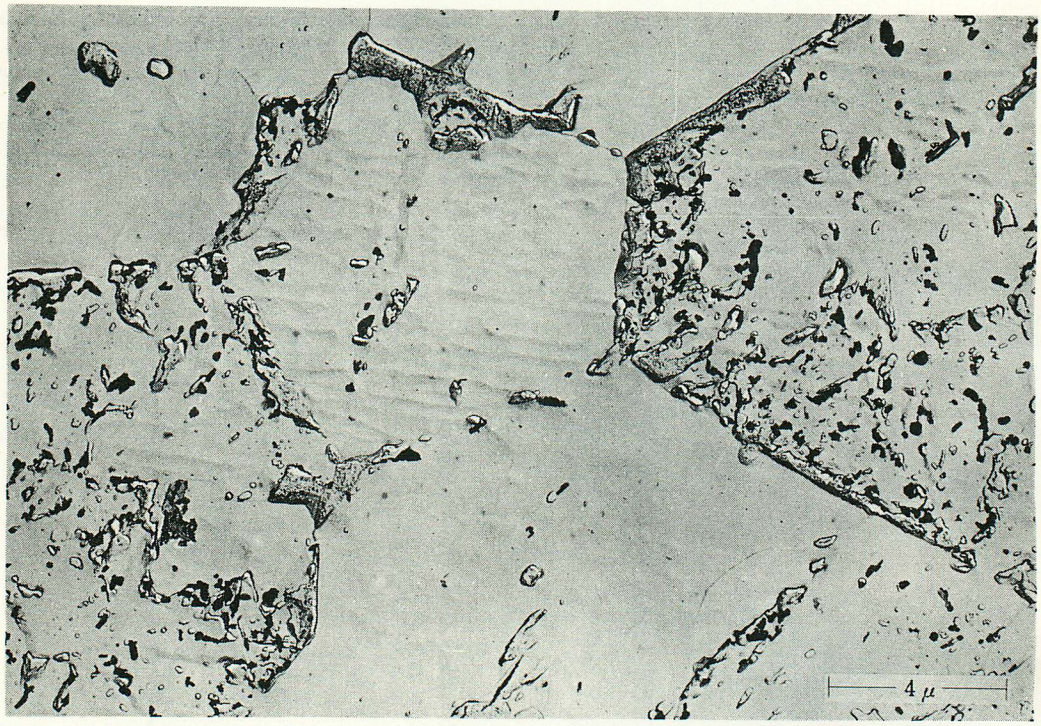

Photo. 3. Electron micrograph of 9% Ni steel slow cooled from 800°C and tempered. The chemical composition of the steel was 0·1%C–0·8%Mn–9%Ni. The heat treatment was 800°C × 1hr, cooled at 2°C/min, +550°C × 1hr WQ.

impact energy and hardness shown in Fig. 4: Higher tempering temperatures are a profitable means of obtaining good impact values to the extent that temper embrittlement does not occur.

2. New ferritic steel having excellent low-temperature toughness

In the investigation on the relation between microstructure and the low-temperature toughness of 9%Ni steel, the following controlling factors were determined[2,3]:

a) Grain refining of the ferritic matrix by formation of finely dispersed austenite islands in the process of tempering.

b) Formation of austenite islands at prior austenite grain boundaries can also prevent temper embrittlement.

c) It is necessary to make the austenite islands more stable even at temperatures as low as –196°C by adding appropriate alloying elements.

Based on these results, a systematic study has been carried out on the effect of alloying elements on the low-temperature toughness of nickel-containing steels. And, at last, the author and his colleagues have found that a steel containing as low as 6%Ni shows the same low-temperature toughness as the commercial 9%Ni steel when 1·0–1·7%Mn and 0·2% Mo are added[7,6]. Furthermore, a special heat treatment involving holding the steel at a temperature in the two-phase region where austenite and ferrite co-exist was developed in order to obtain finer microstructures.

Fig. 5 shows the influence of manganese content and heat treatment on the Charpy impact value at –196°C of the steels. It is obvious that the steels have fairly good impact values even with conventional heat treatments, such as quenching and tempering. But the range of tempering temperatures giving good toughness is rather narrow and varies with minor changes in composition. Both steels containing between 1·1 and 1·7%Mn, however, showed excellent values, higher than 20 kgm/cm², when the special heat treatment was applied after conventional quenching and followed by a final temper[8,9]. Furthermore, the good toughness is obtained uniformly over a wide range of tempering temperatures.

Photo. 4 shows the microstructure of steels containing 6% Ni–1·7% Mn and heat treated by the two heat treatments

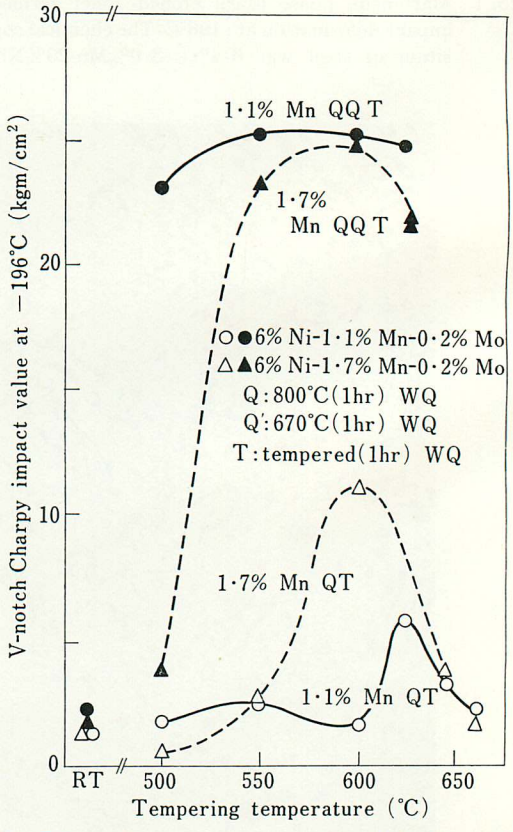

Fig. 5. Effect of manganese content and heat treatment on the Charpy impact value of 6%Ni steel at —196°C.

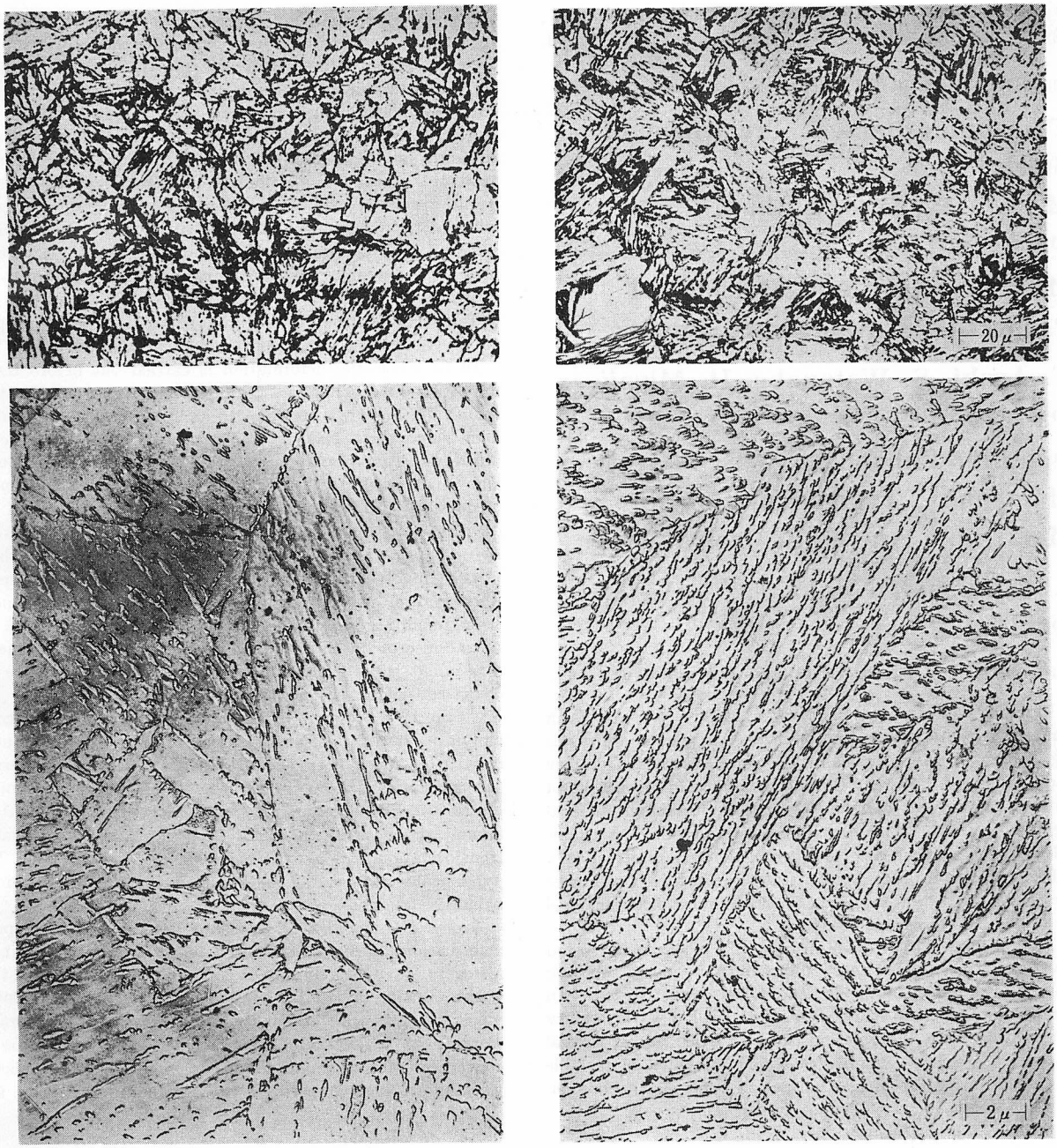

6Ni%-1·1%Mn-0·2%Mo
800°C 1hr WQ+
625°C 1hr WQ

6%Ni-1·1%Mn-0·2%Mo
800°C 1hr WQ +
670°C 1hr WQ +
600°C 1hr WQ

Photo. 4. Optical and electron micrographs of 6%Ni steel heat treated by conventional quench and temper (left) and by special heat treatment (right).

explained in Fig. 5[9]. That is, the structure on the left represents conventional heat treatment and that on the right the new heat treatment. It is clear that the microstructure on the right is finer than that on the left and corresponds to steel having excellent toughness.

3. Conclusions

Based on the results of investigations on 9%Ni steel, a new steel containing 6%Ni, 1·0–1·7%Mn and 0·2%Mo with good toughness as high as 20 kgm/cm² at –196°C was developed.

Furthermore, a new heat treatment involving heating in the two-phase region followed by quenching has been developed. The combination of this heat treatment with conventional quenching or normalizing gives excellent low-temperature toughness as low as –196°C for tempered nickel-containing steels.

1) M. Krön et al.: Mém. Sci. Rev. Mét., **58** (1961), p. 901
2) S. Nagashima et al.: Document No. IX–511–66, X–373–66, Tech. Report, IIW (1966)
3) T. Ōoka et al.: Journal Inst. Metals, Japan, **30** (1966) p. 442
4) H. Sakurai et al.: ibid, **33** (1969), p. 856
5) K. Segawa et al.: Tetsu-to-Hagané, **49** (1963), No. 6, p. 914
6) K. Aoki et al.: Netsushori (Heat Treatment, Japan) **7** (1967), No. 4, p. 211

7) S. Nagashima et al.: To be published elsewhere
8) S. Yano et al.: Tetsu-to-Hagané, **57** (1971), No. 4, p. 199
9) S. Yano et al.: To be published elsewhere

Thermomechanical Treatment of Steels:

M. J. May, D. J. Latham

(pp. 157-169)

Microstructure and Mechanical Properties of Ausformed Steels:

T. Araki, S. Watanabe, H. Miyaji

(pp. 171-181)

Ductility Enhanced by Martensitic Transformation in Metastable Austenitic Iron Alloys:

I. Tamura, T. Maki

(pp. 183-193)

Rapporteur T. Araki (Tokyo University).

It is my honor to comment on these three fine papers in connection with thermomechanical treatment, which is highlighted in this symposium "Toward Improved Ductility and Toughness". For attaining a balanced improvement of both strength and toughness of steel, thermomechanical treatment (TMT), which combines plastic working (mechanical process) with heat treatment (thermal process) is a definitely hopeful process. It is thought that TMT processes are indispensable in obtaining a 350 kg/mm² strength level in bulk steel materials.

Fig. 1 shows TTT diagrams on which various thermal processes are described in combination with plastic working (mechanical processing is indicated by zigzag curves). In the case of low-alloy steels with relatively low hardenability (Fig. 1 a)), plastic deformation can be carried out at several thermal stages, for example, of stable austenite, metastable austenite during the incubation period before ferrite precipitation, or accompanying decomposition of the austenite. In general, the hot-deformed austenite should be rapidly cooled to give a refined structure. In the case of high-alloy and hardenable steels, particularly those containing chromium, molybdenum and tungsten (Fig. 1 b)), there are two representative TMT's: i.e., plastic deformation of a stable austenite at high temperatures and that of metastable austenite in the "bay" between the upper nose and the bainite nose of the TTT diagram, with both processes followed by quenching, usually to martensite. In addition, some processes are concerned with certain aging phenomena, including dynamic aging, tempering and also recovery processes.

Table 1 indicates a classification of TMT of steel in respect to the time of transformation and deformation.

In Group I, the deformation is carried out before transformation on cooling so the lowest working temperature should be higher than the Md point. *A* is the so-called high-temperature TMT (HTMT), including ausforging, semi-hot working and also "controlled rolling and cooling" of lean-alloy high-tensile steels. In these cases, some improvement of ductility and toughness of the steel by refinement of the quenched or rapidly cooled structure is of primary interest. *B* is the so-called low-temperature TMT (LTMT), which usually involves quenching of deformed metastable austenite, known as "ausforming". In this case, pronounced strengthening is obtained and generally is accompanied by no sacrifice of ductility and toughness. This fact is due to a peculiar subcell structure of the final martensite as discussed in the second paper.

Group II represents the case of plastic working accompanying transformation, where *C* 1 is strain-induced martensite and *C* 2 is accelerated transformation of ferrite accompanying carbide precipitation. Isoforming involves plastic working of unstable austenite at a temperature around the nose of the TTT diagram to give accelerated transformation and a dynamic-recovery phenomenon. The dynamically recovered cell structures obtained result in a balanced toughness-to-strength ratio.

Group III includes *D*, accelerated maraging after prior deformation; *E*, dynamic strain aging of interstitials (carbon, nitrogen) at relatively low temperatures (low-temperature warm working or E.T.D., etc.) giving rise to an enhanced yield strength with some loss of ductility; and *F*, warm working at higher temperatures. This last *F* process is concerned with dynamic recovery of martensite by plastic working during tempering, which, according to the first

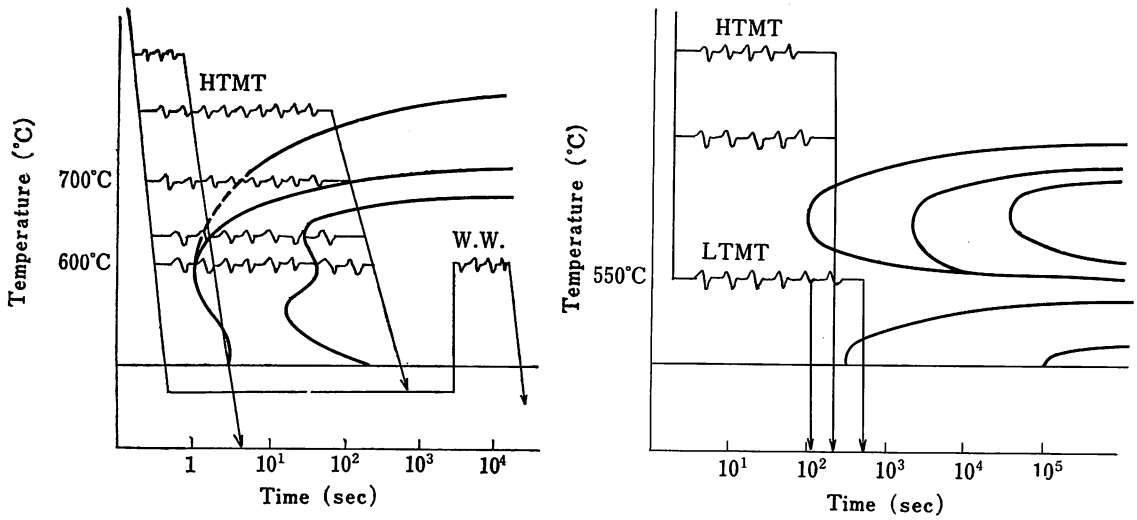

a) Steel with low hardenability.

b) Steel with high hardenability.

Fig. 1. Some TMT curves superimposed on TTT diagrams.

Table 1. Thermomechanical treatments of steel.

Classification of TMT		Nomenclature
I Deformation before transformation T>Md	A,—of stable γ	HTMT
	1.—to M (and/or B) 2.—to F+P (and/or B)	Ausforging (controlled rolling)
	B,—of metastable γ	LTMT (hot-cold working)
	1.—to M (and/or B)	Ausforming (Ausroll temper)
II Deformation accompanying transformation *	C,—of less stable γ	(Strain-induced transformation)
	1.—to M	Zeroll (cold working of γ)
	2.—to F+P	Isoforming (dynamic recovery)
III Deformation and aging	D,—of M (carbon-free)	Marforming (dynamic strain aging) (dynamic recovery)
	E,—of transformed structure	Warmworking
	1.—of M, TM 2.—of F+P, B etc.	E. T. D. etc.
	F,—of M	Warmworking at higher temperatures (dynamic recovery)

* Relevant phenomena: TRIP, etc.

paper, results in a fully recovered cell structure, quite similar to that of isoformed structures, and, therefore, in an improvement in strength and toughness of low-alloy and low-hardenability steels.

A relevant phenomenon of Group II is superplasticity by strain-induced martensitic transformation of steel, which is called TRIP (transformation-induced plasticity). Hopefully; this can be utilized to obtain a high-ductility very strong steel by applying LTMT etc. to a duplex structure of metastable austenite and martensite.

I. Kozasu (Nippon Kokan K. K., Technical Research Center).

The writer would like to point out that as strong crystallographic textures also exist in control-rolled steels as in steels processed by TMT as reported by Prof. Araki and his coworkers. Fig. 1 is such an example where a commercial low-alloy steel was experimentally control-rolled and quenched directly after rolling[1]. Fig. 2 is another example of a plain carbon-silicon-manganese steel, which was strongly rolled in low-temperature range of metastable austenite[2]. They

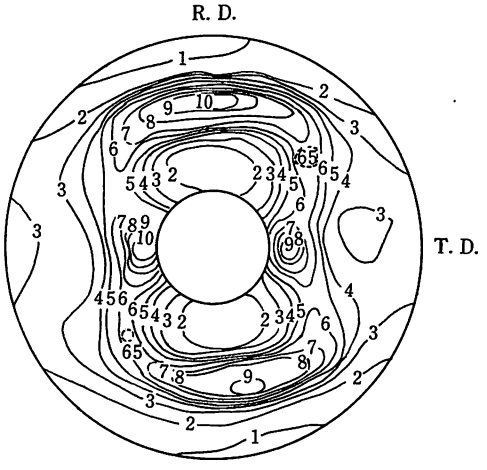

Fig. 1. (200) pole figure of 0·17%C-0·9%Mn-0·95%Cr-0·34%Mo-0·065%Ti steel processed by controlled rolling followed by direct quenching.

are similar in nature to the texture reported by Mr. Terazawa et al. Our general experience is that for such cases there generally exists a difference in the fracture-appearance transition temperature of impact tests in the longitudinal and transverse directions to rolling. FATT in the transverse direction is generally inferior to that in the longitudinal direction. In the examples cited above, 50% FATT of the Charpy V-notch test in the transverse direction was 20°C higher compared to that in the transverse direction. The crystallographic texture implies a preferred orientation of the (100) cleavage plane of ferrite. This is believed to be responsible to some extent for this difference of FATT although the effects of mechanical and crystallographic textures can not be separated out distinctly.

1) H. Kubota, I. Kozasu and T. Shimizu: J. Japan Inst. Metals, **32** (1968), p. 1074–1078
2) I. Kozasu : to be published

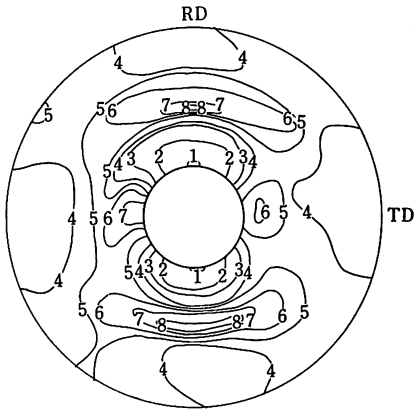

Fig. 2. (200) pole figure of control-rolled and air-cooled 0·18%C-0·44%Si-1·36%Mn steel.

Ductility of Age-Hardenable Martensitic Iron Alloys:

M. Tanaka, J. Yamamoto

(pp. 195-206)

Y. Imai (Tohoku University).

In Fig. 14, the specimen containing 0·1%C differs from the specimen containing 0·03%C in that it shows no decrease in elongation and reduction of area even at maximum hardness and tensile strength. Please explain the reason for this difference.

Author's Response (M. Tanaka).

The alloy in Fig. 14 containing 0·1%C has a similar chemical composition to steel B in Table 2. Table 2 shows that the volume fraction of the austenite was determined as 5–9 vol% in the high-toughness and high-strength states of both steels A and B. It seems that the small amounts of austenite dispersed in the age-hardened martensitic matrix may play an effective role in releasing the stress concentration within the hardened matrix and in impeding the initiation and propagation of microcracks.

高速度工具鋼の靱性におよぼす一次炭化物の影響

清水 欣吾

(pp. 207-237)

古沢 浩一（名古屋工業大学）

高速度鋼の機械的性質や，工具としての耐久力を左右する最大の因子は一次炭化物の形，大きさ，分布であると言っても良い程，それは重大な問題である．本題目の研究については多くの人達が研究してきたので大体のことは，すでに分っていることである．本論文の内容を見ても特に目新しいことはほとんど見当らない．しかし，一定の研究者が，新しい機器を含めた広汎な手段を用いて，これ程組織立った研究をしたのは初めてのことで，この点に関し深い敬意を表したい．またこの点について本論文の価値を高く評価したい．

（質問）試料は鋼塊形状，分塊，圧延条件を適当に組合せて製造したとあるが，この点について具体的に説明して下さい．また，高速度鋼を 1200° で焼入した状態におけるオーステナイト粒度は試料によってかなり異なるが，この場合のオーステナイト粒度を左右する因子にはどのようなものがあるのですか．

出口喜勇爾（新日本製鉄株式会社技術開発部）

この報告においては，靱性におよぼす一次炭化物の影響を高速度工具鋼の硬度約 HRC 65～66 の状態において実験し考察しているが，下記2項目の理由により，硬度がこれよりもさらに低い場合においても，靱性におよぼす一次炭化物の影響は同様な傾向にあると考えてよいかどうか？

①M2 は切削工具として使用するよりも，少しく硬度を低めて（例えば underhardening や焼戻温度の control を行なって）型として使用する場合において，衝撃応力に対する靱性の検討が実用上重要問題となってくるから．

②高速度工具鋼のごとき硬度高く脆い鋼のわずかな靱性の差異を確認する試験法に関しては，従来各種の研究が行なわれているが，その最も適当なる方法の1つとして衝撃的ねじり試験法があげられている．いま M2 につき静的ねじり仕事量と衝撃的ねじり仕事量との関係を試験した結果の一例を示せば Fig. 1（以前日特鋼にて試験）のごとくである．これによれば，2次硬化の前後における焼戻温度の影響（従って硬度の影響）に関し，静的ねじり仕事量によって表示される靱性においては大差なくとも，衝撃的ねじり仕事量によって表示される靱性においては，特に最高硬度よりもむしろ少しく硬度の低い範囲において，影響のあることが明瞭にうかがわれるから．

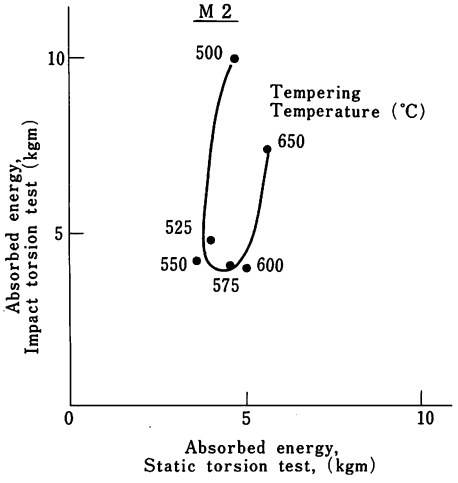

Fig. 1. Results of static and impact torsion tests on M2 test pieces, tempered at various temperatures.

著者回答

1. 本研究は同一化学成分で一次炭化物状態の異なる高速度鋼の性質を論じたもので，その試料製造法は本研究論文の範囲外に属するものと考えています．また本論文の場合，試料作製は研究室的でなく，生産工程を変化させた現場製品の中から抽出したものであり，その製造法の詳細は企業機密に属し，残念ながら公表を許されておりません．

製造因子としては，鋼塊条件3種類，鋼塊から分塊に到る熱的条件4種類，分塊加熱条件3種類，圧延加熱条件2種類を適宜組合わせ，合計 40 種類の約 30 mm φ 棒鋼のミクロ組織を検討し，目的の一次炭化物状態に近いものを6種類選んで実験に供したものであります．それ故，6種類とも製造法は異なり，また多数の因子が交錯しています．

2. オーステナイト結晶粒度は本研究のように同一化学成分においては，一次炭化物のサイズと分布状態によって定まり，さらに同一鍛造比の場合は，主として一次炭化物のサイズにより定まると考えられます。本文 Table 5 の Average area of carbide と Table 7 の Austenitic grain size はよい相関を示しています．

御指摘のごとく，AISI・M2 は切削工具以外に塑性加工工具としても種々使用されている．この場合は，本研究のような高硬度においてでなく，使用条件に応じて HRC 58～63 程度の適当な硬さが選ばれ，underhardening 処理の採用，焼もどし温度の調節が行なわれる．このような場合，いかなる熱処理条件が適当かは一概に定められない．それは靱性と同時に耐摩耗性，必要とする降伏強さなどが使用条件により夫々異なってくるからである．しかしながら，適当な熱処理条件が選定された場合，一次炭化物がどのような作用を及ぼすかについては，本研究の結論ないしは考え方を適用できるものと考えられる．上記低硬度における一次炭化物の影響を考察すると次の通りである．

硬さが低下することは matrix の塑性変形能を増大し，クラックの伝播エネルギーを大にする．しかし，本研究で述べた炭化物の亀裂，剝離に対する抵抗は与えない．すなわち，同一硬さで比較した場合，一次炭化物サイズ，偏析の靱性に及ぼす効果は硬さの絶対値が低いからといって，決して小さくはならない．弾性限が低下すれば塑性変形による転位の炭化物周辺における pile up が進行し，micro-crack を発生しやすくなり（焼なまし材の炭化物の micro-crack が多い事実からも想像される），かえって一次炭化物の影響は大きくなると考えられる．

次に，靱性試験法として衝撃捩り試験が靱性の僅かな差を見出す方法として有利であることを述べておられるが，筆者は衝撃捩りの経験がないので適格に回答することは出来ない．Fig. 1（質疑文中）の結果は静的捩りと衝撃捩りの結果に相関がないことを示し，静的捩りの値の微小の差が衝撃捩りで拡大されて現われることを示しているとは考えられない．むしろ，525

～600°C の範囲では，衝撃捩りでは有意差が出ず，静的捩りでは有意差があると思われる．しかし，硬さが低く，塑性変形能がかなり大きい場合の靱性は衝撃捩りの方が差が大きく現われると解釈すべきではなかろうか．

この現象の差は歪速度の差に起因するもので，靱性に対しどちらが正しい値を示すかと考えるべきものではないと思う．筆者の私見を述べれば，次の通りである．

歪速度が大きい場合は，初期クラックの発生と同時に破壊が進行し，吸収エネルギーは主としてクラックの伝播過程に支配される．それ故，一次炭化物に差がない場合は，硬さが低く，塑性変形能が大きいとき衝撃捩りと静的捩りの差が大きく現われる．歪速度が小さい場合，破壊は次の3工程，すなわち初期クラックの発生（炭化物亀裂）．それがある臨界サイズに成長する過程，最終破断に到る過程にわかれ，前2者の影響が大きいと考えられる．非常に高硬度材の場合は前2工程の差が靱性を決定すると思われ，静的捩りのごとく歪速度の小さい方が525～600°C 焼もどし状態の差を正確に表わすと思われる．また歪速度が小なるときは，試験片各部にクラックの起点を生じているため，第3の過程による吸収エネルギーの増大の割合は歪速度の大なる場合ほど大きくないと考えられる．

以上は筆者の推論であり，確証はないが，今後，機会を得て検討したいと思っている．

日本鉄鋼協会
THE IRON AND STEEL INSTITUTE OF JAPAN

日本金属学会
THE JAPAN INSTITUTE OF METALS

CLIMAX MOLYBDENUM DEVELOPMENT COMPANY (JAPAN) LTD.